

Prashant M. Pawar
Babruvahan P. Ronge
R. Balasubramaniam
Sridevi Seshabhatar *Editors*

Techno-Societal 2016

Proceedings of the International
Conference on Advanced Technologies for
Societal Applications

Techno-Societal 2016

Prashant M. Pawar · Babruvahan P. Ronge
R. Balasubramaniam · Sridevi Seshabhatar
Editors

Techno-Societal 2016

Proceedings of the International Conference
on Advanced Technologies for Societal
Applications

Editors

Prashant M. Pawar
SVERI's College of Engineering
Pandharpur, Maharashtra
India

R. Balasubramaniam
Bhabha Atomic Research Centre
Mumbai
India

Babruvahan P. Ronge
SVERI's College of Engineering
Pandharpur, Maharashtra
India

Sridevi Seshabhatter
SVERI's College of Engineering
Pandharpur, Maharashtra
India

ISBN 978-3-319-53555-5

ISBN 978-3-319-53556-2 (eBook)

DOI 10.1007/978-3-319-53556-2

Library of Congress Control Number: 2017933442

© Springer International Publishing AG 2018

This work is subject to copyright. All rights are reserved by the Publisher, whether the whole or part of the material is concerned, specifically the rights of translation, reprinting, reuse of illustrations, recitation, broadcasting, reproduction on microfilms or in any other physical way, and transmission or information storage and retrieval, electronic adaptation, computer software, or by similar or dissimilar methodology now known or hereafter developed.

The use of general descriptive names, registered names, trademarks, service marks, etc. in this publication does not imply, even in the absence of a specific statement, that such names are exempt from the relevant protective laws and regulations and therefore free for general use.

The publisher, the authors and the editors are safe to assume that the advice and information in this book are believed to be true and accurate at the date of publication. Neither the publisher nor the authors or the editors give a warranty, express or implied, with respect to the material contained herein or for any errors or omissions that may have been made. The publisher remains neutral with regard to jurisdictional claims in published maps and institutional affiliations.

Printed on acid-free paper

This Springer imprint is published by Springer Nature

The registered company is Springer International Publishing AG

The registered company address is: Gewerbestrasse 11, 6330 Cham, Switzerland

Preface

Technology has a remarkable influence on the society in general and on human life in particular. Society has a cyclical and mutual dependence on technology. Technology has created many avenues and opportunities that were hitherto unimaginable. Since it has become a part of people's living rooms, the needs and demands for a safe technology has been on the rise. Improper use of technology has raised many flags of concern over the environment and overall well-being of the society. Technology is needed for activities such as communication, travel, trade and commerce, education, medicine, etc. Technology has begun to play a vital role in simplifying the way things are done. Thus, it is high time to create technologies that are safe and relevant to the societal needs. We have come of age and time to tackle some of society's most compelling issues pronto. It is no longer adequate to work in cells, taking on small sections of the problem at a time. Rather, it is imperative to pool knowledge and resources around the world to create opportunity, empowered by technology, for the society to improve life.

This book is a compendium of selected best papers presented at Techno-Societal: 2016 organized by SVERI's College of Engineering, Pandharpur, India on 20–21 December 2016.

Techno-Societal: 2016 is a first international conference aimed at creating a growing sense of responsibility to solve the challenges of society especially through technology. More than 400 authors submitted their work to the conference. The conference editorial committee decided the acceptance of the submitted papers, with contribution of experts from various fields through double peer review process. A total of 193 full papers of original work were selected. During the conference about 20 keynote speaker sessions were arranged in order to give direction and contribute to specific research areas.

The conference offered various sessions under its name. For the purpose of this book, 108 selected papers and 6 papers from keynote speakers are divided into seven topical areas, viz. 1. Deployable Societal Technologies 2. Sensor-, Image- and Data-driven Societal Technologies 3. Mechatronics, Micro–Nano Related for

Bio and Societal Applications 4. Lab-Level Advanced Societal Technologies 5. Manufacturing and Fabrication Processes for Societal Applications 6. Infrastructure Developments for Societal Applications 7. ICT-based Societal Technologies.

Pandharpur, India
Pandharpur, India
Mumbai, India
Pandharpur, India

Prashant M. Pawar
Babruvahan P. Ronge
R. Balasubramaniam
Sridevi Seshabhatter

Contents

Part I Deployable Societal Technologies

Application of Nuclear Spin-Offs for Societal Development	3
Shrikrishna Gupta and Smita S. Mule	
Role of BARC Technologies in Agriculture for Benefit of Farming Community in India	11
S.T. Mehetre and S. Chattopadhyay	
Use of Photochemical Machining Technology for Producing Metal Artwork	17
N.D. Misal, M. Sadaiah, V.K. Suri and P.M. Pawar	
RuTAG IIT Bombay Floating Fish Cages for Livelihood Opportunities for Tribals in Dimbhe Area	27
Rupali S. Khanolkar, Anand B. Rao and Siddhartha Ghosh	
Evaluation of Multiple Hydrometeorological Factors for Prioritization of Water Stress Areas in the Upper Yerala River Basin, Satara, Maharashtra, India	37
Mustaq Shaikh, Milind Herlekar and Bhavana Umrikar	
Design of Improved Biomass Cook Stove for Domestic Utility	53
S.S. Saiyyadjilani, P.G. Tewari, Rakesh Tapaskar, Ajitkumar P. Madival, Mahesh Gorawar and P.P. Revankar	
Computational and Experimental Investigations on Small Horizontal Axis Wind Turbine for Household Applications	65
Gurushant Koulagi, R.S. Hosmath, Ajitkumar Madival and P.P. Revankar	
Computational and Experimental Studies on Effect of Artificial Roughness on Performance of Solar Air Heater	75
Vishwanath Kardi, A.P. Madival, M.B. Gorwar and P.P. Revankar	

Design and Development of Novel Mini Wind Power Turbine Set	85
B. Magade Pramod and P. Chavan Shirrang	
Treadle Pump Operation with Rotary Motion	93
Pawan Kumar Tiwari, S.N. Singh, Subir Kumar Saha and Davinder Pal Singh	
Biofuels—Sustainable Alternative to Petroleum (Fossil Fuels) and New Revenue for Farmers	101
Tatyaso S. Kadam, Mohit B. Zite and Akshay V. Walanj	
Microcontroller Based Automatic Drip Irrigation System	109
Rahul G. Ghodake and Altaf O. Mulani	
Sustainable Raft Based Hydroponic System for Growing Spinach and Coriander.	117
Smital Kulkarni, Plapallil Steve Abraham, Nimain Mohanty, Nitin N. Kadam and Mansee Thakur	
Effect of Change in Vacuum Pressure on the Performance of Solar Dryers	127
Nikhil S. Mane, O.N. Thigale, A.M. Patil and N.V. Hargude	
Wireless Healthcare Monitoring System	135
Dhiraj D. Kadam, Shailaja C. Patil and D.S. Bormane	
Optimization of Process Parameters for Shutter Type Vertical Axis Wind Turbine	147
Vidya R. Muttagi, Sandeep S. Wangikar, Supriya S. Bhosale and Shrikrushna B. Bhosale	
An Anthropometric Data of Cycle Rickshaw Operators to Approach Ergonomics in Cycle Rickshaw Design	153
M.S. Gorde and A.B. Borade	
Analysis of Thermal Performance of Serpentine Tube in Tube Heat Exchanger.	169
Gayakwad Shiwaji, Nitnaware Pravin and Tapobrata Dey	
Experimental Performance Evaluation on S.I. Engine with Gasoline and Liquefied Petroleum Gas as Fuel	183
Puneet Bansal, Ankit Pandya and Ankit Ahuja	
A Review on the Green Supply Chain Management (GSCM) Practices, Implementation and Study of Different Framework to Get the Area of Research in GSCM	193
Prashant S. Bajaj, Satish V. Bansod and Izzhak D. Paul	

Design and Performance Evaluation of Low-Cost, Innovative, Efficient Small-Scale Wind Power Generation for Rural Community of India 201
 Pradip D. Haridas and Avinash K. Parkhe

Design Modification of Biogas Digester to Avoid Scum Formation at the Surface 215
 Vidyarani S. Kshirsagar and Prashant M. Pawar

Part II Sensor, Image and Data Driven Societal Technologies

Social Influence as a Parameter to Prioritize Social Problems. 231
 Shreyank N Gowda

An Accident Detection System (ADS) for the Mumbai-Pune Expressway Using Vehicular Communication. 239
 Saurabh Patil and Lata Ragha

Data Mining Algorithms for Improving the Efficiency of Governance in Dynamic Social Systems: Case Study of Indian Caste and Tribe Reservations 249
 Rhythima Shinde, Bramka Arga Jafino, Paraskevi Kokosia and Jan van den Berg

An Approach for PCA and GLCM Based MRI Image Classification 265
 Sheetal S. Shirke, Jyoti A. Kendule and Samata G. Vyawahare

Urban Tree Canopy Detection Using Object-Based Image Analysis Approach for High-Resolution Satellite Imagery 275
 Sujata R. Kadu, Balaji G. Hogade and Imdad Rizvi

Delamination Study of Sandwich Beam Coupled with Piezoelectric Actuator Using Cohesive Surface Behavior. 283
 K.R. Jagtap, H.H. Nawale and Sajal Roy

Development of Methodology for Transforming CT Images Indicating Location and Size of Lung Cancer Nodule 293
 Rajani R. Mhetre, Pooja P. Kawathekar, Sneha S. Kadam and Megha B. Gore

A Driver Assistance System Using ARM Processor for Lane and Obstacle Detection 303
 Sandip N. Pawar and S.M. Mukane

Multimodel PID and RST Controller to Control CSTR Process Using Gain Scheduling Technique 315
 D.A. Tamboli and R.H. Chile

Silkworm Eggs Counting System Using Image Processing Algorithm	327
Sanaha S. Pathan and Avinash D. Harale	
Compression of Medical Images Using Lifting Scheme Based Bi-orthogonal CDF Wavelet Coupled with Modified Set Partitioning in Hierarchical Trees (SPIHT) Algorithm	337
Surekha S. Koshti and Jyoti A. Kendule	
Various Traditional and Nature Inspired Approaches Used in Image Preprocessing	345
Sarika Deokate and Nilesh Uke	
FPGA Based Adaptive Filter for Removal of Electromyogram Noise from Electrocardiogram Signal	353
A.M. Kasture, S.S. Sathe, M.A. Deshmukh and A.A. Jadhav	
Feature Extraction of Surface EMG Using Wavelet Transform for Identification of Motor Neuron Disorder.	363
Archana Bhaskarrao Sonone and Suvarna S. Chorage	
Early Diagnosis of Diabetes by Retinopathy	375
Sailee M. Shendkar and Rajashri R. Itkarkar	
Optimal Location of TCSC Using Evolutionary Optimization Techniques.	389
Rahul Agrawal, S.K. Bharadwaj, Anil Bodhe, D.P. Kothari and Bhupendra Deshmukh	
MATLAB Simulation Analysis for Removing Artifacts from EEG Signals Using Adaptive Algorithms	399
Pallavi Jadhav, Dipalie Pujari, Papiya Biswas and Mohua Biswas	
Part III Mechatronics, Micro-Nano Related for Bio and Societal Applications	
Effective Sensing Mechanisms and Techniques for Detection of <i>E. coli</i> Bacteria in Potable Water	411
Saakshi Dhanekar	
Smart Materials for Biosensing Applications	421
Kuldeep Mahato, Anupriya Baranwal, Ananya Srivastava, Pawan Kumar Maurya and Pranjal Chandra	
Comparative Study to Improve Antenna Parameters of Multilayer Microstrip Patch Antenna	433
Mr. A.K. Rathod, Mr. R.G. Sonkamble, Mr. R.R. Sharanabasappa, Mr. M.S. Mathpati and Md. Bhakar	

Investigation of Mechanical Behavior of Industry Waste and Al₂O₃ Reinforced Aluminium Matrix Composites by Powder Metallurgy Technique	447
Imranhusen N. Pirjade, S.G. Kulkarni and S.S. Kulkarni	
Phase Sensitive Detector: Fabrication, Processing, and Applications	457
P.A. Ghadage, U.R. Ghodake and S.S. Suryavanshi	
Microbial Synthesis of Silver Nanoparticles Using <i>Aspergillus flavus</i> and Their Characterization	463
Hemant Bhangale, K.M. Sarode, A.M. Patil and D.R. Patil	
Shape Optimization of Microfluidic Pump Using Fluid-Structure Interaction Approach	471
P.M. Pawar, R.R. Gidde and B.P. Ronge	
Fabrication and Characterizations of Cu/CdS_{0.8}Te_{0.2} Thin Film Schottky Junction Grown by Thermal Evaporation Technique	479
M.S. Kale and D.S. Bhavsar	
Kinetic and Thermodynamic Study of Mixed Crystals of Cadmium-Calcium Levo-Tartrate Dihydrate Grown in Silica Gel	487
N.S. Patil	
Numerical Study on Microchannel Heat Sink with Asymmetric Leaf Pattern	495
V.P. Gaikwad, S.D. Ghogare and S.S. Mohite	
Experimental Study of Thermal Energy Storage System Using Nanofluid	509
K. Krishna Reddy, R. Meenakshi Reddy and B. Durga Prasad	
An Approach to Harness Energy by SnO₂ Thin Film Electrode by Thermal Evaporation	515
S.M. Ingole, Y.H. Navale, D.K. Bandgar, I.A. Dhole, M.A. Chougule, P.S. Kulkarni and V.B. Patil	
Efficient Electrodeposited Nickel Oxide Thin Films for Supercapacitor Electrode	521
I.A. Dhole, Y.H. Navale, S.M. Ingole, R.N. Mulik, Y.M. Jadhav, C.S. Pawar and V.B. Patil	
Effect of Waiting Time on Opto-electronic Properties of Antimony Doped Tin Oxide Thin Films for Transparent Conducting Oxide Applications	527
A.R. Babar, C.S. Pawar and B.R. Karche	

Nanoflakes MnO₂ Thin Film as a Supercapacitor Electrode	531
P.M. Kharade, S.S. Mane, S.D. Chavan, S.B. Kulkarni and D.J. Salunkhe	
Experimental Studies on Curvilinear Laser Bending of Thin Sheets	539
Ravi Kant, Parag M. Bhuyan and Shrikrishna N. Joshi	
A Comparative Study on Mechanical and Tribological Properties of Epoxy Composites Filled with Nano-ZrO₂ and Nano-Al₂O₃ Fillers	549
R.V. Kurahatti, A.O. Surendranathan, A.V. Ramesh Kumar and V. Auradi	
Part IV Lab-Level Advanced Societal Technologies	
Synthesis of TiO₂ Nanofibers for Solar Cells and Their Analysis Using Statistical Tool—ANOVA	561
Sunil Kadam, Prerana Ghatmale, Puneet Garg, P.V. Jadhav, Sachin Shendokar and Sachin Chavan	
Development of Experimental Setup for Measurement of Stored Hydrogen in Solids by Volumetric Method	569
Rohan Kalamkar, Aneesh Gangal and Vivek Yakkundi	
Optimization of Biodiesel Synthesis from Karanja Oil Using Heterogeneous Catalyst by Transesterification Process	579
Satish A. Patil and R.R. Arakerimath	
Parametric Studies on Thermo-electric Power Generation Using Micro Combustor	589
B. Aravind and Sudarshan Kumar	
Validation of in House PCR Using IS6110 for Detection of <i>M. tuberculosis</i> and Its Comparison with ZN Staining, Cultures and RT PCR Kit Methods	599
Girish Pai, Mansee Thakur, Harapriya Kar and D.S. Joshi	
Novel Method for Fabrication and Characterization Porous Structure Using Rapid Prototyping and Thermal Gradient Method	611
Shreepad Sarange and Ravi M. Warkhedkar	
Role of Gene Xpert in Early Diagnosis and Treatment of Tuberculosis	623
Harapriya Kar, Samir Pachpute, Poonam Patil, Yogesh Patil and A.D. Urhekar	

Synthesis and Characterization of MoS₂-Graphene Nanocomposite	629
K.M. Sarode, S.G. Bachhav, U.D. Patil and D.R. Patil	
Heat Transfer Intensification with Different Width Swirl Generator	635
Sarang S. Hole, Hanumant B. Narute and Vishal S. Jagadale	
Synthesis and Characterization of ZnO Nanorod Array on FTO Glass by Using Hydrothermal Method	645
H.P. Suryawanshi, S.G. Bachhav and D.R. Patil	
Design and In-Vitro Evaluation of Nicorindil Biphasic Drug Delivery System for Angina Pectoris	651
H.B. Bansode, O.S. Shende, P.B. Gurav and R.G. Kulkarni	
SILAR Synthesis and Cyclic Voltammetric Study of PPy-Cu(OH)₂ Composite Flexible Electrodes for Supercapacitors	659
Amarsingh V. Thakur, Savita D. Sonawane, Pritesh C. Chavan, Dheeraj C. Muttin and Balkrishna J. Lokhande	
Root Canal Filling Process Enhancement in Simulated Dental Blocks Using a Novel Device	667
Ratnakar Ghorpade, Kalyana Sundaram and Vivek Hegde	
Part V Manufacturing and Fabrication Processes for Societal Applications	
Analysis of Surface Integrity and Dimensional Accuracy During Thin-Wall Machining	681
Gururaj Bolar, Argha Das and Shrikrishna N. Joshi	
Wear Behaviour of D-Gun Sprayed Coatings on Ductile Cast Iron	689
Amardeep Singh Kang and Gurmeet Singh Cheema	
Experimental Analysis of Different Compositions of Carbon Fiber/Epoxy Composite and Its Application in Leaf Spring	699
L.B. Raut and A.R. Katu	
Development of a Friction Welded Bimetallic Joints Between Titanium and 304 Austenitic Stainless Steel	709
Muralimohan Cheepu, V. Muthupandi, B. Srinivas and K. Sivaprasad	
Developing an Empirical Relationship to Predict Tensile Strength and Micro Hardness of Friction Stir Welded Aluminium Alloy Joints	719
Gurmeet Singh Cheema and Amardeep Singh Kang	

New Design Approach of Helical Coil Spring for Longitudinal and Translational Invariance by Using Finite Element Analysis	729
Sagar Namdev Khurd, Prasad P. Kulkarni and S.D. Katekar	
Material Removal Rate and Surface Roughness Optimization in WEDM on Tool Steel EN-31 Using Taguchi Approach	739
Mayur N. Patel, H.G. Shah and Haresh Ghoniya	
Automatic Gear Change Mechanism for Two-Wheeler Automobiles	751
Aditya A. Mairal and Akash B. Pandey	
Analysis of Water Lubricated Bearing with Different Features to Improve the Performance: Green Tribology	761
Anil B. Shinde, Prashant M. Pawar, Sunil Gaikwad, Pakija A. Shaikh and Yashpal Khedkar	
Design and Construction of Briefcase Type Portable Solar Dryer	771
S.S. Gaikwad, Anil B. Shinde, A.A. Mote and P.S. Kachare	
Crashworthiness Improvement for Rollover of Bus Using FEA	779
Vivekanand Phadatare, Pravin Hujare and Chandrakant Inamdar	
Optimization of P-GMAW Welding Parameters Using Taguchi Technique for SS304L Pipes	787
Rudreshi Addamani, H.V. Ravindra and C.S. Darshan	
Impact Analysis and Topology Optimization of Pultruded Automotive Bumper	799
Rohit R. Ghadge and S. Prakash	
Simulation of Micro-indentation Process of Black NiAl Coated Aluminum Substrate Using FEM	809
Vishal B. Bhagwat, Aparna G. Kadam and Dadasaheb Rupanwar	
Assembly Method of Pre Twisted Steam Turbine Blades	819
Dhanaji Chavan and Pravin Kachare	
Thermal Performance of Parabolic Dish Water Heater with Helical Coiled Receiver	833
Atul A. Sagade, Satish J. Aher and Narayani Sagade	
Application of MOORA Method for Friction Stir Welding Tool Material Selection	845
V.S. Gadakh, V.B. Shinde, N.S. Khemnar and A. Kumar	
Development of Prototype of Light Passenger Quarter Car for Improved Vehicle Ride Characteristics	855
Vijay R. Patil and Pradeep V. Jadhav	

Sheet Metal Piercing Punch Material Selection Using Complex Proportional Assessment Method	869
D.P. Hase and V.S. Gadakh	
Investigation of Thermal Performance of FRP Parabolic Trough Collector Using Different Receivers	879
Satish Aher, Atul Sagade and Narayani Sagade	
Investigation of Load Carrying Capacity for Steering System with Polymer Helical Rack and Pinion Gear	891
Yogesh Ashok Ingale, A.P. Kadam, Digvijay G. Bhosale and A.P. Bhosale	
Dry Sliding Wear Performance Optimization of MoS₂ Filled PTFE Composites Using Taguchi Approach	903
Prasad M. Patare and G.S. Lathkar	
Tribological Behavior of Al6061 Alloy Reinforced with Fly Ash Particles	915
D.A. Nayana, Mailareppa Marachakkanavar and Nagaraj Kantli	
A Study on Partial Automation of Lac Bangle Manufacturing in Pandharpur	925
Rohini R. Bhosale and Nitin D. Misal	
Parametric Optimization for Photochemical Machining of Copper Using Grey Relational Method	933
Sandeep Sitaram Wangikar, Promod Kumar Patowari and Rahul Dev Misra	
Part VI Infrastructure Developments for Societal Applications	
Buried Pipelines Deformation Behavior in Different Soils Using Geofoam	947
A.S. Mane, Shubham Shete and Ankush Bhuse	
A Time Dependent Scour Around Circular Piers Under Unsteady Flow	957
Anandrao R. Deshmukh and Rajkumar V. Raikar	
Implementation of Methodology for Wastewater Treatment from Textile Industry	969
D.A. Kumbhar	
Improving Torsional Seismic Response of Plan Asymmetric Structures Using Energy Dissipating Devices	977
Ravindra S. Desai and Shrirang N. Tande	
Optimization of Cables in Cable Stayed Bridge	989
Anuja J. Sohani and Smita Patil	

Vibration Isolation of Single-Degree-Freedom System Using Permanent Magnets	1001
Supriya Choudhari and G.R. Patil	
Study on Behavior of Externally Bonded RC Beams Using Armid Fiber Sheets	1011
M.M. Deshmukh and M.M. Pawar	
Part VII ICT Based Societal Technologies	
Forecasting Monsoon Rainfall Over India Based on Global Climate Parameters.	1023
Vaishalee S. Khotlande and Satishkumar S. Kashid	
Augmented Reality in Higher Education Supported with Web 2.0: A Case Study in Chemistry Course.	1033
Trupti Satpute and Prakash Bansode	
Implementation of QoS Based Policer in Routers for Next Generation Network (NGN)	1043
Santosh D. Bhopale, S.V. Sankpal, D. Jayadevappa and Sharan Kumar	
Wireless Sensor Networks for Societal Applications.	1053
Jayashri Joshi and Neeta Kulkarni	
Topology-Hiding Multipath Routing Protocol: A Modified Approach for Wireless Network	1071
Akshay Suhas Phalke and Manohar S. Chaudhari	
A Cloud Computing Based WSNs for Agriculture Management.	1081
Gorakhnath U. Waghmode and Avinash D. Harale	
Analysis on an MHT Based Integrity Authentication Framework for Cloud Data Security	1089
R.S. Sajjan, Vijay Ghorpade and B.D. Arkas	
Historical Drought Analysis of Maharashtra State by Using SPI Index.	1097
Ajay Chavadekar and S.S. Kashid	
Statistical Downscaling of GCM Output for Generating Future Rainfall Scenarios Using SDSM for Upper Godavari Basin, Maharashtra	1105
S.S. Motegaonkar and S.S. Kashid	
Design of MIMO Antenna for WLAN and Wi-Max Application	1113
Vivek D. Kamble and Mandar R. Jadhav	

Secure Ration Dispensing System Using HAN and Geofencing Through Li-Fi. 1123
Aashish A. Gadgil, Apoorva S. Bendigeri, Diksha D. Halagi,
Gautam Prakash and Shivani A. Nadgouda

Enhanced Digital Image Watermarking in Combination with Encryption. 1133
Ashwini B. Babar, J.A. Kendule and S.M. Shinde

SNR Versus BER Performance and Effect of Changes in Hysteresis on Different Modes of IEEE 802.11a. 1141
Swapnita R. Dhabre

Part I
Deployable Societal Technologies

Application of Nuclear Spin-Offs for Societal Development

Concepts of AKRUTI—DAE ORC—CILLAGE

Shrikrishna Gupta and Smita S. Mule

Keywords Spin-offs · AKRUTI · DAE Out Reach Centre · Rural Techno-Preneurship

These spin-off technologies have been made available to industry for commercialisation through mechanisms of technology transfer on non-exclusive basis as developed at BARC. Also selected technologies are made available for Education Institutions/Trusts/Voluntary organisations/Big Companies for their Corporate Social Responsibility and even individuals for promotion of techno pruners in villages and create work opportunity to them by value addition in rural resources under AKRUTI Tech Pack scheme. BARC is thus connecting Villages based on Science and Technology work plan for large scale deployment of BARC/DAE technologies.

This paper describes development of Concept of AKRUTI, DAE Out Reach Centres and Cillage for inclusive growth of rural areas.

Bhabha Atomic Research Centre offers spin-offs technical know-how for transfer to interested parties. The technologies available for transfer are in the areas of Agriculture and Biosciences, Engineering, Water, Environment, Chemical, Radiation monitoring and Medical equipment.

Illustrative list of technologies found useful for Societal and Rural applications:

1. Soil Organic Carbon Detection Kit
2. Kitchen waste based Bio Gas Plant
3. Domestic Water Purifier Based on polysulfone Membrane
4. Fluoride Detection Kit
5. Chromium (VI) Detection Kit for water
6. Nanocomposite Ultrafiltration Membrane Device for Domestic Drinking Water Purification W.R.T. Arsenic, Iron and Microbial Contaminations
7. Solar Energy Driven Portable Domestic Brackish Water Reverse Osmosis (Bwro) Technology

S. Gupta · S.S. Mule (✉)

Bhabha Atomic Research Centre (BARC), Mumbai, India

e-mail: smule@barc.gov.in



Fig. 1 NPAs and spin-offs for societal and rural applications

8. Process for retaining pericarp colour and extending shelf life of litchi
9. Foldable Solar dryer
10. Vibro Thermal disinfestor
11. Hand held Tele-ECG Module
12. Peripheral pulse Analyser
13. Cobalt-60 Teletherapy machine
14. Digital Radiotherapy Simulator
15. Distress Alarm device-Nirbhaya
16. ... and more

In addition, BARC has developed new seeds through radiation induced mutation and carried out isotope hydrology techniques for rejuvenation of drying springs and identification of perennial source of groundwater in drought prone area (Fig. 1).

1 AKRUTI Programme [1, 2]

To derive nuclear technology enabled societal benefits, the Advanced Knowledge and *RURAL* Technology Implementation (AKRUTI) programme has been formulated and implemented in collaboration with many divisions of BARC, DAE

units, the Rajiv Gandhi Science & Technology Commission (RGSTC) of the Government of Maharashtra (GoM) and NGOs working on technically oriented activities in rural sector. The programme, more popularly known as AKRUTI programme, is promoted as part of DAE Societal Initiative.

Technologies deployed in this programme cover areas related to water, land improvement, agriculture, food processing and urban-rural waste processing for value addition.

2 Demonstration of AKRUTI

To demonstrate the concept of AKRUTI, 3 AKRUTI nodes in three villages were formed with financial assistance from RGSTC, Village resources such as Land, place, infrastructure and HR from villages, NGOs active in that region and Technologies and Technical guidance from BARC Scientists and engineers.

Three AKRUTI nodes set up in Maharashtra State (MS) in collaboration with three NGOs viz. CARD, PARIVARTAN and NIRMITEE were:

1. 'AKRUTI-NIRMITEE' by NIRMITEE at Uddhar, Dist. Raigad, MS
2. 'AKRUTI-PARIVARTAN' by PARIVARTAN at Chiplun, Dist. Ratnagiri, MS
3. 'AKRUTI-CARD' by Community Action for Rural Development Society (CARD), at Khirala village, Dist. Amravati, MS

Technologies deployed in various villages by NGOs, through village working groups under the guidance of BARC experts are: NISARGRUNA, Domestic Water Purifier, Soil Organic Carbon Detection Testing Kit, Foldable Solar Dryer, Vibro Thermal Disinfector and Isotope Hydrology for investigation of underground water resources. A Tissue Culture Laboratory for micropropagation of banana plants with field hardening facility and Fruit Processing Unit have also been set up (Fig. 2).

3 Observations

After studying Formation of AKRUTI and functioning of AKRUTI following two observations are to be noted:

1. Setting up of AKRUTI takes place in 3 steps:
 - (a) Establish technologies in Rural Areas
 - (b) Demonstrate and Facilitate villagers
 - (c) Fabricate, Assemble and deploy in the Fields and Expand
2. Working principles for functioning of AKRUTI are Work, Contribute and Earn.



Fig. 2 Photos of various activities at AKRUTI

4 Rural Techno-entrepreneurship [3]

After experimenting establishing AKRUTIs with the help of NGOs, BARC developed mechanism for providing BARC—AKRUTI technologies for deployment in villages through AKRUTI Tech Pack (ATP) which consists of 9 technologies presently. Any interested agency ready to set up facility in villages can take these technologies at concessional cost. All sections of society desirous to work in/for villages have got a chance by way of deployment of any one or all the technologies in villages. After deployment of taken technologies additionally two consultancies suitable to the region are offered without charges to ATP holder. Detail advertisement is available on BARC website: www.barc.gov.in/akruti-tp/index.html.

Presently BARC has signed 37 AKRUTI tech pack agreements for deployment of technologies in rural sector. The ATP parties include Companies, Engineering colleges, Woman Entrepreneurs, Trusts and Individuals.

AKRUTI Tech Pack is made of optional nine (9) technologies and two consultancy services as given below. License fee for the technologies varies from Rs. 2500/- to Rs. 25,000/-, consultancies are provided without charges to ATP holder (Table 1).

Table 1 Composition of AKRUTI tech pack

S. No.	Technology
1.	Nisargruna—Biogas plant based on biodegradable waste
2.	Soil Organic Carbon Detection & Testing Kit (SOCDTK)
3.	Vibro Thermal Disinfector (VTD)
4.	Foldable Solar Dryer (FSD)
5.	Process for retaining Pericarp Colour and extending shelf life of Litchi, novel process, wherein the fruits after treatment can be stored at low temperature up to 45 days
6.	Domestic Water Purifier (DWP)—a technology to get bacteria free clean drinking water without use of electricity
7.	Solar Energy driven Portable Domestic Brackish Water Reverse Osmosis (BWRO) technology
8.	Dip N Drink (DND) Membrane Pouch, technology to convert the biologically contaminated water into sterile solution for oral consumption, useful during flood, cyclones, tsunami, earthquakes, etc. in remote areas/villages
9.	Banana Tissue Culture (BTC) Technology for mass-production of commercially important banana varieties. This technology can also be used for conservation & multiplication to the desired scale, of several other locally important, elite, endangered and ornamental banana varieties

5 Consultancy

1. Preservation of Agri-Produce by Irradiation

For increasing the rural awareness and benefits of radiation processing, consultancy service for irradiation of agro produce once on trial basis for sample quantity without charges will be provided to ATP holders on separate request.

2. BARC New Seeds

For increasing the spread of new crop varieties developed by BARC, sample seeds shall be made available to ATP holder on separate request as per the suitability in his region.

6 DAE Out Reach Centre (DAE ORC) [4, 2]

With increasing number of ATP holders, need is felt to set up Training Institute for deployment of AKRUTI Tech Pack technologies in villages. A dedicated, trained work force needs to be created to speed up the growth of AKRUTI programme and support the growing network of AKRUTI nodes. To achieve this objective **Rural Human and Resource Development Facility (RHRDF)**, co-located with educational institute has been created under the MoU between BARC and Shri Vithal Education & Research Institute (SVERI), in its Gopalpur campus at Pandharpur,

Maharashtra. Here BARC has interacted with College faculties. This has led to modifications in BARC/DAE technologies to suit to local needs/requirements and SVERI has become Knowledge Partner.

It has created opportunities in rural sector, local technical guidance through participation of educational institute for healthy growth of AKRUTI programme. RHRDF set up at SVERI works as a centre for DAE outreach programmes, for DAE technologies. Initial funding for this activity was sanctioned by Rajiv Gandhi S&T Commission, Govt. of Maharashtra to SVERI.

On similar lines one more DAE Out Reach Centre is being set up at Utkal University, Bhubaneswar, Odisha. Few more education institutes have approached BARC with their own funding.

7 XII Plan Project—DTDDF [4]

Present experience of DAE ORC, Pandharpur activities have demonstrated that unlike AKRUTI (wherein BARC directly communicated with villagers), BARC guided faculties of SVERI who in turn put efforts to train the villagers directly. Hence XII Plan Project has been proposed and got sanctioned for setting up **DAE Technologies Display and Dissemination Facilities** with the help of educational institutions. Accordingly 7 MoUs have been signed till now and 3 more have been approved. Thus under XII Plan Project DTDDF are being set up in states of Karnataka, Chhattisgarh, Telangana, Andhra Pradesh, Odisha, Uttarakhand, Nagaland, Manipur, Tamilnadu and Rajasthan.

8 Corporate Social Responsibility (CSR) Model

The multifaceted activities of DAE have spread widely all over India. Further its scope is being continuously enlarged through various constituent units of DAE, Autonomous Bodies and PSUs. Some of the projects have been bigger than the mega projects. However, recently like other mega projects of govt. or pvt. sectors and MNCs, DAE expansion projects are also facing public opposition. This trend in future can create major hurdles in the progress of DAE.

There is a need to create synergy between CSR and R&R plans. Utilisation of CSR funding on a long term basis should generate proper working space and environment for mega projects to slide in smoothly which will not create a sudden change in the living and occupational conditions of the affected people.

Based on experience of activities of AKRUTI and DAE ORC, Pandharpur, under DAE Societal Initiative, NPCIL/DAE has agreed to demonstrate CSR activities and R & R plan at its installation existing and upcoming. The framework is being proposed with a view of self sustainability and in eco-friendly manner. Focus is on “Water” for distribution of BARC developed Nanocomposite UF

membrane based Domestic Water Purifiers to Nuclear Power Plant projects/stations and villages around sites under CSR.

Presently, at any Rehabilitation Colony, thousands of families from different villages are resident. Good number of working men and women in all ages are looking for new activities around. The Implementing Agency with Locals involved can create right framework of working for them and will show them the safe, secure and progressive future in adapting new technologies for their use in day to day life.

The whole plan can be adopted as future model for all DAE mega projects well in advance.

9 Conclusion—CILLAGE

With the objective of development of rural population through innovation and technologies the concept of Cillage is developed. The place should attract competent researchers to work here to address the regional problems. Cillage becomes centre of innovation to solve the problems of the region and disseminate the developed technologies in the region through AKRUTI nodes. **It is a BARC—DAE Concept.**

References

1. AKRUTI-KRUTIK-FORCE Inclusive Rural Advancement through Technology Deployment, Patankar, A.M., Nuclear India, Nov–Dec 2007, vol 41, no 05–06, pp 9–12
2. “AKRUTI—DAE Societal Initiative AKRUTI—Advanced Knowledge & RUrAl Technology Implementation” Dr. K.B. Sainis, Bio Medical Group and A.M. Patankar, Technology Transfer & Collaboration Division BARC Newsletter Founder’s Day, Special Issue October 2011, pp 182–186
3. BARC Website: <http://www.barc.gov.in/akruti-tp/index.html>
4. Kakodkar A, Ronge B, Patankar A, Mule S, Pawar P (2017) Knowledge and technology enabled development of rural India through the concept of CILLAGE: best of city in a village. Current Science 112(4), 25 February (published under Research Article)

Role of BARC Technologies in Agriculture for Benefit of Farming Community in India

S.T. Mehetre and S. Chattopadhyay

Keywords BARC technologies · Mutation breeding · Soil health · Pest control

1 Technologies for Mutant Seeds

Bhabha Atomic Research Centre, Mumbai (India) is engaged in multidisciplinary research activities including power production, industrial research, health care, agriculture and food preservation. Use of nuclear energy for agriculture purpose has resulted in development of various technologies useful to the farming community of India. Mutation breeding programmes to induce variability and use them in crop improvement began in the early sixties and a large spectrum of variability has been isolated and maintained in the different crops with major emphasis on oilseeds and pulse crops for higher productivity, resistance to biotic/abiotic stress and quality improvement. Since India imports 40% oilseeds and 20% pulses, BARC focused its attention primarily on these crops.

Over the last several years, plant breeders and farmers in India have been looking for ways to improve plant varieties to achieve better crop yields, quantitatively as well as qualitatively. The results have been impressive. Nuclear technology has played its part in helping Indian farmers in their quest for developing new varieties of a number of crops through radiation induced mutation breeding. Today, 42 high yielding and disease resistant varieties of crops such as groundnut, mustard, blackgram, Mungbean, pigeon pea and mustard are grown in large parts of the country. All these varieties are officially notified by the Ministry of Agriculture, Government of India for commercial cultivation. Farmers in virtually every State benefited from the technology. It started in 1973 with Trombay Groundnut (TG-1) cultivated mainly in Gujarat and Maharashtra. Maturing in about 130–135 days, with large seeds, the crop gave a modest increase in yield of 15–20% [1, 4].

S.T. Mehetre (✉) · S. Chattopadhyay
Nuclear Agriculture and Biotechnology Division,
Bhabha Atomic Research Centre, Mumbai 400085, India
e-mail: smehetre@gmail.com

Besides high yield, early maturity and early water use efficiency, some of the Trombay groundnut varieties have fresh seed dormancy of 20–30 days thus preventing in situ germination, a nightmare for farmers due to end of season rains when the crop is ready for harvest [1].

2 Technologies for Soil Health

Radioisotopes are used as a ‘tracer’ or ‘label’, which enable scientists to follow the movement of specific molecules in an organism. Radioisotopes are useful in generating information such as efficiency of fertilizer nutrients, quantifying losses from soil and biological transformations of the sample, mineral plant nutrition and allied investigations. Various fertilizers and agrochemicals labelled with a radioisotope are tailor made and supplied for use.

Organic carbon plays central role in deciding health of soil as all the parameters of soil like crust formation, drainage, salt accumulation, alkalinity, beneficial microbes, pathogens and soil fertility factors are related to organic carbon. If organic carbon is low all above parameters get affected badly. Thus organic carbon is an important parameter of soil health and indicator element for status of soil productivity. So monitoring organic carbon is as essential as other important parameters of crop yield.

Soil organic carbon detection kit developed at BARC is a very important tool for the farmers to decide the nutrient level of soil (Fig. 1). The method has been developed for enhanced extraction of organic matter from soil with reference to the existing method of estimation of organic carbon [2, 6, 10]. This kit analyses the carbon status of soil within short time and therefore farmer doesn't have to rely on other agencies for the results. This ultimately helps farmers to immediately decide the nutrient supply to crop which is very critical for better production.

Fig. 1 Different components of soil organic carbon detection kit





Fig. 2 Different kits are available in the market for soil organic carbon detection

If farmer understand the carbon content of soil easily, he will be in position to decide the rate of application of fertilizer input to the agriculture field resulting in the better crop yield over the period of time. Farmers have become more aware about ill effects of chemical fertilizers day by day and consumers are also demanding organic foods. The kit also helps to test the organic nature of soil.

This kit has following features:

- (i) It is user friendly as any farmer himself can perform this on the field.
- (ii) It gives quick and reliable (comparative to standard methods) results.
- (iii) Evaluates the impact of organic carbon amendments supplemented periodically.
- (iv) It gives idea of amount of organic manure additions necessary for better yield.
- (v) Highly economical as compared with other standard methods.

Technology to commercialize the kit has been transferred to 07 entrepreneurs and different products on the basis of this technology are available in the market (Fig. 2). DAE outreach centre at Pandharpur has also developed this kit and is supplied to the farmers for analysis of the soil.

3 Technologies for Pest Control

Trichoderma species are among the most common fungi frequently isolated as saprotrophs from free soil, soil litter, dead wood and rhizosphere and they are better known as suppressor of plant diseases [3]. *Trichoderma*-based formulations thus dominate the biofungicides market throughout the world. Mass multiplication medium has been developed for enhanced disease control and increasing resistance in the plant [5]. This technology is also commercialized and products based on this technology are available in the market. *Trichoderma virens* wild type strain (MTCC 794) was exposed to gamma radiation (1250 Gy) and a mutant strain morphologically different from the wild type was isolated. This strain (designated as G2) was grown in liquid culture (potato dextrose broth) and the filtrate was assayed for ability to inhibit the growth of the plant pathogen *Pythium aphanidermatum*, causing seed/seedling rot and damping-off in many crops. The results showed that the mutant produces more antifungal substance(s) than the wild type.

This technology has been transferred to M/S Ponnalab, Bangalore and the company has developed a product based on this technology named as Vihaan.

Microfine Neem biopesticide has been jointly developed by BARC and VNIT, Nagpur. This biopesticide has been developed by using a novel technique of making micro size powder of whole neem fruit [8, 9]. Azadirectin after extraction becomes unstable when sprayed on the crop and its anti insecticidal effect is also short lived [7]. Therefore instead of extraction this technology utilizes Azadirectin in its original form as in neem fruit. Further this was developed as powder formulation and as the size of powder is decreased the efficacy increases substantially. Thus the insecticidal effect is much stronger and longer lasting. The technology is ready for transfer to the industries.

4 Food Preservation Technology

BARC has been engaged in R&D work on the technology of preservation and hygeinisation of food by radiation for the past more than 50 years. The Department of Atomic energy has the necessary expertise and know-how for setting up radiation processing plants. It has set up two technology demonstration units, one commissioned in the year 2000 for high dose irradiation at Vashi, Navi Mumbai, primarily for hygeinisation of spices. The facility is being operated by Board of Radiation & Isotope Technology (BRIT). A low dose irradiation facility, KRUSHAK at Lasalgaon, near Nashik, for sprout control during storage of onion, potato, and insect disinfestation of agricultural commodities including quarantine treatment of mango for export is being commercially operated by Maharashtra State Agricultural Marketing Board (MSAMB) under MoU with BARC and BRIT.

5 Conclusion

Peaceful uses of nuclear energy involve different applications for societal applications. BARC technologies thus helped farming community throughout India in terms of increasing the crop yield and also improving soil health for sustainable agriculture of future generations.

References

1. Badigannavar AM, Kale DM, Murty GSS (2002) Assessment of yielding ability of Trombay groundnut varieties through growth analysis. *J Oilseeds Res* 19:38–43
2. Bowman RA, Guenzi WD, Savory DJ (1991) Spectroscopic methods for estimation of soil organic matter. *Soil Sci Soc Am J* 55:563–566

3. Druzhinina IS, Seidl-Seiboth V, Herrera-Estrella A, Horwitz BA, Kenerley CM, Monte E, Mukherjee PK, Zeilinger S, Grigoriev IV, Kubicek CP (2011) *Trichoderma*: the genomics of opportunistic success. *Nat. Rev. Microbiol* 9(10):749–759
4. Kale DM, Mouli C, Murty GSS, Rao MVP (1997) Development of a new groundnut variety, TG-26, by using induced mutations in cross breeding. *Mutat Breed Newslett* 43:25–27
5. Mehetre ST, Mukherjee PK, Kale SP (2012) Mass multiplication medium for *Trichoderma* biofungicide. Indian Patent No. 1236/MUM/2012
6. Moore TR (1985) Spectroscopic determination of dissolved organic carbon in peat waters. *Soil Sci Soc Am J* 49:1590–1592
7. Sunny Y, Szeto Michael, Wan T (1996) Hydrolysis of azadirachtin in buffered and natural water. *J Agric Food Chem* 44:1160–1163
8. Tajane S, Dadhe P, Mehetre ST, Mandavgane SA (2016) Kinetic and thermodynamic azadirachtin extraction from whole neem fine powder formulation. *Ind J Chem Technol* (Paper accepted)
9. Tajane S, Mehetre ST, Dadhe P, Mandavgane SA (2016) Characterization and testing of fine powder formulation of whole neem fruits *Current Science* (in press)
10. Walke AJ, Black IA (1934) Estimation of soil organic carbon by Chromic acid method. *Soil Sci* 37:29–38

Use of Photochemical Machining Technology for Producing Metal Artwork

N.D. Misal, M. Sadaiah, V.K. Suri and P.M. Pawar

Keywords Photochemical machining · Ferric chloride · Photo tool · Brass · Artwork

1 Introduction

Photochemical machining is an engineering production technique for the manufacture of burr free and stress free flat metal components by selective chemical etching through a photographically produced mask [1]. Photochemical Machining (PCM) process is mainly produces thin and complex 2-D components. It is one of the few processes where the complexity of the component is not considered in the component cost and in the delivery time. That makes the PCM process a fast, efficient, cost competitive method of producing metal components with complex designs unmatched by any other conventional metal-forming process. Another advantage of the process is the possibility to etch a wide range of materials such as metals, glasses or ceramics. However, the easiest metals to etch are copper, zinc, steels, magnesium, aluminium, nickel and Kovar (Fe, Ni, Co). Due to the diversity of materials used in the photochemical machining process, a wide range of applications can be found in various areas, such as electronics, automotive, aerospace, medical, optics and other engineering industries. Common applications are the production of television shadow masks, integrated circuit lead frames, suspension head assemblies, mobile telephone gaskets, decoration on watch parts and jewelry.

N.D. Misal (✉) · P.M. Pawar
College of Engineering, Pandharpur, Maharashtra, India
e-mail: ndmisal@coe.sveri.ac.in

M. Sadaiah
Dr. Babasaheb Ambedkar Technological University, Lonere, Maharashtra, India

V.K. Suri
Ex BARC Scientist and MGM College of Engineering and Technology, Kamothe,
Navi Mumbai, Maharashtra, India

The journey of PCM knowledge started from Bronze Age where the ancient Greeks had discovered a fluid, which is referred to as liquid fire that attacked both inorganic and organic materials. The ancient Egyptians etched copper jewelry with citric acid as long ago as 2500 BC. The Hohokam people etched snail shell jewelry with fermented cactus juice around 1000 BC. Chemical etching was used in Europe in the fifteenth century when it was used to decorate suits of armor. Decorative patterns were also etched into swords by means of scribed wax resist. The PCM process description and the progress of PCM was discussed by Allen et al. [1]. The representative studies related to PCM are discussed below.

The PCM of SS 316 was conducted to study the effect of magnetic field on the etch rate and also PCM of a cardiovascular stent was performed [2, 3]. The chemical machining of copper by using cupric chloride and ferric chloride was carried out and its effect on depth of etch and surface roughness was analyzed [4]. The better surface finish obtained using cupric chloride while the good material removal rate was produced by ferric chloride. The parametric effect study for chemical machining of copper and aluminium was performed by Cakir and also carried out the regeneration of cupric chloride etchant [5, 6]. The parametric study of photochemical machining of different materials like ASME 316 steel, Brass and German silver, Monel 400, SS316L, and their optimization using different techniques was carried out [7–11]. The copper microchannel was manufactured using PCM, and its surface study was performed [12].

From the above reported studies, it is clear that PCM process has not yet applied for any societal application. In this paper, development in PCM process for artisans is explained. The efforts made in the direction and finally the commercial products developed is presented.

2 Procedure

The component using chemical etching can be manufactured using two different approaches:

Using electricity—Traditional Photochemical Machining process

Without Electricity—Screen Printing Method

2.1 *Using Electricity—Traditional Photochemical Machining Process*

The PCM process flow diagram is presented in Fig. 1.

The process begins with metal being selected, cleaned and coated with photoresist. The negative type photoresist is applied on the specimen, and then the

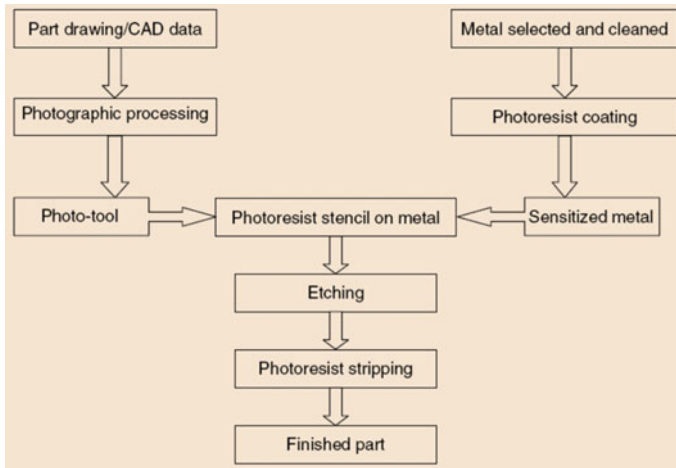


Fig. 1 PCM flow diagram [1]

specimen is exposed under UV light which passes through the transparent areas of the photo tool and becomes hard. The unhardened photoresist (i.e. areas which were protected by the photo tool) is removed by washing in an aqueous solution. The next step is etching. Etchants such as ferric chloride are sprayed onto the surface of the metal. By a chemical reaction (i.e. electrochemical removal process), some areas of the metal are dissolved and the part is produced. The last step is stripping; it consists of removing the hardened photoresist (protecting the metallic areas from etching).

2.2 Without Electricity—Screen Printing Method

The process of screen printing using photosensitive chemical emulsions is explained here. At first, the prepared artwork is to be copied onto a transparency for screen printing. The screen printing can be done on paper, on canvas, or on just about anything made from fabric, like a T-shirt, a tablecloth and napkins, a scarf, a tote bag, or simply a piece of fabric that is framed and hung as art. The object should be clean and ready to absorb the ink. The screen frame is made of wood and is very tightly covered with a fine mesh material. This is the screen through which the ink is transferred onto the object to be printed. Select the proper screen printing ink to transfer the design to the object being printed. The ink is applied and spread on the screen with the help of squeegees which is nothing but comfortable wooden holder with a rubber blade. Apply the mixture of the sensitizer and the emulsion on the Screen. The emulsions are light-sensitive liquid chemicals and become more

sensitive as it dries. The side of the screen that comes in contact with the object to be printed is known as the substrate side, while the side where the ink is placed and pushed through the screen is called the “inkwell” side. Both sides need to be covered with the emulsion mixture, and it is best to begin on the substrate side. Burn the Image onto the Screen. The next steps are to attach the artwork to the screen and expose it all to light in order to burn the image onto the screen, so that the ink can pass through the screen and be transferred to the object being printed. Once the emulsion on the screen is completely dry, and keep the screen in such way that substrate side facing down and the inkwell side facing up. With the exposure to light, the emulsion hardens, and the area of the screen that is covered by the design does not harden. Usually 10–15 min is enough time for this process to be complete. Once the photosensitive emulsion has hardened, users should remove the artwork and rinse the screen under very cold water. The emulsion that was under the design flakes off. It may be necessary to gently rub the area where the emulsion is being removed. At printing use masking tape or painter’s tape so the edges of the screen can be prevented by any sloppy leaks. Next, a small amount of ink is placed on the top of the screen and use a squeegee to pull the ink down across the image. At last, the prepared artwork is carried on preheated oven at 400 °F for just about 30 s. Then the final artwork is printed on required substrate.

3 Development of PCM Process for Artisans

An exhaustive study for the detailed requirements for using PCM method for artisans has been carried out. There is no more challenge in material removal using chemical etching. The developments are given below.

3.1 Photo Tool Development for Artisans

The main challenge is found in photo tool development for producing the products. The negative type photoresist is considered in the study.

Artwork

It is the sketch made by the artist. This may be the output of photo shop software. This artwork not suitable for using as a photo tool.

Photo tool

For converting artwork into photo tool, some processing on the artwork is required. The photo tool helps to passing or blocking of ultraviolet light through it. The precaution should be taken that surface which blocks the UV light passing through it should be Dark and surface which passes UV light should be transparent to light.



Fig. 2 Modification on photo tool

Case study undertaken: Art Work of Shivaji Maharaj

An art work of Shivaji Maharaj shown in Fig. 2a is sample artwork for study created by artisan. This art work if want to convert into a PCM product (metallic component) then certain changes are required in it. Considering negative photo resist in PCM process (commercially available photoregist in market is PR1020), artwork need to be modified. If same art work is used in PCM process, then after etching metal etched is not in one piece. For getting one piece metal piece from artwork, artwork should be modified. Figure 2a shows an artwork to be used as a phototool. The defects in the photo tool are given in Fig. 2b. The defect means there is no continuity in white and black colour. For removing these defects the steps to be followed are presented below:

1. Artwork outside border should be joined with each other.
2. Outer black border once joined together, inside artwork need to be changed. White colour should join together.
3. All such correction are made in artwork then it is considered as PCM process artwork.

After modification the photo tool can be used for PCM as shown in Fig. 2c. The precautions while making photo tool are given below:

- (1) Photo tool should be printed with the dark Laser printer.
- (2) Shading of the picture should be highlighted by dark lines.
- (3) The outer border of the photo tool should be continuous so that only the picture or artwork can easily separate from the surface plat.
- (4) There is possibility of inner surface of the product fall into the etching solution so we need to give connectivity with etch other maintaining appearance of the drawing.
- (5) After completion it should be printed on transparent/tress paper.

For artisan who want to change their artwork into PCM photo tool has to follow one thumb rule, It is—make outer black continuous border and join inside white colour each other without fail.

3.2 *Selection of Metal*

For making the decorative things or photos with the help of PCM, the surface of the metals selected should be more attractive. Because of the golden color and shining nature, brass is selected for the PCM based Artwork. For making photos thin brass sheet of 100 μm is used. These metals are selected on the basis of etching rate and surface finish after etching.

Once the photo tool is ready, then chemical etching can be followed for producing product's using PCM.

3.3 *Workshops for Artisans*

- (1) **First Workshop:** After developing the PCM procedure for artisans, SVERI's college of Engineering, Pandharpur and Bhabha Atomic Research Center (BARC), Mumbai had organized a workshop (1st) on "Photochemical Technology for Artisans Lively hood". This workshop had created awareness amongst the artisans about use of PCM technology for their livelihood. The photographs of first workshop are shown in Fig. 3.
- (2) **Second Workshop:** The second workshop had been arranged by SVERI's college of Engineering, Pandharpur and Bhabha Atomic Research Center (BARC), Mumbai for artisans. The response of artisans is increased and their involvement in the workshop was observed noteworthy. Figure 4a shows the participation of artisans in the second workshop. The different products were developed during the workshop like making of Lord Ganapati, Vithal and Shivaji Maharaj metal frames using PCM. This was the success of the workshops. The outcomes of the second workshop is shown in Fig. 4b.



Fig. 3 Photographs of the 1st workshop



Fig. 4 a Photograph of second workshop, b outcomes of the workshop

4 Commercial Product Development

After two workshops, the products were developed using PCM. The products developed are having quality of commercial products. The products development stages are as shown in Fig. 5.

4.1 Exhibition in Kartiki Vari at Pandharpur

An exhibition on “USE of PCM in Hand-crafts” was held in Pandharpur in Kartiki Vari period. The different products developed using PCM were kept in the exhibition. There was a huge response from pilgrims for this exhibition. The photographs of exhibition are shown in Fig. 6.



Fig. 5 Product development stages



Fig. 6 Photographs of exhibition in Kartiki Vari

4.2 Commercial Products

The commercial products developed are Shivaji Maharaj photos, Lord Vithal photos, etc. The cost accounting has been done for the complete PCM set-up as well as for making of the Lord Vithal photo (Fig. 7). The PCM set-up cost is approximately Rs. 3.00 lac. The Vithal Photo is approximately costing to Rs. 350.00 only.

4.3 Generation Entrepreneurs for PCM Based Artwork

The ultimate success of this work is to create an entrepreneur for PCM based artwork. The first entrepreneur Shri. Akash Gawade emerged out of two workshops.

Fig. 7 Lord Vithal photo made by PCM



5 Conclusions

The photochemical machining is developed for use of artisans for photo making. The main outcomes of the study are summarized below:

- The photo tool making method is developed for using artwork as photo tool.
- Two workshops have been organized for artisans to create awareness about PCM, Hands on Experience in PCM, etc.
- An exhibition using the developed products by artisans has been held in Kartiki vary at Pandharpur.
- The commercial products are developed using PCM like Shivaji Maharaj photo and Lord Vithal photo.
- An entrepreneur Mr. Akash Gawade has emerged out from this two workshops
- Use of PCM can change the livelihood of artisans.

References

1. Allen DM, Photochemical machining: from ‘manufacturing’s best kept secret’ to a \$6 billion per annum, rapid manufacture process. *Galvanotechnik* 97(6)
2. Saraf AR, Sadaiah M (2016) Magnetic field assisted photochemical machining (MFAPCM) of SS316L. *Mater Manuf Process*; (Accepted Article). doi:[10.1080/10426914.2016.1198014](https://doi.org/10.1080/10426914.2016.1198014)
3. Saraf AR, Sadaiah M (2016) Photochemical machining of a cardiovascular stent. *Mater Manuf Processes*; (Accepted Article). doi:[10.1080/10426914.2016.1198025](https://doi.org/10.1080/10426914.2016.1198025)
4. Cakir O, Temel H, Kiyak M (2005) Chemical etching of Cu-ETP copper. *J Mater Process Technol* 162–163:275–279
5. Cakir O (2006) Copper etching with cupric chloride and regeneration of waste etchant. *J Mater Process Technol* 175:63–68
6. Cakir O (2008) Chemical etching of aluminum. *J Mater Process Technol* 199:337–340

7. Sadaiah M, Patil DH (2015) Some investigations on surface texturing on Monel 400 using photochemical machining. In: Proceedings of the 460 ASME 2015 international manufacturing science and engineering conference MSEC2015, Charlotte, North Carolina, USA, 8–12 June 2015. doi:[10.1115/MSEC2015-9294](https://doi.org/10.1115/MSEC2015-9294)
8. Bhasme AB, Kadam MS (2016) Parameter optimization by using grey relational analysis of photochemical machining. *Int Res J Eng Technol* 3:992–997
9. Bhasme AB, Kadam MS (2016) Experimental investigation of PCM using response surface methodology on SS316L steel. *Int J Mech Eng Technol* 7:25–32
10. Mumbare P, Gujar AJ (2016) Multi objective optimization of photochemical machining for ASME 316 steel using grey relational analysis. *Int J Innovative Res Sci Eng Technol* 5:12418–12425
11. Wangikar SS, Patowari PK, Misra RD (2016) Effect of process parameters and optimization for photochemical machining of brass and German silver. *Mater Manuf Processes* (Accepted Article). doi:[10.1080/10426914.2016.1244848](https://doi.org/10.1080/10426914.2016.1244848)
12. Wangikar SS, Patowari PK, Misra RD (2016) Effect of process parameters on surface characteristics of photochemically machined copper microchannel. In: International conference on surface modification technologies SMT30, Milan, Italy, June 29–July 1, 2016

RuTAG IIT Bombay Floating Fish Cages for Livelihood Opportunities for Tribals in Dimbhe Area

Rupali S. Khanolkar, Anand B. Rao and Siddhartha Ghosh

Keywords Livelihood · Aquaculture · Floating fish cages · Rural technology · Inland water body · Fishery

1 Introduction

This paper presents the case study of a technological intervention by Rural Technology Action Group (RuTAG) IIT Bombay to improve the design of the floating fish cages in Dimbheto generate livelihood opportunities and to protect self-respect for dam displaced tribal communities in Pune district of Maharashtra. The improved design has significantly helped in this endeavor.

1.1 Objective

The purpose of this paper is two folds: the first objective is to showcase the 'Floating fish cage intervention' by RuTAG IIT Bombay for livelihood generation for tribals in Ambegaon block of Pune district of Maharashtra. The second one is to highlight the decipherable socio-economic impacts of the intervention on the local communities.

The paper is divided into three broad components. The first part of the paper narrates details about struggle and sufferings of the local tribals due to construction of Dimbhe dam. The second part presents technical details of the RuTAG IITB intervention. And the third part focuses on impacts of the intervention on local tribal communities.

R.S. Khanolkar (✉) · A.B. Rao · S. Ghosh
Indian Institute of Technology Bombay, Mumbai, India
e-mail: rupali.khanolkar@iitb.ac.in

1.2 About Shashwat

Shashwat, a grass root level voluntary organization (NGO) was formed as an outcome of efforts by Smt. Kusum Karnik, an avid social worker and Late Shri. Anand Kapoor, an IIT Kharagpur alumnus. The NGO has played a pivotal role in the initiation of present intervention and facilitating installation of ‘floating fish cages’ in backwaters of Dimbhe, Manikdoh, Bhama-Askhed and Chas-Kaman Dams in Pune district of Maharashtra. Shashwat had earlier helped in the struggle of displaced tribal communities by getting fishing rights and also registration of the local fishermen’s co-op society—Dimbhe Jalashay Shramik Adivasi Macchimar Sahakari Society Maryadit, Dad.

2 Need for the Intervention

2.1 Dimbhe Dam and the Struggle of the Local Communities

Dimbhe dam was constructed on Ghodriver in Ambegaon block of Pune district in Maharashtra. When the dam was made functional in the year 2000, 1253 tribal families had to leave behind best of their agricultural lands and shift towards the hilly slopes in nearby regions with no livelihood opportunities left. In 2003, a few fishermen started fishery in backwaters of the dam with very little success. Shri. P.D. Karandikar, the then divisional commissioner of Pune, invited Central Institute of Fisheries Education (CIFE) to guide the tribals about developing fisheries for livelihood in the year 2006.

2.2 Introducing Aquaculture in Dimbhe Dam

CIFE recommended the introduction of inland aquaculture technology. Aquaculture or cage fishing is the process of controlled and protective rearing of fries (fish seeds) to fingerlings within a cage (a net that allows water to flow) floating in a water body.

CIFE provided first fish cage and also supplied fish seeds of Indian Major Carp (Rohu, Catla and Mrigal) in Dimbhe dam in the year 2006. Indian Major Carp was chosen since it fetches the better market price. CIFE design of fish cage was made of wooden truss made of Sal wood (refer Fig. 1). The buoyancy to the structure was offered by some airtight PVC drums uniformly tied around the structure. The walkway was made of jungle wood. The entire structure was anchored so that it would not float away. Though this structure provided the necessarily protected environment for growing the fish, the tribals faced many difficulties while working on it.

Fig. 1 Close up view of CIFE fish cage structure



2.3 Challenges Faced by the Tribals

After using the fish cages for 2–3 years, people operating on fish cages realized that there was high maintenance cost due to continuous wear and tear of wood used in the structure. Under wave effect, the flotation drums kept hitting the wooden structure and thus weakened it severely over 2–3 years. Also due to deterioration of wood, the walkways sagged, as a result, people, especially women did not feel safe and comfortable to work on cages. The cages needed shifting from one place to other due to changes in water levels in the reservoir. The CIFE structure being very heavy could not be pulled conveniently thus causing difficulties.

3 The RuTAG IIT Bombay Intervention

Late Shri. Anand Kapoorji approached RuTAG IIT Bombay for help in resolving the above issues. Prof. Siddharth Ghosh from Civil Engineering department of IIT Bombay accepted the responsibility of the project as a Principal investigator (P.I.). Mr. Nuli Dharma Teja, worked on the project in partial fulfillment of his master's degree (M.Tech. in civil Engineering) under guidance of Prof. Ghosh along with other volunteers. The project was initiated in April 2012 and completed in April 2014.

3.1 Literature Review

Literature review indicated that very limited research had been done in the subject area till then. Both National as well as International publications on the subject mainly focused on different techniques of aquaculture (pros and cons of specific aquaculture, effect of structure on fish production etc.) and not on the structural design and maintenance of floating cages [1–5].

3.2 RuTAG IIT Bombay Fish Cage Structure

Two alternative models were designed:

1. Model A was fixed truss (frame) structure with all joints fixed
2. Model B was a pinned truss structure with all joints hinged

Linear static analysis was performed for three different load cases using SAP 2000. The results of analysis indicated that Model A i.e. ‘Fixed truss model’ (shown in Fig. 2) was more suitable for cage fishing. Details about the fish cage designed by RuTAG IIT Bombay are available in our fabrication manual.

Salient features of the selected structure are highlighted below:

- The structure is made of hollow pipes connected to each other with help of connectors as shown in Fig. 2. The outer diameter of the pipe is 25 mm and inner diameter being 15 mm. The length of the threading at each end of pipe is 25 mm. (dimensions of structure are shown in Fig. 2 and the units are in meters).
- All pipes and connectors are made of galvanized iron (G.I.) to prevent rusting. All welded parts are either galvanized or fusion bonded epoxy coated to prevent corrosion.
- Sealed empty PVC barrels are tied below the structure to provide buoyancy force. These are recycled drums used in chemical industry of length 975 mm and diameter varying along the length. Each drum is securely tied to the main

Fig. 2 a Top view of fish cages. b Side view of fish cages

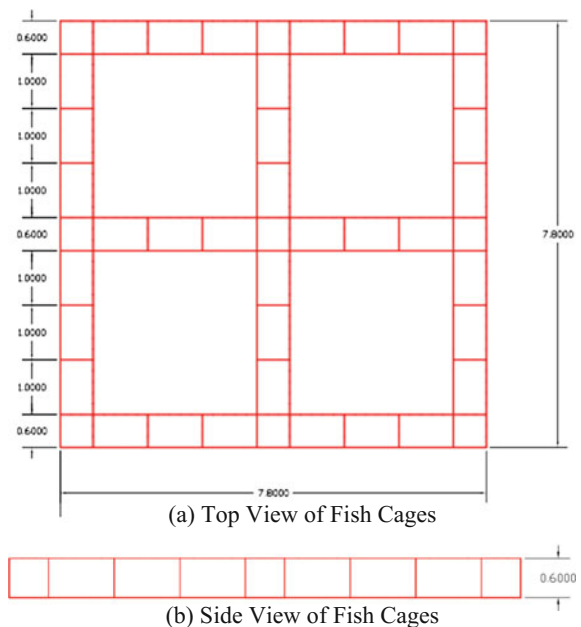


Fig. 3 Structure of fish cages by IIT Bombay



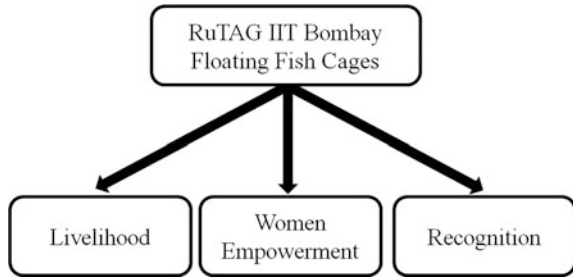
structure at four points with help of a pair of specially designed holders for the drums. The holders are made of mild steel flat and are galvanized to prevent corrosion. This arrangement prevents the drums from continuously hitting and thus damaging the floating structure (as in case of ‘CIFE structure’).

- The walkways for people in earlier structure were made of ordinary jungle wood and were susceptible to damage and sagging. In new structure, wood is replaced by gratings made of GFRP (glass fibre reinforced plastic) which is light weigh, stiff and corrosion free. Square holes of size 3 cm × 3 cm have been provided on the gratings for allowing flow of water thereby reducing impact of water on the structure. This change has remarkably improved the safety aspect of the structure.
- Nylon nets of suitable size are connected to the inner structure using hooks. Each net forms a closed structure of dimension 3 m × 3 m × 3 m. Each one of these closed structures is called as a ‘fish cage’. There are 4 cages in each structure. These cages are used for growing fish from fish seeds in protected environment (Fig. 3).

4 Impact Analysis

The RuTAG IIT Bombay fish cages were installed in Dimbhe dam in April 2014. It was felt that decipherable socio-economic impacts of the new design of fish cages needed to be evaluated. Data collection tools such as observation, focused group discussion and informal interview were used while interacting with the tribals. Mr. Budhaji Damase, Executive Director, Shashwat has been part of the journey for past 20 years or so. An informal discussion with Shri. Budhaji also proved to be quite insightful and provided valuable information. Apart from this, various records maintained in office of ‘Shashwat’ were used as a source of quantitative data. The main areas of impact cited by the tribals have been broadly divided into following three categories (Fig. 4).

Fig. 4 Impact analysis



- Livelihood
- Recognitions
- Women Empowerment.

4.1 Livelihood

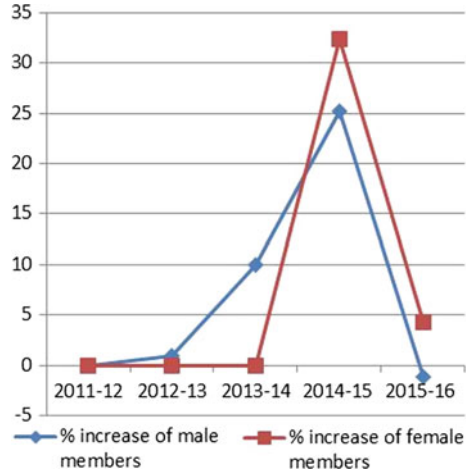
RuTAG IIT Bombay fish cages are stronger and sturdier as compared to the erst-while cages. Due to improvement in safety factor, more number of fisher folks (especially women) is attracted to working on fish cages. After introduction of RuTAG-IITB fish cages in April 2014, there was a sharp increase of 25% in number of male members and 32% in number of women members working on fish cages (refer Figs. 5 and 6). Recently 28 additional cages have been introduced in 4 dam reservoirs with help of grant from GOM. As per current month’s records from Shashwat, additional 452 tribal families have already started working on these cages. This has increased the number of direct beneficiaries to more than 3500. Another major impact is on availability of fish. Financial year 2015–16 recorded 323 fishing days in Dimbhe dam as compared to just 73 days in year 2006–07. Due to the consistent availability of good quality fish throughout the year, wholesale buyers now come to Dimbhe to purchase the fresh fish catch. This has ensured a regular income for the fisher folks.

Financial year	Total members	Male members	Female members	% of female members	% increase of male members	% increase of female members
2010-11	213	142	71	33	-	-
2011-12	213	142	71	33	0	0
2012-13	214	143	71	33	1	0
2013-14	228	157	71	31	10	0
2014-15*	273	179	94	34	25	32
2015-16	275	177	98	36	-1	4

*Introduction of RuTAG IIT Bombay fish cages

Fig. 5 Registered members for fishery at Dimbhe in last five years

Fig. 6 Percent increase in membership at Dimbhe in last five years (gender wise)



4.2 Women Empowerment

Due to enhanced safety at IITB fish cages; there was a sharp rise of 32% in number of women members involved in fisheries at Dimbhe area in year 2014–15. A group of 52 women is working exclusively on cultivation of ornamental fish. The women SHGs have now started their own shops for selling the ornamental fish, fish tanks and other accessories at Dimbhe, Manchar and Junnar. The women are also participating in exhibitions in cities like Pune to sell the ornamental fish and fish tanks. These women have successfully achieved sales figure of Rs. 3,75,000 in year 2015–16. Recently Doordarshan channel (Marathi) has felicitated these women by airing a documentary film based on their life in program—‘JanataDarbar’

Smt. Meeratai Dangat, one of the tribal women while sharing her experience of working on fish cages said, “Women were scared of working on old cages as they used to sag. The new cages are strong, safe and very comfortable for us to work on. IITB cages have really transformed our lives and made us independent”.

4.3 Rewards and Recognitions

After successful operation of RuTAG IITB fish cages in Dimbhe dam for one year, it was felt that benefits of technology developed by RuTAG IITB should also reach the

dam displaced population in 3 neighboring dams. It was proposed to introduce 28 more cages in the backwater of Manikdoh dam, Bhamra Askhed dam, Chas Kaman dam and Dimbhe dam in surrounding areas. Shri. Budhaji Damase and few other representatives of Shashwatalong with Dr. Rupali Khanolkar, Project manager of RuTAG IIT Bombay presented a proposal for introducing ‘RuTAG IITB’ type Fish cages’ to the Tribal Development Department, GOM on 5th February, 2015. The proposal for grant of Rs. 9,921,290 was approved by Shri. Vishnu Sawra, Minister for Tribal Development, GoM in May 2015 via GR no. 201503131600425724. As requested by the Government authorities, RuTAG IIT Bombay is providing technical support for dissemination of these 28 cages.

Today Dimbhe has become a role model for many. Shashwat conducts training for fishermen interested in learning about cage fishing. Students from institutes like IIT Bombay, TISS and CIFE (Central Institute of Fisheries education) visit the dam site every year for study purpose.

“Thanks to the fish cages—we have become famous. Senior government officials and eminent personalities visit our fish cages and praise us. We feel proud that we are able to train other fishermen and also students from eminent institutes like IIT.”

—Mr. Budhaji Damase, Executive Director, Shashwat.

5 Conclusion

The project titled ‘Floating fish cages for aquaculture’ by Rural technology action group (RuTAG) IIT Bombay is a classic example of how technological Institutes like IIT could bring a positive change in the lives of thousands of dam displaced tribals in Pune district of Maharashtra. The intervention has not only improved the livelihood opportunities for these tribals but also has helped in enhancing their self-esteem. The intervention has a positive impact on the tribal women also. There is a wide scope for further improvement and dissemination of this technology in various parts of our country.

6 Scope for Future Dissemination

Though the intervention was originally designed for backwaters of Dimbhe dam, it is suitable for any inland water reservoir in India and other developing countries.

7 Recommendations for Future Research

The cost of each fish cage as per present market value is around Rs. 500,000/-. Based on feedback from NGOs, recommendations for future research is to design low cost fish cages and to make them more affordable without compromising on the strength and stability of the present structure.

Acknowledgements The authors gratefully acknowledge the funding and support from Office of Principal Scientific Advisor to the Government of India under RuTAG IIT Bombay. Rural technology action group (RuTAG) is a project initiated by PSA to the Government of India with the objective of achieving rural development through science and technology interventions. We wish to extend our gratitude to all members of project review committee of RuTAG especially Dr. Ketaki Bapat for their kind support. We also thank (late) Shri. Anand Kapoor and Shri. Budhaji Damge from Shashwat along with members of Dimbhe Jalashay Shramik Adivasi Machhimar Sahakari Sanstha Maryadit without whose enthusiasm, vision, technical and non-technical inputs and feedbacks this project would not have been possible. CIFE has played a pivotal role by providing valuable inputs related to fisheries and the basic structure of fish cages which we have improved, and we are thankful to them. Finally, we would like to acknowledge the students and staff of Civil Engineering Department of IIT Bombay without whose efforts the project would not have been possible. We are thankful to all of them.

References

1. Kapoor A, Damase B (2012) Tribals develop fisheries in Dimbhe dam. https://www.swissaid.ch/sites/default/files/Dimbhe_Fishery_Case_Study_0.pdf
2. Beveridge M, Cage aquaculture, 3 edn. Blackwell Publishing Ltd., Oxford
3. Chen J, Guang, C, Xu H, Yan X, Wang Y, Liu J (2006) A review of cage and Pen aquaculture: China. <http://www.fao.org/3/a-a1290e/a1290e03.pdf>
4. Singh Kohli MP, Langer RK, Dube K, Chandra P, Reddy AK, Somdutt S, Upadhyay RK (2003) Proceedings of Workshop cum demonstration on cage aquaculture in open waters by Central Institute of Fisheries Education held in May 2003. Available at <http://krishikosh.egranth.ac.in/handle/1/2034623>
5. Ghosh S (2015) Design of the floating structure for fishing nets for the purpose of cage fishing: a manual for design and fabrication. IIT Bombay project identifier 12DST052, April 2015

Evaluation of Multiple Hydrometeorological Factors for Prioritization of Water Stress Areas in the Upper Yerala River Basin, Satara, Maharashtra, India

Mustaq Shaikh, Milind Herlekar and Bhavana Umrikar

Keywords GIS · Groundwater stress areas · MCDM techniques · Upper Yerala river basin

1 Introduction

Water is one of the important elements responsible for the life on the earth. Clean, safe drinking water is scarce. Presently, billion people in the developing world don't have access to it. Water is the foundation of life. Many people spend their most of the time for searching water. The total amount of water on the earth is almost constant, but rapid growth in population, increased agricultural/industrial use of water are producing stress in terms of both quantitative and qualitative aspects [1]. The over-extraction of groundwater than the natural recharge of water, for fulfilling the increased demands of the increased population and pollutions from different sources causing fresh water resources decreasing day by day [2]. The present study deals with phreatic/shallow aquifers where groundwater is at the atmospheric condition and dynamic, thus gives quick response to the supply (precipitation/recharge) and demand (draft/discharge). Most of the dug wells are high yielding till winter but as the summer approaches, the groundwater levels starts declining as a result few wells completely dries up indicating the minimum saturation in phreatic aquifers. Thus, during summer months the less availability of water creates water stress [2]. The water stress is difficulty in finding sources of fresh water for utilization during a period when required. It affects, in auxiliary depletion and decline in quality of available water resources in an area [3].

Water stress is primarily experienced because of the water deficit, various reasons for the water stress are, scanty rainfall, groundwater contamination, growing

M. Shaikh (✉) · M. Herlekar · B. Umrikar
Department of Geology, Savitribai Phule Pune University, Pune, India
e-mail: mushtaqshaikh27@gmail.com

population, rise in groundwater withdrawal, decreased groundwater recharge, increase in groundwater abstraction structures as a result groundwater depletes. The water-stressed condition does not allow industrial, agricultural, urban and tourism development to proceed without restrictions on water use and allocation policies especially for tourism and industrial sectors [4, 5].

In the present study, authors have attempted to develop an approach to find out the water stress areas in the Upper Yerala river basin, Satara by using the multi-criteria decision-making technique to target water risk management practices. The GIS techniques have been utilized here in conjunction with the available field datasets to get the desired objective. The spatial interpolation technique of the GIS software is very useful for defining the spatial distribution of various hydrometeorological parameters [5, 6]. The GIS techniques have been used by many researchers in groundwater quality, artificial recharge, groundwater potential studies [7–22]. The present study focuses on the various parameters, namely, groundwater draft, groundwater recharge, groundwater level, rainfall, population and abstraction structures for demarcation of groundwater stress areas by using GIS techniques.

The demarcation of water-stressed zones would be helpful to the decision makers in the groundwater management and identifying prime areas for water conservation structures. As, till now no such studies have been reported from the study area, therefore, the present study is the pioneer work which is crucial for sustainable groundwater management. The results indicate the importance of hydrometeorological parameters, application of GIS and multicriteria decision-making techniques to identify the water stressed regions in the study area.

2 Study Area

Upper Yerala River basin, a tributary of river Krishna is situated in Khatav taluk, Satara district covering southwestern part of Maharashtra, India. The Yerala stream originates at Mol, Shendgewadi villages present in the northern part of the basin and continues its travel through village Vaduj, and finally meets Yerala dam near Yeralwadi village in the south. The Yerala river is the major stream flowing from the study area, which shows, dendritic and parallel drainage pattern. The areal extent of Upper Yerala basin is 745.26 km². The study area is included in the Survey of India toposheet no's 47 K/1, 47 K/5, 47 K/6, and 47 K/10. It lies between 17°30'42"–17°52'55" N latitudes and 74°14'8"–74°37'30" E longitude (Fig. 1). The climate in the study area is semiarid type, and the average annual rainfall is 606 mm. as per the record of Agricultural department of Maharashtra. Temperature may rise in summer up to 45 °C, while the mean annual temperature is about 24 °C. In winter, the temperature drops to 10 °C. The main sources of groundwater recharge in the study area are river and rain water that percolates down to the groundwater system.

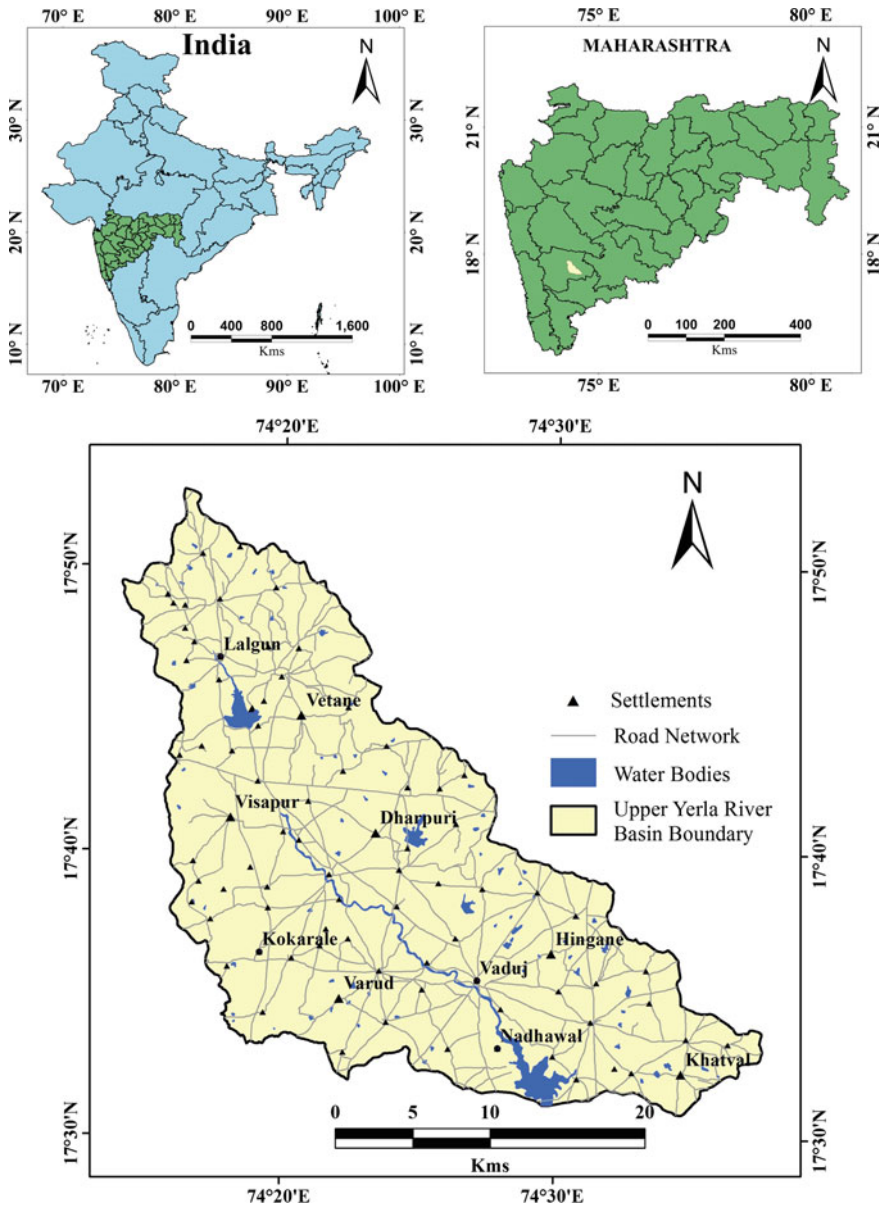


Fig. 1 Study area location map

3 Methodology

Factors controlling water stress are different in space and time, and some of these factors are summarized in Table 1. It involves: (1) groundwater draft as a water utilization factor; (2) groundwater recharge as a water availability factor; (3) groundwater levels which enhance the groundwater availability with the rise in water level and vice versa; (4) rainfall availability as a source of water; (5) population density controls the domestic water utilization of an area and (6) abstraction structures were also considered in this study, since it governs the amount of groundwater withdrawal for agricultural as well as domestic purposes.

All these influencing factors are spatially dependent and restrained to finite regions. For example, in areas with comparatively high rainfall, the availability of water as recharge source will be more and these areas will fall under low water stress category. While, if rainfall is comparatively less, those regions will come under high water stress category.

The Survey of India toposheet maps on a scale of 1:50,000 were used for the preparation of the base map of the study area. In order to assess or prioritize the water stress area, six thematic layers, viz. groundwater draft, groundwater recharge, groundwater water level, rainfall distribution, population, and abstraction structures were chosen as the effective factors. The weights have been assigned to thematic layers based on expert knowledge. A database was built for managing the thematic layers in GIS framework by using Multiple Criteria Decision Making (MCDM) techniques. The integration of these different factors in a logical manner will result in a map showing water stress areas, with a high, moderate and low categories. Furthermore, all these influencing factors have the different degree of influence on water stress condition of the area but also their influence is varying at different levels. The flow diagram of the methodology adopted in the study is shown in Fig. 2.

Table 1 Major influencing factors

Sr. No.	Influencing factor	Influencing element	Controlling element
1	Groundwater draft	Quantity	Groundwater utilization
2	Groundwater recharge	Quantity	Groundwater source
3	Groundwater levels	Depth of water	Water availability
4	Rainfall	Quantity	Groundwater source
5	Population	Density	Groundwater consumer
6	Abstraction structures	Density	Groundwater withdrawal

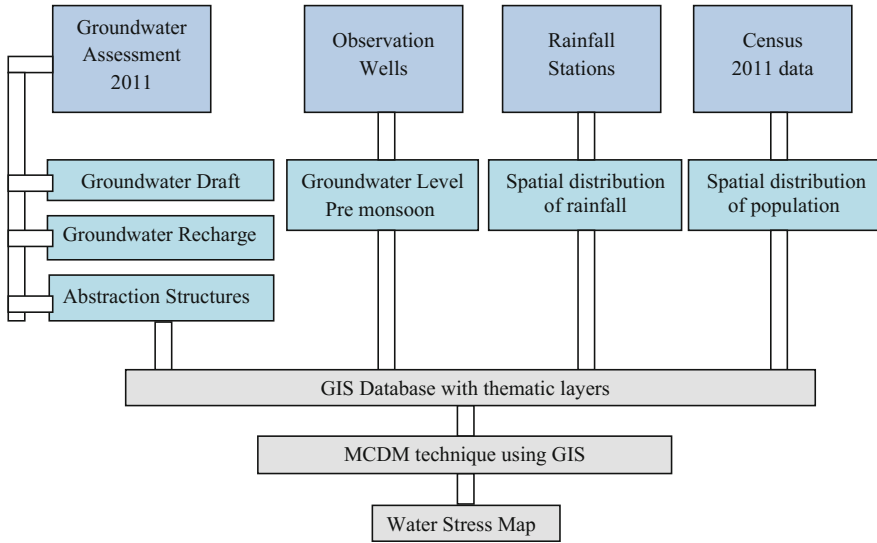


Fig. 2 Flow diagram of approach involved in the study

4 Results and Discussions

4.1 Groundwater Recharge

The major source for groundwater recharge is the rainfall in the study area. The rainfall recharges the shallow phreatic aquifer that decreases the water stress condition of the area by increase in the availability of water. The total estimated groundwater recharge of the study area is 9200 ham. The four major watersheds represent the Upper Yerala river basin, which include (KR 9) Lalgun watershed, (KR 10) Vaduj watershed, (KR 11) Kokrale watershed and (KR 23) Nadhwal watershed. The groundwater recharge values have been estimated by the GEC 97 methodology and obtained from GSDA. The estimated groundwater recharge value for Lalgun, Vaduj, Kokrale and Nadhwal watersheds are 1649, 3341, 1807 and 2403 ham respectively. Further, the groundwater recharge factor was classified into three classes viz., >2800, 2800 to 2200, <2200 ham (Fig. 3 and Table 2). However, this factor is one of the most influencing parameters on groundwater stress conditions; therefore, it was given a weight of 20% for obtaining the water stress map.

4.2 Groundwater Draft

Declining water availability in some areas due to less rainfall will exacerbate the challenge of water stress. Strategies for efficient and sustainable development and

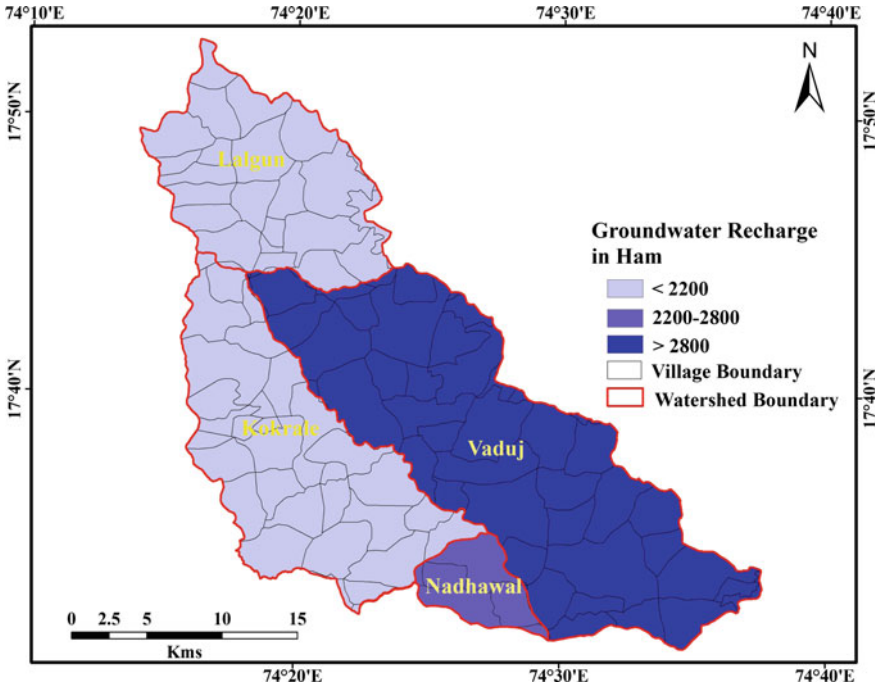


Fig. 3 Spatial distribution of groundwater recharge map

Table 2 Weights and score assigned to evidential themes

Factor	Class	Score	Weight %
Groundwater recharge in ham	<2200	8	20
	2200–2800	6	
	>2800	2	
Groundwater draft in ham	<1500	2	20
	1500–2000	6	
	>2000	8	
Population density persons/sq kms	<1500	2	15
	1500–2500	6	
	>2500	8	
Abstraction structure density wells/sq kms	<8	2	15
	8–12	6	
	>12	8	
Groundwater level in mtr	<765	2	15
	765–815	6	
	>815	8	
Rainfall in mm	<600	2	15
	600–675	6	
	>675	8	

management of water resources are needed to ensure access to the world’s limited water resources and to cope with competing demands [23]. The quantity of water drawn for the fulfillment of regular need of agricultural, industrial and domestic purposes are the important factors while considering the water stress condition. The total estimated groundwater draft of the study area is 7731 ham as per the GSDA report of 2011. The areas where water draft is more will have certainly more water stress than the area where water draft is less. Therefore, high weightage is assigned where the water draft is comparatively more to obtain the water stress map and vice versa. The groundwater draft values have been estimated by the GEC 97 methodology and obtained from the GSDA. The estimated groundwater draft value for Lalgun, Vaduj, Kokrale and Nadhwal watersheds are 1324, 3098, 1524 and 1785 ham respectively.

Further, the groundwater draft factor was classified into three classes viz., >2000, 2000 to 1500, <1500 ham (Fig. 4 and Table 2). However, this factor is also one of the most influencing parameters on groundwater stress conditions; therefore, it was given a weight of 20% for obtaining the final water stress map.

4.3 Population

Population growth is a major contributor to water stress. Growth in populations means growing demand and fight of water for domestic, industrial, and municipal uses. The most stressed areas are typically those with few water resources, high

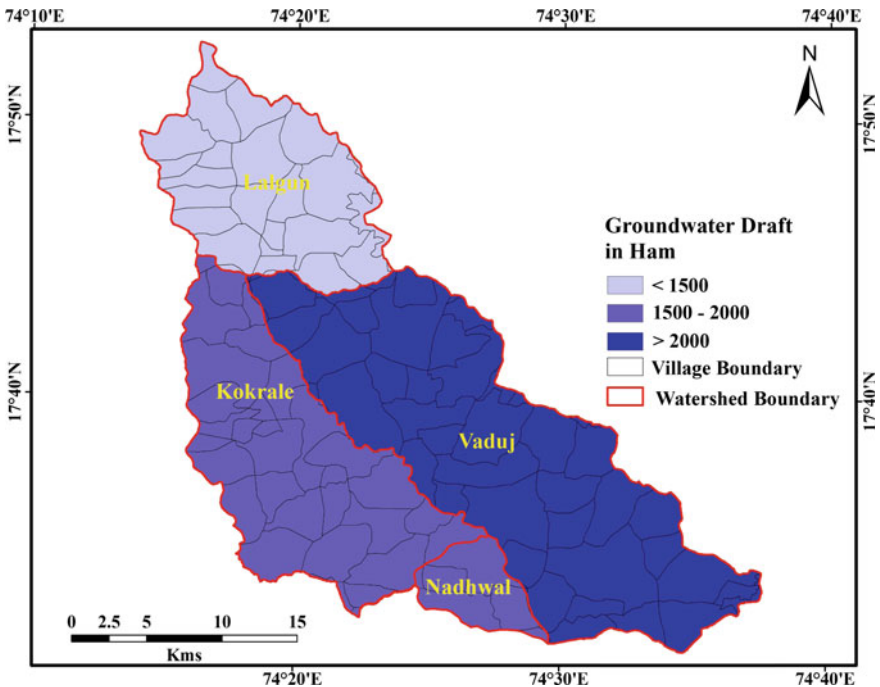


Fig. 4 Spatial distribution of groundwater draft map

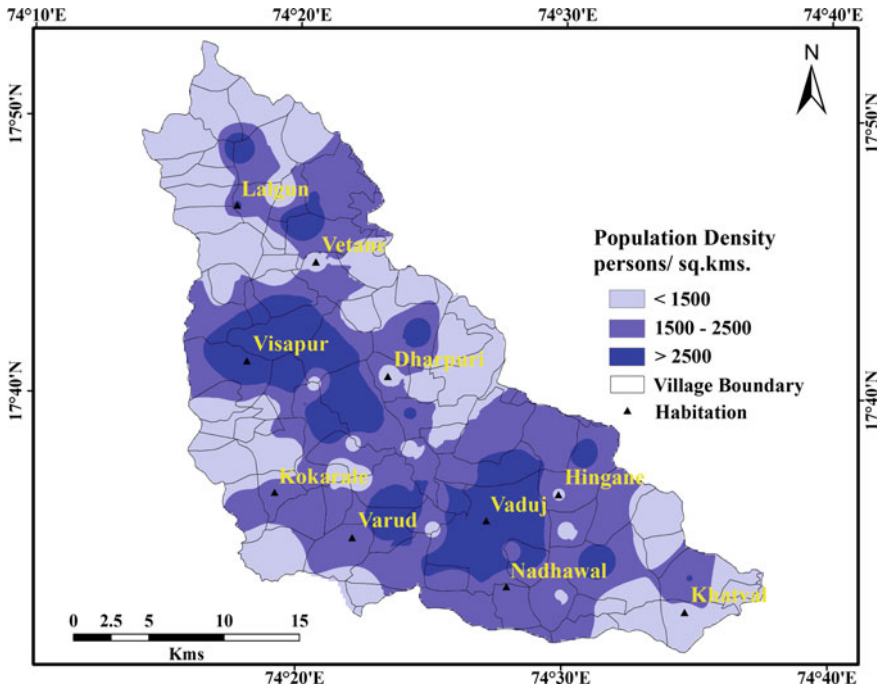


Fig. 5 Spatial distribution of population density map

population densities, and high population growth rates [24]. Population growth leads directly to increase in overall water demand, that leads to the limits of water available per capita. The dense population could expose more people to water shortages, with negative entailments for sustainability of water resources. The village wise population data (census 2011) procured from the statistical department of Government of Maharashtra and utilised to get the population density map in GIS environment. Further, the population density classified into three classes as >2500, 2500 to 1500 and <1500 persons per sq. kms. (Fig. 5 and Table 2).

The high density population occurred around the central portion of the study area and low density occurred around northern, western, and eastern portion of the area.

The stress on freshwater resources due to increased population and growing need is already heading to water scarcity in various locations in Maharashtra. Therefore, high weightages are assigned to dense populated area and vice versa. The population density factor assigned a weight of 15% to obtain the water stress region of the area.

4.4 Abstraction Structures

Agriculture accounts for approximately 70% of global water use, and for as much as 95% of water use in predominantly agriculture-based countries. Agriculture not only requires a large amount of water, but it is also one of the most inefficient uses of water [25]. A growing population requires more food and more water required for agricultural production. Agricultural productivity is a crucial component of global food security. To get the desired quantity of water, more number of bore wells/dug wells constructed since the last two decades in the study area.

The demand for water for industrial use is increasing with rapid industrialization to meet the many needs of a growing population. Therefore, to fulfill the agricultural, domestic and industrial requirement of water, more number of abstraction structures/wells or borewells constructed in an area.

The watershed wise data of number of abstraction structures were obtained from GSDA and utilised to get the abstraction density map in GIS environment. Further, the abstraction density was categorized into three classes as >12, 12 to 8 and <8 abstraction structures per square km (Fig. 6 and Table 2). The high density abstraction structures occurred around major portion of the central area and low density occurred around southern portion of the area. More the density of

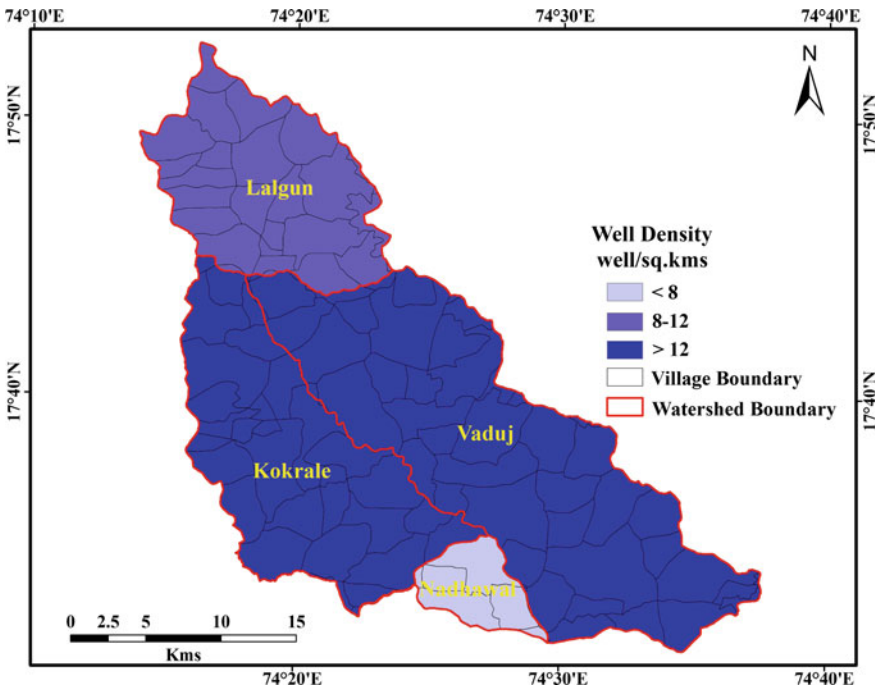


Fig. 6 Spatial distribution of abstraction structure density map

abstraction structures within an area, more will be water stress. Therefore, high weightage have been assigned, where the abstraction structures density is high and vice versa. This factor was assigned a weight of 15% to obtain the water stress region of the area.

4.5 Groundwater Level

The groundwater occurs almost everywhere below the earth surface. Because of the advanced drilling technology the groundwater extraction/exploitation from the greater depth is possible now a days. The groundwater level fluctuates with the extraction or recharge of water into groundwater system. The dug wells or bore wells are not only used for pumping of water but also provides the insights about the condition of groundwater [26]. The pumping of groundwater at a faster rate than it can be recharged, can have adverse effect on groundwater availability and this can be manifested by the depletion of groundwater level. Therefore, the groundwater level factor is considered in this research as one of the important factors for analyzing the water stress condition of an area. The groundwater level readings of pre-monsoon period of 9 observation wells from the last 5 years average data were obtained from the GSDA. The groundwater level was mapped by subtraction of the groundwater elevation data obtained by field data elevation reading from GPS.

The analyzed data was utilised to get the spatial groundwater level map. The deeper groundwater level occurred in the northern part and comparatively shallower groundwater level occurred in the southern part of the area. The reduced groundwater level (surface elevation minus depth to water level) below the ground surface categorized into three classes viz., >815, 815 to 765, <765 m (Fig. 7 and Table 2). Accordingly, the high weightage have been assigned to the areas which shows deeper groundwater level and low weightage assigned to shallow groundwater level areas. The groundwater level factor assigned a weight of 15% to obtain the water stress region of the area.

4.6 Rainfall

The water is added into the groundwater system by recharge from rainfall. The areas with high rainfall rates are relatively water wealthy areas [27]. However, the total annual rainfall, in general, does not exceed 771 mm; this relatively high rainfall region occurs in the central portion of the study area around Khatav village. The minimum annual rainfall value is about 479 mm in the southern part around Katarkhatav and Vaduj villages, and it reaches to 600–675 mm in the central-northern region of the Upper Yerala river basin.

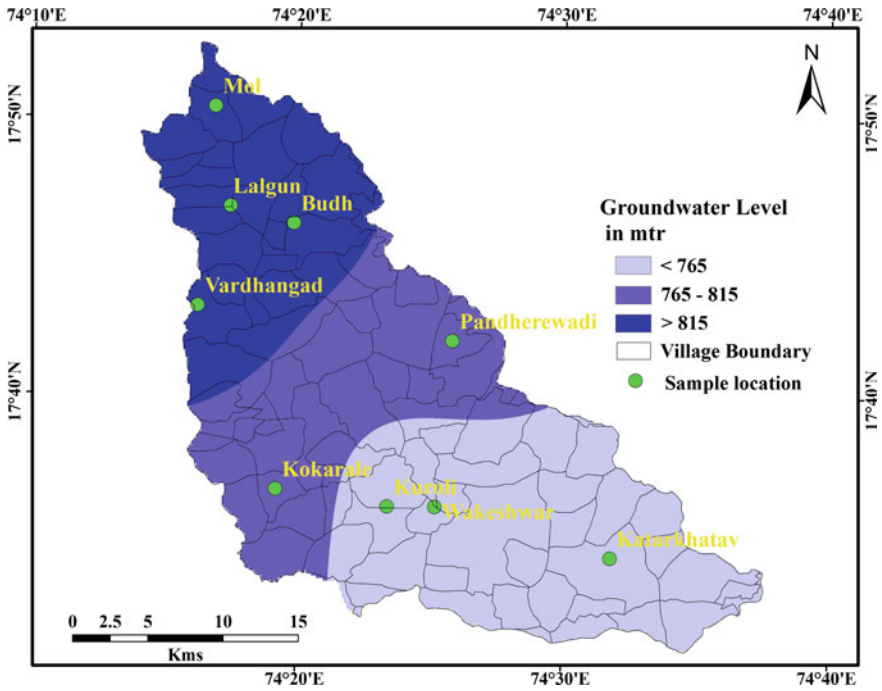


Fig. 7 Spatial distribution of pre-monsoon groundwater level map

The geographic distribution and intensity of rainfall Upper Yerala river basin were analyzed applying the isohyet method. Rainfall data were acquired from the available records of the Agricultural department, Government of Maharashtra. The spatio-temporal distribution of rainfall adding last three years amount was considered to understand the instant reflections of rainfall on water stress conditions in present study to classify the spatial distribution of rainfall map. The resulting map was classified into three major classes <600, 600 to 675, >675 mm/year (Fig. 8 and Table 2). The map shows that the central portion around Khatav village receive much more water from rainfall than the southern part of basin around Vaduj and Katarkhatav villages. The rainfall factor assigned a weight of 15% to obtain the water stress region of the area

The spatial distribution of prioritized water stress area has been obtained from the integration of six parameters by weighted overlay analysis in GIS environment. Further, the spatial distribution of prioritized water stress area classified into three classes low, moderate and high water stressed regions. The high, moderate, low water stressed region includes 5, 24, 67 villages with the areal coverages 34.13 (4.58%), 218.06 (29.26), 493.07 km² (66.16%) respectively (Fig. 9 and Table 3).

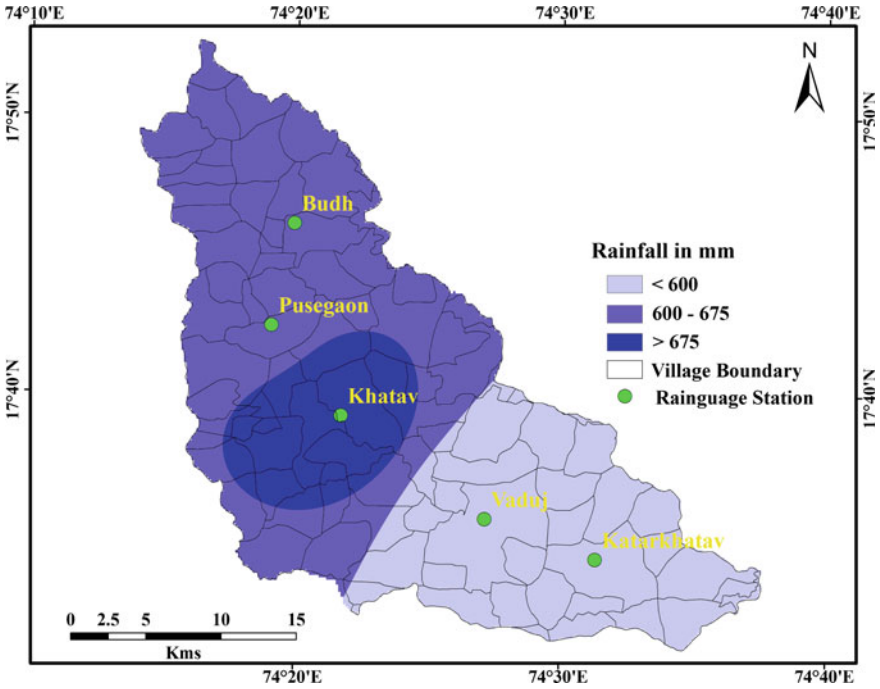


Fig. 8 Spatial distribution of rainfall map

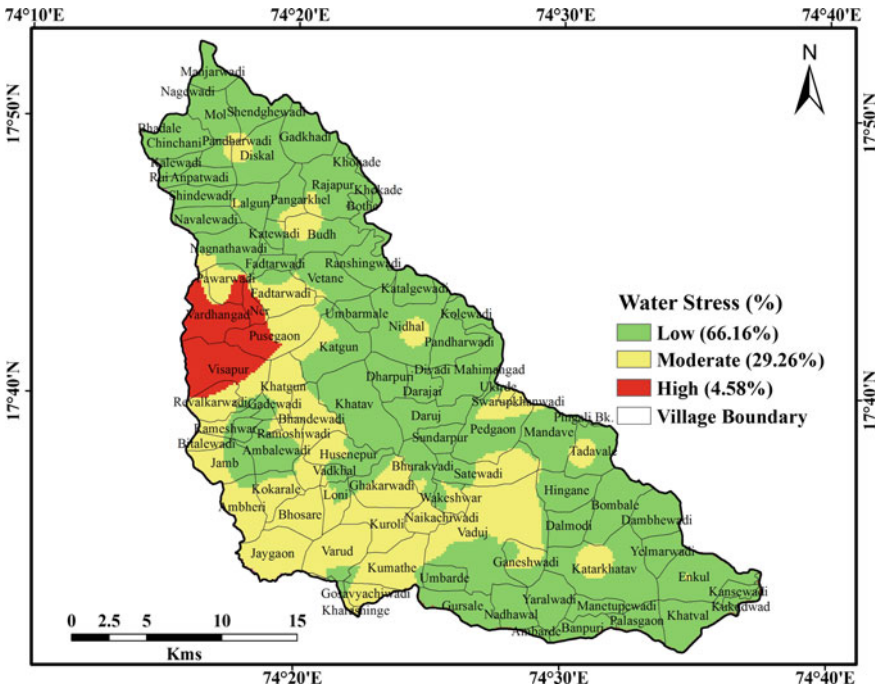


Fig. 9 Priority wise categorization of water stress areas

Table 3 Villagewise classification of water stressed areas in Upper Yerala river basin

	High water stress	Moderate water stress	Low water stress
	Ner, Pawarwadi, Pusegaon, Vardhangad, Visapur (total 5 villages)	Ambheri, Bhandewadi, Bhosare, Bitalewadi, Fadatarwadi, Ganeshwadi, Gharkarwadi, Gosavyachiwadi, Jamb, Jaygaon, Kharshinge, Khatgun, Kokrale, Kumthe, Kuroli, Loni, Naikachiwadi, Rameshwar, Revalkarwadi, Satewadi, Swarupkhanwadi, Vaduj, Varud, Wakeshwar (total 24 villages)	Ambalewadi, Ambarde, Anapatwadi, Banpuri, Bhadale, Bhurakwadi, Bombale, Borjaiwadi, Bothe, Budh, Chinchani, Dalmodi, Dambhewadi, Darjai, Daruj, Dhapuri, Diskal, Divadi Mahimgad, Enkul, Gadewadi, Gadkhadi, Gursale, Hingane, Husenpur, Jakhangaon, Kalewadi, Katgun, Kansewadi, Katalgewadi, Katarkhatav, Katewadi, Khatav, Khatwal, Khokade, Kolewadi, Kukudwad, Lalgun, Loni, Mahimgad, Mandave, Manetupewadi, Manjarwadi, Mol, Nadhwal, Nagewadi, Nagnathwadi, Navalewadi, Nidhal, Palasgaon, Pandharwadi, Pandharewadi, Pandharewadi, Pangarkhel, Pegaon, Pingali Bk, Rajapur, Ramoshiwadi, Rui, Shindewadi, Sundarpur, Tadavale, Ukirde, Umbarde, Umbarmale, Vadhakal, Vetane, Yeralwadi, Yelmarvai (total 67 villages)
Area	34.13 km ²	218.06 km ²	493.07 km ²
%	4.58	29.26	66.16

5 Conclusions

The multiple hydrometeorological factors and GIS based weighted overlay techniques proved to be a valuable tool to explore water stressed areas in basaltic terrain in way such that, time and cost can be saved. It is found that the groundwater recharge, groundwater draft, groundwater levels, annual rainfall, population density and density of abstraction structures were the most effective factors of the sub-surface water conditions and therefore aided in deciphering water stress zones in the area. It has been observed that the zones of water stressed regions are located more precisely when pertinent factors are combined and logically modeled. Most of the high water stressed zones were found in the western central region of the study area around Visapur village. The villages categorized under high water stressed class need to be tackled immediately for the sustainable supply of groundwater. The

sustainability of water supply can be maintained by management of demand side and supply side interventions. Additionally, groundwater availability should be increased by constructing the water conservation structures to arrest the surface runoff. The findings from this study can be used for other similar hydrometeorological regions.

This work demonstrates the integrated use of GIS technique with multicriteria approach to relate the various hydrometeorological, demographical datasets in categorizing the water stress area for future preparedness. Moreover, prioritization of various government and private sectoral schemes on improvement of water availability to implement the managed aquifer recharge projects and for planners in the water resource management for future planning and to target water risk management practices.

References

1. Shaikh M, Birajdar F (2015) Groundwater assessment and feasibility of artificial recharge structures on over-exploited miniwatersheds of MR-12, Osmanabad District. In: IEEE international symposium on international conference on technologies for sustainable development. IEEE Press, pp 1–5
2. Shaikh M, Birajdar F (2015) Mapping of water scarce zones of Osmanabad District by analysis of groundwater levels and rainfall. *Int J Innovations Eng Tech* 5:254–262
3. Rodell M, Velicogna I, Famiglietti J (2009) Satellite based estimates of groundwater depletion in India. *Nature* 460:999–1003
4. Shaikh M, Birajdar F (2015) Anticipation of water scarcity areas and duration: a case study of Osmanabad district, Maharashtra, India. *Int J Latest Technol Eng Manage Sci* 4:1–5
5. Goodchild M, Haining R, Stephen W (1992) Integrating GIS and spatial data analysis: problems and possibilities. *Int J Geogr Inf Syst* 6(5):407–423
6. Kemal S, Ibrahim G (2007) Spatial analyses of groundwater levels using universal kriging. *J Earth Syst Sci* 116(1):49–55
7. Ahn H, Chon H (1999) Assessment of groundwater contamination using geographic information systems. *Environ Geochem Health* 21:273–289
8. Nas B, Berktaş A (2010) Groundwater quality mapping in urban groundwater using GIS. *Environ Monit Assess* 160:215–227
9. Dar I, Sankar K, Dar M (2011) Spatial assessment of groundwater quality in Mamundiyyar basin, Tamil Nadu, India. *J Environ Monit Assess* 178:437–447
10. Shaikh M, Birajdar F (2015) Mapping of feasibility of groundwater for drinking water zones of Akkalkot taluk, Solapur, India using GIS techniques. *Int J Sci Res* 4:1–5
11. Sekar I, Randhir T (2007) Spatial assessment of conjunctive water harvesting potential in watershed systems. *J Hydrol* 334:39–52
12. Rosegrant M, Ximing C (2001) Overcoming water scarcity and quality constraints, water for food production. A 2020 vision for food, agriculture, and the environment. *Vision 2020*
13. Sarkar B, Deota B, Raju P, Jugran D (2001) A geographic information system approach to evaluation of groundwater potentiality of Shamri micro-watershed in the Shimla Taluk, Himachal Pradesh. *J Ind Soc Remote Sens* 29(3):151–164
14. Madani A, Niyazi B (2015) Groundwater potential mapping using remote sensing techniques and weights of evidence GIS model: a case study from Wadi Yalamlam basin, Makkah Province, Western Saudi Arabi. *Environ Earth Sci*. doi:[10.1007/s12665-015-4524-2](https://doi.org/10.1007/s12665-015-4524-2)

15. Srinivasa Y, Jugran D (2003) Delineation of groundwater potential zones and zones of groundwater quality suitable for domestic purposes using remote sensing and GIS. *J Sci Hydrol* 48(5):821–833
16. Saud Al (2010) Mapping potential areas for groundwater storage in Wadi Aurnah basin, western Arabian peninsula, using remote sensing and geographic information system techniques. *Hydrogeol J* 18:1481–1495
17. Dar I, Sankar K, Dar M (2010) Remote sensing technology and geographic information system modeling: an integrated approach towards the mapping of groundwater potential zones in hardrock terrain, Mamundiyyar basin. *J Hydrol* 394:285–295
18. Elewa H, Qaddah A (2011) Groundwater potentiality mapping in the Sinai peninsula, Egypt, using remote sensing and GIS-watershed based modeling. *Hydrogeol J* 19:613–628
19. Mayilvaganan M, Mohana P, Naidu K (2011) Delineating groundwater potential zones in Thuringapuram watershed using geospatial techniques. *Indian J Sci Tech* 4(11):1470–1476
20. Mondal S (2012) Remote sensing and GIS based ground water potential mapping of Kangshabati irrigation command area, West Bengal. *J Geogr Nat Disast* 1(1):1–8
21. Srivastava V, Giri D, Bharadwaj P (2012) Study and mapping of ground water prospect using remote sensing, GIS and geoelectrical resistivity techniques—a case study of Dhanbad district, Jharkhand, India. *J Ind Geophys Union* 16(2):55–63
22. Adji T, Sejati S (2014) Identification of groundwater potential zones within an area with various geomorphological units by using several field parameters and a GIS approach in Kulon Progo Regency, Java, Indonesia. *Arab J Geosci* 7:161–172
23. Gleick P (1998) Water an crisis: paths to sustainable water use. *Ecol Appl* 8(3):571–579 (1998)
24. Ehrlich P, Holdren J (1971) Impact of population growth. *Am Assoc Adv Sci New Series* 171 (3977):1212–1217
25. Madramootoo C, Fyles H (2010) Irrigation in the context of today’s global food crisis. *Irrig Drain* 59:40–52
26. Mohammad H, Johnson R (1985) Municipal demand for water in Kuwait’ methodological issues and empirical result. *Water Resour Res* 21(4):433–438
27. Vorosmarty C, Green P, Salisbury J, Lammers R (2000) Global water resources: vulnerability from climate change and population growth. *Science* 289:284–288

Design of Improved Biomass Cook Stove for Domestic Utility

S.S. Saiyyadjilani, P.G. Tewari, Rakesh Tapaskar,
Ajitkumar P. Madival, Mahesh Gorawar and P.P. Revankar

Keywords Improved biomass cook stove (IBCS) · WBT · Thermal efficiency · Fire power · Specific fuel consumption (SFC)

Nomenclature

WBT Water boiling test
CS Cook stove
CCT Controlled cooking test
IBCS Improved biomass cook stove
KPT Kitchen performance test
CCS Conventional cook stove

1 Introduction

The world's primary energy consumption has been predominantly dominated by conversion through combustion process that accounts for nearly 90% of the total energy used. The major fields of heat and power supply services like food preparation, space heating, ventilation, air conditioning, electricity generation and transportation have been thrust areas where maximum quantity of energy has been expended. The usage of biomass resources for combustion was reduced to 11% on account of a range of other fuels like coal, peat, natural gas, crude and refined oils that were brought to Vogue as combustion fuels. The small biomass cook stoves of 5 kW and smaller rating are in use for a variety of applications practiced by billions

S.S. Saiyyadjilani · P.G. Tewari · R. Tapaskar · A.P. Madival · M. Gorawar ·
P.P. Revankar (✉)
KLE Technological University, Hubballi 580030, Karnataka, India
e-mail: pp_revankar@bvb.edu

R. Tapaskar
e-mail: rptapaskar@bvb.edu

of people worldwide. In contrast to the combustion of fossil fuels, the biomass combustion releases zero net carbon dioxide on account of the fact that biomass fuel is a plant derivative evolving through the photosynthesis reaction and thus maintain the level of carbon dioxide.

As per 2011 Census, India had 25 crore households, with a 31% urbanization, per capita annual income of Rs. 88,536 as per 2015 data and about 1075 kWh of per capita energy consumption. The cooking fuel determines the time required and health impacts of cooking task. For cooking food, 87 and 26% respectively of rural and urban households rely on biomass. The collection of fuel consumes time and requires effort which causes ill effects to health. In India, 400 million women were exposed to smoke from biomass burning resulting in vision and respiratory problems. Women spend the average of 5 h each day for cooking, procuring of fuel also consumes 20% of the time. Switching to efficient and modern fuels is desirable as they will not alter the demand significantly [1].

Standardized chapati dough preparation regarding consistency and rolling characteristics indicating rolled dough sheet to be in the range of 150 mm diameter prepared by sharp edge die. The baking time of 60–180 s per chapati was identified as a standard while operating on Tawa maintained at 202–232 °C temperature. The chapati puff operation that needed 15 s was critical in fixing color and pliability with a slightly higher temperature in the range of 337–340 °C [2]. The Mexican cook-stove showed potential fuel savings of 44–65% over open fire stoves [3]. The tests conducted on gas tandoor oven for chapati making with reported baking operations consuming 30 and 45 s for the two sides of rolled chapatti dough (150 mm). The, controlled hot plate needed 3–5 s for puffing operation performed at about 320 °C [4]. The high fuel moisture resulted in the reduction of stove efficiency without significant influence by wood type and mode of ignition as reported by Kumar et al. [5]. The study developed new biomass-fired cook stoves and investigated them by fuel moisture, a size of wood (fuels), ignition and design method for a comparative study with existing traditional cook stove [5]. Raman et al. adopted improvised test procedure identifying gaps and drawbacks in existing test methods that were less efficient and produced more smoke [6]. Huangfu et al. investigated natural draft semi-gasified cook stove concerning wood pallet moisture content measured to be 5.9, 9.4, 18.2, and 22.1% [7]. Arora et al. investigated Philips natural draft (PN) and forced draft (PF) biomass cook stoves through BIS and WBT. PF and PN stoves had increased CO emissions by 68 and 48% respectively with the batch feeding of fuel in BIS test [8]. The study by Gayad et al. stressed on insulated combustion chamber, ash box for better ash disposal and the air inlet for adequate air supply to complete combustion. The thermal efficiency of 37.65% at 1.73 kg/h wood consumption was reported for the developed cook-stove [9]. Gallagher et al. attributed pollution menace as a precursor to trigger cook stove research in developing countries with committed private sector participation essential to their increased adoption. The Global Alliance for Clean Cook Stoves reported on common yardstick in the form of ten step test biomass safety protocol [10]. Gogoi et al. reported on steady state heat transfer model to predict cook-stove

performance and its validation through field tests on commercial cook-stoves. The test indicated 811 W of heat required in the self sustenance of combustion while the balance was distributed amongst primary air, unburned charcoal, cooking pot, combustion chamber and unaccounted heat [11]. The top lit updraft cook stove investigated by Obi et al. for wood chip, rice husk briquette and coconut shell as fuel indicated lowest cooking time for boiling 1.02 kg of yam (10 min) and lowest SFC (686.26 g/kg) for rice husk briquette [12].

2 Experimental Studies on Improved Cook Stove

In this section detailed design procedure, construction and performance analysis of improved cook stove have been explained. The discussions in this section are related to performance tests on Biomass cook-stoves to evaluate thermal efficiency using water boiling and Roti making tests. The heat transfer analysis to assess heat loss from the cook stove is also indicated.

Moisture content and excess air influences combustion efficiency so these parameters were interrelated by reported literature that used to evaluate combustion efficiency [13]

$$\eta_c = 96.84 - 0.28M_{fuel} - 0.064T_s - 0.065E_A \quad (2.1)$$

The evaluated combustion efficiency value was used to determine the dimensions of combustion chamber.

$$\eta_c = \frac{m_w \times C_p \times \Delta T}{m_{fuel} \times C_v} \quad (2.2)$$

$$\rho_{fuel} = \frac{m_{fuel}}{V_{required}} \quad (2.3)$$

$$V_{required} = \left(\frac{\pi \times d^2 \times l}{4} \right) \quad (2.4)$$

The diameter of the combustion chamber obtained from the calculations using Eqs. (2.1)–(2.4) was 0.117 m.

The mass analysis of ash-free dry wood indicated by the literature was adopted for the present study detailed for pine wood as carbon, hydrogen, nitrogen, oxygen and sulfur were in the scale of 54.9, 5.8, 0.2, 39 and 0.1% respectively [14]. The complete burning of 1 kg of wood 6.6913 kg of air is required. The amount of air required to burn 0.8685 kg of wood was 5.4601 kg. The air to fuel ratio found to be 6.6912. The two models of cook stove were developed with identical dimensions and geometry but differed only in terms of the material of construction.

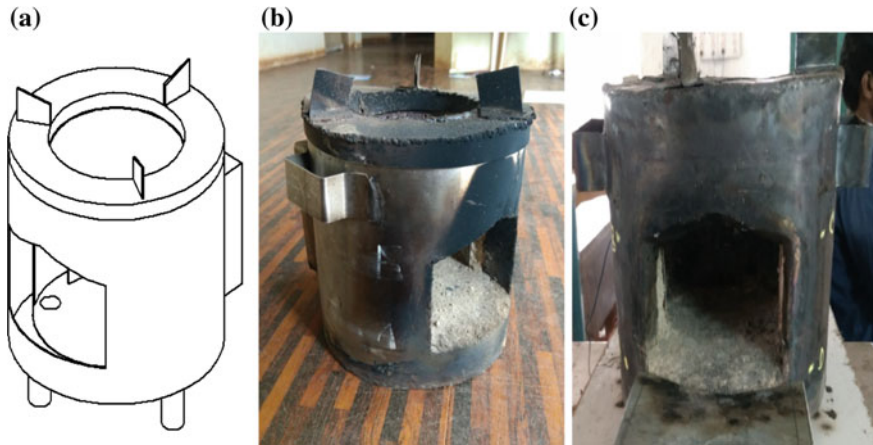


Fig. 1 Pictorial view of IBCS. **a** Conceptual drawing. **b** Model-1. **c** Model-2

Details of Improved cook stove

The final design of cook stove was obtained through the calculations. Figure 1a gives the pictorial representations of assembled view of the system. The two models of cook stove were developed with identical dimensions and geometry but differed only regarding the material of construction. The model-1 represents the stainless steel used during construction of outer chamber and for the construction of model-2 mild steel was used and are shown in Fig. 1b, c.

The WBT protocol version 4.2.3 developed by Shell Foundation was employed for conducting this test. The designed cook stove was evaluated using the protocol for its performance in its three-phase of operation, and test setup for both the models are shown in Fig. 1a, b. The cold start test was started by measurements of initial values of weights for empty pot, pot with water and fuel (pine wood). The initial temperature of water used in the pot was recorded to measure the amount of useful heat gain with time duration as the fuel burning in improved cook stove proceeded. The dimensions of fuel wood used in the study were $0.02\text{ m} \times 0.0025\text{ m} \times 0.001\text{ m}$. The Hot start WBT is conducted immediately following the end of Cold starts WBT for the cook-stove. The difference between these two tests lies in the fact that hot start WBT commences with the cook-stove in heated condition following its operation for a considerable amount of time. The Low power test is performed immediately following the Hot-start WBT to assess the ability of stove to simmer water using the minimum amount of wood. The remaining part of the pre-weighed fuelwood was weighed, and the fire of the furnace was reduced to keep the water as close to $6\text{ }^{\circ}\text{C}$ below the local boiling point as possible. The fire was maintained at this level for next 45 min beyond which temperature of the water in the pot was recorded along with the weight of the remaining water left, char and wood. The roti making test was designed to assess

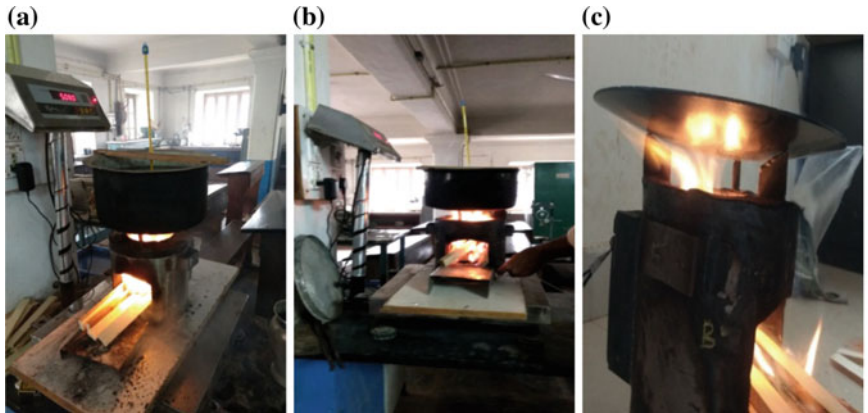


Fig. 2 Test setup of improved cook-stove models, **a** WBT: Model 1, **b** WBT: Model 2, **c** Roti making

the performance of cook stove for the practical utilization through roti baking application. In this test, roti dough was prepared by mixing the pre-determined amount of water with 200 g of wheat flour. The prepared dough after proper kneading was made compatible for making circular roti geometries of 150 mm diameter using a sizing die to cut to the required dimension. The prepared circular roti geometries were puffed on the heated baking pan (tawa) kept over the flame of the Improved cookstove. The time taken to prepare each roti was recorded along with the amount of fuel (wood) consumed during the test calculated by measuring the weight of fuel before and after the test (Fig. 2).

3 Results and Discussions

3.1 Results of IBCS Testing

The WBT test results of three phases conducted for both the constructed models and variation among them is compared with performance parameters of IBCS.

Figure 3 shows difference in thermal efficiency for Model 1 and Model 2 of the improved cookstoves on the WBT (cold start- hot start- simmering). The results indicated the thermal efficiencies respectively to be 29.99, 31.16 and 45.10% for cold start, hot start and simmering tests performed on the 1st model. On the contrary, the thermal efficiency readings were recorded as 32.08, 32.42 and 49.06% for the 2nd model on the WBT. The variations in efficiency noticed at various phases of WBT were due to the additional heat required to heat up cook-stove in the cold start condition that gets accounted as the lost heat fraction. The simmering phase exhibited highest thermal efficiency on account of lower heat losses associated with

Fig. 3 Variation of thermal efficiency

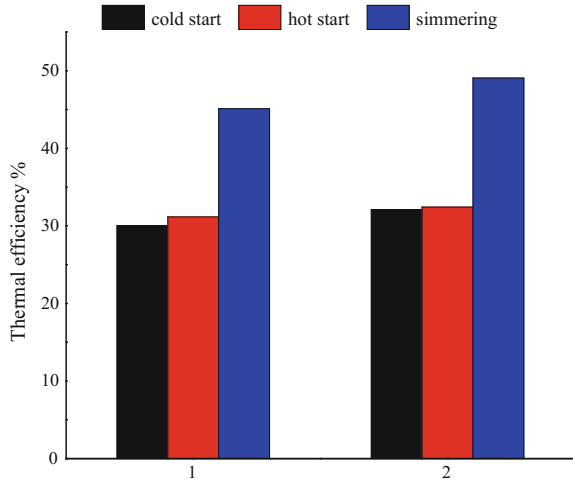
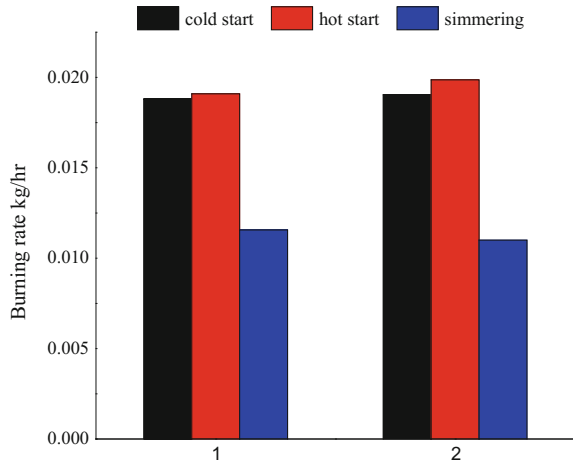


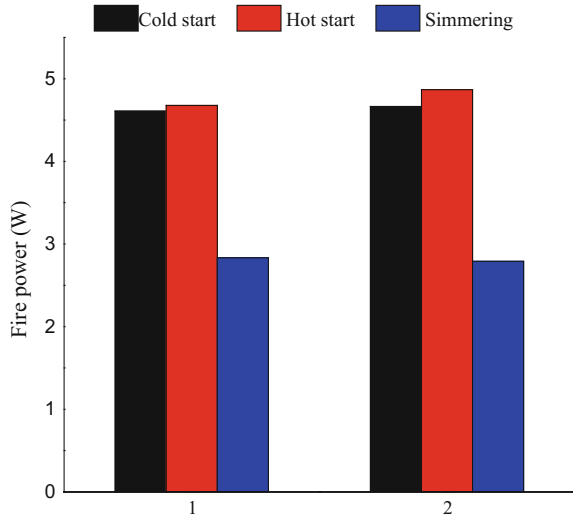
Fig. 4 WBT fuel burning rate of 1st and 2nd model



process undertaken at temperature 6 °C lower to the local boiling point. The performance of Model 2 presented a better performance as compared to Model 1 on account of proper air circulation obtained inside this combustion chamber due to fixing of top-lid thereby leading to lower fuel consumption during tests.

Figure 4 indicates the burning rates in kg/min to be 0.0188 (cold start), 0.0190 (hot start) and 0.01156 (simmering) with respect to 1st model as against values of 0.019, 0.0198 and 0.011 for 2nd model. The lesser the burning rate led to increasing in fuel savings and was found good for 2nd model as compared to the 1st model. The time taken to attain the local boiling point of 97 °C, was respectively 26 and 24 min for the hot start and cold start process on Model 1 as against the time

Fig. 5 Fire power of 1st and 2nd model during WBT



durations of 24 and 23 min for Model-2. The time taken to boil water to its local boiling point, in turn, affects the fuel consumption and cause variation in its performance. The equivalent dry wood consumed for Model 1 was 0.488916, 0.458208, and 0.5203 kg respectively for three phases of WBT as against fuel consumption of 0.4569, 0.4569 and 0.513 kg for 2nd model that relatively lower amongst the two models investigated.

Figure 5 shows the firepower occurred for 1st and 2nd model during testing of water boiling. Cold start exhibits a fire power of 4.60 kW, 4.67 kW for the hot start and 2.83 kW for the simmering phase of the 1st model. Similarly, 4.66, 4.86 and 2.792 kW exhibits for cold start, hot start and simmering phase respectively for 2nd model. The wood energy consumed by IBCS per unit time links to the fire power. Higher fire output is desired and was found in 2nd model. The water vaporization in kg during WBT that was 0.325, 0.30 and 1.53 respectively for cold-hot—simmering phases concerning Model-1 as against the values of 0.325, 0.335 and 1.645 kg respectively for Model 2.

Figure 6 shows the SFC of 1st and 2nd model. Wherein cold start has a 0.113044 kg wood/kg of water, 0.105335 kg wood/kg of water for the hot start and 0.1734 kg wood/kg of water simmering phase of 1st model. Similarly, 0.10565 kg wood/kg of water, 0.105895 kg wood/kg of timber for the hot start and 0.177 kg wood/kg of water for the simmering phase of 2nd model. The SFC of IBCS should be minimum, intern it reflects in less fuel consumption.

Figure 7 shows the surface temperatures of cook stove for an interval of 2 min. The 1st model exhibits a surface temperature of 52.5 °C at 10 min, 64.15 °C at 20 min and 67.55 °C at the end of the test. Similarly, 2nd model exhibits temperature values of 57.15, 74.55 and 80 °C for corresponding timings. The surface

Fig. 6 SFC of 1st and 2nd model during WBT

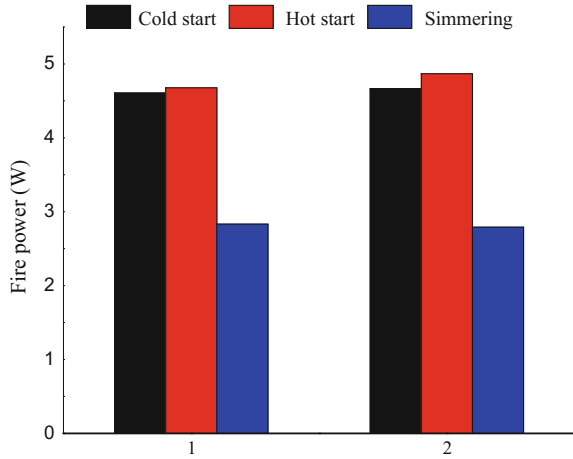
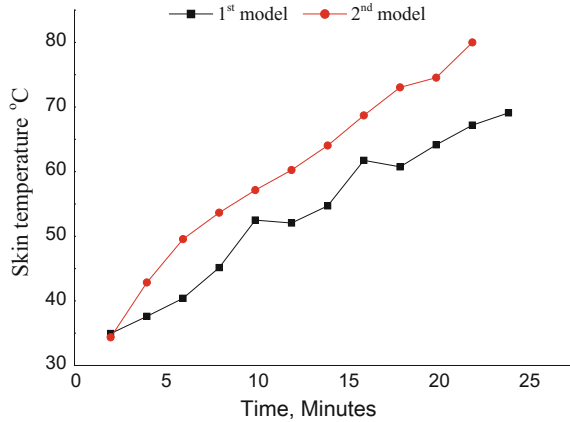


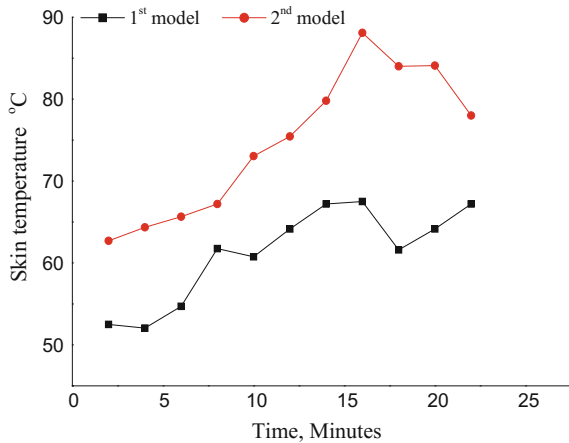
Fig. 7 Variation of skin temperature for WBT (cold start)



temperature depends on the material selected for fabrication and insulation chose, higher temperature need safety precautions to hold the IBCS and leads to corrosion over a period.

Figure 8 shows the surface temperature values of 60.75 °C for 10 min, 64.15 °C for 20 min and 67.2 °C at the end of hot start phase conducted for 1st model. Similarly, variation of 73.05, 84.1 and 78 °C for the same time. The variation in temperature at the various time of IBCS operation depends on fuel feeding interval. The variation of cook stove surface temperature of 67.2, 70.5 and 70 °C at 15, 30 and 45 min for 1st model. Similarly, 2nd model exhibits the values of 79.1, 79.5 and 88.8 °C for the corresponding time interval of simmering phase.

Fig. 8 Variation of skin temperature for WBT (hot start)



3.1.1 Roti Making Test

The Roti making test was conducted to cook an overall weight of 150 g of roti assessing the time taken to complete the cooking task. It was observed that a time duration of 6.50 min was required to prepare five rotis with a total of 150 g each of 150 mm diameter and to average to a weight of 30 g each. The time taken for puffing operation was critical for good color and pliability with, continuous puffing for 15 s necessary to get chapatti with the desired appearance.

3.2 Heat Transfer Analysis

This heat transfer analysis of the IBCS was assessed to ensure that skin temperature of the device does not exceed beyond permissible limits for safe operation. The excessive skin temperature also indicated the higher value of convective and radiation losses from the stove surfaces. This investigation also aimed at selection of appropriate insulating material for the IBCS that ensured a lower skin temperature. The value of natural convective heat transfer coefficient and convective heat transfer coefficient occurred at combustion chamber are more in model-2. The heat loss evaluated through heat transfer analysis was 24.31 W for 1st model where stainless steel was used as the outer cylinder as a material, and 35.27 W was observed for the 2nd type for which mild steel was used for the outer body. The heat carrying capacity of the material determines the heat loss by walls of IBCS; lesser the conductivity lesser would be the heat loss. The material with minimum thermal conductivity is desired for the construction of the model.

4 Conclusions

The conclusions drawn from experimental studies on IBCS are summarized below:

- The moisture content and lower calorific value of pine wood sample used for the study was experimentally determined and was found to be respectively 10.75% and 14700 kJ/kg.
- The significant temperature difference was noticed on the two models of cook-stove that were in the range of 14–15% owing to variability in cook-stove operation on account of two different materials of construction used.
- The results of heat transfer analysis based upon skin temperatures recorded during WBT for the two models showed that 2nd model had higher values over the 1st model values by 13.19, 18.30 and 16.04% for cold start, hot start and simmering phases of WBT respectively.
- The WBT results from w.r.t average thermal efficiency (cold start and hot start phases) of model 1 and model 2 of Improved Cookstove indicated values of 30.85 and 32.25% respectively. The relative thermal efficiency for the two model w.r.t simmering test was observed to be 7.96% more for model 2 of cook-stove.
- The averaged value of fire power for models 1 and two were respectively evaluated to be 4.03 and 4.104 kW and corresponding SFCs were 0.1305 kg wood/kg water and 0.1295 kg wood/kg water.
- The Roti making test indicated that five rotis weighing overall 150 g were puffed in a time duration of 6.50 min with a fuel consumption of 0.1768 kg.
- The heat loss at outer periphery for 1st and 2nd model was evaluated to be respectively 24.31 and 35.27 W owing to lower skin temperature for model 1 over that for model 2.

References

1. http://www.indiaenergy.gov.in/docs/RE_Documentation.pdf
2. Haridas Roa P, Leelavathi K, Shurpalekar SR (1986) Test baking of chapatti—development of a method. *Coreal Chem* 63(4):297–303
3. Berrueta VM, Edwards RD, Masera OR (2008) Energy performance of wood-burning cookstoves in Michoacan, Mexico. *Renew Energy* 33:859–870
4. Gurushree MN, Nandini CR, Pratheeksha K, Prabhasankar P (2011) Gangadharappa Gundabhakthara Hosamane, design, development and performance evaluation of chapatti press cum vermicelli extruder. *J Food Sci Technol* 48(2):218–224
5. Kumar A, Prasad M, Mishra KP (2013) Comparative study of effect of different parameters on performance and emission of biomass cook stoves. *Impact Int J Res Eng Technol* 1(3): 121–126
6. Raman P, Ram NK, Murali J (2014) Improved test method for evaluation of bio-mass cook-stoves. *Energy* 1(17)

7. Huangfu Y, Li H, Chen X, Xue C, Chen C, Liu G (2014) Effects of moisture content in fuel on thermal performance and emission of biomass semi-gasified cook stove. *Energy Sustain Dev* 21:60–65
8. Arora P, Das P, Jain S, Kishore VVN (2014) A laboratory based comparative study of Indian biomass cook stove testing protocol and Water Boiling Test. *Energy Sustain Dev* 21:81–88
9. Gayad N, Tewari PG (2015) Performance enhancement of cook stove. *Int J Renew Energy Environ Eng* 03(01):2348–0157
10. Gallagher M, Beard M, Clifford MJ, Watson MC (2016) An evaluation of a biomass stove safety protocol used for testing household cook stoves, in low and middle-income countries. *Energy Sustain Dev* 33:14–25
11. Gogoi B, Baruah DC (2016) Steady state heat transfer modelling of solid fuel biomass stove: part 1. *Energy* 97:283–290
12. Obi OF, Ezeoha SL, Okorie IC (2016) Energetic performance of a top-lit updraft (TLUD) cook stove. *Renew Energy* 99:730–737
13. Overned RP (2009) Renewable energy sources charged with energy from the sun and originated from earth moon interaction 1:74–75/339–347
14. Ragland KW, Aerts DJ, Baker AJ (1991) Properties of wood for combustion analysis. *Bio-research Technol* 37:161–168

Computational and Experimental Investigations on Small Horizontal Axis Wind Turbine for Household Applications

Gurushant Koulagi, R.S. Hosmath, Ajitkumar Madival
and P.P. Revankar

Keywords Horizontal axis wind turbine (HAWT) · Angle of attack (α) · Lift coefficient (C_L) · Drag coefficient (C_D)

1 Introduction

Renewable energy is defined as the energy that is obtained from non-conventional energy resources such as sunlight, geothermal heat, tides, waves, and the wind. Wind energy being one of the renewable energy resources has gained considerable importance in recent years as it is widely distributed, non-polluting and is sustainable [1]. According to Ministry of New and Renewable Energy (MNRE), the wind power accounts nearly 8.9% of India's total installed power capacity and 61.37% of the total power capacity in renewable energy sector delivering 27,151.4 MW (as on 31.07.2016) of electrical power to the nation. Karnataka ranks fifth in India regarding installed wind power capacity indicating the potential ability of available wind power in the state. According to Karnataka Renewable Energy Development Ltd. (KREDL), the estimated wind power potential in Karnataka is 13,236 MW indicating the scope for development in wind energy sector. The work proposed in this paper deals with the wind potential analysis for the selected site (15.3647°N, 75.1240°E) and development of HAWT for wind energy extraction. The work proposed in the study concentrates on meeting the needs of energy demand in rural locations in Karnataka state (India) for lighting purposes. The rural or remote locations have lower lighting demands which to supply from electrical grids involves higher transmission losses. Thus, a decentralized system which can meet the needs of rural lighting energy demand based on on-site wind power

G. Koulagi (✉) · R.S. Hosmath · A. Madival · P.P. Revankar
Department of Energy Systems Engineering,
BVB College of Engineering and Technology, Hubballi, India
e-mail: gurushantk1@gmail.com

P.P. Revankar
e-mail: pp_revankar@bvb.edu

generation could be an alternative solution. A method by which the rural lighting needs can be met is presented in the paper by designing a suitable wind turbine and whose performance analysis is also presented using computational methods, tools, and experimental analysis.

2 Airfoil and Wind Turbine Basics

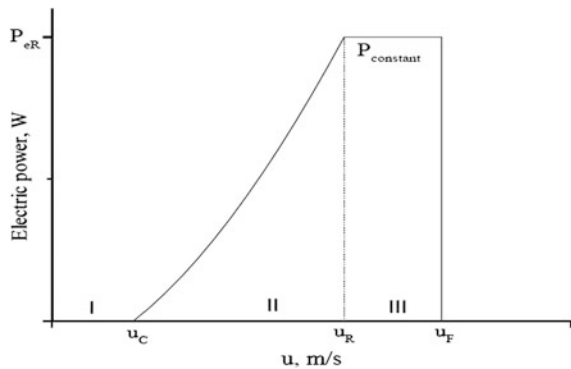
The airfoil structure of blades is one of the most important parameters for the turbine to convert kinetic energy from the wind into mechanical energy. According to Betz limit the wind turbine cannot turn the energy into the wind more than 59.3% of the incoming wind energy i.e. the maximum energy efficiency of a wind turbine which transforms the kinetic energy (KE) of the wind to mechanical energy (ME) of the turbine is only 0.593 and is called the power coefficient (Cp) [2, 3]. The general operating characteristics of a variable speed wind turbine are as shown in Fig. 1.

For the production of energy from the wind turbine, the key factor is operating speeds of wind. The wind speeds about wind turbine can be classified as cut-in, rated and furling wind speeds denoted by u_R , u_p and u_F , respectively [4]. The power variation trend in general for a variable speed wind turbine is represented as indicated in Fig. 1. In Fig. 1 the Region I will not contribute to any electrical power generation as the wind turbine is stationary while Region II and III are responsible for energy production as wind turbine blades start to rotate. The lift coefficient is related to the lifting force of the turbine and determines the ability of the turbine to start to rotate for a particular wind speed. The lift coefficient is given by:

$$C_L = \frac{2 \times L}{\rho \times V^2 \times A}$$

where L —length of the turbine blade, ρ —density of air, V —velocity of air, A —area of aerofoil.

Fig. 1 Power variation trend of a wind turbine [4]



The torque produced by a wind turbine is also the function of the tip speed ratio (TSR). It is observed that the maximum torque is generated at the particular value of TSR denoted by which is given as [4]:

$$\lambda = \frac{\omega R}{u}$$

where ω —angular velocity, R —radius of blade, u —wind velocity.

3 Computational Studies on Small Scale HAWT

Small scale wind turbines in the recent years have evolved largely due to improved technologies in the wind-based electricity power generation by providing a sustainable alternative for energy production. The proposed wind turbine in the present study is a small scale mini (1.25–3 m) [5] wind turbine having a nominal power rating of 350 W at a rated wind speed of 9 m/s and power coefficient to be 0.25. The site considered for installation of the wind turbine generating system should have considerable wind speed to sustain continuous wind power generation. The estimation of wind potential for power generation at the site can be done by statistical analysis taking information about wind speed data and direction of the wind at the selected location [6, 7]. The instruments like anemometer and wind vane also help in accurate measurements of wind data collected at the site [8]. The choice of the aerofoil structure in blade design plays a significant role in determining the performance characteristics of the blade like cut in speed, determining the rated speed and hence the power delivered by the blade. Thus, a suitable aerofoil must be designed so that the turbine operates at its optimal values at the selected site offering the desirable amount of electrical power. The aerofoil development of the blade in the present study is done using as open source software QBlade which is as shown in Fig. 2.

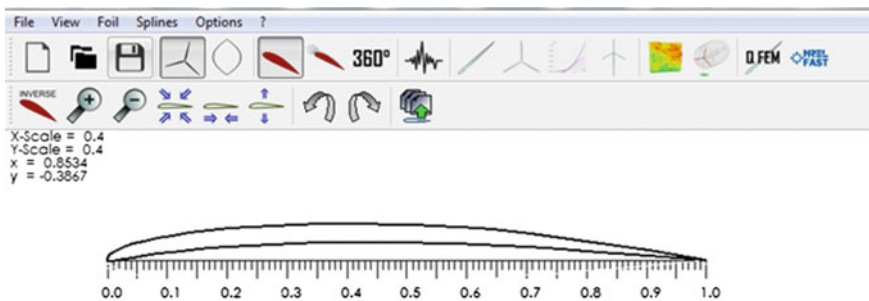


Fig. 2 Aerofoil structure development in QBlade

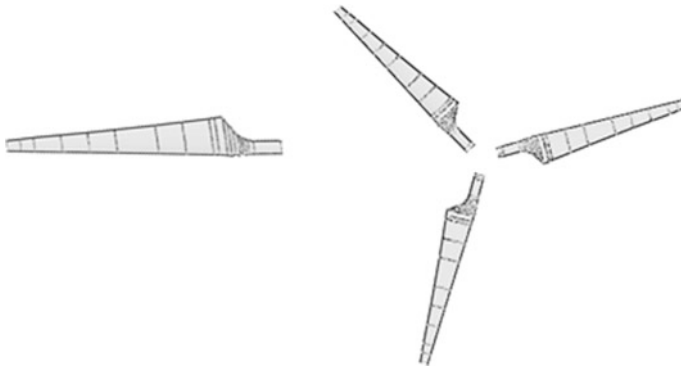


Fig. 3 Blade structure used in the present work

Based on the designed aerofoil shape, a suitable blade structure was developed, and then the performance testing was done to analyze the turbine for various performance parameters using QBlade software. The blade structure developed using QBlade is as shown in Fig. 3.

The aerofoil structure was then imported to CFD simulation tool to study the performance characteristics and ANSYS Workbench 14.5 is used as the computational tool for analysis of proposed aerofoil structure for small-scale wind turbines. The geometry of the airfoil is as shown in Fig. 4.

Triangular unstructured mesh has been used in the present study to obtain accurate results. Figure 5 shows the meshed geometry of aerofoil flow domain. The designed aerofoil was analyzed at various incoming wind speeds and different angle of attacks. The boundary conditions applied to the present study are as shown in Table 1.

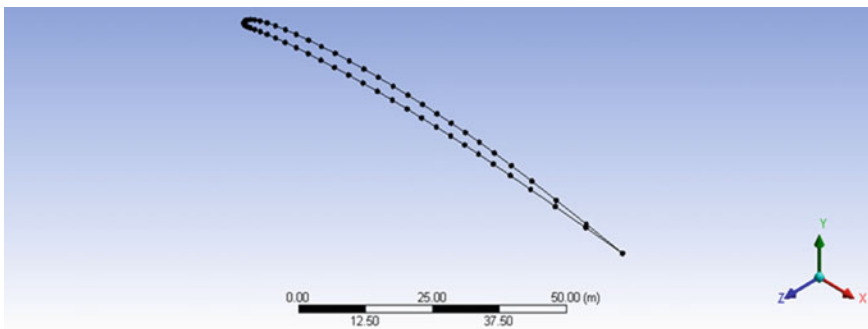


Fig. 4 Geometry of the developed aerofoil structure

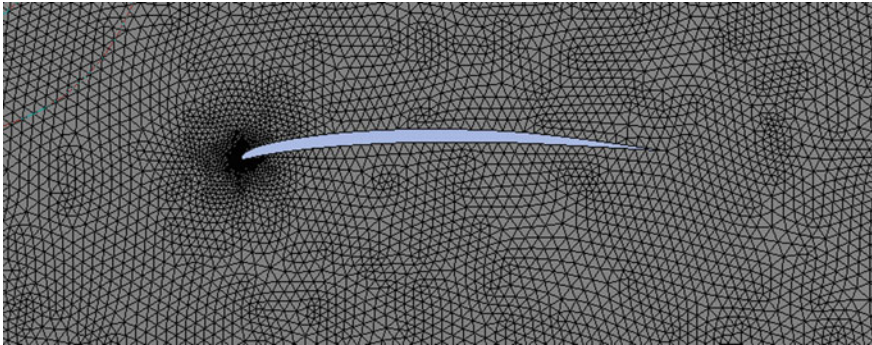


Fig. 5 Mesh generation of flow domain

Table 1 Specified boundary conditions

Parameters	Values
Analysis type	Pressure-based, 2D steady simulation
Turbulent model	SST K- ω
Fluid material	Air
Air density	1.225 kg/m ³
Inlet boundary condition	Flow velocity
Outlet boundary condition	Pressure
Wall condition	Stationary wall with no slip shear condition

4 Experimental Studies on Small Scale HAWT

The Blade design should be efficient to maximize the lift force and minimize the drag force, and the minimum drag force occurs on blade element when an aerofoil section of the blade should face the relative wind in such a way that the smallest possible area is exposed to the wind drag [9]. The wind velocity is constant throughout the rotor area, but the blade velocity increases from the inner edge to the tip. So, neither the magnitude nor the angle of relative wind is constant throughout the length of the blade. Thus the designed aerofoil has to face the relative wind at all points, and it should have a varying pitch angle along the blade. The lift force developed at the tip is higher than that at the inner edge. Hence the tip tries to move faster than the parts near to the center. This produces a stress that may cause blade failure. Moreover, the tension developed at the inner side due to centrifugal force is more than that at the tip. Both these problems can be solved by designing a tapered blade so that the blade area at the tip is less than the inner edge. To achieve a perfect balance of all these forces at all parts of the blade, it may sometimes be desirable to have a varying aerofoil section along the blade. Designing a wind turbine rotor system essentially involves determining the diameter of the rotor, some blades, blade profile, chord length, setting angle and height of the tower.

Fig. 6 Developed HAWT

The diameter of the proposed rotor is 2 m and the radius (turbine), or the length of a blade is 1 m. The HAWT blades designed is as shown in Fig. 6.

The wind turbine after installation at the site was then tested for various incoming wind speeds. Various turbine parameters like tip speed ratio, revolutions per minute (rpm), power content in the wind and the extracted power by the turbine were noted. The recorded parameters were noted, and the turbine produced 350.7 W of mechanical power extracted at rated wind speed of 9 m/s and power coefficient 0.25 and the tip speed ratio was calculated to be 7.19 at rated speed.

5 Results and Discussions

The flow over the developed airfoil is discussed in this section to demonstrate the effect of angle of attack and flow velocity over the lift and the drag coefficient. The aerofoil structure analysis was done in ANSYS (FLUENT) work bench 14.5 to compute and analyze the flow behavior of the fluid (air) around the aerofoil structure of the developed wind turbine blade. The simulation was done for free wind steam conditions the angle of attack considered are $\alpha = 0^\circ, 5^\circ, 7^\circ, 10^\circ$ at wind speed = 3 m/s. The computed pressure contours for various angle of attack and wind speed equal to 3 m/s are as shown in Fig. 7. It can be seen that as the angle of attack increases the stagnation point slowly shifts to the lower surface of the air foil inducing more lift to the aerofoil structure. The pressure distribution on the upper surface of the aerofoil decreases as the angle of attack increases indicating generation of lift.

The computed velocity contours for wind speeds 3 and 5 m/s and varying angle of attacks are as shown in Fig. 8. It can be seen that the velocity contours on the upper as well as on the lower surface decreases for the airfoil. The ability of the

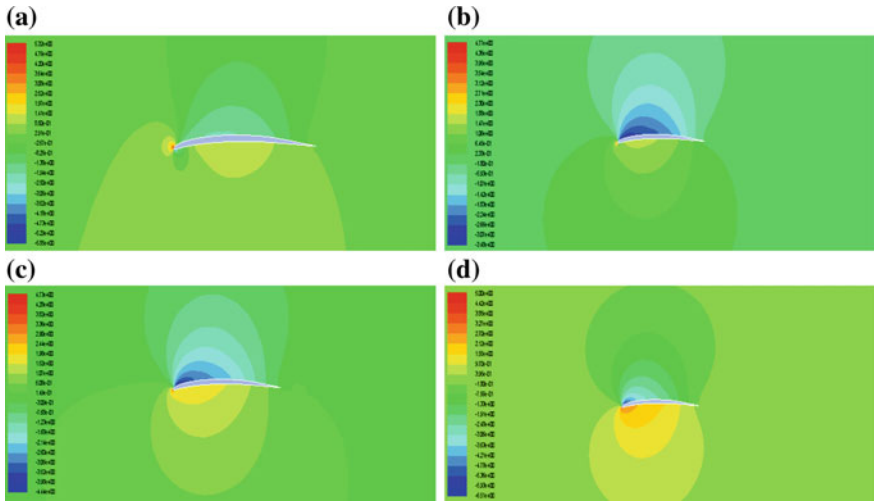


Fig. 7 Pressure contours around the airfoil at $\alpha = 0^\circ, 5^\circ, 7^\circ, 10^\circ$ and wind speed = 3 m/s

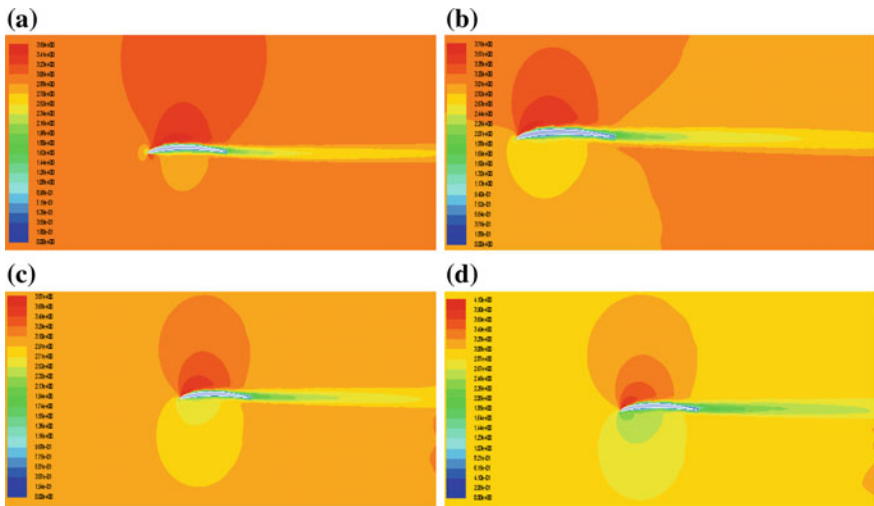
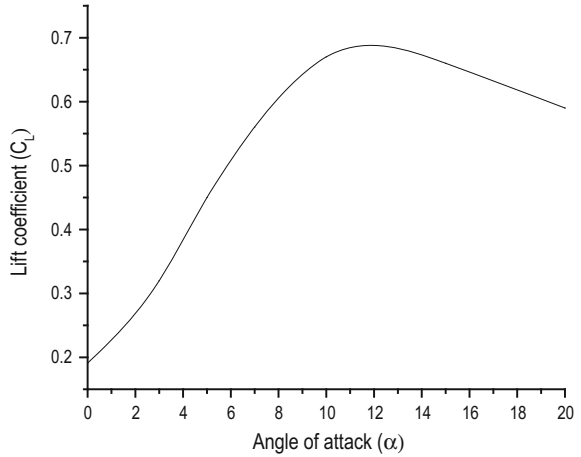


Fig. 8 Velocity contour around air foil at $\alpha = 0^\circ, 5^\circ, 7^\circ, 10^\circ$ and wind speed = 3 m/s

airfoil to lift when it is exposed to an incoming wind can be determined by lift co-efficient. Figure 9 shows the variation of lift co-efficient with the angle of attack. It can be seen that as the angle of attack increases the co-efficient of lift also increases indicating the force exerted on the aerofoil to be increasing giving the

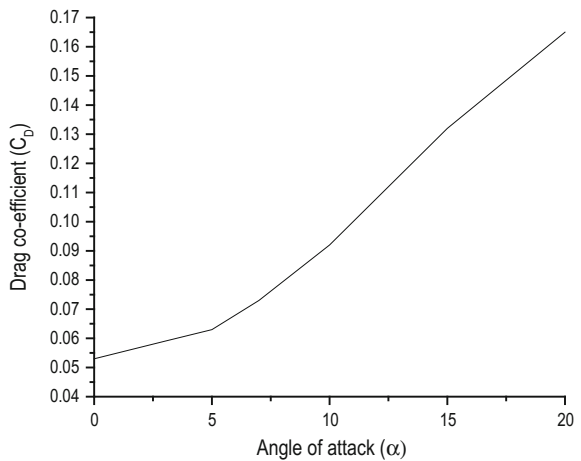
Fig. 9 Variation of lift coefficient with angle of attack



blade more lift. However, at the angle of attack equal to 12° and greater values, the lift generated was found to decrease.

The coefficient of drag is related to the drag force, and it is the force acting in the direction of the motion of the wind. The drag coefficient should be as low as possible so that the wind turbine must be able to produce electric power even at low incoming wind speeds. Figure 10 indicates the variation of drag coefficient with angle of attack depicting an increase in drag coefficient as the angle of attack rises. A maximum drag coefficient of 0.165 was observed for the aerofoil.

Fig. 10 Variation of drag coefficient with angle of attack



6 Conclusions

The work presented the development of a decentralized small scale HAWT for wind power extraction in rural locations. The aerofoil analysis of the blade based on CFD analysis indicated the maximum value of lift coefficient of 0.665 at 12° angle of attack with corresponding drag coefficient 0.09. The performance characteristics of the developed HAWT like cut-in, rated and furling wind speeds were 2.5, 9 and 12 m/s respectively. The tip speed ratio of the wind turbine is 7.19, and the power coefficient is 0.25 at the rated wind speed. The maximum mechanical power extracted was 350.7 W at the rotational speed of 550 rpm at a wind stream of 9 m/s.

References

1. Johnson GL (2001) Wind energy systems (electronic edition)
2. Drumheller DP, Antonio GCD, Chapman BA, Allison CP, Pierrakos O (2015) Design of a micro-wind turbine for implementation in low wind speed environments. In: Systems and information engineering design symposium (SIEDS), pp 125–130
3. Bukala J, Damaziak K, Kroszczynski K, Krzeszowiec M, Malachowski J (2015) Investigation of parameters influencing the efficiency of small wind turbines. *J Wind Eng Ind Aerodyn* 146:29–38
4. Bhadra SN, Kastha D, Banerjee S (2005) Wind electrical systems. Oxford University Press, Oxford
5. Tummala A, Velamati RK, Sinha DK, Indraj V, Hari Krishna V (2016) A review on small scale wind turbines. *Renew Sustain Energy Rev* 56:1351–1371
6. Sun Y, Zhang L (2010) Numerical simulation of the unsteady flow and power of horizontal axis wind turbine using sliding mesh. In: 2010 Asia-Pacific power and energy engineering conference, pp 1–3
7. Salem H, Diab A, Ghoneim Z (2013) CFD simulation and analysis of performance degradation of wind turbine blades in dusty environments. In: 2013 international conference on renewable energy research and applications (ICRERA), pp 827–832
8. Abdelrahman MA, Abdellatif OE, Moawed M, Eliwa A, Misak S (2015) The CFD performance analysis for horizontal axis wind turbine with different blade shapes and tower effect. In: 16th international scientific conference on electric power engineering (EPE), pp 754–759
9. Chaudhary U, Nayak SK (2015) Micro and small-scale HAWT blades airfoils study through CFD for low wind applications. In: 2015 annual IEEE India conference (INDICON), New Delhi, pp 1–6

Computational and Experimental Studies on Effect of Artificial Roughness on Performance of Solar Air Heater

Vishwanath Kardi, A.P. Madival, M.B. Gorwar and P.P. Revankar

Keywords CFD · Solar air heater · Broken rib fin configuration · Chamfered rib fin configuration · Ansys CFX

1 Introduction

Today world the analysis of different types of real systems through computer simulation has become a common practice before its practical application. Which helps to understand the interaction of the parts of a real system, and of the system as a whole. The level of understanding through this method is seldom achievable via any other discipline. This is a wide spread modeling approach which utilizes numerical methods and computer simulations to solve and analyze problems that involve transport phenomena in fluid flows. Lots of commercial and open computer codes are implementing CFD technique: ANSYS FLUENT, ANSYS CFX, FLOW-3D, STAR-CD, COMSOL CFD, Open FOAM, Open FVM and many others. Are similar kind of tools numerical simulation/modeling tools are in practice by the scientists and engineers. Simulation models of the real system are developed based governing equations and suitable boundary conditions, as the complexity of the system increases the model complexity. Hence it difficult develops such types of the simulation model. In the present work CFX, 14.5 was used to develop the simulation model of the cabinet of solar crop dryer to analyze the velocity and temperature components of circulating air inside the collector.

The computer simulation model was developed using CFX 14.5 was based on control volume approach. In this approach, structured numerical algorithms were designed for an infinitesimal small control volume. The governing equations are derived from Navier stroke equations with some boundary conditions used to solve fluid flow and heat transfer problems. Few such examples are the governing equations derived for conserve mass and energy, for the net forces acting on the

V. Kardi (✉) · A.P. Madival · M.B. Gorwar · P.P. Revankar
Department of Mechanical Engineering, BVBCET, Hubballi, India
e-mail: vnath.kardi@gmail.com

control volume is equivalent to the time rate of change of linear momentum and for laminar and turbulent fluid flow systems. These equations are called as, energy equation, momentum equation, and continuity equation.

Energy equation:

$$\frac{\partial \rho E}{\partial t} + \frac{\partial \rho u_j E}{\partial x_j} = \frac{\partial p}{\partial t} - \frac{\partial}{\partial x_j} (U_i \tau_{ij} + Q_{ij}) \quad (1)$$

Momentum equation:

$$\frac{\partial u_i}{\partial t} + u_i \frac{\partial (u_j)}{\partial x_j} = - \frac{1}{\rho} \frac{\partial p}{\partial x_j} \quad (2)$$

Continuity equation:

$$\frac{\partial \rho}{\partial t} + \frac{\partial \rho u_i}{\partial x_i} = 0 \quad (3)$$

The computational studies revealed that artificial roughness helps to produce turbulent flow inside solar collector duct to enhance the heat utilization factor [1]. An early study of the effect of roughness on friction factor and velocity distribution was performed by Yadav [2], who conducted a series of experiments with the numerical investigation to analyze the incompressible flow through artificial roughened solar collector ($3800 < R < 18,000$) with equilateral triangle type rib. Kumar [3] reported on performance study of a solar collector provided with V-shaped, multiple V-shaped fins and gap in multi V-shaped fins artificial roughness using CFD. The fin geometry (V-shaped, multi V-shaped fins) influence on convective heat transfer was investigated using roughness elements, fin spacing and other operating parameters [3]. Geometry and operating parameters of collectors have an impact on fluid flow characteristics. The advanced computer software and development of numerical methods supported efficient and convergent simulations of the collector. It was concluded that CFD was one of the useful tools to detect the better configuration of fin for its optimum thermal performance. The different approaches used to investigate thermal performance of collector were reviewed and explained concerning CFD tool like ANSYS FLUENT [4].

2 Methodology

The present work is done by using ANSYS CFX 14.5 which consists of three important elements viz: (1) a pre-processor, (2) a solver and (3) a post-processor. The first step in any CFD analyses is the definition and creation of geometry of flow region for the CFD calculations. It consists of the input flow problem to a CFD

program using an operator-friendly interface and the subsequent transformation of this input into a form suitable for use by the solver.

Mesh generation constitutes one of the most important steps during the pre-process stage after the definition of the geometry. CFD requires the subdivision of domain into some smaller, non-overlapping of sub-domains to solve the flow physics within the domain geometry that has been created; this results in the generation of a mesh of cells overlaying the whole domain geometry. The accuracy of the CFD solution is governed by the number of cells in the grid.

The use of unstructured mesh has become more relevant and widespread in many CFD applications. Here the cells are allowed to be assembled freely within the computational domain the most typical shape of an unstructured element is a triangle in two dimensions or a tetrahedron in three dimensions, any other elemental shape including quadrilateral, or hexahedral cells are also possible. Triangular or tetrahedral cells in comparison to the quadrilateral or hexahedral cells are usually ineffective to resolve wall boundary layers. The block-structured or multiblock mesh is another special case of a structured mesh. The mesh is assembled from some structured blocks attached to each other. Instead of the block-structured mesh where the attachment of some adjacent blocks is realized at block boundaries, the use of overlapping grids to cover the irregular flow domains further presents another grid generation approach in handling complex geometries. Here, the rectangular, spherical or no orthogonal grids can be combined with the parent Cartesian grids in the solution domain. Block-structured grids with overlapping blocks are sometimes referred as Chimera grids. The mesh generation for the dryer unit is shown in Fig. 1. Over 50% of the time spent in the industry on a CFD project is devoted to the definition of the domain geometry and grid generation.

Once the created body is done in the design modeler, it is then attached to meshing tool. The named selections are edited by specifying the inlet and the outlet for the designed geometry. The inlet is shown with blue and outlet with red. The default option shows the dialogue box for different preferences of creating the mesh. The physical preference is set as CFD and the solver preference to the fluid. The sizing option allows setting the required mesh sizes which effect on the accuracy of the resulting answers. The advance size center is set to on curvature with relevance center fine and smoothing to be the medium and slow transition. Curvature normal angel is set to be 36 °C and remaining the other options to be the default. The inflation options are set to program controlled, and the inflation option is set to smooth transition with maximum layers of 5 and growth rate of 1.2 and all the other options are left to take the default values and the generate mesh is activated. The mesh will create and then the statistics option is selected which shows the total number of nodes and elements and in mesh metric the orthogonal quality is selected which shows the average deviation which should be less than 1 and then saved. The meshing inputs referred during the study were given in Table 1.

The simulation model of proposed system was analyzed by using ANSYS CFX that combines an advanced solver with powerful pre and post processing facilities. It consists of the following inbuilt features: An advanced coupled solver that is both reliable and robust. Integration of definition of the problem, analysis, and

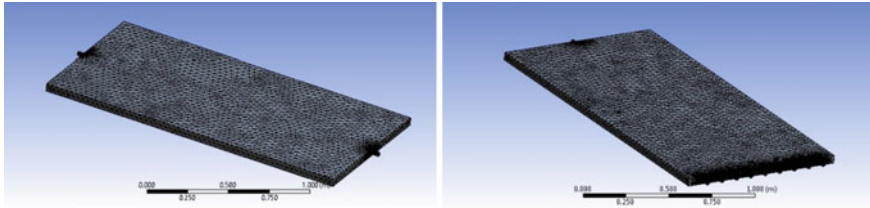


Fig. 1 Grid generated for the computational study

Table 1 Input values for the meshing software

Physical preference	CFD
Solver preference	CFX
Relevance centre	Fine
Smoothing	Medium
Transition	Slow
Inflation	Program controlled
Inflation option	Smooth transition
Nodes	96995
Elements	329046
Mesh metric	Orthogonal quality

presentation of the results. An instinctive and interactive setup process, using set menu and innovative graphics. Navier-Stokes equations are used to derive the governing equations with the boundary conditions involved in the heat transfer and fluid flow solutions.

There is provision for the creation of geometry and geometry can be imported from most major CAD packages using native format. The aim of the simulation in this work is to investigate the effect of some inlets to the collector on the flow distribution and the end results regarding outlet pressure and temperature. One of the cad tool called as SOLIDEDGE has been used to model the flow medium. The number of inlets to the collector has been varied from 1 to 9. The analysis was made for the collector having the dimensions obtained from the preliminary design and having the chamfered fin configuration. Once the model has been imported, it then meshed in the pre-processing stage. The primary domain was divided into number subdivisions by the generation of a mesh. The number of grid cells governs the accuracy of the CFD solution. Figure 1 shows the meshed fluid domain.

The physical models which have to be included in the simulation are selected. Fluid properties and boundary conditions are specified. Table 2 gives the list of boundary conditions applied during the computational study.

The Solver is the primary component which is used to evaluate the CFD problem. The results produced by the Solver in a batch or non-interactive process. The control volumes from the region of interest are applied to integrated partial differential equations. It's nothing but the application of a fundamental law of conservation (Ex. mass or momentum) to each and every control volume. The

Table 2 Details of boundary conditions

Sr. No.	Boundary	Boundary details	Values
1	Inlet	Inlet temperature	28 °C
		Static pressure	1 atm
2	Outlet	Mass flow rate	0.02 kg/s
3	Fin surface	Emissivity	0.2
		Diffuse fraction	0.33
		Emissivity	0.8
4	Glass	Diffuse fraction	1
		Radiation heat source	1000 W/m ²

Fig. 2 Experimental set-up of solar air heater



fabricated air heater was field tested for its performance. The dimensions of fabricated air heater were $2 \times 1 \times 0.01$ m. Having a bed of 5 cm, thick glass wool is used as the insulating material. The experiment was conducted at the terrace of the Mechanical Department of BVBCET, Hubballi having the geographical location 15.3647°N , 75.1240°E . The values of Insolation, collector outlet temperature, and ambient temperature were noted at a period of 10 min. Figure 2 shows the setup of solar air heater.

3 Results and Discussions

The simulation results obtained from ANSYS CFX were represented in the graphical form. The variation in the flow distribution for the different number of collector inlets having broken fin structure is shown in Fig. 3a-i.

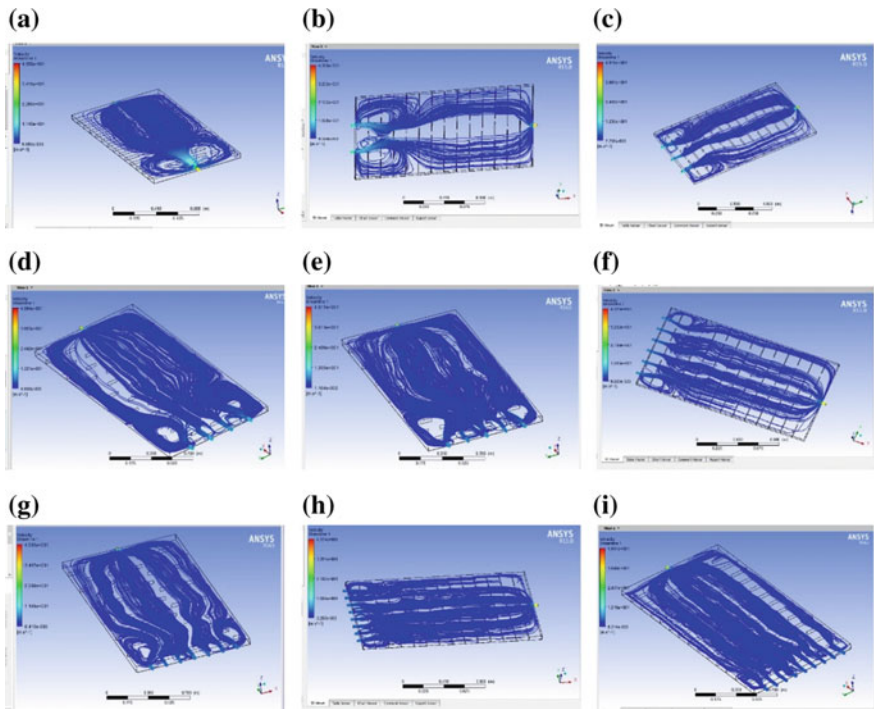


Fig. 3 Flow distribution in solar air heater with 1–9 inlet holes with broken rib fins

The simulation results obtained from ANSYS CFX were represented in the graphical form. The variation in the flow distribution for the different number of collector inletshaving chamfered fin structure is shown in Fig. 4a-i.

Figure 3a shows the distribution of air in the collector with single inlet where two air pockets are created due to back pressure generated at either side of the inlets. Figure 3b shows the distribution of air in the collector with two inlets where two air pockets are created due to back pressure generated at either side of the inlets. Figure 3c, d shows the distribution of air in the collector with three and four inlets where some air pockets created due to back pressure were less than the collector with two inlets. Also, the distribution of flow is better in these configurations. Figure 3e, f shows the distribution of air in the collector with five and six inlets where number air pockets created due to back pressure were less than the earlier collector inlets. Also, the distribution of flow was better in these configurations. Figure 3g, h shows the distribution of air in the collector with seven and eight inlets where number air pockets created due to generated back pressure were less than the earlier collector inlets. Also, the distribution of flow is better in these configurations. Figure 3i shows the uniform flow distribution in the collector with nine inlets which results from better extraction of heat and uniform pressure distribution with less pressure drop. Same results were observed during the simulation

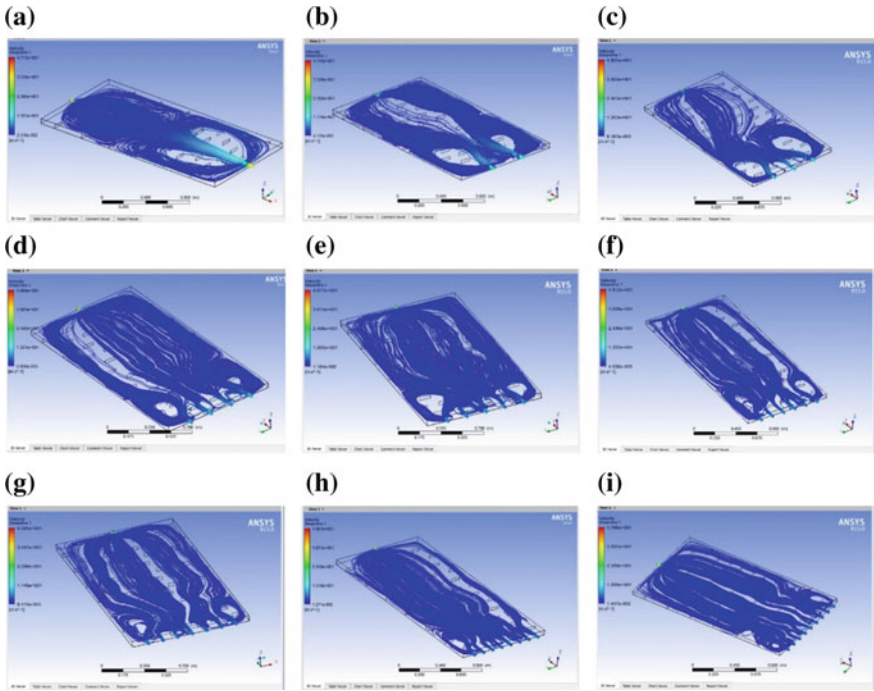
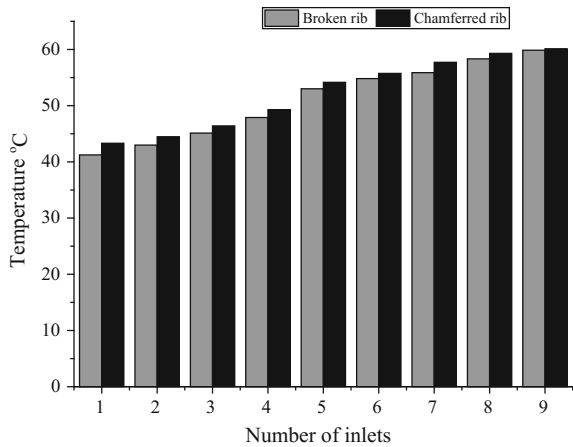


Fig. 4 Flow distribution in solar air heater with 1–9 inlet holes with chamfered rib fins

Fig. 5 Comparison of outlet temperature for broken and chamfered rib collector



of air heater with chamfered fin structures. The variations in flow distribution for chamfer finned air heater with nine-hole configuration were shown in Fig. 4a–i. Simulation results of broken rib and chamfer rib finned collector were studied by considering the outlet temperature and pressure of the collector. Figures 5 and 6

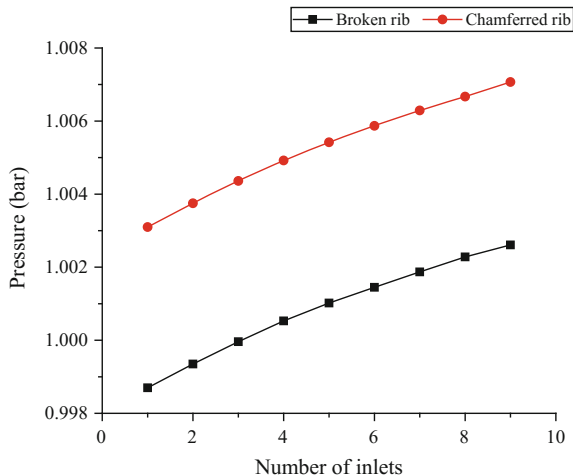


Fig. 6 Comparison of outlet pressure for broken and chamfered rib collector

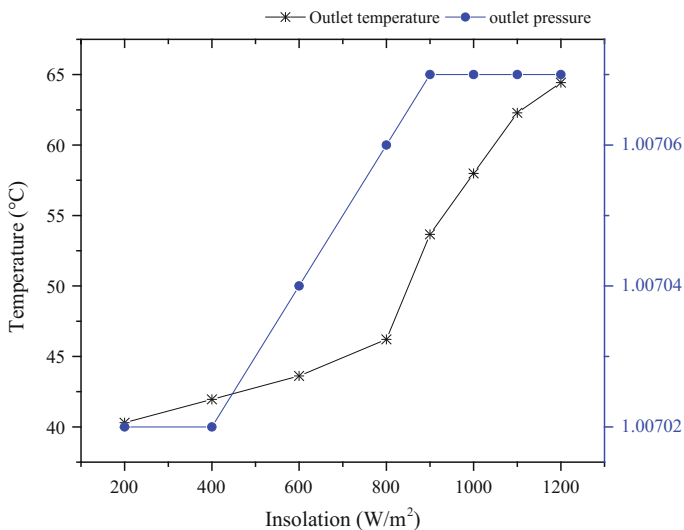


Fig. 7 Effect of solar insolation on outlet temperature and pressure of chamfer finned air heater

show the comparison of both the fin configuration based on temperature and pressure of working fluid and Fig. 7 and 8 shows effect of solar insolation and mass flowrate on outlet temperature and pressure of chamfered rib air heater.

A significant increase in the outlet temperature with the reduction in pressure drop was observed in the case of chamfer finned collector than a broken rib. So the chamfer fin configuration was selected for further investigation of the effect of isolation and mass flow rate on the collector outlet. The effectiveness of heat

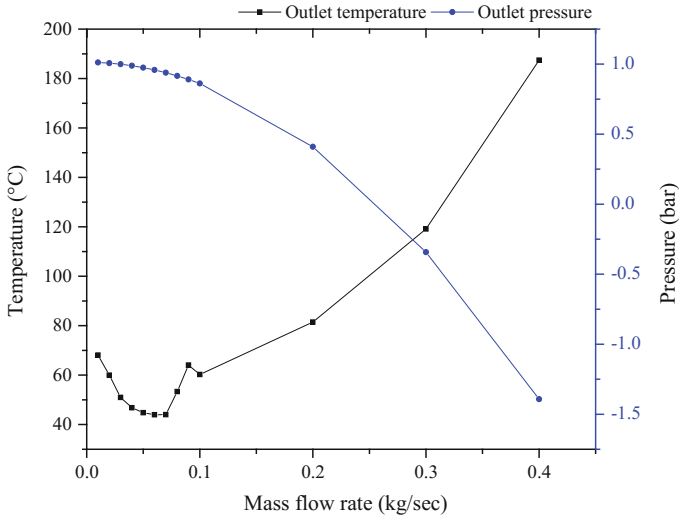
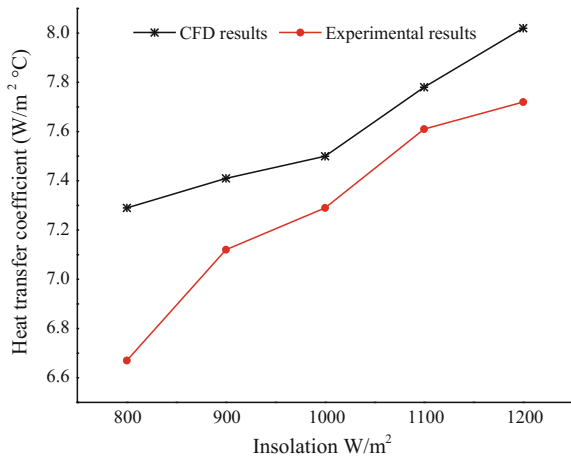


Fig. 8 Effect of mass flow rate on outlet temperature and pressure of chamfer finned air heater

Fig. 9 Comparison of CFD and experimental results



transfer was evaluated for the experimental observations made regarding the convective heat transfer coefficient between the air and absorber plate. The obtained experimental results were compared with simulation results for validation of the same. Figure 9 shows the experimental validation of the obtained CFD results. At an insolation of 1000 W/m², the heat transfer coefficient of 7.5 and 7.29 W/m² °C were obtained through CFD and experimental results respectively.

4 Conclusions

Based on the study, the following conclusions are made

1. The study indicated that use of solar air heater with the nine-hole configuration as against the single hole configuration performed better regarding providing the higher temperature of air with improved heat transfer coefficient.
2. The simulation results showed that the outlet temperature range between 65 and 70 °C was obtained for insolation in the range 1000–1200 W/m² and the better air distribution was obtained for designed model of the solar collector with nine-hole configuration.
3. Chamfered rib configuration is better than broken rib as it shows better heat extraction and reduced pressure drop. An outlet pressure of 0.99 and 1.031 bar obtained for the broken rib and chamfered rib configuration respectively.
4. From the simulation of collector for the different flow rates, it can be concluded that the flow rate of air was assumed to be 0.02–0.03 kg/s so for all the products the same range flow rate was retained and this was to be considered as optimum.
5. CFD results are validated by experimental results. With an insolation of 1000 W/m², the heat transfer coefficient of 7.5 and 7.29 W/m² °C were obtained through CFD and experimental results respectively. About 2–3% of deviation was found in CFD and experimental results.

References

1. Yadav AS, Bhagoria JL (2013) A CFD (computational fluid dynamics) based heat transfer and fluid flow analysis of a solar air heater provided with circular transverse wire rib roughness on the absorber plate. *Energy* 55:1127–1142
2. Yadav AS, Bhagoria JL (2014) A CFD based thermo-hydraulic performance analysis of an artificially roughened solar air heater having equilateral triangular sectioned rib roughness on the absorber plate. *Int J Heat Mass Transf* 70:1016–1039
3. Kumar A (2014) Analysis of heat transfer and fluid flow in different shaped roughness elements on the absorber plate solar air heater duct. *Energy Procedia* 57:2102–2111
4. Gawande VB, Dhoble AS, Zodpe DB, Chamoli S (2016) A review of CFD methodology used in literature for predicting thermo-hydraulic performance of a roughened solar air heater. *Renew Sustain Energy Rev* 54:550–605

Design and Development of Novel Mini Wind Power Turbine Set

B. Magade Pramod and P. Chavan Shrirang

Keywords Blade design · Novel shape · Horizontal axis wind turbine and wind power

1 Introduction

Energy available in various forms as nature's gift has been playing vital role in the progress of world. In fact, there is positive relation between GDP growth and availability of energy. With growing population and industrial revolution the consumption of energy has increased with exponential rate that endangered the conventional energy sources, particularly fossil fuels [1, 2]. As governments of worldwide countries are promoting and pushing for the renewable energy technologies, providing various fiscal/financial incentives, to meet the basic energy needs of communities. Along with all renewable energy options, wind power has caught the attention of world and is today the fastest growing commercially competitive source of green energy. It is because it is available in nature free of cost, widely distributed and do not create pollution. The use of wind machines to harness the energy from wind is not the new concept. It has been used since 2000 B.C. for pumping water from well for irrigation purpose and for grinding grains. Since last two decades, intensive research and development took place for conversion of wind energy into electricity. This development is going to address issue of global warming and climate change which causing towards reducing greenhouse gases [3, 4].

In this study, from survey of various existing windmills, the toy windmill is selected to utilise the wind motions generated on highways due to the traffic motions to obtain electrical energy. The advantage of this turbine is of low starting

B. Magade Pramod (✉) · P. Chavan Shrirang
Walchand College of Engineering, Sangli, India
e-mail: Pramod.magade@gmail.com

P. Chavan Shrirang
e-mail: Chavan.walchand@gmail.com

wind speed of 2–4 m/s. Initially small model of a toy wind turbine is developed with easily available materials with varying number of blades. The corresponding assembly is mounted in proximity to vehicular passageways. The wind created by the traffic will be used to rotate the blades and their attached generators to produce electrical energy. The power generated by the generator can be stored in a battery and can later be used to power the road lights.

2 Design of Turbine

The conversion process utilizes aerodynamic forces (lift and/or drag) to produce a net positive turning moment on a shaft, resulting in the production of mechanical power which can be converted to electrical power [5]

$$P_{wind} = \frac{1}{2} \times \rho \times A \times V^3 \times h \quad (1)$$

The primary objective in wind turbine design is to maximize the aerodynamic efficiency or power extracted from the wind. So it is clear that a longer blade will favor the power extraction. But, with an increase in blade length, deflection of blade tip due to axial wind force also increases. So a blind increase in the length of the blade may lead to a dangerous situation of collision of blade and tower.

For different loading condition (such as point load and UDL) deflection and the equivalent stresses arise in trapezoidal, and micro shape blade is going to calculate by analysis. Stresses occur in the blade is safe or fail is depends on the load applied on the respective sections. The number of nodes used for meshing is 241892. Figure 1 shows the stresses generated for various configurations of turbines and the values of stresses are shown in Table 1.

3 Fabrication of Turbine

In a quest to study the generation of electricity from wind energy, on the basis of the structural analysis, two models of MHAWT are developed. One is of PVC (Polyvinyl Chloride), and another is sheet metal having gauge 26 (thickness of 0.55 mm), with increasing the numbers of blades (i.e., five and eight) for getting maximum torque. Wind energy recaptured from the energy expended by the moving vehicles. In the testing of three, five blades suitable amount of torque is not generated for development of voltage and current, so decided to go for manufacturing of eight blade model. The diameter of the blade was selected 0.85 m from above equation. Following are the models of the corresponding blade is shown in Fig. 2.

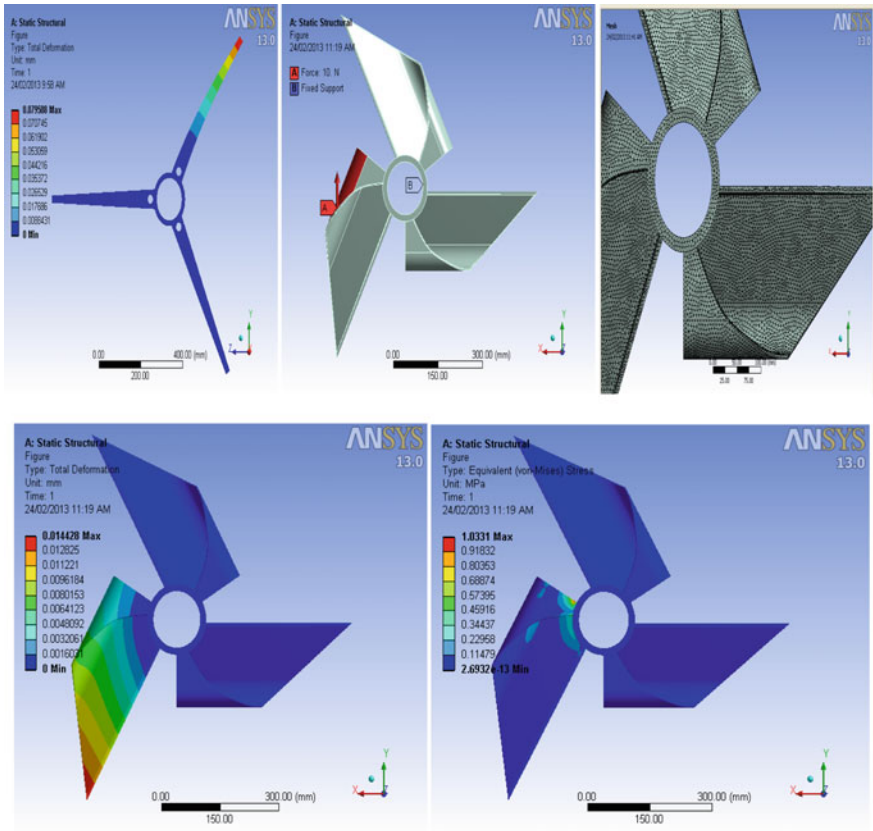


Fig. 1 Structural analysis of PVC and novel shape blade with 10 N load

Table 1 Comparison of the results for two type’s blade model

Sr. No	Shape of blade	Load applied (N)	Total deformation (mm)	Equivalent stresses (MPa)
1.	Trapezoidal blade	Point load 10 N	12.85	21
		UDL of 10 N	0.07	5.17
2	Micro shape blade	UDL of 10 N	0.014	1.03
		UDL of 15 N	0.021641	1.54
		UDL of 20 N	0.028855	2.06

After manufacturing blades and supporting structure, the generator, and shaft of the rotor are directly coupled and mounted on supporting structure as shown in Fig. 3.



Fig. 2 PVC and sheet metal model of five and eight blades



Fig. 3 Assembled model

4 Testing of Mini Wind Turbine

After completing the assembly, in-house testing is carried out with wind speed regulated from 0 to 10 m/s as shown in Fig. 4.



Fig. 4 In-house testing

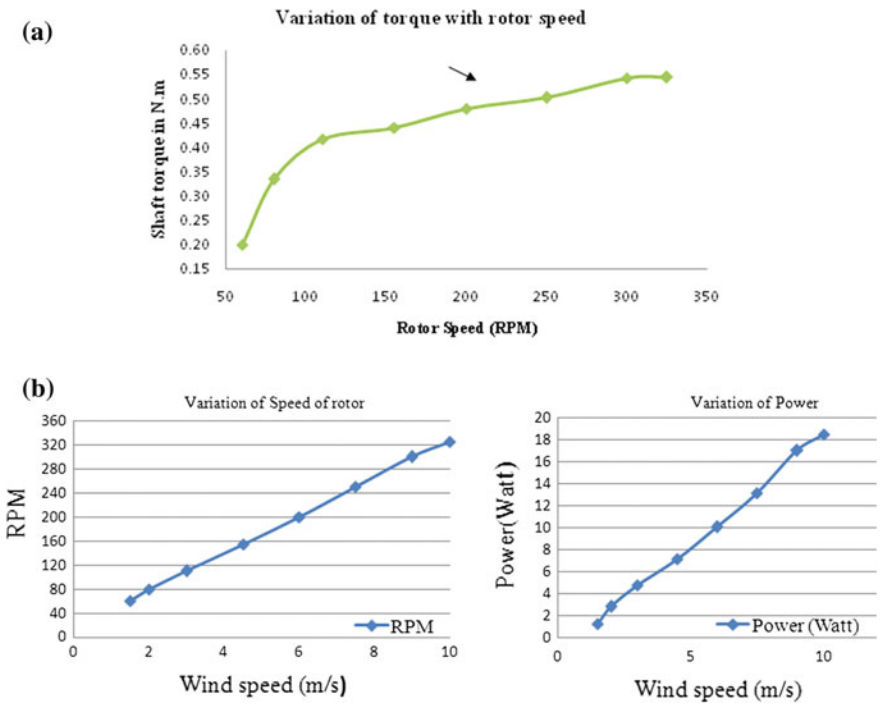


Fig. 5 a Variation of torque with rotor speed b Variation of torque with rotor speed and Variation of speed of motor and power



Fig. 6 Highway testing setup

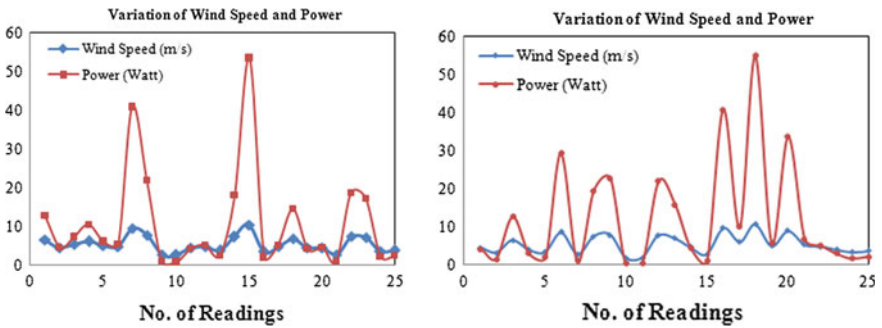


Fig. 7 Onsite measurement of wind speed along of power for two turbines

The shaft torque curve reached a peak value of 0.54 N.m at a rotor speed of 300 RPM, corresponding to a wind speed of 9 m/s and power output of 17–19 W (Fig. 5). RPM and wind velocity relation is directly proportional.

As shown in Fig. 6, an onsite testing is performed on roadside and the variation of wind speed and power measurement are shown in the Fig. 7, respectively.

5 Conclusion

The goal of this study is to come up with a mechanism to harvest the wind energy generated by fast moving vehicles. Conclusions of the study are listed below:

- (1) The new wind power turbine starts generating power at an average wind speed of 1.5 m/s which is lower than the cut-in speeds of most of the wind turbines (usually varying between 3 and 4 m/s) currently available in the market.
- (2) With the external load, the variation in power output was 0 to 18.48 W for wind speed ranging from 0 to 10 m/s.
- (3) The shaft torque versus rotor speed curve showed a peak value of 0.54 Nm at a rotor speed of 300 RPM, corresponding to a wind speed of 9 m/s and power output of 17 W.
- (4) However, it is prudent to mention here that field test results proved the existence of a new concept in wind turbine design. Further, it is the first model of the new wind turbine, after successful lab testing it was subjected to full-scale field testing, these field tests pointed out certain clues for improvement in design. It is, therefore, concluded that the field test results should be viewed as the beginning of a new chapter in wind turbine technology rather than giving an absolute measure of success or failure of the new wind turbine.

References

1. Percival MC, Leung PS, Datta PK (2005) The development of a vertical turbine for domestic electricity generation. University of Northumbria, School of Engineering, Ellison Building, Ellison Place, Newcastle Upon Tyne, Tyne and Wear, UK, NE1 8ST
2. Bilgen AW (2003) Wind power generating system. Patent application No.: 10/741, 544 Filed: 19 Dec 2003
3. Crinion J (2003) Wind driven power generator. Patent application No.: 10/352, 97, Filed: 29 Jan 2003
4. Lockington M, Martin E, Tsai H (2002) Wind power preliminary study. Queen's University Physical Plant Services
5. Wagner H-J, Mathur J (2009) Introduction to wind energy systems-basics, technology and operation. Springer Series in Green Energy and Technology, pp 1–4. ISSN 1865-3529

Treadle Pump Operation with Rotary Motion

Pawan Kumar Tiwari, S.N. Singh, Subir Kumar Saha
and Davinder Pal Singh

Keywords Treadle pump · Rural technology · Improvement · Farmers

1 Introduction

Hand pumps are in use since many years for pumping water from the ground. It consists of a cylinder fitted with a piston and a pushing mechanism for the up and down motion of the piston. A pipe connects the pump to the water source. At the end of the pipe, a non-return valve is fitted that allows water to enter the pipe and stops it from flowing back into the source. When the piston is pushed down, the water is pushed through a small valve in the piston to fill up space above it. When the piston is raised again the water comes out from cylinder to irrigation channel. The downward stroke of the piston once again pushes water through the small valve into space above the piston and the process is repeated. This is a very simple principle used for centuries for lifting water from streams and wells. The amount that can be lifted in this way is usually small, however, because pumps that use this idea are hand operated and the effort required to lift water is considerable [1–3].

To overcome the above-mentioned problems with the pump, hand operated driving mechanism is replaced by the foot operated mechanism. In this improved mechanism, power input is given through treadles. The advantage of this mechanism is that input can be given by comparatively stronger foot muscles. By providing treadles not only effort is minimized but also one can operate this for a longer period. A frugal model of treadle pump is shown in Fig. 1. Based on the principal of operation mentioned above a model has been developed under RuTAG (Rural Technology Action Group) IIT Delhi with certain modification.

P.K. Tiwari (✉) · S.N. Singh
Department of Applied Mechanics, IIT Delhi, Delhi, India
e-mail: pawan8iitd@gmail.com

S.K. Saha · D.P. Singh
Department of Mechanical Engineering, IIT Delhi, Delhi, India

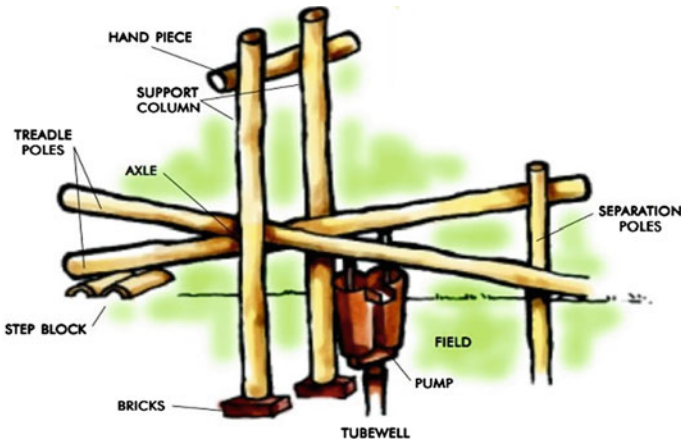


Fig. 1 Existing treadle pump model (Source water and sanitation program, write media)

The idea of treadle pump has been skilfully adapted to this model for use in irrigation, where much greater volumes of water are needed. In this treadle pump, two cylinders are used. Each piston moving in the cylinder is connected to a treadle. The operator stands on the treadles and presses them up and down, and treadles follow a reciprocating motion. All parts used in this model are standard hand pump and pumping parts available in the market. Parts are made detachable so that they can be replaced as per the need. With the current modification now the operation is much smooth than previous models (Fig. 2).

Though providing the driving force for feet and leg made the operation easier, but yet it is not a fully optimized solution. This motivated us to look for an improved design for the following reasons—

1. Providing continuous power even by reciprocating motion through treadles is a tough task.
2. Use of renewable energy resources such as wind/solar in rural areas.
3. To enhance the capacity to lift water from a higher depth and higher overall discharge.
4. Capability to have discharge as continuous.

These points show that there is need to develop a hybrid model which can be operated either by foot or by solar input. Based on these initial observations a 3D model has been developed in Solid Works to convert reciprocating motion into rotary motion (Fig. 3).

A detailed literature survey was done to understand the issues. Fraenkel [1] observed that a reasonably fit, well fed human being between 20 and 40 years old could produce a steady power output of around 75 W for long periods. He summarizes his findings and observations by calculating the discharge and head for an input power of 75 W at 50% efficiency as shown in Table 1.

Fig. 2 Treadle pump (Source RuTAG IIT, Delhi)



Orr et al. [2] indicated that output from a pump depends on a variety of factors, including a suction lift, cylinder diameter, variations in internal friction, occasional air leaks in the installation, hard filters, skills and care of the installation team and the weight and ability of the operator. By their key findings, they have proposed a relationship between suction lift, cylinder diameter, and discharge which is listed in Table 2.

On the basis of their research IDE (International Development Enterprises) has given some pump design feature which is presented in Table 3.

As given in IDE data a typical diameter for the cylinder of the pump is observed to be 100 mm. There are two strokes which are to be considered while designing treadle pump the foot stroke length and the piston stroke length. The foot stroke length is the vertical distance between the feet when one foot is raised, and the other is at its lowest point. If the stroke is too short, the leg muscles tire quickly; if it is too long, the leg muscles are strained. An optimized stroke length can be approximated distance between two bicycle paddles which are around 340 mm.

We cannot keep our piston stroke length equal to bicycle stroke length because it will need more power and will slow the operation. If a choice is given, an operator would usually choose a short stroke length for high heads so that input power can

Fig. 3 A 3D CAD model of improved Treadle Pump

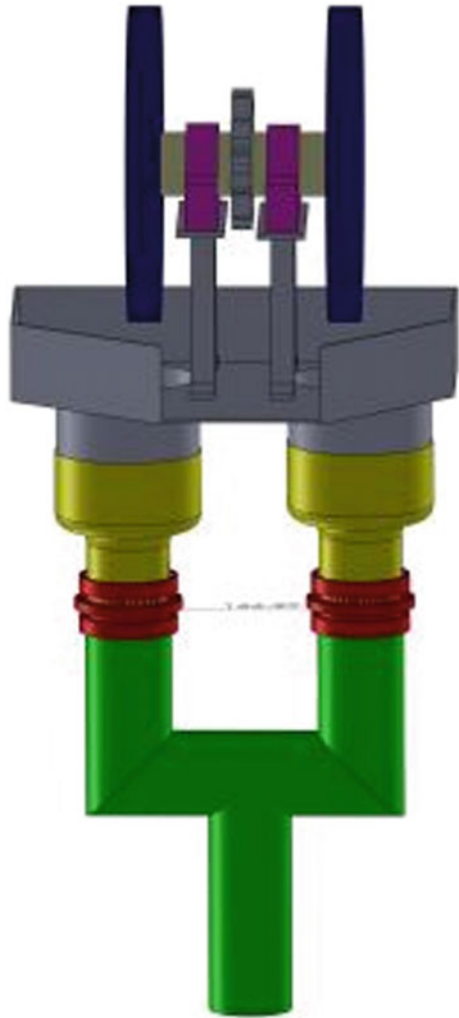


Table 1 Relationship between discharge and head [1]

Head (m)	0.5	1	2.5	5
Discharge (l/s)	7.6	3.8	1.52	0.6

Table 2 Relation between suction lift, discharge and cylinder diameter [2, 4]

Pump cylinder diameter (mm)	76	89	120	152	178
Suction lift (m)	7–8.5	5–7	2.5–5.5	2–2.5	0.5–2
Sustainable discharge (l/s)	1	2	3	4	5
Volume per stroke (l)	1.2–5	1.7	3	5	7

Table 3 Pump design features

Piston diameter (mm)	75–150
Foot stroke length (mm)	100–350
Cadence	About 60 rpm
Foot force	15–50 kgf (150–500 N)
Mechanical advantage	from 0.5 to 4
Treadle spacing (mm)	175–200

Source IDE South Africa

be reduced and a longer stroke for low heads where we need to put comparatively lower effort. As the foot stroke length of the operator is limited to approximately 350 mm, one-third of it is approximated as a suitable piston stroke length. It is found that a cadence up to 60 cycles per minute is comfortable for operation. To make pump suitable for men, women and children foot force limit should be 150–500 N according to their average weight. Suggested mechanical advantage ranges between 0.5 and 4. But to get a higher mechanical advantage one will have to cross the practical upper limit. This might lead to the overturning of the pump. Treadle spacing is the spacing between two treadles which is again approximated with the spacing between two paddles in bicycle and ranges from 175 to 200 mm which is matching with IDE data provided. Theoretically, treadle pump can lift water by suction up to 10.3 m, but in practice, a reasonable limit is 7 m considering all possible losses.

Our assumptions on the basis of literature review

- Head = 5 m
- Average Force = 250 N
- Diameter of piston = 100 mm
- Piston stroke length = 100 mm
- Foot stroke length = 340 mm
- Sprocket = 19.2 mm
- Rpm provided = 40
- Treadle spacing = 180 mm

Calculations

$$P = \omega \times T \text{ (Power supplied)}$$

$$\text{Power supplied} = \text{power required}$$

$$\omega \times T = \Phi g Q h$$

$$\begin{aligned}
 Q &= (\omega \times T \div \rho g h) \text{ m}^3/\text{s} \\
 &= 75 \div (1000 \times 9.81 \times 5) \\
 &= 0.001529 \\
 &= 1.52901/\text{s}
 \end{aligned}$$

Here symbols have their usual meanings. Discharge calculated is theoretical discharge considering 5 m as head and 75-W power as an average power that can be easily produced manually for a longer period. Through our present model, we are getting an approximate discharge of 0.6 l/s.

Use of this pump will affect the rural areas in various ways. Some important effect that can be observed by using this pump can be listed as—

1. Land area under irrigation will increase
2. Easier than bucket irrigation and time-saving
3. Proper irrigation will improve productivity and quality
4. Reduce the level of pollution (Fig. 4).

Places, where this pump can be used, are—

1. Water level up to 7 m
2. Small level irrigation fields where water can be provided with manual work
3. Vegetables and flower forming
4. Small and marginal level crop production
5. Where discharge of around 1 l/s is sufficient

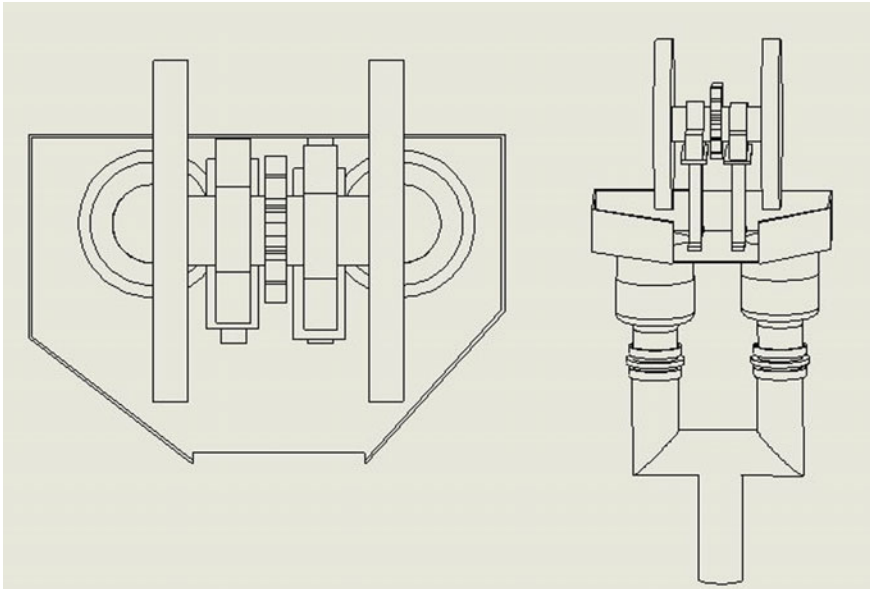


Fig. 4 Top (*left*) and Isometric (*right*) view of modified Treadle Pump

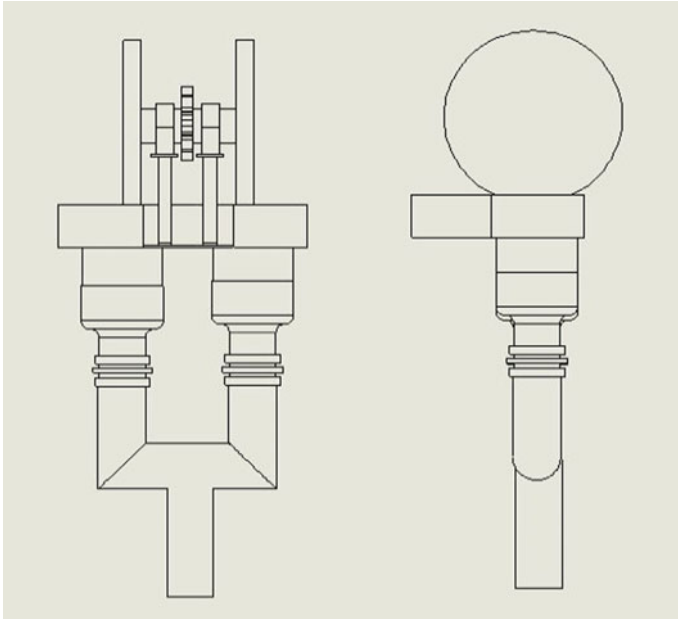


Fig. 5 Front and Side view of modified Treadle Pump

A modified treadle pump with rotary motion was at display in IIT Delhi at the Open House (Fig. 5). An additional sprocket has been provided for connection with battery/solar power driven motor depending on the availability (Fig. 6).

Suggestions for future work

1. We have made arrangement for solar operated model too but it is yet not tested with our model.
2. The present volumetric efficiency is around 40%. This needs to be enhanced.
3. Adjustable seat can be redesigned or improved by considering all aspects of ergonomics.
4. Effort to make the flow continuous is needed.
5. Overall cost of the project is 7000 Rs, which can be further reduced to make it available for all.



Fig. 6 Display in Open House 2016, at IIT Delhi

References

1. Fraenkel PL (1986) Water lifting devices, irrigation and drainage, paper no. 43. Rome
2. Orr A, Nazrul Islam ASM, Barnes G (1991) The treadle pump: manual irrigation for small-scale farmers in Bangladesh. Dhaka, Rangpur Dinajpur Rural Service (RDRS)
3. Daka AE, Elkind JP (1998) The treadle pumps operation and maintenance manual. Lusaka
4. Lambert RA, Faulkner RD (1991) The efficient use of human energy for micro-scale irrigation. *Agric Eng Res* 48:171–183

Biofuels—Sustainable Alternative to Petroleum (Fossil Fuels) and New Revenue for Farmers

Tatyaso S. Kadam, Mohit B. Zite and Akshay V. Walanj

Keywords Biofuels · Ethanol · Renewable energy

1 Introduction

Fuel is anything that can be used to obtain work output. Biomass is one of the abundant and renewable energy source available in the India. When this available biomass is converted into the biofuel by various processes can give a performance as like as petroleum fuels with little or no modifications to the available engine. The climate changes, growing air pollution are the major bad effects of fossil fuel combustion. The amount of CO₂ absorbed during the growth of bioenergy plant (Jatropha, Soybean, Linseed) will help to reduce the global warming and promote green revolution in India. Indian farmers have a great opportunity to help for making the nation more self-sufficient in energy and to reduce air pollution including emissions of Greenhouse gasses. These can provide extra farm income revitalize rural communities and improve the environment at the same time.

The majority of India's labour force works in the agricultural sector therefore in India there is particularly high potential for biofuels to earn the profit, provide employment and contribute to rural development. The production of biofuels will create new job opportunities for rural Indians as well as a new market for crops and agricultural by-products.

T.S. Kadam · M.B. Zite (✉) · A.V. Walanj
Vishwakarma Institute of Information Technology, Pune, India
e-mail: vickyzite5994@gmail.com

T.S. Kadam
e-mail: tatyasokadam88@gmail.com

2 Present Scenario in India

India is the sixth largest in term of energy demand and estimated that will growing at the rate of 5% per annum. The main energy source for India is coal which is mainly used for electricity generation and to meet the demand of transportation sector India need to import the crude oil and hence India ranks the third largest importer of crude oil. It is estimated that the demand for diesel and petrol will rise from 69.4 million metric ton (MMT) and 19.1 MMT respectively in the year 2014–15 to 110 and 31.1 MMT by the year 2021–22 [1–5]. Also, the vehicle population estimates to increase 10% annually and hence to meet the fueling requirement of these vehicles we need to go for alternative fuel considering energy security. In order to strengthen and formalize the country's commitment to promoting sustainable biofuel industry. Indian government adopted the National Policy on Biofuel 2009 (NPB). The policy aims to encourage the use of renewable biofuels and proposes 20% biofuel mandatory by the end of 2017.

3 Biofuel

Biofuels are liquid or gaseous fuels produced from biomass resources and are used as a replacement for diesel, petrol or other fossil fuels for transport, stationary, portable and other applications. In simplest form Biofuels are the fuels which are directly or indirectly produced from biomass or waste organic material. It can also be defined as any hydrocarbon fuel which is produced from organic matter in a short period of time, unlike fossil fuels which take millions of years to form.

3.1 Types of Biofuels

According to the feedstock used for the biofuel production, biofuels are mainly classified into three types: First generation biofuels are produced from sugar and starch using conventional technologies. The major feedstock for the first generation biofuels is from agriculture and food processing industry. Second generation biofuels produced from agricultural, forest and other biological waste. The third generation biofuels are obtained from the algae and specially produced fungus. The two most commonly used biofuel types are Ethanol and Biodiesel.

3.1.1 Ethanol

Ethanol is a type of alcohol having chemical formula C_2H_5OH . It is a clear colorless liquid with characteristic agreeable odour. Ethanol is used as an automotive fuel by

itself or by blending with the gasoline engine. Ethanol is mainly produced from the biomass containing sugar and starch.

3.1.2 Biodiesel

Biodiesel is the monoalkyl esters of long fatty acids derived from renewable feedstock such as vegetable oils or animal fats for use in compression-ignition (diesel) engines. Biodiesel is a renewable fuel obtained from methanol, vegetable oil and animal fats.

4 Properties of Biofuel

See Table 1.

4.1 Properties of Ethanol Oil Compared to the Petrol

Ethanol is an oxygenated fuel hence improves combustion characteristics and the air requirement for complete combustion is less as compared to petrol. Auto-ignition temperature and the flash point of ethanol is higher than petrol and gasoline here if is safer for transportation and storage. The heating value of ethanol is lower than petrol, therefore, BSFC increases.

4.2 Properties of Biodiesel Compared to Diesel Oil

Viscosity is higher than the diesel oil. Calorific value is slightly lower than diesel. Density is slightly higher than the diesel. Flashpoint is much higher than the diesel hence Biodiesel is quite safe to store. In general, biodiesel have higher cetane number than diesel fuel [3].

Table 1 Comparison of properties of biofuels and fossil fuels

Sr. No.	Property	Petrol	Ethanol	Diesel	Biodiesel
1	Density at 20 °C (g/cm ³)	0.755	0.78	0.82	0.8742
2	Boiling point (°C)	95	78	180–360	315–350
3	Viscosity at 40 °C (mm ² /s)	0.710	1.35	3.4	4.63
4	Lower calorific value (KJ/Kg)	44000	26800	44000	38725
5	Self-ignition temperature (°C)	246	415	210	320
6	Octane number	82	94	–	–
7	Cetane number	–	–	45	56

5 Feedstock to Produce Biofuels

The main feedstock for production of Biofuels is biomass. Biomass resources are the biodegradable fraction of products, agriculture residues, forestry and a related fraction of industrial and municipal wastes. The feedstock available to obtain the biodiesel and ethanol is described below.

5.1 Ethanol

Ethanol is produced from primary biomass such as sugar containing materials, like sugar cane, sugar beet, sweet sorghum, etc., starch containing materials such as corn, cassava, algae etc. and, cellulosic materials such as bagasse, wood waste, agricultural and forestry residues. In India ethanol is mainly produced from fermentation of sugarcane molasses.

5.2 Biodiesel

Biodiesel can be extracted from a wide range of oils like Jatropha, Karanj, Soybean, palm, coconut, rapeseed oils. Biodiesel can be made from renewable resources like used vegetable oil, animal fats and another type of wasted biomass. In India Jatropha is the primary feedstock used to make biodiesel. Biodiesel can also be produced from non-edible oils such as Mahua, Neem, and Karanja which will help to reduce food versus fuel conflict.

6 Biofuel Production

Biomass consists of three major components cellulose, hemicellulose and lignin. During the biomass conversion process, these components are breakdown by using two methods viz. Thermochemical and Biochemical. Using thermochemical conversion process the lignin can be recovered and used as a fuel. There are three methods in thermochemical process viz. pyrolysis, gasification, liquefaction used mainly to obtain the syn-oil, bio-syngas and biochemical respectively from biomass [4]. In Biochemical conversion process the hemicellulose components are separated from the biomass for the reduction to be more accessible to the cellulose, while lignin component remains unchanged [5].

6.1 Ethanol

Ethanol is produced by the fermentation (hydrolysis Process). The three major steps involved in the production of ethanol from the lignocellulose biomass are pretreatment, enzymatic hydrolysis, fermentation. The raw biomass is pretreated to improve the accessibility of enzymes and to separate biomass into cellulose. Then this pretreated biomass is undergone through enzymatic hydrolysis process which converts the cellulose component of the biomass into glucose and hemicellulose components into Pentose and Hexoses. Then the obtained glucose is fermented into ethanol by selected microorganisms.

6.2 Biodiesel

Biodiesel is also produced by the method of biochemical conversion using transesterification process also known as alcoholises process in which the glycerine is separated from the fat or vegetable oil. The process leaves behind two products viz. methyl esters (the chemical name for biodiesel) and glycerine.

7 Sustainability of Biofuels with Respect to Petroleum Fuels

Biofuels are the best sustainable in coming years by considering following factor.

7.1 Effect on Engine Parameters and Emissions

Various research and experiments have been conducted using biofuels and some are still going on. Also, there are various papers and literature published regarding the effect of biodiesel on the engine.

7.1.1 Effect on Exhaust Emissions

The transportation sector is considered as one of the major polluting sectors. The combustion of fossil fuels releases the harmful greenhouse gasses such as the CO₂, NO_x, HC and particular matters into the atmosphere. Biofuels are the best fuels to reduce these Greenhouse gasses there are lots of reports that conclude that the combustion of biofuels helps to reduce the harmful gasses in the air. The mixing of biodiesel and bioethanol with diesel significantly reduces the emissions of

particulate matter (PM) because the blended biofuel contains more oxygen [6]. Huang et al. found that the smoke, CO, emissions at 50% load was reduced with blends comparing with diesel fuel [7]. Subbaiah et al. concluded from their investigation that carbon monoxide and smoke hydrocarbon emissions are less during ethanol blend oils as compared with diesel fuel [8]. At high load condition, Ethanol blended diesel fuels have a stronger effect on smoke, NO_x, acetaldehyde emissions and unburnt ethanol emissions with the increase of ethanol smoke, NO_x and CO₂ emissions decreases [9]. Ethanol consists of 35% of oxygen which helps it to complete combustion of fuel and thus reduces vehicular pollutions with a reduction in particulate emissions.

7.1.2 Engine Performance

The heating value of the ethanol is less as compared with gasoline hence BSFC increases but due to the complete combustion in the combustion chamber, it results in the increase in power output. Brusstar et al. obtained the same thermal efficiency up to approximately that of diesel when using biodiesel. They concluded that fuel economy is same for ethanol and gasoline and petroleum engine [10]. Pikunas et al. reported that when ethanol-gasoline blend is used fuel consumption of the engine slightly increases [11]. Song and Zhang mentioned that the engine brake power and torque increases with the increase in biodiesel percentage in the blends [12].

7.1.3 Durability of Engine

The use of biodiesel will increase the life of the engine because it will lead to lower soot formation and inherent lubricity [13]. The latent heat of evaporation of ethanol is 3–5 times greater than diesel results in the increase in volumetric efficiency. Biodiesel is nonflammable and nonexplosive, unlike petrodiesel, due to this property biodiesel-fueled vehicle much safer in accidents than those powered by diesel or gasoline [14].

7.2 Environmental Considerations

The combustion of biofuels like ethanol and biodiesel emits lower emissions such as CO₂, CO, SO₂ and particulate matter (PM) as compared to petroleum fuels which make biofuel environment-friendly. CO₂ which is the main cause for Green House Gas (GHG) and global warming is absorbed during the growing of biofuel plants at its initial stage and after the combustion biofuel obtained from the biomass emits less CO₂ than fossil fuels which will defiantly help to reduce GHG and global warming. Biofuels are biodegradable and hence less effective in the environment. Biofuels are safer to handle and are less toxic as compared to the crude oil. Biofuels

are having higher flash point hence decrease the chances of a fire hazard. Biofuels are the clean source of energy.

7.3 Benefits to the Country

India is an Agricultural country and has a wide range of land resources to grow biofuel feedstock hence in future, India can able to produce its own energy. It will reduce the dependency on foreign countries for fueling the transportation sector. In India, domestic fuel production does not meet it's required consumption this increases the growing gap between production and consumption of crude oil. The use of biofuels will help to reduce this gap between supply and demand in the country. Biofuel industries will create new job opportunities in India and help to rural development with the development of the farming industry. The production and use of biofuels in the country improve our energy security and decreases the reliance on foreign supplies. Under these considerations using the ethanol, biodiesel and their blends are the better than fossil fuels because they are cleaner and harmless to the environment. Biofuels are assumed to be new alternative and sustainable renewable energy source for the automotive fuel.

8 Biofuels as a New Revenue for the Farmer

There is a strong link between biofuel production and agricultural sector. India is an Agricultural industry and about 62% of the population is engaged in agricultural work. Agricultural sector provides food security to the people and on the other hand, it provides raw materials to various agro-based industries. Hence there is a significant potential to expand the biomass production from the agricultural sector. In India, there is a scope for the plantation of bioenergy plants such as sugarcane, Jatropha, Karanj, soya bean, sunflower, corn, wheat, Mahua, Neem and castor. There is a large scope for agricultural residues, biofuels can also be produced from the agricultural residues too hence in coming years there is a huge requirement of agricultural residue. The biofuel energy plantation in rural areas will create new jobs to the workers and there will be a large requirement of skilled and unskilled employees in the biofuel refineries which will help to reduce the unemployment in India. There is a significant potential to expand the current biomass production from the agricultural sector and increase the earning by export. The development of biofuels will create the direct or indirect opportunities from growing bioenergy crops to their manufacturer. The development of biofuel in our own country will reduce the transportation cost and other regarding taxes which lead to the reduction in the petroleum cost on the local scale. Defiantly the biofuel production will become new revenue for farmers which will give profit to them and ultimately prosperity of our country.

9 Conclusion

Fuel consumption is going to increase as compared to its production. It is necessary to develop and create new energy sources that will cope with the current requirement. The biofuel production will decrease the dependency on fossil fuel with various advantages to the society and environment. The biofuel blends or biofuels can be directly used with little or no modification of the engine. Biofuels are the safer and cleaner source of energy. By economical consideration, biofuels will help to reduce import of crude oil and ultimately save in costing. The biofuel industries will create new job opportunities to Indian manpower and will boost the agricultural sector in the country. Also, there is some limitation regarding food security and land equitability but this can be overcome by producing biofuel from non-food feedstock and technological advancement. Finally, Biofuels are the best available sustainable alternative to the fossil fuels and will defiantly be going to increase the profit of farmers.

References

1. Ministry of Petroleum and Natural Gas, Government of India, Annual Report 2015–16
2. Government of India, Ministry of New & Renewable Energy
3. Jayed MH et al (2011) Prospects of dedicated biodiesel engine vehicles in Malaysia and Indonesia. *Renew Sustain Energy Rev* 15:220–235
4. Hassan MH, Kalam MA (2013) An overview of biofuel as a renewable energy source: development and challenges. *Procedia Eng* 56:39–53
5. Simonyan K, Fasinao O (2013) Biomass resources and bioenergy potential in Nigeria. *Afr J Agric* 8(40):4975–4989
6. Hansen AC, Zhang Q, Lyne PWL (2005) Ethanol-diesel fuel blends—a review. *Bioresource Technol* 96:277–285
7. Huang J, Wang Y, Li S, Roskilly AP, H Yu, Li H (2009) Experimental investigation on the performance and emissions of a diesel engine fuelled with ethanol-diesel blends. *Appl Therm Eng* 29(11–12):2484–2490
8. Subbaiah GV, Gopal KR, Hussain SA (2010) The effect of biodiesel and bioethanol blended diesel fuel on the performance and emission characteristics of a direct injection diesel engine. *Iranica J Energy Env* 1(3):211–221
9. He B-Q, Shuai S-J, Wang J-X, He H (2003) The effect of ethanol blended diesel fuels on emissions from a diesel engine. *Atmos Env* 37(35):4965–4971
10. Brusstar M, Bakenhus M (2008) Economical, high-efficiency engine technologies for alcohol fuels. U.S. Environmental Protection Agency. Retrieved 14 Jan 2008
11. Pikunas A, Pukalskas S, Grabys J (2003) Influence of gasoline ethanol blends on parameters of internal combustion engine. *J KONES Intern Combust Engines* 10:3–4
12. Song J-T, Zhang C-H (2008) An experimental study on the performance and exhaust emissions of a diesel engine fuelled with soybean oil methyl ester. *P I Mech Eng D-J Aut* 222:2487–2496
13. Xue J, Grift TE, Hansen AC (2011) Effect of biodiesel on engine performances and emissions. *Renew Sustain Energy Rev* 15(2):1098–1116
14. Qi DH, Chen H, Geng LM, Bian YZH, Ren XCH (2010) Performance and combustion characteristics of biodiesel–diesel–methanol blend fuelled engine. *Appl Energy* 87(5):1679–1686

Microcontroller Based Automatic Drip Irrigation System

Rahul G. Ghodake and Altaf O. Mulani

Keywords Soil moisture sensor · Temperature sensor · PIC microcontroller · Solenoid valve

1 Introduction

Water is the resource that all living species need like human beings, animals, plants, etc. Due to the excessive and continuous extraction of water from earth via wells or bore wells is responsible for the reduction of the water level which leads to making a lot of land in the zones of un-irrigated land. Hence proper planning of water usage is needed. There is an immense demand for new techniques of water saving in irrigation systems [1–4]. The lack of rain water and scarcity of land water also results in the decrement a volume of water on earth. In the drip irrigation technique, the water is provided to the root zone of plants using drip due to which a large amount of water can be saved. Figure 1 shows typical drip irrigation system. At Present, the farmers have been irrigating the land manually in which the farmers must irrigate the lands at every regular interval. This technique may consume extra water. Sometimes to avoid drying of crops, water is provided to roots of the plants. Because of this growth rate becomes slow, the weight of fruits becomes lighter, etc. Automatic drip irrigation system can solve this issue entirely. Today the availability of carrying agricultural activity is less; therefore automation in agriculture is needed. Proposed irrigation system uses valves to turn ON or OFF automatically. Drip irrigation can be applied to a wide range of field conditions. The simple Drip irrigation assembly is shown in Fig. 1.

R.G. Ghodake (✉) · A.O. Mulani
SKN Sinhgad College of Engineering, Pandharpur, India
e-mail: ghodakerg96@gmail.com

A.O. Mulani
e-mail: aksaltaaf@gmail.com

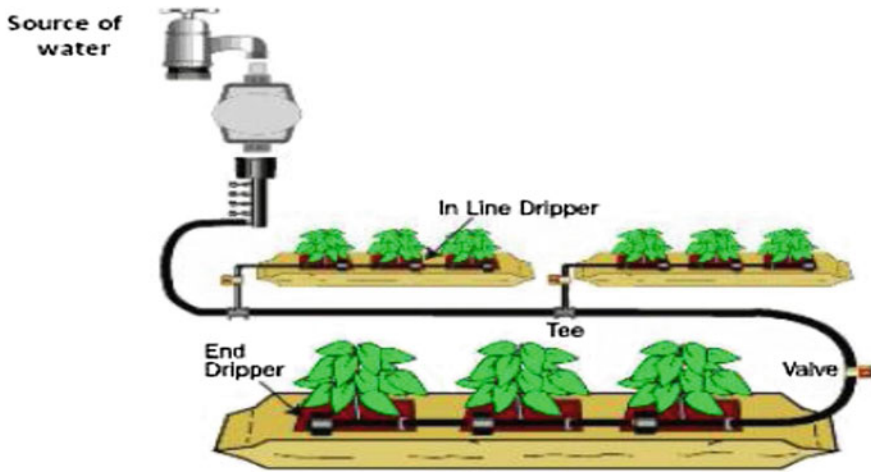


Fig. 1 Drip irrigation assembly [6]

1.1 Components

The components of Microcontroller Based Automatic Drip Irrigation System are as follows [5, 6]:

1. Water Pump
2. Water Filter
3. Solenoid Valve
4. Drip lines with Emitters
5. Soil Moisture and Temperature Sensors
6. PIC Microcontroller Unit
7. GSM (Global System for Mobile Communication).

2 Irrigation

The artificial process of providing water to the soil for growing crops is called as irrigation. Water is undeniable or major resource for living organisms. Agriculture is one of the fields where water is required in very large quantity. Nowadays, insufficiency of water is becoming one of the biggest problems in the world. Hence to overcome this issue, microcontroller based automatic drip irrigation system is presented.

2.1 Types of Irrigation

There are mainly three types of irrigation and can be explained as follows.

1. Surface Irrigation
2. Drip Irrigation
3. Sprinkler Irrigation

1. *Surface irrigation*

It is also called as conventional irrigation. Surface irrigation is the irrigation technique in which water is applied and distributed over the surface by gravity. A surface type irrigation system can wet the lower leaves of the plants. When land is irrigated by using such methods, the soil surface is saturated and stays wet for a long time. These conditions lead to infection the plants. The surface irrigation methods consume a large amount of water. The drip or trickle irrigation is used to solve this problem.

2. *Drip irrigation*

It is also known as micro-irrigation or localized irrigation system, is irrigation method which can save water by allowing it slowly drip at the plant's roots, either onto the soil surface or directly onto the root zone. It consists a network of valves, pipes, tubing, and emitter. Drip irrigation implemented at plant's root zone is shown in Fig. 1.

3. *Sprinkler irrigation*

The irrigation system based on overhead sprinklers in this system, sprayguns, installed permanently on a riser. Water pressure based using guns can also be used to avoid implementation ambiguity.

3 Methodology

There are mainly three methods used for Automation:

- (a) *Time-based system*

The basic aim is to prepare system schedule according to water requirements of the crop. Here time is the basis for operation.

- (b) *Volume-based system*

In this type of system, a land is divided into the small part called a field or section, and every section or field will receive the pre-allocated volume of water.

- (c) *Sensor (priority)-based system*

In this system, sensors give feedback to the controller, depending on which the controller initiates various actions as required.

In this paper, the methods mentioned above (Time based, Volume based and Priority based) are combined in one system.

4 System Architecture

The block diagram of microcontroller based automatic drip irrigation system is as shown in Fig. 2 which consists of various blocks. The function of each block is explained as follows:

- (A) **Sensors:** A sensor is an object or device whose purpose is to transduce events or changes in its environment regarding physical quantity, and then provide relative output.
- (a) *Temperature sensor:* A temperature sensor is a device which provides for temperature measurement through an electrical signal. The LM35 5 V sensor is used to measure the temperature. The LM35 series are precision integrated sensors. The output voltage is linearly proportional to the Centigrade temperature.
 - (b) *Soil moisture sensor:* Soil moisture sensors measure the volumetric water content in soil. Measuring soil moisture is useful for farming applications to help farmers manage their irrigation systems more efficiently. Sensors should be buried properly in the root zone of the plants to be irrigated.
- (B) **Liquid crystal display (LCD):** The LCD shows a matrix of the alphabets, numbers, characters and symbols on the LCD screen. The LCD used in this system is the eight-bit parallel type, and the display size is 16 * 2. It is used for displaying the temperature and moisture value on a display screen.
- (C) **Solenoid valve:** A fluid solenoid valve operates on electromechanical principle. It converts the input electrical energy into mechanical energy. This will internally open and closes the switch automatically. In the case of a valve with two-port the flow is switched on or off; whereas in a three-port valve, switching of outflow is done between the two outlet ports.

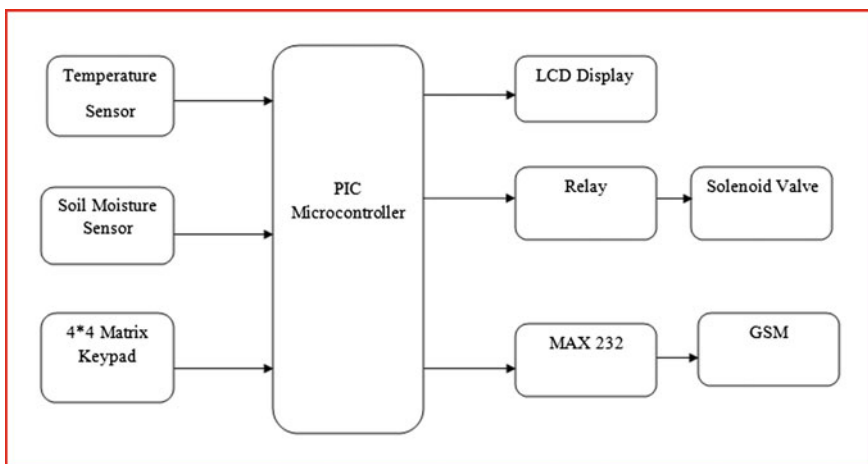


Fig. 2 System block diagram

- (D) **GSM:** GSM (Global System for Mobile Communications), developed by the European Telecommunications Standards Institute (ETSI) to explain the protocols for second-generation (2G) digital cellular networks used by GSM modems. There will be serial communication between microcontroller and GSM. So the information from the microcontroller can be sent as SMS through GSM.
- (E) **PIC microcontroller:** PIC stands for Peripheral Interface Controller is a family of modified Harvard architecture microcontrollers registered trademark of Microchip Technology. In this project, PIC 16F877A microcontroller is used. The important features of PIC 16F877 series are listed below.

Features of PIC 16F877A:

1. High performance
 2. RISC family CPU.
 3. Only 35 instructions.
 4. Single cycle instructions, only for branches of program two cycles instructions are required.
 5. Interrupts available are fourteen.
 6. Different types of addressing modes (direct, Indirect, relative addressing modes).
 7. Power on Reset (POR).
- (F) **Power supply:** A power supply is to be developed for desired load conditions. Power supply unit converts input AC power to DC power required by various parts of the project such as 5–12 V in our system.

5 Results and Discussions

The output of LM35 is in the form of the analog temperature sensor as its output is analog and requires to be converted into digital. The input supply voltage is 5 V. The output will be in the form of voltage (Table 1).

The sensor used for soil moisture measuring is directly connected to the microcontroller. The output is in the digital form and data is sent directly to PIC microcontroller. The output of microcontroller is displayed on LCD screen (Table 2).

Table 1 Output of LM 35 temperature sensors

Temp (°C)	Output voltage in mV
30	300
31	310
32	320
33	330
34	340

Table 2 Output of soil moisture sensor

Moisture level (%)	Output voltage (V)
20	2.75
40	2.10
60	1.39
80	0.71

Fig. 3 Irrigation system

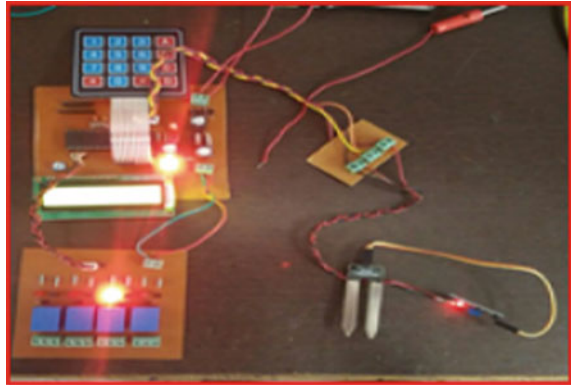


Fig. 4 Output screen 1



When moisture level of soil is low, the solenoid valve is turned ON automatically. When the desired level of water is reached in the soil the valve will be closed automatically (Fig. 3).

Figure 4 shows output screen 1. First, the appropriate system is selected (time-based, priority based and volume based system) for irrigation. If time-based system is selected then, the results are as follows. In time-based system, a significant amount of water is available to irrigate land depending upon crop condition (Table 3).

Table 3 Observation table of time based system

Starting delay in seconds	Motor status	Motor status (end of delay)
10	On (for 10 s)	Off
30	On (for 30 s)	Off
60	On (for 60 s)	Off

Table 4 Observation table of priority based control system

System	Dry (%)	Priority
1	50	2
2	90	1
3	30	3

If the priority based system is selected then, the following results are observed which are as shown in Table 4. Priority is assigned depending upon the dry condition of the field.

6 Conclusion

This paper mainly focuses on designing a fully automated drip irrigation system. The microcontroller based automatic drip irrigation system is implemented and found to be feasible and cost effective. It will be advantageous over manual control as it uses a mechanism like time-based control mechanism, volume based control mechanism, and sensor based control mechanism.

References

1. Goumopoulos C, Flynn BO, Kameas A (2014) Automated zone-specific irrigation with wireless sensor/actuator network and adaptable decision support. *Comput Electron Agric* 105 (Elsevier)
2. Miranda FR, Yoder RE, Wilkerson JB, Odhiambo LO (2005) An autonomous controller for site-specific management of fixed irrigation system. *Comput Electron Agric* 48 (Elsevier)
3. Patil PS, Alai SR, Malpure AC, Patil PL (2014) An intelligent and automated drip irrigation system using sensors network control system. *Int J Innovative Res Comput Commun Eng* 2(12)
4. Gutiérrez J, Villa-Medina JF, Nieto-Garibay A, Porta-Gándara MÁ (2013) Automated irrigation system using a wireless sensor network and GPRS module. *IEEE Trans Instrum Measur* 63(1):166–176
5. Maheshwari CV, Sindha D (2014) Water irrigation system using controller. *Int J Adv Technol Eng Sci* 02(01)
6. Galande SG, Agrawal GH (2013) Embedded controlled drip irrigation system. *Int J Emerg Trends Technol Comput Sci (IJETTCS)* 2(5)

Sustainable Raft Based Hydroponic System for Growing Spinach and Coriander

Smital Kulkarni, Plapallil Steve Abraham, Nimain Mohanty, Nitin N. Kadam and Mansee Thakur

Keywords Hydroponics · Spinach · Coriander · Raft system

1 Introduction

One of the largest challenges of this century in the near future will be maintaining supplies of freshwater fit for human use [1]. This perceived is largely associated with projected global population growth estimates and subsequent increase in food demand. Currently, 70% of freshwater usage is attributable to agricultural practices [2, 4]. Considering that the agricultural industry is the world's leader in freshwater consumption, it would follow that decreasing the water used by this industry will have the greatest impact [2]. Therefore, to prepare for the challenges associated with water scarcity, it is imperative that we develop and implement technologies and processes that maximize agricultural outputs while minimizing inputs.

Hydroponic systems have been utilized as one of the standard methods for plant biology research and also used in commercial production for several crops,

S. Kulkarni · P.S. Abraham
Department of Medical Biotechnology, MGMSBS, MGMIHS, Navi Mumbai, India
e-mail: smitalkulkarni20@gmail.com

P.S. Abraham
e-mail: steveabraham1990@yahoo.com

N. Mohanty · N.N. Kadam
Department of Pediatrics, MGM Medical College, MGMIHS, Navi Mumbai, India
e-mail: nimain.mohanty@gmail.com

N.N. Kadam
e-mail: dr_nnkadam@yahoo.com

M. Thakur (✉)
Department of Medical Biotechnology, MGMSBS, MGMIHS CRL,
MGM Medical College & MGM CET, Navi Mumbai, India
e-mail: mansibiotech79@gmail.com

including lettuce, vegetables and tomato. Within the plant research community, numerous hydroponic systems have been designed. Approximately, it requires 70–95% less water than open field agriculture [3, 4]. This is a method of cultivating plants in a liquid nutrient solution with or without the use of artificial media. Hydroponics offers several advantages over soil-based systems. When removed from soil, root tissue is often mechanically sheared causing loss of tissue or damage. This is particularly true for fine root structures such as lateral roots and root hairs. Hydroponic systems that do not utilize an inert particulate media allow a less invasive separation of root and shoot tissues. In soil systems, nutrient bioavailability changes throughout the soil matrix as nutrients bind to soil particles creating micro-environments within the soil. This heterogeneity could add an extra level of complexity in experiments needing a precise control on the external concentration of nutrients or other molecules [5]. In contrast, the hydroponic solution is homogeneous and can be easily replaced throughout the course of the experiment. The popularity of this technique stems from the fact our food supply is increasingly stressed and the need to grow food faster is in order to keep up with demand. The idea is to grow a plant in such a way that it can tolerate the biotic and abiotic stresses [6]. Hydroponic techniques can provide year round growing opportunities and ease the stress placed on traditional soil but this comes with a cost.

In this paper, a raft based hydroponic protocol that can be easily implemented in laboratories interested in pursuing studies on plant mineral nutrition. Most of the materials described in this protocol can be found easily outside the companies providing scientific supply, making the set up for hydroponic experiments less expensive and convenient. The following protocol provides step-by-step instructions on how to set up a hydroponic system in a laboratory. This protocol has been optimized for *spinach and corianders*; however, similar or in some cases identical steps can be used to grow other species

2 Materials and Procedures

2.1 Seedlings and Cups

Prior to starting the experiment thirty seeds of each type-spinach and coriander were kept in lukewarm water overnight for germination. The next day seeds were further used to grow plant. The seeds were cracked open by giving a gentle press (do not divide the cotyledons into two different parts). Each day the seeds were checked and water was added on and were placed in moist muslin cloth and kept on providing moisture to it. Within a week it has showed pummels and radicals grown from seeds, which were further used to grow plant (Figs. 1 and 2).

1. **Incorporation of germinated seeds in supporting medium:** Soaked the coco peats in the water so that it puffs up. Dig two holes in the coco peats. Place one seed in each hole. Keep on spraying water on coco peats so that it won't get dry.



Fig. 1 Procedure for germinating the coriander seeds **a** cracking open the seeds **b** keep the cracked seed on moist muslin cloth **c** plumules and radicles observed within a week

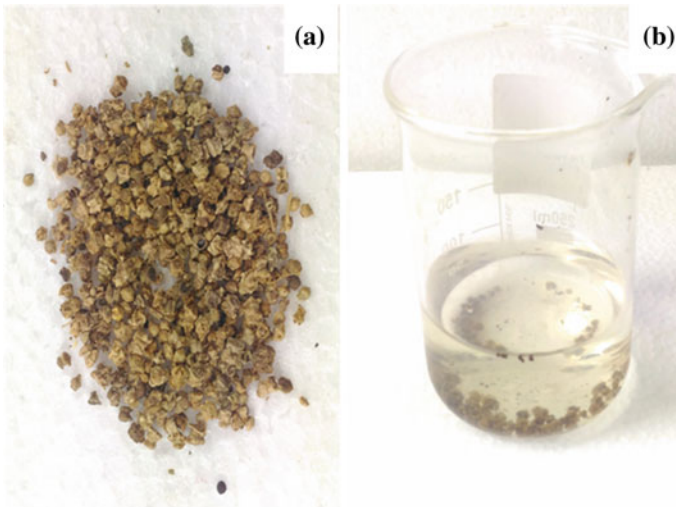


Fig. 2 Procedure for germination of Spinach seeds. **a** Spinach seeds, **b** soaking the seeds in warm water for 12–24 h

2. **Settling up coco peats in seedling tray:** Once the seeds grow to seedling stage, the net cups containing coco peats were placed in seedling tray containing water and required quantity of nutrient solutions as per the given table. They were kept till it grows to plantlet stage. The net cups were placed in such a way that the base of cups should touch the water and nutrient solutions which were added in the tray (Fig. 3).
3. **Preparation of nutrient solution in stock:** Stock solution A and stock solution B (Hoglands medium) were two nutrient solutions used for growth of plants. The following are the ingredients added (Table 1).
4. **Transfer of coco peats to hydroponic crates:** Hydroponic crates were rectangular trays with plastic lids having 12 holes on it. The holes were of suitable size for net cups (size—2 in./5 cm) so that it can be properly fit in it. The size of crate was 60 cm * 40 cm * 10.5 cm and it has capacity of 16 L of water.

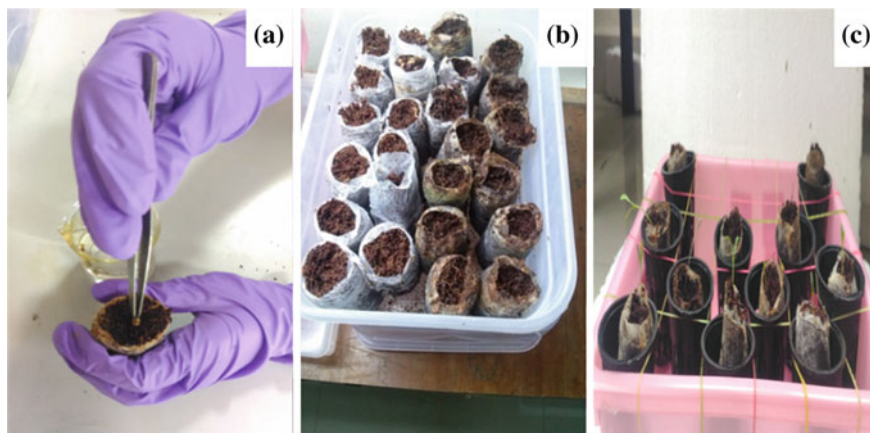


Fig. 3 Spinach and coriander seeds transplant in net pot

Table 1 Nutrient solution mixing ratios at different stages

Media preparation	Stock A	Calcium nitrate	180 g/L
		Potassium nitrate	8.8 g/L
		Ferrous EDTA	5.0 g/L
	Stock B	Monopotassium phosphate	44 g/L
		Potassium sulphate	77 g/L
		Magnesium sulphate	111.5 g/L
		Manganese sulphate	460 mg/L
		Copper sulphate	118 mg/L
		Zinc sulphate	352 mg/L
		Boric acid	343 mg/L
Ammonium molybdate	10.4 mg/L		
Stock A and stock B in equal proportion			and further used as a media
Media concentration	Seedling stage (15 days)	0.5× (2.5 mL/1 L water)	
	Seeding stage (6 days)	0.75× (3.75 mL/1 L water)	
	After seedling stage till fully grown plant	1× (5 mL/1 L water)	

As the plant reaches its plantlet stage, it has been transferred to hydroponic crates in such a way that the water and mixed nutrient solutions should touch the base of net cups. The trays were filled with 13 L of water and accordingly appropriate amount of nutrient solutions were added. The plants were allowed to fully grown stage in these hydroponic crates.

Above each hydroponic crate there were three PL lights adjusted to timer for light and dark cycle for plants. pH and electrical conductivity of water in crates were routinely checked to avoid any obstacle in plants growth.

5. **Control Traditional Growth set-up:** The germinated seedlings were placed in soil and same conditions were maintained as that of hydroponics system such as light and dark cycle 18 hr and 6 hr respectively (using timer), temperature 26–28°C and electrical conductivity of water 1.5–2.5 dS/m.
6. **Height measurements:** Each plant height were measured every three days a week. An average height was taken for each type of plant (spinach and coriander) in centimeters.
7. **Water quality:** pH and salinity were measured using Vernier software logger pro probes. For ammonia, phosphate, and nitrate tests kit was used. A standard thermometer was used to measure temperature in Celsius
8. **Harvesting of fully matured plants:** Both plants took around one month to mature fully. They were cut using sterile and clean blade near the roots.

3 Results and Discussion

In the experiment to explore the growth of hydroponics compared to traditional gardening. The quantitative data that was taken showed a correlation between measurements of plant height. Observations found that the traditional and hydroponic gardening grew at an exceeding rate. Figures 4, 5 and 6 show hydroponic lab set up showing fully grown plants (spinach and coriander) 24 days old. A number of measurements were made to ascertain the physiological state of plants grown in both systems. The study involves different parameters which includes height of plants, estimation of iron and chlorophyll content. The plants grown in hydroponically

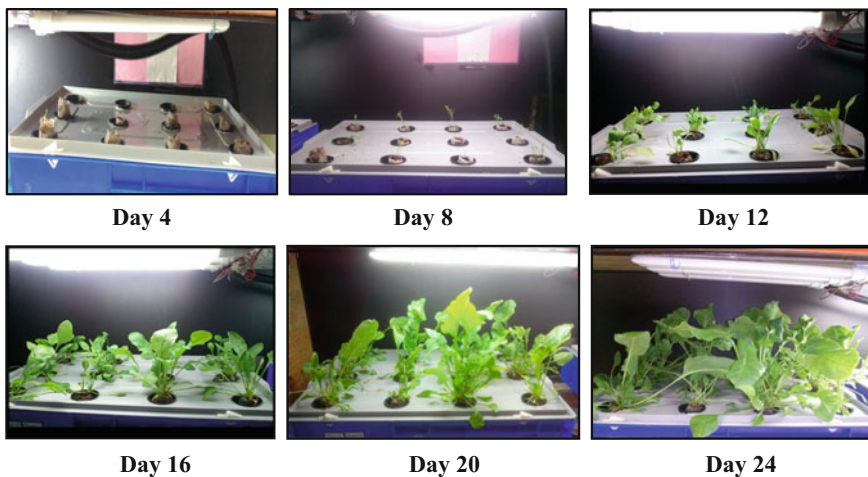


Fig. 4 Healthy spinach being grown in a standard 60 cm * 40 cm * 10.5 cm hydroponic raft based system after 24 days

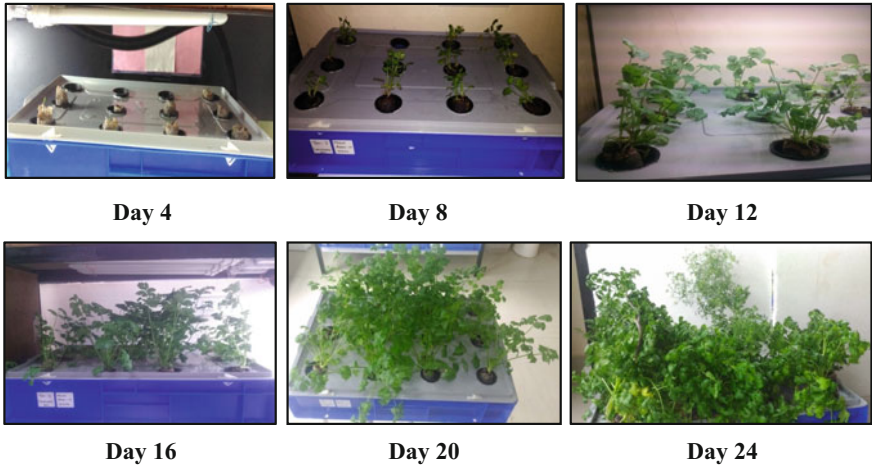


Fig. 5 Healthy coriander being grown in a standard 60 cm * 40 cm * 10.5 cm hydroponic raft based system after 24 days



Fig. 6 Lab-setup

grown conditions (Spinach - 28.33 cm and Coriander - 47.21 cm) were found to have slight more height when compared to soil grown plants (Spinach - 25.22 cm and Coriander - 42.60 cm) (Figs. 7 and 8). The iron content for hydroponics spinach and coriander were found to be 0.5 gm/100 gm and 0.4 gm/100 gm respectively and soil-grown spinach and coriander were found to be 0.45 gm/100 gm and 0.4 gm/100 gm respectively (Table 2). Plants had vibrant green coloration for which total chlorophyll content of hydroponics plant leaves of spinach and coriander were found to be $11.5 \pm 0.4 \mu\text{g mg-DW}^{-1}$ and $10.4 \pm 0.4 \mu\text{g mg-DW}^{-1}$ (mean \pm SD) respectively while soil-grown spinach leaves had $11.6 \pm 0.6 \mu\text{g mg-DW}^{-1}$ and coriander had $10.2 \pm 0.4 \mu\text{g mg-DW}^{-1}$ chlorophyll content (Table 2) and possessed the same growth rates throughout the vegetative growth

Fig. 7 Plant height growth pattern of spinach and coriander during 24 days in hydroponics

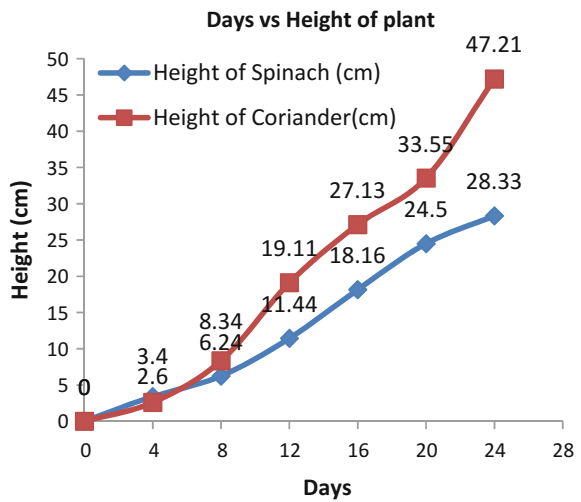


Fig. 8 Plant height growth patterns of spinach and coriander during 24 days in traditionally grown

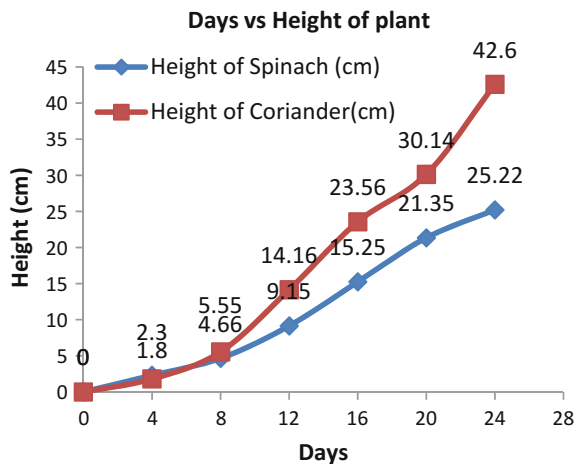


Table 2 Comparative results for iron & chlorophyll content of hydroponics & traditional method

	Hydroponics		Traditional	
	Spinach	Coriander	Spinach	Coriander
Iron content	0.5 gm/100 gm	0.4 gm/100 gm	0.45 gm/100 gm	0.4 gm/100 gm
Chlorophyll content	11.5 ± 0.4 ug mg-DW ⁻¹	10.4 ± 0.4 ug mg-DW ⁻¹	11.6 ± 0.6 ug mg-DW ⁻¹	10.2 ± 0.4 ug mg-DW ⁻¹

cycle (24 days). Therefore, it can be concluded that there were no much differences found in Spinach and Coriander grown in both systems.

pH is a measure of acidity or alkalinity on a scale of 1–14. In a nutrient solution, pH determines the availability of essential plant elements. For pH values above 7.5, iron, manganese, copper, zinc and boron becomes less available to plants. The optimum pH range for hydroponic nutrient solution is between 5.8 and 6.5.

The electrical conductivity indicates the strength of nutrient solution, as measured by an EC meter. The ideal EC range for hydroponics is between 1.5 and 2.5 dS/m. Higher EC will prevent nutrient absorption due to osmotic pressure and lower EC severely affect plant health and yield. When plants take up nutrients and water from the solution, the total salt concentration, i.e., the EC of the solution changes. If the EC is higher than the recommended range, fresh water must be added to reduce it. If it is lower, add nutrients to raise it. In the present study EC up to 24 days was within the range between 1.5 and 2.3 ds/m.

Hydroponic growing methods are growing in popularity and seem to have a positive overtone because of the numerous environmental benefits of soilless methods compared to soil grown crops [7]. Although there are numerous benefits to the hydroponic system, it does not automatically guarantee a high quality product. Advantages of a hydroponics system include, but are not limited to, conservation of resources (including water and soil), extended growing season, space efficiency (no need to rotate crops or to move the structure, and the plants can grow more densely packed), and protection against the elements (pests, high wind, harsh rain, harsh temperatures). As this technology is advancing, it is important to consider the sensory attributes of the hydroponic product since taste is one of the main drivers of consumption [8]. Our study indicated 90% have no differences between hydroponically and soil grown spinach and coriander.

4 Conclusion

Although different types of hydroponic methods are used, they are often far removed from traditional agriculture. Future research includes experiment to be continued and held for a longer time to observe the changes in growth and rate of plants grown under hydroponic conditions. This study leads to an abundance of data and it is the hope that with the arable land degradation, increase in water

scarcity and soil degradation, the hydroponic methods will be successful in growing produce and promote healthy living.

References

1. Simonovic SP (2002) World water dynamics: global modeling of water resources. *J Env Mngt* 66:249–267
2. Wallace JS (2000) Increasing agricultural water use efficiency to meet future food production. *Agr Eco Env* 82:105–119
3. Bradley P, Marulanda C (2000) Simplified hydroponics to reduce global hunger. *Acta Hort* 554:289–296
4. Despommier D (2010) *The vertical farm: feeding the world in the 21st century*. St. Martin's Press, New York, NY. ISBN-10: 0312610696
5. Nguyen NT, McInturf SA, Mendoza-Cózatl DG (2016) Hydroponics: a versatile system to study nutrient allocation and plant responses to nutrient availability and exposure to toxic elements. *J Vis Exp* 113
6. This document is HS943, one of a series of the Horticultural Sciences Department, UF/IFAS Extension. Original publication date June 2003. Revised Nov 2009 and June 2013. Reviewed Mar 2016. Visit the EDIS website at <http://edis.ifas.ufl.edu>
7. Resh HM, Howard M (2012) *Hydroponic food production: a definitive guidebook for the advanced home gardener and the commercial hydroponic grower*. St. Bárbara, EUA. ISBN 9781439878675
8. Ho LC (2004) The contribution of plant physiology in glasshouse tomato soilless culture. *Acta Horticulturae* 19–25

Effect of Change in Vacuum Pressure on the Performance of Solar Dryers

Nikhil S. Mane, O.N. Thigale, A.M. Patil and N.V. Hargude

Keywords Solar energy · Solar dryers · Renewable energy · Grape dryers · Vacuum drying

1 Introduction

In many nations across the globe, the application of solar thermal systems in the agricultural area to conserve vegetables, fruits, coffee and other crops is very common. Drying fruits under the direct sunlight does not involve any cost, but it has some limitations; first one is that this process takes a long time also there are high possibilities of an addition to external contamination as drying material is kept in the open for a long time. In recent years use of solar energy is more common and solar energy is used in many applications [1]. And If the use of solar energy is not increased future shortages in energy might cause major blow on agricultural productivity [2].

Open drying of products is a common technique used due to its simplicity from last thousands of years, but with time small changes in the open drying technique have been incorporated. But the quality of a product is sacrificed in open drying process as it gives poorly dried products. If the improved open drying techniques are adopted then, food products can be dried fastly and bitterly even in the rainy season where the humid and cloudy climate is present [3, 4].

Drying means a simple process in which water is removed by vaporizing it, which require a heat source. Generally to increase heat removal forced convection can be used [5]. When water gets vaporized an air flow should be there to carry away that. Airflow is also required to remove the vapour away from the product.

N.S. Mane (✉) · A.M. Patil · N.V. Hargude
PVPIT, Budhgaon, India
e-mail: manenikhil24@gmail.com

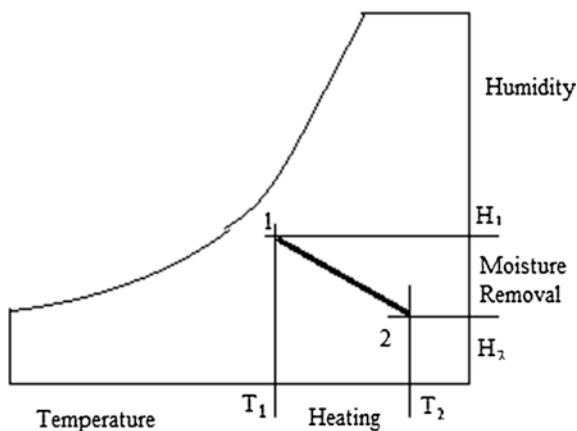
O.N. Thigale
Trinity Polytechnic, Pune, India
e-mail: thigale.onkar05@gmail.com

Vapour otherwise the product will be cooked. Hence increasing a temperature of heat source and velocity of air speed of drying process can be increased. The important objective of the drying process is to vaporize the water content of the product and carry it away from the product to reach the minimum level of moisture content required for storage. To overcome limitations and disadvantages of natural or sun drying process methods like vacuum dryer [6], tunnel dryer [7] can be used. As drying period increases drying rates fall [8] then vacuum drying can be helpful to remove further moisture. Vacuum dryers will give the clean product as drying takes place inside a closed chamber and no physical particle will enter into the drying chamber. Use of forced convection increases the drying rate [9], but if air flow is not maintained properly, then the quality of products from the dryer will not meet required conditions [10–13].

2 Drying Process on Psychrometric Chart

Figure 1 shows the grape drying process representation on the psychrometric chart. It can be observed that in this process grapes are dried from their initial condition 1 to final condition 2. The grape drying process is nothing but the heating and dehumidification process in which dehumidification is done by the removing the moisture from the grapes and heating is given by hot air heated by solar radiations. Due to continuous circulation of air, the drying chamber get heated whose temperature increases from T_1 to T_2 moisture from the grapes are removed, and humidity decreases from H_1 to H_2 .

Fig. 1 Representation of drying on psychrometric chart



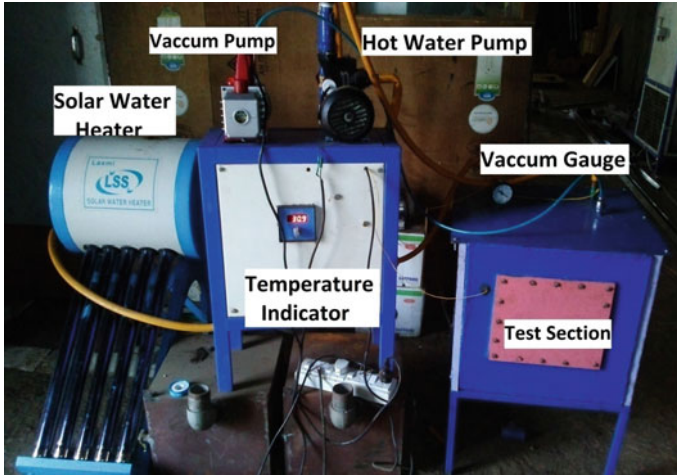


Fig. 2 Experimental setup

3 Experimental Investigation

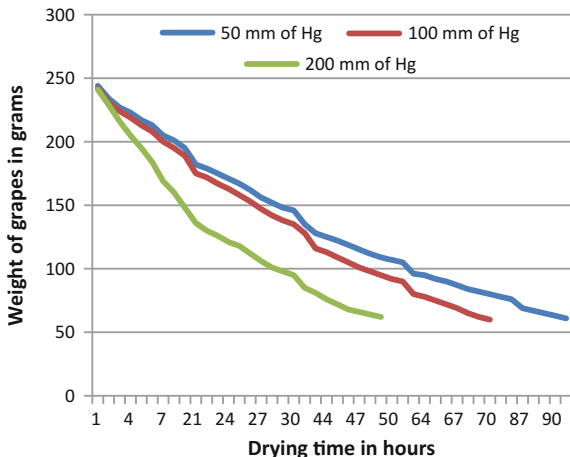
Figure 2 Shows the experimental setup used for this study. In this set up different components and instruments used for various applications can be observed.

4 Results and Discussion

4.1 Drying Time Versus Weight of Grapes

Figure 3 shows the reduction in weight of grapes with the increase in the drying time duration. Graph shows linear behavior which indicates that the decrease in weight of grapes is directly proportional to the drying time. Even though this graph shows some fluctuations at the place of open night drying as the drying process becomes slow at the night when hot water circulation is stopped. The graph also shows that the reduction in weight of grapes is faster at high vacuum pressure. It can be seen that for 50 mm of Hg the weight of grapes goes on increasing from 250 to 63.33 g which is the minimum amount of moisture required in the raisins. At 100 mm of Hg vacuum pressure, Over the period of 76 h the grape samples loses weight from 250 to 60 g due to losing moisture of 190 g as a result of combined drying of vacuum drying and open night drying. For 200 mm of Hg vacuum pressure In first hour 9 g of weight reduction is observed, at the end of first day weight becomes 148 g. After 53 h of drying final weight reduction in grape sample is 62 g, which gives raisins with 25% moisture contents and as good quality raisins requires 25% moisture content, hence no further drying is done.

Fig. 3 Drying time versus weight of grapes



4.2 Drying Time Versus Drying Rate

Figure 4 shows drying rate of grapes in kg/h is shown with drying time in hours. It can be observed from the graph that the drying rate of raisins decreases with increase in drying time. Initially, drying rate is very high, and it reduces as drying time increases. In initial hours at 200 mm of Hg, drying rate is 0.241 kg/h and it decreases up to 0.0013 kg/h at the end of drying process on 53 h. The decrease occurred in the drying rate is due to the reduction in moisture, initially, moisture is more hence it can be removed fastly, so the drying rate is high initially, and as moisture is reduced afterward, efforts required to reduce the moisture content is very high hence drying rate is decreased. For 100 mm of Hg, the drying rate drops

Fig. 4 Drying time versus drying rate

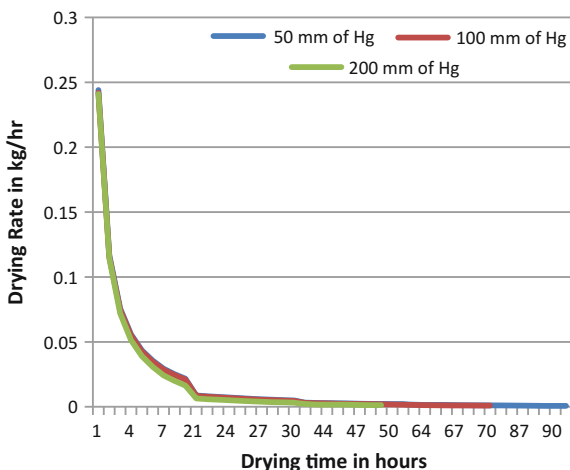
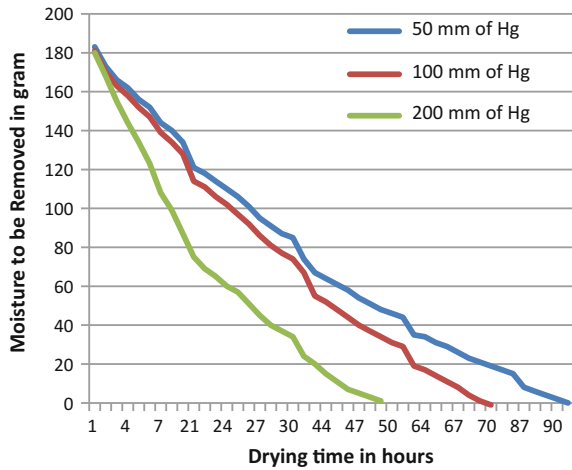


Fig. 5 Drying time versus moisture required to remove



from 0.242 to 0.0009 kg/h over a drying period of 76 h. The reduction in drying rate is a result of the reduction in moisture in the grapes which makes further drying much difficult (Fig. 5).

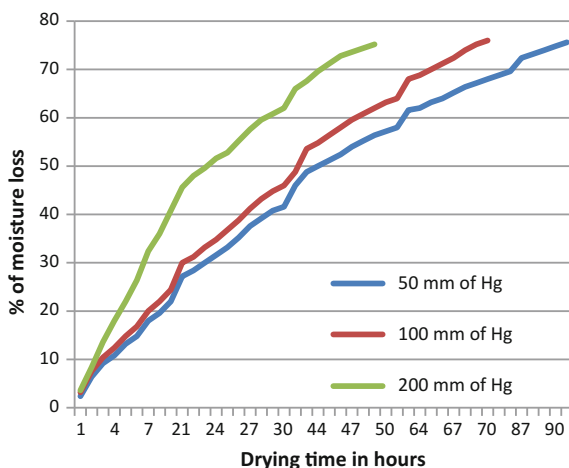
4.3 Drying Time Versus Moisture Content

This graph shows that over a period of 96 h grape sample losses 186.66 g of moisture through mostly vacuum drying and partly due to open night drying at 50 mm of Hg. For 100 mm of Hg vacuum pressure In the grape sample of 250 g, 75% of moisture is to be removed which is 186.66 g hence the drying process is done for removing these 186.66 g of moisture is presented on this graph. It shows that over period of 76 h 186.66 g of moisture is removed from the grape sample of 250 g. As only 186.66 g of moisture is to be removed from grapes to ensure good quality of raisins, the graph only represents the reduction in moisture content which is to be removed and other 63.33 g of moisture is not represented in this graph. For 200 mm of Hg vacuum pressure, at the first hour the gram sample loses 6 g of moisture, and total moisture mean to be removed 180 g. As drying time increases the moisture goes on decreasing and at the end after 53 h, the moisture content remains in the sample is 63 g which should not be removed from grape samples.

4.4 Drying Time Versus Moisture Loss

Figure 6 shows the loss of moisture with time for all the vacuum pressures in the system. The graph shows that for 200 mm of Hg vacuum pressure process of

Fig. 6 Drying time versus moisture loss



moisture removal is faster as compared to the low vacuum pressure. As moisture removal process is faster in high vacuum pressure, it is also seen from the fig that drying process takes less time at 200 mm of Hg vacuum pressure compared to the vacuum pressure at 100 mm of Hg and 50 mm of Hg.

5 Conclusions

The results of this experiment also show that the vacuum pressure in the drying chamber does have an effect on the performance of dryer, moisture removal depends upon the vacuum pressure. It is observed from the results that higher vacuum pressure results in the reduction in drying time. As vacuum pressure increases, drying period required for the production of raisins decreases. For vacuum pressure of 55 mm of Hg the drying period needed for the production of raisins is 96 h. As vacuum pressure increases from 55 mm of Hg to 100 mm of Hg the drying period decreases. It is seen that at 100 mm of Hg pressure drying period is 76 h.

When vacuum pressure further increases to 200 mm of Hg the drying period shows its lowest value of 53 h. When vacuum pressure increases from 55 mm of Hg to 200 mm of Hg the drying period decreases by 45%.

References

1. Voskens RGJH, Out PG, Schulte B (2015) Market opportunities for solar drying. Solar thermal, Ecofys Energy and Environment, Netherlands
2. Trotter WK, Heid WG, McElroy RG Jr (1979) Review of solar energy for agricultural products. U.S. Department of Agriculture Economics, Statistics, and Cooperative Service, Aug 1979

3. Belessiotis V, Delyannis E (2011) Solar drying. *Sol Energy* 85:1665–1691
4. Khalifa AJN, Al-Dabagh AM, Al-Mehemdi WM (2012) An experimental study of vegetable solar drying systems with and without auxiliary heat. *Int Sch Res Netw* 2012:8
5. Sarsavadia PN (2007) Development of a solar-assisted dryer and evaluation of energy requirement for the drying of onion. *Renew Energy* 32:2529–2547
6. Perumal R (2007) Comparative performance of solar cabinet, vacuum assisted solar and open sun drying methods
7. Bala BK, Mondol MRA, Biswas BK, Chowdury BLD, Janjai S (2003) Solar drying of pineapple using solar tunnel drier. *Renew Energy* 28:183–190
8. Lahsasni S, Kouhila M, Mahrouz M, Mohamed L, Agorram B (2004) Characteristic drying curve and mathematical modeling of thin-layer solar drying of prickly pear cladode (*Opuntia Ficus Indica*). *J Food Process Eng* 27(2):103–117
9. Mohanraj M, Chandrasekar P (2009) Performance of a forced convection solar drier integrated with gravel as heat storage material for chili drying. *J Eng Sci Technol* 4(3):305–314
10. Misha S, Mat S, Ruslan MH, Sopian K, Salleh E (2013) Review on the application of a tray dryer system for agricultural products. *World Appl Sci J* 22(3):424–433
11. Vijaya Venkata Ramana S, Iniyamb S, Goicc R (2012) A review of solar drying technologies. *Renew Sustain Energy Rev* 16:2652–2670
12. Sopian K, Othman MY, Zaidi SH, Amin N (2013) Advanced solar assisted drying systems for marine and agricultural products. Solar Energy Research Institute, University Kebangsaan, Malaysia
13. McGruder GR, Torgerson K (2007) Determination of optimal surface area to volume ratio for thin-layer drying of breadfruit. *Int J Service Learn Eng* 2(2):76–88

Wireless Healthcare Monitoring System

Dhiraj D. Kadam, Shailaja C. Patil and D.S. Bormane

Keywords Wireless sensor network · Wearable sensor · Health monitoring · Embedded system · Android system · Google cloud messaging

1 Introduction

Wireless Sensor Network (WSN) is considered as a standout amongst the most essential innovation today. Progress in remote sensor network monitoring system opened up new doors in healthcare monitoring frameworks [1]. With remote sensor monitoring system, it is possible to perform real time monitoring of multiple patient body which help to minimize risk of patient life [2, 3]. Sensor-based innovation has the best alternative to traditional wires associated system found in hospital monitoring. Due to this remote monitoring system there is no need of doctors to visit patient periodically [5–7]. The existing patient monitoring frameworks in hospital facilitates consistent checking of patient parameters, which require the sensors to be hardwired to adjacent, bedside screens or PCs, and basically limit the patient to the bed. In the present system constant monitoring of individuals needs and necessary to note down all the physiological parameters of a given patient by monitoring his/her records physically. Receiving such a strategy is error prone and may prompt catastrophe on account of a human mistake. But now, there is no such relation

D.D. Kadam (✉) · S.C. Patil · D.S. Bormane
Department of Electronics and Telecommunication, Rajarshi Shahu Collage of Engineering,
Savitribai Phule Pune University, Pune, Maharashtra, India
e-mail: dhirajkdm90@gmail.com

S.C. Patil
e-mail: shailaja.patil11@gmail.com

D.S. Bormane
e-mail: bdattatraya@yahoo.com

between the sensors and the bed side equipment's because of the remote sensor monitoring and sensor network. These frameworks don't require the patient to be constrained to his bed and allow him to move around, but requires within a particular range from the bedside screen [4–8].

The paper is organised as follows; Sect. 2 deals with literature review. Section 3 describes system architecture, sensor node, system flow graph, working of the system. Section 4 describes experimental evaluation. Conclusion and future scope described in Sect. 5.

2 Literature Review

From many years, a lot of research work is being carried out in healthcare industry as well as in WSN. Rapid development in the information and communication technology (ICT) opens up many doors for the development of health care technology.

Alemdar et al. [1] gives a significance of addressing to give smart health care services to the elderly and chronically ill children. This work proposes a solid potential for remote sensor systems to open new research point of view of low power, energy efficient deployment of multi-modular sensors for an enhanced nature of medical service. Additionally, it gives few conditions with state of the art like adaptability, energy efficiency, and security. Furthermore it give an advantages and difficulties of this framework. Li et al. [2] proposed a design of wireless health monitoring system that can monitor different vital signs and send them to a hospital or a health care provider through a wireless network. Rathore et al. [3] described a system for biomedical applications, where a patients' condition can be monitored from the place where doctors are sitting and hence proper and timely care to the patient can be given. This will help in losses due to delay in timely care. Further, in case of emergency, the doctor will be informed about the patient via SMS. It will be very beneficial for the patients, as in any case of emergency, doctors can take immediate action. Many effective health care applications based on wireless sensor technology have been proposed till now described in [9–13].

Proposed system in this paper developed with the integration of different technologies like ZigBee, GUI monitoring, GCM, Android Application that can helpful for doctors and family members of the patient(s) to monitor the patient in real time from remote location also. The graphical user interface allows family and other caretakers to monitor patient from anywhere any time. This system provides not only in hospital monitoring but also useful in the outdoor monitoring for elderly and alone people at their home, also in disaster prone area where emergency hospital setup is needed [8, 14].

3 System Architecture

The proposed monitoring system is capable of monitoring multiple patients' physiological parameter wirelessly. Wireless sensor node connected to the patient, will continually collect the sensor data and send this data by using RF module to the base node at remote location. Base node will perform all necessary operation on this data and display it on GUI. If any parameter cross the threshold value it will send an alert to the doctor. Figure 1 shows a block diagram of the system.

This system is mainly divided into four different section as described below;

- **Data input module**

This module consists of sensor that collects the physiological parameter from patients' body. Sensors used in this proposed system are temperature sensor (DS18B20), Heartbeat sensor (RDL), accelerometer sensor (ADXL 335) and stress monitoring sensor. Temperature sensor measure the body temperature, Heartbeat sensor measures the pulses of patient, Accelerometer is used for fall detection and Stress sensor is used to measure body stress.

- **Trans-receiver section**

Trans-receiver used is ZigBee. The sensor data is processed by node this data is then transmitted to base station using ZigBee module.

- **Interface module**

Here base node acts as interfacing device between sensor node and server PC. Beagle bone black is used as base station node. Processing like threshold checking and alert message is generated at the base node and send this data to the server for real time monitoring. This is further displayed on GUI.

- **Graphical user interface**

The GUI is used to analyse the real time monitoring that helps caretakers to monitor patients in real time. In case of any emergency it will send alert message using (GCM) service on android App.

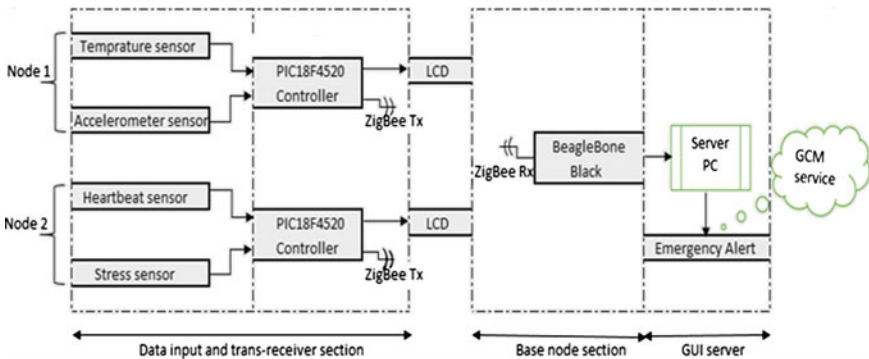


Fig. 1 Block diagram of proposed system

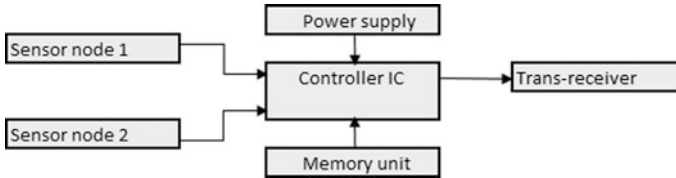


Fig. 2 Node architecture

3.1 Node Architecture

The node is the main part of the WSN. The node consists of sensors, controller board, power supply, trans-receiver section shown in Fig. 2. Node collects the data from different sensors and send them to the controller. Since the sensor data are analog in nature, controller converts this to digital by ADC. ZigBee at the node sends this data to the base station.

Hardware used for designing the system is PIC18F4520, Beagle-Bone Black as a base station, ZigBee and sensors like heartbeat sensor, temperature sensor, an accelerometer and stress sensor.

3.2 System Flow Chart

The proposed system algorithm can be explained with flow graph as shown in Fig. 3.

3.3 Step of Flow Graph

After turning on the system, the node is initialised. The system is designed to take input as physiological parameters of a patients' body. This input collected from the sensors is processed and integrated at the node. LCD is used to display the patients' data at a node that sensors measure and transmits to the base station. This processed data at the node, then transmitted to the base station via ZigBee. Here Beagle-Bone Black acts as a base node which collects the data from the node via ZigBee and then send it to the server PC using GUI which will be later used to monitor. If one or more parameter provided by the sensor is out of range, it will send alert messages by using GCM service otherwise it will go to the next data arrived from the sensor node.

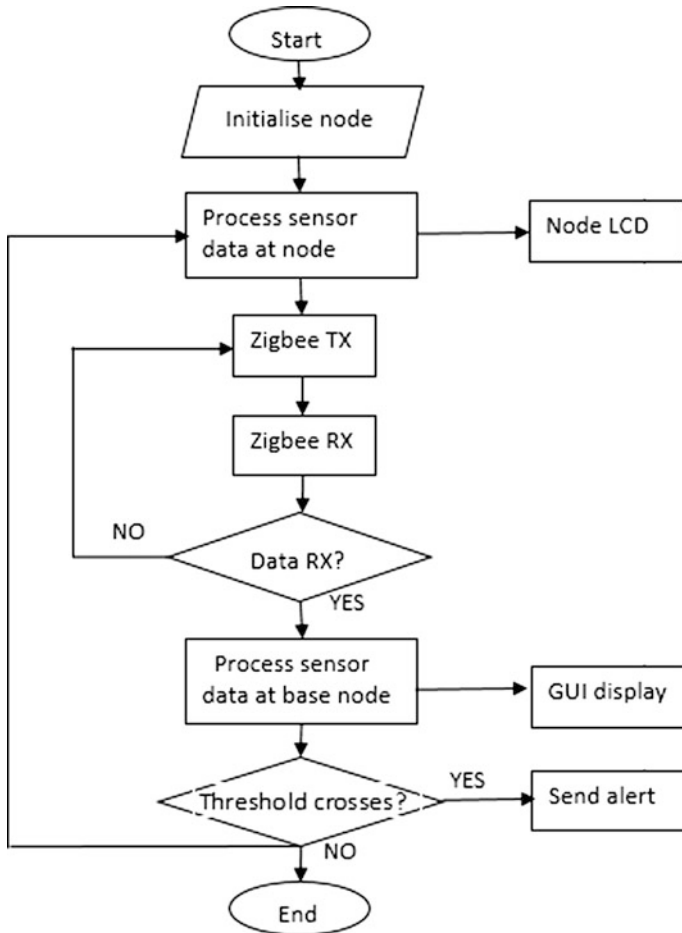


Fig. 3 System flow chart

4 Experimental Evaluation

The main objective of this evaluation is to observe that the software and hardware fulfils the objective and goal of the proposed system. Experimental evaluation is carried out at two different levels, one is Hardware level evaluation and other is Software level evaluation. At the hardware level evaluation, node processes data and send to the base node. At the software level evaluation, this data is displayed in GUI for real time monitoring and Android Application that helps doctors to analyses the patient from remote location also.

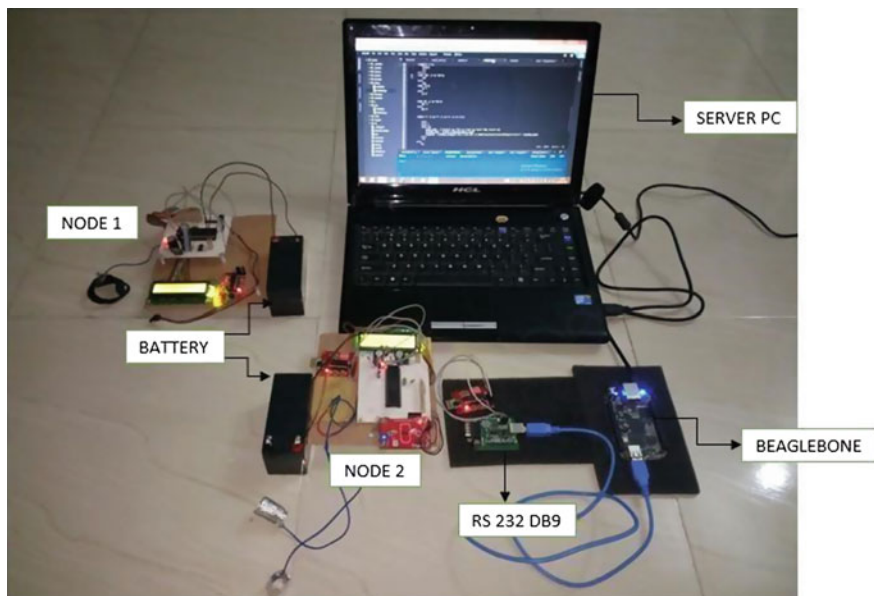


Fig. 4 Experimental setup

Figure 4 shows experimental setup. It consists of sensor node 1, sensor node 2 with DC battery of 12 V 1.3 Ah, Beagle Bone black controller board as a base node, and laptop as a server PC for GUI.

The output this evaluation is as shown below.

4.1 Heartbeat and Stress Sensor

Heartbeat measurement gives the soundness of the human cardiac network. A system to measure the heart rate by detecting the change in blood volume in a finger vein while the heart pumps the blood. It consists of an IR light that transmits a signal through the fingertip of the patient, a part of which is reflected by the blood cells. The reflected sign is recognized by a photo diode sensor which is measured in beats/min. Stress sensor is designed to analyse the body stress. Human skin acts as a resistance to electrical current. With the two electrodes that are placed on two fingertips of the patient, with that Galvanic Skin Response (GSR) is measured. As stress level increases body resistance decreases in proportion with the stress. Usually it is observed that, more stress results in higher voltage. To find out this value we use one resistance in series with skin resistance to form a voltage divider as shown in equation below;

$$v_0 = \frac{R_2}{R_s + R_2} V_{CC} \quad (1)$$

where R_s = skin resistance.

4.2 *Temperature Sensor*

DS18B20 temperature sensor used for monitoring the body temperature. It is one wire Interface i.e. it requires Only One Port Pin for Communication. It measures Temperatures from -10 to $+85$ °C for input voltage ranges from 3 to 5 V with ± 0.5 °C Accuracy.

4.3 *Accelerometer Sensor*

Accelerometer sensor is used to find the fall detection and motion of the patient. ADXL 335 is a thin, low power, accelerometer. It can measure the static acceleration of gravity in motion applications. With the change in the movement of the patient, it will produce signal conditioned voltage outputs. Deflection within the movement is measured using differential capacitors that consists of independent fixed plates and plates attached to the moving mass. Acceleration deflects the proof mass and unbalance the differential capacitor, resulting in a sensor output whose amplitude is proportional to acceleration.

4.4 *GUI and Alert Message*

The GUI is helpful in continuously monitor Patients physiological parameters. At the time of registration important details like the name of the patient, health problems and contact number are stored within the system which is useful for study of the patients' data over a period of time. Database used here is MySQL. Figure 5 shows login page of the GUI.

Figure 6 shows output of sensors displayed on GUI. This fig consist of display of four parameter i.e. Temperature, Accelerometer, Heartbeat and Stress level with patients' ID number. From this ID patients' can be identified.

Figure 7 shows the snapshot of history of the patient. The title of GUI is Medicare. The patients' details is displayed on the screen followed by all the sensor parameter.

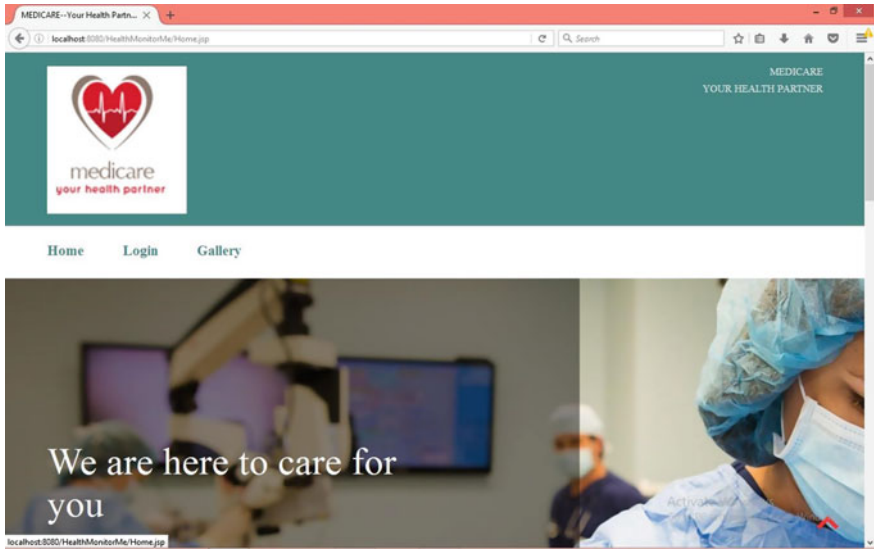


Fig. 5 GUI login page

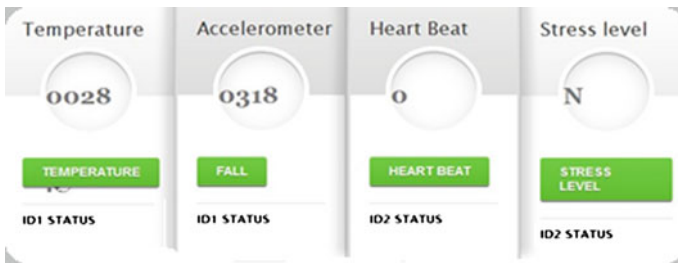


Fig. 6 Sensor output at GUI

It gives all the details of patient with ID 1. This patient is being monitor for fall detection and temperature, hence only two parameters are displayed on the screen. The patient ID 2 is being monitored for heartbeat and stress which is not shown in the screen shot.

Emergency alert system sends an alert message to the care-takers. Figure 8 shows snapshot of emergency alert message displayed on android App. With patient ID and alert message as “condition is abnormal and need emergency help”.

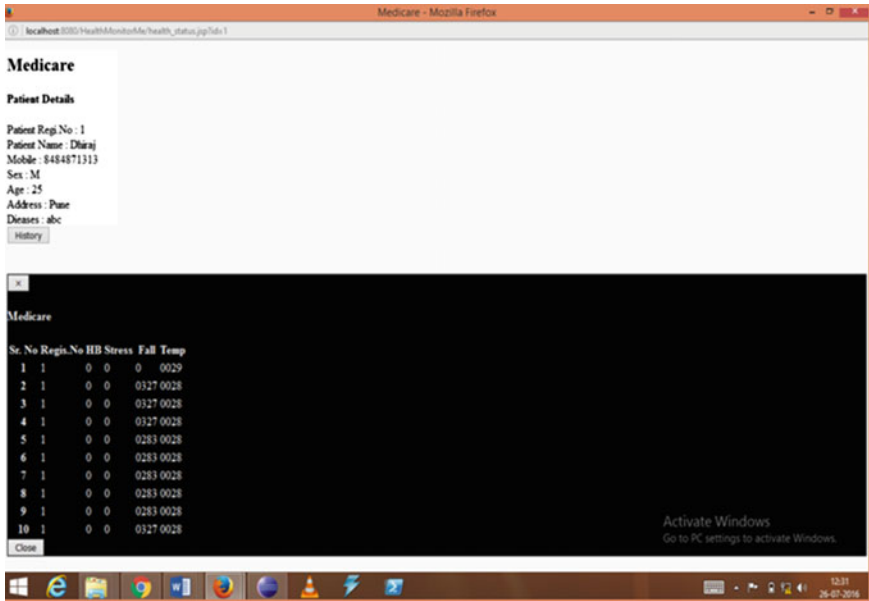
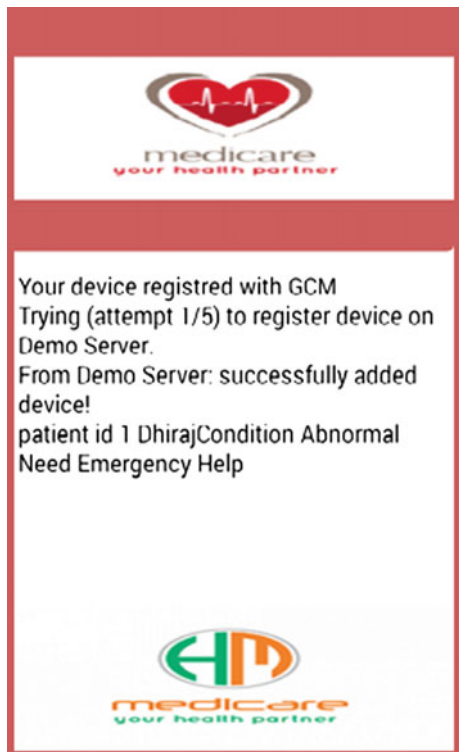


Fig. 7 History of the patient

Fig. 8 Emergency alert message



5 Conclusion

Medical healthcare systems, are being developed rapidly with advances in wireless communication technology. With development in healthcare system and its ease of use it allow doctors to real-time monitor, early diagnose and timely treatment for health hazards. Proposed system gives best alternative over wired associate system present in the hospital environment. From the experimental evaluation, objectives of application have implemented. Output of system can be monitored through GUI. Since communication is carried out with ZigBee thus a wireless network platform has been successfully implemented. This system can give advantages to the doctors and nurses to monitor patients from remote location, also by Emergency alert messaging service which gives alert to the doctors in case of emergency, reduce the further risk of patient life. In future not only in the hospital but also in emergency situation like disaster prone areas where emergency hospital setup is needed, this system can be very effective due to its small size and remote monitoring facility. Also in country like India where huge population and lack of hospital facilities, it is possible to use this system effective to help the society.

References

1. Alemdar H, Ersoy C (2010) Wireless sensor network for healthcare: a survey, vol 54. *ELSVIER Computer Network*, pp 2688–2710
2. Li Z, Feng G, Liu F, Dong JQ, Kamoua R, Tang W (2010) Wireless health monitoring system. In: Applications and technology conference (LISAT), pp 1–4
3. Rathore DK, Lulla D, Upmanyu A (2013) Wireless patient health monitoring 2013 international conference on system. In: *IEEE signal processing and communication (ICSC)*, pp 415–418
4. Ko JG, Lu C (2010) Wireless sensor for health care. In: *Proceedings of the IEEE conference 2010*, vol 98, pp 1947–1960
5. Patil SP, Patil SC (2015) Real time AVR based monitoring system for wireless sensor network. *Int J Innovative Res Sci Technol* 2.5:4–8
6. Krishna RVV, Ganana Vargin R (2014) Implementation of health care monitoring system using low power MCU and ARM Cortex A8, vol 2, pp 521–525
7. Rajasekaran S, Kumaran P (2013) Human health monitoring using wireless sensors network (WSN). *IJAIEEM* 2(12):323–330
8. Lin C-C, Chiu M-J, Hsiao C-C (2006) Wireless health care service system for elderly with dementia. *IEEE Trans Inf Technol Biomed.* 10(4):pp 696–704
9. Wcislik M, Pozoga M, Smerdzynski P (2015) Wireless health monitoring system. *Sci Dir IFAC Pap OnLine* 48(4):pp 312–317
10. Media Aminnian Hamid Reza Naji (2013) A hospital health care monitoring system using wireless sensor network. *Health Med Inf JHMI (an open access journal)* 4:121
11. Junnila S, Kailanto H, Merilahti J (2010) Wireless, multipurpose in-home health monitoring platform: two case trials. *IEEE Trans Inf Technol Biomed* 14(2):447–455

12. Lee R-G, Chen K-C (2007) A mobile care system with alert mechanism. *IEEE Trans Inf Technol Biomed* 11(5):507–517
13. Gonzalez FCJ (2014) Smart multi level tool for remote patient monitoring based on a wireless sensor and mobile augmented reality. *Sensors* 14:17212–17234
14. Somov A, Baranov A, Spirjakin D, Passerone R (2014) Circuit design and power consumption analysis of wireless gas sensor nodes: one-sensor versus two-sensor approach. *IEEE Sens J* 14(6):2056–2063

Optimization of Process Parameters for Shutter Type Vertical Axis Wind Turbine

Vidya R. Muttagi, Sandeep S. Wangikar, Supriya S. Bhosale
and Shrikrushna B. Bhosale

Keywords Shutter type · VAWT · Shutter angle · Wind speed · Taguchi method · ANOVA

1 Introduction

Energy has been the major issue for the mankind for a long time. In the last decade with progress in industry and international communication, energy consumption has been significantly increased. Electric energy consumption is expected to be doubled by 2053 compared with the year 2008. Today utilization of fossil fuel resources of energy is becoming more restricted mainly because of declining in fossil fuel reservoir, threatening global warming and the increase in oil prices. Therefore harnessing clean and renewable sources of energy is becoming the main worldwide topic for many researchers [1]. Wind energy is the kinetic energy associated with the movement of atmospheric air. It has been used for hundreds of years for sailing, grinding grain, and for irrigation. Wind energy system converts this kinetic energy into more useful forms of power. Wind energy systems of irrigation and milling have been in use since ancient times and since the beginning of the 20th century. It is being used to generate electric power. Windmills for water pumping have been installed in many countries, particularly in the rural areas. Wind turbines transform the energy from the wind into mechanical power, which can then be employed directly for grinding etc. or then converting to electric power for generation of electricity. The wind turbines can be used singly or in clusters known

V.R. Muttagi · S.S. Bhosale
Department of Information Technology, SVERI's College of Engineering (Polytechnic),
Pandharpur, India
e-mail: muttagividya@gmail.com

S.S. Wangikar (✉) · S.B. Bhosale
Department of Mechanical Engineering, SVERI's College of Engineering,
Pandharpur, India
e-mail: sswangikar@coe.sveri.ac.in

as ‘wind farms’. Small wind turbines called aero-generators can be used to charge large batteries [2]. The Indian wind energy sector has an installed capacity 7.04 GW (Dec 2016). In terms of wind power installed capacity, India has been successful in achieving 4th rank in the world [3]. Today India is a major player in the global wind energy market. Wind turbines are classified into two general type’s horizontal and vertical axis. A horizontal axis wind turbine (HAWT) has its blades rotating on an axis parallel to the ground. A vertical axis wind turbine (VAWT) has its blades rotating on an axis perpendicular to the ground. There are a number of available designs for both and each type has certain advantages and disadvantages. However, compared with the horizontal axis type, very few vertical axis machines are available commercially. The few advantages of VAWT over HAWT are as: Easier to maintain to as most of their moving parts are located near the ground, yaw device is not needed decreasing the need for this bearing and its cost, low manufacturing cost for VAWT than that for an equivalent HAWT, etc. The representative collection of literature related to VAWT is presented below: A blade vibration monitoring method based on strain gauges for a straight-bladed vertical axis wind turbine with pitch control has been studied by Liang et al. [4]. The effect of design parameters on the performance of casement type vertical axis wind turbine and shutter type vertical axis wind turbine has been performed [5, 6]. The basic research methods have been presented by Jin et al. [7]. Rollin used stereo particle image velocimetry in a wind-tunnel to study boundary layer effects in the wake behind a vertical axis wind turbine [8]. The measurement of velocity distribution in the whole field of a small straight bladed VAWT has been carried out by Li et al. [9]. Li et al. studied the power performance of straight-bladed VAWT experimentally in wind tunnel [10].

In this paper, a process parameter’s effect on the performance of shutter type vertical axis wind turbine is presented. The wind speed and shutter speed are the selected process parameters for the study. The study is carried out using Taguchi L9 orthogonal array. The parameters corresponding to the higher power are given.

2 Methodology

2.1 Experimentation Model of STVAWT

Shutter Type Vertical Axis Wind Turbine (STVAWT) is as shown in Fig. 1. STVAWT consists of three blades with casements. These shutters are mounted in a frame which is attached to the shaft. The wind turbine has a radius of 50 cm and height 85 cm. The three frames of radius 50 cm are fitted on the central hollow shaft of 25 mm diameter. Each frame is having two shutters ($210 \times 290 \times 0.5$ mm) fitted in it with the help of hinges so that the shutters can be adjusted to the desired angle. Also, shutter types can be changes like plain or curved type shutter. There is one thrust and two deep groove ball bearings used for supporting the shaft in the structure.



Fig. 1 Photograph of shutter type vertical axis wind turbine (STVAWT)

2.2 Design of Experiments

In this study, experiments were designed on the basis of the experimental design technique which refers to the planning of experiments, collection, and analysis of data with near-optimum use of the available resource (D.C. Montgomery). It is an experimental method designed and developed for evaluating the effects of process parameters on performance characteristics. It determines the process parameter conditions for optimum response variables. The design of experiments involves proper selection of variables (input factors) and their interactions. The use of statistically derived full factorial design gives the number of experimental runs, to be carried out without affecting the quality of the analysis. The performance of any wind turbine is governed by the power generated. Therefore, the response parameter selected is the mechanical power generated. The main parameters which will have a significant effect on the STVAWT are wind speed and shutter angle. The power is directly proportional to the cube of wind speed. Shutter angle is the angle made by shutter with the frame or blade plane. This angle determines the amount of air passing through the blades at a given wind speed. Therefore, the full factorial design method was used to determine optimal response parameters for maximum power generation with wind speed and shutter angle. The 3k full factorial design consists of all combinations of the k factors taking on three levels. These are high, medium and low levels of factors. Accordingly, to 3k full factorial designs, 9 experiments were planned as per the selected design. The present investigation studied the results of the effects of wind speed and shutter angle on the power

Table 1 Input parameters and their levels

Factor/parameter	Level 1	Level 2	Level 3
Wind speed (m/s)	10	12.5	15
Shutter angle (°)	20	30	40

Table 2 Experimental design matrix with power generated

Expt. No	Wind speed (m/s)	Shutter angle	Power for plain shutters (W)	Power for curved shutters (W)
1	10	20	29.97	45.72
2	10	30	42.16	62.05
3	10	40	22.78	40.75
4	12.5	20	38.93	58.31
5	12.5	30	54.61	78.39
6	12.5	40	28.59	52.05
7	15	20	51.78	74.02
8	15	30	70.98	103.50
9	15	40	35.24	65.29

Table 3 Analysis of variance for power in plain shutter

Source	DF	Seq SS	Adj SS	Adj MS	F	P
Wind speed	2	667.55	667.55	333.77	19.52	0.009
Shutter angle	2	1106.67	1106.67	553.34	32.35	0.003
Error	4	68.41	68.41	17.10		
Total	8	1842.63				

S = 4.13559, R-Sq = 96.29%, R-Sq (adj) = 92.57%

generation in STVAWT. Selected parameters and their levels are shown in Table 1. Table 2 shows experimental design matrix with power generated for plain and curved type shutter.

3 Results and Discussion

All the experiments are conducted and result analysis are calculated and discussed in this section. The analysis of the experimental data was carried out for plain and curved shutter by using ANOVA and main effect plot. Table 3 shows ANOVA for plain shutter and Table 4 shows ANOVA for the curved shutter type vertical axis wind turbine.

From Table 3 of ANOVA of plain shutter type wind turbine shows that the wind speed and shutter angle both has a significant effect on power generation. The major contribution is of shutter angle over wind speed. Also, in a case of curved shutter

Table 4 Analysis of variance for power in curved shutter

Source	DF	Seq SS	Adj SS	Adj MS	F	P
Wind speed	2	1492.39	1492.39	746.20	35.84	0.003
Shutter angle	2	1345.57	1345.57	672.78	32.32	0.003
Error	4	83.28	83.28	20.82		
Total	8	2921.24				

S = 4.56282, R-Sq = 97.15%, R-Sq (adj) = 94.30%

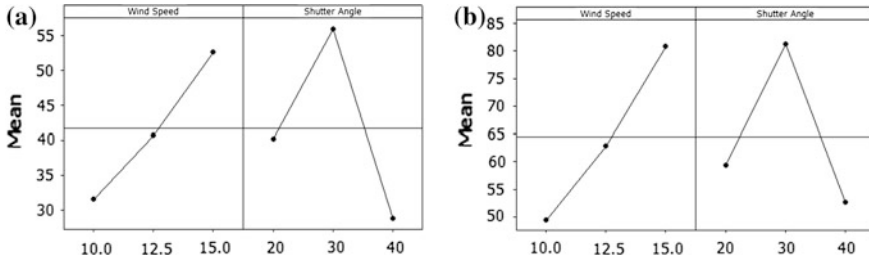


Fig. 2 Main effect plot for power for plain shutter

type wind turbine, as shown in Table 4, it shows a similar trend but the wind speed has more significant parameter as compared to shutter angle. Figure 2a, b show the main effect plots for mechanical power for plain shutter and curved shutter respectively.

From Fig. 2a, b, the trend of wind speed and shutter angle remains same in both plain and curved type shutter. The mechanical power is observed increasing with increase in wind speed within the tested ranges of air velocities. The power increases with increase in shutter angle up to 30° and then decreases with further increase in shutter angle for both the plain and curved shutters. As compared with plain shutters, the power generated using curved shutters is higher. This is due to less resistance to the wind due to the curved shape of the shutter. It is observed that for maximum power generation in plain and curved type shutter wind turbine the significant parameters are wind speed at 15 m/s and shutter angle at 30°.

4 Conclusion

The Shutter Type Vertical Axis Wind Turbine (STVAWT) is developed and the performance analysis is carried out. The following conclusions are drawn from above study:

- Wind speed and shutter angle affects the performance of turbine significantly.
- The power increases with increase in wind speed and having maximum values at wind speed 15 m/s.

- For 30° shutter angle, the power is maximum and it is 70.98 and 103.5 W for plain and curved shutter type wind turbine.
- The power generated using curved shutters found higher than that for plain shutters.

References

1. Saeidi D, Sedaghat A, Alamdari P, Alemrajabi AA (2012) Aerodynamic design & economical evaluation of site specific small vertical axis wind turbines. *Appl Energy* 1–2 (Elsevier)
2. Howell R, Qin N, Edwards J, Durrani N (2010) Wind tunnel and numerical study of a small vertical axis wind turbine. *Renew Energy* 35:412–422
3. Global Wind Energy Council—GWEC (in press) <http://www.gwec.net/india-ranks-4th-in-global-wind-power-installed-capacity-index/>
4. Liang Y, Li J, Meng J (2016) Blade vibration monitoring for a straight-bladed vertical axis wind turbine with pitch control. In: Proceedings of 2016 IEEE international conference on mechatronics and automation, 7–10 Aug, Harbin, China
5. Wangikar SS, Misal ND (2012) Effect of some design parameters on performance of a shutter type vertical axis wind turbine. In: Proceedings of the ASME 2012 gas turbine India conference (GTINDIA2012), 1 Dec 2012, Mumbai, Maharashtra, India
6. Wangikar SS, Jagtap SU, Tarmude AB, Pore AS, Shinde SP (2013) Development and performance analysis of casement type vertical axis wind turbine. Paper Number: GTINDIA2013-3752
7. Jin X, Zhao G, Gao K, Wenbin J (2015) Darrieus vertical axis wind turbine Basic research methods. *Renew Sustain Energy Rev* 42:212–225
8. Rolin V, Porté-Agel F (2015) Wind-tunnel study of the wake behind a vertical axis wind turbine in a boundary layer flow using stereoscopic particle image velocimetry. *J Phys Conf Ser* 625:012012
9. Li Q, Maeda T, Kamada Y, Murata J, Yamamoto M, Ogasawara T, Shimizu K, Kogaki T (2016) Study on power performance for straight-bladed vertical axis wind turbine by field and wind tunnel test. *Renew Energy* 90:291–300
10. Li Q, Maeda T, Kamada Y, Murata J, Furukawa K, Yamamoto M (2016) Measurement of the flow field around straight-bladed vertical axis wind turbine. *J Wind Eng Ind Aerodyn* 151:70–78

An Anthropometric Data of Cycle Rickshaw Operators to Approach Ergonomics in Cycle Rickshaw Design

M.S. Gorde and A.B. Borade

Keywords Anthropometric data · Cycle rickshaw · Cycle rickshaw puller

1 Introduction

A number of studies have been carried out on various aspects of cycle rickshaw like energy expenditure of cycle rickshaw operators of different part of India [1, 2]. A number of anthropometric studies have been reported in India on agricultural workers [3–7], anthropometric data of various part of body have been reported for general population in India [8–11]. In spite of the studies was carried out in order to collect the data anthropometric data for 34 body measurements specially for Eastern India [12]. Studies indicate that Indian population is different in different regions. Stature of Indian population is smaller than other populations [13].

1.1 Cycle Rickshaw

The pedal operated Rickshaw is a modified bicycle, which is used extensively as a mode of transport for carrying passengers and luggage. Tricycle orienginated in Japan around 1868. At that time this man power vehicle was called “Jinriksha”. The word rickshaw comes from Asia, where this vehicle was mainly used as a means of transportation for the social elites. The word derives from the Japanese word jin-

M.S. Gorde (✉) · A.B. Borade
Jawaharlal Darda College of Engineering and Technology,
Yavatmal 445001, Maharashtra, India
e-mail: gordemahesh7@rediffmail.com

A.B. Borade
e-mail: atulborade@gmail.com

rikisha (jin = human, riki = power or force, sha = vehicle), which literally means “human-powered vehicle” Tricycle is widely used in Asian countries in varying styles and names such as Trishaw, Pedicab, cyclo and Becaks. A cycle rickshaw is often hailed as environment-friendly and less expensive mode of transportation. Since it is considered as Indian traditional ride they are seen in each and every part of India ranging villages, small towns, metros, heritage sites etc. It is unorganized sector of India. In metros these are used inside institutional areas, market places and also in narrow and crowded lanes where there is accessibility problem for vehicles. The Cycle Rickshaw is available in various types as per the operation purpose such as for carrying passengers, luggage and merchandise.

1.2 Cycle Rickshaw Operators

In India, a population of about 9 lacks people is engaged in riding cycle rickshaw as occupation. The cycles Rickshaw operator are predominantly males with little or no formal training in the field of their work. Most of them have learnt the riding through observation and hand on experience. Owing to this, the methodology followed by them is unscientific and instinctive. As it is unorganized sector of India, has no representation of any sort and hence any standards are not followed. The cycle Rickshaw is manufacture fabricates and modified as per the local trends. All this has lead to unplanned mushrooming operation in an extremely unscientific way further leading to severe health and occupational hazards to the rider.

2 Research Methodology for Pilot Study

2.1 Motivation and Research Objective

The objective of present study is collect an anthropometric data of Cycle Rickshaw operators specially selected location in Vidrabha region of Weston India as well as compared it with anthropometrics data of Indian population. The anthropometric data and outcome of the research is beneficial for ergonomic design of bicycle, Cycle Rickshaws and similar types of products. The main motive behind this pilot study is the ergonomic design, assessment and optimization of variables affecting the performance of cycle rickshaw puller as per anthropometric data specially for Vidrabha region of Weston India.

2.2 Research Instrument

Body weight and different heights, different lengths statures of the subjects were recorded. The parameters like heights of the eye, acromion and elbow both in standing and sitting postures, knee and popliteal heights in a sitting posture were recorded using anthropometer and flexible measuring tape. A random sampling technique was adopted to select the rickshaw stands in a locality. From each rickshaw stand the rickshaw pullers were selected based on a systemic sampling technique.

2.3 Survey Administration

All subjects were in voluntary basis and have been given a verbal description of the purpose of the study. They were provided with a questionnaire pertaining to their Name, age, gender, experience, etc. All of them underwent a pre interview for obtaining some information's about their job characterizations.

2.4 Respondents' Profiles

Anthropometric data was collected of 550 Cycle Rickshaw riders from selected location of Vidrabha region i.e. Nagpur, Amaravati, Akola, Buldhana, Washim, Yavatmal, Wardha, Chandrapur, Bhandara, Gondia and Gadchiroli districts of India. Research participants are the cycle Rickshaw operator's male between the age 31.2 and 57.6 years with mean age of 44.4 (± 10.9 years). Each cycle Rickshaw puller had a minimum work experience of 1 year. Data of 12 anthropometric parameters were collected from cycle rickshaw pullers ($n = 550$) of different locations at Nagpur ($n = 50$), Amaravati ($n = 50$), Akola ($n = 50$), Buldhana ($n = 50$), Washim ($n = 50$), Yavatmal ($n = 50$), Wardha ($n = 50$), Chandrapur ($n = 50$), Bhandara ($n = 50$), Gondia ($n = 50$) and Gadchiroli ($n = 50$).

2.5 Variables

In this study five variables Stature, Eye, Acromion, Elbow, Crotch in standing condition and seven variables Erect sitting, Eye, Elbow rest, Knee, Popliteal, Lower humber, Upper Lumbar in sitting condition are recorded. The variables were chosen on the basis of previous studies, [4-7, 12] and considering its important in ergonomic design, assessment and optimization of variables affecting the performance of cycle rickshaw puller.

2.6 Hypotheses

Detailed anthropometric survey in India is important the body dimension of Indian population varies from region to region Majumdar [14]. There is much more difference in body dimensions of western and Indian population and even in Indian population, as they vary by region to region. Anthropometric survey of western, northern, central and southern India have been reported by Sen 1964, Sharma et al. [7], Gite and Yadav [6], and Fernandez and Uppugonduri [11]. In spite of the studies was carried out in order to collect the data anthropometric data of cycle rickshaw puller for 34 body measurements specially for Eastern India [12]. However no such anthropometric survey has been done on cycle rickshaw puller in Vidrabha region of Weston India. Due to geographical as well as climate differences it is expected to have significant difference between anthropometric data. This is needs to be examined in the Weston Indian context. As all variables are dependent variables in which stature is prime importance variable. The following hypotheses were formulated on the basis of Stature.

H_0 = There is no significant difference between anthropometric data of Cycle Rickshaw puller of Vidrabha region of Weston India and Eastern India [12].

$$H_0 : P_1 = P_2$$

H_1 = There is a significant difference between anthropometric data of Cycle Rickshaw puller of Vidrabha region of Weston India and Eastern India [12].

$$H_1 : P_1 \neq P_2$$

Similarly

H_0 = There is no significant difference between anthropometric data of Cycle Rickshaw puller of Vidrabha region of Weston India and Indian population [9].

$$H_0 : P_1 = P_3$$

H_1 = There is a significant difference between anthropometric data of Cycle Rickshaw puller of Vidrabha region of Weston India and Indian population [9].

$$H_1 : P_1 \neq P_3$$

3 Results and Discussion

3.1 Anthropometric Data

Table 1 shows the mean value of age, height and weight, the lowest value of age was observed in Akola 31.2 year and the highest age was found in Yavatmal which

Table 1 Physical characteristic of cycle rickshaw operator

	Nagpur	Amaravati	Akola	Buldhana	Washim	Yavatmal	Wardha	Chandrapur	Bhandara	Gondia	Gadchiroli	All places (n = 550)	Pradhan et al. 2010 (n = 880)	Chakrabarti 1997 (n = 710)
Age (year)	42.7 ± 11.3	42.8 ± 10.1	43.3 ± 12.1	45.8 ± 10.8	45.4 ± 11.7	45.2 ± 12.4	44.3 ± 09.6	46.3 ± 11.0	44.4 ± 11.1	44.5 ± 10.3	43.8 ± 10.3	44.4 ± 10.9	37.7 ± 11.3	-
Stature (cm)	163 ± 5.52	165 ± 5.01	164 ± 6.26	163.2 ± 5.21	162.4 ± 4.79	163.3 ± 4.97	163 ± 5.37	164.5 ± 6.94	163 ± 5.32	163 ± 7.18	162.3 ± 4.72	163.27 ± 5.22	161.4 ± 5.94	165 ± 7
Weight (kg)	51.4 ± 8.63	49.8 ± 7.45	50.2 ± 6.78	47.62 ± 10.61	47.5 ± 7.16	48.96 ± 9.39	47.9 ± 7.86	52.61 ± 10.48	51.8 ± 8.93	47.3 ± 6.55	48.6 ± 6.84	49.43 ± 8.24	48.8 ± 6.28	57 ± 11

Values are mean ± SD

is 57.6 years the lowest stature was found in Gondia which was 155.77 cm and the highest stature found in Chandrapur which is 171.4 cm the lowest weight was found in Yavatmal which was 39.6 kg and the highest weight was found in Chandrapur 63.09 kg. When the value of height was compared with Indian data [9, 12], it was found that there was significant difference. The value of stature as reported by other Indian studies (South India) were 160.7 ± 6.0 cm [11] and 161.5 cm [15] (Fig. 1; Tables 2 and 3).

3.2 Anthropology of Indian Cycle Rickshaw Operator

Anthropometric characteristics of Cycle rickshaw operators were different for different area of India as well as Indian population. There is some genetic difference of populations along the different places in India which is always reflected in the anthropometric characteristic of Cycle rickshaw operator. The lower values of Cycle rickshaw operator may be due to their poor socio-economical conditions and the lack of proper nutrition (Table 4).

3.3 Hypothesis Testing

To test hypothesis Statistic Z test were used.

Null hypothesis $H_0: P_1 = P_2$

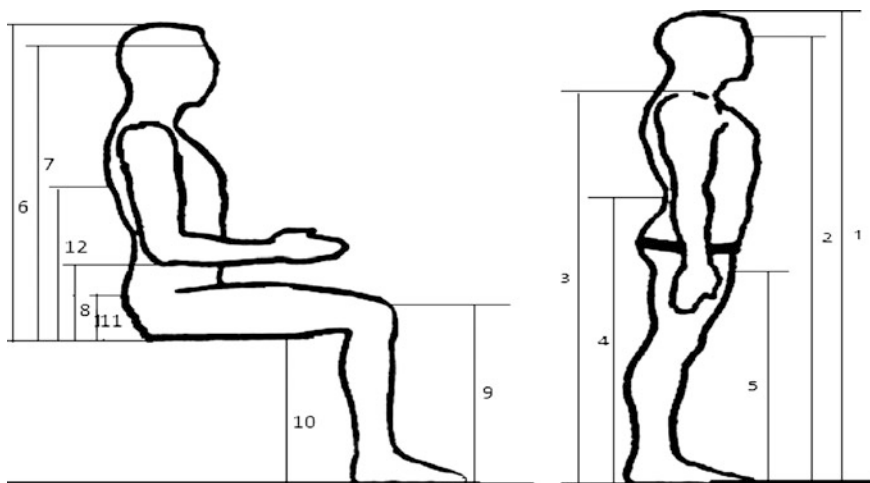


Fig. 1 Illustrations of dimensional landmark with reference numbers

Table 2 Anthropometric measurement of different body height of cycle rickshaw operators during standing

Ref. No.	Variables	Nagpur	Amaravati	Akola	Buldhana	Washim	Yavatmal	Wardha	Chandrapur	Bhandara	Gondia	Gadchiroli	All places
[1]	Stature	163 ± 5.52	164.7 ± 5.01	163.7 ± 6.26	163.2 ± 5.21	162.4 ± 4.79	163.3 ± 4.97	162.7 ± 5.37	164.5 ± 6.94	163.2 ± 5.32	163 ± 7.18	162.3 ± 4.72	163.27 ± 5.22
[2]	Eye	153 ± 5.43	154.3 ± 5.06	153.5 ± 6.30	153.3 ± 5.74	152.1 ± 4.81	152.7 ± 4.97	151.9 ± 6.02	154.4 ± 4.94	153 ± 5.33	153 ± 5.28	152.8 ± 5.06	153.1 ± 5.21
[3]	Acromion	136 ± 5.6	137.3 ± 5.02	136.7 ± 5.78	135.9 ± 5.23	135.6 ± 5.02	136.6 ± 4.80	135.5 ± 5.39	137.1 ± 5.12	137.3 ± 5.45	135 ± 5.56	134.1 ± 4.71	136.05 ± 5.18
[4]	Elbow	103.0 ± 5.52	104.2 ± 6.14	102.3 ± 6.26	101.3 ± 6.24	100.7 ± 5.43	101.2 ± 6.71	100.3 ± 5.37	102.3 ± 6.54	101.9 ± 5.85	101.6 ± 5.74	100.5 ± 5.34	101.8 ± 5.67
[5]	Crotch	77.9 ± 5.52	77.2 ± 5.68	77.4 ± 6.48	77.3 ± 5.56	74.9 ± 4.82	76.2 ± 4.56	75.7 ± 5.63	78.3 ± 4.94	76.7 ± 5.96	75.7 ± 5.28	75.1 ± 5.69	76.582 ± 6.45

Values are mean ± SD in centimeters

Table 3 Anthropometric measurement of different body height of cycle rickshaw operators during sitting position

Ref. No.	Variables	Nagpur	Amaravati	Akola	Buldhana	Washim	Yavatmal	Wardha	Chandrapur	Bhandara	Gondia	Gadchiroli	All places
[6]	Erect Sitting	85.8 ± 5.52	86.1 ± 5.01	85.6 ± 6.26	81.9 ± 5.21	86 ± 4.79	86.6 ± 4.97	85.1 ± 5.37	85.8 ± 4.94	83.9 ± 5.32	84.7 ± 5.28	82 ± 4.72	84.86 ± 5.21
[7]	Eye	74.4 ± 5.43	77.4 ± 5.06	73.6 ± 6.30	73.6 ± 5.74	75 ± 4.81	75.1 ± 4.97	74.8 ± 6.02	74.6 ± 4.94	75.6 ± 5.33	76.4 ± 5.28	76.4 ± 5.06	75.17 ± 5.21
[8]	Elbow rest	22.9 ± 5.52	24.1 ± 6.14	22.2 ± 6.26	23.4 ± 6.24	23.5 ± 5.43	25.1 ± 6.71	21.4 ± 5.37	25.5 ± 6.54	20.9 ± 5.85	25.4 ± 5.74	23.9 ± 5.34	23.48 ± 5.67
[9]	Knee	50.8 ± 5.52	52.8 ± 5.01	50.3 ± 6.26	52.6 ± 5.20	53.7 ± 4.77	55.2 ± 4.98	51.3 ± 5.35	54.6 ± 6.94	52.7 ± 5.32	54.0 ± 7.18	53.7 ± 4.72	52.9 ± 5.22
[10]	Popliteal	36.3 ± 5.6	41.2 ± 5.02	39.4 ± 5.78	41.8 ± 5.23	40.1 ± 5.02	42.5 ± 4.80	36.7 ± 5.39	41.2 ± 5.12	37.5 ± 5.45	39.1 ± 5.56	41.1 ± 4.71	39.7 ± 5.18
[11]	Lower lumbar	13.5 ± 5.52	12.7 ± 5.01	13.1 ± 6.26	13.4 ± 5.21	10.9 ± 4.79	12.8 ± 4.97	11.4 ± 5.37	13.9 ± 6.94	11.2 ± 5.32	10.4 ± 7.18	9.7 ± 4.72	12.1 ± 5.22
[12]	Upper lumbar	24.7 ± 5.51	30.3 ± 5.02	28.7 ± 6.30	31.2 ± 5.21	29.0 ± 4.72	35.6 ± 4.89	26.3 ± 5.41	31.2 ± 6.92	26.1 ± 5.32	32.6 ± 7.17	32.2 ± 4.71	29.8 ± 5.23

Values are mean ± SD in centimeters

Table 4 Comparison of anthropometric measurements of different body height of cycle rickshaw operators

Ref. No.	Variables	All places (n = 550)	Pradhan et al. 2010	Chakrabarti 1997	Ref. No.	Variables	All places (n = 550)	Pradhan et al. 2010	Chakrabarti 1997
[1]	Stature	163.27 ± 5.22	161.4 ± 5.94	165 ± 7	[7]	Eye	75.17 ± 5.21	73.8 ± 3.90	73.2 ± 3.02
[2]	Eye	153.1 ± 5.21	150.8 ± 5.75	153 ± 6.8	[8]	ElbowRest	23.48 ± 5.67	21.5 ± 3.40	22.2 ± 3.12
[3]	Acromion	136.05 ± 5.18	134 ± 5.52	134.9 ± 6.8	[9]	Knee	52.9 ± 5.22	52 ± 3.00	50.1 ± 2.49
[4]	Elbow	101.8 ± 5.67	99.6 ± 4.48	103.8 ± 5.6	[10]	Popliteal	39.7 ± 5.18	42.6 ± 2.80	41.4 ± 2.16
[5]	Crotch	76.582 ± 6.45	74.2 ± 2.73	76.5 ± 5.2	[11]	Lower lumbar	12.1 ± 5.22	10.6 ± 2.60	9.7 ± 0.36
[6]	Erect sitting	84.86 ± 5.21	83.7 ± 4.50	83.9 ± 3.37	[12]	Upper Lumbar	29.8 ± 5.23	30.6 ± 3.00	29.1 ± 1.07

$$Z = \frac{P1 - P2}{\sqrt{\left\{ \frac{P1 * q1}{n1} \right\} + \left\{ \frac{P2 * q2}{n2} \right\}}}$$

where

$$P1 = 163.27/550 = 0.296, q1 = 1 - P1 = 1 - 0.296 = 0.703, n1 = 550$$

$$P2 = 161.4/880 = 0.183, q2 = 1 - P2 = 1 - 0.183 = 0.816, n2 = 880.$$

Statistic Z test

$$Z = \frac{0.296 - 0.183}{\sqrt{\left\{ \frac{0.296 * 0.703}{550} \right\} + \left\{ \frac{0.183 * 0.816}{880} \right\}}}$$

$$Z = 4.9$$

At 5% level which comes as under normal curve area table, $R: |Z| > 1.645$.

The observed value of Z is 4.9 which is in the rejection region and so null hypothesis was reject in favour of there is a significant difference between anthropometric data of Cycle Rickshaw puller of Vidrabha region of Weston India and Eastern India [12].

Similarly Second hypothesis test

i.e. Null hypothesis $H_0: P1 = P3$

$$Z = \frac{P1 - P3}{\sqrt{\left\{ \frac{P1 * q1}{n1} \right\} + \left\{ \frac{P3 * q3}{n2} \right\}}}$$

where

$$P1 = 163.27/550 = 0.296, q1 = 1 - P1 = 1 - 0.296 = 0.703, n1 = 550$$

$$P3 = 165.0/710 = 0.232, q3 = 1 - P3 = 1 - 0.183 = 0.767, n2 = 710.$$

Statistic Z test

$$Z = \frac{0.296 - 0.232}{\sqrt{\left\{ \frac{0.296 * 0.703}{550} \right\} + \left\{ \frac{0.232 * 0.767}{710} \right\}}}$$

$$Z = 2.63$$

At 5% level which comes as under normal curve area table, $R:|Z| > 1.96$.

The observed value of Z is 2.63 which is in the rejection region and so null hypothesis was reject in favour of there is a significant difference between anthropometric data of Cycle Rickshaw puller of Vidrabha region of Weston India and Indian population [9].

4 Variable Factors Consider for Ergonomic Design of Cycle Rickshaw Puller

4.1 Crank Length

Investigators have reported that maximal pedaling power is affected by crank length [16–18]. This optimal crank length is related to leg length [16]. In the mathematical modeled it was found that crank length directly effects on optimal pedaling rate, maximal power produce as well as pedaling speed. Maximum power varied by $0 \pm 10\%$ for crank lengths of 130 ± 210 mm, depending on the dimension of optimal muscle length, and that optimal pedal speed was nearly independent of crank length [18, 19]. But this model may not affect by step wise muscle activation and relaxation, which normally occurs during activation and relaxation periods [20]. Impulse and power were similar for crank lengths of 145 ± 220 mm [14], but they did not report values for maximum power, optimal pedaling rate, or optimal pedal speed. Thus, it seems that the exact effects of crank length on maximum power, optimal pedaling rate, and optimal pedal speed remain to be determined. Therefore, investigation should carried out to determine the effects of crank length on the maximum cycling power, optimal pedaling rate, and optimal pedal. But as per anthropometric data 170 mm crank length is taken for ergonomic design of cycle rickshaw.

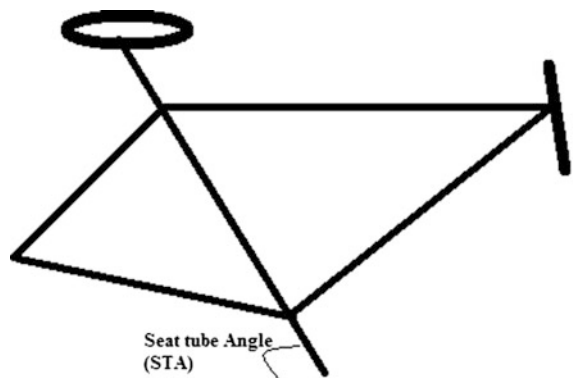
4.2 Seat Tube Angle

The seat tube angle commonly referred as STA, the angle between seat tube and ground is the most important angle [21, 22]. Most of researchers examined the effect of seat tube angle on cardio respiratory measures with steady-state pedaling at angles with various range 60° – 90° and reported oxygen consumption [23]. As the research carried out in steady-state condition the effect of other factors of road pedaling on oxygen consumption is unaccounted. Most of researchers carried of their research by taking other kinematic variables constants and concluded that the changes in performance are related to musculoskeletal changes stemming from the variation in Seat tube angle [23, 24]. By using mathematical model STA is calculated taking seat height, crank length, and foot position of pedal constant 76° [21]. Whereas at constant external power output 300 W the optimal Seat tube angle should be 67° . The differences in power output may be due to altered muscle lengths and moment arms associated with the changes [25]. All the researcher carried out their research by considering other variable constant, but still there is lot of scope on considering other variable or the effect of other variable on the performance on pedaler. Still as per anthropometric data 670 is consider as SAT for ergonomic design of cycle rickshaw (Fig. 2).

4.3 Speed Ratio

The Speed ratio can highly effect the efficiency of peddler. In conventional case speed ratio generally taken as 2, which is capable to provide speed upto 17 km/h. This much of speed is the generally higher limit of for Cycle Rickshaw pullers. To achieve higher speed higher pedaling is required which is not suitable for cycle rickshaw puller. So the speed ratio 2 is higher for cycle rickshaw and it is necessary

Fig. 2 Seat tube angle



to investigate that whether optimum efficiency obtain of lower side of speed ratio i.e. smaller than 2.

4.4 Wheel Diameter

The wheel diameter is the most important factor which highly effect on the efficiency of cycle rickshaw puller. As it is not suitable to used higher speed ratio to overcome this difficulty smaller wheel diameter can be used. This smaller diameter of wheel keep constrained on the speed. The Higher speed ratio is not of much use as peddler does not have capacity to pedal rickshaw at a higher speed. The stability can also increase due to lower center of gravity of smaller wheel diameter. Generally 700, 675 and 650 mm diameter wheel are available in the market. So as per anthropometric data 675 mm is consider for design of cycle rickshaw.

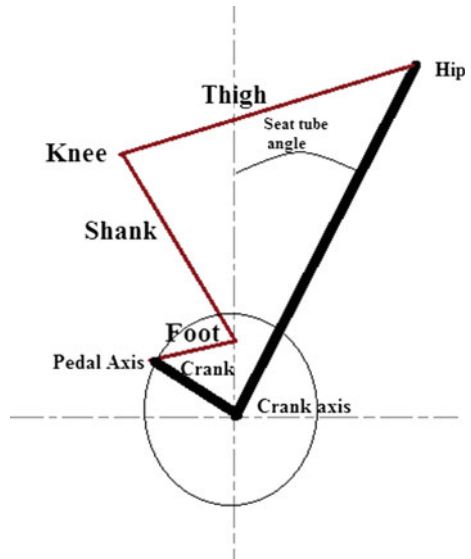
4.5 Load

Load is the critical factor which highly affect on the performance of the peddler. As the cycle rickshaw is commonly use to transport passenger and baggage or load. This load can vary from 50 to 300 kg. So the investigation should carried out to identify what should be the maximum load that cycle rickshaw puller can carry to optimal performance. Still we ergonomically design design cycle rickshaw.

4.6 Kinematics of Pedaling

Pedaling mechanism of Cycle rickshaw is a man- machine system, in which crank and saddle are rigid component of constant lengths whereas thigh and shank length vary from person to person. The Cranking mechanism, Chassis, Chain drive, Front and Rear wheel, Steering mechanism, Puller Seat are the main components of Cycle rickshaw. The front wheel, steering mechanism, crank shaft assembly are hold by chassis having diamond type frame. Whereas rear axle, rear wheel, passengers seat are supported by rear part of chassis. The pedal crank is mounted on crank shaft with 180° to each other and rickshaw puller drive the cycle rickshaw by pedaling this two pedaling crank. Thigh muscles power is used with oscillatory movement to get circular pedaling motion of the cranks. The torque exerted by the feet on crankshaft is transferred to the rear axle through a chain drive to achieve rotation of rear wheel.

Fig. 3 Kinematics of pedaling



The thigh form driving link which oscillates, leg act as a coupler, imparting motion to the crank (Pedal) and the crank which rotates, forms the output link. The fixed link is the frame. This form inversion of four bar chain (Input link, Oscillation, Lever, Output link rotating Crank). With the two legs used from driving the cycle rickshaw has two such mechanisms operating at 180° out of phase (Fig. 3).

5 Result Analysis

The average Age of Cycle rickshaw operator is found 44.4 years. The average value of Stature is 163.27 cm. When the value of Stature was compared with Indian data [9, 12], it was found that there was significant difference [6, 12]. The value of stature as reported by other Indian studies (South India) were 161.5 cm [15], 160.7 cm [11], 165.0 cm [9] and 161.4 cm [12]. The Acromion size is significantly higher and Popliteal size is significantly lower than Indian data [9, 12]. The anthropometric characteristics of cycle rickshaw operators were different from those of the Indian population. The lower value of Stature may be due to their poor social condition and there are also some genetic differences of populations among the different places in India which may reflect the anthropometric characteristic.

6 Conclusion

As the anthropometric characteristics of cycle rickshaw operators were different from those of the Indian population. The cycle rickshaw should be design as per local anthropometric data. Otherwise height of driver's seat from pedal (Crotch height) and the distance between the driver's seat and handle should a have structure with variable adjustments corresponding to the stature of each cycle rickshaw operator. As per the presents research work Seat tube angle should be 67°, maximum speed ratio should be smaller than 2, wheel diameter should be 675 mm as per Vidrabha region stature size. While designing load should be consider as 300 kg including passenger and baggage. The main motive behind this pilot study is the ergonomic design, assessment and optimization of variables affecting the performance of cycle rickshaw puller as per anthropometric data specially for Vidrabha region of Weston India.

Acknowledgements The authors are thankful to Dr. Chandan K. Pradhan, Regional Occupational Health Centre (Eastern), Indian Council of Medical Research, India who assist us in completing research. Authors are also thankful to Cycle rickshaw pullers who voluntarily participated in the study.

References

1. Pradhan CK, Thakur S, Mukherjee AK, Roychowdhury A (2004) Physiological assessment of cycle rickshaw pullers. *Indian J Physiol Allied Sci* 58:113–118
2. Pradhan CK, Thakur S, Mukherjee A, Roychowdhury A (2008) Energy expenditure of cycle rickshaw pullers in different places in India. *Ergonomics* 51:1407–1417
3. Dhara PC, Kar SK, Manna I, Ghosh S, Sau S, Banerjee S (2005) Body dimension and body composition of agricultural workers of Eastern India. *Indian J Physiol Allied Sci* 59:111–123
4. Kar SK, Ghosh S, Manna I, Banerjee S, Dhara P (2003) An investigation of hand anthropometry of agricultural workers. *J Hum Ecol* 14:57–62
5. Yadav R, Tiwari VK, Prasad N (1997) Anthropometric data of Indian farm worker—a module analysis. *Appl Ergon* 21:69–71
6. Gite LP, Yadav BG (1989) Anthropometric survey for agricultural machinery design. *Appl Ergon* 20:191–196
7. Sharma PK, Gupta ML (1983) Anthropometric survey of Indian farm workers. *Agric Mechanisation Asia* 14:27–30
8. Manna I, Pradhan D, Ghosh S, Kar SK, Dhara P (2001) A comparative study foot dimension between adult male and female and evaluation of foot hazards due to using footwear. *J Physiol Anthropol Appl Hum Sci* 20:241–246
9. Chakrabarti D (1997) Indian anthropometric dimensions for ergonomic design practice. National Institute of Design, Ahmedabad
10. Chakrabarti D, Nag PK (1996) Human concept in workspace design (Ch. 8). In: Nag PK (ed) *Ergonomics and work design*. New Age International Publishers, New Delhi, pp 129–157
11. Fernandez JE, Uppugonduri KG (1992) Anthropometry of South Indian industrial workmen. *Ergonomics* 35:1393–1398
12. Pradhan CK, Thakur S, Mukherjee AK (2010) Anthropometric characteristics of Indian cycle rickshaw pullers. *J Hum Ergol* 39(2)

13. Dewangan KN, Prasanna Kumar GV, Suja PL, Choudhury MD (2005) Anthropometric dimensions of farm youth of the north eastern region of India. *Int J Ind Ergon* 35(11):979–989
14. Majumdar DN (1972) Rules and cultures of India. Asia publishing house, New York
15. Sen RN, Nag PK, Ray GG (1977) Some anthropometry of people of Eastern India. *J Indian Anthropol Soc* 12:199–206
16. Inbar O (1983) The effect of bicycle crank length variation upon power performance. *Ergonomics* 26:1139–1146
17. Landwer GE (2000) The effect of pedal crank arm length on joint angle and power production in upright cycle ergometer. *J Sports Sci* 18:153–161
18. Yoshihuku Y (1990) Optimal design parameters of bicycle rider system for maximal muscle power output. *J Biomech* 23:1069–1079
19. Yoshihuku Y (1996) Maximum muscle power output in cycling: a modelling approach. *J Sports Sci* 14:139–157
20. Caizzo VJ (1997) Determination of work produced by skeletal muscle: potential limitation of activation and relaxation. *Am J Phys* 273:1049–1056
21. Gonzalez H (1989) Multivariable optimization of cycling biomechanics. *J Biomech* 22:1151–1161
22. Derrick JP (1997) The relationship between preferred and optimal positioning during submaximal cycle ergometry. *Euro J app physic* 75:160–165
23. Heil DP (1995) Cardiorespiratory responses to seat-tube angle variation during steady state cycling. *J Med Sci Sports Exer* 27:730–735
24. Prince D (1997) Effect of variation in seat tube angle at different seat heights on submaximal cycling performance. *J Sports Sci* 15:395–402
25. Umberger BR (1998) Difference in power output during cycling at different seat tube angles. *J Hum Move Studies* 35:021–036
26. Bharati S, Demarchi DA, Mukherji D, Vasulu TS, Bharati P (2005) Spatial patterns of anthropometric variation in India with reference to geographic, climatic, ethnic and linguistic backgrounds. *Ann Hum Biol* 32:407–444

Analysis of Thermal Performance of Serpentine Tube in Tube Heat Exchanger

Gayakwad Shiwaji, Nitnaware Pravin and Tapobrata Dey

Keywords Serpentine tube · Counter flow · Parallel flow · Nusselt number · Thermal analysis · Heat exchanger

Nomenclatures

T_{hi}	Inlet temperature of hot fluid (k)
T_{ho}	Outlet temperature of cold fluid (k)
T_{ci}	Inlet temperature of cold fluid (k)
T_{co}	Outlet temperature of cold fluid (k)
u	Mean velocity of flow (m/s)
Re	Reynolds number
ρ	Density of fluid (kg/m^3)
D_i	Inner diameter of shell (m)
D_o	Outer diameter of shell
Pr	Prandtl number
δ	Curvature ratio
μ	Coefficient of dynamic viscosity (Ns/m)
k	Thermal conductivity (w/mK)
C_h	Hot fluid capacity
C_c	Cold fluid capacity
C_{min}	Minimum fluid capacity rate
De	Dean number
Q	Actual heat transfer (W)
Q_{max}	Maximum heat transfer (W)
Nu	Nusselt Number
d_i	Inner tube diameter
d_o	Outer tube diameter

Gayakwad Shiwaji (✉) · Nitnaware Pravin · T. Dey
Department of Mechanical Engineering, Savitribai Phule Pune University,
D. Y. Patil College of Engineering, Akurdi, Pune, India
e-mail: shiwajigayakwad@gmail.com; gayakwadshiwaji@gmail.com

1 Introduction

Heat transfer between the surface and the nearby fluid in a heat exchanger is the most a main issue and subject of study. Heat exchanger is important engineering system with the extensive variation of use together with solar water and space heating; also it is used in refrigeration system and air conditioning system, heat recovery system, nuclear reactor etc. The heat transfer occurs by the above three principles which are conduction, convection, and radiation.

Now in the heat exchanger, it is seen that the heat transfer through radiation is not taken into concern because as it is irrelevant in comparison with conduction and convection. The conduction is taking place while the heat transfers from high temperature fluid through the immediate of a solid wall. The conductive heat transfer can take advantage as selecting of a minimum thickness of the wall of an extremely conductive material. But the convection plays the major role in the enhancement of a heat transfer through a heat exchanger [1–4].

Depending on selection criteria there are different types of shell and tube heat exchanger. With respect to the heat exchanger, we may separate the subsequent designs as follows, evaporation-cooled, air-cooled, water-cooled condensers. In the construction, tubes used in heat exchanger, the following types of curved tubes are distinguished as,

- (1) Helically Coiled Tubes;
- (2) Spirally Coiled Tubes; and
- (3) Serpentine Tubes.

A new technology is available for a heat transfer enlargement in heat exchanger is essential to compeers of the solar receiver, refrigerator, and power plants etc. Which is not often stated and therefore more work is too needed in this field for a broad understanding and to develop the uses of new energy sources and contribute to sustainability [5].

The inspiration for starting of this work is a study of all parameters of the heat exchanger and inconvenience in a transfer of heat between the two fluids through a serpentine tube in tube heat exchanger. Here development in heat transfer due to a serpentine tube is described and large trial or theoretical analysis is done for the serpentine tube in tube heat exchanger making an allowance for fluid to fluid heat transfer and a heat transfer distinguishing inside a serpentine tube for considering several boundary conditions.

To examined serpentine tube in tube heat exchanger, which deals with the study of heat transfer region and compute a quantity of heat transfer between two fluids. The simple serpentine tube in tube heat exchanger is facing difficulties for the reason that of the privation of investigational data available concerning the performance of the fluid in the serpentine tube in occasion of heat transfers data. This is not happening on the occasion of a compact heat exchanger. So in the direction of the first of our effort, to design a serpentine tube in tube compact heat exchanger and numerical examination is conceded out to decide the heat transfer appearances

of a heat exchanger by changing the different parameters at different temperature ranges and flow rate and also to govern the fluid flow outline in this heat exchanger Compare preceding study data for another tube type heat exchanger [6, 7].

The material used here for the tube is a copper amount of heat transfer is determined for the stated materials considering various assets. A different method is used for finding numerous thermal constraints for checking the amount of heat transfer such as trial method, Numerical method, and CFD analysis etc.

The objective of this study is improved heat transfer rate and more assessable concentration into the heat transfer progression that take place when a fluid flows in a serpentine tube in tube heat exchanger. The study also concealed the different types of fluid flow, such as counter flow and parallel flow through heat exchanger extending from laminar flow through a transition to turbulent flow.

2 Experimental Setup

The trial set up is shown in Fig. 1 and set up is properly set for counter flow arrangement and also for parallel flow arrangement.

Set the bulk flow rate of both cold water and hot water to a suitable computing instrument. Using a digital thermometer, measure the inlet and exit temperature of hot and cold water and remarks are noted and outcomes are estimated. The graphs

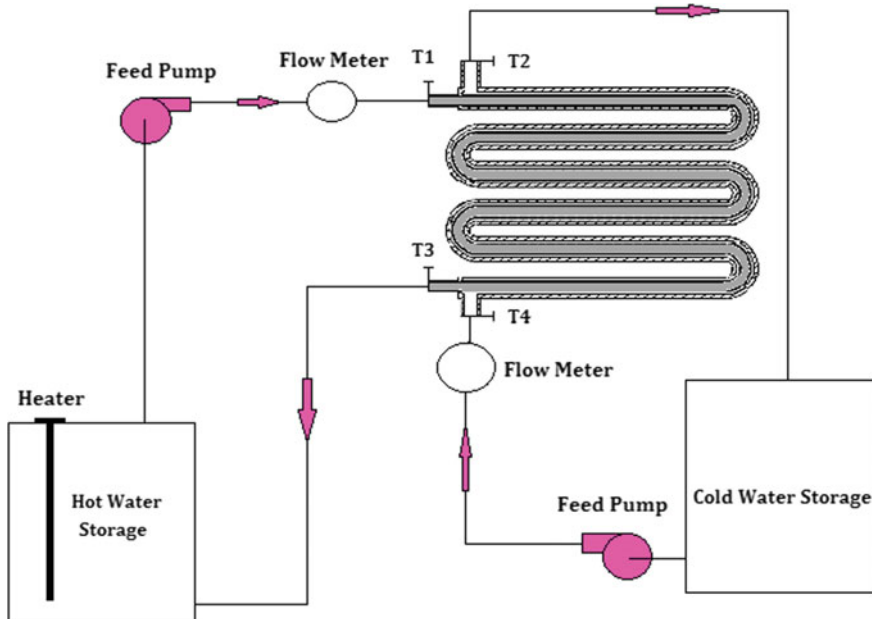


Fig. 1 Experimental rig

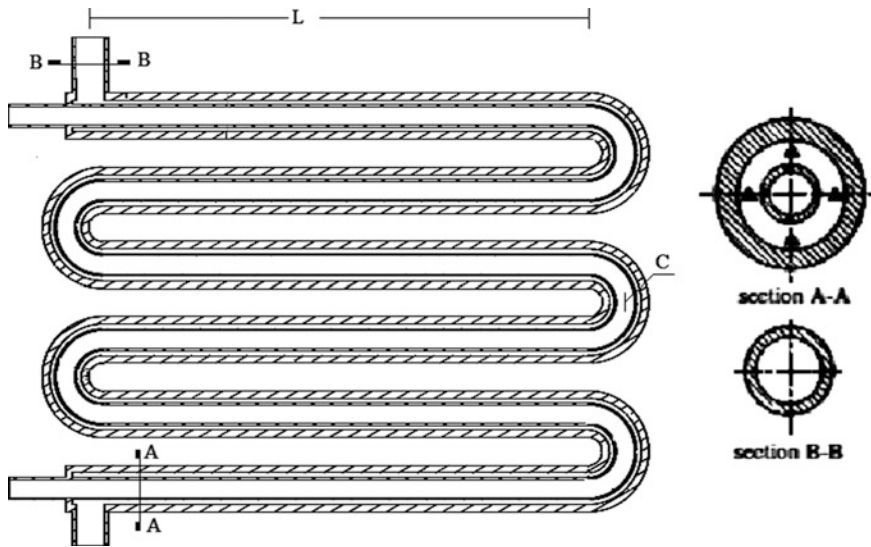


Fig. 2 Schematic diagram of serpentine tube in tube heat exchanger

Table 1 Dimensional parameters of serpentine tube in tube heat exchanger

S. No.	Dimensional parameter	Dimension (mm)
1	Inner diameter of tube	11.7
2	Outer diameter of tube	12.8
3	Inner diameter of shell	35.1
4	Outer diameter of shell	38.1
5	Curvature radius	23

are planned to permit to the attained results. The experiment is to be carried out on the different series of flow rate and flow type and results are collected. Figure 2 illustrates the presentation of the serpentine tube in tube heat exchanger.

The experiment is to be carried out on deciding on proper values, and also the assessment is to be taken concerning the approach of heat transfer.

Dimensional parameters of serpentine tube in tube heat exchanger is shown in Table 1 as follows.

3 Mathematical Analysis

3.1 Analytical Calculations

As flow geometry involve different correlation be used to achieve heat transfer coefficients and calculations of Nusselt number is carried out using this relationship

given by Keys Xin and Roger for curved pipe arrangement Correlation is given by Roger is as follows,

$$Nu = 0.023Re^{0.84}Pr^{0.4}\delta^{0.1} \quad \text{For } Re > 2000$$

In curved pipes, the heat transfer coefficient inside the tube in the presence of heat transfer, the various empirical correlations proposed in the numerous literature is chosen the most widely used being that by Xin and Ebadian. An empirical correlation is developing by Xin and Ebadian for the average fully developed flow, using this, estimate the heat transfer coefficient inside a curved tube. The correlation as follows.

For Laminar flow,

$$Nu = (2.153 + 0.318De^{0.643})Pr^{0.177}$$

$$20 < De < 2000, \quad 07 < Pr < 175, \quad 0.0267 < \delta < 0.088$$

For turbulent flow,

$$Nu = 0.00619Re^{0.92}Pr^{0.4}(1 + 3.455\delta)$$

$$5 \times 103 < Re < 105, \quad 0.7 < Pr < 5, \quad 0.0267 < \delta < 0.0884$$

An empirical correlation is developing by Kalb et al. for the fully developed viscous flow heat transfer in curved circular tubes with uniform wall temperature, using this, estimate the heat transfer coefficient inside a curved tube. The correlation as follows,

$$Nu = 0.83De^{0.5}Pr^{0.1} \quad \text{for } De \geq 80 \text{ and } 0.7 < Pr < 5$$

The Effectiveness of heat exchanger is calculated as,

$$\varepsilon = \frac{Q}{Q_{\max}} = \frac{C_h(T_{h1} - T_{h2})}{C_{\min}(T_{h1} - T_{c1})} = \frac{C_c(T_{c2} - T_{c1})}{C_{\min}(T_{h1} - T_{c1})}$$

3.2 Numerical Calculations

Steady state implicit pressure based solver using Ansys15 environment is being conceded for the numerical solution. For steady state streams for mass and momentum are explained by the major partial differential equations. Using second order up wind scheme, the discretization is complete. Mean Flow Equations are presented in Cartesian tensor notation as follows.

Continuity equation,

$$\frac{\partial}{\partial x_i} (\rho V_i) = 0$$

Momentum Equation,

$$\frac{\partial}{\partial x_i} (\rho V_i V_j) = \frac{\partial P}{\partial x_i} + \frac{\partial}{\partial x_j} \left[\mu \left(\frac{\partial V_i}{\partial x_j} + \frac{\partial V_j}{\partial x_i} \right) \right] - \rho \overline{V_i V_j}$$

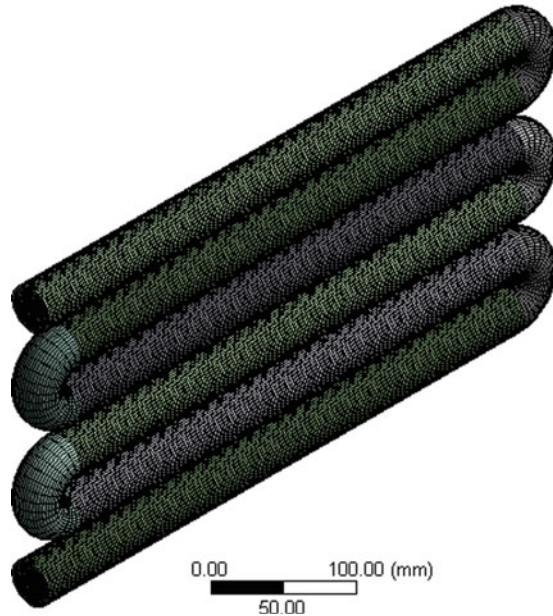
Energy Equation,

$$\frac{\partial}{\partial x_i} (\rho V_i T) = \frac{\partial}{\partial x_j} \left[\frac{\mu}{Pr} \frac{\partial T}{\partial x_j} - \rho V_i t \right]$$

The geometric model of the serpentine tube and straight tube were constructed using workbench in ANSYS 15 environment. In order to arithmetically found the effectiveness of serpentine tube in tube heat exchanger, the tube diameter and length of the tube were presumed to be same that of straight tube. The three-dimensional computational domain modeled is shown in Fig. 3. And this geometry is mesh by using hexagonal mesh is as shown in Fig. 4. Initially a reasonably coarser mesh is

Fig. 3 3D computational domain modeled



Fig. 4 Mesh modeled

made. The whole domain of serpentine tube consists of ≈ 7.8 lakes elements and straight tube consists of ≈ 5.6 lakes elements. For checking the validity of the quality of the mesh in the results are achieved by grid independent test. Further adaptation did not alter the results by more than 0.87% which is occupied as the applicable mesh quality for computation.

A boundary condition such as constant wall temperature is executed on the wall of the tube. Fluid is ready to become cold as it flows through the tube by isolating a wall temperature of 300 K. Pressure outlet boundary conditions are applied at the outlet of both hot and cold fluid. Conservation calculations were committed for the control volume to capitulate water flow in the tube for velocity and temperature fields.

There is two inlet condition and two outlet condition because here two tubes are used. Copper is separated two fluid flows. The inner fluid is taken as hot liquid flow and outer fluid as cold liquid flow.

4 Boundary Conditions

Boundary condition is used permitting to the requisite of the model as mass flow inlet and pressure outlet is well defined at inlet and outlet condition of the hot and cold fluid. The walls are independently identified with corresponding to boundary conditions. No slip condition is deliberated for every single wall. Zero heat flux

Table 2 Boundary conditions

	Hot inlet	Hot outlet	Cold inlet	Cold outlet
Boundary condition type	Mass flow inlet	Pressure outlet	Mass flow inlet	Pressure outlet
Mass flow inlet (kg/s)	0.01–0.03	–	0.01–0.05	–
Temperature (k)	333	–	300	–
Turbulent kinetic energy (m ² /s ²)	0.01	–	0.01	–
Turbulent dissipation rate (m ² /s ²)	0.1	–	0.1	–

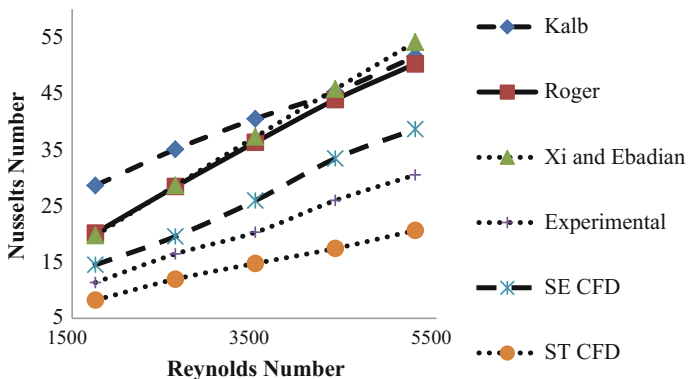


Fig. 5 Reynolds number versus Nusselt number

condition is established at respective wall with the exception of the inner tube wall. The above table demonstrations all boundary condition (Table 2).

5 Result and Discussions

Figure 5 illustrates the effect of Reynolds number on Nusselt number. While calculating Nusselt number a different scientist gives correlations to deliberate various parameters. Hence, five different curves for each correlation were plotted. From above graphs for same Reynolds number, it can be seen that a value of the Nusselt number given by Xin and Ebadian for a curved tube arrangement and is higher than straight tube arrangement. According to Roger, for calculation of Nusselt number they consider the curvature ratios and its results are increased heat transfer due to secondary turbulence occurs at curvature. Thus, the values given by Roger are considered for comparison.

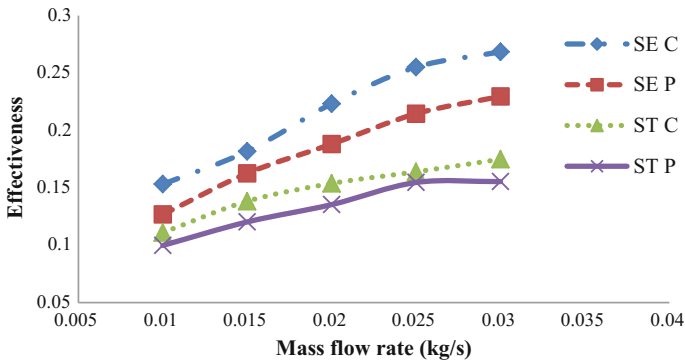


Fig. 6 Mass flow rate versus effectiveness for 0.05 kg/s cold fluid flow

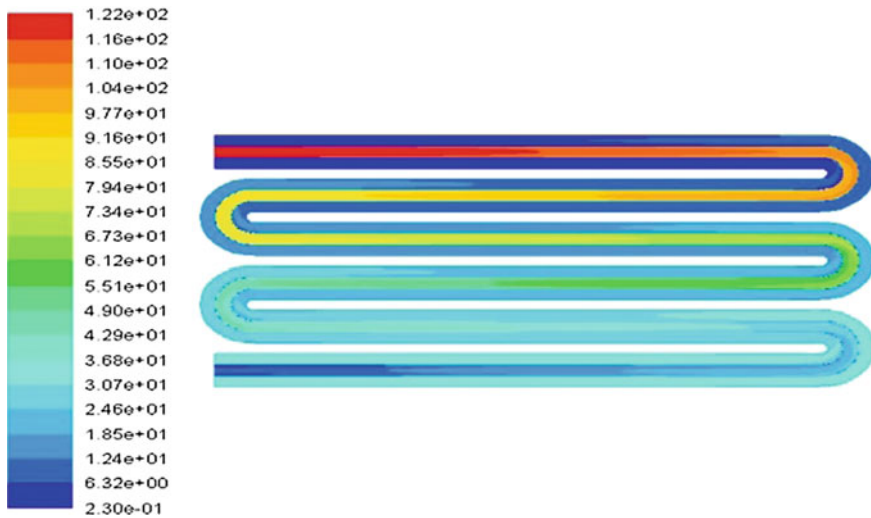


Fig. 7 Contours of total pressure (Pa)

Figure 6 illustrates the variation of effectiveness associate through a mass flow rate of hot water on behalf of together with serpentine tube and straight tube heat exchangers for counter and parallel flow. It is found that for all inlet temperature conditions the effectiveness of serpentine tube in tube heat exchanger is to be greater when related to that of the straight tube heat exchanger. From this result, it is found that the serpentine tube in tube heat exchanger is superior to straight tube heat exchanger.

The total pressure distribution along the serpentine tube in tube heat exchanger can be seen through the contours of total pressure as illustrates in Fig. 7.

Pressure is reduced further at a curved section, as shown in Fig. 8 and which is more advantageous for maximum heat transfer. Figure 8 illustrates the comparison

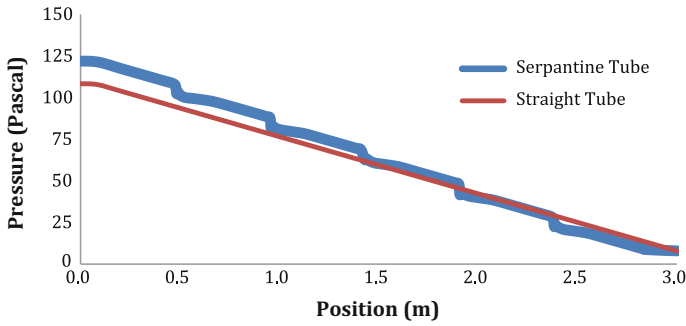


Fig. 8 Variation of total pressure in serpentine tube and straight tube

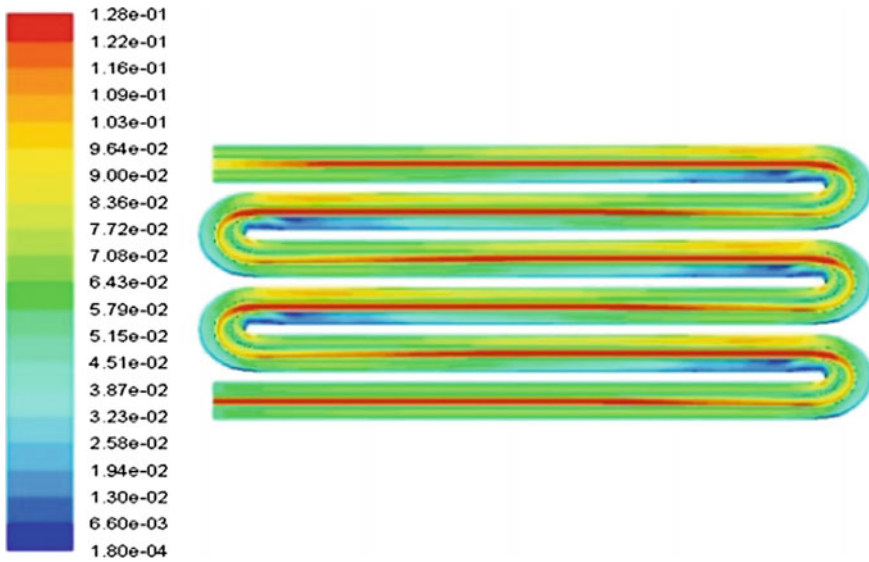


Fig. 9 Contours of velocity magnitude (m/s)

of variation of total pressure in the serpentine tube and straight tube over a tube length.

The velocity distributions in a serpentine tube in tube heat exchanger can be seen through the contour in Fig. 9.

While Fig. 10 shows velocity distributions in a serpentine tube in tube heat exchanger can be seen through the contour.

Figures 11 and 12 illustrate temperature distributions in a serpentine tube and straight tube with a counter. This shows temperature is reducing more at curved section than a straight one.

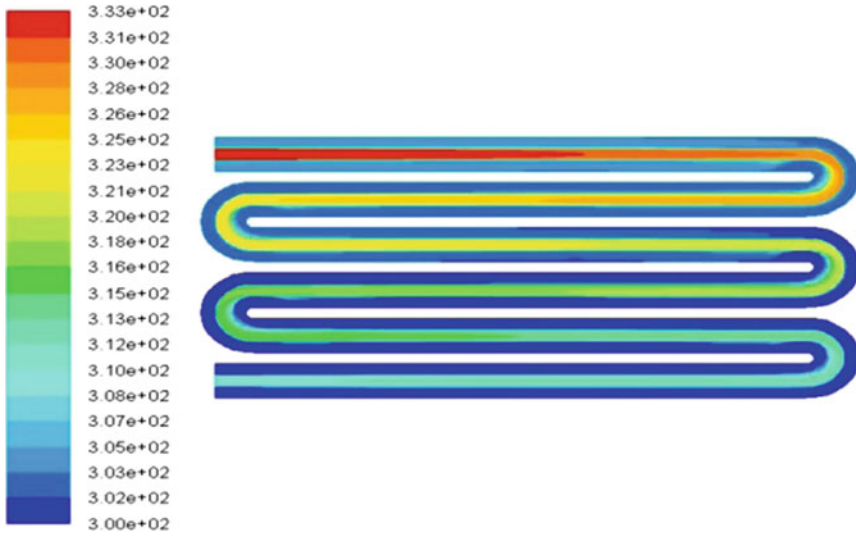


Fig. 10 Contours of total temperature

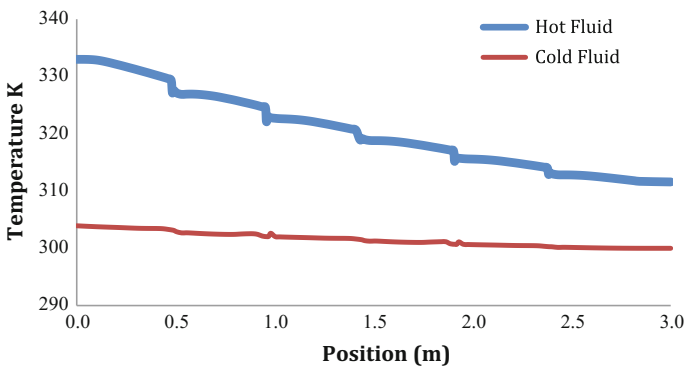


Fig. 11 Temperature distributions in serpentine tube with counter flow

Correspondingly in parallel flow conditions through a serpentine tube and straight tube, more temperature drop occurs in curved section than straight as shown in Figs. 13 and 14.

The contour of turbulent kinetic energy k in m^2/s^2 is shown in Fig. 15. From Fig. 15 Laminar flow is disturbed due to curved section and so turbulent kinetic energy is extreme at curvature.

While Fig. 16, give variations in turbulence intensity through a Serpentine tube and Straight tube over a length

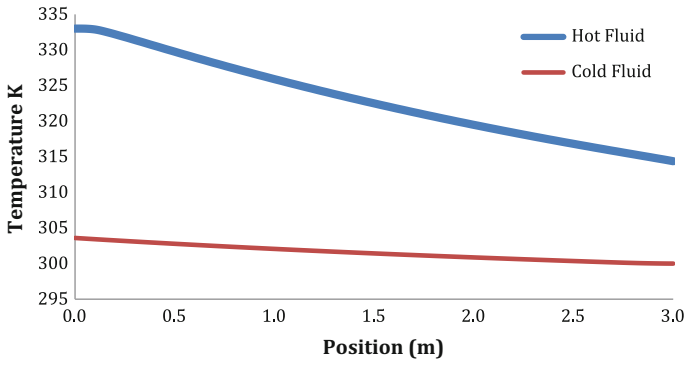


Fig. 12 Temperature distributions in straight tube with counter flow

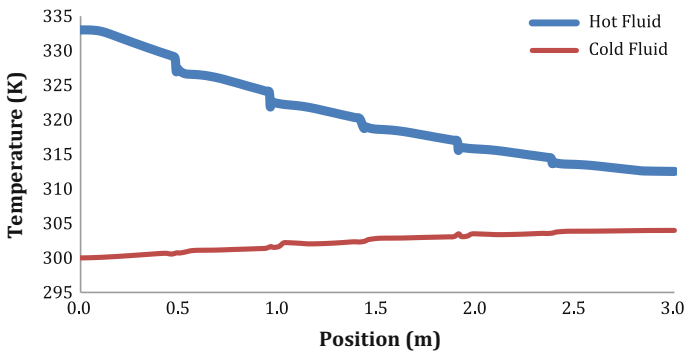


Fig. 13 Temperature distributions in serpentine tube with parallel flow

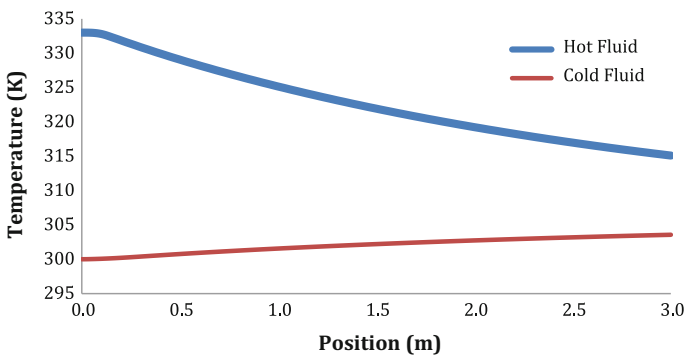


Fig. 14 Temperature distributions in straight tube with parallel flow

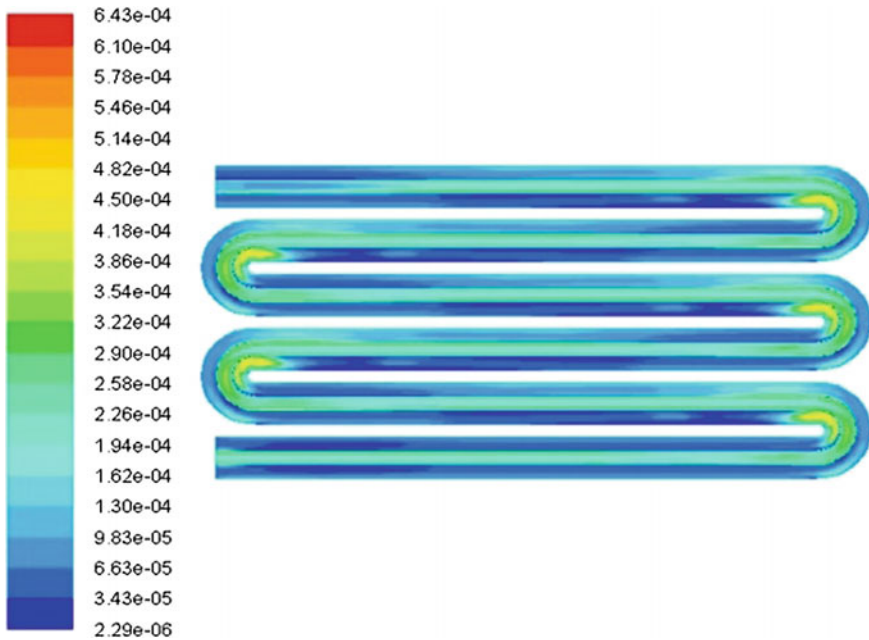


Fig. 15 Contours of turbulent kinetic energy

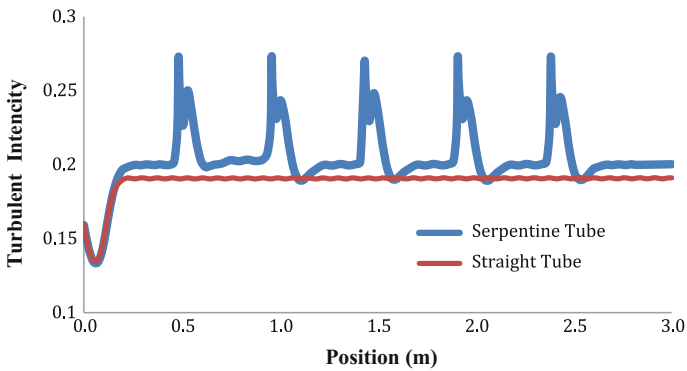


Fig. 16 Turbulence intensity versus position

6 Conclusions

A series of experiment is conducted for a serpentine tube in tube heat exchanger subjected to changing mass flow rate at inlet. During the analysis the following terms are identified. The design technique adopted serpentine tube heat exchanger and results are found in good agreement with the experimental results. By growing

mass flow rate of hot water the effectiveness rises at constant cold water mass flow rate. The effectiveness varies from 0.153, 0.182, 0.223, 0.255, 0.268 for 0.05 kg/s cold fluid flow and hot fluid flow varies from 0.01 to 0.03 kg/s.

When mass flow rate of cold water is preserved at lower value the effectiveness is determined but, when mass flow rates of cold water increases effectiveness decreases correspondingly. The effectiveness varies from 0.335, 0.287, 0.211, 0.181, 0.153 for 0.01 kg/s hot fluid flow and cold fluid flow varies from 0.01 to 0.05 kg/s.

When mass flow rate is 0.05. The variation of overall heat transfer coefficient is 286.5, 443.54, 543.95, 639.56, 695.4 W/m² k the heat transfer rate and overall heat transfer coefficient increases with minimum amount when mass flow rate of cold water is kept 0.01 whereas it is increases with maximum amount. At the constant temperature and constant wall heat flux conditions, representative of the fluid flow is also studied. The fluid elements were experienced an oscillatory motion in both inner tube and outer tube of the serpentine tube in tube heat exchanger due to curvature section and it is established from the velocity vector plot. In evaluation through the inner values beside the outer side of the tubes the velocity and pressure values are greater and it is seen from the pressure, and temperature contours.

Numerical simulation has been carried out for serpentine tube in tube heat exchanger and straight tube heat exchanger subjected to different boundary conditions. Nusselt number, pumping power required, Log mean temperature difference, pressure drop variation with respect to Reynolds number for different l/c ratio is plotted. Following are the outcome of above experimental and numerical study;

With increase in the Reynolds number, the Nusselt number for the inner tube increase. However, with increases in flow rate turbulence between the fluid element increases which will enhance the mixing of the fluid and ultimately the Nusselt number or the heat transfer rate increases.

References

1. Li Q, Flamant G, Yuan X, Neveu P, Luo L (2011) Compact heat exchangers: a review and future applications for a new generation of high temperature solar receivers. *Renew Sustain Energy Rev* 15:4855–4875
2. Rogers GFC, Mayhew YR (1964) Heat transfer and pressure loss in helically coiled tubes with turbulent flow. *Int J Heat Mass Transf* 7:1207–1216. ISSN 0017-9310
3. Ciofalo M, Di Liberto M (2015) Fully developed laminar flow and heat transfer in serpentine pipes. *Int J Thermal Sci* 96:248e266
4. Laskowski R (2015) The black box model of a double-tube counter-flow heat exchanger. *Heat Mass Transf* 51:1111–1119. doi:10.1007/s00231-014-1482-2
5. Cioncolini A, Santini L (2006) An experimental investigation regarding the laminar to turbulent flow transition in helically coiled pipes. *Exp Therm Fluid Sci* 30:367–380
6. Noorani A, El Khoury GK, Schlatter P (2013) Evolution of turbulence characteristics from straight to curved pipes. *Int J Heat Fluid Flow* 41:16–26
7. Zhang L, Chen Z (2011) Convective heat transfer in cross-corrugated triangular ducts under uniform heat flux boundary conditions. *Int J Heat Mass Transf* 54:597–605

Experimental Performance Evaluation on S.I. Engine with Gasoline and Liquefied Petroleum Gas as Fuel

Puneet Bansal, Ankit Pandya and Ankit Ahuja

Keywords S.I. engine · Liquefied petroleum gas (LPG) · Vaporizer · Emissions

1 Introduction

Liquefied Petroleum Gas (LPG) is widely using nowadays in transportation as an alternative fuel because it is economic as well as have lower pollutants as compared to conventional fuels like petrol and diesel [1, 2]. LPG is ready to use in spark ignition engines since LPG has high octane number whereas it has lower cetane number, so it's hard to use in compression ignition engines [3–5].

LPG obtained from hydrocarbons produced during crude oils from heavier natural gas. LPG is a colorless mixture of propane and butane along with ethane. It is very popular due to low cost, low maintenance and environmentally friendly characteristics [6].

LPG gas has a low carbon and high octane number fuel creates lower carbon dioxide (CO₂) emission as compared with gasoline. The use of LPG as an alternative fuel for vehicles has been studied in recent years, i.e., nearly 4 million vehicles are running on LPG worldwide. Most of these were mainly light, medium and heavy-duty trucks originally were nit only operating on gasoline but also later converted to LPG using approved and certified conversion kits [7].

Present work also represents the effectiveness of the use of LPG over gasoline in terms of Emissions and other factors.

P. Bansal (✉) · A. Pandya · A. Ahuja
U.V. Patel College of Engineering, Ganpat University, Mehsana, Gujarat, India
e-mail: punitbansal80@gmail.com

A. Pandya
e-mail: apa@ganpatuniversity.ac.in; ankitpandya195@gmail.com

Table 1 Properties of LPG and gasoline [7]

Characteristics	LPG	Gasoline
Chemical formula	C ₃ H ₈	C ₃ H ₁₈
Boiling point (°C)	-44	30–225
Molecular weight (kg/K mole)	44.1	114.2
Density at 150 °C (kg/l)	0.53	0.7372
Research octane number	100	96–98
Stoichiometric air fuel ratio	15.6	14.7
Flame speed (m/s)	48	52–58
Upper flammability limits in air (% vol)	74.5	7.6
Lower flammability limits in air (% vol)	4.1	1.3
Calorific value (KJ/kg)	46,100	43,000

2 Experimental Detail

2.1 Selection of Fuel

Fuels selected for evaluation of performance were Gasoline and Liquefied Petroleum Gas (LPG). Some properties of selected fuels are giving in Table 1.

2.2 Experimental Setup

2.2.1 S.I. Engine

A 4 stroke spark ignition engine of displacement volume 149 cc with compression ratio 9.5 is used for this study. Detailed specifications of engine are giving in Table 2. Engine coupled with 5 gears with final reduction 2.8. Gear ratios are as follows, first 2.92, second 1.88, third 1.38, fourth 1.08 and fifth 0.92.

2.2.2 Fuel Intake System

LPG (Propane and Butane) is transported and stored as a liquid under pressure. For equipment to be able to use the propane in a storage tank it must undergo a vaporization from liquid to vapor within the cylinder, before being combusted. The natural vaporization is a function of two factors ambient temperature and wetted tank surface. Outside temperature cannot control so there is a need for a device

Table 2 Engine specification

Model	Pulsar 150 cc
Type	Single cylinder, 4 stroke spark ignition
Rated power	15 HP @9000 rpm
Bore and stroke (mm)	57 × 56
Displacement (cubic capacity)	149
Compression ratio	9.5



Fig. 1 Pictorial view of LPG vaporizer

which can increase surface area so that liquefied Fuel can convert into gas this can be functioned by a vaporizer. This Vaporizer does not build additional pressure, but LPG enters in a vaporizer as liquid and exit as gas. Figure 1 shows the picture of vaporizer.

2.2.3 Braking System

A dynamometer is a mechanical device which is used to determine the force, torque and speed when coupled with a prime mover. In the present study, a spring balance Rope break absorbs dynamometer with rope diameter 10 mm and drum diameter 257 mm is used for braking purpose. Load on engine applied through dynamometer. Figure 2 shows the pictorial view of dynamometer.



Fig. 2 Pictorial view of dynamometer

2.2.4 Coupling of Engine with Dynamometer and Speed Measurement

A coupling is a component which is used to connect two shafts, and it is also used for transmitting power from one shaft to another. In the present work, a mild steel sleeve coupling is used to connect the engine with dynamometer so that engine power can transfer to dynamometer and load can be applied to it. The speed of engine cum dynamometer measures through digital pen tachometer. Figure 3 represents the coupling which connects the engine to the dynamometer.

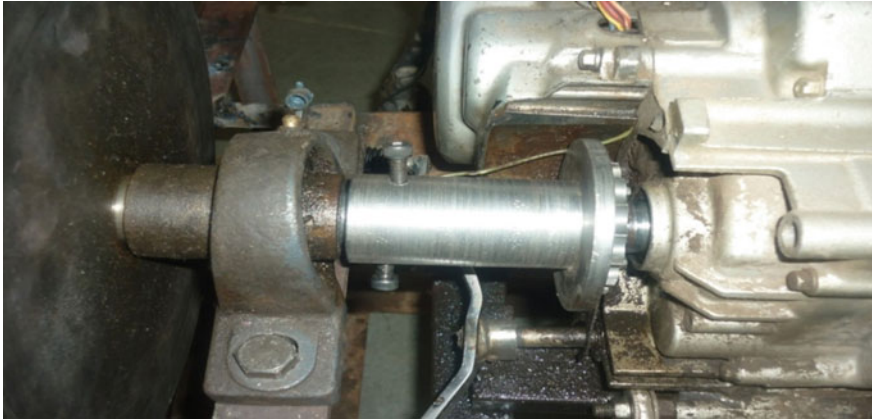


Fig. 3 Image of coupling connects engine to dynamometer

3 Experiment Test Parameter

Experiments did on 149 cc S.I. Engine, first it runs through gasoline and then LPG and measures exhaust gas emissions like CO and HC respectively. Mechanical parameters like torque and break power were also calculated when engine runs by gasoline and LPG respectively.

3.1 Torque

Torque through dynamometer is measured by

$$T = (P * 9.81) * 0.1335$$

Diameter of dynamometer with rope = 0.1335 m, T = Torque in N-m and P = Load in Kg.

3.2 Break Power

Break Power of the engine were calculated by:

$$BP = 2\pi NT / (60 * 1000)$$

where BP = Break Power in KW, N = Break speed in rpm and torque in N m.

3.3 Exhaust Emissions

Exhaust gas emissions like CO and HC were measured by four gas analyzer when engine run through gasoline and LPG respectively.

4 Results and Discussions

Experiments were done on engine to measure exhaust gas emissions like CO and HC, torque and break power while engine run through Gasoline and LPG. Load on engine applied range from 0 to 2 kg by dynamometer while engine run on gear range 0–4.

4.1 Exhaust Emissions

CO is produced when there is the deficiency of Air in a combustion chamber, due to insufficient Amount of air in combustion chamber tends incomplete combustion which leads carbon of fuel in CO. Figure 4 shows the variation of CO on various loading conditions along with gasoline and LPG uses as fuel.

Figure 4 represents that when an engine runs through gasoline emissions almost constant for 1st and 2nd gear but slight increases for 3rd gear and more emissions produces for 4th gear on the other hand CO emissions produced by LPG were always less than emissions produces by gasoline. Maximum CO emission is 2.413 and 1.341 ppm respectively for gasoline and LPG.

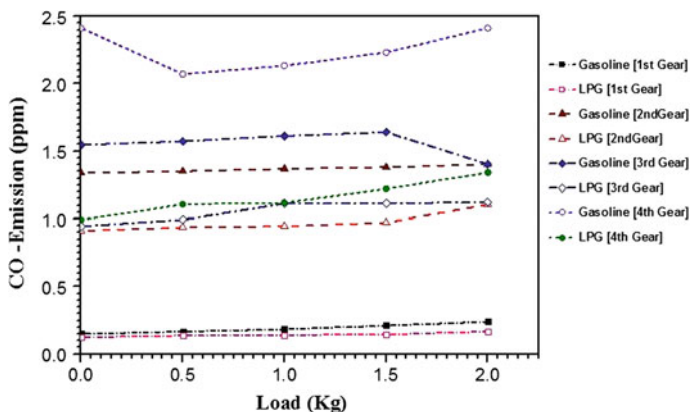


Fig. 4 Variation of CO emission for various loading at different gears

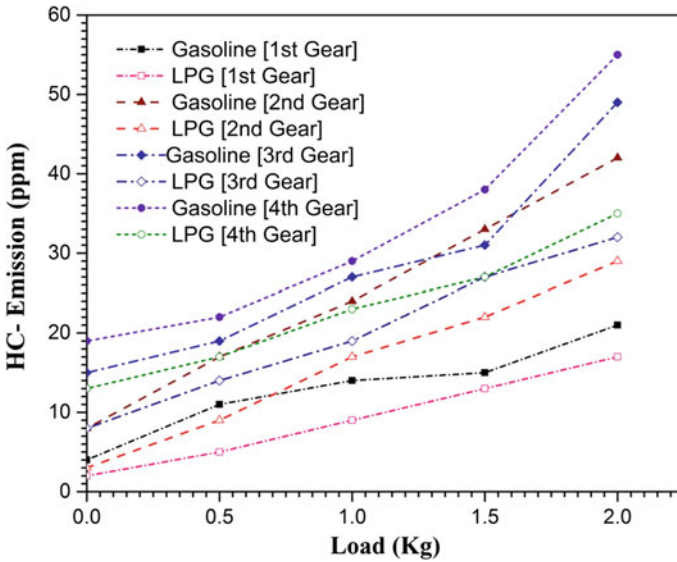


Fig. 5 Variation of HC emission for various loading at different gears

Figure 5 represents that when an engine runs through gasoline HC Emissions increases as gear shifting lifted on the other hand emission produced by LPG were less than Gasoline. Maximum HC emission is 55 and 35 ppm respectively for gasoline and LPG.

Results of emissions are such because LPG is more combustibile as compare to gasoline which results in better combustion so as for produce less CO because combustion will tend to produce more CO₂ and hence results in less CO and as far as emission hazard intensity is concern CO is more hazardous as compare to CO₂. Same for HC, hydrocarbons of LPG will combust efficiently so as-as to produce less HC after combustion.

4.2 Break Power and Torque

Figure 6 represents that Break Power increases as gear lifted up against torque for gasoline as compared to LPG. The maximum value of Break power against torque is 238.43 N m for gasoline on 4th gear, and the maximum value of Break power against torque is 238.43 N m for gasoline on 4th gear and maximum 187.9 N m.

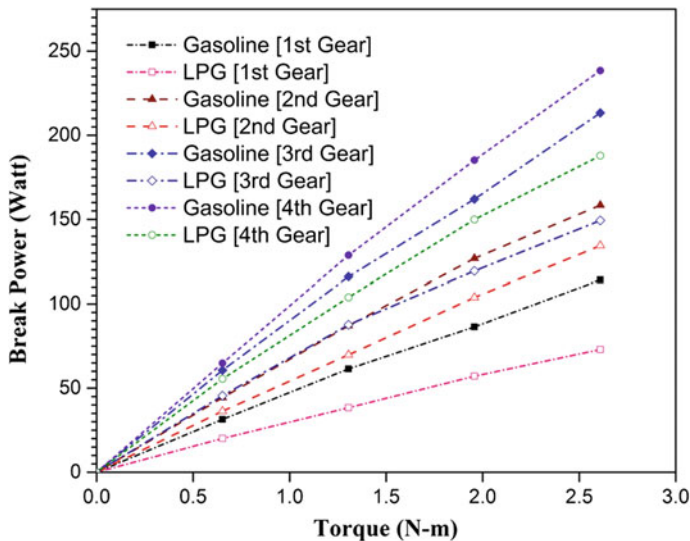


Fig. 6 Variation of break power for various loading at different gears

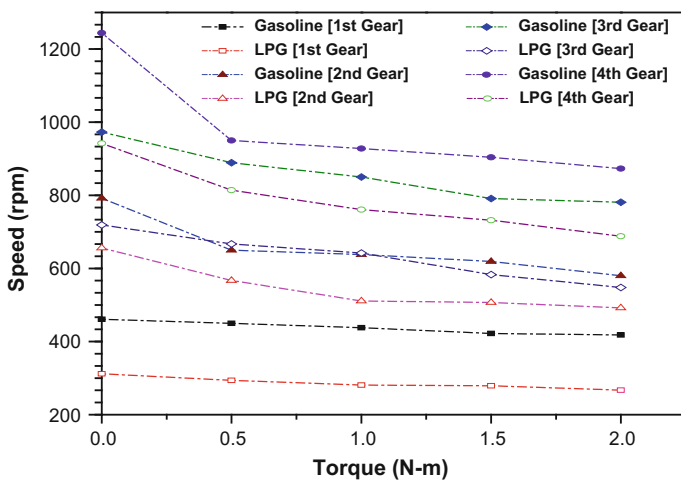


Fig. 7 Variation of speed and torque for various loading at different gears

4.3 Speed and Torque

Figure 7 shows variation of torque against speed, since torque and speed are inversely proportional to each other so as torque increases speed decreases i.e. at higher gear torque is low and speed is high and vice versa for low gear condition.

5 Conclusion

The above study shows that when engine runs through LPG, emissions like HC and CO are less as compared to Gasoline as Fuel at every gear shifting and loading conditions. But LPG driven engine gives less break power as compared with Gasoline, but emissions are under control for LPG driven engine, so LPG driven engines are better than gasoline due to its less emission production rate. This article lead to gives performance and behavior of a 149 cc engine run at various gear engaged at loading conditions to know the actual performance and behavior just as on the road.

References

1. Campbell M, Wyszynski LP, Stone R (2004) Combustion of LPG in a spark-ignition engine. SAE paper; 2004 [2004-01-0974]
2. Oh C, Jang J, Bae C (2010) The effect of LPG composition on combustion and performance in a DME-LPG dual-fuel HCCI engine. SAE paper; 2010 [2010-01-0336]
3. Goto S, Lee D, Shakal J, Harayama N, Honjyo F, Ueno H (1999) Performance and emissions of an LPG lean-burn engine for heavy duty vehicles. SAE paper; 1999 [1999-01-1513]
4. Alam M, Goto S, Sugiyama K, Kajiwara M, Mori M, Konno M et al (2001) Performance and emissions of a DI diesel engine operated with LPG and ignition improving additives. SAE paper; 2001 [2001-01-3680]
5. Gunca C, Razavi MRM, Karim GA (1998) The effects of pilot fuel quality on dual fuel engine ignition delay. SAE paper; 1998 [982453]
6. Saraf RR, Thipse SS, Saxena PK (2009) Comparative emission analysis of gasoline/LPG automotive bifuel engine. IJMAMME 3
7. Mamidi T (2012) Investigations on S.I. engine using liquefied petroleum gas (LPG) as an alternative fuel. Int J Eng Res Appl 362–367

A Review on the Green Supply Chain Management (GSCM) Practices, Implementation and Study of Different Framework to Get the Area of Research in GSCM

Prashant S. Bajaj, Satish V. Bansod and Izzhak D. Paul

Keywords GSCM · GSCM practices · GSCM implementation · Research area in GSCM · GSCM framework

1 Introduction

There is a simple and most famous concept is present behind any type of business i.e. making profit. To be always in profit status industry needs perfect optimization and balance in every aspect encompassing market conditions, Government regulations, investors' support, customer's demand and many other things [1]. This passion of earning profits gives less importance towards the environment aspects. Formerly quality and environment was nonexistence and from 1980s the quality consciousness is increases and the supply chain revolution in 1990s lead to the business for the environmental management parallel with ongoing operations. The world started growing fast and the need of new innovation and new research is increases, this fast growing world forget that this fastness deploying the environment and the health of human being, animals and even earth (our mother land). To overcome this problem, the concept of supply chain management is reintroducing with the term Green Supply Chain Management (GSCM). The Green Supply Chain Management is the Integrating environment thinking into supply chain manage-

P.S. Bajaj (✉) · I.D. Paul (✉)

Department of Mechanical Engineering, SSGB College of Engineering,
Bhusawal, India
e-mail: prashantsbajaj@gmail.com

I.D. Paul

e-mail: izakpaul@gmail.com

S.V. Bansod

Department of Mechanical Engineering, Prof. Ram Meghe Institute
of Technology & Research, Badnera, India
e-mail: svbansod@mitra.ac.in

ment, including product design, material sourcing and selection, manufacturing processes, delivery of the final product to the consumers, and end-of-life management of the product after its useful life. The practices of GSCM lead to Financial Benefits that are increased in the revenue, reduced cost, increase Asset Utilization and enriched not only Financial benefits it also gives the environmental benefits, that are Reduced waste, Increased Energy efficiency, reduced air Emission, reduced Water Emissions, reduced Fuel consumption. The GSCM practices gives the Noise Reduction, Health, Safety and security to society by improving the environment conditions. Thus it can be said that the introducing green in supply chain management will save the environment and will increase the profit too. The GSCM can be defined as the combination of green purchasing, green manufacturing, green distribution and reverse logistics, all this together form the green supply chain. The GSCM can be defined in any way but the meaning will remain the same. There are frameworks proposed by researchers to improve the collaborative bond between the manufacturer and suppliers. There are some performance measuring techniques which will lead to extract the efficiency and effectiveness of an existing system with the alternating system.

The need of GSCM is essential to improve the environment constraint as our environment facing a problem of global warming. The competition increases and based on this the economic growth also increases but this need more energy and material consumption due to which environmental issues occurs. It become a compulsory pressure on the organization to regulate the environment performance [2]. This research paper aims to find the areas of interest in GSCM for further studies by understanding the practices and implementation of GSCM.

2 Literature Review on GSCM

2.1 Concept of GSCM

The Green Supply Chain is the advancement of Supply Chain and the concept of “Green Supply Chain” (GSC) was first proposed by the Manufacturing Research Consortium (MRC) of Michigan State University in the U.S. in 1996, for comprehensively considering environmental impacts and resources optimization of manufacturing supply chains [3]. The aims were to minimize the impacts on environmental i.e. related to the products end-of-use by tracking and controlling the raw material i.e. related to the products end-of-use by tracking and controlling the raw material procurement, in order to ensure compliance with environmental rules and regulations starting from the stage of product R&D. The GSCM improve the life cycle of the products. Green supply chain is implemented right from the planning, and continued till reverse logistics. The entire supply chain is managed as a green system and every process focuses on environmental management and risk control. The GSCM is very similar to Supply Chain Management (SCM), as the goal of SCM is to improve the economical benefits and GSCM did the same with

the decrease in consumption of resources and energy even benefits to society. GSCM Manage the internal and external management. It gives the more complete business models with low carbon in environment i.e. the improvement in whole life cycle right from raw material to delivery stage. GSCM always works in “Cradle-to-Reincarnation”, the product flow is circular and reversible since all product manage throughout the life cycle [4].

2.2 Principal and Practices of GSCM

The principle of the GSCM is to focus on the life cycle of the product and to make the cycle green in all means. GSCM gives the integrated management ideas and methods to improve the supply chain and every long term corporate performance [5].

At present, environmental objectives have become major societal, technological and political imperatives [6]. GSCM is the important practices that being adopted by the companies [7]. The aims of GSCM is to organize and systematize efforts i.e. redesigning according to environment friendly practices, by materials recycling, remanufacturing, reuse of leftovers and eco-design [8]. The companies integrated internal practices, like green manufacturing or eco-design, with external initiatives like cooperation with partners or reverse logistics [9]. The on-going practice of GSCM can minimize the total impact of industrial activity along the entire product life cycle [10]. Studied factors influencing the adoption of green supply chain practices in the logistics industry in Taiwan [2]. The major GSCM practices [11] are Supplier Oriented practices, internal supply Chain Practices and customer oriented practices. The supplier oriented practices says that the Suppliers are the major portion of development and maintenance of green activities in supply chains. There is a need of empowering them and making aware about the GSCM [12] did the strong partnerships with suppliers, which gives a significant success in innovative environmental practices. That means cooperation is needed and proctor the performance of supplier to ensure that the component supplied by them is environmental friendly [13]. Monitoring can be done by gathering and processing supplier information through publicly disclosed environmental records, company-specific questionnaires, environmental audits performed by either the buyer or an independent third party, using environmental criteria in evaluating suppliers, and demanding certified EMS from them. As Green purchasing is the most commonly implemented green supply chain practice which reduces the waste and increases recycling [9, 2]. Internal supply chain practices are the important practices to implement GSCM. There are lots of internal green practices that can be notorious like life cycle assessment, Total quality environment management design for environment and many more. These Practices will create the connection between the other departments and established a teamwork [14]. In design of Environment

the focus is given on reuse, recycling and remanufacturing of components. These activities aim to facilitate the design on reuse basis i.e. material selection and assembly of components repair, rework, and refurbishment activities aiming at returning product to new or better than new condition [15]. By implementing TQM, TQEM, these activities need the support from the upper management as this helps in life cycle management of the component [16, 17]. Customer-oriented practices aims on Green packaging, green distribution and green reverse logistics. The green distribution means green packaging the green packing will reduce the cost and negative impact on environment [15]. The main customers of organization are dealers, retailers, wholesalers, and final consumers. Green distribution means less emission transportation i.e. by selecting appropriate location for ware housing and outlets [18]. Green reverse logistics practices aims return of reusable, remanufacturable, and recyclable products and materials.

The implementation of the practices is increasing now a day because of the pressure from the stakeholder, Government, frequent audits, performance evaluation and competition in the market. In response to this pressure the organization gives training to their employment for the awareness and importance of GSCM with the collaboration of stakeholder.

2.3 Implementation and Frame Works

In the previous article we understand the main practices of GSCM. Now to implement the GSCM there is a need a driver their different drivers and their framework according to the industry. There are two main drivers [19]. External drivers are those that are not from the organization they may be stakeholders that posit pressure on organization, government bodies that means the set of regulations and act that exert pressure on the organization. Customer pressure, NGO's pressure and environmental societies pressure to form the green product [20, 21]. Internal drivers are the practices done internally that is cost saving from waste, recycling and reusing of materials with lower consumptions of energy and efficient resource [21]. To use standards like ISO 14001 and to generate the good publicity for the organization. To emanates mainly from prevalent green culture and awareness in the organization and its supply chain members. This lead these organizations to assume responsibility over product reuse and recycling as an element of environmental management (Fig. 1).

The use of TQM may encourage the firms to implement GSCM. Since these are the drivers which integrate in the firms to reduce the impact on the environment as strategic initiatives [8, 14]. The framework listed above shows that the external drivers act as primary motivators and internal drivers as stronger motivator and supply chain capabilities as catalyst or mechanism for higher level implementation. The organization must understand the importance of internal drivers.

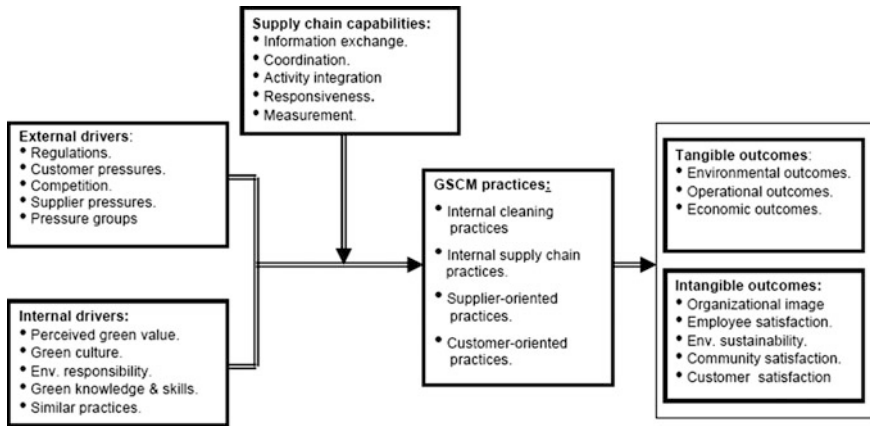


Fig. 1 Conceptual framework of the study (Source Eltayeb [4], p 7)

2.4 Evaluation and Performance of GSCM

GSCM performance and its correlations on financial performance The implementation of GSCM practices leads to the performance increment of the organization. Ala harja and Helo shows that the implementation of GSCM in food company improves the logistics efficiency leading to cost saving in transportation [22]. Reference [23] endeavored to implement the GSCM practices in the electrical and electronics industry in India. This gives the major impact on the organization environment performance and it becomes distinguish from this study that successful implementation of GSCM has major impact on firm’s environment performance and gain long-term benefits. Reference [24] implement the GSCM practices in textile industries as there was the lack of top management support, lack of knowledge regarding the green environment and the lack of awareness it took difficulty to implement but afterwards shows the better performance in textile industries.

From previous researches, there are several samples of GSCM implementation and its linkage to other performance, such as, operational performance, environmental performance, cost performance etc. Nonetheless, limited research has attempted to investigate relationship between GSCM performance and actual firm financial performance, such as, ROA, Inventory turnover ratio, Operating cost ratio, Net profit margin, Asset turnover ratio, etc. This paper examines the impact of the GSCM factors on selected financial ratio where electronics industries in Thailand are chosen as case study. The result maybe vary from industry to industry but similar approach can be replicated to investigate result from different business. Miguel [25] explain the evaluation of effectiveness of implementation of GSCM in organization by using the Analytical Hierarchy Process (AHP). Seles et al. [26] did the case study on the theory generation i.e. the theory previously defined by some

researcher and the results of the case study done. The study done on the automotive battery sector in Brazil. This gives the clear environmental pressure example of stakeholder to implement the GSCM in battery industries. The pressure was developed by frequent audits, Regulations, competitions and demand for the green products. Luthra [27] take the Expert opinions (from academics and industry) and validated that opinion with literature to categorized four dimensions, that are Non Members of Supply Chain (International environmental agreements, Central government legislations, State government legislations and Non government organizations). The another dimensioned is supplier's selection. The another dimensioned is about the input from the organization i.e. the appropriate technologies resources and motivation to the employees. The last dimensioned is the end of life management and customer awareness regarding the greening. Thirty strategies were find out and being evaluated by AHP and Interpretive Ranking Process (IRP).

3 Discussion and Conclusion

The papers clear the practices and implementation of the GSCM in industry. GSCM practices are the new approach towards supply chain. GSCM is not spread widely so it is necessary to find the ways that how to implement the practices of GSCM in various sectors. The awareness of GSCM is needed for each employee and customer also then and only then the GSCM can be fully implemented. The paper tries to explain few concepts with the help of some framework developed by some researchers. There are theories by which we can developed the framework that are porter's theory, RBV, TCT etc. From literature it is clear that the internal and external drivers are important the most is internal drivers, if the company developed internal drivers than more supply chain capabilities can be implement.

While going through the literature many researchers focus on various sectors but less work is incorporated in the automobile, textile, plastic, mining and on small scale industries (that means on supplier) sector. The area where GSCM should implement are Designing of products, production, material purchase, packaging, ware housing and reverse logistics. More effort has to be taken to empower GSCM.

References

1. Shultz CJII, Holbrook MB (1999) Marketing and tragedy of the commons: a synthesis commentary and analysis for action. *J Public Policy Mark* 18(2):218–229
2. Yu LC (2007) Adoption of green supply in Taiwan logistic industry. *J Manage Study* 90–98
3. Practices and innovation of green supply chain. In: CCICED annual general meeting, 2011
4. Eltayeb T, Zailani S (2007) The implementation of green supply chain management practices: a conceptual framework
5. Zhu M (2016) The principle of green supply chain and application proposal in construction industry

6. Klemeš J, Varbanov P, Pierucci S, Huisingh D (2010) Minimizing emissions and energy wastage by improved industrial processes and integration of renewable energy. *J Clean Prod* 18:843–847
7. Zhu Q, Sarkis J, Lai K (2008) Confirmation of a measurement model for green supply chain management practices implementation. *Int J Prod Econ* 111:261–273
8. Seuring S, Muller M (2008) From a literature review to a conceptual framework for sustainable supply chain management. *J Clean Prod* 16:1699–1710
9. Zhu Q, Sarkis J, Lai K (2012) Examining the effects of green supply chain management practices and their mediations on performance improvements. *Int J Prod Res* 50:1377–1394
10. Linton J, Klassen R, Jayaraman V (2008) Sustainable supply chains: an introduction. *J Oper Manage* 25:1075–1082
11. Lippmann S (1999) Supply chain environmental management: elements for success. *Environ Manage* 6(2):175–182
12. Geffen CA, Rothenberg S (2000) Suppliers and environmental innovation: the automotive paint process. *Int J Oper Prod Manage* 20(2):166–186
13. Rao P, Holt D (2005) Do green supply chains lead to competitiveness and economic performance? *Int J Prod Oper Manage* 25(9):898–916
14. Seitz MA, Peatty K (2004) Meeting the closed-loop challenge: the case of manufacturing. *Calif Manag Rev* 46(2):74–89
15. Beamon BM (1999) Designing the green supply chain. *Logistics Inf Manage* 12(4):332–342
16. Sarkis J (1998) Evaluating environmentally conscious business practices. *Eur J Oper Res* 107(1):159–174
17. Lin B, Jones CA, Hsieh C (2001) Environmental practices and assessment: a process perspective. *Ind Manage Data Syst* 101(2):71–79
18. Sarkis J (2003) A strategic decision framework for green supply chain management. *J Clean Prod* 11(4):397–409
19. Porter ME (1991) Towards a dynamic theory of strategy. *Strateg Manag J* 12:95–117
20. Henriques I, Sadosky P (1996) The determinants of an environmentally responsive firm: an empirical approach. *J Environ Econ Manage* 30(3):381–395
21. Porter ME, van der Linde C (1995) Green and competitive: ending the stalemate. *Harvard Bus Rev* 73(5):120–134
22. Tippayawong KY, Tiwatreewit T, Sopadang A (2015) Positive influence of green supply chain operations on Thai electronic firms' financial performance. In: International conference on sustainable design, engineering and construction, Elsevier Procedia Engineering, vol 118, pp 683–690
23. Dyer JH (1997) Effective inter firm collaboration: how firms minimize transaction costs and maximize transaction value. *Strateg Manag J* 18(7):535–556
24. Sarkis J, Zhu Q, Lai K (2011) An organizational theoretic review of green supply chain management literature. *Int J Prod Econ* 130:1–15
25. Sellitto MA, Bitten Court SA, Reckziegel BI (2015) Evaluating the implementation of GSCM in industrial supply chains: two cases in the automotive industry. *Chem Eng Trans* 43
26. Seles BMRP, de Sousa Jabbour ABL, Jabbour CJC, and Dangelico RM (2016) The green bullwhip effect, the diffusion of green supply chain practices, and institutional pressures: evidence from the automotive sector. *Int J Prod Econ* 182,342–355
27. Luthra S, Garg D, Haleem A (2013) Identifying and ranking of strategies to implement green supply chain management in Indian manufacturing industry using analytical hierarchy process. *J Ind Eng Manage JIEM* 6(4):930–962

Design and Performance Evaluation of Low-Cost, Innovative, Efficient Small-Scale Wind Power Generation for Rural Community of India

Pradip D. Haridas and Avinash K. Parkhe

Keywords Small HAWT designs · Light weight rotor blades · Balancing of rotor blades · Hub design · HAWT tail end designs · PMG · Performance curves · Rated output

Nomenclature

GFRC	Glass fibre reinforced composites
HAWT	Horizontal axis wind turbine
R&D	Research and development
RPM	Revolutions per minute
C-WET	Centre for Wind Energy Technology, Chennai
kW	Kilowatt
mW	Megawatt
GW	Gigawatt
NACA	National Advisory Committee of Aeronautics, USA
NREL	National Renewable Energy Laboratory, USA
PMG	Permanent magnet DC generator
ρ	Density of air
A	Swept area
V	Wind speed
C_p	Power coefficient
λ	Tip speed ratio
λ_o	Actual tip speed ratio
η	Efficiency
ω	Linear velocity in m/s
τ	Torque
R	Total radius

P.D. Haridas (✉) · A.K. Parkhe
SVERI's College of Engineering, Pandharpur, District Solapur, India
e-mail: pradipdharidas@yahoo.com

A.K. Parkhe
e-mail: avinashparkhe92@gmail.com

r	New desired radius
C	Chord width
N	Revolution per minute
α	Angle of attack
S_p	Shape parameter
B	No. of blade
C_i	Initial chord width for each section
C_l	Lift coefficient

1 Introduction

The foundation for this research is recognition of the need for sustainable practices and development of renewable energy sources, and acknowledgment of the benefits that such forms of energy can have for individuals and communities, especially when conventional grid-supplied electricity is not available.

This paper envisions the design and appropriate implementation of a 500 W electricity producing wind turbine. The turbine will ideally be intended for implementation in remote communities to power individual house's electrical needs. The aim of the project is to design a wind energy converter comprising of the rotor system, and a generator that will successfully produce the specified electrical power.

The performance criteria necessary in the design of small wind turbine (SWT) are examined, as well as some of the theory and calculations necessary to develop such performance standards. Also, an investigation into the associated design standards and a discussion of how they relate to performance criteria are presented. High initial costs and significant structure of the Large Wind Turbines have given rise to cheaper, Small Wind Turbine market. Small Wind Turbines are lightweight, which allow them to function with the lightest wind. Technical developments have increased the efficiencies of these turbines, which are now being used to power homes and businesses. Due to the advanced technology; the wind turbine blades have become lighter, smaller, but more efficient. Further, a countable number of Small Wind Turbines are also available with wireless connectivity, which enables owners to control the turbine dynamics from a distant location, while some Wind Turbines are fitted with electronic displays. New Wind Turbines can also be used on and off grid, as expected by an owner. Such technological up gradation has made these Wind Turbines more reliable as a source of energy and driven the market for the Small Wind Turbines [1–3].

The most useful and shared type of wind turbine found today is the horizontal axis wind turbine which can be most easily identified by its propeller-like rotor design.

2 Design of HAWT System

The design details of 500 W Horizontal Axis Wind Turbine System is given below in this section (Figs. 1 and 2).

The fundamental principles that govern the operation of a HAWT will be investigated to develop further understanding of the system requirements. These principles will assist in identifying the elements of the design. The major components of this type of design have been designated as Rotor, Generator, Tower and foundation Yaw mechanism with tail, Furling mechanism, Slip rings and electrical cabling, Energy storage or conversion system, Electrical control system, with over-speed and lightning protection One of the fundamental theories of rotor aerodynamics is the one-dimensional (1D) Betz’s Elementary Momentum Theory. Betz’s simple momentum theory considers a stream of air moving through a circular disk. The analysis is based on the following assumptions: (1) Homogeneous, incompressible, steady-state fluid flow (2) No frictional drag (3) An infinite number of blades (4) Uniform thrust over the entire rotor area (5) Non-rotating wake (air stream after passing through rotor) (6) Upstream and downstream static pressures are equal to the undisturbed ambient static pressure. One-dimensional theory considers a moving stream of air passing through a circular disk (Fig. 3). The kinetic energy equation gives the energy in the moving stream of air [4, 5]:

Fig. 1 System diagram

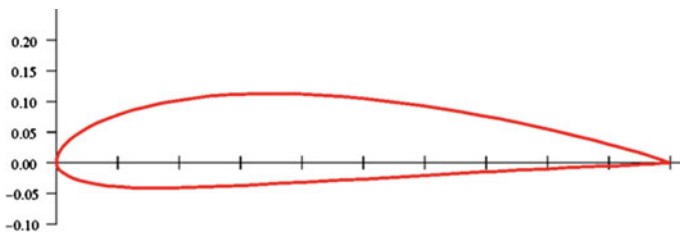
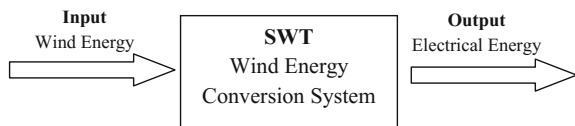


Fig. 2 NACA 4415 aerofoil

Fig. 3 Rotor blade

$$E = \frac{1}{2} mV^2 \quad (1)$$

Energy per unit time gives the power in this air stream:

$$P = E/t = \frac{1}{2} mV^2/t = \frac{1}{2} \frac{m}{t} V^2 = \frac{1}{2} mV^2 \text{ (W)} \quad (2)$$

where 'm' is the mass flow rate of the air stream, and is given by,

$$m = \rho Av \text{ (kg/s)} \quad (3)$$

Thus the power of a moving stream of air, with density ρ and velocity v , that flows through a disk of area A is:

$$P = \frac{1}{2} \rho Av^3 \quad (4)$$

This expression gives the power available in a moving stream of air, but the power that can be extracted from this moving stream is what is required. Thus we can consider a ratio, known as the power coefficient, between the power in the wind, and the power of the rotor:

$$C_p = \text{Rotor Power/Wind Power}$$

In theory, the maximum possible rotor power coefficient is given by the Betz Limit, $C_p = 16/27 = 0.593$ [6]. In practice, however, further inefficiencies cause a decrease in the maximum achievable output power:

So the power output of the SWT can be summarized as:

$$P = C_p \times \eta \times \frac{1}{2} \rho Av^3 \quad (5)$$

2.1 Design of Blade

The blade is one of the most important parts of the wind machine, which converts the kinetic energy into electrical energy. From root to tip the blade is loaded with varying forces. The way to consider such loading is to write the expressions for a small section of the blade at radius ‘r’ and find out the distribution; this is the “blade element theory.”

$$\text{Power} = \frac{1}{2} \times \rho \times A \times V \times C_p \times \eta_g \times \eta_g \quad (6)$$

Using tip speed ratio and blade Solidity graph we have to select the Aerogenerator tip speed ratio.

For that we have to calculate first angular velocity

$$\lambda = R \cdot \omega \quad (7)$$

More factor of safety more reliability hence increases the blade length and cost. Now, Angular velocity ω is calculated by

$$\therefore \lambda = 0.85 \times \omega \quad (8)$$

Now from following equation speed is calculated.

$$\omega = \frac{2\pi N}{60} \quad (9)$$

Hence Tip speed Ratio at ‘r’ is calculated by eq.

$$\lambda_r = \lambda_o \times \frac{r}{T} \quad (10)$$

Chord width is calculated from equation

$$C = r \times \frac{SP}{CL} \times B \quad (11)$$

Torque is calculated by following equation

$$\text{Torque, } \rho = \frac{2\pi N}{60} \quad (12)$$

2.2 Selection of Aerofoil Section

By preferring Blade Element Theory, Now preferring NACA 4415—airfoil i.e. 40% chamber height 40% chord length 15% Thickness of chord length, Now as per design foil software max. Lift occur in NACA—4415, 0018, 63-215 While, CL/C ratio is maximum for 4415. And at $\alpha=50$ i.e. angle of attack is 50. So the airfoil selected for our wind machine blade is NACA 4415 which is shown below and the coordinates for drawing the profile is also given in the table below.

3 Construction of HAWT

Figures 4, 5, 6, 7, 8, 9 and 10

Fig. 4 Rotor hub plate and bush



Fig. 5 Nacelle bed plate with yawing assembly





Fig. 6 Tail vane assembly



Fig. 7 Tower assembly

Fig. 8 PMDC generator assembly

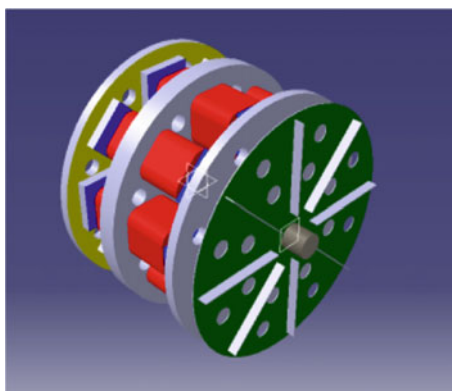




Fig. 9 Wind speed measurement on Anemometer

Fig. 10 Assembly of HAWT



4 General Characteristics of 500 W Small Wind Turbine

Cut-in wind speed	2.7 m/s	Voltage	24 V
Rated wind speed	10 m/s	Tower	Tubular concrete fitted
Cut-out wind speed	15 m/s	Material	Mild steel
Rotor situation	Up wind	Height	3 m
Number of blades	Three	Height from ground	30 m (building + pole ht.)
Blade material	FRP	Yawing system	Fitted at the top of the pole
Rotor diameter	0.55 m	System regulation	Rotor tilting
Generator	PMDC	Emergency brake	Generator short circuit
Rated power	500 W	Weight	30 kg without pole

5 Testing of HAWT

The 500 W small wind turbine is installed on the roof of the International school of Technology, Department of Technology building of the Shivaji University for testing. As micro-siting is done previously the points of maximum wind speed were located, and the wind turbine was installed by constructing the column on a tower of 3-m height, supported by heavy angles which can be quickly lowered to roof level for turbine inspection and maintenance (Table 1).

Table 1 Sample readings of HAWT

S. No.	Wind speed (m/s)	Speed of turbine (RPM)	Voltage (V)	Current (A)	Actual power (W)	Th. power (W)	Efficiency (%)
1	1.2	72	20.5	0.7	14.35	1.07	7.46
2	1.9	122	21.2	1.5	31.8	4.25	13.37
3	0.9	65	21	0.5	10.5	0.45	4.30
4	0.7	52	21.2	0.2	4.24	0.21	5.01
5	0.6	52	21.3	0.19	4.04	0.13	3.30
6	1.7	90	21.5	1.2	25.8	3.04	11.80
7	1.5	75	21.1	1	21.1	2.09	9.91
8	2	110	21.2	1.7	36.04	4.96	13.76
9	2.5	130	21.1	3.4	71.74	9.68	13.50
10	1.2	79	21	0.7	14.7	1.07	7.28
11	0.5	60	20.7	0.17	3.51	0.07	2.20
12	1.4	75	20.8	1	20.8	1.70	8.17
13	4.4	279	21.1	5.3	111.8	52.81	47.22
14	2.3	145	21.1	3.1	65.41	7.54	11.53
15	4.5	270	21.2	5.3	112.3	56.49	50.28
16	3	192	21	3.7	77.7	16.74	21.54
17	3.7	195	21.3	3.4	72.42	31.40	43.36
18	2.7	142	21.1	2.2	46.42	12.20	26.28
19	2.9	171	21.2	3.1	65.72	15.12	23.00
20	4.6	295	21.4	5.9	126.2	60.34	47.79
21	5.4	342	21.7	6.5	141.0	97.62	45.21
22	4.6	280	21.7	5.5	119.3	60.34	50.56
23	0.8	71	21.1	0.5	10.55	0.31	3.00
24	1.1	78	21.2	0.6	12.72	0.82	6.48
25	1.2	78	21.2	0.6	12.72	1.071	8.42

6 Performance Evaluation of Horizontal Axis Wind Machine

The analysis is as per the guidelines available in IEC 61400-12-1, design requirements of a small wind turbine. Through IEC standards 250 h of testing periods, in the present case the IEC procedure was adopted for the performance, characterization of a small wind machine, as time available before monsoon was 1.5 months.

Only power performance guidelines, as per the IEC 61400-12-1, power performance measurements of electricity producing wind turbine for small wind machine is followed. That leads to power curve, power coefficients (C_p curve) and estimation of annual energy production. For small wind turbines, the average data of 15 min was collected and sorted to 0.5–12 m/s wind speed bins. The data collection is complete when the wind speed bins between 1 and 12 m/s of 15 min interval.

Some graphs have been shown related to Performance of Wind Machine.

Graph Fig. 11 shows a variation of turbine speed with wind speed. It is a common phenomenon that as wind speed increases the speed of rotation of turbine enhances. With the system described it is possible to generate sufficient amount of electrical energy.

Graph Fig. 12 shows Wind Speed versus Current. Wind Speed is plotted along X-axis and Current along Y-axis. As the linear wind speed increases from 0 to 6 m/s the current increases from 0 to 10 A.

Graph Fig. 13 shows Current versus RPM. RPM is plotted along X-axis and Current along Y-axis. With the linear increase in Turbine speed from 0 to 600 rpm the current increases from 0 to 10 A.

Fig. 11 Wind speed versus RPM

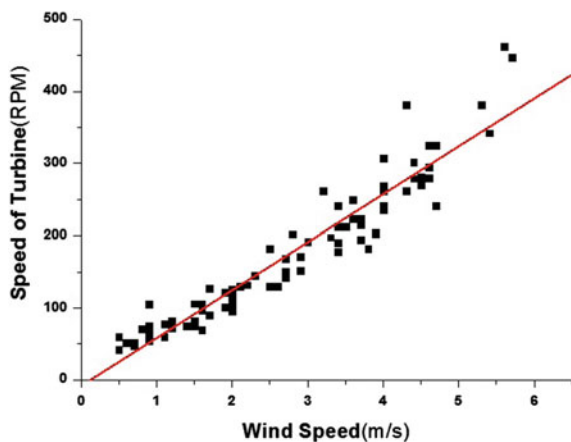


Fig. 12 Wind speed versus current

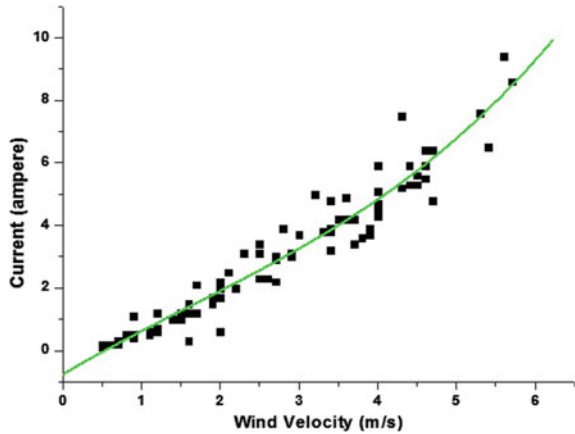
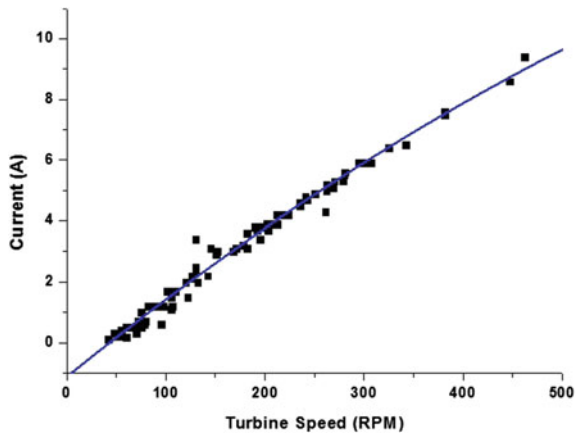


Fig. 13 Current versus RPM



7 Performance Comparison

Graph Fig. 14 shows Wind Speed versus Theoretical power. Wind Speed has been plotted along X-axis and Theoretical power along Y-axis. As the wind speed increases linearly, from 0 to 6 m/s the power increases from 0 to 120 W.

Graph Fig. 15 shows Wind Speed versus Actual power. Wind Speed has been plotted along X-axis and Actual power along Y-axis. As the wind speed increases linearly, from 0 to 6 m/s the power increases from 0 to 200 W.

Fig. 14 Wind speed versus theoretical power

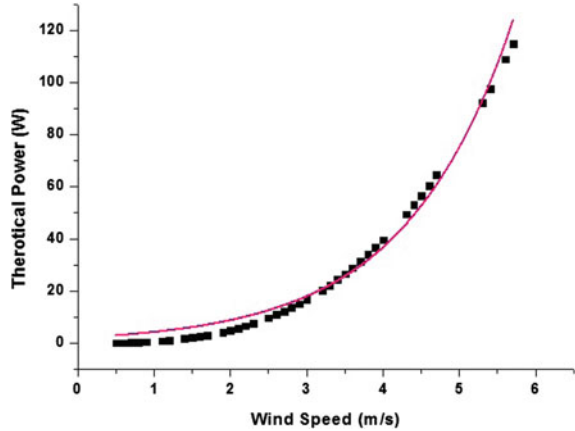
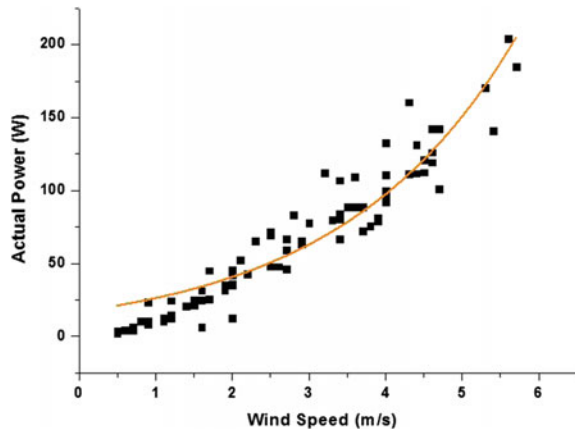


Fig. 15 Wind speed versus actual power



8 Conclusions

Based on the study, the following conclusions are listed

1. Considering the small family of 4–5 persons the daily requirement of electricity is concluded to 1.5 kW for a family.
2. The project work reveals that there is a necessity of developing horizontal axis small wind machines having capacity 200–1500 W which can run at low wind speeds. The project work has therefore considered design, development and testing of a prototype horizontal axis small wind machine of 500 W.
3. The project concludes manufacturing FRP rotor blades and allied PM Generator with suitable components like Shaft, Yawing, Bearing and Tail end, etc.
4. The testing of 500 W horizontal axis small wind machine results is as given below.

- (i) The wind machine was tested in the month of December and January with a minimum wind speed of 0.6 m/s to a maximum wind speed of 10.9 m/s.
- (ii) During testing the machine start at 2.7 m/s at 100 rpm as against design cut in wind speed of 3.5 m/s.
- (iii) The maximum 957 RPM has been observed at 10.9 m/s. Once rotated machine kept running up to around 1.2 m/s. Due to inertia, it has gained but does not generate enough current to charge the battery.
- (iv) The Power Curve Fig. 12 shows that cut in speed of our machine is 2.7 m/s where other is having 4 m/s. Also at rated wind speed it generates 350 W where prototype machine produces 500 W.
- (v) It has been concluded that the machine developed through the Research and Development gives better results and performance than the similar capacity machines available in the market. The prototype device is more feasible than imported machine for local wind conditions.

References

1. Hau E (2000) Wind turbine fundamentals, technology, application, & economics, 2nd edn. Springer Publication, Germany
2. International Electro technical Commission (2005) Wind turbines—Part 12—1: Power performance measurements of electricity producing wind turbines, IEC 61400-12-1:2005(E), International Electro Technical Commission, Geneva, viewed 19 May 2010. <http://www.saiglobal.com.ezproxy.usq.edu.au/online/autologin.asp>
3. Chalmers BJ, Spooner E (1999) An axial-flux permanent-magnet generator for a gearless wind energy system. *IEEE Trans Energy Convers* 14(2):251–257
4. IEC-61400-12-1. Wind turbine generator system, Part 12, Power performance measurement technique
5. IEC-61400-2. Wind turbines, part-2: design requirements for small wind turbines
6. Manwell J, McGowan J, Rogers A. (2002) *Wind Energy Explained: theory design and application*, John Wiley & Sons, Chichester, England

Design Modification of Biogas Digester to Avoid Scum Formation at the Surface

Vidyarani S. Kshirsagar and Prashant M. Pawar

Keywords Anaerobic digester · Computational fluid dynamics (CFD) · Geometrical modifications · Scum · Mixing

1 Introduction

Anaerobic digestion (AD) produces biogas from organic material. In particular, the AD of solid waste can reduce the emission of greenhouse gasses, mainly methane, which may otherwise be released to the atmosphere [1]. Biogas, a clean, efficient, and renewable source of energy, has become popular as a substitute for other types of fuel to save energy and to protect the environment in rural areas [2]. This technique has been evaluated as one of the most energy-efficient and environmentally beneficial technology for bioenergy production [3]. The increase of renewable energy production is of great interest today. Biogas technology can contribute an essential part to a sustainable energy system. Therefore the efficiency of technology has to be improved continually.

McMahon et al. [4] performed experiments using four digesters with different startup strategies operated under continuously mixed conditions and compared the performance with the mixed conditions digesters. This comparative study shows that the level of mixing improved digester performance. Further, the results of continuously mixed digesters show the unstable performance at the higher loading rates, while the minimally mixed digesters performed well for all loading rates evaluated. They have demonstrated the unstable behavior can be stabilized by reducing the mixing level. Karim et al. [5] examined the effect of the mixing modes on biogas production, and found that the digesters with mixing unit produced more biogas than the regular digesters for input as thick manure slurries. Kaparaju et al. [2] evaluated the effect of mixing on anaerobic digestion of manure in lab-scale and pilot-scale experiments. They have demonstrated that various mixing strategies viz.

V.S. Kshirsagar (✉) · P.M. Pawar
Department of Civil Engineering, SVERI's College of Engineering, Pandharpur, India
e-mail: vskshirsagar@coe.sveri.ac.in

continuous mixing, intermittent and minimal mixing improved methane productions by 7, 1.3, and 12.5%, respectively. The effect of mixing in pilot-scale model supported the lab-scale results with an average 7% increase in biogas yields during intermittent mixing compared to continuous mixing. Luděk et al. [6] presented the energy requirement estimate for biogas operation. The result shows that about 7–8% of total electrical energy produced is required for various operations of the biogas plant and from which about 40% is needed just for mixing devices.

Binxin [7] reviewed, the state-of-the-art CFD for biochemical conversion in six major bioreactors. He mentioned that no matter which Bioenergy system is studied but, the primary objective is to create an optimal physical environment that favors the biological process. This requires the use of CFD for quantitative identification of the relation between physical and biological characteristics (e.g. mixing and biomethane fermentation). The importance of mixing in achieving efficient substrate conversion has been reported by several researchers [4, 5, 8] mentioned that, the effective suspension and settling are critical for controlling biomass retention in a bioreactor. He has proposed to the engineers and researchers for the use of CFD in the large-scale digesters for a good mixing performance, to provide a comprehensive predictive control and optimization solution for a biogas plant.

Literature study presents that, most of the researchers carried out the research for increasing the mixing efficiency of biogas digester by implementing the impeller and gas inlet which unfortunately consumes energy. The main objective of this work is to increase the mixing efficiency of the biogas digester without adding a mechanical stirrer. To produce the sufficient turbulence, the author has changed the geometry of existing biogas digester and added the three horizontal passive flaps for the maximization of the surface velocity. This problem has been studied by using time-dependent CFD module and Optimization solver in COMSOL Multiphysics software. The optimization is carried out to find the optimal location and optimal width of the flaps in the digester.

2 Background Information

2.1 Biogas Characteristics

Typical biogas composition mentioned in Table 1. The main constituent of biogas is the CH₄ and CO₂ gas. The biogas burns very well when the CH₄ content is more than 50%. The relative percentage of gasses in biogas depends on the feed material and management of the process.

Table 1 Typical biogas composition

Energy content	20–25 MJ/m ³
Methane (CH ₄)	55–70%
Carbon dioxide (CO ₂)	30–45%
Hydrogen sulfide (H ₂ S)	200–4000 ppm

Source RISE-AT (1998), Braber [9]

Fig. 1 Observed scum in the baseline digester



Table 2 Rheological properties and densities of liquid manure for T = 35 °C

TS (%)	K (Pa S ⁿ)	n	$\dot{\gamma}$ (s ⁻¹)	η_{\min} (Pa s)	η_{\max} (Pa s)	ρ (kg m ³)
2.5	0.042	0.710	226	0.006	0.008	1000.36
5.4	0.192	0.562	50	0.01	0.03	1000.78
7.5	0.525	0.533	11	0.03	0.17	1001.00

Achkari-Begdouri and Goodrich [10], Landry et al. [11], Wu and Chen [12]

2.2 Failure Causes of Biogas Plant

Mixing characteristic produces direct impact upon the microbial structure in the digester. Microbial cells are susceptible to mechanical force, which disrupts the cell membrane and eventually kills some microorganisms, animal cells, and plant cells. Continuous shear, in particular, negatively affects microbial flocks and converted into the formation of thick scum layer on the surface. The observed scum layer in the baseline biogas digester is shown in Fig. 1.

2.3 Rheological Properties

The fluid dynamics in the digester can be affected by the TS related to the slurry rheological behavior. Rheological characteristics of the sludge mentioned in Table 2 were taken from published data to carry out the numerical analysis of baseline and proposed digester model. The impact of TS concentration was studied on the flow pattern in the biogas digester for a constant inlet velocity and the period from 0 to 50 s at the interval 0.05 s.

3 Numerical Methods

A simulation is a powerful tool in science and engineering for predicting the behavior of physical systems, particularly those governed by partial differential equations. CFD emerged in the early 2000s as a tool to predict biomethane yield from covered anaerobic lagoons. Since then considerable research has been done on the various bioreactors for biomethane and biohydrogen production including anaerobic lagoon, plug-flow digester, complete-mix digester, anaerobic biohydrogen fermenter, anaerobic biofilm reactor, and photobioreactor (PBR). Thus, a Computational Fluid Dynamic (CFD) modeling is used to simulate the dispersion behavior of biogas from pressurized release into the atmosphere. CFD is the popular tool used to investigate the behavior of released substance mainly liquid and gas. CFD also equipped with a branch of fluid mechanics that involve algorithm and numerical method to solve the problem related to the fluid flow. Computational Fluid Dynamics (CFD) can assist in studying mixing through numerical simulation of fluid motion (Paul et al. 2004). CFD can allow determination of flow characteristics of a liquid/slurry system with a much lower cost than experimentation. Its advantages are even greater in applications where it is difficult to detect the mixing parameters experimentally.

A time-dependent two-dimensional CFD-based simulation model is prepared using COMSOL Multiphysics fluid flow software. The simulation started with a preprocessing step that included the mesh generation of a bioreactor. This step continued by solving all the governing equations that incorporate in the models. The last step was the post-processing that visualized the flow pattern of biogas inside the tank. The physics controlled extra fine mesh generated in the model. 200 iterations were given to obtain a converged numerical solution. No-slip boundary conditions applied on the walls. An implicit time step of 0.05 s used to ensure the convergence criteria.

3.1 *Mixing*

Optimal mixing is an essential requirement for efficient anaerobic digester operation and biogas production. Research on mixing using CFD will provide theoretical support for design, optimization, and scale-up of the biogas digester. To date, lab-, pilot- and commercial-scale high solid anaerobic digesters have been constructed in which mixing is a key factor. Mixing provides intimate contact between the feed sludge and active biomass, yielding uniformity of temperature, of substrate concentration, of another chemical, physical and biological aspects throughout the digester, and preventing both the formation of surface scum layers and the

deposition of sludge at the bottom of the tank. CFD based COMSOL Multiphysics software enables one to predict the effects of geometry, feed location, physical properties, and operating conditions in the tank. Typical results predict velocity profiles, rates of energy dissipation, concentrations, and flow streamlines as they would occur in the vessel. This tool enables one to appreciate the good and bad features for each considered design. Luděk et al. [6] Presented that, the total electric energy self-consumption by the investigated biogas plants was in the range of 7–8% of the total electrical energy produced. About 40% of the consumed energy is needed just for mixing in digesters.

3.2 Governing Equations

Under most circumstances, the organic wastes such as wastewater sludge and manure slurry may exhibit non-Newtonian behavior [10, 11]. Liquid manure is described using the non-Newtonian Fluid Model:

$$\tau_{ij} = \eta \frac{\partial u_i}{\partial x_j} + \frac{\partial u_j}{\partial x_i}$$

where, η is non-Newtonian viscosity, which is only considered to be a function of the shear rate.

The viscosity in the non-Newtonian power law is expressed as:

$$\eta = K\gamma^{n-1}e^{\frac{T_0}{T}}$$

where K is the consistency coefficient (Pa s^n), γ is the shear rate (s^{-1}), n is the power-law index that determines the class of fluid, T_0 is the reference temperature (K), and T is the slurry temperature (K). For the non-Newtonian power law various model parameters was entered in the model viz. Fluid consistency coefficient (m), Flow behavior index (n) and lower shear rate limit ($\dot{\gamma}_{\text{min}}$).

CFD analysis carried out is explained using the baseline digester. The baseline design of biogas plant contains a circular digester with three vertical baffles parallel to the inlet and outlet arrangement as shown in Fig. 2. The baffle arrangements are made to increase the Hydraulic Retention Time (HRT). Through the direct observation in the baseline model, it is concluded that due to lack of turbulence in the baseline design a hard scum forms at the surface. The 2D geometric design of baseline biogas plant is shown in Fig. 2. The CFD analysis carried out to determine the domain velocity and velocity at the surface of the digester. Further this analysis

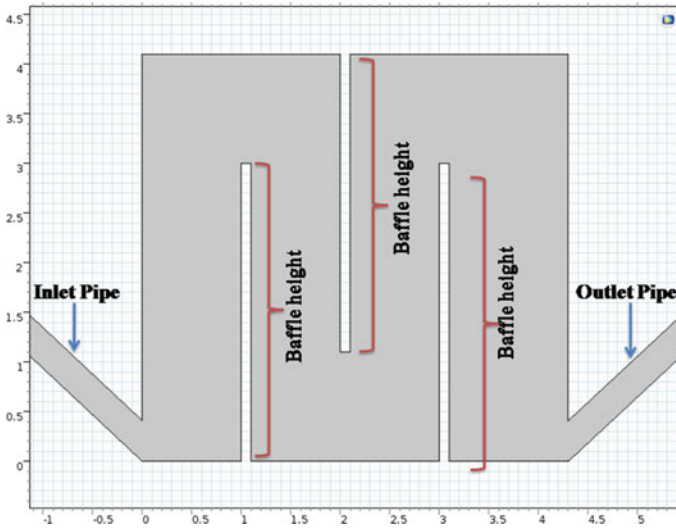


Fig. 2 2D baseline geometry design of biogas digester

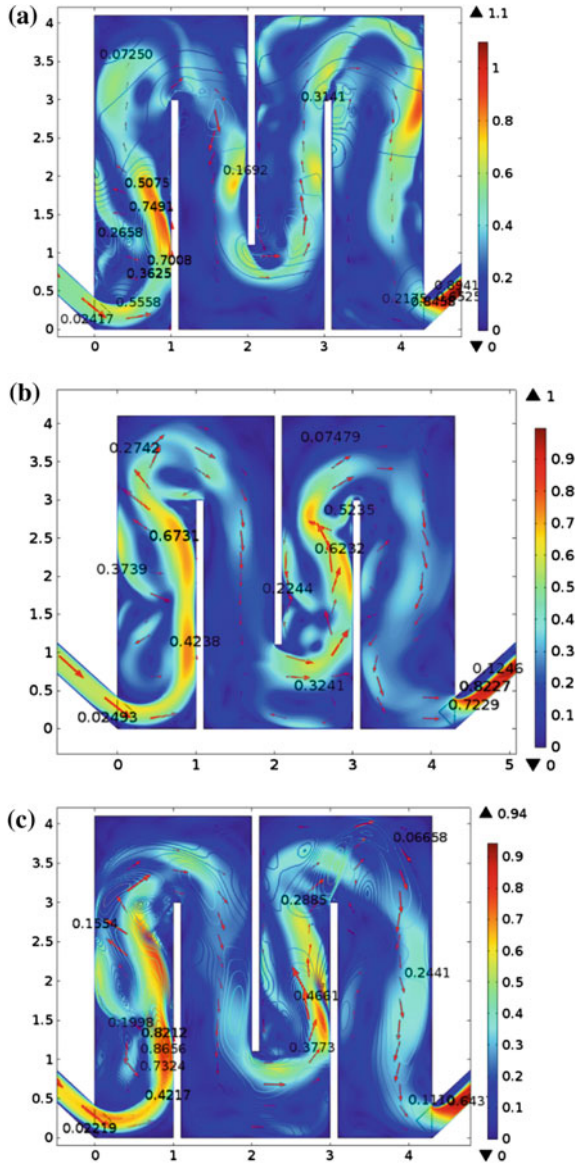
Table 3 Geometric parameters of baseline biogas digester

Notation	Description	Baseline dimensions
h	Digester height	4.1 m
d	Digester width	4.3 m
dh2	Difference in walls	1 m
h1	Baffle height	3 m
w1	Wall thickness	0.1 m
w2	Inlet pipe thickness	0.3 m
ipl1	Inlet pipe length	3 m
tht1	Inlet pipe angle	47°
tht2	Outlet pipe angle	-47°

is used to understand the flow pattern in the baseline design. Parametric dimensions of Baseline Biogas Plant presented in Table 3.

In the present paper, first, the CFD simulation is carried out for the baseline model. The final result means the value about the hydrodynamic of the sludge inside the digester, as velocity fields are noted. Velocity is then considered the most representative parameter of the behavior of flow. The blue color represents lower velocities, and red color represents the higher values of the velocity field in the digester. The observed flow pattern of baseline model is shown in Fig. 3.

Fig. 3 Velocity profile observed in baseline digester design for different TS concentrations. **a** TS 2.5, **b** TS 5.4, **c** TS 7.5



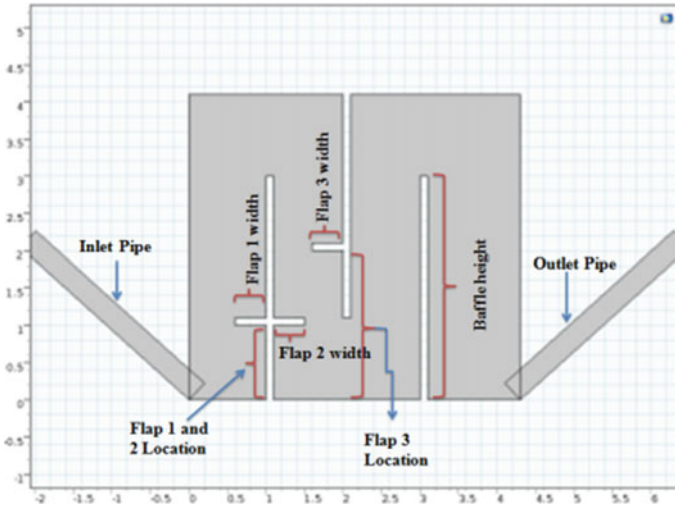


Fig. 4 Proposed digester design

Table 4 Proposed digester design of biogas plant with geometrical dimensions

TS in %	fl1	fl2	fl3	df1	df2	df3	Model
2.5	0.37	0.28	0.39	1.071	0.95	2.00	S-I
5.4	0.39	0.11	0.4	0.005	0.991	2.00	S-II
7.5	0.38	0.20	0.35	0.98	0.97	1.96	S-III

4 Proposed Digester Design for Surface Velocity Improvement

4.1 Problem Statement

For improvement of mixing process and surface velocity, most of the studies provided impellers. However, the digester design for such systems became complicated, and also plant becomes less economical due to the requirement of external energy. In this study, the passive flaps are provided for improving the surface velocity. Figure 4 shows the proposed digester design with three flaps. The proposed digester simulated in COMSOL Multiphysics CFD module with the description details of flaps and its geometrical dimensions provided in Table 4. The simulation was carried for three different TS values mentioned in Table 2.

5 Result and Discussion

A comparative study was carried out for baseline digester and proposed digester. The proposed digester is a modification in the geometry of baseline digester by adding three horizontal flaps. It is observed that the mixing improved due to the addition of flaps in the biogas digester.

The velocity magnitude for the surface is calculated with respect to time 1 to 50 s. The visual performance of the velocity in the domain of the digester for all the models is shown in Figs. 5, 6 and 7. Through the visual report, it is observed that the performance of velocity is increased in the maximum portion of the domain in model S-I, S-II, S-III. Out of all models mentioned above the model S-I for TS 2.5 and for TS 5.4, model S-II for TS 2.5, model S-III for TS 2.5 shows a better turbulence at the surface along with the domain. This type of increase in velocity will help to increase the turbulence in the digester and turn mixing will be achieved.

Fig. 5 Surface velocity behavior of model S-I for TS 2.5%

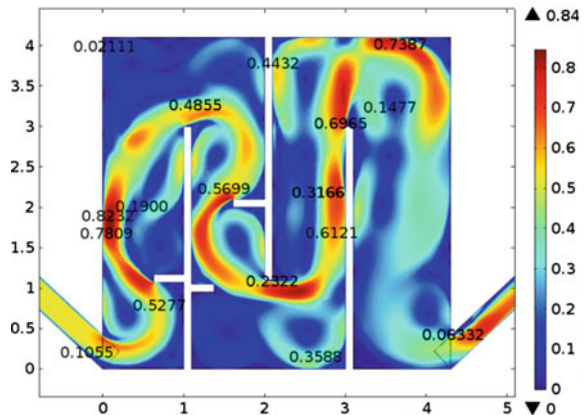


Fig. 6 Surface velocity behavior of model S-II for TS 2.5%

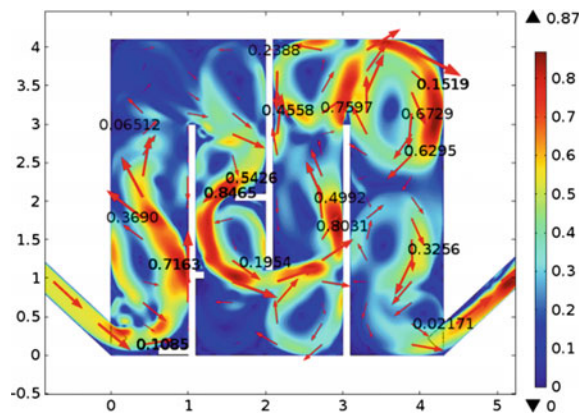


Fig. 7 Surface velocity behavior of model S-III for TS 2.5%

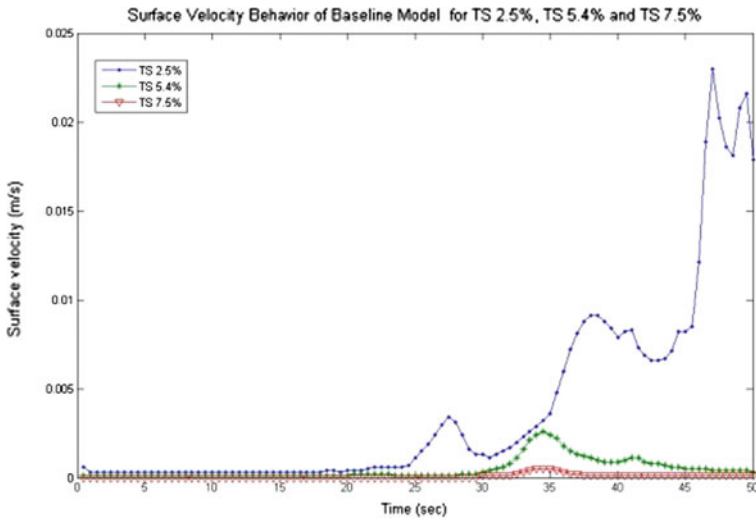
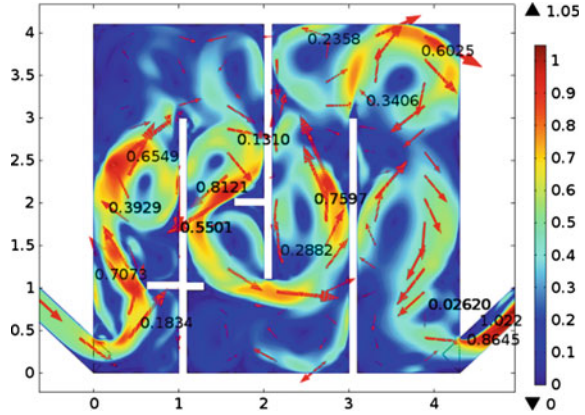


Fig. 8 Baseline model surface velocity performances

5.1 Based on Surface Velocity Maximization

The velocity magnitude in the entire domain and at the surface of the baseline digester is calculated and compared with the Model S-I, S-II, and S-III. The baseline model shows the maximum velocity at the surface of the digester as 0.0230, 0.0026, 0.0005 m/s and in the domain of the digester is 1.1040, 1.1469 and 1.0085 m/s at TS 2.5, TS 5.4 and TS 7.5 respectively Fig. 8. Whereas the proposed models S-I, S-II and S-III shows better values as a maximum velocity at the surface as well as in the domain of the digester which is shown in Figs. 9, 10 and 11.

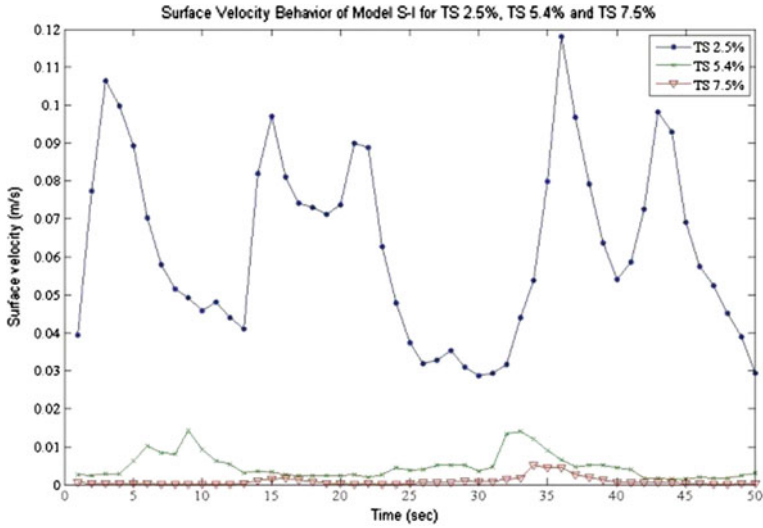


Fig. 9 Model S-I surface velocity performances

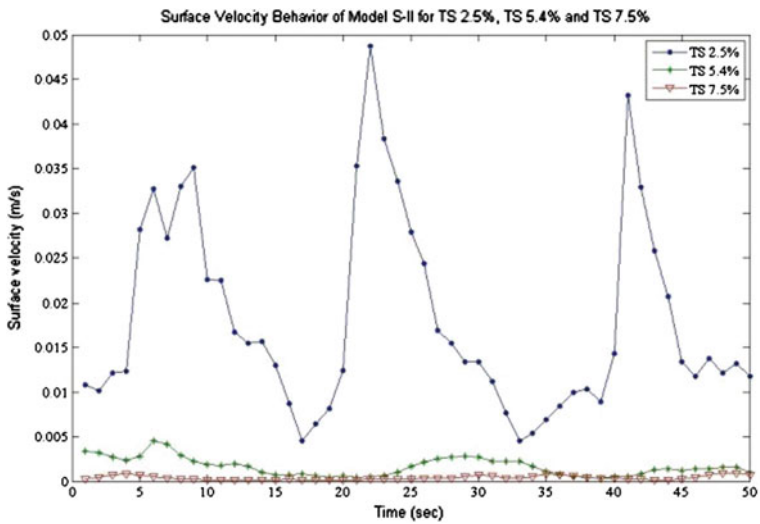


Fig. 10 Model S-II surface velocity performances

Based on surface velocity maximization, the maximum surface velocity in the model S-I is increased appreciably by 80.50, 81.69 and 90.19% for the TS value 2.5, 5.4 and 7.5 respectively on baseline model. The model S-II and S-III also maximizes its surface velocity considerably.

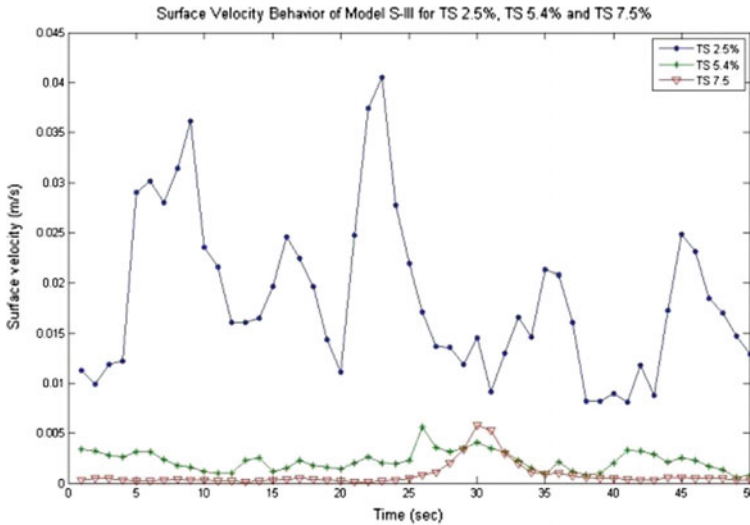


Fig. 11 Model S-III surface velocity performances

6 Conclusion

Based on study, following conclusions are made:

- CFD simulations in a baseline model of an anaerobic digester system have been performed.
- The optimization for finding the optimal location and width of the flaps in the digester for various TS value with a proposed digester design have been performed.
- The CFD simulations for the optimal dimensions have been carried out for various TS value. The observed flow pattern in the digester is noted.
- The different width and location of the flaps have been analyzed, determining an optimum width and location. The particular geometry of the flap for particular TS value shows digester's mixing and thus the overall performance.
- There is a need for further research and improvement of this model to validate the numerical results presented in this paper. Work is ongoing towards this goal.
- In this sense, CFD techniques postulate as a very promising tool for designers to optimize the hydraulic behavior of digesters.

References

1. Amon B, Kryvoruchko V, Amon T, Zechmeister-Boltenstern S (2006) Methane, nitrous oxide and ammonia emissions during storage and after application of dairy cattle slurry and influence of slurry treatment. *Agric Ecosyst Environ* 112:153–162
2. Kaparaju P, Buendia I, Ellegaard L, Angelidakia I (2008) Effects of mixing on methane production during thermophilic anaerobic digestion of manure: lab-scale and pilot-scale studies. *Bioresour Technol* 99(11):4919–4928
3. Weiland P (2010) Biogas production: current state and perspectives. *Appl Microbiol Biotechnol* 85:849–860
4. McMahon KD, Stroot PG, Mackie IR, Raskin L (2001) Anaerobic co-digestion of municipal solid waste and biosolids under various mixing conditions II Microbial population dynamics. *Water Res* 35(7):1817–1827
5. Karim K, Hoffmann R, Klasson T, Dahhan AI (2005) Anaerobic digestion of animal waste: waste strength versus impact of mixing. *Bioresour Technol* 96:1771–1781
6. Luděk K, Stefan P, Gunther B, Michael H (2013) Determination of quality in biogas plant digesters using tracer tests and computational fluid dynamics. *Acta Universitatis Agriculturae et Silviculturae Mendelianae Brunensis* LXI, No. 5, pp 1269–1278
7. Wu B (2013) Advances in the use of CFD to characterize, design and optimize bioenergy systems. *Comput Electron Agric* 93:195–208
8. Vavilin VA, Angelidaki I (2005) Anaerobic degradation of solid material: importance of initiation centers for methanogenesis, mixing intensity, and 2D distributed model. *Biotechnol Bioeng* 89:113–122
9. Braber K (1995) Anaerobic digestion of municipal solid waste: a modern waste disposal option on the verge of breakthrough. *Biomass Bioeng* 9:365–376 (*J Environ Eng* 127(3): 240–248 (2001))
10. Achkari-Begdouri A, Goodrich P (1992) Rheological properties of Moroccan dairy cattle manure. *Bioresour Technol* 40:149–156
11. Landry H, Lague C, Roberge M (2004) Physical and rheological properties of manure products. *Appl Eng Agric* 20:277–288
12. Wu B, Chen S (2008) CFD simulation of Non-Newtonian fluid flow in anaerobic digesters. *Biotechnol Bioeng* 99:700–711

Part II
Sensor, Image and Data Driven Societal
Technologies

Social Influence as a Parameter to Prioritize Social Problems

Shreyank N Gowda

Keywords Facebook · Twitter · Social problems · Social media · R language · IBM Bluemix

1 Introduction

Every city in this world has problems [1]. No city is ever perfect. But most of these problems always tend to be solvable. In India, there are many environmental problems. The sewages, the pollution, the environment state, etc. An excellent example of this can be seen with potholes on big important roads that are not solved quickly enough. Destroying houses for empty lands that end up in the construction of malls [2]. The garbage disposals are done on the main roads that cause a pungent smell in the environment [3] and also dirties the city.

Most developed countries do already have means to overcome most such problems regarding directly dealing with problems. However, these problems persist in developing and underdeveloped countries. According to the Road Accident Report (2014) published by the road transport and highways ministry, while 4726 lives were lost in crashes due to humps, 6672 people died in accidents caused due to potholes and speed breakers. Sources [4] said the actual figure could be much higher since the data was not properly captured by local police while registering accidents and in many cases, these are recorded as any other road crash.

In another separate case study in the city of Dhaka [5], Dhaka city in Bangladesh has been undergoing a process of urbanization and population growth at a very rapid rate. A rapid growth of population, unplanned urbanization and industrialization in the periphery has generated pressure to the changes in land use pattern, which has also caused huge urban expansion. This expansion process, causing problems to cultivated land, wetlands, vegetation and water bodies without considering their impacts on the environment. This study argues that these changes and

S. N Gowda (✉)
Indian Institute of Science, Bengaluru, India
e-mail: kini5gowda@gmail.com

their scale of environmental impacts or sufferings are not equally distributed among the dwellers in Dhaka city. It seeks to explore variations of environmental qualities by people's perceptions.

2 Background

There have been improved methods to ensure that urbanization impact on environment is minimum. There have been new methods to process waste to reduce the impact on environment, but even these methods do not have adverse impact on the environment [6]. The roads have improved, but even then there are many potholes which make it extremely unsafe for driving. These potholes sometimes get covered up in the rain and make it all the more difficult to drive through them. As such there has been no method proposed to sort the way of solving these problems. Hence this will be an innovative way of doing so. The proposed method works for using two different social media: Twitter or Facebook. Reilly et al. [7], describes the preliminary work on a study that ranks users in a directional social network by their influence during a particular period. The method considers a user with high influence as one who has a high ratio of received to sent messages is greater than 1. This helps to rank all users on the social media. Junco [8], studied how Facebook affected the lives of college students. This helped to show the impact a social media platform can have on the lives of the general public, while also showing the number of people using it and how it influenced them. Facebook plays a pivotal role these days in the lives of individuals. It helps create friendships online and acts as a platform to connect [9]. This helps to create a large database of people. Facebook has over a billion users and hence public opinion on any issue will be massive. The voice on public forum will help for the proposed algorithm. The number of users using Facebook is massive [10]. This helps social media act as a platform for public to voice their opinion on any social issue. People can use these social media as a method to gain attention to any causes. This will always help regarding making any decision. Nowadays it is easy to gain the attention of even celebrities for causes that they feel are worth doing, for example, charity. It ensures that when the public is voicing an opinion and any celebrity joins in it only increases the amount of support being generated for that cause. Ultimately it acts as a medium to gain public support over any issue.

3 Proposed Algorithm

There have been improved methods to ensure that environmental impact is minimum. There have been new methods to process environmental waste to reduce the impact it causes, but even this is not completely free of harm for the environment [6]. The roads have improved, but even then there are many potholes which make it

extremely unsafe for driving. These potholes sometimes get covered up in the rain and make it all the more difficult to drive through them. As such there has been no method proposed to sort the way of solving these problems. Hence this will be an innovative way of doing so. The proposed method works for using two different social media: Twitter or Facebook. Reilly et al. [7], describes the preliminary work on a study that ranks users in a directional social network by their influence during a particular period. The method considers a user with high influence as one who has a high ratio of received to sent messages is greater than 1. This helps to rank all users on the social media. Junco [8] studied of how Facebook affected the lives of college students. This helps to show the impact a social media platform can have on the lives of the general public, while also showing the number of people using it and how it influenced them. Facebook plays a pivotal role these days in the lives of individuals. It helps create friendships online and acts as a platform to connect [9]. This helps to create a large database of people. Facebook has over a billion users and hence public opinion over any issue will be massive. A lot of people get to have their say, and this will help for the proposed algorithm. The number of users using Facebook is massive [10]. This helps social media act as a platform for public to voice their opinion on any social issue. People can use these social media as a method to gain attention to any causes. This will always help regarding making any decision. These days it is easy to gain the attention of even celebrities for causes that they feel are worth doing, for example, charity. This ensures that when the public is voicing an opinion and any celebrity joins in it only increases the amount of support being generated for that cause. Ultimately it acts as a medium to gain public support over any issue. The application was developed by using the IBM Bluemix platform. A Mongo database was taken which would store the pictures as a series. Also in the case of Twitter, we would use a particular hashtag such as #CleanBengaluru and the mongo database would store all tweets using that particular hashtag in it.

The proposed algorithm will vary for the two social media under consideration. So let us separate them out and explain the algorithm for each.

- (A) Twitter: The first step to being done is the posting of series of pictures. All these have to be done using a particular hashtag. For example, say the person in charge is looking to help speed up problem-solving in Bengaluru, he could then use #cleanbl18April2016 and post each picture using that same hashtag.

The date is given so new problems could be posted every week and could also include unsolved problems from the previous week. He releases each and every image as a protected image which will ensure that the public cannot see it and it is protected to only people he is following.

This should be done since the problems will persist to only those people living in those cities. So someone from Mumbai should not have a say on the road problems or the garbage problems in Bengaluru more than the Bengaluru citizens themselves. Another method to solve this was to use the location feature to filter out only eligible people to have their say or cast a vote.

Next, after he has released a series of tweets using a particular hashtag he gives a time of one week for the public to cast their opinion by either “retweeting” or “liking” the tweet, they are options to endorse your support for a tweet.

After this, these tweets are analyzed by using a program written in R Language to count the image which has maximum retweets and favorites. Should a case occur where more than 1 picture has the same total of retweets and favorites than the picture with more retweets is selected.

This shows that particular problem is what the public wants to be solved first since they are expressing a lot of opinions to solve that first. The counting could also be done manually as well.

Also, all the problems for that week could be sorted out, and as many problems as possible are solved. The remaining unsolved ones are added to the list of problems that were going to be given for the next week.

To do this, we use smappRpackage [11]. Using this package, we can easily find and even sort the tweets by retweets or favorites/likes. Figure 1 shows an explanation of the algorithm.

Manual solving this problem will take a lot of time and also unnecessary wastage of time since this could be done much faster by making use of a system.

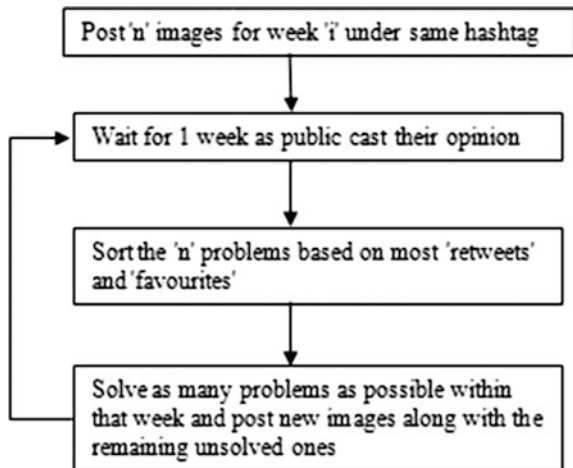
- (B) Facebook: The person in charge could create a closed group for that particular city. A closed group would ensure only people of that particular city are in the group.

More importantly, a closed group will ensure that only the people in the group can see what is happening in the group. This ensures a lot of privacy.

Next after creating a closed group the person in charge can create an album say April 2nd week or date it and name the album as April 18th–24th.

In this album the person in charge can post any number of images that are deemed to be social problems. Once this is done, he can wait for a week. Also, the

Fig. 1 Workflow of algorithm for Twitter



people themselves can add any problems they deem necessary and which are not present in the group already.

In this time the public get to ‘vote,’ ‘share’ and ‘comment’ on each picture. For example, if the person in charge is in charge of Bengaluru he can create a closed group called Bengaluru and allow only Bengaluru citizens to enter the group.

Once they see the set of problems and cast their votes by liking, sharing and commenting on these problems, the person in charge could again either through a data analytic language determine which is the problem the public wants to be solved first by counting the likes, shares, and comments and choosing the one with maximum likes and shares.

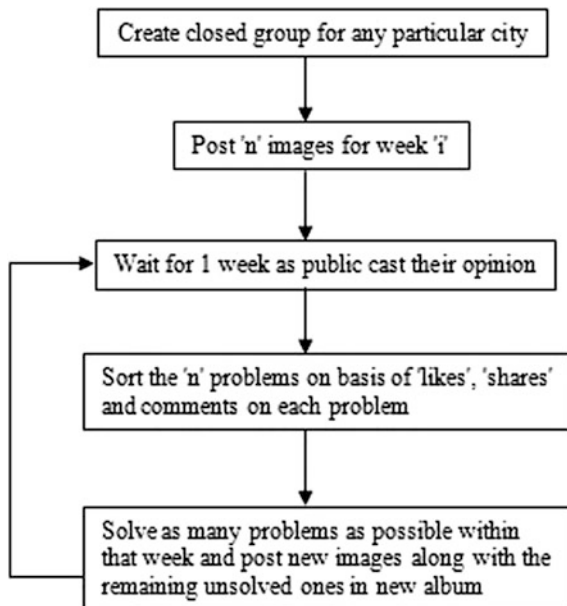
This could also be done manually, but again will be leading to a lot of unnecessary wastage of time.

Also, the ‘n’ pictures could be sorted out to determine the order of solving the problems. For the next week the unsolved problems will be added to a new set of problems, and again the process is repeated.

This will ensure the public gets to have their say in matters that affect them, while also helping the person in charge to make more informed decisions. This also helps to make unbiased decisions, decisions that are made largely by the public.

The working of this can be seen in Fig. 2. Also, Facebook has much more monthly active users in comparison to Twitter. But none the less each social platform does help to get as much public attention as needed. Analytics of Facebook data can be performed by using R which makes use of the Facebook [12] platform.

Fig. 2 Workflow of the algorithm when the case of social media is Facebook



4 Experimental Analysis

As an example let us consider the following 3 images posted on Twitter using #cleanbengaluruNovember182015.

Figure 3 was taken from www.fakingnews.firstpost.com, represents a pothole in one of the main roads of Bengaluru.

Figure 4 was taken from www.nationalinterest.in and also is another pothole in one of the most important roads in Bengaluru.

Figure 5 was taken from www.dajiworld.com and represents a common problem in Bengaluru, dumping of garbage on the roads itself.



Fig. 3 Pothole in Bengaluru



Fig. 4 Another pothole in Bengaluru



Fig. 5 Garbage dumped on the road

Table 1 Results of Twitter analytics

S. No.	Picture	No. of retweets	No. of favorites
1.	Pothole 1	14	7
2.	Pothole 2	16	9
3.	Garbage dump	11	16

All three images are social problems in Bengaluru that currently exist. These were uploaded to Twitter as part of the test experiment using the hashtag #cleanBengaluruNovember182015.

Table 1 shows the results of Twitter analytics on the given 3 images. The testing was done on 21 such problems to varied results.

Using the results obtained above we can see that the person in charge would resort to solving the problem associated with the garbage dump first. Also, it can be clearly seen that using this as the method ensures public involvement is kept at a maximum.

5 Conclusion

Getting public opinion on public matters is one of the most important things a person in charge can do. The public is the people affected by the surroundings, and it will only do justice to give them a say on what is affecting them. Hence the proposed approach ensures that each person gets to have a say and only the real majority get the final say. In that regard, the proposed approach uses social media as the best way to get public involved in their problems and also use this as a medium to voice their concerns over any other problems. Also, the given approach could

still cause bias as the person in charge could create fake profiles just to increase the value of the problem he wants to be solved first. So it is important to be able to verify users as well. Recent developments have occurred as well such as the Twitter feature of a poll. However, this does not verify user location and does not give the option to insert images to depict a problem.

References

1. Jardine N (2011) The 10 biggest problems in the world according to the EU. <http://www.businessinsider.com/the-10-biggest-problems-in-the-world-according-to-the-eu-2011-10?IR=T>, Oct 2011
2. Varma P (2013) Ejjipura: how many malls do Bangaloreans need? <https://bangalorecaptured.com/2013/01/28/ejjipura-how-many-malls-do-bangaloreans-need/>, Jan 2013
3. Anila Kurian (2012) The garden city to the garbage city: Bangalore gets a new name. <http://www.youthkiawaaz.com/2012/06/the-garden-city-to-the-garbage-city-bangalore-gets-a-new-name/>, June 2012
4. Dash DK (2015) Over 11000 people killed by potholes, speed breakers last year. <http://timesofindia.indiatimes.com/india/Over-11000-people-killed-by-potholes-speed-breakers-last-year/articleshow/48950267.cms>, Sept 2015
5. Islam MS, Rana MMP, Ahmed R (2013) Environmental perception during rapid population growth and urbanization: a case study of Dhaka city. Springer Science + Business Media, Dordrecht, pp 443–453
6. Zakkour P, Haines M (2007) Permitting issues for CO₂ capture, transport, and geological storage: a review of Europe, USA, Canada and Australia. *Int J Greenhouse Gas Control* 1 (1):94–100
7. Reilly CF, Salinas D, De Leon D (2014) Ranking users based on influence in a directional social network. In: International conference on computational science and computational intelligence vol 2, pp 237–240, 10–13 Mar 2014
8. Junco R (2011) The relationship between frequency of Facebook use, participation in Facebook activities, and student engagement. *Comput Educ* 58:162–171
9. Ellison NB, Steinfield C, Lampe C (2007) The benefits of Facebook “Friends:” social capital and college students’ use of online social network sites. *J Comput Med Commun* 12 (4):1143–1168
10. Chilana P, Holsberry C, Oliveira F, Ko A (2012) Designing for a billion users: a case study of Facebook. In: SIGCHI conference human factors in computing system, pp 419–432, May 2012
11. Open source code for Twitter Analytics. <https://github.com/SMAPPNYU/smappR>
12. Open source code for Facebook Analytics. <https://github.com/PabloBarbera/Rfacebook>

An Accident Detection System (ADS) for the Mumbai-Pune Expressway Using Vehicular Communication

Saurabh Patil and Lata Ragha

Keywords Vanet · Accident detection · Raspberry Pi · Mumbai-Pune expressway

1 Introduction

The population of the world has shown a steady increase, with India being the most densely-populated country. Correspondingly, road traffic has also been getting more congested, as a higher population and increased business activity result in a greater demand for cars and vehicles for transportation. Nowhere is this truer than in India's first six-lane, concrete, high-speed Mumbai-Pune tolled expressway connecting the financial capital, Mumbai, with the industrial and educational centre, Pune. The expressway that helped reduce travel time between the two cities by over 90 min has become one of India's busiest roads [1]. The traffic on the Mumbai-Pune section of National Highway 4 was expected to increase from 60,755 passenger car units per day in 1990 to a projection of 100,000 passenger car units per day by 2004. The expressway is 94 km long and is witnessing a large number of traffic crashes, fatalities and serious injuries. Over 14,500 accidents have so far taken place on this stretch in which around 1400 people have died in the last 14 years since it became operational [2].

A close look at the statistics reveals that traffic accidents turned into casualties and serious medical conditions owing to the time lapse between the occurrence of the accident and the arrival of medical assistance. The so called 'Golden Hour' [3] after a car crash is the time within which medical or surgical intervention by a specialized team has the greatest chance of saving lives. Hence, early reporting of accident alerts to an emergency system may reduce fatalities and the severity of injuries.

S. Patil · L. Ragha (✉)

Terna Engineering College, Nerul, Navi Mumbai, Maharashtra, India
e-mail: lata.ragha@gmail.com

S. Patil

e-mail: saurabh.terna@gmail.com

The process of arriving at a feasible solution could include an Accident Detection System (ADS) on the expressway that can zone in on accidents and offer information updates on the status of accidents. On the Mumbai-Pune Expressway, the calling booths installed can be used to pass on information about accidents or ask for assistance. These, however, have major drawbacks in terms of: (i) The time taken for the emergency system to be activated and reach the location, (ii) The inputs provided, which are not appropriate enough to initiate precise emergency rescue steps, and (iii) The fact that the vehicles following behind are unaware of an accident having taken place, and consequently block the expressway, holding up all traffic instead of taking a diversion and so resolving the bottleneck. Recent trends involving the use of wireless communication between vehicle-to-vehicle (V2V) and vehicle-to-infrastructure (V2I), called Vehicular Ad hoc Networks (VANETs), can reduce human intervention and ensure faster message propagation.

Vehicular ad hoc networks, an advanced application of Mobile Ad hoc Networks (MANETs), can help effect improvements in the areas of congestion detection, emergency notification, accident detection, post-accident rescue, traffic clearance for emergency vehicles and a cooperative collision warning by providing an intelligent transport system [3]. V2V and V2I systems are supported by the IEEE 802.11p *wireless access in vehicular environments* (WAVE), a standardization effort that provides a protocol suite solution to support vehicular communications in the licensed frequency band at 5.9 GHz (5.85–5.925 GHz).

In this paper, we propose a framework titled **An Accident Detection System (ADS) for the Mumbai-Pune Expressway**. The ADS will detect and report accidents to the central emergency handling system on the 94.5 km stretch of the expressway. The proposed system will be responsible for post-accident status message dissemination containing such details as the location, type of vehicle, direction, and sensor values on the vehicle. Message authentication and integrity are taken into consideration, ensuring that no false messages are propagated and no one misuses our system [4].

2 The Proposed ADS System

In the proposed ADS architecture for the Mumbai-Pune Expressway, cost and usability are high priorities. It is a challenge to develop a structure that can be deployed in minimal time and without burdening vehicles using the toll road. Indian road structures, and the vehicles plying on them are not fully equipped with VANET-supported hardware. A VANET solution for accident detection needs vehicle-to-vehicle (V2V) and vehicle-to-infrastructure (V2I) communication, requiring vehicles to have an On-Board Unit (OBU) and a Roadside Unit (RSU) for infrastructure support. An OBU installed on a vehicle will have a processing unit and a communication interface. It collects vehicle statuses on the road periodically and shares them with peer vehicles using V2V communication, and communicates the current situation by sharing it with the RSU. RSUs are communicating units

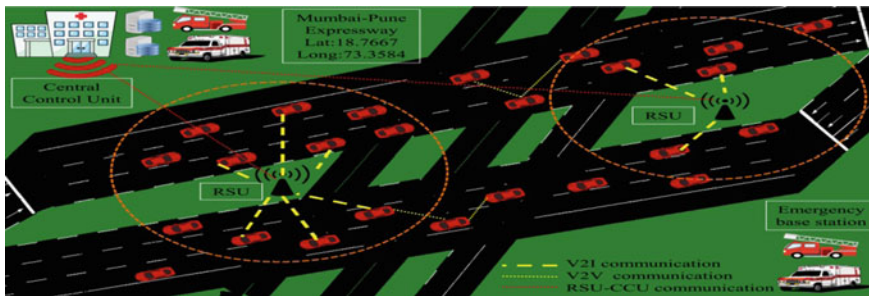


Fig. 1 Proposed ADS architecture at the Mumbai-Pune expressway

installed beside roads, and collect information by establishing a short communication network with vehicles within the radio communication range. The ADS architecture for the Mumbai-Pune Expressway is depicted in Fig. 1, at an interaction point near Khandala Exit.

In the deployed ADS, vehicle sensor values are processed together in the OBU to identify possible collisions. Vehicles involved in an accident shall immediately start sending out messages to the surrounding vehicles and the roadside unit, alerting them about the crash. A crash alert message, carrying details of the location so as to assist casualty at the accident spot, will be processed by the control center unit as well as the nearest ambulance and hospital. Sharing the same information also alerts approaching vehicles on the same route as the crash vehicle to slow down and stop at a safe distance, thus circumventing traffic congestion and saving people from injury and loss of life. The ADS is expected to be particularly helpful during bad weather, in tandem with low visibility.

The OBU in the proposed system is designed using the Raspberry Pi [5], which lets users enjoy sophisticated VANET solutions in their current vehicles, doing away with investments on expensive OBUs. Raspbian supports most current networking hardware, eliminating the common problems encountered with other embedded operating systems.

Raspberry Pi is configured for node discovery using a dynamic host configuration protocol (DHCP). It also enables ip-forwarding for multi-hop communication, where a peer OBU interface is used to forward packets to the destination node. Further, routing tables are updated as vehicles travel along the road. All network parameters are released at the exit point to avoid misuse, and a GPS device is triggered every 300 ms for location updates. The proposed OBU design is easily scalable to software and hardware updates, in line with newer technology.

The roadside unit also plays a vital role in detecting and sending accurate information to the control centre unit. RSU installation and configuration is a major financial burden in the deployment of the ADS. Consequently, in our proposed system, we have decided on fewer RSUs stationed only at major locations, especially accident-prone zones and those susceptible to natural calamities, all along the Mumbai-Pune Expressway. RSUs compute messages delivered by vehicles, analyse



Fig. 2 RSU installation locations on the Mumbai-Pune expressway

the said messages, and forward their statuses to the central control unit. In line with coverage requirements, a total of 12 RSUs need to be installed in critical areas. Figure 2 depicts sample installation locations of RSUs with their coordinates (latitude and longitude) and unique RSU-Ids, assigned to update vehicle messages with id flags.

The third tier of the architecture is deployed with the Central Control Unit (CCU), equipped with high-end configuration and high-speed connectivity for quick connections and replies to safety messages. The CCU is responsible for the following tasks: (i) Carrying out data mining on the accident scenario database and understanding the situation, (ii) Routing alert messages to the emergency system with exact information about the scenario, (iii) Broadcasting messages for the RSU to update the vehicles following on the status of the road, (iv) Maintaining revocation and active lists to track rules and regulations on the expressway, and (v) Ensuring security by providing a proper handshake between the OBUs in the vehicles and the RSUs in the network.

3 Framework Design for the ADS

3.1 Initial Handshaking

When a vehicle reaches the entry point at the Mumbai-Pune Expressway, it communicates with the first RSU installed. The first phase of the Accident Detection System (ADS) commences from the initial handshaking process.

Certain notations—such as ENCZ (M), DECZ (M) and SIGZ (M), as well as the message M using the key Z—are being used to denote encrypting, decrypting and signing, respectively, from now on.

3.1.1 Vehicle V_i Meets the First RSU $R_{(Id)}$

Digital Signature: It ensures non-repudiation, i.e., the vehicle's driver cannot deny that he has not sent a message. A digital signature is affected by signing its RID,

MACAddr, Timestamp (TS), and Random Number (RADNUM), using its Vehicle Registration Identification number (RID). Given that the RID is unique, that particular property can be utilized for replays and pretend attacks. $X = \text{SIG}_{(\text{RID})} [\text{RID}, \text{MACAddr}, \text{TS}, \text{RADNUM}]$.

Vehicle (V_i) thereafter encrypts the RID and $\text{SIG}_{(\text{RID})} [\text{RID}, \text{MACAddr}, \text{TS}, \text{RADNUM}]$ using the control centre unit (CCU) public key, PKTA, and sends the $\text{ENC}_{\text{PKCC}} (\text{RID}, X)$ to the RSU, which forwards it to the TA.

3.1.2 Verification of the Vehicle by the CCU

The CCU, receiving the encrypted packet of Vehicle V_i from the RSU, decrypts the block and verifies the RID. It ascertains if all the data received is valid and that the RID is not in its active and revocation lists. The active list maintains a list of all vehicles registered at the entry point of the expressway and updates it as vehicles leave the expressway network.

The CCU stores the (RID, V_{PK_i} , MACAddr, V_{PK_i} , RADNUM) in its repository and forwards the V_{PK_i} through $A = \text{ENC}_{\text{SKR}} (V_{\text{PK}_i}, \text{SIG}_{\text{SKTA}} (V_{\text{PK}_i}))$ to the RSU, where SK_R are the conventional shared secret keys between the RSU and the CCU. The CCU passes the V_{PK_i} to the vehicle in B. $B = \text{ENC}_{\text{RADNUM}} (V_{\text{PK}_i}, \text{SIG}_{\text{SKTA}} (V_{\text{PK}_i}))$ is encrypted using the random number passed by the vehicle during its initial handshake.

3.1.3 Shared Key Generation

Vehicle V_i decrypts Y to obtain t_{id} and verifies it using a challenge response with the RSU. Similarly, it decrypts X to obtain s and V_{PK_i} and verifies the CCU's signature on them, following which it computes its shared secret with the CCU using $V_{\text{S}_i} = V_{\text{PK}_i} \oplus \text{RID} \oplus \text{MACAddr}$.

3.2 Vehicle Message Dissemination

After the initial registration process, the vehicle's OBU is programmed to periodically collect data from sensors. Every vehicle is equipped with multiple sensors and a Raspberry Pi (a vehicle OBU) system configured to gather data on the driver's environment. Sensors can provide information such as the location, abrupt breaking, speed and acceleration. In case of an accident or a slowing down of the vehicle, certain of these components and their statuses will vary according to the conditions on the road.

The OBU is responsible for collecting the data and generating packets at specific time intervals. The number of messages generated by each vehicle congests the RSU, degrading the system's performance. So then, instead of forwarding each

packet to the RSU, the ADS has it processed at the vehicle's OBU unit. Packets with fluctuating data are prioritized and forwarded to the RSU for further processing and action. This concept optimizes messages on the communication medium and the number of RSUs required is also reduced.

3.3 Vehicle Accident Data Processing

The vehicle's data collection and processing modules get activated after the OBU initialization handshake. The data collection module collects values from all the connected sensors at two different time intervals: (i) Every 300 ms it collects values for speed, acceleration, direction and the timestamp. (ii) Every 1 s it collects values for seatbelts, GPS location, airbags, ABS and crash sensors. Consequently, all the sensors do not need to be activated simultaneously to collect information effectively to help in process scheduling. After observing the importance of the data, it is subsequently categorized. After the sensors provide values, the processing module starts analyzing the speed recorded by the vehicle.

3.3.1 Speed Aggregation and Message Format

An assessment of the value of the speed helps identify the state of the vehicle on the expressway. The speed of a vehicle can indicate whether it is moving steadily or slowly owing to a traffic jam, or has ground to a complete halt as a result of an accident. The speed of a vehicle can indicate whether it is moving steadily or slowly owing to a traffic jam, or has ground to a complete halt as a result of an accident. According to the interpretation of the speed, the values of the other sensors are standardized for the purpose of generating a warning message. Our system focuses on optimizing messages exchanged on the communication line, so we aggregate data at the OBU. The aggregation function is executed on a 20 s interval, if data values collected in the last 20 s do not show signs of an accident. With aggregate speed as (1), calculate distance $D_{(x,y)}$ as (3) and time $T_{(x,y)}$ as (2) from location x to y . S_i indicates the speed at time i , n denotes the number of samples and the speed aggregation register (S.A.R).

$$S.A.R \cong \frac{\sum_{i=2}^n |S_i - S_{i-1}|}{n - 1}$$

$$T(x, y) \geq 0 \text{ for time from } x \text{ to } y, D(x, y) \geq 0 \text{ for distance from } x \text{ to } y$$

$$x = (lat, long)_{at = 1}, \quad y = (lat, long)_{at = n = 1}$$

The message format in our system has options for accidents as well as alerts. Messages are propagated, carrying the aggregate information for controlled speeds with no fluctuations in sensor values. In case the OBU evaluates variations in speed,

the option accident gets attached to the payload displaying speed, acceleration and sensor values. The complete payload has a unique t_{id} and location, digitally signed using the vehicle’s verification public key (V_{PKi}) to avoid non-repudiation.

3.4 Central Control Unit

The CCU, responsible for every decision broadcast on the network, is connected to every component of the ADS and ensures a flawless performance. The process tracks vehicles throughout their journey on the expressway. The CCU ensures the exchange of security parameters for confidentiality and message integrity. The OBU processes messages to the RSU, which acts as a message collector, passing messages to the CCU for action. The CCU takes charge after receiving notification messages from the RSU. It takes responsibility for warning messages, obtaining information from appropriate vehicles, and notifying the emergency services about the conditions under which the accident occurred. Given that the expressway has multiple emergency service base stations, the nearest is identified and informed, depending on the location of the accident. The CCU stores each activity in the database and uses it to study the received values prior to declaring that an accident has taken place. It also maintains a list of vehicles that exceed the speed limit, calling them to a halt on the expressway and passing on the information at the exit point for the authorities concerned to take action (Fig. 3).

In the ADS, emergency alerts are broadcast at continuous intervals to provide updates of emergency service arrival times, and redirect traffic to eliminate traffic snarls. Quite apart from accidents, the Mumbai-Pune Expressway has always had problems with avalanches/landslides at certain locations, declared critical areas. If

Fig. 3 Message alert format for the proposed ADS

t_{id} (tempory vehicle ID)		Aggregated Vehicle Values
Location		
$T_{(x,y)}$	$D_{(x,y)}$	
X	Y	
Speed	Accelerat ion	Accident
Direction	Time-stamp	
Speed	Accelerat ion	
Crash Censor Values		
ABS	Airbag	
Vehicle Signature (V_{PKi})		Sign-ature

the speed limit is reset in this area as a consequence and vehicles noting the changes slow down accordingly, sensors for fog lights and wipers are activated. If such inclement conditions are identified, the system advises the authorities on route diversion and generates messages to that effect.

4 Conclusion

In this paper, we presented an Accident Detection system for the Mumbai-Pune Expressway, which allows for the detection of accidents, improves assistance to injured passengers by reducing the response time of emergency services and disseminating information on the conditions at the scene of the accident using a combination of V2V and V2I communications. This architecture, in line with current efforts at integrating technology with workable solutions, has also eliminated human errors—such as incomplete or incorrect information at inappropriate times—in the notification of accidents. The development of a low-cost prototype shows that it is feasible to implement a universal OBU. Future work in this area includes deploying the system and testing it on Indian roads in a real-time environment with OBUs installed in real vehicles to check the system’s behavior at high speeds (Fig. 4).

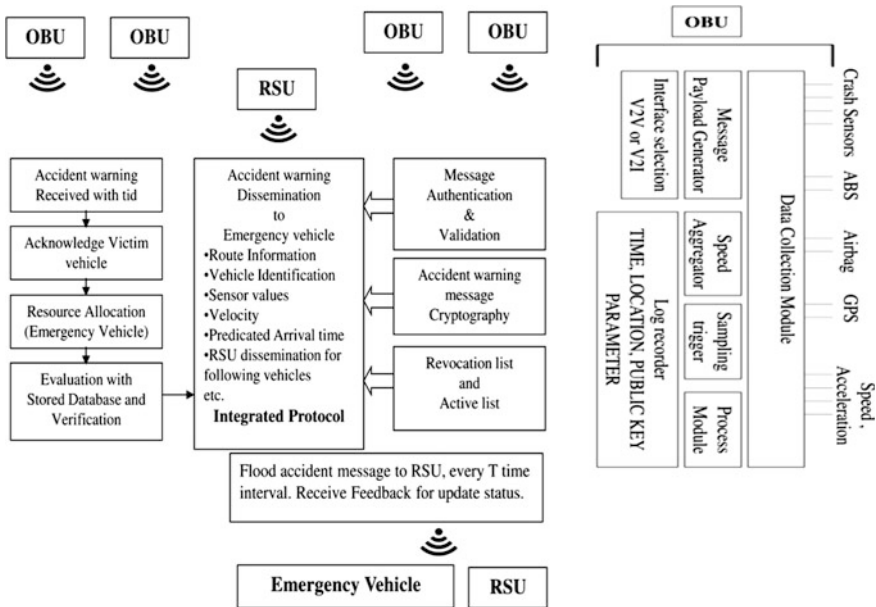


Fig. 4 Framework for the proposed ADS

References

1. Mumbai-Pune expressway may soon have eight lanes. The Times of India, 23 Feb 2013
2. <http://indianexpress.com/article/pune/pune-mumbai-expressway-accident-14500-accidents-1400-deaths-in-14-years-maharashtra-govt-turns-deaf-ear-agencies-play-blame-game-2836472/>
3. Fogue M, Garrido P, Martinez FJ, Cano JC, Calafate CT, Manzoni P (2013) A novel approach for traffic accidents sanitary resource allocation based on multi-objective genetic algorithms. *Expert Syst Appl* 40(1):323–336
4. Al-Sultan S et al (2014) A comprehensive survey on vehicular ad hoc network. *J Netw Comput Appl* 37:380–392
5. Mitchell G (2012) The Raspberry Pi single-board computer will revolutionise computer science teaching [For Against]. *Eng Technol* 7:26

Data Mining Algorithms for Improving the Efficiency of Governance in Dynamic Social Systems: Case Study of Indian Caste and Tribe Reservations

Rhythima Shinde, Bramka Arga Jafino, Paraskevi Kokosia
and Jan van den Berg

Keywords One-class classification · Reservation system · Attributes · Support vector machine · Principal component analysis · Naïve Bayes · k -nearest neighbors

1 Introduction

During the times India was ruled by the British, historical-social classes of the people were used to smoothen administrative procedures (only those with higher social class were given jobs). This hierarchy of classes was defined based on the occupation the people had. When India gained its independence in 1947, India committed to develop policies that would improve the well-being of its people who were oppressed by the hierarchical caste system. The disadvantaged castes who historically had suffered from such discrimination due to the hierarchical caste system got facilitated using the system of “reservation” from the 1950s [1].

R. Shinde (✉) · B.A. Jafino · P. Kokosia
Faculty of Technology, Policy and Management, Delft University of Technology,
Delft, The Netherlands
e-mail: rhythimashinde@gmail.com

R. Shinde
Faculty of Electrical Engineering, Mathematics and Computer Science,
Delft University of Technology, Delft, The Netherlands

J. van den Berg
Section of ICT, Faculty of Technology, Policy and Management,
Delft University of Technology, Delft, The Netherlands

J. van den Berg
Section of Cyber Security, Faculty of Electrical Engineering,
Mathematics and Computer Science, Delft University of Technology,
Delft, The Netherlands

J. van den Berg
Institute of Security and Global Affairs, Faculty of Governance and Global Affairs,
Leiden University, Leiden, The Netherlands

For example, in education, reservation means using a quota, where a portion of school vacancies must be reserved for members of these castes. This reservation system has been allocated based on the socio-economic attributes of these castes (i.e. income, education level, etc.) and is used to decide which castes need support and thus would be labeled as “scheduled” or “reserved.” Such systems can be labeled as the “dynamic socio-political systems” which evolve along with the interactions within the society and political changes, and thus have the property of dynamism due to increasing amount of information generated and transferred in communities, leading to faster changes in the societies [2]. There have been many debates over the existence of this reservation system today as it is no more allocated by the socio-economic attributes but only based on the historical record of the parents’ castes (social status). To complicate the matter, the socio-economic conditions of these castes have changed vastly, and the debates around them have led to many violent protests [3]. This demands an insight into the efficiency and the accuracy of the reservation by considering the dynamism of indicators.

This paper aims at answering the following research question: “Is the reservation system for scheduled caste and scheduled tribe efficient for different states equally and is it well defined by the socio-economic indicators?” To unravel this, we dive into the following sub-research questions:

1. For the scheduled castes and tribes, is there any difference between the northern states and the southern states with regard to the efficiency of reservation system?
2. Do the socioeconomic conditions in all states justify the reservation system?
3. What can be an effective way to define reservation system in India for the future based on the continuously changing indicators?

Predictive modeling is used as a tool to check if the socio-economic indicators decide the reservation and thus justify the system based on the 2011 census data [4]. The explanatory model is not used in this study since the research doesn’t aim at improving the socio-economic indicators but at improving the reservation system; while explanatory models focus on the variables (attributes) primarily [5]. Different prediction algorithms will be compared for improving the prediction accuracy of similar sociopolitical systems.

This paper is organized by the following four sections. Section 2 lays down the conceptualization and methodology followed for answering the research questions. Section 3 includes the data analysis part. In this section, the dataset is preprocessed and then compared carefully by selecting the algorithm. In the validation part, one-class Support Vector Machine (SVM), one class Naïve Bayes (ONB), k -nearest neighbor (k -NN) and Principal Component Analysis (PCA) are selected and tested out respectively. Then, the results obtained from the methods are presented and analyzed in Sect. 4. Finally, brief conclusions with limitations and recommendations of the results, as well as discussion for future work follow in Sect. 5.

Table 1 Attributes used for the analysis

Attribute	Description
IPTP	Illiterate percentage in the caste
PELP	Students in primary education per-literate population in the caste
GALP	Graduate and above educated per-literate population in the caste
SMLP	Secondary or matric educated per literate population in the caste
SMSC	Total surviving male per total surviving children
SCMW	Total surviving children per total married women
CLTC	Percentage of child-labor in the caste
TWTP	Total employment rate in the caste

2 Conceptualization and Methodology

To respond the questions formulated before, we take following steps in data analytics to understand the models' accuracy in dynamic sociopolitical systems:

1. For the first question, the dataset from the northern states is trained on the dependent variables of the "caste allotted" and the independent socio-economic attributes which are shown in Table 1. The trained model is then tested for the southern states. These attributes are believed to have high predictive power because the reservation system is based on the assumption that lower castes have lower value of socio-economic attributes, and that there is no discrepancy between the northern and the southern states.
2. For the second question, the training set and the test set come from randomly splitting the whole data (both northern and southern states) several times with the same ratio.
3. For the third question, if the model has high accuracy, it cannot be directly concluded that the reservation system is efficient enough because there might be inaccuracies in the model itself. Thus, different models are chosen and if all the models have high accuracy, it can be considered that the reservation system is efficient enough. If some models peculiarly fail, those models are investigated in comparison to those who have good accuracy. If all models fail, then it can be said that there is some inherent flaws in the reservation system itself. Then, the most accurate predictive model is suggested for efficient reservations.

3 Data Analysis

(a) Pre-processing of Data

Available indexes were given in Census of India for the year 2011 and are used as the data source. Datasets used in this study are employment, education, social and healthcare indicators. The datasets are extracted from the available census data by

creating excel macros and cleaning castes with unavailable attributes data. A more detailed explanation of the process is discussed in detail in Appendix. The prime indicators are shown in Table 1.

(b) Choice of Models/Algorithms

Predictive analysis models use various statistical, data mining and machine learning algorithms. There are three basic forms of predictive algorithms: classification, clustering and regression [6, 7]. Classification is a supervised learning method which predicts categorical class labels, classifies the data based on the training set and allots values to new class [8]. Clustering creates different groups (clusters) which consist of a set of objects that are similar, and regression is a supervised learning method which is mainly used for continuous response values.

In this study, classification algorithms are used to compare the scheduled (positive class) and non-scheduled (negative class). Due to a limitation in census data (only available data for scheduled castes and tribes are available, and there is no caste-wise data for the non-scheduled castes), One class classification (OCC) has been used. OCC tries to find out the objects of a specific class amongst all objects by learning from a training set which contains the objects of that class. Therefore, a classifier is determined only from positive and unlabeled samples in a semi-supervised way [9, 10].

OCC can be applied in three different ways: density estimations, boundary methods, and reconstruction methods. The goal of density estimation is to estimate the density of the attribute that has to be observed e.g. in Gaussian model and Parzen density estimators. Boundary methods find the distance from the vector to a learned boundary and are based on numeric data and can be applied to Support Vector Data Description (SVDD) and k -centers. Reconstruction method calculates the reconstruction error and the algorithms based on the category of the data. Literature studies in OCC lead to the selection of the final methods choices, which could be well representative for the different types of OCC method: SVM and k -NN (boundary method), ONB (density method), and PCA (reconstruction method) [11–16]. Moreover, the type of features which classifier takes as inputs and the characteristics of the classification method such as number of training examples, number and independence of features, linearity, space dimensionality, training time, sensitivity to the errors in training data and accuracy are in order to select these specific algorithms [17–20].

(c) Application of models

Method 1: Support Vector Machines (SVM)

SVM builds a hyperplane that best separates the high-dimensional input vectors for classification purpose [1, 2]. One-class SVM (OSVM) uses parameter ‘ ν ’ as both an upper limit of the outliers’ fraction and the lower limit of the support vector fraction, which ranges between 0 and 1. To implement the OSVM, built-in module One-Class SVM from scikit learns library in python (sklearn.svm) was used and modified. Firstly, the dataset from states which belong to ‘North’ category was used as the

training set. The model was then applied to the dataset from states which belong to 'South' category by initially setting the ν parameter to 0.1. Thus, it was assumed that the maximum percentage error of the training set was 10% (non-positives). The percentage error of the test dataset (the southern states) was then compared to the percentage error of the training dataset. For validation, sensitivity analysis was conducted by running the model 20 times with the parameter varied between 0.01 and 0.2. The second analysis came from conducting split test 10 times, where 80% of the whole data points in the dataset (both northern and southern states) were used as the training set while the remaining 20% acted as the test set. The aim of this split test was twofold: (i) studying the discrepancies of the attributes of the scheduled caste/tribe in random order instead of seeing the northern-southern states differences, and (ii) evaluating the sensitivity of the algorithm.

Method 2: One Class Naïve Bayes (ONB)

ONB is a classification method which makes a prediction based on the probabilities of each attribute in the dataset fitting into each class [3]. The ONB determines the Gaussian probability density function for each attribute of the training set, calculates the target rejection threshold T , and compares each data instance's probability score. If the test data instance has higher probability score, it is considered as positive data.

A sensitivity analysis was executed by using different T threshold values toward the northern and the southern states. The assumption made in the analysis was that there was a certain percentage of the currently scheduled castes and tribes which was overqualified to be categorized as scheduled. Thus, a range between 1st to 20th percentiles with an interval of one was used for the threshold value. Further, ten random data splits were done on the whole data into train and test dataset. The ONB presents a few limitations regarding the probability estimation along with the assumption that there is at least one negative class to estimate the probability given the negative class. In cases where the attributes of the dataset are continuous, the algorithm might underperform, which may also occur in the case of using a large number of attributes [5].

Method 3: k -nearest neighbor (k -NN)

k -NN is a simple non-parametric classifier which selects the k samples whose attribute values are closer than the sample that has to be classified. One class k -NN uses the principle of the local density estimation which is inversely proportional to the distance from the nearest neighbor. If the local density of a point from the testing set is larger than the local density of its nearest neighbor, then that point is accepted as the class entity (in OCC). Otherwise, it is rejected from the class [6].

In this case, a python code was developed where the southern states were treated as the testing set while the northern ones as the training set, to check whether the reservation systems were equally efficient in the northern and southern states. Second, for different values of k , this analysis was repeated. Finally, different split tests were tested on this to check the variation of the results based on the data.

Method 4: Principal Component Analysis (PCA)

PCA can be used to reduce the dimensionality of the data, where each attribute is represented as a vector which indicates how that attribute contributes to the principal components. For the OCC, PCA can be used by setting a threshold value by eigenvectors which are set as the mean values. In this study, the eight attributes were reduced to 2-dimensional space and then those which were above the set threshold were considered as anomalies or outliers, which did not belong to that class. Next, cross validation was done to check the model with the best accuracy, which involved choosing different threshold values. PCA was implemented in Matlab, first for the northern and southern regions (where the southern region was the testing set) and then for the overall overview of the method in the dataset (random thresholds from 0.5 times the standard deviation to 4 times the standard deviation are taken) to get the maximum accuracy from the model [7].

4 Results and Interpretation

4.1 One-Class SVM Results

By assuming a ν value of 0.1, the percentage error of the OSVM for both scheduled castes and tribes can be seen in Table 2. The percentage errors of the test set for both categories are more than 16% higher compared to that of the training set, showing a significant difference in the reservations between northern and southern states. To further verify this result, a sensitivity analysis was conducted by varying the ν parameter from 0.01 to 0.2. The result shown in Fig. 1 indicates that for larger values of ν , the gap between the test and the training set's percentage errors gets wider. The gap is even wider for scheduled caste, confirming the difference between the two states.

The final analysis was conducted by applying ten random data splits for the whole dataset and the result can be seen in Fig. 2. The graph shows that if all data points are taken together, the reservation system looks efficient in itself. For instance, the percentage error of the test dataset for scheduled caste with ν parameter of 0.2 ranges between 15 and 25%, which is close to 20%. However, the low variance of the results might also simply indicate that OSVM is an adequate technique to analyze this case.

Table 2 Percentage error result of OSVM, $\nu = 0.1$

	Scheduled caste (%)	Scheduled tribes (%)
% error of the training set (north States)	9.83	9.69
% error of the test set (south states)	25.91	27.52

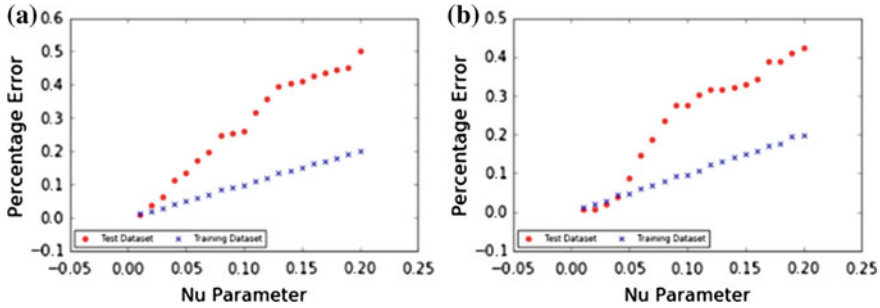


Fig. 1 Comparison of percentage error between test and training dataset for **a** scheduled caste and **b** scheduled tribe

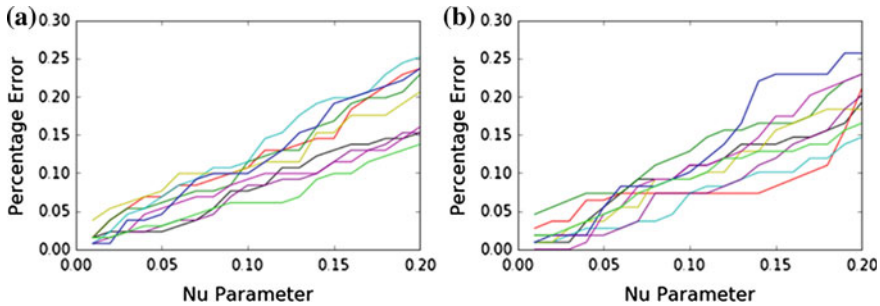


Fig. 2 Comparison of test dataset's percentage error with 10 random data splits for **a** scheduled caste and **b** scheduled tribe

4.2 ONB Results

Using theoretical threshold T value, which is the minimum probability score from the training dataset, as the cutoff point of the ONB leads to 99.5 and 100% of positive class data instances for SC and ST, respectively. Two explanations can be derived from this result: (1) values of all attributes in the dataset are normalized values between zero and one: therefore, generating Gaussian probability distribution will result in a limited range of probability distribution, which tends to create an overlap between the training and the test dataset, or (2) some outliers might exist in the training dataset; thus, taking theoretical threshold T value for the analysis will result in an extremely small value of probability score since it also considers the probability score of the outliers.

Based on the two deficiencies explained above, using the theoretical threshold T value of minimum training dataset probability scores is not sufficient for this case study. Therefore, sensitivity analysis was conducted, and the result is displayed in Fig. 3. The percentage of positive class data instances from the train dataset decreases along with the increase of the threshold T value as expected. The decrease

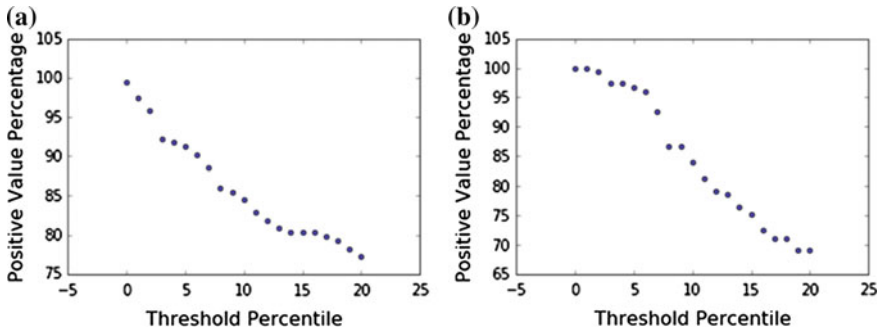


Fig. 3 Positive-class percentage of the test dataset (the southern states) for **a** scheduled caste and **b** scheduled tribe

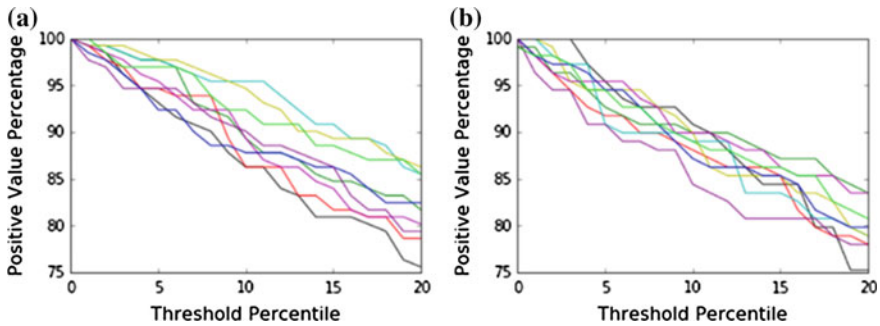


Fig. 4 Comparison of test dataset’s positive-class percentage with 10 random data splits for **a** scheduled caste and **b** scheduled tribe

shows the positive class percentage does not drop more than 25% when 20th percentile of the training dataset’s probability score is used. For tribes, by assuming that 20% of training dataset is outliers, the positive-class percentage of the test dataset decreases by around 30%. Ten random data split tests were also conducted for the ONB and can be shown shown in Fig. 4. The ranges of both scheduled caste and tribe are quite diverse; for the 20th percentile, the reduction of the positive class percentage is between 15 and 25%. To conclude, either there is a high algorithm accuracy or there is no significant difference of socioeconomic attributes for the whole scheduled population.

4.3 k-NN Results

The *k*-nearest neighbors results show an increasing accuracy for the increasing value of *k* as shown in Fig. 5; this is expected as the number of *k* increases the local

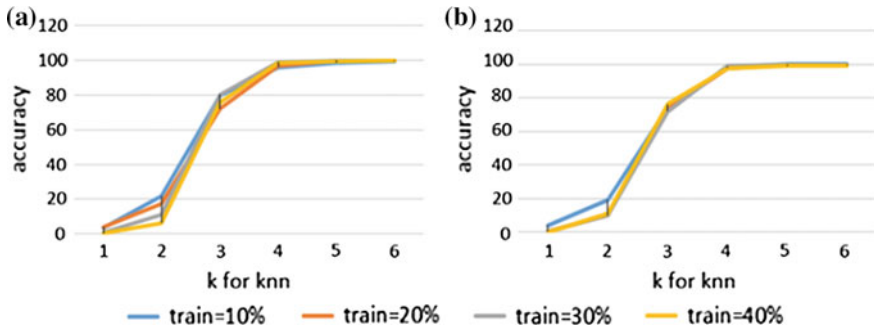


Fig. 5 Accuracy versus the value of k in k -nearest neighbors (for complete data set) for **a** scheduled caste and **b** scheduled tribe

density of the training data becomes smaller, and thus more testing data fits. Figure 5 also helps in showing that the number of positive class castes accepted as the reserved caste is high for $k > 3$. This shows that the reservation system is equally efficient in both of the northern and southern states.

To verify if this holds true for the complete dataset, four different split ratios with train data of 10, 20, 30 and 40%, were taken. The resulting accuracies are very close for different splits, showing that there is either a very high algorithm accuracy or that there is no significant difference of socioeconomic attributes for the whole scheduled population.

4.4 PCA Results

The dimensionality reduction achieved from PCA can be seen in Fig. 6 for the northern, southern and all states, respectively. The results are depicted for outliers with the value of two times the standard deviation added to the mean. The dashed line depicts the threshold and the points within this threshold are considered as positive class.

Based on the results from dimensionality reduction, for every set of data i.e. the northern states, southern states and all states, the error in the PCA is measured as the function of the outlier value, as seen in Fig. 7. The error of the model decreases with increasing value of standard deviations. The scheduled castes' and tribes' results both show a very small gap between the error percentages, depicting that the systems are almost equally efficient for both the northern and southern states. For all states, the error of the scheduled castes seems to be lower compared to the northern and southern states. If two times standard deviation is considered for the outlier, then for the scheduled caste, the error percentages for northern, southern and all states are around 7.5%. As for the scheduled tribes, it is in the range of 5–7.5% (7.5% for all states, 5%

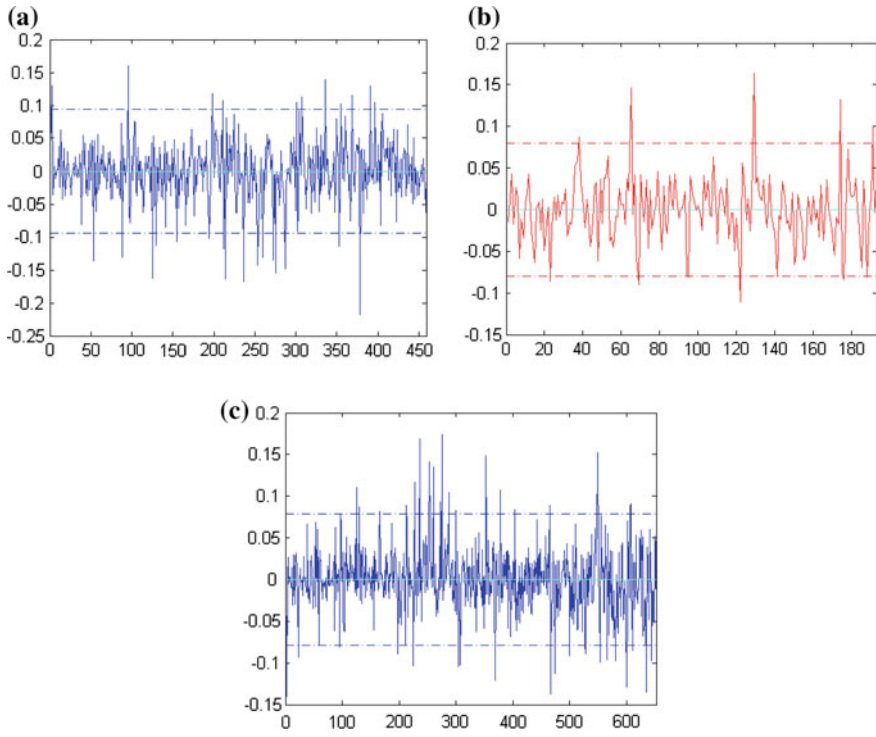


Fig. 6 PCA results with respect to threshold equal to mean over 2 times the standard deviation **a** the northern states, **b** southern states and **c** all states

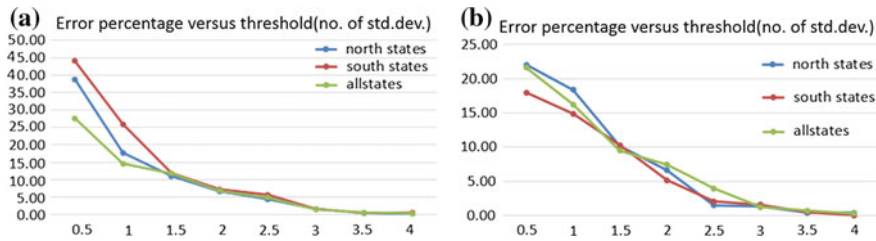


Fig. 7 Error percentage versus number of standard deviation above the mean value for PCA **a** scheduled caste and **b** scheduled tribe

for southern states and around 6% for northern states). This shows that the results of both scheduled castes and tribes are almost similar for northern, southern and all states. PCA does not distinguish them significantly, and the reservation system is equally efficient for all of them.

4.5 Comparative Results

The results obtained from the data splits for the first sub-question into northern and southern states where northern states were taken as the train set, while southern as the test set can be found in Table 3 column 3. SVM and k -NN (for $k \leq 3$) results show that the reservation system in the north and the south is different. ONB, k -NN ($k > 3$) and PCA indicate that the difference is low, with PCA showing the smallest difference. Tribes present a higher difference for all the methods except SVM. This shows that there does exist a difference in the reservation system for both the northern and southern states, and especially for tribes.

To answer the second research sub-question and also verify the above-stated results, split tests have been performed for SVM, ONB, and k -NN. For PCA, different values of standard deviation were tested for the complete dataset. Table 3 column 4 reports the results. All results (k -NN with $k > 3$) show that the accuracy of the model is more than 75%, with the highest accuracy for PCA, followed by k -NN, SVM, and ONB in decreasing order. The third sub-research question suggests the model with highest accuracy. This also reports some differences in the northern and southern states due to their differences in reservation allocation. That would be the k -nearest neighbors, with $k > 3$.

Table 3 Results of all algorithms

1	2	3	4
		North-south (training/test set)	Split tests (except for PCA)
SVM (boundary)	SC	Different: 16% difference	Slightly justified (error for 20% parameter: 15-25%)
	ST	Different: 16% difference	
ONB (density)	SC	Similar: 5% max. difference	Slightly justified (error for 20 percentile: 17-27%)
	ST	Slightly different: 10% max. difference	
k -NN (boundary)	SC	Slightly different: difference 0-15%	Justified (0-25% for $k = 3$ and 0-5% for $k > 3$)
	ST	Different: difference 0-25%	
PCA (reconstruction)	SC	Similar: 0% difference (2 time std. dev.)	Justified (error for 2 times Std. dev.: 7.5%)
	ST	Similar: 0-2.5% diff. (2 time std. dev.)	

5 Conclusion and Reflection

Indian reservation system is a hot debate, which questions the system's efficiency. From a data analysis point of view, this is a question of predictive modeling as the class of whether a caste/tribe is labeled as "scheduled" is decided based on attributes values. As the non-scheduled caste data is not available, OCC method was used for predictive modeling by applying four different methods: SVM, ONB, k -NN and PCA.

The exploration of the main research question through the three sub-questions has revealed several insights. Firstly, the boundary methods show that the difference between the north-south is much larger than what is shown by density method, while the reconstruction method has the lowest difference. The reason behind this can be twofold: the difference in quota (% of reservation) for some of the southern states is very high (as high as 69%), while this is not the case in the north (in 2014, only some of the north states got quota above 50%) [8]. Further, the boundary methods have lower accuracy because they define the boundaries very clearly as compared to the density and reconstruction methods where boundaries are based on a distribution and not the exact distance as in k -NN.

The socioeconomic conditions justify the reservation systems with an accuracy of around 80% with boundary methods (in k -NN, for $k \leq 3$), around 78% with density method and around 92.5% with the reconstruction method. Overall, the reservation system is not perfect but is not completely inefficient.

The k -NN method with $k > 3$ seems to be the most suitable method because it does not only show the difference in north and south states to some extent, but also has a higher accuracy (lower than PCA, but PCA shows no difference between the south and the north, which is not correct). This model would be most suitable for future predictions of the reserved castes in India to make the reservation system efficient.

Finally, rather than using OCC (because of its limitation to comment over the negative set and disability to give results as false positives and true negatives), future researches should be able to use binary or multi-class classification. Furthermore, there should be more attributes-based data available for non-scheduled castes and tribes.

Appendix

1. Attributes used for the analysis

The indicators (attributes) are chosen such that it can be seen that how backward a caste is, and based on the assumption that a backward caste should only technically demand reservation in an efficient reservation system. The educational indicators comprise of illiterate percentage, students in primary education per literate, graduate and above educated per literate, and secondary/metric educated per literate in the caste to understand the educational levels distribution in the caste. The distribution

is important to be understood because the level of education describes the level of progress or backwardness of caste (with the assumption that more “backward” caste is one with lower education, economic and health level). The health indicators comprise of studying total surviving children per total married women to understand the average health of a woman and a child. This also helps in understanding the willingness to carry more than two children, which is associated to traditional beliefs against contraception, but this is not the target of study here. Total surviving male per total surviving children is a social indicator which helps in understanding if a wide discrepancy in the female and male population (relating to female genocides/feticide) relates to the backwardness of a caste and thus demands more reservation. The employment indicators include the percentage of child-labor in the caste (forcing children to work due to the poverty or lack of education in the families) and the total employment rate (Table 4).

Table 4 Description of the attributes used for the analysis in detail [4]

Code	Description/title	Indicator extracted
SC—05/ ST—05	Marginal workers and non-workers seeking/available for work classified by educational level, age and sex	<ul style="list-style-type: none"> • Illiterate population/total population: illiterate percentage in the caste • Literate people with primary education/total literate population: students in primary education per literate in the caste • Literate people with graduate and above education/total literate population: graduate and above educated per literate in the caste • Literate people with secondary or matric education/total literate population: secondary/matric educated per literate in the caste
SC—12/ ST—12	Number of women and ever married women by present age, number of surviving children and total surviving children by sex	<ul style="list-style-type: none"> • Total surviving male per total surviving children: surviving male children/total surviving children • Total surviving children per total married women • Total surviving children/total married woman
SC—10/ ST—10	Population age 5–19 attending school/college by economic activity status and sex	<ul style="list-style-type: none"> • Total child labour/total children population: percentage of child-labor in the caste
A10/A11	Individual scheduled caste primary abstract data	<ul style="list-style-type: none"> • Total working population/total population: total employment rate in the caste

Table 5 States and their codes

Andhra Pradesh	28	Meghalaya	17	Karnataka	29	Tamil Nadu	33
Assam	18	Mizoram	15	Kerala	32	Tripura	16
Chhattisgarh	22	Orrisa	21	Madhya Pradesh	23	Uttarakhand	5
Delhi	7	Punjab	3	Manipur	14	Rajasthan	8
Goa	30	Uttar Pradesh	9	Haryana	6	Bihar	10
Gujarat	24	Maharashtra	27	Himachal Pradesh	2	West Bengal	19
Jammu Kashmir	1	Sikkim	11	Jharkhand	20		

2. Northen and Southern States

Different states are divided based on their codes (which are given geographically) and the code till 27 is used as north, and from 27 onwards are used as southern state as shown in Table 5.

References

1. Ambedkar.org (2015) Reservations in India. Available: <http://www.ambedkar.org/News/reservationinindia.pdf>. Accessed 2016
2. Korotaev AV (2006) Introduction to social macrodynamics: compact macromodels of the world system growth. Editorial URSS 2006
3. Nitisha (2015) Reservation in India: controversy, justification, and controversy. Yourarticle company. Available: <http://www.yourarticlelibrary.com/reservation-system/reservation-in-india-controversy-justification-and-criticism/47114/>. Accessed July 2016
4. Office of the Registrar General & Census Commissioner, India, Census India, Ministry of Home Affairs, Government of India, 2011. Available: <http://www.censusindia.gov.in/2011-Common/CensusData2011.html>. Accessed 2016
5. Cerrito PB (2006) The difference between predictive modeling and regression. In: MWSUG conference, Louisville, KY
6. Bari A, Chaouchi M, Jung T (2016) How to choose an algorithm for a predictive analysis model. Predictive analytics for dummies. Available: How to choose an algorithm for a predictive analysis model. Accessed 2016
7. Howard J, Bowles M (2012) The two most important algorithms in predictive modeling today. Conferences Oreilly. Available: <http://conferences.oreilly.com/strata/strata2012/public/schedule/detail/22658>. Accessed 2016
8. Kollios G (2012) Classification. Available: www.cs.bu.edu/fac/gkollios/ada01/LectNotes/Classification1.ppt. Accessed 2016
9. Mazhelis O (2007) One-class classifiers: a review and analysis of suitability in the context of mobile-masquerader detection. Arima J 6:29–48
10. Wang K, Stolfo S (2003) One class training for masquerade detection. ICDM: workshop on data mining for computer security

11. Denis F, Gilleron R, Tommasi M (2002) Text classification from positive and unlabeled examples. In: 9th international conference on information processing and management of uncertainty in knowledge-based systems
12. Liu B, Lee W, Yu P, Li X (2002) Partially supervised classification of text documents. In: Proceedings of ICML
13. Dempster A, Laird N, Rubin D (1977) Maximum likelihood from incomplete data via the em algorithm. J R Stat Soc
14. de Ridder D, Tax DM, Duin RP (1998) An experimental comparison of one-class classification methods. In: Proceedings of the 4th annual conference of the advanced school for computing and imaging
15. Munroe D, Madden M (2005) Multi-class and single-class classification approaches to vehicle model recognition from images. In: Irish conference on artificial intelligence and cognitive science, Portstewart
16. Letouzey F, Denis F, Gilleron R (2000) Learning from positive and unlabeled examples. In: Algorithmic learning theory: 11th international conference, Sydney
17. Data School (2015) Comparing supervised learning algorithms. Data School. Available: <http://www.dataschool.io/comparing-supervised-learning-algorithms/>
18. Chen E (2016) Choosing a machine learning classifier. Available: <http://blog.echen.me/2011/04/27/choosing-a-machine-learning-classifier/>. Accessed 2016
19. Amatriain X. What are the advantages of different classification algorithms? Quora. Available: What are the advantages of different classification algorithms?
20. Schapire R (2015) Machine learning algorithms for classification. Princeton University, Princeton

An Approach for PCA and GLCM Based MRI Image Classification

Sheetal S. Shirke, Jyoti A. Kendule and Samata G. Vyawahare

Keywords PNN-RBF classifier · PCA and GLCM · MRI brain tumor images

1 Introduction

The human brain is a complicated organ. It commands our body, receives information, examines information, and reserves information (our memories) [1–3]. Brain tumors are abnormal and uncontrolled proliferations of cells [4]. Some originate in the brain itself, in which case they are termed primary. Others spread to this location from somewhere else in the body through metastasis, and are termed secondary [5]. Primary brain tumors do not spread to other body sites and can be malignant or benign [6]. Secondary brain tumors are always malignant. Both types are potentially disabling and life-threatening. Because the space inside the skull is limited, their growth increases intracranial pressure and may cause edema, reduced blood flow, and displacement, with consequent degeneration, of healthy tissue that controls vital functions. Brain tumors [7] are, in fact, the second leading cause of cancer-related deaths in children and young adults.

Classification of the tumor is to identify what type of tumor is prevailing [8]. The conventional methods, which are present in diagnosis, are Biopsy, Human inspection, Expert opinion, etc. In early stage brain tumor diagnose mainly includes Computed Tomography (CT) scan, Magnetic Resonance Imaging (MRI) scan, Nerve test, Biopsy, [9], etc. At present, the doctor usually refers MRI image and

S.S. Shirke (✉) · J.A. Kendule · S.G. Vyawahare
E&TC Department, SVERI's College of Engineering, Pandharpur, India
e-mail: shitalshirke32@gmail.com

J.A. Kendule
e-mail: jyotikendule@rediffmail.com

S.G. Vyawahare
e-mail: sgvyawahare@coe.sveri.ac.in

make the report about the MRI analysis of the patient. Texture analysis [10] is an important task in many computer applications of Computer Image Analysis for classification, detection or segmentation [11] of images.

2 Proposed Method

The proposed design is to overcome the disadvantage of pre-existing methods which can detect and classify MRI brain images only into normal and abnormal. A brain tumor is one of the most regular and poisonous diseases in the world. Tracking the brain tumor in its initial stage is the key to its cure. This proposed method explains how to classify MRI Brain Images into normal, benign tumour images and malignant tumour images, using a Probabilistic Neural Network with radial basis function.

The objectives which will be fulfilled by the proposed system are:

1. To extract feature using PCA, GLCM and classification using PNN-RBF network.
2. To classify MRI image to detect brain tumor and analyze its structure.
3. To regulate stages of brain tumor, that is benign, malignant or normal.

This paper scopes for medical images and also for face recognition system. A brain tumor is abnormal growth of cells within the brain or the central spinal canal. So detection of brain tumor is very important.

3 Proposed Methodology

A Large amount of information is needed to represent an image, and this information occupies a large amount of memory. The features are extracted from the image. The extracted features contain the relevant information about the image. The extracted features are used as input to the classifier for classification. Features are said to be properties that describe the whole image. It can also refer to an important piece of information which is relevant to solving the computational task related to the specific application. The purpose of feature extraction is to reduce the original data set by measuring certain features. The extracted features act as input to a classifier by considering the description of relevant properties of the image into feature space (Fig. 1).

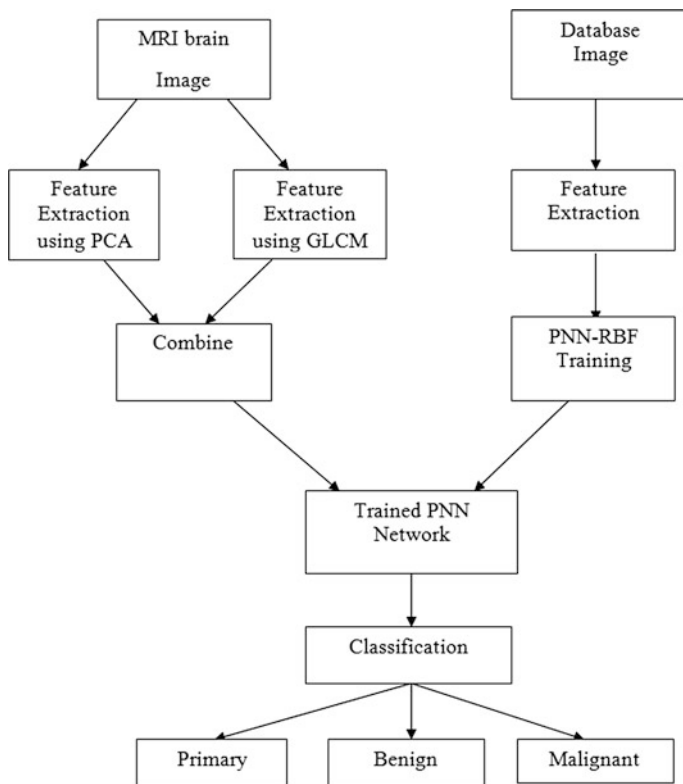


Fig. 1 Flow chart of proposed methodology

3.1 Feature Extraction Using PCA

PCA is a transformation that converts the set of correlated variables into a set of uncorrelated variables. The first principal component has maximum variance.

PCA is a well-established technique for feature extraction and dimensionality reduction. It is based on the assumption that most information about classes is contained in the directions of which the variations are the largest. The most common derivation of PCA regards a standardized linear projection which maximizes the variance in the projected space. Therefore, each original data vector can be represented by its principal component vector with dimensionality m . Principal Component Analysis (PCA) is a standard technique for dimensionality reduction and has been applied to a broad class of computer vision problems, including feature selection, object recognition and face recognition. While PCA suffers from some shortcomings such as its implicit assumption of Gaussian distributions and its

restriction to orthogonal linear combinations, it remains popular due to its simplicity. The idea of applying PCA to image patches is not novel. Our contribution lies in rigorously demonstrating that PCA is well-suited to representing key point patches.

3.2 Feature Extraction Using GLCM

In statistical texture analysis, texture features are computed from the statistical distribution of observed combinations of intensities at specified positions about each other in the image. According to the number of intensity points (pixels) in each combination, statistics are classified into first-order, second-order and higher-order statistics. The Gray Level Co-occurrence Matrix (GLCM) method is a way of extracting second order statistical texture features. The approach has been used in some applications. A GLCM is a matrix where the number of rows and columns is equal to the number of gray levels, G , in the image.

It was initially proposed by R.M. Haralick, the co-occurrence matrix illustration of texture features explores the gray-level spatial dependence of texture. A co-occurrence matrix is characterized by an image by the method of partitioning of co-occurring ideas at a given offset. Whether considering the grayscale values of the image or various measures of color, the Gray level co-occurrence matrix is mainly used for the measurement of the texture of the image. Because Gray level co-occurrence matrices are consistently large and occasional, Features generated using this method is defined as Haralick features. GLCM calculates the co-occurrence matrix of an image by computing how often a pixel with a certain intensity i occurs in relation with another pixel j at a certain distance d and orientation.

The following features are used:

- Homogeneity, Angular Second Moment (ASM):

$$ASM = \sum_{i=0}^{G-1} \sum_{j=0}^{G-1} \{P(i, j)\}^2$$

ASM is a measure of homogeneity of an image. A homogeneous scene will contain only a few gray levels, giving a GLCM with only a few but relatively high values of $P(i, j)$. Thus, the sum of squares will be high.

- Contrast:

$$CONTRAST = \sum_{n=0}^{G-1} n^2 \left\{ \sum_{i=1}^G \sum_{j=1}^G P(i, j) \right\}, |i - j| = n$$

This measure of contrast or local intensity variation will favor contributions from $P(i, j)$ away from the diagonal, i.e. $i \neq j$.

- Local Homogeneity, Inverse Difference Moment (IDM):

$$IDM = \sum_{i=0}^{G-1} \sum_{j=0}^{G-1} \frac{1}{1 + (i - j)^2} P(i, j)$$

IDM is also influenced by the homogeneity of the image. Because of the weighting factor $(1 + (i - j)^2)^{-1}$, IDM will get small contributions from inhomogeneous areas ($i \neq j$). The result is a low IDM value for inhomogeneous images and a relatively higher value for homogeneous images.

- Entropy:

$$ENTROPY = - \sum_{i=0}^{G-1} \sum_{j=0}^{G-1} P(i,j) \times \log(P(i, j))$$

Inhomogeneous scenes have low first order entropy, while a homogeneous scene has high entropy.

- Correlation:

$$CORRELATION = \frac{\sum_{i=0}^{G-1} \sum_{j=0}^{G-1} \{i \times j\} \times P(i,j) - \{\mu_x \times \mu_y\}}{\sigma_x \times \sigma_y}$$

Correlation is a measure of gray level linear dependence between the pixels at the specified positions from each other.

- The Sum of Squares, Variance:

$$VARIANCE = \sum_{i=0}^{G-1} \sum_{j=0}^{G-1} (i - \mu)^2 P(i, j)$$

This feature puts relatively high weights on the elements that differ from the average value of $P(i, j)$.

- Sum Average:

$$AVER = \sum_{i=0}^{2G-2} iP_x + y(i)$$

- Sum Entropy

$$\text{SENT} = - \sum_{i=0}^{2G-2} P_x + y(i) \log(P_x + y(i))$$

- Difference Entropy:

$$\text{DENT} = - \sum_{i=0}^{G-1} P_x + y(i) \log(P_x + y(i))$$

- Inertia:

$$\text{INERTIA} = - \sum_{i=0}^{G-1} \sum_{j=0}^{G-1} \{i - j\}^2 \times P(i, j)$$

- Cluster Shade:

$$\text{SHADE} = \sum_{i=0}^{G-1} \sum_{j=0}^{G-1} \{i + j - \mu_x - \mu_y\}^3 \times P(i, j)$$

- Cluster Prominence:

$$\text{PROM} = \sum_{i=0}^{G-1} \sum_{j=0}^{G-1} \{i + j - \mu_x - \mu_y\}^4 \times P(i, j)$$

3.3 Classification

The neural network is the best tool in recognition and discrimination between different sets of signals. To get best results using the neural network, it is necessary to choose a suitable architecture and learning algorithm. The best way to do that is to choose what is expected to be suitable according to our previous experience and then to expand or shrink the neural network size until a reasonable output is obtained. The PNN has three layers: the Input Layer, hidden and the output layer. The input image for classification is first to given to the Input layer. Hidden Layer finds vector distances between the input vector and row weight vectors in weight matrix. Radial Basis Function ascends the obtained distances. Output Layer finds the shortest distance among matrices, and thus finds the training pattern closest to

the input pattern based on their distance. Here, supervised learning with non-knowledge based classifier will be used for image classification. The neural network model PNN is used here to act as a classifier with radial basis function for network activation function.

Finally, the image is classified into normal, benign or malignant.

3.4 Segmentation

Image segmentation is based on the division of the image into regions. Division is done by similar attributes. Similarities are separated out into groups. The basic purpose of segmentation is the extraction of affected regions from the image, from which information can easily be perceived. Thresholding is used for segmentation as it is most suitable for the present application to obtain a binarized image with gray level 1 representing the tumor and gray level 0 representing the background.

Threshold Segmentation: Thresholding often provides an easy and convenient way to perform the segmentation by the different intensities or colors in the foreground and background regions of an image. A thresholding operation is applied typically on a grayscale or color image. Black pixels correspond to background and white pixels correspond to the foreground. If the pixel's intensity is higher than the threshold, the pixel is set to white, in the output. If it is less than the threshold, it is set to black. Segmentation is accomplished by scanning the whole image pixel by pixel and labeling each pixel as object or background according to its binarized gray level.

4 Morphological Operators

After converting the image to the binary format, morphological operations are applied to the converted binary image. The purpose of the morphological operators is to separate the tumor part of the image. Now only the tumor portion of the image is visible, shown as white color. This portion has the highest intensity than other regions of the image.

5 Results

It classifies the images between normal, benign and malignant images (Figs. 2, 3, 4, 5, 6 and 7).

Initially, when input MRI image (patient's MRI brain image) is taken then after filtering PCA and GLCM features are extracted and then combined and Classified using PNN-RBF. Depending on the size of a brain tumor in a pixel the tumor is

Fig. 2 Input image

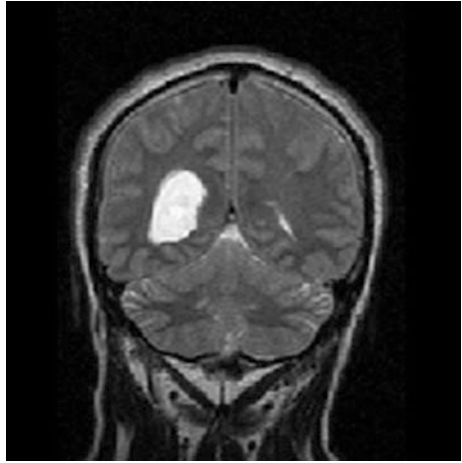


Fig. 3 Filtered image

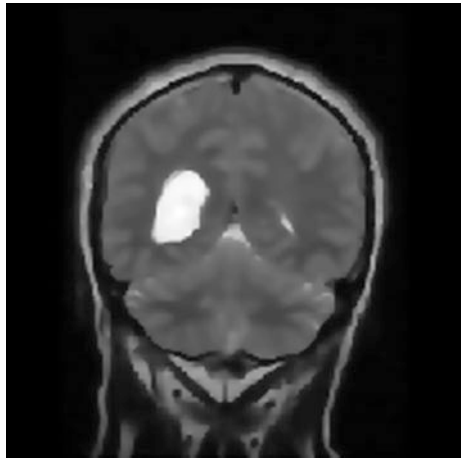


Fig. 4 PNN classifier



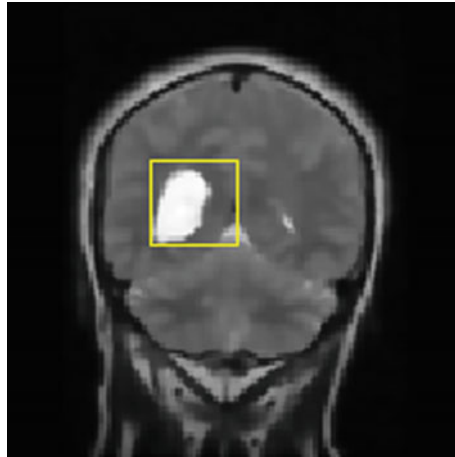


Fig. 5 Locating bounding box

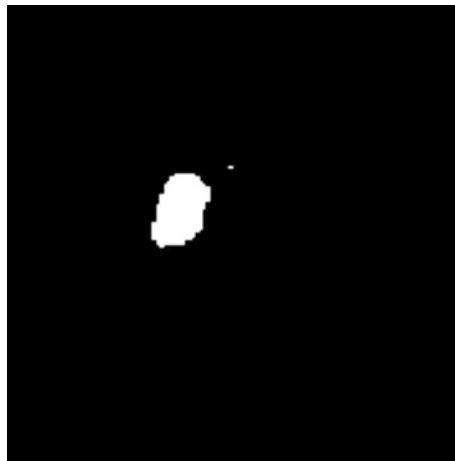


Fig. 6 Segmented tumor



Fig. 7 Final result

classified as three main stage. If the pixel size is less than 200, then it Primary brain tumor. If it is between 200 and 700, then it is Binign Tumor, and if the pixel size is greater than 700, then it is Malignant Tumor.

6 Conclusion

This proposed work will be developed to classify between normal, benign and malignant MRI brain images using automatic classification technique. Features will be extracted from images using feature extraction algorithms GLCM and PCA and will be classified further using PNN-RBF classifier. The recommended approach gives very auspicious results in classifying MR images.

References

1. Natarajan P, Krishnan N, Kenkre NS, Nancy S, Singh BP (2012) Tumor detection using threshold operation in MRI brain images. IEEE international conference on computational intelligence and computing research
2. Joshi DM, Rana NK, Misra VM (2010) Classification of brain cancer using artificial neural network. IEEE international conference on electronic computer technology, ICECT
3. Amin SE, Mageed MA (2012) Brain tumor diagnosis systems based on artificial neural networks and segmentation using MRI. IEEE international conference on informatics and systems, INFOS 2012
4. Sapra P, Singh R, Khurana S (2013) Brain tumor detection using neural network. Int J Sci Mod Eng IJISME 1(9). ISSN 2319-6386, Aug 2013
5. Goswami S, Bhaiya LKP (2013) Brain tumor detection using unsupervised learning based neural network., IEEE international conference on communication systems and network technologies
6. Rajeshwari S, Sharmila TS (2013) Efficient quality analysis of MRI image using preprocessing techniques. In: IEEE conference on information and communication technologies, ICT
7. George EB, Karnan M (2012) MRI brain image enhancement using filtering techniques. Int J Comput Sci Eng Technol IJCSET
8. Singh D, Kaur K (2012) Classification of abnormalities in brain MRI images using GLCM, PCA and SVM. Int J Eng Adv Technol (IJEAT) 1(6). ISSN 2249-8958
9. Gadpayleand P, Mahajani PS (2013) Detection and classification of brain tumor in MRI images, Int J Emerg Trends Electr Electron IJETEE 5(1). ISSN 2320-9569
10. Shasidhar M, Sudheer Raja V, Vijay Kumar B (2011) MRI brain image segmentation using modified fuzzy C-means clustering algorithm. IEEE international conference on communication systems and network technologies
11. Preethi G, Sornagopal V (2014) MRI image classification using GLCM texture features. In: Green Computing Communication and Electrical Engineering (ICGCCEE)

Urban Tree Canopy Detection Using Object-Based Image Analysis Approach for High-Resolution Satellite Imagery

Sujata R. Kadu, Balaji G. Hogade and Imdad Rizvi

Keywords High-resolution images · OBIA · Multiresolution segmentation · Urban area

1 Introduction

Urban Tree Canopy (UTC) is the layer of leaves, stems and branches of trees that cover the ground when viewed from above. A canopy of urban trees includes Public area like parks, streets, riparian corridors, neighborhood as well as a private area like residential, commercial, industrial areas, etc. [1]. Trees make life nice. It has been shown that spending time among green spaces and trees reduces the amount of stress that we carry around with us in our daily lives. Trees offer many environmental benefits. Trees reduce the urban heat island effect through evaporative cooling and decreasing the amount of sunlight that reaches parking lots and buildings. It is especially true in areas with large impervious surfaces, such as parking lots, stores, and industrial complexes. With half of the world population living in areas dominated by conurbations of asphalt, sealed surfaces, and polluted air, the attention has been centered on how to improve the living conditions of urban dwellers and on how to reduce the environmental effects of urban sprawl [2]. One way to achieve this is through the management of urban forest in the metropolitan area. Urban forest may be defined as the collection of all trees in

S.R. Kadu (✉) · I. Rizvi
Department of Electronics and Telecommunication Engineering,
Terna Engineering College, Navi Mumbai 400706, India
e-mail: sujatakadu@gmail.com

B.G. Hogade
Department of Electronics Engineering, Terna Engineering College,
Navi Mumbai 400706, India

stands and groups as well as single trees within and close to urban area. These includes for examples trees in woods, parks, private gardens, streets, as well as a tree planted around factories, offices, hospitals, and schools. Benefits of Urban forest are trees provide shade and lower surface temperatures on roads, walkways and other paved surfaces, reducing the heating of rainwater that runs across its surface. It minimizes the fast, hot and dirty impact of runoff pollution [3].

UTC provides many benefits such as:

- Improving the Quality of Water
- Reducing Air Pollution
- Saving Energy
- Lowering Temperatures of the City
- Increasing Property Values
- Mitigating Storm Water Runoff Costs
- Providing Wildlife Habitat
- Facilitating Educational and Social Opportunities
- Providing Aesthetic Benefits
- Tourism etc.

2 Study Area

In this study, WorldView-2 imagery of the urban area of Mumbai City is considered. Very high spatial resolution of WV 2, with the increased spectral reliability, provides additional data which is necessary for classification. The image has a radiometric resolution, and there are nine spectral bands in WV-2 imagery. Eight multispectral bands with a resolution of 2 m and one panchromatic band with a spacial resolution of 0.5 m. Pansharpening is also called as resolution merging. Pansharpening uses spatial information in the high-resolution grayscale band and color information in the multispectral band to create a single high-resolution color image. WV-2 is the first high-resolution satellite imagery with four new bands in addition to NIR and RGB [4].

3 Methodology

An expert system in an OBIA environment must employ a repeated approach that mimics human analytical process. It involves iterative segmentation, classification and refinement of image object until the desired land cover classification is achieved [5]. Such an approach effectively incorporates the elements of manual

image interpretation and essentially converts the procedure used by human analyst into series of rules. Authors have evaluated the method of image classification with two approaches Nearest neighbor classification and rule set method [6].

The powerful practicality of eCognition is that it will produce the objects with totally completely different scale parameters and at different levels. An image is comprised of features of varied sizes. The Higher scale parameter values produce greater objects, therefore if those objects area unit solid are going to be extracted at higher level itself whereas for heterogeneous areas to get detailed objects they are divided further with smaller scale parameter values.

(A) *Segmentation:*

Segmentation means subdividing entities like objects, into smaller partitions. In eCognition Developer segmentation is any operation that creates new image objects. It means segmentation can be a combine operation, a reshaping operation or subdividing operation.

There are two basic segmentation principles:

- Top-down strategy which is cutting something big into smaller pieces
- A bottom-up strategy which is merging small pieces to get something bigger. Bottom-up segmentation means, assembling objects to create larger objects [7]. It can but does not have to start with the pixels of the image. Examples are multi-resolution segmentation [8] and classification-based segmentation. The Multiresolution Segmentation algorithm merges existing image objects or pixels. The procedure identified single image objects of pixel in size and combined with their neighbors and based on relative homogeneity criteria (Fig. 1).

(B) *Classification:*

This homogeneity criterion is a combination of shape criteria and spectral. Assign Class allocate a class to an image object with certain features, using a threshold value. The Assign Class algorithm is the most simple classification algorithm. A threshold condition determines whether an image object matches a condition or not. Classification uses the class description to assign a class.

Here, the nearest neighbor classifier is used to classify the segmented objects. The method classifies image objects with the help of given samples and by a given feature space representing the concerned class and then after a representative set of sample objects has been declared for every class, the algorithm searches for the closest sample object in the feature space for every image object. If an image object's closest sample object belongs to class A, then the object will be assigned to Class A.

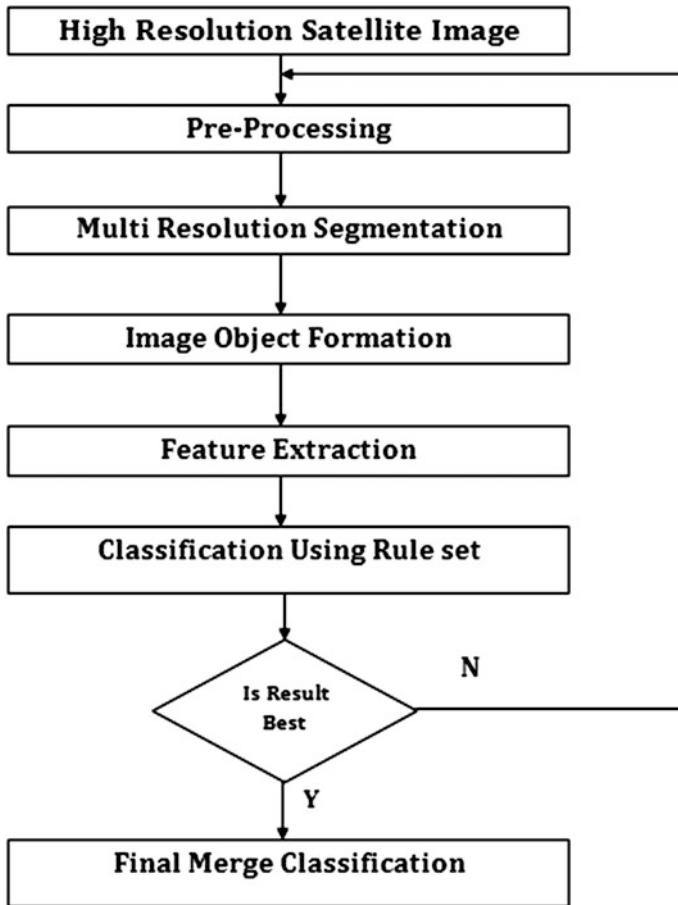


Fig. 1 Methodology used for object-based classification [9]

4 Results and Discussion

Urban forests provide a broad range of environmental, economic, and social benefits as an integral part of a green infrastructure network. These benefits improve the quality of life within the urban environment by reducing storm water runoff of city, improving air quality, mitigating the urban heat island effect, conserving energy, and increasing property values while providing access to nature and improving the experiential vitality and aesthetic richness of city [10]. An urban canopy assessment will be used to map the spatial distribution and extent of existing (Existing UTC) and possible tree cover (Possible UTC). To establish a citywide canopy goal that



Fig. 2 Original image. For three band image (using MATLAB)

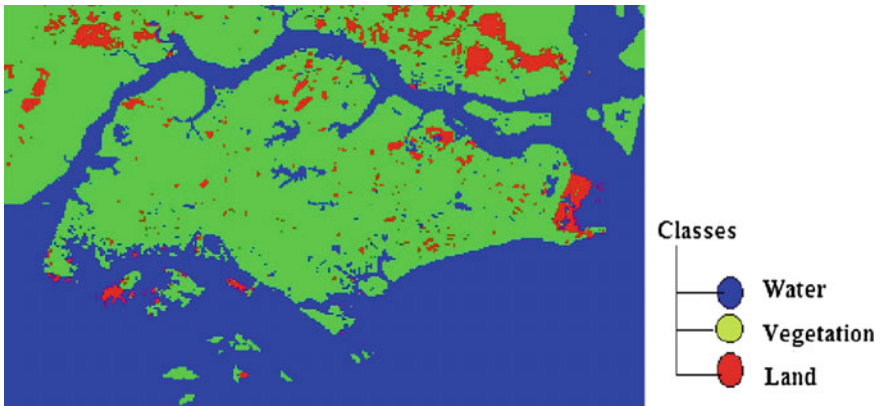


Fig. 3 Classified image (classified using MATLAB). For three band image (using eCognition)

outlines preferable canopy increases and guides management strategies that will enhance the extent and benefits provided by the urban canopy [11]. Satellite image of 3 bands has been classified by MATLAB [12] (Figs. 2, 3, 4 and 5).



Fig. 4 Classified image of water (using eCognition)



Fig. 5 Classified image (using eCognition)

5 Conclusion

This study proposed a method to detect grass and tree information in an urban environment from high-resolution remote sensing imageries. The accuracy result shows that the method is reliable to obtain the desired information. The desired information can refer to other thematic information, for example, water surface, impervious surface, and so on. MATLAB and eCognition have classified satellite image of 3 bands and 8 bands have been classified using eCognition. In future 8 bands, satellite image will be classified using MATLAB. The goal of research to find vegetation which further can be classified in trees and grass or different types of

canopy. The results can be made more accurate with LIDAR data which provides height and intensity data with the help of such data trees and grassland, towers and small buildings can be accurately classified.

References

1. McGee JA, Day SD, Wynne RH, White MB (2012) Using geospatial tools to assess the urban tree canopy: decision support for local governments. *J Forestry*
2. <http://www.nmmconline.com>. Accessed: 15 Nov 2015
3. <http://forestsforwatersheds.org/>. 15 Aug 2015
4. Rizvi IA, Mohan BK (2011) Object-based image analysis of high-resolution satellite images using modified cloud basis function neural network and probabilistic relaxation labeling process. *IEEE Trans Geosci Remote Sens* 49(12):4815–4820
5. Rizvi IA, Mohan BK (2012) Object-based analysis of world view-2 imagery of urban area. In: 2012 IEEE international geoscience and remote sensing symposium (IGARSS), pp 431–434
6. Walker JS, Briggs JM (2007) An object-oriented approach to urban forest mapping in Phoenix. *Photogram Eng Remote* 73(5):577–583
7. <http://community.ecognition.com/home>. Accessed: 5 July 2016
8. Rizvi IA, Buddhiraju KM (2010) Improving the accuracy of object-based supervised image classification using cloud basis functions neural network for high-resolution satellite images. *Int J Image Process* 4(4):342–353
9. Zhang X, Feng X (2005) Detecting urban vegetation from IKONOS data using an object-oriented approach. In: IEEE international proceedings on geoscience and remote sensing symposium. IGARSS'05
10. https://www.itc.nl/library/papers_2012/phd/ardila.pdf. Accessed: 16 Oct 2015
11. Basu S, Ganguly S, Nemani RR, Mukhopadhyay S, Zhang G, Milesi C, Michaelis A, Votava P, Dubayah R, Duncanson L, Cook B, Yu Y, Saatchi S, DiBiano R, Karki M, Boyda E, Kumar U, Li S (2015) A semiautomated probabilistic framework for tree-cover delineation from 1-m NAIP imagery using a high-performance computing architecture. *IEEE Trans Geosci Remote Sensing* 53(10)
12. Buddhiraju KM, Rizvi IA (2010) Comparison of CBF, ANN and SVM classifiers for object-based classification of high-resolution satellite images. In: IEEE international geoscience and remote sensing symposium (IGARSS), pp 40–43

Delamination Study of Sandwich Beam Coupled with Piezoelectric Actuator Using Cohesive Surface Behavior

K.R. Jagtap, H.H. Nawale and Sajal Roy

Keywords Sandwich beam · Cohesive behavior · Delamination · FEA · FRFs · Frequency

1 Introduction

The use of sandwich composite structures has been increasing consistently in the various fields of engineering like aerospace, civil, mechanical, marine etc. due to their advantageous characteristics. One of the most beneficial property that sandwich structures having is their light weight and high strength to weight ratio, so they are most preferable in the area's where high flexural rigidity is required. Sandwich structure consists of two thin skins (face sheets) and one thick light weight core, inserted between two skins. Skins are made up of composite sections while core is made up of isotropic material such as, PVC foam, balsa wood, honey comb etc. Though sandwich composite structures are strong enough and they are having high strength, they prone to delamination when subjected to high impact loading or shocks. Delamination is the most frequent damage that can occurs in the composite material at any movement without giving any signal or information, and can collapse whole system. Delamination is the process of separation of composite laminate from one another. In case of sandwich structure, delamination may occur

K.R. Jagtap (✉) · H.H. Nawale
Department of Mechanical Engineering, Sinhgad Institute of Technology
and Science, Pune 411041, India
e-mail: krjagtap_sits@sinhgad.edu

H.H. Nawale
e-mail: harshad.nawale5212@gmail.com

S. Roy
R&DE(E), Defence Research and Development Organization, Pune 411015, India
e-mail: roysajal@rde.drdo.in

between various laminas of skins or between skin and core. Delamination occurrence at any location reduces the stiffness of the structure and changes its dynamic characteristics. Due to changing in dynamic characteristics, modal parameters like natural frequency, mode shapes, damping ratio etc. may vary depending upon the degree of damage.

Piezoelectric materials have intrinsic electromechanical coupling effect due to which they have found many applications in smart devices such as electromechanical transducers, actuators etc. Piezoelectric material is such that when it is subjected to mechanical load or stress, it generates electric charge called piezoelectric effect. Conversely if piezoelectric material stress electrically by voltage, its dimension changes called as inverse piezoelectric effect. Piezoelectric materials have wide scope in structural health monitoring of composite structures. Piezoelectric actuators can be used to generate perturbation in the structure and its response can be monitored using sensors, which gives the health condition of the structures.

Tate et al. [1] studied the effect of delamination on natural frequency of composite beam coupled with piezoelectric actuator. FRFs are plotted from dynamic response by performing transient analysis and concluded that natural frequency decreases as damage increases. Macro et al. [2] studied identification of low velocity impact damage in composite laminate using vibration testing and conducted experiment by doing drop weight impact test. Finally, concluded that relative changes in mode shapes are greater than natural frequency to detect low velocity impact damage. Zeki et al. [3] studied the effect of impact failure on free vibration responses of composite cantilever beam and concluded that frequency decreases as damage increases. Zeki et al. [4] presented the effect of root crack on natural frequencies of sandwich beam numerically as well as experimentally. Crack is generated at the interface between skins and core and concluded that presence of root crack affects natural frequency of cantilever beam. Daniel and Glauco [5] presented the application of small library of three dimensional cohesive elements and ABAQUS finite element software (FEA) is used to define the three dimensional cohesive elements. They chose the PPR, potential based traction separation relation to describe the elements constitutive model. Xiangting et al. [6] studied the algorithm of cohesive elements in ABAQUS and gives the idea of 3D crack propagation in quasi brittle material with the help of cohesive elements.

In this paper, effect of delamination on natural frequency of sandwich composite cantilever beam coupled with piezoelectric actuator is presented. Transient analysis of the beam is performed by exciting beam with piezoelectric actuator and obtained its dynamic responses, using ABAQUS FEA software. From dynamic responses, FRFs are obtained by developing MATLAB code. Delamination of various sizes are modeled at different locations using cohesive surface behavior and effect of delamination on natural frequency for healthy and damaged beam is observed.

2 Material and Dimensions

A simple sandwich composite cantilever beam with piezoelectric actuator, is used for simulation, which consist of two thin skins and one thick core inserted between two skins. The dimensions of sandwich cantilever beam are shown in Fig. 1.

- Length of beam = 300 mm
- Width of beam = 30 mm
- Total thickness of the beam = 15.4 mm
- Thickness of each skin = 1.7 mm
- Thickness of skin lamina = 0.425 mm
- Thickness of core = 12 mm
- Size of piezoelectric actuator = 10 × 10 × 1 mm

Material used for skin is carbon fibre UD T-700, which is made up of composite section and material used for light weight core is PVC foam. Material properties used for skin and core are mentioned in Tables 1 and 2 respectively.

Interaction between various layers of the sandwich beam has been defined using cohesive surface behavior. Cohesive element properties for lamina to lamina and skin to core interaction for non-delaminated region are mentioned in Tables 3 and 4 respectively. To model the delamination at various locations, cohesive element properties for delaminated region are mentioned in Table 5. The sandwich beam is excited using piezoelectric actuator and mechanical strain is generated in the beam. PZT 5H is used as piezoelectric actuator with thickness 1 mm and size 10 × 10 mm and is glued on upper surface of top skin of sandwich composite cantilever beam located 10 mm from free end.

Piezoelectric coupling matrix (Strain coefficients) for PZT 5H is

$$\begin{bmatrix} 0 & 0 & 0 & 741 & 0 & 0 \\ -274 & 593 & -274 & 0 & 0 & 0 \\ 0 & 0 & 0 & 0 & 0 & 741 \end{bmatrix} \times 10^{-12} \text{ M/V}$$

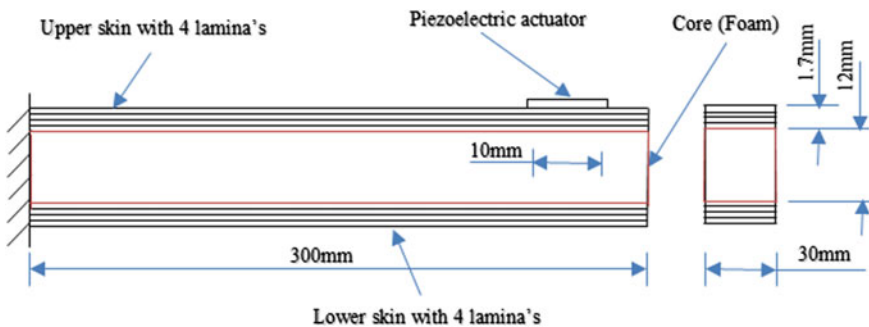


Fig. 1 Sandwich composite cantilever beam

Table 1 Carbon fibre unidirectional T-700

ρ (kg/m ³)	E_1 (GPa)	E_2 (GPa)	E_3 (GPa)	G_{12} (GPa)	G_{23} (GPa)	G_{13} (GPa)	ν_{12}	ν_{23}	ν_{13}
1500	112	7.7	7.7	6.7	6.7	6.7	0.2	0.2	0.2

Table 2 Poly vinyl chloride (foam)

ρ (kg/m ³)	E_1 (GPa)	ν_{13}
100	130	0.3

Table 3 Cohesive behavior interaction between skin laminas for non-delaminated region

Interaction between laminas	K_{nn} (MPa)	K_{ss} (MPa)	K_{tt} (MPa)
	1×10^6	1×10^6	1×10^6

Table 4 Cohesive behavior interaction between skin and core for non-delaminated region

Interaction between skin and core	K_{nn} (MPa)	K_{ss} (MPa)	K_{tt} (MPa)
	1×10^8	1×10^8	1×10^8

Table 5 Cohesive behavior interaction between delaminated regions

Property	K_{nn} (MPa)	K_{ss} (MPa)	K_{tt} (MPa)
Cohesive stiffness for delamination	1×10^3	1×10^3	1×10^3
Quadratic traction damage initiations stiffness	61	68	68

Table 6 Material properties for PZT-5H

ρ (kg/m ³)	E_1 (GPa)	E_2 (GPa)	E_3 (GPa)	G_{12} (GPa)	G_{23} (GPa)	G_{13} (GPa)	ν_{12}	ν_{23}	ν_{13}
7500	60.6	60.6	48.31	23	23.5	23	0.512	0.289	0.408

Dielectric matrix for PZT 5H is given as,

$$\begin{bmatrix} 1.505 & 0 & 0 \\ 0 & 1.301 & 0 \\ 0 & 0 & 1.505 \end{bmatrix} \times 10^{-8} \text{ F/M}$$

PZT actuator is modeled by giving piezoelectric properties such as permittivity matrix and piezoelectric matrix. Material properties of piezoelectric actuator (PZT-5H) are mentioned in Table 6.

3 Methodology

Modeling of the sandwich composite cantilever beam has been done by using ABAQUS FEA software. Surface to surface cohesive behavior has been used to define the contact between various layers of sandwich beam. Then sandwich beam is excited using piezoelectric actuator coupled on upper surface of the top skin and transient dynamic analysis of the beam is performed and acceleration vs. time history is computed on node near the piezoelectric actuator. From acceleration vs. time history, FRFs are plotted using MATLAB program. From FRFs, we get the natural frequencies of the sandwich beam for various modes. Properties used for lamina to lamina interaction have smaller strength than lamina to core interaction. Surface of the beam where no delamination is present, is modeled with properties mentioned in Tables 3 and 4. To model delamination at various locations, quadratic traction damage initiation criteria have been used with cohesive stiffness's mentioned in Table 5. For modeling delamination between any two laminas, node sets are created between those two laminas and defined with limit bonding cohesive behavior. For delamination modeling, using limit bonding cohesive behavior, clearance of 1×10^{-4} mm has been used. Continuum shell element has been used for laminas of skins and 8 noded brick element has been used for PVC core to mesh the model. To study delamination, five different cases of delamination are considered from which Case: I is shown in Fig. 2 for more understanding.

Case: I Delamination length of 90 mm between 2nd and 3rd lamina located 60 mm from fix end

Case: II Delamination length of 120 mm between 2nd and 3rd lamina located 60 mm from fix end

Case: III Delamination length of 120 mm between 3rd and 4th lamina located 60 mm from fix end

Case: IV Delamination length of 60 mm between upper skin and core located 60 mm from fix

Case: V Simultaneous delamination of 90 and 60 mm between 2nd and 3rd lamina and upper skin and core respectively, located 60 mm from fix end

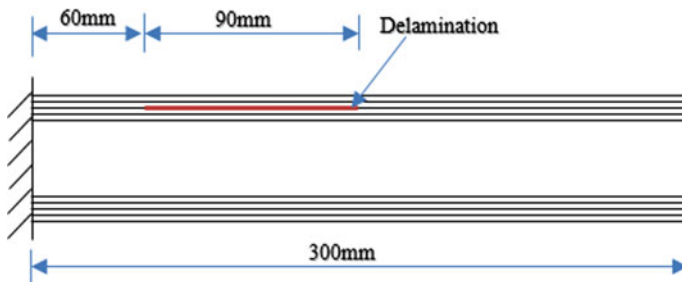


Fig. 2 Delamination of 90 mm between 2nd and 3rd lamina near fix end

The contact between piezoelectric actuator and upper skin is defined by hard contact and normal behavior. An electric potential degree of freedom is coupled by giving zero potential to one side of the actuator to provide electric coupling between two materials. The other side of the actuator is given voltage of 5 MV to excite the structure. Simulation is run for 1 s with time step of 1.25×10^{-4} and 8000 time increments are taken to perform the transient analysis of healthy beam. To get the dynamic response of delaminated beam, delamination is modeled in the beam at various locations and same voltage is applied as used in case of healthy beam. For delaminated beam, to get more accuracy 16,000 time increments are taken with time step 6.25×10^{-5} .

4 Results and Discussions

Transient analysis of healthy as well as damaged (for various cases of delamination) sandwich composite cantilever beam coupled with piezoelectric actuator for symmetric quasi isotropic $([0/45/-45/90]_s)$ fibre orientation has been performed in ABAQUS FEA and FRFs are plotted by developing MATLAB code. Overlaying plots of FRFs of damaged and healthy model are compared and certain conclusions are drawn as follows.

To check the effect of delamination size on natural frequency, overlaying plot of FRFs of healthy beam, 90 mm delamination between 2nd and 3rd lamina located 60 mm from fix end (Case: I) and 120 mm delamination between 2nd and 3rd lamina located 60 mm from fix end (Case: II) is shown in Fig. 3.

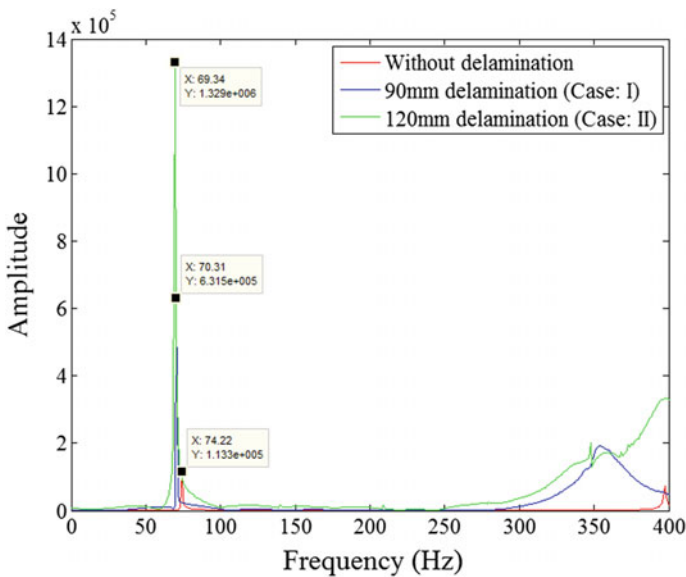


Fig. 3 FRFs for healthy beam, Case: I and Case: II of delamination

From Fig. 3, it is observed that, natural frequencies in Case: I and Case: II are smaller than healthy beam. Also natural frequencies for Case: I are bigger than Case: II. So due to presence of damage, stiffness of beam is reduced and natural frequencies are decreasing after introducing delamination. By comparing Case: I and Case: II, it is also observed that, if size of delamination is more reduction in natural frequency is also more.

To observe the effect of delamination location on natural frequency, overlaying plot of healthy beam, Case: II and Case: III is shown in Fig. 4, where location of delamination is different but size of delamination (120 mm) is same. From Fig. 4, it is observed that natural frequencies for Case: III are smaller than Case: II. It means that stiffness degradation of the beam is more in Case: III and decrease in natural frequency of the beam is also dependent on location of delamination.

To check the effect of skin to core delamination on natural frequencies, Case: I and Case: IV are compared. Overlaying plot of healthy beam, 90 mm delamination between 2nd and 3rd lamina (Case: I) located 60 mm from fix end and 60 mm delamination between upper skin and core (Case: IV) located 60 mm from fix end, is shown in Fig. 5. From Fig. 5, it is observed that natural frequencies for Case: I are higher than Case: IV and difference of natural frequencies in both cases is much higher. So it can conclude that, stiffness degradation of the sandwich beam is more if delamination is between skin and core than in various laminas of skins.

To check the effect of simultaneous delamination at two different locations overlaying plot of Case: I, Case: IV and Case: V is shown in Fig. 6. In case: V, delamination length of 90 and 60 mm is modelled simultaneously at two different

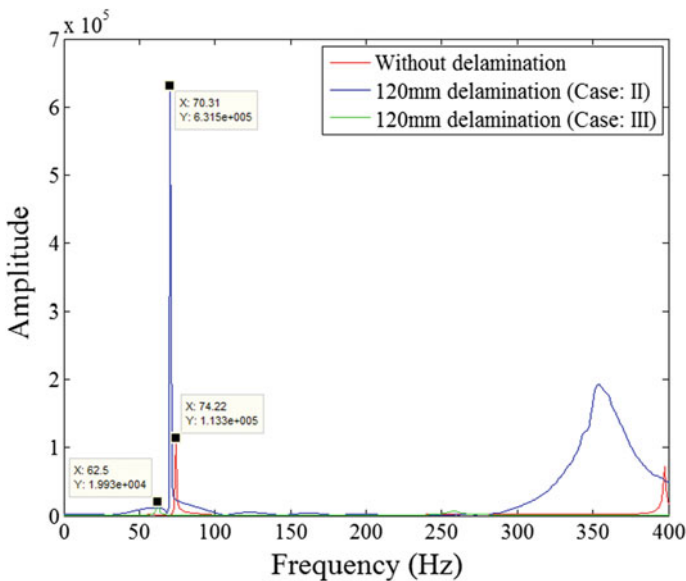


Fig. 4 FRFs for healthy beam, Case: II and Case: III

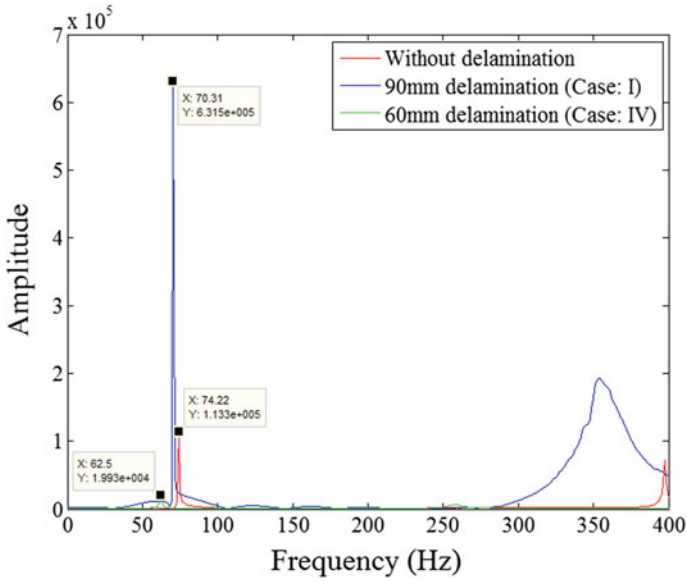


Fig. 5 FRFs for healthy beam, Case: I and Case: IV of delamination

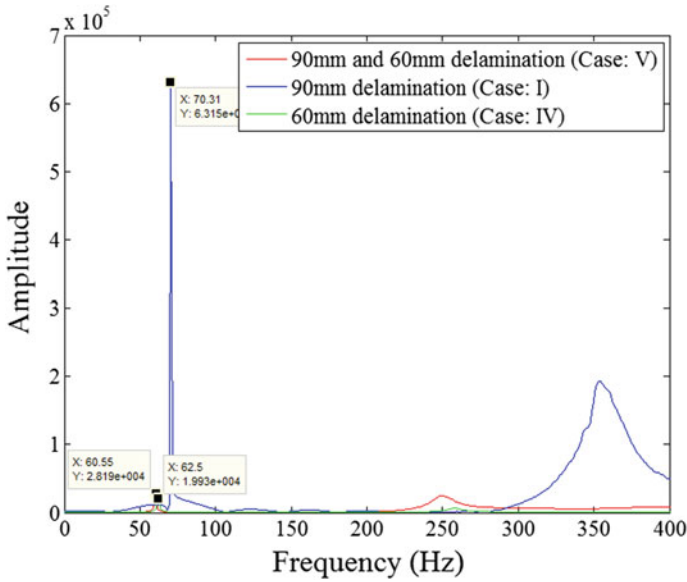


Fig. 6 FRFs for Case: I, Case: IV and Case: V

locations, where as in Case: I and Case: IV delamination length of 90 and 60 mm is modelled individually. From Fig. 6, it is observed that natural frequencies for Case: V are smaller than Case: I and Case: IV. So as damage in Case: V is more, stiffness degradation is also more. So it can be concluded that, stiffness degradation of the beam is more if simultaneous delamination is present at two different locations than individual delamination at the same locations.

5 Conclusions

Delamination study of sandwich composite cantilever beam coupled with piezoelectric actuator has been done. Transient dynamic analysis of the beam is performed in ABAQUS FEA and FRFs for damage and undamage states are plotted by using MATLAB code. By comparing FRFs for damage and undamage states, some important points are concluded which are given as follows.

- Natural frequency of sandwich beam decreases after introducing delamination in it.
- If the size of delamination is more, decrease in natural frequency is also more.
- Decrease in natural frequency of sandwich beam is also dependent on location of delamination.
- Stiffness degradation of the sandwich beam is more if delamination is between skin and core than in various laminas of skins.
- Stiffness degradation of the beam is more if simultaneous delamination is present at two different locations than individual delaminations at the same locations.

References

1. Tate IV, Roy S, Jagtap KR (2014) Delamination detection of composite cantilever beam coupled with piezoelectric transducer using natural frequency deviation. *Procedia Eng* 97:1293–1304
2. Marco AP, Liuis G, Sergio O (2014) Impact damage identification in composite laminates using vibration testing. *Compos Struct* 108:267–276
3. Zeki K, Icten BM, Binnur GK (2012) Effect of impact failure on the damping characteristics of beam-like composite structures. *Compos B* 43:3053–3060
4. Zeki K, Everen TM, Binnur GK, Sayman O (2013) Effect on root crack on lateral buckling loads and natural frequency of sandwich composite beam. *Compos B* 53:308–313
5. Daniel WS, Glaucio HP (2014) A growing library of three-dimensional cohesive elements for use in ABAQUS. *Eng Fract Mech* 14, S0013-7944-00100-3
6. Xiangting S, Zhenjun Y, Guohua L (2013) Finite element modelling of complex 3D static and dynamic crack propagation by embedding cohesive elements in ABAQUS. *Acta Mech Solida Sin* 23(3):0894–9166

Development of Methodology for Transforming CT Images Indicating Location and Size of Lung Cancer Nodule

Rajani R. Mhetre, Pooja P. Kawathekar, Sneha S. Kadam
and Megha B. Gore

Keywords Lung cancer · Computed tomography · Region growing algorithm

1 Introduction

The most recent estimates according to the latest statistics provided by World Health Organization indicates that around 7.6 million deaths occur worldwide each year because of this type of cancer. Furthermore, mortality from cancer are expected to rise, to become around 17 million worldwide in 2030. Cancer is one of the most serious health problems in the world field. If the cancer is detected earlier then survival rate of patient will increase [1]. Now a day's different CAD systems are available for early detection of cancer stages. The proposed work is having Image Processing background to develop a methodology which indicates a location and size of lung cancer nodule.

Giuseppe Coppini et al. used a neural-network-based system for the computer aided detection of lung nodules in chest radiograms. Their approach is based on multiscale processing and artificial neural networks (ANNs). The problem of nodule detection is faced by using a two-stage architecture including: (1) an attention focusing subsystem that processes whole radiographs to locate possible nodular regions ensuring high sensitivity; (2) a validation subsystem that processes regions of interest to evaluate the likelihood of the presence of a nodule, so as to reduce false alarms and increase detection specificity [2].

Iyad Jafar et al. developed a computer aided diagnosis software prototype that simultaneously processes the CT, attenuation-corrected PET, and attenuation uncorrected PET volumes to detect tumors in the lungs. The system applies optimal thresholding and multiple gray-level thresholding with volume criterion to extract the lungs and to detect tumor candidates, respectively. A fuzzy logic based approach

R.R. Mhetre (✉) · P.P. Kawathekar · S.S. Kadam · M.B. Gore
Department of Electronics and Telecommunication,
SVERI's College of Engineering Pandharpur, Pandharpur, India
e-mail: rrmhetre@coe.sveri.ac.in

is used to reduce false-positive tumors. The remaining set of tumor candidates are ranked according to their likelihood of being actual tumors. They show the preliminary results of a retrospective evaluation of clinical PET/CT images [3].

Yang et al. [4] presented a new method to automatically detect both tumors and abnormal lymph nodes based on the low-level intensity and neighborhood features and high-level contrast-type features, with a two-level SVM classification. One level of conditional random field (CRF) is based on unary level contextual and spatial features and pair wise-level spatial features. Other level is based by relabeling the detected tumors as positive or mediastinum by filtering the high-uptake myocardium areas.

Chen et al. [5] incorporated the VDE technology in CADe scheme. The VDE technology suppressed rib and clavicle opacities in CXRs while maintaining soft-tissue opacity by use of the MTANN technique that had been trained with real dual-energy imaging. Their scheme detected nodule candidates on VDE images by use of a morphologic filtering technique. Sixty morphologic and gray-level-based features were extracted from each candidate, from both original and VDE CXRs. A nonlinear support vector classifier was employed for classification of the nodule candidates.

Ada et al. developed methodology for Early Detection and Prediction of Lung Cancer Survival using Neural Network Classifier. In this paper Histogram Equalization is used for preprocessing of the images and feature extraction process and neural network classifier to check the state of a patient in its early stage whether it is normal or abnormal. After that Author predict the survival rate of a patient by extracting features. Experimental analysis is made with dataset to evaluate the performance of the different classifiers [6].

The Objective of this paper is to develop a method for calculating size and location of lung cancer nodule. The paper is organized into VI sections including this introduction. Section 2, look after the main five objectives of study. Section 3, tell about dataset used for proposed method. Section 4 explains about actual proposed method and various steps need to be carrying out like, preprocessing, segmentation and feature extraction. Section 5 includes experimental results which are then followed by conclusion and references.

2 Objectives of Study

The objectives of this study are as follows:

- To have image database of lung cancerous and noncancerous images.
- To use image enhancement method for preprocessing.
- To segment the image for selecting region of interest.
- To select and apply appropriate feature extraction algorithms for calculation of size of lung cancer nodule.
- To obtain a final image with location and size of lung cancer nodule.

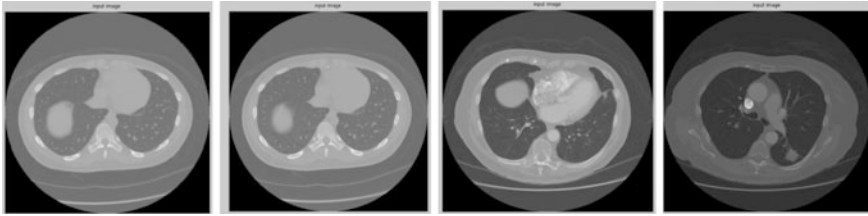


Fig. 1 Sample CT scan images of lung cancer from dataset

3 Dataset

The database used here is LIDC-IDRI obtained from www.cancerimagingarchive.net. The images in this database are CT scan images, and are in standard dicom format. The intent of the Lung Imaging Database Consortium (LIDC) initiative was to support a consortium of institutions to develop consensus guidelines for a spiral CT lung image resource and to construct a database of spiral CT lung images. The investigators funded under this initiative have created a set of guidelines and metrics for database use and for developing a database as a test-bed and showcase for those methods. The database is available for researchers and users through the Internet and has wide utility as a research, teaching, and training resource [7] (Fig. 1).

4 Proposed Method

There are three steps which are required to be followed as:

(i) **Preprocessing:**

Pre-processing is applied on images at the lowest level of abstraction and aim of this is to reduce undesired distortions. The key function of preprocessing is to improve the image such that it increases the chances for success of other processes. Here, the following image processing techniques are used to enhance the image quality (Fig. 2).

Digitization noise and high frequency components are some of the unwanted regions present in the CT scan images. These can be removed by using median filter. The advantage of using median filter is that it can remove the noise without disturbing the edges. By applying the lung border extraction technique, the lung region border is obtained [1]. Further edge is detected using sobel operator. Finally, to fill the obtained lung border with the lung region flood fill algorithm is used. The lung region is extracted from the CT scan image after the application of these algorithms. Finally the resultant lung region is used further for the segmentation in order to detect the cancer nodule.

Fig. 2 Preprocessing steps

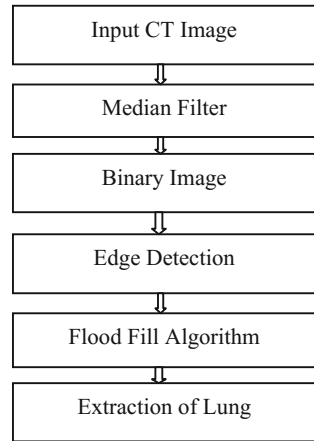
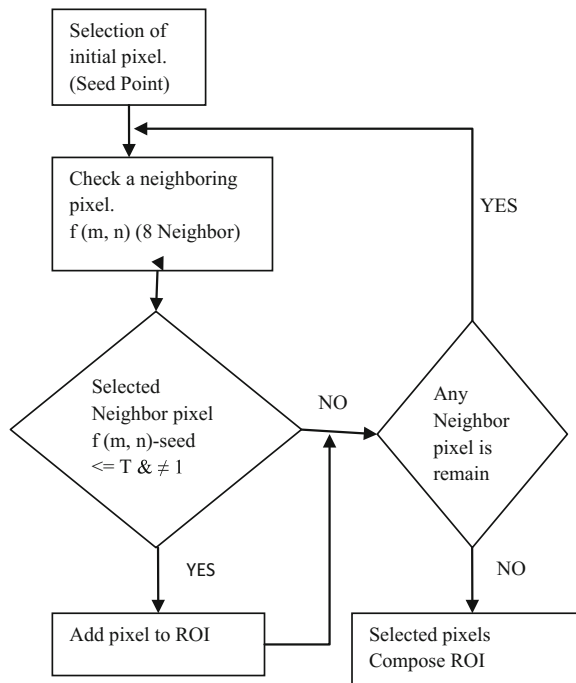


Fig. 3 Segmentation using region growing algorithm



(ii) **Segmentation:**

For segmentation, region growing algorithm is used (Fig. 3).

Step I: Select a pixel in the input image and make it a Seed point. Add the seed pixel into an empty queue.

Step II: From top of the queue, start finding immediate 8-connected neighbors of each unprocessed pixel and for each neighbor point, check whether the

gray level value of that neighbor pixel is within the specified deviation from the seed pixels gray level value. $F(m, n) - \text{seed} \leq T$. Where, $f(m, n)$ is the grey level value of the current pixel and the threshold $T = 0.0003$. If the current pixel satisfies the criteria then it is added to the queue.

Step III: Step II is repeated till all the pixels in the queue are processed. If some pixel is encountered, that is already on the queue then ignore it and process the next pixel in the queue [8].

(iii) **Feature extraction:**

(A) **Area:** It is the scalar value that gives actual number of overall nodule pixel in the extracted ROI. Transformation function creates an array of ROI that contains pixels with 255 values.

$$\text{Area} = A = (A_{i,j}, X \text{ ROI [Area]} = I, \text{ROI [Area]} = j)$$

where, i, j are the pixels within the shape. ROI is region of interest. $X \text{ ROI []}$ is vector contain ROI x position, $Y \text{ ROI []}$ is vector contain ROI y position. It is the simplest property and gives the total number of white pixels in the extracted area [9].

(B) **Perimeter:** It is a scalar value that gives actual number of the nodule pixel. It is the extracted ROI boundary. Transformation function create array of edge that contain pixel with 255 values that have at least one pixel which contain 0 values.

$$\text{Perimeter} = p = (P_{i,j}, X \text{ edge [P]} = I, Y \text{ edge [P]} = j)$$

where, $X \text{ edge []}$ and $Y \text{ edge []}$ are vectors represents the co-ordinate of the i th and j th pixel forming the curve, respectively [9].

(C) **Radius:** By considering the shape of lung cancer nodule as a approximately circular, the radius will be calculated as

$$\text{Radius (R)} = \text{Sq.rt (Area/Pi)}$$

(D) **Diameter:** Once calculated the Area and Radius, Diameter can be calculated as

$$\text{Diameter (D)} = 2R$$

(E) **Eccentricity:** This metric value is also called as roundness or circularity or irregularity complex (I) equal to 1 only for circular and it is less than 1 for any other shape [9].

$$\text{Eccentricity} = \frac{\text{Length of Major Axis}}{\text{Length of Minor Axis}}$$

- (F) **Centroid:** It is 1×2 Vector; the center of mass of the region. The first element of the centroid is the horizontal co-ordinates of the center of mass, and second is the vertical co-ordinate. Function `regionprops` is the toolbox's principal tool for computing region descriptors. This function has the syntax

$$D = \text{regionprops}(L, 'Centroid')$$

where, L is label Matrix.

- (G) **Location:** First calculate the number of columns present in that image, then find out the mid of the image. If the nodule is present at left side of mid then it is present in left lung otherwise in right lung. In this way, the features can be obtained in order to find Location and Size of the Lung cancer nodule.

5 Experimental Results

CT images are difficult to elucidate. The aim of preprocessing is to improve the image data that suppresses unwanted distortions or enhances some image features important for further processing. For preprocessing as shown in Fig. 4, median filter is applied on original image, then binarize the filtered image, then clear the border and edge is detected followed by flood fill algorithm. We get extraction of lung from original image. Figure 5 shows the result of segmentation by using region growing method.

Feature Extraction for calculation of Size and Location of Lung Cancer Nodule, the tabular representation is as shown below. In following tables the feature

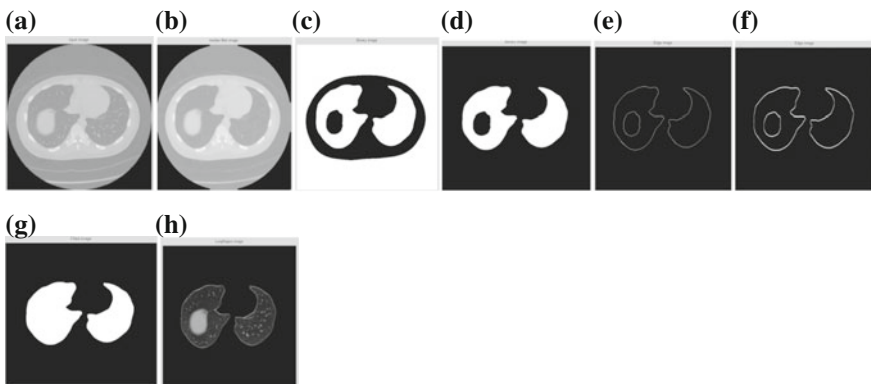


Fig. 4 a Input image; b median filtered image; c binary image; d clear border; e edge detection; f dilation of image; g flood fill algorithm applied on image; h extraction of lung

extraction data is represented for twenty five images. In that features like area, radius, diameter, and perimeter are calculated in number of pixel values for calculation of size of lung cancer nodule. In Table 1 these features are shown as follows:

From above table, the variation in the size of the lung cancer nodule in different patients. Smallest nodule detected in image number 11 i.e. 365 pixels and the largest nodule detected in image number 25 i.e. 6055 pixels. So, here we can significantly see the variation in nodule size.

Eccentricity and centroid co-ordinates are calculated in order to find the location of nodule in lung. These data for twenty five images are shown in Table 2.

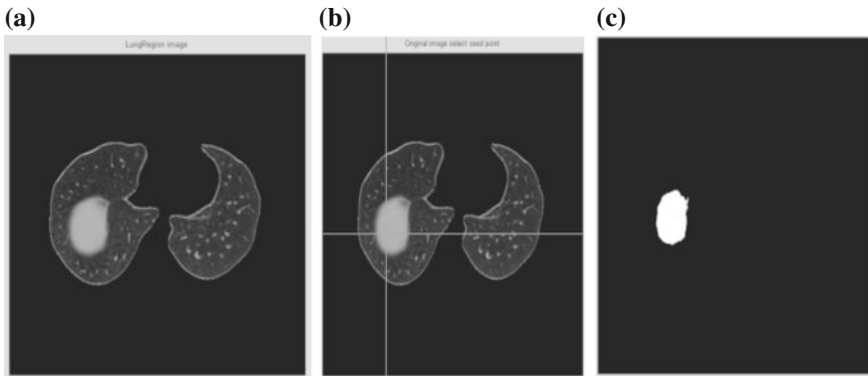


Fig. 5 Result of segmentation **a** preprocessed image; **b** selection of seed point; **c** extraction of lung cancer nodule

Table 1 Features for calculation of size

Image No.	Area	Radius	Diameter	Perimeter
	In number of pixels			
1	3713	34.3785	68.7571	227
2	2113	25.9343	51.8686	158
3	3775	34.6644	69.3288	265
4	3600	33.8514	67.7028	214
5	2752	29.5971	59.1942	174
6	5559	42.0652	84.1305	254
7	1573	22.3764	44.7527	142
8	2255	26.7916	53.5832	165
9	936	17.2609	34.5218	104
10	3514	33.4446	66.8892	203
11	365	10.7788	21.5577	77
12	5320	41.151	82.3021	268
13	2448	27.9146	55.8291	175

(continued)

Table 1 (continued)

Image No.	Area	Radius	Diameter	Perimeter
	In number of pixels			
14	1178	19.3641	38.7282	131
15	3573	33.7242	67.4484	210
16	1830	24.1352	48.2704	149
17	4072	36.0022	72.0044	224
18	4491	37.8091	75.6182	242
19	3079	31.3062	62.6123	186
20	545	13.1711	26.3423	90
21	4895	39.4731	78.9462	269
22	4364	37.2707	74.5414	235
23	4946	39.6782	79.3564	247
24	800	15.9577	31.9154	112
25	6055	43.9018	87.8036	274

Table 2 Features for calculation of location

Image No.	Eccentricity	Centroid coordinates		Location
		X	Y	
1	0.369864	138.774	274.766	Left lung
2	0.370405	136.396	276.481	Left lung
3	0.32716	370.513	298.63	Right lung
4	0.236913	146.297	245.308	Left lung
5	0.238176	147.414	242.295	Left lung
6	0.234733	144.78	247.182	Left lung
7	0.239608	146.065	244.177	Left lung
8	0.326416	169.08	214.643	Left lung
9	0.333166	165.946	216.11	Left lung
10	0.320675	170.872	213.15	Left lung
11	0.447147	317.836	369.855	Right lung
12	0.4541	164.989	212.996	Left lung
13	0.472523	160.927	214.728	Left lung
14	0.476759	160.509	215.876	Left Lung
15	0.466489	162.511	214.109	Left lung
16	0.474775	160.833	215.537	Left lung
17	0.462759	163.562	213.802	Left lung
18	0.459495	163.905	213.493	Left lung
19	0.469882	161.571	214.496	Left lung
20	0.479064	159.389	217.222	Left lung
21	0.456627	164.784	213.321	Left lung
22	0.236277	145.532	246.569	Left lung
23	0.235562	145.112	246.836	Left lung
24	0.240225	144.031	248.141	Left lung
25	0.234033	144.405	247.181	Left lung

6 Conclusion

The expert physicians diagnose the disease and identify the stage of cancer by experience. The treatment includes surgery, chemotherapy, radiation therapy and targeted therapy. These treatments are lengthy, costly, and painful. Hence, an attempt is made to atomize this procedure to detect the lung cancer using image processing techniques. CT scan images are acquired from publicly available database on internet. These images include less noise as compared to X-ray and MRI images. The time factor is taken into account to discover the abnormality issues in target images. The CT captured images are processed. The region of interest i.e., tumor is identified accurately from the original image. Median filter, binarization of image, clearing the border, edge detection, dilation and flood fill algorithm have given the best result for the preprocessing stage.

Also after preprocessing of original image, we have extracted the nodule portion from the preprocessed image by selecting a seed point and applying the region growing algorithm. Finally features like area, perimeter, eccentricity and centroid co-ordinates are calculated in order to find the size and location of lung cancer nodule.

References

1. Shaik S, Kavita C (2013) Detection of lung cancer nodules using automatic region growing method. IEEE
2. Giuseppe C, Stefano D, Massimo F, Natale V, Guido V (2003) Neural networks for computer-aided diagnosis: detection of lung nodules in chest radiograms. IEEE Trans Inf Technol Biomed 7(4)
3. Iyad J, Hao Y, Anthony FS, Otto M (2006) Computerized detection of lung tumors in PET/CT images. In: Proceedings of 28th IEEE, EMBS annual international conference, New York City, USA, 30 Aug–3 Sept 2006
4. Yang S, Weidong C, Jinman K, David DF (2012) A multistage discriminative model for tumor and lymph node detection in thoracic images. IEEE Trans Med Imaging 31(5)
5. Chen S, Suzuki K, Member IEEE (2013) Computerized detection of lung nodules by means of ‘virtual dual-energy’ radiography. IEEE Trans Biomed Eng 60(2)
6. Ada RK (2013) Early detection and prediction of lung cancer survival using neural network classifier. IJAIEM 2(6)
7. www.cancerimagingarchive.net
8. Kumar S, Dhir V, Mehra S (2014) Analysis and implementation of contrast enhancement techniques using medical image. IJARCSSE 4(5). ISSN: 2277 128X
9. Vijay AG, Gajdhane A, Deshpande LM (2014) Detection of lung cancer stages on CT scan images by using various image processing technology. IOSR 16(16)

A Driver Assistance System Using ARM Processor for Lane and Obstacle Detection

Sandip N. Pawar and S.M. Mukane

Keywords Driver assistance · Lane deletions · Obstacle detection · Raspberry pi

1 Introduction

Driver assistance (DA) is a system which helps the driver or aimed at aiding the driver of the vehicle. For example, a relatively simple DA system can be one that automatically turns on or off windshield wipers when there is water detection. On the other side, the pedestrian detection is an example of an advanced DA system. It is implemented in a few high end automobiles. A variety of sensors allow the DA system to interface with the world these sensors include microphones, GPS devices, and radar [1]. It allows the drivers increased control, thus facilitates vehicular operation [2].

The number of vehicle accident victims has increased annually with an increase in a number of vehicles. The main reason behind this is a lack of awareness about driving conditions due to driver carelessness or visual interference [3]. Over 19,000 people died on U.S. highways due to road departures in 2008 [4]. Due to the driver errors, more than 90% of accidents have happened [5]. Also, there is a serious problem of traffic in many countries [6].

There are many solutions developed for the problems discussed above. But all the system implementing the solutions is too costly to buy. These systems are implemented only in the luxurious vehicles like Audi, BMW, and Volvo, etc. The common people cannot purchase these vehicles due to lack of money. Thus the aim of the research presented in this paper is to provide a low cost system which can detect the obstacle and lane and warn the driver to prevent any possible accident. Looking at all these aspects, driver assistance system lane and obstacle detection using ARM processor are proposed. Lane detection is carried out by capturing the

S.N. Pawar (✉) · S.M. Mukane
Department of Electronics and Telecommunication Engineering,
SVERI's College of Engineering, Pandharpur, India
e-mail: sandip.pawar91@gmail.com

video with the help of a camera. Also, the obstacle detection is proposed to implement using ultrasonic sensors.

The embedded image processing system integrates all the functions such as image capturing, displaying and processing [7]. Taking into account the advantages of small size and low power consumption, the ARM processor as used in [7, 8] is chosen for the prototype development of the system.

1.1 Lane Detection

In the lane detection, the painted lane markings or boundaries on the road surface are located with little knowledge of the road geometry. One or more cameras are used in vision-based lane detection. In this, data in the form of video or an image sequence are acquired. This data is analyzed to extract features that closely correspond to the desired lane markers [1].

In automotive research and development, the Camera based lane change assistance (LCA) is very important. Collisions due to unintentional lane departure caused by driver distractions, fatigue, or driving under the influence of a controlled substance can be avoided by continually monitoring the position of a vehicle within a lane [1].

The number of deaths can be reduced by warning the driver of a lane departure using safety systems on vehicles, such as lane departure warning (LDW) systems [4]. The result [7] showed that the system could realize fast acquisition, compression, and storage of images if it is based on ARM and Linux. This system uses low cost, high performance of ARM processor.

Different techniques for lane detection are the transformation of an image into hue-saturation-value and the application of morphological filters to reduce noise, the use of a Canny edge detector that produces single pixel wide edges, histogram equalization, filtering, clustering and polyline extraction, grayscale conversion and the application of a Gaussian low-pass filter to remove noise, smoothing, and the spitting of an image etc. [9].

Looking at all above points the camera based system for lane detection is decided to be implemented. The Raspberry Pi board contains the ARM processor. This board has CSI connector to interface the Raspberry camera. The HDMI display can be easily interfaced with the board to show the lanes detected. It can also be used for displaying the different warning messages. The warning messages are useful for altering the driver.

1.2 Obstacle Detection

While driving the, there should be a safe distance between the vehicle and other vehicles running on the road or any other obstacles. If this distance is not safe,

then there is the possibility of an accident due to the collision. Also, while reverse parking the vehicle, the driver cannot look what is there at back side of the vehicle. It is not possible to predict the safe distance from obstacles like a two-wheeler, stone, etc. In such a case the vehicle may be get damaged badly if the driver is unaware of the obstacles very close to the vehicle. So, there should be the system which will provide information about the front as well as back side obstacles and warn the driver about it. The forward collision avoidance is implemented in [5] using the ultrasonic sensor. In [10] system is proposed with an ultrasonic sensor as a short range collision warning system or a parking assistance system for application in a congested traffic environment, where vehicle speeds are relatively low. It acts as an assistive device for hearing impaired person as vibration method implemented as a warning.

The ultrasonic waves have frequencies greater than 20 kHz, and they fall in the category of sound waves. As human ear's audible perception range is 20 Hz–20 kHz, the ultrasonic waves are inaudible to human ears. Thus the ultrasound waves can be used for applications in vehicles without hindering human activity. Ultrasonic transducers are used to convert electrical energy into ultrasound waves and vice versa. When there is a change in, medium of propagation, the waves are reflected back. This property can be used for detecting obstacles. The time duration of the transmitted pulse and the received echo is used to calculate the distance of the object from the sensor. The important properties of ultrasound waves are given below [11].

1. They need a medium for propagation.
2. Their velocity varies with the nature of the medium.
3. They can be reflected.
4. A unique property of ultrasonic waves is that, as their frequency f is very high, they can be used to sense small objects.

Also, it is stated in [11] that the ultrasonic sensors can be used to detect the obstacle because they have several advantages over other types of sensors in short-range object detection. Thus ultrasonic sensor HC-SR04 is selected to implement the objective of the obstacles detection. It has a detection range from 2 cm to 4 m.

2 Proposed System Model

Figure 1 represents the system block diagram.

To accomplish the objectives of the proposed system, following prototype model is designed. It is designed considering the all above discussed points. The main blocks of the system are ARM processor, front and back side camera and two ultrasonic sensors and one HDMI display. The Raspberry Pi board is chosen as a development platform as it satisfies all the system requirements.

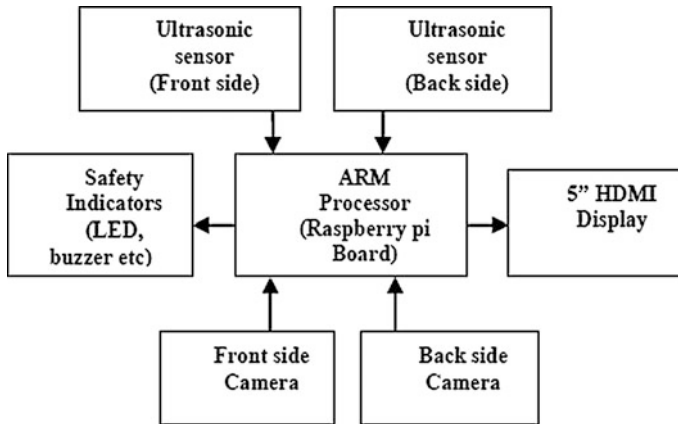


Fig. 1 System block diagram

2.1 *Ultrasonic Sensor*

It detects the obstacles and gives the feedback to the system. It can detect the obstacle within a range from 2 cm to 4 m. It is used to protect the vehicle from a collision with obstacles. It is needed to supply a short 10 μ s pulse to the trigger input to start the ranging, and then the module will send out an 8 cycle burst of ultrasound at 40 kHz and raise its echo. The range can be calculated through the time interval between sending trigger signal and receiving echo signal.

2.2 *Front Side Camera*

It is used for capturing the front side part of the vehicle and to send this video to the board so that it can be processed for the purpose of lane detection.

2.3 *Backside Camera*

It should turn on when the vehicle is moving in a back direction. It will capture the back side part of the vehicle and send it to the board. The video is displayed on display to assist the driver in reverse parking.

2.4 Safety Indicators

The buzzer and LED can be used as the indicators. It will warn the driver if any obstacle is detected. The threshold value for the distance from the obstacle can be set in code thus minimum safe distance is maintained between vehicle and obstacle. Indicator will also alert the driver if the vehicle is crossing the lane.

2.5 Display

5" HDMI display is used for displaying the lane markings that are detected after processing the video sent by front camera. It is also used for displaying the warning messages. It also shows the video captured from back side when the vehicle is moving in back or reverse direction. Thus, the vehicle can be prevented from the collision.

2.6 DC Motors

The DC motors are used to run the wheels of the vehicle. The two DC motors are used to develop demo vehicle model.

3 Implementation

The proposed system is decided to be implemented on a Raspberry Pi platform. The Raspberry Pi development board is available easily which is based on ARM processor. It is a credit card sized single board computer developed in the UK by the Raspberry Pi Foundation. This board has micro sd slot where the 8 GB memory card installed with Raspbian OS is inserted. There are four USB slots. Among which the one slot is used to connect the USB camera to board. This camera is used for the purpose of reverse parking and connected at the back side. The raspberry camera can be interfaced at CSI connector. It is used to find out lane markings on the road, and this camera is connected at the front side. The ultrasonic sensors, led, buzzer, switches can be interfaced with GPIO port of board. The 5" HDMI display is used to show the detected lane and the warning messages to the driver.



Fig. 2 Raspberry Pi board

This display can be connected to HDMI port of board. The warning system is designed using buzzer and LED.

The board is as shown in Fig. 2.

3.1 Connection Diagram

As proposed the two ultrasonic sensors are connected to the GPIO 3, GPIO 5 and GPIO 7, GPIO 11 pins of Raspberry board respectively. The Display is connected using HDMI cable. The buzzer and LED are connected to GPIO 13 and GPIO 18 pins of the board. Backside camera switch is connected to the GPIO 26 pin. The USB camera is connected to the USB port. The Raspberry camera is connected to the CSI connector.

The connection with the Raspberry Pi board is as shown in Fig. 3.

3.2 Flowchart

The flowchart shows the steps of execution of the python script developed to accomplish the objectives of proposed prototype. The Python is high level scripting language and has the advantage of ease of use and simplicity. The raspbian os is installed on Raspberry board. There are two scripts; the main script contains the task of lane detection and object detection. The other script is developed for back side camera to achieve the objective of safe reverse parking. This script is run as a subprocess in the main script. The libraries like GPIO, cv2, time, camera subprocess are some important libraries needed to include in the script.

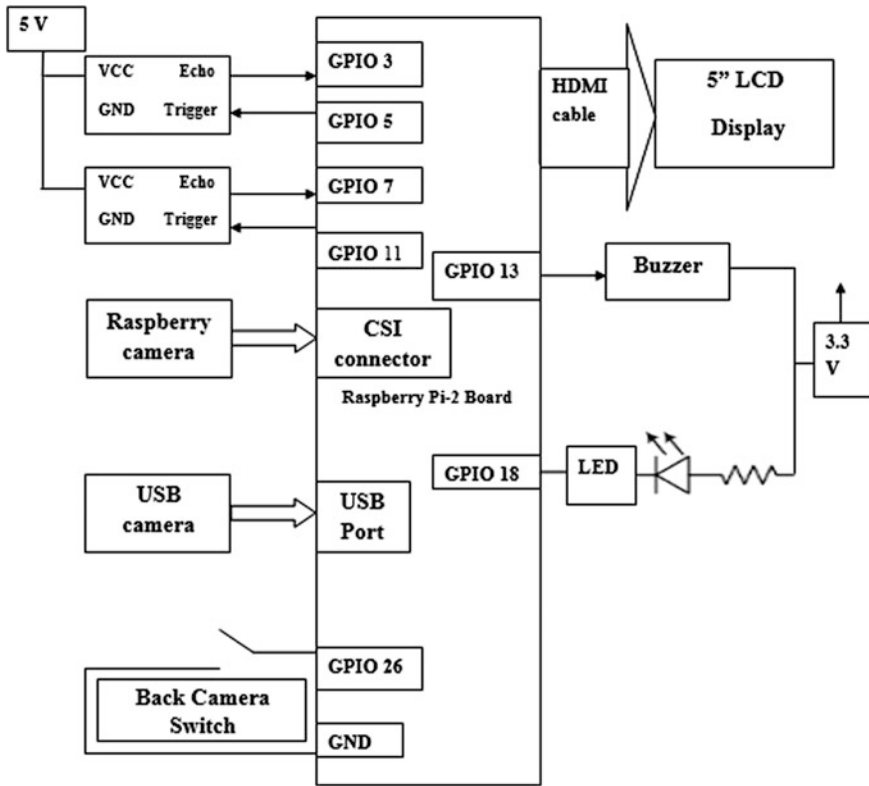


Fig. 3 Connection diagram

The SD Formatter and Win32DiskImager are software required to install the raspbian os on the SD card. SD Formatter is used to format sd card, and Win32DiskImager is used to copy the os setup on the sd card. The setup of the raspbian os, SD Formatter, Win32DiskImager is available on the internet as free-ware software. The flow chart of proposed system is developed as shown in Fig. 4.

4 Experimental Results

A hardware demo model with the Raspberry Pi platform is implemented. The core processor is Quad-core ARM Cortex-A7 with 900 MHz CPU, 1 GB RAM, Dual Core VideoCore IV GPU. The demo model works on 5 V supply. Following are the results of the experiment under different conditions (Figs. 5, 6, 7, 8, 9, 10, 11, 12 and 13).

Fig. 4 Flowchart of proposed system

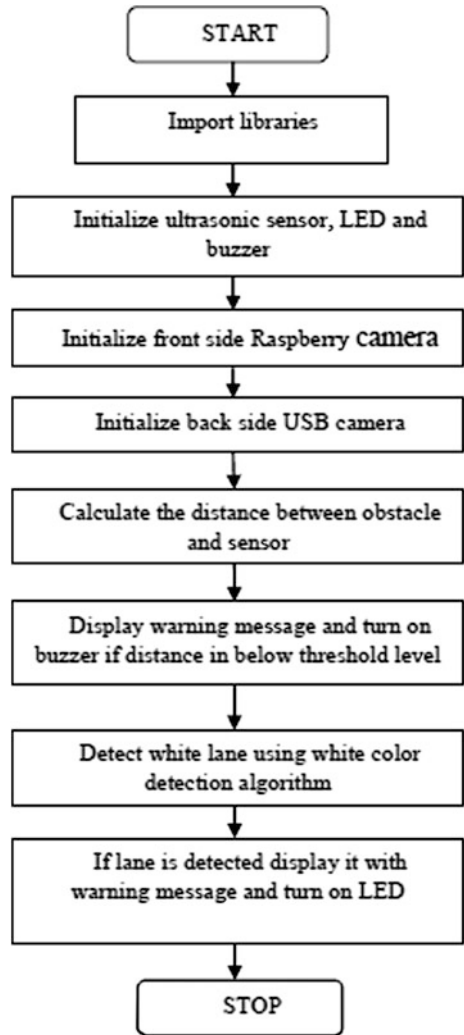


Fig. 5 Output in normal condition

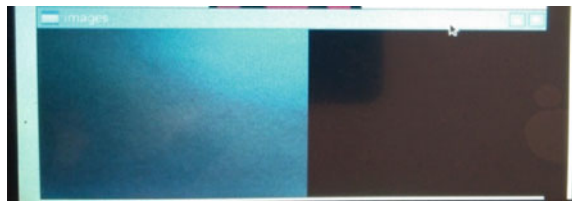


Fig. 6 Output when lane is detected



Fig. 7 Output when back side obstacle is detected

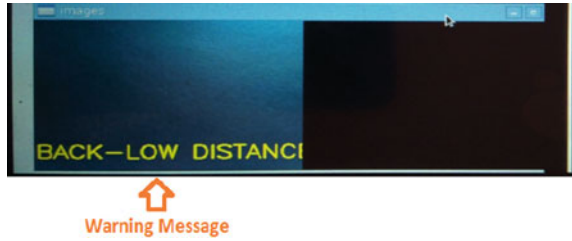


Fig. 8 Output when front side obstacle is detected

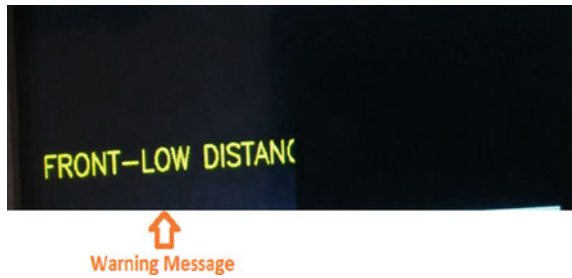


Fig. 9 Output when lane and back side obstacle is detected



Fig. 10 Output when lane and front side obstacle is detected

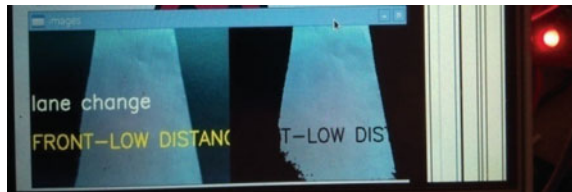


Fig. 11 Output when lane, front side, and back side obstacle is detected



Fig. 12 Output when back side camera is turned on

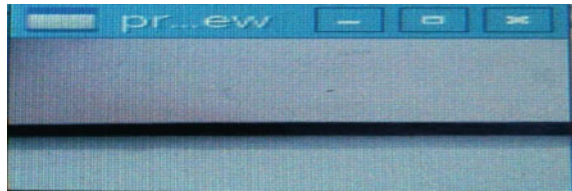
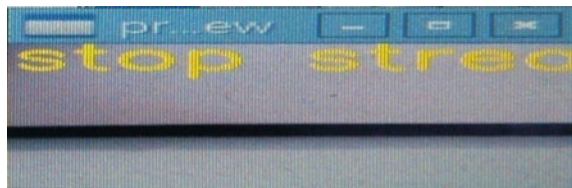


Fig. 13 Output when back side camera is turned off



5 Conclusion and Result Analysis

In this paper, the lane detection and obstacle detection system based on the Raspberry pi platform are implemented. The lane detection algorithm is based on the white color detection method. The above experimental results show that the lane markings on the roads can be detected with the help of a camera. The detected marking are displayed on the HDMI display. Also, the warning message is displayed on the screen if demo vehicle model is crossing the lane markings. The LED is also turned on to provide the indications during a lane change.

The obstacle detection is implemented using HC-SR04 ultrasonic sensors. The ultrasonic sensors can find out the obstacles on the front as well as back side of the vehicle model. The buzzer is turned on if the distance between obstacle and vehicle model is below a threshold value. It helps the driver during reverse parking of a vehicle and to put a safe distance between the vehicle and any obstacle. The back side camera can be turned on during reverse parking of vehicle to provide the back side visualization on display to the driver.

References

1. Borkar A, Hayes M, IEEE Fellow, Smith MT (2012) A novel lane detection system with efficient ground truth generation. *IEEE Trans Intell Transp Syst* 13(1)
2. Chiang HH, IEEE Member, Chen YL, IEEE Senior Member, Wu BF, IEEE Fellow, Lee TT, IEEE Fellow (2014) Embedded driver assistance system using multiple sensors for safe overtaking maneuver. *IEEE Syst J* 8(3)
3. Yoo H, Yang U, Sohn K, IEEE Senior Member (2013) Gradient-enhancing conversion for illumination-robust lane detection. *IEEE Trans Intell Transp Syst* 14(3)
4. Rose C, Britt J, Allen J, Bevely D (2014) An integrated vehicle navigation system utilizing lane-detection and lateral position estimation systems in difficult environments for GPS. *IEEE Trans Intell Transp Syst* 15(6)
5. Alghamdia W, Shakshukia E, Sheltamiba TR (2012) Context-aware driver assistance system. *Procedia Comput Sci* 10:785–794
6. Wu CF, Lin CJ, IEEE Member, Lee CY (2012) Applying a functional neurofuzzy network to real-time lane detection and front-vehicle distance measurement. *IEEE Trans Syst Man Cybern Part C Appl Rev* 42(4)
7. Liu Y, Liang Y, Cheng Y (2011) Design and implementation of image acquisition system based on ARM and Linux. In: International conference on electronics and optoelectronics (ICEOE). IEEE
8. Strovnal V, Machacek Z, Hercik R, Slaby R (2010) Intelligent car control and recognition embedded system. In: Proceedings of the international multiconference on computer science and information technology. IEEE, pp 831–836
9. Gaikwad V, Lokhande S (2014) Lane departure identification for advance driver assistance. *IEEE Trans Intell Transp Syst*
10. Kassim AM, James MS, Aras MSM, Rashid MZA (2012) Design and development of vibration method for vehicle reverse system (VRS). *Procedia Eng* 41:1114–1120
11. Agarwal V, IEEE Senior Member, Venkata Murali N, Chandramouli C (2009) A cost-effective ultrasonic sensor-based driver-assistance system for congested traffic conditions. *IEEE Trans Intell Transp Syst* 10(3)

Multimodel PID and RST Controller to Control CSTR Process Using Gain Scheduling Technique

D.A. Tamboli and R.H. Chile

Keywords CSTR · RST · RLS · Multiple model · Gain scheduler

1 Introduction

As the industry is an enlivening field of society and chemical processes such as CSTR are reveal enormously non-linear nature. It changes its properties with load or with respect to time giving a slower reaction, inferior transient response, delayed convergence, and probably may cause an unstable system if proper control action has not taken. The controller should identify such situations and take necessary control action at a faster rate, with high accuracy, and in a stable fashion to have adaptability in its behavior. Robust controllers such as PID are the most common tools, but the controllers tuned at particular operating condition don't give a satisfactory performance in all operating conditions [1] unless the operating boundaries are known well in advance.

To tackle such situation Gao et al. [2] proposed a local model control of CSTR using nonlinear PID controller. A nonlinear MPC and nonlinear PID controller have been proposed by Prakash and Srinivasan [3] to control the concentration of CSTR. In this research, a weighted MPC output has calculated by designing several linear MPC at the various operating point. Vinodha et al. [4] use three control strategies Neural network-based gain scheduled to extract PID parameters, local model MPC and Multiple Models based PID controller. An output Concentration has used as a variable for the scheduler. Manimozhi and Saravanakumar [5] presented Fault Detection and diagnosis using Multi Model Adaptive linear H^∞ filter

D.A. Tamboli (✉)
SVERI's College of Engineering, Pandharpur, India
e-mail: datamboli@coe.sveri.ac.in

R.H. Chile
S.G.G.S. Institute of Engineering and Technology, Nanded, India

(MMALH ∞ F). The author uses gain scheduling technique to estimate the states of nonlinear CSTR in the presence of unknown noise statistics and unmodeled dynamics.

This work mainly focused on controlling the concentration of non-linear CSTR process at large set point changes in MATLAB Simulink. For that firstly the process is represented by Multiple Linear Models at the various operating condition and Multiple PID controllers are designed which takes control action using Gain Scheduling Algorithm based on output concentration. Secondly, Multiple Self-Tuning Regulator (RST) are designed using RLS estimator and Pole Placement controller for each case and demonstrated through simulation results.

The paper organizes as follows: Sect. 2 discusses Modeling of CSTR process. Section 3 presents Multiple Model PID Control Design at Multiple operation points. Section 4 is dealing with the design of Multiple Self Tuning Regulator. Then the gain scheduler strategy is an implementation for CSTR using both controller techniques. Extensive simulation results and discussions are carried out in Sect. 5 followed by conclusion in Sect. 6.

2 Modeling of CSTR Process

A Continuous Stirred Tank Reactor (CSTR) is a highly nonlinear chemical process which mixes two chemicals to turn out a product having concentration $C_a(t)$ and the temperature $T(t)$. In proposed constant volume CSTR, an irreversible, exothermic reaction $A \rightarrow B$ takes place to slow down the reaction by removing the heat with a coolant flow rate $q_c(t)$. Numerical values of CSTR process has specified in [3], and same parameters are taken for the simulation study. The control objective is to maintain the product concentration as per set point changes by manipulating the coolant flow rate $q_c(t)$. The following differential equations are used to model process the [6]:

$$\frac{dC_a(t)}{dt} = \frac{Q}{V}(C_{a0} - C_a(t)) - k_0 C_a(t) e^{\left(-\frac{E}{RT(t)}\right)} \quad (1)$$

$$\frac{dT(t)}{dt} = \frac{Q}{V}(T_0 - T(t)) - k_1 C_a(t) e^{\left(-\frac{E}{RT(t)}\right)} + k_2 q_c(t) \left(1 - e^{\left(-\frac{k_3}{q_c(t)}\right)}\right) (T_{c0} - T(t)) \quad (2)$$

If the steady state behavior of CSTR has studied by linearising it around various equilibrium values of C_a , it observed that CSTR behaves differently at each operating concentrations and the nonlinearities in the second order model give drastic variation in damping factor. For high values of operating points, the responses

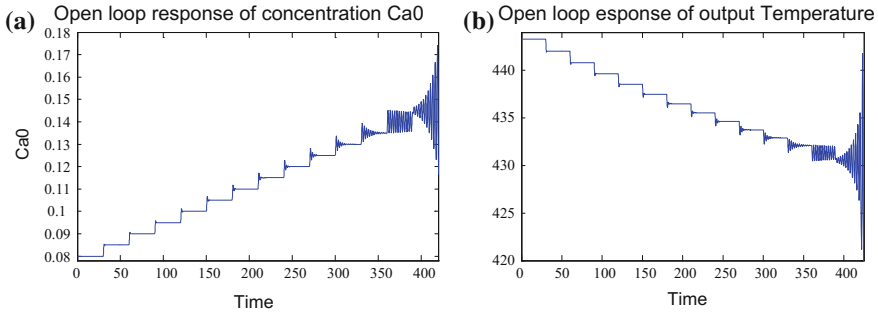


Fig. 1 Open loop **a** Concentration $Ca(t)$. **b** Temperature response $T(t)$ for nonlinear CSTR

become unstable as depicted in Fig. 1 which can overcome by using some adaptive strategy such as gain scheduling control is proposed in successive section, designs Multiple Models at each operating point and a corresponding controller.

3 Multiple Model PID Control Design

This section projects on structuring Multiple PID controllers originated by forming several linear models. The CSTR has linearised at six steady state operating point on the base of output concentration Ca using Eqs. (1) and (2). The global model formed with six local models gives an excellent trade-off between the performance quality and a number of local models. For analysis purpose the CSTR process model is found to be following second order transfer function as follows:

$$G_i(s) = \frac{C_a(s)}{q_c(s)} = \frac{K_i}{s^2 + 2\zeta_i w_{n,i}s + w_{n,i}^2} \quad \forall i = 1 : 6 \quad (3)$$

The calculation of tuned PID parameters is based on IMC tuning using rule suggested by Morari and Zafriou [7]. It accepts following control parameters for each model.

$$K_{c,i} = \frac{2\zeta_i}{w_{n,i}K_{p,i}\lambda}; \quad T_{r,i} = \frac{2\zeta_i}{w_{n,i}}; \quad T_{d,i} = \frac{1}{2\zeta_i w_{n,i}}$$

The process gain, damping factor, undamped natural frequency and PID parameters for all operating conditions has reported in Table 1. It can conclude that lambda (λ), the filter time constant plays a significant role in deciding the performance of the controller. To get optimum robustness and performance the value of lambda is considered as 0.5.

Table 1 Operating points, process gain (K_p), damping factor (ζ) and undamped natural frequency (W_n) and PID parameters for six models

Operating point	K_p	ζ	W_n	K_c, i	Tr, i	Td, i
$Ca_1 = 0.08$ mol/l, $T_1 = 443.309$ K, $qc_1 = 97.264$ l/min	0.00284	0.6535	3.9089	$117.734/\lambda$	0.3344	0.1957
$Ca_1 = 0.09$ mol/l, $T_1 = 440.794$ K, $qc_1 = 100.547$ l/min	0.00327	0.5218	3.592	$88.848/\lambda$	0.2905	0.2668
$Ca_1 = 0.10$ mol/l, $T_1 = 438.544$ K, $qc_1 = 103.406$ l/min	0.00374	0.4029	3.313	$65.033/\lambda$	0.2432	0.3746
$Ca_1 = 0.11$ mol/l, $T_1 = 436.506$ K, $qc_1 = 105.908$ l/min	0.00427	0.2953	3.0591	$45.214/\lambda$	0.1931	0.5535
$Ca_1 = 0.12$ mol/l, $T_1 = 434.641$ K, $qc_1 = 108.104$ l/min	0.00485	0.1934	2.833	$28.151/\lambda$	0.1365	0.9126
$Ca_1 = 0.13$ mol/l, $T_1 = 432.920$ K, $qc_1 = 110.031$ l/min	0.00556	0.0967	2.614	$13.307/\lambda$	0.0740	1.9781

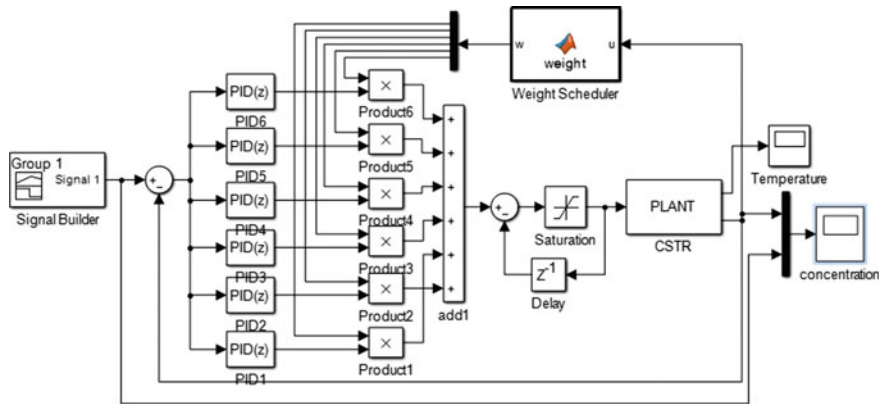


Fig. 2 Block diagram of multiple model PID controller

Weight Scheduler Design

To control CSTR in the wide operating region and getting better transient performance a Gain Scheduling technique is implemented through six PID controller. At every sampling instant certain weight (gain scheduling) has been assigned to each tuned controller based on actual value of measured output concentration [4]. The value of the weight varies between [0–1]. As in this work six operating conditions has been considered, the control signal applied as an input to the plant is a weighted sum of six outputs. The implemented MATLAB Simulink block diagram for Multiple Model PID controller has shown in Fig. 2.

4 Multiple Model Self-tuning Regulator (RST) Design

In Self-Tuning Regulators estimator estimates the parameters of the model online recursively using RLS Algorithm. These estimated parameters and design specifications provided by the designer develops the control law based on Minimum Degree Pole Placement (MDPP) algorithm [8]. At each sampling interval, controller parameters have updated whose Simulink control structure has explained in Fig. 3.

4.1 Recursive Least Square Algorithm

The principle of RLS algorithm is to monitor changes in the behavior of the process in real time by identify the unknown parameters of second order discrete time incremental model for CSTR given in Eq. (4) and form the base for RST controllers [8]. The error in the estimation which is a deviation between actual and estimated output has optimized by the sum of error square. For the nonlinear process, without online estimation, it is intricate to provide zero mean data which is fundamentals requirement of estimation. This condition is because, at each operating point, the steady-state control input and the desired output are nonlinear with each other. The system should energize with a Pseudo Random Binary Sequence (PRBS), a rich frequency content signal.

$$(q^2 + a_1q + a_0)\Delta C_a(k) = (b_1q + b_0)\Delta q_c(k) \tag{4}$$

Here

$$\Delta C_a(k) = (1 - q^{-1})C_a(k) \quad \text{and} \quad \Delta q_c(k) = (1 - q^{-1})q_c(k) \tag{5}$$

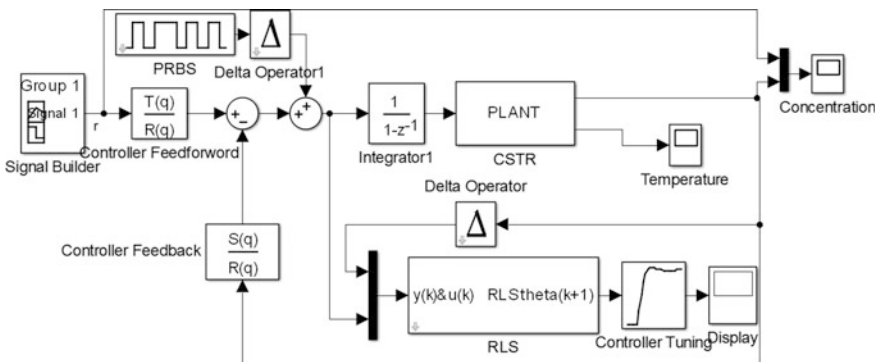


Fig. 3 Simulink schematic of single model pole-placement adaptive controller

Consider a SISO stochastic process with following ARX model for designing Pole-Placement Self-tuning control [8].

$$A(q)y(k) = B(q)u(k) + \varepsilon(k) \quad (6)$$

where $u(k)$, $y(k)$ and $\varepsilon(k)$ are the process input, output, and white noise respectively, and the polynomials in the forward shift operator are $A(q)$ and $B(q)$. Four parameters a_0 , a_1 , b_0 and b_1 of this second-order model can be estimated recursively using Recursive Least Squares algorithm (RLS), with exponential forgetting.

$$\hat{\theta}(k+1) = \hat{\theta}(k) + P(k+1)\varphi(k+1)[y(k+1) - \varphi^T(k+1)\hat{\theta}(k)] \quad (7)$$

$$P(k+1) = \left[P(k) - \frac{P(k)\varphi(k+1)\varphi^T(k+1)P(k)}{\lambda + \varphi^T(k+1)P(k)\varphi(k+1)} \right] \frac{1}{\lambda} \quad (8)$$

where $\hat{\theta}(k)$, $P(k)$ and $\varphi(k)$ are parameter vector, covariance matrix, and regression vector respectively. As the exponential forgetting factor λ in Eq. (8) indicates exponentially discarding in past measurements and plays a vital role in system performance by developing the capability to track variations in dynamically changing behavior. The small value can handle the nonlinearities and fast changes in the system and larger values near to 1 results in slower forgetting, and can be suitable for the slow changing process. Here the value of forgetting factor used is 0.956. The next step is to design control algorithm by using MDPP.

4.2 Self-tuning Pole-Placement Control

The control law to be implemented has given as

$$R(q)u(k) = T(q)r(k) - S(q)y(k) \quad (9)$$

Here $r(k)$, $u(k)$ and $y(k)$ are the set points, input, and output of plant respectively and $R(q)$, $S(q)$ and $T(q)$ are the polynomials of the controller in the forward shift operator. The Diophantine equation for the closed loop characteristic polynomial becomes

$$A_{cl} = A_m(q)A_0(q) = \hat{A}(q)R(q) + \hat{B}(q)S(q) \quad (10)$$

To get optimum time domain performance the specifications to design controller are of natural frequency $\omega_n = 6.35$ rad/min and damping factor = 0.707. Thus

Table 2 Identified models and RST controller parameters

Identified models parameters		Polynomials of R-S-T controller	
Model 1		R1	$1 + 0.521531 q^{-1} + 1.539928e-07 q^{-2}$
a_0, a_1	-1.481725, 0.5999154	S1	$4345.181098 - 5631.236191 q^{-1} + 2038.234522 q^{-2}$
b_0, b_1	0.000182, 0.000154	T1	752.179429
Model 2		R2	$1 + 0.557370 q^{-1} + 1.343996e-07 q^{-2}$
a_0, a_1	-1.580894, 0.687373	S2	$4620.029243 - 6242.777621 q^{-1} + 2347.8183580 q^{-2}$
b_0, b_1	0.000185, 0.000163	T2	725.0699793
Model 3		R3	$1 + 0.587467 q^{-1} + 1.207002e-07 q^{-2}$
a_0, a_1	-1.670005, 0.7653893	S3	$4898.798619 - 6828.205323 q^{-1} + 2636.436198 q^{-2}$
b_0, b_1	0.000187, 0.000171	T3	707.029495
Model 4		R4	$1 + 0.612930 q^{-1} + 1.106776e-07 q^{-2}$
a_0, a_1	-1.74969, 0.834700	S4	$5175.929860 - 7386.877562 q^{-1} + 2906.346473 q^{-2}$
b_0, b_1	0.000187, 0.000176	T4	695.398771
Model 5		R5	$1 + 0.634623 q^{-1} + 1.030865e-07 q^{-2}$
a_0, a_1	-1.820783, 0.896166	S5	$5449.009921 - 7920.479207 q^{-1} + 3159.967222 q^{-2}$
b_0, b_1	0.000187, 0.000180	T5	688.497937
Model 6		R6	$1 + 0.653186 q^{-2} + 9.718747e-08 q^{-1}$
a_0, a_1	-1.884062, 0.950561	S6	$5717.113303 - 8431.256193 q^{-1} + 3399.399844 q^{-1}$
b_0, b_1	0.000186, 0.000183	T6	685.256954

$A_m(q) = q^2 - 1.15q + 0.4074$, $B_m(q) = 0.148q + 0.1094$ and $A_0(q) = (q - 0.006)^3$ is observer polynomial. The controller of lowest degree considering the condition of causality is obtained by solving Eq. (10) to find R(q) and S(q) which is known as minimum-degree solution for polynomial R and S. Polynomial T can be calculated as $T(q) = A_m(1)/B(1)$.

Consequently, six RST controllers for each local model are calculated. The values of identified models and its RST parameters at operating conditions specified in Sect. 3 are summarized in Table 2. A weight scheduling algorithm have intended in the same way as that for PID controller.

5 Simulation Results and Discussions

Two control schemes designed above using Gain Scheduling Technique has implemented for CSTR process for three set point configuration. In the first case small step size of 0.005 mol/l from 0.08 to 0.10 mol/l is implemented where though

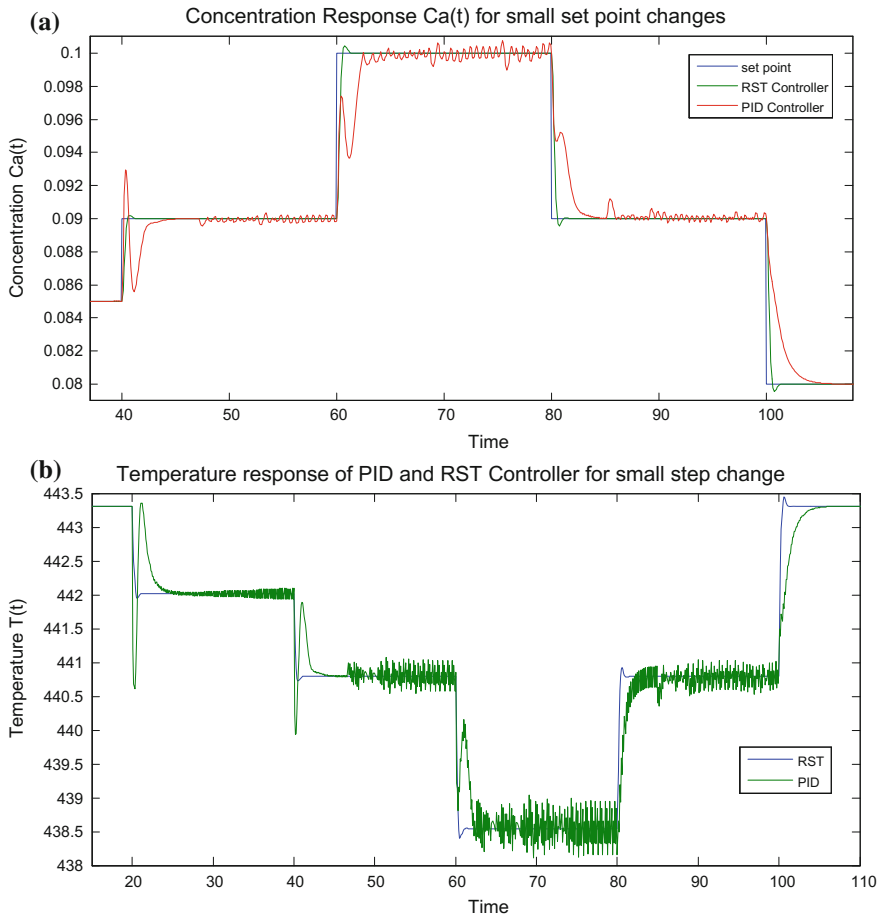


Fig. 4 **a** Concentration. **b** Temperature response of PID and RST controller for small set point changes

both the controllers perform well but the response of RST controller is better regarding peak overshoot and settling time. The concentration and temperature response of the first case has shown in Fig. 4a, b respectively. Figure 5a, b explains the natures of coolant flow rate and temperature response respectively at the various set point of RST controller.

The drastic performance difference is observed in the second scenario when the set point is varied with the step change of 0.01 mol/l over the full range from 0.08 to 0.15 mol/l. The zoomed response of both controllers has observed in Figs. 6 and 7.

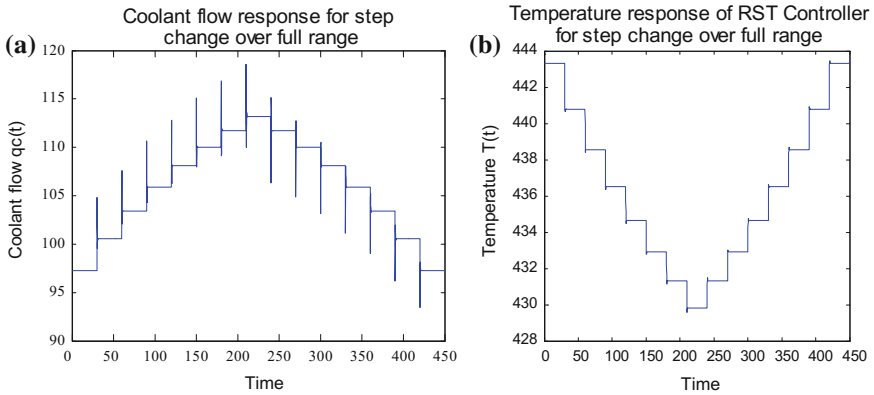


Fig. 5 a Coolant flow rate. b Temperature response of RST controller for various step changes

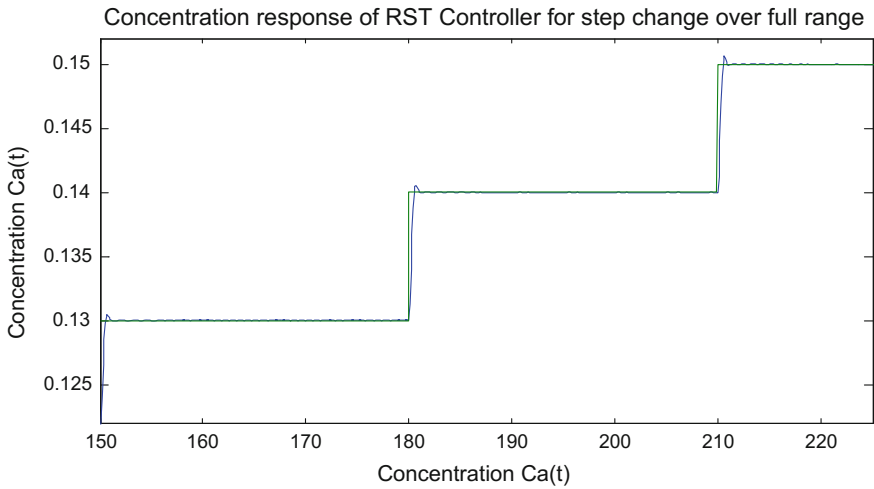


Fig. 6 Zoomed concentration response of RST controller for set point change over full range

Here PID Controller works well up to set point of 0.13 mol/l after which system shows continuous oscillations showing excessive overshoot. The RST controller shows not only minimum overshoot less than 0.6% but also settles to its steady state value within one cycle. In a third configuration large set point change from 0.08 to 0.13 mol/l and 0.08 to 0.15 mol/l are considered where PID deteriorated its performance at a set point around 0.15 mol/l giving constant oscillations.

Table 3 Performance analysis of system for different set point configuration

Set point Ca	PID		RST		Set point Ca	PID		RST	
	Case 1					Case 2			
	% Mp	Ts min	% Mp	Ts min		% Mp	Ts min	% Mp	Ts min
0.085	5.88	5	0.235	1.25	0.09	0.11	6	0.55	1.3
0.09	3.33	2.5	0.22	0.5	0.10	0	2.5	0.50	1
0.10	0	2.5	0.5	0.5	0.11	0.27	2	0.36	0.53
	Case 3				0.12	0.33	1.8	0.33	0.5
0.13	2.31	5	7.69	1	0.13	2.31	2	0.31	1
0.15	33.33	Osc.	14.66	0.9	0.14	2.93	Osc.	0.36	1.5
					0.15	33.33	Osc.	0.40	1.3

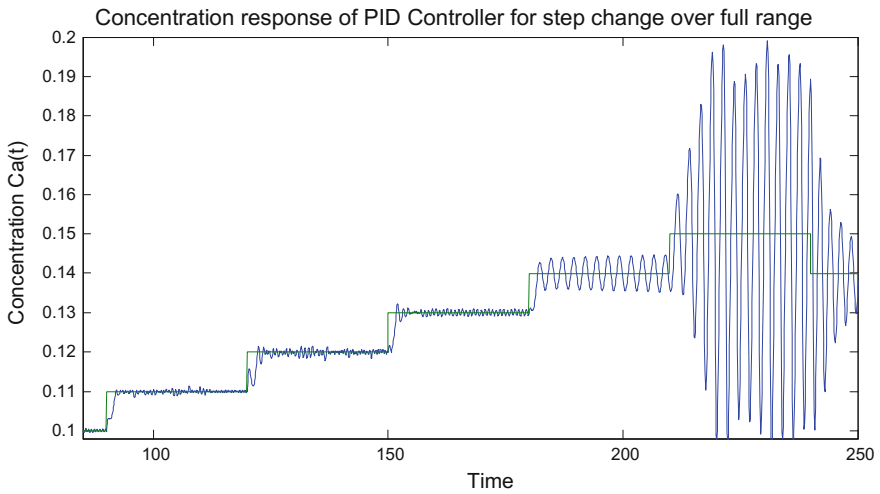


Fig. 7 Zoomed concentration response of PID controller for set point change over full range

Table 3 summarizes transient performance result of all configurations at each set point. As illustrated by Fig. 8a, b though the peak overshoot of RST controller is larger than the previous two configurations but the settling time is negligible and overall performance is much better than PID controllers.

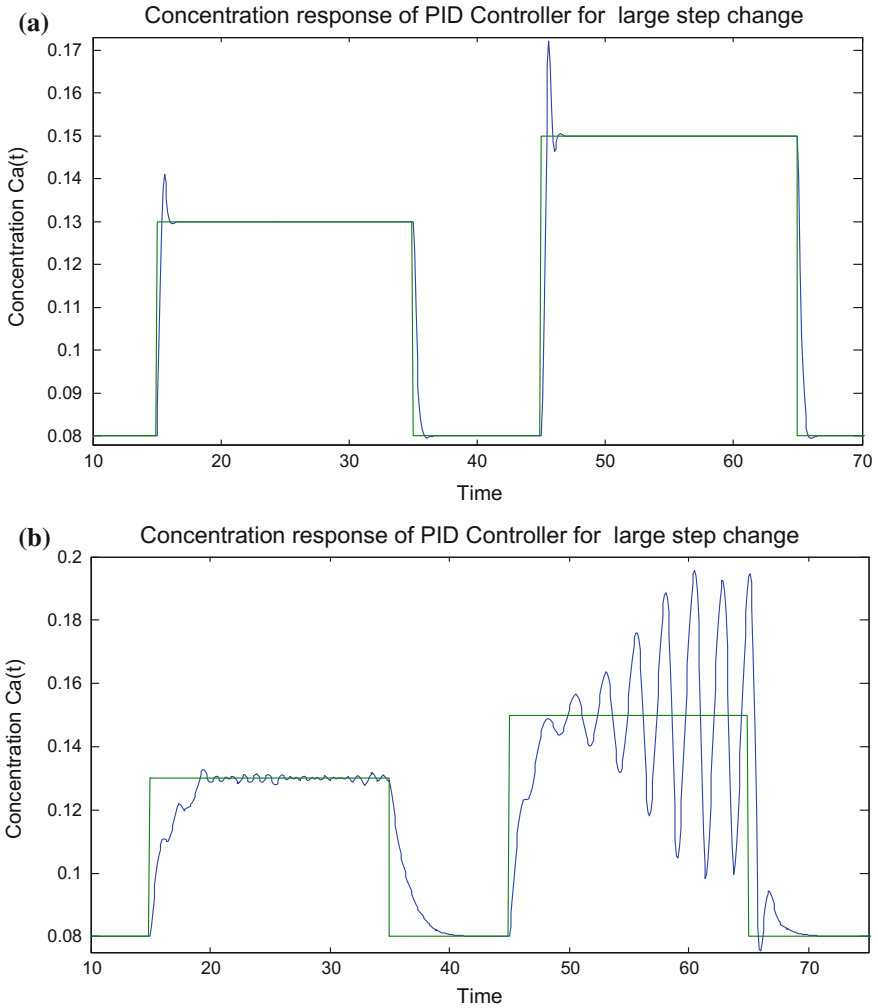


Fig. 8 Concentration response of a RST and b PID and controller for large step changes

6 Conclusion

This simulation study concludes that implementation of adaptive algorithms such as Multiple Model Self Tuning Regulators using Gain Scheduling Techniques is very efficient in handling large set point changes and nonlinearities in the case of chemical process CSTR. The extensive simulation study shows that

MultiModel RST Super performs over Multiple PID giving a better transient performance in term of peak overshoot and settling time. The performance can be further improved by introducing switching strategy in Multiple Model.

References

1. Doyle FJ, Packard AK, Morari M (1989) Robust controller design for a Nonlinear CSTR. *Chem Eng Sci* 44(9):1929–1947
2. Gao R, O'Dwyer A, Coyle E (2002) A nonlinear PID controller for CSTR using local model networks. In: *Proceedings of the 4th world congress on intelligent control and automation*, pp 3278–82
3. Prakash J, Srinivasan K (2009) Design of nonlinear PID controller and a nonlinear model predictive controller for a continuous stirred tank reactor. *ISA Trans* 14(3):273–282
4. Vinodha R, Lincoln S, Prakash J (2011) Design and implementation of simple adaptive control schemes on a simulated model of CSTR process. *Int J Modell Ident Control* 14(3):159–169
5. Manimozhi M, Saravanakumar R (2014) Fault detection and diagnosis in non-linear process using multi model adaptive H^∞ filter. *Int J WSEAS Trans Syst* 13:660–667
6. Bequette BW (2002) *Process control-modelling, design, and simulation*. Prentice Hall PTR, India
7. Morari M, Zafiriou E (1989) *Robust process control*. Prentice Hall, Upper Saddle River
8. Landau ID, Zito AG (2006) *Digital control systems, design, identification and implementation*. Springer, London

Silkworm Eggs Counting System Using Image Processing Algorithm

Sanaha S. Pathan and Avinash D. Harale

Keywords Image acquisition · Preprocessing · Area based thresholding · Object counting

1 Introduction

A center for the production of a large number of silkworm eggs is grainages which provide silkworm eggs to sericulturists and farmers. For producing cocoons with high yields and rich silk content, farmers required disease free commercial seeds [1]. For offering a great opportunity for employment and economic growth to our nation, sericulture organization is to be developed [2]. Production of eggs is labor intensive, and for various processes of egg production, it requires a significant number of laborers.

Manual counting is done with the help of one transparent paper, the transparent paper is covered on DFL sheet then it counts eggs manually with pen or marker by marking on every egg one by one, due to pen quality, eggs may be damaged and grainages cause loss. Continuous counting may cause eye fatigue, headache and dizziness and effects on the accuracy of results. However, the process of counting objects in more quantity is not always trivial or straight forward; even it is performed manually. Most counting methods have a rarity that makes them tricky to take on. For example, the objects may occur in large number, small in size and overlapped to each other making counting tricky and tedious that in cause error also inaccuracy. The manual method must be replaced by computer vision or in hardware installation as the results of manual methods are erroneous and time

S.S. Pathan (✉) · A.D. Harale
SKN, Sinhgad College of Engineering, Korti, Pandharpur, India
e-mail: sanaha.pathan@gmail.com

A.D. Harale
e-mail: haraleavinash@yahoo.co.in

consuming and required extra manpower. Counting is also used for counting cells, vehicle and number of people [3–5].

Pandit et al. [6] present the method for vision based counting system for silk-worm eggs. The method is implemented by using LABVIEW graphical programming environment. Image acquisition, grayscale color conversion and contrast enhancement are used to improve the quality of the image. Top hat filtering is used for removing noise and lightening condition. Adaptive thresholding is applied for image segmentation, after segmentation image is divided into two regions foreground region and the background region. Morphological operation erosion is used for removing unwanted particles. The dual combination of opening and closing is used to filtrate and removing small particles. Connected component method and watershed segmentation these two different methods can be analyzed for segmenting overlapping eggs. For counting eggs, IMAQ count command is applied on the segmented image. The accuracy of results depends on the lighting conditions of background, size of objects and number of erosions to separate connected objects.

Kiratiratanapruk et al. [7] presented a method for analysis silkworm eggs. This method is useful to find out eggs type and objects. The first part is regarding object detection and the second part is classification. In object detection process, an egg color object image is converted into a binary image. After that adaptive thresholding technique is used for separating foreground pixel from the background. For different types of eggs different color conversion system is used. On binary image, morphological erosion operation is performed which calculates only unconnected eggs. For connected region component labeling is applied after that based on centroid value thresholding is applied. In object classification, Gaussian Mixture Model (GMM) is used for the color composition of each type of egg. Using this technique egg quality can be controlled with 86.82, 87.89% accuracy.

Venkatalakshmi and Thilagavathi [8] introduced method for red blood cell counting by using Hough transform. The first step is image acquisition. After that color transformation is performed by converting the original image into HSV, from that HSV based image analyzed saturation component S, S image shows clear and bright objects such as WBC and platelets so that there is easy to distinguish red blood cells. After analyzing segmentation is performed. The morphological operation is useful to describe, region shape and boundaries of the segmented image. After segmentation different Morphological operation is performed on object point and background point which fills small holes present in the binary images. Feature extraction is done using Hough transform, for detection of parametric curves. Equation of Hough transform to find a circle characterized by a center point x_0 , y_0 and radius r by equation

$$(x - x_0)^2 + (y - y_0)^2 = r^2 \quad (1)$$

The last step is the detection of RBC cell and counting of RBC, by using segmentation red blood cell can be detected and by using Hough transform it can easily count red blood cell.

2 Proposed Method

The proposed method is offline eggs counting method, so the database of silkworm eggs which is in the form of DFL sheets are collected from the BAIF Center, Urulikanchan (India). Different types of resolution cameras are used for capturing DFL sample. The image is captured by using Sony digital camera with 15 megapixel resolution, Nokia XL mobile with 8 megapixel resolution camera and Samsung Duos mobile with 8 megapixel resolution cameras. Some sample of DFL sheet is shown in Fig. 1.

Figure 2 is DFL sample image captured by using a digital camera, and for further processing, it is saved in image JPEG format with a suitable size. Figure 2 contains 578 eggs which are calculated by the manual method. Algorithm is analyzed by comparing the manual count of DFL sample with the method developed by using image processing algorithm.

Evolution of image processing algorithm for silkworm eggs counting is very difficult and challenging because some DFL sample has dark background. Some DFL sample has a light background. Every time shape, size, and area occupied by eggs is varying; sometimes more eggs are overlapped. In some DFL sample background, text and dark border present. Illuminating all these difficulties is difficult.

Software used for development of silkworm eggs counting system using image processing algorithm is Matlab 2014. Block diagram of proposed method is shown in Fig. 3.

Detail description of proposed block diagram and information related to every step is explained below.

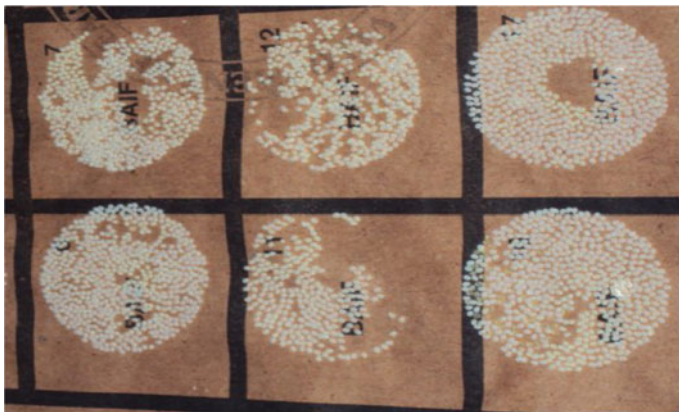


Fig. 1 Sample of DFL sheet with dark background



Fig. 2 Sample of DFL

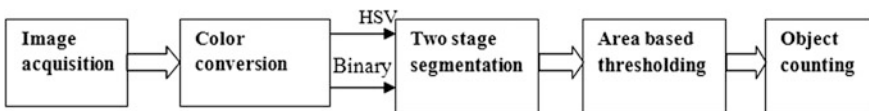


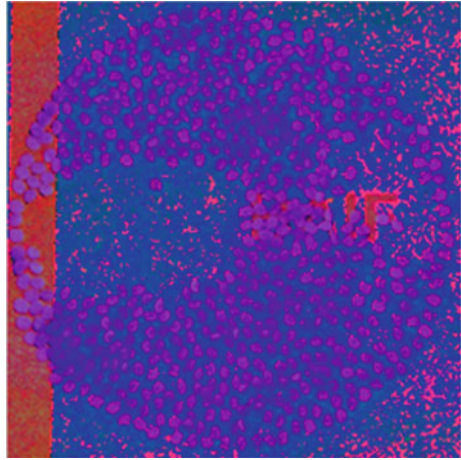
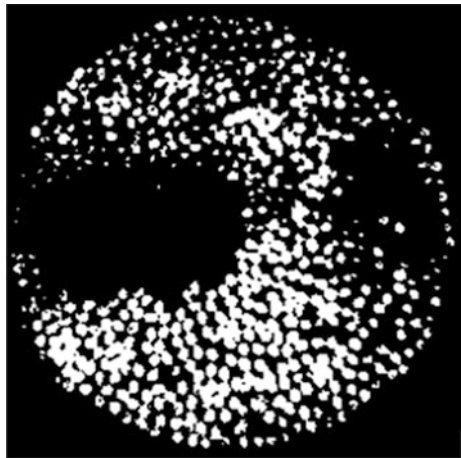
Fig. 3 Block diagram of proposed method

2.1 Image Acquisition

The accuracy of results entirely depends upon brightness, intensity level and quality of acquisition image, so for image acquisition, different types of resolution cameras are used as mention in above section and generate a database with suitable size i.e. 256 verses 256 pixels. Size can be adjusted directly in Matlab by using *imresize* function.

2.2 Color Conversion

RGB color model does not contain useful information for segmentation [8]. So after image acquisition and resized image is converted into HSV color space because of visual properties of HSV color space. HSV color is also useful in content-based image retrieval applications, and HSV color space will give the maximum distance value between background and foreground distinctly as compare with the other

Fig. 4 Colour transformation**Fig. 5** Binary image

color space [5]. Same RGB image converted into a binary image to find out the position of x as well as y coordinate of the white pixel. HSV color transformation image and binary image are shown in Figs. 4 and 5.

2.3 Two Stage Segmentation

For counting a total number of particles, segmentation is useful. Segmentation is used to separate foreground pixels from background pixels [9]. Before two stage segmentation, HSV color information is mapping with a binarized image for determining eggs pixels position. Segmentation is the process of determining egg

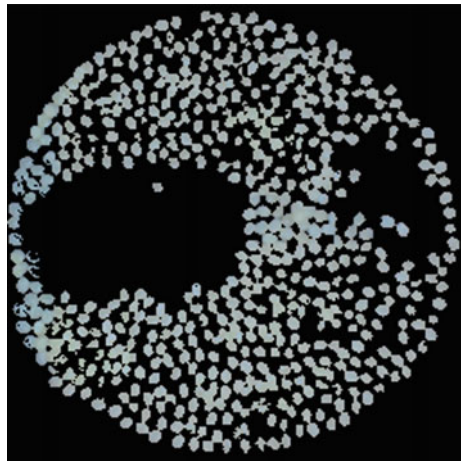
portion and eliminating non-egg portion. For removing non-egg portion from useful information thresholding method is used. The equation for thresholding is below.

$$g(x, y) = \begin{cases} 1, & \text{if } f(x, y) \geq T \\ 0, & \text{otherwise} \end{cases} \quad (2)$$

The threshold value was decided based on the average mean value of HSV information. For calculating the level of local threshold mean value is useful [10]. There are two main approaches of first stage segmentation method. First is eliminating non-egg information and noise and keep pixel information as it is which is related to egg portion. By deciding average mean value thresholding is applied, if average mean threshold value does not meet the threshold value, the pixel is considered as non-egg portion. The second approach is related to determining information related to overlapping eggs. Another thresholding condition based on pixel intensities of HSV image and the original image is used to find out the difference between barriers of pixels and overlapping eggs. After second threshold condition barriers considered as non-eggs portion and it is eliminated, and egg information keeps as it is.

The second stage of segmentation is related to determining individual eggs information. This segmentation stage depends on thresholding method, if the distance between the HSV mapping information and the original image does not satisfy threshold condition then information is not related with individual egg, and it is eliminated. Result collected after two-stage segmentation containing information regarding eggs portion, and non-eggs portion will be removed. After two-stage segmentation, output is segmented image contain the position of individual eggs and overlapping eggs and other portion is dilated. The final segmented image does not contain much information for further processing, so it is converted into a binary image. Effect of two-stage segmentation method is shown in Fig. 6.

Fig. 6 Final segmented image



2.4 Area Based Thresholding

For further analysis of the image, physical information of silkworm eggs is a very essential factor [11]. The area based thresholding is used based on the area of the individual object. For applying thresholding based on area, it is necessary to find out properties of image i.e. perimeter, area, size, distance, pixel list, etc. The threshold value was decided based on comparing the satisfactory result with the different value of the threshold. If the area meets the threshold value, it is considered as fine particles and eliminated, remaining portion contain egg information is used for further egg counting. The result after area based thresholding is shown in Fig. 7.

2.5 Object Counting

Object counting is calculated a total number of objects present in an image; it counts all eggs by considering each egg as an individual object. Based on these final count displayed with above 90% accuracy. The result of counted eggs is shown in Fig. 8.

Fig. 7 Area based thresholding

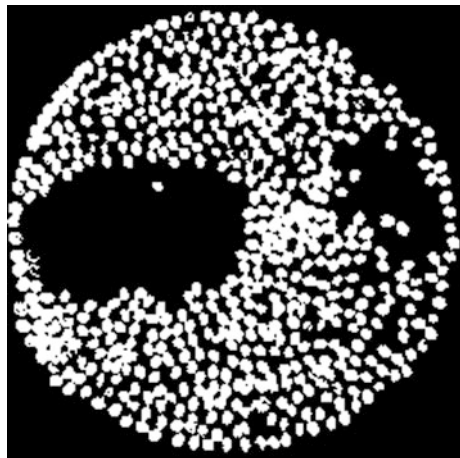


Fig. 8 Object counting

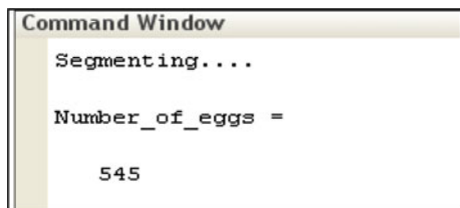


Table 1 Results of proposed method

DFL sheet	Manual count of eggs	Count by silkworm eggs counting algorithm	Percentage of accuracy
1	578	545	95.61
2	530	512	96.6
3	411	385	93.67
4	592	576	97.29
5	630	586	93.01

3 Result and Discussion

The result of proposed method is presented in Table 1 applied to 5 different samples of DFL. Figure 3 contains 545 eggs by using silkworm eggs counting algorithm which is near about manual count 578. DFL sheet 1 from the Table 1 present count of Fig. 2 by using silkworm eggs counting by image processing algorithm.

The proposed method has average accuracy above 90%. The accuracy of counting algorithm was checked out by comparing algorithm count with 10 different DFL's accurate count. After analyzing results, it is observed that in some images, eggs had very small size, they were considered as noise particles. And such eggs are not considered as individual egg or overlapping egg in the determination of two-stage segmentation. In some images, eggs were tightly overlapped so that in segmentation process it's hard to determine overlapping eggs. Some eggs have low-intensity level, so it was below a threshold level and due to this, it was not counted while counting the number of eggs. But proposed method has satisfactory results for a different number of DFL images.

4 Conclusion

This paper presents an image processing algorithm for silkworm eggs counting. Proposed method counted silkworm eggs from a lower quality of images; images contain a watermark, border, also images that have a different background with above 90% accuracy. Counting algorithm is not only useful in sericulture field, but in the medical field and agricultural field also it is useful to count small blood cells and bacteria. The project can also extend in future for hardware implementation based on real-time object counting system.

Acknowledgements I would like to thanks, BAIF research foundation Uralikanchan for supported regarding database of images. I express a deep sense of gratitude and sincere thanks for valuable assistance that I have received from my guide Prof. Avinash D. Harale, I also express gratitude to HOD and all staff of E&TC dept, who guided me, supported me during this work.

References

1. Narasimhanna MN (1988) Manual on silkworm egg production. 1st ed Central Silk Board
2. Directorate of Sericulture. Assam Sericulture manual Khanapara. Guwahati-22
3. Barbedo JGA (2012) Method for counting microorganisms and colonies in microscopic images. In: IEEE, ICCSA, 12th international conference on computational science and its application, Brazil
4. Pornpanomchai C, Stheitsthienchai F, Rattanachuen S (2008) Object detection and counting system. In: IEEE, congress on image and signal processing, Thailand, pp 61–65
5. Prem kumar V, Barath V, Prashanth K. Object counting and density calculation Using matlab
6. Pandit A, Rangole J, Shastri R, Deosarkar S (2014) Vision system for automatic counting of silkworm eggs. ICICES, Chennai
7. Kiratiratanapruk K, Methasate I, Watcharapinchai N, Sinthupinyo W (2014) Silkworm eggs detection and classification using image analysis. IEEE, pp 340–345
8. Venkatalaksmi B, Thilagavathi K (2013) Automatic red blood cell counting using hough transform. In: Chennai, IEEE conference on information and communication technology, pp 267–27
9. Rahman MS, Islam MR (2013) Counting objects in an image by Marker controlled watershed segmentation and thresholding. In: IEEE 3rd international conference on advanced computing, Bangladesh, pp 1251–1256
10. Ramin M, Ahmadvand P, Sepas-Moghaddam A, Dehshibi MM (2012) Counting number of cells in immunocytochemical images using genetic algorithm. In: 12th international conference on hybrid intelligent systems, pp 185–190, Iran
11. Mello CAB, dos Santos WP, Rodrigues MAB, Candeias ALB, Gusmao CMG (2008) Image segmentation of ovitraps for automatic counting of *Aedes aegypti* eggs. In: 30th annual international IEEE EMBS conference Vancouver, British Columbia, Canada, pp 3103–3106

Compression of Medical Images Using Lifting Scheme Based Bi-orthogonal CDF Wavelet Coupled with Modified Set Partitioning in Hierarchical Trees (SPIHT) Algorithm

Surekha S. Koshti and Jyoti A. Kendule

Keywords Lifting scheme · Bi-orthogonal CDF wavelet · MSPIHT · Compression of medical images

1 Introduction

Medical images need a large amount of storage space especially medical images such as magnetic resonance (MR) images, ultrasound images, positron emission tomography (PET) images and computed tomography (CT) images [1]. It is necessary to use compressed images to limit the amount of data to be stored and transmitted. In this paper, we propose the lifting structure algorithm for MRI image compression [2]. This gives better compressing results with good image quality. During this process, the input image is decomposed into wavelet coefficient using lifting based CDF 9/7 bi-orthogonal wavelet transform and the resultant form is encoding using the modified SPIHT algorithm.

2 Lifting Scheme

The lifting scheme is a technique for both designing wavelets and performing the discrete wavelet transform. During the lifting implementation, no extra memory buffer is required. A lifting step can be modified to operate on integers while

S.S. Koshti · J.A. Kendule (✉)
E&TC Department, Sveri's College of Engineering, Pandharpur, India
e-mail: jyotikendule@rediffmail.com

S.S. Koshti
e-mail: surekhakoshti12@gmail.com

preserving the reversibility. The lifting-based wavelet transform consists of splitting, lifting, and scaling modules and the wavelet transform is treated as prediction error decomposition [3]. Let X denote the input signal, and X_{L1} and X_{H1} be the decomposed output signals, constructing wavelets using lifting scheme. Thus consists of three steps.

2.1 Splitting

In this module, the original signal X is divided into two disjoint parts, i.e. $X_e(n) = X(2n)$ and $X_o(n) = X(2n + 1)$ that denote all even indexed and odd-indexed samples of X , respectively [4].

2.2 Lifting

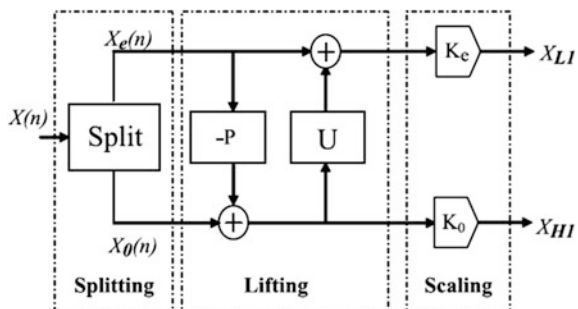
In this module, the prediction operation P is used to estimate $X_o(n)$ from $X_e(n)$ and results in an error signal $d(n)$ which represents the detailed part of the original signal. Then we update $d(n)$ by applying it to the update operation U , and the resulting signal is combined with $X_e(n)$ to $s(n)$ estimate, which represents the smooth part of the original signal.

2.3 Scaling

A normalization factor is applied to $d(n)$ and $s(n)$, respectively. In the even-indexed part $s(n)$ is multiplied by a normalization factor K_e to produce the wavelet sub-band X_{L1} . Similarly, in the odd-index part the error signal $d(n)$ is multiplied by K_o to obtain the wavelet sub-band X_{H1} (Fig. 1).

The lifting-based scheme has several advantages; the computation complexity can be reduced by a factor of two. No auxiliary memory is needed.

Fig. 1 Block diagram of lifting based wavelet transform [3]



3 Bi-orthogonal Wavelets CDF 9/7

Wavelet 9/7 is part of symmetric bi-orthogonal wavelet CDF. The low pass filters associated with wavelet 9/7 have $p = 9$ coefficients in the analysis, $p = 7$ coefficients to synthesize. The coefficients are described in Table 1. They are more symmetrical and very close to orthogonality. It has been widely used by in image coding [5, 6] and used by the JPEG-2000 codec [7].

The Lifting Scheme of the bi-orthogonal transform 9/7 goes through of four steps: two prediction operators and two update operators as shown in Fig. 2 [8, 9].

The following equation describes the four “lifting” steps and the two “Scaling” steps.

$$\begin{aligned}
 X(2n + 1) + (a \times [X(n) + X(2n + 2)]) &\rightarrow Y(2n + 1) \\
 X(2n) + (b \times [Y(2n - 1) + Y(2n + 1)]) &\rightarrow Y(2n) \\
 Y(2n + 1) + (c \times [Y(2n) + Y(2n + 2)]) &\rightarrow Y(2n + 1) \\
 Y(2n) + (d \times [Y(2n - 1) + Y(2n + 1)]) &\rightarrow Y(2n)
 \end{aligned}
 \tag{1}$$

$$\begin{aligned}
 -K \times Y(2n + 1) &\rightarrow Y(2n + 1) \\
 (1/K) \times Y(2n) &\rightarrow Y(2n)
 \end{aligned}
 \tag{2}$$

where the values of the parameters are:

$$\begin{aligned}
 a &= -1.586134342, \\
 b &= -0.0529801185, \\
 c &= 0.8829110762, \\
 d &= -0.4435068522, \\
 k &= 1.149604398.
 \end{aligned}
 \tag{3}$$

Table 1 (a) The analysis filter coefficients. (b) The synthesis filter coefficients

I	Low-pass filter	High-pass filter
<i>(a)</i>		
0	0.6029490182363579 0.6029490182363579	+1.115087052457000
±1	+0.266864118442875	+0.591271763114250
±2	-0.078223266528990	-0.057543526228500
±3	-0.016864118442875	-0.091271763114250
±4	+0.026748757410810	
<i>(b)</i>		
0	+1.115087052457000	0.6029490182363579
±1	-0.591271763114250	-0.266864118442875
±2	-0.057543526228500	-0.078223266528990
±3	+0.091271763114250	+0.016864118442875
±4		+0.026748757410810

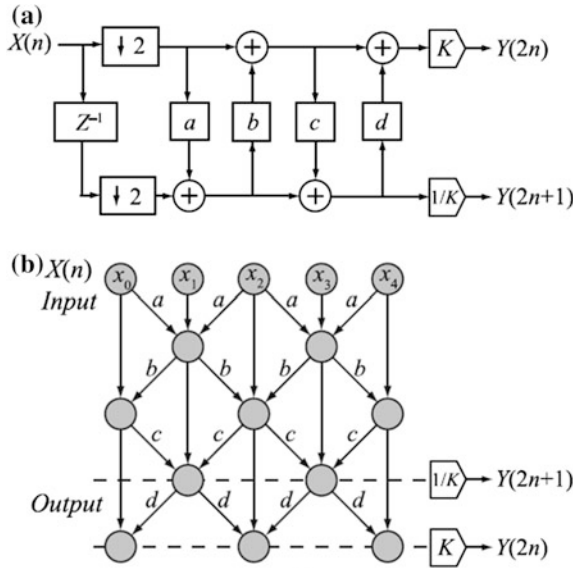


Fig. 2 Split, predict and update steps of forward CDF 9/7 wavelet using lifting scheme [3, p. 226]. **a** Lifting implementation of the analysis side of the CDF 9/7 filter bank. **b** Structure of the CDF 9/7

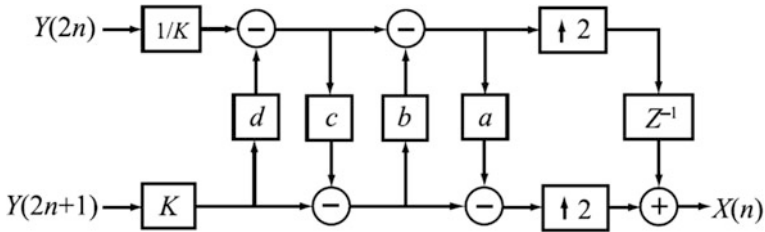


Fig. 3 Lifting implementation of the synthesis side of the CDF 9/7 filter bank [3, p. 226]

The synthesis side of the filter bank simply inverts the scaling and reverses the sequence of the lifting and update steps. Figure 3 shows the synthesis side of the filter bank using lifting.

4 MSPIHT

SPIHT is Set Partitioning in Hierarchical Trees. It is a method of coding and decoding the wavelet transform of an image. It has three lists to store the values. They are List of Insignificant Pixels (LIP), List of Significant Pixels (LSP), List of

Insignificant Sets (LIS) [10]. In SPIHT, the usage of three temporary lists is quite memory consuming. In the proposed MSPIHT algorithm, the sorting pass and the refinement pass are combined as one scan pass. Modified set partitioning in hierarchical trees is based on prior scanning and ordering the coefficients. The coefficients or sets were sorted according to the number of surrounding significant coefficients before being coded. The previous significant coefficients were refined as soon as the sets around which there existed any significant coefficients had been scanned. The scanning order was confirmed adaptively and did not need any extra storage.

5 Compression Quality Evaluation

The Peak Signal to Noise Ratio (PSNR) is the most commonly used as a measure of the quality of reconstruction in image compression. The PSNR are identified using the following formulae

$$PSNR = 10 \log_{10} \left(\frac{(\text{Dynamics of image})^2}{MSE} \right). \tag{4}$$

Mean Square Error (MSE) which requires two $M \times N$ gray scale images I and I^\wedge , where one of the images is considered as a compression of the other is defined as:

$$MSE2 = \frac{1}{M \times N} \sum_{i=1}^{i=M} \sum_{j=1}^{j=N} ((I(i,j) - I^\wedge(i,j))^2) \tag{5}$$

Compression Ratio (CR) is the ratio of the size of compressed data set to the size of the original image. It measures the ability of data compression.

$$CR = \frac{\text{Size of compressed image}}{\text{Size of original image}} \tag{6}$$

6 Results

Lifting based wavelet transforms considered is CDF 9/7. All the Classical wavelets produced less PSNR around 30 dB [11]. The lifting-based wavelet transforms produced high PSNR and compression ratio. The original size of the image is in MB (Fig. 4; Table 2).

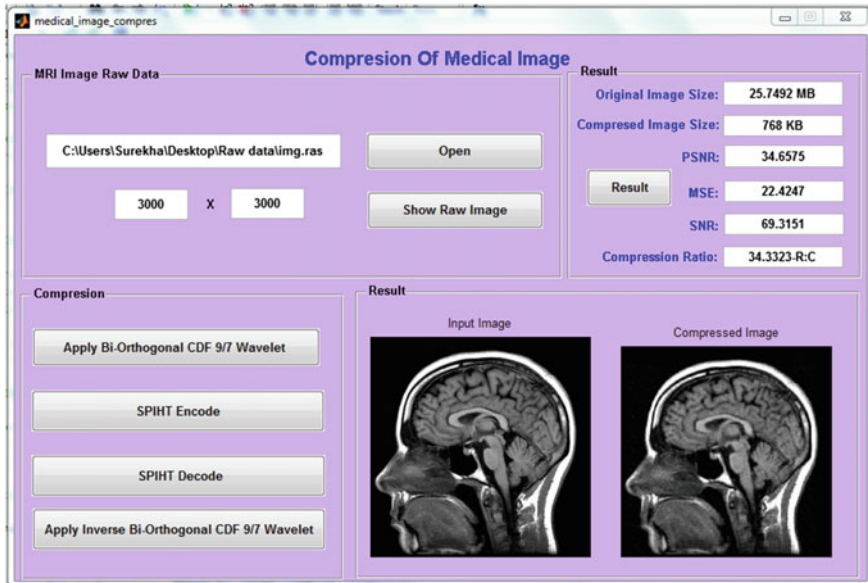
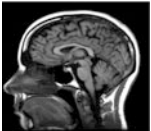
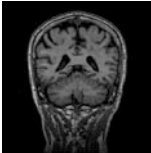
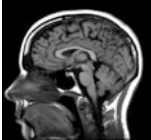



Fig. 4 Screen shot of GUI (MATLAB)

Table 2 PSNR and CR of medical images are given below

Image	Original size (MB)	Compressed size (KB)	PSNR	CR	MSE	SNR
	25.7492	768	34.6575	34.3323R:C	22.4247	69.3151
	46.3964	768	37.3092	61.8619R:C	12.1775	74.6184
	71.8693	768	34.6778	95.8257R:C	22.3205	69.3555
	106.5983	768	33.8371	142.1311R:C	27.0874	67.6743

References

1. Anitha E, Kousalya Devi S (2015) Squeezing of medical images using lifting based wavelet transform coupled with modified SPIHT algorithm. *Int J Innov Res Sci Eng Technol* 4(6) (An ISO 3297: 2007 Certified Organization)
2. Beladgham M, Bessaid A, Abdelmounaim ML, Abdelmalik TA (2011) Improving quality of medical image compression using biorthogonal CDF wavelet based on lifting scheme and SPIHT coding. *Serb J Of Electr Eng* 8(2)163–179
3. Beladgham M, Bessaid A, Moulay-Lakhdar A, Ben Aissa M, Bassou A (2010) MRI image compression using biorthogonal CDF wavelet based on lifting scheme and SPIHT coding. *Quatrième Conférence Internationale sur le Génie Electrique CIGE'10*, 03–04 Novembre 2010, Université de Bechar, Algérie
4. Miaou SG, Chen ST, Chao SN (2003) Wavelet-based lossy-to-lossless medical image compression using dynamic VQ and SPIHT coding. *Biom Eng Appl Basis Commun* 15 (2003):235–242
5. Said A, Pearlman WA (1996) A new fast and efficient image codec based on set partitioning in hierarchical trees. In: *IEEE transaction on circuits and systems for video technology*, vol 6, pp 243–250
6. Villasenor JD, Belzer B, Liao J (1995) Wavelet filter evaluation for image compression. *IEEE Trans Image Process* 4(8):1053–1060
7. Sharma N, Agarwal A, Khyalia PK (2014) Squeezing of color image using dual tree complex wavelet transform based preliminary plan. *Signal Image Process Int J (SIPIJ)* 5(3)
8. Pau G (2006) Advanced wavelets and space-time decompositions; application to video coding scalable. Ph.D. thesis, National school of Telecommunications, Paris
9. Savakis A, Carbone R (2005) The discrete wavelet transforms core for image processing applications. In *Proceedings of SPIE-IS and T electronic imaging, SPIE*, vol 5671
10. Nikhil SJ (2014) Image compression using lifting based wavelet transform. *Int J Eng Res Technol (IJERT)* 3(2). ISSN: 2278-0181
11. Abdullah MS, Subba Rao N (2013) Image compression using classical and lifting based wavelets. *Int J Adv R Comput Commun Eng* 2(8)

Various Traditional and Nature Inspired Approaches Used in Image Preprocessing

Sarika Deokate and Nilesh Uke

Keywords OCR · Segmentation · Feature extraction · Preprocessing · Nature inspired optimization

1 Introduction

Due to the globalization, it becomes very necessary to digitize the each and every document/record. As the number of users and documents are increasing it is becoming very crucial to preserve these records digitally. So the historical documents can either printed or handwritten are digitized for future availability. For this purpose OCR systems are becoming very popular. Many issues need to consider at the time of construction of OCR e.g. writing style, language strokes in writing etc.

The concept of OCR started around 1929 with the first idea. At that time it was a dream to have a machine to read the hard documents. But actual concept became realization after computer evolution i.e. after 1950. Very initially the images were captured with a mechanical rotating disk with photomultiplier. It was bit slow and costly. Subsequently research was improved towards fast OCR.

Nature has tremendous aspects to learn like healing technique to come out of the problem, problem solving in optimized way, learning new methods and techniques by its own, and self disciplined working. Nature itself takes care of utilization of available resources in effective manner. So the researchers used the nature concept to get optimized or best result for the available problems and successfully implemented and got the best result for many complex problems.

In this paper the traditional techniques are discussed with nature inspired optimization algorithms, which are used for image processing e.g. binarization, edge detection, segmentation etc.

S. Deokate
JJT University, Jhunjhunu, Rajasthan, India

N. Uke (✉)
Pimpri Chinchwad College of Engineering, Pune, India
e-mail: nilesh.uke@gmail.com

2 Pre-processing

It is very necessary to do the pre-processing of the documents like document enhancement, binarization, normalization etc. As there is lot of noise in the image so need to remove it. There may be a variance (rotation, transformation, and scale), dots, and spots in the image due to the scanning [1, 2]. Following methods are implemented in the pre-processing.

2.1 *Layout Analysis/Zoning*

The documents available for processing are having their own structure with lot of ambiguities e.g. misalignment of document, noise in the document, overlapping of characters, issues at the time of scanning, available background etc. Like this many other factors we have to consider at the time of document pre-processing. Local analysis gives the region of interest from the scanned image.

2.2 *Line Removal*

The different type of lines are removed from the document with different font style size and type. Text line detection and removal is done for avoiding confusion between the background lines and the original text. There are many methods have been developed for the removal of line from the document [2].

2.3 *Enhancing the Document (Cleaning and Smoothing)*

Scanning document image may contain a lot of noise, due to the scanner resolution, broken words/characters, or the methods used for binarization. Due to this problem it may degrade the recognition process, which can be avoided using the enhancing and smoothing methods. Smoothing methods include the removing of the gaps, repair the broken characters etc. the different methods used here are zoning, thinning, smoothing, normalization.

In addition to smoothing, pre-processing usually includes normalization. The normalization is applied to obtain characters of uniform size, slant and rotation. To be able to correct for rotation, the angle of rotation must be found. For rotated pages and lines of text, variants of Hough transform are commonly used for detecting skew. However, to find the rotation angle of a single symbol is not possible until after the symbol has been recognized [2-4].

2.4 *Thresholding/Binarization*

All the color or greyscale document images are converted to either greyscale or binary form for better and accurate result. Main purpose of thresholding to find out the pixels of interests [ROI]. In this method the original foreground pixels (region) will be true or 0 and background pixels (region) will be false of 1 [5, 6]. Multi-plane thresholding is one of the technique used for the region matching and segmentation of the object.

Tuba et al. invented the method of fireworks algorithm for the multilevel image thresholding. As the firework explodes, a shower of sparks fills the local region near about the firework. Author evaluate the system proving the better result over Particle swarm intelligence, cuckoo search and differential evolution using the kapoor's entropy indicator [7].

2.5 *Deskewing*

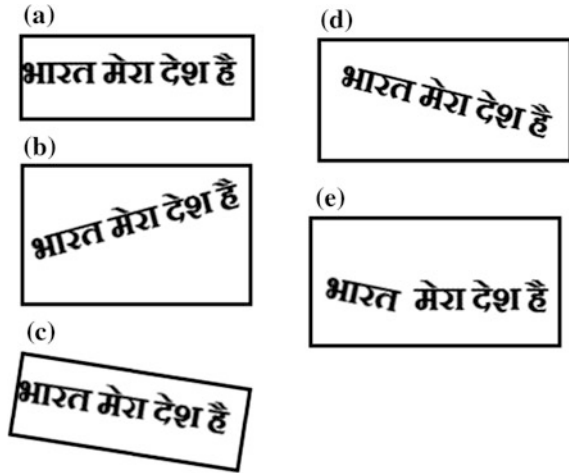
Skew is defined as the angle of falsehood in the given image or recognized word. Several times the angle of the document image gets rotated at the time of scanning or some skew is there in the words due to the writing style. Thus, before applying further pre-processing methods, it essential to de-skew the document. If there is skew in the word, then word is rotated in either clockwise or anticlockwise or by specific angle to correct it. Normally Hough transformation method is developed for deskewing the document and words [4]. Nowadays huge research is going on the implementation of the nature inspired algorithm in different areas.

A Roy et al. proposed the candidate path to perform both Skew detection as well as the segmentation. This candidate path is nothing but a graphical path which is generated using the segmenting points obtained from the handwritten patterns of bangla letters. Around 150 dataset is referred for skew detection and correction of handwritten bangla script [8]. Biological Cell model is proposed to detect the skew by detecting local orientation perceptron [9] (Fig. 1).

2.6 *Despeckle*

There can be a number of spots or dots in the original or scanned document. It very essential to remove these positive and negative spots from the image and smooth the edges.

Fig. 1 Skew detection and correction



2.7 Normalization

Before applying classification, the document is normalized to its customary position. The angle of skew (rotation) need to be detected before applying any standardized method. Normalization is done to get uniformity in size, length, angle, and strokes. Hough transformation method is used to detect the rotated/skewed angle. Different algorithms are used like KNN, moments, cross correlation PCA and many more [4, 6].

2.8 Character Segmentation

Once we get the separate words from the document it is important task to separate out the characters for finalization and then individually recognized. We need to apply the methods for removing overlapped or connected characters, differentiating the text and graphics objects, removing noise from text. Vertical and horizontal pixel projection methods used by many researchers for the character segmentation [2, 10]. Edge detection is one of the main methods accepted for the segmentation purpose.

2.8.1 Edge Detection

In 2015, Yongsheng Pan et al. proposed the bacterial foraging base (BFED) edge detection algorithm in cell image segmentation to track the bacteria. They have checked and evaluated this system against Canny, Verma's algorithm, active

contour model and SUSAN algorithm to detect the edges of cell images. As per the author's result edge detection is done more effectively and accurately using the BFED [11].

Dawson et al. proposed the ant colony optimization on GPU with combination of CUDA to perform the parallel task to improve the speed [12]. In [13], researchers used the Multi threading based Ant colony optimization (ACO) with the concept of Multi threading and semaphore on multiprocessor. It is less complex and time consuming compared to ACO.

3 Character Recognition

Actual identification of segmented characters is done in character recognition. To recognize the segmented characters we need a strong database with us, else it will create a false result. Clustering, feed forward, back propagation ANN methods are used for character recognition. There may be chances of false recognition in letters like 6 or 9 p or Q 1 or 7 in, Hindi क and फ, च and ज, ब and व, भ and म. The different methods used are explained here.

3.1 *Template/Matrix Matching*

In this method a number of character object images are collected. In this stage the dissimilarity or similarity measure is calculated between each extracted character template T_i and the already saved image S_i in the database. Threshold is set to check the perfect similarity match. The template with highest similarity is separated, if similarity measure is above a specified threshold then character is classified, else it is discarded [14].

3.2 *Feature Extraction*

The main aim of the feature extraction is to identify the features and then apply the suitable method for the extraction of objects from the image. The obtained features are used as input to the classification process. In feature extraction, the global or local neighbourhood method is used to find the feature region e.g. size, shape, statistical properties etc. [1, 2]. This process improves the accuracy at the time of object recognition. Researchers used binary bat algorithm in image processing for feature selection [15], classification, image matching (Fig. 2).

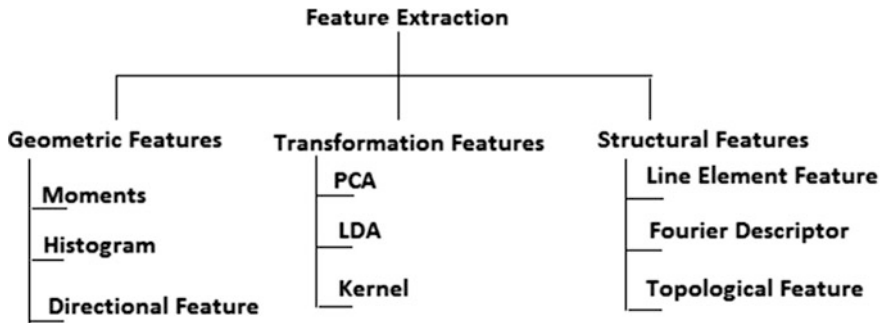


Fig. 2 Feature extraction methods

3.2.1 Moments

In feature extraction methods, shape is also considered as one of the main feature. Moments e.g. Zernike moment, central moment, Tcheblchef moment provide the methods for recognizing the character's or object's scale, rotation variance/ Invariance and translation. The number of different nonlinear functions were developed by Hu for geometric moments [6].

Zernike Moments: Zernike moments are used by many researchers for character recognition of mainly greyscale image. These moments can be used for two dimensional image patterns. Zernike moments are used to check the angle of rotation of any object, to recognize the object from the given shape etc.

3.2.2 Histogram

Greyscale or binary image can be represented using a function $f(x, y)$ i.e. the pixel values can be represented on X and Y axis in given vector plane. Histogram is used as one of the method for structural analysis. Histogram method can be used for line and word segmentation. It consists of two types (1) Horizontal Projection (2), Vertical Projection [10, 14].

3.2.3 Hough Transform

IT is a global process to find out the curves, straight line, or any specific shape from images with the huge amount of data. Hough transform method is used for detecting lines, separating the noise as well as to detecting and correcting skew. It uses a Hough space with distance d , a line with an angle of T . It consists of two methods of Hough Transform (1) Randomized Hough Transform, (2) Standard Hough Transform. Hough transform method is also used for detecting the text lines [2, 4].

3.2.4 Fourier Descriptors

It is very necessary to take out the required object shape from the given image. Many methods are available for retrieving the shapes from the image. Fourier descriptor is one of the efficient method used for this. It define the shape in terms of frequency domain. Fourier Descriptors are used to encode the 2D image shape by considering its boundary. Inverse Fourier transform can be used to get the original shape. The complex valued vector is used to calculate the edge pixel coordinates of a given shape. The properties of Fourier transform are inherited by Fourier descriptor like scaling, invariance, rotation [6].

3.2.5 Orientation Features

In every language the words and characters consists of curves, lines, or different shapes. Orientation of the writing word plays an important role in OCR. In each and every language human writing style is different and hence need more concentration on the orientation to differentiate the words and characters. To achieve this stroke orientation angle is divided into one range and it is considered as feature value. Histogram can be used to represent these type of features. The different ways to find out the orientation are contour chaincode, stroke segment and skeleton orientation [2, 6].

3.2.6 Topological Features

In topological features it consists of the features related to topological properties like boundaries, connectedness of image object. In OCR the segmentation paths can be calculated using the linking feature points on the word skeleton. These feature points are (1) Branch Points, (2) End Points, (3) Cross Points [2].

4 Conclusion

Many algorithms are implemented from the decades for image processing. But nature inspired algorithms are creating the revolution in the computer systems. In this paper we provided the number of algorithms used for the different task of image processing mostly on OCR. Nature inspired algorithms—Bio inspired algorithms like Ant Colony optimization, Bat algorithm, Fireworks algorithm, Flower pollination etc. are used in preprocessing feature extraction of images. Mainly these algorithms are used for the optimization and having huge scope in the future.

References

1. Trier I, Jain AK, Torfinn T (1996) Feature extraction methods for character recognition—a survey. *Pattern Recognit* 29(4):641–662
2. Vamvakas G, Gatos B, Stamatopoulos N, Perantonis SJ (2008) A complete optical character recognition methodology for historical documents. In: *The eighth IAPR workshop on document analysis systems 2008 IEEE*. 978-0-7695-3337-7/08
3. Seethalakshmi R, Sreeranjani TR, Balachandar T (2005) Optical character recognition for printed Tamil text using unicode. *J Zhejiang Univ Sci* 6A(11):1297–1305
4. Jundale TA, Hegadi RS (2015) Skew detection and correction of Devanagari script using hough transform. *Procedia Comput Sci* 45(2015):305–311
5. Nürogiannis K, Gatos B, Pratikakis I, Senior Member IEEE (2013) Performance evaluation methodology for historical document image binarization. *IEEE Trans Image Process* 22(2):1057–7149
6. Cheriet M, Nawwaf K, Liu CL, Suen CY (2007) *Character recognition systems a guide for students and practioners*. Wiley, New York. ISBN 978-0-471-41570-1
7. Tuba M, Bacanin N, Alihodzic A (2015) Multilevel image thresholding by fireworks algorithm. In: *Radioelektronika (RADIOELEKTRONIKA), 2015 25th international conference*. 978-1-4799-8117-5
8. Roy A, Bhowmik TK, Parui SK, Roy U (2005) A novel approach to skew detection and character segmentation for handwritten Bangla words. In: *Digital imaging computing: techniques and applications DICTA IEEE 2005*. 0-7695-2467-2/05
9. Liu X, Cao Z, Ai K, Jiao J, Tan M (2014) A general image skew detection approach with a bio-inspired mechanism. In: *Proceeding of the 11th world congress on intelligent control and automation Shenyang, China, June 29–4 July*. 978-1-4799-5825-2/14
10. Bansal V, Sinha RMK (1998) Segmentation of touching characters in Devanagari. In: *Proceedings CVGIP Delhi*, pp 371–376
11. Pan Y, Zhou T, Xi Y (2015) Bacterial foraging based edge detection for cell image segmentation. In: *Engineering in medicine and biology society (EMBC), 2015 37th annual international conference of the IEEE 25–29 Aug 2015*
12. Dawson L, Stewart IA (2014) Accelerating ant colony optimization-based edge detection on the GPU using CUDA. In: *2014 IEEE congress on evolutionary computation (CEC), Beijing, China, July 6–11*. 978-1-4799-1488-3/14
13. Aslam A, Khan E, Beg MMS (2015) Multi-threading based implementation of ant-colony optimization algorithm for image edge detection. *IEEE INDICON 2015*. 978-1-4673-6540-6/15
14. Choudharya A, Rishib R, Ahlawat S (2013) A new character segmentation approach for off-line cursive handwritten words. In: *Information technology and quantitative management (ITQM2013) Procedia Computer Science*, vol 17, pp 88–95
15. Yang XS (2014) *Nature-inspired optimization algorithms*. Elsevier Science Publishers, Amsterdam, pp 141–154

FPGA Based Adaptive Filter for Removal of Electromyogram Noise from Electrocardiogram Signal

A.M. Kasture, S.S. Sathe, M.A. Deshmukh and A.A. Jadhav

Keywords Adaptive filter · Xilinx system generator (XSG) · ECG signal · MIT-BIH database · Simulink · Electromyogram (EMG)

1 Introduction

Coronary heart disease (CHD) is the measure cause of death in India, which may become a grave problem in future. CHD is caused by a narrowing of the coronary arteries that supply blood to the heart, and sometimes it may result in a heart attack. Each year, about millions humankind, suffers from the heart attack. About half of those deaths occur within 1 h of the start of symptoms and before the person reaches the hospital. Hospitalization and possibly intensive care is required at that time [1]. Continuous ECG monitoring as well as removing of noise component from ECG signal is required for providing best treatment to a patient immediately, because life-threatening arrhythmias (irregular heartbeats) is the leading cause of death in the first few hours of a heart attack.

ECG is a very important biomedical signal. Typical ECG signal is shown in the Fig. 1. For the correct diagnosis, the ECG trace should be free from noise. ECG signal may be corrupted by various kinds of sound. For meaningful and accurate detection, steps have to be taken to discard all these noise sources, which is termed as filtering of the ECG. The best performance of an ECG processing system can achieve if input data is free from noise. Electromyogram noise consists of Muscle contraction, Electromagnetic interference, etc. Due to muscle contraction million volt potential gets generated. The signal resulting from muscle contraction can be assumed to be transient bursts of zero mean band limited Gaussian Noise. Electromyogram (EMG) interferences produce rapid fluctuation which is very faster

A.M. Kasture (✉) · S.S. Sathe · M.A. Deshmukh · A.A. Jadhav
Electronics and Telecommunication, SVERI COE, Pandharpur, Maharashtra, India
e-mail: amkasture@coe.sveri.ac.in

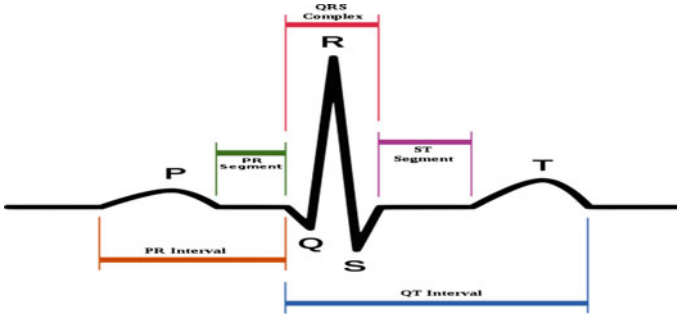


Fig. 1 Schematic of normal ECG waveform

than ECG wave. Its frequency content is DC to 10 kHz and duration is 50 ms. Electrosurgical noise can completely destroy ECG signal. It is represented by a large amplitude sinusoid with frequencies approximately between 100 kHz and 1 MHz [2, 3].

Digital filters play a very significant role in the analysis of the frequency components in ECG signal [4]. Adaptive filters are digital signal processing systems, which are stable systems, in which automatic coefficient is adjusted using feedback system. Distributed algorithms are preferred over traditional algorithms because they can greatly reduce hardware size utilization and which results in high-speed execution. They are widely used in recent FPGA digital signal processing to achieve the Adaptive digital filter to become very real needs [5, 6].

2 Proposed System

2.1 MIT-BIH ECG Database

In the present work ECG signal required for analysis is collected from Physionet MIT-BIH Arrhythmia Database where annotated ECG signals are described by a text header file (.hea), a binary file (.dat) and a binary annotated file (.atr). Header file consists of detailed information such as the format of ECG signal, type, and the number of ECG leads, patient's history, the number of samples, sampling frequency, and detailed clinical information. The database contains 48 records, each of the record is slightly over 30 min long. Each record is sampled at 360 Hz frequency with a resolution of 11 bits [4]. The sample data file 100.dat from MIT-BIH arrhythmia database is extracted and considered as $s(k)$ be the original ECG signal with no noise and noise $n(k)$ to be added to the ECG signal, to make noisy ECG signals $x(k)$ before it is received for analysis or information extraction, which is

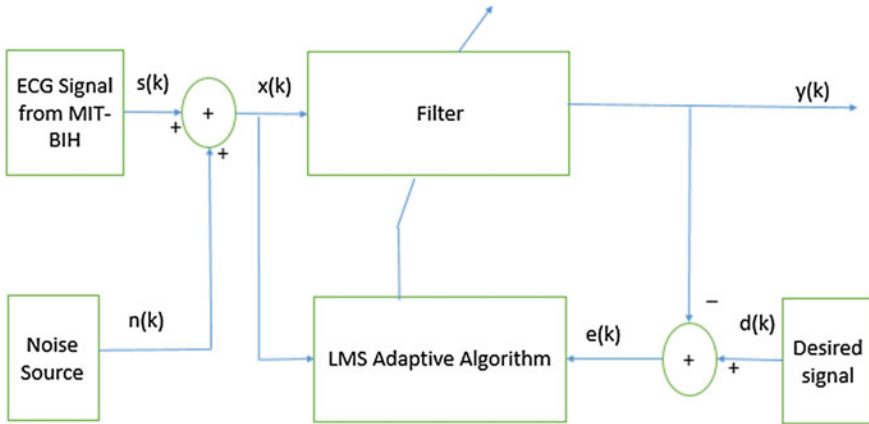


Fig. 2 A typical adaptive filter block diagram

shown in Fig. 2. The purpose of the procedure of de-noising is to extract original ECG signal from $s(k)$ from noisy ECG signal $x(n)$ so that it can be used for intended purposes.

2.2 LMS Adaptive Algorithm

LMS Algorithm is used more among different algorithm for automatic updating coefficients of an Adaptive filter because of its low computational processing tasks and high robustness. Windrow and Hoff in 1960 developed this algorithm.

$$W(k + 1) = w(k) + 2\mu * e(k) * X(k) \tag{1}$$

$$e(k) = d(k) - y(k) \tag{2}$$

$$y(k) = \sum_{i=0}^{N-1} w(j, k) * x(k - j) \tag{3}$$

where, $W(k) = [(w(0, k)), (w(1, k)), \dots, (w(N - 1, k))]$ is the filter coefficients at time n , $X(k) = [(x(k)), (x(k - 1)), \dots, (x(k - N+1))]$ are the last N samples the reference input at time n , $e(k)$ is error signal at output side, $d(k)$ is desired or reference signal and μ is a positive parameter controlling the stability and the convergence speed. A larger value for μ can increase the convergence speed, but smaller value can assure better stability.

3 Implementation Techniques

To implement, Xilinx system generator software version 14.2 is used. This software installs the Xilinx block sets required for hardware implementation in Matlab-Simulink Library Browser. Figure 3 shows the Adaptive Filter implementation using Xilinx system generator tool. IN and OUT block decides the boundary of hardware. Clean ECG is taken from MIT_BIH which is added with electromyogram noise. The simulation was done on SIMULINK available with MATLAB (2013). Equation (5) is used to calculate SNR of filtered signal $e(k)$ at the output side, mean square error (MSE) is calculated from (6) and (4) is used to calculate SNR of input signal $x(k)$ at the input side. Figure 3 shows Adaptive filtering using Xilinx system generator tool. Adaptive Filter implementation using Spartan-3s400pq208-4 board and Xilinx system generator tool is shown in Fig. 4. Detailed internal structure of first order Adaptive filter is shown in Fig. 5.

$$SNR = 10 \log 10 \frac{\sum_{i=0}^N x(k)^2}{\sum_{i=0}^N n(k)^2} \tag{4}$$

$$SNR = 10 \log 10 \frac{\sum_{i=0}^N e(k)^2}{\sum_{i=0}^N (x(k)^2 - e(k)^2)} \tag{5}$$

$$MSE = \sum_{i=0}^N (x(k)^2 - e(k)^2) \tag{6}$$

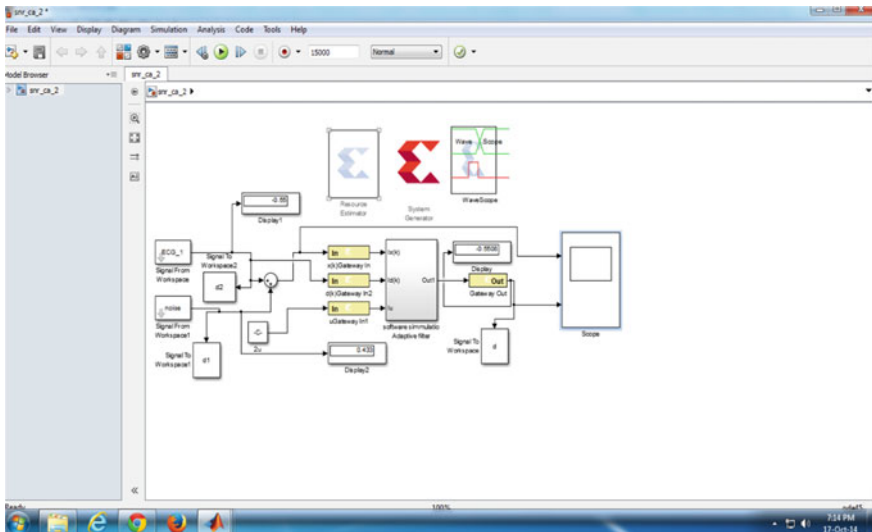


Fig. 3 Adaptive filter implementation using Xilinx system generator tool

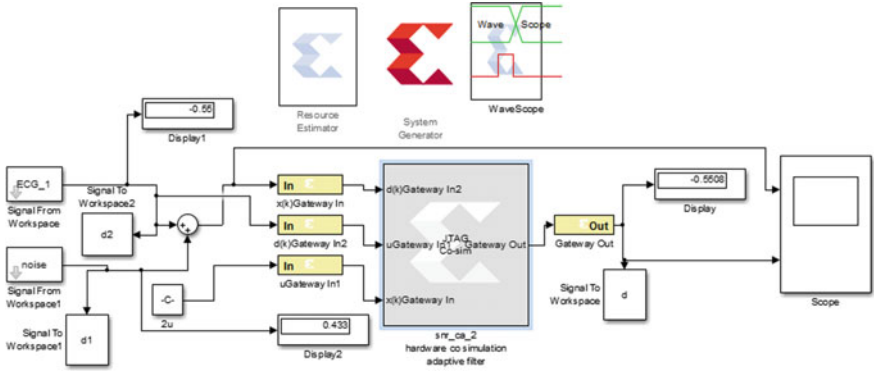


Fig. 4 Adaptive Filter implementation using Spartan-3s400pq208-4 board and Xilinx system generator tool

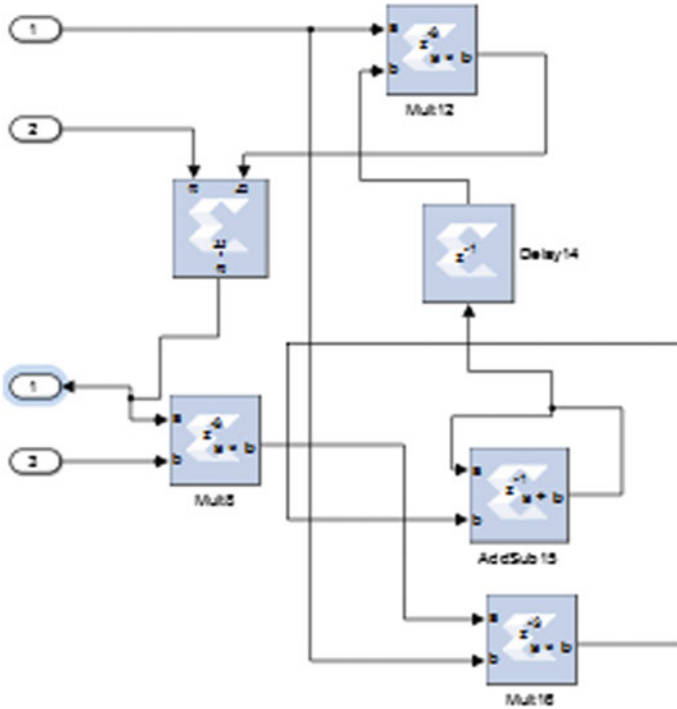


Fig. 5 First order detailed the architecture of LMS-based adaptive filter sub-system

4 Results and Discussion

Clean ECG is taken from MIT_BIH which is added with Electromyogram noise. The simulation was done on SIMULINK available with MATLAB (2013b). Figure 6 shows results of Adaptive filter implemented on Xilinx system generator. Within Fig. 6 above graph shows input signal which is mixed with Electromyogram noise and lower graph shows filtered ECG signal. Similar results obtained on hardware using Spartan-3s400pq208-4 board, as shown in Fig. 7. Table 1 and

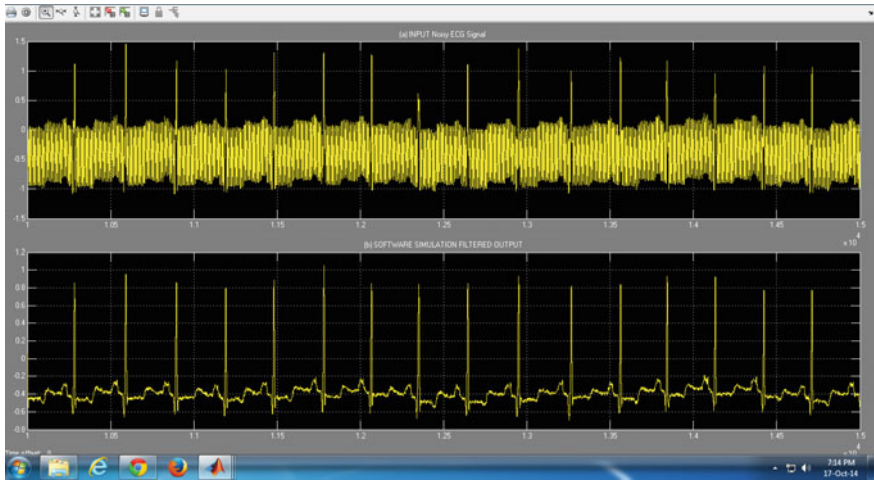


Fig. 6 Adaptive filtering results implemented on software simulation

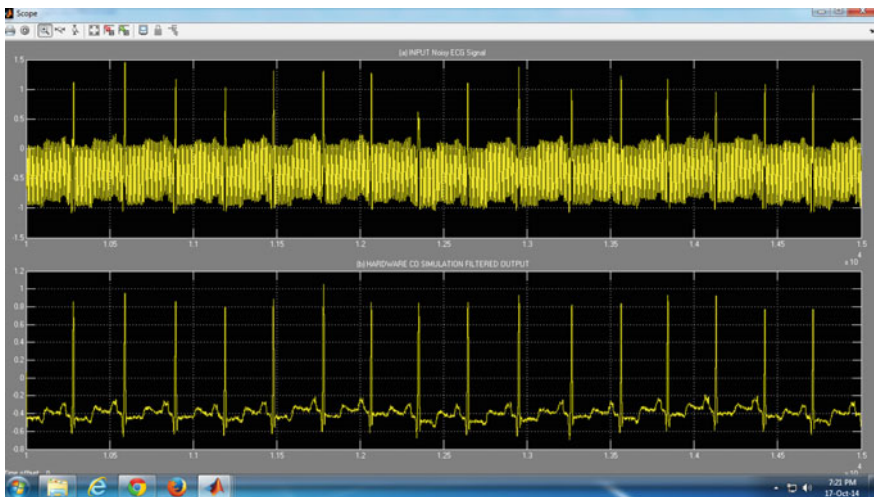


Fig. 7 Adaptive filtering results implemented on hardware co-simulation on Spartan-3s400pq208-4 board

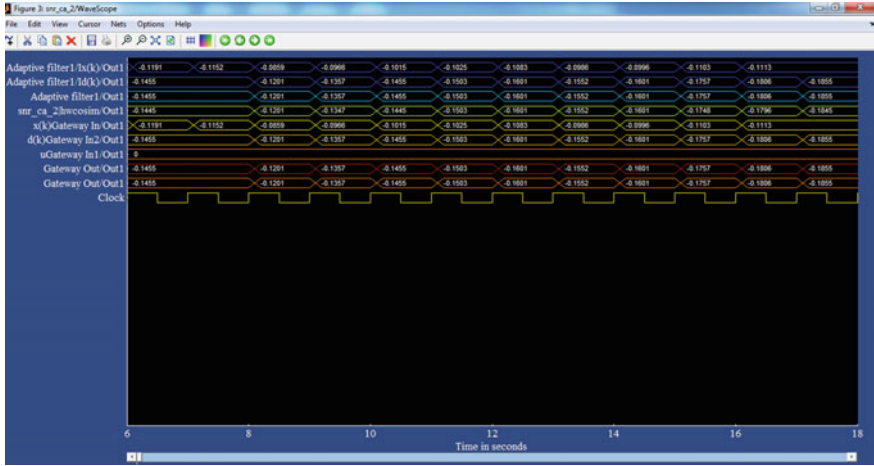


Fig. 8 The result of adaptive filtration on wave scope of system generator

Table 1 shows comparison for the different order of adaptive filter

Sr. No.	Adaptive filter order	1	2	3	6	Available on Spartan-3
1	Number of slice flip flops	100	197	303	603	7168
2	Number of 4 LUT inputs	93	164	231	408	7168
3	Number of occupied slices	92	154	237	442	3584
4	Number of logic containing only related logic	92	154	237	442	442
5	Number of logic containing unrelated logic	0	0	0	0	442
6	Total number of 4 input LUTs	93	164	231	408	7168
7	Number used as logic	81	140	207	384	
8	Number used as shift register	12	24	24	24	
9	Number of bonded IOBs	49	49	49	49	141
10	Number of MULT 18 × 18s	3	5	7	13	16
11	Number of BUGFMUXs	1	1	1	1	8
12	Power utilization(mW)	66	68	70	74	-
13	SNR(db) at output side	26.678	26.678	26.678	26.678	-
14	SNR(db) at input side	0.760	0.760	0.760	0.760	-
15	MSE	4.83	4.83	4.83	4.83	-
16	Average fan out of non-clock nets	1.93	1.63	2.00	2.04	-

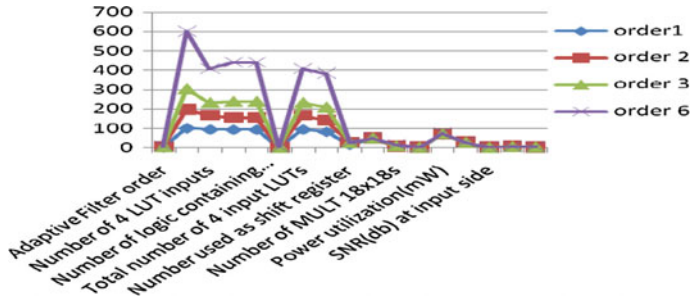


Fig. 9 Graph showing different resources required for different order

Fig. 9 show the comparison of the different order of LMS Adaptive Filter for a different parameter. The result of Adaptive filtration using wave Scope of System Generator is shown in Fig. 8. Figure 10 Represents Distribution of total path delay.

From Table 1 it can be analyzed that first order Adaptive filter effectively removes the low-frequency Baseline noise without distortion of the ECG signal. Higher order Adaptive filter design increases the number of filter coefficient which leads to the large memory requirement and problems in hardware implementation. In lower order, fewer components are required as compared to the higher order.

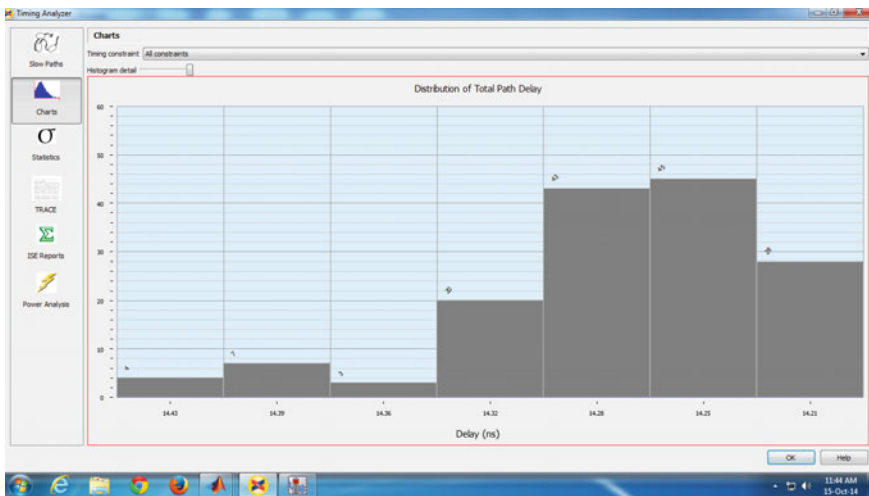


Fig. 10 Distribution of total path delay

5 Conclusion

In this research paper, the implementation of LMS Adaptive using FPGA and Xilinx system generator tool has been introduced. It has been investigated that, first order Adaptive filter is producing the same SNR as it producing to higher order. To measure the performance of de-noising, SNR of processed ECG is calculated, and MSE was determined to find the degree of mismatch between noisy ECG and filtered. The designed Adaptive filter works excellent in removing Electrocardiogram noise. From Table 1 and Fig. 9, it can be analyzed that first order Adaptive filter which provides same SNR, MSE, requires less power and utilizes less hardware component as compared to higher order Adaptive filter. So, first order Adaptive filter is efficient as compared to the higher order.

References

1. Bhogeshwar SS, Soni MK, Bansal D (2014) Design of Simulink Model to denoise ECG signal using various IIR & FIR filters. In: IEEE international conference on reliability, optimization and information technology-ICROIT 2014, India, 6–8 Feb 2014, pp 477–483
2. Bagha SBS (2013) Removal of 50 hz powerline interference for quality diagnosis of ECG signal. *Int J Eng Sci Technol* 5:1149–1155
3. Leelakrishna M, Selvakumar I (2013) FPGA implementation of high speed FIR low pass filter for EMG removal from ECG. *Int J Eng Res Technol* 2(5):855–863
4. Youssef SM (2011) Analysis of non-stationary electrocardiogram signals using iterative wavelet decomposition. In: IEEE international conference on mechatronics and automation, 7–10 Aug 2011, Beijing, China, pp 1125–1130
5. Vullings R, de Vries B, Bergmans Jan WM (2011) An adaptive Kalman filter for ECG signal enhancement. *IEEE Trans Biomed Eng* 58 (4):1094–1103
6. Chang C-H, Chang K-M, Ko H-J (2011) Removal of random noises for electrocardiogram (ECG) signals using adaptive noise canceller without reference input. *Int J Phys Sci* 6 (24):5699–5705

Feature Extraction of Surface EMG Using Wavelet Transform for Identification of Motor Neuron Disorder

Archana Bhaskarrao Sonone and Suvarna S. Chorage

Keywords Amyotrophic lateral sclerosis (ALS) · Electromyography (EMG) · Motor nerve unit (MNU) · Motor nerve disorder (MND) · sEMG (surface EMG)

1 Introduction

Human body consists of large number of many bundles of muscle fibers. These are arranged functionally into different individual motor unit activated by nerve impulse provided by the nerve impulse by the brain's nervous systems. These impulse travels through the whole length of muscle fiber spread in the body. Small electric currents are generated by these muscle fibers during muscle force production. The electromyography (EMG) signal which is an electrical responses generated in the form of electric pulses from the contraction and relaxation of bundles of muscles throughout the body. Surface EMG (sEMG) is an electrical signals associated with the upper layer surface of muscle activity which is controlled by motor nerve unit control of brain [1]. It gives the information in the form of electrical impulses about the various muscle activities in the body. This sEMG signals recording are of two different types. First one is recording with a surface electrodes and second one is insertion needle electrode so called intra electrode. By applying conductive elements or electrodes to the skin surface surface EMG recording is done. sEMG signals contain important information related to the activity, status of health, and the characteristics of muscles. There are two categories of EMG signals which are (1) Surface EMG (sEMG), (2) Intramuscular EMG (iEMG). In sEMG collection of muscle information from the uppermost layer surface of muscle. Whereas in a the case of iEMG collection of information is done from the deep inside the muscles in the body. To get qualitative information from surface EMG signal, different ways of different time domain, frequency domain and time-frequency domain methods have

A.B. Sonone (✉) · S.S. Chorage
Department of Electronics & Telecommunications,
BVs College of Engineering for Women, Pune 411043, India
e-mail: archanasonone19@gmail.com

been analyzed. EMG is an important nerve disorder diagnostic tool used to identify many nervous disorders [1]. ALS is among those MND category. ALS stands for Amyotrophic Lateral Sclerosis, which is a pro-gressive neurodegenerative disorder which affects the muscular activities of the body due to change in the muscle action configuration [1]. As the surface EMG signal is used widely in many fields including engineering as well, it is the obvious inspiration for the exploration of some more effective methods to extract the different features of surface sEMG and reduce the error rate in the process of diagnosis. The Electromyography (EMG) signal is playing an important role in medical field and technology field applications [2]. The EMG is nothing but an electrical activities in the body. The classification of EMG is necessary so as to use EMG signal as diagnostic tool for the motor nerve disorder patients. For the classification of different MND diseases, feature extraction of sEMG is very important. These Feature extraction techniques are based on wavelet transforms [1, 2].

The rest of the paper has been arranged as, in the next section which is Sect. 2, the work related is stated. Section 3 explains the methodology of the identification using feature extraction. The Sect. 4 talks about the results obtained in the process and it's analysis which is in the terms of discussion. In the last Sect. 5 conclusions is stated.

2 Related Work

A. Time-Frequency Domains sEMG Signal Analysis

Complicated time variation pattern is present in the sEMG signal. Hence to classify them directly based on time variation pattern of the sEMG signal will not be the reliable method as by seeing the complicated sEMG and classifying them directly on the bases of difference in the appearance in the waveform will not be the correct way. Time variation significance features in the sEMG signal of normal person and ALS patients is not uniquely distributed. Hence to differentiate the time variations of normal and ALS patient's sEMG, energy content in different frames of the sEMG signal are to be first calculated. Energy distribution in the frames of sEMG in both normal and ALS patients is to be calculated. RMS values of amplitude corresponding to the ALS patients fluctuates very abruptly in the initial and final frames as compares to normal persons sEMG [1, 3]. The middle portion of the frames remains constant in both the cases of normal and ALS patients. In normal person sEMG database values do not change abruptly but it changes very abruptly in ALS patients' sEMG database. Therefore for the correct comparison between normal and ALS class sEMG middle portion should be taken into consideration [1]. Hence middle portion of frames are taken into consideration for the analysis. Useful information is concentrated in the low frequency region of the sEMG hence low pass filter is to be used to extract the specific useful information which will be used

for classification of the normal and ALS patients [1]. Hence low pass filtered signal will be the right method for the feature extraction for the classification of the normal and ALS patients. ZCR which is one of the most important time domain feature is well accepted in medical technology and has simple methodology of calculating it [1]. Along with time domain features a frequency domain features are also used for classification. Mean frequency, which is one of the frequency domain, obtained using Fast Fourier Transform (FFT) is also used to analyze sEMG of normal and ALS patient.

B. Wavelet Domain Feature of sEMG Signal

The discrete Wavelet transform (DWT) is a technique that represents both time and frequency domain. It is capable of representing a signal in two dimensional function of time and frequency. DWT has many advantages over conventional frequency domain transform methods. DWT has multi-dimensional localization in both time and frequency domain. The DWT has features of good frequency resolution at low frequencies and good time resolution at high frequencies. Wavelet transform has low computational efforts and ease of implementation [1]. While analyzing the signal DWT offers different frequency bands with different resolutions. Low frequency region in the sEMG signals, is the more important part than the high-frequency content. Hence our region of interest is low frequency ranges where DWT would give high resolution which would be very beneficial while analyzing the sEMG for the identification and classification. The DWT coefficients having higher values are utilized as features to distinguish between the both class [1, 4].

C. KNN Classification

KNN is used for pattern recognition. There are many pattern recognition algorithms but will be using KNN for classification. KNN stands for k-nearest neighborhood algorithm (KNN). KNN has very simple method of classification and most reliable and simple method of classification of objects based on closest training of samples. This algorithm is based on the learning and which is the instance-based learning or lazy learning. The KNN classifier is used for the classification of the sEMG data into two classes based on the time and frequency domain features [5].

3 Methodologies

A. Wavelet Transform

Wavelet transform is a powerful tool for biomedical signal processing because it can process non stationary and time varying in nature signals. Wavelet transform technique is of two types. (1) discrete wavelet transform (DWT), (2) continuous wavelet transform (CWT). We have chosen DWT because our application is real time engineering application. In discrete wavelet transform technique, it iteratively transforms interested real time signals into multi-resolution subsets of coefficients of wavelet transform.

B. Different Features

- (1) Mean Absolute Value (MAV): It is also known as average rectified value (ARV), averaged absolute value (AAV), integral of absolute value (IAV). MAV feature is an average of absolute values of the EMG signal amplitude.
- (2) Root Mean Square (RMS): Root mean square (RMS) is one of the well known features in analysis of the EMG. It is the mean value of square rooted values of the signal.
- (3) Waveform length (WL): Waveform length (WL) describes the complexity of the EMG signal. It is the cumulative length of the EMG waveform over the particular time period segment.
- (4) Zero Crossing Rate (ZCR): The zero-crossing rate is the rate of sign-changes in any signal. Means the rate at which the signal changes from positive amplitude to negative amplitude or vice a versa. In some cases only the “positive-going” or “negative-going” crossings are counted, rather than counting all the crossings—since, logically, between a pair of adjacent positive zero-crossings there must be one and only one negative zero-crossing and vice a versa. Hence it is sufficient to count either positive or negative going edge in any signal rather than counting both the edges unnecessarily.
- (5) DWT coefficients: As we are using 3 level decomposition in our wavelet transform for feature extraction, maximum valued co-efficient will be used as feature. Coefficients of high pass filter are the values of DWT coefficients. Greater value among them will be used as feature of EMG frames to identify the difference in the normal EMG and the ALS EMG [1]. For both the datasets normal and MND we are using KNN classifier to extract the above said features.

C. Evaluation Using Graphs

Different features of EMG frames are shown in the form of line graph and stem graph. In the line graph, amplitude feature can be clearly evaluated. Here we have shown baseline removed signal, low pass filter and high pass filter coefficients stem graph, DWT coefficient graph for every EMG frames in the both normal and ALS patients.

4 Results and Discussions

We have taken EMG database of 30 normal male and 15 normal females of age between 22 and 35 having normal body shape. For ALS patients also we have taken 30 male and 15 female EMG database. Amplitude in case of ALS EMG frames fluctuates more as compares with normal EMG frames. Mean frequency is higher in ALS EMG as compares to normal person EMG. Various graphs for the extracted features are shown in the graphs as bellow. Figure 1 shows the baseline removed signal in normal EMG. Baseline removing process is important in feature extraction process to as to remove any errors introduced in the signals. If in the signal acquisition process signal is shifted then it is necessary to bring the signal to the

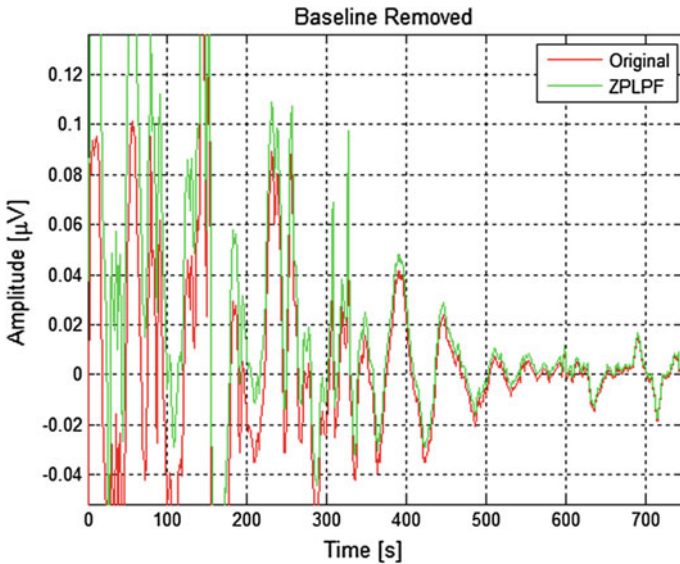


Fig. 1 Baseline removed normal EMG

original baseline. Hence it is necessary part of our study. Figure 2 shows the frequency plot in normal EMG. It shows the frequency distribution of EMG signal in normal as well as in MND patients. Figure 3 shows the MATLAB result of normal matched class. Here as we have used the database for normal and MND patients which included 45 person in each class. Hence we have programmed in MATLAB to classify the signal being tested in two categories. Figure 3 shows that MATLAB result only. Figure 4 shows decomposition of low pass filter. Figure 5 shows decomposition of high pass filter (Figs. 6, 7 and 8).

Fig. 2 Frequency plot in normal EMG

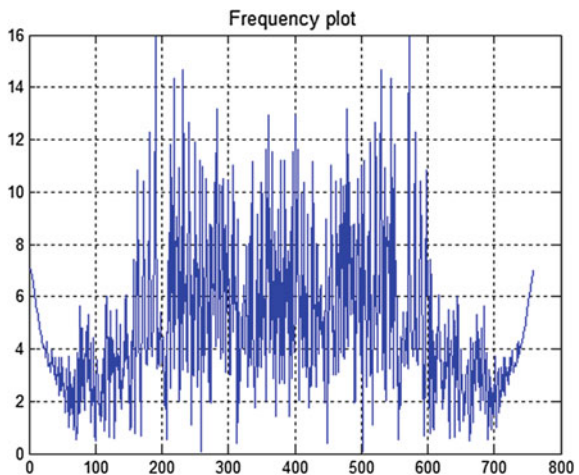


Fig. 3 Result of normal matched class

```
Mean frequency is 190
MAV is 1.038117e-01
Root Mean Square is 2.063552e-01
Waveform Length is 774
Energy of D1 is 4.174631e-01
Energy of D2 is 3.058429e+00
Energy of D3 is 1.993445e+01
Energy of D4 is 3.572913e+01
Energy of C4 is 4.086053e+01
ZCR rate is 5.092105e-01
Matched Class is NORMAL
```

Fig. 4 Decomposition of low pass filter

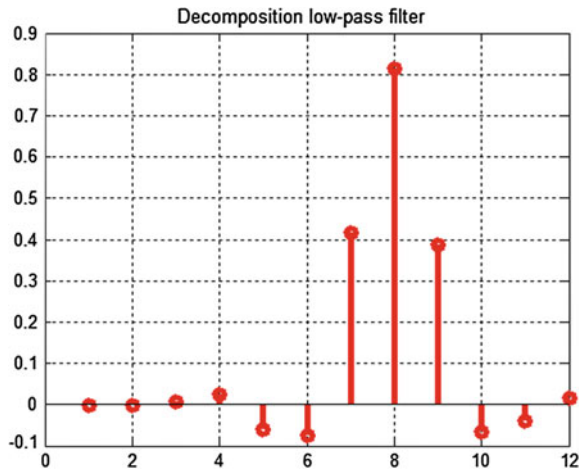
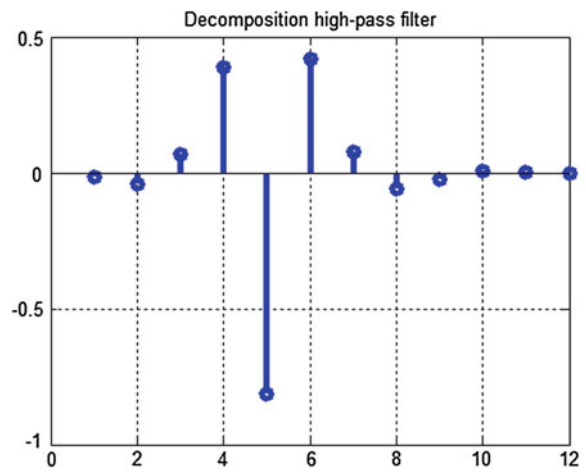


Fig. 5 Decomposition of high pass filter



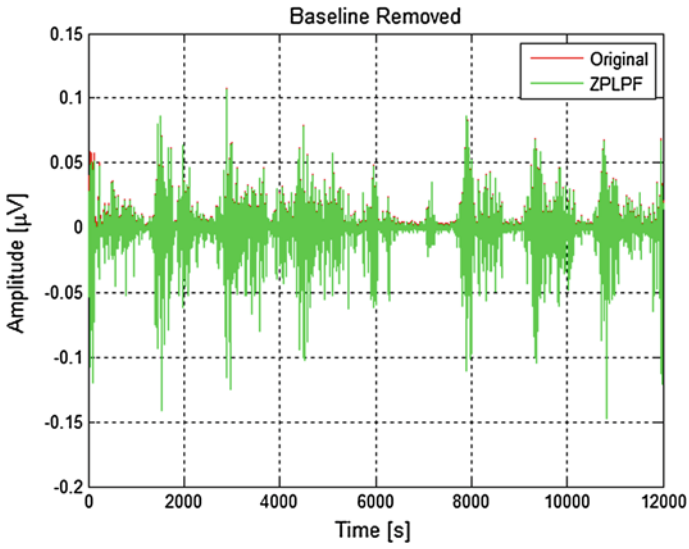
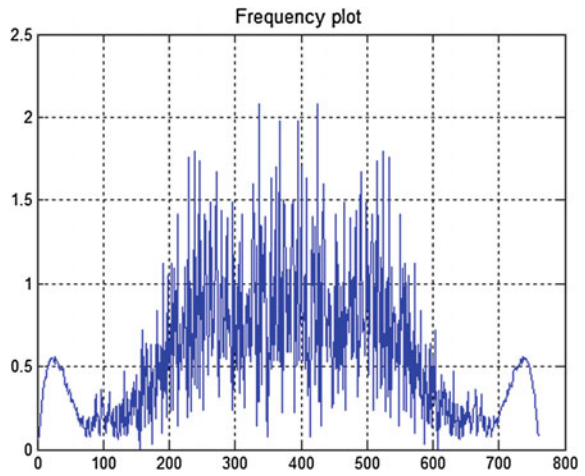


Fig. 6 Baseline removed in ALS EMG

Fig. 7 Frequency plot in ALS EMG



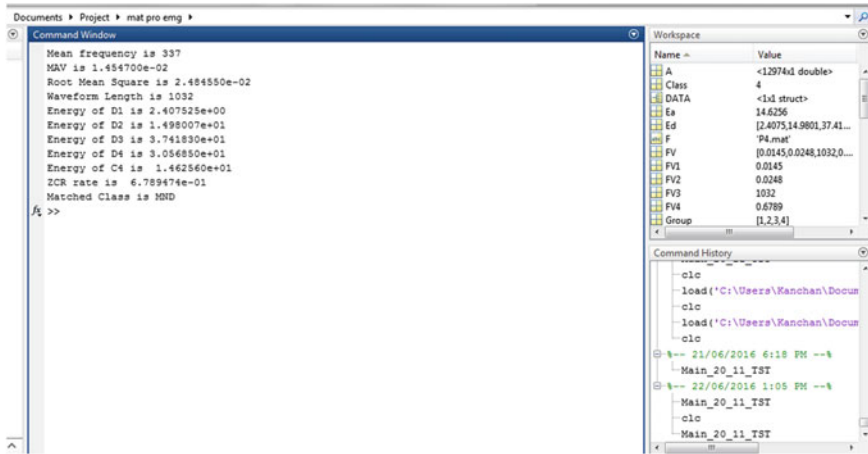


Fig. 8 Result of ALS matched class

5 Conclusion

To identify ALS patient, surface EMG has been used. Wavelet transform coefficients give the better results than the other considered features. For classification between normal and ALS patient, different parameters are considered such as mean frequency, mean absolute value, root mean square, zero crossing rate, waveform length etc. The values of different parameters are to be considered for the comparison. Feature extraction using wavelet transform gives accurate results to diagnose the disease of motor nerve disorder. Mean frequency in case of normal person EMG feature extraction has comes out to be 503 Hz in females; but in some cases it has varied from 744 to 1058 Hz. Mean frequency in case of normal males found out to be 503 and 502 Hz; but was varying from 248 Hz to 603 in some cases. Mean frequency in ALS female case was found out to be 503 Hz throughout in all the cases and that of in male was found out to be 503 Hz and sometimes was varying by small and large values. MAV in normal females was found out as 1.2–5.8 varying in different cases and that of in male was 1.5–7.8 varying in this range for every different samples. MAV in ALS females was 1.07–9.7. ZCR in normal females was 4.701195e–01 to 5.796813e–01 that of male was 4.490040e–01 to 5.107570e–01. Waveform length of normal females was found out to be 2360–2910 and that of males was 2254–2564. Waveform length in

case of ALS female was 2428–2690 and that of in males was 2168–2694. Characteristic table of features and their values in normal and ALS are shown as follows (Figs. 9, 10 and Tables 1, 2).

Fig. 9 Decomposition of high pass filter

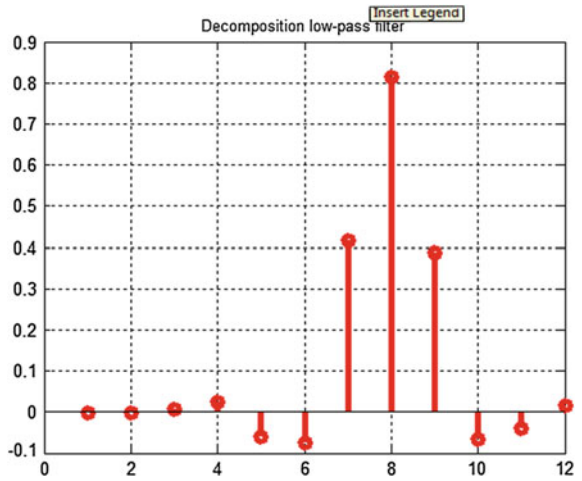


Fig. 10 Decomposition of low pass filter

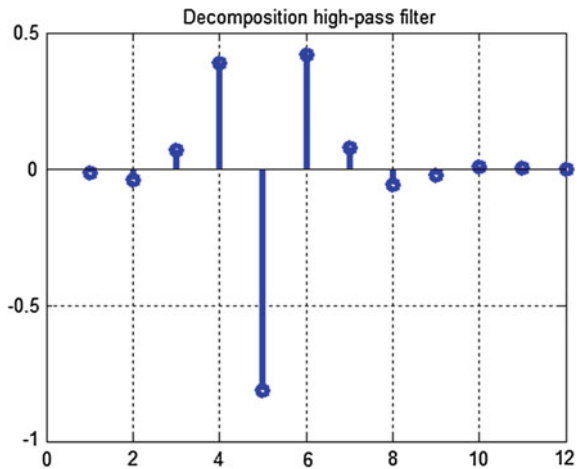


Table 1 Features and their values in Normal person EMG

Sr. No.	Parameter	Values
1.	Mean frequency	503
2.	Mean absolute value	1.2–5.8 in female 1.0–9.8 in male
3.	Root mean square	2.1–8.3 in female 1.1–8.8 in male
4.	Waveform length	2360–2910 in female 2254–2564 in male
5.	Energy of D1	1.1–9.9 in female 1.2–9.0 in male
6.	Energy of D2	2.5–9.5 in female 1.2–6.7 in male
7.	Energy of D3	3.8–9.9 in female 1.2–9.3 in male
8.	Energy of D4	2.1–3.4 in female 1.5–3.2 in male
9.	Energy of C4	5.4–7.2 in female 5.1–8.0 in male
10.	ZCR	4.7–5.7 in female 4.4–5.1 in male

Table 2 Features and their values in ALS person EMG

Sr. No.	Parameter	Values
1.	Mean frequency	503
2.	Mean absolute value	1.5–7.8 in female 1.07–9.7 in male
3.	Root mean square	1.01–9.3 in female 1.2–9.2 in male
4.	Energy of D1	1.1–9.1 in female 1.0–4.0 in male
5.	Energy of D2	3.0–9.3 in female 1.0–8.8 in male
6.	Energy of D3	5.3–8.2 in female 1.0–9.1 in male
7.	Energy of D4	2.7–3.2 in female 1.8–3.07 in male
8.	Energy of C4	6.0–6.7 in female 5.8–7.7 in male
9.	Waveform length	2428–2690 in female 2168–2694 in male
10.	ZCR	4.8–5.3 in female 4.3–5.3 in male

Acknowledgements I would like to thank my all the staff members of BVCOEW, Pune for being moral support through the period of my project study in BVCOEW, Pune whose help and shared knowledge was the main support to my work in project.

References

1. Fattah SA, Doulah ABMSU, Iqbal MA, Shahnaz C, Zhu WP, Ahmad MO (2013) Identification of motor neuron disease using wavelet domain features extracted from EMG signal. In: IEEE
2. Lolure A, Thool VR (2011) Wavelet transform based EMG feature extraction and evaluation using scatter graphs. In: 2015 international conference on industrial instrumentation and control (ICIC), College of Engineering Pune, India, 28–30 May 2011
3. Doulaht ABMSU, Iqbal MA, Jumana MA (2015) ALS disease detection in EMG using time frequency method. In: IEEE/OSA/APR international conference on infonnatics, Electronics and Vision 2015
4. Parsaei H, Gangeh MJ, Parsaei H, Gangeh MJ, Kamel MS (2015) Augmenting the decomposition of EMG signals using supervised feature extraction techniques. In: 34th annual international conference of the IEEE EMBS San Diego, California USA, 28 Aug to 1 Sept 2015
5. Al-Timemy AH, Bugmann G, Escudero J, Outram N (2013) Classification of finger movements for the dexterous hand prosthesis control with surface electromyography. *IEEE J Biomed Health Inform* 17(3)

Early Diagnosis of Diabetes by Retinopathy

Sailee M. Shendkar and Rajashri R. Itkarkar

Keywords Diabetic retinopathy · Blood vessels · Exudates · Gabor wavelet transform · Adaptive histogram equalization · Discrete wavelet transform · Support vector machine

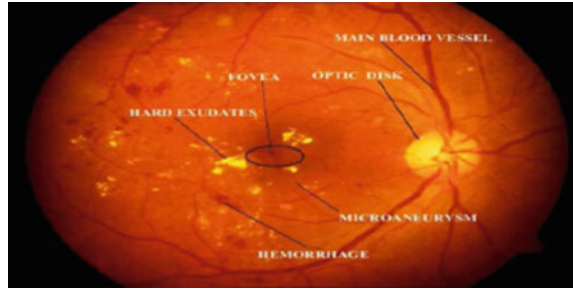
1 Introduction

A standout amongst the most critical infections that bring about retinal veins structure to change is diabetic retinopathy that prompts visual impairment. Diabetes influences very nearly 31.7 million Indian populace and has related difficulties, for example, stroke, vision misfortune and heart disappointment. Diabetes happens when the pancreas does not discharge enough measure of insulin. This illness influences the circulatory framework including the eye gradually. Retinal vein structure in retinal pictures has a critical part in the location of diabetic retinopathy. There are a few techniques present for program retinal vein division. Retinal vein division is the fundamental establishment for creating retinal screening frameworks since veins serve as one of the primary retinal historic point properties [1]. The most widely recognized manifestations of diabetic retinopathy incorporate cotton fleecy spots, hemorrhages, hard exudates and widened retinal veins. A patient with diabetic retinopathy illness needs to experience an immediate screening of retina. Hence, here we have proposed a method in which we have used Gabor wavelet transform for vessel enhancement [2].

Introduction—Sect. 1, Related Work—Sect. 2, Proposed Methodology—Sect. 3, Implementation and Results—Sect. 4, Conclusion—Sect. 4 (Fig. 1).

S.M. Shendkar (✉) · R.R. Itkarkar
JSPM's RSCOE, Tathawade, Pune, India
e-mail: saileeshendkar@gmail.com

Fig. 1 Different features of diabetic retinopathy



2 Related Work

In this paper, the segmentation of the veins from retinal pictures has been finished with incredible exactness due to the utilization of Gabor Wavelet Transform. Robotized vein division is advantageous to handle retinal vessel images under different conditions with sensible precision, and consistent quality for restorative analysis is proposed by Akram and Khan [3]. In this paper, we have attempted to introduce a novel strategy to fragment veins and optic plate in the fundus retinal pictures. The technique could be utilized to bolster noninvasive conclusion in modern day ophthalmology since the morphology of the vein, and the optic circle is an important pointer for maladies like diabetic retinopathy, glaucoma, and hypertension. Our strategy makes as first stride the extraction of the retina vascular tree utilizing the diagram cut technique. The vein data is then used to appraise the area of the optic circle. The optic circle division is performed utilizing two options strategies. The Markov arbitrary field (MRF) picture remaking strategy portions the optic plate by expelling vessels from the optic Circle district, and the pay component technique sections the operation tic circle utilizing the earlier nearby force information of the vessels. The proposed strategy has been tried on three open datasets, DIARETDB1, DRIVE, and STARE. The outcomes and correlation with option strategies demonstrate that our strategy accomplished remarkable execution in portioning the vein and Gonzalez et al. proposed optic circle [2]. This paper has shown a robotized framework which can recognize typical and anomalous vasculature on the optical circle. It could shape part of a framework to lessen manual evaluating workload or an instrument to organize understanding reviewing lines. Bolster Vector Machine was utilized as a classifier. Bolster Vector Machine (SVM) classifiers have shown Premanandan et al. has proposed astounding execution in an assortment of example acknowledgment issues [4]. Another imperative for visual Circle recognition has been proposed where the real veins are distinguished first, and after that, their crossing point is utilized to locate the estimated area of the optic plate. This point is further restricted using shading properties. It is additionally demonstrated that a large portion of the elements, for example, the veins, exudates and microaneurysms and hemorrhages can be identified precisely utilizing different morphological operations connected fittingly is proposed by

Sharma and Kaushik [5]. This paper presents the division of retinal vasculature by Gabor wavelet highlight based bit classifier (Support Vector Machine) and its utilization for the location of early side effects of Diabetic Retinopathy. Execution assessment is directed utilizing openly accessible database DRIVE concerning the physically sectioned pictures given in the database. The classifiers’ performance is assessed as far as Sheeba et al. proposes exactness, affectability, and specificity [1, 6, 7].

3 Proposed Methodology

The Designing and implementation of a mechanical structure for detection of Diabetic Retinopathy using Image Processing have been divided into two phases— Training phase and Testing phase. The aspects of the system are as follows:

Training Phase

- Step 1 To pre-process training database retinal images with the use of 2-D Gabor Wavelet Transform and Adaptive Histogram Equalization Method.
- Step 2 To eliminate the optic disk by using Morphological operators.
- Step 3 To extract feature like blood vessels in the retinal image using Adaptive Thresholding and exudates using Discrete Wavelet Transform.
- Step 4 To calculate mean of blood vessels and area of exudates.

Figure 2 shows the proposed block diagram of the system for Training phase.

Testing Phase

- Step 1 To pre-process testing database retinal images by using 2-D Gabor Wavelet Transform and Adaptive Histogram Equalization Method.
- Step 2 To remove optic disk by using Morphological operators.

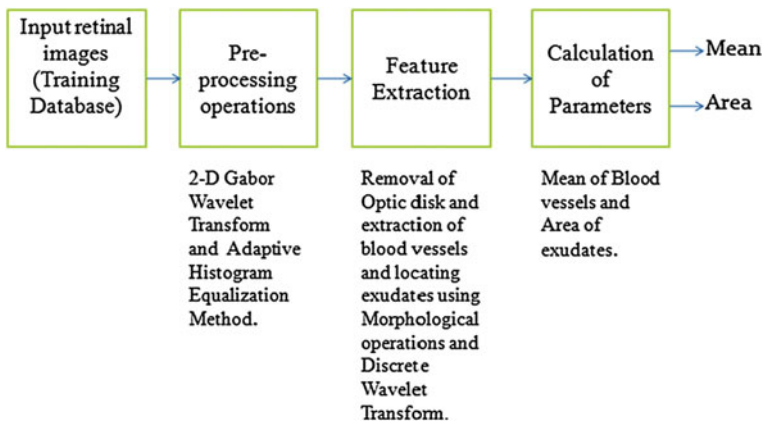


Fig. 2 Block diagram of proposed methodology for training phase

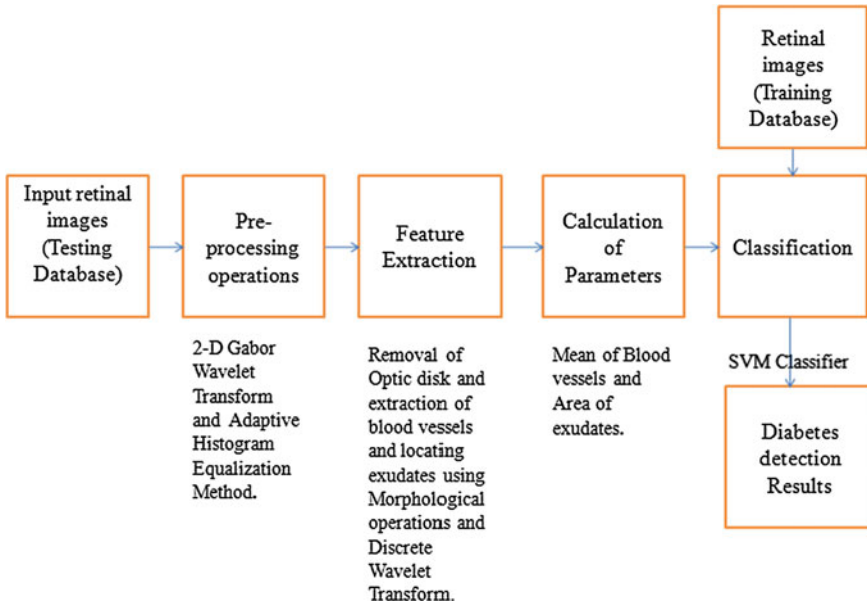


Fig. 3 Block diagram of proposed methodology for testing phase

- Step 3 To extract feature like blood vessels in the retinal image using Adaptive Thresholding and exudates with the use of Discrete Wavelet Transform.
- Step 4 To measure mean of blood vessels and area of exudates.
- Step 5 To train the SVM classifier using the mean values of the blood vessels and the area of the exudates of the training database which has been calculated in Step 4 of the Training phase.
- Step 6 To classify the images of the testing database using Support Vector Machine Classifier into Healthy or Diabetic retinal images.

Figure 3 shows the proposed block diagram of the system for Testing phase.

3.1 Explanation

A. Input retinal images

A fundus camera is used to record retinal images of the part on the surface of the eye by Fundus Retinal Photography, to report the proximity of defects and screen their change over time. A fundus camera or retinal camera is a little power amplifying lens with a joined camera to capture the part within the surface of the eye, including the retina, retinal vasculature, optic circle, macula, and back post (i.e. the fundus). Conspicuous locale and have a clearer point of view of the back of the

Fig. 4 Low power microscope with fundus camera



eye. The Training and Testing database are obtained from the authorized hospital (Fig. 4).

Step 1 Pre-processing Operations.

(a) Image Enhancement using 2-D Gabor Wavelet Transform.

2-D Gabor wavelet used for the vessel given their ability to enhance directional structures. Segmentation of veins from the picture is a difficult task as a result of thin vessels and low quality between container edges and background. It enhances the vascular portion using 2-D Gabor wavelet. The original retinal picture is in RGB shading model has a cleanse blue band. However, the red band is consistently drenched yet green channel gives an incredible representation of retinal picture highlights. In revised green channel, veins appear to be lighter than the establishment that is the reason we have used turned around the green channel. 2-D Gabor wavelet is associated with turned around the green channel to enhance the vascular illustration, especially, the thin and less unmistakable vessels. Gabor wavelets have directional identity capability. They go about as low level organized edge discriminators besides filter out the establishment uproar of the image. Wavelet response gives better results, especially for shaky vessels [3].

The analyzing Wavelet is defined as,

$$\Phi_{b,\theta,a} = a^{-1} \varphi(a^{-1} r_{-\theta}(x-b)) \tag{1}$$

b is displacement vector; a is dilation parameter and θ is rotation angle.

Step 1 Pre-processing Operations.

(b) Image Enhancement using Adaptive Histogram Equalization Method.

Spreading out the deep levels in a picture with the goal that they are uniformly circulated over their range. Histogram of the resultant image is as level as possible. Visually satisfying results over a more extensive scope of pictures [3].

Step 2 Removal of an Optic disk using Morphological Operators and extraction of features using Adaptive thresholding and Discrete Wavelet Transform.

Morphological Opening operation.

Opening operation is performed by using a ball shaped structuring element to remove the optic disk so that we can concentrate only on the blood vessels. Opening separates out the optical disk from the blood vessels. This image is subtracted from the enhanced image to obtain a picture which consists of only blood vessels. Thus the optic disk is eliminated.

Adaptive Thresholding.

The image is divided equal size blocks, and each image block is assigned a threshold and the pixel values below the threshold is assigned with 0 and pixel values above the threshold are assigned with 1. This makes only the blood vessels visible.

Discrete Wavelet Transform.

The image is decomposed into detailed, and approximate components into horizontal, vertical and diagonal directions to extract exudates using Discrete Wavelet Transform.

Step 3 The Calculation of various parameters

Mean of each line (column) of blood vessels in extracted image is calculated and is stored as a vector. Area of exudates located image is calculated.

$$\text{Mean} = 1/N \sum_{i=0}^{N-1} x_i \quad (2)$$

N Total number of pixels in a column

X pixel value

Area Total number of pixels in the located exudates region

Steps 1–4 are performed on both training and testing images.

Step 4 Training of the SVM classifier using the mean values of the blood vessels and the area of the exudates of the training database is calculated in Step 4. of the Training phase.

Support Vector Machines are based on the concept of decision planes that describes decision boundaries. A decision plane separates a set of objects which do not have same class memberships. Here an arrangement plane is one that separates the parameters, i.e., mean of blood vessels and area of exudates of healthy and diabetic images. SVM is trained for 30 images of training dataset, i.e., 15 healthy and 15 diabetic retinal images. The mean of the blood vessels and area of exudates

of Training images are saved, and they are classified into healthy and diabetic by training retinal images. Here, linear SVM is used.

Step 5 Classification of the images of the testing database with the use of Support Vector Machine Classifier into Healthy or Diabetic retinal images

The test image is diabetic if the Euclidean distance of both means of the blood vessels and area of exudates is minimum. And the test image will be healthy if the Euclidean distance of both means of the blood vessels and area of exudates is maximum [2].

$$E = \sqrt{(x - a)^2 + (x - b)^2} \tag{3}$$

- a Mean of blood vessels and area of exudates of an image in training database (healthy or diabetic)
- b Mean of blood vessels and area of exudates of an image in the testing database (healthy or diabetic).

B. ROC—Curves for SVM Classification.

In measurements, a beneficiary working trademark (ROC), or ROC bend, is a graphical plot that outlines the execution of a double classifier framework as its segregation edge differs. The curve is made by plotting the actual positive rate (TPR) against the false positive rate (FPR) at different edge settings. The true positive rate is otherwise called affectability. The false-positive rate is otherwise called the dropout and can be computed as (1—specificity). True positive: Diabetic images accurately recognized as diabetic.

- False negative: Diabetic images not exactly recognized as healthy.
- False positive: Healthy images not exactly recognized as diabetic.
- True negative: Healthy images accurately identified as healthy.

Therefore:

$$\text{Accuracy} = \frac{TP + TN * 100}{TP + TN + FP + FN} \tag{4}$$

Here, the accuracy achieved is 94.88%.

4 Implementation and Results

The proposed implementation is done using MATLAB2014.

Step 1 Graphical User Interface for creating the database, training the database and testing the database (Fig. 5).

Fig. 5 Graphical user interface

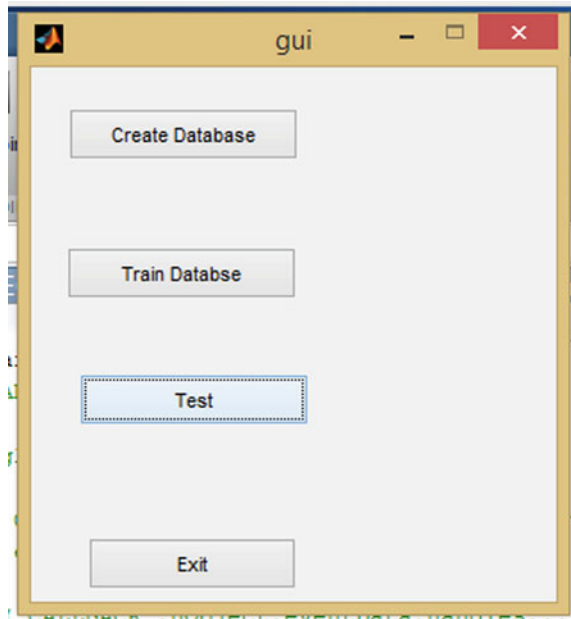
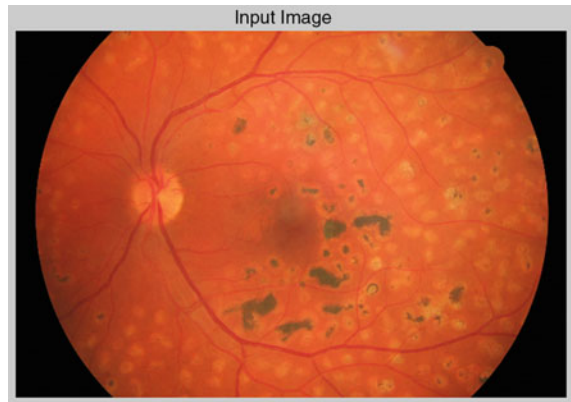


Fig. 6 Input image



- Step 2 Input image was taken from an authorized hospital (Fig. 6).
- Step 3 Green color extracted image with the inverted green channel (Fig. 7).
- Step 4 To pre-process training database retinal images by using 2-D Gabor Wavelet Transform and Adaptive Histogram Equalization Method (Figs. 8 and 9).
- Step 5 To delete optic disk by using Morphological operators (Fig. 10).

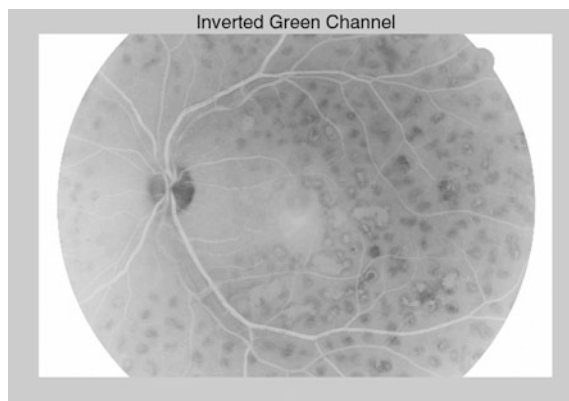


Fig. 7 Inverted green channel

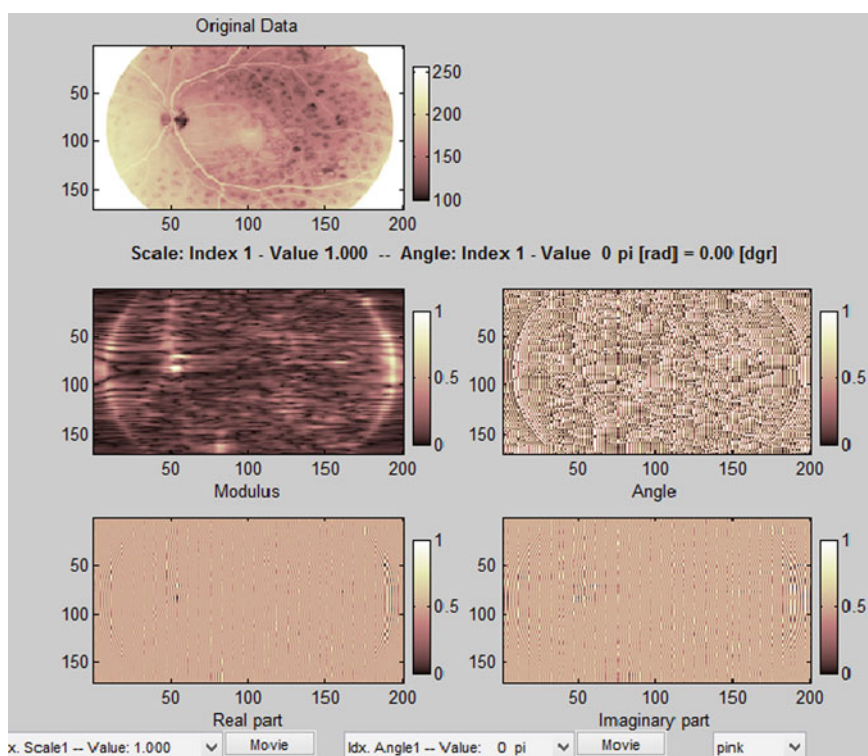


Fig. 8 Continuous wavelet transform-2D wavelet transform

Fig. 9 Enhancement using adaptive histogram equalization

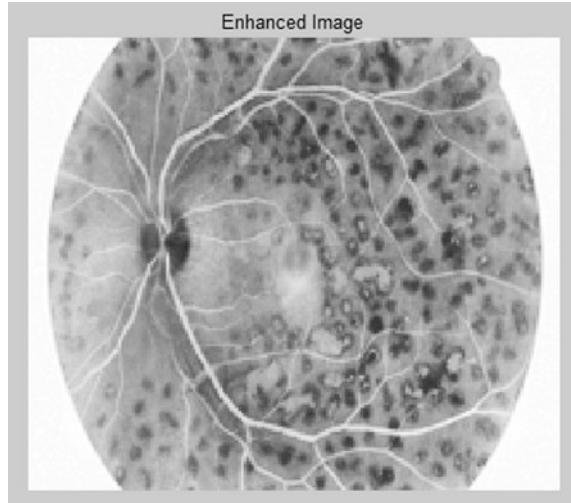


Fig. 10 Optic disk removal using morphological operations



- Step 6 To extract feature like blood vessels in the retinal image using Adaptive Thresholding and exudates using Discrete Wavelet Transform (Figs. 11, 12 and 13).
- Step 7 To calculate mean of blood vessels and area of exudates.
- Step 8 To train the SVM classifier using the mean values of the blood vessels and the area of the exudates of the training database which is calculated in Training phase.

Fig. 11 Histogram of optic disk removed image

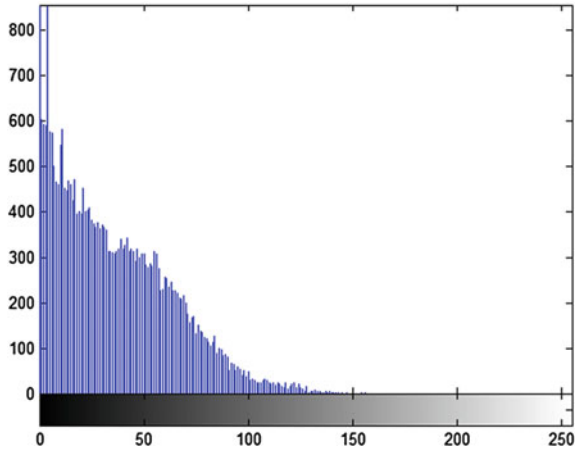


Fig. 12 Extraction of blood vessels

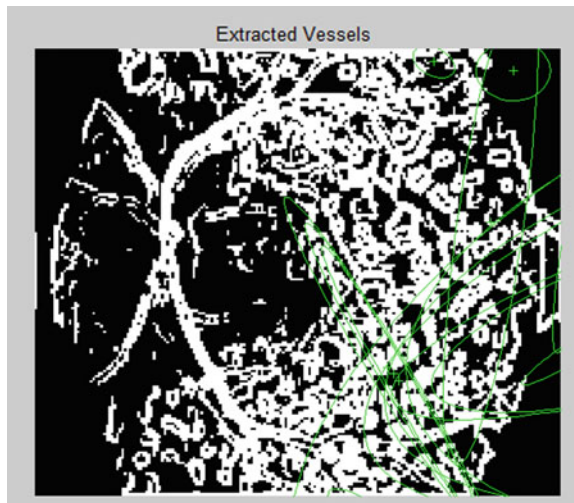


Fig. 13 Locating exudates

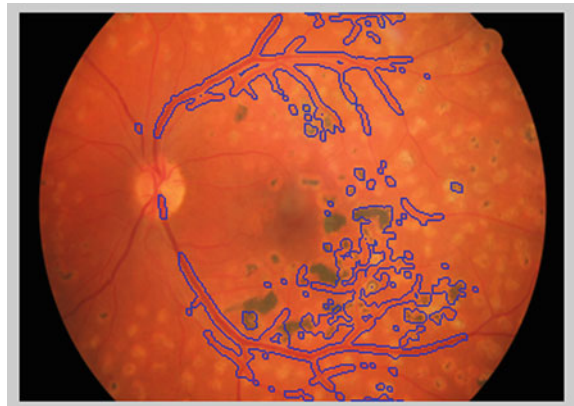


Fig. 14 Detection of diabetes using SVM

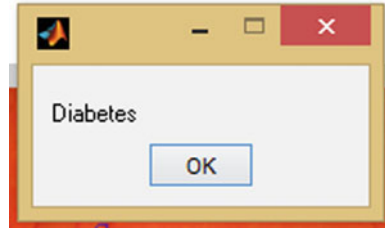


Fig. 15 ROC—Curves for SVM classification

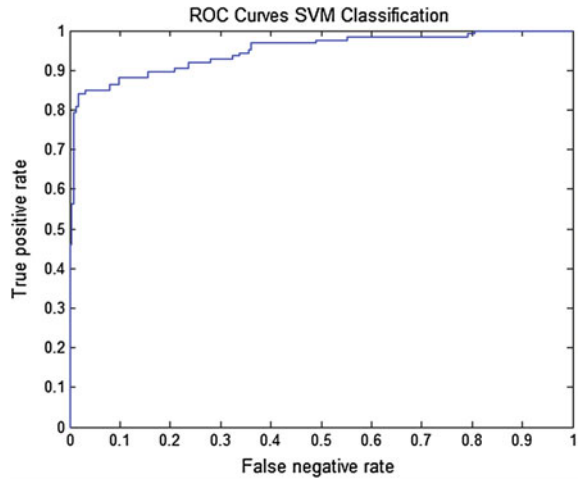


Fig. 16 Accuracy of SVM classifier

```
>> ROC
Accuracy of SVM classifier
94.8854|
```

Step 9 To classify the images of the testing database using Support Vector Machine Classifier into Healthy or Diabetic retinal images (Fig. 14).

4.1 Results

See Figs. 15, 16 and Tables 1, 2.

Table 1 Results of SVM classifier

Classifier	Total no. of images (N)	True positive (TP)	False negative (FN)
SVM	15 Diabetic	12	03
Classifier	Total no. of images (N)	False positive (FP)	True negative (TN)
SVM	15 Healthy	02	13

Table 2 Comparison of accuracy for different methodologies

Classifier	Methodology	Accuracy (%)
SVM	Gabor wavelet transform	94.88
k-NN	Gabor wavelet transform [5]	90.34
k-NN	Matched filter [10]	88.51

5 Conclusion

For initial detection of diabetes using Image Processing Algorithm, An automated system has been brought into practice in which Gabor Wavelet Transform and Adaptive Histogram Equalization is used for enhancing directional structures of vessels. Blood vessels are extracted using Adaptive Thresholding. The Morphological Operation is used to delete optic disk as it is necessary for us to concentrate only on blood vessels and exudates. Discrete Wavelet Transform locates the exudates. DWT is used for decomposition of an image into its approximate and detailed components. Parameters like the mean of blood vessels and area of exudates are calculated. Support Vector Machine classifier is used to classify the images into Healthy or Diabetic images by the values of mean and area. The accuracy achieved using Gabor Wavelet Transform, and SVM Classifier is 94.88%. These results are compared with the results in which algorithm is implemented using Gabor Wavelet Transform and k-Nearest Neighbour Classifier and the accuracy was found to be 90.34%. So SVM classifier along with Gabor Wavelet Transform gives better accuracy and better results as compared to kNN classifier along with Gabor Wavelet Transform.

Acknowledgements We thank Dr. Kiran Bahirwade, Department of Ophthalmology, LTMMC & SION Hospital, Mumbai for providing the Retinal database for Diabetic Retinopathy.

References

1. Sheeba O, Ajitha SS (2015) Detection of diabetic retinopathy from fundus camera images. *Int J Eng Trends Technol* 24(4)
2. Gonzalez AS, Kaba D, Li Y, Liu X (2014) Segmentation of the blood vessels and optic disk in retinal images. *IEEE J Biomed Health Inform* 18(6)
3. Akram MU, Khan SA (2013) Multilayered thresholding-based blood vessel segmentation for screening of diabetic retinopathy. *Eng Comput* 25:165–173

4. Premanandan G, Selvakumar R (2014) Identification of diabetic retinopathy in fundus images by using segment features and morphological features. *Int J Innov Res Comput Commun Eng* 2 (2)
5. Sharma C, Kaushik G (2014) Automatic diagnosis of diabetic retinopathy using fundus images. *Int J Adv Res Comput Sci Softw Eng* 4(5)
6. Fraz MM, Basit A (2008) Evaluation of retinal vessel segmentation based on a combination of vessel center lines and morphological processing. In: *IEEE ICET08*, pp 232–236
7. Paithane AN, Borman DS (2014) Analysis of the nonlinear and non-stationary signal to extract the features using Hilbert-Huang, transform. In: *International conference on computational intelligence and computing research (ICCIC), IEEE 2014*

Optimal Location of TCSC Using Evolutionary Optimization Techniques

Rahul Agrawal, S.K. Bharadwaj, Anil Bodhe, D.P. Kothari
and Bhupendra Deshmukh

Keywords PSO · TLBO · Transmission loss · TCSC

1 Introduction

Present day power systems, are developing in span and complication, are portrayed by long distance mass energy transmissions and zone interconnections. In a power system, steady and secure operation of power supply is required to meet the load demand along with the minimum power loss. The power can be consumed more efficiently if losses will be as minimum as possible or move towards optimal value. To meet the power demand either new transmission line is added to the existing power system or latest technology should be used [1]. But the environmental and economical constraints prohibited the commissioning of new transmission line. The best suited available technology for the same is a Flexible AC Transmission System (FACTS), its allow the utilities to enhance power system performance. The FACTS devices, control the line impedance, terminal voltage and phase angle of the transmission line in an expeditious and efficacious way [2]. Apart from the main function of the FACTS devices, i.e. control of power flow, it is also useful in improving the dynamic behavior of the system and thus refinement of system

R. Agrawal (✉) · A. Bodhe
Department of Electrical Engineering, SBPCOE, Indapur, MH, India
e-mail: yourrahul1@gmail.com

A. Bodhe
e-mail: anilindore1987@gmail.com

S.K. Bharadwaj
Department of Electrical Engineering, MANIT, Bhopal, India

D.P. Kothari
Gaikwad-Patil Group of Institutions, Nagpur, MH, India
e-mail: dpkvits@gmail.com

B. Deshmukh
K.K. Wagh Institute of Engineering Education & Research, Nashik, MH, India

reliability. Moreover, optimal location of FACTS devices increases the system load ability. TCSC, SSSC, SVC, STATCOM, IPFC and UPFC are the example of FACTS devices.

To find the suitable location of TCSC to enhance security and minimize the generation cost of the IEEE 30, IEEE 57 and IEEE 118 bus systems using fuzzy logic with Harmony search algorithm were examined by [3]. The optimal power flow with TCSC to minimize transmission loss, fuel cost and emission cost using Symbiotic Organism Search (SOS) algorithm are witnessed in [4]. Reference [5] have developed non dominated sorting PSO [NSPSO] algorithm for TCSC and SVC to enhance the static voltage stability margin SVSM, reduces real power losses (RPL) and load voltage deviation (LVD). In [6] Genetic Algorithms and Particle Swarm optimization is used to minimize the investment cost and line loading of the power system with TCSC. The optimal location, number and rating of TCSC were considered as an optimization parameter.

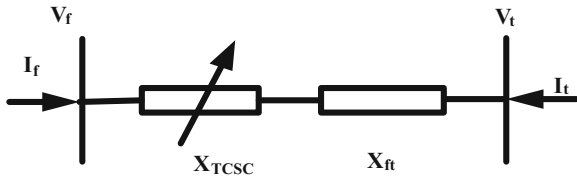
It is revealed from the literature review that many evolutionary optimization techniques along with FACTS devices is used for solving the various issued as address above. In this paper Teaching Learning Based Optimization and Particle Swarm Optimization are used in conceiving the suggested objective.

Kennedy and Eberhart [7] present the Particle Swarm Optimization in 1995. PSO is an evolutionary optimization method based on the behavior of the swarm intelligence. It consist a group of particle called a swarm. Every particle flies with a certain velocity in the search area, searching for the optimal result. Every particle remembers it, personal best (pbets) value and global best (gbest) value. Based on the pbest and gbest, each particle updates its velocity and position in the search area. Rao et al. [8] present a meta-heuristic optimization method named as Teaching-Learning-Based Optimization (TLBO) algorithm which is based on the idea of classroom process i.e. teaching and learning process in a classroom. There are two phases to explain TLBO algorithm properly, one is called 'teacher phase' and another one is called 'learner phase'. In teacher phase, the learners gain knowledge from the knowledge of the teacher. In teacher stage, the learner learns the knowledge from the teacher and teacher try to enhance the learner knowledge up to his knowledge level.

2 Modeling of TCSC

To minimize the transmission system losses along with the maintaining voltage profile under certain inequality constraints in which power system operates, a power system engineer should know the optimal location and the optimal value of the Thyristor Controlled Series Capacitor (TCSC). TCSC consist a capacitor of constant value along with variable inductance, whose value is varied using the firing angle of an anti parallel thyristor. It is connected between the lines where tap-setting transformers are not present. In Fig. 1, the TCSC is modelled as a variable series reactance with a variable reactance X_{TCSC} .

Fig. 1 Model of TCSC



The analysis of a TCSC i.e. parallel LC circuit with a variable inductance gives the steady state voltage and current equations and therefore the expression of TCSC equivalent reactance, as a function of the TCSC firing angle β is given by,

$$X_{TCSC} = X_c - \frac{X_c^2}{(X_c - X_L)} \frac{(2\beta + \sin 2\beta)}{\pi} + \frac{4X_c^2}{(X_c - X_L)} \frac{\cos^2 \beta}{(k^2 - 1)} \frac{(k \tan k\beta - \tan \beta)}{\pi} \quad (1)$$

The total reactance of transmission line ‘ X_{line} ’ after inserting TCSC and considering the degree of compensation ‘ k ’ is expressed as follows:

$$X_{line} = (k + 1)X_{ft} \quad (2)$$

where X_{ft} is reactance of a transmission line between node f and t, kX_{ft} is the reactance of the TCSC interms of degree of compensation.

3 Objective Function

The power flow is a most convincing algorithms used for steady state analysis of electric power system. An objective function is formulated to find out a solution consisting of both the TCSC location and size that minimizes the total power loss, installation cost and maintain the voltage profile at the all buses, described as follows.

3.1 Minimize the Active Power Loss

The Mathematical objective function is in term of the transmission loss is formulated as follows:

$$\min f_1 = P_{loss} = \sum_{\substack{k=1 \\ j \neq i}}^{nline} G_{kj} [V_k^2 + V_j^2 - 2V_k V_j \cos(\delta_k - \delta_j)] \quad (3)$$

where $nline$ represent the total number of transmission lines, G_{kj} is the conductance between the line ‘ $k - j$ ’, V_j and V_k are the bus voltage magnitude at bus j and k respectively, δ_j and δ_k are the angles of the bus j and k respectively.

3.2 Maintain Voltage Profile

The second objective function can be expressed as

$$\min f_2 = \sum_{i=1}^k |V_{\text{iref}} - V_i| \quad (4)$$

where V_i represent the magnitude of voltage at the i th bus, V_{iref} is the reference voltage of the i th bus and 'k' is the number of load buses for which bus voltage limit is violated.

3.3 Minimize the Installation Costs

The cost of the TCSC device expressed mathematically as

$$C_{\text{TCSC}} = 0.0003S^2 - 0.3051S + 127.38 \quad \text{US\$/kVAR} \quad (5)$$

The installation cost (IC) of the TCSC in term of cost of TCSC device C_{TCSC} and operating range 'S' is expressed as

$$\min f_3 = \text{IC} = C_{\text{TCSC}} \times S \times 1000. \quad (6)$$

The above objective function is subjected to equality and inequality constraints of the power system. The single objective function is formulated using a weighted factor method as follows:

$$F = wF_1 \times f_1 + wF_2 \times f_2 + wF_3 \times f_3 \quad (7)$$

where wF_1 , wF_2 and wF_3 are the weighting factor.

4 Implementation of TLBO for the Optimal Placement of TCSC

The step by step implementation of the TLBO algorithms of the Eq. (7) is presented in this section as follows

Step I Input the IEEE 14 bus power system data.

Step II Initialize the position and rating of the TCSC as a design variable of TLBO.

- Step III Read the line data, bus data, shunt data and generator data Run the Newton Raphson power flow without TCSC and determine voltage, active power and reactive power for all the buses.
- Step IV Evaluate the real power loss before the placement of TCSC.
- Step V Initialize the TLBO parameter as per Table 1.
- Step VI Generate the population (learners) based on the number of design variable and population size as per Eq. (8)

$$x_i = x_j^{\min} + (x_j^{\max} - x_j^{\min}) * rand(P, D) \tag{8}$$

where ‘D’ represents the number of design variations, ‘P’ is the class size, x^{\min} is the minimum value of the jth parameter, x^{\max} is the maximum value of the jth parameter and *rand* represents uniformly distributed random number between the (0, 1).

- Step VII Update the line data, bus data and run the Newton Raphson load flow method for each design variable ‘i’ at the buses.
- Step VIII Calculate the fitness function for each design variable.
- Step IX Update teacher phase for each design variable ‘i’ using Eq. (9)

$$x_i^{new} = x_i + Difference_mean_D \tag{9}$$

where *Difference_mean_D* is the difference mean and x_i^{new} , x_i are the existing population and updated population of the ith learners.

- Step X Update the learner phase for each design variable ‘i’.
- Step XI Check the termination criterion, otherwise go to step V.
- Step XII Enumerate the transmission losses after the placement of TCSC.
- Step XIII Terminate the program and print the result.

The flow chart of the proposed TLBO algorithms with optimal location and sizing of FACTS devices is given in Fig. 2.

Table 1 Parameter values for PSO and TLBO

PSO parameter		TLBO parameter	
Parameter	Value	Parameter	Value
Number of iterations	35	Termination criterion	35
Number of design variable	2	Number of subjects	2
Population size	20	Number of students	20
Inertial weight, w	0.88–0.38	Rand	0–1
Constant, C1	1.5		
Constant, C2	2.5		
Rand1	0–1		
Rand2	0–1		

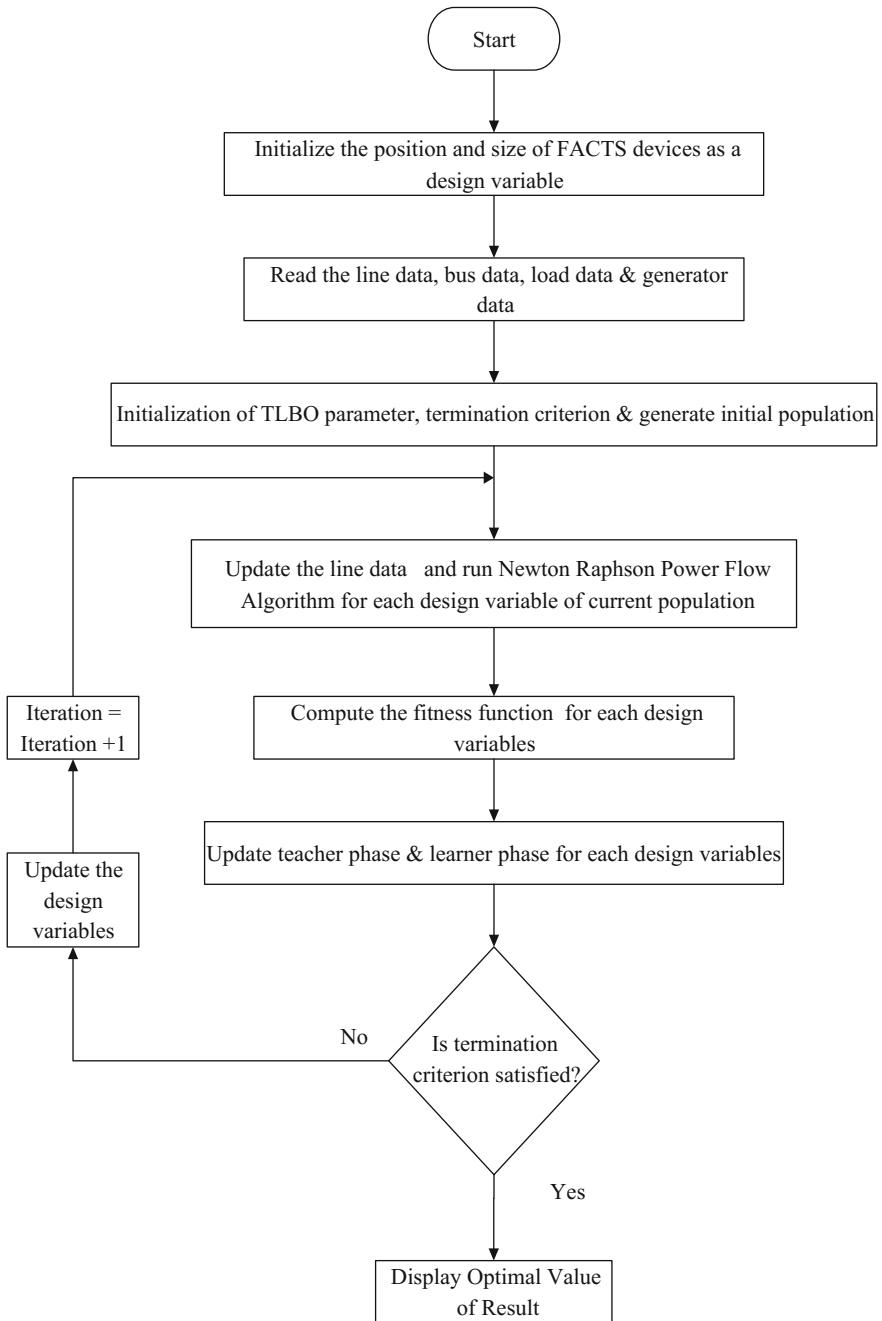


Fig. 2 Flow chart of TLBO algorithm for optimal placement of TCSC

5 Test Results and Discussion

The IEEE 14 bus power system data are taken from [9]. The parameter values of the PSO and TLBO optimization methods are listed in Table 1.

From the Table 2 it is observed that with TCSC both the optimization techniques PSO and TLBO reduced the real power transmission loss. It is evident that total real power transmission loss without TCSC at the base loading is 13.9612 MW whereas with after placing TCSC using PSO and TLBO the real power transmission loss at same loading is 13.8212 and 13.8201 MW respectively. It is shown in Table 2 that after placing TCSC the real power transmission loss at all the different loading condition is also reduced with the use of TLBO and PSO. From the Table 2 it is clear that results obtained from TLBO are better as compared to those obtained from PSO.

The simulation results of the real power transmission loss for the parameter value as listed in Table 1 for the normal loading using TLBO and PSO with TCSC is shown in Fig. 3. From the Fig. 3 it is observed that with the iteration, the real power transmission loss is reduced. It is also seen from the Fig. 3 that the real power transmission loss obtained from TLBO, in the first iteration is lower as compared to the PSO. The results converge faster with TLBO as compared to PSO is also depicted in the figures.

Table 2 Real power transmission loss at different loading condition

Loading condition	Total real power transmission loss in MW		
	Without TCSC	With TCSC and PSO	With TCSC and TLBO
Normal loading	13.9612	13.8212	13.8201
110	17.2595	17.0843	16.2467
120	20.9975	20.7777	19.1757
130	25.3087	24.9449	23.785
140	29.943	27.6104	26.6105

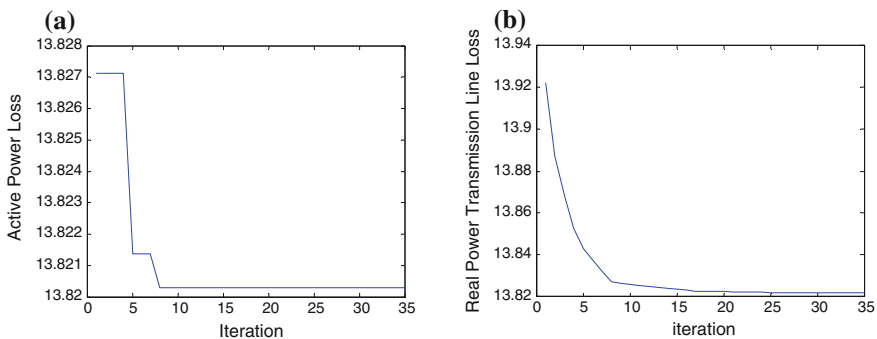


Fig. 3 a TCSC with PSO. b TCSC with TLBO

Table 3 Comparison of installation cost

Loading condition	With TCSC and PSO				With TCSC and TLBO			
	Line number	k	X _{tcsc} (p.u.)	Installation cost (US\$)	Line number	k	X _{tcsc} (p.u.)	Installation cost (US\$)
Normal	2	23.29	-0.0519	7989.7	2	24.78	-0.0491	7545.5
110	2	23.23	-0.0518	7967.5	2	20.36	-0.0454	6984.9
120	2	23.39	-0.0522	8022.8	2	9.48	-0.0212	3252.7
130	2	23.49	-0.0524	8055.8	2	15.31	-0.0341	5249.8
140	2	23.79	-0.0531	8159.4	2	19.18	-0.0428	6577.4

Where k = degree of compensation

The installation cost, optimal value, optimal position and degree of compensation obtained from TLBO and PSO is demonstrated in Table 3. Table 3 shows that if TCSC is installed in the line number 2 with capacitive reactance 5.19 and 4.91% of the line for the base case, using TLBO and PSO respectively, the real power transmission losses are decreased. The installation cost obtained from PSO for the base case is 7989.7 US\$ whereas with TLBO it is 7545.5 US\$. The installation cost and rating of TCSC obtained from TLBO is superior as compared to PSO at all the different loading condition as mentioned in Table 3.

6 Conclusion

In this paper a new heuristic algorithm, Teaching Learning Based Optimization (TLBO) has been presented in order to determine the optional location of Thyristor Controlled Series Capacitor (TCSC) of the given power system. The algorithms discover the best location and setting of TCSC by optimizing the objective function. The minimization of real power transmission loss, installation cost and improved the voltage stability are considered as an object function. From the result, it is evident that both installation cost and real power installation cost are reduced in the IEEE-14 bus system. From the result, it is also shown that the after placement of TCSC in the line, active power loss of the line is minimized and voltages of the buses are improving. The performance of the proposed algorithms named TLBO and Particle Swarm Optimization (PSO) has proven through to obtain results and may consider it for a proposed work. The proposed algorithms are effective and beneficial for the utilities in decision making.

References

1. Agrawal R, Bharadwaj SK, Kothari DP (2016) Transmission loss and TCSC cost minimization in power system using particle swarm optimization. *Int J Innov Res Electr Electron Instrum Control Eng* 4 (3):226–231
2. Hingorani NG, Gyugyi L (2000) Understanding FACTS, concepts and technology of flexible AC Transmission Systems In: IEEE Press
3. Pandiarajan K, Babulal CK (2016) Fuzzy harmony search algorithm based optimal power flow for power system security enhancement. *Int J Electr Power Energy Syst* 78:72–79
4. Prasad D, Mukherjee V (2016) A novel symbiotic organisms search algorithms for optimal power of power system with FACTS. *Int J Eng Sci Technol* 19(1):79–89
5. Benabid R, Boudour M, Abido MA (2009) Optimal location and setting of SVC and TCSC devices using non-dominated sorting particle swarm optimization. *Electr Power Syst Res* 79:1668–1677
6. Rashedl GI, Shaheen HI, Cheng SJ (2007) Optimal location and parameter settings of multiple TCSCs for increasing power system loadability based on GA and PSO techniques. In: IEEE international conference on natural computation
7. Kennedy J, Eberhart R (1995) Particle swarm optimization. *IEEE Int Conf Neural Netw* 4:1942–1948
8. Rao RV, Savsani VJ, Vakharia DP (2012) Teaching–learning-based optimization: an optimization method for continuous non-linear large scale problems. *Inf Sci* 183:1–15
9. Verma MK (2005) Voltage stability considered power system security assessment and its enhancement using FACTS controllers. Ph.D. thesis, IIT Kanpur

MATLAB Simulation Analysis for Removing Artifacts from EEG Signals Using Adaptive Algorithms

Pallavi Jadhav, Dipalie Pujari, Papiya Biswas and Mohua Biswas

Keywords EEG · Ocular artifacts (EOG) · Least mean squared · Normalized least mean squared · MSE · SNR · Convergence · Stability EEG signal · Depth of anesthesia · DoA

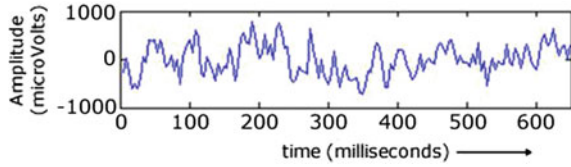
1 Introduction

EEG signal is the record of cerebrum activity. Thus, EEG is a non-stationary signal. These signals are affected by noise called as artifacts. Simple filters and Non-adaptive filtering technique is not able to remove noise such as EMG, ECG and EOG. The increasing value of EMG in EEG signal could raise the BIS index which results in inaccurate amount of DoA. For removing the artifacts from EEG signal adaptive filters are required [1–3] (Fig. 1).

2 Database

500 PSG records belonging to sixteen subjects were selected from the MIT-BIH Polysomnographic Database. All subjects are aged 44 ± 12 years. This database contains over 80 h of four-, six-, and seven-channel PSG recordings. All of them contain EEG, ECG and Blood Pressure (BP) signals, some of them have Nasal or Plethysmograph Respiratory signals, five of them have O₂ Saturation signal, EOG and EMG signals. All the subjects have ECG signals annotated beat-by-beat, and EEG and respiration signals annotated by an expert with respect to sleep stages and apnea. In this work were used only the EEG, ECG and EOG signals, all of them were sampled at 250 Hz [4].

P. Jadhav (✉) · D. Pujari · P. Biswas · M. Biswas
Sveri's College of Engineering, Solapur University, Pandharpur, India
e-mail: pmjadhav@coe.sveri.ac.in

Fig. 1 EEG signal

3 Adaptive Filter Algorithms

3.1 Least Mean Square Algorithm

The algorithm was developed by Widrow and Hoff in 1966 and was the first linear adaptive-filtering algorithm for solving problems such as prediction and communication [5].

The filter tap weights of the adaptive filter are updated according to the following formula:

$$w(n+1) = w(n) + 2\mu e(n) x(n);$$

where $x(n)$ is the input vector of time delayed input values.

3.2 Normalized Least Mean Square Algorithm

One of the primary disadvantages of the LMS algorithm is that it has a fixed step size parameter for each iteration and this is overcome by NLMS algorithm. When the convergence factor μ is large, the algorithm experiences a gradient noise amplification problem. In order to solve this difficulty we can use the NLMS algorithm. The correction applied to the weight vector $w(n)$ at iteration $n+1$ is “normalized” with respect to the squared Euclidian norm of the input vector $x(n)$ at iteration n [6].

4 Artifacts

By artifacts, it is understood that all signals which appear in the EEG record which don't come from the brain. The common artifacts occurred in EEG signal are EOG, EMG and ECG.

4.1 *Electro-oculogram (EOG)*

The major noise source of EEG signal is EOG. It is because of the movement of the eye ball causes an electric field around the eye and affected the electric field of the scalp. EOG is considered as a signal with high amplitude and low frequency. Amplitudes of EOG are in the range of 0.05 and 3 mV. EOG occurs in 0–16 Hz of EEG signal.

4.2 *Electromyogram (EMG)*

An electromyography detects the electrical potential which is generated by the muscle cells. These are the constant peak signals which affect the entire amplitude of EEG signal. EMG has less effect on frequency of EEG signal. EMG makes EEG signal spiky which results in wrong EEG analysis. Amplitude range of EMG is from 0 to 10 mV (peak-to-peak) or 0–1.5 mV (rms). Frequency range is 12–300 Hz. Most of the spectrum lies between 30 and 150 Hz.

4.3 *Electrocardiogram (ECG)*

The electrical artifact actually is the ECG, as recorded from head electrodes. The P wave and T wave are usually not visible, because of the distance from the heart and the sub-optimal axis. Essentially, the artifact is a poorly formed QRS complex. It is the most prominent, when the neck is short. Amplitude level is from 1.15 ± 0.69 mV. Frequency range is 0.3–30 Hz.

5 Simulation Diagram

For simulation we require the recorded EEG signal and then it will be given as an input as shown in Simulink model for LMS filter. Recorded EEG Noise samples also taken and then it will be added with original signal. The recorded noise taken might be EOG, EMG and ECG. Added signal is subtracted from the output of the adaptive filter and then given to the display. By changing the filter parameters we can use LMS as NLMS filter. Filter order is 32 for LMS filter and 40 for NLMS filter. The step size for LMS and NLMS filter is 0.027 and 0.8 resp. MATLAB function blocks are created by user for statistical parameters such as MSE, SNR and convergence rate. Sampling of the EEG signal and noise signal is already done. 'sig' signal is the pure EEG signal and 'nio' signal is noise signal which is any i. e. EOG, EMG and ECG. Around 1000 samples are taken for the simulation (Fig. 2).

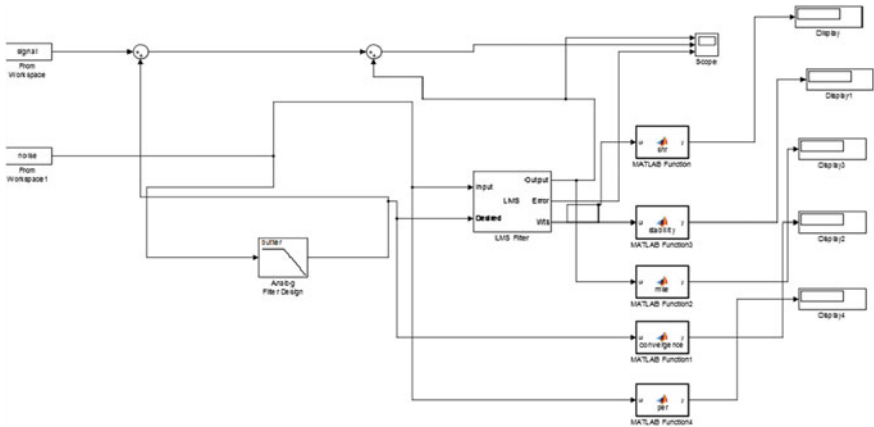


Fig. 2 Simulink model for LMS filter algorithm

6 Results

The Simulation is done to remove the noise of an EEG signal which is corrupted by various types of interferences and distortions. Figure 4 shows de-noise EEG signal by LMS filter algorithm.

6.1 Simulation Result for EOG Artifact Removing Using LMS Filter

See Fig. 3.

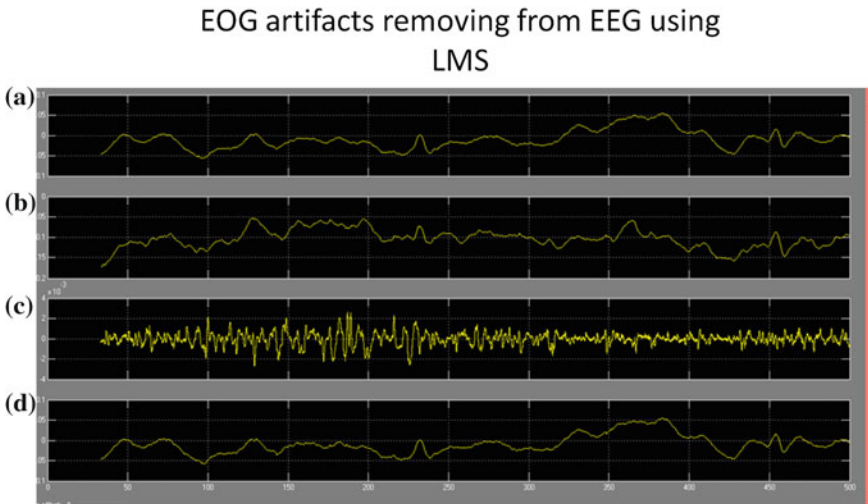


Fig. 3 a Pure EEG signal. b EEG + EOG. c Error signal. d De-noised EEG signal

6.2 Simulation Result for EOG Artifact Removing Using NLMS Filter

See Fig. 4.

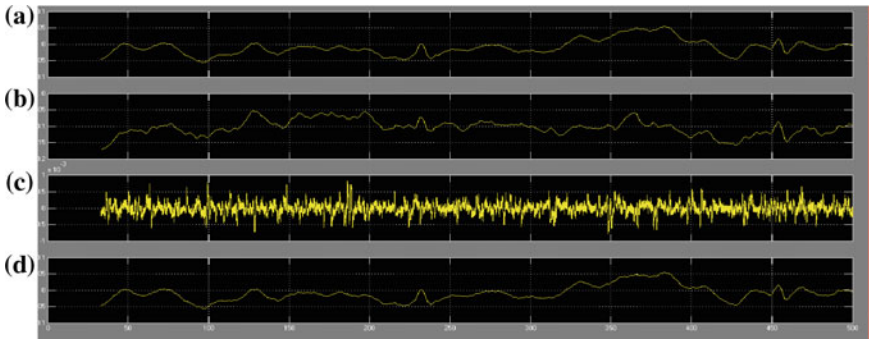


Fig. 4 a Pure EEG signal. b EEG + EOG. c Error signal. d De-noised EEG signal

6.3 Simulation Result for EMG Artifact Removing Using LMS Filter

See Fig. 5.

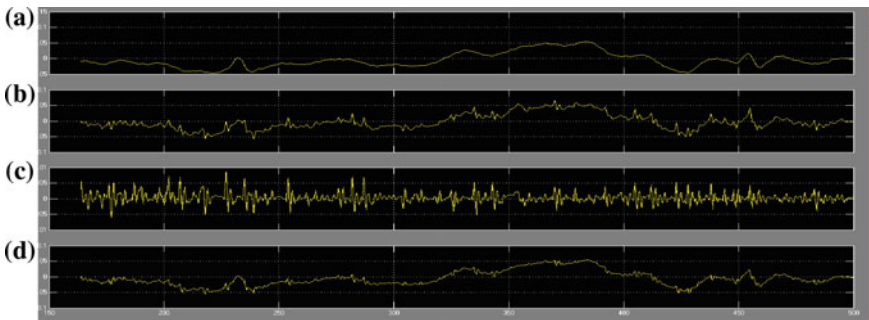


Fig. 5 a Pure EEG signal. b EEG + EMG. c Error signal. d De-noised EEG signal

6.4 Simulation Result for EMG Artifact Removing Using NLMS Filter

See Fig. 6.

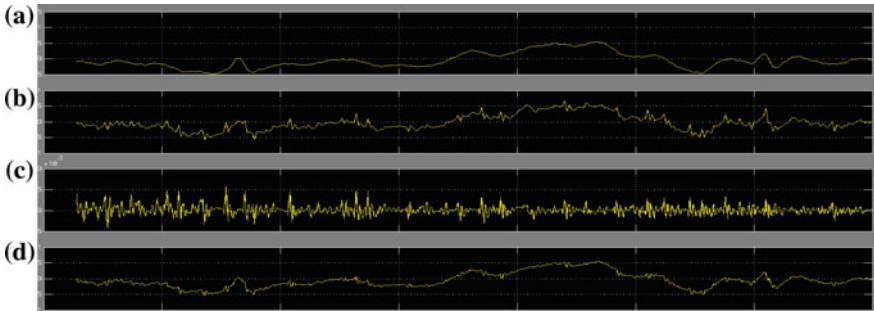


Fig. 6 a Pure EEG signal. b EEG + EMG. c Error signal. d De-noised EEG signal

6.5 Simulation Result for ECG Artifact Removing Using LMS Filter

See Fig. 7.

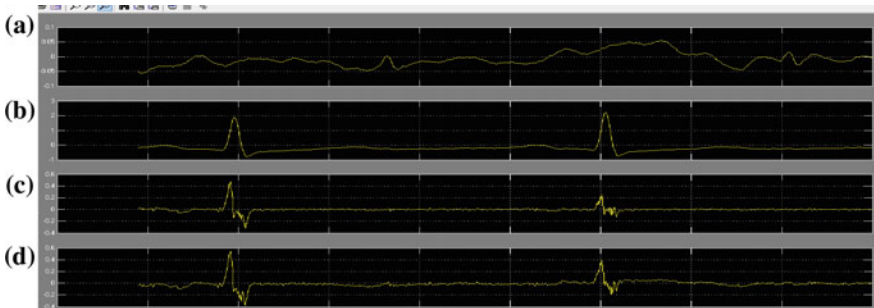


Fig. 7 a Pure EEG signal. b EEG + ECG. c Error signal. d De-noised EEG signal

6.6 Simulation Result for ECG Artifact Removing Using NLMS Filter

See Fig. 8, Tables 1, 2 and 3.

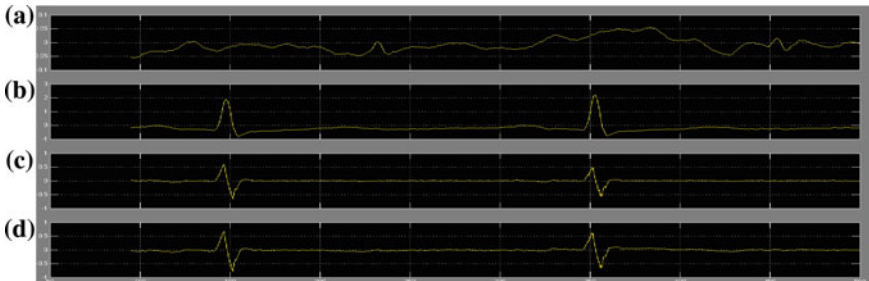


Fig. 8 a Pure EEG signal. b EEG + ECG. c Error signal. d De-noised EEG signal

Table 1 Comparison of LMS and NLMS algorithm for EOG removal based on statistical parameters

Sr. No.	Algorithm	SNR	MSE	Convergence speed
1.	LMS	-6772	0.00774	0.85
2.	NLMS	-6755	0.00772	0.95

Table 2 Comparison of LMS and NLMS algorithm for EMG removal based on statistical parameters

Sr. No.	Algorithm	SNR	MSE	Convergence speed
1.	LMS	-3.6e+7	0.00116	0.885
2.	NLMS	-1.6e+7	0.00109	0.985

Table 3 Comparison of LMS and NLMS algorithm for ECG removal based on statistical parameters

Sr. no.	Algorithm	SNR	MSE	Convergence speed
1	LMS	-925.55	0.3399	0.985
2	NLMS	-949.54	0.3300	0.985

Selection of Order and Step Size for LMS and NLMS Filter

(a) For step size = 0.5

Order of filter	MSE for LMS	MSE for NLMS
5	0.00812	0.007754
10	0.00804	0.007753
20	0.00786	0.007746
32	0.00777	0.007729
40	0.007754	0.007730

(b) For step size = 0.3

Order of filter	MSE for LMS	MSE for NLMS
5	0.008092	0.007787
10	0.008065	0.007786
20	0.007912	0.007769
32	0.007792	0.007741
40	0.07762	0.007738

7 Conclusion

For EOG artifact SNR and MSE values are better for NLMS as compared to LMS. The NLMS filter of order 40 and step size of 0.5 is selected for minimum value of MSE. For more convergence speed NLMS filter with order 40 and step size 0.9 is selected. For EMG artifact SNR and MSE values are better for NLMS as compared to LMS. The NLMS filter of order 40 and step size of 0.9 is selected for minimum value of MSE. For more convergence speed NLMS filter with order 40 and step size 0.15 is selected. NLMS gives better SNR and minimum value of MSE. Convergence speed of NLMS is more as compared to LMS. The NLMS is mainly used to remove EOG noise in EEG signal. EOG artifacts are largely reduced to improve BIS index in DoA. During the simulation for NLMS algorithm, SNR is improved as compared to LMS. Mean square error is less for NLMS compared to LMS which is close to zero. EMG artifacts are largely reduced which increases the BIS index, which is useful in correct DoA. Hence NLMS algorithm is better than that of LMS algorithm.

References

1. Google Image. <https://www.google.co.in/search?q=adaptive+filter>
2. Majkowski A (2005) Denoising based on wavelet and pca signal compression intelligent signal processing. In: IEEE international workshop, pp 70–73, 1–3 Sept 2005
3. SuyiLi (2009) Comparisons of wavelet packet, lifting wavelet and stationary wavelet transform for de-noising ECG. In: 2nd IEEE international conference on computer science and information technology, ICCSIT 2009, 8–11 Aug 2009
4. Banerjee A, Basuand K, Chakraborty A (2010) Prediction of EEG signal by digital filtering
5. Walters-Williams J, Li Y (2012) BMICA-independent component analysis based on B-spline mutual information estimation for EEG signals. Can J Biomed Eng Technol 3(4)
6. Szalai J, Haller P, Marthi Z (2012) Adaptive filtering of EEG signals. In: The 6th edition of the interdisciplinarity in engineering international conference Petru Maior. University of Tirgu Mures, Romania

Part III
Mechatronics, Micro-Nano Related for Bio
and Societal Applications

Effective Sensing Mechanisms and Techniques for Detection of *E. coli* Bacteria in Potable Water

Saakshi Dhanekar

Keywords Biosensors · *E. coli* · Bacteria detection · Potable water · Sensing techniques · Societal applications

1 Introduction

Since the time nanotechnology has stepped in the world of research and development, the conventional technology seems to be obsolete or insignificant. The monitoring of microbial water contamination is performed through some indicator tests which are time consuming, labor intensive, bulkier and require a trained personal [1]. The recent and emerging techniques are much more efficient, easy to use and rapid. A biosensor is required to be responsive in real time to a problem so that the solution can be provided quickly. It is known from various resources that the *E. coli* outbreak has caused serious illness and many deaths in the past [2, 3]. The most harmful strain of *E. coli* is O157:H7 known for its pathogenicity and virulency. It is the deadliest coliforms responsible for food and water borne diseases [4]. Our natural resources like rivers, wells, oceans etc. are vulnerable to microbial exposure due to seasonal change or sudden events. Thus, there are various factors stimulating the water contamination level which can be industry and human made. Accurate, rapid and high throughput sensor measurements are mandate for knowing the status of potable water. A good knowledge of microbial activity and its dynamics can help in interpreting the signals received during process of water quality testing [5, 6]. It is crucial to collect large number of data for longer durations and shorter frequencies for inferring the trend of microbial activity.

In this work, different efficient techniques for detection of *E. coli* bacteria in water are presented. These have been compared for understanding their advantages

S. Dhanekar (✉)

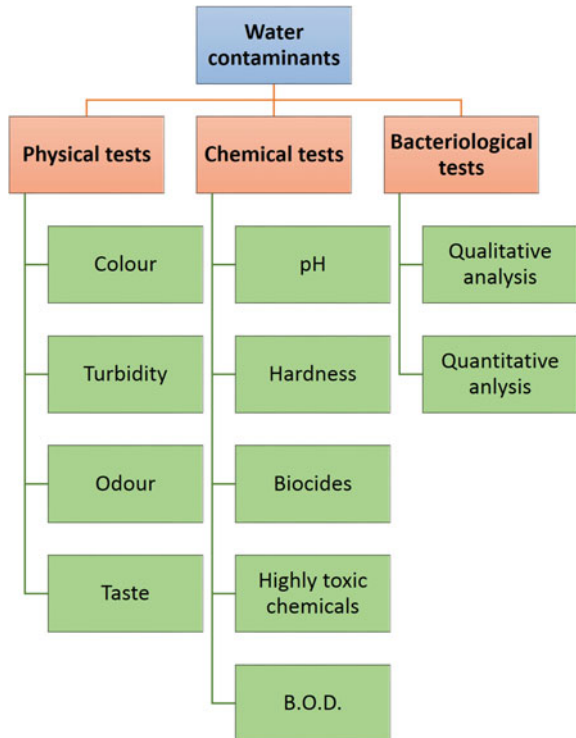
Centre for Applied Research in Electronics (CARE), Indian Institute of Technology (IIT) Delhi, Hauz Khas, New Delhi 110016, India
e-mail: sdhanekar@care.iitd.ac.in

and limitations. It also describes the tests that are performed for assessing the quality of potable water and various substrates and parameters calculated for setting the benchmark of water quality.

2 Tests for Water Contamination: Conventional and Contemporary

Figure 1 shows the tests that are performed for analysis of water quality. These include physical tests one of which can visually analyse the quality of water for qualitative analysis. Color in water may be due to the presence of minerals such as iron and manganese or algae and weeds. Turbidity is defined as the amount of small particles of solid matter suspended in water and measured by the amount of scattering and adsorption of light rays caused by the particles [7, 8]. It may be due to dredging of eroded soil or because of growth of micro-organisms. Odour and taste can be linked to presence of living microscopic organism or industrial wastes or decaying organic matter. Chemical tests are performed to measure the presence of a group of chemical parameters. pH is a measure of hydrogen ion concentration in water. Potable water should have pH between 6.5 and 8.5. Biochemical oxygen

Fig. 1 Different tests performed for assessing the quality of potable water



demand (B.O.D) denotes the amount of dissolved oxygen needed (i.e., demanded) by aerobic biological organisms to break down organic material present in a given water sample at certain temperature over a specific time period. A very low value (<5 ppm) and higher value adversely affect the quality of water.

3 *E. coli* Biosensors: Substrates, Parameters and Techniques

Biosensor is a device whose properties gets manipulated upon interaction with bio-analytes. There are few important parameters for judging the biosensor capability and these are substrate types, biological recognition elements, materials used for detection, sensing techniques and sensor parameters [9]. These are diagrammatically represented in Fig. 2. Different substrates can be chosen depending on the application, feasibility, bio-molecules and cost. These include silicon wafer, glass or polymer (flexible) substrates. There are various bio-recognition elements that can be used for bio-sensing like enzymes, antibodies or DNA strands. Materials like carbon nanotubes, porous materials (including porous silicon, aluminium oxide etc.), metal oxides (ZnO, TiO₂, MoO₃ etc.) can be explored for increasing the surface area to volume ration and for providing a platform for bio-molecules to bind. However, it also strongly depends on both the material and analyte properties for efficient attachment. Different techniques are used for implementing bio-sensor tests. This largely depends on the kind of environment where tests are being performed, if it is lab or field tests. The techniques chosen for field tests are generally required to be robust, light weight and low cost while the environmental conditions are controlled in case of lab tests. The parameters which grade the sensor quality are sensitivity, response time, limit of detection, reusability etc.

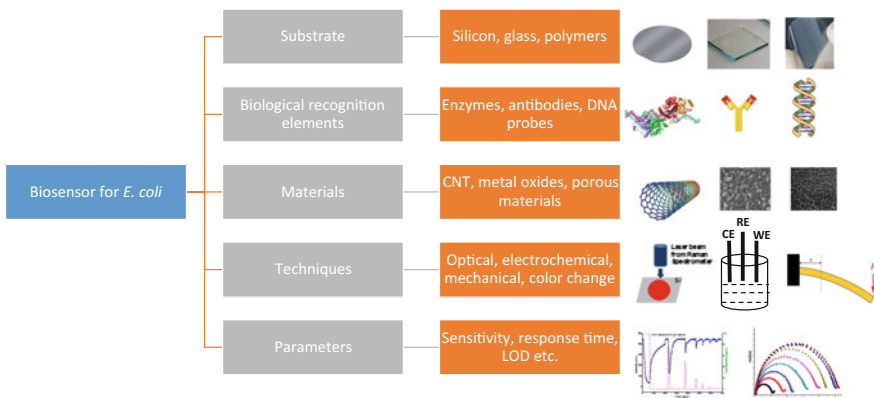


Fig. 2 Various substrates for biosensors, bio-sensing techniques and parameters of bio-sensors [10, 11]

4 Techniques Employed for *E. coli* Detection in Water

Various techniques have been employed for detection of coliform in water. These include culture based detection methods like PCR, electrical, electrochemical, optical, microfluidic and some nanoparticle based techniques. A schematic of all techniques is shown in Fig. 3. It summarizes the different methodologies used for testing a bio-sample. Figure 3(i) portrays that the sample with bio-molecule attached when exposed to light source, shows a change in optical response. The signal intensity varies depending on the concentration of the bacteria. A different mechanism is shown in Fig. 3(ii) where inter-digitated electrodes (IDEs) are fabricated on the sample to acquire the change in current flowing through the samples. This current varies as per the change in concentration of bacteria. Figure 3(iii) displays the change in deflection of a cantilever beam upon exposure to bio-analytes whereas Fig. 3(iv) shows the impedance change in an electrochemical cell with sample as the working electrode (WE). Figure 3(v) demonstrates a method which is most suitable for rural society. It depicts the change in color upon exposure to bio-analytes. This method is low in cost however is only qualitative and not quantitative.

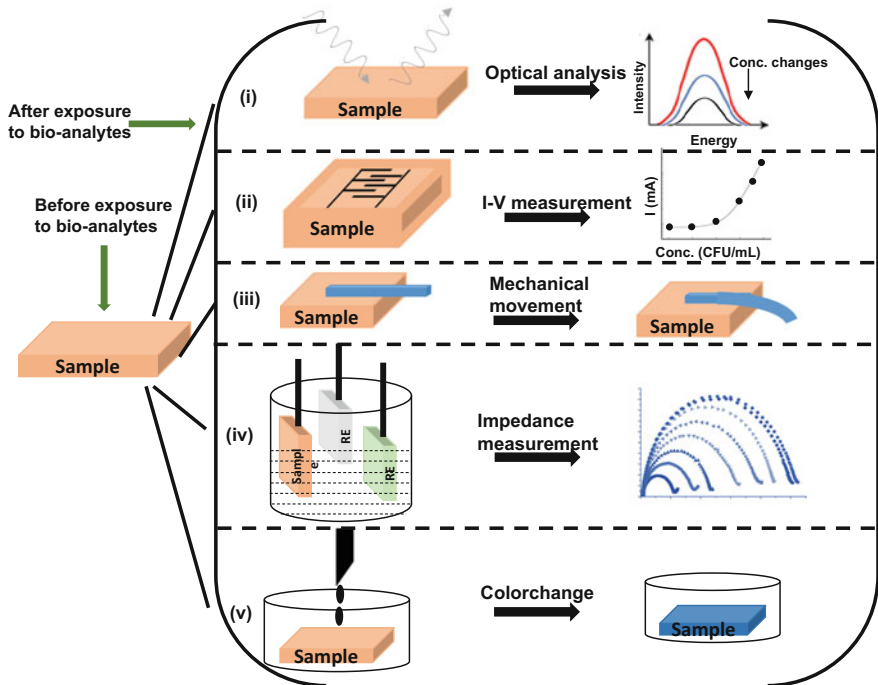


Fig. 3 Techniques used for bio-sensing tests

There are reports where bacteria detection in water is shown. A real time PCR based method for on-site detection of bacteria in seven minutes has been demonstrated [12]. Advanced Nucleic Acid Analyzer (ANAA) has been used as a portable equipment which consists of different reaction modules and a laptop computer. Bacteria with concentration of 500 CFU were taken and subjected to a series of thermal cycle settings and lysing. The thermal cycling time was decreased from 38 to 17 s, followed by a decrease in signal amplitude and detection time from 15 to 7 min. One of the electrochemical techniques is anodic stripping voltammetry (ASV) which has been used as a sensitive electrochemical immunoassay for rapid detection of *E. coli* [13]. Core-shell Cu@Au nanoparticles were used as anti-*E. coli* antibodies labels. *E. coli* was immobilized on polystyrene modified ITO chips and were made to interact with the nanoparticles. This technique could detect 30 CFU/mL of bacteria in 2 h and upon an addition of pre-enrichment step, a concentration of 3 CFU/10 mL of *E. coli* could be detected. Self-assembled peptide nanotubes have been used for fabrication of an electrochemical immunosensor for detection of bacteria [14]. The nanotubes prepared by sol-gel method were deposited on screen-printed carbon paste electrode. The antibodies against *E. coli* by themselves reacted with the nanotubes and this was confirmed by fluorescence microscopy. This antibody modified electrode (probe) was then exposed to antigens in presence of $[\text{Fe}(\text{CN})_6]^{3-/4-}$ and the binding was checked by increase in electron transfer resistance using cyclic voltammetry measurements.

Optics based measurements are known to be more sensitive and expensive. Flow cytometry (FCM) is one of the commonly used techniques for high throughput measurements [15]. It is simple to perform the tests using this technique if the organism exhibits auto fluorescence or fluorescence reported genes. Other organisms like small bacteria need to be stained with a dye in order to make it distinctly different from background. An on-line FCM technique has been developed for real water samples subjected to natural events with fully automated analysis of data over a long period of time. An on-line optical bacteria sensor has been reported with only 10 min time resolution [16]. The sensor is based on 3D image recognition in which the obtained pictures are examined with pre-saved algorithms. The sensor is able to detect and quantify bacteria in pure and mixed suspensions. This image processing based technique has been shown to be superior to flow cytometry as the latter requires staining whereas the former does not have any pre-requisites. The sensor was tested on field and could detect bacteria in the range of 1.6×10^2 to 1.5×10^6 cells/ml and could distinguish between bacteria and abiotic particles with a certainty of $90 \pm 7\%$.

A rapid technique based on optical response from a charge-coupled detector camera and imaging and analysis software has reported with response time as 1 min with LOD of 10^4 cells/mL [17]. This sensor was based on star-burst dendrimer film containing a lipophilic fluorophore. The reporter molecule was embedded in the dendrimer layer using host-guest interaction. The cells concentration range was from 1×10^4 to 1×10^8 cells/mL. The sensor was found to be responsive and selective for bacterial species among all biological and non-biological contamination. A different technique has been introduced as nanoparticle amplification

method for sensitive detection of bacteria. This uses quartz crystal microbalance (QCM) as a substrate for immobilizing thiolated ss-DNA probe specific to *E. coli*. Upon hybridization i.e., exposure of ss-DNA to complementary DNA, a frequency change of QCM was noticed. Streptavidin conjugated Fe_3O_4 nanoparticles were used as 'mass enhancers' which in turn reflected a change in frequency of QCM. As low as 2.67×10^2 CFU/mL of *E. coli* was detected. Since, QCM DNA sensors had limited sensitivity and not great detection limit, several ways have been attempted to enhance its sensitivity. These methods include optimization of probe immobilization and use of signal amplification strategies. Another work reported by Oberoi et al., have demonstrated a microwave biosensor to check *E. coli* contamination in water [18]. The scheme consists of a 3×3 array of polystyrene cylinders of which eight are filled with poly vinyl chloride solid cylinders and the centre is kept hollow for placing the test liquid. These cylinders have dielectric constant same as that of polystyrene. The sensor is placed on a copper cavity designed at 7.7 GHz. A vector network analyzer is used for determining the shift in frequencies and quality factors for unloaded and loaded cavity. The sensor takes 4–5 min for sensing 1–2 CFU of *E. coli*. The technique is thus rapid and sensitive.

RF MEMS is also an emerging field of study in the area of bio-sensors. One of the ways of detection using this technique has been described as involvement of a coplanar waveguide (CPW) and distributed microelectromechanical systems transmission line (DMTL) [19]. RF MEMS has a key advantage of easy integration with microfluidic systems due to its single sided planar configuration. A simulation study has been presented to show how RF characteristics including characteristic impedance, S_{11} parameter and voltage standing wave ratio (VSWR) change with respect to frequency upon attachment of bacteria to the surface. Polyzoiev et al. [20] presented a concept of integration of super paramagnetic particles sandwich assay onto a microcantilever beam wherein the gold coated beam is functionalized with anti-*E. coli* IgG. The antigens are introduced on the surface and these specifically bind to antibodies. Magnetic particles are then dropped on the surface so that these capture the bacteria. An external magnetic field is applied for enhancement of cantilever deflection and optical lever is used to quantify the deflection. The sensor was found to be suitable for detection range 100–4500 CFU/mL.

Very recently, Gunda et al. [21] have described the application of plunger-tube assembly containing hydrogel matrix for detection of bacteria in water. A hydrogel based porous matrix (built in filter with 0.45 μm pore size) was used for encapsulation of chemical compounds. A formulation of new chemical composition has been described which is impregnated with the hydrogel matrix. The work is shown to be superior to 96-well plate method as the latter requires preconcentration of bacteria. In case of plunger-tube assembly, the preconcentration and colorimetric detection happens in sequential steps. The colorimetric detection picture is sent to the web cloud via an app created in the phone. This sends information on the quantitative measure of bacteria. A detection range of 400– 4×10^6 CFU/mL has been presented with detection time of maximum 60 min depending on the concentration of bacteria. The technique is limited by the size of the commercially available plunger-tube assembly which is presently being scaled up for increasing

the quantity of water being taken in the tube. The researchers anticipate this method of detection to be low cost and very useful for people in poorly resourced communities.

Immense work in the area of bio-sensors has been published describing the role of microfluidics. A small explanatory description is shown in Fig. 4. These microfluidic devices can be integrated with any of the existing technologies for improving the efficiency of the bio-sensor. Microfluidics deals with the branch of science where the flow of fluid (liquid/gas) in a microscopic channel is studied [22]. The width of the channel may be same as that of human hair. There are large number of genes and proteins in the human body. The complexity increases when these are extracted in large quantities in large sample volumes. The approach designed for better analysis is to have more number of bio-molecules in lesser sample volume. This can be easily achieved using microfluidics. Thus, microfluidics greatly reduces reagent volumes and cost. It is also easy to study the reaction kinetics in a microfluidic channel due to controlled speed of reaction and easy visibility of the same under the microscope. A cross-sectional view of a microfluidic channel in silicon is shown in Fig. 4. It shows the inlet (IN) and outlet (OUT) points of the channel. The channel can be of varying depth typically in the order of microns. Firstly, a solution is made to pass through the channel which leaves a binding layer in the channel. This layer easily allows antibodies to attach to the surface. Now, antigens are introduced on the surface of which the specific ones bind to the antibodies and after this, the sample (liquid) can be collected at the output for further processing. This whole system can be integrated with optical, electrical, mechanical techniques for efficient bio-sensor operation.

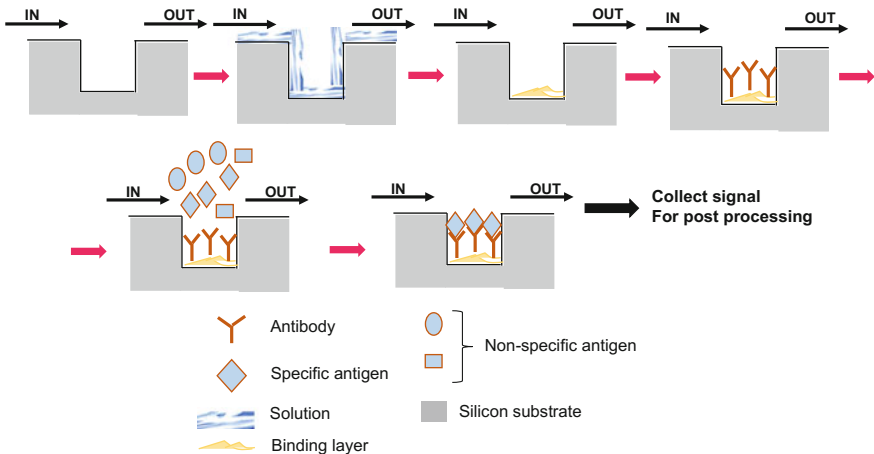


Fig. 4 Role of microfluidics in bio-sensor technology

5 Challenges

Even with the abundant number of techniques available for bacteria detection in water, it is still challenging to fabricate field deployable, low cost, wafer scalable and sensitive sensors for the rural sector. For such an application, the sensor is required to be battery operated, working at room temperature, robust, adaptable to wide range of temperature/humidity, low cost, rapid, reusable and easily used by the common man. This not only has fabrication challenges but also testing difficulties. It is also true that few companies have started coming up with low cost bio-sensors however, commercialization of such sensors and its availability to the society still remains a major challenge.

6 Conclusion

This work highlighted various conventional and contemporary tests used to rate the quality of water. It also discussed the various materials, substrates, processes and techniques used for bio-sensor technology. A detailed comparison has been done among techniques like electrical, electrochemical, optical, mechanical etc. for better realization of these used in development of bacteria sensors in water. A role of microfluidics was also sighted which shows the easy integration of microfluidics with other existing technologies. This kind of integration can improve the sensitivity to a great extent and also reduce the cost of device per chip.

Acknowledgements The author is thankful to Department of Science and Technology (DST), Ministry of Science and Technology, Govt. of India for providing financial and research support through its grant no. DST INSPIRE Faculty IFA-12 ENG-13.

References

1. Wang R, Lum J, Callaway Z, Lin J, Bottje W, Li Y (2015) A label-free impedance immunosensor using screen-printed interdigitated electrodes and magnetic nanobeads for the detection of *E. coli* O157:H7. *Biosensors* 5:791–803
2. Rangel JM, Sparling PH, Crowe C, Griffin PM, Swerdlow DL (2005) Epidemiology of *Escherichia coli* O157:H7 Outbreaks, United States, 1982–2002. *Emerg Infect Dis*. 11(4)
3. Olsen JS, Miller G, Breuer T, Kennedy M, Higgins C, Walford J, McKee G, Fox K, Bibb W, Mead P (2002) A waterborne outbreak of *Escherichia coli* O157:H7 infections and hemolytic uremic syndrome: implications for rural water systems. *Emerg Infect Dis* 8:370–375
4. Radke SM, Alcocilja EC (2005) A high density microelectrode array biosensor for detection of *E. coli* O157:H7. *Biosens Bioelec* 20:1662–1667
5. Ibrišimović N, Ibrišimović M, Kesić A, Pittner F (2015) Microbial biosensor: a new trend in the detection of bacterial contamination. *Montash Chem* 146:1363–1370
6. Noble RT, Weisberg SB (2005) A review of technologies for rapid detection of bacteria in recreational waters. *J Water Health* 03:381–392

7. Bhardwaj J, Gupta KK, Gupta R (2015) A review of emerging trends on water quality measurement sensors. In: International conference on technologies for sustainable development (ICTSD-2015), 6 p, IEEE Press, Mumbai, India
8. O'Dell J (1993) Method 180.1 determination of turbidity by nephelometry. Environmental Monitoring Systems Laboratory Office of Research and Development, US Environmental Protection Agency, Cincinnati, OH 8
9. Dhanekar S, Jain S (2013) Porous silicon biosensor: Current status. *Biosens Bioelec* 41:54–64
10. Dhanekar S, Sharma I, Islam SS (2016) Optical measurement of trace level water vapours using functionalized porous silicon: selectivity studies. *RSC Adv* 6:72371–72377
11. Dwivedi P, Dhanekar S, Das S (2016) Synthesis of α -MoO₃ nano-flakes by dry oxidation of RF sputtered Mo thin films and their application in gas sensing. *Semicond Sci Tech* 31 (115010) (7 pages)
12. Belgrader P, Benett W, Hadley D, Rishards J, Stratton P, Mariella R Jr, Milanovich F (1999) PCR detection of bacteria in seven minutes. *Science* 284:449–450
13. Zhang X, Geng P, Liu H, Teng Y, Liu Y, Wang Q, Zhang W, Jin L, Jiang L (2009) Development of an electrochemical immunoassay for rapid detection of *E. coli* using anodic stripping voltammetry. *Biosens Bioelectron* 24:2155–2159
14. Cho EC, Choi J, Lee M, Koo K (2008) Fabrication of an electrochemical immunosensor with self-assembled peptide nanotubes. *Colloids Surf A: Physicochem Eng Aspects* 313–314: 95–99
15. Besmer MD, Weissbrodt DG, Kratochvil BE, Sirgist JA, Weyland MS, Hammes F (2014) The feasibility of automated online flow cytometry for in-situ monitoring of microbial dynamics in aquatic ecosystems. *Front Microbiol* 5:1–12
16. Højris B, Christensen SCB, Albrechtsen H, Smith C, Dahlqvist M (2016) A novel, optical, on-line bacteria sensor for monitoring drinking water quality. *Sci Rep* 6(23935):1–10
17. Ji J, Schanzle A, Tabacco MB (2004) Real-time detection of bacterial contamination in dynamic aqueous environments using optical sensors. *Anal Chem* 1411–1418
18. Oberoi S, Daya KS, Tirumalai PS (2012) Microwave sensor for detection of *E. coli* in water. In: Sixth international conference on sensing technology (ICST), pp 614–617
19. Pallavi S, Prince A (2013) RF MEMS-based biosensor for pathogenic bacteria detection. *Bio Nano Sci*, 321–328
20. Polyzoev V, Enikov E, Heinze H, Yoon J (2009) Magnetic particle enhanced microcantilever biosensor for rapid and sensitive *E. coli* detection. In: International symposium on optomechatronic technologies, IEEE explore
21. Gunda NSK, Chavali R, Mitra SK (2016) A hydrogel based rapid test method for detection of *Escherichia coli* (*E. coli*) in contaminated water samples. *Analyst* 141:2920–2929
22. Dhanekar S, Chandra S, Balasubramaniam R (2016) Micro-mixer device with deep channels in silicon using modified RIE process: fabrication, packaging and characterization. *Microsyst Technol* 22:515–522

Smart Materials for Biosensing Applications

**Kuldeep Mahato, Anupriya Baranwal, Ananya Srivastava,
Pawan Kumar Maurya and Pranjal Chandra**

Keywords Smart materials · Biosensors · Nano-conjugated systems · pH-sensitive materials · Piezoelectric materials

1 Introduction

Materials are known for its usage since ages, from the stone age to the modern silicon age. Historically, usage of materials played a very important role in building various civilizations. Timeline of such civilizations is also demarcated by the ages after the name of the materials used mostly during that time, such as iron age, bronze age, cement age, and silicon age. Advances in material research paved the synthesis of novel materials including composite materials, nano-material, and smart materials [1]. Smart materials are known for its appropriate, reversible, and repeatable response towards the external stimuli such as stress, temperature, moisture, pH, magnetic and electric stimuli [2]. Various categories of the smart materials are being used globally viz. shape memory alloys, pH sensitive polymers, thermo-responsive materials, nanobiomaterials composites, biosensing material etc. Also, smart materials have found a number of applications in diverse domains such as; structure building, healthcare services, heat engine manufacturing, microelectromechanical systems, building damp proof mechanism, sophisticated instrumentations etc. Apart from these applications smart materials have also been used in the actuators and sensors. Actuators are the sets in which smart materials are used to trigger the

K. Mahato · A. Baranwal · P. Chandra (✉)
Department of Biosciences and Bioengineering, Indian Institute of Technology Guwahati,
Guwahati 781039, Assam, India
e-mail: pchandra13@iitg.ernet

A. Srivastava
Department of Chemistry, Indian Institute of Technology New Delhi, New Delhi 110016,
India

P.K. Maurya
Amity Institute of Biotechnology, Amity University Uttar Pradesh, Noida 201303, U.P., India

response of material against the stimulus whereas sensors generally involve detecting the impact of the stimulus on sensing platforms. Biosensor, being a multidisciplinary emerging domain of the research, which finds the wide and diverse approach supported by various precision technologies [3, 4]. Various biosensors have been developed till date including commercially available ones viz. glucometer, malaria, typhoid, and pregnancy dipsticks etc. [5]. The introduction of micro-technologies have not only contributed the cheaper cost to the diagnoses but also offered detection of biomarkers in remote area in miniaturised settings [6]. Material used for these miniaturized handy equipments decides its efficiency as well as commercial viability. Furthermore, transducers and supports (platform) of the biosensors play a critical role in achieving a low limit of detection, greater selectivity, and dynamic ranges to these devices [5]. Though the efficacy of sensing mechanism is greatly influenced by the environmental conditions under which the detections are being performed, but transducers types also increase the sensor output in terms of amplified signals which offers ultrasensitive detection. Smart materials based transducers and supports have resolved a number of issues for the application of biosensors in diverse settings, viz. rejection of implanted biosensors under in vivo conditions, shelf life, signal amplification etc. The smart (material based) platform in biosensor facilitates the improved quality of sensing by introducing the selective and easy accession of analyte as in the pH sensitive polymeric support where a specific pH allows the system available for sensing [7]. Transducers are the essential component of biosensor that converts physical phenomenon to measurable signals. In conventional biosensing devices, transducers are coupled with the enzymatic entities that generally helps to produce signal. There are several strategies which have been adopted to achieve greater selectivity, however, few biosensors are limited in use for real applications due to its instability, low sensitivity, and robustness. Therefore, to address these shortcomings, new researches in material science and nanotechnology have paved the path by adding various smart (material based) transducers for affordable, sensitive, specific, user-friendly, rapid and robust, equipment free and deliverable biosensors (ASSURED) to end-users [8].

1.1 Smart Material Based Biosensors

For a biosensor, it is desirable to have significantly better amplification in the signal to screen out the noise in order to achieve a better signal-noise ratio. Various strategies using smart materials have been adopted to obtain excellent output to minimize such limitations. The essential component of biosensor is the support for transducer, such as; electrodes in the electrochemical sensors, microfluidic strip for colorimetric detection etc. These play important role in facilitating the biosensing mechanisms. Additionally, in some cases these materials allow controlled access of analyte to the sensory element, pH-sensitive polymers are the best examples, which initiates working when the sample solution attains a particular pH. Apart from this, some other materials have been smartly crafted in the excellent structures for

biosensing. For instance, the microfluidic biosensing channels that are being operated in ultra-low dimensions require less energy for the flow due to the capillary action of embedded channels. For instance, a polydiacetylenic membrane mimicking material containing cell surface receptor and sialic residue have been used for colorimetric detection of the influenza virus and bacterial toxin. This polymeric supramolecular structure facilitates the recognition and transduction by a single functional unit that is convenient for micro-fabrication usage [9]. In addition to the abovementioned example, another type of polymers including electroactive polymers and natural polymer scaffold have been widely used for the biosensing applications [10, 11]. Along with these polymeric smart materials, there are several other smart materials which have been used for biosensing such as; carbon nanotubes, nanoparticles, nanodots, conjugated polymers, 2D materials, and fluorescent active materials [12].

2 Properties and Biosensing Application of the Smart Materials

In general, smart materials have been extensively used in the smart structure building, shape memory alloys, and other allied applications. In recent days, these materials are also being used for various biosensing prototypes, however, these are limited to pH-responsive polymer, conductive polymers, electro-active polymers, piezoelectric materials (used in mechano-sensors). Apart from these, nanotechnology crafted smart material viz. nanoparticles, nano-rods, nano-cages have widely been exploited for the various types of biosensors [12, 13].

2.1 Biosensing Properties of Smart Nanomaterial

Nanoparticles, nanorods, and nanostructures such as; graphene, graphene oxides are collectively called nano-materials. The dimensions of nanoparticles are in general taken from 1 to 100 nm [14, 15]. Owing to the excellent catalytic, magnetic, electrical, chromophoric, and surface properties, nowadays metallic and polymeric nanomaterials are being used to develop various optical and electronic biosensors. The properties of these nanomaterials greatly depend on the size and aspect ratio, surface charges, and functional group attached on it [16–18]. Furthermore, spectral properties, optical properties, and surface plasmon resonance of such particles are influenced by the size of nanoparticles [15]. Apart from these bio-conjugated nanoparticles have been extensively studied for the biosensing applications [19–21]. In addition to these conjugated polymers having the delocalized electronic backbone are being used in optoelectronic devices since long because of its semiconducting properties which have been studied for sensitive biosensing

prototypes. Additionally, these conjugated polymeric substances have been used in DNA, protein, and cell detection in simplistic manner etc. [22–24].

2.2 *Biosensing Properties of pH Sensitive Polymers*

pH sensitive or pH-responsive polymers are the materials which respond to the pH fluctuation in surrounding medium. These materials, in general, swells or collapse depending on the pH of the environment. This property is exhibited by materials due to the presence of certain functional groups in polymeric chains. There are two types of functional groups present in the polymeric chains. These can be either acidic or basic; acidic groups ($-\text{COOH}$, $-\text{SO}_3\text{H}$) swell in the basic pH, for example, polyacrylic acid. Polymer like chitosan consisting the basic groups ($-\text{NH}_2$) swells in acidic pH [25]. The biosensor fabricated from these materials have unique capabilities to perform sensing in the restricted pH range. So far sensing model that have appreciated worldwide is the theranostic device for the diabetic patient, where the patient has been treated with insulin carried by pH sensitive carrier within the body. The moment patient's blood pH level attains pH of 5.8 due to the formation of gluconic acid in glucose rich environment, pH sensitive carriers release the Insulin after swelling [26]. For example, glucose-sensitive hydrogel synthesized using the copolymerization of diethylaminoethyl methacrylate and poly (ethylene glycol) monomethacrylate assisted by functionalized glucose oxidase, catalase, and tetra (ethylene glycol) dimethacrylate [26]. Apart from these, various pH sensitive polymeric smart materials have been used as non-toxic extracellular pH sensing biosensors, for example, Zhang et al. have reported a high throughput biosensor for extracellular pH monitoring, which is developed from pH sensitive polymer Poly (*N*-(2-hydroxypropyl)methacrylamide) [27]. Another example of pH sensitive polymer has been shown by Li et al. where urea has been detected using a biosensor based on a sensitive photonic polymeric crystal [28].

2.3 *Biosensing Properties of Piezoelectric Materials*

Piezoelectric materials have also been employed in biosensing applications, where the sensing of the molecules have been done using the electromechanical properties of the sensor and that is transduced to electrical signal using piezoelectric sensors. In this case, the biosensing has been achieved by exploiting their intrinsic properties. In general, the sensing principle includes piezoelectric crystal that vibrates under the influence of electric field in various frequencies where the resonating vibrational frequency depends on various factors, such as thickness, adsorption area, and mass of the crystal [29]. When there is a change in the system on functionalized tip of the vibrating crystal, the resonate frequency differs resulting the desired analyte to be sensed. The major drawback of this system is they are

highly prone to the atmospheric humidity and analyte-selectivity. However, selectivity can be enhanced by using the functionalized systems, such as antibody/aptamer immobilization on the tip which helps to adhere the specific molecule which significantly increased selectivity. Predominantly quartz, owing an extraordinary piezoelectric property has also been used in various mechanosensing applications [30]. Several techniques have been employed to fabricate piezoelectric based biosensor coupled with various biosensing techniques based on DNA, protein, enzyme, and cells [31]. The immobilization of these biorecognition elements on the sensing probe of piezoelectric crystals have been done by using polymer nanofiber, chemicals, polymer coating etc. [32, 33].

3 Fabrication Technique of Smart Materials and Strategies for Biosensing Modulation

Fabrication of the smart materials has been extensively studied. This section will elaborate the standard methods that have been employed to synthesize various smart materials, which are used in biosensing application, viz. nano-materials, pH sensitive materials etc. Some of these methods have been shown in Fig. 1. This section will also highlight the fabrication strategies of these materials for biosensor design and application.

3.1 Synthesis of Nanomaterial: Application in Biosensor

In general, the nanomaterial can be synthesized by two approaches, bottom-up and top-down approach. The bottom-up approach essentially includes assembly of atoms and molecules to form nanoparticles or quantum dots. Top-down approach involves formation of nano-sized particles by breakdown of the bigger units by means of any external agent [14]. Generally, the bottom-up approach is mediated by chemical synthesis which sometimes introduces monodispersity enabling them for excellent precise catalytic properties. Metallic nanomaterial comprises of nanoparticles, nanorods of various metals including the oxide of some other metals. Among different varieties of nano-materials, so far, nanoparticles have been exploited for various biosensing mechanisms. these nanoparticles are synthesized by several methods using various recipes, but only few considered as standard methods by which these are being synthesized, for example citrate, sodium borohydrate, ascorbate methods are used for gold, silver, and platinum nanoparticles by reducing metal salts using these reducing agents and cetyl trimethylammonium bromide, Polyvinylpyrrolidone are used as stabilizer. Nanoparticles carry excellent catalytic properties which catalyzes the reaction involving chromophoric groups and electroactive molecules, thereby assisting the detection of target in

ultrasensitive manner. This essentially involves redox reaction for sensing where electron plays a key role to generate signal [9]. The functionalization involves addition of the biorecognition molecules in order to enhance selectivity, dynamic range, and limit of detection [34].

3.2 pH Sensitive and Stimuli Responsive Polymers Synthesis

pH-responsive polymers are sensitive to pH due to the functional groups associated with polymeric chains. Conventionally, synthesis of the pH sensitive polymer has been performed by radical and ionic techniques as in emulsion polymerization using water soluble initiators. Also, these have been synthesized by using controlled polymerization technique, such as; anionic and group transfer polymerizations [35]. Besides the chemical synthesis, the stimuli-responsive polymeric systems can be fabricated by using layer by layer self-assembly technique which is dependent on the strong intra-molecular interactions rather than weaker binding interactions. For example polyelectrolyte multilayers fabricated systems. Such systems can be applied for encapsulation of bioactive molecule development, here the top layer of capsule remains active and could be used to encapsulate drugs, fragrances, additives etc. these can be affected by the pH and salts concentration [36]. pH-sensitive polymers are being exploited in various applications such as; theranostics, biosensors, targeted drug delivery etc. pH-sensitive polymers are polyelectrolytes of either charge and operate by widening of mesh sizes therefore, using this property it has been profoundly used in drug delivery and biosensing applications.

3.3 Piezoelectric Materials for Biosensor Fabrication

There exists plethora of piezoelectric materials including tourmaline, topaz, quartz, Rochelle salt, and cane sugar [37]. Apart from these, there are several other piezoelectric materials which have been used for the sensing purpose are as follows: lead zirconate titanate/polyvinylidene difluoride, polar poly(γ -benzyl α ,L-glutamate)/poly(methylmethacrylate) etc. [38]. The general piezoelectric biosensors fabrication process includes immobilization of receptors on sensing probe that is essentially made up of a piezoelectric transducer. In operating mode the piezoelectric crystals generates electrical signals which have been detected by the detector unit [30]. For example, piezo-sensors have been successfully employed to achieve the quick detection of the cancer biomarker CM15.3 using quartz crystal microbalance (QCM) with ZnO nanorods [30, 39]. Apart from this, microbial (*Escherichia coli*) detection have also been reported by using QCM [40]. In another example, aptamer based QCM biosensors have been reported by Chandra et al.

where the smart conducting polymer 2,2':5',2''-terthiophene-3'-(*p*-benzoic acid) is used for detection of daunomycin drug [3].

4 Operating Principle of Biosensors Using Smart Materials

Though there are several strategies that have been employed for the working on these materials, only a few of them have managed to attain the establishment for common biosensing mechanisms. In biosensors, nanomaterials used as a catalyst that selectively catalyzes the biosensing reactions. For instance, a nonenzymatic uric acid sensor reported by Kumar et al. where gold nanoparticles have been exploited as a catalyst to sense the uric acid, a well known biomarker for hyperuricemia and gout. Briefly, this mechanism involves a chromophoric agent 3,3',5,5'-Tetramethylbenzidine, gold nanoparticles, hydrogen peroxide, and target analyte; uric acid. The results obtained clearly shows the importance of highly crafted smart material *i.e.* the nano-catalyst which mediated the reaction to provide a quantitative as well as qualitative analytical signal for uric acid detection [41]. Several other mechanisms have been reported for biosensing in electrochemical mode of detections. These essentially involve the electrode immobilized with biological recognition unit that introduces better selectivity and sensitivity. For example a biosensor prototype reported by Chandra et al. where the cancerous cell and anti-carcinogenic drug daunomycin interaction have been detected using gold nanoparticle deposited on conducting polymer assisted electrochemical reactions [3]. Same group has also developed smart nanoconjugates using conducting polymer-gold nanoparticles composite that has been used to detect inducible nitric oxide synthase [42]. Similarly, hydrazine-gold nanoparticle-aptamer bioconjugate have been utilized for the ultrasensitive and selective electrochemical detections of breast cancer [43]. pH sensitive polymers, in this regard, follow the swelling mechanism in particular pH and facilitates the biosensing and theranostic signal generation. There are several other applications that has employed pH sensitive polymers. For example pH-sensitive field-effect transistor (pH-FET) reported by the Dzyadevych et al. for the detection of phenolic compounds from bovine serum albumin following electrochemical mode of biosensing [44]. Additionally, Shul'ga et al. have demonstrated a pH-FET based conductometric device for urea and glucose using enzyme electrode system. Briefly, the enzyme urease and glucose oxidase catalyze the respective substrates that generate carbonate and hydrogen ions leading to the change in pH of the medium [45]. Piezoelectric sensors, in this context have been practiced in various modes including thickness shear mode, bulk acoustic wave and quartz crystal microbalance modes [30].

5 Conclusion and Outlook

Smart materials are self-responsive, intelligent materials that respond according to the environments stimuli. Recently, the outstanding properties of smart materials have been coupled to various type of biosensor including optical, electrochemical etc. for better selectivity and sensitivity. In addition to this, such smartly crafted materials can serve as an alternative to the expensive enzyme based biosensing mechanisms by introducing the low cost enzyme mimetic strategies. Thus, smart materials can be seen as a potential alternative platforms for next generation biosensor development.

Acknowledgements This work is supported by DST-ECRA research grant (ECR/2016/000100) and DST Ramanujan Fellowship (SB/S2/RJN-042/2015) awarded to Dr. Pranjali Chandra.

Declaration of Interest Authors report no conflict of interest in this work.

References

1. Xu H (2016) Design, fabrication properties and applications of smart and advanced materials. CRC Press, Boca Raton
2. Contributors W. Smart material. https://en.wikipedia.org/wiki/Smart_material
3. Chandra P, Noh H-B, Won M-S, Shim Y-B (2011) Detection of daunomycin using phosphatidylserine and aptamer co-immobilized on Au nanoparticles deposited conducting polymer. *Biosens Bioelectron* 26:4442–4449
4. Chandra P, Noh H-B, Pallela R, Shim Y-B (2015) Ultrasensitive detection of drug resistant cancer cells in biological matrixes using an amperometric nanobiosensor. *Biosens Bioelectron* 70:418–425
5. Chandra P (2016) Nanobiosensors for personalized and onsite biomedical diagnosis. The Institution of Engineering and Technology, London
6. Mahato K, Prasad A, Maurya P, Chandra P (2016) Nanobiosensors: next generation point-of-care biomedical devices for personalized diagnosis. *J Anal Bioanal Tech* 7:e125
7. Li Y, Yang HY, Lee DS (2016) Polymer-based and pH-sensitive nanobiosensors for imaging and therapy of acidic pathological areas. *Pharm Res* 33:2358–2372
8. Parolo C, Merkoci A (2013) Paper-Based nanobiosensors for diagnostics. *Chem Soc Rev* 42:450–457
9. Song J, Cheng Q, Zhu S, Stevens RC (2002) “Smart” materials for biosensing devices: cell-mimicking supramolecular assemblies and colorimetric detection of pathogenic agents. *Biomed Microdevices* 4:213–221
10. Pallela R, Chandra P, Noh H-B, Shim Y-B (2016) An amperometric nanobiosensor using a biocompatible conjugate for early detection of metastatic cancer cells in biological fluid. *Biosens Bioelectron* 85:883–890
11. Zhu Y, Chandra P, Song K-M, Ban C, Shim Y-B (2012) Label-free detection of kanamycin based on the aptamer-functionalized conducting polymer/gold nanocomposite. *Biosens Bioelectron* 36:29–34
12. Song Y, Wei W, Qu X (2011) Colorimetric biosensing using smart materials. *Adv Mater* 23:4215–4236

13. Prasad A, Mahato K, Maurya PK, Chandra P (2016) Biomaterials for biosensing applications. *J Anal Bioanal Tech* 7:e124
14. Baranwal A, Mahato K, Srivastava A, Maurya PK, Chandra P (2016) Phytosynthesized metallic nanoparticles and their clinical applications. *RSC Adv.* 6:105996–106010
15. Jana J, Ganguly M, Pal T (2016) Enlightening surface plasmon resonance effect of metal nanoparticles for practical spectroscopic application. *RSC Adv.* 6:86174–86211
16. Chhetri S, Kuila T, Murmu NC (2016) Graphene Composites. *Graphene technology: from laboratory to fabrication* 18:22
17. Kuilla T, Bhadra S, Yao D, Kim NH, Bose S, Lee JH (2010) Recent advances in graphene based polymer composites. *Prog Polym Sci* 35:1350–1375
18. Chandra P, Das D, Abdelwahab AA (2010) Gold nanoparticles in molecular diagnostics and therapeutics. *Digest J Nanomater Biostruct (DJNB)* 5:363–367
19. Jiang S, Win KY, Liu S, Teng CP, Zheng Y, Han M-Y (2013) Surface-functionalized nanoparticles for biosensing and imaging-guided therapeutics. *Nanoscale* 5:3127–3148
20. Qhobosheane M, Santra S, Zhang P, Tan W (2001) Biochemically functionalized silica nanoparticles. *Analyst* 126:1274–1278
21. Fu Y, Li P, Xie Q, Xu X, Lei L, Chen C et al (2009) One-pot preparation of polymer–enzyme–metallic nanoparticle composite films for high-performance biosensing of glucose and galactose. *Adv Funct Mater* 19:1784–1791
22. Gaylord BS, Heeger AJ, Bazan GC (2002) DNA detection using water-soluble conjugated polymers and peptide nucleic acid probes. *Proc Natl Acad Sci USA* 99:10954–10957
23. Duan X, Yue W, Liu L, Li Z, Li Y, He F et al (2009) Single-Nucleotide Polymorphism (SNP) genotyping using cationic conjugated polymers in homogeneous solution. *Nat Protoc* 4:984–991
24. Feng X, Liu L, Wang S, Zhu D (2010) Water-soluble fluorescent conjugated polymers and their interactions with biomacromolecules for sensitive biosensors. *Chem Soc Rev* 39:2411–2419
25. Contributors W. pH-sensitive polymers. https://en.wikipedia.org/wiki/PH-sensitive_polymers
26. Podual K, Doyle IJ, Peppas NA (2000) Preparation and dynamic response of cationic copolymer hydrogels containing glucose oxidase. *Polymer* 41:3975–3983
27. Zhang L, Su F, Kong X, Lee F, Day K, Gao W et al (2016) Ratiometric fluorescent pH-sensitive polymers for high-throughput monitoring of extracellular pH. *RSC Adv* 6:46134–46142
28. Li L, Long Y, Gao J-M, Song K, Yang G (2016) Label-free and pH-sensitive colorimetric materials for the sensing of urea. *Nanoscale* 8:4458–4462
29. Noh H-B, Chandra P, Moon JO, Shim Y-B (2012) In vivo detection of glutathione disulfide and oxidative stress monitoring using a biosensor. *Biomaterials* 33:2600–2607
30. Skládal P (2016) Piezoelectric biosensors. *Trends Anal Chem TrAC.* 79:127–133
31. Lec RM (2001) Piezoelectric biosensors: recent advances and applications. In: *Proceedings of the IEEE international frequency control symposium and PDA exhibition*, pp 419–429
32. Wessa T, Rapp M, Ache HJ (1999) New immobilization method for SAW-biosensors: covalent attachment of antibodies via CNBr. *Biosens Bioelectron* 14:93–98
33. Barié N, Rapp M, Sigrist H, Ache HJ (1998) Covalent photolinker-mediated immobilization of an intermediate dextran layer to polymer-coated surfaces for biosensing applications. *Biosens Bioelectron* 13:855–860
34. Chandra P, Singh J, Singh A, Srivastava A, Goyal RN, Shim YB (2013) Gold nanoparticles and nanocomposites in clinical diagnostics using electrochemical methods. *J Nanopart Res* 2013:12
35. Dai S, Ravi P, Tam KC (2008) pH-responsive polymers: synthesis properties and applications. *Soft Matter* 4:435–449
36. Kharlampieva E, Sukhishvili SA (2003) Ionization and pH stability of multilayers formed by self-assembly of weak polyelectrolytes. *Langmuir* 19:1235–1243
37. Contributors W. Piezoelectricity. <https://en.wikipedia.org/wiki/Piezoelectricity>

38. Pramanik S, Pingguan-Murphy B, Osman NAA (2013) Developments of immobilized surface modified piezoelectric crystal biosensors for advanced applications. *Int J Electrochem Sci* 8:8863–8892
39. Wang X, Yu H, Lu D, Zhang J, Deng W (2014) Label free detection of the breast cancer biomarker CA15. 3 using ZnO nanorods coated quartz crystal microbalance. *Sens Actuators, B* 195:630–634
40. Farka Z, Kovář D, Skládal P (2015) Rapid detection of microorganisms based on active and passive modes of QCM. *Sensors* 15:79
41. Kumar A, Hens A, Arun RK, Chatterjee M, Mahato K, Layek K et al (2015) A paper based microfluidic device for easy detection of uric acid using positively charged gold nanoparticles. *Analyst* 140:1817–1821
42. Chandra P, Koh WCA, Noh H.-B, Shim Y.-B (2012) In vitro monitoring of I-Nos concentrations with an immunosensor: the inhibitory effect of endocrine disruptors on I-NOS release. *Biosens Bioelectron* 32:278–282
43. Zhu Y, Chandra P, Shim Y-B (2013) Ultrasensitive and selective electrochemical diagnosis of breast cancer based on a hydrazine–Au nanoparticle-aptamer bioconjugate. *Anal Chem* 85:1058–1064
44. Dzyadevych SV, Mai Anh T, Soldatkin AP, Duc Chien N, Jaffrezic-Renault N, Chovelon JM (2002) Development of enzyme biosensor based on pH-sensitive field-effect transistors for detection of phenolic compounds. *Bioelectrochem* 55:79–81
45. Shul'ga A, Soldatkin A, El'skaya A, Dzyadevich S, Patskovsky S, Strikha V (1994) Thin-film conductometric biosensors for glucose and urea determination. *Biosens Bioelectron* 9: 217–223

Comparative Study to Improve Antenna Parameters of Multilayer Microstrip Patch Antenna

Mr. A.K. Rathod, Mr. R.G. Sonkamble, Mr. R.R. Sharanabasappa,
Mr. M.S. Mathpati and Md. Bhakar

Keywords Bandwidth · VSWR · HFSS · Directivity · Multilayer · Techniques

1 Introduction

Different shape has brought out the new technique for improving the bandwidth of the Multilayer rectangular microstrip patch antenna by means of modifying the structure instead of changing the dielectric material. Different shapes employ modification in the design structure which in general case found to be plane. Different shape has brought out the new technique for improving the bandwidth of the Multilayer rectangular microstrip patch antenna by means of modifying the structure instead of changing the dielectric material. Different shapes employ modification in the design structure which in general case found to be plane [1, 2]. The commonly used technique for realizing a broadband microstrip antenna (MSA) is to cut slots of different shapes—such as a U-shaped slot, a V-shaped slot, an L-shaped slot, or a pair of rectangular or toothbrush shaped slots—at an appropriate position inside the patch. The psi-shape is used to improve the bandwidth and

Mr. A.K. Rathod · Mr. R.R. Sharanabasappa
Department of Electronics and Telecommunication Engg,
SSDGCT's Sanjay Ghodawat Group of Institutions, Atigre, Kolhapur, India
e-mail: rathod.ak@sginstitute.in

Mr. R.G. Sonkamble
Department of Computer Engineering, SSDGCT's Sanjay Ghodawat
Group of Institutions, Atigre, Kolhapur, India

Mr. M.S. Mathpati (✉)
Department of Electronics and Telecommunication Engg,
SVERI's College of Engineering, Pandharpur, India
e-mail: msmathpati@coe.sveri.ac.in

Md. Bhakar
Department of Electronics and Communication Engg,
G.N.D. Engineering College, Bidar, India

antenna parameters [3]. The design of microstrip patch antenna at 2.4 GHz is done. Further by introducing fractal concept to the star-shaped microstrip antenna Koch curve antenna is designed. The Koch island fractal patch antenna is introduced in order to reduce the antenna size. By space-filling property of fractal geometry, this antenna reveals lower resonant frequency. Based on experimental result, it is found that as iteration and iteration factor increases, the resonant frequency of this patch antenna decreases. Broad band operation with size reduction is obtained [4]. Microstrip patch antennas are widely used because of their many advantages, such as the low profile, light weight, and conformity. However, patch antennas have a main disadvantage i.e. a narrow bandwidth. Researchers have made many efforts to overcome this problem and many configurations have been presented to broaden the bandwidth. A new, compact, simple and gap coupled broadband microstrip patch antenna with multilayer stacked configuration is presented in this paper. The computer Simulation results show that the antenna can realize wide band characters [5]. There are different feeding techniques but co-axial fed compact rectangular microstrip antenna with multi-layer arrangement for WLAN band (2.4–2.48, 5.15–5.825 GHz) applications. The designed antenna consist of rectangular patch with two open ended L shaped slots and ground plane with of two open ended rectangular slots. The antenna with single layer arrangement shows two resonant bands in PCS (1.851–1.91 GHz) and Wi MAX (3.287–3.934 GHz) frequency range [6]. A simple microstrip antenna with multilayer structure having 20% bandwidth and spreading over 4.4/5.3 GHz Wi-Fi communication band is introduced. Due to the stacking of two substrates and slotted patches, a wide bandwidth is obtained as Compared to simple rectangular patch antenna, It gives a moderate gain over a whole frequency band with good radiation characteristics [7].

2 Design Steps of Microstrip Antenna

Step 1 Calculation of the width of patch (W)

The width of the Microstrip antenna is given as

$$W = \frac{c}{2f_0 \sqrt{\frac{\epsilon_r + 1}{2}}} \quad (1)$$

For $c = 3 \times 10^8$ m/s, $f_0 = 2.4$ GHz, $\epsilon_r = 4.4$. Then We get $W = 38$ mm.

Step 2 Calculation of effective dielectric constant (ϵ_{reff})

Fringing makes the Microstrip line look wider electrically compared to its physical dimensions. Since some of the waves travel in the substrate and some in air, an effective dielectric constant given as:

$$\epsilon_{reff} = \frac{(\epsilon_r + 1)}{2} + \frac{(\epsilon_r - 1)}{2} \left(1 + 12 \frac{h}{w} \right)^{-\frac{1}{2}} \quad (2)$$

For $\epsilon_r = 4.4$, $h = 1.6$ mm, $W = 38$ mm. Then We get $\epsilon_{reff} = 4.085$.

Step 3 Calculation of length of patch (L)

The effective length due to fringing is given as:

$$L_{eff} = \frac{c}{2f_0 \sqrt{\epsilon_{reff}}} \quad (3)$$

For $c = 3 \times 10^8$ m/s, $\epsilon_{reff} = 4.085$, $f_0 = 2.4$ GHz. Then We get $L_{eff} = 30.91$ mm.

Due to fringing the dimension of the patch increased by ΔL on both the sides given as:

$$\Delta L = 0.412h \frac{(\epsilon_{reff} + 0.3) \left(\frac{w}{h} + 0.264 \right)}{(\epsilon_{reff} - 0.258) \left(\frac{w}{h} + 0.8 \right)} \quad (4)$$

For $W = 38$ mm, $h = 1.6$ mm, $\epsilon_{reff} = 4.085$. Then We get $\Delta L = 0.7388$ mm

Hence the length the of the patch is:

$$L = L_{eff} - 2\Delta L = 29.44 \text{ mm} \quad (5)$$

Step 4 Calculation of Substrate dimensions (L_s and W_s)

$$\begin{aligned} L_s &= L + 2 * 6h & L_s &= 2 * 6h + L \\ L_s &= 2 * 6(1.6) + 29.44 = 48.64 \text{ mm} \end{aligned} \quad (6)$$

$$\begin{aligned} W_s &= W + 2 * 6h & W_s &= 2 * 6h + W \\ W_s &= 2 * 6(1.6) + 38.76 = 57.23 \text{ mm} \end{aligned} \quad (7)$$

Step 5 Calculation of feed point (X_f , Y_f)

The position of the coaxial cable can be obtained by using

$$X_f = \frac{L}{2\sqrt{\epsilon_{reff}}} = \frac{29.44}{2\sqrt{4}} = 7.36 \cong 7.5 \quad (8)$$

$$Y_f = \frac{W}{2} = \frac{38.76}{2} = 19.38 \quad (9)$$

3 Simulation Tool

With availability of dimensions it is required to model the design in the software based tool for example the software from Ansoft called HFSS. It is found to be precise antenna simulation software available in the market with ease of user friendly interface. Building of the 3-D drawing in HFSS is far easy because of its dynamic selection of geometrical shapes. The three different ground planes are designed by using Boolean and subtraction operation available in the HFSS.

4 Design Shapes

4.1 Simulated Results of Different Shape Multilayer MSA

To study the effect on Bandwidth, Return loss, VSWR and radiation pattern of Multilayer rectangular MSA due to changing the shapes of Micro strip patch antenna, three different shapes has been considered i.e. Rectangular, E-shape and Psi-shape. Following models in Figs. 1, 2 and 3 respectively shows the different shape.

Fig. 1 Multilayer RMSA

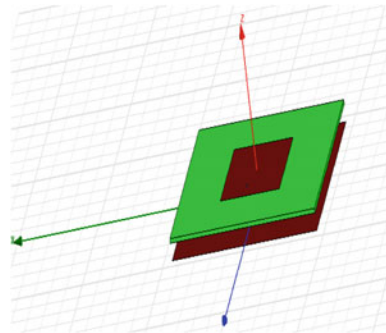


Fig. 2 Multilayer E-shape MSA

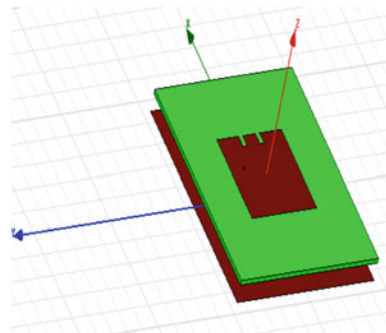
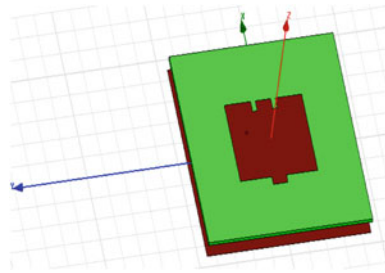


Fig. 3 Multilayer Psi-shape MSA



5 Simulated Results of Multilayer Different Shapes MSA

5.1 Return Loss

See Figs. 4, 5 and 6.

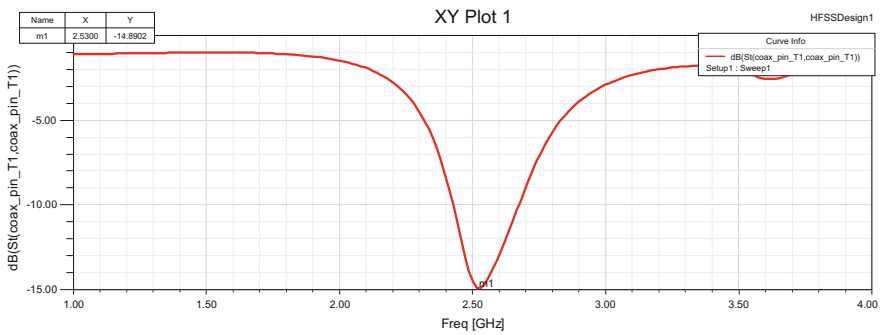


Fig. 4 Return loss of RMSA

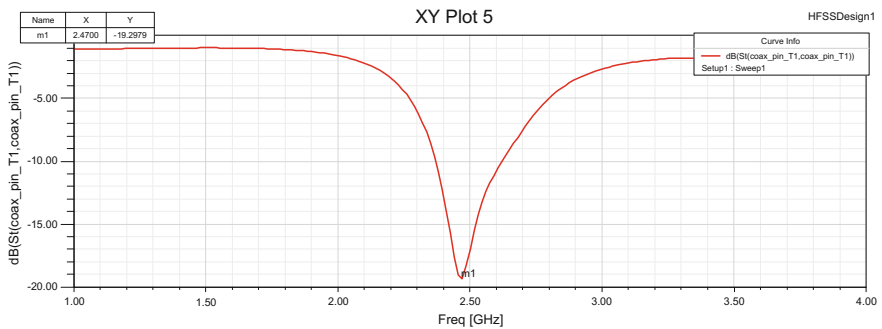


Fig. 5 Return loss of E-shape

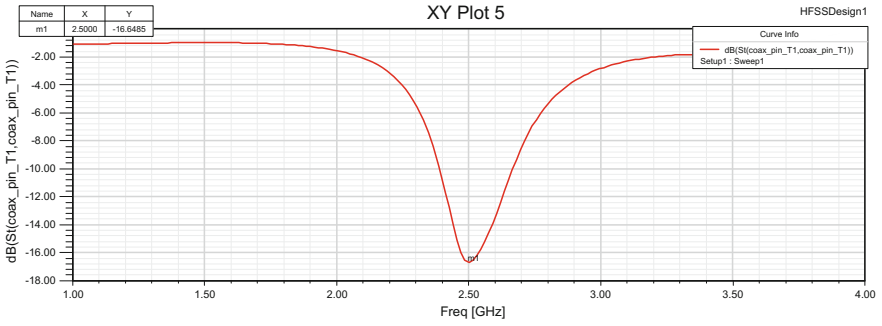


Fig. 6 Return loss of Psi-shape

5.2 Bandwidth

See Figs. 7, 8 and 9.

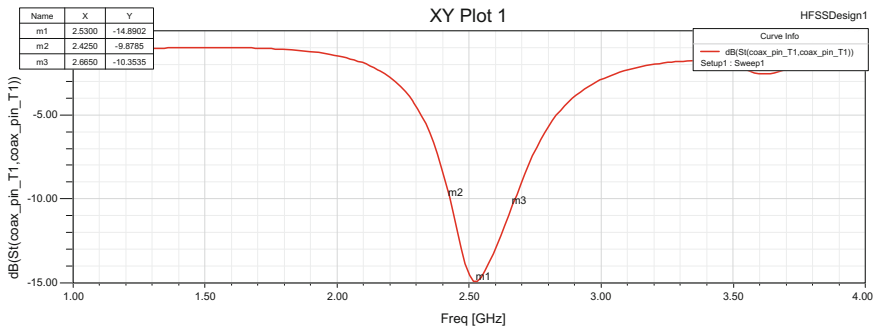


Fig. 7 Bandwidth of RMSA

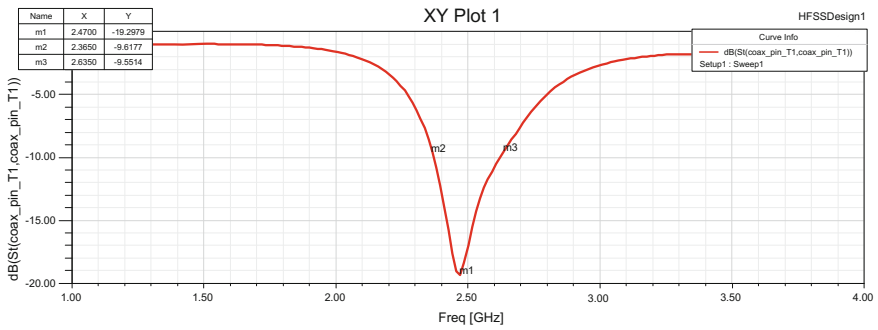


Fig. 8 Bandwidth of E-shape

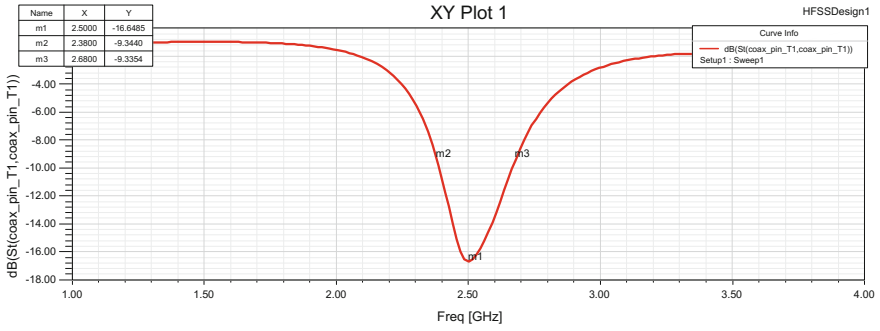


Fig. 9 Bandwidth of Psi-shape

5.3 VSWR

See Figs. 10, 11 and 12.

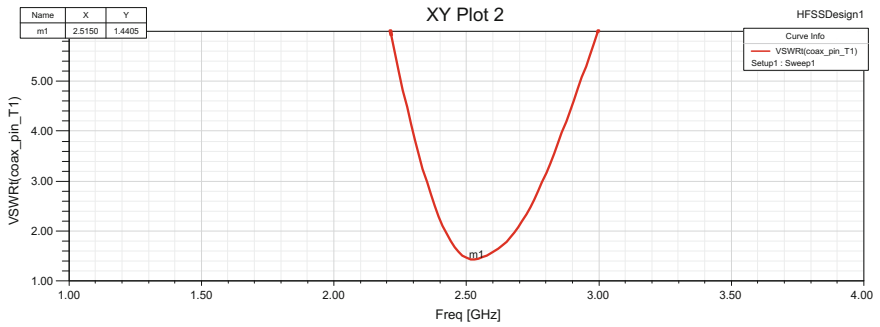


Fig. 10 VSWR of RMSA

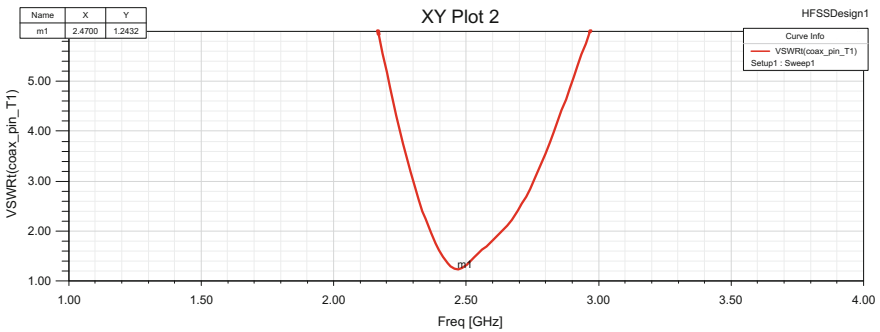


Fig. 11 VSWR of E-shape MSA

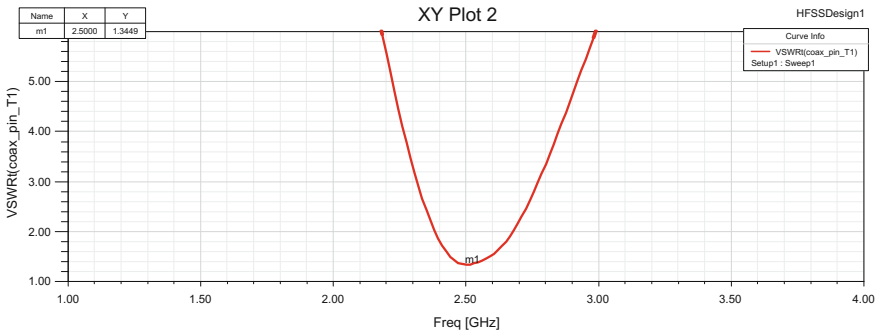


Fig. 12 VSWR of Psi-shape MSA

5.4 Directivity

See Figs. 13, 14 and 15.

Fig. 13 Directivity of RMSA

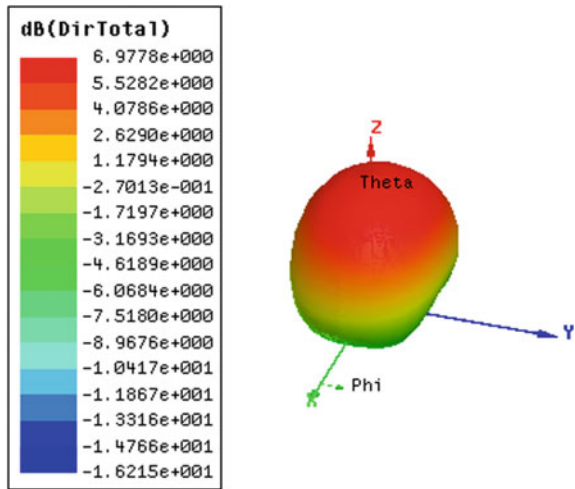


Fig. 14 Directivity of E-shape

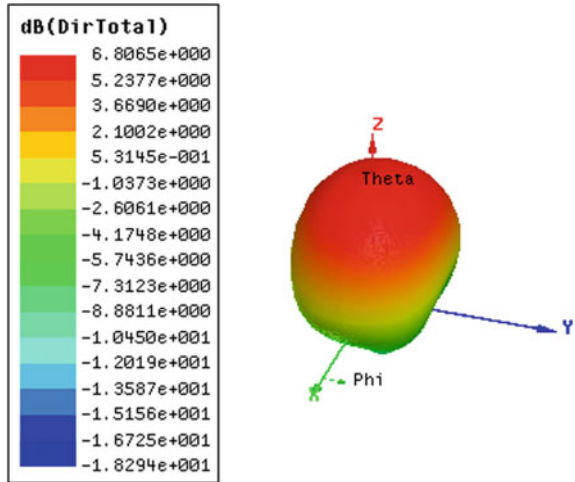
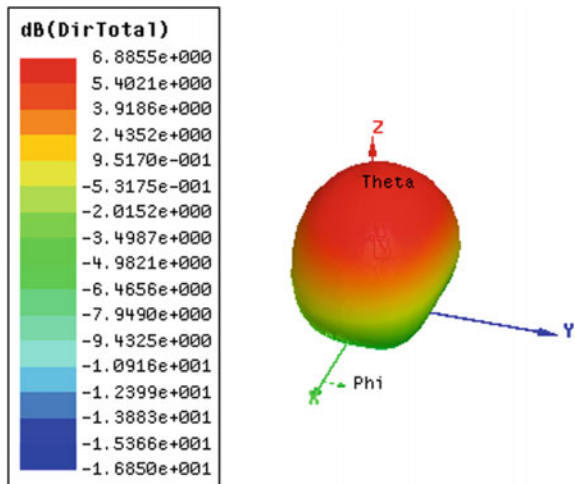


Fig. 15 Directivity of Psi-shape



5.5 Gain

See Figs. 16, 17 and 18.

Fig. 16 Gain of RMSA

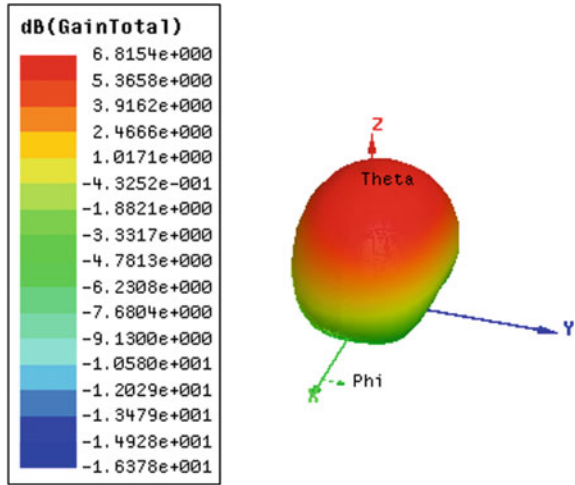
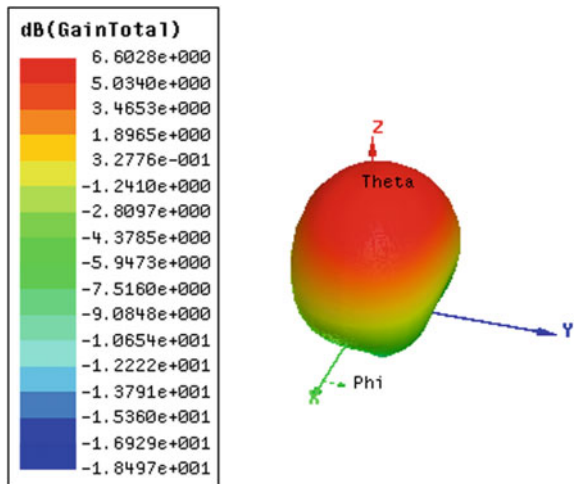


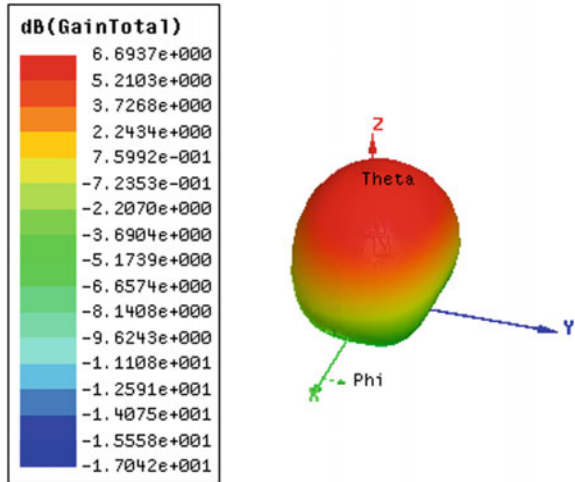
Fig. 17 Gain of E-shape



5.6 Radiation Pattern

Figures 4, 5, 6, 7, 8 and 9 show the bandwidth and return loss variations due to various structured antenna. The variation in return loss is observed in the range of

Fig. 18 Gain of Psi-shape



Name	Theta	Ang	Mag
m1	0.0000	0.0000	4.1443

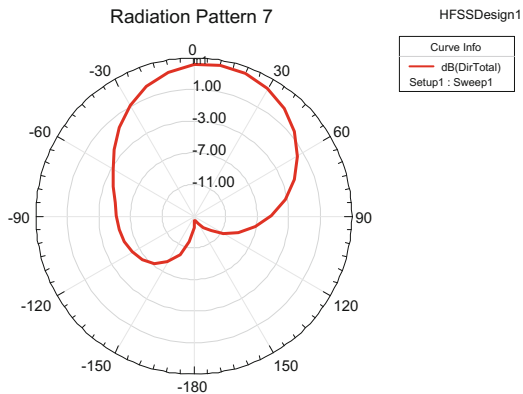


Fig. 19 Radiation pattern of RMSA

-14.8902 to -19.2979 dB and variation in the bandwidth is in the range of 240–300 MHz. Similarly the variation in the VSWR is observed as shown in Figs. 10, 11 and 12 (Figs. 19, 20 and 21).

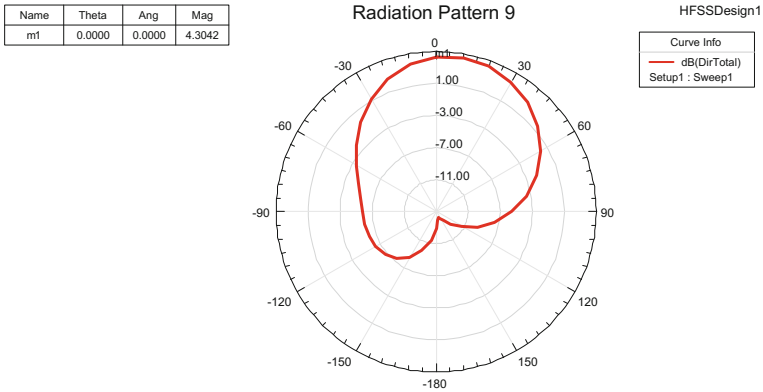


Fig. 20 Radiation pattern of E-shape

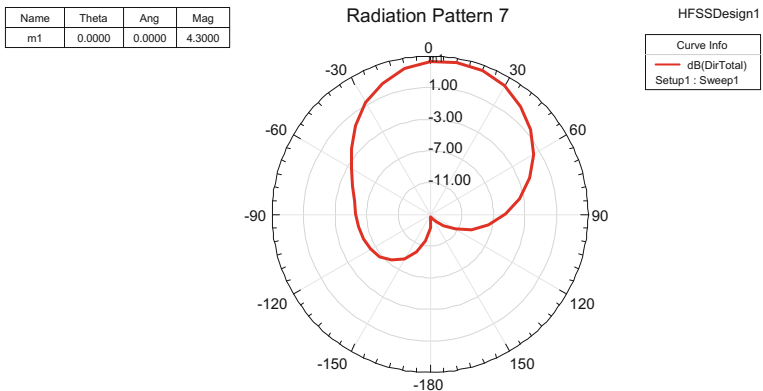


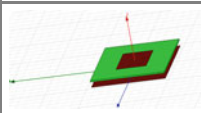
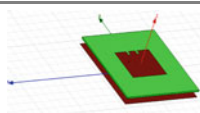
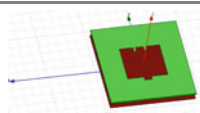
Fig. 21 Radiation pattern of Psi-shape

6 Conclusion and Result Analysis

After simulating the three designed models, the results for the parameters such as Bandwidth, Gain, VSWR and Return Loss are observed to be different for the same dimensioned patch antenna.

Design of different structured Multilayer MSA has been simulated using Ansoft HFSS (High Frequency Structure Simulator) software. It has been observed that, the bandwidth of Multilayer Psi-shape MSA is improved over RMSA and E-shape MSA. Multilayer Psi-shape MSA can be considered as better candidate for wireless applications (Table 1).

Table 1 Comparison table for different shapes in multilayer MSA with parameter

Parameters	Multilayer rectangular MSA	Multilayer E-shape MSA	Multilayer Psi-shape MSA
Design shape			
Operating frequency (GHz)	2.4250–2.6650	2.3650–2.6350	2.3800–2.6800
Return loss (dB)	-14.8902	-19.2979	-16.6485
Bandwidth (MHz)	240	270	300
VSWR	1.4405	1.2432	1.3449
Directivity (dB)	6.9778	6.8065	6.8855
Total gain (dB)	6.8154	6.6028	6.6937

Acknowledgements Authors would sincerely like to thank Dr. S.R. Chougule, (H.O.D. ENTIC) from SGI, Kolhapur for their precious guidance and valuable suggestions throughout the work.

References

1. Balanis CA (2004) Antenna theory. Wiley, New York
2. He W, Jin R, Geng J (2008) E-Shape patch with wideband and circular polarization for millimeter-wave communication. *IEEE Trans Antennas Propag* 56(3):893–895
3. Amit A, Deshmukh, Ray KP (2013) Analysis of broadband Psi (Ψ)-shaped microstrip antennas. *IEEE Antennas Propag Magazine* 55(2)
4. Jadhav B, Pawar MM (2014) Bandwidth and gain improvement by using suspended Fractal MSA at 2.4 GHz. *IOSR J Electron Commun Eng (IOSR-JECE)* 9(4, Ver. V):29-33. e-ISSN: 2278-2834, p- ISSN: 2278-8735
5. Mendhe SE, Kosta YP (2014) Broadband multilayer stacked rectangular micro strip patch antenna using edge coupled patches. In 2nd international conference on emerging technology trends in electronics, communication and networking (ET2ECN), IEEE Conference Publications
6. Kundu A, Roy B, Batabyal S, Chakraborty U, Bhattacharjee AK (2014) A coaxial fed compact rectangular microstrip antenna with multi-layer configuration for WLAN 2.4/5.2/5.8 GHz band applications. In 9th international conference on industrial and information systems (ICIIS), IEEE Conference Publications
7. Tiwari K, Pujara D (2015) Multilayer slotted microstrip antenna for Wi-Fi application. In IEEE international symposium on antennas and propagation & USNC/URSI national radio science meeting, IEEE Conference Publications

Investigation of Mechanical Behavior of Industry Waste and Al₂O₃ Reinforced Aluminium Matrix Composites by Powder Metallurgy Technique

Imranhusen N. Pirjade, S.G. Kulkarni and S.S. Kulkarni

Keywords Aluminium matrix composites (AMCs) · Powder metallurgy · Industrial waste · Alumina · Mechanical properties

1 Introduction

Aluminium (Al) is most abundant metal in earth's crust. Al acquires about 8% by weight of earth's solid surface. Al is widely used due to its availability, high strength to weight ratio, due to enhanced machinability, durability, ductility and malleability. Further, Aluminium based Metal Matrix composites (MMCs) have received increasing attention in recent decades as engineering materials due to their enhanced high strength to weight ratio, good mechanical properties, good corrosion resistance, enhanced thermal conductivity, better machinability and recyclability. It is one of the most prospective matrix metals for the production of composites. Aluminium matrix composites have increasing potential due various applications like aircraft pump parts, automotive transmission cases, aircraft fittings and control parts, water-cooled cylinder blocks, brake rotors, cylinder liner, engine parts, pistons, cylinder heads, etc. [1–5].

Aluminium is widely used as a structural material especially in the aerospace industry because of its light weight property. However, the low strength is a problem for pure aluminium. A cheap method is introduced to solve this problem by using the reinforcement elements such as fly ash, SiO₂, bagasse ash, Al₂O₃, SiC particles in to the matrix. The addition of these ceramics and alloying elements particles addition make it possible to increase the specific elastic modulus of aluminium, improve its mechanical, tribological and thermal properties etc. [3–5].

The several methods are available including powder metallurgy, stirring methods, etc. to manufacture the aluminium composites and produce a homogenous distribution of reinforcement particle in matrix [1, 5].

I.N. Pirjade (✉) · S.G. Kulkarni · S.S. Kulkarni
Department of Mechanical Engineering, SKNSCO Engineering, Pandharpur, India
e-mail: imapirjade11@gmail.com

Table 1 Composition of 99.7% pure aluminium

Name of constituent	Al	Fe	Cu	Mn	Mg	Zn	Other
Percentage	99.7	0.17	0.00159	0.0023	0.0016	0.0053	0.1192

1.1 Matrix Material

Matrix material used in present investigation is 99.7% pure aluminium as a base metal in composites. The composition limit of 99.7% pure Al shown below in Table 1.

Percentage of aluminium in matrix above 99.0% belongs to 1xxx Al-alloy series. It offers better machinability, good corrosion resistance, high thermal and electrical conductivity, etc. along with that its specific application in the manufacturing of car tank or truck bodies, foil and strip for packaging, electrical bus bar installation and in sheet metal work [6].

1.2 Reinforcement Material

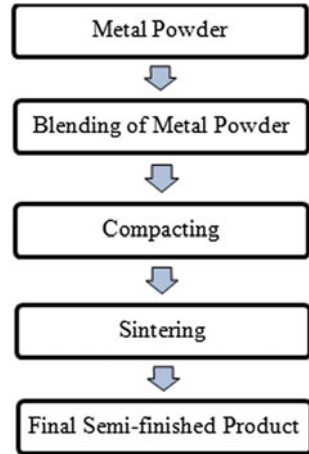
In present work during manufacturing of AMCs fly ash, bagasse ash and alumina are used as reinforcement materials. Fly ash is a by-product of coal power stations, it is also known as flue-ash, is one of the residues generated in combustion, and comprises into the fine particles that rise with the flue gases [7, 8]. Bagasse is a by-product from the sugar industry and it is usually burnt at the mill to provide process powder or steam that provides energy for process machineries [10, 11]. Therefore, usability of these industrial waste materials i.e. fly ash and bagasse ash have been reviewed extensively decreases the production cost concurrently enhancing the property of the materials [7–11].

2 Experimentation

There are different manufacturing processes to manufacture the AMCs by distributing the reinforcement particles into the matrix homogeneously. In general, the most common manufacturing AMC technologies are divided primarily into two main parts: liquid and solid phase fabrication technique. The liquid phase fabrication technique contains different manufacturing processes such as stir casting, squeeze casting, compo casting and on the other hand; solid phase fabrication technique contains diffusion bonding, powder metallurgy (P/M), etc. [12, 13].

In present work, to manufacture the AMCs powder metallurgy technique is used. Powder metallurgy can be defined as the art of producing powders of metals, alloys, ceramics, etc. mixing them in required quantities, compacting and sintering into

Fig. 1 Powder metallurgical process



machine parts is known as powder metallurgy [1]. The P/M covers various stages as shown in Fig. 1. The role of different stages of the manufacturing process of P/M specimen is described as given in Fig. 1

2.1 *Metal Powder*

Generally, first identified the product for manufacturing using P/M process; then important step is selection of material and process parameters to be required. In present work 99.7% pure aluminium powder is used as a matrix material and alumina as a reinforcement material both are taken from the chemical industry. The reinforcement materials fly ash and bagasse ash are taken it from the power generation plant and sugarcane industry respectively. The fly ash and bagasse ash are sieved into size of 75 μm .

2.2 *Blending of Metal Powder*

In the next stage of P/M process, the required metal powders are mixed in different ratios using stirrer to prepare powders in homogeneous form for the period of 30 min by using ethanol as a binder during mixing of composite mixture [14]. P/M is frequently used to improve various material properties and to prepare advanced materials that are different or impossible to be obtained by traditional techniques. The homogeneous mixture of aluminium along with various reinforcement material in different percentage is carried as shown in Table 2.

2.3 Compacting

The die-punch assembly is used to compress the above powder mixture on the Universal Testing Machine (UTM) to get required shape specimen. As shown below in Fig. 2 for tensile and impact test specimen and as shown in Fig. 3 for lateral compression test.

Compaction is the first step in the shaping of loose powders into a product of desired size and provide sufficient strength for handling specimen. But during compacting of an aluminium metal powder it is necessary to maintain the compacting ratio 2.6693 g/cm^3 for aluminium. It is mostly done by unidirectional or uniaxial compaction on a punch or to a lesser extent by cold isostatic pressing (CIP). In a first stage the particles are rearranged leading to a better packing. Increasing pressure provides better packing of metal particle with reinforcement particle and helps to decreasing the porosity.

Table 2 Mechanical alloying elements in different weight percentage

Sr. No.	Name of material	% Reinforcement
1	Pure aluminium	100% Al
2	Al-5% fly ash composites	95% Al + 5% FA
3	Al-10% fly ash composites	90% Al + 10% FA
4	Al-15% fly ash composites	85% Al + 15% FA
5	Al-5% bagasse ash composites	95% Al + 5% BA
6	Al-10% bagasse ash composites	90% Al + 10% BA
7	Al-15% bagasse ash composites	85% Al + 15% BA
8	Al-5% alumina composites	95% Al + 5% Al_2O_3
9	Al-10% alumina composites	90% Al + 10% Al_2O_3
10	Al-15% alumina composites	85% Al + 15% Al_2O_3

Fig. 2 Die compacting for tensile and impact test specimen



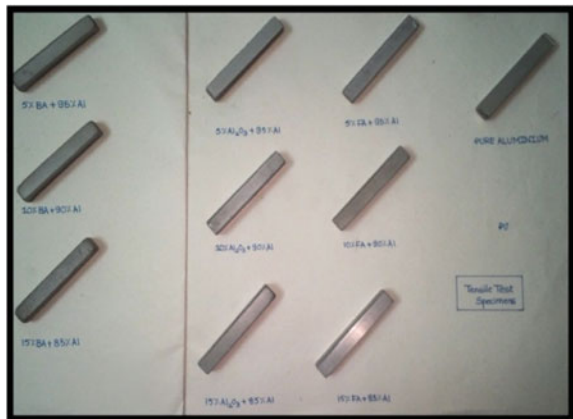
2.4 Sintering

After compacting powder it is necessary to provide heat in a protective atmosphere to a temperature below the melting point of the major component, a densification of the powder occurs by eliminating pores and a sintered product of increased mechanical strength is formed. During sintering process, cohesion of particle takes place as necks form and grows at the points of particle contact. According to ASTM standard sintering temperature for aluminium is typically in between 600 and 650 °C [15]. In present work sintering is done by using the muffle furnace at 630 °C. The composites manufactured by using powder metallurgy process are purposefully shaped as per ASTM test standard. Figure 4 shows tensile test specimen and Fig. 5 Charpy impact test specimen.

Fig. 3 Die compacting for lateral compression test specimen



Fig. 4 Tensile test specimen of 10 × 10 × 70 mm



3 Results and Discussion

3.1 Ultimate Tensile Strength (UTS)

Tensile test behavior of all the prepared specimen of pure aluminium matrix and various reinforced composites are determined to investigate the ultimate tensile strength behavior of all composites. Tensile test of rectangular specimen is carried out according to the ASTM standard E8-610 [15] on 300 kN capacity of UTM with gage length of 50.00 ± 0.05 and width 10.00 ± 0.05 . The overall dimensions of specimen $70 \times 10 \times 10$ mm.

The ultimate tensile strength of all the reinforced composites is shown in Table 3. The ultimate tensile strength of all the types of reinforced composites is found to be increases as the % reinforcement increases. The UTS increases in all type of reinforcement but UTS of bagasse ash reinforced composites is found more as compared to fly ash and alumina reinforcement composites as shown in Fig. 6.

Fig. 5 Charpy impact test specimen of $10 \times 10 \times 55$ mm

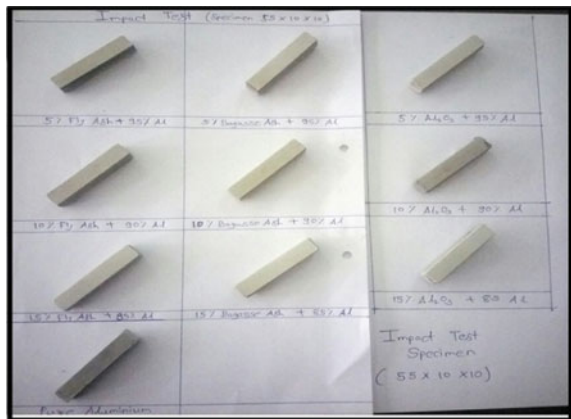


Table 3 Ultimate tensile strength of all reinforced composites

Sr. No.	Name of material	Ultimate tensile strength (Mpa)
1	Pure aluminium	159.015
2	Al-5% fly ash composites	186.882
3	Al-10% fly ash composites	187.236
4	Al-15% fly ash composites	187.813
5	Al-5% bagasse ash composites	172.560
6	Al-10% bagasse ash composites	186.882
7	Al-15% bagasse ash composites	206.444
8	Al-5% alumina composites	167.102
9	Al-10% alumina composites	188.136
10	Al-15% alumina composites	193.663

The strength of composite material increases due to strengthening effect produced in composite material due to reinforcement addition [16, 17].

3.2 Impact Strength

Impact strength behavior of pure aluminium specimen and all the specimens of various reinforced composites are determined to investigate the sustainability of all composites. Impact test of rectangular specimen is carried out according to the ASTM standard E23-B823 on impact test equipment by Charpy Impact test method. The overall dimensions of specimen required for charpy impact test is $55 \times 10 \times 10$ mm [15]. Impact strength behavior in terms of joule (J) of all sintered specimen is tabulated in Table 4.

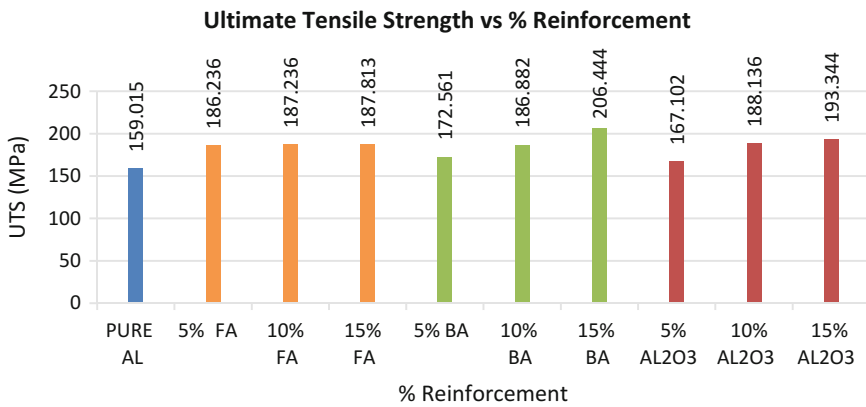


Fig. 6 Ultimate tensile strength versus % reinforcement

Table 4 Impact strength of all reinforced composites

Sr. No.	Name of material	Impact strength (J)
1	Pure aluminium	1
2	Al-5% fly ash composites	2
3	Al-10% fly ash composites	2.5
4	Al-15% fly ash composites	3.5
5	Al-5% bagasse ash composites	1.5
6	Al-10% bagasse ash composites	2
7	Al-15% bagasse ash composites	4
8	Al-5% alumina composites	2
9	Al-10% alumina composites	3
10	Al-15% alumina composites	4

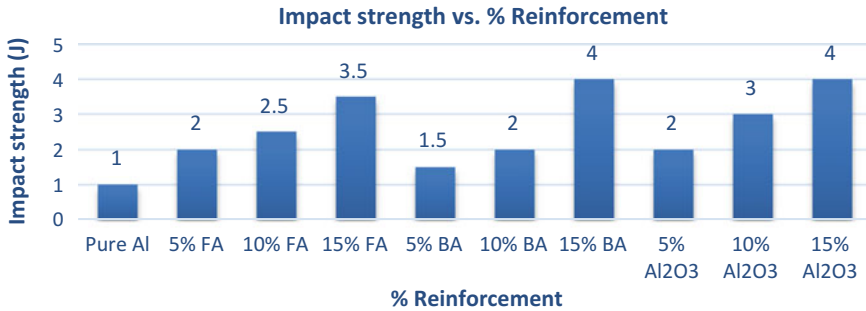


Fig. 7 Impact strength versus % reinforcement

From Table 4 and Fig. 7 it is observed that 15% bagasse ash and 15% alumina shows the highest impact strength than pure aluminium. 75% increment is observed than the pure aluminium. Also, from above table and figure it was observed that 5% bagasse ash shows the less percentage increment among all the reinforcement materials. So, finally among the all three reinforced materials Al_2O_3 shows the more impact strength by weight percentage than bagasse ash, fly ash and pure aluminium.

4 Conclusions

The pure aluminum is successfully reinforced by commercially used alumina and industrial waste fly ash and bagasse ash as a reinforcement material to manufacture the AMCs by the route of powder metallurgy. Industrial waste fly ash and bagasse ash reinforcement gives the better mechanical properties as compared to pure Al.

The ultimate tensile strength (UTS) of all the reinforced material increases with increase in percentage reinforcement due to resistance offered by the hard reinforcement particle. The UTS of Al bagasse ash composites found to be more than other reinforcement material and shows 29.82% increment than pure Al. Therefore, UTS trend observed to be more in bagasse ash reinforced composites while least in fly ash reinforced composites. However alumina reinforced composites found in between bagasse ash and alumina reinforced composites.

Impact strength increases with increase in percentage reinforcement of all Al composites due to hard particles of bagasse ash, fly ash and alumina sustain the impact stroke. Therefore, impact strength trend observed to be more in alumina reinforced composites while least in fly ash reinforced composites. However bagasse ash reinforced composites found in between alumina and fly ash reinforced composites.

References

1. Radhaa P, Chandrasekaran G, Selvakumar N (2015) Simplifying the powder metallurgy manufacturing process using soft computing tools. *J Appl Soft Comput Tool* 27:191–204 (Elsevier)
2. Bharat Admile SG, Kulkarni SA (2014) Sonwane; review on mechanical & wear behavior of aluminum-fly ash metal matrix composite. *IJETAE* 4(5):863–866
3. Torralba JM, da Costab CE, Velasco F (2003) P/M aluminum matrix composites: an overview. *J Mater Process Technol* 133:203–206 (Elsevier)
4. Nassa AE, Nassar EE (2015) Properties of aluminum matrix nano composites prepared by powder metallurgy processing. *J King Saud Univ Eng Sci* (Elsevier)
5. Kulkarni SG, Menghani JV (2016) Achchhe Lal; investigation of mechanical properties of fly ash and Al_2O_3 reinforced A356 alloy matrix hybrid composites manufactured by improved stir casting. *Int J Eng Mater Sci* 23:27–36
6. The Aluminum Association (1998) Book of selection and application of aluminium alloy
7. Kulkarni SG, Menghani JV (2014) Achchhe Lal; effect of fly ash hybrid reinforcement on mechanical property and density of aluminium A356 alloy. *J Procedia Mater Sci* 5:746–754 (Elsevier)
8. Wu X, Xia K (2007) Back pressure equal channel angular consolidation—application in producing aluminium matrix composites with fine fly ash particles. *J Mater Process Technol* 192:355–359 (Elsevier)
9. Senapati AK et al (2014) An extensive literature review on the usage of fly ash as a reinforcement for different matrices. *IJISME* 2(3):4–9
10. Usman AM, Raji A, Waziri NH, Hassan MA (2004) Production and characterisation of aluminium alloy—bagasse ash composites. *IOSR J Mech Civ Eng* 11(4):38–44
11. Anas M, Khan MZ (2015) Comparison of hardness and strength of fly ash and bagasse ash Al-MMCs. *IJSART* 1(7):88–93
12. Singh H, Sarabjit NJ, Tyagi AK (2011) An overview of metal matrix composite: processing and sic based mechanical properties. *J Eng Res Stud* 2(4):72–78
13. Attar S, Nagaral M, Reddappa HN, Auradi V (2015) A review on particulate reinforced aluminum metal matrix composites. *JETIR* 2(2):225–229
14. Abdizadeh H, Ebrahimiard R, Baghchesara MA (2014) Investigation of microstructure and mechanical properties of nano MgO reinforced al composites manufactured by stir casting and powder metallurgy methods: a comparative study. *J Compos: Part B* 56:217–221 (Elsevier)
15. ASTM International standards Standard practices for production and preparation of powder metallurgy (P/M) test specimens. Designation: B 925–03
16. Aigbodion VS (2014) Thermal ageing on the microstructure and mechanical properties of Al–Cu–Mg alloy/bagasse ash particulate composites. *J King Saud Univ Eng Sci* 26:144–151
17. Guo RQ, Rohatgi PK (1997) Preparation of aluminium–fly ash particulate composite by powder metallurgy technique. *J Mater Sci* 32:3971–3974

Phase Sensitive Detector: Fabrication, Processing, and Applications

P.A. Ghadage, U.R. Ghodake and S.S. Suryavanshi

Keywords Phase sensitive detector · Phase difference · Amplitude

1 Introduction

The amplitude and phase of a test signal with a reference signal or wideband Gaussian noise was detected and measured by using various techniques like Phase sensitive detection, Lock-in-amplification, Lock-in-detection [1, 2]. The Phase Sensitive Detector (PSD) is one of the versatile electronic devices which detects the phase difference between two signals. The PSD has also been used as a null detector in many applications like calibration of AC bridges, susceptibility measurement devices [3, 4]. Due to low cost and high reliability of the detector circuit, could produce best results in harsh environments, medium precision applications [5]. Here we had designed and fabricated a detector circuit on a single printed circuit board by using low-cost Single Pole Double Throw (SPDT) switch.

P.A. Ghadage · S.S. Suryavanshi (✉)
Department of Physics, Solapur University, Solapur 413255, Maharashtra, India
e-mail: sssuryavanshi@rediffmail.com

P.A. Ghadage
e-mail: ghadagepa@gmail.com

U.R. Ghodake
Department of Electronics, Shri. Shivaji Mahavidyalaya,
Barshi 413411, Maharashtra, India
e-mail: urghodake@rediffmail.com

2 Experimental Details

2.1 Design and Fabrication Process

The detector circuit is designed and fabricated on a single printed circuit board. The low cost and easily available chemicals like FeCl_3 were used for the etching process. The inverting amplifier is connected at the input stage of the PSD. The output of the inverting amplifier is then connected to a simple Zener regulator circuit through a diode. The Zener diode is connected in reverse bias, which acts as a zero crossing detector (ZCD). The output of ZCD produces a square wave, which is considered as a reference signal.

2.2 Operating Mechanism of PSD

The schematic circuit diagram of PSD is shown in Fig. 1. The sinusoidal test signal has been amplified to assume reasonable amplitude and then applied to the switching system.

The switching of the signals is done by using an SPDT switch like IC 7512DI. If the contactor of the switch goes in an upward direction, the second amplifier circuit acts as a non-inverting adder [6]. The output voltage at the non-inverting terminal were determined by using the principle of superposition theorem, which is shown in the following equations [3]:

$$V_r = \frac{R_2}{R_3 + R_2} V_i \quad (1)$$

where, $V_r = V\sin(\omega t + \phi_1)$ and Eq. (1) can also be written as,

$$V_r = \frac{1}{3} V_i \quad (2)$$

But the amplifier gain is,

$$A = 1 + \frac{R_f}{R_1} = 3 \quad (3)$$

Hence the total gain of the amplifiers shows that $A(+1) = A(-1)$.

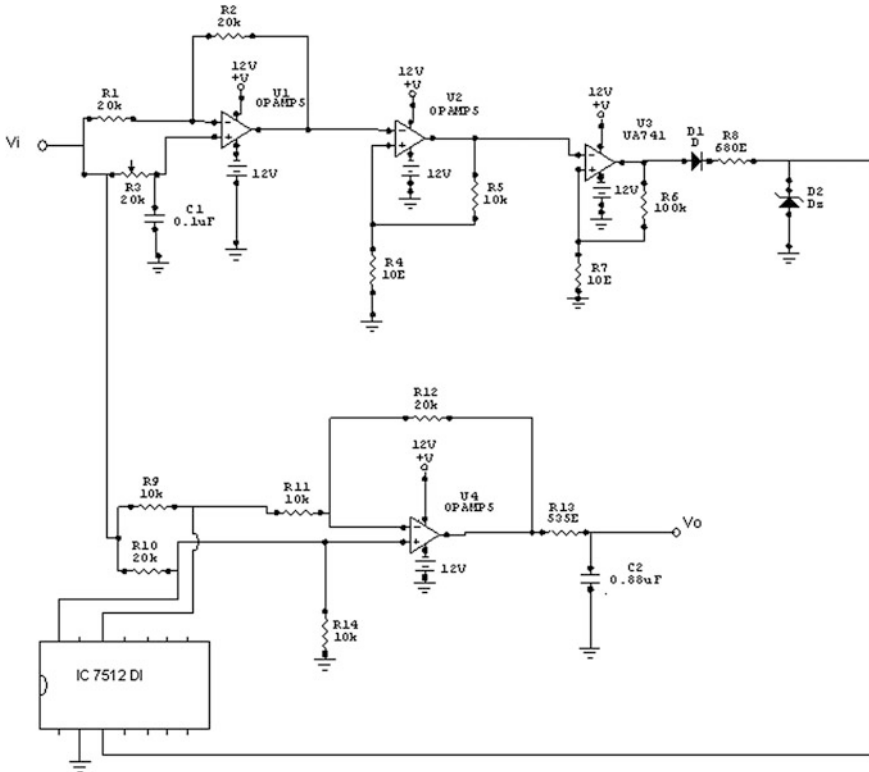


Fig. 1 Circuit diagram of PSD for measurement of phase angle

3 Results and Discussions

The output measurements of the detector circuit show that when there is a phase difference between the test signal and the reference signal, the average output voltage or the meter reading is a function of phase angle ϕ of the test voltage with respect to the reference voltage. The output results are also measured on cathode ray oscilloscope, which are similar with reported waveforms shown in Fig. 2 [2].

The d.c. output voltages obtained from the PSD circuit for different phase angles are shown in Table 1.

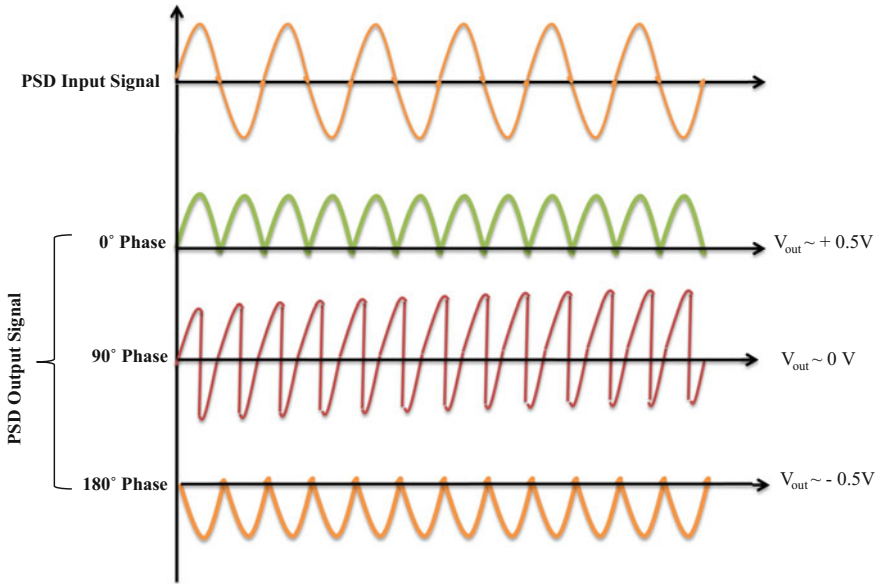


Fig. 2 Output waveforms of PSD at various phase angles

Table 1 Output measurements of PSD

Observation No.	Phase difference	D.C. output voltage
1	0°	+5
2	90°	0
3	180°	-5

4 Conclusions

In this study, we have successfully designed a schematic circuit of Phase Sensitive Detector which is fabricated on a single printed circuit board and is very useful for various applications. The output measurements of detector circuit give the d.c. The output voltage for a respective change in phase of a test signal. Hence if the test signal and reference signals are in phase, the output of PSD has been similar to an AC to DC converter.

References

1. Blair DP, Sydenham PH (1975) Phase-sensitive detection as a means to recover signals buried in noise. *J Phy E Sci Instrum* 8:621
2. Smith RWM, Freeston IL, Brown BH, Sinton AM (1992) Design of a phase-sensitive detector to maximize signal-to-noise ratio in the presence of gaussian wideband noise. *Meas Sci Technol* 3:1054–1062

3. Wobschall D (1961) Sensitive output indicator for differential transformer displacement determinations. *Rev Sci Ins* 32:71
4. de Sa A (1994) Signal-conditioning integrated circuits for magnetic susceptibility measurements. *Meas Sci Technol* 5:55–57
5. Sydenham PH, Taing V, Mounsey DJ, Yu WX (1995) Low-cost, precision, flat inductive sensor. *J Meas* 15:179–188
6. Bissel PR, Webster E, Babasanya-Craig CA (1978) Phase-sensitive detector experiments in the teaching laboratory. *Phys Educ* 22(2):122

Microbial Synthesis of Silver Nanoparticles Using *Aspergillus flavus* and Their Characterization

Hemant Bhangale, K.M. Sarode, A.M. Patil and D.R. Patil

Keywords *Aspergillus flavus* · Silver nanoparticles · Biosynthesis · UV · SEM · TEM

1 Introduction

Nanotechnology is the design, characterization, production and applications of structures, devices, and systems by controlled manipulation of size and shape at the nanometer scale that produces structures, devices, and systems with at least one novel/superior characteristics or property [1]. Nanoparticles are the fundamental units of the nanotechnology. Nanoparticles are typically in the range from 1 to 100 nm and can be tuned in various sizes and shapes, each having different quantum mechanical properties and hence different exploitation. The size of the nanoparticles is the most important quality of nanoparticles.

Silver nanoparticles have potential applications in the field of photonics [2], electronics [3], optical receptor [4], Biolabeling [5] and antimicrobial agents [6], water filters and also used in solar energy applications. Several methods like physical and chemical routes are employed to prepare silver nanoparticles of various shapes and sizes which are found to be expensive and involve the use of toxic chemicals. There is a growing need to develop cost effective and environmentally friendly technique for the synthesis of silver nanoparticles. Exploitation of microbial cells is a novel approach for the synthesis of metal nanoparticles [7]. The biological route is the reliable protocol for the synthesis of nanoparticles over a range of chemical composition, sizes, and high monodispersity. Biological synthesis takes place within living organisms and is catalyzed by enzymes.

H. Bhangale (✉) · K.M. Sarode · A.M. Patil · D.R. Patil
Nanomaterial Research Laboratory, R.C. Patel ACS College, Shirpur, Maharashtra, India
e-mail: hgbhangale67@gmail.com

Attempts were made to prepare silver nanoparticles using the fungus *Aspergillus flavus* by optimizing the conditions and the corresponding surface Plasmon resonance was studied.

2 Materials and Methods

2.1 Preparation of Cell Filtrate and Synthesis of Silver Nanoparticles

The fungus culture *Aspergillus flavus* (NCIM650) was obtained from National Chemical Laboratory culture collection center, Pune, India. It was sub-cultured and maintained in the Microbiology Lab of R.C. Patel College, Shirpur. The biomass of *Aspergillus flavus* has grown aerobically in potato dextrose broth for seven days at 30 °C. After seven days the mycelia was separated, washed thoroughly with distilled water three times to remove any media components. Fresh 5 g of biomass was re-suspended in 100 ml distilled water. The flask was again incubated at 37 °C at 120 rpm. After 72 h, biomass was separated by filtering through Whatman filter paper, and the cell filtrate was used for the synthesis of silver nanoparticles [8, 9].

For the synthesis of silver, nanoparticles-cell filtrate was challenged with the equal amount of 1 mM silver nitrate solution at optimized pH value, and the flask was incubated at 37 °C at 120 rpm for 96 h. A control containing cell filtrate without silver nitrate solution was run simultaneously as standard with the experimental flask.

2.2 UV-Visible Characterization

Change in color of the cell filtrate incubated with silver nitrate solution was visually observed over a period. The bio-reduction of precursor silver ions was monitored at different time intervals. UV-visible spectra were also carried for three months to check the stability of the synthesized silver nanoparticles.

2.3 XRD Measurements

The prepared silver nanoparticles solution was centrifuged at 8000 rpm for half an hour to obtain purified silver nanoparticles which were then re-suspended in deionized water and again centrifuged under same conditions. The collected pellets were air dried at room temperature for obtaining the powder form. X-ray diffraction technique was used to analyze the metallic nature of the nanoparticles after bio-reduction.

2.4 FTIR Measurements

The presence of proteins and potential biomolecules responsible for the synthesis of silver nanoparticles was analyzed by FTIR spectroscopy.

2.5 Scanning Electron Microscopy

The solution of silver nanoparticles was obtained in powder form for scanning electron microscopy.

2.6 TEM Measurements

A drop of colloidal silver nanoparticles solution was placed on the carbon-coated copper grid and dried by allowing water to evaporate at room temperature. Electron micrographs were obtained using Philips CM 200 transmission electron microscopy.

3 Result and Discussion

3.1 Biosynthesis of Silver Nanoparticles

The filtrate was pale yellow in color before the addition of silver nitrate solution and this change to brown in color on completion of the reaction with Ag^+ ions after 48 h (Fig. 1). The appearance of the brown color of the solution containing the cell

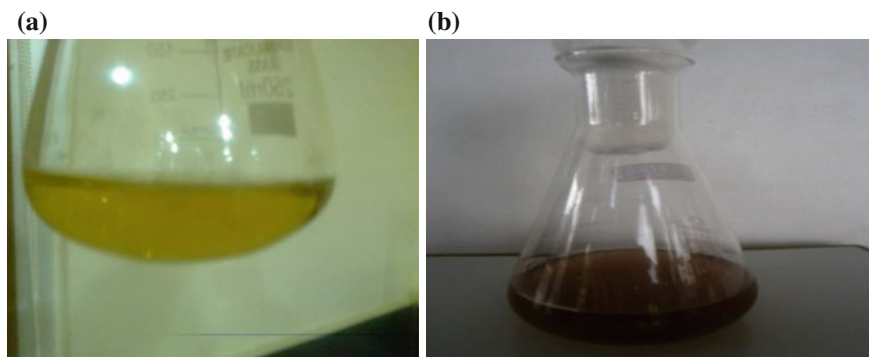


Fig. 1 a Flavus filtrate before treatment of AgNO_3 b after treatment

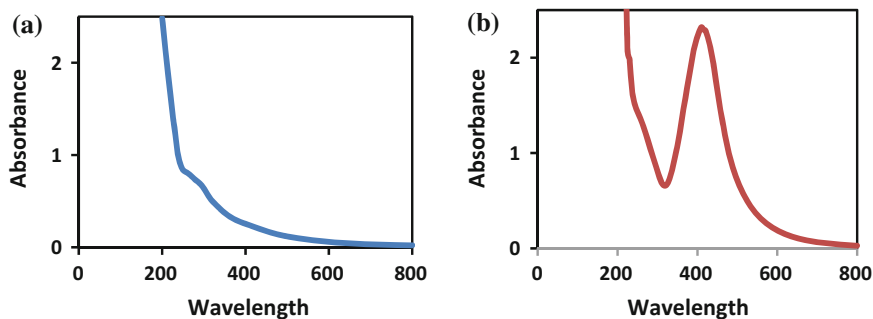


Fig. 2 UV-visible spectra of *Aspergillus flavus* filtrate (a) and filtrate treated with silver nitrate (b)

filtrate indicates the formation of silver nanoparticles in the reaction mixture [10]. After 48 h no significant change in the color was observed.

3.2 UV-Visible Spectra

The UV-visible spectra of only *Aspergillus flavus* filtrate and filtrate treated with silver nitrate solution is depicted in Fig. 2a, b respectively. Figure 2a does not show any absorbance band while in Fig. 2b the absorbance peak was observed at 409 nm at 12 h and attained the maximum intensity after 48 h. After 48 h no change in the maximum intensity was observed indicating the complete reduction of silver ions. The absorbance peak at 409 nm is due to surface Plasmon resonance band occurring due to collective oscillation of free electrons in metal nanoparticles in resonance with the light wave [11, 12]. The result correlates with Shivaraj Ninganaogouda's result [9].

3.3 XRD Analysis

XRD analysis of biosynthesized silver nanoparticles was used to study the crystalline nature of the particles. XRD pattern of the prepared sample is shown in Fig. 3. The diffracted intensities were recorded from 10° to 80° through 2θ angles, and it reveals that particles were crystalline in nature with FCC structure.

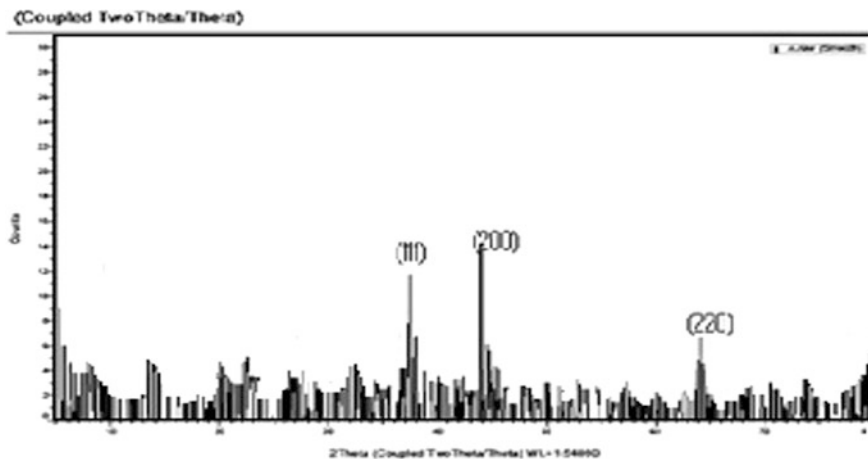


Fig. 3 XRD spectrum of synthesized silver nanoparticles

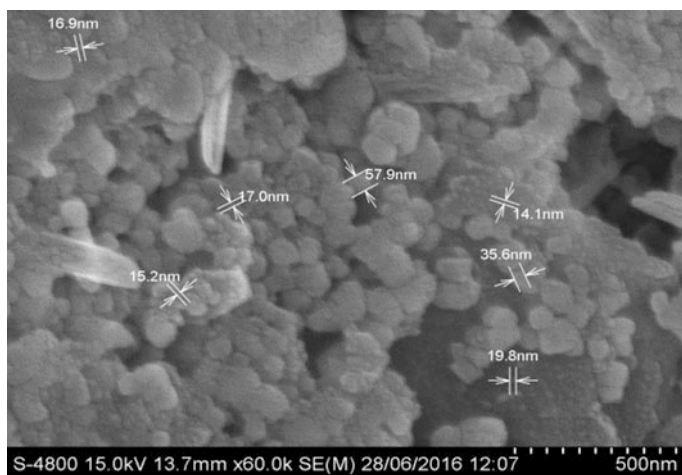


Fig. 4 Scanning electron micrograph of the silver nanoparticles

3.4 SEM

The scanning electron micrograph of silver nanoparticles synthesized by treating cell filtrate with 1 mM silver nitrate solution is depicted in Fig. 4. Which clearly shows surface deposited silver nanoparticles and some agglomeration was also observed.

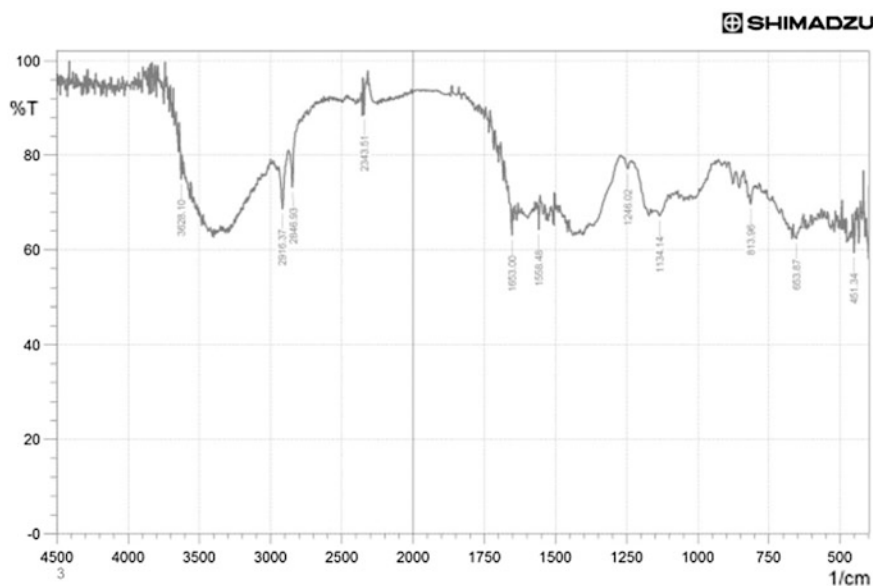


Fig. 5 FTIR spectra of silver nanoparticles

3.5 FTIR Measurements

FTIR spectrum of the prepared sample of silver nanoparticles is shown in Fig. 5. The study of FTIR spectra confirms the presence of proteins in the samples of silver nanoparticles.

3.6 TEM

TEM image of the drop coated film of silver nanoparticles showed distinct shape and size of the nanoparticle (Fig. 6). The particles were spherical in shape with mean of 7.13 nm. Silver nanoparticles are uniformly distributed with some agglomeration was noticed. The selected area diffraction pattern confirms the crystalline FCC structure of metallic silver.

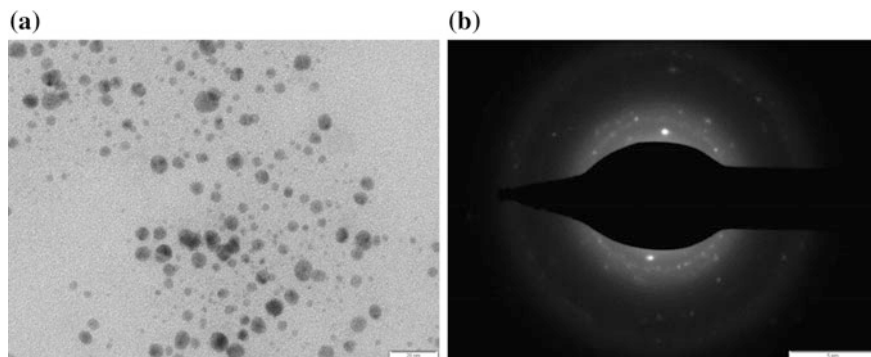


Fig. 6 **a** TEM of silver nanoparticles, **b** diffraction pattern of silver nanoparticles

4 Conclusions

The fungus *Aspergillus* has a potential to synthesize silver nanoparticles extracellularly and is the developing nano factories because of downstream processing and handling of biomass would be simple. UV-visible spectra show the maximum absorption at 409 nm with a single SPR band confirm that the particles are spherical. SEM observations show that the particles synthesized in the range between 10 and 55 nm with spherical in size. FTIR analysis confirms the presence of the proteins in the cell filtrate solution of silver nanoparticles. The synthesized silver nanoparticles were found to stable over a period of three months. TEM reveals that the particles were spherical with the average size of 7.13 nm and diffraction pattern exhibit the FCC structure.

References

1. Sharon M, Sharon M, Pandey S, Oza G (2012) Bio-nanotechnology concepts and applications. Ane Books, New Delhi
2. Velicov KP, Zegers GE, Von Blaaderen A (2003) Synthesis and characterization of large colloidal silver particles. *Langmuir* 19:1384
3. Rao CNR, Kulkarni GU, Thomas PJ, Edwards PP (2000) Metal nanoparticles and their assemblies. *Chem Soc Rev* 29:27–35
4. Schultz S, Smith DR, Mock JJ, Schultz A (2000) Single target molecule detection with nonbleaching multicolor optical immunolabels. *Proc Natl Acad Sci* 97:996
5. Hayat MA (1989) Colloidal gold: principles, methods and applications. *Chem Phys* 90:51
6. Valodkar M, Bhadorai A, Pohnerkar J, Mohan M, Thakore S (2010) Morphology and antibacterial activity of carbohydrate stabilized silver nanoparticles. *Carbohydr Res* 345:1767–1773
7. Vala AK et al (2014) Biogenesis of silver nanoparticles by marine derived fungus *Aspergillus Flavus* from Bhavnagar coast, Gulf of Khambhat, India. *J Mar Biol Oceanogr* 3:1

8. Vigneshwaran N, Ashtaputre NM, Varadarajan PV, Nachane RP, Paralikar KM, Balasubramanya RH (2007) Biological synthesis of silver nanoparticles using the fungus *Aspergillus flavus*. *Mater Lett* 61:1413–1418
9. Ninganagouda S, Rathod V, Jyoti H, Singh D, Prema K, Ul Haq M (2013) Extracellular biosynthesis of silver nanoparticles using *Aspergillus Flavus* and their antimicrobial activity against gram negative MDR strains. *Int J Pharm Bio Sci* 4(2):222–229
10. Natrajan K, Selvaraj S, Ramchandra Murty V (2010) Microbial production of silver nanoparticles. *Digest J Nanomater Biostruct* 5:135–140
11. Taleb A, Petit C, Pileni MP (1998) Optical properties of self assembled 2D and 3D superlattices of silver nanoparticles. *J Phys Chem B* 102:2214
12. Link S, Sayed MAEI- (2003) Optical properties and ultrafast dynamics of metallic nanocrystals. *Annu Rev Phys Chem* 54:331

Shape Optimization of Microfluidic Pump Using Fluid-Structure Interaction Approach

P.M. Pawar, R.R. Gidde and B.P. Ronge

Keywords Shape optimization · Microfluidic pump · Micropump · Fluid-structure interaction · Parametric study

1 Introduction

A micropump is one of the important devices for medical applications, which can generate flow in the range of milliliters to microliters. Some potential applications for micropumps are still being investigated, involving in drug delivery, biological detection, a clinical analysis in medicine, etc. A nozzle/diffuser pump, also known as a valveless micropump is one of the most extensively investigated micropumps, which mainly consists of a flexible diaphragm propelling the flow and a microvalve directing the flow. The oscillation of the diaphragm above pump chamber excited by the actuators propels the flow. The conventional actuation mechanisms include piezoelectric [1], electrostatic [2], electromagnetic [3], shape memory alloy (SMA) [4], etc. A valveless micropump [5] designed for biological analysis and investigated the dependence on the properties of the pumped biological medium. Some of the main advantages of such micropump are the absence of moving parts (flap valves), the simple planar design, and high pump performance concerning

P.M. Pawar (✉)

Department of Civil Engineering, SVERI's College of Engineering,
Pandharpur 413304, India
e-mail: pawarpm@gmail.com

R.R. Gidde · B.P. Ronge

Department of Mechanical Engineering, SVERI's College of Engineering,
Pandharpur 413604, India
e-mail: ranjitsinhag1@rediffmail.com

B.P. Ronge

e-mail: ronge_bp@rediffmail.com

pressure head and flow rate. The performances of the diffuser/nozzle elements in valveless micropump analyzed by using commercial software Fluent [6]. Therefore, in this study, a three-dimensional finite element model of the diffuser/nozzle micropump was built in COMSOL Multiphysics, including the pump diaphragm and the working fluid and analyzed the effect of the geometric parameters on the flow rate to design a micropump.

2 Numerical Modeling

2.1 Description of Micropump

The fluid flow inside the pump is assumed to be laminar. The estimated force of the electromagnet is applied to the diaphragm of the three-dimensional micropump model. The dimensions of a model of the micropump selected for simulations are as follows: chamber diameter $D_c = 6$ mm, nozzle/diffuser length $L_d = 1.1$ mm, neck width $w_1 = 100$ μm , divergence angle $\theta = 10^\circ$ and height of the chamber $h_c = 500$ μm .

2.2 Governing Equations

The governing equation of forced vibration of a thin clamped plate is can be expressed as (Fox and Chen 2007):

$$D\nabla^4 W + \rho_p \frac{\partial^2 W}{\partial t^2} = f_e - P \quad (1)$$

where,

$$D = \frac{Et_d^3}{12(1 - \nu^2)} \quad (2)$$

and D is the plate stiffness, ∇^4 is the two-dimensional double Laplacian operator, E is the Elastic modulus, ν is the Poisons ratio of the diaphragm, t_d is the thickness of the diaphragm, and ρ_d is the density of the diaphragm. f_e is the periodic actuating force, and P is the dynamic pressure exerted on the diaphragm by the liquid. In this case, the pump diaphragm is assumed to be clamped.

The fluid flow can be considered as an incompressible laminar flow, which can be described using the Navier–Stokes equation (3) and the mass continuity equation (4) (Fan et al. 2004).

$$\rho_L \frac{D\vec{V}}{Dt} = \rho_L \vec{g} + \mu \nabla^2 \vec{V} - \nabla P \quad (3)$$

$$\frac{\partial \rho_L}{\partial t} + (\vec{V} \cdot \nabla) \rho_L = 0 \quad (4)$$

where, ρ_L is the density of the liquid; \vec{V} is the velocity vector; μ is the viscosity of the liquid.

2.3 Boundary Conditions

An estimated sinusoidal force of 0.020 N, is applied to the diaphragm at frequency 20 Hz. For the fluid part, zero pressure boundary condition is used at inlet and outlet. At the fluid-structure interface, the fluid receives deflection data from the diaphragm. A no-slip boundary condition was used for all the walls.

3 Simulation Results and Parametric Study

Figure 1a presents the total displacement. However, streamline velocity contours inside the chamber of micropump as shown in Fig. 1b.

It can be observed that during the first half cycle, the flow coming through the inlet into the pump chamber is more as compared to the flow coming back through the outlet. On the other hand, during the second half cycle, the flow going out through the outlet is more as compared to the flow going back through the inlet. The difference between the two curves provides the net flow that occurs from the inlet to the outlet in each cycle. As a result, the fluid flows from the inlet to outlet. However, the difference in the pressure drop across nozzle and diffuser elements cause a flow rectification as shown in Fig. 2a. The flow rate delivered by the micropump for different frequencies is, as depicted in Fig. 2b.

3.1 Optimization of Divergence Angle and Diffuser Length

The effect of the divergence angle and nozzle/diffuser length on the net flow rate is presented in Fig. 3a, b. It is observed that the net flow rate is maximum at divergence angle 10° . At smaller values of divergence angle, the rectification efficiency is low and thus the net flow rate increases with increase in divergence angle. In the same way, at higher values divergence angles, there is a possibility of flow

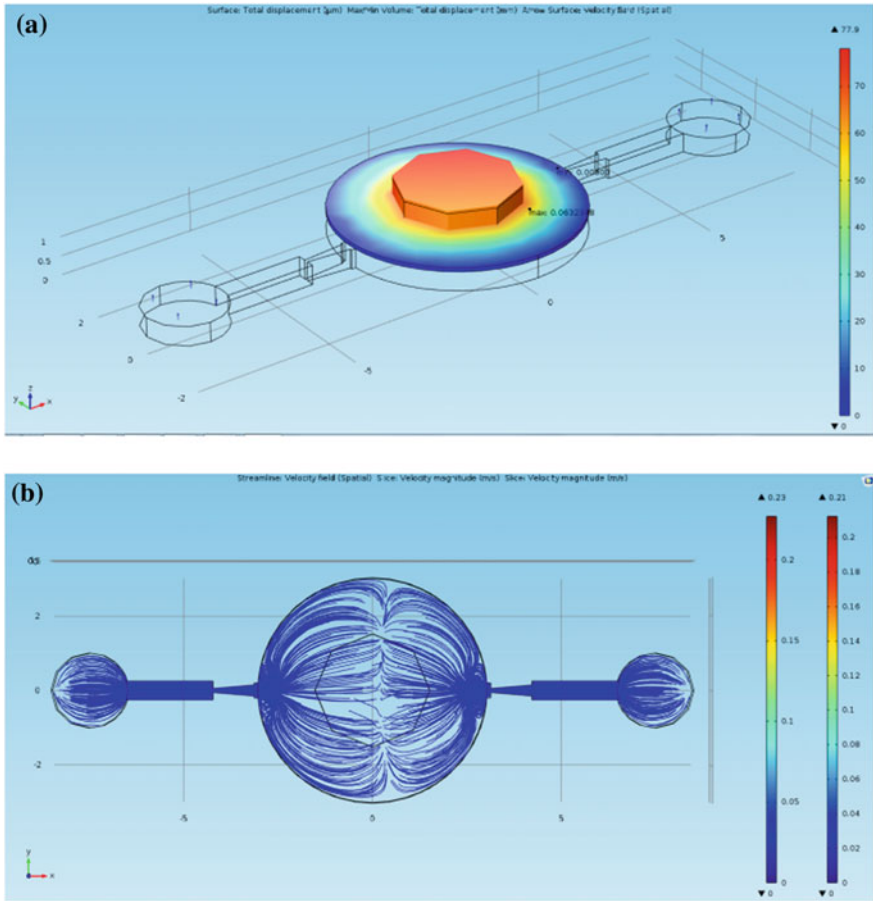


Fig. 1 a Total displacement of diaphragm (left). b Streamline velocity contours inside the chamber of micropump

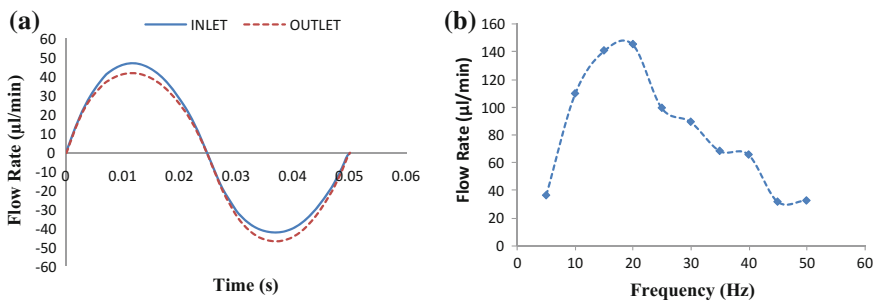


Fig. 2 a Flow rate through the inlet and outlet a function of time. b Flow rate versus frequency

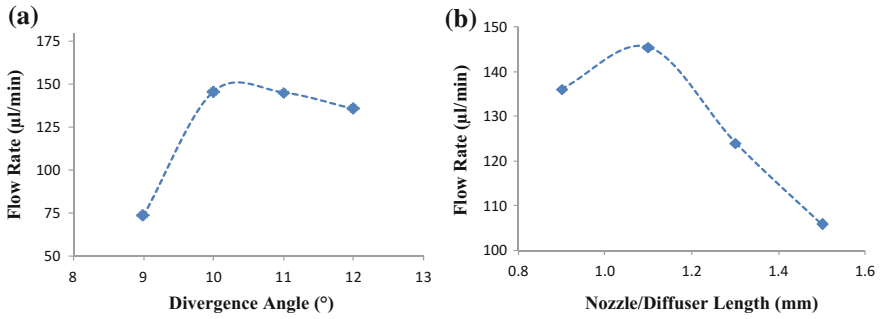


Fig. 3 a Net flow rate versus divergence angle. b Net flow rate versus nozzle/diffuser length

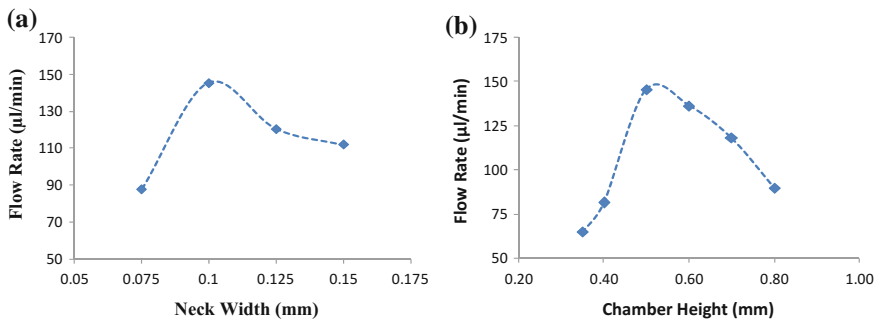


Fig. 4 a Net flow rate versus neck width. b Net flow rate versus chamber height

separation, which leads to the decrease in the net flow rate. It was also observed that net flow rate is higher at 1.1 mm diffuser length and lower at 1.5 mm.

3.2 Optimization of Neck Width and Chamber Height

The effect of neck width on the net flow rate is depicted in Fig. 4a. Flow rate becomes maximum for the neck width of 100 μm and minimum for the neck width of 150 μm . At the lower value of neck width, the net flow rate is found to be less which may be due to ‘clogging effect.’ A Higher value of neck width renders lower flow rectification and thus the net flow rate decreases.

The effect of the chamber height h_c on the net flow rate is studied by varying the chamber height in the range 300–500 μm for different neck width, as shown in Fig. 4b. It was observed that the net flow rate becomes the maximum for a chamber height of 500 μm . However, at larger chamber heights, due damping provided by the fluid, force transferred by the diaphragm to the fluid may be less. Thus net flow rate decreases with further increase in the chamber height more than 500 μm .

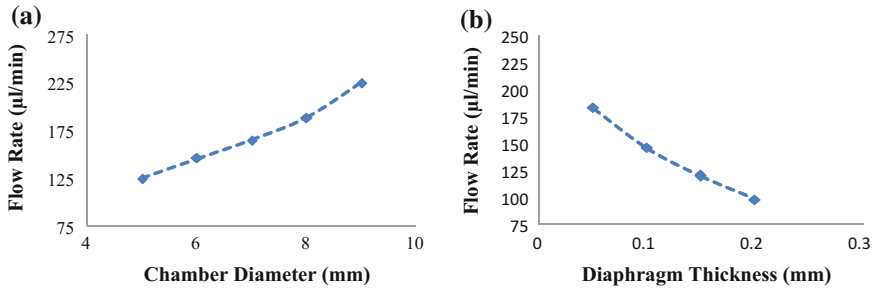


Fig. 5 **a** Net flow rate versus chamber diameter. **b** Net flow rate versus diaphragm thickness

3.3 Optimization of Chamber Diameter and Diaphragm Thickness

It was observed that the net flow rate increases with increase in chamber diameter as depicted in Fig. 5a. This may be due to the increase in stroke volume. The deflection of the diaphragm decreases with increase in the diaphragm thickness, and thus the net flow rate decreases as depicted in Fig. 5b.

4 Conclusion

In this study, diffuser/nozzle micropump was simulated. The effect of the geometrical parameters on the net flow rate the micropump was investigated using fluid-structure interaction approach. The simulation results are summarized as follows:

1. The net flow rate is maximum at divergence angle 10° . At smaller values of divergence angle, the rectification efficiency is low and thus the net flow rate increases with increase in divergence angle. Also at higher values divergence angles, the net flow rate decreases due to the possibility of flow separation. Thus the net flow rate is higher at 1.1 mm diffuser length and lower at 1.5 mm diffuser length.
2. The net flow rate is found to be less due to ‘clogging effect’ at lower values of neck width. Also at a higher value of neck width, the net flow rate decreases due to lower flow rectification. Thus it is maximum at 100 µm neck width. The net flow rate becomes the maximum for a chamber height of 500 µm. However, at larger chamber heights, due damping provided by the fluid, force transferred by the diaphragm to the fluid may be less. Thus net flow rate decreases with further increase in the chamber height.

3. The net flow rate increases with increase in chamber diameter due increase in stroke volume. Also, the net flow rate decreases as with an increase in diaphragm thickness as the deflection of the diaphragm decrease with increase in the diaphragm thickness.

References

1. Kim JH, Kang CJ, Kim YS (2004) A disposable polydimethylsiloxane based diffuser micropump actuated by piezoelectric-disc. *Microelectron Eng* 71:119–124
2. Patrascu M, Gonzalo-Ruiz J, Goedbloed M, Brongersma SH, Crego-Calama M (2012) Flexible, electrostatic microfluidic actuators based on thin film fabrication. *Sens Actuators A* 186:249–256
3. Chang HT, Lee CY, Wen CY, Hong BS (2007) Theoretical analysis and optimization of electromagnetic actuation in a valve less microimpedance pump. *Microelectron J* 38 (2007):791–799
4. Xu D, Wang L, Ding G, Zhou Y, Yu A, Cai B (2001) Characteristics and fabrication of NiTi/Si diaphragm micropump. *Sens Actuators A* 93(2001):87–92
5. Andersson H, van der Wijngaart W, Nilsson P, Enoksson P, Stemme G (2001) A valve-less diffuser micropump for microfluidic analytical systems. *Sens Actuators B* 72(2001):259–265
6. Singhal V, Garimella SV, Murthy JY (2004) Low Reynolds number flow through nozzle-diffuser elements in valveless micropumps. *Sens Actuators A* 113(2004):226–235

Fabrication and Characterizations of Cu/CdS_{0.8}Te_{0.2} Thin Film Schottky Junction Grown by Thermal Evaporation Technique

M.S. Kale and D.S. Bhavsar

Keywords XRD · SEM · Photo sensing · Cu/CdS_{0.8}Te_{0.2} Schottky diode

1 Introduction

Metal semiconductor (MS) structure fabrication has drawn much attention because of its usefulness in the fabrication of various electronics and opto-electronics devices [1]. The metal semiconductor interface properties can be altered by chemical compositions and surface preparation conditions [2, 3]. Many researchers develop various models to understand the behaviors of MS junction. Most of the efforts are being carried to realistic interpretation of Schottky diode parameters [4]. I-V measurement method has been extensively used to evaluate the ideality factor and Schottky barrier height (SBH) of Schottky diode [5]. The MS contact is one of the fundamental structures in electronic devices [6]. MS contacts are used frequently in ICs, various electronic devices, solar cells and high-current rectifiers.

In the present work the structural and photo sensing properties of thermally evaporated CdS_{0.8}Te_{0.2} thin film are discussed. Further work is extended to formation of Cu/(n)-CdS_{0.8}Te_{0.2} metal semiconductor junction and investigation of I-V characteristics of metal semiconductor junction.

2 Experimental

The ternary compound of CdS_{0.8}Te_{0.2} was prepared by melt quench method and the prepared compound is used in MS junction. The Schottky junction was formed by sequentially depositing ohmic contact, semiconductor layer and a metal layer onto the glass substrate by using thermal evaporation technique (model—Hind Hi Vac

M.S. Kale (✉) · D.S. Bhavsar

Department of Electronics, Pratap College, Amalner, Jalgaon, Maharashtra, India
e-mail: milinkale616@yahoo.com

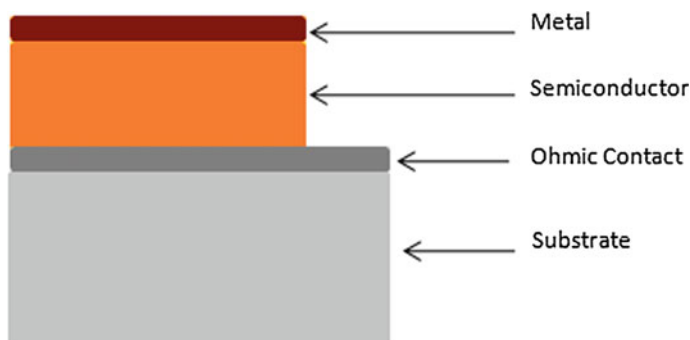


Fig. 1 Schematic of Cu/(n)-CdS_{0.8}Te_{0.2} Schottky diode

12A4D) under the pressure of 2×10^{-5} torr. The deposition rate was kept in the range of 8–10 Å/s and growth was monitored on Digital Thickness Monitor (DTM-101) provided by Hind-Hi Vac. Before deposition, the glass substrates were cleaned thoroughly using detergent, distil water, chromic acid and acetone.

2.1 Preparation of Samples

First of all, the ohmic contact was formed by depositing the Al thin film of 1000 Å thickness on glass substrate. Next, a semiconductor layer of CdS_{0.8}Te_{0.2} of 3000 Å thickness was deposited on Al thin film. Finally, onto the semiconductor layer the Cu thin film was deposited to form Schottky diode. Then the prepared sample was annealed at 100 °C. The schematic of Schottky diode is shown in Fig. 1.

The deposited CdS_{0.8}Te_{0.2} thin film was characterised under the XRD to determine the nature of the material and crystal structure. The surface morphology of CdS_{0.8}Te_{0.2} thin film was studied by using SEM technique. The photo sensing coefficient of CdS_{0.8}Te_{0.2} thin film was determined by photo sensing experiment. I-V measurements of Cu/CdS_{0.8}Te_{0.2} thin film metal semiconductor contact were determined by using Keithley model.

3 Results and Discussion

3.1 XRD Analysis

The XRD pattern of CdS_{0.8}Te_{0.2} thin film is shown in Fig. 2. The sample was scanned within the 2θ range of 20°–80°. The multiple XRD peaks show that CdS_{0.8}Te_{0.2} thin film is polycrystalline in nature [7]. The diffraction angles 2θ peaks

observed at degree 25.2°, 26.6°, 34.0° and 41.4° corresponds to (040), (330), ($\bar{1}01$) and ($\bar{1}21$) reflection planes respectively. The peaks are well matches with JCPDS data. The dominant peak belongs to orthorhombic crystal structure. From the JCPDS data the lattice parameters a, b and c were found 14.31, 14.07 and 14.56 Å respectively.

3.2 SEM Analysis

The SEM photographs of the CdS_{0.8}Te_{0.2} thin film is shown in Fig. 3. The SEM image reveals that the grown sample was homogeneous. The spherical shaped nano-grains were closely packed and uniformly distributed and covers the almost area of substrate. The samples is free from any microscopic defects like cracks or peeling off. It is also seen that the grains are made up of small particle and forms clusters [8, 9]. The average cluster size is found to be near about 150 nm.

Fig. 2 XRD pattern of CdS_{0.8}Te_{0.2} thin films

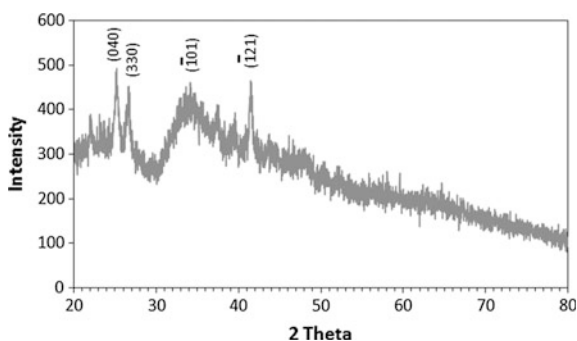
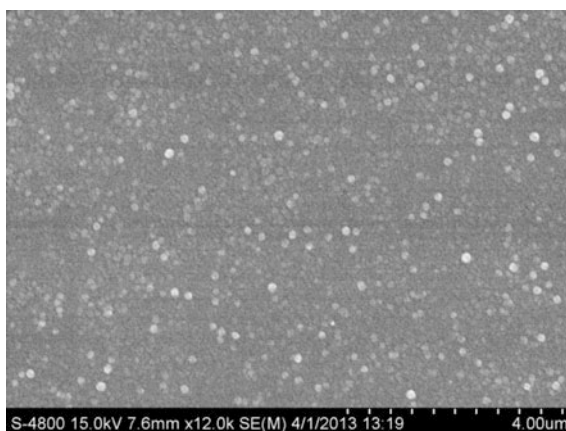


Fig. 3 SEM image of CdS_{0.8}Te_{0.2} thin films



3.3 Photo Sensing Analysis

The opto-electronics performance of CdS_{0.8}Te_{0.2} thin films determined from I-V response. Supply voltages was varied from 0 to 10 V.

Figure 4a–d shows the I-V plots of CdS_{0.8}Te_{0.2} thin films under the luminance and dark conditions for various thicknesses. From these figures, the recorded I-V plots reveal that the current increases with the voltage. The amount of current always depends upon the number of charge carriers [10]. From Fig. 4a, b it is clear that the current under the luminance is slightly higher than the dark current for thickness 1000 and 2000 Å. However, for thickness 2500 and 3000 Å, the light current was relatively lower as compared to the dark current. It may be due to the recombination of carrier generated by the photon. Photosensitivity of grown CdS_{0.8}Te_{0.2} thin films is calculated by Hernandez [11]:

$$S = \frac{I_l - I_d}{I_d} \tag{1}$$

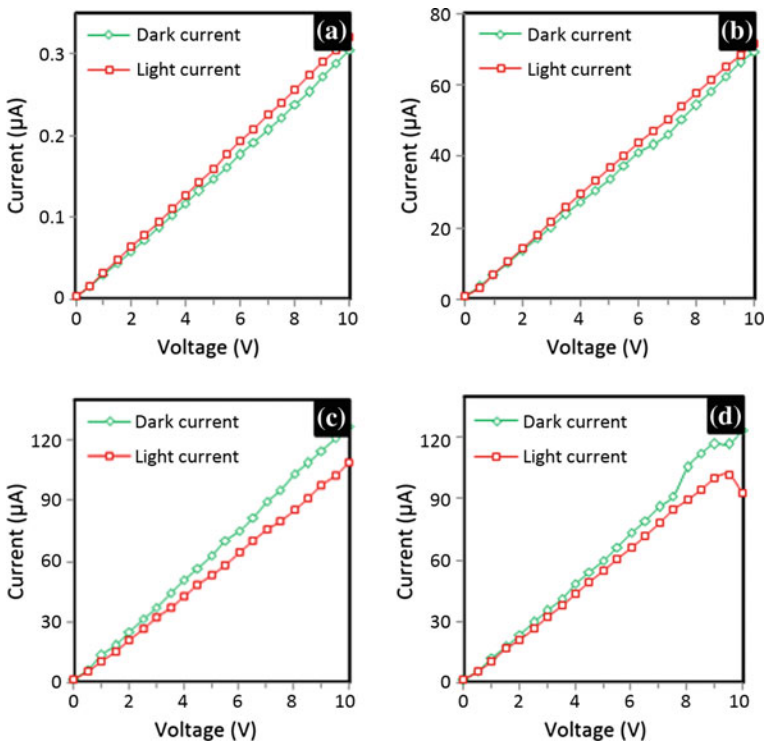


Fig. 4 I-V plot of CdS_{0.8}Te_{0.2} thin films for **a** 1000 Å **b** 2000 Å **c** 2500 Å **d** 3000 Å

where I_l is the light current and I_d is dark current of thin film. The CdS_{0.8}Te_{0.2} thin film was found to be photosensitive which can be further utilized in absorber layer in solar cell and various optoelectronic applications. The photo sensitivity of CdS_{0.8}Te_{0.2} thin films was found to be 0.0743, 0.0478, -0.1633, -0.1017 for 1000, 2000, 2500, 3000 Å thickness respectively.

3.4 I-V Characteristics of Schottky Diode

The current-voltage analysis is commonly used to study the nature of the barriers, developed across the metal semiconductor contact. Figure 5 shows current-voltage characteristics of Cu(n)-CdS_{0.8}Te_{0.2} Schottky diode.

The carrier transport occurs across the barrier due to the thermionic emission obeys the relation [12, 13]:

$$I = I_0 \exp\left(\frac{qV}{\eta kT}\right) \left(1 - \exp\frac{-qV}{kT}\right) \tag{2}$$

where, q is the electronic charge, V is the applied voltage, η is the diode ideality factor, k is Boltzmann’s constant, T is the temperature in Kelvin and I_0 is the saturation current. The ideality factor (η) of a Schottky diode can be expressed as:

$$\eta = \left(\frac{q}{kT}\right) \left(\frac{\partial V}{\partial \ln J_0}\right) \tag{3}$$

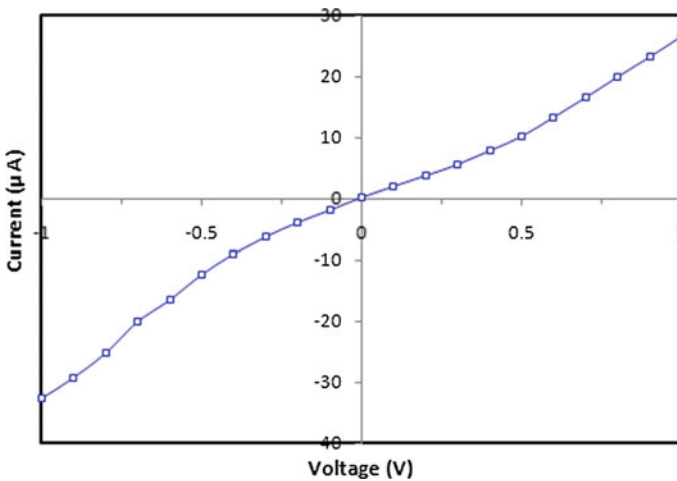
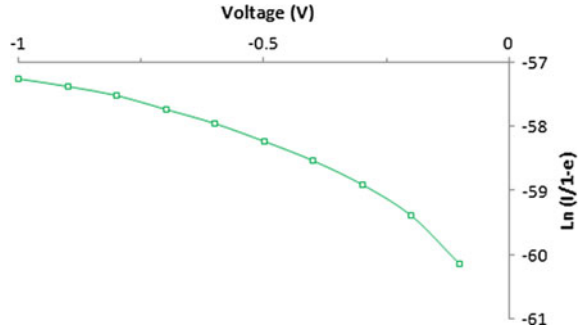


Fig. 5 I-V characteristics of Cu(n)-CdS_{0.8}Te_{0.2} junction

Fig. 6 Plot of voltage versus $\ln(J_0)$ for Cu/(n)-CdS_{0.8}Te_{0.2} junction



where, J_0 is saturation current density. Figure 6 shows the plot of voltage versus $\ln(J_0)$ for Cu/(n)-CdS_{0.8}Te_{0.2} Schottky diode.

The Schottky Barrier Height (SBH) can be formulized as:

$$\phi_B = \frac{kT}{q} \ln A^* \frac{T^2}{J_0} \quad (4)$$

where, ϕ_B is the Schottky barrier height, A^* is effective Richardson constant, J_0 is a saturation current density. Parameters of Cu/(n)-CdS_{0.8}Te_{0.2} Schottky device are found to be $J_0 = 27.76 \times 10^{-3}$, $\eta = 0.93$ and $\phi_B = 0.45$ eV. The ideality factor has been found almost equal to 1.

4 Conclusions

The Cu/(n)-CdS_{0.8}Te_{0.2} thin films Schottky junction was formed by thermal evaporation technique. The CdS_{0.8}Te_{0.2} thin film has polycrystalline nature having orthorhombic crystal structure. The SEM image revealed that the CdS_{0.8}Te_{0.2} thin films were smooth and uniform. The photo sensing coefficient of CdS_{0.8}Te_{0.2} thin films were determined by photo sensing experiment. It was clear that CdS_{0.8}Te_{0.2} thin film is photosensitive and it can be used in fabrication of various optoelectronic applications. I-V characteristic confirmed the formation of Schottky barrier at metal semiconductor interface. The ideality factor has been calculated 0.93 which is approximately equal to 1.

References

1. Reddy DS, Reddy MB, Reddy NK, Reddy VR (2011) Fabrication and electrical characterizations of Cu/(n)-CdS_{1-x}Se_x Thin Film Schottky Diode. *J Mod Phys* 2(3):113–123
2. Sarpatwari K (2009) Ph.D. thesis, the Graduate School, the Pennsylvania State University, pp 4–6 (2009)

3. Rhoderick EH, Williams RH (1988) Metal-semiconductor contacts. Clarendon Press, Oxford, p 20
4. Mathai AJ, Patel KD, Srivastava R (2010) Stability and phase transition studies of Ga-pWSe₂ Schottky diode by current—voltage—temperature method. *Thin Solid Films* 518(10): 2695–2700
5. Jang M, Kim Y, Jun M, Lee S (2005) *J Semicond Technol Sci* 5(2):69–76
6. Mahesha MG, Kasturi VB, Shivakumar GK (2008) Characterization of thin film Al/p-CdTe Schottky Diode. *Turk J Phys* 32:151–156
7. Kale MS, Toda YR, Bhole MP, Bhavsar DS (2014) Structural, optical and thermo electrical properties of nanostructured vacuum evaporated CdS thin films. *Electron Mater Lett* 10:21–25
8. Kale MS, Talele NT, Bhavsar DS (2014) Preparation and Studies of Nanostructured thin films of (CdS)_{0.8} Se_{0.2}. *Int J Sci Res Publ* 4(2):1
9. Kale MS, Talele NT, Bhavsar DS (2014) Synthesis and Characterization of Nanostructured thin films of (CdS)_{0.6} Se_{0.4} for Solar Cell. *IOSR J Appl Phys* 6(1):58–62
10. Shaikh SU, Desale DJ, Siddiqui FY, Ghosh A, Birajadar RB, Ghule AV, Sharma R (2012) Effects of air annealing on CdS quantum dots thin film grown at room temperature by CBD technique intended for photosensor. *Mater Res Bull* 47:3440–3444
11. Hernandez GP, Enriquez JP, Morales BE, Hernandez DM, Flores LD, Jimenez CR, Mathews NR, Mathew X (2012) A comparative study of CdS thin films deposited by different techniques. *Thin Solid Films* 4
12. Farag AAM, Yahia IS, Fadel M (2009) Electrical and photovoltaic characteristics of Al/n-CdS Schottky diode. *Int J Hydrogen Energy* 34:4906–4913
13. Gupta S, Patidar D, Saxena NS, Sharma K, Sharma TP (2008) Electrical study of Cu-CdS and Zn-CdS Schottky junctions. *Optoelectron Adv Mater Rapid Commun* 2(4), 205–208

Kinetic and Thermodynamic Study of Mixed Crystals of Cadmium-Calcium Levo-Tartrate Dihydrate Grown in Silica Gel

N.S. Patil

Keywords Cadmium-calcium mixed Levo-tartrate crystals · Gel growth · Thermogravimetric analysis · Kinetic parameter · Thermodynamic parameter

1 Introduction

Crystal is clearly visible in industries like semiconductors, optics, etc. This type of crystal inventions of LASER, and the field of the nonlinear optics and the practical implementations was possible with the applications of nonlinear optical crystal. The effect of dopant on a various purpose of a crystal is keen interest from solid state science as well as technological point of view. The crystals of CCT grown in a silica gel medium have already been reported [1]. In the present work we have attempted to grown Barium doped Cadmium Tartrate crystal by Gel Technique. This Growth experiment yielded crystal in the Gel using solution Gel Technique [2]. Most of the tartrate compounds are insoluble in water and decompose before melting. Hence, such type of compounds cannot be grown by either slow evaporation or melt technique. But can be produced by solution gel method. A single diffusion method [3] was employed to grown mixed crystal of CCT in the gel method [4].

2 Experimental

The AR grade (Loba) chemicals were used for the present work. The crystallization apparatus employed was Borosilicate glass tubes (25 mm diameter and 200 mm length). Gel was prepared by mixing sodium metasilicate solution of appropriate

N.S. Patil (✉)

Bhusawal Arts Science and P.O. Nahata Commerce College Bhusawal,
Bhusawal, Jalgaon, Maharashtra, India
e-mail: narendrap65@rediffmail.com

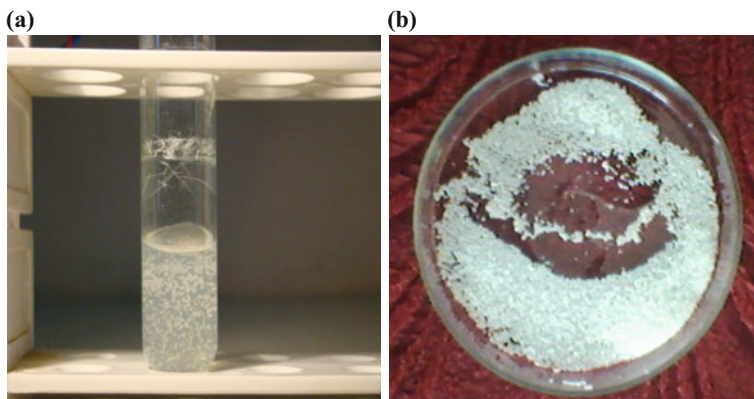
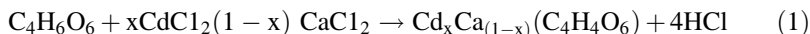


Fig. 1 a Ca crystals, b Cd crystals

specific gravity and 1 M solution of tartaric acid so that the desired pH of the mixture could be obtained. The specific gravity and pH were varied between 1.04–1.05 g/cc and 4–5 respectively. After mixing the solution was allowed to set for about 48 h. Over the set Gel, mixing of 1 M cadmium chloride solution + 1 M Calcium chloride was gently poured with the help of a pipette, so as to allow the solution to fall steadily along the walls of the tube without disturbing the gel surface. The supernatant ions (Ca^{++} and Cd^{++}) slowly diffuse into the gel medium where it reacts with the inner reactant. The open end of the test tube was closed with cotton to avoid dust from the entering into the glass tube. The test tubes were kept undisturbed at room temperature. To grow the crystals for different concentration of an aqueous solution of Barium chloride of varying concentration 0.2–1.0 M was mixed with the top of the solution. After one month the crystal was taken out from the test tube and cleaned for the further characterization [5]. The best quality crystals were grown for 4.2 pH as shown in Fig. 1



3 Result and Discussion

3.1 Powder X-ray Diffraction

X-ray diffraction technique is used to investigate the internal arrangement of atoms or molecule in the crystalline material. The grown CCT crystals were subjected to powder diffraction pattern of the grown crystal was carried out using BRUKER AXSD8-Advance model Germany. X-ray diffraction with $\text{CuK}\alpha 1$ radiation of wavelength ($\lambda = 1.54056 \text{ \AA}$) operating at a voltage of 40 kV and a current 20 mA.

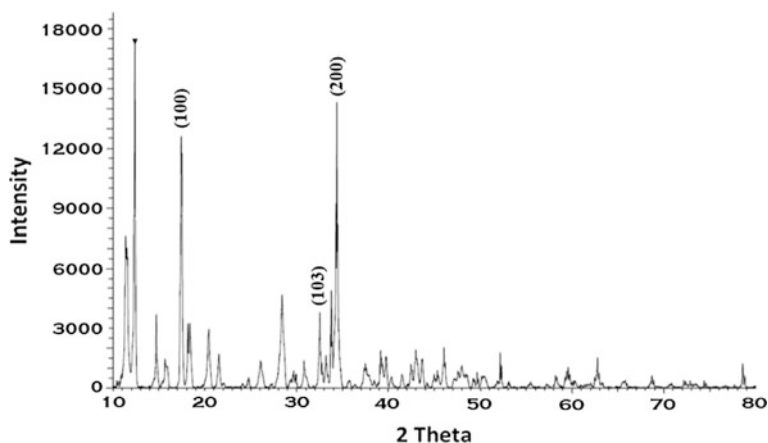


Fig. 2 Powder X-ray diffraction of CCT crystal

The scanning rate was maintained at $2^\circ/\text{min}$ over a 2θ range of $20\text{--}80^\circ$. In the present study of XRD powder pattern of CCT crystal is shown in Fig. 2. The sharp peaks with maximum intensity characterized by XRD pattern, indicating the formation of well-defined crystallites. The spectrum matches with the data reported in JCPDS file No. 65-2018. From this diffraction pattern intensity and hkl values were computed. The observation table gives the index XRD data for the grown crystals value, and hkl plane was calculated the unit cell parameter satisfied the condition for the hexagonal system that the lattice parameters a, b, c, v was found to be 5.98, 5.98, 9.65, 299.28 respectively ($a = b \neq c$). While the α , β , γ was found to be at 90° . The XRD spectrum reveals that the sample is polycrystalline having the hexagonal structure. Percentage of crystallinity is excellent; it is 79.99%. The grain size was 6.148 nm calculated by using the following formula:

$$D = 0.9\lambda / \beta \cos\theta \quad (2)$$

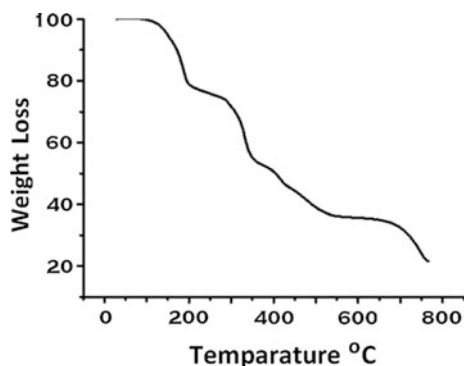
where β is full width at half maximum ($\text{FWHM} = 0.235$), $\lambda = 1.54060$ is the wavelength of X-ray, 2θ is diffraction angle. The observed and calculated d values are given in Table 1. The diffracting index observed d values are in good agreement with calculated values [6].

3.2 Thermal Analysis of CCT Crystal (TGA)

The TGA used to study percentages of the weight loss in the different stages of decomposition. There is four stage of decomposition starting from 45°C temperature there is no decomposition of the sample up to temperature 100°C . The TGA curve for CCT gel grown crystals is as shown in Fig. 3. The TGA used to study

Table 1 Powder diffraction data of CCT crystal

From present work				From JCPDS file			
2 θ	Observed d-value	Intensity I/I ₀	hkl values	2 θ	Standard d-value	Intensity I/I ₀	hkl values
17.445	5.07956	12296	100	17.099	5.07950	505	100
32.531	2.75019	3743	103	32.733	2.75010	371	103
34.382	2.60622	13287	200	34.595	2.60628	49	200

Fig. 3 TGA curve of calcium cadmium tartrate crystal

percentages of the weight loss in the different stages of decomposition. The TGA were obtaining with the help of Diamond TGA/DTG thermal analyzer, at Department of Chemical Science NMU Jalgaon. The TG curve did not show the substantial weight change in the temp range 70–100 °C indicating that the CCT crystal is thermally stable in this range and no transformation took place. It was observed that the decomposition beginning at 270 °C. And crystals are unstable beyond 270 °C. It was found that in the temperature range 70–100 °C in which weight loss of 4%, agrees very well with the calculated weight loss of 4.91%. It is clear that strontium cadmium tartrate crystal are hydrated and the weight loss calculation clearly indicates that strontium cadmium tartrate crystal have one water molecules as a water of crystallization. A small curve observed in the temperature range 70–100 °C single the loss of first H₂O molecule, curve between 100 and 200 °C to 270 °C indicated the temperature range between the total weight loss of 23% is seen which is due to the loss of 2CO₂. This is in good agreement with calculated weight loss of 24.4%. Then an anhydrous strontium cadmium tartrate decompose into strontium cadmium oxalate. The curve between the temp 270–340 °C indicates the temperature range between the total loss of 8% is seen which is due to loss of CO₂H₂ this is well agreement with calculated weight loss 8.75% is attributed to the stable calcium cadmium carbonate. In the fourth step of decomposition total weight loss 8% was observed in the temperature range 340–535 °C which corresponds to the loss of CO. This weight loss agrees very well with the

calculated weight loss 8.34% is attributed to the stable calcium cadmium oxide. Plateau in the temperature range 535–750 °C is attributed to the stable CaO and CdO. DTA and DTG curve of the same compound shows its endothermic peaks.

3.3 Kinetic Parameter of Dehydration and Decomposition

The use of thermogram data to evaluate kinetic parameter of solid state reaction involving weight has been investigated by many workers [7]. The shape of the curve is determined by the kinetic parameters of CCT such as an order of reaction, frequency factor, and energy of activation. Reported Kotru et al., Fig. 3 shows thermogram of CCT crystal. The value of theoretical weighted percentage and observed weight percentage at different stages was motioned in the table. From the thermogram, it was found that the CCT crystal were first dehydrated and decomposition. A kinetic and thermodynamic parameter can be evaluated from the thermogram. In present investigation the Coats and Redfern relation [8]. It was use to evaluate the kinetic parameter from the thermo gram as shown in Fig. 3 [8–12]. The Coats-Redfern relation is as follows:

$$\log 10 \left[\frac{1 - (1 - \alpha)^{1-n}}{T^2(1-n)} \right] = \log 10 \left[\left(\frac{AR}{\alpha E} \right) \left(1 - \frac{2RT}{E} \right) \right] - \left\{ \frac{E}{2.3 RT} \right\} \quad (3)$$

For $n \neq 1$

where α = fraction of original substance decomposed at time t , n = order of reaction.

A = frequency factor, E = activation energy of the reaction, R = gas constant, a = heating rate in °C/min.

To determine the value of activation energy and order of reaction, Coats-Redfern plot,

$Y = -\log 10 \left[\frac{1 - (1 - \alpha)^{1-n}}{T^2(1-n)} \right]$ verses $X = 1/T$ is drawn for different values of n and the best linear plot gives the correct value of activation energy Eq. (1) cannot be use for $n = 1$, Therefore it is modified as follows:

$$-\log 10 \left[-\log 10 \frac{(1 - \alpha)^{1-n}}{T^2} \right] = \log 10 \left[\left(\frac{AR}{\alpha E} \right) \left(1 - \frac{2RT}{E} \right) \right] - \left\{ \frac{E}{2.3RT} \right\} \quad (4)$$

For $n \neq 1$

In present investigation the best linear fit was obtained for $n = 2$. The values of activation energy and frequency factor are found.

3.4 *Thermodynamic Parameter of Dehydration and Decomposition*

The various thermodynamic parameters applying well known formulae. The standard entropy of activation $\ddagger S^\circ$ (subscript \ddagger is for activation and subscript $^\circ$ is for standard). Entropy change associated with the activation reaction can be calculated by the following formula:

$$\Delta^{++}S^\circ = 2.303 \times R \times \log 10 \left(\frac{Ah}{kTm} \right) \quad (5)$$

where A is the frequency factor, k is Boltzmann constant and h is planks constant, R is gas constant, T is absolute temperature in Kelvin.

The standard enthalpy activation $\ddagger H^\circ$ can be calculated by the formula:

$$\Delta^{++}H^\circ = E - 2RT \quad (6)$$

Enthalpy is the straight function whose absolute value can't be known. $\ddagger H^\circ$ can be asserted either by a direct method or indirect. An increasing the enthalpy of the system for which $\ddagger H^\circ$ is positive referred as the endothermic process. Conversely loss of heat from a system for which $\ddagger H^\circ$ is negative value is known as an exothermic process. The standard gives energy difference between transition state of reaction and GND state of the reaction is known as standard Gibbs energy of activation. The standard Gibbs energy of activation $\ddagger G^\circ$ can be calculated by

$$\Delta\ddagger G^\circ = \Delta\ddagger H^\circ - T \Delta\ddagger S^\circ$$

The standard change in internal energy of activation $\ddagger U^\circ$ can be calculated by the formula

$$\Delta\ddagger U^\circ = E - RT$$

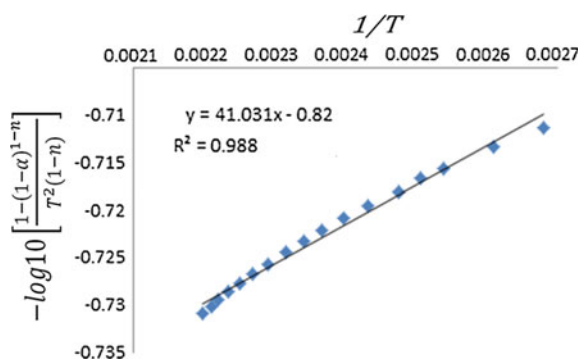
The value of the different thermodynamic parameter of dehydration and decomposing can be calculated by 398 k temperature. Here negative values of $\ddagger S^\circ$ shows that the process is in non-spontaneous, whereas the positive value of $\ddagger H^\circ$ shows that the enthalpy is increasing during the process and such process is an endothermic process. Positive value of $\ddagger G^\circ$ indicates that the CCT is thermodynamically unstable. Comparing with the earlier report work [12] considerable change in the value of kinetic and thermodynamic parameter clearly indicates that the effect of variation of volume concentration of supernatant solution on the grown crystal. The enthalpy involved in the thermal dehydration and decomposition process obtained by the Coats and Redfern integration method do not correspond to the value given in Tables 2 and 3 (Fig. 4).

Table 2 Kinetic parameter of dehydration and decomposition of CCT crystal

Kinetic parameter	Symbol	Value
Activation energy	E	0.7856 kJ/mol ⁻¹
Frequency factor	A	7.0794 × 10 ⁵
Order of reaction	n	2

Table 3 Thermodynamic parameter of dehydration and decomposition of CCT

Thermodynamic parameter	Symbol	Value (kJ/mol ⁻¹)
Standard entropy of activation	Δ [‡] S°	956.36
Standard enthalpy of activation	Δ [‡] H°	785.62
Standard Gibbs energy of activation	Δ [‡] G°	4482.27
Standard internal energy of activation	Δ [‡] U°	2769.79

Fig. 4 Coats and Redfern plot of CCT crystal

4 Conclusion

Gel method is found suitable for growing mixed CCT crystal. The growth of CCT crystal was accomplished using single test tube diffusion method. Optimum condition for growth were worked out. Different habits of CCT crystal can be obtained by changing parameters like gel density, gel aging, pH of gel, concentration of reactants and change in the morphology of the crystals as well as kinetic and thermodynamic parameter was observed with the change in volume concentration of the supernatant solution. From TG curve it was found that the crystals were thermally unstable upon heating they become anhydrous and decompose into metal oxide through a single stage of carbonates. The kinetic parameter evaluated for both the stage by using coats and Redfern relation and thermodynamic parameter were evaluated for both the stages by using standard relation. The XRD pattern reveals that the grown crystals exhibits crystalline nature and confirms the unit cell parameter value with those available in the literature.

References

1. Henisch HK, Dennis J, Hanola JI (1965) *J Phys Chem Solid* 26:493
2. Arora SK, Abraham T (1981) *Indian J Pure Appl Phys* 19:203
3. Hennisch HK (1973) *Crystal growth in gels*. Pennsylvania State University Press.
4. Patel AR, Rao AV (1983) *Bull Mater Sci* 4:527
5. Patel AR, Bhat HL (1972) *J Cryst Growth* 12:288
6. Henisch HK (1970) *Crystal growth in gels*. Pennsylvania University Press, Pennsylvania
7. Joshi MS, Rao PM, Antoni AV (1981) *Bull Mater Sci* 2:127
8. Arora SK, Patel V, Chudasama B, Amin B (2005) *J Cryst Growth* 5:657
9. Suryanarayana K, Dharmaparakasha SM (2000) *Mater Lett* 42:92
10. Arora SK, Patel V, Kothari A, Amin B (2004) *Cryst Growth Des* 4:343
11. Jain A, Razdan AK, Kotru PN (1996) *Mater Chem Phys* 45:180
12. Mevada KC, Patel VD, Patel KR (2012) *Arch Phys Res* 3(4):258–263

Numerical Study on Microchannel Heat Sink with Asymmetric Leaf Pattern

V.P. Gaikwad, S.D. Ghogare and S.S. Mohite

Keywords Leaf pattern microchannel · Temperature gradient · Electronics cooling

1 Introduction

In 21st century owing to continuous increasing demand of highly compact ultra-fast computers and electronic devices around the world, emphasis is to dissipate heat generated by the device to provide a thermally stable device. Maximum allowable temperature for the device is 700 °C. Above that the device fails. For better performance and to provide a reliable electronic device and to increase its life span, there is a need to go for alternative options for cooling the device other than conventional method. Liquid cooling with micro-channel heat sink gives an assuring solution for such devices. Advantage of using micro-channel heat sink is it provides removal of significant amount of heat from small surface area. Other superior features associated with micro-channel heat sink are large surface area to volume ratio, high convective heat transfer coefficient, and little coolant inventory.

The concept of fabricating cooling microchannels in silicon wafer was first introduced by researchers at Stanford University [1]. A conventional microchannel heat sink (MCHS) usually employs straight channels in which the flow becomes fully developed after travelling past the first few diameter lengths, and then remains developed throughout the remainder of the channel. As a result, the fluid mixing

V.P. Gaikwad (✉)

Textile and Engineering Institute, Ichalkaranji 416115, India

e-mail: gvinayak2002@gmail.com

S.D. Ghogare · S.S. Mohite

Mechanical Engineering Department, Government College of Engineering,

Karad 415124, India

e-mail: shwetali.ghogare@gmail.com

S.S. Mohite

e-mail: mohitess@yahoo.com

becomes poor and the heat transfer is insufficient. Those small channels experience a very high pressure drop penalty as well. Furthermore, significant temperature variations throughout the chip can persist since the heat transfer performance deteriorates in the flow direction because of the thickening boundary layers and significant heat gain by the coolant as it travels downstream. The temperature gradients across the chip can compromise the reliability of integrated circuits and result in thermal runaway or early failures.

A number of heat transfer enhancement techniques in microchannel heat sink have been explored by researchers to overcome the above mentioned issues.

Steinke and Kandlikar [2] reviewed the passive and active enhancement techniques. The passive techniques include (a) flow disruptions by using the sidewalls to obstruct the flow, or placing obstacles in bulk of microchannel, (b) channel curvature, (c) re-entrant obstructions, (d) secondary flows by adding smaller channels between main channels, (e) out of plane mixing, (f) fluid additives, and (g) surface roughness. The effective techniques include (a) vibration, (b) electrostatic field and (c) flow pulsation.

Sui et al. [3] employed wavy microchannels of rectangular cross section to cause Dean Vortices to enhance convective fluid mixing and heat transfer. They concluded that for the entire range of Reynolds number and wavy amplitude considered the enhancement in heat transfer always moderately or significantly exceeds the pressure drop penalty. Colgan et al. [4] experimentally showed that the combined offset strip fin and manifold microchannel configuration gives enhanced microchannel cooling for high heat flux applications with reasonable pressure drop penalty.

Rubio-Jimenez et al. [5] proposed branching in the microchannel a phenomenon observed in nature to reduce the non uniform temperature profile. The branching was based on two laws: Biomimetic tendency and Allometric law. The temperature profile in these microchannels showed a different non uniform temperature profile where the maximum temperature occurs at the mid region. Secondary flows are also observed in nature like in leaf venation. Wang et al. [6] compared the symmetric and asymmetric leaf venation network with tree like branching networks in microchannel design. Even though the results showed that the leaf networks perform better, they proposed that further work is needed due to the simplifications made in the study.

Secondary flow helps in promoting better fluid mixing and has been widely used in conventional channels. One way to obtain secondary flows is by connecting two parallel channels by a smaller channel at an angle. This method was employed by Lee et al. [7]. They used oblique fins which connect the parallel channels. The oblique fin diverts a small fraction of the flow into adjacent main channels. The breakage of a continuous fin into oblique section leads to the re-initialization of the thermal boundary layer, improves fluid mixing which serves to enhance heat transfer.

To get the uniform thermal behaviour, introducing secondary flows at many locations along the primary flow is one of the alternatives. Such form is found in nature in leaf or in mammalian respiratory system and hence leaf venation is our

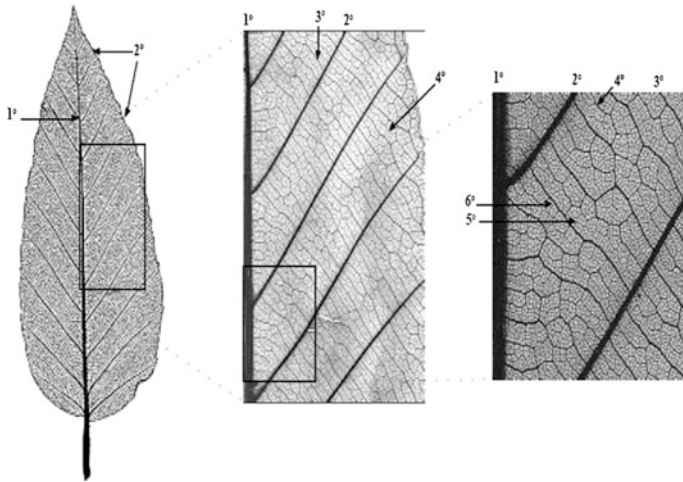
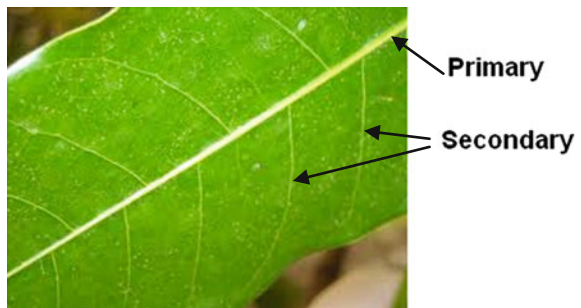


Fig. 1 Pinnate type leaf venation primary and higher order veins [8]

Fig. 2 Pinnate type of leaf venation



source of inspiration. Natural forms of leaf consists of a general form, a primary channel of decreasing hydraulic diameter and it branches out at many locations in two or more sub channels of decreasing diameter. Primary (1°), secondary (2°), tertiary (3°), and higher order veins of a leaf is shown in the Figs. 1 and 2. In general, the primary and secondary veins are the major structural veins of the leaf, while the tertiary and higher order veins are the largest veins that fill the field of the leaf [8]. The branching of secondary veins can be of symmetric (Fig. 1) or asymmetric (Fig. 2) in nature.

The main objective of this work focuses on the study of fluid flow and heat transfer in enhanced microchannels having asymmetric leaf venation pattern. The present work develops the idea of breaking up of the developing flow profile. The result is a continually developing flow that maintains a very high heat transfer coefficient which results in lower maximum surface temperature (T_{max}) and less temperature difference (ΔT) along the length of heat sink.

2 Numerical Simulation

2.1 Geometry of Microchannel

The geometry of the microchannel model is shown in Fig. 3. It consists of primary veins running along the length of heat sink and secondary veins branching out from primary veins. Primary channels are either converging or diverging type. All secondary channels are of converging nature which helps in improving the heat transfer rate and requires less pumping power. In a set of three primary channels, the outlet of central primary channel is blocked to ensure adequate supply of coolant through the secondary veins. The central primary channel is connected by secondary channels asymmetrically with the adjacent primary channels. The geometrical dimensions for conventional and leaf pattern microchannel heat sinks are tabulated in Table 1.

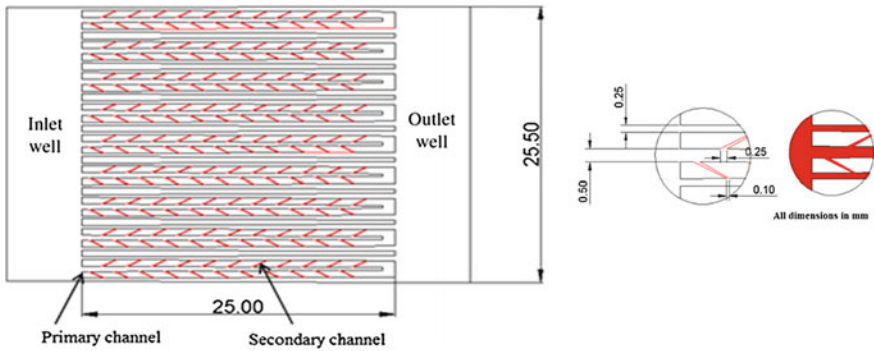
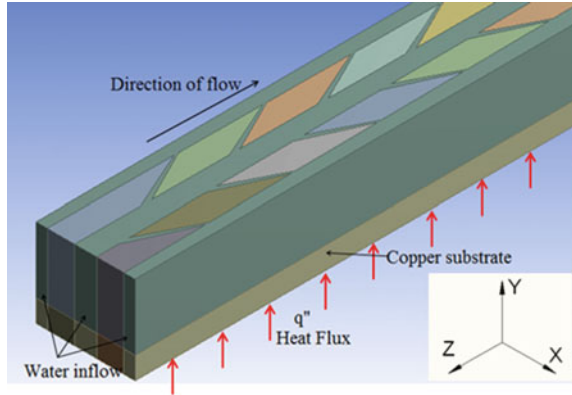


Fig. 3 Plan view of microchannel heat sink

Table 1 Geometrical details for conventional straight and leaf pattern micro channels

Characteristic	Conventional straight microchannel	Leaf pattern microchannel
Material	Copper	Copper
Footprint width × length (mm × mm)	2.5 × 25	2.5 × 25
Main channel width, W_{ch} (μm)	500	500
Channel depth, H_{ch} (μm)	1500	1500
Aspect ratio α	3	3
Primary channel start width (μm)	–	500
Primary channel end width (μm)	–	250
Secondary channel start width (μm)	–	250
Secondary channel end width (μm)	–	100
Secondary channel gap (mm)	–	2
Bifurcation angle θ (°)	–	27

Fig. 4 Simplified computational domain of leaf pattern MCHS



The conventional microchannel and microchannel with leaf pattern were generated using ANSYS Workbench. As seen from the geometry, the microchannels exhibit periodicity along the width. Only one set of primary channels connected by secondary channels are considered for numerical simulation (Fig. 4). Such a simplification is necessary since the simulation of entire computational domain is very expensive. A hexahedral mesh is generated in the specified computational domain.

2.2 Governing Equations

Computational Fluid Dynamics (CFD) commercial software ANSYS Fluent v15 is used to study the fluid flow, heat transfer and associated physical phenomena for the MCHS. The three-dimensional microchannel heat sink is analyzed using deionized water as the cooling fluid. A uniform surface heat flux is applied at the bottom surface of the heat sink. The heat flux available over bottom surface of the microchannel causes an increase in temperature of the fluid. This temperature rise in combination with fluid momentum transport results in the development of hydrodynamic and thermal boundary layers which help to establish heat flow by conduction within the boundary layer and by bulk movement in the free stream of the fluid. These physical phenomena are represented in mathematical form using continuity, momentum and energy equations as follows:

Continuity equation:

$$\nabla \cdot (\rho \vec{v}) = 0 \tag{1}$$

Momentum equation:

$$\nabla \cdot (\rho \vec{v} \vec{v}) = -\nabla P + \nabla \cdot (\mu \nabla \vec{v}) \tag{2}$$

Energy equation for fluid:

$$\nabla \cdot (\rho \vec{v} c_p T) = \nabla \cdot (k \nabla T) \quad (3)$$

Energy equation for solid:

$$\nabla \cdot (k \nabla T) = 0 \quad (4)$$

The microchannel inner faces are declared as walls and other walls are said as walls with insulation boundary but the bottom most face as shown in Fig. 4 is declared as the wall subjected to constant heat flux boundary condition. This declaration helps to detect and recognize flow simulation for boundary condition and zone assignment.

2.3 Boundary Conditions

The inlet temperature of the coolant (liquid–water in this case) was set at room temperature 300 K (27 °C). A uniform flow profile is applied at the inlet and pressure outlet condition is prescribed at the outlet. In the 3D conjugate simulation, the substrate material is copper. Constant heat flux (65 W/cm²) is supplied evenly from the bottom of the substrate while the top surface of the copper micro-channel is assumed bonded with an adiabatic material. A residual of 1×10^{-3} is set as the convergence criteria for the continuity equation, X velocity, Y velocity and Z velocity while that for the energy equation is set as 1×10^{-6} . Figure 4 shows the geometry of a simplified computational model of MCHS, indicating the direction of fluid flow and heat input.

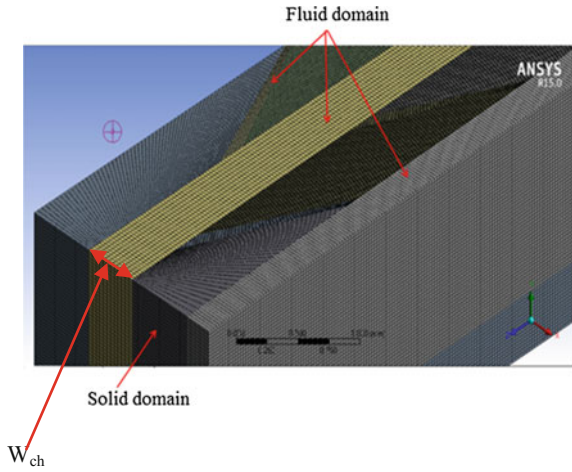
Once the mesh is created, the boundary conditions and other properties are applied to the mesh in FLUENT, the 3D double precision pressure based solver is selected with standard SIMPLE algorithm as its pressure–velocity coupling method. Standard discretization scheme is used for the pressure equation while second order upwind discretization scheme is selected for both the momentum and energy equations (Fig. 5).

With regard to the material selection, water–liquid from the FLUENT material database is selected for working fluid while copper with thermal conductivity, $K_{cu} = 387.6$ W/m K is assigned as the heat sink substrate material. The density, specific heat capacity, thermal conductivity and dynamic viscosity of water are evaluated at the mean fluid temperature (average of the fluid inlet and outlet temperatures) using the following formulas.

Density,

$$\rho(T) = \frac{a_0 + a_1 T + a_2 T^2 + a_3 T^3 + a_4 T^4 + a_5 T^5}{1 + bT} \quad (5)$$

Fig. 5 Schematic of meshing of solid and fluid domain



where,

$a_0 = 999.8396$	$a_4 = 1.49756 \times 10^{-7}$
$a_1 = 18.22494$	$a_5 = -3.93295 \times 10^{-10}$
$a_2 = -7.92221 \times 10^{-3}$	$b = 1.81597 \times 10^{-2}$
$a_3 = -5.54485 \times 10^{-5}$	T has the unit of $^{\circ}C$

Specific heat capacity,

$$C_p(T) = 8958.9 - 40.535T + 0.11243T^2 - 1.0138 \times 10^{-4}T^3 \tag{6}$$

Thermal conductivity,

$$K(T) = -0.58166 + 6.3555 \times 10^{-3}T - 7.9643 \times 10^{-6}T^2 \tag{7}$$

Dynamic viscosity,

$$\mu(T) = 2.414 \times 10^{-5} \times 10^{\frac{247.8}{T-140}} \tag{8}$$

For the calculation of specific heat capacity, thermal conductivity and dynamic viscosity, the temperature, T , should have unit of Kelvin (K).

3 Results and Discussion

3.1 Velocity and Temperature Profile

Simulation results reveal a clear flow field difference between the conventional straight microchannel and leaf pattern microchannel. Figure 6 shows the velocity contour at mid-depth ($y = 0.75$ mm) and mid-portion region along the length of microchannel ($z = 12.5$ mm).

From Fig. 6a, it is seen that the velocity contours do not change along the length of conventional microchannel. In Fig. 6b, it is observed that velocity contours are not uniform along the length, the secondary channels disrupts the velocity profile at each entrance of the downstream channel and causes the hydrodynamic boundary layer development to reinitialize at every downstream secondary channel. This results in the boundary layer thickness reducing significantly in comparison with the conventional straight microchannel. Thus, the velocity profile is maintained in the developing region for this leaf pattern, thereby enhancing the heat transfer.

Figure 7 shows the axial velocity profile at mid depth along the width of conventional and leaf pattern microchannel. The width is converted to a Dimensionless parameter $X1 = (\frac{x}{W_{ch}})$. The velocity profile of conventional microchannel is parabolic in nature while the velocity profile for leaf pattern microchannel at different locations along the length is skewed due to the presence of secondary channel. The velocity profile is skewed towards $X1 = 0$ in the leaf pattern microchannel compared to the symmetric velocity profile of conventional microchannel. Since the

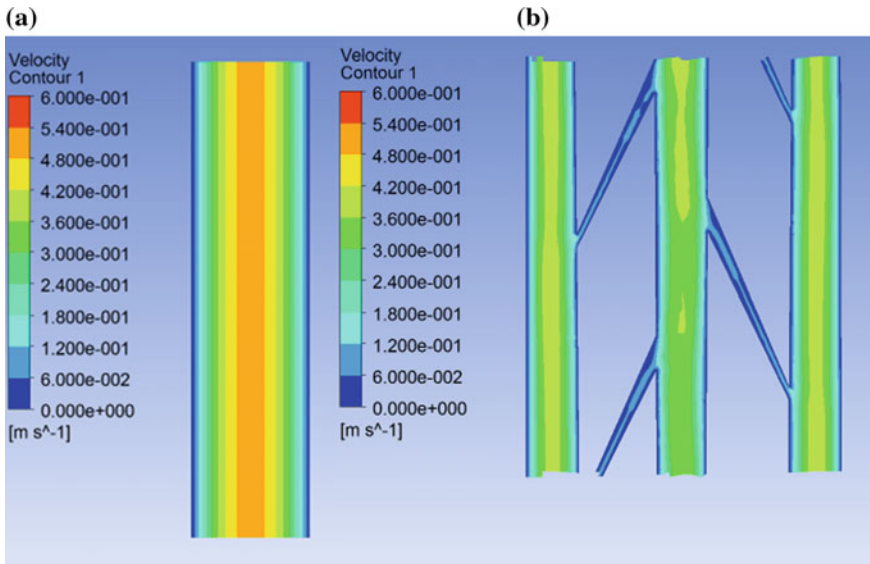


Fig. 6 Velocity contour for flow inside **a** conventional MCHS and **b** asymmetric leaf pattern MCHS

Fig. 7 Axial velocity profile at mid depth plane at $z = 12.5$ mm

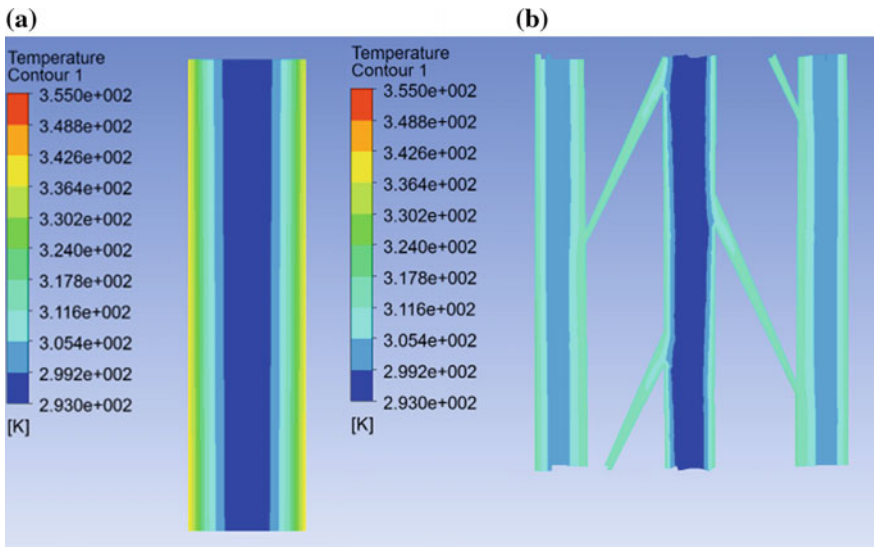
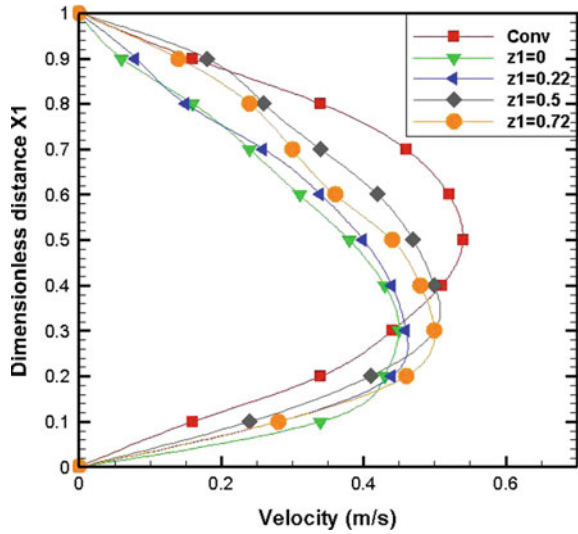


Fig. 8 Temperature contour in the fluid region **a** conventional MCHS and **b** asymmetric leaf pattern MCHS

central primary channel has secondary channels of leaf pattern, the velocity profile is skewed alternately towards left or right side. Consequently leaf pattern microchannel will have thinner boundary layer even though the average velocity in main channel is lower compared to conventional microchannel.

Figure 8 shows the Temperature contour at mid-depth ($y = 0.75$ mm) and mid-portion region along the length of the microchannel ($z = 12.5$ mm).

From Fig. 8a, it is seen that the temperature contours do not change along the length of conventional microchannel. In Fig. 8b, out of the three primary channels the central primary channel has lower fluid temperature compared to the other two channels.

As convection occurs, heat is conducted from channel wall into fluid particles and propagates further into the fluid core. Due to the significant flow field difference, a large fluid temperature distinction is found between the conventional straight microchannel and leaf pattern microchannel. It can be observed from Fig. 8a, that the fluid temperature difference is 49 K which is from 293 to 342 K in the conventional straight microchannel. It is observed that the temperature gradient ($\partial T/\partial z$) between the near wall fluid and core fluid is highly developed and the thermal boundary layer keeps increasing as the fluid travels downstream in the conventional straight microchannel. This phenomenon deteriorates the convective heat transfer and reduces the cooling effect on the copper surface. However, in Fig. 8b, the temperature contour inside the leaf pattern microchannel exhibits a more uniform fluid temperature distribution from 293 to 318 K (difference = 25 K). A portion of the main flow is diverted into the secondary channel due to the presence of the secondary channels. This secondary flow, which carries momentum driven by the pressure difference, injects into the adjacent main channel and disrupts the boundary layer as well as accelerates the heat transfer into the core fluid. This results in a better fluid mixing and superior heat transfer performance which lead to lower surface temperature.

3.2 Heat Transfer Characteristics

Due to the secondary flow and entrance effect in leaf pattern microchannel, superior convective heat transfer performance is achieved, and these results in a uniform and lower surface wall temperature compared to conventional straight microchannel. Figure 9 shows the bottom surface wall temperature comparison between conventional straight and leaf pattern microchannel. It is observed that the maximum wall temperature T_{\max} for the leaf pattern microchannel is 324.5 K and the difference between maximum and minimum wall temperature is at 14.5 K. In the case of the conventional straight microchannel, the maximum wall temperature T_{\max} is 354.9 K and the temperature difference between maximum and minimum wall temperature (ΔT) is at 30.8 K. Therefore, the introduction of secondary channels results in substantial decrease of the maximum wall temperature T_{\max} by 30.4 K and the temperature difference (ΔT) by 16.3 K.

3.3 Pressure Drop Characteristics

Figure 10 depicts the pressure drop comparison between conventional and leaf pattern microchannel heat sink. The pressure drop increases as the Reynolds

Fig. 9 Heater temperature of conventional and leaf pattern MCHS

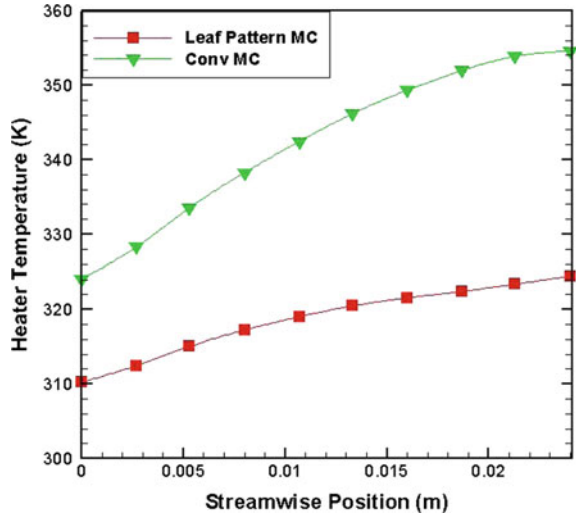
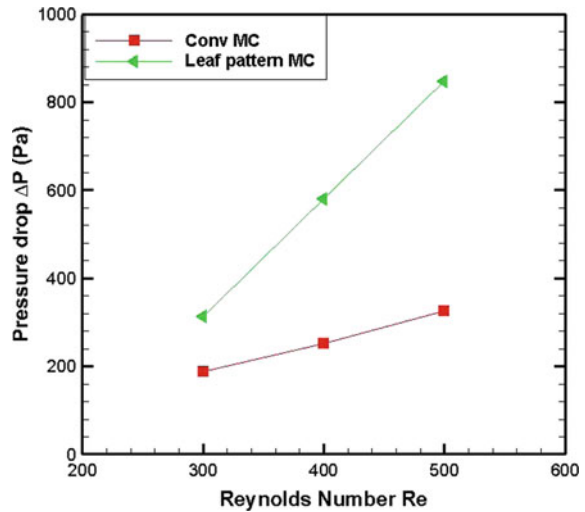
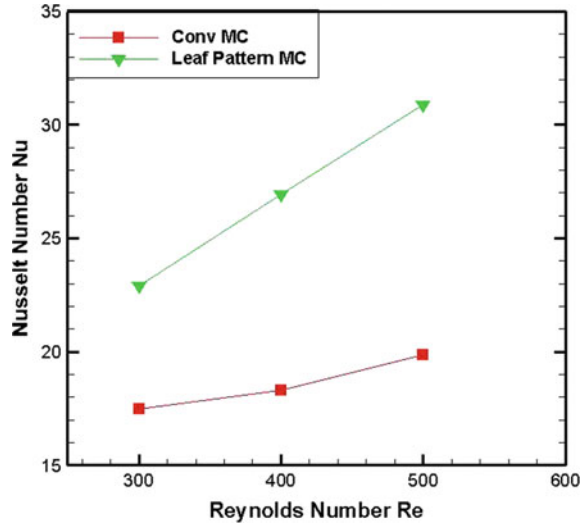


Fig. 10 Pressure drop for conventional and leaf pattern MCHS



number increases because as the coolant flow rate increases, the more frictional loss it faces as it transverses through the heat sink. As the Re increases, a higher percentage of coolant is diverted into the secondary channels. This creates stronger a secondary flow which further augments the heat transfer but incurs additional pressure drop penalty. Therefore pressure drop for leaf pattern heat sink increases more than conventional configuration. Therefore the leaf pattern heat sink generates secondary flow which enhances its heat transfer performance yet maintains a comparable pressure drop compared with conventional heat sink ΔP .

Fig. 11 Nusselt number for conventional and leaf pattern MCHS



From Fig. 11 it is seen that the Nu for both microchannel heat sinks increase with Reynolds number because the thermal boundary layer thickness decreases with increased fluid velocity. Nevertheless, the heat transfer performance for the microchannel with leaf pattern is significantly higher than conventional heat sink. The heat transfer performance increment is 31% greater than conventional microchannel heat sink. This remarkable enhancement in heat transfer is due to the combined effect of thermal boundary layer redevelopment at the leading edge of leaf pattern microchannel and the uniform secondary flows generated by flow diversion through secondary channels.

4 Conclusions

Heat transfer and pressure drop characteristics of single-phase flow through leaf pattern microchannel heat sink are numerically investigated. Its cooling effectiveness is compared with conventional straight microchannel heat sinks through numerical simulations in ANSYS Fluent. Numerical study reveals that highly augmented and uniform heat transfer performance is achievable with such design. The following key conclusions are drawn from this study:

- Simulation results showed a clear distinction in the flow fields between the conventional straight microchannel and leaf pattern microchannel, creating uniquely skewed velocity and temperature profile. It is found that boundary layer thickness is reinitialized and redeveloped from the velocity and temperature profile analysis of the leaf pattern microchannel. Better fluid mixing and superior heat transfer performances are caused by the secondary flow

generation. This leads to a lower surface temperature as evident from the temperature profile analysis for the leaf pattern microchannel.

- The combined effect of redevelopment of boundary layer and generation of secondary flow results in thinner boundary layer that leads to better heat transfer performance and higher pressure drop. The increased pressure drop was somehow compensated by pressure recovery due to the “diffuser” effect at each branching region.
- The Nusselt number for the leaf pattern microchannel heat sink increases by 31% as compared with the conventional straight microchannel heat sink.
- Demerits of leaf pattern microchannel heat sink include complex construction geometry, and a significant pressure drop across the primary channel.

References

1. Tuckerman DB, Pease RF (1981) High performance heat sinking for VLSI. *IEEE Electron Device Letters*, EDL 2
2. Steinke ME, Kandlikar SG (2004) Review of single phase heat transfer enhancement techniques for application in microchannels, minichannels and microdevices. *Heat Technol* 22
3. Sui Y, Lee PS, Teo CJ (2011) An experimental study of flow friction and heat transfer in wavy microchannel with rectangular cross section. *Int J Thermal Sci* 50:2473–2482
4. Colgan EG, Furman B, Gaynes M, Graham WS, LaBianca NC, Magerlein JH, Polastre RJ, Rothwell MB, Bezama RJ, Choudhary R, Marston KC, Toy H, Wakil J, Zitz JA, Schmidt RR (2007) A practical implementation of silicon microchannel coolers for high power chips. *IEEE Trans Compon Packag Technol* 30(2):218–225
5. Rubio-Jimenez CA, Hernandez-Guerrero A, Rubio-Arana JC, Kandlikar SG (2009) Natural patterns applied to the design of microchannel heat sinks. In: *Proceedings of the ASME 2009. IMECE*
6. Wang XQ, Peng X, Mujumdar AS, Yap C (2010) Flow and thermal characteristics of offset branching network. *Int J Therm Sci* 49:272–280
7. Lee YJ, Lee PS, Chou SK (2013) Numerical Study of fluid flow and heat transfer in the enhanced microchannel with oblique fins. *ASME J Heat Transf* 135
8. Ash A, Ellis B, Hickey LJ, Johnson K, Wilf P, Wing S (1999) *Manual of leaf architecture*. Smithsonian Institution Leaf Architecture, Working Group Department of Paleobiology, Washington, DC

Experimental Study of Thermal Energy Storage System Using Nanofluid

K. Krishna Reddy, R. Meenakshi Reddy and B. Durga Prasad

Keywords Nanofluids · Phase change material · Thermal energy storage system

1 Introduction

Depletion of the fossil fuels and the exponential increase in energy demand due to urbanization and rapid industrial growth have made the researchers and policy makers to focus on the utilization of naturally available renewable resources. The significant contribution for the global warming is due to exponential increase in the usage of thermal energy in the various sectors, particularly in the buildings which demand the need for alternate energy resources. Solar energy as a renewable energy source receives greater importance for its clean, inexhaustible, non-polluting, and freely available. However, the main problem associated with the solar energy is intermittent in nature and demand of energy for different applications is also time dependent, but in a different pattern and phase from the solar energy supply. The gap of time between the supply and demand is to be matched dynamically through the integration of an energy storage system for effective utilization of solar energy. Among the various energy storage systems, the thermal energy storage (TES) is of great significance, in particular, the latent heat thermal energy storage (LHTS) system, in which a higher energy density is stored using the phase change materials (PCMs) in a narrower operational temperature range. In the last decade, substantial amounts of experimental as well as theoretical research were done to investigate the thermo physical behaviour of nanofluids. All these studies reveal the fact that micro structural characteristics of nanofluids have a significant role in deciding the

K. Krishna Reddy (✉)

Brindavan Institute of Technology and Science, Kurnool 518218, AP, India
e-mail: kkrreddy64@yahoo.com

R. Meenakshi Reddy

G. Pulla Reddy Engineering College, Kurnool 518007, AP, India

B. Durga Prasad

JNTUA College of Engineering, Anantapur, Ananthapuramu 515002, AP, India

effective thermal conductivity of nanofluids. There are many reviews on nanofluid thermal conductivity research [1]. The LHTS system is used successfully in different applications such as energy management in buildings [2], telecom shelter [3], food storage [4] and space cooling [5] in order to improve the overall system performance. Various types of PCMs are commercially used in the LHTS system, out of these the stearic acid is more widely used in many applications, as they start to melt/solidify exactly without any sub-cooling.

2 Experimental Setup

Preparation of nanoparticle suspension in water is the first step in applying nanofluid for heat transfer enhancement. In this study, Al_2O_3 water Nano fluids were prepared separately by dispersing nano particles into the base liquid, water. Nanofluids with two different volume concentrations (0.02, 0.08%) were prepared to measure the time required to transfer the heat in charging process from nanofluid to PCM. Al_2O_3 nano particle of mean size, <50 nm were dispersed in distilled water as base fluid in different concentrations. The nano fluid was circulated by means of a pump. The ambient, inlet and outlet temperatures were measured with the help of thermocouples at flow rate of 2 l/min. The amount of Al_2O_3 nanoparticles are required to prepare nanofluids of different percentage volume concentration in a 20 l of base fluid (water) is shown in Table 1.

An experimental set-up is shown in Fig. 1 which is designed, fabricated and commissioned to collect thermal performance data on the thermal energy storage tank using spherical capsule. A spherical capsule of 150 mm diameter and containing PCM as stearic acid is shown in Fig. 2. TES tank specifications are given in Table 2.

3 Results and Discussions

3.1 Charging Process

Experiments were carried out with nano fluid and with out nano fluid to ensure that enhancement in heat transfer. The experimental readings were tabulated in Table 3 regarding to charging process. The nanoparticles were added in 0.02 and 0.08% into base fluid volume based.

Table 1 Volume concentration and weight of nanoparticles

S. No.	Volume concentration (%)	Weight of nanoparticles (g)
1	0.02	15.61
2	0.08	62.44

Fig. 1 Thermal energy storage system



Fig. 2 Spherical capsule in TES tank



It is significant from fig. 3 that the charging time decreases with the inclusion of 0.02% volume concentrated Nano fluid along with the base fluid with a mass flow rate of 2 lit/min. The thermal energy supplied to the TES tank through nanofluid

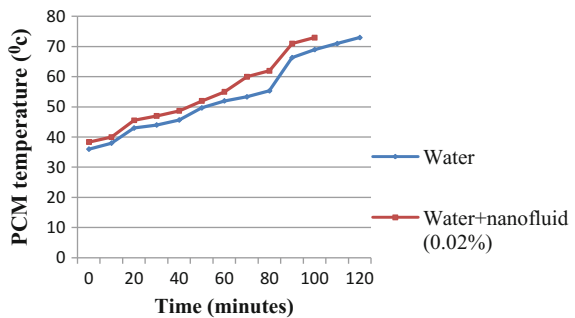
Table 2 Specifications of TES tank

S. No.	Specifications	Units (cm)
1	Length	30
2	Width	30
3	Height	26
4	Thickness	5

Table 3 Time versus PCM temperature for 2 l/min flow rate

S. No.	Time (min)	PCM temperature (oC)	
		Without nano fluid	With nano fluid (Al ₂ O ₃)
1	0	32	32
2	10	38	41
3	20	41	43
4	30	42	45
5	40	45	47
6	50	47	52
7	60	54	58
8	70	57	60
9	80	62	64
10	90	65	72
11	100	72	78
12	110	77	–
13	120	78	–

Fig. 3 Variation of PCM charging process temperature with time



infused HTF in a given time increases in comparison to HTF devoid of nanofluid. This further causes reduction in charging time with the usage of nano fluids.

Fig. 4 pin points that the charging time decreases with the usage of Nano fluid (with a volume concentration of 0.08%) along with the base fluid having a mass flow rate of 2 lit/min. Also the thermal energy supplied to the TES tank through HTF in a given time increases which causes a reduction in charging time with the usage of nano fluids.

Fig. 4 Variation of PCM charging process temperature with time

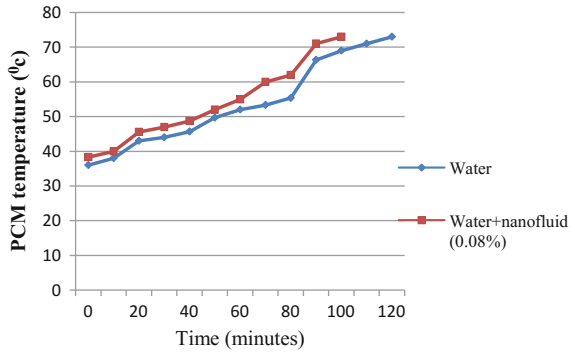
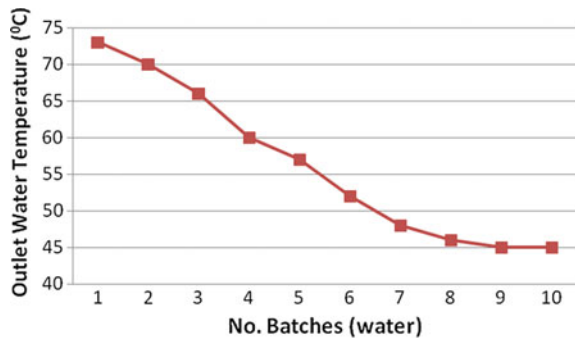


Fig. 5 Variation of outlet water temperature versus batches of water



3.2 Discharging Process

The discharging process was carried in a batch wise manner where hot water (20lit) is discharged from the storage tank in each batch. The average temperature of the collected discharge water in the bucket is measured using a thermometer. The time difference between the consequent discharges is 20 min. The water at (30°C) is supplied into the TES tank. The batchwise withdrawing of hot water is continued till the temperature of the outlet water reaches 45°C. Fig.5 depicts gradual decrease in temperature with batch wise withdrawal of water from TES tank where last two batches have no remarkable change in temperature and discharging process was stopped.

4 Conclusions

A thermal energy storage system using the concept of combined sensible and latent heat is developed for the supply of hot water at an average temperature of 45 °C for various applications such as solar water heating, air heating, solar cooking, building applications, printing on the cotton cloths and dyeing the threads and kitchen

purpose etc. Experiments were conducted on the TES unit to study its performance by integrating it with constant heat source. The variables studied include temperature of PCM with nano fluid and with out nano fluid for charging of TES system for different volume concentrations. While using HTF without nano particles the charging time of PCM is around 120 min and in the case of HTF with nano particles the charging time of PCM is around 100 min. Here observed that reduction in charging time with the use of nano fluids. The discharging process allowed to collect 200 l of water at an average temperature of 45 °C.

References

1. Özerinç S, Kakaç S (2010) Enhanced thermal conductivity of nanofluids: a state-of-the-art review. *Microfluidics Nanofluidics* 8:145–170
2. Behzadi S, Farid MM (2010) Energy storage for efficient energy utilization in buildings. In: 1st international high performance buildings conference, Purdue University, USA
3. Shanmuga Sundaram A (2010) An experimental investigation on passive cooling system comprising phase change material and two-phase closed thermosyphon for telecom shelters in tropical and desert regions. *Energy Buildings* 42:1726–1735
4. Oro E et al (2010) Experimental study on the selection of phase change materials for low temperature applications. *Renew Energ* 57:130–136
5. Zalba B et al (2004) Free-cooling of buildings with phase change materials. *Int J Refrig* 27:839–849
6. Nallusamy N, Sampath S, Velraj R (2006) Study on performance of a packed bed latent heat thermal energy storage integrated with solar water heating system. *J Zheziang Univ Sci A* 7:1422–1427
7. Velraj R et al (1999) Heat transfer enhancement in a latent heat storage system. *Sol Energy* 65:171–180
8. Meenakshi Reddy R (2012) Solar energy based thermal energy storage system using phase change materials. *Int J Renew Energy* 3:11–23
9. Wu W et al (2009) Thermal energy storage behavior of $Al_2O_3-H_2O$ nanofluids. *Thermochim Acta* 483:73–77
10. Kumaresan V et al (2013) Role of PCM based nanofluids for energy efficient cool thermal storage system. *Int J Refrig* 36:1641–1647
11. Zalba B, Marin JM, Cabeza LF, Mehling H (2003) Review on thermal energy storage with phase change material heat transfer analysis and applications. *Appl Therm Eng* 23:251–283
12. Felix Regin A, Solanki SC, Saini JS (2008) Heat transfer characteristics of thermal energy storage system using PCM capsules: a review. *Renew Sustain Energy Rev* 12:2438–2458
13. Jegadheeswaran S, Pohekar Sanjay D (2009) Performance enhancement in latent heat thermal storage system: a review. *Renew Sustain Energy Rev* 13:2225–2244
14. Liu Y-D, Zhou Y-G, Tong M-W (2009) Experimental study of thermal conductivity and phase change performance of nanofluids PCMs. *Micro Fluid Nanofluid* 7:579–584

An Approach to Harness Energy by SnO₂ Thin Film Electrode by Thermal Evaporation

S.M. Ingole, Y.H. Navale, D.K. Bandgar, I.A. Dhole, M.A. Chougule,
P.S. Kulkarni and V.B. Patil

Keywords Thermal evaporation · SnO₂ electrode · XRD · SEM · CV

1 Introduction

In recent years, rising demands for power sources of transient high-power density have stimulated a huge importance in electrochemical supercapacitor with applications in electric vehicles, digital communications, memory back-up devices, burst power generation and other related devices which require high-power pulses. The prospective applications of electrochemical supercapacitors consist of the power enhancement and cycle life improvement of primary power sources such as fuel cells and batteries. Electrochemical supercapacitors are also attractive for other applications such as power sources for lasers, camera flash equipment, and cellular phones. Electrochemical supercapacitors are separated into two categories according to different charge-storage mechanisms (i) redox supercapacitors and (ii) electric double layer capacitors (EDLCs). In redox supercapacitor, the pseudo capacitance arises from faradic reactions happening at the electrode interface and, in electric double layer capacitors the capacitance arises from the charge separation at the electrolyte/electrode interface. The most important materials that have been deliberate for the supercapacitor electrode are (i) conducting polymers, (ii) transition metal oxides and (iii) carbon [1, 2].

Various transition-metal oxides, such as Fe₂O₃, RuO₂, NiO, Co₃O₄, IrO₂, MnO₂, SnO₂, etc. those are being studied for the supercapacitor applications. Among the

S.M. Ingole · Y.H. Navale · D.K. Bandgar · I.A. Dhole · M.A. Chougule ·
P.S. Kulkarni · V.B. Patil (✉)
Functional Materials Research Laboratory, School of Physical Sciences,
Solapur University, Solapur 413255, Maharashtra, India
e-mail: drvbpatil@gmail.com

metal oxides electrode materials, tin oxide-based nanostructures are presenting themselves as one of the most imperative classes due to their various tunable physicochemical properties [3]. Tin oxide is an important n-type wide-band-gap semiconductor. Tin oxide (SnO_2) with the advantages of inexpensive, efficient semiconducting nature and environmental safety has been applied commonly [4, 5]. SnO_2 -based supercapacitors have been compensated significant attention due to their elevated electrochemical capacitor (EC) and chemical stability [6, 7]. Tin oxide (SnO_2) thin films can be deposited by various methods such as pulsed laser deposition [8], co-precipitation [9], similar [10], chemical bath deposition [11], electrodeposition [12], spray pyrolysis [13], hydrothermal [14] and thermal evaporation [15]. Thermal evaporation technique is chosen among these techniques, due to its process simplicity, low-cost infrastructure, easy-to-handle equipment and high throughput. Also, the thermal evaporation offers significance including the high degree of control, good uniformity over a large area for the film growth and high reproducibility.

In the present study, we first time report the synthesis of SnO_2 electrodes for supercapacitor by thermal evaporation method. These electrodes were characterized by XRD and SEM. The supercapacitor behavior of SnO_2 electrode was investigated by cyclic voltammetry and charge-discharge in 1M Na_2SO_4 electrolyte. The effect of scan rate on the super capacitance of SnO_2 electrode has been explored.

2 Experimental Detail

Tin oxide (SnO_2) electrode was synthesized by a thermal evaporation method on precleaned stainless steel substrate from tin (Sn) powder with high purity 99.99% Aldrich make. Sn powder was taken in a mole sodium boat connected to the power supply. The pressure inside the chamber was maintained at 1.5×10^{-5} torr. The required current increased to evaporate Sn powder. During the process, the source and target were maintained at 12 cm apart. The deposited thin film annealed at 700 °C temperature for 30 min in the presence of ambient air in the tubular zone furnace.

The crystalline structure of SnO_2 thin film electrode was examined by X-ray diffractometer (Rigaku, Ultima IV, Cu kb/40 kV/40 mA, $k = 1.5406 \text{ \AA}$) with scan range 10–80° under the scan rate of 1° min^{-1} . The surface morphology of SnO_2 thin film electrode was analyzed using SEM (Model: JEOL-6300F) plane-view digital images. The electrochemical supercapacitor study of SnO_2 thin film electrode was measured by the CHI608E electrochemical workstation.

3 Results and Discussion

3.1 Structural and Morphology Analysis

XRD patterns of the SnO₂ thin film electrode was shown in Fig. 1a. The figure shows well-defined X-ray diffraction peaks of crystallized SnO₂ were indexed to the tetragonal rutile SnO₂ phase, which is consistent with the JCPDS card no. 41-1445. In the given XRD pattern of SnO₂, there is no other peaks are present, indicates the no other phase detected and high purity of the final product. The surface morphologies of SnO₂ thin film prepared by thermal evaporation method were investigated by SEM, and the micrograph is shown in Fig. 1b. As confirmed by the SEM observations that the prepared electrode posses a porous and granular nanoparticles grown in very high density. It is familiar that the surface porosity significant to penetrate the electrolyte and improving electrolyte/electrode junction [16] and such kind of morphology improves the supercapacitor performance.

3.2 CV, Charge/Discharge and Cyclic Stability Study

The SnO₂ thin films deposited by thermal evaporation were used in the development of super capacitors and their performance was examined by studying CV curves. Figure 2a shows the CV curves of the SnO₂ electrode with different scan rates in 1M Na₂SO₄ electrolyte within the voltage range of -1.1 to 0 V. It was found that the current under the curve was gradually increased with scan rate.

This shows that the cyclic voltammetric currents are directly proportional to the scan rates of CV, indicating an ideally supercapacitive behavior [17]. The specific capacitance CS (F g⁻¹) of SnO₂ electrode was calculated using following relation;

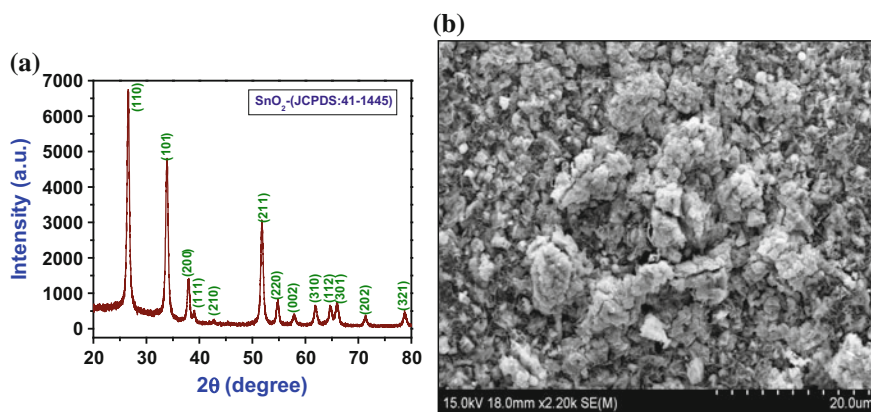


Fig. 1 a XRD and b SEM image of SnO₂ thin film

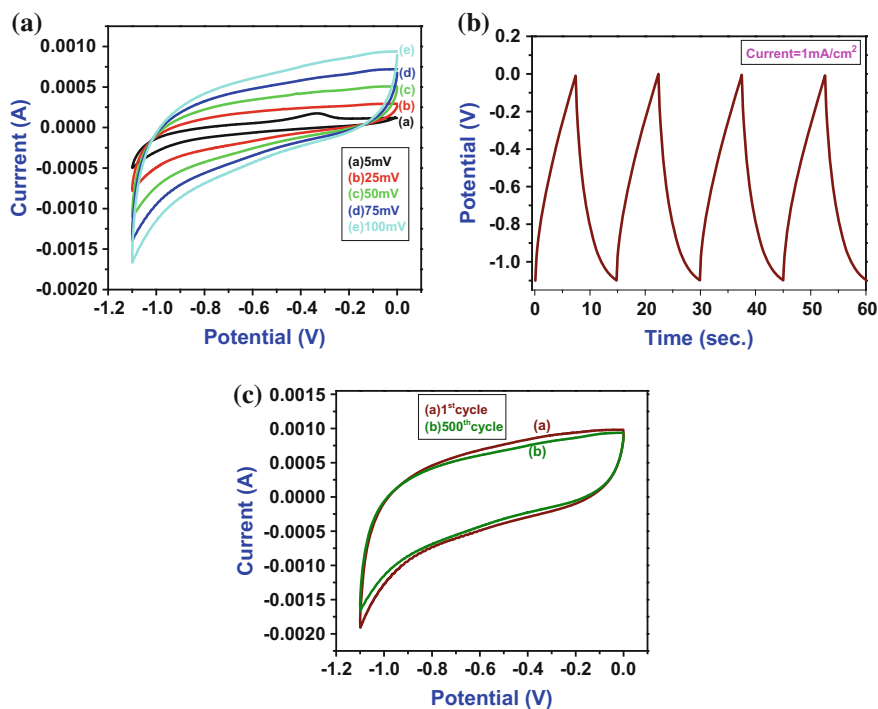


Fig. 2 a Cyclic voltammograms of SnO₂ thin film electrode at different scanning rate, b charge/discharge curve of SnO₂ electrode and c cyclic stability of SnO₂ thin film electrode

$$C_s = \frac{I_{\max}}{\left(\frac{dv}{dt}\right) \cdot W} \quad (1)$$

where, I_{\max} is the average current in ampere (A), dv/dt is the voltage scanning rate in volt (V), and W is the weight of SnO₂ material dipped in the electrolyte. The SnO₂ electrode exhibited the maximum specific capacitance of 328 F g⁻¹ at 5 mV scan rate. The charge/discharge cycles of SnO₂ electrode was studied by galvanometric charge/discharge technique under a constant current of 1 mA cm⁻² between -1.1 and 0 V. Figure 2b shows galvanostatic charge/discharge plot of the SnO₂ electrode in 1 M Na₂SO₄. A good linear relation of potential against time was observed in given charge-discharge profile, being regarded as a typical ideal behavior [18]. Figure 2b shows CV scan of SnO₂ electrode 1st and 500th cycle at 100 mV scan rate. The SnO₂ electrode retained 89% of its initial capacity even after 500 cycles, indicating the material has potential application for the energy-storage device.

4 Conclusion

In summary, SnO₂ thin film electrode has been developed by simple and inexpensive thermal evaporation method. XRD pattern revealed that the SnO₂ thin film exhibits crystalline tetragonal rutile phase. From scanning electron micrograph images it is seen that SnO₂ film surface was porous with granular nanoparticles. The SnO₂ electrode exhibited the high specific capacitance of 328 F g⁻¹ with good cycle stability. These results demonstrate that SnO₂ thin film deposited by thermal evaporation is a good candidate as the electrode material for the electrochemical capacitor.

Acknowledgements Prof. V.B. Patil would like thank to CSIR, for financial support through the scheme no. 3(1319)/14/EMR-II.

References

1. Kulal PM, Dubal DP, Lokhande CD, Fulari VJ (2011) Chemical synthesis of Fe₂O₃ thin films for supercapacitor application. *J Alloy Compd* 509:2567–2571
2. Navale YH, Ingole SM, Navale ST, Stadler FJ, Mane RS, Naushad M, Patil VB (2017) Electrochemical synthesis and potential electrochemical energy storage performance of nodule-type polyaniline. *J Colloid Interface Sci* 487:458–464
3. Zhao Q, Ma L, Zhang Q, Wang C, Xu X (2015) SnO₂-Based Nanomaterials: Synthesis and Application in Lithium-Ion Batteries and Supercapacitors. *Nanomaterials*. Article ID 850147
4. Pusawale SN, Deshmukh PR, Lokhande CD (2011) Chemical synthesis of nanocrystalline SnO₂ thin films for supercapacitor application. *J Appl Surf Sci* 257:9498–9502
5. Lim SP, Huang NM, Lim HN (2013) Solvothermal synthesis of SnO₂/graphene nanocomposites for supercapacitor application. *J Ceram Int* 39:6647–6655
6. Dai YM, Tang SC, Peng JQ (2014) MnO₂@SnO₂ core-shell heterostructured nanorods for supercapacitors. *J Mater Lett* 130:107–110
7. Li R, Ren X, Zhang F, Du C, Liu J (2012) Synthesis of Fe₃O₄@SnO₂ core-shell nanorod film and its application as a thin-film supercapacitor electrode. *J Chem Commun* 48:5010–5012
8. Pham DP, Phan BT, Hoang VD, Nguyen HT, Ta TKH, Maenosono S, Tran CV (2014) Control of preferred (222) crystalline orientation of sputtered indium tin oxide thin films. *J Thin Solid Films* 570:16–19
9. Du Y, Yan J, Meng Q, Wang J, Dai H (2012) Fabrication and excellent conductive performance of antimony-doped tin oxide-coated diatomite with porous structure. *J Mater Chem Phys* 133:907
10. Yıldırım MA, Akaltun Y, Ates A (2012) Characteristics of SnO₂ thin films prepared by SILAR. *J Solid State Sci Technol* 14:1282–1288
11. Pusawale SN, Deshmukh PR, Gunjekar JL, Lokhande CD (2013) SnO₂-RuO₂ composite films by chemical deposition for supercapacitor application. *J Mater Chem Phys* 139:416–422
12. Yang J, Li X, Bai SL, Luo RX, Chen AF, Lin Y, Zhang JB (2011) Electrodeposition and electrocatalytic characteristics of porous crystalline SnO₂ thin film using butyl-rhodamine B as a structure directing agent. *J Thin Solid Films* 519:6241–6245
13. Yadav AA, Pawar SC, Patil DH, Ghogare MD (2015) Properties of (200) oriented, highly conductive SnO₂ thin films by chemical spray pyrolysis from non-aqueous medium: Effect of antimony doping. *J Alloy Compd* 652:145–152

14. Chiu HC, Yeh CS (2007) Hydrothermal Synthesis of SnO₂ Nanoparticles and Their Gas-Sensing of Alcohol. *J Phys Chem C* 111:7256–7259
15. Kim HW, Shim SH, Lee C (2006) SnO₂ microparticles by thermal evaporation and their properties. *J Ceram Int* 32:943–946
16. Navale ST, Mali VV, Pawar SA, Mane RS, Naushad M, Stadler FJ, Patil VB (2015) Electrochemical supercapacitor development based on electrodeposited nickel oxide film. *J RSC Adv* 5:51961–51965
17. Gujar TP, Shinde VR, Lokhande CD, Kim WY, Jung KD, Joo OS (2007) Spray deposited amorphous RuO₂ for an effective use in electrochemical supercapacitor. *J Electrochem Commun* 9:504–510
18. More PD, Jadhav PR, Ingole SM, Navale YH, Patil VB (2017) Preparation, structural and electrochemical supercapacitive properties of sprayed manganese oxide film electrode. *J Mater Sci Mater Electron* 28:707–714

Efficient Electrodeposited Nickel Oxide Thin Films for Supercapacitor Electrode

I.A. Dhole, Y.H. Navale, S.M. Ingole, R.N. Mulik, Y.M. Jadhav, C.S. Pawar and V.B. Patil

Keywords NiO thin film · Electrodeposition · Nanostructure · XRD · SEM · CV

1 Introduction

In recent years, supercapacitors derived from metal oxide thin films are attracting great attention as energy storage systems because of their potential applications in micro-electronic devices, household appliances, backup power sources, in clocks, video equipment, and other devices. Various transition metal oxides, such as RuO_2 , Co_3O_4 , NiO , MnO_2 , Fe_2O_3 , Ir_2O_3 , SnO_2 etc., are being studied for the supercapacitor applications with their charge storage mechanisms based on pseudocapacitance. Between these metal oxides for supercapacitor electrodes, amorphous hydrous ruthenium oxide is the most capable material for supercapacitors because of its elevated specific capacitance, excellent reversibility and long cycle-life [1, 2]. The Powder forms of amorphous and hydrous ruthenium oxide ($\text{RuO}_2 \cdot x\text{H}_2\text{O}$) have been produced by the sol-gel method and found to be capable material for electrochemical capacitor with high power density and energy density [3]. However, RuO_2 is high-priced toxic and naturally less abundant which has restricted their commercial use. Also RuO_2 requires the use of a strong acidic electrolyte such as sulfuric acid. The acidic media can liquefy the metal oxide over extended cycling leading to weaken in the specific capacitance with cycle-life. As a result, various metal oxides have also been tested as probable candidates for electrochemical supercapacitor devices. Candidate systems include IrO_2 [4] or CoO_x , [5] but they suffer from limitations similar to RuO_2 , that is, they are high-priced and require

I.A. Dhole · Y.H. Navale · S.M. Ingole · R.N. Mulik · Y.M. Jadhav · V.B. Patil (✉)
Functional Materials Research Laboratory, School of Physical Sciences,
Solapur University, Solapur 413255, Maharashtra, India
e-mail: drvbpatil@gmail.com

I.A. Dhole · C.S. Pawar
Material Science Research Laboratory, Department of Physics,
Shankarrao Mohite Mahavidyalaya, Akulj 413101, Maharashtra, India

strong acidic or alkaline electrolyte. Additionally the potential window over which they operate reversibly is considerably smaller than that for RuO₂. On the other hand NiO, Co₃O₄ and MnO₂ [6] systems seem promising mostly due to their lower cost. Therefore largely the interest is focused on different electrode materials that are low-priced and demonstrate ruthenium oxide like capacitive behaviour. NiO_x is one of the potential candidates for electrode materials in pseudocapacitors and it may serve as an alternative for RuO₂. The electrochemical properties make them useful in batteries, fuel cells, electrochromic devices. The specific capacitance of 245 F g⁻¹ was reported in Liu and Anderson for porous NiO film [7]. Nickel oxide is the most abundantly studied oxide. It is a well studied oxide in sight of its technologically important application in power sources. For super-capacitor application, it is been studied by numerous authors. Some examples are: nanocrystalline NiO [8], nanoporous electrodeposited nickel oxide films [9], nickel oxide/hydroxide nanoplatelets [10], nickel oxide films on different substrates [11], NiO electrode via electrochemical route [12], nanosized NiO [13].

In the current study, we report the preparation of nickel oxide thin film electrode by electrodeposition method on stainless steel substrate at room temperature. The Nickel hydroxide films were annealed at 400 °C in air. Obtained films of NiO were characterized for XRD, SEM and CA. Electrochemical capacitance performance of the films was broadly studied using the method of cyclic voltammetry (CV) and galvanostatic charge–discharge tests in 1 M NaOH aqueous solution electrolyte. A maximum specific capacitance of 259.3 F g⁻¹ was achieved suggesting that; nickel oxide electrode is a capable electrode material for electrochemical supercapacitors.

2 Experimental Details

The NiO thin film electrode was prepared by using AR grade Nickel acetate as a source of Ni. The stainless steel substrate (SS) (grade 304, 0.22 mm thick) was polished with emery paper to a rough finish, washed free of emery particles and then air-dried. The electrochemical synthesis of NiO was performed in a conventional three-electrode electrochemical cell, containing stainless steel substrate, saturated calomel electrode (SCE) and platinum wire as working electrode, reference electrode and counter electrode respectively. The electrochemical synthesis was carried out onto stainless steel substrates from aqueous alkaline solution containing 0.1 M Nickel acetate at room temperature (300 K). The deposition of well adherent and uniform gray colored was observed by applying a constant potential of +1.8 V/SCE for the deposition time 30 min. The obtained Ni(OH)₂ was annealed at 400 °C for 60 min in tubular furnace for the formation of NiO.

3 Result and Discussions

3.1 X-ray Diffraction Study

Figure 1a shows the XRD pattern of stainless steel (SS) and Fig. 1b shows XRD pattern of NiO thin film on SS substrate. In XRD pattern there is no diffraction peak observed other than SS substrate, which clearly indicates that the film consisted of NiO particles which are in amorphous phase. The symbol (SS) indicates the peak obtained due to stainless steel substrate. Due to easy diffusion of ions in the bulk of the active material, amorphous phase of the oxide material is probable for supercapacitor application [14].

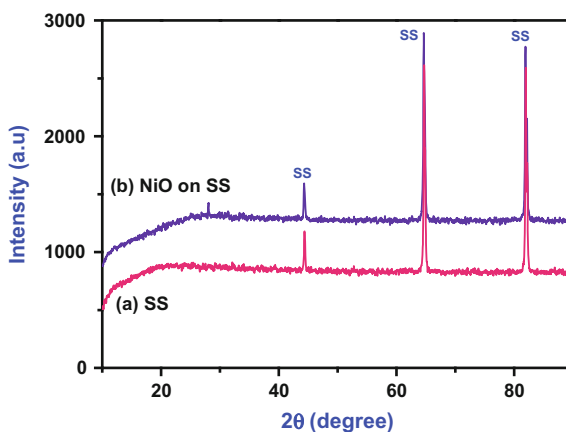
3.2 Surface Morphology Study

Figure 2a shows Scanning electron micrograph of annealed nickel oxide thin film. The NiO thin film micrograph looks smooth with high porosity. The nickel oxide film surface is well covered without any cracks and pinholes. Such type of morphology can give greater surface area for electrode, which is the basic requirement of supercapacitor [15].

3.3 Wettability Study

Figure 2b shows the contact angle image of NiO thin film. As water contact angle is less than 86° (less than 90° means more wettability), the NiO films are hydrophilic in nature. We believe, this was because of the strong cohesive force between the

Fig. 1 XRD pattern of NiO thin film on stainless steel substrate



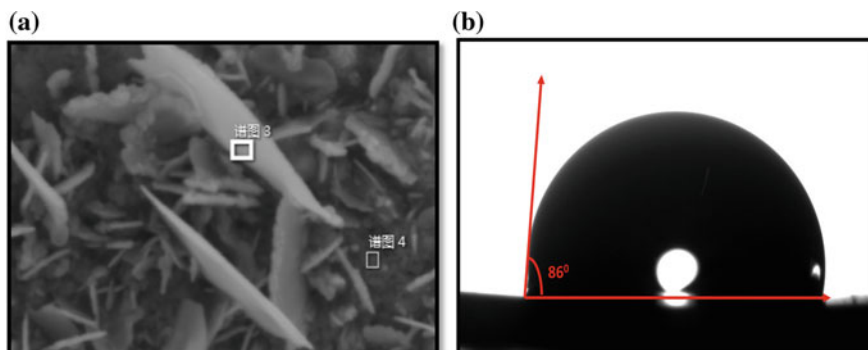


Fig. 2 **a** SEM image of NiO electrode. **b** Contact angle measurement of NiO electrode

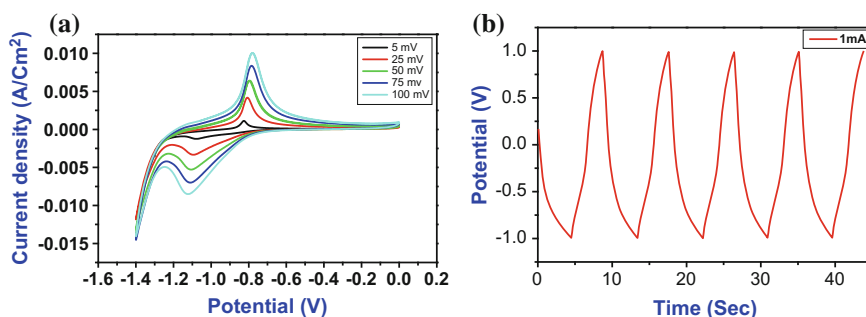


Fig. 3 **a** Cyclic voltammetry of NiO electrode at different scanning rates. **b** The charge–discharge curve of nickel oxide electrode

oxide present in the nickel oxide compound and water droplet. This specific property is useful for making intimate contact of aqueous electrolyte with electrode surface in supercapacitor application. It is well known that hydrophilic surface nature of the electrode is an essential factor for better performance in the electrochemical capacitors [16].

4 Supercapacitive Studies

4.1 Cyclic Voltammetry

In general, cyclic voltammetry (CV) is used to characterize capacitive behaviour of an electrode material. The CV curves of NiO electrode in 1 M NaOH electrolyte at different scan rates within voltage range of -1.4 to $+0.1$ V are shown in Fig. 3a.

It was found that, the area under curve was slowly increased with the scan rate. This shows that the scan rates of CV are directly proportional to current, which demonstrates that, an ideal capacitive behavior [17].

4.2 Galvanostatic Charge–Discharge Studies

The charge–discharge behavior of nickel oxide electrode was studied by chronopotentiometric charge–discharge method at a constant current of 1 mA cm^{-2} . Figure 3b shows the typical charge–discharge curve of nickel oxide electrode. The discharge profile usually includes two parts, first a capacitive component related to the voltage change due to change in energy within the capacitor and a resistive component arising from the sudden voltage drop representing the voltage change due to the internal resistance. From Fig. 3b the symmetric behavior of voltage–time curve is also seen. The electrochemical parameters such as, specific energy (E), specific power (P) and coulomb efficiency ($\eta\%$) are calculated using following equations:

$$E = (V \times I_d \times T_d)/W \quad (1)$$

$$P = (V \times I_d)/W \quad (2)$$

$$\eta\% = (T_d/T_c) \times 100 \quad (3)$$

where I_d , T_d and T_c are the discharge current, discharge time and charge time respectively. The W is the mass of nickel oxide film electrode. The specific energy was 10.42 Wh kg^{-1} . The specific power and coulomb energy efficiency of nickel oxide electrode were 9.47 kW kg^{-1} and 95.47% respectively.

5 Conclusions

In this work, we have effectively synthesized nanostructure NiO electrode for electrochemical supercapacitor by electrochemical method. XRD pattern revealed that the NiO thin film exhibits amorphous nature. From scanning electron micrograph it clear that NiO film surface was smooth with very high porosity. Contact angle measurement showed NiO surface was hydrophilic with contact angle 86° . The specific capacitance of NiO electrode was 259.3 F g^{-1} . These results demonstrate that chemically deposited NiO thin film is a capable candidate as electrode material for electrochemical supercapacitor.

Acknowledgements Prof. V.B. Patil would like thank to CSIR, for financial support through the scheme no. 03(1319)/14/EMR-II.

References

1. Soudan P, Lucas P, Ho HA, Jobin D, Breau L, Belanger D (2001) *J Mater Chem* 11:773
2. Yoon YS, Cho WI, Lim JH, Choi DJ (2001) *J Power Sour* 101:126
3. Zheng JP (1999) *Electrochem Solid State Lett* 2:359
4. Conway BE, Birss V, Wojtowicz J (1997) *J Power Sour* 66:1
5. Lin C, Ritter JA, Popov BN (1998) *J Electrochem Soc* 145:4097
6. Wang X, Wang X, Huang W, Sebastian PJ, Gamboa S (2005) *J Power Sour* 140:211
7. Liu KC, Anderson MA (1996) *J Electrochem Soc* 143:124
8. Zhang F, Zhou V, Li H (2004) *Mater Chem Phys* 83:260
9. Wu MS, Huang YA, Yang CH, Jow JJ (2007) *Int J Hydrogen Energy* 32:4153
10. Wu MS, Hsieh HH (2008) *Electrochim Acta* 53:3427
11. Wu M, Gao J, Zhang S, Chen A (2006) *J Power Sour* 159:365
12. Nam KW, Kim KB (2002) *J Electrochem Soc* 149:346
13. Deng MG, Yang BC, Hu YD, Gongcheng C (2005) *J Mater Eng* 26:319
14. Feng ZP, Li GR, Zhong JH, Wang ZL, Ou YN, Tong YX (2009) *Electrochem Commun* 11:706
15. Navale ST, Mali VV, Pawar SA, Mane RS, Naushad M, Stadler FJ, Patil VB (2015) *RSC Adv* 5:51961
16. Navale YH, Ingole SM, Navale ST, Stadler FJ, Mane RS, Naushad M, Patil VB (2017) *J Colloid Interface Sci* 487:458
17. More PD, Jadhav PR, Ingole SM, Navale YH, Patil VB (2017) *J Mater Sci Mater Electron* 28:707

Effect of Waiting Time on Opto-electronic Properties of Antimony Doped Tin Oxide Thin Films for Transparent Conducting Oxide Applications

A.R. Babar, C.S. Pawar and B.R. Karche

Keywords Thin film · Antimony doped tin oxide · Optical properties · Electrical properties

1 Introduction

Now a days, SnO₂ doped materials is attracting great attention for their potential application as one of the indium tin oxide (ITO) substitution. From literature it is observed that tin oxide thin films doped with antimony exhibit interesting electro-chemical properties in different electrode processes [1], such as low temperature electrochemical combustion of organic pollutants, ozone production and organic electro-synthesis [2]. Also ATO is a transparent conducting oxide (TCO), which has been focus of intensified study due to its technological importance as a solar energy material, electrochemical properties, thermal and environmental stability, low cost and easy fabrication [3]. Usually SnO₂ is doped with Sb because the substitution of Sn⁴⁺ by Sb⁵⁺ leads to a donor centre very close to the conduction band. Thus ATO exhibits interesting properties, which arise from the coexistence of oxygen vacancies with antimony doping. It is found that ATO thin films have been deposited by using a wide variety of physical and chemical techniques. It is possible to tailor the properties by controlling the preparative conditions, which in turn makes ATO suitable for a particular application. Therefore, the preparation technique plays a vital role. Spray pyrolysis (SP) is a simple and inexpensive technique having advantages like ease of adding dopant material, reproducibility, high growth rate and mass production capability for uniform large area coatings, which are desirable for industrial, solar cell and gas sensor applications. In the present paper, we have studied effect of waiting time (waiting time in sec) in producing ATO films of lower electrical resistivity and higher optical transmittance as well as highest figure of merit.

A.R. Babar (✉) · C.S. Pawar · B.R. Karche
Materials Science and Thin Film Laboratory, Department of Physics,
Shankarrao Mohite Mahavidyalaya, Akluj 413101, India
e-mail: babarar2008@gmail.com

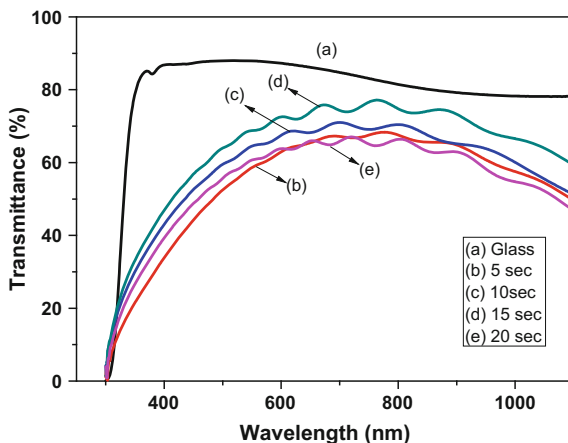
2 Results and Discussion

2.1 Optical Properties

The optical transmittance spectra of ATO thin films prepared with different waiting times are shown in Fig. 1. From the transmittance spectra, it is understood that the increase in waiting time results into increase in transmittance. The maximum transmittance of $\approx 75\%$ was obtained for the film deposited with 15 s waiting time and further decreases for higher waiting time. The high transparency is associated with a good structural homogeneity or may be due to reduced grain boundary scattering. The decrease in transmittance at higher waiting time may be due to the increased scattering of photons by crystal defects or because their layered structure reduces the free charge mobility and allows the formation of Sb in its unusual oxidation state 4^+ (between Sb^{3+} and Sb^{5+}), which produces a sample blue darkening. In general, in the visible region of the spectrum, the transmission is very high due to the fact that the reflectivity is low and there is no (or less) absorption due to transfer of electrons from valence band to conduction band owing to optical interference effects, it is possible to maximize the transmission of thin film at particular region of wavelengths [4]. Estimated values of bandgap (direct) for the films are observed to be vary from 3.58 to 4.04 eV respectively. The increase in band gap value is attributed to the increased carrier concentration which is due to Brustein–Moss effect [5]. The calculated IR reflectivity was found to be in the range of 92–97% for the films prepared with various waiting times.

Figure 2a shows room temperature photoluminescence (PL) excitation spectra for optimized sample and Fig. 2b emission spectra for all the samples. The excitation spectra (Fig. 2a) showed two prominent peaks, one around 325 nm (3.8 eV) and other around 385 nm (3.22 eV). The emission spectra (Fig. 2b) taken at 325 nm excitation showed a strong blue-green emission band around 488 nm in all

Fig. 1 Optical transmittance of ATO films deposited with different waiting times



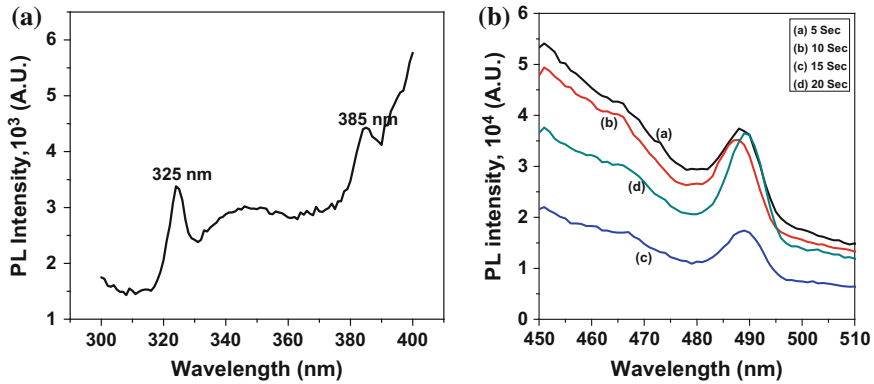
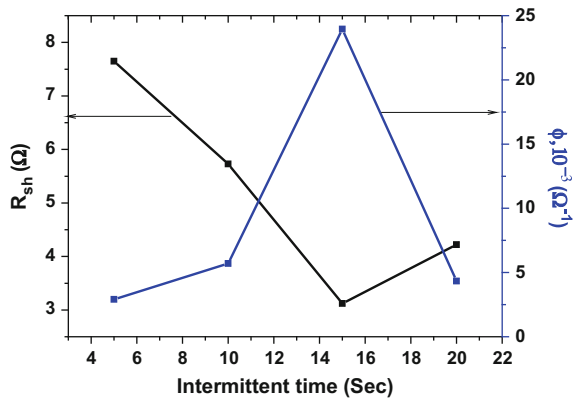


Fig. 2 Photoluminescence **a** excitation and **b** emission spectra of ATO thin films deposited with different waiting times. Optical transmittance of ATO films deposited with different waiting times

Fig. 3 Variation of sheet resistance and figure of merit with waiting time



samples, which can be attributed to singly charged oxygen vacancies (VO) in the films [6]. The slight shift in PL peak with waiting time is due to the various concentrations of oxygen vacancies at various waiting times.

2.2 Electrical Properties

Figure 3 shows the variation of sheet resistance with waiting time. Both sheet resistance (R_s) and electrical resistivity (ρ) were found to be decreased with increasing waiting time initially but then increased for higher waiting times. The ϕ values were found decreased from the value of 7.2×10^{-4} to $4.2 \times 10^{-4} \Omega \text{ cm}$ with increase in waiting time up to 15 s. The mean free path value of carriers varies from 27.23 to 28.76 Å. The calculated Fermi energy is in the range of 0.81–1.04 eV.

2.3 Figure of Merit

For optoelectronic device applications, the figure of merit (ϕ) plays an important role. The sheet resistance (R_S) is a main factor for figure of merit, which is calculated by van der Pauw technique. Figure 3 also shows variation of figure of merit (ϕ) with waiting time. The variation figure of merit with different waiting time shows reverse trend of sheet resistance. The highest value of figure of merit observed in this study is $23.95 \times 10^{-3} \Omega^{-1}$ which is higher than the values reported in the literature. This may be due to the fact that 15 s waiting time is good for structural growth of ATO thin films. This value is higher than the values of ϕ reported in literature for ATO films prepared by spray pyrolysis technique is no need to include page numbers or running heads; this will be done at our end. If your paper title is too long to serve as a running head, it will be shortened. Your suggestion as to how to shorten it would be most welcome.

3 Conclusions

The antimony doped tin oxide thin films were prepared by using the chemical spray pyrolysis technique and Effect of waiting time on the physical characteristic was studied. The high transmittance of $\sim 75\%$ was obtained for the film deposited with 15 s waiting time. Oxygen vacancies are the dominant luminescent centers for the emission of blue-green light in thin films. In this work highest figure of merit and the minimum resistivity achieved for antimony doped tin oxide thin films.

Acknowledgements One of the authors (A.R. Babar) is highly grateful to Mr. Jaysingh Mohite-Patil President Shikshan Prasark Mandal, Akluj for the inspiration and support. I am also thankful to Secretary and all management of Shikshan Prasark Mandal. I also acknowledge to Dr. A.L. Deshmukh, Principal, Shankarrao Mohite Mahavidyalaya, Akluj for his co-operation, encouragement, love and homely behavior given to me in every movement of this work, which helped me a lot.

References

1. Yao P (2011) Desalination 267:170–174
2. Wang YH, Chan KY, Li XY, So SK (2006) Chemosphere 65:1087–1093
3. Montero J, Guillén C, Herrero J (2011) Sol Energy Mater Sol Cells 95:2113–2119
4. Yadav AA, Masumdar EU, Moholkar AV, Spallart MN, Rajpure KY, Bhosale CH (2009) J Alloy Compd 488:350–355
5. Burstein E (1954) Phys Rev 93:632–633
6. Dua L, Biswas PK (2013) Appl Surf Sci 280:33–41

Nanoflakes MnO₂ Thin Film as a Supercapacitor Electrode

P.M. Kharade, S.S. Mane, S.D. Chavan, S.B. Kulkarni
and D.J. Salunkhe

Keywords Electrodeposition · Manganese oxide · Scanning electron microscope · Cyclic voltammetry · Charging-discharging

1 Introduction

Energy storage devices have become more demanded due to the fast growing market of portable electronic devices and hybrid electric vehicles (HEVs) [1]. Electrochemical capacitors (ECs), also called supercapacitors or ultracapacitors, have received great interest over last decades because of their higher power density and longer cycle life than batteries and high energy density compared to conventional capacitor [2–5]. Based on the charge storage mechanism, there are two major categories [6]: (1) electric double-layer capacitors (EDLC) which store energy by utilizing the double-layer capacitance arising from the charge separation at the electrode–electrolyte interface, (2) pseudocapacitors which store energy by utilizing the pseudocapacitance arising from the fast and reversible Faradic reactions.

Generally the electrode materials are of three types, carbon materials, conducting polymers and transition metal oxides. Because of their high conductivity and better electrochemical stability metal oxides have also been explored as a possible electrode

P.M. Kharade · S.S. Mane · D.J. Salunkhe (✉)
Nano-Composite Research Laboratory, K.B.P. Mahavidyalaya,
Pandharpur 413304, India
e-mail: djsalunkhe@rediffmail.com

S.D. Chavan
Department of Physics, DBF Dayanand College, Arts and Science,
Solapur, India

S.B. Kulkarni
Physics Department, The Institute of Science, Mumbai 400032, India

material for pseudocapacitors. The majority of research concerns with ruthenium oxide. This is because other metal oxides have yet to obtain comparable capacitances. A very high specific capacitance of up to 786 F g^{-1} was obtained for hydrous RuO_2 prepared by cathodic electrodeposition techniques [7]. However, the high cost and toxic nature of this noble material limit its further commercial applications. Hence the efforts have been aimed at searching for alternative inexpensive electrode materials with good capacitive characteristics e.g. MnOx , NiOx , CoOx [8]. Thus, a major area of research is to utilize cheap metal oxide and the development of fabrication methods to reduce the cost of ruthenium oxide, without reducing the performance [3, 9]. MnOx has been considered as a promising electrode material for electrochemical capacitors because of its low cost and excellent capacitive performance in the aqueous electrolytes.

In the present work, efforts have been taken to study the structural, morphological and supercapacitive properties of galvanostatically deposited MnO_2 electrode.

2 Experimental Details

2.1 Chemicals

All precursor's were purchased in refined grade and used without further purification Manganese chloride (MnCl_2) were purchased from SD Fine Chem Limited and Potassium hydroxide (KOH) was purchased from Fisher Scientific. In all the process distilled water was used as a solvent. The Stainless Steel (SS) strips used the substrates and these substrates were polished with emery polish paper to rough finish. Then these substrates were cleaned with detergent and followed by rinsing with distilled water and acetone.

2.2 Synthesis of MnO_2 Thin Films

The MnO_2 thin films were synthesized following procedure reported earlier [10]. The MnO_2 thin films were galvanostatically deposited on SS substrates with constant current density of 5 mA cm^{-2} for 600 s. To stabilize MnO_2 the films thus grown were annealed at $200 \text{ }^\circ\text{C}$ for 1 h.

2.3 Characterization Techniques

The deposited films were characterized by XRD for crystallographic study using Bruker axes D8 Advance Model with copper radiation (K_α of $\lambda = 1.54 \text{ \AA}$) in the 2θ

range from 20° to 80°. The surface morphology was studied using scanning electron microscope (SEM, ZESIS). The cyclic voltammetry and galvanostatic charge-discharge studies were carried out using electrochemical workstation (CHI 660 A). An electrochemical cell was constituted using three electrode system, deposited film as a working electrode, graphite as a counter electrode and saturated calomel electrode (SCE) as a reference electrode.

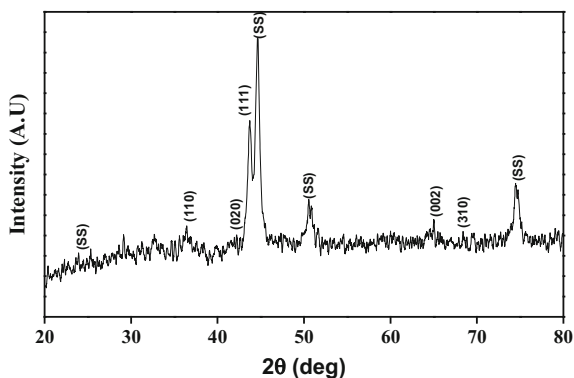
3 Results and Discussions

3.1 Structural and Surface Morphological Studies

To get information about the crystal structure of the deposited MnO₂ electrodes, XRD techniques were carried out in the 2θ range between 20° and 80°. Figure 1 shows the XRD pattern of the MnO₂ electrode. The MnO₂ electrode shows cubic crystal symmetry [11]. The peak marks (SS) in the XRD pattern are due to the ss substrates only.

The surface morphology of the deposited MnO₂ electrodes was characterized by scanning electron microscopy techniques and displayed in Fig. 2. It was observed that MnO₂ thin film shows porous and nanoflakes like morphology [12]. The average length and diameter of MnO₂ thin film appears to be 180 and 20 nm. The nanostructure and porous morphology is a most essential in supercapacitor [13]. Such nanosized grains may provide increase in surface area which are mostly useful for supercapacitor.

Fig. 1 X-ray diffraction pattern of MnO₂ thin film



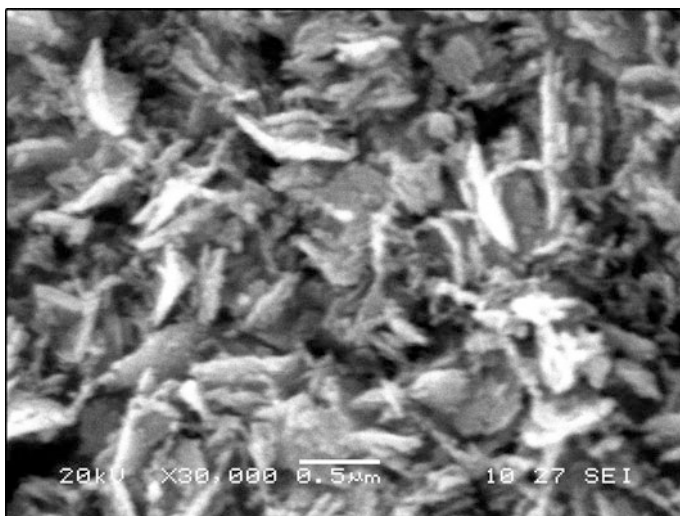


Fig. 2 SEM image of MnO₂ thin film

3.2 Supercapacitive Studies

3.2.1 Cyclic Voltammetric Study

Cyclic voltammetry is a most important tool to examine the capacitive behavior of materials. Ideal capacitive nature is to be identified by indication of rectangular shape and enormous amount of current density in anodic as well cathodic directions i.e. in symmetric forms of voltammograms [14].

Figure 3 shows cyclic voltammetric curve of MnO₂ film electrode within potential range between -1.0 V and $+1.0$ V/SCE in 0.5 M Na₂SO₄ electrolyte. The SR was varied as 50 , 100 and 150 mV s. The interfacial capacitance (C_{in}) value of MnO₂ film electrode was calculated by using the following formula,

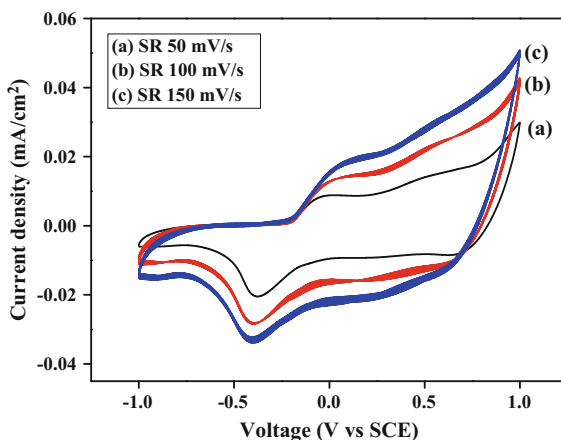
$$C_{in} = i/(dV/dt) \quad (1)$$

where 'i' is the average current in the ampere, dV/dt is the scan rate. Specific capacitance values (C_{sp}) of Mn₂O₃ film electrode was calculated by following formulae,

$$C_{sp} = C_{in}/m \quad (2)$$

where, m—the mass of deposited MnO₂ film electrode on the SS substrate. From Fig. 3, it was observed that all the curve shows pair of redox peaks which remarks that current-potential performance is voltage dependent and supercapacitance mainly arises due to the redox reactions of the MnO₂ thin film with electrolyte. As

Fig. 3 Cyclic voltammetry of MnO₂ thin film



scan rate increases current under curve increases and potential of the curve shifts more towards positive and negative direction. This remarks that pseudocapacitive behaviour of the prepared MnO₂ film electrode. MnO₂ film electrode shows maximum specific capacitance of 340 F g⁻¹ at the SR of 50 mV s⁻¹. Xia et al. [15] have been reported maximum specific capacitance of nanostructured MnO₂ thin film at 230 F g⁻¹ by using facile solution method without any assistance of template or surfactant. Zhu et al. [16] have been reported the specific capacitance of nanostructured MnO₂ to be 240 F g⁻¹ by using hydrothermal synthesis route. The value of specific capacitance in this case is may be due to nanostructure and porous morphology of the MnO₂ thin film electrode.

3.2.2 Galvanostatic Charge-Discharge Study

Galvanostatic charge-discharge is a most accurate method to determine the specific capacitance other supercapacitor parameters. Figure 4 shows galvanostatic charging-discharging curves of MnO₂ thin film electrode in 0.5 M Na₂SO₄ electrolyte at constant current density of 5 mA cm⁻². It was observed that both charging-discharging curves are symmetric and straight line which demonstrates that the process is to be a faradic reaction one. The values of coulombic efficiency, specific capacitance, specific power and specific energy are calculated using the following formulae and tabulated in Table 1.

$$\text{Coulombic efficiency}(\eta) = (T_d/T_C) * 100 \quad (3)$$

$$\text{Specific Capacitance} = I_d * T_d/V * W \quad (4)$$

Fig. 4 Charging-discharging curve of MnO₂ thin film

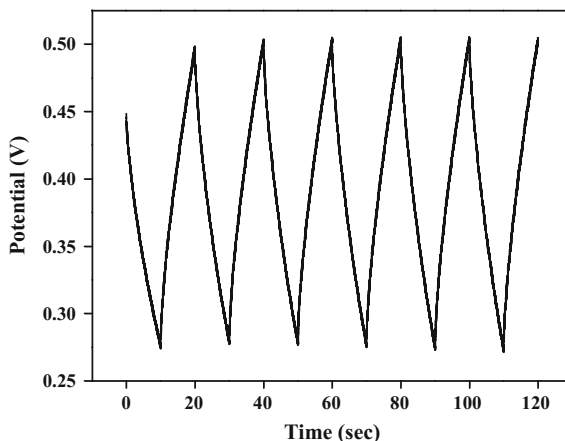


Table 1 Values of coulombic efficiency, specific capacitance, specific energy and specific power of Mn₂O₃ thin film electrode obtained from charging-discharging technique at constant current density of 0.5 mA cm²

Electrodes in ES	Coulombic efficiency η (%)	Specific capacitance (F g ⁻¹)	Specific energy (Wh kg ⁻¹)	Specific power (KW kg ⁻¹)
Mn ₂ O ₃	99.32	323.05	191.53	19.25

$$\text{Specific energy} = (V * I_d * T_d)/W \quad (5)$$

$$\text{Specific power} = (V * I_d)/W \quad (6)$$

where, T_C and T_d is charge and discharge time respectively, V is voltage window (in volt), I_d is discharge current (in ampere) and W is the mass of active material (in grams).

It was observed that the MnO₂ thin film electrode shows a good electrochemical reversibility with a large specific capacitance 323.05 F g⁻¹. The values of specific capacitance obtained from galvanostatic charging-discharging and CV technique are nearly comparable.

4 Conclusions

A galvanostatic electrodeposition method is used to synthesize nanoflakes of MnO₂ thin film. Cubic crystalline phase of MnO₂ thin film electrodes were confirmed from the XRD study. The morphology of the MnO₂ thin film electrode shows porous and nanoflakes like structure which is feasible for supercapacitor application. It is observed that MnO₂ thin film offer better values of coulombic efficiency, specific

capacitance, specific energy and specific power. Thus, galvanostatically deposited MnO₂ thin film electrode is a superior candidates for supercapacitor.

Acknowledgements Authors are thankful to *Materials Research Laboratory*, Department of Physics, Institute of Science, Mumbai, for providing electrochemical Characterization.

References

1. Zhang LL, Tianxin W, Wenjuan W, Zhao XS (2009) Manganese oxide–carbon composite as supercapacitor electrode materials. *Microporous and Mesoporous Mater* 123:260–267
2. Conway BE (1999) *Electrochemical supercapacitors: scientific fundamentals and technological applications*. Kluwer Academic/Plenum, New York
3. Kftz R, Carlen M (2000) Principles and applications of electrochemical capacitors. *Electrochim Acta* 45:2483–2498
4. Sarangapani S, Tilak BV, Chen CP (1996) Materials for electrochemical capacitors. *J Electrochem Soc* 143:3791
5. Frackowiak E, Beguin F (2001) Carbon materials for the electrochemical storage of energy in capacitors. *Carbon* 39:937
6. Arbizzani C, Mastragostino M (1996) Polymer-based redox supercapacitors: a comparative study. *Electrochim Acta* 41:21–26
7. Zheng Y-Z, Ding H-Y, Zhang M-L (2008) Hydrous–ruthenium–oxide thin film electrodes prepared by cathodic electrodeposition for supercapacitors. *Thin Solid Films* 516:7381–7385
8. Zhao D, Yang Z, Kong ES, Xu C, Zhang Y (2011) Carbon nanotube arrays supported manganese oxide and its application in electrochemical capacitors. *J Solid State Electrochem*. doi:10.1007/s10008-010-1182-x
9. Burke A (2000) Ultracapacitors: why, how, and where is the technology. *J Power Sources* 91:3750
10. Kharade PM, Chavan SG, Salunkhe DJ, Joshi PB, Mane SM, Kulkarni SB (2014) Synthesis and characterization of PANI/MnO₂ bi-layered electrode and its electrochemical supercapacitor properties. *Mater Res Bull* 52:37–41
11. Zhang Y, Li GY, Yan LV, Wang LZ, Zhang AQ, Song YH, Huang BL (2011) Electrochemical investigation of MnO₂ electrode material for supercapacitors. *Int J Hydrogen Energy* 36:11760–11766
12. Wu MQ, Snook GA, Chen GZ, Fray D (2004) Redox deposition of manganese oxide on graphite for supercapacitors. *J Electrochem Commun* 6:499–504
13. Kandalkar SG, Dhawale DS, Kim C-K, Lokhande CD (2010) Chemical synthesis of cobalt oxide thin film electrode for supercapacitor application. *Synth Met* 160:1299
14. Hassan S, Suzuki M, El-Moneim A-A (2012) Capacitive behavior of manganese dioxide/stainless steel electrodes at different deposition currents. *Am J Mater Sci* 2(2):11–14
15. Xia H, Xiao W, Lai MO, Lu L (2009) Facile synthesis of novel nanostructured MnO₂ thin films and their application in supercapacitors. *Nanoscale Res Lett* 4:1035–1040
16. Zhu T, Zheng SJ, Chen YG, Luo J, Guo HB, Chen YE (2014) Improvement of hydrothermally synthesized MnO₂ electrodes on Ni foams via facile annealing for supercapacitor applications. *J Mater Sci* 49:6118–6126

Experimental Studies on Curvilinear Laser Bending of Thin Sheets

Ravi Kant, Parag M. Bhuyan and Shrikrishna N. Joshi

Keywords Laser bending · Laser forming · Buckling mechanism · Curvilinear irradiations · Edge effect · Step line heating

1 Introduction

In laser bending, plastic deformation of metal sheets is carried out using thermal stresses induced by controlled laser beam irradiation. The process can be carried out with or without application of the mechanical load. When the bending is carried out with only laser beam irradiation, it is called laser bending while a combination of laser beam irradiation with a mechanical load, is termed as laser assisted bending [1]. It is a non-contact tool-less forming process that has important advantages such as the ability to process at inaccessible area; no need of specific tool; and ability to deform brittle materials [2]. The advantages also include less springback, small heat affected zone (HAZ), easy control, good accuracy and cost effective for small size production [3]. However, the process is relatively slow and costly for mass production applications [4].

R. Kant (✉)

Department of Production Engineering and Industrial Management,
College of Engineering, Pune, India
e-mail: rk.prod@coep.ac.in

P.M. Bhuyan

Technische Hochschule Ingolstadt, Ingolstadt, Germany

S.N. Joshi

Indian Institute of Technology Guwahati, Guwahati 781039, India
e-mail: snj@iitg.ac.in

The laser beam can be focused on a very small spot which makes the process suitable for MEMS applications. The process is suitable for low volume requirements in forming of ship planks and production of the aerospace fuselage. The high flexibility of the process makes it suitable for production in space and rapid prototyping [5].

The laser bending can be performed with three mechanisms i.e. temperature gradient mechanism (TGM), buckling mechanism (BM) and upsetting mechanism (UM). TGM occurs when there is a steep temperature gradient along the workpiece thickness. A bend angle up to 2° can be generated in a single scan with TGM dominated process conditions [2]. The BM occurs when temperature gradient along the workpiece thickness is negligible and buckling stiffness of the workpiece is less. The bend angle in a scan is high and can go up to 20° [4]. The UM dominates when temperature gradient along the workpiece thickness is negligible, but the geometry of the workpiece is stiff enough to prevent buckling. In UM, workpiece thickens and shortens in the heated region [6].

Most of the work reported in the literature is carried out with TGM because it can be controlled certainly. The BM is difficult to control because bending direction as well as bend angle is not certain and depends on the pre-stresses, pre-curvature, external load and irradiation strategies. Some work is reported by researchers on laser bending with BM dominated process conditions. Li and Yao [7] showed that a certain bending direction away from the laser source could be obtained when irradiation starts from a location near the middle instead of from an edge of the worksheet. It was a result of extra mechanical constraints added by surrounding material to sustain the initial convex deformation. Ojeda and Grez [8] showed that the directional certainty could be obtained by using appropriate modulation of the laser energy. Jamil et al. [9] found that the beam geometry plays an important role in the temperature distribution and deformation behavior during buckling mechanism laser bending of workpiece. Shi et al. [6] proposed a critical condition based on laser energy parameters, workpiece thickness, and workpiece material properties to know whether the process is dominated with TGM or BM. Shi et al. [10] derived an inequality condition to determine the bending mechanism and bending direction of the workpiece.

The reported work on laser bending with BM is focused on straight line irradiation. However, curvilinear irradiation is more appropriate to generate complex shapes as it makes the process easy and efficient. Investigation on curvilinear irradiation with TGM showed that the temperature distribution and deformation behavior is significantly affected by the scanning path curvature [3]. BM can produce larger bend angle in a scan as compared with TGM, and therefore it is important to investigate curvilinear laser bending process with BM dominated process conditions. The present work is an attempt in this direction. In this study, curvilinear laser bending of galvanized iron (GI), thin sheets with BM process conditions has been carried out, and the effect of process parameters on bend angle and edge effect (non-uniform bend angle along the scanning path) is investigated.

2 Experimental Setup

This section explains the details of experimental setup which includes details of CO₂ laser setup, design, and development of fixture, material selection, workpiece geometry, bend angle measurement, and irradiation strategies.

2.1 CO₂ Laser Machine Setup

The experiments were performed on an industrial LVD Orion 3015 2.5 kW continuous wave CO₂ laser cutting machine. The machine has three-dimensional control to the laser irradiation. Laser head can move along an axis in the horizontal direction; laser bed has access to move in the horizontal direction perpendicular to the motion of laser head, and laser head is also free to move in the vertical direction. The vertical movement of laser head adjusts the laser beam diameter while horizontal movement of the laser head and machine bed helps to track the laser heating along a specified path. The positioning of the laser head and machine bed is accomplished by servo motor units, from which the rotary motion is converted into a linear motion by a rack and pinion transmission. The focusing mirror of focal length 5" or 7.5" can be used to control the laser beam coming from the cavity/resonator. In this work, experiments were conducted at a spot beam diameter of 4 mm using a lens of 5" focal length.

2.2 Workpiece Holding Fixture

A fixture designed by Hemanth [11] shown in Fig. 1; was used to hold the workpiece on the machine bed during experiments. The fixture was also having a capability of installing pyrometer at the bottom of the workpiece for temperature analysis during laser beam irradiations. The fixture is made up of the main bracket and is fitted to machine langerones through the slots provided in the main bracket as shown in Fig. 2. A spirit level is used to adjust the main bracket parallel to the laser machine bed. The adjustment is made by operating the M12 nut. This ensured a perpendicular laser irradiation on the workpiece surface. The specimens of size up to 100 mm width can be fitted on the bracket. A top bracket is fitted on the specimens to apply enough force that holds the specimens rigidly during laser irradiation.

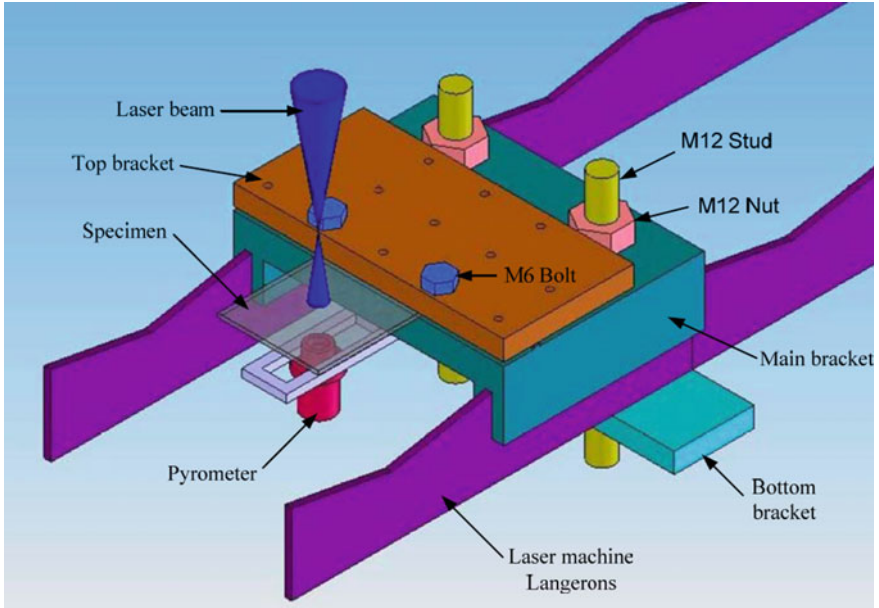


Fig. 1 3-D model of fixture used to hold the workpiece on laser machine bed [11]

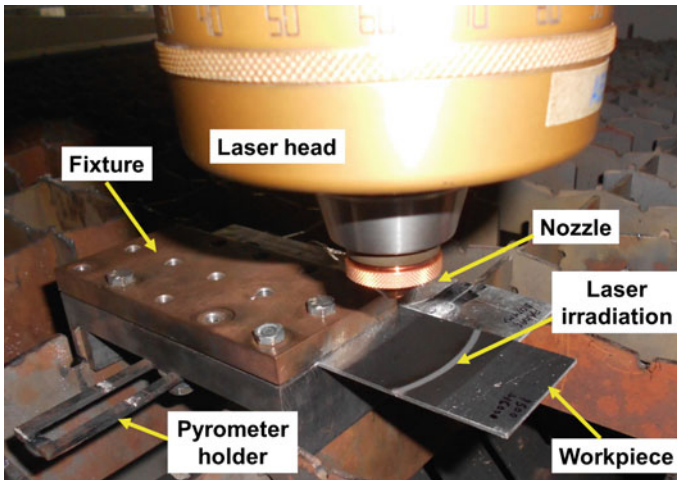


Fig. 2 Workpiece arrangement on the laser machine bed

2.3 Workpiece Details

Experiments were carried out on galvanized iron (GI) thin sheets of size 80 mm length, 50 mm width and 0.5 mm thickness. The specimens were cleaned and were coated with graphite spray. The coating was applied to increase the absorptivity so that energy loss due to reflection can be minimized and also to ensure uniform absorptivity along the scanning path.

2.4 Irradiation Details

The experiments were carried out with curvilinear parabolic irradiations. The parametric equations of a parabola can be given as

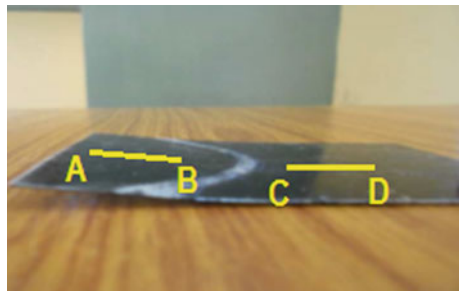
$$x = 2at \quad \text{and} \quad y = 2at^2 \tag{1}$$

where x and y are the coordinates at various positions along the curve; a is the distance between vertex and focus of parabola and t is the controlling parameter. It should be noted that the curvature of parabola increases with the increase in the value of a . At an infinite value of a parabola becomes a straight line. Laser power and scanning speed were varied to control the process while the beam diameter was kept constant i.e. 4 mm.

2.5 Bend Angle Measurement

The workpiece was bent due to laser irradiation, and the bend angle was measured by using coordinate measuring machine (CMM). The bent specimen is shown in Fig. 3. The bend angle is measured between two lines AB and CD on both sides of the laser irradiation respectively (see Fig. 3). A line on the one hand of radiation was selected by choosing two points (A, B or C, D) on that side. The bend angle is

Fig. 3 Laser bent specimen with single curvilinear irradiation



calculated on an average of three measurements about middle position of the scanning path. The data points were collected manually by moving the probe in x, y and z directions.

3 Analysis of Results

This section presents a discussion of the results obtained during BM dominated curvilinear laser bending of GI sheets. Effect of laser power, scanning speed, and number of irradiations are displayed on bend angle. The results are also discussed on the distribution of bend angle along the scanning path.

3.1 Studies on Bend Angle

3.1.1 Effect of Laser Power

Figure 4 shows the effect of laser power on the bend angle at a constant scan speed of 700 mm/min. It can be seen that the bend angle has non-linearly increasing trend with the increase in laser power. This is because at lower laser power there is lesser heat absorption whereas at higher power there is a higher heat absorption which results in greater plastic deformation and hence a larger bend angle is observed at higher power. The rate of increase in bend angle is more at higher laser power. It is because the temperature gradient decreases with the increase in laser power which favors the buckling mechanism and hence larger bend angle is realized.

Fig. 4 Effect of laser power on bend angle

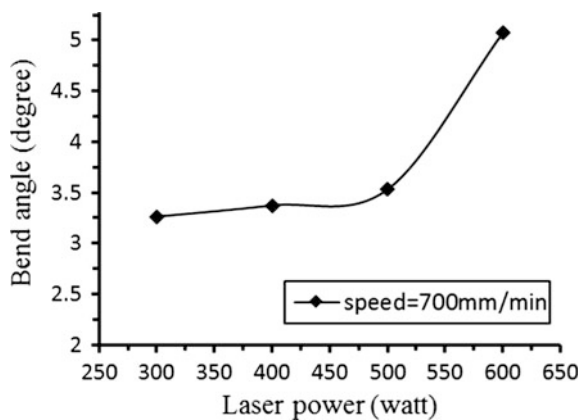


Fig. 5 Effect of scanning speed on bend angle

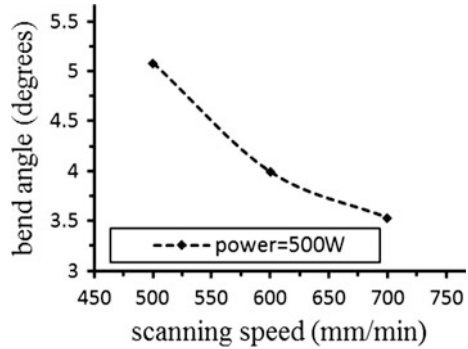


Fig. 6 Parabolic heating with step line irradiation

3.1.2 Effect of Scan Speed

Figure 5 shows the effect of scanning speed on bend angle at a laser power of 500 W. It is illustrated that the bend angle non-linearly decreases with the increase in scan speed. It is because the contact time between laser beam and workpiece surface decreases with the increase in scan speed. It reduces the energy absorption per unit length. It can also be imagined easily that the temperature gradient increases with the increase in scan speed. In BM, the bend angle decreases with the increase in the temperature gradient. Therefore, the bend angle decreases with the increase in scan speed due to combined effect of less energy absorption and the increase in temperature gradient.

3.2 Parabolic Heating with Step Irradiations

In this section, the results are presented on step irradiations carried out along a parabolic path as shown in Fig. 6. The effect of step irradiation on bend angle is studied at different levels of laser power and scanning speed.

Fig. 7 Variation of bend angle with number of step line heating

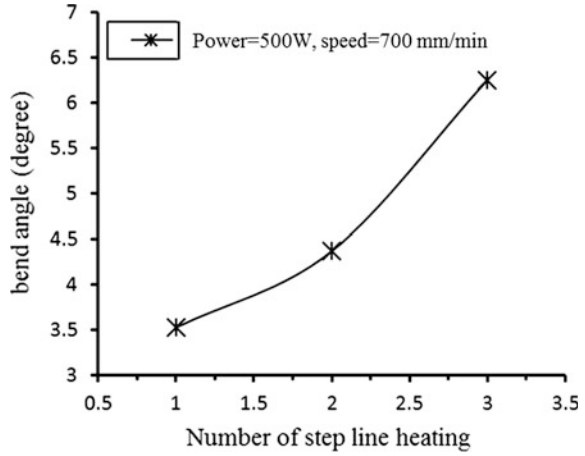
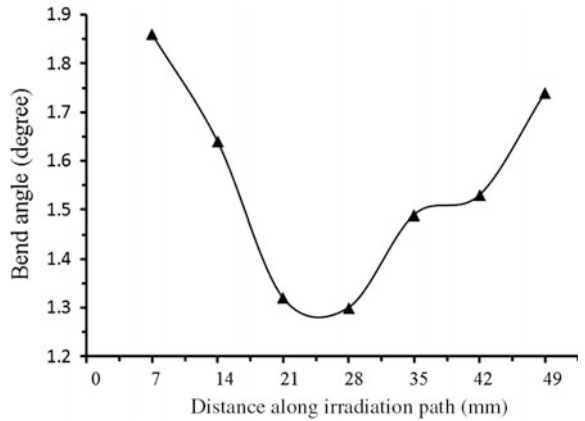


Fig. 8 Variation of bend angle along the scanning path



The bend angle of the successive irradiations is studied for three step line irradiations as shown in Fig. 6. The bend angle was measured for all the three stages. Figure 7 demonstrates the effect of step irradiations on bend angle. It can be seen that the bend angle increases with the number of line irradiations. This is because, after each irradiation, the sheet bends by a particular angle and hence the total bend angle keeps on increasing or in other words the sheet turns incrementally.

3.3 Variation in Bend Angle Along Scanning Path (Edge Effect)

The edge effect is the variation of bend angle along the laser scanning path. The distribution of bend angle along the scanning path is shown in Fig. 8. Total seven

equidistant points have been chosen along the curvilinear scanning path for the evaluation of edge effect. It can be observed that the bend angle is maximum at the edges and minimum in the middle of the scanning path. This is because thermal conduction is not present towards the free ends of the workpiece. Therefore, near the edges, heat flow is more along the workpiece thickness. It reduces the temperature gradient in the thickness direction. It results in the higher bend angle near the edges as compared with the middle of the scanning path.

4 Conclusions

In this work an experimental study on curvilinear laser bending of galvanized iron thin sheets with buckling mechanism dominated process conditions has been carried out. The effect of laser power, scanning speed and number of step line heating on bend angle was investigated. The distribution of bend angle along the scanning path was also investigated. Results showed that the bend angle non-linearly increases with the increase in laser power and decreases with the increase in scanning speed. Probably, the reason for non-linearity is the variation in bending mechanism (temperature gradient) with varying parameters. However, it was not explored in the present work and can be a future scope of the work. The total bend angle was increased with number of step line heating. It justifies the use of step line irradiation for incremental bending applications. Studies on the distribution of bend angle showed that the bend angle is not uniform along the scanning path. The bend angle was maximum near the edges, and it was minimum in the middle of the scanning path. The variation in bend angle was significant and therefore, one should be careful while using laser for bending applications. The present work will be useful for generation of complex shapes using laser bending process.

References

1. Kant R, Joshi SN (2013) Finite element simulation of laser assisted bending with moving mechanical load. *Int J Mechatron Manuf Syst* 6:351–366
2. Dixit US, Joshi SN, Kant R (2015) Research on laser forming system: a review. *Int J Mechatron Manuf Syst* 8:160–205
3. Kant R, Joshi SN (2014) Numerical modeling and experimental validation of curvilinear laser bending of magnesium alloy sheets. *Proc IMechE [B] J Eng Manuf* 228:1036–1047
4. Kant R, Joshi SN, Dixit US (2015) Research issues in the laser sheet bending process (Chap. 4). In: Devim Paulo J (ed) *Materials forming and machining*. Woodhead/Elsevier, UK
5. Kant R, Joshi SN (2016) Thermo-mechanical studies on bending mechanism, bend angle and edge effect during multi-scan laser bending of magnesium M1A alloy sheets. *J Manuf Processes* 23:135–148
6. Shi Y, Yao Z, Shen H, Hu J (2006) Research on the mechanisms of laser forming for the metal plate. *Int J Mach Tools Manuf* 46:1689–1697

7. Li W, Yao YL (2001) Numerical and experimental investigation of convex laser forming process. *J Manuf Processes* 3:73–81
8. Ojeda VC, Grez RJ (2009) Bending of stainless steel thin sheets by a rasterscanned low power CO₂ laser. *J Mater Process Tech* 209:2641–2647
9. Jamil MC, Sheikh MA, Li L (2011) A study of the effect of laser beam geometries on laser bending of sheet metal by buckling mechanism. *Optics Laser Tech* 43:183–193
10. Shi Y, Liu Y, Yao Z, Shen H (2008) A study on bending direction of sheet metal in laser forming. *J Appl Phys* 103:053101
11. Hemanth KV (2011) Experimental study on laser bending of steel sheet using CO₂ laser. M. Tech thesis, IIT Guwahati

A Comparative Study on Mechanical and Tribological Properties of Epoxy Composites Filled with Nano-ZrO₂ and Nano-Al₂O₃ Fillers

R.V. Kurahatti, A.O. Surendranathan, A.V. Ramesh Kumar
and V. Auradi

Keywords Polymer nanocomposites · Wear · Mechanical properties

1 Introduction

In the previous few decades, polymer composites are being widely used as structural materials in aerospace, automotive and chemical industries as they provide lower weight relative to conventional metallic materials. They are used as tribological components such as gears, cams, bearings, seals etc., where their self-lubrication properties are of special advantage. The feature that makes them promising in industrial applications is the possibility to tailor their properties with special fillers with different volume fraction, shape and size. The incorporation of well-dispersed nano- or micro-size inorganic particles into a polymer matrix has been demonstrated to be quite effective to improve their performance which includes friction and wear properties [1–4].

Comparing to the conventional microscale particles, nanoparticles have some unique features [5, 6]. Firstly, the much higher specific surface area can promote stress transfer from matrix to nanoparticles. Secondly, the required amounts of

R.V. Kurahatti (✉)

Basaveshwar Engineering College, Bagalkot, Karnataka, India
e-mail: rajukurahatti@gmail.com

A.O. Surendranathan

National Institute of Technology Karnataka, Surathkal, India
e-mail: aos_nathan@yahoo.com

A.V. Ramesh Kumar

Naval Physical and Oceanographic Laboratory, Kochi, Kerala, India
e-mail: avramesh.kumar@gmail.com

V. Auradi

Siddaganga Institute of Technology, Tumakuru, Karnataka, India
e-mail: vsauradi@gmail.com

nanoparticles in polymer matrices are usually much lower than those of the corresponding micro particles. Therefore, many intrinsic merits of pure polymers such as low weight, ductility, good processability, will be retained after the addition of nanoparticles. Thirdly, the mechanical behavior of the bulk materials can be improved while the often disturbing abrasiveness of the hard microparticles decreases remarkably by reduction of their angularity.

However, the unique nanocomposite effects can only be effective, if the nanoparticles are well dispersed in the surrounding polymer matrix. It has been shown that, a considerable improvement of the mechanical and tribological properties can already be achieved at very low filler volume content, somewhere in the range of 1–5 vol% [7, 8]. Especially for epoxy/TiO₂ nanocomposites Rong et al. presented experimental results which indicate that the wear performance significantly depends on the dispersion state and the micro structural homogeneity of the fillers [5].

Nanoparticles can be introduced into the polymers by different technologies. On the one hand by direct incorporation using chemical methods, and on the other hand by the application of high shear forces during a mechanical powder dispersion process [9, 10]. This process is necessary in order to transfer the nanoparticles from the agglomerated state into a homogeneously dispersed state. For thermoplastic matrices mainly twin screw extrusion is the method for manufacturing nanocomposites. In case of low viscosity liquid thermosetting resins, the dissolver technique in which a metal disc rotates with high speed inside the resin/particle mixture is used. Ultrasound vibration also helps to improve the dispersion state of nanoparticles [11]. Chemical methods are able to generate individual and non-agglomerated nanoparticles “in situ” within a thermosetting polymer [12]. An additional chemical treatment of the particle surface may further enhance the composite’s properties by improving the filler-matrix coupling quality [13, 14].

Epoxyes exhibit superior qualities such as high glass transition temperature (T_g), high modulus, high creep resistance, low shrinkage at elevated temperature and good resistance to chemicals due to their densely cross-linked structure. Having ability to adhere to a variety of fillers, they are used for high-performance coatings for tanks and structures in the chemical process industry, potting of electrical components and as fiber-reinforced circuit boards. There are special grades of epoxy for elevated-temperature service to about 176 °C.

Zirconia and alumina are famous for their hardness and are often used as grinding medium. They would not be suitable fillers in the micro scale particulate form due to their angularity which tends to abrade the mating counter face. The materials in the nanoscale particulate form have much lower angularity and thus they are not that abrasive.

In the present work, nanoparticles filled epoxy nanocomposites have been prepared by using high speed mixing process for particle dispersion. The filler content was varied in the range of 0.5–10 wt%. An effort is made to study the effect of weight fraction of nanoparticles on the mechanical and tribological properties of nanocomposites. To have more information, we compare the friction and wear properties of nano-ZrO₂/epoxy and nano-Al₂O₃/epoxy composites.

2 Experimental

2.1 Resin System

Epoxy. Epoxy resin (LY 556, Diglycidyl ether of Bisphenol A) and curing agent (HY 951, Triethylene tetramine) were purchased from Huntsman, Mumbai.

2.2 Fillers

Zirconium dioxide (ZrO_2) and Aluminum oxide (Al_2O_3). ZrO_2 and Al_2O_3 represent the ceramic nano crystalline phase and consist of primary particles in the size of 100 nm. They have a specific surface area of $100\text{ m}^2/\text{g}$. They were provided as dry powder and purchased from Aldrich, Bangalore.

2.3 Fabrication of Epoxy Nanocomposites

The nanoparticles were added into epoxy resin of known weight (grams). The mixture was stirred by using homogenizer (Fig. 1 Micra D-9) for 2 h. The temperature of mixture was not allowed to rise beyond $50\text{ }^\circ\text{C}$. The mixture was kept in

Fig. 1 Homogenizer



vacuum for 30 min (min) to remove the air bubbles entrapped during stirring. The hardener (10 wt% of epoxy) was mixed. The final mixture was poured into molds and cured at room temperature. Post-curing at 100 °C for 1 h was done. Specimens of required shape and size were obtained.

2.4 Characterization

Flexural properties. Three-point bend tests of pure epoxy resin and composites were carried out by using universal testing machine (UNITEK 9450PC, Blue star) as per ASTM D 790 at a deformation rate of 1 mm/min. The flexural strength and moduli were determined for each sample. The average of the three readings is reported. The dimensions of flexural, impact and wear test specimens are shown in Fig. 2.

Impact strength. Un-notched Charpy impact tests were conducted by using impact tester (IT-30, FIE).

Tribological properties. Dry slide wear tests as per ASTM G 99 were conducted on pin-on-disc machine (TR-201CL, Ducom). The disc material was made of En-32 steel (dia. 160 mm and thickness 8 mm) having hardness of 65 HRC. The surface roughness of the disc was about 0.02–0.06 μm . Before each test, the surfaces were polished with metallographic abrasive paper of 600 grade. Then the samples and the counter surface were cleaned in acetone and thoroughly dried. A constant 80 mm track diameter was used for all tests. Sliding was performed at 25 °C for 1 h (h) at a sliding velocity 0.84 m/s and normal pressure 0.8 MPa. The samples were weighed before and after the wear runs with electronic balance to determine the wear loss. The coefficient of friction was calculated by considering the normal load and the frictional force. The specific wear rate K_s was calculated by using equation:

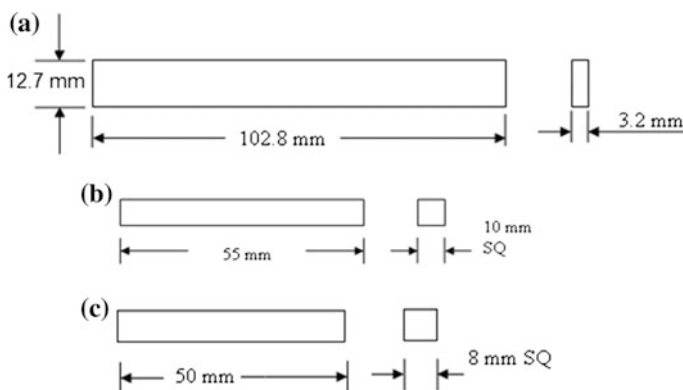


Fig. 2 Flexural test specimen (a), impact test specimen (b) and wear test specimen (c)

$$K_s = \frac{\Delta m}{\rho \times F_N \times L} (\text{mm}^3/\text{Nm}) \quad (1)$$

where Δm is mass loss (g), ρ is measured density of the sample (g mm^{-3}), F_N is normal load (N), and L is sliding distance (m).

These tests were carried out to assess the suitability of epoxy nanocomposites as they need to have good strength, toughness and wear resistance properties.

3 Results and Discussion

A homogeneous dispersion of the nanoparticles is believed to contribute better to the property improvement. Achieving homogeneous dispersion is very difficult because of the strong agglomerating tendency of the nanoparticles. The following results were obtained.

3.1 Mechanical Properties

The mechanical properties of the composites containing different contents of ZrO_2 are shown in Table 1. It is expected that incorporated filler particles impart high stiffness to the matrix due to elastic deformation occurring in the polymer/filler interfaces [15]. As the filler content increased from 0.5 to 10 wt%, the moduli of samples increased which is attributed to the increase in interfacial area between the matrix and filler particles. Samples with 5 wt% nano- ZrO_2 exhibited flexural strength and modulus of 76.8 MPa (+108%) and 5.15 GPa (+47%). The stiffness of composite materials is a reflection of the capability of composite interface to transfer elastic deformation [16]. It is clear that the addition of zirconia increased the stiffness of the matrix.

With a rise in filler content, the modulus increased mainly due to the contribution of the hard zirconia particles. The measured moduli depend also on the dispersion state of the nanoparticles. In contrast to conventional micro particulate-epoxy composites characterized by reduced strength in comparison with that of unfilled

Table 1 Mechanical properties of epoxy- ZrO_2 nanocomposites

Nano- ZrO_2 content (wt%)	Flexural strength (MPa)	Flexural modulus (GPa)	Impact strength (kJ/m^2)
0	36.9	3.5	18.68
0.5	48.3	5.2	19.2
1	54.2	4.8	18.3
5	76.8	5.15	15.2
10	63.8	5.43	14.3

Table 2 Mechanical properties of epoxy- Al_2O_3 nanocomposites

Nano Al_2O_3 content (wt%)	Flexural strength (MPa)	Flexural modulus (GPa)	Impact strength (kJ/m^2)
0	36.9	3.5	18.68
0.5	94.7	6.65	31.87
1	56.6	4.9	16.85
5	34.7	4.4	16.36
10	41.4	4.7	18.19

matrix [17], the current nanocomposites are stronger than neat epoxy. This implies that the bonding between the particles and the matrix is effective enough to transfer plastic deformation.

The zirconia particles are able to provide epoxy with higher impact toughness. Singh et al. [18] considered that crack front trapping is the primary extrinsic toughening mechanism involved in zirconia filled thermoset polymer. Impact values of the filled samples are higher compared to neat epoxy at low filler content (0.5 wt%). For higher filler contents, the impact toughness increased slightly. Though filler-matrix adhesion is improved, agglomeration of the particles is more severe at high filler contents.

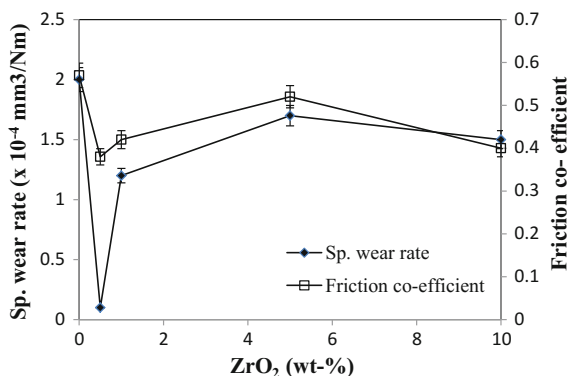
The mechanical properties of the composites containing different contents of Al_2O_3 are shown in Table 2. It is seen that flexural and impact strengths increased by the addition of alumina with the highest values being obtained at 0.5 wt%. This shows that stresses are efficiently transferred via the interface. However, the values decreased with increase in alumina content above 0.5 wt%. It is inferred that higher content of alumina is unfavorable for increasing the mechanical properties. Samples with 0.5 wt% filler exhibited highest flexural strength of 94.7 MPa (+156%) and modulus of 6.65 GPa (+88%) compared to epoxy. The increments in flexural strength and modulus were more for alumina-filled samples compared to the zirconia-filled ones.

3.2 Tribological Properties

Wear properties of polymers are affected by many factors like nature of materials, physical, mechanical and chemical behavior of interacting bodies, test environment, tribochemical reactions, etc. For nanocomposites, several additional factors contribute to the friction and wear damage. These include hardness, particle shape, aspect ratio, orientation and concentration of the fillers in the polymer matrix.

It was found that the epoxy-zirconia samples exhibited decreased sp. wear rate (K_s) compared to the epoxy (Fig. 3). The K_s sharply decreased when filler content was below 0.5 wt%. Although, the K_s increased with increasing zirconia content above 0.5 wt%, it was still lower compared to epoxy. 0.5 wt% samples showed the

Fig. 3 Tribological properties of epoxy-ZrO₂ nanocomposites



K_s value of $0.1 \times 10^{-4} \text{ mm}^3/\text{Nm}$ (-95%) compared to epoxy value of $2.0 \times 10^{-4} \text{ mm}^3/\text{Nm}$.

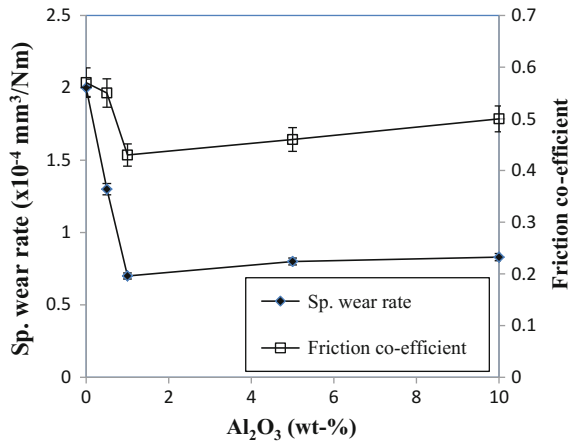
Rong et al. [5] examined the influence of microstructure on the tribological performance of nanocomposites by different compounding methods. They confirmed that the dispersion state of the nanoparticles and micro-structural homogeneity of the fillers improve the wear resistance significantly. However, a further increase in filler loading leads obviously to a deterioration of the K_s value. A change in the wear mechanism could be involved which may be ascribed to the large amount of zirconia particles causing a higher abrasive wear. Some aspects of the reinforcing role that ceramic microparticles can play in the tribological behavior were studied by Durand et al. [19], who found that large particles protect the matrix better than smaller ones because they can shield the polymer if they are not pulled out. Small particles, on the other hand, were removed and then involved in an abrading wear process.

Besides improving the wear resistance, the nanoparticles also reduce the frictional coefficient of epoxy. Evidently, the nanocomposite with 0.5 wt% zirconia exhibited the lowest friction coefficient. The coefficient of friction decreased from 0.57 for unfilled epoxy to 0.38 at 0.5 wt%. When the composites with nanoparticles are subjected to wearing, detachment of nanoparticles and small amount of the surrounding matrix plays the leading role in material removal due to wear. The detached nanoparticles act as solid lubricant. These account for the low wear rates and frictional coefficients of the composites.

It was found that the epoxy-nano Al₂O₃ composites exhibited decreased K_s relative to neat epoxy (Fig. 4). The K_s sharply decreased when filler content was below 1 wt%. Epoxy with 1 wt% alumina exhibited the lowest K_s . Although, the K_s increased with wt% of alumina above 1 wt%, it was lower compared to the neat epoxy. Epoxy with 1 wt% alumina showed the lowest K_s value of $0.7 \times 10^{-4} \text{ mm}^3/\text{Nm}$ (-65%) compared to the epoxy value of $2.0 \times 10^{-4} \text{ mm}^3/\text{Nm}$. The friction coefficient decreased from 0.57 for unfilled epoxy to 0.43 at 1 wt%.

Epoxy-zirconia composites have shown improved tribological properties relative to epoxy-alumina composites. This may be due to the greater extent of interaction

Fig. 4 Tribological properties of epoxy- Al_2O_3 nanocomposites



of nano zirconia filler with the polymer matrix, which makes the composite more wear resistant.

It is difficult to establish the relation between mechanical and tribological properties from the data presented here. The bonding between the polymer matrix and fillers decides the yield strength of the filled composite. In the same way, the difference in reducing the friction coefficient and improving the wear resistance ability of epoxy nanocomposites should result mainly from the filler-matrix adhesion strength.

4 Conclusions

This study focused on the development of nanocomposites with properties superior to the neat matrix. The following conclusions were drawn:

- (1) Epoxy composites with 0.5 wt% alumina showed highest flexural strength of 94.7 MPa (+156%) and modulus of 6.65 GPa (+88%) relative to neat epoxy. Samples with 5 wt% nano- ZrO_2 exhibited flexural strength and modulus of 76.8 MPa (+108%) and 5.15 GPa (+47%). The increments in flexural strength and modulus were more for alumina-filled samples compared to the zirconia-filled ones.
- (2) Epoxy with 1 wt% alumina showed the K_s value of $0.7 \times 10^{-4} \text{ mm}^3/\text{Nm}$ (-65%) compared to neat epoxy. The friction coefficient was 0.43.
- (3) Epoxy with 0.5 wt% zirconia showed the lowest specific wear rate and friction coefficient ($0.1 \times 10^{-4} \text{ mm}^3/\text{Nm}$ and 0.38 respectively) than neat epoxy, for which the values were much higher ($2 \times 10^{-4} \text{ mm}^3/\text{Nm}$ and 0.57 respectively).

References

1. Wang Q, Xue Q, Liu W, Shen W (1999) Tribological properties of micron silicon carbide filled poly (ether ether ketone). *J Appl Polym Sci* 74:2611–2615
2. Durand JM, Vardavoulias M, Jeandin M (1995) Role of reinforcing ceramic particles in the wear behaviour of polymer based model composites. *Wear* 181–183:833–839
3. Zhang MQ, Rong MZ, Yu SL, Wetzel B, Friedrich K (2002) Effect of particle surface treatment on the tribological performance of epoxy based nanocomposites. *Wear* 253: 1086–1093
4. Lin J-C (2007) Compression and wear behavior of composites filled with various nanoparticles. *Compos Part B Eng* 38:79–85
5. Rong MZ, Zhang MQ, Liu H, Zeng HM, Wetzel B, Friedrich K (2001) Microstructure and tribological behavior of polymeric nanocomposites. *Ind Lubr Tribol* 53:72–77
6. Rong MZ, Zhang MQ, Zheng YX, Zeng HM, Friedrich K (2001) Improvement of tensile properties of Nano-SiO₂/PP composites in relation to percolation mechanism. *Polymer* 42:3301–3304
7. Ng CB, Schadler LS, Siegel RW (1999) Synthesis and mechanical properties of TiO₂-epoxy nanocomposites. *Nanostruct Mat* 12:507–510
8. Wang Q, Shen W, Xue Q (1997) The friction and wear properties of nanometer SiO₂ filled polyetheretherketone. *Tribol Int* 30(3):193–197
9. Avella M, Errico ME, Martelli S, Martuscelli E (2001) Preparation methodologies of polymer matrix nanocomposites. *Appl Organometal Chem* 15:434–439
10. Dennis HR, Hunter DL, Chang D, Kim S, White JL, Cho JW, Paul DR (2001) Nanocomposites: the importance of processing. *Plast Eng* 1:56–60
11. Wang Q, Xia H, Zhang C (2001) Preparation of polymer/inorganic nanoparticles composites through ultrasonic irradiation. *J Appl Polym Sci* 80:1478–1488
12. Adebahr T, Roscher C, Adam J (2001) Reinforcing nanoparticles in reactive resins. *Eur Coat J* 4:144–149
13. Rong MZ, Zhang MQ, Zheng YX, Zeng HM, Walter R, Friedrich K (2000) Irradiation graft polymerization on nano-inorganic particles: an effective means to design polymer based nanocomposites. *J Mater Sci Lett* 19:1159–1161
14. Becker C, Krug H, Schmidt H (1996) Tailoring of thermomechanical properties of thermoplastic nanocomposites by surface modification of nanoscale silica particles. *Mat Res Soc Symp Proc* 435:237–242
15. Wang Q, Xue Q, Shen W, Zhang J (1998) The friction and wear properties of nanometer ZrO₂-filled polyetheretherketone. *J Appl Polym Sci* 69:135–141
16. Zhang M, Zeng H, Zhang L, Lin G, Li RKY (1993) Fracture characteristics of discontinuous carbon fibre-reinforced PPS and PES-C composites. *Polym Polym Compos* 1:357–365
17. Spanoudakis J, Young RJ (1984) Crack Propagation in a Glass Particle Filled Epoxy Resin. Part 2. Effect of Particle-Matrix Adhesion. *J Mat Sci* 19:487–496
18. Singh RP, Zhang M, Chan D (2002) Toughening of a brittle thermosetting polymer: effects of reinforcement particle size and volume fraction. *J Mat Sci* 37:781–788
19. Durand JM, Vardavoulias M, Jeandin M (1995) Role of reinforcing ceramic particles in the wear behavior of polymer-based model composites. *Wear* 181–183:833–839

Part IV
Lab-Level Advanced Societal Technologies

Synthesis of TiO₂ Nanofibers for Solar Cells and Their Analysis Using Statistical Tool—ANOVA

Sunil Kadam, Prerana Ghatmale, Puneet Garg, P.V. Jadhav,
Sachin Shendokar and Sachin Chavan

Keywords Analysis of variance (ANOVA) · Design of experiments (DoE) · Electrospinning

1 Introduction

Electrospinning or electrostatic fiber spinning is the simplest form of producing polymer nanofibers in sub-micron to a nanometric range by applying high voltage supply. Among the different techniques to synthesize nanofibers, electrospinning is most commonly used method due to reasons such as ease of use, cost efficiency, and non-mechanical characteristics. The produced electrospun TiO₂ nanofibers demonstrated excellent features such as high surface to volume ratio, adjustable porosity and possible high control over the morphology of the nanofibers. The potential applications of the synthesized TiO₂ nanofibers can be found in energy storage, filtration, biomedical engineering, cosmetics, etc. [1, 2].

Titanium dioxide or Titania is a semiconductor material with compulsive properties such as high refraction index, low absorption coefficient, and transparency to light. It is available in nature in 3 crystalline forms namely Rutile, Anatase and Brookite. Among the three, Rutile and Anatase are the two main polymorphs and exhibit excellent photolytic behavior. The brookite phase is the orthorhombic variant of TiO₂. Preparing nanofibers from Titania has made a pathway to combine the two major properties together i.e. high surface area and

S. Kadam · P. Ghatmale (✉) · P. Garg · P.V. Jadhav · S. Chavan
Bharati Vidyapeeth Deemed University College of Engineering, Pune, India
e-mail: prerana_ghatmale@outlook.com

S. Kadam
e-mail: s.kad@rediffmail.com

P. Garg
e-mail: pkgbme@outlook.com

S. Shendokar
Bharati Vidyapeeth College of Engineering, Lavale, India

semiconductor properties. The characteristic property of being very photoactive of Anatase phase makes it applicable in various electronic domains such as sensors, catalytic devices, solar cells, optoelectronic devices, etc. Whereas the rutile phase properties make it a viable option for applications in a cosmetic field [3–5].

The Design of Experiments (DoE) approach is implemented by statistical tool—Analysis of Variance (ANOVA) which helps in determining the effect of the various electrospinning parameters along with the solution parameters on the output i.e. the nanofiber diameter.

2 Experimental Procedure

2.1 Materials

Titanium Isopropoxide (TiP) (MW = 284.22 g/mol, 97% purity), polyvinylpyrrolidone (PVP) (MW = 1,300,000 g/mol, 100% purity). Acetic acid (MW = 60.05 g/mol, 99.5% purity) and ethanol (MW = 46.07 g/mol, 99.5% purity) are all purchased from Sigma–Aldrich, Inc., NSW, Australia.

2.2 Preparation of TiO_2

Solution A is made by adding 1.5 ml of Titanium Isopropoxide (TiP) and 3.0 ml of acetic acid. This mixture is then stirred for 1 h on a magnetic stirrer to get the homogenous mixture.

Solution B is made by adding 0.45 g of polyvinylpyrrolidone (PVP), (MW = 1,300,000 g/mol, 100% purity) and 10.0 ml of ethanol. This mixture is also stirred for 1 h on a magnetic stirrer. Solution B is slowly added to solution A and stirred continuously for 1 h. The resultant solution is placed in a 2.0 ml syringe with a metallic needle attached. The solution is kept at different electrospinning parameters for the duration of minimum 1 h, and further optimization is carried out for the parameters using ANOVA technique.

2.3 Electrospinning Experiments

ESPIN NANO-MODEL V1 unit is purchased from Physics Equipment Corporation Chennai, India to fabricate electrospun nanofibers. The two primary sections of electrospinning machine are spinning chamber and control panel. The spinning chamber consists of collector drum, syringe pump, discharge stick, cabin light, exhaust fan, jack and height adjustment mount. The control panel has an HV Power

Table 1 Design of experiments in uncoded form

Readings	Distance (cm)	Flow rate (ml/h)	Voltage (kV)
1	20	1.5	18
2	20	1.5	15
3	20	1.0	18
4	20	1.0	15
5	15	1.5	18
6	15	1.5	15
7	15	1.0	18
8	15	1.0	15

Table 2 Low (−1) and high (+1) values in design of experiments

Parameters	Nomenclature	Low (−1)	High (+1)
Distance	cm	15	20
Flow rate	ml/h	1.0	1.5
Voltage	kV	15	18

Supply control, Syringe pump control and drum collector control. The prepared solution is loaded in 2.0 ml syringe along with the stainless needle. The needle tip to collector distance is adjusted according to the values obtained from the DOE (as shown in Table 1). The distance parameter is adjusted in between 15 and 20 cm. Similarly, the flow rate is set in between 1.0 and 1.5 ml/h. The voltage parameter is set between 15 and 18 kV.

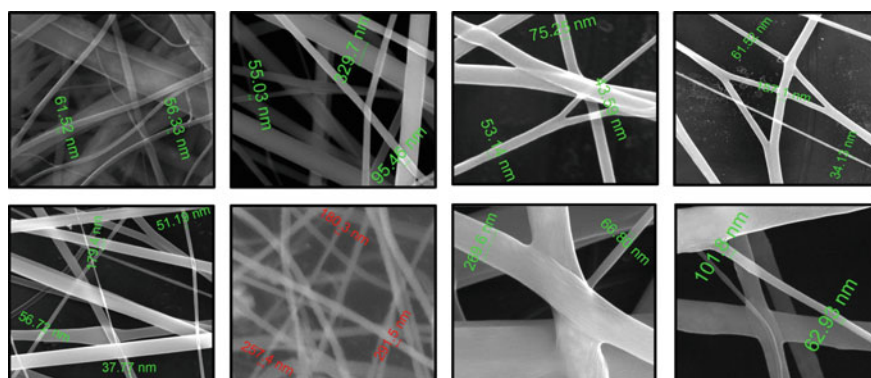
2.4 Design of Experiments

When multiple factors are involved in the electrospinning technique, it becomes necessary to determine which factor has the maximum effect on the thickness of the nanofiber or in other terms which parameter gives the minimum nanofiber diameter. Thus a design of experiments is set up to determine the individual effect of parameters involved in the electrospinning process [6]. The analysis is carried out by the Minitab software using the statistical tool ANOVA. A full factorial design with two levels—low (−1) and high (+1) are used. Three independent parameters are varied at two levels (low and high) as shown in Table 2.

Thus 2^k defines the output of the full factorial design where k is the number of process parameters that are to be varied. For three parameters eight different experiments are carried out. The three parameters considered are a distance from the

Table 3 Design of experiments in coded form

S. No.	Distance (cm)	Flow rate (ml/h)	Voltage (kV)
1	+1	+1	+1
2	+1	+1	-1
3	+1	-1	+1
4	+1	-1	-1
5	-1	+1	+1
6	-1	+1	-1
7	-1	-1	+1
8	-1	-1	-1

**Fig. 1** SEM images of the TiO₂ fibers prepared using parameters in Table 1

positive electrode (tip of the needle) to collector drum, a voltage applied and the flow rate of the polymer solution. For the electrospinning process, the two levels low and high and the three factors are given as input values to generate the coded table of DOE as shown in Table 3.

3 Characterization

The electrospun TiO₂ nanofibers are characterized by Scanning electron microscope (SEM) to study the fiber morphology, topology, composition and crystallographic structure. The SEM images of the synthesized TiO₂ nanofibers (as shown in Fig. 1) reported the average diameter range from 76.42 to 262.13 nm (as shown in Table 4).

Table 4 Average diameter of the TiO₂ nanofibers using various parameters

Readings	Distance (cm)	Flow rate (ml/h)	Voltage (kV)	Average diameter (nm)
1	20	1.5	18	130.67
2	20	1.5	15	114.27
3	20	1.0	18	77.48
4	20	1.0	15	76.42
5	15	1.5	18	100.13
6	15	1.5	15	262.13
7	15	1.0	18	158.11
8	15	1.0	15	127.14

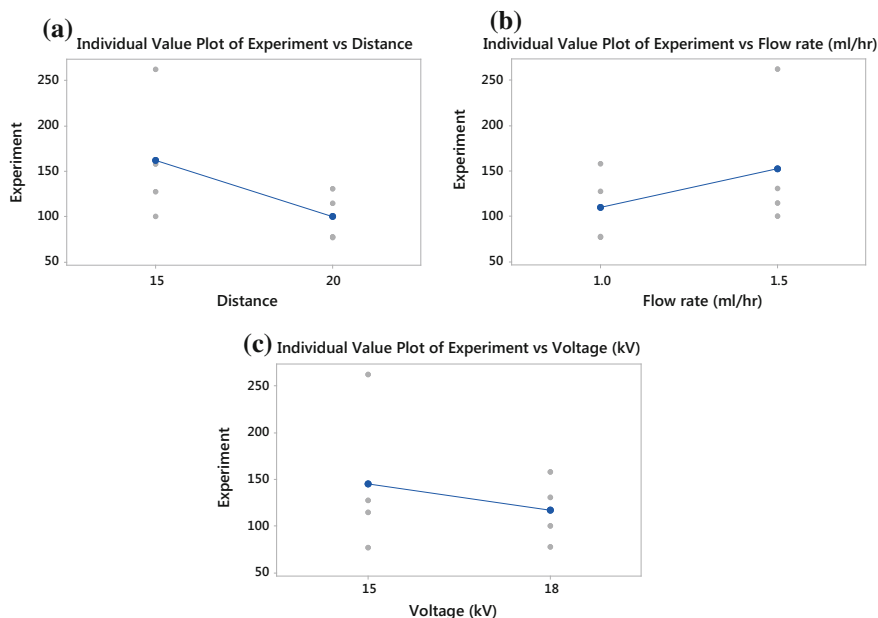


Fig. 2 Individual value plots obtained using one way ANOVA: **a** distance versus average diameter; **b** flow rate versus average diameter and **c** voltage versus average diameter

4 Results and Discussion

4.1 Optimization by One-Way ANOVA

One way Analysis of Variance is performed on the dataset obtained with an average diameter as the response and distance, flow rate and voltage as the input factors. Individual value plots for each independent factor versus response graphs are shown in Fig. 2. As can be seen, one way ANOVA by comparing the means of the two data groups indicates that at the greater distance, lower flow rate and greater

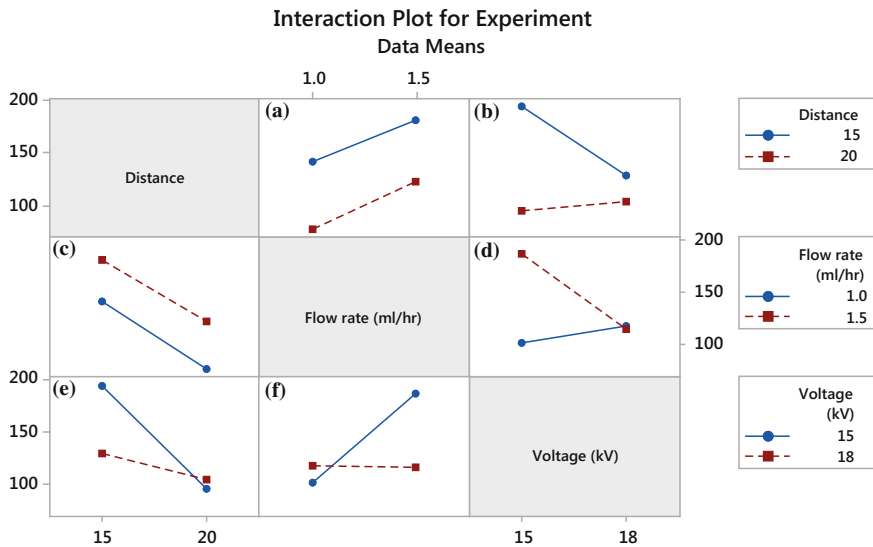


Fig. 3 Interaction plots of three factors with one another

voltage, we will obtain the thinnest TiO₂ nanofibers. From the slopes of the three parameters, it can be observed however that the distance parameter has the highest affect on the nanofiber diameter.

4.2 Interaction Plots

The interaction plots between the three factors on the average diameter are shown in Fig. 3. It is clearly visible (from Fig. 3a, c) that distance and flow rate have no effect on each other what-so-ever. However, a clear interaction between distance and voltage and also flow rate and voltage can be observed (see Fig. 3b, d–f). Further, it can be stated that the interaction of factors voltage and flow rate is more as compared to distance and voltage. Both the subplots (Fig. 3d, f) of voltage and flow rate show interaction whereas only one out the two subplots (Fig. 3b, e) of distance and voltage show the interaction (Fig. 3e).

5 Applications

Electrospun nanofibers have numerous applications in different domains such as filtration, water purification, fuel cells, drug delivery, wound healing and tissue engineering [7]. TiO₂ nanofibers can have potential application in energy storage

domain. The two main limitations of conventional solar cells of less efficiency and high manufacturing cost can be surpassed by the use of nanotechnology equipped solar cells. TiO₂ due to its properties are widely used in the energy harvesting field and Dye-Sensitized Solar Cells (DSSCs) which are likely to improve the efficiency and reduce the manufacturing cost in comparison to the conventional solar cells [8]. The synthesized nanofibers have a thinner diameter which can provide more surface to volume ratio for increased light harvesting thus improving the efficiency of DSSCs. Moreover, the manufacturing process mentioned is comparatively simple and thus can be used for the bulk manufacture of TiO₂ nanofibers.

6 Conclusion

Electrospun TiO₂ nanofibers are synthesized by the novel technique of electrospinning. The average diameter obtained from the synthesized TiO₂ nanofibers is in the range from 76.42 to 262.13 nm. The nanofibers are optimized by performing DOE and Analysis of variance (ANOVA). It is found that distance had the maximum effect on the fiber diameter. The interaction plots show the interaction of the three parameters with one another. Figure 3a, c shows no interaction between the factors distance and voltage, whereas Fig. 3b, e and d, e shows an interaction of distance with voltage and also voltage and flow rate.

References

1. Chen Z, Foster MD, Zhou W, Fong H, Reneker DH, Resendes R, Manners I (2001) Structure of poly (ferrocenyldimethylsilane) in electrospun nanofibers. *Macromolecules* 34(18): 6156–6158
2. Fong H, Reneker DH (2001) *Electrospinning and the formation of nanofibers*, vol 6
3. Banfield JF, Veblen DR, Smith DJ (1991) The identification of naturally occurring TiO₂ (B) by structure determination using high-resolution electron microscopy, image simulation, and distance-least-squares refinement. *Am Mineral* 76(3–4):343–353
4. Hanaor DA, Sorrell CC (2011) Review of the Anatase to rutile phase transformation. *J Mater Sci* 46(4):855–874
5. Di Paola A, Bellardita M, Palmisano L (2013) Brookite, the least known TiO₂ photocatalyst. *Catalysts* 3(1):36–73
6. Dunn PM (1997) James Lind (1716-94) of Edinburgh and the treatment of scurvy. *Arch Dis Child Fetal Neonatal Ed* 76(1):F64–F65
7. Ghatmale P, Garg P, Kadam S, Chavan SS (2016) Review: electrospinning technique and factors affecting electrospun nanofibers and some applications. *Int J Sci Res Dev* 4(4):681–686
8. Chuangchote S, Sagawa T, Yoshikawa S (2008) Efficient dye-sensitized solar cells using electrospun TiO₂ nanofibers as a light harvesting layer. *Appl Phys Lett* 93(3):33310

Development of Experimental Setup for Measurement of Stored Hydrogen in Solids by Volumetric Method

Rohan Kalamkar, Aneesh Gangal and Vivek Yakkundi

Keywords Hydrogen storage · PC isotherms · Kinetics · Gas absorption/desorption

1 Introduction

Energy plays an important role in human activity. The rapid depletion of crude oil reserves and environmental problems associated with petroleum combustion give rise to an urgent need to establish an alternative fuel for the transport sector. One of the possible alternatives to the transport fuel is the use of Hydrogen. Technologists working in this field feel that Hydrogen Energy System will be a solution to the projected global crisis in energy supply because of its properties like abundance, inexhaustibility, cleanliness and convenience. It is highly reactive and reacts with almost all elements in the periodic table. The safety record has been excellent in production as well as transportation. Hydrogen is high in energy (heating value 127 MJ/kg) and for sourcing electrical power to applications, fuel cell technology used. Applications can use fuel cell as a battery which is constantly replenished by adding Hydrogen and Oxygen as fuel to prevent the fuel cell performance deterioration [1]. The Hydrogen based application requires Hydrogen generator and storage medium. Hydrogen can be stored in a number of states, as a compressed gas, cryogenic liquid and component in a solid chemical media. Particularly, fuel cell vehicle, storing sufficient Hydrogen on board is a key issue. Conventionally, Hydrogen is stored as compressed gas in high-pressure cylinders or as a liquid in cryogenic containers. Since these methods are energy intensive and have associated

R. Kalamkar (✉)
Gharda Institute of Technology, Lavel, India
e-mail: rohanhirve@gmail.com

A. Gangal
Rajaram Shinde College of Engineering, Pedhambe, India

V. Yakkundi
Lokmany Tilak College of Engineering, Koperkhairane, India

safety issues, Hydrogen storage in the form of solid compounds is considered to be a promising option [2]. The extremely low density of hydrogen 0.089 kg m^{-3} makes the storage of it a major hurdle in implementation of Hydrogen fueled applications [3]. Significant research and development activities are being carried out in order to increase the efficiency of Hydrogen storage systems to make them competitive with current fossil fuels for transportation and stationary applications. In order to develop and demonstrate viable Hydrogen storage technologies, a set of objectives have been proposed by the US Department of Energy (DOE), based on achieving a driving range of 500 km for a Hydrogen powered vehicle. These objectives fix a target of 2 kW h kg^{-1} (6 wt%), 1.5 and 4 kW h^{-1} for 2010 and of 3 kW h kg^{-1} (9 wt%), 2.7 and 2 kW h^{-1} for 2015. It is important to note that these are system targets, which implies that the weight of the storage system as a whole must be taken into account [4]. Literature review shows use of this apparatus for production of Nd–Fe–B permanent magnets, giant magnetostrictive REFe_2 alloys using hydrogen decrepitation process, for the nitrogenation of $\text{RE}_2\text{Fe}_{17}$ and REFe_{12} magnet materials [5], thermal decomposition study for ammonia borane and CNTs materials [3] and metal-Hydrogen systems [6].

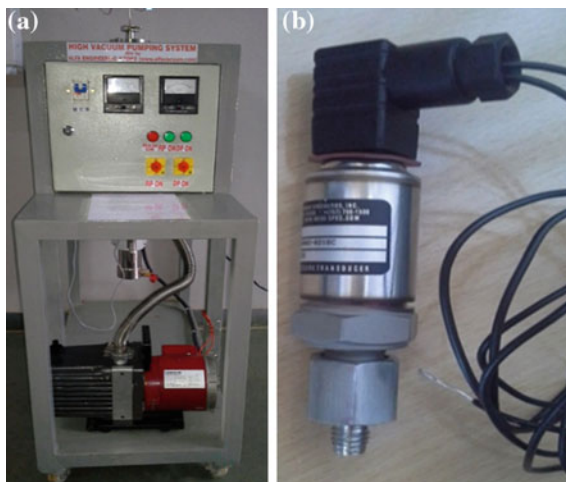
The purpose of this work is to prepare experimental setup which can measure the amount of Hydrogen stored in solids, its absorption and desorption properties and kinetics of the reaction based on pressure reduction method to develop a low-cost high-capacity. Hydrogen storage material having favorable thermodynamics and kinetics characteristics as well as stability with cycling. Estimation of wt% of Hydrogen is done to conclude use of a solid material technique to store Hydrogen seems to be a valid alternative compared with the traditional storage techniques.

2 High Pressure Experimental Setup

2.1 High Vacuum System and Pressure Sensor

The high vacuum system is a device that removes gas molecules from a sealed volume in order to leave behind a partial vacuum. The quality of a partial vacuum refers to how closely it approaches a perfect vacuum. It consists of rotary and diffusion pump. The rotary pump gives roughing side vacuum at least in 10^{-1} mbar range and diffusion pump further improve vacuum up to 10^{-5} mbar range. A pressure sensor acts as a transducer and it generates a signal as a function of the pressure imposed. It converts changes in pressure of a gas into an electrical signal by means of a pressure sensing device and generates an analog output proportional to the pressure or a switching output which operates at a particular pressure level. The pressure sensor which is used takes an input of 9–30 V DC and gives an output

Fig. 1 **a** Photograph of high vacuum system setup, **b** photograph of pressure sensor



of 4–20 mA with the accuracy of $\pm 0.25\%$ BFSL (Best fit straight line method). Figure 1a, b show Photograph of High vacuum system setup and Photograph of Pressure sensor respectively.

2.2 *Temperature Controller, Temperature Indicator and Thermocouples*

Temperature controller is needed for situation requiring a given temperature to be kept stable and where an object is required to be heated, cooled or both and to remain at the target temperature (set point), regardless of the changing environment around it. The temperature indicator is a cost-effective control device that helps to determine and display temperatures. Measurement results can easily be read out from large LED display. K type thermocouples consist of two wire legs welded together at one end, creating a junction at which the temperature is measured. Figure 2a, b shows conceptual setup and photograph of measuring and reactor setup.

2.3 *Reactor and Measuring Chamber*

Sievert's type apparatus is used for measurements of Hydrogen absorption/desorption characteristics, such as reversible Hydrogen intake capacity, kinetics, plateau pressure of alloys and inter-metallic compounds in the ranges $0.05 < P/\text{bar} < 50$ and $300 < T/\text{K} < 723$, based on the pressure reduction method as well as PC isotherm and decomposition studies.

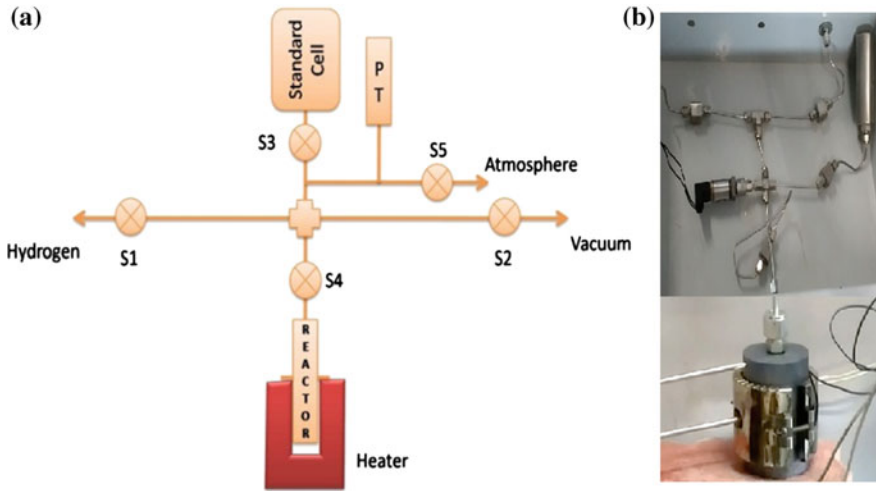


Fig. 2 a Conceptual setup (Source [3], p. 33), b photograph of measuring and reactor setup

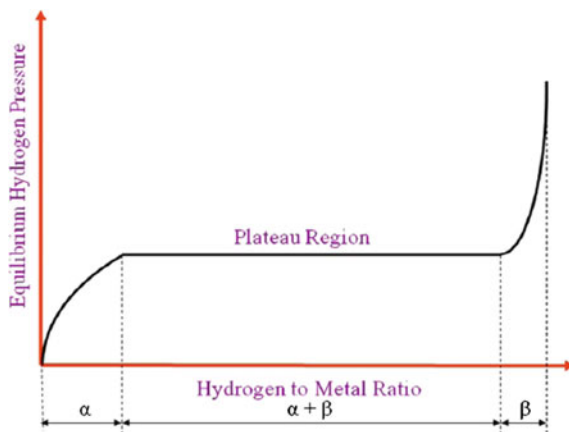


Fig. 3 Photograph showing fabricated experimental setup

3 Methodology

Experiments are performed on Hydrogen storage materials to estimate their Hydrogen sorption properties and thermal decomposition. The volumetric technique is used to measure the amount of Hydrogen absorbed/desorbed based on the measure of change in the pressure which corresponds to the change in Hydrogen contents of the material [5]. Knowing the volume and temperature of gas, change in pressure can be related to number of moles of Hydrogen with the help of van-der Waal’s equation. Figure 3 shows photograph showing fabricated experimental setup.

Fig. 4 Pressure composition (PC) isotherm (Source [3], p. 38)



When Hydrogen is allowed to interact with the material, it gets absorbed in the material (Van-der Waal's interactions). In both the cases if the volume of the reactor is fixed then the pressure of the gas decreases. The adsorption of a gas on a surface is a consequence of the yield force at the surface of the solid, called the adsorbent which attracts the molecules of the gas or vapour, called adsorbate. The forces of attraction emanating from a solid may be of two main kinds, physical or chemical, and they give rise to physical, i.e. Van-der Waals, or chemisorptions respectively [3]. The results of these measurements are a pressure-composition isotherm. It is a fingerprint of Hydrogen storage characteristics of the material and consists of three distinct regions. The initial steep slope corresponds to Hydrogen forming the solid solution or α -phase. At the saturation limit of the solid solution, hydride begins to form as a second phase also called as β -phase. During this pressure remains constant while the concentration of Hydrogen increases due to conversion of α -phase to β -phase. Finally, in the third region, further addition of Hydrogen leads to the second solid solution phase which is the dissolution of Hydrogen in the hydride and this causes a steep rise in the Hydrogen pressure. The flat or the constant pressure region in the PC isotherm is plateau region. The value of the plateau pressure represents the pressure of Hydrogen in equilibrium with the material-material hydride phases at the temperature concerned (Fig. 4).

The charging/discharging times are associated with the rate of hydrogenation/dehydrogenation i.e. how fast these reactions occur. The measurement of decomposition data with respect to time is done to determine the rate of reaction and finally to estimate the kinetic parameters namely the activation energy and the pre-exponential factor. Estimation of wt% of Hydrogen taken up by a sample is done using applied pressure, equilibrium pressure, ambient temperature and sample temperature. This calculation is tedious because there exists a temperature gradient within the reactor and the temperature difference between sample holder and rest of the system. To account for this temperature gradient the total volume is divided into two regions, namely hot volume and cold volume. Finally, the amount of Hydrogen

absorbed was estimated using the Van-der Waal's Equation for real gas considering hot and cold volume [3]. Finding the best adsorbents for Hydrogen storage basically involves optimizing three parameters: the characteristic binding energy of the Hydrogen molecule with the material, the available surface for adsorption processes and the bulk density of the adsorbate. Both of the latter can be combined with an average surface available per unit volume of the adsorbent which should be maximized. The binding energy determines the operating temperature of a Hydrogen storage system based on the solid [3, 4].

4 Calibration of Experimental Setup

For estimating the unknown volumes in the apparatus calibration of the experimental setup is done and for that gas expansion method was employed. Figure 5 conceptual setup for volume calibration with Van-der Waal's equation for real gas. Setup is made up of several tubing linkages fitted to the reactor, cylinder, inlet and outlet. For estimation of wt% of Hydrogen evolved or absorbed it is required to calculate a volume of tubing system using van-der Waal's equation. Initially pressure of Hydrogen in standard cell is known and it is used in a calculation of number of moles of Hydrogen and further calculations are carried out by taking number of moles as a constant value. By calculating number of moles of Hydrogen absorbed or desorbed using equation, weight of Hydrogen can be calculated as $(n_1 - n_2) \times 2$ where n_1 are number of moles before reaction and n_2 are number of moles after the reaction.

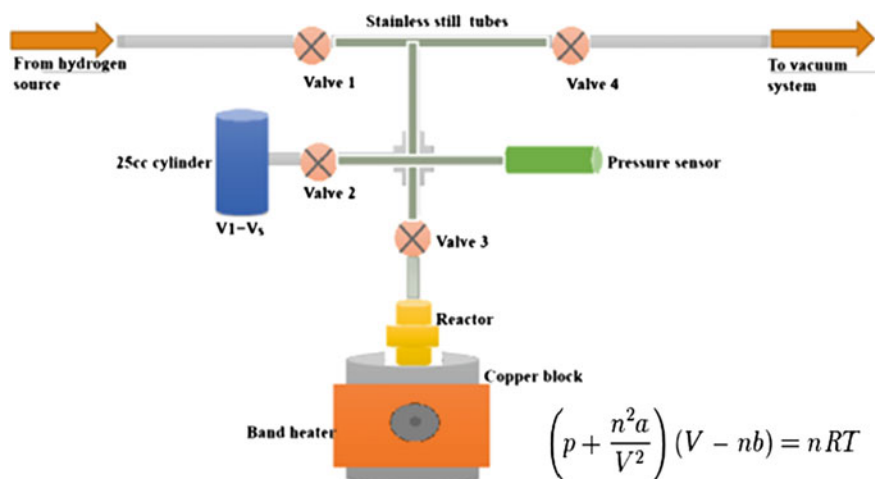


Fig. 5 Conceptual setup for volume calibration with Van-der Waal's equation for real gas

The nomenclatures of equation are p is pressure, n is number of moles of gas, V is volume, T is absolute temperature, a is correction for intermolecular forces which is $0.0248 \text{ J m}^3/\text{mol}^2$, b is correction for finite molecular size which is $2.66 \times 10^{-5} \text{ m}^3/\text{mol}^2$, standard volume of cylinder is 0.025 L and R gas constant 8.314 J/K mol .

Initially, the test of Hydrogen absorption experiment is conducted on 60–80 nm size Mg and Si particles. The sequence of changes occurring in the material-Hydrogen system can be followed experimentally by monitoring the changes in Hydrogen pressure and concentration of Hydrogen at a constant temperature in a closed system. Magnesium hydride combines a high H_2 storage capacity of 7.7 wt% with the benefit of the low cost of the richly available magnesium [6]. Five numbers of magnesium Hydrogen tests are conducted. Average of test results shows optimum Hydrogen uptake of 1.85 wt% at the temperature of $250 \text{ }^\circ\text{C}$ and at 12.4 bar pressure. Theoretically SiH_x system has 3.44, 6.66 and 9.67 wt% of Hydrogen for $x = 1, 2, 3$ respectively [7]. The reactivity of Si with Hydrogen strongly depends on coverage and surface temperature [8]. Emission of molecular Hydrogen produced from the heat induced decomposition of SiH_x groups homogeneously covering the PS nanostructures makes this material suitable for its application as a Hydrogen reservoir [9]. Silicon-Hydrogen test is repeated five numbers of times. Average of test results shows optimum Hydrogen uptake of 2.55 wt% at the temperature of $110 \text{ }^\circ\text{C}$ and at 12.6 bar pressure for silicon Hydrogen test. Further, the dehydrogenation test on Ammonia Borane (AB) having Hydrogen content (19.6 wt%) per mass is conducted. The decomposition of AB takes place in three steps at desorption temperatures of about 100, 140 and above $1000 \text{ }^\circ\text{C}$ respectively releasing 1 mol of Hydrogen in each step [10]. AB is a white crystalline solid at room temperature, it's non-toxic, environmentally benign, and stable material that can be safely transported without Hydrogen loss, which dictates the success of any chemical for hydrogen storage [11]. Five numbers of tests are conducted on an isothermal decomposition of AB. Average test results show wt% released for neat AB is 1.15 for temperature $100 \text{ }^\circ\text{C}$. The dehydrogenation test on magnesium hydride is also repeated five times. Magnesium hydride, MgH_2 has the highest energy density (9 MJ/kg) of all reversible hydrides applicable for hydrogen storage [12]. Average test results show isothermal decomposition of MgH_2 and wt % released is 0.24 for temperature $90 \text{ }^\circ\text{C}$. Each test of the sample material is repeated five times and average results are noted in Table 1. Figure 6a, b shows graph of absorption of H_2 by Mg and absorption of H_2 by Si. Similarly Fig. 7a, b shows graph of desorption of NH_3BH_3 and desorption of MgH_2 .

Table 1 Summary of experiments conducted on fabricated setup

Type of experiment	Sample	Pressure (bar)	Temperature ($^\circ\text{C}$)	Total wt% absorbed/desorbed
Hydrogenation	Mg	12.44	250	1.85
Hydrogenation	Si	12.62	110	2.55
Dehydrogenation	NH_3BH_3	2.52	100	1.15
Dehydrogenation	MgH_2	1.54	90	0.24

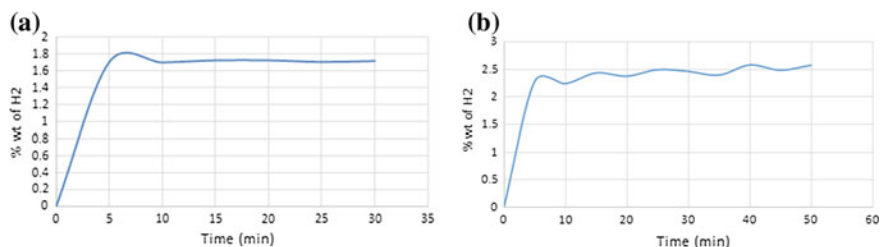


Fig. 6 a Graph of absorption of H₂ by Mg, b graph of absorption of H₂ by Si

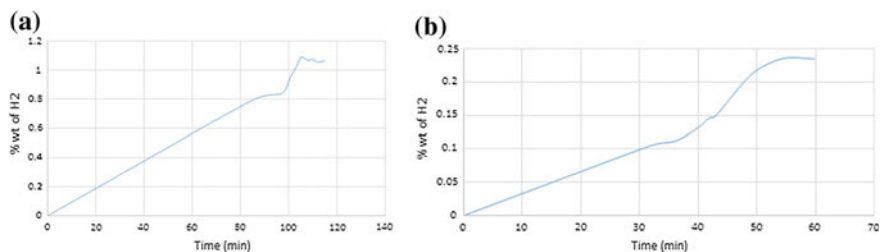


Fig. 7 a Graph of desorption of NH₃BH₃, b graph of desorption of MgH₂

5 Conclusion

A promising storage alternative for Hydrogen systems relies on the chemical or physical binding of Hydrogen with other elements through sorption of Hydrogen on or in a solid substrate to overcome the difficulties in conventional Hydrogen fuel storage methods. The pilot tests on Mg, Si, NH₃BH₃ and MgH₂ are carried out for calibration and results are compared with the previously published research works which are found to be similar to validate the fabricated setup. The apparatus allows hydrogenation/dehydrogenation study and desorption kinetics as well as PC isotherm measurement of the material–Hydrogen system over a wide range $0.05 < P/\text{bar} < 50$ and $300 < T/\text{K} < 723$. The apparatus developed has found to be reliable with observed experimental errors around 7%.

Acknowledgements Authors are thankful to the Gharda Institute of Technology, Lavel and University of Mumbai for jointly funding the research work.

References

1. Vishwanathan B, Scibioh MA (2006) Fuel cells. Hyderabad University Press
2. Hausdorf S, Baitalow F, Wolf G, Mertens F (2008) A procedure for the regeneration of ammonia borane from BNH waste products. *Int J Hydrogen Energy* 33:608–614

3. Gangal AC (2013) Ammonia borane as hydrogen storage material, Thesis, Department of Energy Science and Engineering, IIT Bombay
4. Bénard P, Chahine R (2007) Storage of hydrogen by physisorption on carbon and nanostructured materials. *Scripta Materialia* 56:803–808
5. Ramaprabhu S, Rajalakshmi N (1998) Design and development of hydrogen absorption/desorption high pressure apparatus based on the pressure reduction method. *Int J Hydrogen Energy* 23:797–801
6. Zhu M, Wang H, Ouyang LZ (2006) Composite structure and hydrogen storage properties in Mg-based alloys. *Int J Hydrogen Energy* 31:251–257
7. Kale PG, Gangal AC (2011) Investigation of hydrogen storage behavior of silicon nano-particles. *Int J Hydrogen Energy* 37:3741–3747
8. Durr M, Hofer U (2006) Dissociative adsorption of molecular hydrogen on silicon surfaces. *Surf Sci Rep* 61:465–526
9. Rivolo P, Geobaldo F, Rocchia M, Amato G (2003) Joint FTIR and TPD study of hydrogen desorption from p± type porous silicon. *Phys Status Solidi A* 197:217–221
10. Gangal AC, Edla R (2012) Effect of zeolites on thermal decomposition of ammonia borane. *Int J Hydrogen Energy* 37:3712–3718
11. Ramachandran VP, Gagare DP (2007) Preparation of ammonia borane in high yield and purity, methanolysis and regeneration. *Inorg Chem* 46:7810–7817
12. Sakintuna B, Lamari-Darkrim F, Hirscher M (2007) Metal hydride materials for solid hydrogen storage: a review. *Int J Hydrogen Energy* 32:1121–1140

Optimization of Biodiesel Synthesis from Karanja Oil Using Heterogeneous Catalyst by Transesterification Process

Satish A. Patil and R.R. Arakerimath

Keywords Transesterification · Catalyst · Heterogeneous · Optimization · Renewable

1 Introduction

1.1 Importance

Diesel fuels are used in many areas and have importance for the economy of countries. Interest in the use of alternative fuels for diesel engines has risen with the decrease of petroleum reserves and the rise in environmental consciousness. Because of the energy and global warming crisis, development of renewable energies, for example, H₂ energy, solar energy and biodiesel have been focused worldwide.

Due to the properties like high degradability, no toxicity, low emission of carbon monoxide, particulate matter and unburned hydrocarbons biodiesel has gained international attention as a source of alternative fuel. Biodiesel can be used in conventional compression ignition engines, which need almost no modification. It can be used as heating oil and as fuel.

1.2 Biodiesel

The fuel which will be alternated to diesel fuel must be suitable and acceptable technically, Biodiesel which can be produced from vegetable oils and animal fats is

S.A. Patil (✉)

Mechanical Engineering, DYPIET, Pune, Maharashtra, India

e-mail: sapcoeh@rediffmail.com

R.R. Arakerimath

G. H. Raisoni College of Engineering and Management, Wagholi, Pune, India

e-mail: rachayya.arakerimath@raisoni.net

an alternative fuel for diesel engines. It is long-chain fatty acid alkyl ester and is one of the interesting alternative fuels which can be produced from renewable sources and provides complete combustion with less gaseous pollutant emission. Biodiesel is an ecofriendly and alternative energy source for diesel engines that can be synthesized by transesterification of vegetable oil or animal fat with alcohols.

1.3 Heterogeneous catalyst

To avoid catalyst removal operations and soap formation and most important to save lots of waste stream, much effort has been expended on the search for solid acid or basic catalysts that could be used in a heterogeneous catalyzed process. In the heterogeneous process, the catalyst is very stable with no metal leaching. There is no formation of either glycerate salts or metal soaps which affords the advantages: no neutralization step is required, there is no introduction of water and there is no salt formation; these accounts for exceptional glycerol purity.

1.4 Transesterification Process

To avoid catalyst removal operations and soap formation and most important to save lots of waste stream, much effort has been expended on the search for solid acid or basic catalysts that could be used in a heterogeneous catalyzed process. Here a new continuous process is described, where the transesterification reaction is promoted by a completely heterogeneous catalyst.

1.5 Steps for Transesterification Process

- (1) Take one liter of Vegetable oil in round bottom flask and heat unto 65–70 °C
- (2) Check the FFA content of the oil. If it is more than 5% then esterification is essential.
- (3) Dissolve catalyst in alcohol, and then it is poured into the round bottom flask containing heated Vegetable oil.
- (4) Stirring of the mixture continuously.
- (5) Maintain the temperature for 1 h and then allow the reaction products to settle under gravity for 6 h in a separating funnel.
- (6) The color of Vegetable oil changed from deep brown to reddish yellow.
- (7) Vegetable oil methyl ester (biodiesel) and glycerol from upper and lower layers respectively.
- (8) Separate out biodiesel, catalysts, methanol and glycerol.

2 Experimental Setup for Biodiesel Production by Transesterification Process

This experimental set up contains 1000 ml four necked round bottom flask as a reactor. The flask has placed in heating mantle whose temperature could be controlled. One of the two side necks has equipped with a condenser and the other has used as a thermo well. A thermometer has placed in the thermo well containing little glycerol for temperature measurement inside the reactor (Figs. 1 and 2).

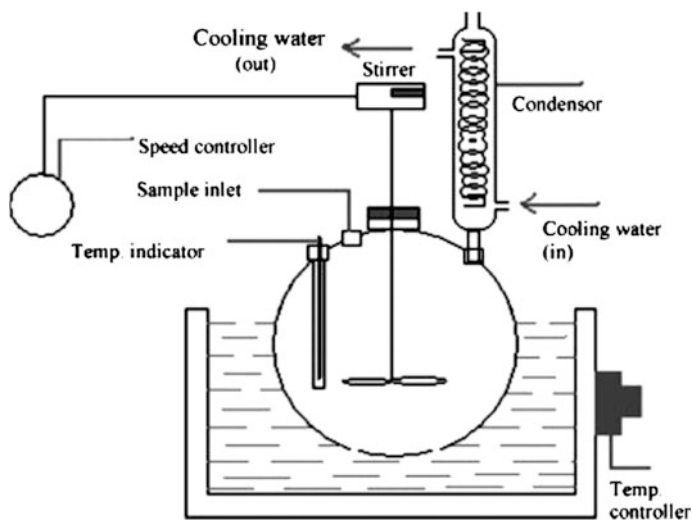


Fig. 1 Sketch of transesterification process setup

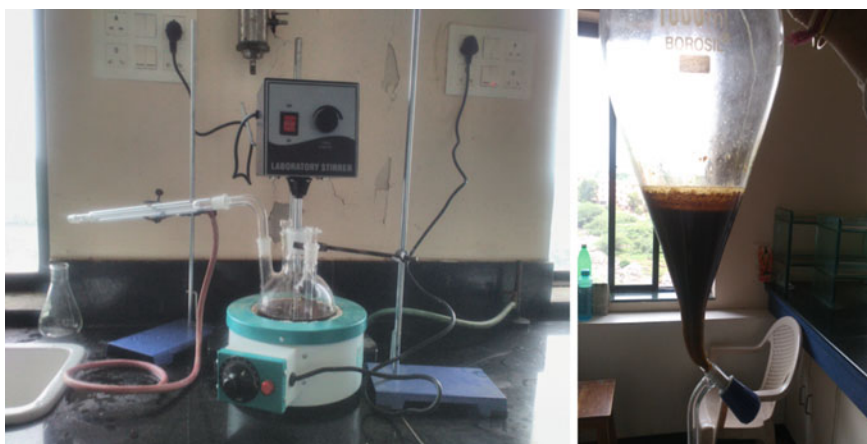


Fig. 2 Experimental setup of transesterification process

Condenser has used to reflux alcohol vapors back to the reactor to prevent any reactant loss. A blade stirrer has passed through the central neck, which has connected to a motor along with speed regulator for adjusting and controlling the stirrer speed. The transesterification reactions were performed in various conditions to determine the optimum conditions of transesterification. Variable quantities of catalyst were dissolved in various amount of methanol as described in each test. The reaction was carried out by taking 100 ml of Karanja oil and 0.4 wt% of CaO catalyst with oil to methanol molar ratio 1:4.

After 2–3 h the transesterification reaction was completed and mixture was withdrawn from the reactor and poured in the funnel separator to separates biodiesel from glycerol. Separation of two phases which is performed by gravity requires at least 4 h.

3 Different Parameters Affecting the Transesterification Process

Effect of different parameters studied as follows.

- (1) Variation of Molar Ratio in reaction.
- (2) Effect of amount of catalyst.
- (3) Effect of temperature on reaction.
- (4) Effect of stirring speed on reaction.

All these parameters were studied separately for yield optimization.

4 Results by Variation of Different Parameters Obtained for Karanja Oil with CaO Catalyst Are as Follows

To avoid catalyst removal operations and soap formation and most important to save lots of waste stream, much effort has been expended on the search for solid acid or basic catalysts that could be used in a heterogeneous catalyzed process. Oxide of calcium (CaO) has been tried as solid base catalyst owing to their easy availability, low cost and non-corrosive nature.

4.1 Effect of Molar Ratio

Variation of Molar Ratio for different catalyst percentages is done by keeping other parameters Speed—600 rpm, Temp—60 °C constant. Table 1 shows different Variation of Molar Ratio for different catalyst percentages (Fig. 3).

Table 1 Variation of Molar Ratio for different catalyst percentages

Molar Ratio	Catalyst				
	0.40%	0.60%	0.80%	1.00%	1.20%
1:4	42	55	64	69	70
1:6	47	63	72	74	74
1:8	55	69	79	84	85
1:10	59	76	80	89	88
1:12	69	77	82	91	87

Fig. 3 Comparison of variation of Molar Ratio for different catalyst percentages

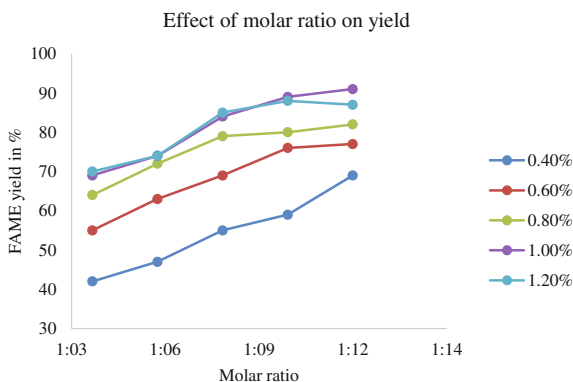
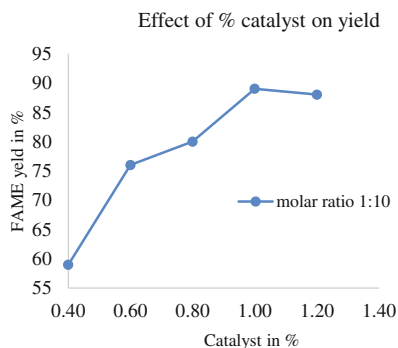


Fig. 4 Variation of catalyst is done by keeping the other parameters constant such as speed—600 rpm, temp—60 °C and Molar ratio 1:10



4.2 Effect of Catalyst %

Variation of catalyst is done by keeping the other parameters constant such as Speed—600 rpm, Temp—60 °C and Molar Ratio 1:10 (Fig. 4).

The effect of catalyst on yield was studied with catalyst concentration varying from 0.4 to 1.2% considering the weight oil in gram. Heterogeneous catalyst CaO was used and reactions were carried out at 60 °C. At the catalyst amount 1.0 wt%, yield was maximum. Further addition of catalyst has decrease the yield of methyl ester (Table 2).

4.3 Effect of Reaction Temperature

Temperature variation has done from 45 to 70 °C at all other parameters kept constant i.e. Speed—600 rpm, Catalyst 1.0% and Molar Ratio 1:10. The obtained yield is as shown in Table 3.

The graph shows that temperature has an important influence on speed of reaction and led to higher conversion of ester. With increasing temperature of reaction, yield of biodiesel increased quickly to near the boiling point of alcohol. At higher temperature than boiling point of methanol, alcohol evaporates and the yield was decreased.

Figure 5 variation of temperature is done from 45 to 70 °C at all other parameters kept constant i.e. Speed—600 rpm, Catalyst 1.0% and Molar ratio 1:10.

4.4 Effect of Reaction Time

Variation of Time from 25 to 75 min done by keeping other parameters Speed—600 rpm, Catalyst 1.00%, Molar Ratio 1:10 and Temp 65 °C constant (Table 4).

Table 2 Variation of Molar Ratio for different catalyst percentages

Catalyst %	Yield %
0.40	59
0.60	76
0.80	80
1.00	89
1.20	88

Table 3 Temperature variation has done from 45 to 70 °C at all other parameters kept constant

Temp. (°C)	Yield %
45	57
50	70
55	79
60	88
65	90
70	87

Fig. 5 Variation of temperature is done from 45 to 70 °C at all other parameters kept constant i.e. Speed—600 rpm, Catalyst 1.0% and Molar ratio 1:10

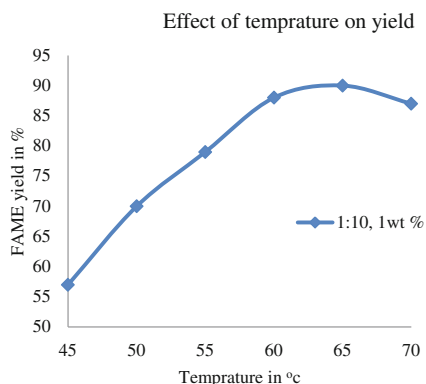
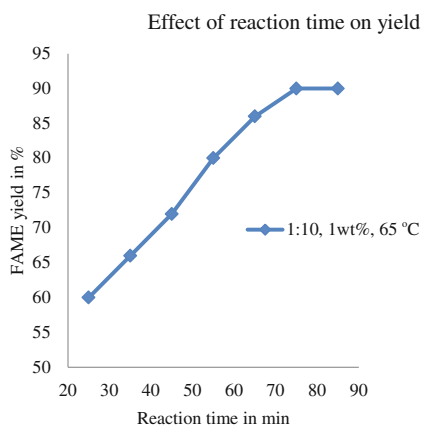


Table 4 Variation of time from 25 to 75 min done by keeping other parameters

Reaction time in min	Yield %
25	60
35	66
45	72
55	80
65	86
75	90
85	90

Fig. 6 Variation of Time from 25 to 75 min done by keeping other parameters Speed—600 rpm Catalyst 1.00%, Molar Ratio 1:10 and Temp. 65 °C constant

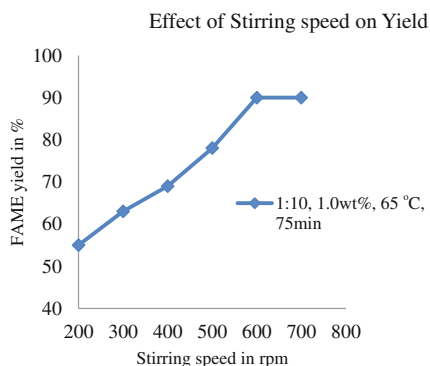


In 25 min of reaction time, 60% conversion of biodiesel was obtained, which increased gradually with an increase in time. A reaction time of 75 min was found to give maximum yield 86% of biodiesel. A further increase in time could not increase the yield of biodiesel. It was because of maximum triglyceride get converted into its particular ester (Fig. 6).

Table 5 Stirring speed variation is done from 200 to 700 rpm at all other parameters Catalyst 1.00%, Time 75 min, Molar ratio 1:10, Temp. 65 °C kept constant

Stirring speed	Yield %
200	55
300	63
400	69
500	78
600	90
700	90

Fig. 7 Stirring speed variation is done from 200 to 700 rpm at all other parameters Catalyst 1.00%, Time 75 min, Molar ratio 1:10, Temp. 65 °C kept constant



4.5 Effect of Reaction Speed

Stirring speed variation is done from 200 to 700 rpm at all other parameters Catalyst 1.00%, Time 75 min, Molar Ratio 1:10, Temp 65 °C kept constant (Table 5).

The rate of stirring was varied from 200 to 700 rpm. The yield was maximum with 600 rpm of agitation. With the agitation lower than 600 rpm, a lesser yield was obtained. With an agitation rate higher than 600 rpm, no more increase in either yield was observed (Fig. 7).

5 Conclusion

The parameters that affected the Transesterification reaction are Molar Ratio of alcohol to oil, catalyst concentration, temperature of reaction, time of reaction, stirring speed. All these parameters were studied separately for yield optimization. The result shows that biodiesel production using CaO catalyst is a considerable potential in biodiesel production process. A large number of experiments were carried out on transesterification of Karanja oil with methanol to produce biodiesel under different reaction conditions and an attempt has been made to analyze the effect of various reaction conditions on biodiesel yield. Maximum yield for the

production of methyl esters from Karanja oil was found to be 90% under the condition of temperature of 65 °C, the Molar Ratio of methanol to oil of 10:1, catalyst concentration of 1 wt%, stirring speed of 600 rpm and a reaction time of 75 min.

References

1. Hawash S, El Diwani G, Abdel Kader E (2011) Optimization of biodiesel production from *Jatropha* oil by heterogeneous base catalysed transesterification. *Int J Eng Sci Technol*
2. Agarwal AK, Bajaj TP (2009) Process optimisation of base catalyzed transesterification of Karanja oil for biodiesel production. *Int J Oil Gas Coal Technol* 2(3)
3. Bobade SN, Khyade VB (2012) Preparation of methyl ester (Biodiesel) from Karanja (*Pongamia Pinnata*) oil research. *J Chem Sci* 2(8):43–50
4. Mansourpoor M, Shariati A (2012) Optimization of biodiesel production from sunflower oil using response surface methodology. *J Chem Engg Process Technol* 3:5
5. Yimer S, Sahu O (2014) Optimization of biodiesel production from waste cooking oil. *Sustainable Energy* 2(3):81–84
6. Chavan SB, Kumbhar RR, Sharma YC (2014) Transesterification of *Citrullus colocynthis* (Thumba) oil optimization for biodiesel production. *Adv Appl Sci Res* 5(3):10–20
7. Romero R, Martínez SL, Natividad R (2009) Biodiesel production by using heterogeneous catalysts. In: Lee D-W, Park Y-M, Lee K-Y (eds) *Heterogeneous base catalysts for transesterification in biodiesel synthesis*. vol 13, pp 63–77 (*Catal Surv Asia*)
8. Guo F, Wei N-N, Xiu Z-L, Fang Z (2012) Transesterification mechanism of soybean oil to biodiesel catalyzed by calcined sodium silicate. *Fuel* 93:468–472
9. Viriya-Empikul N, Krasae P, Nualpaeng W, Yoosuk B, Faungnawaki K (2012) Biodiesel production over Ca-based solid catalysts derived from industrial wastes. *Fuel* 92:239–244
10. Sharma Yogesh C, Singh B, Korstad J (2011) Latest developments on application of heterogeneous basic catalysts for an efficient and ecofriendly synthesis of biodiesel: a review. *Fuel* 90:1309–1324
11. Etefagh MM, Sadeghi MH, Pirouzpanah V, Tash HA (2008) Knock detection in spark ignition engines by vibration analysis of cylinder block: a parametric modeling approach. *Mech Syst Signal Pr* 22(6):1495–1514
12. Lee DW, Park YM, Lee KY (2009) Heterogeneous base catalysts for transesterification in biodiesel synthesis. *Catal Surv Asia*, 13:63–77

Parametric Studies on Thermo-electric Power Generation Using Micro Combustor

B. Aravind and Sudarshan Kumar

Keywords Micro-combustor · Heat recirculation · Flame stability · Thermoelectric modules

1 Introduction

Combustion driven microdevices are receiving propelled attention and interest from the combustion research community due to the intense demand for small-scale portable power sources. Because of their tremendous advantages such as high energy density, compact size and sustainably high power supplying time (approximately 6 times compared to conventional devices), combustion based power devices can be considered as the competitive alternative for conventional electrochemical batteries [1]. Thermal and radical quenching are the two key issues associated with the flame stability in micro-combustors due to the high surface to volume ratio [2]. Proper thermochemical management techniques can be adopted to curtail the quenching issues [3]. Many researchers have come up with promising techniques to solve these stability issues by performing excess enthalpy combustion [4]. Catalytic combustion [5], Porous media combustion [6] and use the of stepped combustors [7, 8] are some of the useful strategies proposed to circumvent the quenching issues. Hydrocarbon fuel driven power sources with a conversion efficiency of 5%, results in six times higher power density than the conventional chemical batteries due of its high energy density [4]. Such power generation systems with higher conversion efficiency are yet to be explored in detail. One of the earlier breakthrough research carried out at the MIT Gas Turbine Laboratory provided a clear insight into the micro power generation methods [9].

B. Aravind (✉) · S. Kumar
Indian Institute of Technology Bombay, Powai, India
e-mail: aravindpillai69@gmail.com

Moving components in these types of conversion devices are frequently subjected to maintenance problems and in turn, results in lower conversion efficiencies. Thus, many researchers are focussing on direct conversion devices such as photovoltaic cell [10, 11], thermoelectric generators [12, 13], fuel cell [14] integrated to the micro-combustor. Yang et al. [11] developed a thermophotovoltaic (TPV) based micro a power generation system by incorporating it with backward facing step combustor. They found that channel diameter and step size are the crucial factors affecting the performance of the system. Jiang et al. [10] fabricated a planar combustor, which facilitates high temperature (above 1300 K) with superior uniformity in the temperature profile. An Overall system efficiency of 4.1% was achieved by integrating high-performance TPV into the planar combustor. One of the earliest development in TEM by Schaevitz et al. [15] is that MEMS thermoelectric power generation system using catalytic combustion. This generator was stable up to 500 °C and achieved a conversion efficiency of 2% with the output voltage of 7 V. Shimokuri et al. [12] prototyped a mesoscale vortex combustor for the thermoelectric power generation. Vortex flow enhances the heat transfer from burnt gas to the combustion chamber. This system successfully generated 0.7% of conversion efficiency. Yadav et al. [16] developed a power generation system using a rearward facing stepped micro combustor with heat recirculation cup. The conversion efficiency of 4.26% was achieved with four modules at 6.5 m/s velocity.

The present study investigates the thermal characteristics and flame stability of three step backward facing step combustor with heat recirculation cup. A parametric study is performed by varying the material and geometric aspects of the cup to understand the optimized design for micro combustor—cup arrangement for power generation. Thermoelectric modules are further placed on the top and bottom sides along with the cooling jacket on the cup to achieve electric power. This study also investigates the effect of porous media on the flame stability and surface temperature of the cup.

2 Experimental Methodology

2.1 *Micro Combustor Configuration*

A three step backward facing micro combustor made up of mild steel has been chosen for the present study. Steps provided in the combustor creates recirculation zone and thereby enhances the flame stability limit. Dimensions of the combustor are taken as per the previous works by the author's research group [7, 8]. A recirculation cup is provided at the outlet of the combustor to improve flame stability further by preheating the reactant mixture. Figure 1 represents the configuration of micro combustor—cup arrangement adopted in the present study.

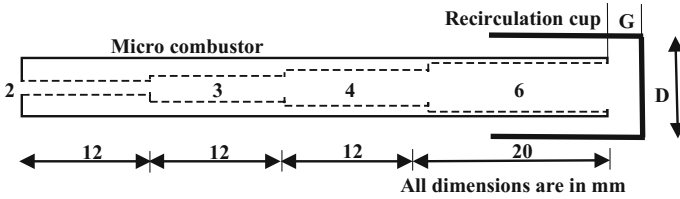


Fig. 1 Configuration details of micro combustor recirculation cup arrangement

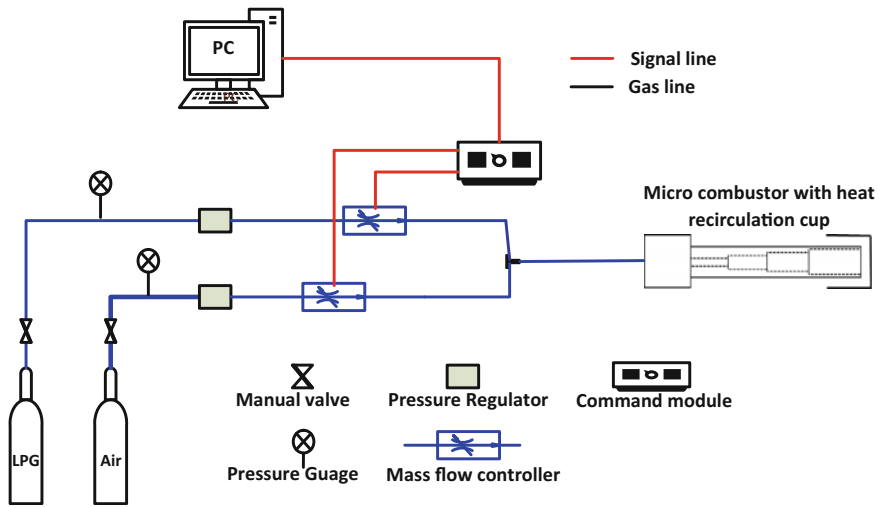


Fig. 2 Schematics of the experimental setup

2.2 Details of Experimental Method

The experimental setup consists of LPG and air feed systems, high precision electric mass flow controllers (5 LPM, 0.5 LPM for air and LPG respectively), the command module and backward facing step micro combustor. Fuel and air are thoroughly mixed before introducing into the combustor at ambient conditions. The outer wall temperatures are measured using K-type thermocouples with 0.5 mm bead diameter. Coupled system of computer and command module accurately controls and monitor the flow rate to the combustor. Figure 2 depicts the schematic of the experimental setup.

3 Results and Discussions

3.1 Thermal Characteristics and Flame Stability Limit

Experimental studies were conducted to understand the thermal characteristics and flame stability limit of the micro-combustor with heat recirculation cup using premixed LPG air mixture. Effect of cup material, porous media, and equivalence ratio and inlet flow velocity on the flame stability have been investigated. Figure 3 represents the temperature distribution in the heating cup captured using the high precision infrared camera. The uniform temperature profile on the cup surface as shown in the Fig. 3 was obtained for different surfaces of the cup, which would aid in the power generation.

3.1.1 Effect of Thermal Conductivity of Heating Cup

To understand the effect of thermal conductivity of heating cup, three different materials copper, aluminium and mild steel were chosen for the cup. It can be observed from Fig. 4 that, surface temperature of the cup goes on increasing with the inlet velocity. The heat transfer to the wall increases with the inlet velocity due to the higher fuel consumption. The surface temperatures of mild steel are lower than aluminum for all values of velocity within flame stability limits, but such is not in the case of copper whose values exceed that of aluminum at inlet velocities lower than ~ 3.75 m/s. This observation is attributed to the higher thermal diffusivity of copper due to which at lower velocities, the thermal diffusion to the surface is higher for copper in comparison to Aluminium. However, at higher inlet velocities, as heat transfer coefficient increases, the proportion of heat lost to ambient is larger for copper than that in the case of Aluminium. In fact, it is found to be so high that beyond ~ 4.5 m/s, the surface temperature for copper falls below that of even mild steel. This is clearly counter-intuitive. The wall temperature variation is due to the fact that heat dissipation can be due to the interplay of two phenomenon: heat loss at surface and heat

Fig. 3 Temperature profile of heating cup captured using infrared camera (*side view*)

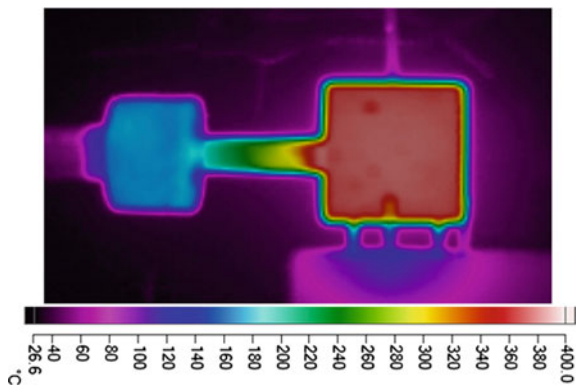


Fig. 4 Variation of surface temperature with inlet velocity and material at $\phi = 1.0$ ($D = 11, G = 3$ mm)

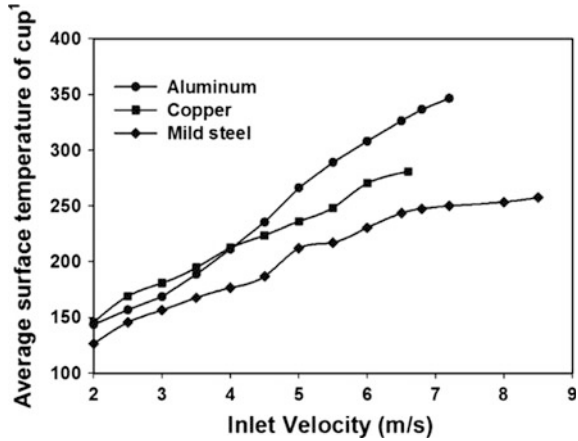
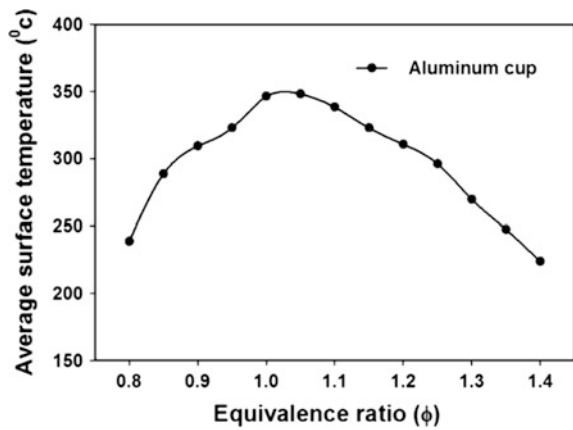


Fig. 5 Variation of surface temperature with equivalence ratio for aluminium cup of $D = 11, G = 3$ mm



recirculated through the combustor wall to the incoming premixed mixture, the relative proportion of both of which influence flame temperature. Figure 5 shows the variation of surface temperature with the equivalence ratio for aluminium cup. The maximum temperature at slightly rich mixture is due to the higher adiabatic flame temperature. Figure 6 represents the flame stability diagram for the proposed micro combustor with the aluminium-heating cup. The operating regime of the given combustor lies between nearly 1–8 m/s for all the equivalence ratios.

3.1.2 Effect of Porous Media on the Flame Stability

In order to understand the effect of porous media on flame stability, glass wool of 2 mm thickness is placed inside the recirculating cup. Experiments were conducted for lean and stoichiometric mixtures as a preliminary analysis. The upper flammability limit is enhanced with the use of porous media which ensures the wide

Fig. 6 Variation of surface temperature with inlet velocity in aluminium recirculation cup at $\phi = 0.8$ and 1 using ceramic wool inside the recirculation cup (*configuration of combustor cup arrangement with the porous media is indicated in the inset*)

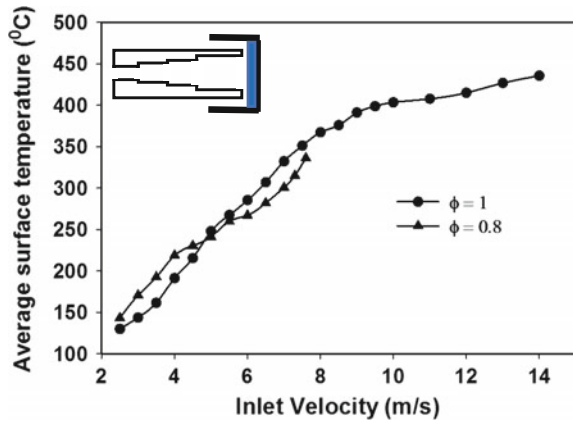
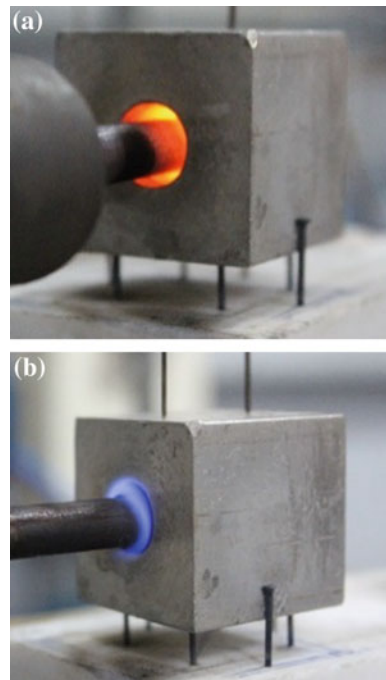


Fig. 7 Direct photography of flame with and without porous media



operating limit of the system. Figure 6 shows the variation of surface temperature with the inlet velocity for different equivalence ratios. It is observed that only a slight improvement in the surface temperature using the porous media. The ceramic wool itself burns to sustain the flame in between the gap of combustor outlet. Porous media traps heat inside the pores in it and heat up the solid matrix by means of convection and conduction. Eventually, it becomes red hot and liberates heat through radiation in addition to the convection and conduction as shown in Fig. 7.

3.2 Integration of the Combustor and Thermoelectric Generators

Experimental studies were conducted to determine the overall efficiency with which the micro combustor-heat recirculation cup combination converts the chemical input to electrical power. An HZ-2, HZ Technology Inc. thermoelectric modules (TEM) were used for the experiment. These modules use bismuth-telluride based alloys and having 98 p-n couples. Two modules were sandwiched between the heating cup and water cooled copper jackets on the top and bottom faces of the cup as shown in Fig. 8. Ceramic wafers were used on the either side of the TEM to ensure the electrical insulation. The Assembly was compressively loaded which would maximize the heat transfer across the interface. The voltage developed by each module is measured by an independent multimeter.

Fig. 8 Experimental setup for two modules configuration

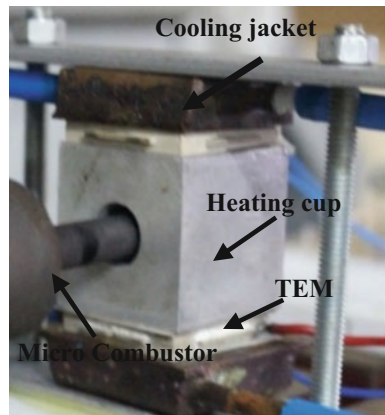
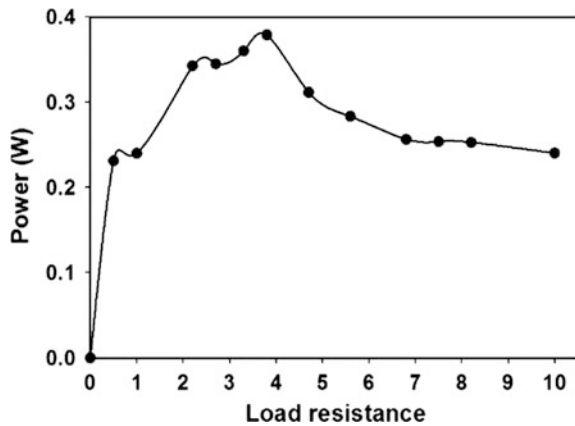


Fig. 9 Variation of power with load resistance at $\phi = 0.9$ and inlet velocity of 6 m/s for two-module configuration



The power developed by both module is added to obtain the total power. Maximum Power Point Tracking (MPPT) method was carried out to determine the internal resistance of the TEG, at $\phi = 0.9$ and inlet velocity of 6 m/s as represented in Fig. 9. A maximum power of ~ 0.4 W is obtained from each module at 3.8 Ω resistance. Conversion efficiency is calculated based on the thermal input and is found to be 1.2%. Further enhancement in the efficiency is possible by introducing more modules and improving the upper flame stability via porous media.

4 Conclusion

The thermal characteristics and flame stability limits of a rearward facing three-step micro combustor with a heat-recirculating cup were studied. It was observed that the cup wall temperature increases with the mixture flow rate due to the higher thermal input to the micro-combustor. The investigations show that aluminium is the suitable material for the heating cup as it offers higher surface temperature compared to the copper and mild steel cups. Two thermoelectric modules were mounted onto the micro-combustor—heating cup configuration to generate electricity. An overall conversion efficiency of 1.2% is achieved for two-module configuration at a mixture flow velocity of 6 m/s and the equivalence ratio of 0.9. Further increase in the power can be realized by mounting more number of modules. The use of porous media greatly improves the upper flammability limit of the combustor and thereby providing enhanced power generation. However, the effect of porous media needs to be explored in detail to understand the optimum power generation.

References

1. Epstein AH, Jacobson SA, Protz JM, Frechette LG (2000) Shirtbutton-sized gas turbines: the engineering challenges of micro high speed rotating machinery. In: Proceedings 8th international symposium on transport phenomena and dynamics of rotating machinery, Honolulu, HI
2. Fernandez-Pello AC (2002) Micropower generation using combustion: issues and approaches. *Proc Combust Inst* 29(1):883–899
3. Maruta K, Parc J, Oh K, Fujimori T, Minaev S, Fursenko R (2004) Characteristics of microscale combustion in a narrow heated channel. *Combust Explosion Shock Waves* 40 (5):516–523
4. Ju Y, Maruta K (2011) Microscale combustion: technology development and fundamental research. *Prog Energy Combust Sci* 37(6):669–715
5. Maruta K, Takeda K, Sitzki L, Borer K, Ronney PD, Wussow S, Deutschmann O (2001) Catalytic combustion in microchannel for MEMS power generation. In: Third Asia-Pacific conference on combustion, Seoul, Korea
6. Li J, Li Q, Shi J, Liu X, Guo Z (2016) Numerical study on heat recirculation in a porous micro-combustor. *Combust Flame* 171:152–161
7. Taywade UW, Deshpande AA, Kumar S (2013) Thermal performance of a micro combustor with heat recirculation. *Fuel Process Technol* 109:179–188

8. Khandelwal B, Deshpande AA, Kumar S (2013) Experimental studies on flame stabilization in a three step rearward facing configuration based micro channel combustor. *Appl Therm Eng* 58(1):363–368
9. Epstein AH, Senturia SD, Anathasuresh G, Ayon A, Breuer K, Chen K-S, Ehrich F, Gauba G, Ghodssi R, Groshenry C (1997) Power MEMS and microengines. In: IEEE international conference on solid state sensors and actuators TRANSDUCERS'97 Chicago
10. Jiang D, Yang W, Tang A (2015) Development of a high-temperature and high-uniformity micro planar combustor for thermophotovoltaics application. *Energy Convers Manag* 103:359–365
11. Yang W, Chou S, Shu C, Li Z, Xue H (2007) Experimental study of micro-thermophotovoltaic systems with different combustor configurations. *Energy Convers Manag* 48(4):1238–1244
12. Shimokuri D, Hara T, Ishizuka S (2014) Development of a portable power system with meso-scale vortex combustor and thermo-electric device. *J Phy: Conf Series IOP Publishing*
13. Yadav S, Yamasani P, Kumar S (2015) Experimental studies on a micro power generator using thermo-electric modules mounted on a micro-combustor. *Energy Convers Manag* 99:1–7
14. Ahn J, Ronney PD, Shao Z, Haile SM (2009) A thermally self-sustaining miniature solid oxide fuel cell. *J Fuel Cell Sci Technol* 6(4):041004
15. Schaevitz SB, Franz AJ, Jensen KF, Schmidt MA (2001) A combustion-based MEMS thermoelectric power generator. In: *Transducers' 01 Eurosensors XV*, Springer, Berlin, pp 30–33
16. Yadav S, Sharma P, Yamasani P, Minaev S, Kumar S (2014) A prototype micro-thermoelectric power generator for micro-electromechanical systems. *Appl Phys Lett* 104(12):123903

Validation of in House PCR Using IS6110 for Detection of *M. tuberculosis* and Its Comparison with ZN Staining, Cultures and RT PCR Kit Methods

Girish Pai, Mansee Thakur, Harapriya Kar and D.S. Joshi

Keywords *Mycobacterium tuberculosis* · Conventional PCR · Diagnosis · IS6110

1 Introduction

Tuberculosis causes significant morbidity and mortality all over the world. World Health Organization has recognized India as a major hot-spot region for tuberculosis and as the leading cause of death. Factors such as antibiotic resistance and HIV infection compound the severity and spread of the disease rapidly among communities. The current treatment and control regime of revised national tuberculosis control program (RNTCP) has achieved a marginal reduction in the prevalence of pulmonary tuberculosis [1]. Pulmonary tuberculosis is the most common form and Ziehl-Neelsen (ZN) staining of sputum smear is still the method of choice for diagnosis in most of the hospitals and laboratories. The method is not very sensitive and is prone to problems with microscopy competency of even the trained technician. Radiological examination, tuberculin skin test, and immunological assays methods has shown inadequate in sensitivity and specificity.

G. Pai (✉) · M. Thakur

Department of Biotechnology, MGM Institute of Health Science & MGM College of Engineering & Technology, Kamothe, Navi Mumbai 410209, India
e-mail: girishpai123@gmail.com

M. Thakur

e-mail: mansibiotech@gmail.com

H. Kar

Department of Medical Microbiology, MGM Institute of Health Sciences, Kamothe, Navi Mumbai 410209, India
e-mail: harapriya.kar@gmail.com

D.S. Joshi

Department of Biotechnology & Genetics, MGM Institute of Health Sciences, Kamothe, Navi Mumbai 410209, India
e-mail: josharvind@gmail.com

Definitive identification of *Mycobacterium tuberculosis* by culture in Lowenstein Jensen (LJ) medium after extensive processing of sputum samples, or automated mycobacterium culture system in automated blood culture system such as BacT/Alert 3D takes weeks to give a result [2]. Integrated procedures involving Nucleic acids of particular organism could be used for the purpose of diagnostic. Before disease can be treated, a diagnosis needs to be made in an efficient and timely manner. The availability of various techniques for Nucleic acid detection in compatible format is required in diagnostic field for particular organism. In our study we have evaluated different PCR based Nucleic acid detection test for MTB. There is need to evaluate comparative efficiency of the various procedures, methods and integrate and this could be useful for development of integrated optimize protocol. Polymerase chain reaction (PCR) is a known valuable technique for disease diagnosis from a variety of clinical samples. Only a very few studies exist in the literature on the evaluation of sputum samples by PCR compared to acid fast staining, from tropical developing countries [3, 4]. Quintanilla et al. [5] reported the application of a hemi nested PCR in smear negative and culture positive sputum samples with a high sensitivity. Gengvinji et al. [6] developed a nested PCR (nPCR) for the detection of pulmonary tuberculosis from sputum specimens by targeting 16S rRNA gene. However, the study was not clinically evaluated. Recently, several reports on the detection of *M. tuberculosis* from sputum specimens using real-time PCR [5, 7, 8] and line probe assay [9] have been reported. These assays, though sensitive and specific than conventional PCR, need expertise and cannot be routinely performed due to lack of specialized equipment and expensive instrumentation even in a tertiary care hospital setting in India. The objective of this prospective study efficacy of the conventional PCR targeting IS6110 to that of sputum smear findings in identification of *M. tuberculosis* from sputum samples.

2 Methodology

2.1 Sample Collection

Samples were collected at various institution 1. MGM Hospital and MGMCRL, Kamothe and from Jai Clinic Govandi (Under IERC Approval for Project on TB Diagnosis-MGMIHS/RS/2010/605).

2.2 Sample Processing

Sputum Sample decontamination, AFB staining and culture processes were performed by the staff in the Microbiology laboratory of MGM Central Research

Laboratory as this was part of the procedure of their clinical service following the guidelines by the Clinical and Laboratory Standards Institute (CLSI). (CLSI 2008) Clinical sputum specimens collected were first liquefied and decontaminated according to *N*-acetyl-L-cysteine-sodium hydroxide (NALC–NaOH) method in order to avoid bacteria overgrowth which may obstruct the recovery of mycobacterium. Specimen was tested for the presence of mycobacterium tuberculosis. AFB smear were prepared stained with Ziehl-Neelsen (ZN) staining procedure. ZN Staining provides a rapid, but preliminary, result. The specimen was also inoculated for culture. Medium used were Middlebrook 7H9 broth medium, 7H11 agar slope and Lowenstein-Jensen medium. The culture was incubated for 4–8 weeks and growth was observed [10, 11].

2.3 *Mycobacterial DNA Extraction from Sputum*

100 µl of Decontaminated sputum sample was taken in 1.5 ml of eppendorf tube. Briefly add 20 µl lysozyme was added and incubate at 37 °C for 90 min. Next 10 µl of 20% SDS added and incubated at 37 °C for 30 min. DNA was extracted by Enzymatic Lysis Method Cell walls and other protein content was digested with Lysozyme (10 mg/ml), Proteinase K (Himedia) (10 mg/ml). In following step, 20 µl Proteinase K and 200 µl of AL Buffer (Quiagen DNA Extraction kit) was added and incubated at 56 °C for 30 min. Lysis by boiling method was carried by at 95 °C for 15 min. To the total suspension 200 µl ethanol added and vortex for 15 s. After these steps, suspension was carried out for DNA extraction as per Quiagen column based Bacterial DNA extraction method. After transferring the content to spin column, spin was given at 8000 rpm for 1 min. In subsequent steps, column was washed with Alkaline Wash Buffer 1 (Quiagen Kit) with intermediate spin at 8000 and 13,000 rpm for 1 and 3 min respectively. In the last step Elution buffer was added about 100 µl and eluted by spin at 8000 rpm for 1 min. Collected DNA then processed for purity and concentration by spectrophotometric reading at 260 nm and OD 280 nm using Thermo fisher UV 6000 Spectrophotometer. The processed samples were stored at 2–8 °C for up to 8 h, or stored at –70 °C for long time use.

Amplification of 123 bp DNA segment belonging to IS 6110. The extracted DNA was amplified by PCR assay. The amplification was carried out in 25 µl final volume, in which 12 µl amplification Master Mix (reaction buffer with MgCl₂, dNTPs, Taq DNA polymerase), *M. tuberculosis* complex specific primers 1.25 µl of 0.5 µM concentration of each, (Table 1) 4.5 µl of Molecular PCR grade water and 5 µl DNA template. The amplification was carried out in a thermo cycler (Peqlab, Germany). After initial denaturation at 94 °C for 5 min, 35 amplification cycles were performed within thermo cycler. Each cycle consisted of denaturation at 94 °C for 1 min, annealing of primer at 60 °C for 1 min and primer extension at 72 °C for 1 min and Final Extension and Cooling at 72 °C for 5 min and cooling at 4 °C for 1 min respectively.

Table 1 List of primers used in conventional PCR assay for MTBC detection [12]

Assay	Name	Type	Sequence (5'–3')	Length (bp)
IS6110 one-tube	IS-F	Forward primer	CCT GCG AGC GTA GGC GTC GG	20
Real-time PCR for M. Tb	IS-R	Reverse primer	CTC GTC CAG CGC CGC TTC CGG	21

2.4 Analysis of Amplified Product

PCR products were analyzed by gel electrophoresis in 08% PAGE (Sigma-MO USA) prepared in Tris-Borate EDTA buffer containing. The Gel was stained by silver staining and was examined in a gel documentation system (Vilber Lourmat-QUANTUM ST4) for a 123 bp using standard molecular marker. Presence of a single band equivalent to 123 bp was taken a positive result.

2.5 RT-PCR with Commercial Kit

200 sputum samples were assayed by RT-PCR. For the purpose RT-PCR was performed using the Genosense RT PCT MTBC Commercial kit according to the manufacturer's instructions. As per instruction of kit three channels were used in the RT-PCR reaction (*M. tuberculosis* complex, MOTT, internal control). Results were interpreted as the guidelines available with the kit. Signals for FAM, HEX, and Cy5 (fluorescent material fixed to the TaqMan probe) were measured in different channels. Each taqman probe gives signal accordingly Real time monitoring performed by instrument and crossing point (Cp) values calculate by software which gives information of presence or absence of MTB. *M. tuberculosis* was considered present if the Cp of was less than 45 on each signal.

2.6 Statistical Analysis

The data obtained were statistically analyzed for diagnostic values (Sensitivity, Specificity, positive predictive value, negative predictive value). The sensitivity, specificity, and the diagnostic odds ratio of different detection methods were calculated by MedCalc®. MedCalc—User-friendly statistical software which has different statistical test, procedures and graphs ROC curve analysis, Distribution plots, Correlation Scatter diagram and regression line, Crosstabs (categorical data), Method comparison and evaluation (Fig. 1).

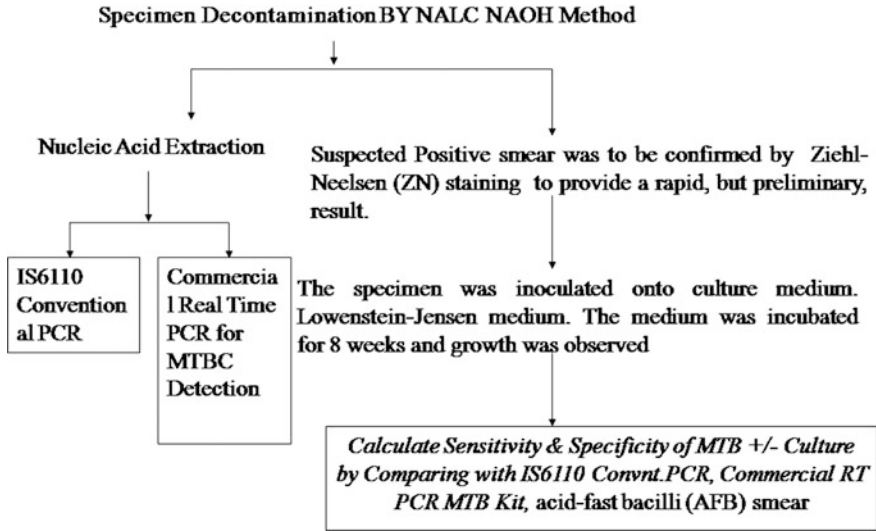


Fig. 1 Overall methodology starting from sputum processing to detection has been shown in the flowchart

3 Results

3.1 In-House Conventional PCR

DNA extracted from sputum sample obtained from suspected MTB positive patients were processed by Conventional PCR method. The protocol was used to monitor results of Conventional PCR product obtained from 200 DNA samples using IS6110 as target sequence. The amplified product 123 bp band was observed on 8% PAGE. Representative Gel pictures are shown in Fig. 2.

3.2 AFB Smear Negative—Culture Positive and PCR Positive

Suspected MTB infection Samples found to be negative for AFB staining but positive by culture and conventional PCR implies its positive result by observing 123 bp amplified product band on 8% PAGE, It has observed that in general majority of nonspecific amplification due to conventional PCR results in multiple bands, mainly observed positive due to presence of 123 bp amplified product.

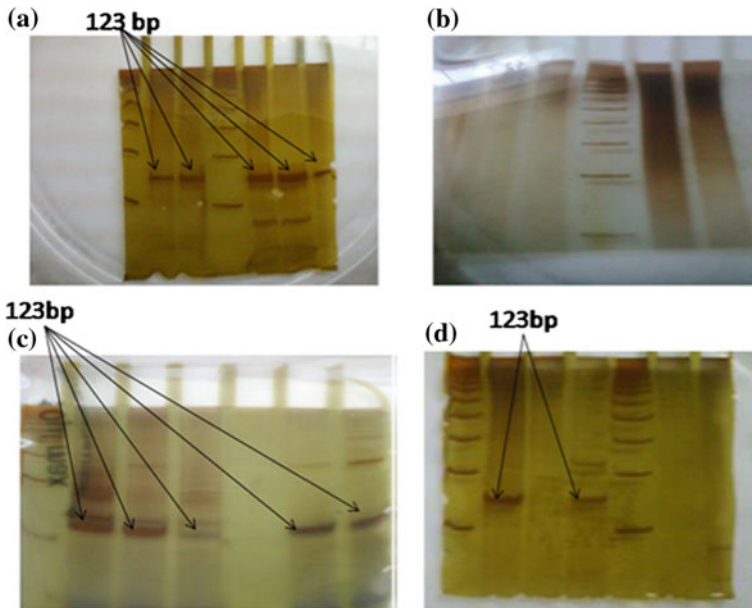


Fig. 2 8% PAGE for separation of 123 bp amplified product positive for MTBC from. PCR amplification of 123 bp region of IS6110 gene of *M. tuberculosis* in conventional PCR, representation of some clinical samples. **DNA ladder**—50 bp DNA Marker ladder used for 123 bp band location. Gel A:1,4: B:4, C:1,D:1,5. **Positive control (MTB DNA)** Gel A: 3, C: 4, D: 2 were show positive control DNA amplification of 123 bp band. **Negative control** Gel B: 1:2:3, C: 5, D: 7 of negative samples PCR product which did not show any amplification, only smear observed on gel

3.3 Comprehensive Comparison of Different Techniques

The amplification confirms the positive diagnosis of MTB in suspected samples. The data from 200 DNA samples has been presented in Table 2. After examination of 200 suspected tuberculosis samples, MTBC were detected positive in 34% (n = 67) samples with Culture; 26% (n = 51) positive samples from ZN Staining; 34% (n = 67) positive samples from with IS6110 Conventional PCR. Combination of both ZN Staining and Culture positive samples were 21% (n = 51). 62% (n = 124) samples were negative by all three method. PCR alone was positive in 4% (n = 8) among 132 clinical samples that were negative by both conventional bacteriological techniques-smear and culture for AFB. And 4% (n = 8) samples were positive by both Conventional bacteriological methods but negative by Conventional PCR. About 9% (n = 17) sample which were smear Negative and Culture positive were also found positive by IS6110 Conventional PCR Such comparative assessment helps in establishing the relative sensitivity and efficiency of various techniques (Table 3).

Table 2 Validation of in house PCR for detection of *M. tuberculosis* & its comparison with ZN staining, cultures and RT PCR kit methods

Methods used			Results					
			ZN staining		Culture		RT PCR kit	
			(PS)	(NS)	(PS)	(NS)	(PS)	(NS)
			n = 51 (25.5%)	n = 149 (74.5%)	n = 67 (33.5%)	n = 133 (66.5%)	67 (33.5%)	133 (66.5%)
Conventional PCR	(PS)	n = 67 (33.5%)	42 (21.0%)	25 (12.5%)	59 (29.5%)	8 (4.0%)	59 (29.5%)	8 (4.0%)
	(NS)	n = 133 (66.5%)	9 (4.5%)	124 (62.0%)	8 (4.0%)	125 (62.5%)	8 (4.0%)	125 (62.5%)

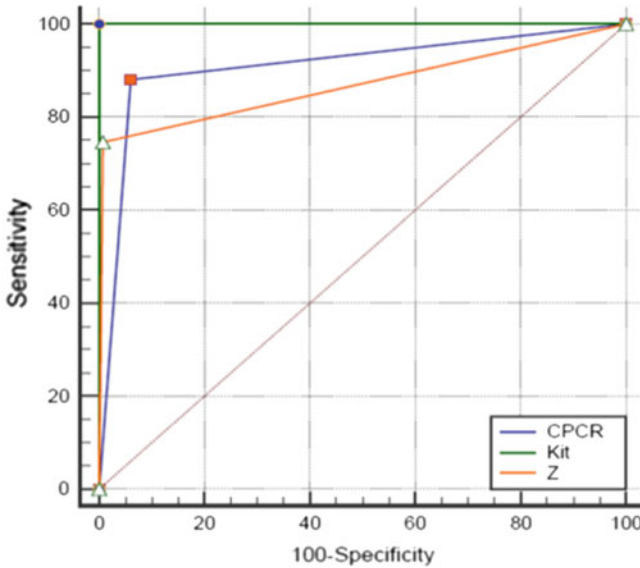
Key: PS (+) positive sample, NS (-) negative sample

Table 3 Statistical analysis of the results obtained within house PCR used for detection of *M. tuberculosis*

	Method to be compared with culture as gold standard method					
	ZN staining [95% confidence level]		Genosens's MTB complex/MOTT RT PCR kit [95% confidence level]		In-house conventional PCR [95% confidence level]	
Sensitivity	74.63%	62.51–84.47	100.00%	94.64–100.00	88.06%	77.82–94.70
Specificity	99.25%	95.88–99.98	100.00%	97.26–100.00	93.98%	88.49–97.37
AUC (area under curve)	0.87	0.81–0.91	1.00	0.98–1.00	0.91	0.86–0.95
Positive predictive value	98.04%	89.55–99.95	100.00%	94.64–100.00	88.06%	77.82–94.70
Negative predictive value	88.59%	82.36–93.21	100.00%	97.26–100.00	93.98%	88.49–97.37

4 ROC Curve Analysis

In order to compare the sensitivity and specificity of the diagnostic techniques namely In-house Conventional PCR, ZN Staining, Commercial Genosens's MTB Complex/MOTT RT PCR Kit and Culture; ROC curves and Forest plot were plotted to calculate the statistical significance of each technique. ROC curves have been plotted using Sensitivity and 100-Specificity. The left hand upper corner value showed 100% sensitivity and specificity when compare with gold standard microbiological method Culture. Results of culture are considering as standard for plotting other methods ROC curves. Other methods plot were obtained area under curve (AUC) were plotted comparing with culture method. The overall diagnostic sensitivity was 100% for the Genosense commercial Real Time PCR kit assay and 88.06% for the IS6110 conventional PCR assay, while the overall diagnostic specificity for the commercial kit was 100% whereas for Conventional PCR was



Comparison of ROC curves

Variable 1	CPCR
Variable 2	Kit
Variable 3	Z
Classification variable	C

Sample size	200
Positive group ^a	67 (33.50%)
Negative group ^b	133 (66.50%)

^a C = 1
^b C = 0

Variable	AUC	SE ^a	95% CI ^b
CPCR	0.910	0.0225	0.862 to 0.946
Kit	1.000	0.000	0.982 to 1.000
Z	0.869	0.0270	0.815 to 0.913

Fig. 3 ROC (receiver operating curves) in combination for in-house conventional PCR, Genosens’s MTB complex MOTT RT PCR kit, ZN staining method compare with Culture as Gold Standard Method. In which *AUC* area under the curve; *SE (AUC)* standard error of AUC; *SE* standard error. *CPCR* conventional PCR, *Kit* Genosens’s MTB complex MOTT RT PCR kit, *ZN*-*ZN* staining, *C* culture

93%. The test results showed that the two assays had significant difference in diagnostic performance for clinical respiratory specimens. The ROC curve for the two assays showed that the AUC was 1.00 for Commercial RT PCR kit assay and 0.8204 for the IS6110 Conventional PCR. A significant difference of 0.0892 could be observed between the AUC of the two assays ($P < 0.0001$). ROC Curves has been explain graphically in Fig. 3. 95% confidence interval line of each test and other statistical information also given in figure.

5 Conclusion

In India, the diagnosis of tuberculosis is primarily based on clinical features, microscopy based identification of acid fast bacilli and Culture. Nucleic acid amplification based method to detect *M. tuberculosis* in clinical specimens is increasing used as a tool for TB diagnosis. Many variants of PCR assays are presently available; our in-house PCR assay was based on the amplification of a fragment of the IS6110, which is specific for the *M. tuberculosis* complex. The amplification of IS6110 insertion sequence, which belongs to IS3 family and is found in almost all members of the *M. tuberculosis* complex. Most strains of *M. tuberculosis* carry 10–15 copies, which are present in a wide variety of chromosomal sites [12]. Application of molecular methods in routine diagnosing in developing country like ours depends on various factors like high cost and availability of skilled personnel to perform the test. In our study the overall efficacy of PCR reaction on suspected tuberculosis cases was found to be 67 (34%) positive by PCR test with efficiency of 88% detection when compare to culture as standard, while 40 (26%) were smear positive and efficiency of detection was 75%. PCR amplification method is useful for the rapid detection of *M. tuberculosis* with reported sensitivity of 55–95% in the smear negative and culture positives cases and 100% in both smear and culture positive clinical cases [13, 14]. Similar results were reported by Negi et al. in 2005 and they reported PCR efficiency 74.4%, while smear sensitivity was of 50% [15]. In another study, PCR positivity of clinical specimens was 100% in both smear and culture positive and 69.4% in culture positive and smear negative specimens [16]. In this study there are 8 false positive results was observed by Conventional PCR test. This could be due to the ability of the PCR test to detect very low number and even dead bacteria in a sample which can be present in a symptomatic individual [17–20]. In our study, Conventional PCR Positive predictive value and Negative predictive value was 88–93% respectively. To conclude, molecular diagnosis of tuberculosis by PCR has a great potential to improve the clinicians' ability to diagnose tuberculosis. This will ensure early treatment to patients and prevent further transmission of disease [20]. However, further work is needed for improving sensitivity, specificity and reproducibility of this test and to make it more user friendly and cost effective.

References

1. Jaggarajamma K, Sudha G, Chandrasekaran V, Nirupa C, Thomas A, Santha T, Narayanan PR (2007) Reasons for non-compliance among patients treated under Revised National Tuberculosis Control Programme (RNTCP), Tiruvallur district, South India. *Ind J Tub* 54(3):130

2. Aslanzadeh J, De la Viuda M, Fille M, Smith WB, Namdari H (1998) Comparison of culture and acid-fast bacilli stain to PCR for detection of *Mycobacterium tuberculosis* clinical samples. *Mol cell probes* 12(4):207–211
3. Nolte FS, Metchock B, McGowan JE, Edwards A, Okwumabua O, Thurmond C, Shinnick T (1993) Direct detection of *Mycobacterium tuberculosis* in sputum by polymerase chain reaction and DNA hybridization. *J Clin Microbiol* 31(7):1777–1782
4. Kocagöz T, Yilmaz E, Ozkara S, Kocagöz S, Hayran M, Sachedeva M, Chambers HF (1993) Detection of *Mycobacterium tuberculosis* in sputum samples by polymerase chain reaction using a simplified procedure. *J Clin Microbiol* 31(6):1435–1438
5. García-Quintanilla A, García L, Tudó G, Navarro M, González J, de Anta MTJ (2000) Single-tube balanced heminested PCR for detecting *Mycobacterium tuberculosis* in smear-negative samples. *J Clin Microbiol* 38(3):1166–1169
6. Gengvinij N, Pattanakitsakul SN, Chierakul N, Chairprasert A (2001) Detection of *Mycobacterium tuberculosis* from sputum specimens using one-tube nested PCR
7. Lemaître N, Armand S, Vachée A, Capilliez O, Dumoulin C, Courcol RJ (2004) Comparison of the real-time PCR method and the Gen-Probe amplified *Mycobacterium tuberculosis* direct test for detection of *Mycobacterium tuberculosis* in pulmonary and nonpulmonary specimens. *J Clin Microbiol* 42(9):4307–4309
8. Takahashi T, Nakayama T (2006) Novel technique of quantitative nested real-time PCR assay for *Mycobacterium tuberculosis* DNA. *J Clin Microbiol* 44(3):1029–1039
9. De Beenhouwer H, Lhiang Z, Jannes GA, Mijs W, Machtelinckx L, Rossau R, Portaels F (1995) Rapid detection of rifampicin resistance in sputum and biopsy specimens from tuberculosis patients by PCR and line probe assay. *Tuber Lung Dis* 76(5):425–430
10. Della LP (2004) Mycobacteriology and mycobacterial susceptibility tests. In Henry D (ed) *Clinical microbiology procedures handbook*, 2 edn. ASM Press
11. Kim SJ (2005) Drug-susceptibility testing in tuberculosis: methods and reliability of results. *Eur Respir J* 25(3):564–569
12. Negi SS, Anand R, Pasha ST, Gupta S, Basir SF, Khare S, Lal S (2007) Diagnostic potential of IS6110, 38 kDa, 65 kDa and 85B sequence-based polymerase chain reaction in the diagnosis of *Mycobacterium tuberculosis* in clinical samples. *Indian J Med Microbiol* 25(1):43
13. Shawar RM, El-Zaatari FA, Nataraj A, Clarridge JE (1993) Detection of *Mycobacterium tuberculosis* in clinical samples by two-step polymerase chain reaction and nonisotopic hybridization methods. *J Clin Microbiol* 31(1):61–65
14. Eisenach KD, Siford MD, Cave MD, Bates JH, Crawford JT (1991) Detection of *Mycobacterium tuberculosis* in sputum samples using a polymerase chain reaction. *Am Rev Respir Dis* 144(5):1160–1163
15. Negi SS, Khan SF, Gupta S, Pasha ST, Khare S, Lal S (2005) Comparison of the conventional diagnostic modalities, bactec culture and polymerase chain reaction test for diagnosis of tuberculosis. *Indian J Med Microbiol* 23(1):29
16. Banavaliker JN, Bhalotra B, Sharma DC, Goel MK, Khandekar PS, Bose M (1998) Identification of *Mycobacterium tuberculosis* by polymerase chain reaction in clinical specimens. *Indian J Tuberc* 45:15–18
17. Bechnoosh A, Lieberman JM, Duke MB (1997) Stutman comparison of quantitative polymerase chain reaction, therapy for pulmonary tuberculosis. *Diag Microb Infect Dis* 29(2):9–73
18. D'Amato RF, Hochstein LH, Colaninno PM, Scardamaglia M, Kim K, Mastellone AJ, Miller A (1996) Application of the Roche Amplicor, *Mycobacterium tuberculosis* (PCR) test to specimens other than respiratory secretions. *Diagn Microbiol Infect Dis* 24(1):15–17

19. Singh KK, Muralidhar M, Kumar A, Chattopadhyaya TK, Kapila K, Singh MK, Tyagi JS (2000) Comparison of in house polymerase chain reaction with conventional techniques for the detection of *Mycobacterium tuberculosis* DNA in granulomatous lymphadenopathy. J Clin Pathol 53(5):355–361
20. Rimek D, Tyagi S, Kappe R (2002) Performance of an IS6110-based PCR assay and the COBAS AMPLICOR MTB PCR system for detection of *Mycobacterium tuberculosis* complex DNA in human lymph node samples. J Clin Microbiol 40(8):3089–3092

Novel Method for Fabrication and Characterization Porous Structure Using Rapid Prototyping and Thermal Gradient Method

Shreepad Sarange and Ravi M. Warkhedkar

Keywords Rapid prototyping (RP) · Biomaterial · Hydroxyapatite

1 Introduction

Porous hydroxyapatite (Hap) is expected to have desired mechanical and biological properties for biomedical application [1]. However, due to material processing problems, till date, this material can only be prepared by conventional techniques. In this paper, we report the route to prepare porous Hap structure with the help of Rapid Prototyping (RP) and thermal gradient method. The cardinal challenge for rapid fabrication of Biomaterial by Rapid Prototyping (RP) is the preparation of photoinitiator (with properties viscosity and UV reactivity). In Present process consists of firing the hydroxyapatite slurry particle while they are in free-fall. When the mixture is in nozzle, it should be pseudoplastic with viscosity of some thousand CPS and droplets must have sufficient residence time for getting dried and other parameters like air temperature, velocity and flow of mixture are controlled and this droplet when deposited on platform further heating is carried out. This is a new technique developed for complex 3-D microstructure parts. In conventional vector by vector process laser beam is deflected by scanning mirror on the surface of layer. This may cause continuous change in laser size which may affect resolution of micro structure.

S. Sarange (✉)

Government College of Engineering Aurangabad, Aurangabad, India

e-mail: sarangeshreepad@gmail.com

R.M. Warkhedkar

Government College of Engineering Awasari, Ambegaon, India

e-mail: raviwar.wildorchid@gmail.com

2 Method of Preparation of Hydroxyapatite

Figure 1 shows overview of slurry preparation heating arrangement for deposition of Biomaterial on substrates. Hydroxyapatite powder (Sigma-Aldrich) of high resolution is used as raw material. The slips were prepared by dispersing the HA powder in solvent (66% powder + 34% solvent by mass), using mechanical stirring. The dispersion behavior of the HA particles was studied as a function of the pH of the slurry and with the addition of dispersing agent, organic (ammonium polyacrylate (NH₄PAA) 0.3 wt%) solution. This mixture is milled for 24 h to get uniform distribution of particle size and viscosity. PH is maintained ~10. In this beam is stationary and platform is moving and heated uniform continuously. In Primary heating, a laser beam is used to bind the powder without the addition of binder directly. The powder is heated to the temperature (T_m/2) at which fusion of particle takes place. The process continues with formation of neck between the adjacent particles. In this RP Process primary laser Nd:YAG laser is for melting (Fusion) and for consolidation [CO]₂ is used.

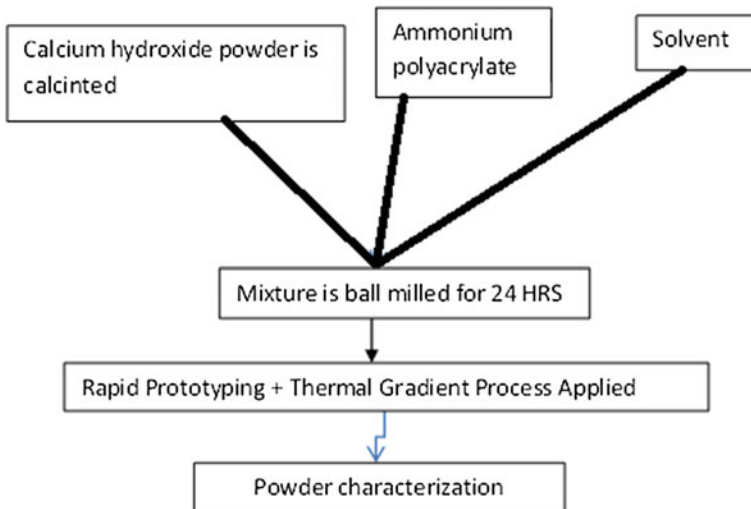


Fig. 1 Overview of rapid prototyping, thermal gradient process and material characterization

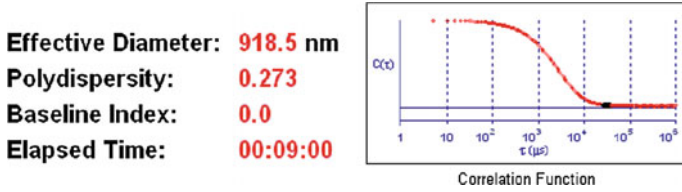


Fig. 2 Slurry analysis by DLS technique

3 Particle Size Distribution

As shown in Fig. 2 Dynamic light scattering technique is used for particle size and characteristics of the particle. In small size particle surface area is more and lower temperature of melting and bonding. But strongly influenced by inter particulate forces, high shrinkage. Slurry is of polydispersity index of 0.273 and effective diameter of 918.5 nm.

In order to avoid agglomeration, ultrasonic treatment was used. Settling time since this process requires time and slip viscosity is low for this deflocculating and the viscosity needs to be adjusted.

The surface area increases by square of the radius as the particle size decreases. Surface chemistry dominates over the slip Rheology, thus making PH and concentration Key variables (2). Higher the particle size higher the temperature to melt coarse grain structure which eases the process. To optimize the process, the moderate particle size is selected average particle size (923 nm).

4 Construction and Working Principle

Slurry prepared as per procedure in Fig. 1 it will pass through cylindrical taper nozzle to operate at low pressure simultaneously small power Nd:YAG laser will melt this slurry partial so that inter particle bonding begins (solid-solid) as soon as this primary laser switched off and secondary CO₂ laser switched on which facilitates surface diffusion. Initial melting takes place at the surface if heating is too rapid. Thermal stresses may cause part cracking, which can be avoided using heating with electrical heaters around syringe. Primary Heating with Nd:YAG laser layer melt, it flows in the interparticle pores and subsequently can penetrate the grain boundaries in the particles.

Laser power density, porosity, scanning speed will be control by computer control as shown in Fig. 3.

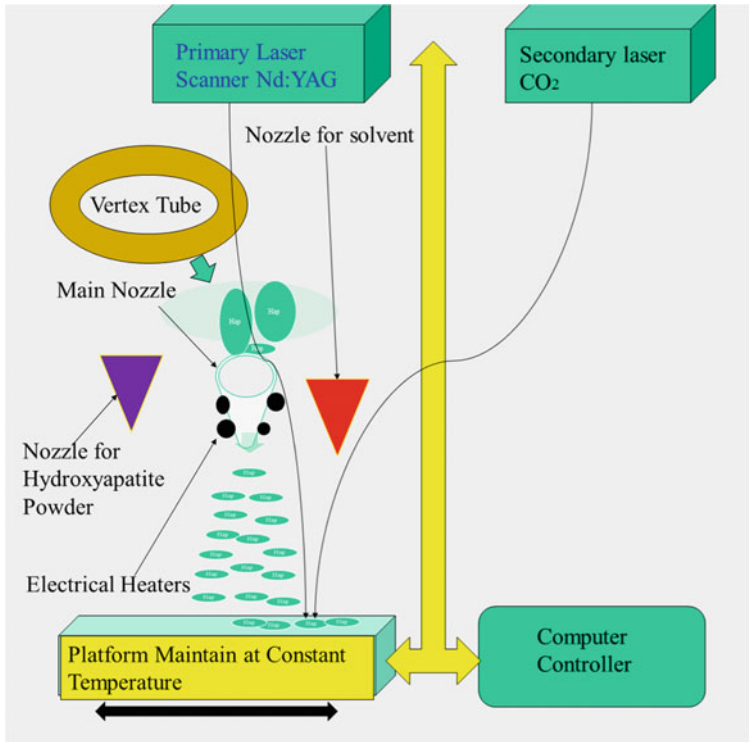


Fig. 3 Experimental arrangement

5 Layer-Wise Slurry Deposition (LSD) Process

3-D computer graphics (Catia V6) is used to prepare model and exported as stereo lithography (Stl) format. Rectangular scaffold was made of size 15 mm × 6 mm. The LSD process utilizes a.stl CAD file to define the geometry of an object to be fabricated. According to thickness, cross section is sliced into number of thin layer. Each scanned layer represents a cross section of the sliced CAD model with stereo lithography (Stl) format. Finally, an object is integrated by sequentially thermal bonding the layers with a scanning laser beam.

Rapid Prototyping (RP) and thermal Gradient is used to fabrication of porous hydroxyapatite (HAP) has been attempted by depositing porous HA on prosthetic material like zirconium, copper. Efforts were put to develop pure Hap that is chemically compatible and stable with HA at elevated temperatures.

The slurry is then made to pass through specially designed nozzle and heated to predetermined temperature as shown in Fig. 4. While deposition Nd:YAG laser is used, and secondary heating CO₂ laser is used which heats the layer upto 1350 °C. While rapid heating with Nd:YAG and CO₂ laser enhances gas blowing, pH

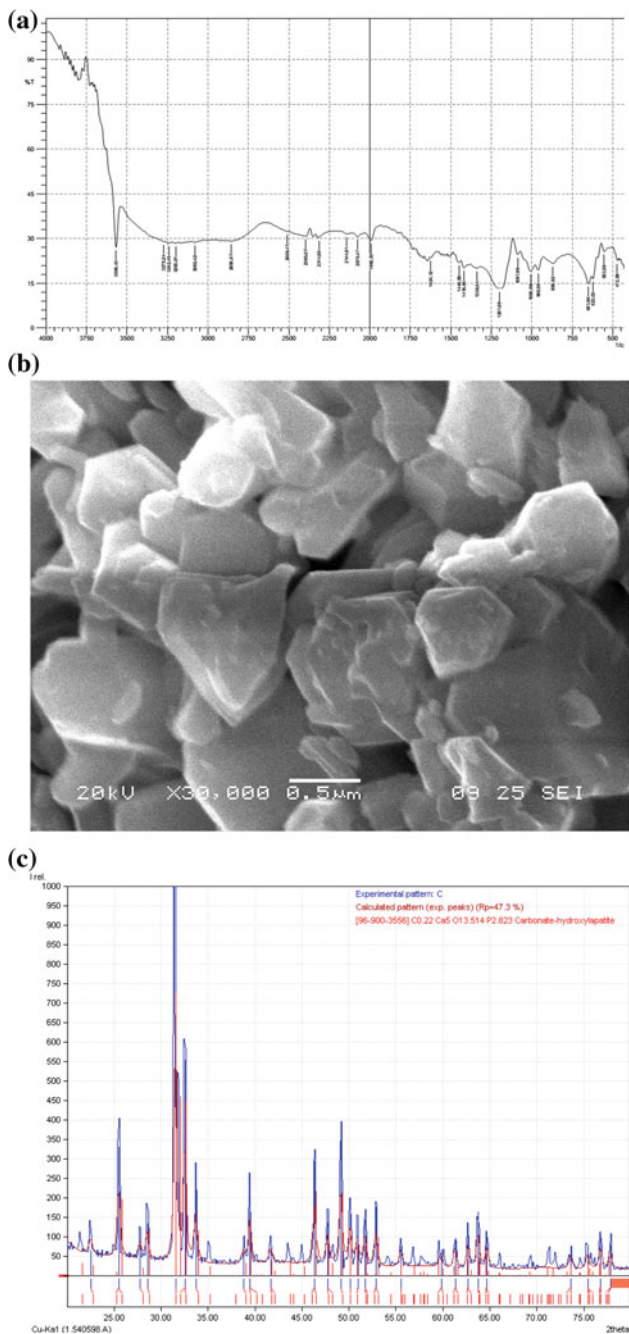


Fig. 4 a FTIR. b SEM image. c XRD. d EDX results of fabricated HaP. e TGA analysis

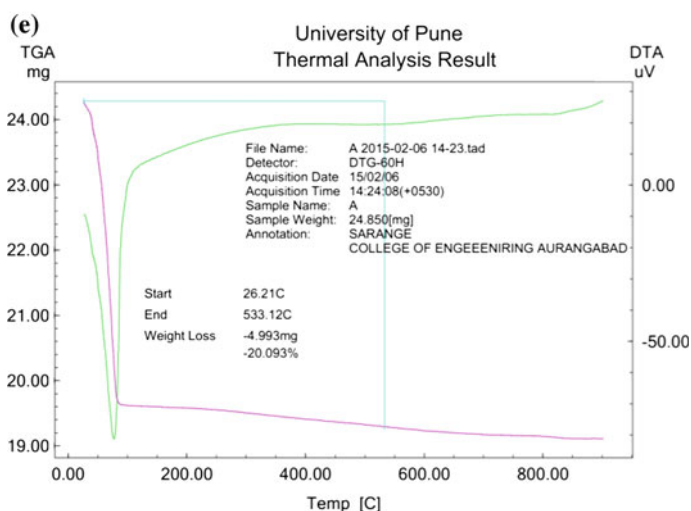
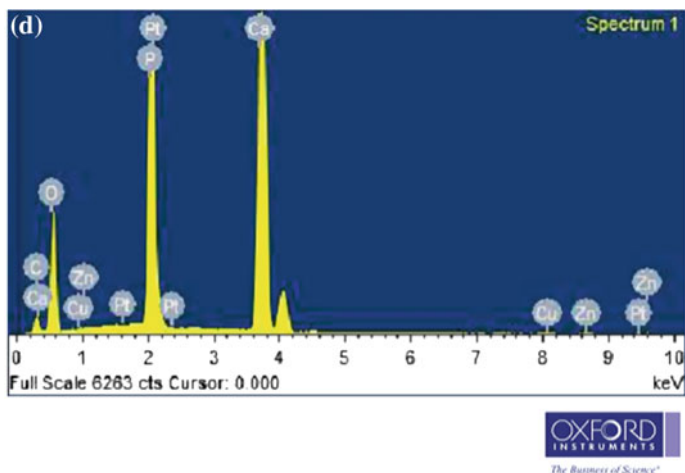


Fig. 4 (continued)

increment, which is accelerated by cross linking agents decomposition, provides better cross linking. Thus interconnected and well-established macroporous structures produced easily and rapidly [2].

5.1 Mechanism

When temperature is close melting point viscosity and surface tension may cause molten particle to aggregate and form large droplet this is called balling. Some particles may burn out especially on top surface and sometimes causes nonuniform

heating. This problem can be avoided by using two laser and Q-switching technique.

The primary Laser Nd:YAG is employed to heat powder up to temperature $T_m/2$ at which fusion between particles occurs without melting. T_m –melting temperature [3].

The process began with formation of neck between adjacent powder particles and subsequent fusion by reducing surface energy. For fusion process the vacancy concentration is main driving force. The vacancy is large at curved surface than flat surface. This induces vacancy gradient which increases the neck size. Due to shrinkage effect may cause formation of cracks this can improve by utilizing Secondary laser [CO]₂ used for further reheating up to T_m .

6 Characterization of Fabricated Hydroxyapatite Bio Film

Characterization of SEM, XRD, FTIR shows hydroxyapatite $Ca_{10}(PO_4)_6O_x(OH)_2(1-x)$ (HOA), ZrO_2 , and trace amounts of α -tricalcium phosphate phases were detected. Results showed that the proposed process is feasible for preparing porous Hap with improved physical and mechanical properties and promising bioactivity for orthopedic applications especially for bone and dental applications.

6.1 FT-IR Analysis

FT IR spectral data aided to assess the reaction chemistry of deposited Hap. Figure 4a shows the FT-IR spectra of fabricated HA. The characteristic bands observed in the samples are listed in (Table 1). Bands at 3568.43 and 623.03 cm^{-1} are due to stretching mode of hydrogen and liberation mode of hydrogen bonded (OH^-) ions respectively.

The band at 1087.89 cm^{-1} arises from $\nu_3 PO_4$, the bands at 623.03 and 533.59 cm^{-1} arise from $\nu_4 PO_4$. The FT-IR analysis demonstrated all traditional absorption bands of hydroxyapatite. Apart from normal bands, few carbonate content was also seen (CO_3^{2-} as peak at 1600 cm^{-1}), which is an indication of the presence of carbonate apatite. This might have originated through the absorption of carbon dioxide from the atmosphere [4].

Table 1 Infrared assigned for the fabricated hydroxyapatite bio coating

Infrared frequency (cm^{-1})	Assignment
533.59	PO_4 bend ν_4
623.03	OH structural
1087.89	PO_4 bend ν_3
3568.43	OH structural

A gradual decrease in intensity band at 960.58 and 1006.68 attributed to oxy hydroxyapatite functional group that would appear around 1200 °C. Broad band from 1200 to 950 cm^{-1} which corresponds to TTCP and α -TCP. C=O Observed to wave number at 1624.12 cm^{-1} .

6.2 SEM Analysis

Figure 4b SEM micrograph of a fabricated structure of bio coating is one of the crucial factors influencing the integrity of the scaffolds, Scanning Electron Microscope (SEM) result shows deposited structure fairly and uniformly interconnected which will contribute to activity when immersed in simulated Body Fluid (SBF) [1].

Analysis SEM micrograph of this has been done using magniSci software. Results as shown in Table 2 shows Hap aggregated into irregular granules. The particles had a spherical shape with a uniform average size of 1–4 μm . Necking of particle is formed due to localized heating.

Table 2 Grain characterization

Sr.No.	Description	Variables	Estimated Values	Unit
1	Number of grains per mm^2	Na	8.922	$1/\text{mm}^2$
2	Average grain area	AM	125569.321	μm^2
3	Average diameter of grains	DM	349.432	μm
4	Number of intercepts per mm	NL	3.306	$1/\text{mm}$
5	Mean linear intercept line	LM	311.298	μm
6	ASTM Grain Size Number	G	0.162	G

6.3 XRD Analysis

XRD pattern for Hap coating Film is as shown in Fig. 4c from the pattern it is revealed that pure hydroxyapatite phase with high crystalline structure and fluorapatite, chlorapatite. The X-ray diffractometer was used to determine the phase structure of the Hap. XRD patterns were obtained in a 2θ angle ranging from 10° – 80° at a scanning speed of $2^\circ/\text{min}$. The straight base line and the sharp peaks of the diffractogram confirmed the biomaterial film was well crystallized. The XRD patterns indicated that Secondary phase CaO (calcium oxide) was observed and traces of other impurities were not detected by this technique.

XRD pattern matches with the standard pattern; it showed a stoichiometric hydroxyapatite characterized pattern (XRD JCPDS data file No. 9-432). The intensity of (200) lattice plan of CaO confirm pure phase of HA as in the Afshar et al. [5] research.

Small amount of CaO presence does not affect biocompatibility of HA [6]. Controlling parameters during synthesis commands the developing of HA purity and impurities in biofilm [6]. The X-ray diffraction (XRD) HaP is consistent with FT IR.

6.4 Elemental Analysis

Figure 4d. The result of estimation of elemental composition (Ca and P content) and Ca/P molar ratio are summarized in Table 3. The bulk Ca/P molar ratio was determined as 1.71. The measured Ca/P ratio for this produced Bio coating was higher than stoichiometric ratio (1.667) expected for a pure HAp (stoichiometric formula $\text{Ca}_{10}(\text{PO}_4)_6(\text{OH})_2$) phase. According to the XRD patterns that showed existence of small amounts of CaO phase.

6.5 DTA and TGA Analysis

The DTA and TGA curves for the Hydroxyapatite slurry prepared are illustrated in Fig. 5e. The first endothermic region range from 90 to 1055°C with a peak at about 100°C which is attributed to dehydration of sample loss of absorbed water. The weight loss in this region is 16%. With increasing temperature from 100 to 800°C no peak has been observed, except a small weight loss of observed which is

Table 3 Ca and P content in the fabricated hydroxyapatite bio coating and Ca/P ratio

Element	Measured content (wt%)	Ca/P ratio
Ca	38.63	1.71
P	17.48	

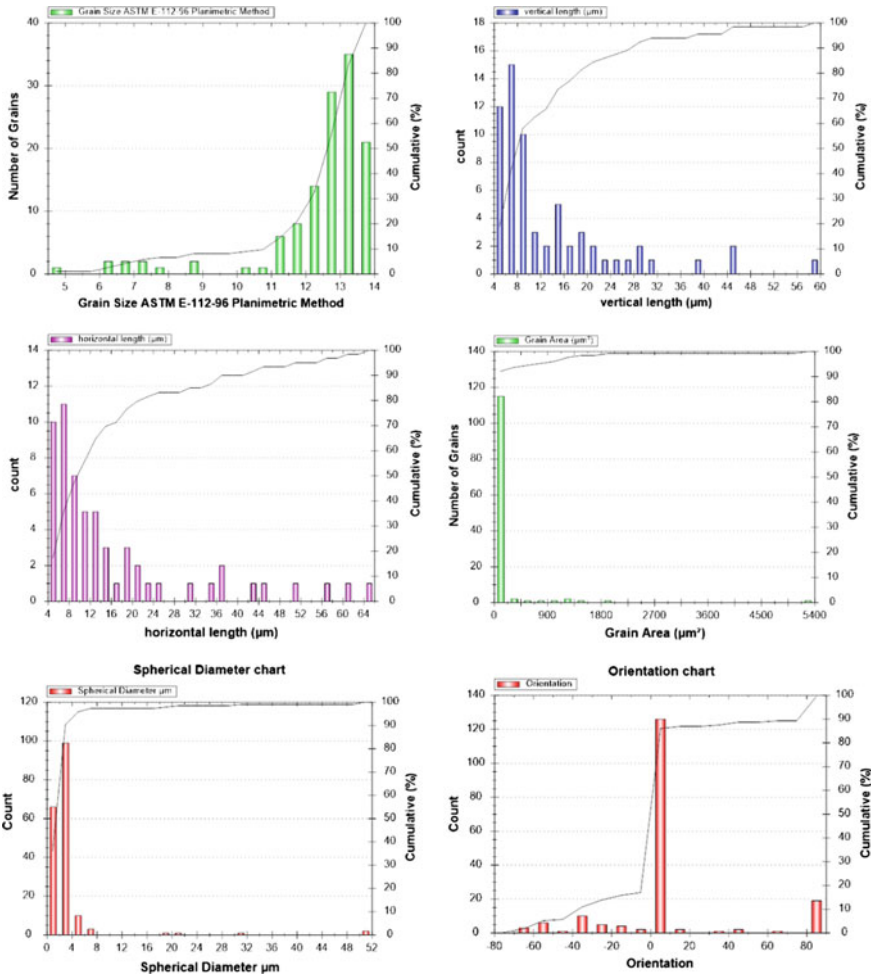
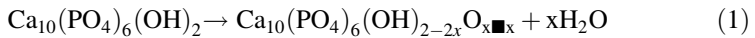


Fig. 5 Grain characterization

attributed to gradual dehydroxylation of HA Slurry. This can be explained by Eq. (1) reaction [7]:



According to the equilibrium phase diagram of CaO/P₂O₅, HAP will decompose into TTCP and a TCP at 1350 °C [8]. To monitor the process and evaluation of chemical bonds is important in determining the bioactivity. The material with more lattice defect would be expected to be more reactive this fact has been verified experimentally.

The high temperature and long duration will be resulting in crystalline structure. Therefore, to enhance the bioactivity low temperature and short duration is used for fabrication. It's critical to find optimal operating parameters for fabrication of porous structure.

7 Conclusions

This method tried to fabricate Porous Hap using Rapid Prototyping (RP) and thermal Gradient. IR spectra; SEM XRD shows interconnected pores and uniformly distribution of Hap. There is covalent bonding exist between HAP and titanium, zirconium. This covalent bonding makes stronger adhesion to prosthetic.

Rapid Prototyping (RP) and thermal Gradient can be evaluated for the preparation of porous scaffolds which have superior properties for bone tissue engineering.

The SEM and EDS indicate uniform and regular distribution of Hap, calcium carbonate, phosphate product. It's showing bonding with zirconium, titanium best interfacial bonding is getting with Alumina.

Therefore, the current modification method may provide a better feasible solution to fabricate HAP as one substitute material with high interfacial bonding and performance.

Many small Nano particles aggregate together to form one higher sized micro particle is called Balling and product of different temperature solidify on the layer is called recasting is dominates the process. By optimizing the operating parameter these problem can be minimized.

References

1. Ripamonti U (1996) Osteoinduction in porous hydroxyapatite implanted in heterotopic sites of different animal models. *Biomaterials* 17(1):31–35. doi:[10.1016/0142-9612\(96\)80752-6](https://doi.org/10.1016/0142-9612(96)80752-6)
2. Rao R, Roopa HN, Kannan TS (1997) Solid state synthesis and thermal stability of HAP and HAP- β -TCP composite ceramic powders. *J Mater Sci Mater Med* 8(8):511–518. doi:[10.1023/A:1018586412270](https://doi.org/10.1023/A:1018586412270)
3. Lobo SE, Arinzeh TL (2010) Biphasic calcium phosphate ceramics for bone regeneration and tissue engineering applications. *Materials* 3(2):815–826. doi:[10.3390/ma3020815](https://doi.org/10.3390/ma3020815)
4. Komath M, Varma HK (2003) Development of a fully injectable calcium phosphate cement for orthopedic and dental applications. *Bull Mater Sci* 4:22–415
5. Afshar A, Ghorbani M, Ehsani N, Saeri MR, Sorrell CC (2003) Some important factors in the wetprecipitation process of hydroxyapatite. *Mater Design* 24:197–202
6. Rameshbabu N, Kumar TSS, Rao KP (2006) Synthesis of nanocrystalline fluorinated hydroxyapatite by microwave processing and its in vitro dissolution study. *Bull Mater Sci* 29:5–611
7. Murray MGS, Wang J, Pontoon CB, Marquis PM (1995) An improvement in processing of hydroxyapatite ceramics. *J Mater Sci* 30:74–3061
8. Riboud PV (1973) Composition and stability of appetites in the system CaO-P₂O₅-iron oxide-H₂O at high temperature. *Ann Chim* 8:90–381

Role of Gene Xpert in Early Diagnosis and Treatment of Tuberculosis

Harapriya Kar, Samir Pachpute, Poonam Patil, Yogesh Patil
and A.D. Urhekar

Keywords Tuberculosis · Gene Xpert · MTB/RIF · AFB · Culture · MGIT · PCR

1 Introduction

India accounted for about one-third of global Tuberculosis deaths. Approximately nine million people worldwide are infected with Mycobacterium Tuberculosis and develop active disease. The percent number of Tuberculosis positive cases reported in India by the year 2014 are 29% of the total global burden (i.e. 1.61 million out of 9 million cases globally) [1]. The high risk of transmission from person to person and the emergence of Multi-Drug Resistant—TB and extensively drug resistant TB [2]. To eradicate this highly infectious disease, rapid diagnosis and treatment are the only ways to control the spread of the disease. On the other hand, conventional diagnostic techniques such as Acid Fast Bacilli—smear microscopy for acid-fast bacilli have poor sensitivity and a poor positive predictive value. [3] Also “gold standard” Culture methods take several weeks for detection of *M.tuberculosis* [4].

A meta-analysis of nucleic acid amplification techniques (NAAT) showed wide variability for the performance of in-house tests and sensitivity for commercial tests of below 60% [5]. Individual reports of the use of in-house PCR have reported higher sensitivities, particularly with multiplex PCR techniques; however, these tests can be difficult to implement with appropriately rigorous quality controls in

H. Kar (✉) · S. Pachpute · A.D. Urhekar
Department of Microbiology, MGM Medical College, Navi Mumbai, India
e-mail: harapriya.kar@gmail.com

A.D. Urhekar
e-mail: dradurhekar@gmail.com

P. Patil
Department of Biotechnology, MGMIUDBS and CRL, Navi Mumbai, India

Y. Patil
Department of Biotechnology, MGM CET and CRL, Navi Mumbai, India

resource-limited, high-burden health care centers, where the need is greatest [6]. Thus, rapid identification, which is essential for earlier treatment initiation, improved patient outcomes, and more effective public health interventions, relies on nucleic acid amplification techniques. The development of an automated, fully integrated DNA extraction and amplification system, the Gene Xpert MTB/RIF assay (Cepheid, CA, USA) has addressed some these limitations. Gene Xpert can be performed in decentralized locations outside reference laboratories by staff with minimal laboratory training (1–2 days). Gene Xpert can detect the presence or absence of both *Mycobacterium tuberculosis* (MTB) complex DNA and rifampicin drug resistance (strongly correlated with MDR-TB) in less than 2 h [7–10].

So, this study was conducted in a tertiary care Hospital to evaluate the diagnostic accuracy of Gene Xpert MTB/RIF assay for rapid and accurate diagnosis of pulmonary tuberculosis and also detection of rifampicin resistance in high-risk groups (patients requiring tuberculosis retreatment and drug resistant Tuberculosis contact).

2 Materials and Methods

2.1 Method

This prospective study was conducted from January 2016 to June 2016, in Central Research Laboratory (CRL), Department of Microbiology, MGM Medical College, Navi Mumbai, India. All Tuberculosis suspected Patients and patients are requiring retreatment and contacts of drug resistant Tuberculosis visiting outpatient of MGM Medical Hospital, were screened and clinically examined for tuberculosis. Sputum samples were collected from these patients and were processed in TB laboratory for smear microscopy by acid-fast bacillus staining (Ziehl-Neelsen [ZN] staining), TB culture by MGIT-culture method (BACTECTM MGITM 960-semi automated) and Gene Xpert MTB/RIF assay. Gene Xpert MTB/RIF assay is based on nucleic acid amplification (NAA) test which simultaneously detects DNA of *Mycobacterium tuberculosis* complex (MTBC) and resistance to Rifampicin (RIF) (i.e. mutation of the *rpoB* gene) in less than 2 h. The primers in the Xpert MTB/RIF assay amplify a portion of Marker sequences of *Mycobacterium tuberculosis* complex and also the sequences of the *rpoB* gene containing the 81 base pair “core” region responsible for the activity of rifampicin drug. The probes can differentiate between the conserved wild-type sequence and mutations in the core region that is associated with rifampicin resistance. The sputum is mixed with the reagent that is provided with the assay, and a cartridge containing this mixture is placed in the Gene Xpert machine. All processing from this point is fully automated. In comparison, standard cultures can take 2–6 weeks for *Mycobacterium tuberculosis* Complex (MTBC) to grow and conventional drug resistance tests can add three more weeks. This system integrates and automates sample processing, nucleic acid amplification, and detection of the target sequences.

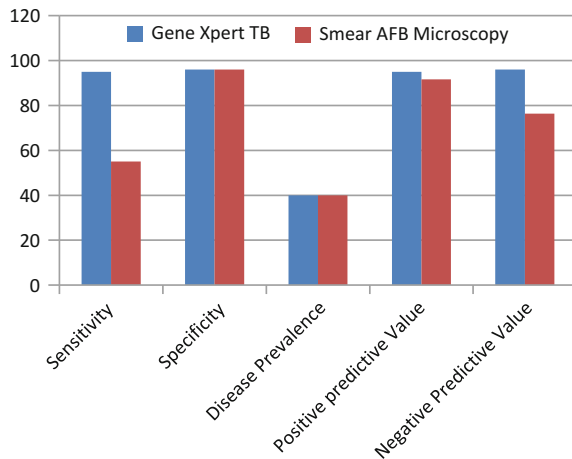
3 Results and Discussion

A total of 100 respiratory specimens with suspected Tuberculosis infection were assayed for tuberculosis detection mainly by three techniques—Acid Fast Bacilli by Smear Microscopy, Liquid Culture system, and Xpert MTB assay. Out of 100 sputum samples examined, 22 (22%) were positive for acid-fast bacilli by Smear Microscopy, 40 (40%) were positive by Liquid culture (MGIT) and 38 (38%) were found positive with Xpert MTB/RIF out of which 8 samples were drug resistance MDR-TB (21%). All the 40 culture-positive samples were further processed with TBcID (Becton Dickinson, Sparks, MD) analysis, which showed that two tests were negative for Mycobacterium tuberculosis complex. This was in agreement with Gen Xpert TB assay results. The overall mean time periods to detect Mycobacterium in culture were 35.70 ± 4.56 days. Considering the liquid medium MGIT culture results as the “gold standard,” the sensitivity of Acid Fast Bacilli (Z-N) staining and Gene Xpert were 55.0, 95% respectively, whereas the specificity were 96.67 and 96.67% respectively (Table 1). The positive and negative predictive values of the methods are also shown in Fig. 1.

Table 1 Comparison of sensitivity and specificity of rapid methods AFB smear microscopy and Gen Xpert for pulmonary tuberculosis with MGIT culture as gold standard

Parameters	Gene Xpert TB (%)	Smear AFB microscopy
Sensitivity	95.00	55.0%
Specificity	96.67	96.67%
Disease prevalence	40	40%
Positive predictive value	95.00	91.67
Negative predictive value	96.67	76.32

Fig. 1 Graphical comparison of Gene Xpert and smear microscopy for diagnosis of pulmonary tuberculosis



4 Conclusion

Conventional laboratory techniques such as smear microscopy for diagnosis of tuberculosis from clinical specimens are less sensitive as compared to the culture based techniques because large bacillary load (10⁵/ml) will be required for a smear to become positive [10]. Moreover the conventional culture-based systems are time consuming, require's Biosafety environment, trained laboratory personnel's [11] and also the accurate prediction of Mycobacterium tuberculosis complex was not as good as due to presence of Mycobacterium other than tuberculosis (MOTT) which leads to prediction of false positive results and also needs further conformational tests such as TBC ID test. The Gene Xpert MTB/RIF assay is a rapid molecular biology based assay that can be used close to the point of care by operators with minimal technical expertise. The technique enables quick diagnosis of TB. The extra advantage is the convenience of sample processing where unprocessed sputum samples, as well as clinical specimens from extra pulmonary sites, can be directly assayed [10].

In the present study, we have evaluated the diagnostic accuracy of Xpert MTB/RIF assay for pulmonary samples and compared it with the conventional techniques. Out of 100 Tuberculosis, suspects 38 (38.0%) were Gene Xpert MTB positive and 22 (22.0%) Acid Fast Bacilli—smear positive and 78 (78%) smear negative cases. Here, the on time Xpert MTB/RIF assay added an advantage of much lower turnaround time and also accurate detection of TB as well as Drug resistant TB(MDR-TB). Batz et al. in their study reported a better detection rate with Xpert when compared to smear microscopy and culture [12]. Compared to our study where 100% of the smear and culture positive cases (Table 1) were positive by Gene Xpert, Batz et al. observed positive results in 95% cases with Gene Xpert. In concordance with this study Zeka et al. also reported 100% specificity of MTB/RIF test in 110 clinically and microbiologically diagnosed tuberculosis patients [13].

Our Study shows that the Gene Xpert MTB/RIF assay is a useful tool for rapid diagnosis of pulmonary Tuberculosis as it has greatly shortened the time of detection up to two hours as compared to other techniques [14, 15]. This advantage is translated into clinical management of the patients as the Xpert MTB/RIF assay reduces the time of the diagnosis and to start treatment for positive patients from several weeks to just a few days [16, 17]. The sensitivity of Acid Fast Bacilli Smear Microscopy (AFB), Gene Xpert were found 55, 96% respectively and specificities were 96.67 and 96.67% respectively considering culture as a Gold standard. Gene Xpert assay was able to detect more Tuberculosis cases than Acid Fast Bacilli Smear microscopy alone. This technique though expensive is much quicker as compared to the conventional methods and is more sensitive and specific. This method could offer a new approach for accurate tuberculosis diagnosis, especially in remote regions of the world where culture is not available and needs a specific environment for Sample processing and Growth of Bacteria.

References

1. Boehme CC et al (2010) Rapid molecular detection of tuberculosis and rifampin resistance. *N Engl J Med* 363:1005–1015
2. Boehme CC et al (2011) Feasibility, diagnostic accuracy, and effectiveness of decentralised use of the Xpert MTB/RIF test for diagnosis of tuberculosis and multidrug resistance: a multicentre implementation study. *Lancet* 377(9776):505–1495
3. Helb D et al (2010) Rapid detection of mycobacterium tuberculosis and rifampin resistance by use of on-demand, near-patient technology. *J Clin Microbiol* 48:229–237
4. Teran R, de Waard JH (2015) Recent advances in the laboratory diagnosis of tuberculosis. *J Int Fed Clin Chem Lab Med* 26(4):295–309
5. Marlowe EM et al (2011) Evaluation of the Cepheid Xpert MTB/RIF assay for direct detection of mycobacterium tuberculosis complex in respiratory specimens. *J Clin Microbiol* 49:1621–1623
6. Pai M, Flores LL, Pai N, Hubbard A, Riley LW, Colford JM Jr (2003) Diagnostic accuracy of nucleic acid amplification tests for tuberculous meningitis: a systematic review and meta-analysis. *Lancet Infect Dis* 3:633–643
7. Ho J, Marais BJ, Gilbert GL, Ralph AP (2013) Diagnosing tuberculous meningitis—have we made any progress? *Trop Med Int Health* 18:783–793
8. Ioannidis P, Papaventsis D et al (2011) Cepheid GeneXpert MTB/RIF assay for *Mycobacterium tuberculosis* detection and rifampin resistance identification in patients with substantial clinical indications of tuberculosis and smear-negative microscopy results. *J Clin Microbiol* 49:3068–3070
9. Blakemore R et al (2010) Evaluation of the analytical performance of the Xpert MTB/RIF assay. *J Clin Microbiol* 48:2495–2501
10. Lawn SD, Nicol MP (2011) Xpert® MTB/RIF assay: development, evaluation and implementation of a new rapid molecular diagnostic for tuberculosis and rifampicin resistance. *Fut Microbiol* 6:1067–1082
11. Hillemann D, Rüsçh-Gerdes S, Boehme C, Richter E (2011) Rapid molecular detection of extra pulmonary tuberculosis by the automated GeneXpert MTB/RIF system. *J Clin Microbiol* 49:1202–1205
12. Batz HG, Cooke GS, Reid SD (2011) Towards lab-free tuberculosis diagnosis. Treatment Action Group, the TB/HIV Working Group of the Stop TB Partnership, Imperial College, and the MSF Access Campaign, pp 1–34
13. Zeka AN, Tasbakan S, Cavusoglu C (2011) Evaluation of the GeneXpert MTB/RIF assay for rapid diagnosis of tuberculosis and detection of rifampin resistance in pulmonary and extrapulmonary specimens. *J Clin Microbiol* 49:4138–4141
14. Vadwai V, Boehme C, Nabeta P, Shetty A, Alland D, Rodrigues C (2011) Xpert MTB/RIF: a new pillar in diagnosis of extrapulmonary tuberculosis? *J Clin Microbiol* 49:2540–2545
15. Van Rie A, Menezes C, Scott L (2011) High yield, sensitivity and specificity of Xpert MTB/RIF for *M. tuberculosis* detection in fine needle aspirates from HIV-infected TB suspects; conference paper: on retroviruses and opportunistic infections, Boston, MA, USA
16. Vadwai V, Boehme C, Nabeta P, Shetty A, Alland D, Rodrigues C (2011) Xpert MTB/RIF: a new pillar in diagnosis of extrapulmonary tuberculosis? *J Clin Microbiol* 49:2540–2545
17. Lawn SD, Nicol MP (2011) Xpert® MTB/RIF assay: development, evaluation and implementation of a new rapid molecular diagnostic for tuberculosis and rifampicin resistance. *Fut Microbiol* 6:1067–1082

Synthesis and Characterization of MoS₂-Graphene Nanocomposite

K.M. Sarode, S.G. Bachhav, U.D. Patil and D.R. Patil

Keywords Bulk MoS₂ · MoS₂ · Graphene · MoS₂-graphene nanocomposites

1 Introduction

Nowadays, Two-dimensional (2D) layered materials such as transition metal dichalcogenide [1–5], graphene [6–8], hexagonal boron nitride [9, 10] are emerging class of new materials due to their favorable electrical and optical properties.

Molybdenum disulfide (MoS₂) is one type layered transition-metal dichalcogenide material TMDCs have X-M-X sandwich-type layered structure, characterized by the chemical formula MX₂. Here M is a transition metal atom (usually Mo or W) and X a chalcogen (S, Se or Te) [11]. The interaction of chalcogen and transition metal atoms in a X-M-X layer is strong covalent bonding, while the X-M-X layers form bulk material via relatively weak van der Waals force [12]. Bulk MoS₂ has an indirect band gap about 1.3 eV, while the single-layer MoS₂ nanosheets have a 1.9 eV direct band gap [13, 14].

Graphene is a new class of carbon nanomaterials consisting of a sp² carbon network with a thickness of one atom. Graphene holds great promise as the next wonder material due to extraordinary properties such as enhanced electrical conductivity, great mechanical strength, high thermal conductivity, and high impermeability to gasses and optical transparency [15–18].

In the present work, we synthesized a novel kind of MoS₂/graphene nanocomposite material by lithiation-assisted exfoliation method. Instrumental characterization shows that exfoliated MoS₂ is supported graphene material.

K.M. Sarode · S.G. Bachhav · U.D. Patil · D.R. Patil (✉)

Nanomaterial Research Laboratory, R.C. Patel ACS College, Shirpur, Maharashtra, India
e-mail: dr.drpatil@gmail.com

2 Experimental

2.1 Synthesis of Graphene Nanosheets (RGO)

Graphene oxide (GO) was synthesized by the chemical oxidation of graphite flasks by a improve Hummers method [19]. In a typical synthesis, GO (200 mg) was loaded in a round bottom flask and water (200 mL) was then added, yielding an inhomogeneous yellow-brown dispersion. This dispersion was sonicated using an ultrasonic bath cleaner (170 W) until it became clear with no visible particulate matter. A certain amount of Hydrazine hydrate was then added and the solution heated in an oil bath at 100 °C under a water-cooled condenser for 24 h which yielded a black precipitation of reduced graphene oxide powder. After cooling to room temperature, this product was filtered, washed in succession with water and methanol and then resulting black material was dried at 60 °C temperature under vacuum for 12 h [20].

2.2 Synthesis of MoS₂/Graphene Nanocomposite

In a typical synthesis, 1.0 g of MoS₂ powder was dispersed in 10 mL of n-butyl lithium solution in hexane in a flask filled with N₂ gas. The mixture was soaked at room temperature for 48 h, and the produced Li_xMoS₂ was filtered and washed repeatedly with hexane to remove excessive lithium and organic residues and dried under the nitrogen atmosphere. After that, the powder was immersed in water and the suspension was ultrasonicated for 1 h to obtained aqueous suspension of MoS₂ nanosheets. Subsequently, the synthesized graphene nanosheets were dispersed in ethanol (3 mg/mL) and ultrasonicated for 30 min to produce graphene suspension. The produced graphene suspension was then slowly added to the MoS₂ layers and the reaction mixture was ultrasonicated and stirred at room temperature for 3 days. After that, two drops of concentrated hydrochloric acid were added and the reaction mixture was allowed to stir in a round bottom flask for another day. The single layers of MoS₂ were very sensitive to temperature and would restack turbostratically on the surface of graphene when heating [21]. The resultant black were collected by centrifugation with deionized water and ethanol several times and then dried in a vacuum oven at 80 °C for 12 h. The different mass ratios of LiMoS₂/graphene are taken as 100/12.5, 100/25, 100/50, 100/100 and the corresponding products are denoted as MG1, MG2, MG3, and MG4. As a control, the restacked MoS₂ without any graphene was also synthesized.

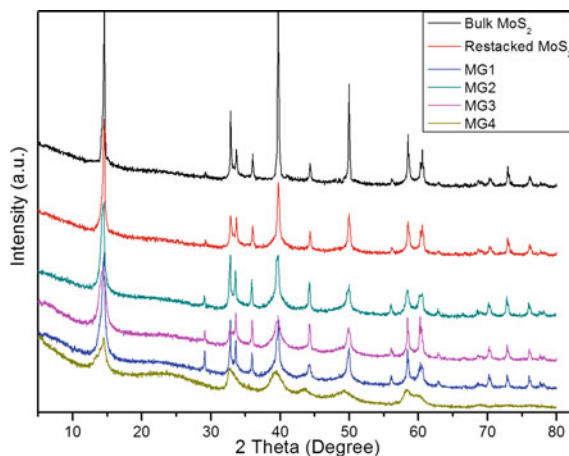
2.3 Characterization

Field emission scanning electron micrograph (FE-SEM) was acquired on Zeiss Ultra-55, X-ray diffraction (XRD) measurements were performed on EMPYREAN Diffractometer with Cu K-alpha radiation ($k = 1.54056 \text{ \AA}$) operated at 45 kV and 30 mA. A Fourier transform infrared spectroscopy (FT-IR) spectrum was recorded on a shimadzu IR Affinity spectrophotometer.

3 Results and Discussion

The XRD patterns of bulk MoS₂, restacked MoS₂, MG1, MG2, MG3, and MG4 nanocomposite are shown in Fig. 1. The bulk MoS₂ exhibited all the sharp peaks can be readily indexed to a hexagonal phase (JCPDS no. 37-1492). The strong (002) peak with a d-spacing of 0.61 nm significances a well-stacked layered structure along the c-axis. In comparison, restacked MoS₂ shows a much shortened (002) peak and broadened peaks [22]. This specifies that the mean crystallite size and the number of layers along the c-axis are very smaller than those of bulk MoS₂. Moreover; the MoS₂-graphene composites essentially retain the position of the diffraction peaks of MoS₂, while the intensity becomes even weaker. This indicates that the incorporation of graphene further restrains the stacking of MoS₂ layers. Also, we can hardly detect the (002) diffraction peak of graphene at $2\theta = 240$, this denoting that the graphene nanosheets seldom stack together. It may be attributed to the layered MoS₂, which is anchored onto the surface of graphene and inhibits the stacking of graphene [23].

Fig. 1 XRD patterns of bulk MoS₂, restacked MoS₂, MG1, MG2, MG3, and MG4, nanocomposite



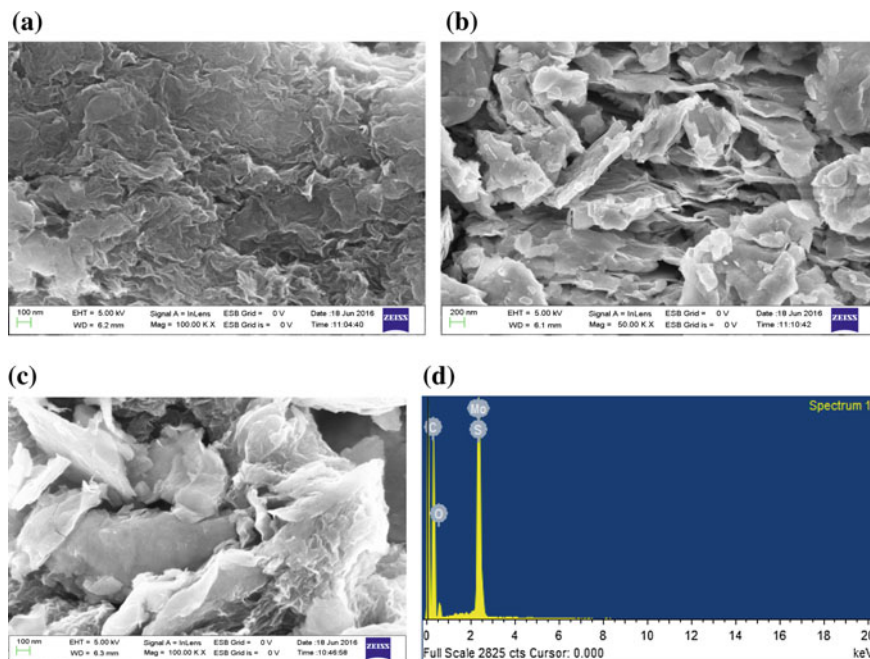


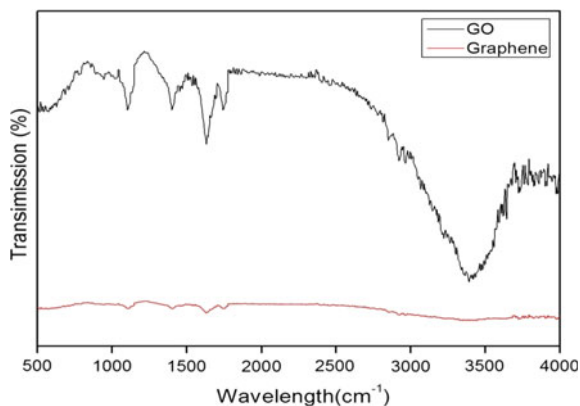
Fig. 2 FESEM images of **a** graphene and **b** restacked MoS₂ **c** MG4 nanocomposite **d** EDX of MG4 nanocomposite

The FE-SEM images of RGO and MoS₂ are shown in Fig. 2a, b. The RGO material displays randomly aggregated, thin, crumpled sheets closely associated with each other, while MoS₂ shows nanoflakes which are stacked together. Figure 2c shows the FESEM image of MG4. The morphologies of MG1, MG2 and MG3 are similar to that of MG4. It is clearly observed that the MoS₂ stacked together on the surface of RGO.

The EDX mapping of MoS₂-graphene nanocomposites is shown in Fig. 2 the studies confirm the presence of C, Mo, S, and a small quantity of O. Further demonstrates that MoS₂ is homogeneously distributed on the graphene substrate.

FT-IR spectra of the as-synthesized GO and graphene are shown in Fig. 3 the result obtained are similar to the result reported earlier [24]. The characteristic peaks of GO appear at around 3400 cm⁻¹(O-H), 1735 cm⁻¹ (C=O), 1620 cm⁻¹ (C=C), 1395 cm⁻¹ (C-O), and 1095 cm⁻¹(C-O), For graphene nanosheets, those vibrations become much weaker and even harder to be detected, signifying that the oxygen-containing groups have been largely removed.

Fig. 3 FTIR spectra of
a graphene oxide (GO) and
b graphene



4 Conclusion

In summary, MoS₂/graphene nanocomposite was successfully fabricated by a lithiation-assisted exfoliation method. Instrumental characterization shows that the MoS₂ is supported on the surface of graphene nanosheets and some of the interlayer spacing of MoS₂ is enlarged with the intercalation of graphene.

References

1. Shi Y, Huang J-K, Jin L, Hsu Y-T, Yu SF, Li L-J, Yang HY (1839) *Sci Rep* 2013:3
2. Chhowalla M, Shin HS, Eda G, Li L-J, Loh KP, Zhang H (2013) *Nat Chem* 5:263
3. Mak KF, He K, Lee C, Lee GH, Hone J, Heinz TF, Shan J (2013) *Nat Mater* 12:207
4. Huang X, Zeng Z, Zhang H (1934) *Chem Soc Rev* 2013:42
5. Li H, Wu J, Huang X, Lu G, Yang J, Lu X, Xiong Q, Zhang H (2013) *ACS Nano* 7:10344
6. Lv R, Li Q, Botello-Mendez AR, Hayashi T, Wang B, Berkdemir A, Hao Q, Elias AL, Cruz-Silva R, Gutierrez HR et al (2012) *Sci Rep* 2:586
7. Lim G, Chen Z, Clark J, Goh RGS, Ng W, Tan H, Friend RH, Ho PKH, Chua L (2011) *Nat Photonics* 5:554
8. Bao Q, Zhang H, Wang Y, Ni Z, Yan Y, Shen ZX, Loh KP, Tang DY (2009) *Adv Funct Mater* 19:3077
9. Liu Z, Ma L, Shi G, Zhou W, Gong Y, Lei S, Yang X, Zhang J, Yu J, Hackenberg KP et al (2013) *Nat Nanotechnol* 8:119
10. Jo I, Pettes MT, Kim J, Watanabe K, Taniguchi T, Yao Z, Shi L (2013) *Nano Lett* 13:550
11. Wilson JA, Yoffe AD (1969) *Adv Phys* 18:193; Wang QH, Kalantar-Zadeh K, Kis A, Coleman JN, Strano MS (2012) *Nat Nanotechnol* 7:699
12. Chhowalla M, Shin HS, Eda G, Li L-J, Loh KP, Zhang H (2013) *Nat Chem* 5:263
13. Mak KF, Lee C, Hone J, Shan J, Heinz TF (2010) *Phys Rev Lett* 105:136805
14. Splendiani A, Sun L, Zhang YB, Li TS, Kim J, Chim CY, Galli G, Wang F (2010) *Nano Lett* 10:1271
15. Geim AK, Novoselov KS (2007) *Nat Mater* 6:183–191
16. Zhu YW, Murali S, Cai WW, Li XS, Suk JW, Potts JR, Ruoff RS (2010) *Adv Mater* 22:3906–3924

17. Allen MJ, Tung VC, Kaner RB (2010) *Chem Rev* 110:132–145
18. Novoselov KS, Geim AK, Morozov SV, Jiang D, Zhang Y, Dubonos SV, Grigorieva IV, Firsov AA (2004) *Science* 306:666–669
19. Marcano DC, Kosynkin DV, Berlin JM, Sinitskii A, Sun Z, Slesarev A, Alemany LB, Lu W, Tour JM (2010) *Article*, vol 4
20. Stankovich S, Dikin DA, Piner RD, Kohlhaas KA, Kleinhammes A, Jia Y, Wu Y, Nguyen ST, Ruoff RS (2007) *Carbon* 45:1558–1565
21. Du G, Guo Z, Wang S, Zeng R, Chen Z, Liu H (2010) *Chem Commun* 46:1106
22. Chang K, Chen WX (2011) *ACS Nano* 5:4720
23. Park S, An J, Potts JR, Velamakanni A, Murali S, Ruoff RS (2011) *Carbon* 49:3019–3030
24. Lin LX, Zhang SW (2012) *J Mater Chem* 22:14385

Heat Transfer Intensification with Different Width Swirl Generator

Sarang S. Hole, Hanumant B. Narute and Vishal S. Jagadale

Keywords Reynolds number · Nusselt number · Heat transfer augmentation · Twist ratio · Swirl generator

1 Introduction

Shou-Shing and Huang [1] conducted experimental studies for heat transfer and pressure drop of laminar flow in horizontal tubes with/without longitudinal inserts. They reported that enhancement of heat transfer as compared to a conventional bare tube at the same Reynolds number to be a factor of 16 at $Re \leq 4000$, while a friction factor rise of only 4.5. Monheit [2] made a comparative study of the thermal performance of ordinary full-width full-length twisted tapes with tapes having modified surface configurations. Eiamsa-ard et al. [3] experimentally find the heat transfer rate and thermo hydraulic efficiency of the combined devices of twisted tape and wire coil by arranging in the form D-coil and DI-coil while the twisted tape was made with two different twist ratios. Dasmahapatra and Raja Rao [4] studied augmentation of heat transfer to viscous non-Newtonian fluids in laminar flow using full width interrupted twisted tapes under the uniform wall temperature condition.

S.S. Hole (✉) · H.B. Narute
Dhole Patil College of Engineering, Wagholi, India
e-mail: saranghole441089@gmail.com

V.S. Jagadale
SVERT's College of Engineering, Pandharpur, India

2 Methodology

2.1 Experimental Procedure

Initially the experiment is carried out without any insert (plain tube experiment). The working fluid air flows through the pipe section with least resistance. The experiment is carried out in similar fashion with straight tape inserts and twisted tape inserts with twist ratios 3 and 5 for widths of 26, 18 and 10 mm. the inserts are made of aluminium. Different types of inserts used are shown in Table 2.1. Each insert is taken and inserted into the test section axially. It is taken care that the strip does not scratch the inner wall of the pipe and get deformed. The presence of the insert in the pipe causes resistance to flow and increases turbulence. For the case of reduced width tapes, the gap between the tube wall and the tape was maintained constant throughout the tube length by brazing metal pins to the edges of the tape.

2.2 Heat Transfer Calculations

2.2.1 Reynolds Number Evaluation

Average Surface temperature of the working fluid, ($^{\circ}\text{C}$)

$$T_s = \frac{T_2 + T_3 + T_4 + T_5}{4}$$

Bulk temperature, ($^{\circ}\text{C}$)

$$T_b = \frac{T_1 + T_6}{2}$$

Equivalent height of air column, (m)

$$h_a = \frac{\rho_w \times h_w}{\rho_a}$$

Air discharge through test section, (m^3/s)

$$Q_a = C_d \times A_o \times \sqrt{2gh_a}$$

Table 1 Different types of inserts used

S. No.	Twist ratio (T.R)	Width of tape insert (mm)
1	3 and 5	26, 18 and 10
2	Straight tape	26, 18 and 10
3	Plain tube	–

where

A_0 Cross sectional area of orifice.

Air velocity through test section, (m/s)

$$V = \frac{Q_a}{A}$$

Reynolds number (experimental) for plain tube,

$$Re = \frac{V \times D}{\nu}$$

where

V Velocity of the fluid

ν Kinematic viscosity of the fluid.

Reynolds number (experimental) with tape inserts

$$Re = \frac{V \times D_h}{\nu}$$

where

D_h hydraulic diameter (m) = $\frac{4A}{P}$.

2.2.2 Nusselt Number Evaluation

For internal flow conditions, if Reynolds number (Re) is greater than 4000 then the flow is said to be turbulent. After the flow is decided i.e. laminar or turbulent then the Nusselt number can be calculated. Nusselt number for plain tube (theoretical) calculated below without considering friction which is theoretical Nusselt number and then calculated by considering friction which will be experimental Nusselt number.

$$Nu_{the} = 0.023Re^{0.8}Pr^{0.4}$$

This equation is called Dittus-Boelter equation.

Total heat transferred to air (Q), (W)

$$Q = m \times Cp \times (T_1 - T_6)$$

Experimental convective heat transfer coefficient, (W/m² K)

$$h = \frac{Q}{A(T_s - T_b)}$$

Nusselt number (experimental) for plain tube

$$\text{Nu} = \frac{h \times D}{K}$$

Nusselt number (experimental) with tape inserts

$$\text{Nu}_i = \frac{h \times D_h}{K}$$

2.2.3 Friction Factor Evaluation

Friction factor (theoretical) for plain tube

$$f_{\text{the}} = 0.25(1.82 \times \log_{10} \text{Re}_D - 1.64)^{-2}$$

This equation is used to find friction factor and is called as Petukhov equation for smooth surface.

Friction factor (experimental) for plain tube

$$f = \frac{\Delta P}{\frac{L}{D} \frac{V^2 \rho_a}{2}}$$

where,

ΔP pressure difference at both ends of test pipe.

L length of test pipe.

D Inner diameter of pipe.

Friction factor (experimental) with tape inserts

$$f_i = \frac{\Delta P}{\frac{L}{D_h} \frac{V^2 \rho_a}{2}}$$

where

D_h hydraulic diameter (m) = $\frac{4A}{P}$.

Over all enhancement ratio

$$\eta = \frac{\text{Nu}_i}{\text{Nu}} \left[\frac{f_i}{f} \right]^{0.333}$$

3 Thermal Characteristic

3.1 Heat Transfer Characteristics

The variation of Nusselt number with Reynolds number for straight tape inserts is shown in Fig. 1. Highest Nusselt number was obtained for full width straight tape. The mean heat transfer gain for straight tape inserts varied from 5 to 23% compared to plain tube. This is due to strong turbulence intensity generated by tape inserts leading to rapid mixing of the flow causing heat transfer enhancement.

The variations of friction factor with Reynolds number for straight tape inserts are presented in Fig. 2. It is observed that the friction factor gradually reduced with rise in Reynolds number. It is observed to be maximum for full width straight tape insert.

Fig. 1 Variation of Nusselt number with Reynolds number for straight tape inserts

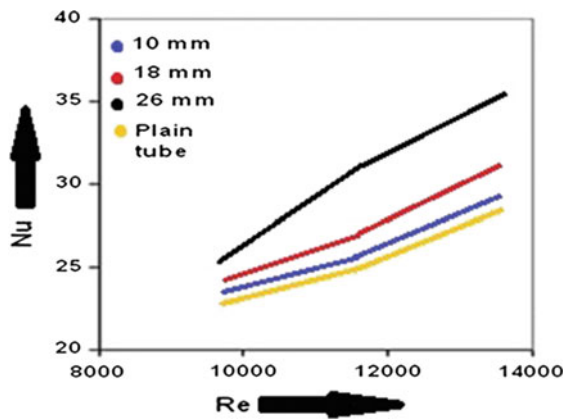


Fig. 2 Variation of friction factor with Reynolds number for straight inserts

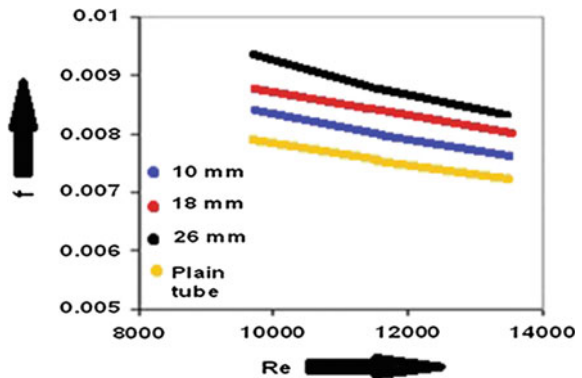


Fig. 3 Variation of Nusselt number with Reynolds number for twist ratio = 3

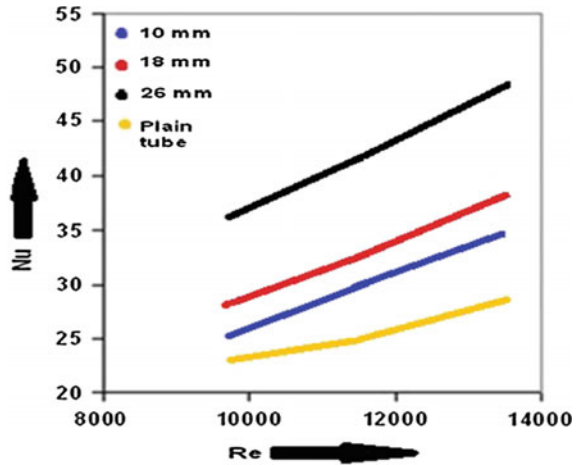
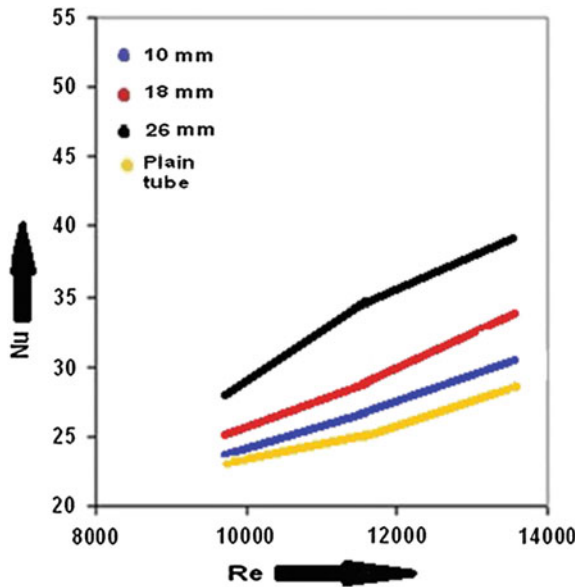


Fig. 4 Variation of Nusselt number with Reynolds number for twist ratio = 5



It is evident from Figs. 2 and 3, that when a twisted tape is inserted into a plain tube there is a significant improvement in Nusselt number, this enhancement is mainly due to the centrifugal forces resulting from the spiral motion of the fluid and partly due to the tape acting as fin. It is observed that the reduction in tape width causes reduction in Nusselt numbers as well as reduction in pressure drop. From Fig. 4, the percentage increase in Nusselt numbers for reduced width tapes compared to plain tube are about 12–24% and 21–35% respectively for tape widths of

10 and 18 respectively for twist ratio = 3. For full width tapes, the percentage increase is observed to be 60–68% compared to plain tube.

From Fig. 4, the percentage increase in Nusselt numbers for reduced width tapes compared to plain tube are about 3–7% and 8–17% respectively for tape widths of 10 and 18 mm respectively for twist ratio = 5. For full width tapes, the percentage increase is observed to be 29–38% compared to plain tube.

3.2 Overall Enhancement Characteristics

The overall enhancement ratio is useful to evaluate the quality of heat transfer enhancement obtained over plain tube at constant pumping power. It is found to be more than unity for all the tape inserts used. Variations of overall enhancement ratio η against Reynolds number for twist ratios 3 and 5 are shown in Figs. 5 and 6 respectively. It is observed that overall enhancement ratio tended to decrease gradually with the rise of Reynolds number for all twist ratios. The maximum value of overall enhancement ratio is 1.62 for full width twisted tape insert with twist ratio equal to 3.

It is seen in Fig. 4 that, for tapes of widths 26, 18 and 10 mm curves are of decreasing order in the range of Reynolds number from 7000 to 14,000. It is observed from Fig. 5 that even the tapes of 10 mm width have an η value of about 1.03–1.20 times over the plain tube. The gradual reduction of these curves basically represents the same performance of reduced width tapes as that of the full width

Fig. 5 Variation of overall enhancement with Reynolds number for twist ratio = 3

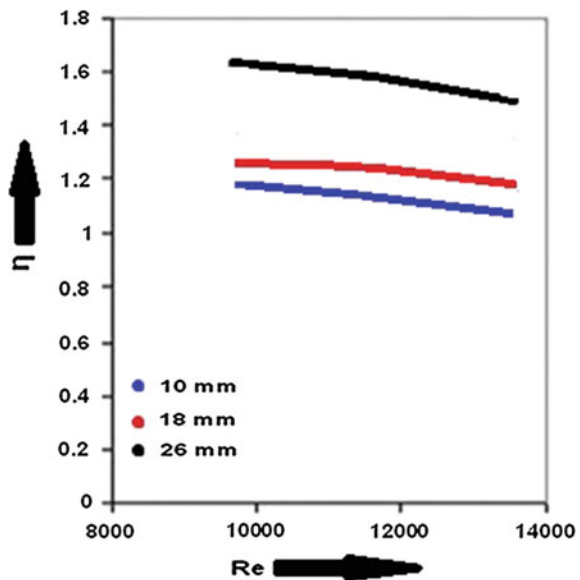
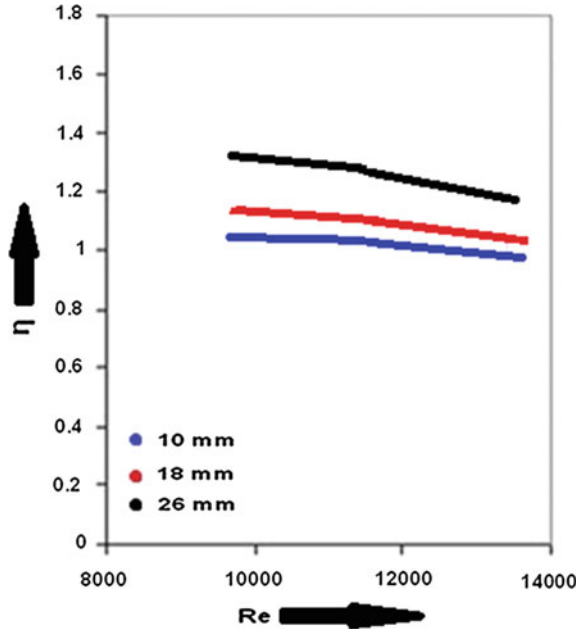


Fig. 6 Variation of overall enhancement with Reynolds number for twist ratio = 5



tape. Thus the same performance can be achieved using reduced width tapes with 15–61% material saving at higher Reynolds number and/or lower twist ratios.

4 Conclusions

This Paper present experimental investigation of reduced width twisted tape inserts to enhance the rate of heat transfer in a horizontal circular tube with inside diameter 27.5 mm with air as working fluid. The effects of parameters such as twist ratio, Reynolds number on the heat transfer and overall enhancement ratio are studied. The following conclusions can be drawn.

- The enhancement of heat transfer with twisted tape inserts as compared to plain tube varied from 35 to 49% for full width. This enhancement is mainly due to the centrifugal forces resulting from the spiral motion of the fluid.
- Reduction in tape width causes reduction in Nusselt numbers as well as friction factors. The maximum friction factor rise was about 19% for 26 mm and only 17.3% for reduced width inserts compared to plain tube.
- The overall enhancement ratio of the tubes with full width twisted tape inserts is 1.62 for full width—26 mm.
- Nusselt numbers decreased by a maximum of 29%, for tape widths of 10 mm, respectively compared to full width twisted tape inserts.

References

1. Shou-Shing H, Huang IW (2000) Heat transfer and pressure drop of laminar flow in horizontal tubes with/without longitudinal inserts. *J Heat Transfer* 122:465–475
2. Monheit M (1987) Experimental evaluation of the convective characteristics of tubes with twisted tape inserts. *Adv Enhan Heat Transf AMSE* 68:11–18
3. Eiamsa-ard S, Nivesrangsarn P, Chokphoemphun S, Promvongse P (2010) Influence of combined non-uniform wire coil and twisted tape inserts on thermal performance characteristic. *Int Commun Heat Transf* 37:850–856
4. Dasmahapatra JK, Raja Rao M (1991) Laminar flow heat transfer to generalized power law fluids inside circular tubes fitted with regularly spaced twisted tape elements for uniform wall temperature condition. *Fundam Heat Transf Non-Newton Fluids ASME* 174:51–58

Synthesis and Characterization of ZnO Nanorod Array on FTO Glass by Using Hydrothermal Method

H.P. Suryawanshi, S.G. Bachhav and D.R. Patil

Keywords ZnO · Hydrothermal · ZnO nanorod · Nanorod array · ZnO nanowires

1 Introduction

ZnO is a wide bandgap semiconductor with a direct bandgap of about 3.37 eV and relatively high exciton binding energy (60 meV) at room temperature. ZnO has attracted increasing interest due to its unique ability to form a variety of nanostructures such as nanowires, nanoribbons, nanobelts, nano combs, etc. The ZnO in the form of nanorods (NRs) or nanowires arrays vertically arranged on the substrate has unique properties. The ZnO nanorods or nanowires array have high confinement effect on photons and carriers, so it has novel optical and electrical properties.

The ZnO nanorods can be synthesized by a gas phase method such as Vapor-liquid-solid (VLS) growth [1], chemical vapor deposition (CVD) [2], metal organic chemical vapor deposition (MOCVD) [3], physical vapour deposition (PVD) [4], Hydrothermal [5] etc. It is reported that these methods are costly, complicated and require high temperature. On the other hand solution phase synthesis method in which the growth reactions are carried out in aqueous or organic solution. It requires relatively low temperature (<200 °C). Among several approaches, hydrothermal synthesis method is effective due to the many point defects of ZnO nanowires mainly due to the presence of oxygen vacancies. Baruah et al. [6] synthesized ZnO nanowires by using a hydrothermal method, and they showed that photocatalytic activities were enhanced by creating defects in the crystal lattice

H.P. Suryawanshi · S.G. Bachhav · D.R. Patil (✉)
Nanomaterial Research Lab, R. C. Patel Arts, Commerce & Science College,
Shirpur, Dhule 425405, Maharashtra, India
e-mail: dr.drpatil@gmail.com

H.P. Suryawanshi
e-mail: harish.suryawanshi32@gmail.com

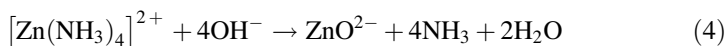
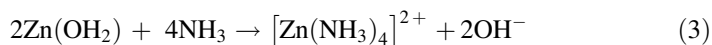
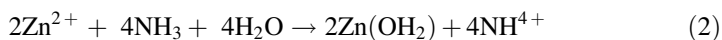
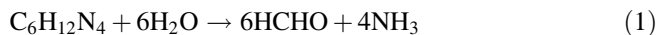
without doping with transition metals. Xu et al. [7] used the hydrothermal method to develop high scale orientation of ZnO nanowires array using Zinc foil at 60 °C without using any oxidant, seed layer and catalyst and subsequently the photocatalytic activity of ZnO nanowires array was studied for the degradation of naphthalene in air. Kenanakis and Katsarakis [8] was studied the photocatalytic activity of ZnO nanowire grown on seeded glass substrate. The ZnO nanowire was grown with hydrothermal method and its photocatalytic activity also studied for the degradation of stearic acid. Wang et al. [9] were synthesized well aligned ZnO nanowires using hydrothermal growth process. He studied the effect of the seed layer, colloid concentration, precursor concentration on the alignment control of ZnO nanorod array. The alignment of ZnO nanorod array was controlled by the colloid concentration of seed layer. Al-Sabahi et al. [10] were synthesized ZnO nanorods using microwave hydrothermal process. The density of surface defect states in ZnO nanorods was controlled by annealing the nanorods at moderate temperature. The PL and XPS analysis showed maximum surface defect at 350 °C. The average length and diameter of ZnO nanorods were found 4.3 μm and 100 ± 10 nm. The ZnO nanorods with the utmost surface defect show the highest photocatalytic degradation rate for phenol which is 72% of 5 h duration.

In the present work, well-aligned one-dimensional ZnO nanorod arrays were synthesized by a simple hydrothermal process on the FTO glass substrate. The effect of temperature and growth time on the morphology of ZnO nanorods arrays was studied.

2 Experimental

To Synthesize ZnO nanorods by hydrothermal method. Initially, seed layer was deposited on Fluorine doped Tin oxide (FTO) glass substrate with 10 mM zinc acetate in ethanol. For this, a substrate was coated by spin coating at 3000 rpm for few minute and repeat this step for four times and subsequently the substrate was heated at 350 °C for 30 min for better adhesion of seed layer. In next step was the ZnO nanorods were grown via hydrothermal process at 95 °C for 2 h in the aqueous solution prepared by mixing 20 mM of zinc nitrate ($\text{Zn}(\text{NO}_3)_2$) and hexamine (HMTA) in the Teflon jar. The jar was inserted in stainless steel autoclave for the particular period. After hydrothermal reaction the reactor cooled down to room temperature and substrate was washed with plenty of distilled water.

The reaction mechanism of ZnO nanorod under hydrothermal synthesis was given below. The ZnO nanorods were grown on the quartz glass substrate. The HMT was hydrolyzed at the temperature of 700 °C, and it produced ammonia (Eq. 1). Ammonia reacts with Zinc ions to produce $\text{Zn}(\text{OH})_2$ (Eq. 2). It further reacts with ammonia to form ammonia compound $[\text{Zn}(\text{NH}_3)_4]^{2+}$ (Eq. 3). This complex again reacts with OH^- to obtained ZnO molecule (Eqs. 4 and 5)



2.1 Characterizations

The morphology of seed layer and ZnO nanorods array were observed by field-emission scanning electron microscope (FE-SEM Hitachi S-4800 Type-II). The element study was confirmed by EDAX analysis combined with FE-SEM. The optical property was examined by using UV-Visible spectrophotometer (Shimadzu UV-2450).

3 Results and Discussion

The FE-SEM images of synthesized ZnO nanorods array on FTO glass substrates are shown in Fig. 1a. The diameters of nanorods are observed to be about 100 nm with hexagonal structure. The FE-SEM images clearly indicate that the ZnO nanorods grown on a glass substrate are quite aligned. The magnifying images of ZnO nanorod are shown in Fig. 1b.

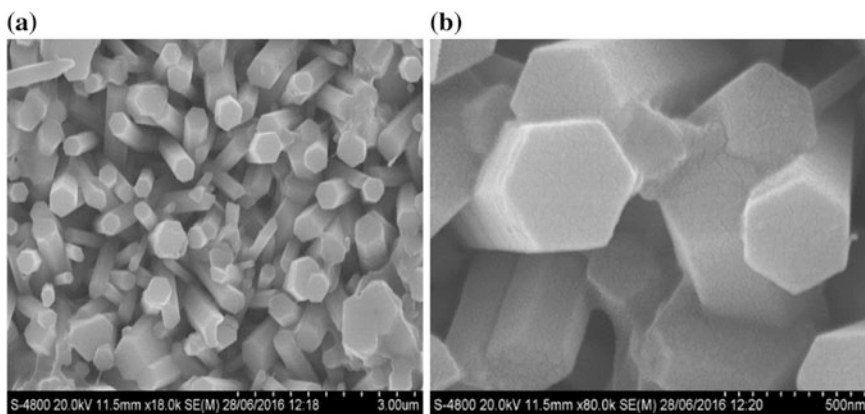
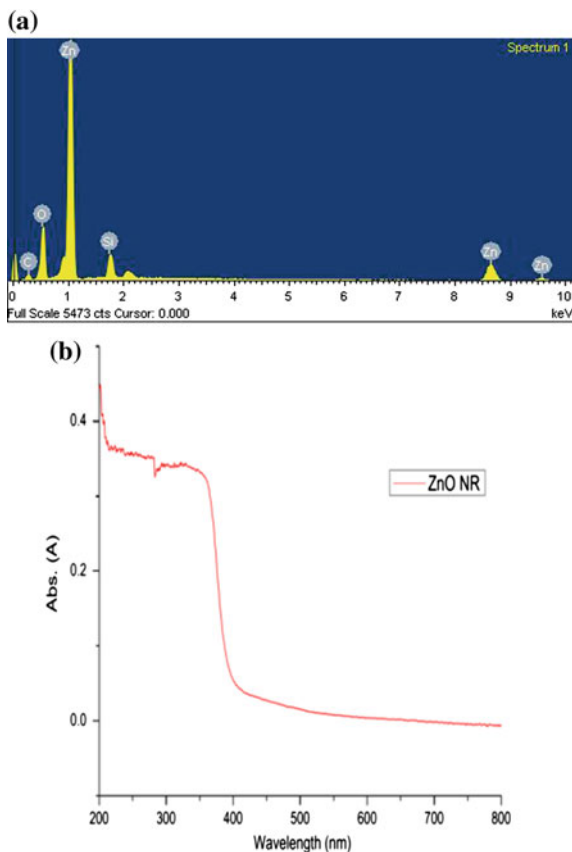


Fig. 1 a FE-SEM image of ZnO nanorods. b Magnifying image of ZnO nanorods

Fig. 2 **a** EDAX image of ZnO nanorod. **b** UV-Vis spectra of ZnO nanorods array



The EDAX analysis is shown in Fig. 2a. The characteristics peaks of only Zinc and Oxygen was only observed, and no other peaks of impurity were observed. The presences of small intensity peaks correspond to the gold coating of the sample.

The UV-Vis spectrum of ZnO nanowires has been represented in Fig. 2b. It has been observed that the maximum absorbance occurred in UV region, which attributed to the fundamental band gap of ZnO.

4 Conclusions

In this work the ZnO nanorods array was successfully obtained by the hydrothermal method. It showed vertically grown ZnO nanorods arrays are hexagonal and aligned structure. The diameters are in the range of 120–180 nm and length 1 μ m respectively. Only Zinc and oxygen are present in the nanorods array substrate. Therefore, it has been predicted that nanostructure ZnO is low cost and an

environment-friendly solution can be used for photocatalyst, solar cell, photoelectrochemical cell and gas sensing devices.

Acknowledgements The authors are thankful to management of R.C. Patel Education Trusts, Shirpur for providing research facilities.

References

1. Petersen EW, Likovich EM, Russell KJ, Narayanamurti V (2009) Growth of ZnO nanowires catalyzed by size-dependent melting of Au nanoparticles. *Nanotechnology* 20(40), Article ID 405603
2. Protasova LN, Rebrov EV, Choy KL (2011) ZnO based nanowires grown by chemical vapour deposition for selective hydrogenation of acetylene alcohols. *Catal Sci Technol* 1(5):768–777
3. Ashraf SA, Jones C, Bacsa J (2011) MOCVD of vertically aligned ZnO nanowires using bidentate ether adducts of dimethylzinc. *Chem Vapor Deposition* 17(1–3):45–53
4. Wang L, Zhang X, Zhao S, Zhou G, Zhou Y, Qi J (2005) Synthesis of well-aligned ZnO nanowires by simple physical vapor deposition on c-oriented ZnO thin films without catalysts or additives. *Appl Phys Lett* 86(2), Article ID 024108
5. Yengantiwar A, Sharma R, Game O, Banpurkar A (2011) Growth of aligned ZnO nanorods array on ITO for dye sensitized solar cell. *Curr Appl Phys* 11:S113–S116
6. Baruah S, Rafique RF, Dutta J (2008) Visible light photocatalysis by tailoring crystal defects in zinc oxide nanostructures. *NANO: Brief Rep Rev* 3:399–407
7. Xu F, Yuan Z, Du G, Ren T (2006) Simple approach to highly oriented ZnO nanowire arrays: large-scale growth, photoluminescence and photocatalytic properties. *Nanotechnology* 17:588–594
8. Kenanakis G, Katsarakis N (2010) Light-induced photocatalytic degradation of stearic acid by c-axis oriented ZnO nanowires. *Appl Catal A: Gen* 378:227–233
9. Wang M, Xing C, Cao K (2014) Alignment-controlled hydrothermal growth of well-aligned ZnO nanorod arrays. *J Phys Chem Solid* 75:808–817
10. Al-Sabahi J, Bora T, Al-Abri M, Datta J (2016) Controlled defect of ZnO nanorods for efficient visible light photocatalytic degradation of phenol. *Material* 9:238–248

Design and In-Vitro Evaluation of Nicorindil Biphasic Drug Delivery System for Angina Pectoris

H.B. Bansode, O.S. Shende, P.B. Gurav and R.G. Kulkarni

Keywords Biphasic tablet · Nicorandil · Olibanum gum · Tamarind seed polysaccharide

1 Introduction

Pharmacological therapies either require or benefit from the administration of drugs in a sequential manner. These combined formulations function from a single dosage form, which simplifies the therapy and reduces or eliminates the chances of improper administration. Bilayer formulations carry more than one drug and deliver each of them without any pharmacokinetic or dynamic interactions, with their individual rate of delivery (immediate, timed or sustained). Bilayer tablet technology is improved beneficial technology to overcome the shortcoming of the single layered tablet. Usually conventional dosage form produce wide ranging fluctuation in drug concentration in the blood stream and tissues with consequent undesirable toxicity and poor efficiency. The goal in designing sustained or controlled delivery systems is to reduce the frequency of the dosing or to increase effectiveness of the drug by localization at the site of action, reducing the dose required or providing uniform drug delivery. The primary objective of sustained release drug delivery is to ensure safety and to improve efficacy of drugs as well as patient compliance. Bilayer tablet is suitable for sequential release of two drugs in combination, separate two incompatible substances and also for sustained release tablet in which one layer is immediate release as initial dose and second layer is maintenance dose [1].

H.B. Bansode (✉) · O.S. Shende · P.B. Gurav
Department of Pharmaceutics, SVERI's College of Pharmacy, Pandharpur, India
e-mail: hemant07bansode@gmail.com

R.G. Kulkarni
Department of Pharmaceutical Chemistry, SVERI's College of Pharmacy,
Pandharpur, India

Bi-layer tablet is suitable for sequential release of two drugs in combination, separate two incompatible substances and also for sustained release tablet in which one layer is immediate release as initial dose and second layer is maintenance dose. There is various application of the bi-layer tablet it consist of monolithic partially coated or multilayered matrices. In the case of bi-layered tablets drug release can be rendered almost unidirectional if the drug can be incorporated in the upper non-adhesive layer its delivery occurs into the whole oral cavity. Bilayer tablet is new era for the successful development of controlled release formulation along with various features to provide a way of successful drug delivery system. Advantages of bilayer tablet are as they are used as an extension of a conventional technology, Potential use of single entity feed granules, Separation of incompatible components, patient compliance is enhanced leading to improved drug regimen efficacy, patient convenience is improved because fewer daily doses are required compared to traditional delivery system, maintain physical and chemical stability. Certain limitation of the same, adds complexity and bilayer rotary presses are expensive, insufficient hardness, layer separation, reduced yield, inaccurate individual layer weight control, cross contamination between the layers [2, 3]. So need of bilayer tablet for the administration of fixed dose combinations of different APIs, prolong the drug product life cycle, buccal/mucoadhesive delivery systems; fabricate novel drug deliver, systems such as chewing device and floating tablets for gastro-retentive drug delivery. controlling the delivery rate of either single or two different active pharmaceutical ingredients, to modify the total surface area available for API layer either by sandwiching with one or two in active layers in order to achieve erodible barriers for modified release, to separate incompatible Active pharmaceutical ingredient (APIs) from each other, to control the release of API from one layer by utilizing the functional property of the other layer (such as, osmotic property) [4]. General properties are it should have graceful product identity free of defects like chips, cracks, discoloration, and contamination: should have sufficient strength to with stand mechanical shock during its production, packaging, shipping and dispensing, should have physical and chemical stability, the bi-layer tablet must release drug in an expectable and reproducible manner, must have a chemical stability shelf life, so as not to follow alteration of the medicinal agents.

2 Materials

Nicorandil is obtained as gift sample from Okasa Pharma, Satara Microcrystalline cellulose pH 102 and Croscarmellose sodium from Loba Chemie., Mumbai.

3.3 Preparation of Multiple Compressed Tablets

For the preparation of the biphasic delivery system the die of tableting machine was progressively filled by hand with the weighed amount (290 mg) of the fast release component. One mini-tablet (120 mg) was putted on that component and again 290 mg of fast release component filled by hand prior to compression. Multiple compressed tablets i.e. Biphasic formulations, weighing 700 ± 10 mg were prepared by direct compression, with concave punch and dies with 12 mm diameter.

3.4 Evaluation of Tablets [6, 7]

The important parameters in the evaluation of tablets can be divided into Physical and chemical parameters.

3.4.1 Weight Variation

Twenty tablets were weighted individually and the average weight was calculated. The individual weights were then compared with the average weight, The tablets passes the test if not more than two tablets fall the percentage limit and none of the tablets differ by more than double the percentage limit given below.

Average weight of the tablet	Percentage deviation
80 mg or less	± 10
More than 80 mg and less than 250 mg	± 7.5
250 mg or more	± 5.0

3.4.2 In-Vitro Dissolution Studies

The in vitro dissolution profile of each formulation was determined on a USP XXIV dissolution apparatus type II. Under pH condition simulative of the gastrointestinal tract. 900 ml of dissolution media was taken. The paddle rotation was adjusted to 50 rpm, the temperature being maintained at 37 ± 0.5 °C throughout the study. A buffer of pH 1.2 was used as dissolution medium for the first 1 h and after that dissolution medium was replaced by phosphate buffer 6.8 for remaining time period. One tablet was used in each test. 1 ml of the sample of dissolution medium was withdrawn and replaced with the fresh dissolution medium. Samples were filtered through Whatmann filter paper No. 41 and were analyzed spectrophotometrically at 218 nm [7, 8].

4 Results and Discussion

4.1 Friability

To determine the absolute strength of tablet, hardness testing along with friability is necessary and it is one of the early detection method for capping and lamination. Friability was related to tablet ability to withstand both shock and abrasion without physical damage during the handling of manufacturing, packaging, shipment and consumer use. Friability of formulations F1, F2, F3, F4, F5, F6 and F7 were, 0.579, 0.581, 0.286, 0.435, 0.291, 0.507 and 0.501. The result shown in Table 2.

4.2 Hardness

The hardness of tablet depend upon the flow properties. The tablet hardness was found to be in the range of 4.4–5.5 kg/cm². The highest hardness was 5.5 kg/cm² of F7 formulation, and lowest was for F4 formulations were 4.4 kg/cm². The result shown in Table 2.

4.3 Thickness

The thickness was found to be 4.95–5.48 mm.

The composition of the immediate release component should provide a hard and rapidly disintegrating tablet at low compression forces, and the compaction of the biphasic tablet system should not affect the structure of the release behaviour of these mini-tablets. Visual inspection of the fracture surfaces of the biphasic system revealed that the appearance of the mini-tablets in the compact system was similar to the original mini-tablets. The mini-tablets tended to keep their integrity when

Table 2 Evaluation of tablets

Formulation code	% Friability	Hardness (kg/cm ²)	Thickness	Weight variation	Drug content (mg) (%)
F1	0.579	5.4 ± 0.22	5.31 ± 0.18	694.03 ± 2.65	95.45
F2	0.581	4.5 ± 0.21	5.13 ± 0.22	692.0 ± 2.83	95.45
F3	0.286	5.2 ± 0.27	4.95 ± 0.23	700.0 ± 2.32	93.75
F4	0.435	4.4 ± 0.30	5.09 ± 0.24	692.50 ± 1.84	91.02
F5	0.291	4.8 ± 0.29	4.98 ± 0.27	687.99 ± 2.06	96.70
F6	0.507	5.1 ± 0.26	5.39 ± 0.28	692.0 ± 1.87	99.43
F7	0.501	5.5 ± 0.22	5.48 ± 0.26	701.0 ± 2.18	94.31

Table 3 In-vitro dissolution profile formulations F1 in 0.1 N HCL pH 1.2 & PBS pH 6.8

S. No.	Time (min)	Cumulative amount of drug released						
		F1	F2	F3	F4	F5	F6	F7
1	0	0	0	0	0	0	0	0
2	15	13.71	12.85	13.52	15.28	16.07	16.45	14.76
3	30	23.14	21.85	24.87	26.06	25.80	26.33	26.89
4	45	33.42	31.71	33.6	34.15	33.84	33.73	36.43
5	60	47.14	51.00	48.87	51.68	49.49	48.96	51.18
6	120	60.00	63.85	62.4	65.16	63.03	62.94	66.36
7	180	68.14	66.42	69.81	73.25	74.03	74.05	77.63
8	240	81.00	80.57	74.61	88.08	84.60	83.52	80.24
9	420	93.85	88.28	80.72	96.17	90.52	84.75	82.84

compacted and remained as coherent individual units after the process of tableting. The result shown in Table 3.

4.4 Drug Content

Drug content for all the formulations was determined by UV method and found to be in the range of 91.02–99.43%. Drug content estimation data for all the formulations was found to be within prescribed limits (NLT 91.0% and NMT 107.5%). The result shown in Table 2.

4.5 IR Spectra of F4 Formulation

The prominent peaks of Nicorandil was observed in the region of 1654 cm^{-1} due to the $-\text{OH}$ stretching, a peak at 1609 cm^{-1} due to $\text{N}-\text{H}$ stretching and a peak 1388 cm^{-1} due to aromatic $\text{O}-\text{H}$ stretching. Peaks at 2981 cm^{-1} showed presence of aliphatic $\text{C}-\text{H}$ stretching, 1577 and 1454 cm^{-1} due to $\text{C}=\text{C}$ aromatic stretching. The IR spectra of physical mixture of the drug with Croscarmellose Sodium showed the shape and location of peaks in the region 3362 cm^{-1} $-\text{OH}$ stretching, a peak at 3292 cm^{-1} due to $\text{N}-\text{H}$ stretching had dramatically not changed. Same results were found in case of Sodium alginate grades. This suggests that drug interactions were totally absent (Fig. 1).

The Nicorandil was profile from biphasic tablet systems system gives a biphasic drug release. The drug release profile characterized by a burst release, followed by a sustained release phase. Biphasic tablet system was rapidly disintegrated into both powder and individual sustained release mini-tablets, in which powder releasing the immediate dose of drug that is loading dose of drug. The immediate release

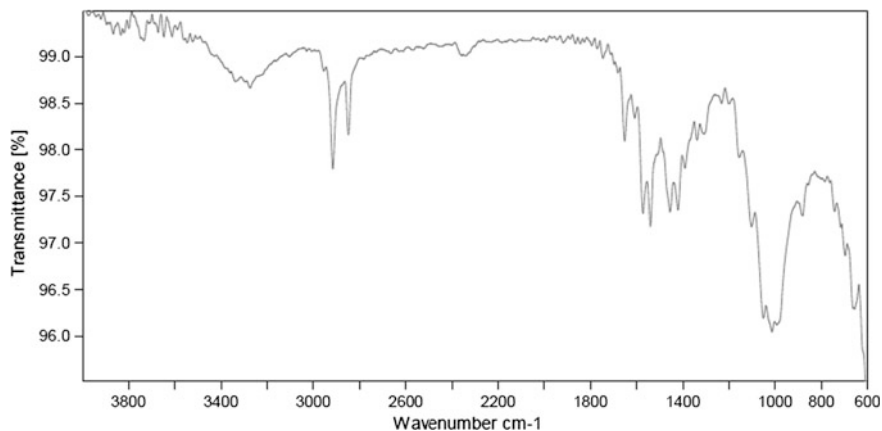


Fig. 1 IR spectra of F4 formulation

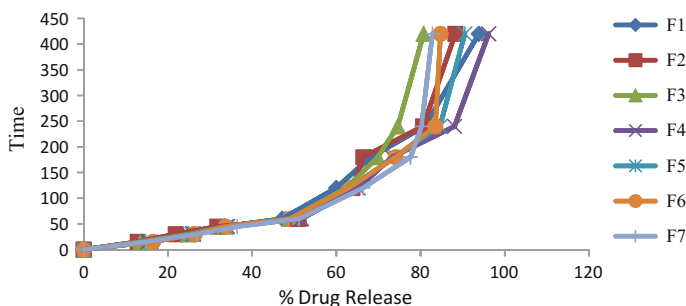


Fig. 2 In vitro drug release study of Nicorandil bilayer tablets

component was disintegrated within few minutes (less than 2 min) due to contact of sodium croscarmellose with dissolution media it get swells very quickly. The percentage of Nicorandil was released was different during initial phase and latter phase. The latter phase was characterized by lag time which was depends on the polymer concentration of the mini-tablets.

All formulation gave sustained drug release up to 7–8 h. Ideally, drug release should not be affected by the compaction process. The aim of compaction of mini-tablets is to convert Multi-unit dosage forms into Single-unit dosage form having same properties, as the individual mini-tablets. Percentage cumulative drug release for formulation F4 having 96.17% drug release and F3 having lowest 80.72% (Fig. 2).

The Nicorandil was profile from biphasic tablet systems system gives a biphasic drug release. The drug release profile characterized by a burst release, followed by a sustained release phase. Biphasic tablet system was rapidly disintegrated into both powder and individual sustained release mini-tablets, in which powder releasing the

immediate dose of drug that is loading dose of drug. The immediate release component was disintegrated within few minutes (less than 2 min) due to contact of sodium croscarmellose with dissolution media it get swells very quickly. The percentage of Nicorandil was released was different during initial phase and latter phase. The latter phase was characterized by lag time which was depends on the polymer concentration of the mini-tablets. All formulation gave sustained drug release up to 7–8 h. Ideally, drug release should not be affected by the compaction process. The aim of compaction of mini-tablets is to convert Multi-unit dosage forms into Single-unit dosage form having same properties, as the individual mini-tablets. Percentage cumulative drug release for formulation F4 having 96.17% drug release and F3 having lowest 80.72%.

References

1. Kumar AH, Kavitha K, Kumar SA, Kumar MP, Singh SJ (2013) Novel approach of Bilayer tech.—a review. *Int J Pharm Chem Bio Sci* 3(3):887–893
2. Mishra A, Bhatt GK, Kothiyal P (2013) Review: Bilayer tablet and evaluation. *Int J Drug Res Tech* 3(2):21–30
3. Verma R, Devre K, Gangarde T (2014) Bi-layer tablets for various drugs: a review. *Scholars Acad J Pharm* 3(3):271–279
4. Panchal HA, Tiwari AK (2012) A novel approach of Bilayer tablet tech: a review. *Int Res J Pharm* 3(5):44–49
5. Karwa P, Kasture PV (2011) Formulation and in vitro evaluation of Bilayer tablets of zolpidem tartrate for biphasic drug release. *Int J Pharm Tech Res* 3(4):1919–1929
6. Reddy P, Rao DV, Kumar RK (2013) Bilayer tech—an emerging trend: a review. *Int J Res Dev Pharm Life Sci* 2(3):404–411
7. Karthikeyan D, Vijayalaxmi A, Kumar CS (2013) Formulation and evaluation of biphasic delivery system of aceclofenac mini-tablets in hard gelatin capsules. *Int J Novel Trends Pharm Sci* 3(2):39–45
8. Rahman S, Abdullah AM, Sharmin F, Islam SM, Reza S (2012) Formulation and evaluation of bi-layered sustained release matrix tablets of tramadol hydrochloride. *J App Pharm Sci* 2(6):129–134
9. Babu AK, Reddy VR, Reddy N, Vidyasagar J (2010) Evaluating the post compression parameter of ibuprofen by using super disintegrants. *An Int J Adv Pharm Sci* 1(2):247–253

SILAR Synthesis and Cyclic Voltammetric Study of PPy-Cu(OH)₂ Composite Flexible Electrodes for Supercapacitors

Amarsingh V. Thakur, Savita D. Sonawane, Pritesh C. Chavan,
Dheeraj C. Muttin and Balkrishna J. Lokhande

Keywords Polypyrrole · Thin films · SILAR · Electron microscopy · Electrochemical properties · Energy storage

1 Introduction

Energy dependent world inevitably relies on the high energy and high power storage devices. Electrochemical super capacitors are applicable in hybrid electric vehicles, fuel cells and electronic devices etc. [1]. In double layer capacitors, the energy is stored in an electrostatic way at the interface between a solid electrode and electrolyte, while in pseudo-capacitors it is in an electrochemical way by fast faradic reactions at the solid electrode surface at appropriate potential [2, 3]. Conducting polymers have been investigated by the scientists for their use as electrode materials due to their ease of production, no constraints on the size and charge storage throughout the volume and conductivity by means of the shifting of conjugate bonds [4, 5]. Several conducting polymers like polyaniline (PANI) [6], polythiophene (PTh) [7], polyethylene dioxythiophene (PEDOT) have been used as electrode materials for the supercapacitors. Polypyrrole (PPy) has few salient features viz. low oxidation potential, water soluble monomer, high charge storage ability, good conductivity. PPy shows electrical conductivity by means of free

A.V. Thakur · B.J. Lokhande (✉)
School of Physical Sciences, Solapur University, Solapur 413255,
Maharashtra, India
e-mail: bjlokhande@yahoo.com

S.D. Sonawane
SVERI College of Pharmacy, Pandharpur, Maharashtra, India

P.C. Chavan
SVERI College of Engineering, Pandharpur, Maharashtra, India

D.C. Muttin
SKN Sinhgad College of Engineering, Korti, Pandharpur, Maharashtra, India
e-mail: radheyrajput7@gmail.com

electron movements across the conjugate double bonds. Thus PPy has been used as electrode material for the super capacitive energy and power applications [8]. Shinde et al. [9] reported the successful synthesis of pristine PPy thin film electrodes exhibiting nanograin like morphology showing maximum specific capacitance of 329 F/g in 0.5M H₂SO₄. Shi and Zhitomirsky [10] reported similar kind of morphology for pure PPy synthesized by Electrodeposition. Metal oxides have been used as electrode materials for supercapacitors [11–15]. Cu oxides and hydroxides are being one of the best choices [16]. Zang et al. reported the synthesis of CuO with flowerlike nanostructure giving SC 133.6 F/g in KOH [16, 17]. Lokhande et al. prepared the thin film of CuO multilayer nanosheet, shows SC 43 F/g in Na₂SO₄ [18, 19]. Wang et al. [20] prepared CuO nanosheet arrays grown on nickel foam gives specific capacitance (SC) 569 F/g in KOH. Jadhav et al. [21] prepared anodized copper hydroxide nanostructure with SC 230 F/g. The inquisitiveness to observe the effect of hybridization of PPy with different metal oxides has forced the researchers throughout the universe to try different combinations of PPy and metal oxide [22]. The incorporation of CuO into PPy matrix was attempted for enhanced stability, high electrical conductivity, and superior electrochemical performance. Yin et al. synthesized the CuO/PPy 1D core-shell nanohybrids as the anode for Lithium ion batteries by wire templet method showing the initial capacity 991 mAh/g [23]. The hydroxide phase of metal gives more specific capacitance oxide. Successive ionic layer adsorption by reaction (SILAR) method was preferred over all the other methods of thin film deposition like chemical bath deposition [9], chemical vapor deposition, electrodeposition [24], spray pyrolysis [25, 26], sol-gel, spin coating etc. The advantages of SILAR over the other methods are (i) It put no constraints on the size of substrates, (ii) It does not need any special mechanical arrangements like the vacuum, temperature management, spray unit etc. and (iii) It does not cause evolution of any poisonous gas by heating hence it is eco-friendly.

Very few literature survey is observed on the synthesis of PPy-Cu(OH)₂ nano-hybrids by SILAR and their electrochemical study using cyclic voltammetry (CV), chronopotentiometry (CP) and electrochemical impedance spectroscopy (EIS). Thus present research work aims to grow the PPy-Cu(OH)₂ hybrid thin films on stainless steel substrates by SILAR technique. It was interesting to see an effect of dip time on their electrochemical behavior hence work was extended in that way.

2 Experimentation

2.1 Precursors

All the chemicals used for the synthesis were of analytical grade and used without any further purification. Extra pure pyrrole and H₂SO₄ were purchased from Sigma-Aldrich while Cu(NO₃)₂ and H₂O₂ (30 wt%) were purchased from SD fine chemicals. H₂O₂ used without any dilution.

2.2 Electrode Preparation

In the electrode preparation—Thin strips of stainless steel (SS) of 304 grade (size = 1 cm × 5 cm) were used as conducting substrates. All the substrates were mirror polished using silicon carbide polish paper (grade 600) to get the rough finish. These substrates cleaned ultrasonically for 20 min in double distilled water at 310 K. As PPy material adheres more to the stainless steel treated with the nitric acid [27], substrates were again treated with the dilute HNO₃ solution.

After the pre-treatments, substrates were first immersed in 0.1 M pyrrole (Py) dissolved in 0.5 M H₂SO₄ for variable time periods (5–20 s), where the polaron cations were adsorbed on the surface of SS substrates. Then these substrates were immersed in 30 wt% H₂O₂ bath for 30 s. After that, these substrates were immersed for different time periods (40–55 s) in 0.1 M of Cu (NO₃)₂ dissolved in 0.5 M H₂SO₄, which is followed by the immersion in the H₂O₂ bath again for 30 s. Finally, these substrates were washed vigorously and pressure cleaned by the jets of double distilled water to remove loosely bound species from electrode material, in order to get the uniform coating of electrode material on the substrate surface. This completes one SILAR deposition cycle. 120 of such SILAR deposition cycles were carried out to study the effect of cycle numbers on the thickness and electrochemical behavior of the film. Deposition parameters and sample codes are given in Table 1.

2.3 Characterizations

2.3.1 Structural Characterizations

X-ray diffractometer (Ultima IV Rigaku D/max2550Vb +18 kw with CuK α , λ = 1.54056 Å) in the range of diffraction angle (2 θ) 10°–90°, FTIR spectrophotometer (Nicolet iS 10, Thermo scientific, USA) was used to verify the formation of polypyrrole, Scanning electron microscope (SEM S4300 HITACHI, Japan) was used to check the surface morphology. Weight of the deposited material was

Table 1 Sample codes with preparative parameters for electrode samples prepared using acidic solutions of Pyrrole and CuNO₃, and their S.C. values at 5 mV s⁻¹ in 0.5 M H₂SO₄

Sample codes	Dip time in 0.1 M pyrrole Dt ₁ (s)	Dip time in oxidizer H ₂ O ₂ (s)	Dip time in 0.1 M CuSO ₄ Dt ₂ (s)	Dip time in oxidizer H ₂ O ₂ (s)	Dip cycles Dc	Specific capacitance SC (F/g)
N ₁	05	30	55	30	120	35.51
N ₂	10	30	50	30	120	42.00
N ₃	15	30	45	30	120	45.02
N ₄	20	30	40	30	120	56.05

measured by weight difference method using high accuracy analytical microbalance (Tapson-100TS, USA) with least count 10^{-2} mg.

2.3.2 Electrochemical Characterizations

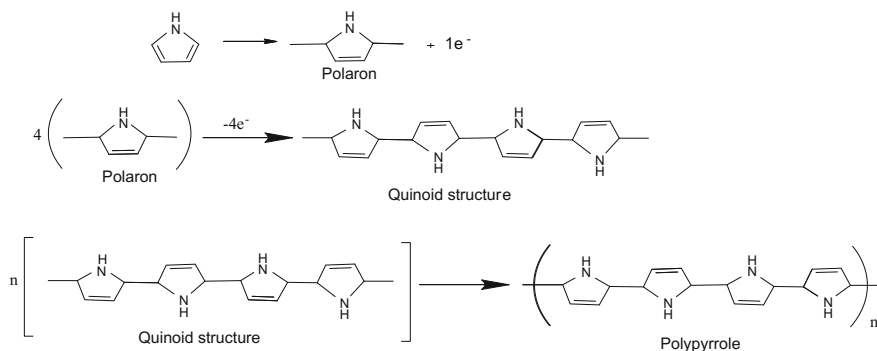
Electrochemical characterizations of the deposited electrodes were carried out using Electrochemical analyzer (CHI 408C, USA) with standard three electrodes cell in which prepared electrode was working electrode, platinum wire was a counter electrode while the saturated Ag|AgCl was a reference electrode. Cyclic voltammetry (CV) for nearly 1 cm^2 surface area of the deposited material was carried to calculate the specific capacitance (SC) using Eqs. 1 and 2 given in the text. The scan rate variations were applied to all electrodes within the potential window -0.5 to 0.7 V in $0.5 \text{ M H}_2\text{SO}_4$.

3 Results and Discussion

3.1 Film Formation Mechanism

In the acidic medium, pyrrole loses one electron to form the polaron. Polarons come together and form a bipolaron, trimer, quinoid structure and finally polypyrrole chain. Two electrons lost during the formation of polarons are taken by the H_2O_2 to form the OH^- ions. Cu^{2+} ions adsorbed on the substrate, combine with the hydroxyl ions to form the $\text{Cu}(\text{OH})_2$. As the film grows layer by layer, the $\text{Cu}(\text{OH})_2$ goes into the polymer matrix and forms the uniform hybrid $\text{PPy-Cu}(\text{OH})_2$. The film formation mechanism is shown in Fig. 1.

Polymerization of pyrrole to polypyrrole



Formation of Cu hydroxide

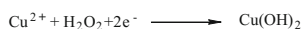


Fig. 1 Film formation mechanism

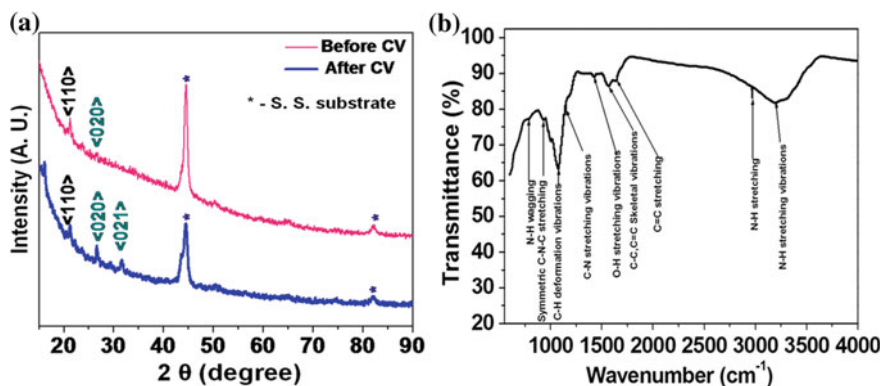


Fig. 2 **a** XRD patterns of the electrode N_4 before and after C.V. analysis, **b** FTIR patterns of the electrode N_4

Table 2 XRD details for the N_4 electrode

Samples	Std. 2θ ($^\circ$)	Observed 2θ ($^\circ$)	Std. 'd' (\AA)	Observed 'd' (\AA)	h	k	l	JCPDS Card no.
N_4 before C.V.	21.50	21.26	4.1290	4.1757	1	1	0	42-0638
N_4 after C.V.	26.51	26.62	3.3450	3.3450	0	2	0	72-1248
	31.51	31.53	2.8347	2.8347	0	2	1	76-0754

3.2 Physical Characterizations

The XRD patterns of PPy-Cu(OH)₂ hybrid electrode (N_4) shows mostly amorphous nature with small peaks of monoclinic Cu(OH)₂ at the $2\theta = 21.50^\circ$ (Fig. 2a). The standard and observed values (interplanar spacing) closely match as per the JCPDS card no. 42-0638 (Table 2). The peaks marked with asterisk are due to the SS substrate as per the JCPDS card no. 351375. The peaks closely matching the JCPDS cards 72-1248 and 760754 are indicating the formation of CuSO₄ during the CV reactions.

The FTIR spectrophotographs of the electrode N_4 (Fig. 2b) shows the peaks at wavenumber 1570 cm^{-1} corresponding to C–C and C=C skeletal (ring) vibrations and 1658 cm^{-1} due to C=C stretching, peaks at 1091 cm^{-1} are due to C–H deformation vibration, peaks at 1140 and 1354 cm^{-1} are due to the C–N stretching, peaks at 796 cm^{-1} are due to N–H wagging, peaks at 2970 and 3186 cm^{-1} are due to N–H stretching and vibrations. The peak at 3307 cm^{-1} is due to $\equiv\text{C-H}$ stretching. All these peaks confirm the existence of PPy in the electrode N_4 .

The scanning electron microscopic image of N_4 shows (Fig. 3a) the nanoclusters and nanolaminae. This morphology is different from the pristine PPy [10, 11] and this may be the reason for the improved electrochemical stability of the electrode. The elemental dispersive X-ray spectrum (EDX) of N_4 electrode shows the

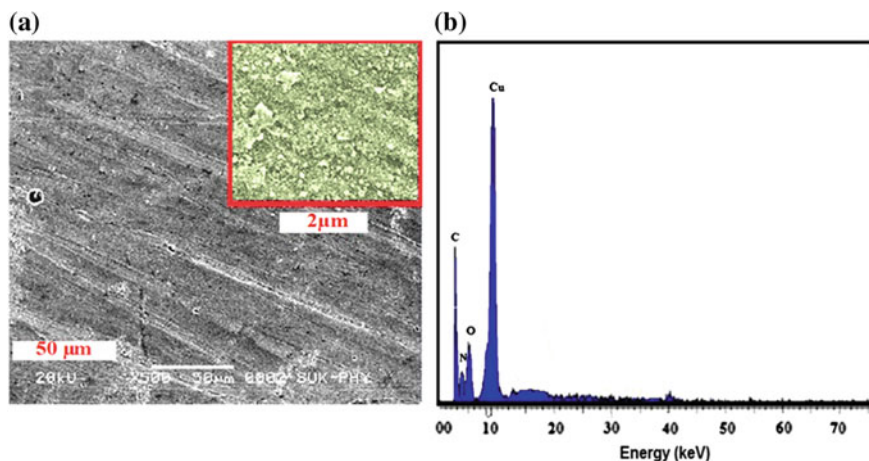


Fig. 3 **a** Nano-lamellae observed for sample N_4 , **b** EDX pattern of the electrode N_4

existence of C, N, O and Cu which is one more evidence of the formation of the composite (Fig. 3b).

3.3 Cyclic Voltammetry

To study the capacitive behavior, all the electrodes N_1 , N_2 , N_3 and N_4 were scanned at 5 mV s^{-1} in $0.5 \text{ M H}_2\text{SO}_4$ within a potential window -0.7 to 0.5 V (Fig. 4a). It was observed that the current integral increases with increase in the dip time in pyrrole bath. The values of capacitance (C) and specific capacitance (SC) for different electrodes were calculated by using following equations.

$$\text{Capacitance } C = \frac{\int_{v1}^{v2} Idv}{V \frac{dV}{dt}} \quad (1)$$

$$\text{Specific Capacitance } SC = \frac{C}{m} = \frac{\int_{v1}^{v2} Idv}{m(V) \frac{dV}{dt}} \quad (2)$$

where, I is the average current in the redox cycle, V potential window, dv/dt is the voltage sc rate, C is the capacitance, m is the mass of the active material dipped in the electrolyte. Electrode N_4 shows maximum value of SC 56.054 F g^{-1} at 5 mV s^{-1} in $0.5 \text{ M H}_2\text{SO}_4$. The values of SC for these electrodes are mentioned in Table 1. The variations of SC with the variations in the potential sc rate in $0.5 \text{ M H}_2\text{SO}_4$ was studied (Fig. 4b) and values are tabulated in Table 3. The electrode

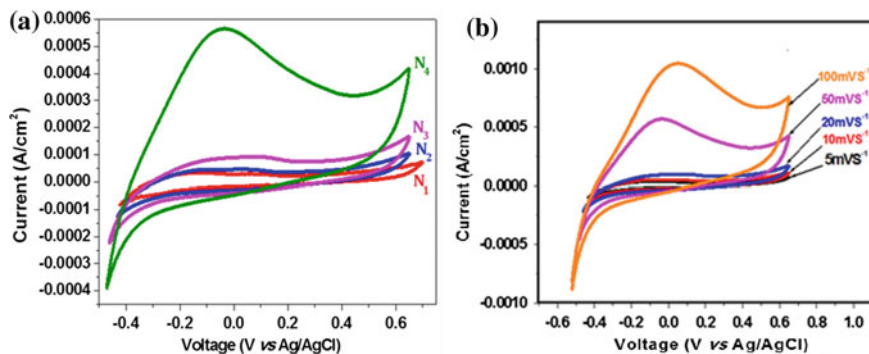


Fig. 4 Cyclic voltammograms of **a** electrodes prepared with different dip times, **b** N₄ electrode at different scan rates

Table 3 Variation of SC with sc rate for the N₄ electrode

Sc rates (dv/dt) mV s ⁻¹	Specific capacitance (SC) F g ⁻¹
5	56.05
10	41.96
20	35.50
50	27.02
100	23.85

shows symmetry on the redox profiles at lower sc rates. With increase in the sc rate, the broad peaks on the oxidation curve goes on increasing. It is observed that as the sc rate increases, the current integral increases. However, the increase was not proportionate as the rate of doping and de-doping as well as the number of faradaic interactions does not increase proportionately with increase in the sc rate hence the specific capacitance decreases with increase in the sc rate.

4 Conclusions

Growth of PPy-Cu(OH)₂ nano-hybrids on the stainless steel substrate by SILAR deposition is possible. Prepared electrodes exhibit partly crystalline and partly amorphous nature due to an existence of triclinic Cu(OH)₂ in the hybrid. FTIR spectrophotograph confirms the presence of PPy in the hybrid. Mixed capacitive behavior due to the presence of faradaic charge storage in the bulk as well as redox reaction at the electrode-electrolyte interface is observed. The electrode shows maximum specific capacitance of 56.05 F g⁻¹ at 5 mV s⁻¹. The electrode has relatively fast discharging indicating its eligibility for power applications.

References

1. Conway BE (1999) *Electrochemical supercapacitors: scientific fundamentals and technological applications*. Kluwer-Plenum, New York
2. Dubal DP, Patil SV, Kim WB, Lokhande CD (2011) *Mater Letter* 65:2628–2631
3. Dubal DP, Lee SH, Kim JG, Kim WB, Lokhande CD (2012) *J Mater Chem* 22:3044–3052
4. Rudge A, Davey J, Raistrick I, Gottesfeld S (1994) *J Power Sour* 47–89
5. Shoa T, Madden JD, Fok CE, MirfaKhari T (2008) *Adv Sci Tech* 61:26
6. Wang H, Hao Q, Yang X, Lu L, Wang X (2010) *Appl Mater Interfaces* 2:821
7. Ambade RB, Ambade SB, Shrestha NK, Nah YC, Sung-Hw HSH, Lee W, Lee SH (2013) *Chem Commun* 49:2308
8. Davies A, Audette P, Farrow B, Hass F, Chen Z, Choi JY, Yu A (2011) *J Phys Chem C* 115:17612
9. Shinde S, Gund GS, Kumbhar VS, Patil BH, Lokhande CD (2013) *Europe Polym J* 49:3734–3739
10. Shi C, Zhitomirsky I (2010) *Nanoscale Res Lett* 5:518–523
11. Zang J, Bao S-J, Li CM, Bi H, Cui X, Bao Q et al (2008) *J Phys Chem C* 112:14843–14847
12. Sharma RK, Rastogi AC, Desu SB (2008) *Electrochim Acta* 53:7690–7695
13. Zhou C, Zhang Y, Li Y, Liu J (2013) *Nano Lett* 13:2078–2085
14. Qu Q, Zhu Y, Gao X, Wu Y (2012) *Adv Energy Mater* 2:950–955
15. Liu Y, Zhang B, Yang Y, Chang Z, Wen Z, Wu Y (2013) *J Mater Chem A* 1:13582–13587
16. Zhang H, Zhang M (2008) *Mater Chem Phys* 108:184–187
17. Zhang H, Feng J, Zhang M (2008) *Mater Res Bull* 43:3221–3224
18. Dubal DP, Dhawale DS, Salunke RR, Jamadade VS, Lokhande CD (2010) *J Alloys Compd* 492:26–30
19. Patake VD, Joshi SS, Lokhande CD, Joo OS (2009) *Mater Chem Phys* 114:6–9
20. Wang G, Huang J, Chen S, Gao Y, Cao D (2011) *J Power Sour* 196:5756–5760
21. Jadhav VV, Shinde DV, Patil SA, Zate MK, Pawar S, Osta A, Mane RS, Han SH (2014) *J Nanoeng Manuf* 4:1–5
22. Liew SY, Thielemans W, Walsh DA (2010) *J Phys Chem C* 114:17926
23. Yin Z, Ding Y (2012) *Electrochemistry Comm* 20:40–43. doi:10.1016
24. Karaca E, Pekmez NO, Pekmez K (2014) *Electrochim Acta* 147:545–556
25. Lokhande BJ, Ambare RC, Mane RS, Bhardwaj SR (2013) *Curr Appl Phys* 13:985–989
26. Lokhande BJ, Patil PS, Uplane MD (2004) *Mater Chem Phys* 84:238–242
27. Fraoua K, Aeiyaach S, Aubard J, Delamar M, Lacaze PC, Ferreira CA (1999) *J Adhes Sci Technol* 13(4):517

Root Canal Filling Process Enhancement in Simulated Dental Blocks Using a Novel Device

Ratnakar Ghorpade, Kalyana Sundaram and Vivek Hegde

Keywords Gutta Percha (GP) · Downpack · Obturation

1 Introduction

Root canal treatment (RCT) is a treatment used to repair and save the tooth that is decayed or becomes infected. Dentist treats the inner aspects of a tooth called root canal. It is a part of Endodontics (means inside the tooth). It is important to know the reasons to obturate root canal, which includes prevention of re-infection of root canals that have been biomechanically cleaned, creating a favorable biologic environment, sealing within the system any irritants that cannot be fully removed during canal cleaning and shaping procedures, and finally preventing material leakage from the canal into the periarticular region. Successful root canal obturation requires the use of materials and techniques capable of densely filling the entire root canal system and providing a fluid tight seal from the apical segment of the canal to the cavo-surface margin to prevent reinfection. Thus, the goal of 3D obturation is to provide an impermeable fluid tight seal within the entire root canal system, to prevent oral and apical microleakage.

In the current study, an experiment was performed on 20 dental acrylic block (of DENTSPLY make). These blocks were divided into two groups, ten blocks in each group. Ten samples in the first group were experimented by using varying

R. Ghorpade
Mechanical Engineering Department, BRACT's V.I.T., Pune 411037, India

K. Sundaram (✉)
R&D, V.I.T., Pune 411037, India
e-mail: dr.kksundaram@gmail.com

V. Hegde
Department of Conservative Dentistry & Endodontics,
MA Rangoonwala College of Dental Sciences & Research, Pune, India

frequency at the dental pin (from 10 to 100 Hz). Initially, blocks were filled with an inert filling material i.e. Gutta Percha (a rubbery material having temperature dependent elastic and plastic properties) without activating vibration at the dental tip; the weight was recorded. Subsequently, the same block was filled with activating vibration at the dental tip, and weight was recorded after filling. Thus weight enhancement was calculated based on the weight analysis method given in the section below. Likewise, other blocks were also experimented based on the same procedure. Ten samples in the second group were experimented as using above procedure with and without the aid of vibration at the dental tip, here vibration frequency was constant (50 Hz) used for all 10 sample of the second group. Molven and Halse [1] assumed "Success to depend on the elimination of root canal infection present when treatment starts, and the prevention of both contamination during treatment and re-infection later. So success rates reflect the standard of the cleaning, shaping, and filling of root canals". For sealing biomechanically prepared root canal cavity, an inert material is expected which is Gutta Percha. The gutta-percha polymer is obtained from the coagulation of latex produced by trees of the Sapotaceae family and mainly derived from *Palaquium gutta* bail. It is a trans-1,4-polyisoprene [2]. Among most of the materials tried, none of the materials met the requirements of an ideal obturating material. The search for a suitable Root canal filling material ended with the discovery of "Gutta-percha" [3]. Pagavino et al. [4] have done the comparative analysis of the percentage of gutta-percha filled area (PGP), for varying the penetration depth and function of the pluggers (heat versus heat plus vibration) using Endo Twinn in simulated root canals. The samples were sectioned horizontally at the levels 1.25, 2.5 and 4.0 mm from the working length and the PGP was evaluated. 0.8 taper canals showed significantly higher PGP than 0.4 taper canals. At the 1.25 mm level, PGP found significantly greater when the vibration function was activated. Jain [5] invented a novel root canal obturating device having adjustable temperature control and sonic vibrations. The obturator has an integrated micro cylindrical sonic vibrator motor of 3V DC used to give the working end sonic vibratory motion. On application heat to the Dental Gutta percha i.e. present in the beta form, it gets transformed from beta phase to alpha phase (60–70 °C). At the transition temperature i.e. alpha phase gutta percha flows best. The sonic vibrations allow the formation of a homogenous mass of GP that is void free along with it the vibratory strokes enables the GP to flow into lateral canals, achieving better lateral canal seal. Goodman et al. [6] studied the fact that the crystalline phase of Gutta Percha appears in two forms: the α phase and the β phase. Transformation occurs in the crystalline structure during heat application that takes place going from the β to the α form, and from the α to the amorphous phase. Schilder et al. [7] demonstrated that for the β - to the α -form the transformation temperatures were found to be 42–49 °C and for the α - to the amorphous form it was 53–59 °C. Overheating gutta-percha up to close to 300 °C with an uncontrolled heat source, causes its degradation.

2 Materials and Methodology Adopted for Obturation of the Root Canal System

Two groups of samples, each containing ten dental blocks was obturated. The first group of ten sample blocks was obturated with conventional down-pack technique as 'Heat and Compaction' for varying frequency of vibration at the dental tip (from 10 to 100 Hz). Sample weights were recorded before and after filling. This was followed by obturation over the same blocks using new proposed method as 'heat, vibration and compaction' and the results were recorded for weights after vibration aid. The same experiment was conducted for the second group (consisting of 10 sample blocks) but at the constant frequency (of 50 Hz) at the dental tip.

2.1 Obturation of the Root Canal System Involves

- (i) Removal of decayed and infected pulp (nerve): In this phase, the tooth is opened to access the Root canal space.
- (ii) Cleaning and shaping of the root canal: the Special instrument (files) is used to clean the infection.
- (iii) Filling of canals and tooth cavity: Canal is then filled with inert material as Gutta-Percha, using pluggers, thus it is sealed with a filling material.
- (iv) Capping of treated tooth.

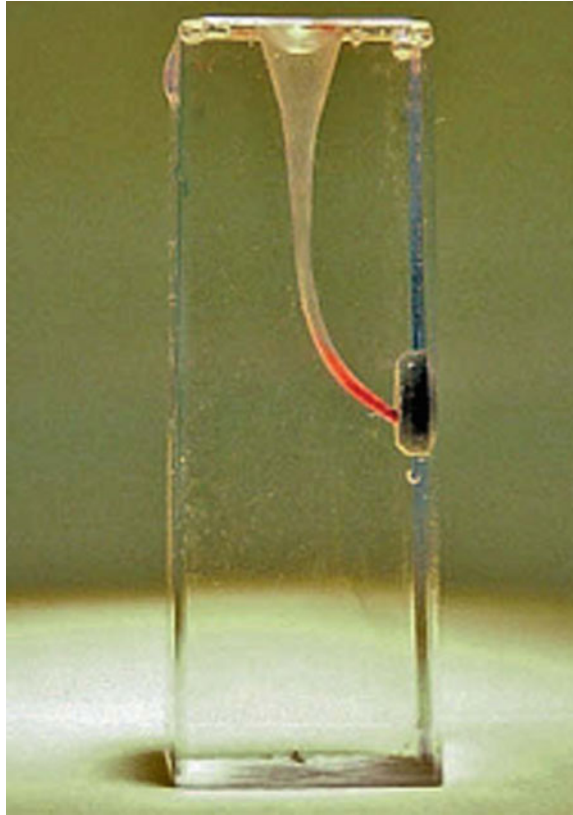
Figure 1 shows the dental blocks (DENTSPLY) with the configuration of a single block used during obturation (Fig. 2).

2.2 Filling Canals with GP Using Dual Energy Technique

Steps taken in obturation of the canals using 'Heat, Vibration and Compaction' technique are listed under

1. Biomechanical preparation of canals: Canals are flared by using 2 and 6% taper files to the required size.
2. Cleaning root canal cavity and application of Sealer: After biomechanical preparation root, canal cavity is cleaned with water and dried with absorbent points. Then sealer is applied inside the root canal cavity prepared in an acrylic block, which seals the micro gap and it acts as anti-bacterial. The coating is done with the sealer over to the entire surface inside of the acrylic block. A master

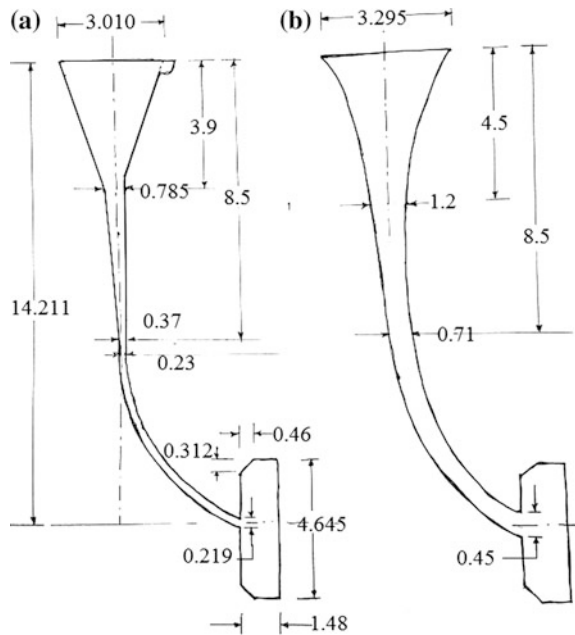
Fig. 1 Dental block
(DENTSPLY)



cone is selected and placed (with sealer) in the Root canal prepared in an acrylic block.

3. Heat application and compaction of GP by plugger: The point is heated, and a relatively small amount of GuttaPercha is removed from the canal leaving a softened portion of GuttaPercha within the canal. This portion is subjected to vertical compression by a tool called a plugger to form a relatively densely compressed mass within the canal of the tooth.
4. Apply Vibration to tip and subsequent compaction: Once the GP starts melting and flowing down, the vibration is given by an eccentric motor which is set at the excitation frequency of 50 Hz. This process is continued for 5–10 s maximum.
5. Same Procedure is repeated by using heat only.

Fig. 2 One block showing Root canal configuration **a** before and **b** after biomechanical preparations. *Source* measurement of the dimensions (all in mm) before and after biomechanical preparations were taken on 'Profile Projector' at Metrology Laboratory, MIT, Pune

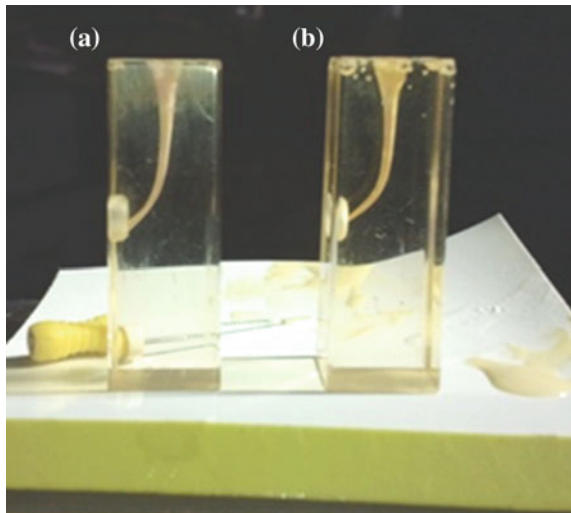


3 Weight Analysis of Blocks After Filling GP

3.1 Comparison of Blocks

After filling GP in Acrylic block, by using Heat-Vibration and using only heat, the percentage of GP for these two categories is compared the compaction of GP in Root canal (Fig. 3).

Fig. 3 Two separate blocks showing compacted GP in root canal using **a** heating, compaction and vibration, **b** heating and compaction only



3.2 *Weight Analysis of Dental Blocks*

Weight analysis is carried out to determine Percentage enhancement in Compaction of GP in Acrylic Blocks by using Vibration given to dental pin.

3.3 *Evaluation of Percentage GP Enhancement in Simulated Dental Blocks*

3.3.1 **Blocks Utilized in the Current Study**

Following categories of blocks were used in the study

- (i) Block without biomechanical preparation (with original root canal)
- (ii) Block with biomechanically prepared root canal (a)
- (iii) Biomechanically prepared root canal filled by heat and compaction only (b)
- (iv) Biomechanically prepared root canal occupied by heat, compaction and Vibration (c).

3.3.2 **Percentage Enhancement in GP Compaction (with and Without Vibration)**

Percent enhancement in filling GP in biomechanically prepared root canal by conventional method 'heat and compaction only' (PGP_{HC})

$$PGP_{HC} = \left(\frac{b - a}{a} \right) \times 100\% \quad (1)$$

Percent enhancement in filling GP in biomechanically prepared root canal by new method 'heat, compaction and Vibration' (PGP_{HCV})

$$PGP_{HCV} = \left(\frac{c - a}{a} \right) \times 100\% \quad (2)$$

4 **Mass of GP Compacted in Root Canal**

M_{HC} = Mass of GP filled with conventional method of heat and compaction,

M_{HCV} = Mass of GP filled with new method of heat, compaction and vibration,

W_P = Weight of Block with biomechanically prepared root canal,

W_{HC} = Weight of Block filled by heat and compaction,

W_{HCV} = Weight of Block filled by heat, compaction and vibration

$$M_{HC} = W_{HC} - W_P \tag{3}$$

$$M_{HCV} = W_{HCV} - W_P \tag{4}$$

5 Volume of Root Canal Based on Mass of Material Compacted

V_{HC} = Volume of Block filled by heat and compaction

V_{HCV} = Volume of Block filled by heat, vibration and compaction

Based on (a), (b) and (c),

$$V_{HC} = (M_{HC})/(\rho_{GP}) \tag{5}$$

$$V_{HCV} = (M_{HCV})/(\rho_{GP}) \tag{6}$$

Basis to evaluate extra volume of GP compacted 9 (i.e. Accessory canal volume)

$$V_{AC} = V_{HCV} - V_{HC} \tag{7}$$

6 Statistical Analysis Using ‘Student-t test’

It suitable for samples less than 30 and population standard deviation is not known. We have 10 different values of % GP enhancement through 10 experiments. We wanted to test the hypothesis that % GP enhancement is less than or equals to 21%.

6.1 Case 1: For Varying Excitation Frequencies 10–100 Hz at Dental Tip

See Tables 1, 2, 3.

Table 1 Case 1: (for varying excitation frequencies 10–100 Hz at dental tip)

Number of experiments	Frequency at dental tip (Hz)	% GP enhancement	$X_i - X'$	$(X_i - X')^2$
1	10	7.142857143	-19.17589001	367.7147575
2	20	17.94871795	-8.370029201	70.05738882
3	30	23.68421053	-2.634536623	6.940783218
4	40	35	8.681252851	75.36415106
5	50	38.0952381	11.77649095	138.685739
6	60	35	8.681252851	75.36415106
7	70	26.82926829	0.510521143	0.260631838
8	80	28.20512821	1.886381056	3.558433488
9	90	28.20512821	1.886381056	3.558433488
10	100	23.07692308	-3.241824072	10.50942332
		$X' = \sum(X_i)/N$ 26.31874715		$\sum(X_i - X')^2$ = 752.0138928

Table 2 Case 2: (for constant excitation frequencies of 50 Hz at dental tip)

Number of experiments	Excitation frequency (Hz)	% GP enhancement	$X_i - X'$	$(X_i - X')^2$
1	50	30	1.806555099	3.263641324
2	50	40.54054054	12.34709564	152.4507707
3	50	30.55555556	2.362110654	5.579566742
4	50	41.02564103	12.83219612	164.6652574
5	50	21.42857143	-6.764873473	45.7635131
6	50	17.07317073	-11.12027417	123.6604976
7	50	16.66666667	-11.52677823	132.8666165
8	50	35.8974359	7.703990996	59.35147727
9	50	36.84210526	8.648660362	74.79932605
10	50	11.9047619	-16.288683	265.3211938
		$X' = \sum(X_i)/N$ N = 28.1934449		$\sum(X_i - X')^2$ = 1027.72186

Table 3 Two groups of experimental results (Student-t test)

Groups	Mean	SS	SD	t (calculated)
Varying excitation frequencies 10–100 Hz (10 samples)	26.3187	752.0139	9.1409	1.8399 ^a
Constant excitation frequencies of 50 Hz (10 samples)	28.1934	1027.7219	10.686	2.1287 ^a

^at (table) = 1.833 for 5% confidence with one-tailed test

Table 4 ANOVA for the two groups of experimental results

S.No.	Source of variation	SS (sum of squares for variance)	DOF (degrees of freedom)	MS (mean square)	F (ratio)	5% F-limit
1	Between sample	17.572	=n - 1 = 2 - 1 = 1	17.572	0.1777	F(1, 8) = 5.32
2	Within samples	1779.7	=N - n = 20 - 2 = 18	98.874		
3	Total	1797.31	19			

6.2 Case 2: For Constant Excitation Frequencies of 50 Hz at Dental Tip

See Table 4.

Therefore % GP Enhancement is 21% for varying frequency at the dental tip (For Case-1: Variable test conditions.) Also % GP Enhancement is 21% for the constant frequency of 50 Hz at the dental tip. (For Case-2: Constant test conditions).

7 Statistical Analysis Using One Way Analysis of Variance

We have two separate groups of results, 1st group containing ten values with constant excitation frequency, and 2nd group containing ten values with varying excitation frequency. We want to observe whether the difference in % GP

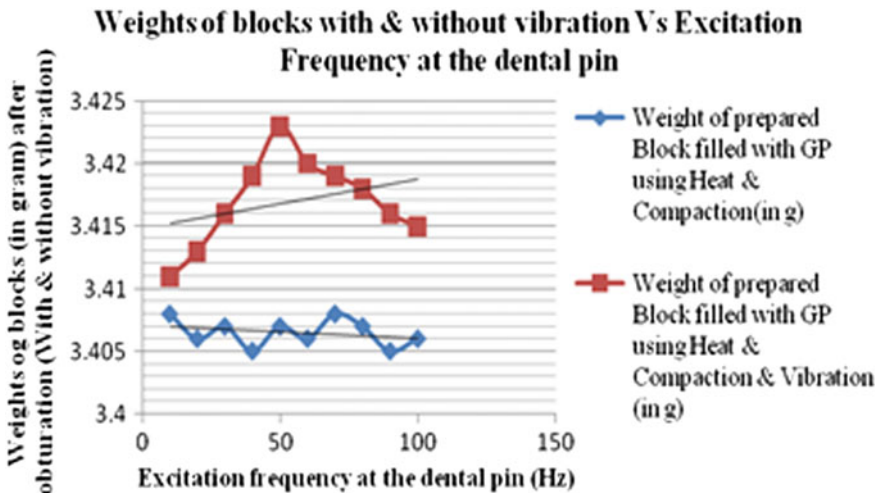


Fig. 4 Dental blocks filled with ‘heat vibration and compaction’ (in red) and with ‘heat and compaction’ (in blue) for various excitation frequencies at dental pin

compaction due to constant frequency and varying frequency is significant or insignificant based on this test.

As, $F(\text{cal}) < F(\text{limit})$ Hence the difference in % GP compaction due to varying frequency and constant frequency is insignificant (Fig. 4).

8 Conclusion

- (i) The difference in % GP compaction due to varying frequency and constant frequency is found insignificant based on One-way ANOVA ($F = 0.05$).
- (ii) Compaction using the new method that uses heat, vibration and compaction together gives better compatibility as compared with the conventional ‘heat and compaction’ method.
- (iii) It is seen that the mechanical vibration at the tip of the device resulted in enhancement of the filling and percentage compaction of GP in root canal over conventional compaction technique by about 21% (Fig. 5).



Fig. 5 Device based on a new method of ‘heat vibration and compaction’ used to perform obturation

Acknowledgements Current research was funded by BCUD, Savitribai Phule Pune University (Formerly, University of Pune), during the year 2012–2014. Grant Reference letter No. OSD/BCUD/230/61 dated 14th May 2012 (of University of Pune).

References

1. Molven O, Halse A (1988) Success rates for gutta-percha and Kloroperka N-O root fillings made by undergraduate students: radiographic findings after 10–17 years. *Int Endod J* 21:243
2. Gutmann JL, Witherspoon DE (2002) Obturation of the cleaned and shaped root canal system. In: Cohen S, Burns RC (eds) *Pathways of the pulp*, 8th edn. Mosby, St. Louis, pp 293–364
3. Prakash R, Gopikrishna V, Kandaswamy D (2005) Gutta-Percha—an untold story, *endodontology*
4. Pagavino G, Giachetti L, Nieri M, Giuliani V, Scaminaci Russo D (2006) The percentage of gutta-percha-filled area in simulated curved canals when filled using Endo Twinn, a new heat device source. *Int Endod J* 39:610–615
5. Jain SD (2012) HYBROSONIC: re-inventing root canal obturation technique using heat + sonic vibration. *Int J Sci Eng Res* 3(5):1–3. ISSN 2229-5518
6. Goodman A, Schilder H, Aldrich W (1974) The thermo mechanical properties of gutta-percha. II. The history and molecular chemistry of gutta-percha. *Oral Surg Oral Med Oral Pathol* 37(6):954–961
7. Schilder H, Goodman A, Aldrich W (1974) The thermomechanical properties of gutta-percha. III. Determination of phase transition temperatures for gutta-percha. *Oral Surg Oral Med Oral Pathol* 38(1):109–114

Part V
Manufacturing and Fabrication Processes
for Societal Applications

Analysis of Surface Integrity and Dimensional Accuracy During Thin-Wall Machining

Gururaj Bolar, Argha Das and Shrikrishna N. Joshi

Keywords Thin-wall machining · End milling · Surface roughness · Dimensional accuracy · Surface defects

1 Introduction

Aerospace, marine, consumer electronics and power industries often require thin-walled structures. Traditional fabrication process basically involves two stages—first, the production of various sub-parts using various machines with different setups and then assembly of these sub-parts through riveting or welding process. Due to numerous set-ups and costs involved machining thin-walled part as a ‘monolithic part’ is an alternative to the traditional process thus reducing setup costs and enhancing the productivity. Due to poor stiffness and low rigidity, these thin sections elastically deform under the action of cutting forces making it quite difficult to maintain the dimensional accuracy and impart desired surface finish [1]. Hence proper selection of machining parameters and strategies are necessary which can result in increased productivity with reduced deformation and improved surface finish of thin-walled parts.

Some aspects of thin-wall machining such as analytical modeling, numerical modeling using finite element based methods, application of CAD/CAM tools have been reported in the literature. Budak and Altintas [2] analyzed the machining accuracy and error compensation using finite element method (FEM) for milling thin-wall components within elastic range. Ratchev et al. [3, 4] investigated on force-induced errors in machining of thin-wall structures. Rai and Xirouchakis [5, 6] developed a FEM based transient milling simulation model to predict tem-

G. Bolar · A. Das · S.N. Joshi (✉)
Department of Mechanical Engineering, Indian Institute of Technology Guwahati,
Guwahati, Assam 781039, India
e-mail: snj@iitg.ac.in

perature distribution in work piece, displacements of thin-walls, and stresses. Aijun and Zhanqiang [7] developed analytical model for prediction of static deformations of thin-walled plate with low rigidity. Campa et al. [8], Seguy et al. [9] reported that process instability due to chatter significantly affects the surface roughness. Thevenot et al. [10] also used the linearized stability lobes theory to determine the critical and optimal cutting conditions for productive peripheral milling of thin-walled structures. They employed both modal measurement and FEM to establish a three-dimensional (3D) representation of stability lobes. Based on various research works it is noted that experimental studies are mainly carried out either to measure cutting forces or to verify the results predicted by the respective numerical/analytical models. Scant work is reported on experimental studies on overall deformation and surface roughness improvement during thin-wall machining operation. In this study, the effects of machining parameters on the surface roughness and part deformation in milling of aluminum thin-wall parts are investigated.

2 Experimental Details

Experiments were carried out on a 3-axis vertical machining centre (PMK India, Model: MC-3/400) with Siemens Sinumerik controller. Four fluted solid carbide flat-end milling cutter having a diameter of 8 mm and helix angle of 45° was used for finish machining of the thin-wall parts. Test specimens were made up of aluminium alloy 2024. Climb milling method was employed to facilitate minimal forces on the thin-walls. The radial depth of cut was fixed at 1.25 mm and the wall thickness was reduced from 2.5 to 1.25 mm. The surface roughness was measured using Taylor Hobson optical profilometer at three different points on the machined surface. The measurement of wall thickness after the machining operation was carried out offline by using a 3-D coordinate measuring machine (CMM Carl Zeiss make). The thickness measurement was carried out at five points and the average thickness was considered for study. The details of the experimental and analysis process work are shown in Fig. 1.

3 Results and Discussion

The experiments were conducted based on factorial design and the results obtained are listed in Table 1.

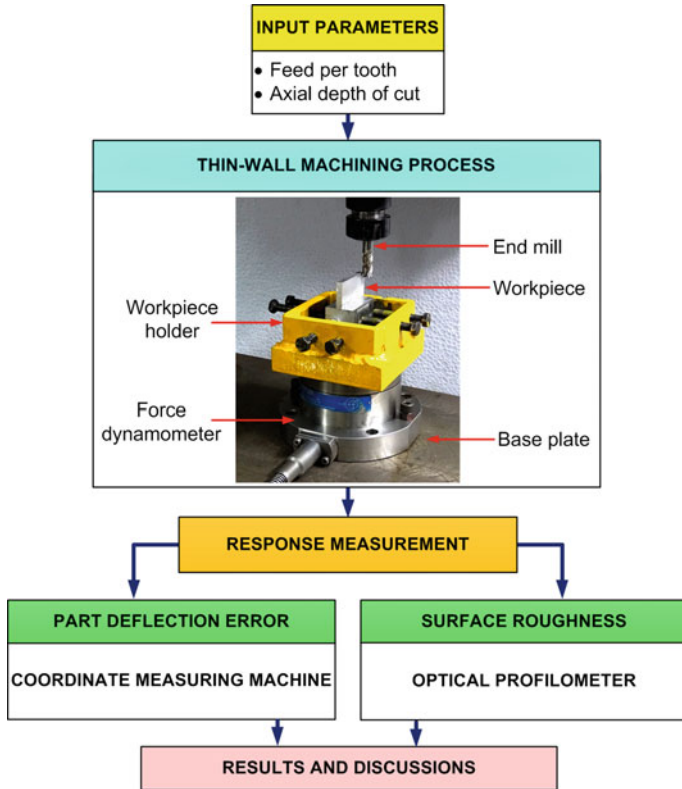


Fig. 1 Schematic of the experimental procedure and analysis

Table 1 Experimental cutting parameters and resultant data

Exp. No.	Feed rate (mm/z)	ADOC (mm)	Average thickness error (mm)	Average surface roughness (µm)
1	0.06	8	0.616	0.705
2	0.02	8	0.202	0.425
3	0.02	12	0.326	0.513
4	0.02	24	0.547	0.443
5	0.06	24	0.178	0.758
6	0.04	24	0.227	0.625
7	0.06	12	0.34	0.908
8	0.04	12	0.223	0.645
9	0.04	8	0.394	0.615

3.1 Analysis of Dimensional Accuracy

During machining of thin-walls, the wall deflects thereby affecting the dimensional accuracy. When the thickness of the wall reduces, it loses its rigidity thus leading to higher deflection. The wall dimensional accuracy (thickness error) variation for two process parameters is shown in Fig. 2. Better dimensional accuracy was observed for lower feed and depth of cut values. As observed from Fig. 2a, increase in feed rate leads to rise in overall deflection. An increase in feed rate resulted in increased chip load and thereby increased the cutting force. As ADOC increases, length of engaged flutes increases leading to increase in cut area. This in turn increases the chip load and the cutting forces resulting in higher deflection (Fig. 2b). The minimum thickness error was observed at lower feed rate and ADOC values as seen in Fig. 2c. Maximum error was observed at highest feed and ADOC values. It was observed that, the thickness error of the straight cantilever wall decrease from the free end of the wall to the fixed base and the error was zero at the base. This is due to the fact that, when the material is removed from the wall, rigidity of the upper portion of the wall decreases. But the rigidity of the lower part is comparatively more as it is supported by the surrounding bulk material.

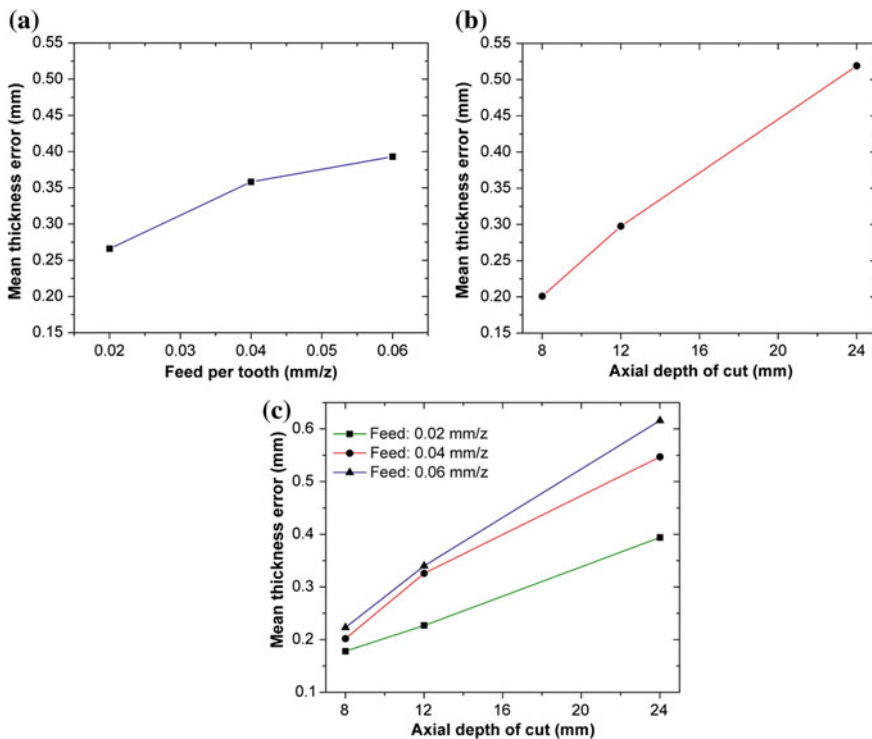


Fig. 2 Effects of machining parameters on dimensional accuracy

3.2 Analysis of Surface Finish and Surface Integrity

The 3-D surface plots as shown in Fig. 3 indicate surface damage such as lay patterns (feed marks), re-deposited work. material (chips), surface tearing, chip layer formation and material adhesion onto the machined surface (Fig. 3a-e). Figure 3a displays the feed marks formed perpendicular to the tool feed direction on the milled surface. Furthermore, there was evidence of surface tearing occurring on the machined surface due to the built-up edge (BUE) deposition and plucking out of re-deposited materials (Fig. 3b). The chip fragments which were torn during machining were smeared onto the surface (Fig. 3c). Re-deposited materials were evidently visible between the feed marks as shown in Fig. 3d. Formation of chip layer formation can be seen in Fig. 3e.

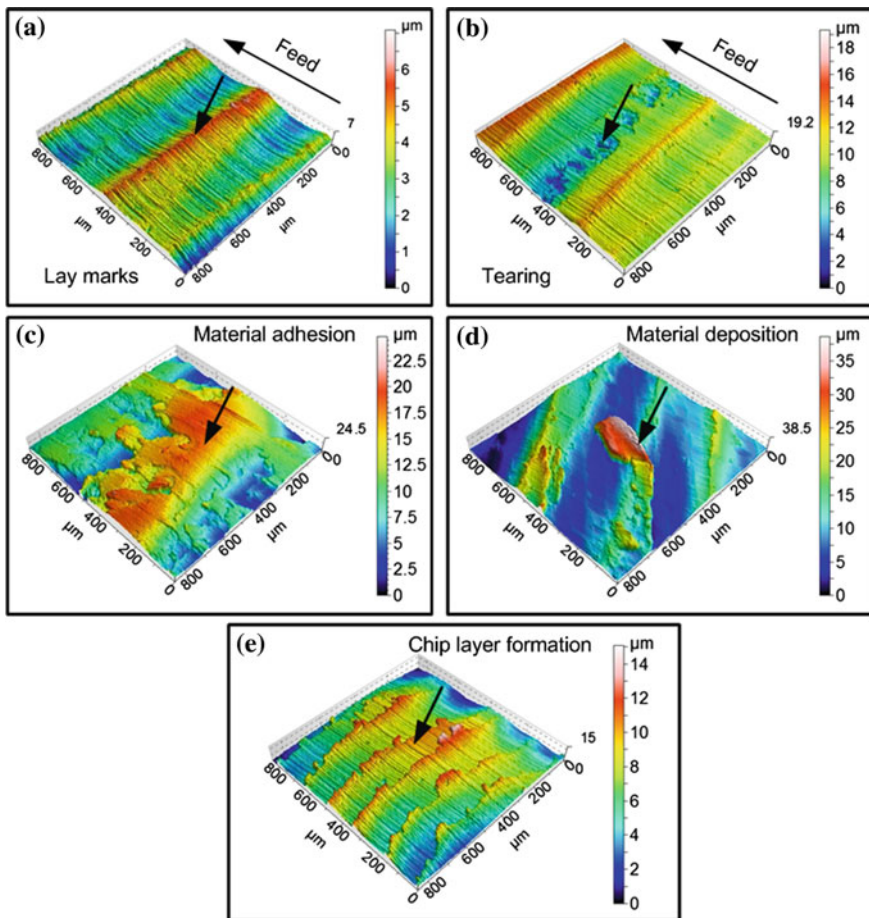


Fig. 3 Images of the main surface defects in dry milling of aluminum alloy

It was observed that due to constant deflection of free end of the thin-walled part, free end resulted in having higher roughness in comparison to the fixed end. The effect of feed rate and ADOC on surface roughness was analysed. Lower surface roughness was observed while the part was machined using low feed rate as seen in Fig. 4a. An increase in the feed rate results in an increase in chip load and thereby increases the overall cutting force. This caused the free end of the wall to deflect leading to poor finish. The axial depth of cut influenced the surface roughness and machining using full axial depth of cut resulted in slight reduction in roughness (Fig. 4b). This was due to the machining of the entire surface in a single go as compared to two pass cuts, where second pass resulted in surface smearing.

The interaction effect of feed and ADOC on the workpiece surface finish at the free end of cantilever is shown in Fig. 4c. During machining of the thin-wall, the spring-back of wall is more prominent during the engagement and disengagement of cutting tool with the work piece. This generated cutter marks (chatter) and affected the surface roughness. Chatter marks were observed at the free end of the surface (Fig. 5a) while a quite a smooth surface observed at the fixed end (Fig. 5b). Phenomenon of built-up edge (BUE) formation was observed in cases of high feed and high axial depth of conditions.

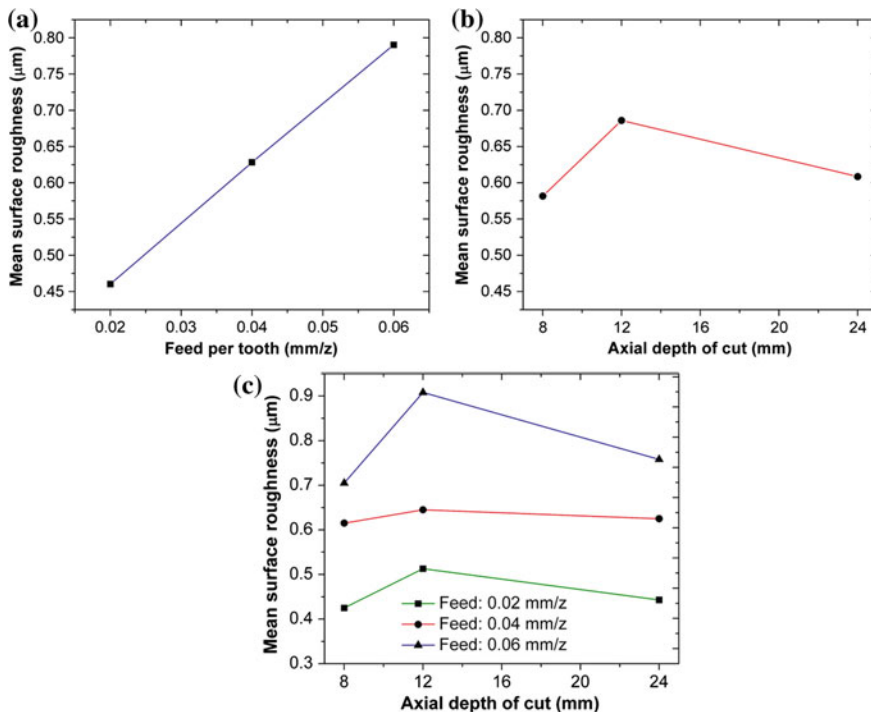


Fig. 4 Effects of machining parameters on surface roughness

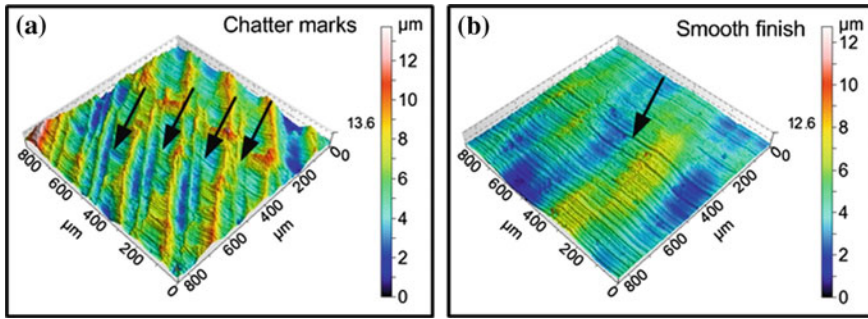


Fig. 5 3-D surface profile **a** chatter surface, **b** smooth surface

4 Conclusions

This paper presents a study on the effect of cutting parameters viz. feed per tooth and axial depth of cut on the surface integrity and dimensional accuracy in thin-wall machining of aluminum 2024 alloy. During the machining process, several surface defects such as lay patterns (feed marks), re-deposited work material (chips), surface tearing, chip layer formation and material adhesion were observed. Formation of built up edges (BUE) was observed at higher feed and depth of cut condition which subsequently led to surface tears. Use of lower feed rate resulted in better surface finish. The deflection of thin-walls during the machining process caused deviation of the wall thickness from its intended value. The feed rate and axial depth of cut were noted to have a profound effect on part deflection. Higher values of feed and depth of cut led to larger deflection. The wall deflection was higher at free ends of the cantilever wall as compared that to at the fixed end. This generated rough surface finish at the free ends. Further investigation is in progress on selection of proper cutting strategies and optimum parameters (feed rate and cutting depth) that to be employed to achieve defect-free good quality thin-walled components of aluminum.

Acknowledgements This work was supported by the Science and Engineering Research Board (SERB), Department of Science and Technology, Government of India (Grant number SR-S3-MERC-0115-2012).

References

1. Bolar G, Joshi SN (2016) Three-dimensional finite element based numerical simulation of machining of thin-wall components with varying wall constraints. *J Inst Eng India Ser C*:1–10 doi:10.1007/s40032-016-0246-9
2. Budak E, Altintas Y (1995) Modeling and avoidance of static form errors in peripheral milling of plates. *Int J Mach Tools Manuf* 35:459–476

3. Ratchev S, Govender E, Niko S, Phuah K, Tsiklos G (2003) Force and deflection modeling in milling of low-rigidity complex parts. *J Mater Process Technol* 143–144:796–801
4. Ratchev S, Liu S, Huang W, Becker AA (2004) A flexible force model for end milling of low-rigidity parts. *Int J Mach Tools Manuf* 153–154:134–138
5. Rai JK, Xirouchakis P (2008) Finite element method based machining simulation environment for analyzing part errors induced during milling of thin-walled components. *Int J Mach Tools Manuf* 48:629–643
6. Rai JK, Xirouchakis P (2009) FEM-based prediction of workpiece transient temperature distribution and deformations during milling. *Int J Adv Manuf Technol* 42:429–449
7. Aijun T, Zhanqiang L (2008) Deformations of thin-walled plate due to static end milling force. *J Mater Process Technol* 206:345–351
8. Campa FJ, Seguy S, López de Lacalle LN, Arnaud L, Dessein G, Aramendi G (2007) Stable milling of thin-walled parts with variable dynamics. 6th international conference on high speed machining. San Sebastian, Spain, pp 367–372
9. Seguy S, Dessein G, Arnaud L (2008) Surface roughness variation of thin wall milling, related to modal interactions. *Int J Mach Tools Manuf* 48:261–274
10. Thevenot V, Arnaud L, Dessein G, Larroche G (2006) Influence of material removal on the dynamic behavior of thin walled structures in peripheral milling. *Mach Sci Technol* 10(3): 275–287

Wear Behaviour of D-Gun Sprayed Coatings on Ductile Cast Iron

Amardeep Singh Kang and Gurmeet Singh Cheema

Keywords Thermal spray coatings · Piston rings · Hard chrome coating · Ni–Cr coating · WC–Co–Cr

1 Introduction

Serviceable engineering components not only rely on their bulk material properties but also on the design and characteristics of their surface. This is especially true in wear resistant components, as their surface must perform many engineering functions in a variety of complex environments. Rajasekaran et al. [1] explained in his studies that detonation gun spraying, a kind of thermal spraying, is well known for its characteristic feature of producing coatings of high hardness with compressive residual stresses. It exhibited superior performance under rolling contact conditions compared to plasma spraying.

Murthy and Venkataraman [2] in their study deposited the tungsten carbide-based and chromium carbide-based coatings by high velocity processes like high velocity oxy-fuel (HVOF) and detonation gun spray (DS) techniques which are known to provide best wear performance for a variety of wear resistance applications. Sundararajan et al. [3] have characterized large varieties of detonation sprayed coatings. From the results and experimental data they concluded that the coatings are substantially poorer than bulk material of identical composition and that the hardness and tribological properties of the coatings are more strongly influenced by the coating process parameters themselves rather than micro structural parameters like phase content and distribution, porosity, etc. Karoonboonyanan et al. [4] in his studies compared two different thermal spray coatings, namely HVOF-sprayed

A.S. Kang (✉) · G.S. Cheema
Bhai Gurdas Institute of Engineering and Technology, Sangrur, Punjab 148001, India
e-mail: amardeepkang@gmail.com

WC/Co and plasma-sprayed $\text{Al}_2\text{O}_3\text{-TiO/NiAl}$, on carbon steel rotary tiller blades. The wear rates of the WC/Co-coated blades were significantly lower than those of the uncoated blades, indicating a great improvement in the wear protection provided by the coatings. Murthy et al. [5] studied the effect of grinding on the erosion behavior of a WC-Co-Cr coating. A detailed analysis indicates that the increase in residual stress in the ground specimen is a possible cause for the improvement in erosion resistance.

In the present work, the wear characteristics of piston ring coatings are evaluated. In this study three different D-Gun sprayed coatings, namely WC-Co-Cr, Ni-Cr and $\text{Cr}_3\text{C}_2\text{NiCr}$ were deposited on ductile cast iron rings. The coated piston rings were tested in actual field environment by running in a 4 cylinder, 60 Horse Power tractor engine. Simultaneously, these coatings were also tested for wear in laboratory using pin-on-disc apparatus.

2 Experimental

2.1 Materials and Coatings

Piston rings and the substrate used in the experiment were made from ductile cast iron with a composition given in Table 1. As it is clear from the literature survey that carbide coatings are sometimes preferred for tribological applications. Among various carbides, tungsten carbide and chromium carbide are most preferred [1]. As the piston rings are mainly subjected to an adhesive wear, tungsten carbide cobalt chromium (WC-Co-Cr), chromium carbide nickel chrome ($\text{Cr}_3\text{C}_2\text{-NiCr}$) and nickel chromium were selected as the coating materials on ductile cast iron rings and specimens because of their good wear resistance characteristics. In this study, the WC-Co-Cr, $\text{Cr}_3\text{C}_2\text{-NiCr}$ and Ni-Cr were deposited by detonation gun spray (D-Gun) technique. D-Gun process was selected as coating technique because it minimizes decomposition of the carbide phase due to lower heat enthalpy and shorter duration involved in the coating process. In addition higher particle velocity during deposition provides several advantages such as lower porosity, higher bond strength and hardness [1].

Table 1 Chemical composition (wt%) of ductile cast iron

Grade	% elements								
Ductile cast iron	C	Mn	Si	S	P	Ni	Cr	Mo	V
	3.15	0.5	3.60	0.11	0.12	0.01	0.2	0.01	0.02

2.2 Coating Powders

Three types of coating powders namely (1) $\text{Cr}_3\text{C}_2\text{-NiCr}$ (2) Ni-Cr (3) Wc-Co-Cr are selected for Detonation Spray Coating Process after comprehensive literature survey. Pertinent review of literature shows that the above coatings have excellent bond strength and wear resistance.

1. **Chromium Carbide-Nickel Chromium Powder ($\text{Cr}_3\text{C}_2\text{-NiCr}$):** Chromium Carbide and Nickel Chromium (75/25) powder, when sprayed using the Detonation Spray process, it produces coatings, which are very hard, dense and excellent bonded. Chromium Carbide and Nickel Chromium coating is recommended for resistance to wear by fretting, abrasive particles oxidation. The powder is supplied by H C Starck, Germany under the product code Amperit 584. The powder is agglomerated and sintered having particle size as 10–45 μm .
2. **Ni-Cr:** NiCr powder when sprayed using the Detonation Spray process, it produces coatings which are very dense and homogeneous. The various constituents of the powder are Carbon (0.25%), Molybdenum (5.5%), Nickel (3.0%), Iron (1.0%), Chromium (29.0%), Silicon (1.0%), Manganese (0.5%), and Cobalt (59.75%). The powder is supplied by H.C. Starck, Germany under the product code Amperit 536. The powder particle size is 15–53 μm .
3. **Tungsten Cobalt Chromium (WC-Co-Cr):** Tungsten Cobalt Chromium powder, when sprayed using the Detonation Spray process, it produces coatings, which exhibit excellent abrasive wear resistance under dynamic loading. In addition higher particle velocity during deposition provides several advantages such as lower porosity, higher bond strength and hardness. It also has excellent corrosion resistance in acidic environment. The powder is supplied by H.C. Starck, Germany under the product code Amperit 556. The powder is agglomerated and sintered having particle size as 15–45 μm .

2.3 Deposition of Coatings by Detonation Spray Process

The Ni-Cr , $\text{Cr}_3\text{C}_2\text{-NiCr}$ and WC-Co-Cr powders were successfully deposited on ductile cast iron substrate material by the Detonation Spray Process. Prior to the application of the coatings, the specimens were grit blasted using Al_2O_3 (mesh size 30) to thinly remove the metal surface layer and to create a rough contour on the surface necessary for the adhesion of the coatings. The blasted surfaces, with the surface roughness of about 8–10 $\mu\text{m Ra}$, were then thermally sprayed with three above said powders. The process parameters employed during deposition of coating are tabulated in Table 2.

Table 2 Detonation spray parameters for Ni–Cr, Cr₃C₂–NiCr and WC–Co–Cr coating

Parameters	Coatings		
	WC–Co–Cr	Cr ₃ C ₂ –NiCr	N–Cr
Pressure of fuel gas (Oxygen) (bar)	2	2	2
Pressure of fuel gas (Acetylene) (bar)	1.5	1.5	1.5
Pressure carrier gas (Nitrogen) (bar)	3	3	3
Flow rate of fuel gas (Oxygen) (LPM)	2960	2640	2800
Flow rate of fuel gas (Acetylene) (LPM)	2400	2320	2240
Flow rate of carrier gas (Nitrogen) (LPM)	720	720	820
Stand-off distance (mm)	165	165	165
Substrate temperature (°C)	110	110	110
Coating thickness (μm)	180–220	180–220	180–220

2.4 Wear Test Using Pin-on-Disc Apparatus

2.4.1 Experimental Set up

The wear tests were conducted on uncoated and detonation spray coated cylindrical specimens using a pin-on-disc machine (Wear and Friction Monitor Tester TR-201) conforming to ASTM G99 standard. The tests were conducted at room temperature. The pin-on-disc test is generally used as a comparative test in which controlled wear is performed on the samples to study. Wear tests were performed on the specimens that had flat surfaces at the end faces of pins. The pin was held stationary against the counter face of a rotating disc made of carbon steel (En-31) at 80 mm track diameter. En-31 steel is a plain carbon steel; case hardened 62–65 HRC as provided with the pin-on-disc machine.

2.4.2 Sliding Wear Studies

The uncoated as well as coated specimens were prepared for sliding wear studies. The pins were polished with emery paper and both disc and the pin were cleaned and dried before carrying out the test. The pin was loaded against the disc through a dead weight loading system. The wear tests for coated as well as uncoated specimens were conducted under three normal loads of 30N, 40N and 50N and a fixed sliding velocity of 1 m/s. The track radii for the pins were kept at 80 mm. It is equipped with a variable speed motor and the speed can be changed at any time during the tests. The speed of rotation of the disc (239 rpm) for all the cases was so adjusted so as to keep the linear sliding velocity at a constant value of 1 m/s. A variation of ± 5 rpm was observed in the rpm of the disc. Wear tests have been carried out for a total sliding distance of 5400 m (6 cycles of 5, 5, 10, 10, 20, 40 min duration), so that only top coated surface was exposed for each detonation sprayed specimen. Weight losses for pins were measured after each cycle to

determine the wear loss. The pin was removed from the holder after each run, cooled to room temperature, brushed lightly to remove loose wear debris, weighed and fixed again in exactly the same position in the holder so that the orientation of the sliding surface remains unchanged. All weight measurements were carried out on a 0.1 mg precision balance.

2.4.3 Wear Rate

The wear rate data for the coated as well as uncoated specimens were plotted with respect to sliding distance to establish the wear kinetics. The specific wear rates for the coated and uncoated material were obtained by

$$W = \delta w / L\rho F$$

where

- W denotes specific wear rates in, Bowden (B) ($1B = 10^{-6} \text{ mm}^3/\text{N m}$)
- δw is the weight loss measured in, g
- L the sliding distance in, m
- ρ the density of the worn material in g/mm^3 and
- F the applied load in N.

2.4.4 Wear Volume

The wear volume loss was also calculated from the weight loss and density of the coatings as well as substrate material for all the investigated cases. These data were reported in the form of plots showing the cumulative wear volume loss versus cumulative time for all the cases.

$$\text{Volume} = \text{mass}/\text{density}$$

$$\text{Wear Volume Loss} = (\delta w/9.81)/\rho$$

where

- δw is the weight loss in, g and
- ρ is the density of material, g/mm^3 .

2.5 Field Trial and Assessment

In order to test the wear behaviour of the thermally sprayed piston rings in field condition, a 4 cylinder, 60 Horse Power tractor engine is chosen to run for 80 h at Standard Corporation India Ltd., Handiaya village, District Barnala, Punjab, India.

The piston rings was fitted on to the piston which was further put into cylinder liner of 3456 cc, 60 Horse Power liquid cooled engine and torque 180 Nm at a speed of 2200 rpm run for 8 h a day. Average fuel consumption was about 10 l/h.

Wear of the piston rings was assessed by weighing each ring before and after each experimental period to determine the weight loss. The measured weight losses were then divided by the density of the base material for the hard chrome coated piston ring and by the coating densities for the other coated rings. The volume losses were used as an indicator of the amount of wear. Wear rate was defined as the volume loss per unit time; the unit is millimeter cube per hour (mm^3/h). The wear resistance index was calculated as the wear rate of the hard chrome coated ring divided by that of the other coated one. The higher the wear resistance index, the coating is more protective. The coated piston rings are shown in Fig. 1.

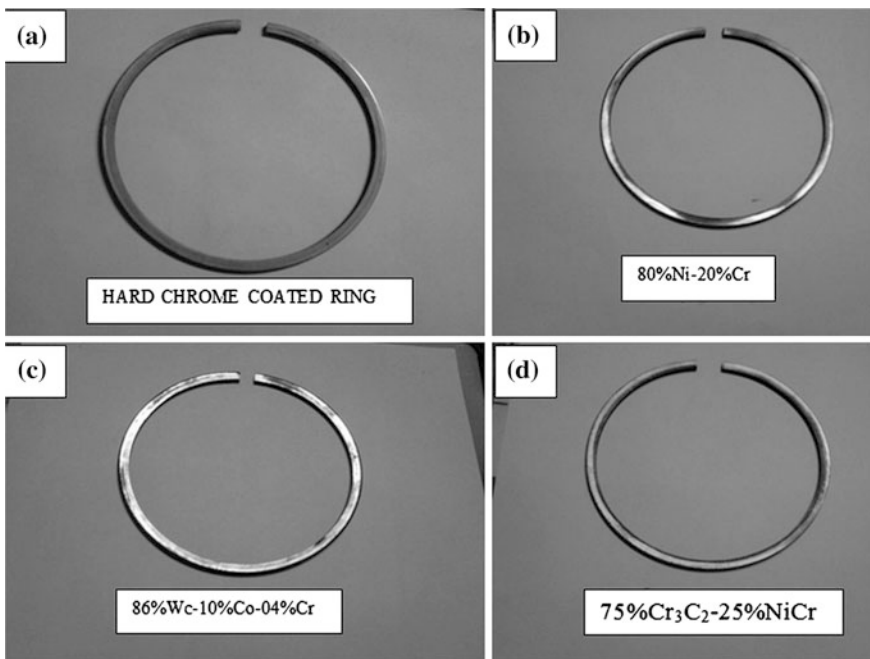


Fig. 1 D-Gun sprayed piston rings

3 Result and Discussion

3.1 Wear Behavior

3.1.1 Laboratory Test

Three samples of each coating i.e. Cr_3C_2-NiCr , $WC-Co-Cr$ and $Ni-Cr$ on ductile cast iron were subjected to wear on Pin-On-Disc wear test rig at normal loads of 30N, 40N and 50N respectively. Three samples of hard chrome coating were also subjected to wear on Pin-On-Disc wear test rig at the same loads. The cumulative volume loss versus time for each sample is plotted as shown in Fig. 2. It is observed from the results (Fig. 2) that the three coatings; Cr_3C_2-NiCr , $WC-Co-Cr$ and hard chrome have shown lower wear resistance as compared to $Ni-Cr$. The wear rate of hard chrome is also more as compared to other coatings which is shown by a curve between CVL and time in Fig. 2.

It is observed from the results that $Ni-Cr$ is showing almost negligible cumulative volume loss as compared to other coatings. Therefore the wear resistance of Detonation sprayed coatings on ductile cast iron in their decreasing order can be given as $Ni-Cr < WC-Co-Cr < Hard\ Chrome < Cr_3C_2-NiCr$.

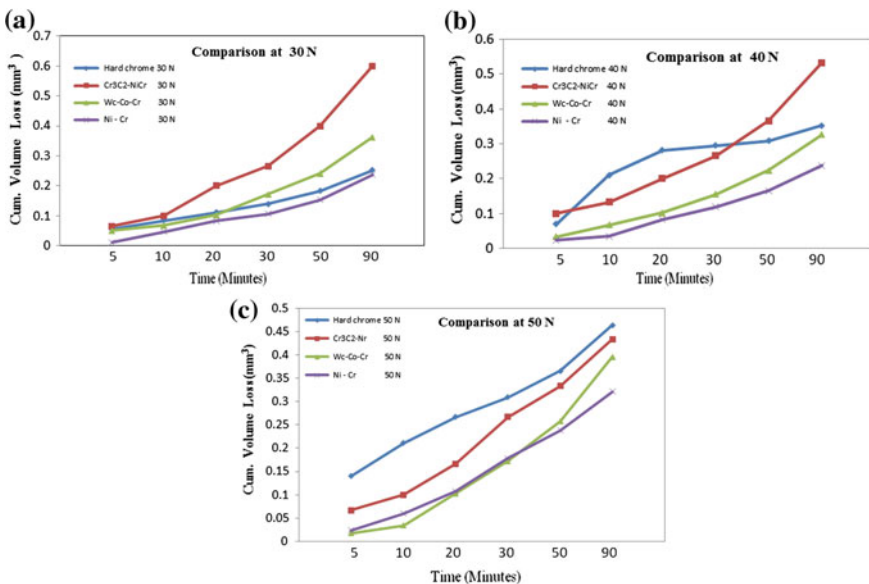
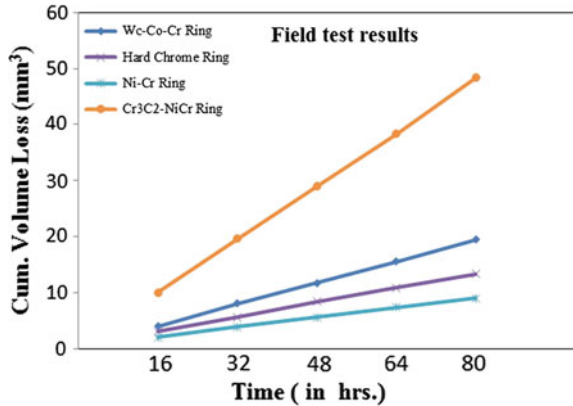


Fig. 2 Cumulative volume loss (mm^3) comparison of Cr_3C_2-NiCr , $WC-Co-Cr$ and $Ni-Cr$ with Hard Chrome Coating at **a** 30N **b** 40N **c** 50N

Fig. 3 Field test results (cumulative volume vs. time)



3.1.2 Field Trial Observations

The coated piston rings were fitted onto the piston in place of the standard rings and the field experiment was carried out on 60 H.P. 4 cylinder Engine. After the test, the rings revealed various amount of wear as shown in Fig. 3. The extent of wear is quantifiable even though the test was conducted for a short time.

3.1.3 Weight Loss and Wear Rate Assessment

In order to obtain a precise wear rate of each ring, the cumulated volume losses of the tested rings at various intervals were plotted against the time (Fig. 3), by using the wear data obtained.

The wear resistance index (WRI), indicating the superiority of the tested ring in comparison with the hard chrome coated ring, is calculated by dividing the wear rate of hard chrome coated ring with wear rate of other coated rings.

The wear resistance indices of the tested rings are presented in Table 3.

Table 3 Wear rates and wear resistance indices of D-Gun sprayed rings in the field test

Coating	Wear rate (mm ³ /h)	WRI
Chrome coated ring	0.1672	1
Ni-Cr coated ring	0.1132	1.4770
Cr ₃ C ₂ -NiCr coated ring	0.6041	0.2767
WC-Co-Cr coated ring	0.2435	0.6866

4 Conclusions

Based upon experimental results obtained in the present work, the following conclusions have been drawn:

1. Detonation Sprayed Ni–Cr, Cr₃C₂–NiCr, and WC–Co–Cr coatings have successfully been deposited on ductile cast iron.
2. Among the detonation sprayed Ni–Cr, Cr₃C₂–NiCr, and WC–Co–Cr coated ductile cast iron specimens, Ni–Cr showed significantly lower cumulative volume loss.
3. Ni–Cr hard chrome coating substrate combination has shown minimum cumulative volume loss among all the combinations.
4. Field test of WC–Co–Cr coated ring show some wear damage, while the Cr₃C₂–NiCr coated ring show very large wear damage, on the other hand Ni–Cr coated ring shows almost negligible wear damage. The WRIs for Ni–Cr, Cr₃C₂–NiCr and WC–Co–Cr coated rings are 1.4770, 0.2767, and 0.6866, respectively. Therefore, the Ni–Cr coated ring will be more reliable and more capable at lengthening the service life of the piston ring.

References

1. Rajasekaran B, Ganesh Sundara Raman S, Joshi SV, Sundararajan G (2009) Effect of grinding on plain fatigue and fretting fatigue behaviour of detonation gun sprayed Cu–Ni–In coating on Al–Mg–Si alloy. *Int J Fatigue* 31:791–796
2. Murthy JKN, Venkataraman B (2006) Abrasive wear behaviour of WC–Co–Cr and Cr₃C₂–20 (NiCr) deposited by HVOF and detonation spray processes. *Surf Coat Technol* 200:2642–2652
3. Sundararajan G, Sen D, Sivakumar G (2005) The tribological behaviour of detonation sprayed coatings: the importance of coating process parameters. *Wear* 258:377–391
4. Karoonboonyanan S, Salokhe VM, Niranatlumpong P (2007) Wear resistance of thermally sprayed rotary tiller blades. *Wear* 263(1–6):604–608
5. Murthy JKN, Rao DS, Venkataraman B (2001) Effect of grinding on the erosion behaviour of a WC–Co–Cr coating deposited by HVOF and detonation gun spray processes. *Wear* 249 (7):592–600

Experimental Analysis of Different Compositions of Carbon Fiber/Epoxy Composite and Its Application in Leaf Spring

L.B. Raut and A.R. Katu

Keywords Composite mono leaf spring · Optimization · Compressive strength · Natural frequency

1 Introduction

Currently, the fuel efficiency, as well as emission gas regulation of automobiles, are two important issues. To fulfill this problem, the automobile industries are trying to make new designs of vehicle which will provide high efficiency with less cost. The best method to improve the fuel efficiency is to minimize the weight of the vehicle. The weight reduction can be obtained mainly by the introduction of better material, design optimization, and better manufacturing processes. The achievement of weight reduction with an adequate improvement of mechanical properties has made composite a very good replacement material for conventional steel. In automobile car one of the components of automobile which can be easily replaced is leaf spring. A leaf spring is a simple type of spring, commonly utilized for the suspension in wheeled vehicles. The suspension of leaf spring is the area which needs to focus to improve the suspension system for the comfort ride. The suspension leaf spring is one of the potential items for weight reduction in an automobile as it accounts for 10–20% of unsprung weight. It is well known that, springs are designed to absorb shocks. So the strain energy of the material becomes a major factor in designing the springs. The introduction of composite material will make it possible to reduce the weight of the leaf spring without reduction in load carrying capacity and stiffness. Since the composite material has more strength to weight ratio and have more elastic strain energy storage capacity as compared with steel. Thus composite material offer high strength and light weight. In this work, leaf

L.B. Raut (✉) · A.R. Katu
SVERI's College of Engineering, Pandharpur, India
e-mail: lbaut@coe.sveri.ac.in

A.R. Katu
e-mail: amitkatu@gmail.com

springs of automobile light passenger vehicle is considers for further investigation. The suspension quality can be improved by minimizing the vertical vibrations, impacts and bumps due to road irregularities which create the comfortable ride [1].

2 Experimental Procedure

2.1 Materials and Methods

(a) Matrix Material

Epoxy resins are thermosetting polymers which are used as adhesives, high-performance coating, sand plotting and encapsulating materials. These resins have excellent electrical properties, low shrinkage, good adhesion to many metals and resistance to moisture, thermal and mechanical shock. Viscosity, epoxide equivalent weight, and the molecular weight are the important properties of epoxy resins [2].

(b) Fiber Material

Carbon fibers (CF) or graphite are fibers about 5–10 μ m in diameter and composed mostly of carbon atoms. To create a carbon fiber, the carbon atoms are bonded together in crystals that are more or less aligned parallel to the long axis of the fiber as the crystal alignment gives the fiber high strength-to-volume ratio. The thousand of carbon fibers are bundled together to form a tow, which may be used by itself or woven into the fabric. The properties of carbon fibers, such as high stiffness, high tensile strength, low weight, high chemical resistance, high-temperature tolerance and low thermal expansion, make it very popular in aerospace, civil engineering, military, and motorsports, along with other competition sports [3].

The carbon fiber/epoxy composite is fabricated using simple hand layup technique and details of volume fraction are shown in Tables 1 and 2.

Table 1 Details of sample prepared

Matrix	Volume %	Reinforcement	Volume %
Epoxy	65	Carbon fiber	35
Epoxy	55	Carbon fiber	45
Epoxy	45	Carbon fiber	55

Table 2 Weight of fiber and matrix in carbon/epoxy laminate

No.	Laminate	Total Wt. (W_T) g	No. of plies	Wt. of fibre (W_f) g	Wt. of matrix (W_m) g	Actual % of carbon fibre	Thickness of laminate (mm)
1	35:65	391	10	180	211	36.25	3
2	45:55	412	13	234	178	46.70	3
3	55:45	434	16	288	146	56.80	3

3 Results and Discussion

3.1 Mechanical Testing

The fabrication involves three dissimilar compositions of composites where the composite plates are cut down according to the ASTM standards in order to conduct tensile, flexural and impact test on every specimen. Tensile test, 3-point bend test and impact test were performed in accordance with ASTM D3039, ASTM D790 and ASTM D6110 standards [4].

Tensile Test. The tensile testing was performed on universal testing machine (Table 3).

The tensile test is conducted for three different cases. Figure 1 shows the results for three different series of Carbon fiber Epoxy. From Fig. 1, it is clear that 45:55% by volume of Carbon fiber epoxy has higher tensile strength as compared to other two volume percentages.

Flexural Test. The flexural test gives the determination of maximum load bearing capacity of the materials at the one set of plastic deformation of the composites. From this ultimate flexural stress and flexural strain are computed. Flexural strength was determined using three points simply supported bending equipment attached with the precision dial gauge and digital load indicator (Table 4).

The bending test is carried out for different volume percentage of Carbon fiber epoxy composites. Figure 2 shows the results for three different series of Carbon fiber epoxy.

From the Fig. 2, it is clear that, the volume percentage of 55:45% of Carbon fiber epoxy has the highest bending strength as compared to other two volume percentages.

Impact Test. Impact test was performed using Charpy impact test. Impact tests are used for studying the toughness of material. A material’s toughness is a parameter of its ability to absorb energy during plastic deformation. Variation of the impact energy along and across the laminates for three different compositions of composites is as shown in Fig. 3 and Table 5.

From Fig. 3, it is clear that, volume percentage of 55:45% of carbon fiber epoxy has the highest impact strength as compared to other two volume percentage.

Table 3 Tensile strength testresult

Sr. No.	Sample description	Tensile strength (MPa)	Elongation (%)	Modulus (MPa)
1	Carbon fiber 35%	552.66	6.23	20666
2	Carbon fiber 45%	604.88	6.13	23826
3	Carbon fiber 55%	550.75	6.00	26389

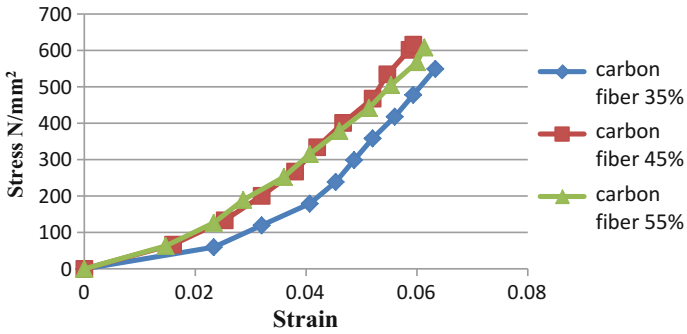


Fig. 1 Comparison of tensile strength for different composition

Table 4 Flexural strength test result

Sr. No.	Sample description	Flexural strength (MPa)	Modulus (MPa)
1	Carbon fiber 35%	474.4	32475.5
2	Carbon fiber 45%	440.4	40481.5
3	Carbon fiber 55%	513.0	40133.0

Fig. 2 Comparison of bending strength for different composition

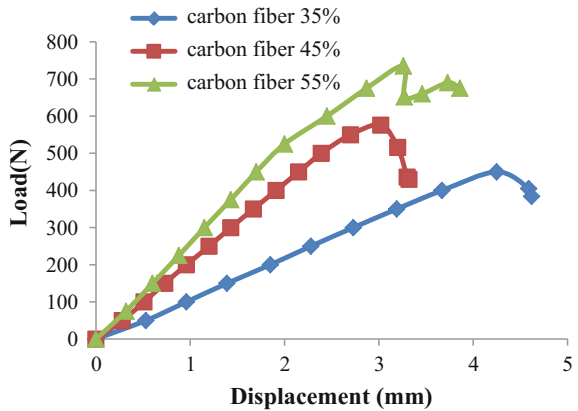
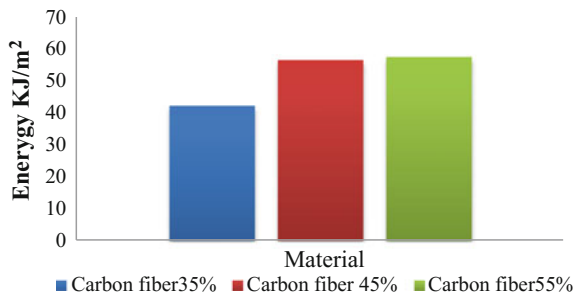


Fig. 3 Impact strength for different composition



3.2 Experimental Testing Using FFT Analyzer

Normally natural road frequency is 12 Hz. Hence more the natural frequency of leaf spring is required. But the conventional steel leaf spring frequency is more than road frequency. Therefore calculating natural frequency of composite leaf spring is important and for that we use FFT analyzer and compare the result with FEA results. Here we have tested both steel and composite mono-leaf spring on FFT analyzer [5].

3.2.1 Modal Analysis

When an elastic system free from external loads can disturb from its equilibrium position and vibrates under the influence of inherent forces and is said to be in the state of free vibration. It will vibrate at its natural frequency and its amplitude will gradually become smaller with time due to energy dissipated by motion. The natural frequencies as well as the mode shapes are important parameters in the design of a structure for dynamic loading conditions. Modal analysis is used to determine the vibration characteristics such as natural frequencies and mode shapes of a structure or a machine component while it is being designed. The rotational speed is controlled by lateral stability considerations [6] (Table 6).

The comparison between natural frequencies obtained from steel and composite material leaf spring is shown in Figs. 4, 5 and 6. It is seen that composite material leaf spring is having higher frequency than the steel leaf spring (Table 7).

Static Load Test. The primary concern behind carrying a Static load test lies in determining the performance characteristics of a Steel leaf spring and a composite leaf spring. The performance characteristics include load carrying capacity and weight Table 8 comparison. The steel and composite leaf springs are tested in the UTM [7].

Table 5 Impact strength test result

Sr. No.	Sample name	Test result (kJ/m ²)
1	Carbon fiber 35%	42.12
2	Carbon fiber 45%	56.46
3	Carbon fiber 55%	57.40

Table 6 Results of FFT analyzer test

Frequency	Steel (Hz)	Carbonfiber/epoxy (Hz)
1st natural frequency	82	134
2nd natural frequency	228	278
3rd natural frequency	421	508

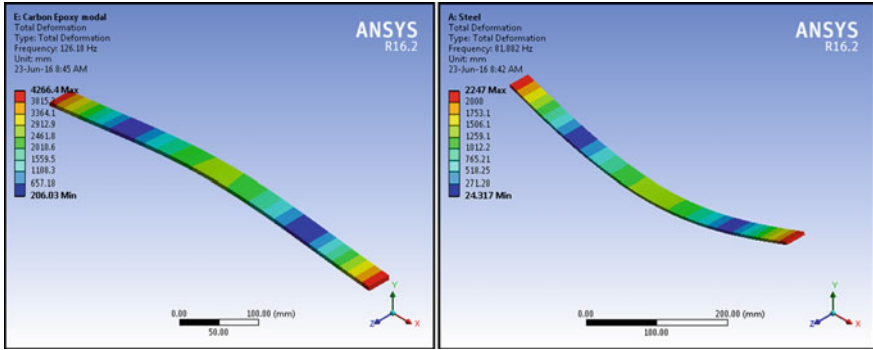


Fig. 4 First natural frequency of composite leaf spring and steel leaf spring

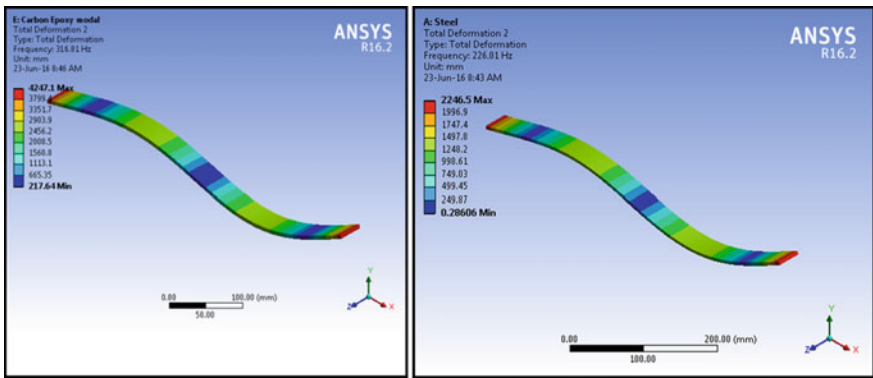


Fig. 5 Second natural frequency of composite leaf spring and steel leaf spring

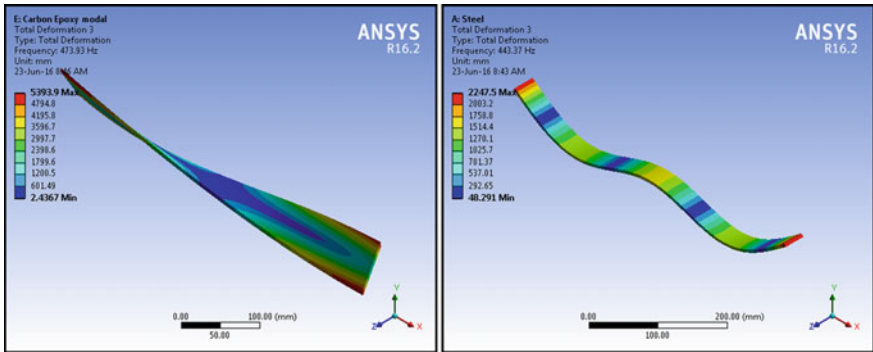


Fig. 6 Third natural frequency of composite leaf spring and steel leaf spring

Table 7 Finite element analysis result

Frequency	Composite material leaf spring (Hz)	Steel leaf spring (Hz)
1st frequency	126.18	81.9
2nd frequency	316.81	226
3rd frequency	473.93	443.4

Table 8 Deflection of spring at different load

Load (N)	Deflection (mm)	
	E-carbon leaf spring	Steel leaf spring
0	0	0
50	4.5	0.33
90	9.72	1.53
180	26.26	3.74
270	33.51	5.78
320	36.33	6.55
360	38.21	7.89
410	39.62	8.63
450	42.1	9.97

3.2.2 Comparison Between Experimental and FEA Results

From Fig. 7, it is observed that the results obtained from FEA are in good agreement with the results obtained from experimental solution. Hence, the design of composite material leaf spring is accurate enough to work properly in working conditions.

Comparison results of load and weight. After conducting tests, the composite leaf spring results are compared with the steel leaf spring and the comparison is made based on weight, which is shown in Table 9.

3.2.3 Comparison Between Steel and Composite Leaf Spring

The difference in results is compared for mass and the fundamental natural frequency and deflection, also the difference has been found in natural frequency using ANSYS 16.2. Table 10 shows that the comparison between steel and composite material leaf spring in which applied same load for steel and composite leaf spring, Minimum requirement of natural frequency is 80 Hz which can be achieved by both steel and Composite leaf spring. Composite leaf spring is having very low weight of 0.131 kg whereas steel shaft of weight is 1.118 kg.

Fig. 7 Comparison between experimental and FEA results of natural frequency of composite leaf spring

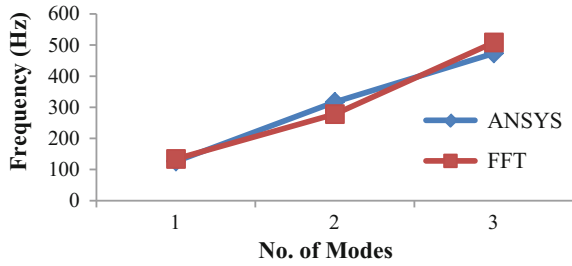


Table 9 Weight of leaf spring

Leaf spring	Steel	Carbon fiber epoxy
Weight (kg)	1.118	0.131

Table 10 Comparison between steel and composite leaf spring

Parameter	Steel leaf spring	Composite leaf spring
Natural frequency (f_n)	82 Hz	134 Hz
Mass (m)	1.118 kg	0.131 kg
% saving in mass	88.43%	

4 Conclusions

A one-piece composite material leaf spring for light weight vehicle has been designed optimally by using classical lamination theory with the objective of minimization of weight of the unsprung mass which was subjected to the constraints such as natural frequency.

1. The weight of the composite leaf spring is reduced by 88.43% as compared to steel leaf spring with same stiffness.
2. It is found that 55:45 volumetric fraction gives optimum results.
3. A comparative study has been made between composite leaf spring and steel spring with respect to weight, natural frequency and deflection.
4. A composite leaf spring can be used on smooth road condition as well as rough condition.

References

1. Gebremeskel SA (2012) Design, simulation, and prototyping of single composite leaf spring for light weight vehicle. Global J Res Eng Mech Mechn Eng 12(7):Version 1.0 Year 2012
2. Samuel John D, Rajenrapasad G (2013) Experimental investigation of mechanical behavior of glass epoxy composites. Int J Adv Trends Comput Sci Eng 2(1):541–548

3. Bankar P, Shivananda HK (2012) Preparation and characterization of the carbon fibre reinforced epoxy resin composites. IOSR, J Civil Mech Eng 1(2). ISSN: 2278-1684
4. Suhas JDQ, Davangiri MB (2016) Investigation on different compositions of e-glass/epoxy composite and its application in leaf spring. IOSR J Mech Civil Eng 11(1)
5. Eranpurwala M, Ajuvath S, Experimental and computational methods to find the modal frequencies of e-glass/epoxy mono composite leaf spring designed for TATAACE HD
6. Anil Kumar M, Charyulu TN, Ramesh CH (2012) Design optimization of leaf spring. Int J Eng Res Appl (IJERA) 2(6), 759–765, 759. ISSN: 2248-9622
7. Patil RM, Harote SM, Patil VS (2014) Fabrication and testing of composite leaf spring for light passenger vehicle. Int J Curr Eng Technol. ISSN 2277-4106 © 2014 INPRESSCO

Development of a Friction Welded Bimetallic Joints Between Titanium and 304 Austenitic Stainless Steel

Muralimohan Cheepu, V. Muthupandi, B. Srinivas and K. Sivaprasad

Keywords Friction welding · Dissimilar materials · Aluminium interlayer · Intermetallic compounds · Mechanical properties

1 Introduction

In recent years, joining of dissimilar materials was investigated because of its complex functions and several applications in the variety of sectors such as nuclear industries, petrochemical, aerospace, automobile and marine applications [1–3]. In many cases it is necessary to make a metallurgical bond between two metals. Various techniques available for joining dissimilar metal combinations are generally limited to those which do not result in the melting and solidification of the materials to be welded. The joining of dissimilar metals such as Ti alloys to stainless steels is a derogatory issue due to the occurrence of stress concentration, chemical segregation and formation of brittle intermetallic compounds. To solve this problem, researchers have tried many joining processes such as brazing, explosive and diffusion welding. Brazing is frequently associated with cracks that

M. Cheepu (✉) · V. Muthupandi
Department of Metallurgical and Materials Engineering, National Institute of Technology, Tiruchirappalli 620015, Tamil Nadu, India
e-mail: muralicheepu@gmail.com

M. Cheepu
Department of Advanced Materials and Industrial Management Engineering,
Dong-Eui University, Busan 47340, Republic of Korea

B. Srinivas
Department of Mechancial Engineering, MVGR College of Engineering,
Vizianagaram 535005, Andhra Pradesh, India

K. Sivaprasad
Advanced Materials Processing Laboratory, Department of Metallurgical
and Materials Engineering, National Institute of Technology, Tiruchirappalli
620015, Tamil Nadu, India

occur and develop in the joint because of the formation of intermetallic compounds [4, 5]. The use of interlayer foils like Al, Ni, Nb, Cu, Va and Ta as an intermediate layer influences the quality of the joints formed during the solid state process. Diffusion bonding of SS to Ti with suitable interlayers has led to some success, though formation of undesirable intermetallic phases like Fe–Ti, Cr–Ti, Ni–Ti could not be entirely eliminated [6] and it offers excellent resistance to high temperature [7]. However, it is a time consuming technique and leads to high residual stresses in the welds. Explosion welding that results in formation of brittle intermetallics such as FeTi and Fe₂Ti and accumulation of significantly high residual stresses at interface of the welds has also been used to bond SS to Ti in many applications [8]. Friction welding, apart from other welding techniques is distinguished by very short welding times and thus extremely short cycle times [9, 10]. In friction welding, heat for welding is produced by relative motion of the two surfaces being joined, under normal conditions no interfacial melting occurs. While the friction welding of mono and multi-metallic combinations exhibiting either perfect or limited solubility in the solid state does not present any metallurgical problems materials which interact among themselves forming intermetallic compounds often pose difficulties in obtaining quality joints. In the study made by Dey et al. on welding of Ti to 304 SS friction welding parameters were optimized to produce joints that were stronger than Ti base material but the presence of intermetallics could not be avoided [11]. The use of Ta, V and Ni as interlayers either singly or in combination was reported for friction welding of Ti to SS to achieve joints with better mechanical properties and the absence of brittle intermetallic phases [12]. Muralimohan et al. [13] showed that friction welding between Ti and SS with Ni interlayer shifted the tensile fracture from the SS/weld interface to the Ti/weld interface and could avoid the formation Fe–Ti intermetallics.

In the present investigation, titanium was joined to SS 304 by friction welding with aluminium interlayer adopting three different combinations of welding parameters. Microstructures of the weld interfaces and elemental distribution across the interfaces were characterized. Mechanical properties of the welds were assessed by tensile test and hardness survey.

2 Experimental Method

Titanium and type 304 stainless steel rods of 16 mm diameter having chemical composition (wt%) Ti–0.17O–0.03Fe–0.014H–0.03N–0.09C and Fe–19Cr–8.2Ni–0.08C–0.38Si–1.74Mn, respectively were the base material considered. Mechanical properties of the Ti and SS 304 were: yield strength 285 and 246 MPa, tensile strength 460 and 542 MPa, and elongation 42 and 67% respectively. A KUKA constant drive friction welding machine operated at a constant speed of 1125 rpm was considered for the joining experiments. The main parameters used to produce the joints were: heating phase-heating pressure and heating time and forging phase-upset pressure and upset time. Parameters employed in performing the three

Table 1 Parameters used in the friction welding trials

Trials	Heating pressure (MPa)	Heating time (s)	Upsetting pressure (MPa)	Upsetting time (s)
P1	85	2	160	5
P2	110	4	160	5
P3	145	6	160	5

trials P1, P2 and P3 are given in Table 1. Friction welding was carried out in two steps to complete the weld. In the first step SS 304 rods were joined to rods of commercially pure Al. In the joint Al rod was cut down to 2 mm thick. Resultant SS-Al was joined to Ti by making Al to face Ti. Thus the welding was completed to yield joints of SS to Ti with Al interlayer. The joints were characterized by narrow heat affected zone, presence of plastically deformed material at the weld area (flash), and the absence of the fusion zone. The 2 mm thick aluminium interlayer was selected to form good bond strength and to avoid the diffusion of atoms between two base metals. Selection of heating time and heating pressure was focused at the interface between the Al and Ti to prevent the formation of intermetallics at Al/Ti interface. Thus the Ti-SS interaction was minimized, and the risk of the formation of brittle intermetallics due to the direct interaction between the Ti and the SS component was diminished.

Diametrically cut longitudinal sections of the joints were prepared for metallographic observations as per standard the procedure. Microstructures of the weld interfaces were recorded and analyzed using an optical microscope and SEM. The composition across the interface was examined using SEM-EDS system using a line scan mode. Hardness survey was conducted across the interfaces of the weld using a Zwick 3212 Vickers microhardness tester. Tensile properties of the joints were assessed using a Universal Testing Machine of model TFUC-400. Tensile fractured surfaces were characterized by SEM.

3 Results and Discussion

3.1 Mechanical Properties

The micro-hardness survey was conducted across the weldment covering base material, HAZ (thermo-mechanically affected zone) and interlayer, in both 304SS and Ti sides. Figure 1 shows the cross-sectional hardness profile. It can be seen from the figure, all the three trials P1, P2 and P3 exhibit a similar trend in microhardness distribution. Steep increase in hardness in titanium side near the interface can be related directly to the microstructure formed in the weld as a result of the strain hardening due to extensive plastic deformation. However, there is no appreciable increase in hardness in 304SS side compared to initial hardness of the base metal indicating that strain hardening is less and the extent of deformation is

Fig. 1 Hardness profile across the Ti/Al/SS joint

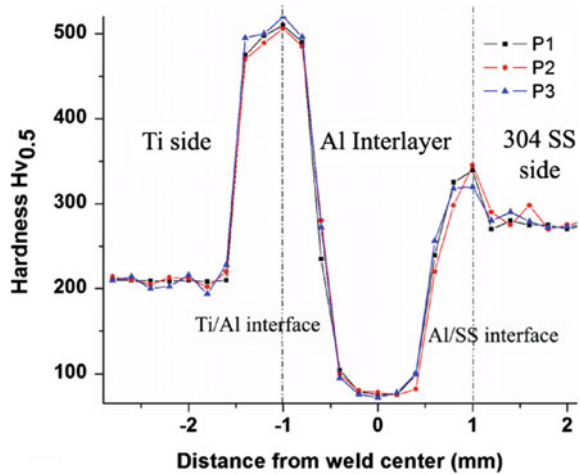


Table 2 Obtained tensile strength values

Trials	Heating pressure (MPa)	Heating time (s)	Tensile strength (MPa)
P1	85	2	208
P2	110	4	256
P3	145	6	232

limited in 304SS compared to Ti. The peak hardness recorded at Ti/Al interface can be attributed to the formation of intermetallic compounds of Al–Ti. Generally, these hard intermetallics tend to have detrimental effects on mechanical strength and consequently on the quality of the joint. Increase in hardness at Al/SS interface can be attributed to plastic deformation accumulated in Al interlayer. Aluminum interlayer recorded the lowest hardness 72 Hv. However, it is higher than the initial hardness 45 Hv of the Al base material, the increase in the hardness in Al interlayer is due to the strain hardening effect.

Tensile test is used to determine the strength of weld joints and besides parameters settings, optimization and qualification of welding procedures and processes. The influence of heating pressure and heating time on the strength of the welds were examined in welding of equal diameter parts. The acquired tensile strengths for all three trials for which upsetting pressure and time are 160 MPa and 5 s, respectively, are given in the Table 2.

Tensile strength of the joints varies with friction welding parameters. In all the trials, the strength of the weld joint is lesser than that of Ti. Tensile fracture occurred at the Ti/Al weld interface as a result of the intermetallics formed at this interface. The test results are plotted between heating pressure, heating time and fracture strength and are shown graphically in Figs. 2 and 3. It can be observed from Figs. 2 and 3, tensile strength of the Ti/Al/SS friction welded joints for constant upsetting pressure and time, increases with increase in the heating time and heating pressure and reaches a maximum.

Fig. 2 Relation between heating pressure and tensile strength

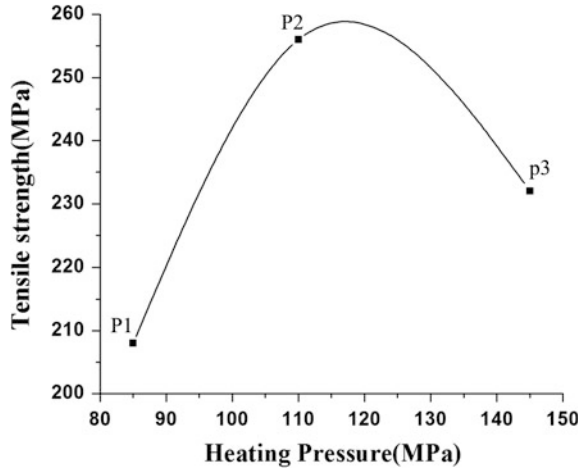
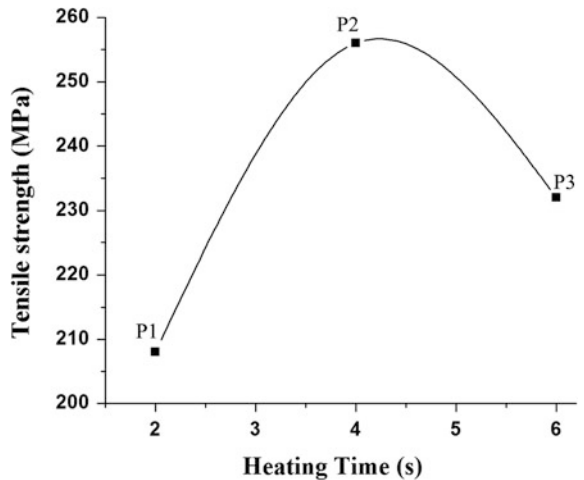


Fig. 3 Relation between heating time and tensile strength



Subsequent increase in these parameters results in reduction in the tensile strength. Existing literature reports [14] that heating time and heating pressure have a direct effect on joint strength. Heating pressure and time jointly decides the maximum temperature attained at the interface they also independently influence the degree of deformation and the extent of diffusion of individual alloying elements, respectively. Though in all the joints tensile failure occurred at Ti/Al weld interface in brittle mode, increase in heating time and heating pressure could have affected the nature, amount and morphology of the brittle intermetallics which in turn affected the bond strength adversely. Therefore, the variation in weld strength with heating pressure and time can be attributed to the formation of range of Al-Ti intermetallics.

3.2 Microstructural Observations

Figure 4 shows a typical friction welded Ti/Al/SS joint. These welds exhibit characteristic flash formation at the weld interface. A macrograph of transverse cross sectional view of the weld specimen is shown in Fig. 5. In the joint, flash formation is confined to Al interlayer. Further the deformation on both sides of the joints is asymmetric. In the case of dissimilar metal joint by friction welding, the formation of flash depends on the mechanical and thermo physical properties of the substrates involved [15].

The microstructure of the cross section of the SS to Ti joints with Al interlayer is shown in Fig. 6. It indicates that Ti deformed to a greater extent due to the frictional heat produced by heating time and heating pressure. Ti was subjected to plastic deformation at elevated temperatures. However, possible dynamic recrystallisation had resulted in fine equiaxed grains near the weld zone. Appreciable change is not observed in grain size of stainless steel. The mechanical deformation and frictional heat at the interface that dissipated through the substrates had resulted in a

Fig. 4 Photograph of friction welded Ti/Al/SS joint

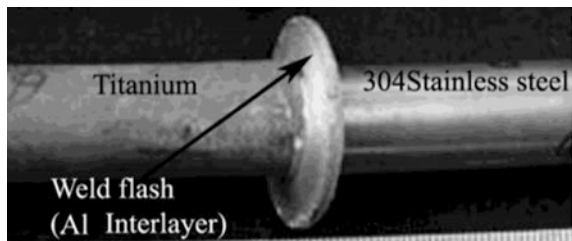


Fig. 5 Macrograph showing the cross section of the joint

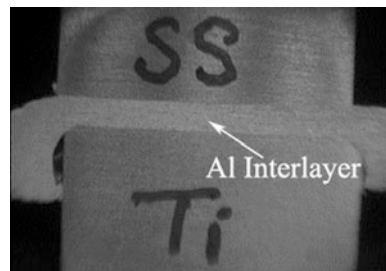
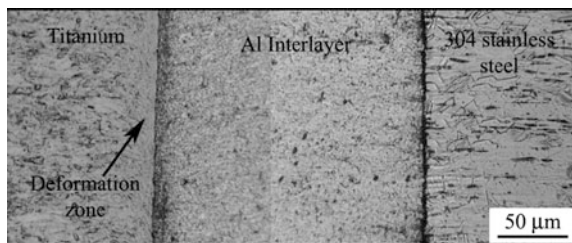


Fig. 6 Macrostructures of the cross sections of the Ti/Al/SS joints



temperature gradient causing materials with different microstructures. Moreover, application of pressure to bring joint pair together by plastic deformation results in dynamic recrystallisation that leads to grain refinement in the central region of the weld [16]. A thin transition layer at the Al–Ti interface is revealed for all the trials. The Al–Ti interface is characterized by a thin transition layer with irregular interface at the interface area whereas the interface between SS–Al is planar in character. The microstructure of the SS consists of austenite phase with twin boundary and the width of the etched zone is between Al interlayer and SS interface is smaller than that the Ti–Al interface.

SEM energy dispersive X-ray analysis is employed to investigate the diffusion of elements across the interface during welding. EDS line scan analysis was used in the examinations. The EDS line scan analysis across the Al/SS interface reveals the intermixing of Fe, Al, Ni and Cr, and also observed that the diffusion of Al into SS. The chemical composition at diffusion zone results in formation of FeAl_2 . The concentration profile of the Al/Ti interface is shown in Fig. 7. The EDS results confirm that Al–Ti interface contain some brittle intermetallic compounds. The atomic percent of the chemical elements at Ti/Al interface represents the formation of Al_3Ti and AlTi intermetallics. Therefore, formation of brittle intermetallic compounds degrades the strength of the joints.

3.3 Fracture Morphology Studies

In tensile tests fracture occurred taken at Al/Ti interface. EDS results revealed the formation of intermetallics. The SEM fracture surface analysis showed that the fracture was a combination of ductile and brittle mode (Fig. 8). The presence of Al–Ti intermetallics was the source of fracture in the welds and it caused reduction in the weld strength.

Fig. 7 SEM-EDS line scan across the Ti/Al interface

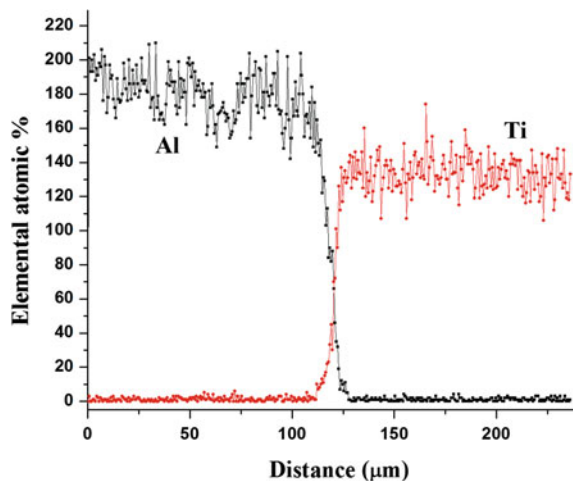
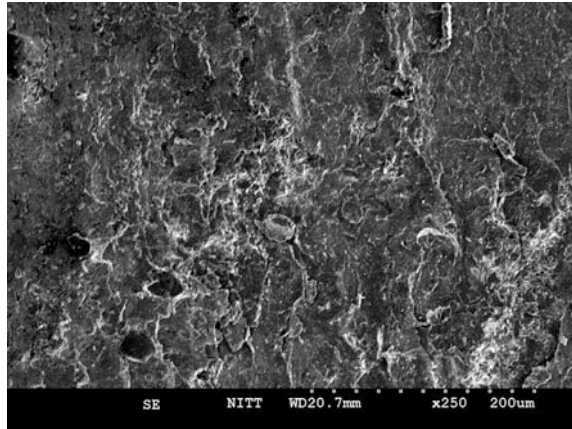


Fig. 8 SEM image of fracture surface on Ti side



4 Conclusion

In the present study, SS and Ti materials were welded successfully. Optimum welding parameters should be properly selected in the friction welding of parts. The joint strength increased and then decreased after reaching a maximum value, with increasing friction time. A longer friction time caused the excess formation of an intermetallic layer. However, the welds showed lower strength than that of Ti because of the presence of Al_3Ti and $AlTi$ intermetallics at the interface. The hardness of Ti/Al interface is higher than the Al/SS interface, which is attributed to Ti–Al intermetallics. Fractography also reveals that presence of intermetallics is the cause for the reduction in tensile strength. EDS analysis predicts the possible of formation of intermetallics such as $AlTi$, Al_3Ti and $FeAl_2$. Microstructural studies SEM and optical microscopy prove that the formation of transition layer at interface and crack free bonding of the Ti/Al/SS welds. Though with the use of Al inter layer, the presence of highly brittle Fe–Ti and Cr–Ti intermetallics can be avoided, it is not altogether possible to avoid the formation of intermetallics.

References

1. Muralimohan CH, Ashfaq M, Ashiri R, Muthupandi V, Sivaprasad K (2016) Analysis and characterization of the role of Ni interlayer in the friction welding of titanium and 304 austenitic stainless steel. *Metall Mater Trans A* 47(1):347–359
2. Muralimohan CH, Muthupandi V, Sivaprasad K (2014) Properties of friction welding titanium-stainless steel joints with a nickel interlayer. *Proc Mater Sci* 5:1120–1129
3. Muralimohan CH, Muthupandi V, Sivaprasad K (2014) The influence of aluminum intermediate layer in dissimilar friction welds. *Int J Mater Res (Former: Zeitschrift für Metallkunde)* 105(4):350–357
4. Winiowski A (2010) Mechanical and structural properties of joints of stainless steel and titanium brazed with silver filler metals containing tin. *Arch Metall Mater* 55:991–1000

5. Laik A, Shirzadi AA, Tewari R, Kumar A, Jayakumar T, Dey GK (2013) Microstructure and interfacial reactions during active metal brazing of stainless steel to titanium. *Metall Mater Trans A* 44:2212–2225
6. Kundu S, Ghosh M, Laik A, Bhanumurthy K, Kale GB, Chatterjee S (2005) Diffusion bonding of commercially pure titanium to 304 stainless steel using copper interlayer. *Mater Sci Eng A* 407:154–160
7. Muralimohan CH, Muthupandi V (2013) Friction welding of type 304 stainless steel to Cp titanium using nickel interlayer. *Adv Mater Res* 794:351–357
8. Manikandan P, Hokamoto K, Deribas AA, Raghukandan K, Tomoshige R (2006) Explosive Welding of titanium/stainless steel by controlling energetic conditions. *Mater Trans* 47:2049–2055
9. Muralimohan CH, Haribabu S, Hariprasada Reddy Y, Muthupandi V, Sivaprasad K (2015) Joining of AISI 1040 steel to 6082-T6 aluminium alloy by friction welding. *J Adv Mech Eng Sci*, 57–64
10. Muralimohan CH, Haribabu S, Hariprasada Reddy Y, Muthupandi V, Sivaprasad K (2014) Evaluation of microstructures and mechanical properties of dissimilar materials by friction welding. *Proc Mater Sci* 5:1107–1113
11. Dey HC, Ashfaq M, Bhaduri AK, Prasad Rao K (2009) Joining of titanium to 304L stainless steel by friction welding. *J Mater Process Technol* 209:5862–5870
12. Ashfaq M, Prasad Rao K, Khalid Rafi H, Murty BS, Dey HC, Bhaduri AK (2011) Friction welding of titanium to 304L stainless steel using interlayers. *Pract Metallogr* 48:188–207
13. Cheepu M, Muthupandi V, Loganathan S (2012) Friction welding of titanium to 304 stainless steel with electroplated nickel interlayer. *Mater Sci Forum* 710:620–625
14. Sahin M, Misirli C (2012) Mechanical and metalurgical properties of friction welded aluminium joints, aluminium alloys—new trends in fabrication and applications. Prof Zaki Ahmad (Ed.) (2012)
15. Li W-Y, Min Y, Li J, Zhang G, Wang S (2009) Characterization of 21–4N to 4Cr9Si2 stainless steel dissimilar joint bonded by electric-resistance-heat-aided friction welding. *Mater Des* 30:4230–4235
16. Ozdemir N, Sarsilmaz F, Hasçalık A (2007) Effect of rotational speed on the interface properties of friction welded AISI 304L to 4340 steel. *Mater Des* 28:301–307

Developing an Empirical Relationship to Predict Tensile Strength and Micro Hardness of Friction Stir Welded Aluminium Alloy Joints

Gurmeet Singh Cheema and Amardeep Singh Kang

Keywords Aluminium alloy · Friction stir welding · Mathematical models

1 Introduction

Aluminium is one of the lightest engineering metals, having strength to weight ratio superior to that of steel. The products developed from aluminum and its alloys are essential to the aerospace industry, transportation and structural materials [1, 2]. Friction-stir welding (FSW) is a solid-state joining process where coalescence occurs by the heat generated between the tool and the work piece material [3]. A non consumable rotating tool is fed at constant rate into clamped workpiece. The probe is slightly shorter from the weld required weld depth. The shoulder of the tool rotates at the top surface of the workpiece [4]. The heats generated by the friction between tool and workpiece and due to this stirred become soften without melting. As the pin moves forward, a special profile on its leading face forces plasticized material to the rear where clamping force assists in a forged consolidation of the weld and hence joins the work piece [5].

2 Experimental

To investigate an understanding about the relationship of various FSW process parameters selected for study and their effect on weld characteristics, Response Surface Methodology (RSM) was used to develop second order regression equation relating response characteristics and process parameters.

G.S. Cheema (✉) · A.S. Kang

Bhai Gurdas Institute of Engineering and Technology, Sangrur 148001, Punjab, India
e-mail: gcheemamand@gmail.com

Plan of Experiments

1. Selection of material
2. Identification of important friction stir welding parameters
3. Development of the design matrix and experimentation
4. Selection of mathematical models
5. Development of model.

2.1 Selection of Material

The material selected for the study was aluminium alloy 6061 which have a better strength to weight ratio than that of high strength steel. Chemical composition and mechanical properties of base material of the original alloy have been presented in Tables 1 and 2 respectively. A proper selection of tool material and tool design plays a vital role to achieve good mechanical as well as microstructural properties with Friction stir welding process [6]. The various options are available for the selection of tool material, but it is necessary to select appropriate steel with specific characteristic behaviors that would apply to joining of aluminium alloys. It can be seen from literature review that the tool materials have a great influence on weld appearance and quality [7]. High chromium high carbon steel was selected as a tool material and the chemical composition of selected material are given in the Table 3. The diameter of the tool pin was 6 mm and the length of the pin was 5.8 mm. To prepare the fixture mild steel (MS) was selected for its availability and easy machineability.

2.2 Identification of Important Friction Stir Welding Parameters

To design the experiments, the central composite rotatable design was adopted. Three parameters as tool rotational speed (N), welding speed and shoulder diameter

Table 1 Chemical composition of base material

Si	Fe	Cu	Mn	Mg	Al
0.57	0.35	0.22	0.12	1.1	Bal

Table 2 Mechanical properties of base material

Ultimate tensile strength (MPa)	Elongation	Hardness (Hv)
280	20	100

Table 3 Chemical composition of high carbon high chromium high carbon steel

Elements	C	Mn	Si	Cr	Ni	Mo	V	Co	Cu	Fe
wt%	1.40–1.60	0.60	0.60	11–13	0.30	0.7–1.20	1.10	1.10	0.25	Balance

Table 4 Welding parameters and their levels

Parameter	Notation	Units	Levels		
			-1	0	+1
Tool rotational speed	N	Rpm	800	1000	1200
Welding speed	S	mm/min	40	60	80
Shoulder diameter	D	Mm	16	18	20

(D) were selected and varied up to three levels. The parameters and their levels were selected from the trial runs and with the help of literature review. The selected parameters and their levels are presented in Table 4.

2.3 Development of Design Matrix

The final experiment was performed as per design matrix as presented Table 5. The material used in this investigation was 100 mm × 100 mm × 6 mm in size and the appropriate size for weld was 200 mm × 100 mm. Thirty six plates of size 100 mm × 100 mm were sliced to obtain eighteen friction stir welded joints with different parameters. Then cut edges are finished with milling operation so that interfaces can be properly matched. For welding process vertical milling machine was used as shown in Fig. 1. Fixture was first fixed on the machine table with help of clamps. The welds were prepared opposite to the rolling direction of the workpiece. Some welded specimens are shown in Fig. 2. Visual inspection was carried out for all the weld joints to find out macro weld defect on the welded specimens. Tensile test specimens were prepared as per ASTM-E8M-08 guidelines [8]. Three tensile test specimens were prepared from each weld and average of the tensile test results is presented in Table 5.

2.4 Selection of Mathematical Model

The response function (Y) of friction stir welded joints are function of tool rotational speed (N), welding speed (S), and shoulder diameter (D) and it can be expressed as [9]

$$Y = f(N, S, D)$$

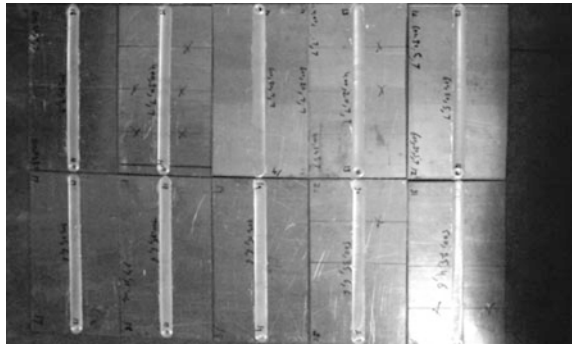
Table 5 Central composite rotatable experimental design (in coded and actual levels of three factors and three levels)

Experiment No.	Coded factors			Actual factors			Tensile strength (MPa)	Percentage elongation %	Micro hardness (Hv)
	N (rpm)	S (mm/min)	F (kN)	N (rpm)	S (mm/min)	D (mm)			
1	-1	-1	-1	800	40	16	164	4.1	66
2	+1	-1	-1	1200	40	16	180	5.4	70
3	-1	+1	-1	800	80	16	183	7.2	69
4	+1	+1	-1	1200	80	16	179	5.1	74
5	-1	-1	+1	800	40	20	192	3.5	72
6	+1	-1	+1	1200	40	20	194	5.3	71
7	-1	+1	+1	800	80	20	191	6.2	78
8	+1	+1	+1	1200	80	20	200	5.3	65
9	-1	0	0	800	60	18	186	5.4	60
10	+1	0	0	1200	60	18	205	6.1	85
11	0	-1	0	1000	40	18	185	5.3	76
12	0	+1	0	1000	80	18	198	6.4	82
13	0	0	-1	1000	60	16	190	5.4	75
14	0	0	+1	1000	60	20	201	6.4	83
15	0	0	0	1000	60	18	221	7	110
16	0	0	0	1000	60	18	225	6.8	112
17	0	0	0	1000	60	18	226	7.3	111
18	0	0	0	1000	60	18	220	7.4	109

Fig. 1 Vertical milling machine



Fig. 2 Friction stir welded specimens



The second order polynomial (regression equation) used to represent the response surface for K factors is given by

$$Y = b_0 + \sum b_i X_i + \sum b_{ij} X_i X_j + \sum b_{ii} X_i^2 + e$$

where ‘bo’ is the free term of the regression equation and provides a mean value of the response factor, ‘bi’ is the linear term, ‘bij’ is the interaction term, ‘bii’ is the quadratic term of the polynomial and ‘e’ is the residual error. The coefficients bo, bi, bij and bii are the least square estimates of true polynomial, representing the response surface. These coefficients represent the strength of the respective process parameters and their interactions. These are also called the parameters of the response function. The experiments were designed using software, Design Expert version 6.0 (State Ease). The same software was used for statistical analysis of the experiments data. For three factors, the selected polynomial can be expressed as given Eq. (1).

$$Y = b_0 + b_1(N) + b_2(S) + b_3(D) + b_{12}(NS) + b_{13}(ND) + b_{23}(SD) + b_{11}(N^2) + b_{22}(S^2) + b_{33}(D^2) \tag{1}$$

2.5 Development of Model for Tensile Strength

The adequacy of the developed model for tensile strength was tested by ANOVA as presented in Table 6. As per ANOVA the Model F-value of 10.22 implies the model is significant. There is only a 0.16% chance that an F-value this large could occur due to noise. Values of “Prob > F” less than 0.0500 indicate model terms are significant. In this case N, S, D, N², S², D² are significant model terms. Values greater than 0.1000 indicate the model terms are not significant. If there are many insignificant model, model reduction may improve the model. The “Lack of Fit F-value” of 8.82 implies there is a 5.15% chance that a “Lack of Fit F-value” this large could occur due to noise. Non significant Lack of fit is good the model [10]. This relatively low probability (<10%) is troubling. After dropping the insignificant co-efficient the final model is given below.

$$\text{Tensile Strength } Y = 223 + 4.02N + 3.29S + 6.55D - 11.25N^2 - 12.66S^2 - 11.25D^2$$

The values of the coefficients of the polynomials were calculated with the help of the statistical software Design-expert 6.0. All the co-efficient were tested for their significance at 95% confidence level applying F-test using design expert software. To test the goodness of the fit and validation of the developed models, adequacy was determined by the analysis of variance technique (ANOVA). The “R-Squared” of 92% is in reasonable agreement with the “Adj R-Squared” of 83%.

Table 6 Anova for response surface quadratic model tensile strength

Source	Sum of squares	Degree of freedom	Mean square	F value	p-value Prob > F	Significant
Model	4691.79	9	521.31	10.22	0.0016	Yes
Tool rotational speed (N)	221.13	1	221.13	4.33	0.0009	Yes
Welding speed (S)	147.38	1	147.38	2.89	0.0077	Yes
Tool shoulder dia (D)	586.53	1	586.53	11.49	0.0095	Yes
NS	21.13	1	21.13	0.41	0.5379	No
ND	0.13	1	0.13	2.450E-003	0.9617	No
SD	21.13	1	21.13	0.41	0.5379	No
N ²	1600.22	1	1600.22	31.36	0.0005	Yes
S ²	2027.93	1	2027.93	39.74	0.0002	Yes
D ²	1600.22	1	1600.22	31.36	0.0005	Yes
Residual	408.21	8	51.03			
Lack of fit	382.21	5	76.44	8.82	0.0515	Not significant
Pure error	26.00	3	8.67			
Cor total	5100.00	17				

Scatter diagrams, which show the predicted and the observed values of responses, were also drawn so as to test the validity of these models. A good agreement was found to exist between the actual and the predicted responses of tensile strength as shown in Figs. 3 and 4 respectively.

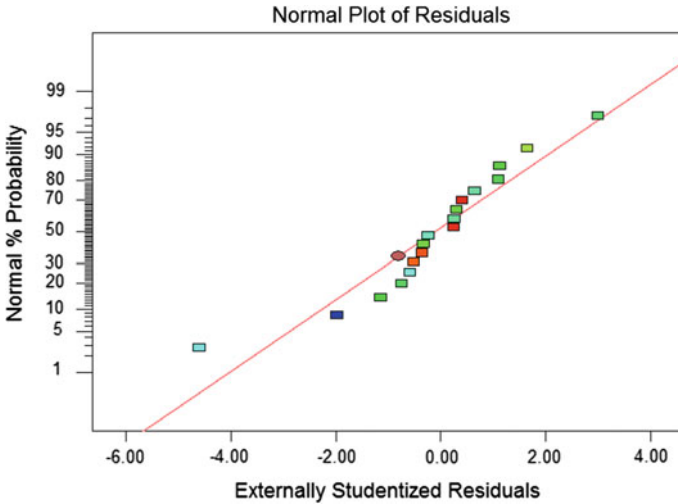


Fig. 3 Normal plot of residuals for tensile strength (MPa)

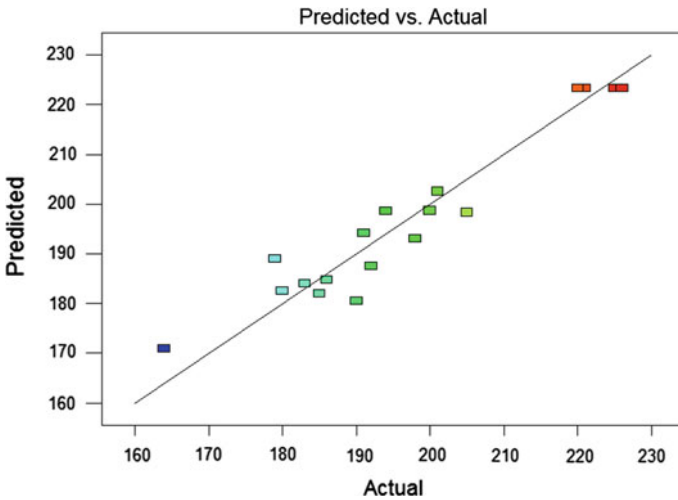


Fig. 4 Predicted v/s actual plot for tensile strength (MPa)

2.6 Development of Model for Percentage Elongation

The adequacy of the developed model for percentage elongation was tested by ANOVA as presented in Table 7. As per ANOVA the Model F-value of 6.52 implies the model is significant. There is only a 0.73% chance that an F-value this large could occur due to noise. Values of “Prob > F” less than 0.0500 indicate model terms are significant. In this case N, S, NS, N2, S2, D2 are significant model terms. Values greater than 0.1000 indicate the model terms are not significant. If there are many insignificant model terms, model reduction may improve your model. The “Lack of Fit F-value” of 5.73 implies there is a 9.08% chance that a “Lack of Fit F-value” this large could occur due to noise. After dropping the insignificant co-efficient the final model is given below.

$$\text{Percentage Elongations} = 7.15 + 0.094N + 0.54S - 0.59N^2 - 0.56S^2 - 0.51D^2 - 0.76NS$$

All the co-efficient were tested for their significance at 95% confidence level applying F-test using design expert software. To test the goodness of the fit and validation of the developed model, adequacy was determined by the analysis of variance technique (ANOVA). The “R-Squared” of 88% is in reasonable agreement with the “Adj R-Squared” of 874%.

Table 7 Anova for response surface quadratic model percentage elongation

Source	Sum of squares	Degree of freedom	Mean square	F value	p-value Prob > F	Significant
Model	17.60	9	1.96	6.52	0.0073	Yes
Tool rotational speed (N)	0.12	1	0.12	0.40	0.0055	Yes
Welding speed (S)	3.96	1	3.96	13.19	0.0067	Yes
Tool shoulder diameter (D)	2.420E-003	1	2.420E-003	8.071E-003	0.9306	No
NS	4.65	1	4.65	15.51	0.0043	Yes
ND	0.36	1	0.36	1.20	0.3043	No
SD	1.250E-003	1	1.250E-003	4.169E-003	0.9501	No
N ²	4.44	1	4.44	14.82	0.0049	Yes
S ²	3.93	1	3.93	13.11	0.0068	Yes
D ²	3.68	1	3.68	12.29	0.0080	Yes
Residual	2.40	8	0.30			
Lack of fit	2.17	5	0.43	5.73	0.0908	Not significant
Pure error	0.23	3	0.076			
Cor total	20.00	17				

2.7 Development of Model for Micro Hardness

The adequacy of the developed model for micro hardness was tested by ANOVA as presented in Table 8. As per the ANOVA, the Model F-value of 13.56 implies the model is significant. There is only a 0.06% chance that an F-value this large could occur due to noise. Values of “Prob > F” less than 0.0500 indicate model terms are significant. In this case N, S, D, N², S², D² are significant model terms. Values greater than 0.1000 indicate the model terms are not significant. If there are many insignificant model terms, model reduction may improve the model. The “Lack of Fit F-value” of 36.22 implies the Lack of Fit is not significant. There is only a 0.70% chance that a “Lack of Fit F-value” this large could occur due to noise. Significant lack of fit is bad. After removing the insignificant co-efficient the final model for micro hardness is given below

$$\text{Micro hardness} = 110.70 + 2.71N + 1.25S + 1.50D - 14.34N^2 - 12.04S^2 - 12.4D^2$$

All the co-efficient were tested for their significance at 95% confidence level applying F-test using design expert software. To test the goodness of the fit and validation of the developed models, adequacy was determined by the analysis of variance technique (ANOVA). The “R-Squared” of 93% is in reasonable agreement with the “Adj R-Squared” of 86%.

Table 8 Anova for response surface quadratic model micro hardness

Source	Sum of squares	Degree of freedom	Mean square	F value	p-value Prob > F	Significant
Model	4681.58	9	520.18	13.56	0.0006	Yes
Tool rotational speed (N)	100.49	1	100.49	2.62	0.0042	Yes
Welding speed (S)	21.39	1	21.39	0.56	0.4766	Yes
Tool shoulder diameter (D)	30.64	1	30.64	0.80	0.0076	No
NS	15.13	1	15.13	0.39	0.5475	No
ND	66.13	1	66.13	1.72	0.2256	No
SD	6.13	1	6.13	0.16	0.6999	No
N ²	2600.06	1	2600.06	67.78	<0.0001	Yes
S ²	1833.33	1	1833.33	47.79	0.0001	Yes
D ²	1833.33	1	1833.33	47.79	0.0001	Yes
Residual	306.87	8	38.36			
Lack of fit	301.87	5	60.37	36.22	0.7000	Not significant
Pure error	5.00	3	1.67			
Cor total	4988.44	17				

3 Conclusions

Based upon the present research work, the following conclusions were drawn.

1. A three level three factor full factorial design matrix based on the central composite rotatable design technique could be effectively used for the development of mathematical models to predict the tensile strength, percentage elongations and micro hardness.
2. Response surface design was found to be an effective technique for developing mathematical models to accurately predict the main, quadratic and two-way interaction effects of various input parameters on different responses.
3. All models developed showed either linear or quadratic relationship between input process.

References

1. Lakshminarayanan AK, Balasubramanian V (2008) Process parameters optimization for friction stir welding of RDE-40 aluminium alloy using Taguchi technique. *Trans Nonferrous Met Soc China* 18:548–554
2. Woo W, Choo H, Brown DW, Feng Z (2007) Influence of the tool pin and shoulder on microstructure and natural aging kinetics in a friction-stir-processed 6061-T6 aluminum alloy. *Metall Mater Trans* 38A:69–76
3. Balasubramanian N, Mishra RS, Krishnamurthy K (2011) Process forces during friction stir channeling in an aluminum alloy. *J Mater Process Technol* 211:305–311
4. Rajakumar S, Muralidharan C, Balasubramanian V (2011) Predicting tensile strength, hardness and corrosion rate of friction stir welded AA6061-T6 aluminium alloy joints. *Mater Des* 32:2878–2890
5. Karthikeyan L, Senthil Kumar VS (2011) Relationship between process parameters and mechanical properties of friction stir processed AA6063-T6 aluminum alloy. *Mater Des* 32:3085–3091
6. Rajakumar S, Muralidharan C, Balasubramanian V (2010) Establishing empirical relationships to predict grain size and tensile strength of friction stir welded AA6061-T6 aluminium alloy joints. *Trans Nonferrous Met Soc China* 20(10):1863–1872
7. Dhanapal A, RajendraBoopathy S, Balasubramanian V (2011) Developing an empirical relationship to predict the corrosion rate of friction stir welded AZ61A magnesium alloy under salt fog environment. *Mater Des* 32:5066–5072
8. ASTM-E8M (2008) Standard test method for tension testing of metallic materials. ASTM Intentional
9. Rajakumar S, Muralidharan C, Balasubramanian V (2010) Optimization of the friction-stir-welding process and tool parameters to attain a maximum tensile strength of AA7075-T6 aluminium alloy. *Proc Inst Mech Eng Part B J Eng Manuf* 224(8):1175–1191
10. Bilici MK (2012) Application of Taguchi approach to optimize friction stir spot welding parameters of polypropylene. *Mater Des* 35:113–119

New Design Approach of Helical Coil Spring for Longitudinal and Translational Invariance by Using Finite Element Analysis

Sagar Namdev Khurd, Prasad P. Kulkarni and S.D. Katekar

Keywords Analysis by FEA · Response surface modeling (RSM) · Simulation

1 Introduction

The main function of the spring is to provide flexibility between two mating parts subjected to fluctuated loads. Few research works show that when spring is manufactured from composite material the efficiency of vehicle increase as the weight of the vehicle reduces. Because composite material has high weight to force ratio, also it can withstand high temperature and corrosion [1]. Composite helical spring with rubber core gives better performance under compressive load and spring constant [2]. Most of the researchers focused on investigating the static behavior of the helical spring under compressive loading in combination with finite element analysis [3–5]. Normally the spring is designed in CAD software's and file is then imported to analysis software for analysis purpose but this is very tedious process. This work gives idea about designing the helical compression spring by using ANSYS work bench which reduces the time of designing and ANSYS process.

2 Design of Helical Coil Spring

Firstly the helical spring is designed theoretically and the theoretical parameters like deformation and maximum shear stress is compared with results obtained by FEA and practical analysis.

S.N. Khurd (✉)

Department of Mechanical Engineering, Sveri's College of Engineering,
Pandharpur, India
e-mail: sagarkhurd88@rediffmail.com

P.P. Kulkarni · S.D. Katekar

Department of Mechanical Engineering,
SKN Sinhgad College of Engineering, Korti, India

Table 1 Maximum shear stress theoretically and maximum shear stress analytically with load

Load (N)	Theoretical maxi. shear stress (N/mm ²)	ANSYS maxi. shear stress (N/mm ²)
500	230.929	251.42
600	277.115	289.12
700	323.301	342.89
800	369.487	386.14
900	415.67	445.87
1000	461.85	468.12

2.1 Variation of Maximum Shear Stress Theoretically and Maximum Shear Stress Analytically with Load

As shown in Table 1 of Load versus maximum shear stress, in the ANSYS and the analysis has been carried out. From the theoretical and ANSYS values compared, the stress having more difference than the experimentally.

3 Finite Element Analysis of Helical Compression Spring by Using ANSYS

Modeling is used ANSYS 14 (workbench) and Analysis is also carried out by using ANSYS 14.0 software for better understanding. SOLID one eight five element is a higher order 3-D, 8-node element. SOLID185 is used for 3-D modeling of solid structures. It is defined by 8 nodes having 3 degrees of freedom at each node: translations in the nodal x, y, and z directions. The element has plasticity, stress stiffening, creep, hyper elasticity, large deflection, and large strain capabilities. It is a mixed formulation capability for simulating deformations of nearly isotropic and elastoplastic materials and fully incompressible hyper elastic materials. The load is applied along Fy direction. To apply load, it is necessary to select the remote force for centre load application associated at the center along y direction, so it is necessary to observe the remote force associated at the center along z and x direction, because the applied force needs to be transfer to the top surface of spring geometry. After the preprocessing, the solution has to be done. From solution phase, choose the new analysis as static, then solve the current load step problem, the solution will be done, Load versus von mises stresses shown in Fig. 4.

As shown in Figs. 1, 2, 3 and 4, the numerical analysis of helical compression spring by using Finite Element Analysis has been carried out. Figure 1 is geometric model which is drawn in workbench itself and analysis also carried out in ANSYS (workbench), so we can vary parameters as per requirement which is not possible in other method. Static analysis is performed to find the Von-Mises stress and maximum shear stress by using FEA software (workbench) from the analysis getting the exact value of total deformation which validate with practically.

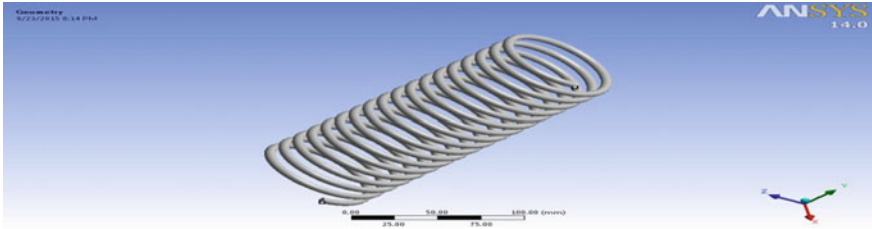


Fig. 1 Spring geometry model in ANSYS

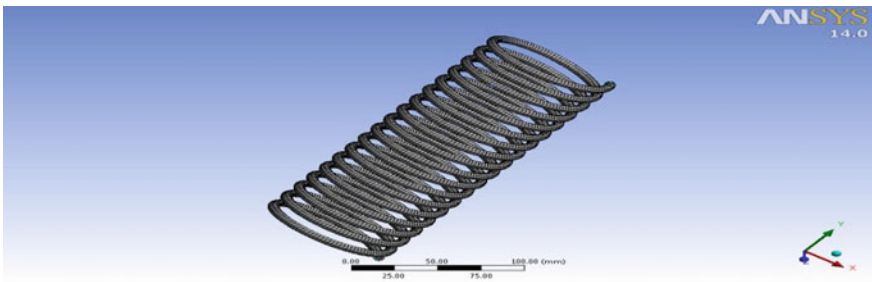


Fig. 2 Geometry meshed modal

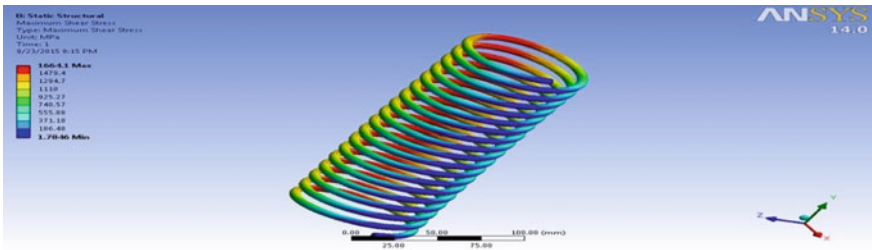


Fig. 3 Maximum shear stress

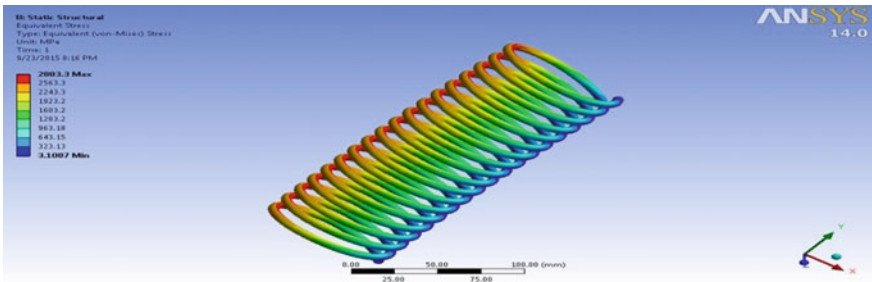


Fig. 4 Von-Mises stresses

4 Experimental Approach for Analysis

4.1 Testing of Helical Compression Spring for Load and Deflection

The helical compression springs are to be used for tested load, deflection by using load checking machine. The experimental set up is shown in Fig. 5 the springs are tested by using design procedures standards. The spring is loaded from zero to the prescribed maximum deflection.

As shown in Fig. 5 experimental set for testing helical coil spring for experimentation the computerized universal testing machine is used.

The load, deflection of helical compression springs are measured and tabulated as shown in Table 2. Figures 6 and 7 shows free and solid length of helical compression spring. Table 2 shows that the load verses deflection values. Loads are applied in the steps of 500 N. By taking the slope of above curve, we can calculate the stiffness of helical compression spring.

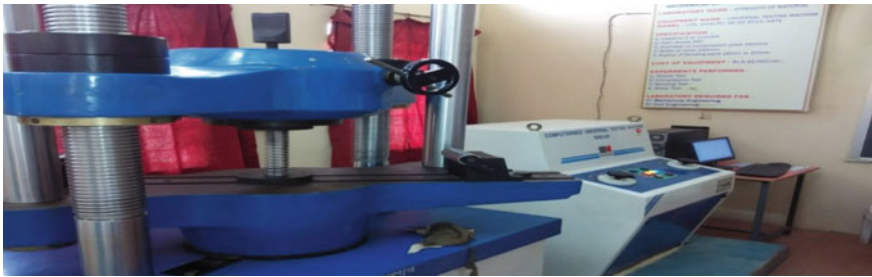


Fig. 5 Experimental set up for analysis of helical spring

Table 2 Experimental load, deflection of helical compression spring

Sr. No.	Load (N)	Deflection (mm)
1	500	55.5
2	600	63.4
3	700	74.7
4	800	80.6
5	900	91.6
6	1000	111.2

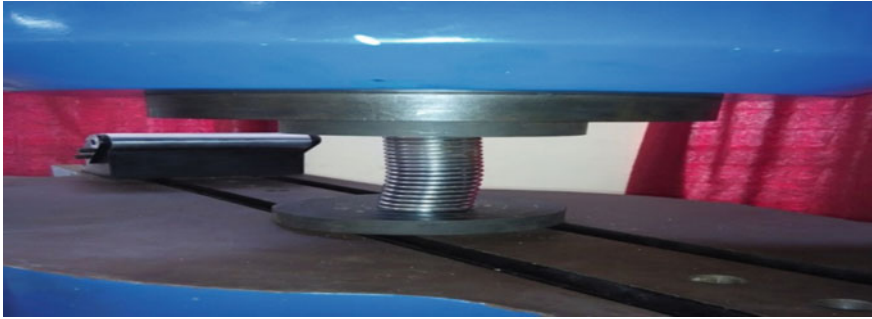
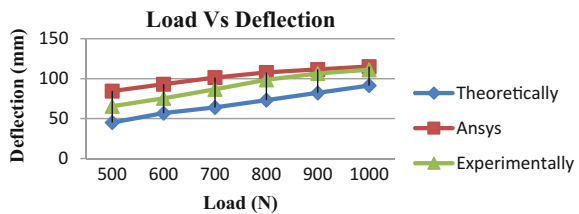


Fig. 6 Solid length of helical spring

Fig. 7 Load and deflection curve of helical compression spring



5 Probabilistic Design of Helical Coil Spring for Longitudinal Invariance by Using Finite Element Method

This longitudinal invariance represents a new approach to design helical coil spring. Response surface modeling and analysis of helical compression spring by considering longitudinal invariance have been carried out. Design parameters are wire diameter, mean diameter, the force, elastic modulus in Y and Z direction varied. It is observed that material property and force are significant parameters which effect on the strength of helical coil spring.

In response surface modeling, analysis of helical compression spring has been carried out. Normally the analysis of helical coil spring carries out by importing the CAD or CATIA file in ANSYS, but in ANSYS workbench we can draw the path and can analysis there itself. If we want to vary the parameter it is easily possible than previous by using workbench. Force, material properties can also change easily.

In RSM we can give a range of parametric values, for example, if the range of force gives between 950 and 1100 N, it will take automatically 950, 951, 952, 953 ... 1100 N and shows the value of total deformation at each point and other parameter will be constant. Same like range of wire diameter is given between 5 and 6 mm, it will take 5.1, 5.2, 5.3 ... 6 and it will show deformation for each value. Response surface modeling gives optimum design values of helical compression spring (Table 3).

Table 3 Corresponding parameters according to response surface modeling (RSM)

Force Y component (N)	Mean diameter (mm)	Wire diameter (mm)	Young's modulus Y direction (Pa)	Young's modulus Z direction (Pa)	Total deformation maximum (mm)	Equivalent stress maximum (Pa)
-1000	25.50	6.55	6.53E+09	6.53E+09	12.389	1.79E+09
-1000	25.50	6.55	5.88E+09	6.53E+09	12.394	1.79E+09
-1000	25.50	6.55	7.18E+09	6.53E+09	12.384	1.79E+09
-1000	25.50	6.55	6.53E+09	5.88E+09	12.409	1.79E+09
-1000	25.50	6.55	6.53E+09	7.18E+09	12.372	1.8E+09
-1100	25.50	6.55	6.53E+09	6.53E+09	13.628	1.97E+09
-900	25.50	6.55	6.53E+09	6.53E+09	11.150	1.61E+09
-1000	25.50	6.10	6.53E+09	6.53E+09	16.451	2.21E+09
-1000	25.50	7.00	6.53E+09	6.53E+09	9.514	1.48E+09
-1000	25.00	6.55	6.53E+09	6.53E+09	11.853	1.76E+09
-1000	26.00	6.55	6.53E+09	6.53E+09	12.940	1.83E+09
-1028.33	25.64	6.42	6.34E+09	6.34E+09	13.966	1.97E+09

6 Probabilistic Design of Helical Coil Spring for Translational Invariance by Using Finite Element Method

This Translational invariance represents a new approach to design helical coil spring. Response surface modeling and analysis of helical compression spring by considering longitudinal and invariance have been carried out. Design parameters are wire diameter, mean diameter, the force, elastic modulus in X and Z direction varied. It is observed that material property and force are significant parameters which affect the compressive strength of helical coil spring (Table 4).

7 Result and Discussion

7.1 Comparison Based on Load Verses Deflection

The deformation of a spring, load versus deflection as shown in Table 5. In this table, comparison is done between theoretical, ANSYS values of load versus displacement. Here step size of load value is 500 N from table it's obtained that the values of theoretical and experimental near than the ANSYS value.

7.2 Comparison Results of Maximum Shear Stress and Deflection

In above table overall Comparison results of Maximum shear stress and deflection stress has been carried out. From above result observed that actual stresses and deflection getting from ANSYS. As shown in Fig. 7. Between load verses Theoretical, Experimental, and ANSYS displacement. The load acting on the x-axis and deflection on the y axis. The line of theoretical and experimental is a straight line, but in ANSYS it is not a straight from load 500–1000 N. The comparison of variation of load versus deflection as shown in Fig. 7 by the tabulated bar chart. At lower loads, both theoretical and experimental and FEA results are very close, but when the load increases the FEA results uniformly increase as compared to theoretical results. The result of theoretical and experimental is close to each other and it is linear.

Table 4 Corresponding parameters according to response surface modeling (RSM)

Force Y component (N)	Mean diameter (mm)	Wire diameter (mm)	Young's modulus X direction (Pa)	Young's modulus Z direction (Pa)	Total deformation maximum (mm)	Equivalent stress maximum (Pa)
-1000.00	25.50	6.6	6.53E+09	3.4E+10	12.389	1.79E+09
-1000.00	25.50	6.6	5.88E+09	3.4E+10	12.409	1.79E+09
-1000.00	25.50	6.6	7.18E+09	3.4E+10	12.372	1.8E+09
-1100.00	25.50	6.6	6.53E+09	3.4E+10	13.628	1.97E+09
-900.00	25.50	6.6	6.53E+09	3.4E+10	11.150	1.61E+09
-1000.00	25.50	6.1	6.53E+09	3.4E+10	16.451	2.21E+09
-1000.00	25.50	7.0	6.53E+09	3.4E+10	9.514	1.48E+09
-1000.00	25.00	6.6	6.53E+09	3.4E+10	11.853	1.76E+09
-1000.00	26.00	6.6	6.53E+09	3.4E+10	12.940	1.83E+09
-1000.00	25.50	6.6	6.53E+09	3.06E+10	12.525	1.8E+09
-1000.00	25.50	6.6	6.53E+09	3.74E+10	12.277	1.79E+09
-1028.33	25.36	6.4	6.34E+09	3.5E+10	13.584	1.95E+09

Table 5 Comparison results of maximum shear stress and deflection

S. N.	Load (N)	Theoretically		Practically		Analytical	
		Max. shear stress (mm)	Deflection (mm)	Max. shear stress (mm)	Deflection (mm)	Max. shear stress (mm)	Deflection (mm)
1	500	230.92	45.10	235.29	55.5	251.42	64.514
2	600	277.11	56.85	285.15	63.4	289.12	73.112
3	700	323.30	63.99	330.40	74.7	342.89	81.450
4	800	369.48	73.13	375.14	80.6	386.14	88.895
5	900	415.67	82.27	425.47	91.6	445.87	99.614
6	1000	461.85	91.41	402.65	98.2	468.12	105.201

8 Conclusion

Based on the study, the following conclusions are made:

1. Parametric modeling and finite element analysis of helical compression spring is successfully carried out in ANSYS WORKBENCH.
2. A new methodology for design of helical coil spring i.e. probabilistic design has been implemented successfully.
3. Response surface modeling (RSM) carried out by using FEA where as compressive stress as objective function for helical compression spring. In response surface modeling the Longitudinal, Translational invariance on a helical compression spring has been carried out through FEA. Dynamic analysis of shock absorber having helical coil spring has been carried out successfully.
4. The theoretical and experimental results were compared with FEA result. The results show good approximate with theoretical and experimental test results.
5. Effect of design parameters on compressive strength is obtained.
 - (a) It is observed that if wire DIA. increases stress on helical spring reduces.
 - (b) Increase in coil diameter results in an increase in stress.
 - (c) If the load increases the stresses also increases.
 - (d) If free length increases stresses increase.
 - (e) Probabilistic design gives better judgment for selection of composite material.

References

1. Singh S (2012) Optimization of design of helical coil suspension system by combination of conventional steel and composite material in regular vehicle. *Int J Appl Eng Res* 7(11). ISSN 0973-4562
2. Chiu C-H, Hwan C-L, Tsai H-S, Lee W-P (2007) An experimental investigation into the mechanical behaviors of helical composite springs. *Compos Struct* 77:331–340
3. Frikha A, Carried P (2013) Fabien trussed “Mechanical modeling of helical structures accounting for translational invariance. Part 1: static behavior” Frikhaetal. *Int J Solids Struct* 50:138–1373
4. Mulla TM, Kadam SJ, Kengar VS (2012) Finite element analysis of helical coil compression spring for three wheeler automotive front suspension. *Int J Mech Ind Eng (IJMIE)* 2(3). ISSN No. 2231-6477
5. Becker LE, Chassies GG (2002) On the natural frequencies of helical coil springs. *Int J Mech Sci* 44:825–841

Material Removal Rate and Surface Roughness Optimization in WEDM on Tool Steel EN-31 Using Taguchi Approach

Mayur N. Patel, H.G. Shah and Haresh Ghoniya

Keywords Wire cut electric discharge machining · Taguchi's method of optimization · Material removal rate · Surface roughness

1 Introduction

Now a day materials with high hardness, toughness, and impact resistance have more demand due to progress in mechanical industry. However, these materials are difficult to machine using traditional methods of machining. There arise a concept of a non-traditional method of machining of such material with electrochemical machining, ultrasonic machining, electrical discharging machine (WEDM), etc. One of non-conventional machining method is Wire Cut Electrically discharge machining process, popularly known as WEDM process [1].

WEDM process finding tremendous application in area of machining of various material used in modern tooling application such as wafering of silicon and machining of compacting dies made of sintered carbide, and capable of generating precise and intricate profiles with small corner [2]. Another area of application is machining of advance ceramic materials such as diamond, boron carbide (B₄C), silicon infiltrated silicon carbide (SiSiC), niobium carbide (NbC) and titanium carbide (TiC), etc. WEDM process is also capable of machining of modern composite material such as metal matrix composites (MMC), carbon fiber and reinforced liquid crystal polymer composites [2].

M.N. Patel (✉) · H. Ghoniya
Uka Tarsadia University, Bardoli, Surat, Gujarat, India
e-mail: mayurn.patel20@gmail.com

H.G. Shah
SVMIT, Bharuch, Gujarat, India

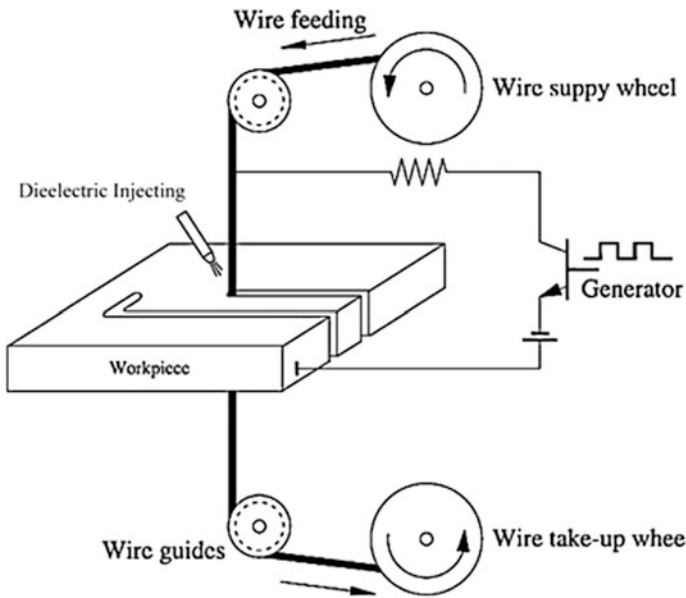


Fig. 1 Principle of WEDM [7]

Automobile industry, tool making industry, aerospace, mold industry, and die making industries are the major applicants of WEDM process. WEDM process also finds tremendous application in the medical, optical and ornament industries where precision and accuracy are of great importance [2]. The material removal mechanism of WEDM is very similar to the conventional EDM process consisting of the erosion effect produced by the electrical discharges (sparks). In WEDM, material is eroded from the work piece by a repetitive sparks occurring between the gap of work piece and the wire, which is separated by a stream of dielectric fluid, which is continuously fed to the machining zone [3]. A voltage more than a breakdown voltage of gap is required to initiate a discharge across the gap. A large number of sparks occurs as a result of formation of conducting path. Main reason behind such occurring is a great amount of discharge per second within minor part of second. This increases both temperature (15,000–21,000 F) and pressure in the spark channel [1]. Particles (chips) so produced through material removal process are carried away from work piece surface through flow of dielectric fluid with the help of nozzle attached to them. And another function of flushing system is to maintain temperature of work piece as it may change work piece's properties. An absence of this cooling system, thermal expansion within workpiece so created can affect positional accuracy and workpiece size [2] (Fig. 1).

2 Materials and Methods

The experiments are conducted on the ECOCUT WEDM machine from Electronica India Pvt Ltd. A brass wire of 0.25 mm diameter was used as the cutting tool. EN-31 having 1.07% Carbon are used as the specimen. The specimens are of rectangular shape having a thickness of 31.4 mm. The deionized water was used as dielectric. The four input process parameters namely Pulse duration on and off time (TON and TOFF), Peak Current (IP) and Cutting speed (CV) are chosen as variables to study their effects on Material removal rate (MRR) and Surface roughness (SR) as response parameter. The ranges of input parameters are selected from the literature survey, machine capability and as shown in Table 1, with a list of fixed parameter. The average surface roughness was measured using the Samsonite Roughness Tester (Model no: TR 200) having the range of 0.025–12.5 μm. Taguchi’s method of optimization was used to determine the effect of input process parameters.

Apart from the parameters mentioned above following parameters are kept constant at a fixed value during the experiments (Figs. 2, 3 and 4):

5. Work material:	EN 31
6. Cutting tool:	Brass wire of diameter 0.25 mm
7. Peak voltage:	2 unit (110 V DC)
8. Flushing pressure:	1 unit (15 kg/cm ²)
9. Wire feed rate:	3 unit
10. Wire tension:	8 unit (1000 gm)
11. Spark gap set voltage:	21 V
12. Servo feed setting:	2080 unit
13. Conductivity of dielectric:	20 mho
14. Height of material:	31.58 mm
15. Density of material:	8.75 × 10 ⁻⁶ kg/mm ³

Table 1 Process parameters and their levels

Factors	Parameters	Levels		
		L1	L2	L3
A	Cutting speed (mm ² /min)	50	60	70
B	Peak current (A)	35	40	45
C	Pulse on time (machine unit)	123	126	130
D	Pulse off time (machine unit)	30	32	34

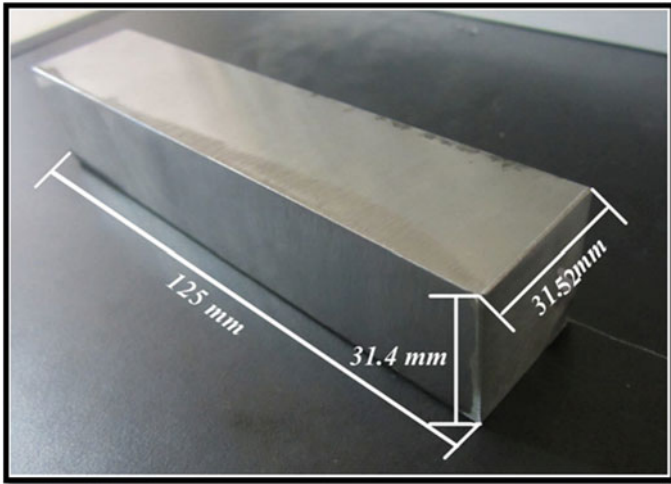
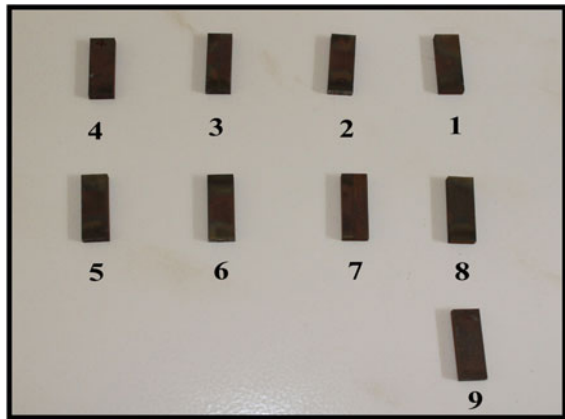


Fig. 2 Work piece material-EN 31

Fig. 3 Specimens lied horizontally



3 Design of Experiments

Taguchi proposed to acquire the characteristic data by using orthogonal arrays and to analyze the performance measure from the data to decide the optimal process parameters. The designed combination of input parameters and its corresponding Material removal rate and surface roughness is shown in Table 2 and 3 respectively.

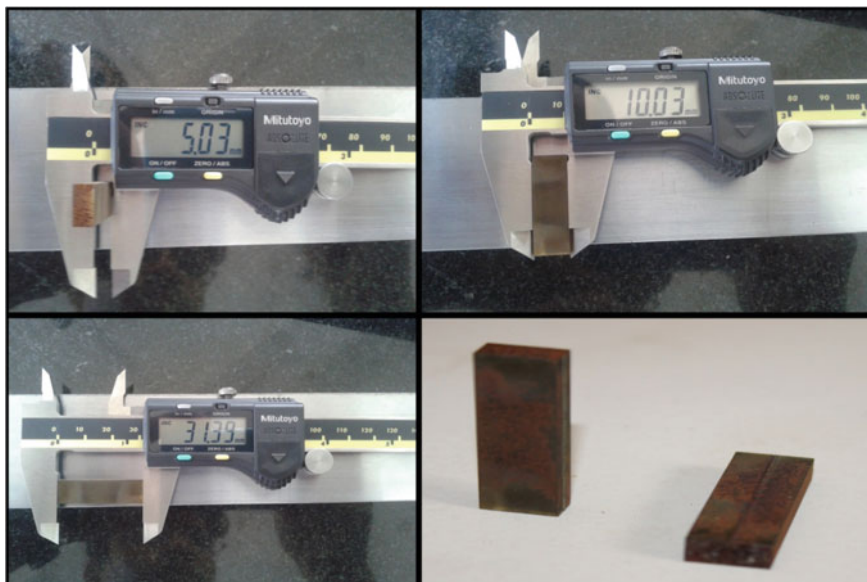


Fig. 4 Preparation of specimens

Table 2 Input parameters

Ex no.	Cutting speed (CV)	Peak current (IP)	Pulse on time (TON)	Pulse off time (TOFF)
1	50	35	123	30
2	50	40	126	32
3	50	45	130	34
4	60	35	126	34
5	60	40	130	30
6	60	45	123	32
7	70	35	130	32
8	70	40	123	34
9	70	45	126	30

4 Taguchi's Optimization Technique

Optimization of process parameters is the key step in the Taguchi method to achieve high quality without increasing cost [4]. However, originally Taguchi method is designed to optimize single performance characteristics [5]. According to Taguchi method, the S/N ratio is the ratio of Signal to Noise, where signal represents the desirable value and noise represents the undesirable value. The response

Table 3 Material removal rate and surface roughness

Trial no.	MRR (mm ³ /min)		S/N ratio	Surface roughness (μm)		S/N ratio
	Y1	Y2		Y1	Y2	
1	23.231	28.420	28.1093	1.342	1.393	-2.7201
2	40.000	40.700	32.1159	3.006	3.128	-9.736
3	49.710	50.352	33.9842	2.460	2.516	-7.9176
4	55.570	56.031	34.9325	3.666	3.659	-11.2756
5	62.200	63.951	35.9947	3.616	3.605	-11.1514
6	51.830	53.070	34.3931	2.937	2.952	-9.3803
7	47.200	48.210	33.5698	3.909	3.922	-11.8558
8	61.470	64.550	35.9804	3.490	3.480	-10.8441
9	46.89	47.500	33.4774	3.150	3.186	-10.0159

Where, Y1 and Y2 are the result for the same experiment conducted twice

MRR and SR reported in Table 3, which is used to calculate the Signal to Noise Ratio (S/N) using the Eqs. (1) and (2). The experimental results are now transformed into a signal-to-noise (S/N) ratio [6]. Since Material removal rate is subjected to be increased and surface roughness is desired to be at the minimum, so Higher the better and Lower the Better characteristic is used for S/N ratio calculation. The S/N Ratio for the experiments conducted is shown in Table 3.

1. Larger the Better:

$$(S/N)_{HB} = -10 * \log(MSD)_{HB} \tag{1}$$

where,

$$MSD_{HB} = \frac{1}{R} \sum_{j=1}^R *(1/y^2j)$$

2. Smaller the Better:

$$(S/N)_{LB} = -10 * \log(MSD)_{LB} \tag{2}$$

where,

$$MSD_{LB} = \frac{1}{R} \sum_{j=1}^R *(y^2j)$$

Experiments are conducted using L9 OA to find the effect of process parameters on the response variable. First of all, ANOVA table is carried out for all process

parameters to determine the significant ones. Then, response curves are plotted to detect the influence of important parameters in a response.

5 Results and Discussion

In the present study all the designs, plots, and analysis have been carried out using Minitab statistical software. Larger material removal rate and lower amount of surface roughness show the high productivity of Wire EDM. Therefore, large the better and small the better are applied to calculate the S/N ratio of material removal rate and surface roughness respectively.

5.1 Effect on Material Removal Rate (MRR)

The analysis of variance (ANOVA) indicates that that pulse on time is having least significance for material removal rate with the comparison to other three parameters. It is clear that pulse on time, pulse off time, cutting speed and peak voltage significantly affect both the mean and the variation in the MRR values. The ranks and the delta values (from response Table 4) show that cutting speed have the greatest effect on material removal rate and is followed by peak current, pulse off time and pulse on time. As material removal rate is the “higher the better” type quality characteristic, it can be seen from Fig. 5 that the two level of cutting speed (A2), two level of peak current (B2), three level of pulse on time (C3), three level of pulse off time (D3) provide maximum value of material removal rate.

Prediction of mean (MRR)

Prediction of the optimum value of Material removal rate (MRR) is done at the optimal levels of significant variables, which have been identified as Cutting speed (A2), peak current (B2), pulse on time (C3) and pulse off time (D3) (Tables 4, 5 and

Table 4 Response table for material removal rate (raw data)

Level	Cutting speed (CV)	Peak current (IP)	Pulse on time (TON)	Pulse off time (TOFF)
1	38.74	43.11	47.10	45.37
2	57.11	55.48	47.48	46.84
3	52.64	49.89	53.60	56.28
Delta	18.37	12.37	6.51	10.92
Rank	1	2	4	3

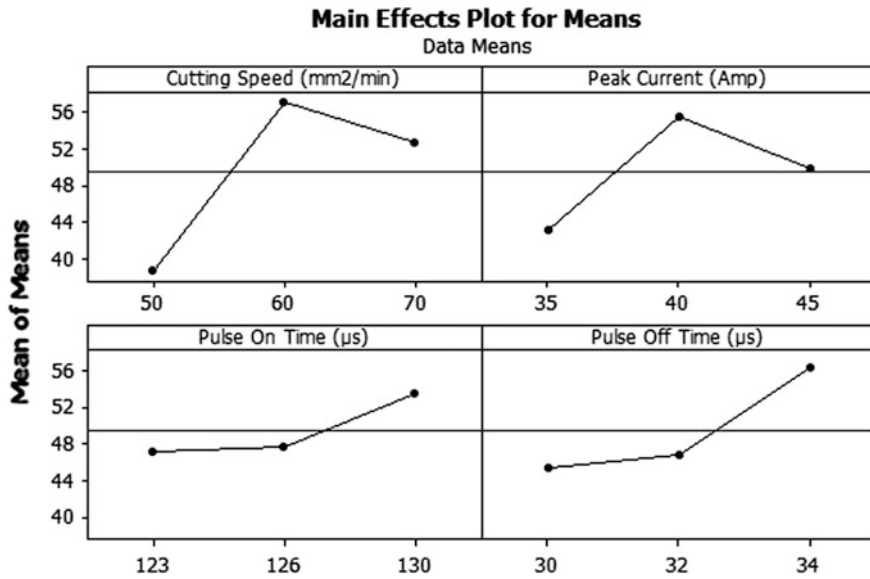


Fig. 5 Effects of process parameters on material removal rate (raw data)

Table 5 Pooled analysis of variance for material removal rate (raw data)

Source	DF	Seq SS	Adj SS	Adj MS	F	% Contribution
Cutting speed	2	550.81	550.81	275.41	7.18	44.38
Peak current	2	230.17	230.17	115.09	3.00	14.36
Pulse off time	2	210.52	210.52	105.26	2.74	12.53
Error	2	76.73	76.73	38.36		28.73
Total	8	1068.23				100

DF Degrees of freedom, SS Sum of squares, MS Mean squares (variance), F Ratio of variance of a source to variance of error

Fig. 5). The estimated mean of the response characteristic (MRR) can be determined [6] as

$$\mu_{MRR} = \underline{A}_2 + \underline{B}_2 + \underline{C}_3 + \underline{D}_3 - 3\underline{T}$$

where,

\underline{T} = overall mean of material removal rate = $(\epsilon Y1 + \epsilon Y2)/18 = 49.49361 \text{ mm}^3/\text{min}$.

Where, Y1 and Y2 are taken from the Table 3, and the values of \underline{A}_2 , \underline{B}_2 , \underline{C}_3 and \underline{D}_3 are taken from the Table 4.

A_2 = Average value of MRR at second level of cutting speed	=57.11 mm ³ /min
B_2 = Average value of MRR at second level of peak current	=55.48 mm ³ /min
C_3 = Average value of MRR at third level of pulse on time	=53.60 mm ³ /min
D_3 = Average value of MRR at third level of pulse off time	=56.28 mm ³ /min

Substituting the values of various terms in the above equation,

$$\mu_{MRR} = 57.11 + 55.48 + 53.60 + 56.28 - 3(46.54528) = 73.9891 \text{ mm}^3/\text{min}$$

5.2 Effect on Surface Roughness (SR)

The analysis of variance (ANOVA) indicates that that peak current (IP) is having least significance for surface roughness with the comparison to other three parameters. It is clear that cutting speed, pulse on time, pulse off time and peak voltage significantly affect both the mean and the variation in the SR values.

The ranks and the delta values (from response Table 6) show that cutting speed has the greatest effect on surface roughness and is followed by the pulse on time, pulse off time and peak current. As surface roughness is the “lower the better” type quality characteristic, it can be seen from Fig. 6 that the first level of cutting speed (A1), three level of peak current (B3), first level of pulse on time (C1), first level of pulse off time (D1) provide minimum value of surface roughness.

Prediction of mean (SR)

Prediction of the optimum value of Surface roughness (SR) is done at the optimal levels of significant variables, which have been identified as Cutting Speed (A₁), peak current (B₃), pulse on time (C₁), pulse off time (D₁) (Tables 6, 7 and Fig. 6). The estimated mean of the response characteristic (SR) can be determined [6] as

$$\mu_{SR} = \underline{A}_1 + \underline{B}_3 + \underline{C}_1 + \underline{D}_1 - 3\underline{T}$$

where,

$$\underline{T} = \text{overall mean of surface roughness} = (\epsilon Y1 + \epsilon Y2)/18 = 3.078722 \text{ }\mu\text{m}.$$

Table 6 Response table for surface roughness (raw data)

Level	Cutting speed (CV)	Peak current (IP)	Pulse on time (TON)	Pulse off time (TOFF)
1	2.307	2.982	2.599	2.715
2	3.406	3.388	3.299	3.309
3	3.523	2.867	3.338	3.212
Delta	1.215	0.512	0.739	0.594
Rank	1	4	2	3

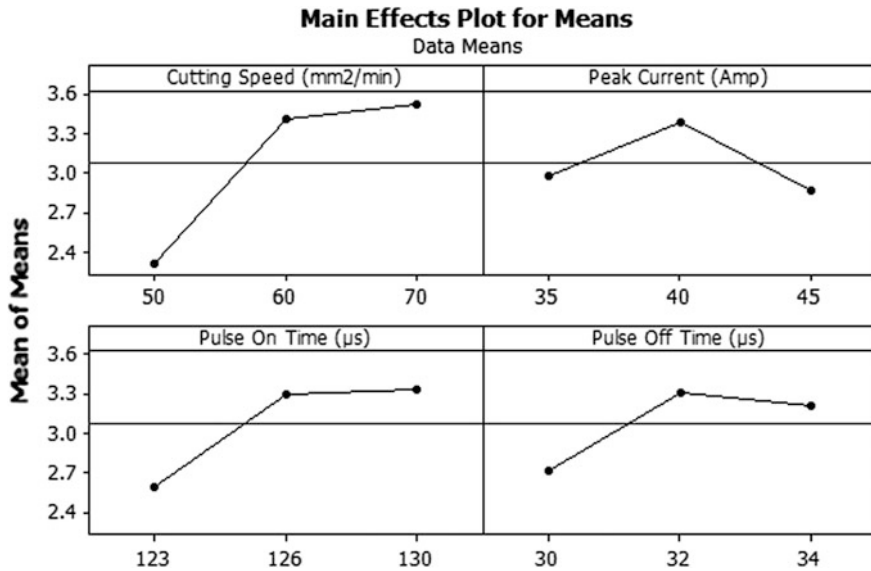


Fig. 6 Effects of process parameters on surface roughness (raw data)

Table 7 Pooled analysis of variance for surface roughness (raw data)

Source	DF	Seq SS	Adj SS	Adj MS	F	% Contribution
Cutting speed	2	2.6971	2.6971	1.3485	6.01	46.92
Pulse on time	2	1.0379	1.0379	0.5189	2.31	12.29
Pulse off time	2	0.6084	0.6084	0.3042	1.36	3.33
Error	2	0.4489	0.4489	0.2244		37.46
Total	8	4.7922				100

DF Degrees of freedom, SS Sum of squares, MS Mean squares (variance), F Ratio of variance of a source to variance of error

Where, Y1 and Y2 are taken from the Table 3, and the values of A_1 , B_3 , C_1 and D_1 are taken from the Table 6.

A_1 = Average value of surface roughness at first level of cutting speed	=2.307 µm
B_3 = Average value of surface roughness at third level of peak current	=2.867 µm
C_1 = Average value of surface roughness at first level of pulse on time	=2.599 µm
D_1 = Average value of surface roughness at first level of pulse off time	=2.715 µm

Substituting the values of various terms in the above equation,

$$\mu_{SR} = 2.307 + 2.867 + 2.599 + 2.715 - 3(3.078722) = 1.251834 \mu\text{m}$$

Table 8 Predicted optimal values and results of confirmation experiments

Performance measures	Optimal set of parameters	Predicted optimal value	Actual value	Error (%)
Material removal rate	A ₂ B ₂ C ₃ D ₃	73.9891 mm ³ /min	68.035 mm ³ /min	8.75
Surface roughness	A ₁ B ₃ C ₁ D ₁	1.251834 μm	1.250 μm	0.14

6 Confirmation Experiment and Conclusion

For validation purpose of results so obtained from analysis, only one confirmation experiment is conducted for Material removal rate (MRR) as well as Surface roughness (SR) at optimal levels of the process parameters. The values of the each quality characteristics so obtained from validation experiment are compared with the predicted values. The summary of results is shown in Table 8.

- ANOVA results for Material removal rate (MRR) show that Cutting speed, peak current and pulse off time are highly significant parameters and pulse on time is less significant for obtaining higher value of Material removal rate (MRR). Pulse-on time has least-significance effect on Material removal rate, with comparison to other three parameters. Percentage contribution of cutting speed (44.38%), Peak current (14.36%), Pulse off time (12.53%) have been found to be dominate percentage contribution for error (28.73%) for raw data.
- The optimized value for Material removal rate (MRR) obtained through Taguchi single response optimization technique has been found to be as higher as 73.9891 mm³/min is obtained at the optimized values of Cutting speed is 60 mm²/min, Peak current is 40 A, Pulse on time 130 machine unit, and pulse off time is 34 machine unit.
- ANOVA results for Surface roughness (SR) show that Cutting speed, Pulse on time, and pulse off time are highly significant parameters and Peak current is less significant for obtaining minimum value of Surface roughness (SR). Peak current has least-significance effect on Surface roughness (SR), with comparison to other three parameters. Percentage contribution of cutting speed (46.92%), Pulse on time (12.29%), Pulse off time (3.33%) have been found to be dominate percentage contribution for error (37.46%) for raw data.
- The optimized value for Surface roughness (SR) obtained through Taguchi single response optimization technique has been found to be as minimum as 1.251834 μm is obtained at the optimized values of Cutting speed is 50 mm²/min, Peak current is 45 A, Pulse on time is 123 machine unit, and pulse off time is 30 machine unit.
- However, error percentage in result is seems to be quite low, and that can be overcome by considering more process parameter other than the selected ones.

References

1. Sarkar S, Sekh M, Mitra S, Bhattacharyya B (2008) Modeling and optimization of wire electrical discharge machining of γ -TiAl in trim cutting operation. *J Mater Process Technol* 205:376–387
2. Ho KH, Newman ST, Rahimifard S, Allen RD (2004) State of art in wire electrical discharge machining (WEDM). *Int J Mach Tools Manuf* 44:1247–1259
3. Puri AB, Bhattacharyya B (2003) An analysis and optimization of the geometrical inaccuracy due to wire lag phenomenon in WEDM. *Int J Mach Tools Manuf* 43:151–159. [2] Green MA (1987) High efficiency silicon solar cells. Trans Tech Publications, Switzerland
4. Esme U (2009) Application of Taguchi method for the optimization of resistance spot welding process. *Arab J Sci Eng* 34(2B):519
5. Sathiya P, Abdul Jaleel MY (2010) Grey based Taguchi method for optimization of bead geometry in laser bead-on-plate welding. *Adv Prod Eng Manage* 5(4):225. Clem PG, Rodriguez M, Voigt JA, Ashley CS (2001) U.S. Patent 6,231,666
6. Ross PJ (2005) Taguchi techniques for quality engineering. McGraw-Hill Book Company, New York
7. Shayan AV, Afza RA, Teimouri R (2013) Parametric study along with selection of optimal solutions in dry wire cut machining of cemented tungsten carbide (WC-Co). *J Manuf Process* 15:644–658

Automatic Gear Change Mechanism for Two-Wheeler Automobiles

Aditya A. Mairal and Akash B. Pandey

Keywords Automatic gear shifting mechanism · Microcontroller · DC motors · Sensor · Solenoid actuator

1 Introduction

In automatic gear transmission system, decision of gear shifting is made by the cars on computer board, without direct interference of driver. This system shifts gears based on the speed of vehicle according to the accelerator, brake or other vehicle running or load conditions. The automatic transmission in car is computer controlled and programmed to keep the engine running at optimum speed (rpm). When the speed (rpm) level increases above the top limit, the transmission automatically shifts into higher gears so that engine will turn slower under same power. When the speed level decreases beyond the lower limit (engine is running too slow) the transmission automatically shifts into a lower gear and the engine will turn faster under the same power [1]. Advantages of these automatic transmissions include simplicity of mechanical design and savings in transmission weight and size, which are beneficial in terms of fuel economy and production costs. This enables gain in fuel economy while meeting drivability and performance goals. The ultimate aim of the research work is to transmit the gears without the human interference and to attain efficient, safe and easy driving in cost effective way. The most popular form of automated transmission as found in automobiles is the hydraulic automatic transmission. This system uses a fluid coupling in place of a friction clutch, and accomplishes gear changes by locking and unlocking a system of planetary gears. Besides the traditional automatic transmissions, there are also other types of automated transmissions, such as a continuously variable transmission (CVT) and semi-automatic transmissions that free the driver from having to shift gears manually, by using the

A.A. Mairal (✉) · A.B. Pandey

Department of Mechanical Engineering, The M.S. University of Baroda,
Vadodara, Gujarat, India
e-mail: adi.mairal@gmail.com

transmission's computer to change gear [2]. The automatic gear change can be ensured by continuously checking the rpm of the automobile through sensors which sends the signal to the input of Microcontroller. The Microcontroller is a small computer on a single integrated circuit containing a processor core, memory, and programmable input/output peripherals. Whenever the speed is increased or decreased as compared to the predefined speed for a particular gear, the Microcontroller through its logic circuits sends the signals to the actuators via its output pins. The actuators apply necessary force on the clutch and then the gear pedal to cause the change of gears [3].

2 System Description

2.1 Complete Product Package

Working: The system developed here aims to change the gears automatically by sensing the speed of the vehicle. Inductive proximity sensors sense the speed of the vehicle and the data is received in the form of pulses by the microcontroller at regular intervals. When the speed sensed by the sensor increases the defined value as entered in the controller the controller takes the decision according to the logic provided and sends the signal first to the actuator for clutch and then the gear. The clutch is actuated by means of a DC motor for gradual engaging and disengaging and the gear with the solenoid actuators for spontaneous thrusts. The microcontroller samples the data in the same time interval as required for one gear change in order to avoid hunting of gears. The system block diagram is shown in Fig. 1.

The system was mounted on a two-stroke motor cycle named "SUZUKI SAMURAI". By using automatic gear change system, effective controlling by automation can be easily achieved. Moreover, the automatic gear change system not

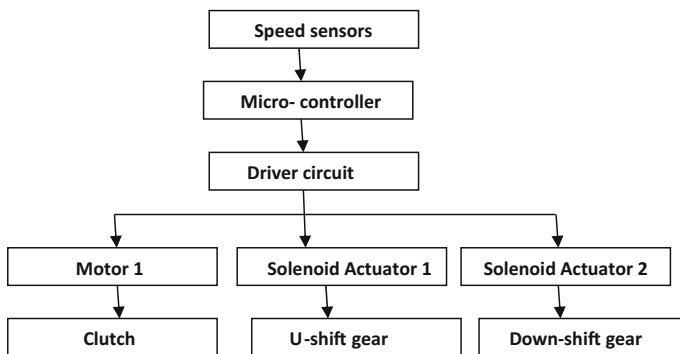


Fig. 1 System block diagram

only reduces human effort but also helps in proper gear changes at the required time.

Cost Analysis: The sensor used in this system is Inductive proximity sensor which would cost around Rs. 700. The Arduino Uno is a microcontroller board based on the ATmega328. There is 8-bit architecture in Arduino. It serves as brain to the system and controls all the actions of the system such as sensing and actuating. It selects the transmission gear as per speed of the vehicle without any human interference, the cost of which is around Rs. 1500. The Actuators here are DC motor (High torque 10 kg cm) and Spring Loaded linear solenoid actuator (12 V 16 mm 4 kg Pull type Tubular) which cost around Rs. 1500 each. The power source i.e. a battery of 12 V would cost Rs. 1000 approximately. The cost for housing and other connections could be approximated as Rs. 1000, which gives the total cost of the system as Rs. 8700.

2.2 Selection of Sensors, Controller and Actuator

Sensors provide the windows through which microprocessor-based systems can observe their environment. They are generally used to detect the presence, absence, or motion of an object. Various sensors available are: Optical sensors, Magnetic sensors, IR sensors and Inductive proximity sensors. Inductive proximity sensors (Fig. 2) operates under the electrical principle of inductance. Upon detection of the target, the sensor's output is switched 'ON' [4]. The Advantages of inductive proximity sensors are:

- Ignores water, oil, dirt, and non-metallic particles.
- Insensitive to target color or target surface finish.
- Short-circuit resistant.
- Withstands high shock and vibration environments.
- Wide range of measurements can be made by only one sensor.

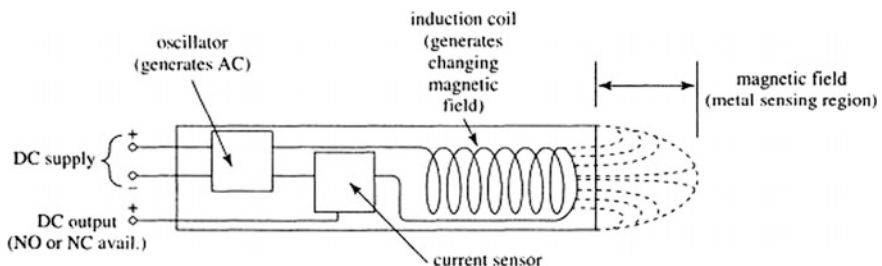


Fig. 2 Inductive proximity sensor

Microcontroller (sometimes abbreviated μC , **uCor MCU**) is a small computer on a single integrated circuit containing a processor core, memory, and programmable input/output peripherals.

The Arduino Uno (Fig. 3) is a microcontroller board based on the ATmega328 (datasheet). It has 14 digital input/output pins (of which 6 can be used as PWM outputs), 6 analog inputs, a 16 MHz ceramic resonator, a USB connection, a power jack, an ICSP header, and a reset button. It contains everything needed to support the microcontroller; simply connect it to a computer with a USB cable or power it with an AC-to-DC adapter or battery to get started [5].

The reasons behind a spontaneous selection of this are mentioned below:

- Easy to interface with its peripherals.
- Flexibility.
- Availability being it as an Open Source platform.
- Ease in programming.
- Does not need a separate loader for a program to load and can be loaded via USB port.
- In-built Analog to Digital Convertor (ADC).

Actuator is something that converts energy into motion. It also can be used to apply a force. Various actuators available are divided into two main categories: Motors and linear actuators. Linear solenoid's basically consist of an electrical coil wound around a cylindrical tube with a ferromagnetic actuator or “plunger” which is free to move or slide “IN” and “OUT” of the coils body. The advantages of linear solenoid actuators are:

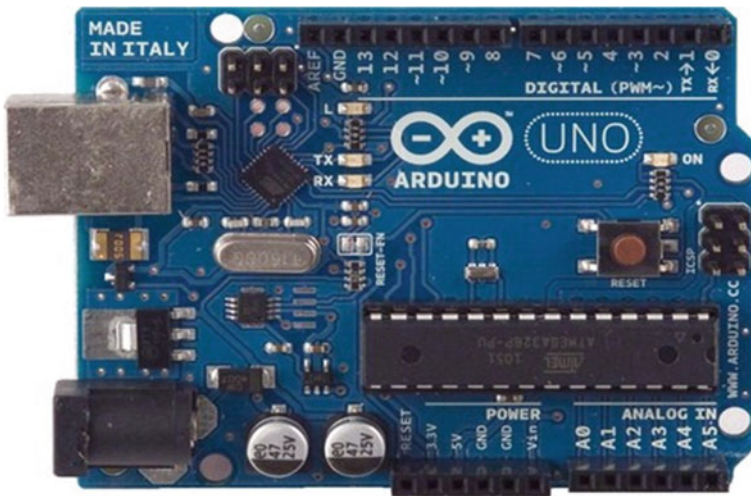


Fig. 3 Arduino UNO controller

- Simple and safe.
- Clean movement with accurate and smooth motion control.
- High spontaneous thrust suitable for changing gears.
- Compared to both hydraulic and pneumatic systems an actuator is a lot easier to install.
- It takes up less space [6].

The **actuation** of clutch should be gradual for the smooth running of the vehicle which makes DC motors the best choice for clutch actuation. The advantages of DC motors are:

- Higher efficiencies
- High reliability
- Low electrical noise
- Good speed control
- Compact size
- Low weight.

The force required for the actuation of clutch wire and gear pedal was found experimentally to be 10 and 4 kg cm respectively. Hence the actuators were selected accordingly.

2.3 Interfacing and Control

In order to interface the system peripherals with the microcontroller some important components need to be used. The details of the Interfacing Circuits shown in Fig. 4 are shown below:

ULN2003: The ULN2003A is an array of seven NPN Darlington transistors capable of 500 mA, 50 V output. The ULN2003 is known for its high-current, high-voltage capacity. The drivers can be paralleled for even higher current output. Even further, stacking one chip on top of another, both electrically and physically, has been done. Since the solenoid actuator requires 12 V current to operate the

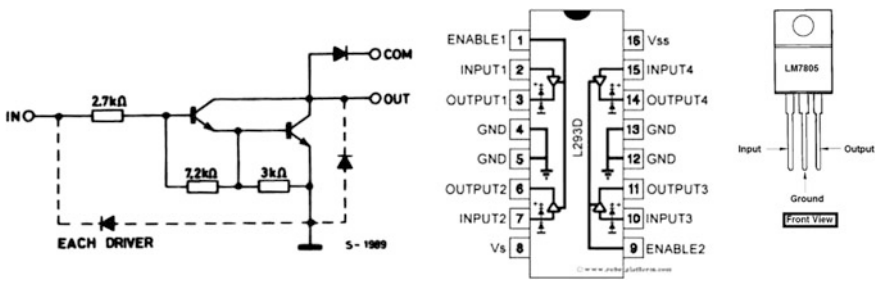


Fig. 4 Interfacing circuits

ULN2003 is used to allow 24 V to pass through actuator upon receiving 5 V from the Arduino controller.

L293D: L293D IC is a dual H-bridge motor driver IC. One H-bridge is capable to drive a dc motor in bidirectional. L293D IC is a current enhancing IC as the output from the sensor is not able to drive motors itself so L293D is used for this purpose. L293D is a 16 pin IC having two enables pins which should always be remain high to enable both the H-bridges. In order to drive the motor actuating the clutch this IC is used.

LM7805: A voltage regulator IC in order to maintain a constant voltage of 5 V to the Arduino.

2.4 Adaptation with Existing Automobile

The system developed can be peripherally attached to any two-wheeler with minor modifications in the connections. For sensing the speed of the rear wheel a small metal protrusion can be welded without disturbing the balancing of the wheel. An inductive proximity sensor could be housed near the metal protrusion to sense the rpm through

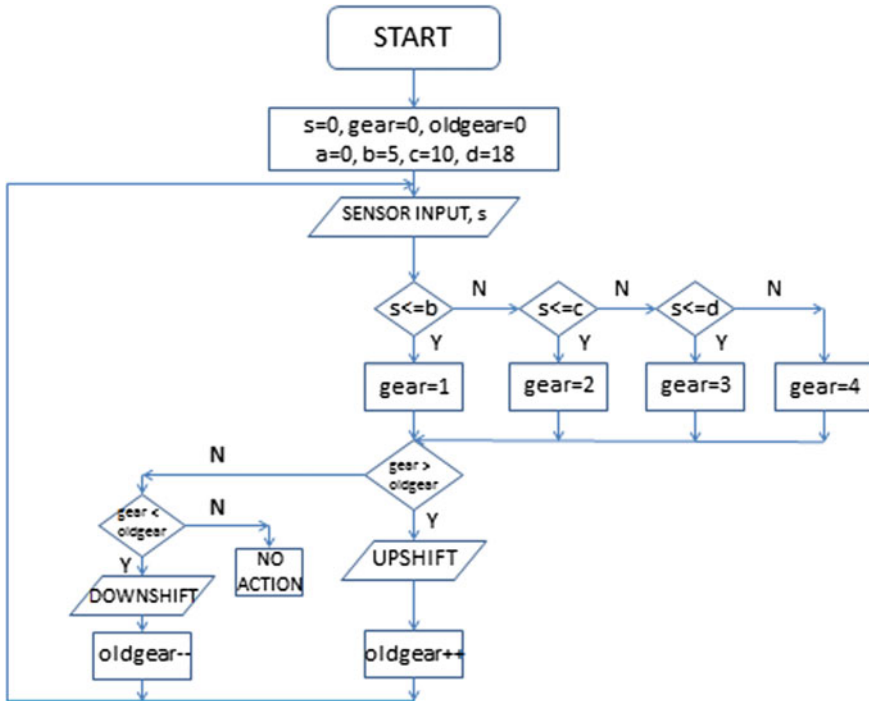


Fig. 5 Control logic

the calibration table. If a gear change is sensed by the controller then it would send the signal to the motor to actuate the clutch by pulling the wire. The next signal would be sent to suitable linear solenoid actuator for either up shifting or down-shifting the gear, which would be realized by the actuator pulling the wire attached to the gear pedal. The power required to drive the motor and actuator would be provided by a battery which can be placed along with the controller and required driving circuits in a housing close to the space near foot rest. This is implemented using the logic diagram shown in Fig. 5 and implemented using the circuit diagram.

The system can be engaged and disengaged as per the will of the rider. The speed sensed is that of the rear wheel, which gives a real-time input for processing considering the load conditions. As no significant modifications are required in the existing automobile the system provides an easy and cost effective solution for automating the cumbersome task of gear-change. As the gear engagement also affects the efficiency of the engine, this system ensures that the engine is always running at an optimum efficiency. The decision for gear change manually can be erroneous as it depends on individual perception, but the automated process always ensures the optimum efficiency of the engine (Fig. 6).

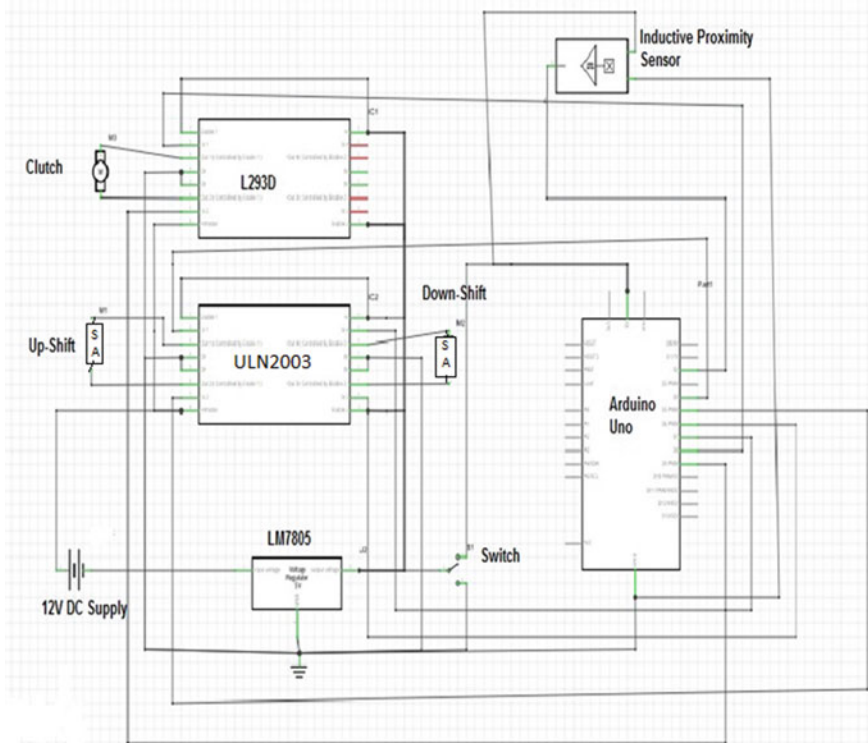


Fig. 6 Complete system connections

3 Results

The system is mounted on a Suzuki Samurai bike and the time required for gear change was observed for the bike first accelerating and then decelerating. The speed sensor calibration results are shown in Table 1. The speed is sampled for 3 s time interval. Based on speed calibration as shown in Table 1, the gear value is decided as shown Table 2. The gear value is compared with the present gear value. In case the new gear value is higher, interrupt signal is sent to upshift circuit. The motor is actuated first in the upshift circuit, and it takes 2–3 s to declutch. Then the solenoid actuator takes not more than 1 s to actuate the clutch. The motor then rotates in opposite direction to clutch the drive. The new gear value is stored in the controller. The cycle repeats itself. Hence the complete cycle time for a gear change was found out to be around 7.5–8 s (Fig. 7).

Table 1 Speed-sensor calibration table

Condition	Speed	Sampling time (s)	Actuation time (s)
Gear-1	0	3	–
Gear-1	5	3	–
Gear-2	10	3	4.5
Gear-2	15	3	–
Gear-3	20	3	4.5
Gear-3	25	3	–
Gear-4	30	3	4.5
Gear-4	40	3	–
Gear-4	30	3	–
Gear-3	25	3	4.5
Gear-3	20	3	–
Gear-2	15	3	4.5
Gear-2	10	3	–

Table 2 Speed-gear calibration

Sensor pulses	Speed (kmph)	Gear position
≤ 5	≤ 7	Gear 1
≤ 10	≤ 14	Gear 2
≤ 18	≥ 26	Gear 3
≥ 19	≥ 27	Gear 4

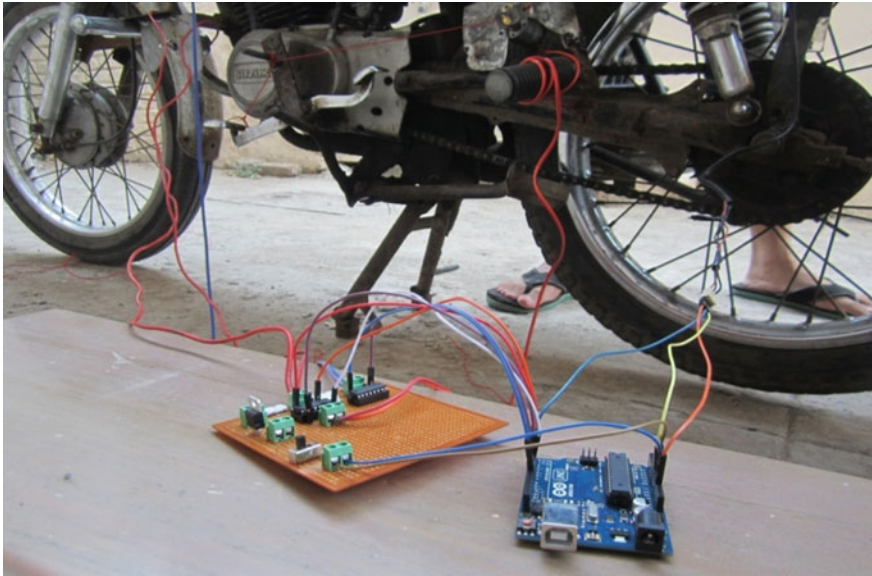


Fig. 7 Actual connected system

4 Discussion and Future Scope

4.1 Discussion and Comparison with Existing Methods

The recent methods incorporated for automatic gear transmission in a four-wheeled automobile include Continuous Variable transmission (CVT), Dual clutch transmission and automated manual transmission. The CVTs have been used since decades but the limited torque and reliability have inhibited their growth. Dual clutch also called as Twins clutch transmission uses two separate clutches for odd and even gear sets. This system is operated fully in automatic mode and it has an ability to allow the driver to shift gear manually in semi-automatic mode. The construction is very complicated and bulky. Also the repairing costs are very expensive. The automated manual transmission is the mix of automated and manual transmission. This system is most efficient, but can be applied in a four-wheeled automobile as due to large space availability the hydraulic unit which is an integral part of this transmission can easily be accommodated [7]. The method discussed in this paper consists of applying AMT to a two-wheeler automobile. Due to space and weight constraint, the hydraulic unit of the AMT is replaced with solenoid actuators, which would develop an efficient system for automatic gear change in two-wheelers.

4.2 Future Scope

- Use of more sophisticated engineering components like torque convertors, planetary gear sets, multi-plate clutches, etc. for this purpose can impart efficient driving attributes.
- Predictive gear shifting system can be employed which can provide required gear ratios while cornering.
- If sufficiently optimized by using better fuel systems, injection systems, use of turbocharger and controlled valve operations these vehicles based on this technology will be more driver and environment friendly.
- The given system can be modified for a semi-automatic gear shifting mechanism wherein the gear would be shifted by the press of a button provided to the rider. This would reduce the effort for changing the gear and would give a convenient and rider-friendly mechanism.

5 Conclusion

The system described delegates the most critical operation while driving a geared two-wheeler automobile- gear change- to the sensor-controller-actuator mechanism which is not only efficient but also cost effective. The real time data is sensed and the gears are changed automatically so as to give the rider a comfortable ride. The system is not automobile specific and can be applied to any given automobile peripherally without any significant modifications in the existing one. This system is of cardinal importance to one-leg amputees and sophomores who would now be able to ride a geared automobile with ease and comfort.

References

1. Alexandar P (2012) Research on automatic gear transmission using embedded system. Int J Adv Res Eng Technol (IJARET). ISSN 0976-64
2. Kluger MA, Fussner DR (1997) An overview of current CVT mechanisms, forces and efficiencies. SAE paper no. 970688, in SAE SP-1241, Transmission and driveline systems symposium, pp 81–88. SAE
3. US Patent No: 4884201 Titled automatic gear change device dated 28 Nov 1989
4. <http://www.ab.com/en/epub/catalogs/12772/6543185/12041221/12041227/Inductive-Proximity-Sensors.html>
5. Mazidi MA, Mazidi JG, Mckinlay RD (2009) The 8051 micro controller & embedded system using assembly and C, 2nd edn. Pearson Education
6. <http://www.linak.com/about/?id3=2339>
7. Borse A, Deshmukh A. 2nd International conference on recent trends in engineering science and management: automatic gear transmission system. ISBN: 978-81932074-3-7

Analysis of Water Lubricated Bearing with Different Features to Improve the Performance: Green Tribology

Anil B. Shinde, Prashant M. Pawar, Sunil Gaikwad, Pakija A. Shaikh and Yashpal Khedkar

Keywords Surface features · Pressure · Load carrying capacity · Numerical analysis

1 Introduction

The world's seas, oceans and rivers are a vast global resource of non-polluting, endlessly renewable energy and with the ever increasing demand for electrical power. Many companies and countries have invested heavily in journal bearing systems that will generate power and yet still withstand the harsh underwater environment. The water passes the bearing through the longitudinal grooves as well as moves radially between the propeller shaft and the bearing face in a thin film. Once this film, or wedge, has developed the journal aft does not actually come into contact with the bearing. The eccentricity of the journal is related to the pressure that will be generated in the bearing to balance the radial load. Hence, it is necessary to analyze the fluid film of lubricant.

Most of the researchers were much attracted in investigating the theories and experiments of hydrodynamic lubrication and paid no attention to how to improve load carrying capacity of a hydrodynamic journal bearing. Reduction of environment pollution and energy saving are important issues in machine design [1]. Water-lubrication system is convenience, green, safe and energy saving. The application of water-lubricated journal bearings is widespread, such as ship building, transportation industry, food industry, industrial machinery and equipment, and pharmaceutical industry [2]. The drawback of water as a lubricant is that its viscosity is much lower than that of oil and other lubricants [3]. The numerical analysis is carried out for smooth surface journal bearings to find out performance characteristics [4–8].

A.B. Shinde (✉) · P.M. Pawar · S. Gaikwad · P.A. Shaikh · Y. Khedkar
Shri Vithal Education and Research Institute's College of Engineering,
Pandharpur, India
e-mail: abshinde@coe.sveri.ac.in

In the present work, a 3 dimensional CFD model is developed, using COMSOL Multiphysics software, to study the behavior and the performance of a journal bearing with a water lubricant. A Reynolds equation is used to obtain the pressure distribution and load carrying capacity. This Reynolds equation is solved theoretically and implemented in COMSOL to get the simulation results. The results of the CFD model are compared with results of Gao [9] and found to be in good agreement.

The validated model is used to analyze the effect of surface features like triangular, circular and rectangular positive slot to study the development of pressure and load carrying capacity.

2 Model of Plain Hydrodynamic Journal Bearing

Figure 1 shows the coordinate and the schematic of a simple plain journal bearing in an equilibrium-state configuration. The plain journal bearing is immersed in water lubricant. The hydrodynamic action creates dynamic pressure in water lubricant, mainly in the convergent part of the journal bearing gap, to counteract the load thereby separating the journal surface from the bearing surface with a thin water lubricant film. The hydrodynamic pressure ultimately terminates in the divergent part of the gap, and the pressure may go below the vapor pressure. When equilibrium state is reached, the journal is displaced from the bearing with a center distance (e), which is referred to the journal eccentricity. The eccentricity ratio (ϵ) and the clearance (C) are important parameters to measure the load carrying capacity and pressure distribution of the journal bearing. With the help of these parameters, lubricant film thickness is determined.

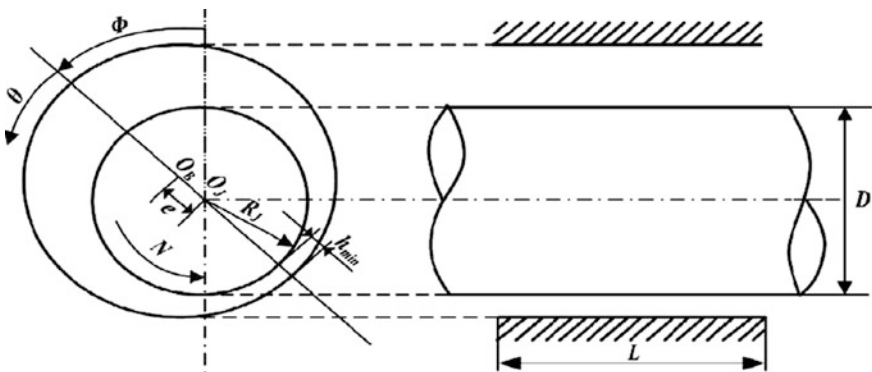


Fig. 1 Co-ordinate and model of a plain hydrodynamic journal bearing

3 CFD Model—Analysis

3.1 Governing Equations

The theory applied to the hydrodynamic water lubricated bearing is given by Reynolds's Equation. This equation is based on several assumptions that were adopted to simplify the mathematical derivations. The following are the some basic assumptions of hydrodynamic lubrication theory (1) the fluid flow is laminar, (2) the fluid lubricant is continuous, incompressible, and Newtonian, (3) there is no slip at the boundary, (4) the velocity component in y direction is negligible in comparison to the other two velocity components in the x and z directions, (5) velocity gradients along the thin and z directions, are small and negligible relative to the velocity gradients across the film, (6) the effect of the curvature can be ignored, (7) the pressure variations in the y direction are very small, and their effect is negligible in the equations of motion, (8) the force of gravity on the fluid is negligible, (9) fluid viscosity is constant.

The Reynolds equation for Newtonian, incompressible and constant viscosity fluid in a thin clearance is given by;

$$\frac{\partial}{\partial x} \left(\frac{h^3}{\mu} \frac{\partial p}{\partial x} \right) + \frac{\partial}{\partial z} \left(\frac{h^3}{\mu} \frac{\partial p}{\partial z} \right) = 6U \frac{\partial h}{\partial x} \quad (1)$$

This Reynolds equation is commonly used for solving the pressure distribution of hydrodynamic bearings. Where, h is the variable film thickness is due to the journal eccentricity;

$$h = C(1 + \varepsilon \cos \theta) \quad (2)$$

3.2 Parameters and Variables

3.2.1 Parameters

The parameters used for analysis are given in Table 1.

3.2.2 Variables

The variables used for analysis are given in Table 2.

Table 1 Parameters set for analysis

Name	Expression	Description
R	40 mm	Journal radius
H	80 mm	Journal height
c	0.04 mm	Clearance between the bearing and the journal
ω	$1500/60 * 2 * \pi$ rad/s	Journal angular velocity
ϵ	0.8	Eccentricity ratio
R_{min}	0.02 mm	Base, width and diameter of triangular, rectangular and circular slot respectively
h	0.01 mm	Height of triangular, rectangular and circular positive slot respectively
d	4 mm	Axial pitch distance
S	20	No. of positive slot

Table 2 Variables set for analysis

Name	Expression	Description
θ	$\text{atan2}(y, x)$ [rad]	Angle along circumference
h	$c*(1 + \epsilon*\cos(\theta))$	Lubricant film thickness
u	$-\omega*R*\sin(\theta)$	x-component of journal velocity
v	$\omega*R*\cos(\theta)$	y-component of journal velocity

3.3 Material Properties and Boundary Conditions

3.3.1 Material Properties

Water is used as a lubricant. The density and dynamic viscosity of water are 1000 kg/m^3 and 0.001 Pa s respectively.

3.3.2 Boundary Conditions

The governing equations are solved in equilibrium state, taking no account of gravity force, and the operating pressure is set to 1 atm. The boundary conditions of the inlet and outlet are respectively “pressure inlet” and “pressure outlet” with gauge pressure at zero Pascal. The inner surface of the water film is modeled as “sliding wall” with an absolute rotational speed which equals the velocity of the journal.

3.4 Analysis and Results

3.4.1 Analysis of Plain Journal Bearing

In the design of journal bearing, various surface features like circular, rectangular and triangular positive slots incorporated. The major dimensions are mentioned in Table 1. In the analysis of plain journal bearing, effect of eccentricity ratio is studied. The results are shown in Fig. 2. The results of the CFD model with water lubricant are compared with results of Gao [9] as shown in Fig. 3 and shows same trend.

3.4.2 Results of Plain Journal Bearing

Eccentricity ratio (ϵ) is an significant parameter to increase pressure distribution and load carrying capacity of plain journal bearing. In order to study the relationship between eccentricity ratio (ϵ) and distribution of pressure produced by hydrodynamic lubrication, the effect of the different eccentricity ratio (ϵ) are used in the

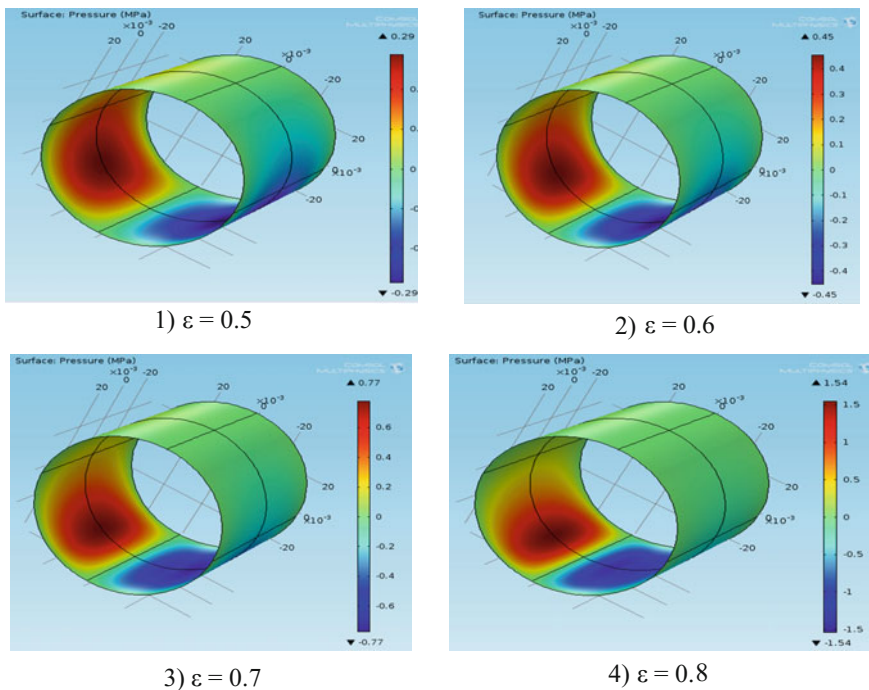


Fig. 2 CFD results of effect of eccentricity ratio (ϵ) on increase in pressure distribution of plain journal bearing

Fig. 3 Effect of eccentricity ratio (ϵ) on pressure distribution for water lubricant, *blue colour* present analysis results, *red colour* Gao [9]

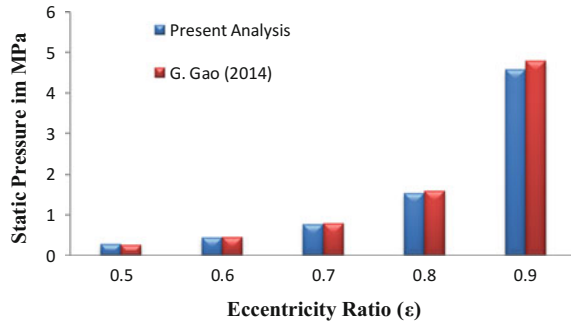
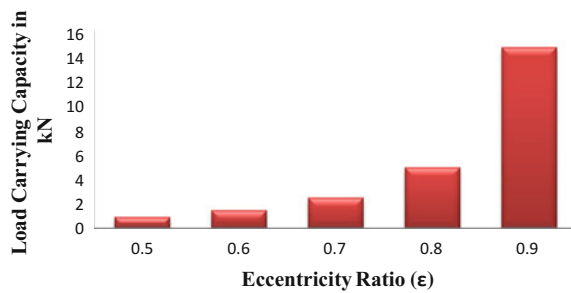


Fig. 4 Effect of eccentricity ratio (ϵ) on load carrying capacity of plain journal bearing

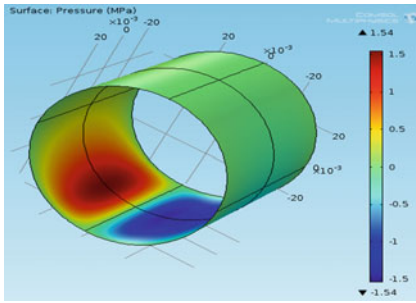


numerical analysis. Figure 3 shows graph for the pressure distribution versus the eccentricity ratio (ϵ). Hydrodynamic performances of plain journal bearing mainly depend on the size and distribution of the positive pressure on the zones. It is observed that, with increase in eccentricity ratio, there is increase in pressure distribution. From Fig. 3, it is seen that maximum pressure is developed for eccentricity ratio $\epsilon = 0.9$.

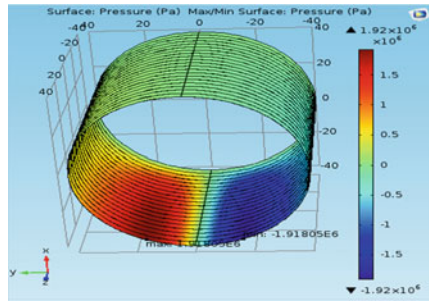
Similar to pressure distribution, load carrying capacity is also depends upon eccentricity ratio. From Fig. 4, it is observed that, as eccentricity ratio increases, load carrying capacity also increases.

3.4.3 Analysis of Journal Bearing with Different Surface Features

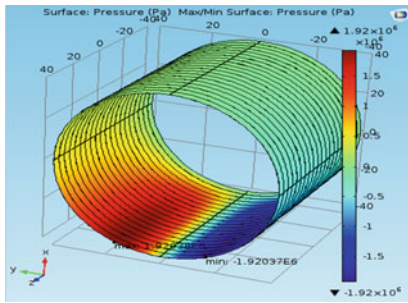
The validated model is used to analyze the effect of surface features like triangular, circular and rectangular positive slot in the development of pressure and load carrying capacity. From the CFD analysis of journal bearing with surface features, it is observed that, micro features on the surface of journal bearing enhancing the pressure distribution. Figure 5 shows CFD results for pressure distribution of plain journal bearing and bearings with surface features at same eccentricity ratio ($\epsilon = 0.8$).



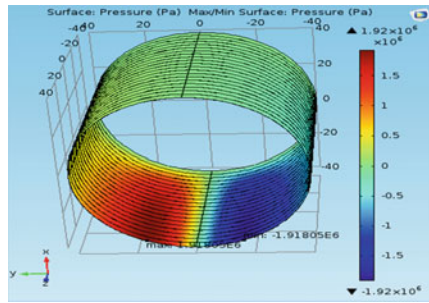
Plain Journal Bearing ($\epsilon = 0.8$)



Bearing Triangular positive slot ($\epsilon = 0.8$)



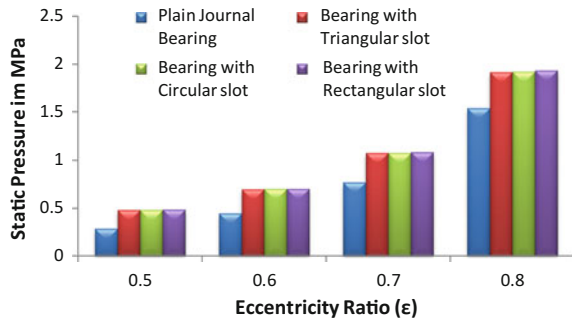
Bearing Circular positive slot ($\epsilon = 0.8$)



Bearing Rectangular positive slot ($\epsilon = 0.8$)

Fig. 5 CFD results for pressure distribution of plain journal bearing and bearings with surface features at same eccentricity ratio ($\epsilon = 0.8$)

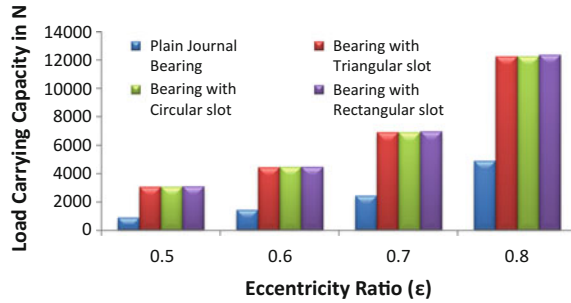
Fig. 6 Comparison of pressure distribution between plain journal bearing and bearings with features at different eccentricity ratio



3.4.4 Results of Journal Bearing with Different Surface Features

From Fig. 6, it is observed that, for 1500 rpm speed of journal with 0.001 Pa s viscosity of water lubricant, maximum pressure is developed in journal bearing with rectangular positive slot.

Fig. 7 Comparison of load carrying capacity between plain journal bearing and bearings with features at different eccentricity ratio



Similar to pressure distribution, load carrying capacity of plain journal bearing and bearing with surface features studied. From analysis, it is found that, journal bearing with rectangular positive slot have more load carrying capacity as compared with others as shown in Fig. 7.

4 Conclusions

The pressure distribution and load carrying capacity of the hydrodynamic journal bearing with water lubricant has analyzed. Based on the results, following conclusions can be made for journal bearing with different surface features studied. Using Reynolds equation, present CFD model of plain journal bearing is simulated and compared with result of Gao [9] and found to be in good agreement. It is found that, the pressure and load carrying capacity increases as of eccentricity for a plain journal bearing increases. Further analysis of bearings with different surface features, it is found that journal bearing with rectangular positive slot have maximum pressure development and load carrying capacity as compared with journal bearing with triangular and circular positive slots. This may be due to development of less film thickness at feature location.

References

1. Wang X, Koji K, Koshi A, Kohj A (2003) Loads carrying capacity map for the surface texture design of SiC thrust bearing sliding in water. *Tribol Int* 36:189–197
2. Santos EN, Blanco CJC, Macedo EN, Maneschy CEA, Quaresma JNN (2012) Integral transform solutions for the analysis of hydrodynamic lubrication of journal bearings. *Tribol Int* 2012(52):161–169
3. Hiroki Y, Shinya S, Tsuneo K, Nagayoshi S (2011) Effects of laser surface texturing on friction behavior of silicon nitride under lubrication with water. *Tribol Int* 2011(44):579–584
4. Cabrera DL, Woolley NH, Allanson DR, Tridimas YD (2005) Film pressure distribution in water-lubricated rubber journal bearings. *Proc Inst Mech Eng, Part J: J Eng Tribol* 2005(219): 125–132

5. de Kraker A, van Ostayen RAJ, Rixen DJ (2007) Calculation of Stribeck curves for (water) lubricated journal bearings. *Tribol Int* 40:459–469
6. Gertzos KP, Nikolakopoulos PG, Papadopoulos CA (2008) CFD analysis of journal bearing hydrodynamic lubrication by Bingham lubricant. *Tribol Int* 41(2008):1190–1204
7. Mane RM (2013) Analysis of hydrodynamic plain journal bearing. In: Excerpt from the proceedings of the 2013 COMSOL conference in Bangalore
8. Wang YQ, Li C (2011) Numerical analysis of hydrodynamic lubrication on water-lubricated rubber bearings. *Adv Mater Res* 2011(299–300):12–16
9. Gao G, Yin Z, Jiang D, Zhang X (2014) Numerical analysis of plain journal bearing under hydrodynamic lubrication by water. *Tribol Int* 75:31–38

Design and Construction of Briefcase Type Portable Solar Dryer

S.S. Gaikwad, Anil B. Shinde, A.A. Mote and P.S. Kachare

Keywords Solar dryer · Forced convection · Solar energy

1 Introduction

The heated air from a separate solar collector is passed through a grain bed in the dryer, and at the same time, the drying cabinet absorbs solar energy directly through the transparent walls and roof. This project presents the design, construction and performance of a briefcase type portable solar dryer for food preservation. The project consists of efficient utilization of solar energy by natural as well as forced convection to improve efficiency of solar dryer. Food drying is a very simple, ancient skill. It is one of the most accessible and hence the most popular processing technology. Sun drying of fruits and vegetables is still practiced mostly unchanged from ancient times. Conventional sun drying takes place by storing the product under direct sunlight. Sun drying is only possible in areas where, in an average year, the weather allows foods to be dried immediately after harvest. The major advantages of sun drying are low capital and operating costs and the fact that little expertise is required. The main limitations of this method are as follows: contamination, theft or damage by birds, rats or insects; slow or intermittent drying and no protection from rain or dew that wets the product, encourages mould growth and may result in a relatively high final moisture content; low and variable quality of products due to over- or under-drying; vast areas of land needed for the shallow layers of food; laborious since the crop must be turned, moved if it rains; direct exposure to sunlight reduces the quality (colour and vitamin content) of some vegetables and fruits. The quality of foods which is sun dried can be improved by

S.S. Gaikwad (✉) · A.B. Shinde · A.A. Mote · P.S. Kachare
SVERI's College of Engineering, Pandharpur, India
e-mail: ssgaikwad@coe.sveri.ac.in

S.S. Gaikwad · A.B. Shinde · A.A. Mote · P.S. Kachare
Solapur University, Solapur, Maharashtra, India

reducing the size of pieces to achieve faster drying and by drying on raised platforms, covered with cloth or netting to protect against insects and animals.

Solar dryers have advantages over sun drying when correctly designed. They give faster drying rates by heating the air to 10–300 °C above ambient, which causes the air to move faster through the dryer, reduces its humidity and deters insects. The faster drying reduces the risk of spoilage, improves quality of the product. They can be constructed from locally available materials at a relatively low capital cost and there are no fuel costs. Thus, they can be useful in areas where fuel or electricity are expensive, land for sun drying is in short supply or expensive, sunshine is plentiful but the air humidity is high.

Xiea et al. [1] developed recent version of concentrated solar energy applications and solar energy concentration technology using Fresnel lens is an effective way to make full use of sunlight. Sharma et al. [2] carried out work regarding a comprehensive review of the various designs and details of construction and operational principles of the wide variety of practically realized designs of solar energy drying systems using Fresnel lenses. Bolin et al. [3] proposed direct and indirect drying, with some work also being done on combination drying procedures. In direct solar dryers, the product to be dried is usually either inside a tent, greenhouse, or a glass-topped box, where the product to be dried is heated by the direct rays from the sun and the moist air is removed by ambient with indirect drying, the opposite is true, where most require powered fans for forced air circulation. Rathi and Mujumdar [4] carried out simulation of solar dryer is to be carried out. Sarsilmaza et al. [5] carried out drying of apricots in a newly developed rotary column cylindrical dryer (RCCD) equipped with a specially designed air solar collector (ASC) was investigated and optimum drying air rate and rotation speed of dryer, to maintain uniform and hygienic drying conditions and to reduce drying times.

Mohanraj and Chandrashekhar [6] mentioned that forced convection solar dryer is more suitable for sun drying process. S. Misha et al. discussed several design of tray dryer system for drying agricultural products and its performance. Most of the dryer systems have been developed are using solar energy because the systems run at low operating cost [7]. Ronald et al. [8] stated that the processes that are used to dry crops at temperatures greater than 50 °C could benefit from solar drying as a supplemental system. B.K. Bala et al. mentioned that the dryer consists of a transparent plastic covered flat plate collector and a drying tunnel connected in a series to supply hot air directly into the drying tunnel using two dc fans operated by a solar module. This dryer is simple in construction and it can be constructed using locally available materials. The solar tunnel dryer can be operated by a photovoltaic module independent of the electrical grid. The photovoltaic system has the advantage that the temperature of the drying air is automatically controlled by the solar radiation. The photovoltaic driven solar tunnel dryer must be optimized for efficient operation [9].

2 Constructions

2.1 Solar Panel

Solar panel refers to a panel designed to absorb the sun's rays as a source of energy for generating electricity or heating. A photovoltaic (in short PV) module is a packaged, connected assembly of typically solar cells. Solar Photovoltaic panels constitute the solar array of a photovoltaic system that generates and supplies solar electricity in commercial and residential applications.

2.2 Battery

It is the oldest type of rechargeable battery. Most of the world's lead–acid batteries are automobile starting, lighting and ignition batteries. Their low cost, makes it attractive for use in motor vehicles to provide the high current required by automobile starter motors.

2.3 Exhaust Fans

A fan is a machine used to create flow within a fluid, typically a gas such as air. The fan consists of a rotating arrangement of vanes or blades which act on the fluid. The rotating assembly of blades and hub is known as an impeller, a rotor, or a runner. Usually, it is contained within some form of housing or case. This may direct the airflow or increase safety by preventing objects from contacting the fan blades. Most fans are powered by electric motors.

2.4 Reflector

A mirror reflects light in such a way that, for incident light in some range of wavelengths, the reflected light preserves many or most of the detailed physical characteristics of the original light. The most familiar type of mirror is the plane mirror, which has a flat screen surface. Curved mirrors are also used, to produce magnified or diminished images or focus light or simply distort the reflected image.

2.5 Glass

Glass is a non-crystalline amorphous solid that is often transparent and has wide-spread practical, technological, and decorative usage in, for example, window panes and tableware. Glass will transmit, reflect and refract light; these qualities can be improved by cutting and polishing to make prisms, optical lenses, fine glassware, and optical fibers for transmission of high speed data by light.

2.6 Heating Element

Heating element is device used to produce the heat by supplying dc current. The current is supplied by using battery.

2.7 Assembly

Briefcase type solar dryer works on the principle of natural as well as forced convection with the help of reflector food is dried naturally and forced convection is achieved by blowing air on the heating element (Figs. 1 and 2).

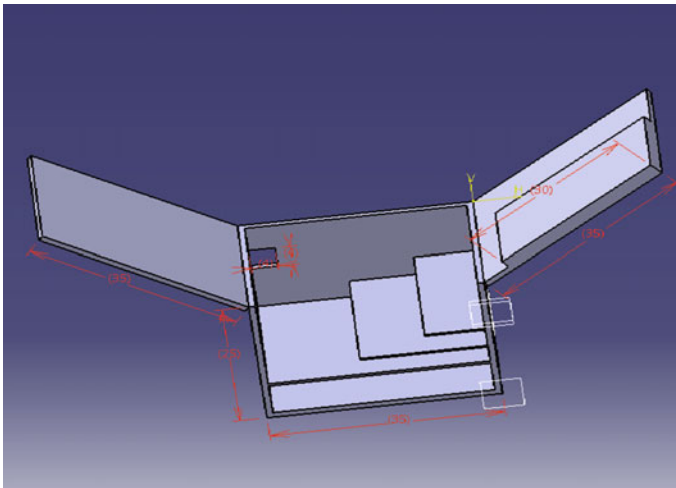


Fig. 1 CATIA solar dryer design assembly

3 Experimentation

- Initial mass of each component = 200 gm
- Calculation:

$$\text{Moisture (\%)} \text{ Removed} = \frac{\text{Initial Mass} - \text{Final Mass}}{\text{Initial Mass}}$$

3.1 Experimentation on Potato

See Table 1, Figs. 3 and 4.



Fig. 2 Fabrication assembly of solar dryer

Table 1 Experimentation on potato

Sr. no.	Time (H)	Solar drying (g)	Open sun drying (g)	Moisture (%) removed (solar drying)	Moisture (%) removed (open sun drying)
1.	1	106.7	120.8	46.6	39.6
2.	2	70.29	83.7	64.85	58.15
3.	3	43.49	61.79	78.25	69.10
4.	4	30.72	43.87	84.64	78.06

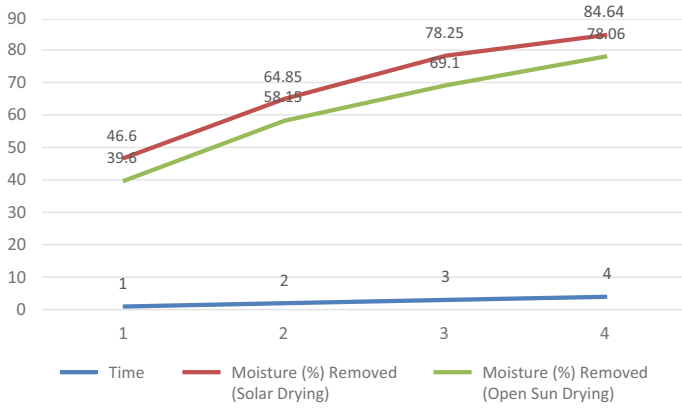


Fig. 3 Moisture (%) removed (solar drying and open sun drying) versus time

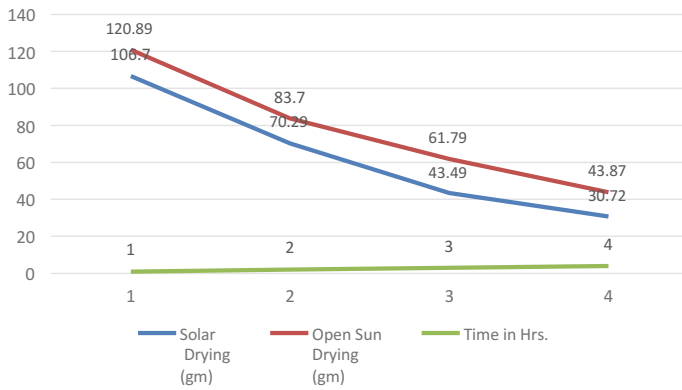


Fig. 4 Solar drying (gm) and open sun drying (gm) versus time

3.2 Experimentation on Tulasi

See Table 2, Figs. 5 and 6.

Table 2 Experimentation on tulasi

Sr. no.	Time (H)	Solar drying (gm)	Open sun drying (gm)	Moisture (%) removed (solar drying)	Moisture (%) removed (open sun drying)
1.	1	114.02	131.87	42.99	34.06
2.	2	82.12	96.99	58.94	51.50
3.	3	64.7	79.9	67.65	60.05
4.	4	52.6	65.4	73.70	67.30

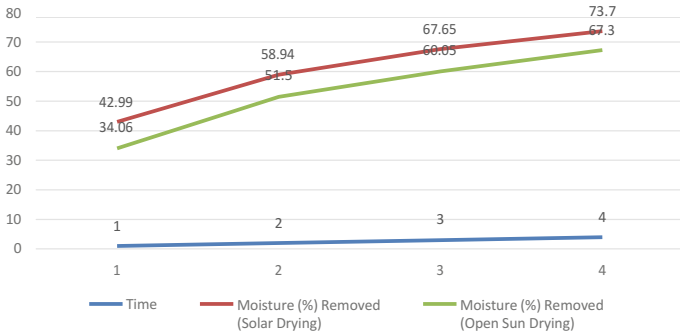


Fig. 5 Moisture (%) removed (solar drying and open sun drying) versus time

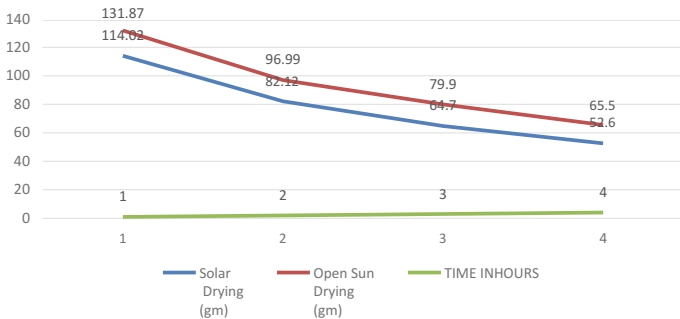


Fig. 6 Solar drying (gm) and open sun drying (gm) versus time

4 Conclusions

After construction and experimentation on solar dryer, we conclude that, after comparing the drying kinetics of solar drying with open sun drying, we observed that efficiency of solar drying is increased in measurable amount. Solar dryer is easy to handle by using trolley mechanism i.e. portable. Dryer is able to work during night hours. Solar dryer is easy to handle by using trolley mechanism. By using heaters in the drying compartment we can increase the efficiency of dryer. In future scope instead of using solar flat plate collector use solar photovoltaic panel. Also increase the no. of trays and no. of heaters in the drying compartment we can improve the efficiency of the dryer.

References

1. Xiea WT, Daia YJ, Wanga RZ, Sumathyb K (2011) Concentrated solar energy applications using Fresnel lenses: a review. *Renew Sustain Energy Rev* 15:2588–2606
2. Sharma A, Chen CR, Lan NV (2009) Solar-energy drying systems: a review. *Ren Sustain Energy Rev* 13:1185–1210
3. Bolin HR, Salunkhe DK, Lund D (1982) Food dehydration by solar energy. *CRC Crit Rev Food Sci Nutr* 16:327–354
4. Rathi C, Mujumdar AS (1997) Solar drying of foods: modeling and numerical simulation. *Sol Energy* 60(3–4):151–157
5. Sarsilmaza C, Yildizb C, Pehlivan D (2000) Drying of apricots in a rotary column cylindrical dryer (RCCD) supported with solar energy. *Renew Energy* 21:117–127
6. Mohanraj M, Chandrashekhar P (2008) Comparison of drying characteristics and quality of copra obtained in a forced convection solar dryer and sun drying. *J Sci Ind Res* 67:381–385
7. Misha S, Mat S, Ruslan MH, Sopian K, Salleh E (2013) Review on the application of a tray dryer system for agricultural products. *World Appl Sci J* 22:424–433
8. Voskens RGJH, Out PG, Schulte B, Market opportunities for solar drying. Solar thermal, Ecofys energy and environment, Netherlands
9. Bala BK, Mondol MRA, Biswas BK, Das Chowdury BL, Janjai S (2003) Solar drying of pineapple using solar tunnel drier. *Renew Energy* 28:183–190

Crashworthiness Improvement for Rollover of Bus Using FEA

Vivekanand Phadatare, Pravin Hujare and Chandrakant Inamdar

Keywords Bus rollover · Finite element analysis (FEA) · Ls-dyna · Residual space

1 Introduction

The most commonly used way of transportation in India and in many countries are the road transport among the various modes of vehicle crashes, rollover crashes are threatening to vehicle occupants. Hence, the Automotive Industry Standard (AIS-031) in India specifies the requirements and methods to calculate the strength of superstructure of buses during and after rollover. The bus structure may collapse due to impact load as shown in Fig. 1.

In rollovers, passengers can be ejected, partially ejected, or become the victims of roof intrusion. Today the European regulation “ECE R66” (Economic commission for Europe) is force to prevent such rollover accidents thereby ensuring the safety of bus and coach passengers. AIS 031 is for rollover setup. The aim of this study was to findout the impact on passenger residual space as per AIS 031 regulation.

Karliński et al. [1] presented the modelling of a bus superstructure and strength analysis of bus structure and evaluates the requirements of Regulation ECE R66 using the finite element method, with consideration of nonlinearity of materials and geometry. Kumar [2] presented the study of bus rollover according to “Automotive Indian Standard Regulation No. 031” (AIS 031)/ECE R66 (Economic commission for Europe Regulation No. 66) conditions. The aim of this study was to investigate

V. Phadatare (✉) · P. Hujare
Sinhgad Academy of Engineering, Kondhwa, Pune, India
e-mail: vivekanand8792@gmail.com

P. Hujare
e-mail: pphujare.sae@sinhgad.edu

C. Inamdar
Virtual Simutech Pvt. Ltd, Pune, India



Fig. 1 Damaged structure of bus in the case of rollover [1]

the impact on passenger residual space as per AIS 031 regulation. Micu and Iozsa [3] presented computer simulation of a bus rollover, on a complete vehicle and can be used as approval method. Sergeevich and Nikolaevich [4] focused on study which contains the search for methods of verification of bus rollover finite element simulation which can replace a full-scale verification rollover test using single bus section. Kyoung Tak Kang [5] discuss a new carbon-epoxy composite roll bar installed in a bus. This focused on benefits of new material like lowers center of gravity, reduced mass and roll moment inertia of the vehicle. Belsare [6] presents a physical rollover test on a complete vehicle. Kadir Elitok [7] presented bus rollover analysis with LS-DYNA.

Marianski and Szosland [8] discuss the research on the strength of standard bus bodies at rollover on the side. The objectives such as to prepare FE model of bus for rollover test, to check whether the total energy remained constant during the roll-over event and to check performance of structure is good and it is not intruding with the residual space, and is not violating the roll-Over Code.

The methodology of investigation can be explained as firstly preparing the model for rollover with roll-bar structure, FE modelling is done by the specialized pre-processing or meshing software HyperMesh. Results of rollover test applied on superstructure is displacement plot and energy plot.

2 Rollover Analysis of Bus

In case of rollover, the bus first comes into contact with the ground and then starts absorbing energy by elasto-plastic deformation and bends at the plastic hinge zones.

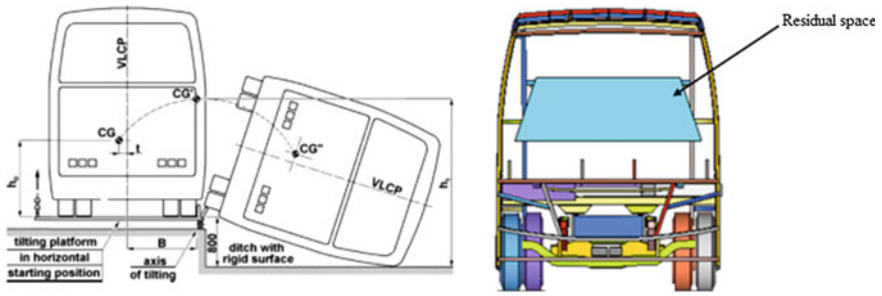


Fig. 2 Positioning of the vehicle on the platform in rollover test [1]

2.1 Theory of Rollover Test on Bus

Rollover test on bus model is used to find strength of superstructure of bus. The rollover test on a complete vehicle is the most objective and reliable but due to economic reasons these tests are performed using other equivalent methods.

The rollover test carried out on that side of the vehicle which is more dangerous with respect to the residual space. The roll-over test platform for a complete vehicle is shown in Fig. 2. It gives stating for rollover test. Where 'h' is distance between two C.G.

3 Finite Element Modelling

The main aim of finite element model of the bus is to capture the deformation and interaction of bus systems during rollover impact. FE modelling process involves CAD data, pre-processing, meshing, deck preparation, and processor (LS-DYNA). Also post-processor, displacement plot and energy plot.

3.1 CAD Model (Geometric Model)

Geometric modeling of the bus was carried out using CAD software CATIA. The mid-surfaces of these CAD model were extracted, since most geometrical features of the bus have been defined with thickness, to proceed for shell-meshing. The first stage was to prepare the geometric model of the external shape of the structure. The strength calculations were conducted using specialized software which implements an explicit algorithm for computing simultaneous differential equations. The geometric model of the bus is shown in Fig. 3.

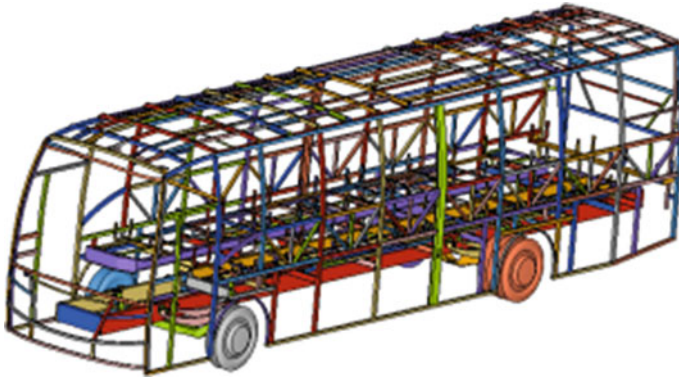


Fig. 3 CAD model of bus structure

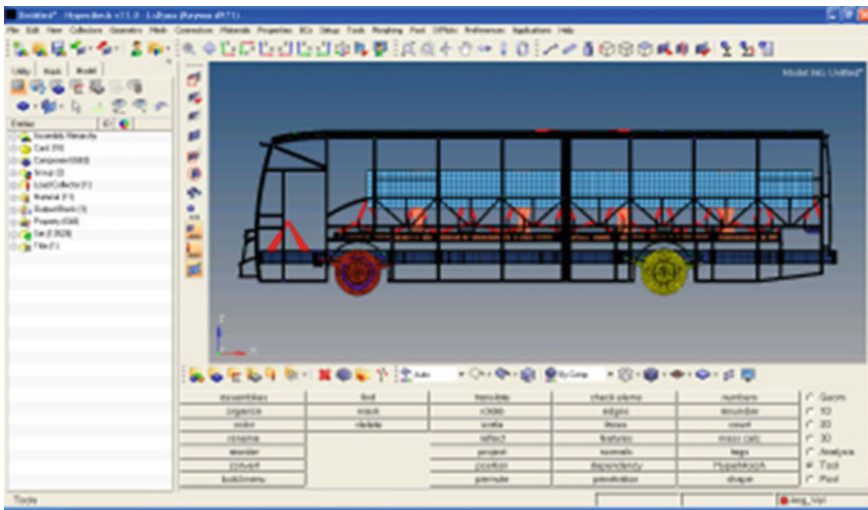


Fig. 4 Meshing of structure of bus

3.2 Meshing of Bus Structure

HyperMesh software is used for meshing purpose [9]. The CAD model of the bus with highly mesh quality was imported into HyperMesh (Fig. 4) and meshing parameters are shown in Table 1.

Table 1 Meshing parameters (quality check)

Sr. No.	Quality checking parameter	Allowable value
1	Minimum length of element	<7 mm
2	Aspect ratio	>5
3	Warping angle	>5°
4	Skew angle	>60°
5	Jacobian	>0.7

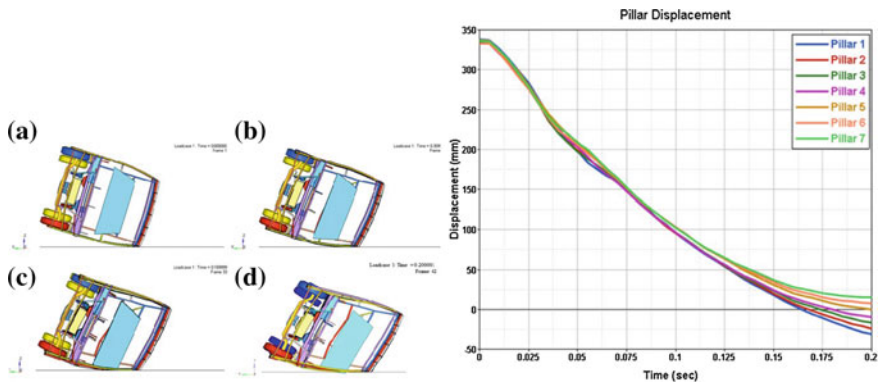


Fig. 5 Distance between pillars and residual space versus time

4 Numerical Analysis

This consists imposing meshed model of bus superstructure into explicit solver LS-DYNA [10] and post-processing of data in Hyper View. The analysis is performed by assuming initial velocity $v = 2.98 \text{ m/s}$, energy applied to the structure $E = 57.71 * 10^6 \text{ J}$ and it taken as initial boundary condition.

After left hand side (LHS) rollover of bus, the displacement of residual space is obtained and shown in Fig. 5. After crash of bus, distance gradually decreases and it crosses zero. It indicates that residual space intruding into frame. This is not acceptable.

4.1 Design Suggestions for New Bus Model

To improve strength and stiffness requirements of bus structure and to avoid above problem, we need to add stiffeners as shown in Fig. 6. Stiffeners having dimensions of $50 \times 50 \times 2.5 \text{ mm}$ with material as mild steel (M.S.).

Old roll bar or pillars are modified by joining stiffeners or brackets at corner of joining pillars and roll bar of roof structure. For stiffer superstructure, addition of stiffeners in bus structure with CAD model are shown in above Fig. 6.

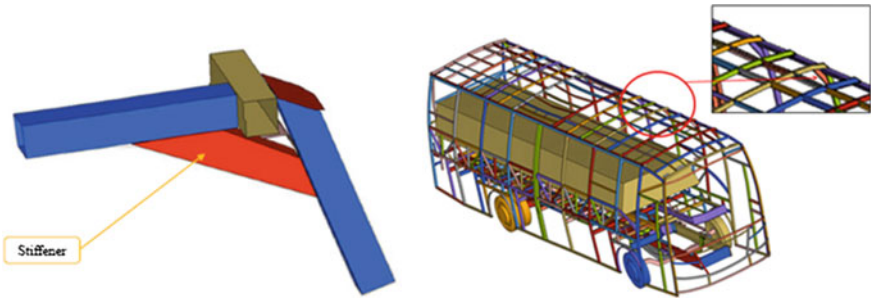


Fig. 6 Design suggestions

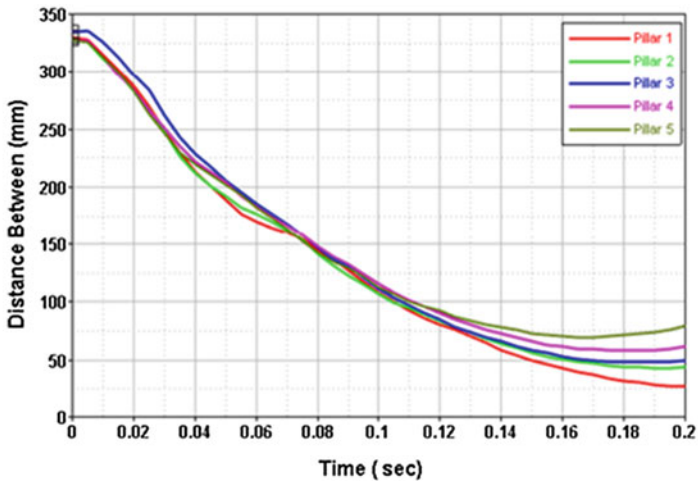
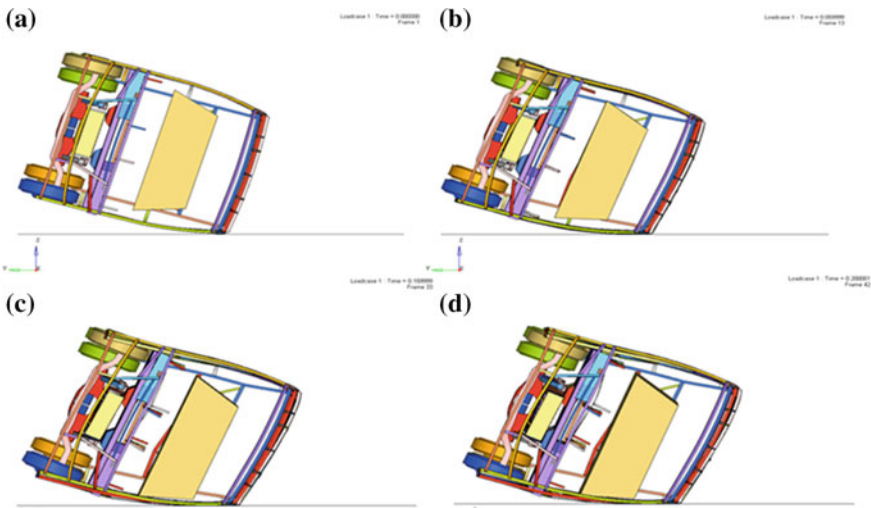


Fig. 7 Distance between pillars and residual space versus time for stiffer (new) bus

Table 2 Distance between superstructure and residual space for pillar

Sr. No.	Pillar name	Distance between superstructure and residual space at time = 0.2 s (mm)	
		Base bus model	Stiffer (new) bus model
1	Pillar 1	-32.785	36.087
2	Pillar 2	-18.436	46.233
3	Pillar 3	38.467	112.507
4	Pillar 4	-2.137	84.680
5	Pillar 5	16.667	88.419

Table 3 Comparison of energy transfer for old bus and modified bus model

Time 't' to transfer energy (s)		% Improvement
Old bus model	Stiffer (modified) bus model	
0.129	0.1425	9.473

4.2 Rollover with Redesigned Model (Stiffer/New Model)

The sequential pictures from the simulation results for selected time steps ($t = 0$ to 0.2 s) (see Fig. 7). The minimum distance between superstructure and residual space was greater than zero, that not crossing road surface, on door side as per AIS 031.

5 Results

See Tables 2 and 3.

6 Conclusion

Following points are concluded regarding new bus structure

- (i) The deformed part of the stiffer (new) bus structure does not intrude into the residual space.
- (ii) No part of the survival space or residual space projects outside the deformed structure.
- (iii) The superstructure of the bus has sufficient strength during and after rollover test.
- (iv) Improved the crashworthiness performance of bus superstructure for rollover analysis

From FEA, it conclude that, there is increase in energy transfer time for stiffer (new) bus model. The energy transfer time increase by 9.473%.

References

1. Karliński J, Ptak M, Działak P, Rusiński E (2014) Strength analysis of bus superstructure according to Regulation No. 66 of UN/ECE. Elsevier, pp 342–353
2. Kumar S (2012) Rollover analysis of bus body structure as per AIS 031/ECE R66. Volvo Group Trucks Technology, Bangalore, India
3. Micu DA, Iozsa DM (2011) Analysis of the rollover behavior of the bus bodies. ANALELE UNIVERSITĂȚII
4. Sergeevich RP, Nikolaevich OL (2015) Verification of computer simulation results of bus body section rollover. *J Traffic Transp Eng* 3:118–127
5. Kang KT, Chun HJ, Park JC, Na WJ, Hong HT, Hwang IH (2012) Design of a composite roll bar for the improvement of bus rollover crashworthiness. Elsevier, pp 1705–1713
6. Belsare V (2012) Rollover analysis of passenger bus as per AIS-031. *IJERD* 4(5):49–59
7. Elitok K, Güler MA, Avcı FH, Stelzmann U (2005) Bus rollover analysis with LS-DYNA. TEMSA A.S
8. Marianski M, Szosland (2012) A Research on the strength of standard bus bodies at rollover on the side, Technical University of Lodz
9. Altair HyperMesh Tutorials, Altair Engineering Inc., 2004
10. LS-DYNA keyword user's manual (2003) Livermore Software Technology Corporation, April 2003

Optimization of P-GMAW Welding Parameters Using Taguchi Technique for SS304L Pipes

Rudreshi Addamani, H.V. Ravindra and C.S. Darshan

Keywords Pulsed gas · SS304L · Taguchi technique · ANOVA

1 Introduction

Pulsed Gas Metal Arc Welding is widely used process, especially in pipe welding. It offers an improvement in quality and productivity over regular Gas Metal Arc Welding (GMAW). The process enables stable spray transfer with low mean current and low net heat input. It applies waveform control logic to produce a very precise control of the arc through a broad wire feed speed range. With precise control of arc dynamics, Pulsed Gas Metal Arc Welding (P-GMAW) can be used as a fast-follow process at high travel speeds, or it can be run as a high deposition rate, fast-fill process. A variation of the spray transfer mode, pulse-spray is based on the principles of spray transfer but uses a pulsing current to melt the filler wire and allow one small molten droplet to fall with each pulse. The pulses allow the average current to be lower, decreasing the overall heat input and thereby decreasing the size of the weld pool and heat-affected zone while making it possible to weld thin work pieces. The pulse provides a stable arc and no spatter, since no short-circuiting takes place. This also makes the process suitable for nearly all metals, and thicker electrode wire can be used as well. The smaller weld pool gives the variation greater versatility, making it possible to weld in all positions. In comparison with short arc Gas Metal Arc Welding (GMAW), this method has a somewhat slower maximum speed (85 mm/s or 200 in/min) and the process also requires that the shielding gas

R. Addamani (✉) · H.V. Ravindra
Department of Mechanical Engineering, P.E.S. College of Engineering,
Mandya, India
e-mail: rudreshaddamnai@gmail.com

C.S. Darshan
Department of Mechanical Engineering, Bangalore Technological Institute,
Bangalore, India

be primarily argon with a low carbon dioxide concentration. Additionally, it requires a special power source capable of providing current pulses with a frequency between 30 and 400 pulses per second. However, the method has gained popularity, since it requires lower heat input and can be used to weld thin work pieces, as well as nonferrous materials.

2 Literature Review

Sapakal and Telsang [1] presented a research on the optimization of MIG welding parameters using Taguchi design method. In their research they considered welding current, welding voltage and welding speed as input variables and penetration depth as output variable. MS C20 was selected as work piece material. A plan of experiments based on Taguchi technique has been used to acquire the data. An orthogonal array, signal to noise (S/N) ratio and Analysis of Variance (ANOVA) were employed to investigate the welding characteristics of MS C20 material and optimize the welding parameters. Their experimentation results that the lower current.

Suresh Kumar et al. [2] have investigated for welding aspects of AISI 304 and 316 by Taguchi technique for the process of TIG and MIG welding. Mechanical properties of austenitic stainless steel for the process of TIG and MIG welding have discussed here. The voltage has taken constant and various characteristics such as strength, hardness, ductility, grain structure, tensile strength breaking point, HAZ have observed in these two processes.

Meshram and Pohokar [3] have done a research on optimization of process parameters of gas metal arc welding to improve the quality of weld bead geometry. In their work, a grey-based Taguchi method was adopted to optimize the gas metal arc welding process parameters. Many quality characteristic parameters were combined into one integrated quality parameter by using grey relational grade or rank. The welding parameters considered in their research were arc voltage, wire feed rate, welding speed, nozzle to plate distance and gas flow. The quality characteristics consider were penetration, reinforcement and bead width. Analysis of variance has performed to find the effect of individual process parameter on quality parameters. The Taguchi L_{25} array was adopted to conduct the experiments. The stainless steel (AISI410) was used as welding specimen.

Kumar and Roy [4] have obtained the use of Taguchi's parameter design methodology for parametric study of Gas Metal Arc Welding of Stainless Steel and Low Carbon Steel. The input process variables considered here include welding current, welding voltage and gas flow rate. A total number of 9 experimental runs were conducted using an L_9 orthogonal array, and calculate the signal-to-noise ratio. Subsequently, using Analysis of Variance (ANOVA) the significant coefficients for each input parameter on tensile strength and Hardness (PM, WZ and HAZ) were determined.

Pandey et al. [5] performed their analysis on optimization of resistance spot welding parameters using Taguchi method. The experiments were conducted under varying pressure, welding current and welding time. The output characteristic considered was tensile strength of the welded joint. The material used was low carbon steel sheets of 0.9 mm. Their conclusion leads that the contribution of welding current holding time and pressure towards tensile strength is 61, 28.7 and 4% respectively as determined by the ANOVA method.

Patil and Waghmare [6] presented their work on optimization of MIG welding parameters for improving welding strength. They presents the influence of welding parameters welding current, welding voltage, welding speed on ultimate strength of welded joints of AISI mild steel materials. A plan of experiments using Taguchi has decided. Experiments were performed and result was confirmed. From this study they concluded that the welding current and welding speed are the major factors affecting tensile strength of welded joints

Hooda et al. [7] has done their research on optimization of MIG welding parameters in order to improve yield strength of AISI 1040 mild steel. The process parameters welding current, voltage, gas flow rate and wire speed were studied. The experiments were conducted based on four factors, three level orthogonal arrays.

In the present work, it is planned to analyze the different input parameters in Pulsed Gas Metal Arc Welding to improve both Ultimate Tensile Strength and Hardness of the welding joint using Taguchi's technique.

3 Experimental Details

The experiments have been conducted using a Pulsed Current Lorch welding machine having 400 A maximum current with air type cooling and automated welding set up. In this welding machine automated Metal Inert Gas torches as well as automatic feeder wire feeding units have provided.

3.1 Material Selection

The present study has been carried out SS304L pipes. Most common uses are in refineries and plants when gasses or fluids are transported at high temperatures and pressures (Table 1).

Table 1 Chemical composition of SS304L pipe material

Element	C	Mn	P	S	Si	Cr	Ni	N	Fe
%	0.21	1.27	0.030	0.001	0.35	18.10	8.02	0.053	Balance

3.2 Taguchi Technique

The Taguchi method developed by Genuchi Taguchi is a statistical method used to improve the product quality. Optimization of process parameters is the key step in the Taguchi method for achieving high quality without increasing cost. This is because optimization of process parameters can improve quality characteristics and the optimal process parameters obtained from the Taguchi method are insensitive to the variation of environmental conditions and other noise factors. Basically, classical process parameter design is complex and not easy to use. A large number of experiments have to be carried out when the number of process parameters increases. To solve this task, the Taguchi method uses a special design of orthogonal arrays to study the entire process parameter space with a small number of experiments only. A loss function is then defined to calculate the deviation between the experimental value and the desired value. Taguchi recommends the use of the loss function to measure the deviation of the quality characteristic from the desired value. The value of the loss function is further transformed into signal-to-noise (S/N) ratio.

3.3 S/N Ratio

The signal to noise ratios (S/N), which are log functions of desired output, serve as the objective functions for optimization, help in data analysis and the prediction of the optimum results. There are 2 signal-to-noise ratios of common interest for optimization of Static Problems.

1. Smaller the better is given by

$$\eta = -10 \log[(\Sigma Y_i^2)/n]$$

2. Larger the better is given by

$$\eta = -10 \log[(\Sigma 1/Y_i^2)/n]$$

where, η = signal to noise ratio
 Y_i = ith observed value of response
 n = no. of observations in a trial
 y = average of observed response.

3.4 Experimental Parameter

Input parameters: Welding Current, Gas Flow Rate and Wire Feed Rate.
 Output parameters: Ultimate Tensile Strength (UTS) and Hardness.

3.5 Experimental Work

Experiments were conducted using pulsed current Lorch welding machine by DC electrode positive power supply. Test pieces of size outer diameter of 25 mm, length of 300 mm with wall thickness of 3 mm were cut into length of each 150 mm initially with an edge preparation of 45° and tack welded as shown in Fig. 1. Copper coated Mild steel electrode of 1.2 mm diameter was used for welding. Argon (85%) and CO₂ (15%) gas mixture was used for shielding. The experimental setup used consists of a rotating disk into which work sample was attached as shown in Fig. 2. Welding speed (157 mm/min) has been kept constant for all twenty trails. Single pass welding was performed on pipes by varying the parameters as shown in Table 2. The working ranges for the process parameters were selected from the American Welding Society handbook. Based on the designed L₂₇ orthogonal array combination a series of joining processes was performed in welding machine. Ultimate Tensile Strength and hardness are considered as objectives. For the calculation of the responses of welded specimens, tensile test were performed using Advanced Universal Testing Machine model number; UTM US-1000 kN and make; Akash Industries Hardness test was performed using Vickers hardness testing machine (Table 3).

Fig. 1 Sample specimen with dimension

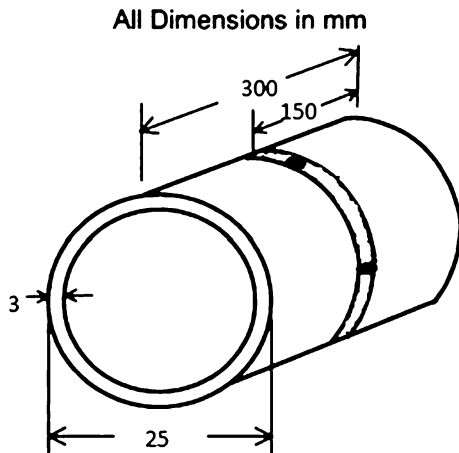




Fig. 2 Experimental set up

Table 2 Control factors and their level

S. No	Symbol	Factors	Unit	Level 1	Level 2	Level 3
1	A	Welding current	A	55	60	65
2	B	Gas flow rate	l/min	12	13	14
3	C	Wire feed rate	mm/min	110	115	120

Table 3 Welding performances using L_{27} orthogonal array

Runs	Current (A)	Gas flow rate (l/min)	Wire feed rate (mm/min)	Ultimate tensile strength (N/mm ²)	Hardness (VHN)
1	55	12	110	313	102.83
2	55	12	115	311	103.83
3	55	12	120	315	111.91
4	55	13	110	321	106.30
5	55	13	115	318	102.56
6	55	13	120	324	112.90
7	55	14	110	326	108.34
8	55	14	115	323	112.07
9	55	14	120	325	118.23
10	60	12	110	341	102.71
11	60	12	115	344	104.44
12	60	12	120	345	113.18
13	60	13	110	347	104.40
14	60	13	115	346	114.35
15	60	13	120	348	117.90

(continued)

Table 3 (continued)

Runs	Current (A)	Gas flow rate (l/min)	Wire feed rate (mm/min)	Ultimate tensile strength (N/mm ²)	Hardness (VHN)
16	60	14	110	350	110.30
17	60	14	115	354	112.07
18	60	14	120	352	118.23
19	65	12	110	356	107.35
20	65	12	115	355	108.89
21	65	12	120	359	111.69
22	65	13	110	363	114.87
23	65	13	115	361	112.07
24	65	13	120	362	113.56
25	65	14	110	367	108.91
26	65	14	115	365	114.44
27	65	14	120	368	127.20

4 ANOVA Table and Response Calculation

The purpose of the Analysis of Variance (ANOVA) is to examine which design parameters significantly affect the quality characteristic. This is accomplished by separating the total variability of the S/N ratios, which is measured by the sum of the squared deviations from the total mean S/N ratio, into contributions by each of the parameters and the error. The ANOVA table for both Ultimate Tensile Strength and hardness are shown in Tables 4 and 5. The response table for both UTS and hardness are shown in Tables 6 and 7.

Table 4 ANOVA table for ultimate tensile strength

Source	DOF	SS	MS	F	P (%)
A	2	5.44629	2.72315	1339.4	93.8*
B	2	0.30195	0.15098	74.27	5.2*
C	2	0.017070	0.00583	4.20	0.29*
Error	2	0.04066	0.00203		
Total	8	5.80597			

SS sum of squares; *DOF* degree of freedom; *%P* percentage contribution
 *level of significance at 95% confidence level

Table 5 ANOVA table for hardness

Source	DOF	SS	MS	F	P (%)
A	2	0.54393	0.2719	5.06	10.44*
B	2	1.3296	0.6644	12.37	25.53*
C	2	2.2596	1.1297	21.02	43.38*
Error	2	1.0749	0.5375		
Total	8	5.20801			

Table 6 Response table for ultimate tensile strength

Levels	A	B	C
1	50.09	50.56	50.69
2	50.82	50.70	50.66
3	51.17	50.81	50.73
Delta	1.08	0.26	0.06
Rank	1	2	3

Table 7 Response table for hardness

Levels	A	B	C
1	40.72	40.62	40.61
2	40.88	40.90	40.77
3	41.07	41.16	41.29
Delta	0.35	0.54	0.68
Rank	3	2	1

5 Result and Discussion

(1) Optimum parameter selection from S/N ratio for UTS

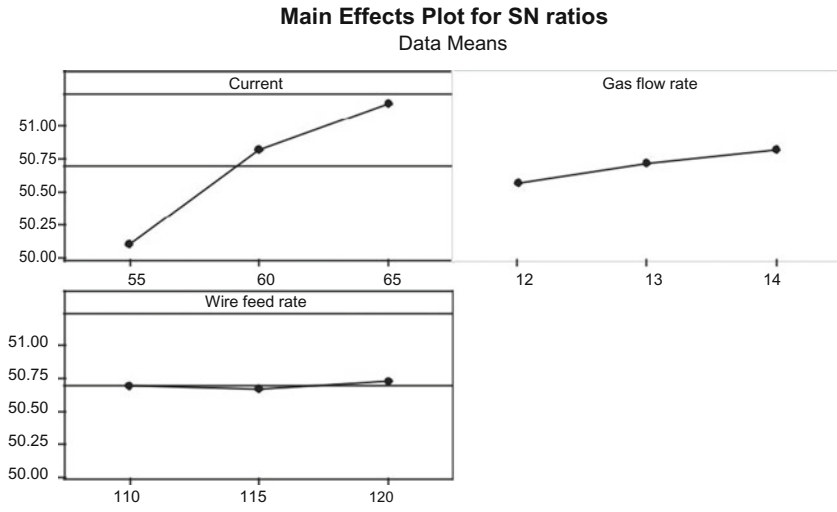
Ultimate Tensile Strength is larger-the-better type quality characteristic higher values of Ultimate Tensile Strength are considered to be optimal. It is clear from Fig. 3, that Ultimate Tensile Strength is highest at third level of welding current, third level of gas flow rate and third level of wire feed rate.

(2) Optimum parameter selection from S/N ratio for hardness

Hardness is larger-the-better type quality characteristic higher values of hardness are considered to be optimal. It is clear from Fig. 4, that hardness highest at third level of welding current, third level of gas flow rate and third level of wire feed rate.

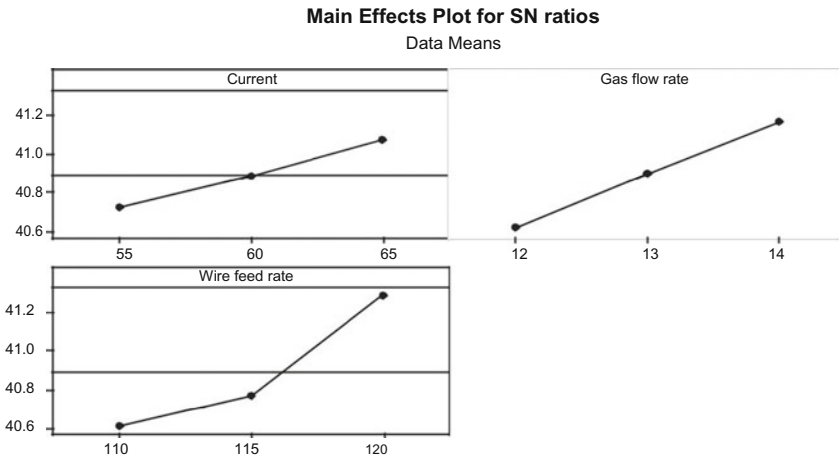
(3) Analysis of Variance (ANOVA) for Ultimate Tensile Strength

The calculated values of Analysis of Variance for Ultimate Tensile Strength of welding joint are listed in Table 4. The calculated values of ANOVA present the



Signal-to-noise: Larger is better

Fig. 3 Main effects plot for ultimate tensile strength



Signal-to-noise: Larger is better

Fig. 4 Main effects plot for hardness

percentage effect of each parameter on Ultimate Tensile Strength of the joint. From the analysis, it is seen that current is the most contribution factor and the wire feed rate is the least contribution factor for Ultimate Tensile Strength of joint.

Table 8 Results of verification experiment

Condition description	Initial set of parameters	Optimal parameters
Level	A2B3C1	A3B3C3
UTS (N/mm ²)	350	378
Hardness (VHN)	110.30	128.5

(4) Analysis of Variance (ANOVA) for Hardness

The calculated values of Analysis of variance for hardness of welding joint are listed in Table 5. The calculated values of ANOVA present the percentage effect of each parameter on hardness of the joint. From the analysis, it is seen that wire feed rate is the most contribution factor and the current is the least contribution factor for hardness.

6 Verification Experiment

The confirmation run was conducted using same experimental setup by taking optimized parameters for SS316L pipes considered in this present work. The results obtained from the confirmation runs are tabulated in Table 8.

From Table 8; one can observe that, the optimized parameters have considerable effect on the response variables i.e. Ultimate Tensile Strength and hardness of SS304L pipes. Ultimate Tensile Strength was at 350 N/mm² for initial settings of parameters and the value has been increased to 378 N/mm² after setting parameters to optimized values. Similarly, the hardness has been increased from 110.30 to 128.5 VHN.

7 Conclusion

In this present work the optimization of the process parameters for Pulsed Gas Metal Arc welding of SS304L pipes with larger Ultimate Tensile Strength and hardness has been reported. A Taguchi orthogonal array, the signal-to-noise (S/N) ratio and Analysis of Variance (ANOVA) were used for the optimization of welding parameters and it is found that (i) optimum condition for maximum Ultimate Tensile Strength is (A3B3C3) i.e. current = 65 A, gas flow rate = 14 L/min and wire feed rate = 120 mm/min (ii) optimum condition for hardness is (A3B3C3) i.e. current = 65 A gas flow rate = 14 L/min and wire feed rate = 120 mm/min. ANOVA for UTS shows that current is the most significant factor, followed by gas flow rate. ANOVA for hardness indicates that wire feed rate influences most significantly, followed gas flow rate. Confirmation experiment was also conducted and verified the effectiveness of the Taguchi optimization method.

Acknowledgements We express our sincere thanks to Mr. Bhasheer Ahmed, Director, Sri Sidhi Vinayaka fabrications Pvt. Ltd. Bangalore, India and P.E.S. College of Engineering, Mandya, India for their support to carry out experimentation.

References

1. Sapakal SV, Telsang MT (2012) Parametric optimization of MIG welding using Taguchi design method. *Int J Adv Eng Res Stud*, 1(4):28–30
2. Sureshkumar L. et al. (2011) Experimental investigation for welding aspects of AISI 304 & 316 by Taguchi technique for the process of TIG & MIG welding. *Int J Eng Trends Tech*, 2(2)
3. Meshram SR, Pohokar NS (2013) Optimization of process parameters of Gas Metal Arc Welding to improve Quality of Weld bead geometry. *International journal of Engineering, Business and Enterprise Applications*, 46–52
4. Kumar P, Roy DB (2013) Nishant “Parameters Optimization for Gas Metal Arc Welding of Austenitic Stainless Steel (AISI 304) & Low Carbon Steel using Taguchi’s Technique”. *Int J Eng Manag Res*, 3:2250–0758
5. Pandey AK, Khan MI, Moeed KM (2013) Optimization of resistance spot welding parameters using Taguchi method. *Int J Eng Sci Technol* 5(2):234–241
6. Patil SR, Waghmare CA (2013) Optimization of MIG welding parameters for improving strength of welded joints. *Int. J. Adv. Engg. Res. Studies/II/IV/July-Sept*, 14:16
7. Hooda A, Dhingra A, Sharma S (2012) Optimization of mig welding process parameters to predict maximum yield strength in AISI 1040. *Int J Mech Eng Robot Res (IJMERR)*, ISSN, 2278–0149
8. Lin JL, Lin CL (2002) The use of the orthogonal array with grey relational analysis to optimize the electrical discharge machining process with multiple performance characteristics. *Int J Mach Tool Manu* 42(2):237–244
9. Choudhury N, Bandyopadhyay A, Rudrapati R (2014) Design optimization of process parameters for TIG welding based on Taguchi method. *Int J Cur Eng Tech* 12–16
10. Patel CN, Chaudhary SANDIP (2013) Parametric optimization of weld strength of metal inert gas welding and tungsten inert gas welding by using analysis of variance and grey relational analysis. *Int J Res Mod Eng Emerg Technol* 1(3):48–56
11. Lakshminarayanan AK, Balasubramanian V, Elangovan K (2009) Effect of welding processes on tensile properties of AA6061 aluminium alloy joints. *Int J Adv Manuf Technol* 40(3): 286–296

Impact Analysis and Topology Optimization of Pultruded Automotive Bumper

Rohit R. Ghadge and S. Prakash

Keywords Pultruded FRP beam · Impact bumper · Pedestrian safety · Three point bend test · Ball drop test · Topology optimization

1 Introduction

In an automobile, bumper system is designed basically to avoid the damage to the radiator and lighting system in the low impact condition. In the present study, the existing steel bumper is replaced by laminated pultruded composite beam of square cross section. Insurance companies majorly look at these performances to decide insurance cost. There are couple of tests to evaluate the performance of the system. Different standards in IIHS, RCAR, ECER42 and Part581 are majorly used in world wide. The major role of beam in the bumper system is to avoid the damage on radiator. Lot of research is going on to design and optimize the bumper cross section, manufacturing process on metals as well as composites. Composite are still under development due to its manufacturing constrains as well as cost. High reinforcement content, better mechanical properties, inexpensive tooling [1], continuous process and fast cycle times, part will have continuous fibers. These are the major advantages which makes to select the pultruded composite parts. As we required larger elongation as well as cost effectiveness we have selected the pultruded beam made with E-glass fibers.

R.R. Ghadge (✉) · S. Prakash
Sathyabama University, Chennai, Tamil Nadu, India
e-mail: rohitghadge@gmail.com

In this paper, both numerical and experimental methods are used to test and compare the force versus deflection data as well as damage due to impact. Based on the proper correlation, the topology optimization is performed. The stress-strain data obtained experimentally is used for FEA based optimization procedure. This input is used for both quasi-static, impact as well as cross section optimization in FEA. Basic theoretical calculation are performed on pure bending theory for square cross section with it's section modulus under the yield limit. Material is assumed as isotropic as the fibre direction remains along the length and normal to the load direction.

2 Theoretical Calculations

For the current study, hollow square cross section of size $50 \times 50 \times 3$ mm is considered. Pultruded beam is subjected to pure bending. Similar to the case of three point bend test, reaction forces are calculated by bending formula.

$$M/I = F/Y$$

For three point bend test UTS is found to be 516 MPa for the span of 0.88 m and corresponding maximum reaction force is 5.29 kN. The maximum bending moment can be evaluated based on this result.

3 Material Data

Tensile test is performed to get stress stain data as per ASTM D 638 (Table 1).

3.1 Correlation with FEA

Once we have stress stain data we can convert it into true values for FEA. Then performed same tensile test in FEA and compare with test lab results just to check the FEA model stability. As fibre orientation is along the length so tensile test also conducted in the same direction in UTM as indicated in the Fig. 1. There is almost 90% correlation is achieved.

Table 1 Mechanical properties of FRP pultruded beam

Mechanical properties	Symbol	Units	E-Glass
Young's modulus	E	GPa	33
Poisson's ratio	μ	–	0.28
Density	ρ	Kg/m ³	1900
UTS	Sut	MPa	516

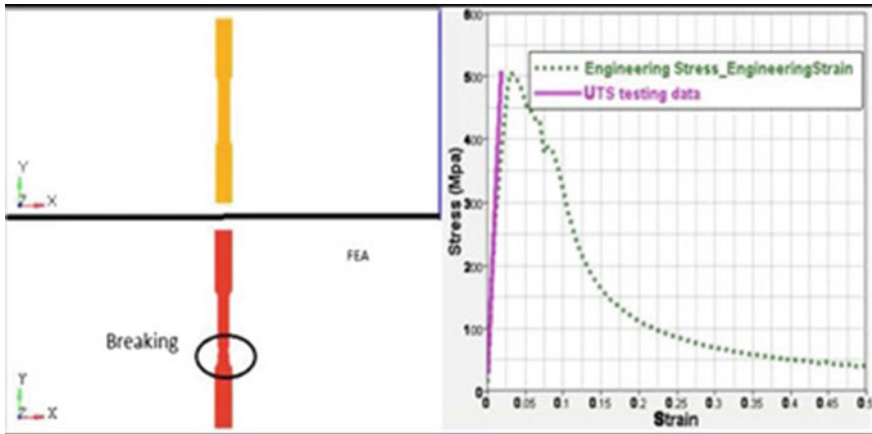


Fig. 1 Stress strain data correlation between testing and FEA

4 Experimental Data

To validate the FRP pultrusion beam section properties we performed two major tests. One is three point bend test and other one is Ball impact test both as per ASTM standard.

4.1 Three Point Bend Test

Three point bend test is performed on the span of 0.88 m under ASTM D 790 [2–4]. Speed of impact is 20 mm/min. Performed on two parts of 1 m length and 50×50 mm cross section. Force versus deflection data was plotted (Fig. 2). Data is found correlated for these two test specimens with minor deviation on both data.

4.2 Ball Impact Test

Ball drop test [5] is performed to check the damage on part. 47×120 mm sample specimen is cut from the beam and ball is impacted against it. Impactor diameter is 32 mm and Weight is 1.44 kg. Ball is impacted from 2 m height with velocity of 6.264 m/sec. After the impact damage is measured. Level of damage is minor but permanent deformation is observed on the specimen.

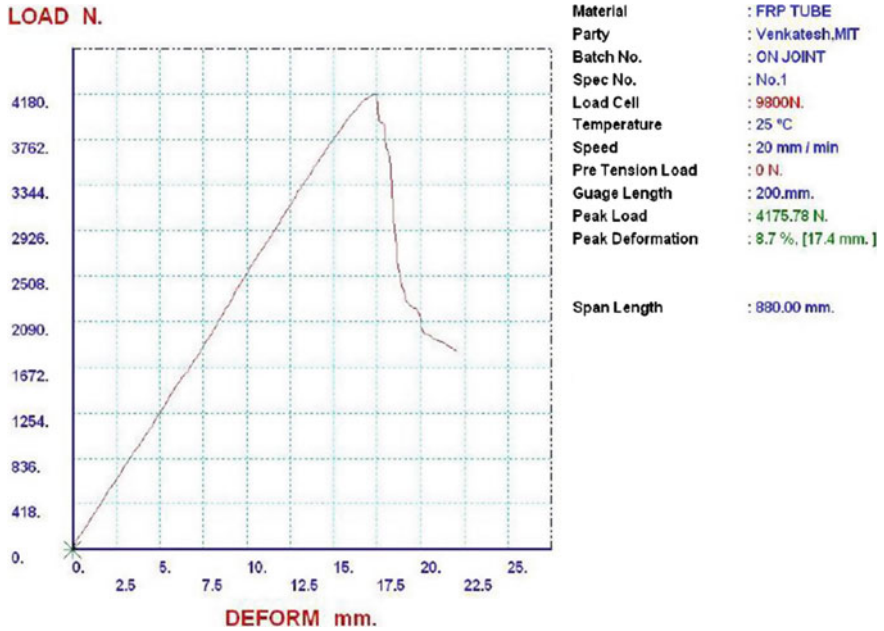


Fig. 2 Three point bend test—force versus deflection data

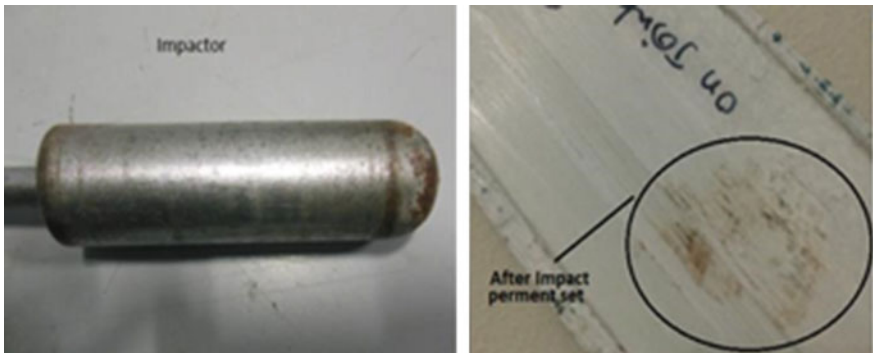


Fig. 3 Level of damage in ball impact test

Initially specimen tried with height of 1 m. As level of damage is invisible so increased the height of impact to 2 m to get the greater level of damage Fig. 3, so that it is convenient to visualize and compare with FEA. Find the below figure for the level of damage

5 FEA Analysis

All experimental data is validated by finite element analysis which is performed for both three point bend test as well as ball drop test.

5.1 Three Point Bend Test

Meshed model is built for square cross section using shell elements. Update thickness as 3 mm and already material model was developed. Updated the material model to beam of length of 1 m. Now total weight is 1.072 kg. Beam is resting on rollers of 50 mm diameter. Impactor is in other side and constantly moving against the beam. Failure stain is added in FEA model so that once strains are reached that level elements automatically removed from calculation. FEA model is in below picture Fig. 4. Reactions loads are extracted from the beam and posted in the results. Model was checked when the strains reach 0.0105 as we know this is failure strains. That point of time we have taken loads into account for further comparison. Mostly overall load is reaching 4837 N in FEA. LS Dyna the tool is used for conducting the 3 point bend test.

5.2 Ball Drop Test

FEA ball drop test is conducted using LS Dyna tool to measure the damage in terms of strains. Ball is made of rigid elements in FEA. Ball is impacted [5] against the plate of 47×120 mm. Weight of impacted ball is 1.44 kg. Ball is impacted at high of 2 m. Plate is rested on flat area and having the passage of 33 mm so that ball can pass through only that passage through specimen. Due to 2 mm height velocity of ball at the time of impact is 6.26 m/sec. In the FEA we have constrained resting area.

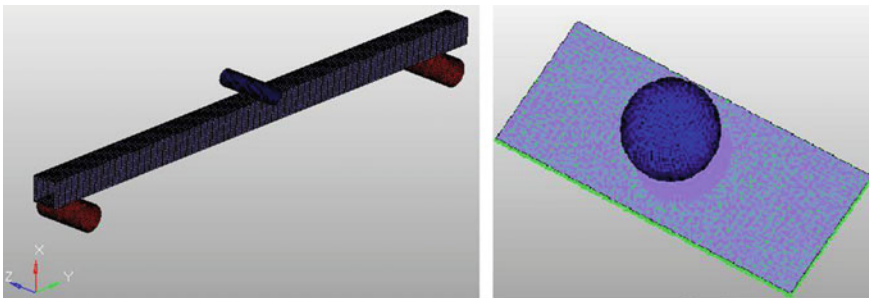
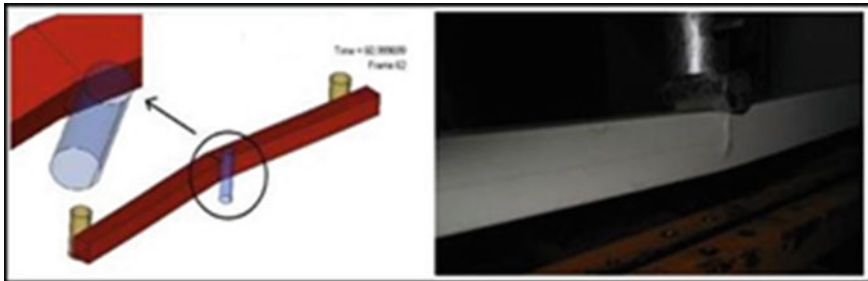


Fig. 4 FEA modal for 3 point bend test and ball drop test

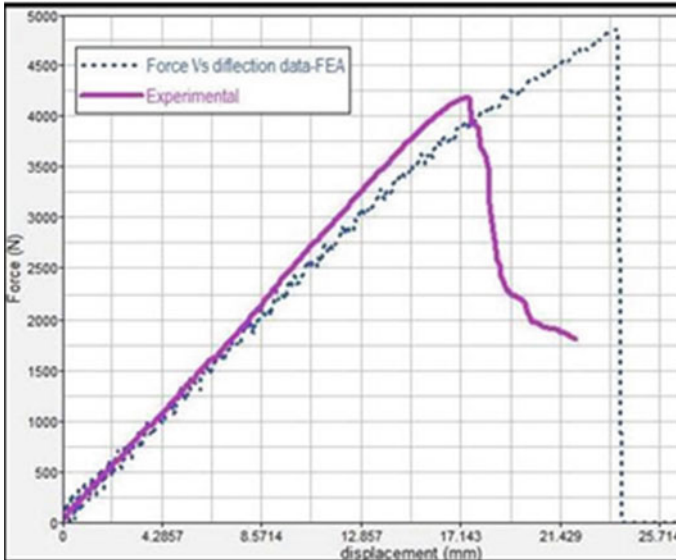
6 Result and Discussions

Once we have both FEA and testing results then the next step is correlation. Finally we found the reasonable correlation between FEA as well as Experimental results.

On Three points bend test load for testing is 4170 N. In FEA we have found it is 4837 N which is a good correlation. The main reason for results deviation is the material as it is not homogeneous. We can find the correlation in below picture Fig. 5a, b. The FEA material is reaching failure strain then it starts eroding elements at that location (highlighted area)

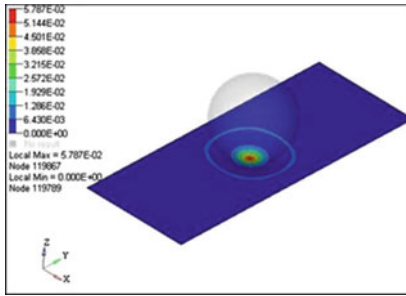


(a) Three point bend test-Level of damage in impact



(b) Three point bend test-Force Vs Deflection comparison

Fig. 5 a Three point bend test- Level of damage in impact. b Three point bend test—force versus deflection comparison



(a) Ball Impact-Stain plot



(b) Ball Impact actual photograph

Fig. 6 a Ball impact–stain plot. b Ball impact actual photograph

On the other hand, we have conducted the impact test on rectangular plate. There is observation that permanent set as well as breakage was observed on both FEA as well as testing Fig. 6a, b. In testing we have observed brakeage along the axis. This is due to joint on that location and driving that brakeage.

7 Topology Optimization

After getting proper correlation in FEA and testing, the cross Section optimization of the beam against impact is performed.

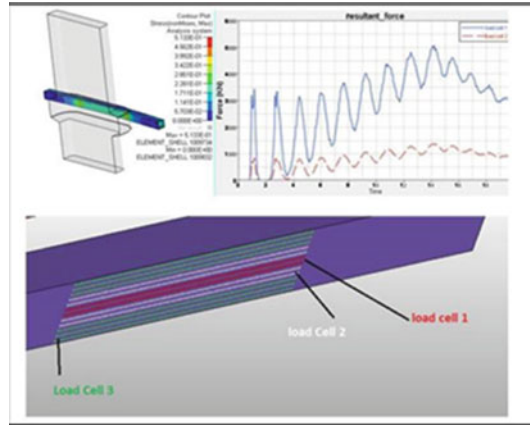
7.1 Load Tracking in Impact

To extract loads against impact we have performed FEA under Part581 regularations. This is pendulum impact with 4 kmph. Pendulum impacted [6] against the freely roll back vehicle.

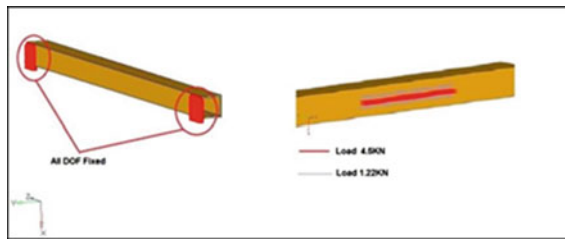
In this we extracted loads under the stress limit and used it for optimization. In FE model, load cells between impactor and our cross section beam have been added. When stress reaches UTS value, load was plotted as Fig. 7a.

7.2 Cross Section Optimization

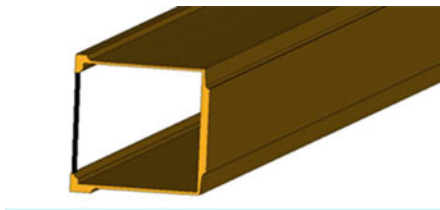
For Cross section optimization [6, 7] we have done the Topology optimization using Optistruct Software. Topology optimization technique yields a new design and optimal material distribution. Topology optimization is performed on a baseline design, resulting in a design that is lighter in most cases, and also performs better



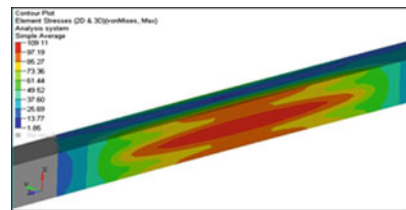
(a) Showing load plots. Load Cell.1- 4.5kN Load Cell.2 - 1.22 kN



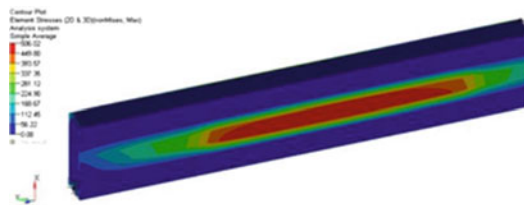
(b) Showing Constraints plot and load plots. Load Cell. 1-4.5KN Load Cell.2 -1.22KN



(c) Optimized cross section



(d) Stress plot of original model



(e) Stress plot of optimized model

Fig. 7 **a** Showing load plots. Load Cell 1–4.5 kN Load Cell 2–1.22 kN. **b** Showing constraints plot and load plots. Load Cell 1–4.5 kN Load Cell 2–1.22 kN. **c** Optimized cross section. **d** Stress plot of original model. **e** Stress plot of optimized model

than the baseline one. For the optimization meshed model is built by using hexahedral elements. All Dofs have been fixed on one side of the tube along 40 mm distance from the end and loads have been applied as per impact load data as shown in Fig. 7b.

7.3 Result and Discussions

New cross section after the optimization is shown in Fig. 7c. As per software result the material is removed from the back side of the beam. But for better strength and shape we are adding a material of 1.5 mm thickness along the length as shown with black line. The weight of new design is 0.435 kg.

Stress obtained in the original design is 109.11 MPa and optimized design is 506.2 MPa (shown in Fig. 7d, e respectively). These stresses are less than the UTS value of the material.

8 Conclusion

Experimental results and FEA results have been correlated and found satisfactory. The optimization study helped in achieving the weight reduction of 56.5% and also stresses below the UTS value of the material. Thus, pedestrian safety issue has been reported in the present study. To cater to this need weight optimization of composite pultruded beam have been done.

References

1. The Pultrux-Pultrusion global design manual, vol 3. Creative Pultrusions, Inc.
2. Ochelski S, Gotowicki P (2009) Experimental assessment of energy absorption capability of carbon epoxy and glass epoxy composites. *Compos Struct* 87:215–224 (Elsevier)
3. Liu Q, Xing H, Ju Y, Ou S (2014) Quasi static axial crushing and transverse bending of double hatched shape CFRP tubes 117:1–11 (Elsevier)
4. Mohagheghian I, McShane GJ, Stronge WJ (2015) Impact perforation of monolithic polyethylene plates: projectile nose shape dependence. *Int J Impact Eng* 80:162–176 (Elsevier)
5. Bienias J, Jakubczak P (2012) Low velocity impact resistance of aluminium carbon epoxy fiber metal laminate. *Compos Theor Pract*, 193–197
6. Belingardi G, Beyene AT, Koricho EG (2013) Geometric optimization of bumper beam profile made up of pultruded composite by numerical simulation. *Compos Struct* 102:217–225 (Elsevier)
7. Jimenez MA, Miravete A, Larrode E, Revuelta D (2000) Effect of trigger geometry on energy absorption in composite profiles. *Compos Struct* 48:107–111 (Elsevier)

Simulation of Micro-indentation Process of Black NiAl Coated Aluminum Substrate Using FEM

Vishal B. Bhagwat, Aparna G. Kadam and Dadasaheb Rupanwar

Keywords Indentation · Micro-indentation · Solar water heater systems (SWHSs) · Vickers indenter · Young's modulus

1 Introduction

In solar water heater system (SWHSs), solar energy is directly converted into thermal energy using solar collectors. In recent solar water heaters, materials used for tubing systems are copper, aluminum or stainless steel etc. In present study, Aluminum material is used for solar collectors tubing system. On these aluminum pipes, black paint coating is applied to increase the efficiency of solar collector systems by absorbing more solar radiations. Although black coating materials used in SWHSs nowadays, have high solar absorptance, they also suffer from the high infrared emissivity. Moreover after some period, this low quality coating is getting separated from collector surface either because of corrosion or erosion. To replace traditional black paint coating, nowadays new solar selective coatings were introduced in market. Several solar selective coatings are available in the market to increase absorptance and lower emittance. One of the widely used solar absorbers is black nickel coating this coating have good solar absorptivity and also low emissivity but, this coating is not chemically and physically stable when working above 200 °C temperature condition [1]. To replace this coating new electroplated black chromium coating was introduced as it is stable up to 300 °C [2]. Although black chromium provides good spectral properties, while, electro deposition of black chrome on collector pipes requires higher density current and also the hexavalent form of chromium is known to be toxic and therefore it must be considered as a weak candidate for paint application in SWHSs. Recently Alshamaileh [3] used modified black NiAl coating which was fabricated by embedding NiAl alloy

V.B. Bhagwat (✉) · A.G. Kadam · D. Rupanwar
Department of Mechanical Engineering, Vidya Pratishthan's
Kamalnayan Bajaj Institute of Engineering and Technology, Baramati, India
e-mail: vishal.bhagwat@vpkbiet.org

particles into black paint to increase the efficiency of solar water heater system. It has high solar absorptivity and low emissivity. In cost/benefit analysis it was shown that for a very small percent increase (around 1%) in the cost of the system, a gain of an average of 5 °C (around 10%) is fairly acceptable especially with larger installations [3]. But this coating must have high wear resistance and strength. However, the coating must be sustainable as its subjected in high temperature or varying environment conditions.

Hardness is nothing but resistance to wear or resistance to indentation. Thus we can measure wear resistance property by measuring mechanical properties such as hardness, young's modulus etc. of material. To measure mechanical properties of small material with more accuracy, microindentation process can be used. In this study, microindentation experiments were carried out on THV-1 digital micro Vickers hardness tester. FE simulation was carried out to investigate elastic/plastic deformation of black NiAl coated aluminum substrate under gradually increasing loading conditions. Aim of the present study is to measure mechanical properties of black NiAl coated aluminum solar collectors and compare these properties with traditional black painted aluminum substrate to select more reliable/sustainable coating for SWHSs.

2 Material Preparation and Experimentation

2.1 Coating Process of Black NiAl Coating on Aluminum Substrate

Black NiAl mixture was prepared by embedding NiAl alloy into black paint. To produce homogeneous coating, an electric mixer was used to mix the paint with the 20% NiAl per ml of black paint. This mixture was diluted with acetone to ease the application of a uniform layer by immersion or brush painting.

Black NiAl coating was applied on Aluminum 6061 T6 alloy specimen. Before processed for coating, specimen must be cleaned for contaminations, soil, oil, grease etc. For this, aluminum plates were kept in acetone for 35 min and then cleaned with distilled water. Black NiAl coating was done on aluminum plate as mentioned [3, p. 1639]. Aluminum 6061 T6 specimen of the size 100 × 50 × 2 mm was processed for black NiAl plating.

2.2 Micro-indentation Experiment

The microindentation test carried out on a THV-1 Digital micro hardness tester to measure the hardness of coated substrate with a loading range from 0.1 to 10 N. Four-sided square based Vickers diamond pyramid indenter with an apex angle

between opposite edges is 136° was used to apply load on specimen. An indenter is pressed into the specimen up to maximum load, held constant for 10 s dwell period at maximum load. While unloading, load is slowly removed up to zero load. Diagonals of square impression obtained on substrate after unloading was measured using microscope. The mean diagonal was found out. Low loads are applied on the specimen and indentation diagonal is measured to calculate Vickers hardness of specimen. The Vickers hardness number is the applied load (kgf) divided by surface area of the indentation $(\text{mm})^2$.

$$H = \frac{P_{\max}}{A}$$

Young's modulus is a measure of stiffness of an elastic material. Indentation Depth after unloading can be found out from diagonals obtained after indentation from the formula given below [4]:

$$h = 0.14285d$$

Young's modulus of black NiAl coated aluminum can be found out from experimental Load-Depth plot by measuring stiffness of material (slope of tangent drawn to the unloading curve from maximum load).

Stiffness of material,

$$S = \left(\frac{dP}{dh} \right)_{\max}$$

3 Finite Element Procedure

A 3D axisymmetric Vickers indentation model was created in CREO PARAMETRIC 3.0 modeling software and simulated in ANSYS 14.5 simulation software. FE simulation was carried out to investigate elastic/plastic deformation of black NiAl coated aluminum substrate under gradually increasing loading conditions and load was applied using Vickers indenter. The total deformation of both black NiAl coated aluminum substrate and black painted aluminum substrate was obtained by applying gradually increasing load followed by unloading. Young's modulus of specimen was predicted from load-depth plot obtained after FE simulation.

In simulation of Vickers indentation process, 3-D axisymmetric model was designated by master (Vickers indenter) and slave (substrate) surfaces. Material processed for modeling was $3 \times 3 \times 2$ mm rectangular plate of aluminum 6061 T6 alloy. On top surface of aluminum plate, NiAl coating of thickness $70 \mu\text{m}$ was

deposited. The Vickers square pyramid indenter was considered as rigid diamond material of angle between opposite faces is 136° . The indentation obtained here was very small as compared to size of the sample. For accuracy, fine mesh generated for coating near the contact area of indenter and for other regions coarse meshing. Mapped quadrilateral face meshing generated for indenter. The total numbers of nodes and elements were 29,657 and 14,857 respectively. The fixed boundary condition was applied at the bottom of aluminum plate. Because of geometric symmetry, only one fourth part of whole domain was considered for modeling indentation process.

One of the important parameters necessary for the simulation is the assignment of the material properties for Vickers indentation model. In present case, for NiAl alloy coating nonlinear, isotropic homogeneous behavior was considered to define elastic properties and bilinear isotropic hardening was considered to define plasticity. Vickers indenter was considered as rigid, isotropic diamond indenter. Material properties of aluminum alloy, NiAl alloy and indenter are shown in Table 1 given below:

The assumptions made in contact between two solids and in analysis of the indentation process [5]:

1. The contact between the indenter and coating is frictionless.
2. The force transmitted only in normal direction between the indenter and specimen.
3. Materials are considered as fully homogeneous, free from contaminate and defects.
4. Bonded contact between coating and aluminum specimen interfaces.

Table 1 Material properties of substrate, coating and Vickers indenter

Sr. No.	Name of part model	Properties
1	Substrate	Material = Aluminum alloy 6061
		Elastic modulus = 70,000 MPa
		Poisson's ratio = 0.33
		Density = 2700 kg/m ³
		Tensile yield strength = 290 MPa
2	Coating	Material = NiAl
		Elastic modulus = 115,000 MPa
		Poisson's ratio = 0.32
3	Indenter	Material = Diamond
		Elastic modulus = 1141000 MPa
		Poisson's ratio = 0.07

In micro indentation process, elastic deformation occurs at beginning. To find out occurrence of plastic deformation Von-mises yield criteria can be used. The equation of

Von-mises stress is given by the expression as follows:

$$\sigma_{\text{Mises}} = \left[\frac{(\sigma_1 - \sigma_2)^2 + (\sigma_2 - \sigma_3)^2 + (\sigma_3 - \sigma_1)^2}{2} \right]^{\frac{1}{2}}$$

4 Results and Discussion

4.1 Experimental Results

Micro indentation experiment was carried out to find Vickers hardness of black NiAl coated aluminum substrate and hardness of black painted aluminum sample. This was found out by applying load ranging from 0.5 to 10 N using Vickers indenter followed by unloading up to zero load. Imprint diagonal obtained after indentation was measured using microscope. From applied load and diagonal value after indentation, Vickers hardness values obtained for black painted aluminum alloy and black NiAl alloy coated aluminum substrate at different loads are shown in Tables 2 and 3. Indentation depth after load removal can be measured from diagonal values which is useful to plot load-Depth curve. From Load-Depth curve young's modulus of coated substrate can be found out.

Average Vickers hardness value obtained for black painted aluminum alloy is 108.58 HV.

Average Vickers hardness value obtained for black NiAl alloy coated aluminum substrate is 273 HV.

Young's modulus was obtained using experimental Load –Depth curve from the slope of tangent drawn to the unloading curve from maximum load. Young's modulus values for black painted aluminum and black NiAl coated aluminum substrate are 43.576 and 71.457 GPa (Figs. 1 and 2).

Table 2 Measurement of Vickers hardness for black painted aluminum substrate

Load (N)	Mean diagonal (μm)	Depth (μm) $h = 0.14285 d$	Hardness (HV)
0.5	69	7.62	108.9
1	79	11.28	118
3	153	21.856	114
5	181	25.85	117
10	260	37.141	85
Average Vickers hardness for black painted aluminum substrate			108.58 HV

Table 3 Measurement of Vickers hardness for black NiAl coated aluminum substrate

Load (N)	Diagonal (μm)	Depth (μm) $h = 0.14285 d$	Vickers hardness (HV)
0.1	16.5	2.375	269
0.25	22	3.14	383
0.5	32.5	4.64	349
1	48	6.86	322
2	66.5	9.5	335
3	101.5	14.5	216
5	146.5	20.9	172
10	220	31.426	145.8
Average Vickers hardness for black NiAl coated aluminum substrate			273 HV

Fig. 1 Experimental load-depth curve (P-h) for black painted aluminum 6061 substrate

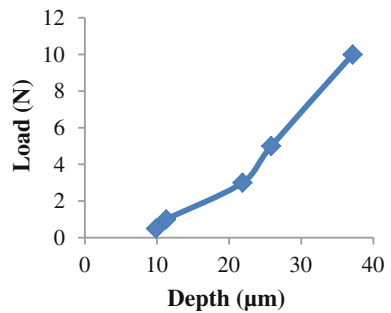
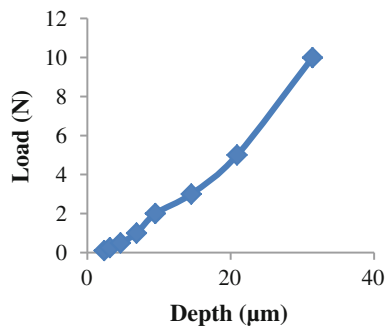


Fig. 2 Experimental load-depth curve (P-h) for black NiAl coated aluminum substrate



4.2 Finite Element Analysis

In indentation process, a gradually increasing load was applied using Vickers indenter up to some specified maximum load (10 N) followed by unloading up to zero. After unloading square indentation is obtained on specimen. If the total deformation is very less then stiffness of material is more and vice versa. Using

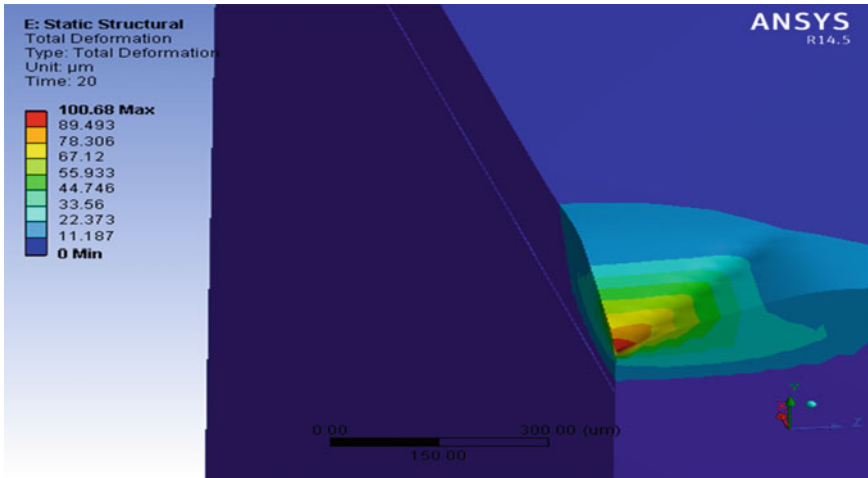


Fig. 3 Total deformation of black painted aluminum substrate for 10 N max load

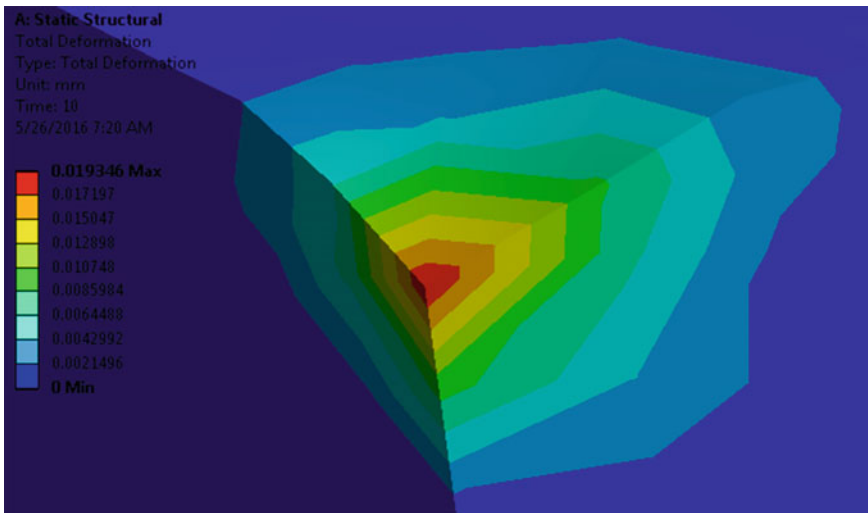


Fig. 4 Total deformation of black NiAl coated aluminum substrate for 10 N max load

three dimensional (3-D) indentation model, plastic deformation occurred on black NiAl coated aluminum substrate and black (Cellulose Nitrate) painted aluminum substrate was investigated to know the plastic deformation in the specimen at the interface i.e. between the indenter and substrate which is initiated at the beginning and then propagated as load increases.

Total deformation obtained for black (Cellulose Nitrate) coated aluminum substrate and black NiAl coated aluminum substrate is as shown in Figs. 3 and 4.

total permanent deformation for black painted aluminum is 100.68 μm at 10 N maximum load. total permanent deformation for black NiAl coated aluminum is 19.346 μm at 10 N maximum load which is very small as compared to the total deformation obtained for black coated aluminum substrate.

From maximum load slope obtained from load-depth at unloading curve gives value of young's modulus. Young's modulus value was obtained from FE simulation for black Painted aluminum is 41.02 GPa whereas Young's modulus value obtained for black NiAl coated aluminum is 69.234 GPa (Figs. 5 and 6).

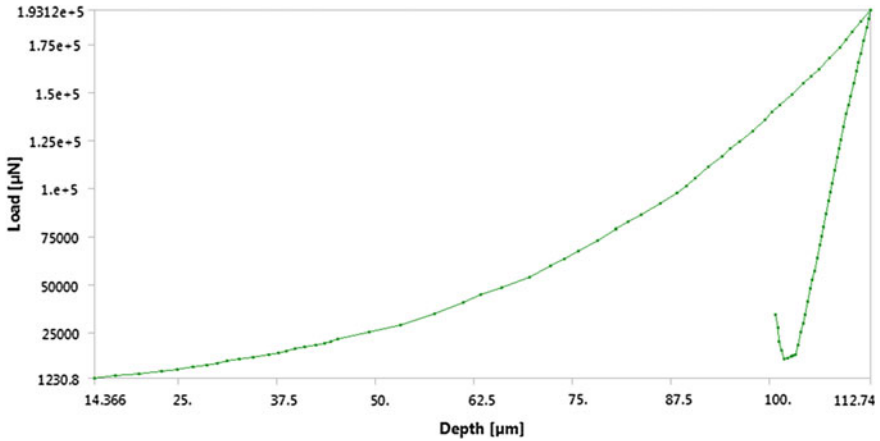


Fig. 5 Load-depth plot for black painted aluminum substrate from FE simulation

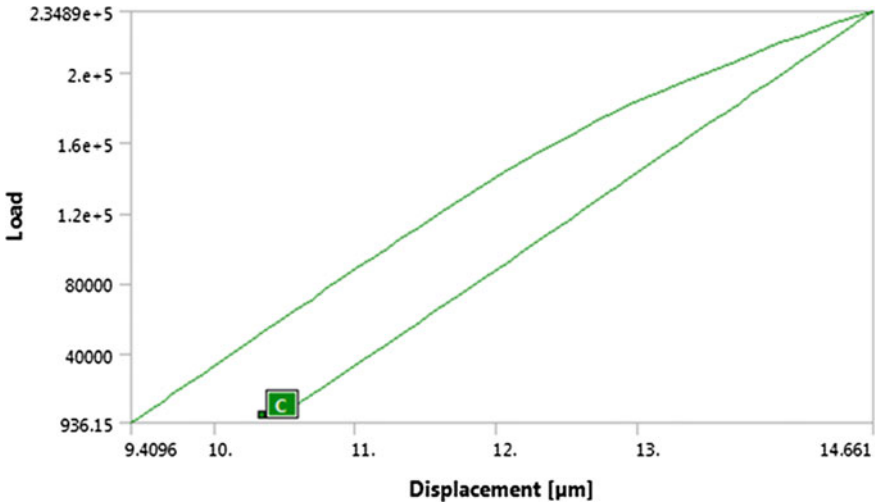


Fig. 6 Load-depth plot for black NiAl coated aluminum substrate from FE simulation

5 Conclusion

Mechanical properties of black painted aluminum substrate and black NiAl coated aluminum substrate were found out using micro indentation experiments. FE simulation is a useful technique to simulate indentation process.

Average Vickers hardness value obtained for black NiAl coated aluminum substrate is 273 HV which is higher than the hardness value of black painted aluminum substrate i.e. 108 HV. Also, young's modulus values obtained experimentally was in good agreement with FE simulation. It is found from FE simulation that total deformation obtained for black NiAl coated aluminum substrate is 19.346 μm which is very small whereas for black painted (Cellulose Nitrate) aluminum substrate i.e. 100.68 μm .

These concludes as, black NiAl coated aluminum substrate is having better mechanical properties than black painted aluminum substrate. It is more suitable for solar applications. Black paint coating can be replaced with black NiAl coating as it has more good wear resistance properties as compared with black painted aluminum substrate.

References

1. Wackelgard E (1998) Characterization of black nickel solar absorber coatings electroplated in nickel chlorine aqueous solution. *Solar Energy Mater Solar Cells* 56:35–44
2. Bayati MR, Shariat MH (2005) Design of chemical composition and optimum working conditions for trivalent black chromium electroplating bath used for solar thermal collectors. *Renew Energy* 30:2163–2178
3. Alshamaileh E (2010) Testing of a new solar coating for solar water heating applications. *Int J Solar Energy* 84:1437–1443
4. Iankov R, Cherneva S, Stoychev D (2008) Investigation of material properties of thin copper films through finite element modeling of microindentation test. *Appl Surf Sci* 5460–5469
5. Pandure PS, Jatti VS (2014) Finite element simulation of nano-indentation of DLC coated HSS substrate. *Int Conf Mater Process Charact* 1619–1624

Assembly Method of Pre Twisted Steam Turbine Blades

Dhanaji Chavan and Pravin Kachare

Keywords Fixture · Pre twist · FFT analyzer · Natural frequency · Steam turbine · Fork root

1 Introduction

The present theory relates to methods and systems for assembling blade having a shroud and a fork root onto the rim of a turbine wheel, particularly to assure complete accurate mechanical coupling between adjacent shrouds in final assembly. Shrouded turbine blades used in steam turbines, require the shroud edges to be in mechanical contact with one another, eliminating any gap between adjacent shrouds. The shrouds typically support application of tip seals to provide improved turbine thermal efficiency. High levels of mechanical reliability are also required under service conditions. A shroud having a predominantly rhombic configuration satisfies these design characteristics. Blades having integral shroud of rhombic configuration with fork root in rotor disc. Blades having rhombic shaped shrouds have been previously used in low, intermediate and high pressure turbine applications. Integrally shrouded blades, however, become increasingly difficult to assemble as airfoil stiffness is increased, as airfoil aspect ratio (i.e., radial height/axial width) is reduced, or as higher pre-twist stresses are required. Problems associated with assembly of blade having rhombic configured shrouds and tangential entry fork root. Generating adequately high tangential forces needed to eliminate gaps between adjacent shrouds (i.e., to pack together) and to produce an adequate pre twist of the blade airfoils. The level of pre-twist must be sufficient to assure that the adjacent shrouds remain in contact, i.e. are mechanically coupled, during all normal phases of turbine operation. Tangential assembly forces required to adequately pack blades together on a turbine wheel can become very high for

D. Chavan (✉) · P. Kachare
Department of Mechanical Engineering, SVERI's College of Engineering,
Pandharpur 413304, Maharashtra, India
e-mail: dhanaji.chavan301@gmail.com

blade of the size employed in large steam turbine applications. Also, as the blades are packed together, the fork root undergoes rotation, which in turn reduces the level of pre-twist applied to the blade airfoils. Fork root rotation must be limited to assure an adequate assembly. Further, the blades in their packed configuration must be constrained from backing away from each other as additional blades are installed on the wheel. The tendency to back away is associated with the forces developed at the shroud contact surfaces, and the orientation of these surfaces relative to the tangential direction. Accordingly, there is a need for an assembly method and system which will overcome the mentioned problems associated with assembly of shrouded blades on a turbine rotor; and which will in turn permit the blades to meet all efficiency and reliability objective.

Many researchers have done research on assembly method of pre twisted steam turbine blades. Ramannagari et al. [1] invented a shrouded blade in a turbo machine. Method and a blade for a turbine or, more generally a turbo machine are described With the blade having at a top end a shroud segment designed to engage With shroud segments of adjacent blades one an ring-shaped assembly at least partly by means of assembling the blades With the shroud segment having a central indentation along an engaging face. The moving blades are designed to have a root at the bottom end to assemble with rotor and a shroud at the top end to engage with the shrouds of adjacent blades forming a ring. The moving blades are assembled on to the rotor having grooves in axial or circumferential direction. The axial grooves can be straight or curved.

Tulsidasa and Shantharaja [2] studied effect of taper and twist in steam turbine blades and found that centrifugal stress must be calculated because it is considered as a main source of stresses in rotor blades. This study reveals that value of centrifugal stress can be controlled by simply tapering blades and twisting the blade can incorporate the moment which are developed in blades. Deallenbach et al. [3]: invented relates to methods and systems for assembling blades having a shroud and a tangential entry fork onto the rim of a turbine wheel, particularly to assure complete accurate mechanical coupling between adjacent shrouds in final assembly. Shrouded turbine blades, e.g. for use in steam turbines, require the shroud edges to be in mechanical contact with one another, eliminating any gap between adjacent shrouds. The shrouds typically support application of tip seals to provide improved turbine thermal efficiency. High levels of mechanical reliability are also required under service conditions. Guengant et al. [4]: studied Turbine blade assembly for improving efficiency and safety in large steam or gas turbines leads to all or some of the blades being made with a head, the heads of the blades in a given row being adjacent, and thus forming a substantially continuous strip covering the blades at the end opposite to their fixing feet. This arrangement gives a reduction in leakage losses, an increase in the characteristic vibration frequency of the blades, and may damp accidental vibration. The present invention also relates to a process for placing these blades in position with an initial twist, hereinafter called the "ultimate twist," which process is particularly advantageous in the case in which all the blades are similar and are fitted by being slid by the foot into circumferential grooves in the periphery of the rotor element of the turbine.

2 Method of Pre Twisted Steam Turbine Blade Assembly

In this method of assembling a plurality of blades on a rotor wheel wherein each blades includes an airfoil terminating at opposite ends in a shroud and a fork root, respectively, comprising the step of pre-twisting the shroud and airfoil of each blades in a rotational direction about a generally radial axis in response to applying a tangential assembly force to interference fit shroud contacting surfaces thereby imparting a rotational bias to the airfoil enabling subsequent rotation of the shroud and airfoil into final assembly with the shroud edges of adjacent blades in contact with one another and gap between adjacent blades at root portion.

In a further preferred embodiment of the present invention, a method of assembling a plurality of blades on a rotor wheel wherein each blades includes an airfoil terminating at opposite ends in a shroud and a fork root respectively, comprising the steps of: providing a lug on the shroud of each blades; releasable securing a fixture on each lug carried by the shroud of each blades, the fixture and lug of respective adjacent blades having generally complementary tapered surfaces at acute angles relative to the tangential direction; and wedging the fixture carried by the shroud of each blades being installed against the tapered surface of the lug carried by the shroud of the adjacent blades previously installed on the rotor rim to pre-twist the shroud and airfoil of the blades.

In a further preferred embodiment of the present invention, a turbine wheel and blades assembly comprising a plurality of blades each including an airfoil, a shroud adjacent the tip of the airfoil and a fork adjacent a root of the airfoil; a lug carried by each shroud; a fixture releasable secured to each lug and having a projection extending in a tangential direction for overlying a portion of a lug of a previously assembled blades onto the wheel, the adjacent shrouds having interference fit contacting surfaces; at least one of the lug and the fixture projection having a tapered surface in contact with a surface of another of the lug and fixture projection to pre twist the shroud and airfoil being installed.

3 System of Pre Twisted Blade Assembly

3.1 Detailed View of Blade Assembly

Various aspects and embodiments of the invention will now be described in connection with the accompanying figures.

3.2 Drawing Description

Referring now to the drawings, particularly to Fig. 1, there is illustrated a turbine rotor wheel including a wheel rim having a rib and groove configuration, i.e. a fork

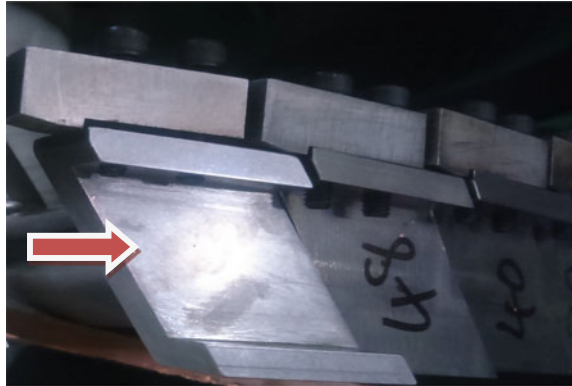
Fig. 1 View illustrating blade with rhombic shaped shrouds



root configuration along opposite axial sides thereof about the circumference of the wheel. Also illustrated in Fig. 1 is a plurality of blades generally designated each blade includes an airfoil having a fork root projecting from the root of the airfoil and a shroud adjacent the tip of the airfoil. It will be appreciated that the fork has a mating corresponding rib and groove arrangement, i.e., a fork root configuration complementary to the fork configuration of the wheel fork. Thus, the blades constitute tangential entry blades whereby the blades are disposed in a radial slot shown on the wheel and slightly disposed about the turbine wheel with contact faces of the fork and contact edges of the shrouds in respective engagement with corresponding parts of adjacent blades. Also illustrated in Fig. 1 is an anti-rotation key which extends about the outer periphery of the fork of the rotor wheel and which engages in a corresponding slot at the base of the fork to minimize or preclude rotation of the fork and hence blade during assembly and operation. In Fig. 1, each of the blades is illustrated as including a lug projecting radially outward from the forward edge of shroud. The lug is preferably formed integrally with the shroud and is in part removed from each blade and shroud after final assembly. Also illustrated in Fig. 1 is a fixture mounted on each of the respective lugs and which fixtures project axially forwardly. Each fixture is bolted to an associated lug by bolts.

As best illustrated in Fig. 2, the shrouds have a rhombic configuration. It will be appreciated that in final assembly, the angled margins or tangential edges of the shrouds about one another. However, those adjoining angled edges which typically extend about to 60° relative to the tangential axis or direction have an extant interference condition at their mating shroud contact surfaces when the blades are

Fig. 2 View of a pair of blades as viewed looking inwardly towards the radially outer faces of the shrouds in the course of assembly of the blades onto the wheel



assembled to the turbine wheel and the adjacent fork faces contacts one another. That is, there is an excess amount of material on the contact edges of the shrouds so that the shroud edges would theoretically overlap one another when the fork faces of adjacent blades are in contact one with the other.

Because of this shroud interference condition at the shroud contacting surfaces 32, the adjacent fork faces 34 cannot be brought into full flush contact with one another until a rotation or twisting of the shroud 20 occurs. By rotating the shroud about a blade radial axis, a change in the shroud cover tangential pitch occurs which permits the blade assembly to accommodate the shroud interference condition. That is, the excess amount of material forming the edges 30 of the adjacent shrouds is taken up by rotation of the shrouds about generally radial axes of the blades to produce a twisting of the shrouds as well as an elastic pre twist of the blade airfoils. Because of the angle of the shroud edges 30, a twisting of the shroud reduces the tangential width of the shroud as the shroud rotates about the generally radial axis until all of the interference is taken up. By twisting the shroud, the airfoil acts as a torsional spring, which serves to maintain the contact load between adjacent shroud contact surfaces 32 at all normal operating conditions of the blade to pre-twist the airfoil during assembly, a substantial tangential assembly force is required to generate the required twisting moment, i.e., torque on the shroud which occurs through the bearing forces on the shroud contact surfaces 32. The tangential assembly force must also overcome the frictional forces associated with sliding one contact surface 32 relative to the adjacent contact surface 32.

There is provided shroud contact surfaces having a shallow angle, i.e., approximately 15° relative to the tangential axis creates a wedging effect as the blades are tangentially assembled. Large bearing forces are thus generated on the shroud contact surfaces for the steep angle design and are oriented principally in the axial direction creating a substantial twisting moment on the shroud. The component of the assembly force in the tangential direction, however, is relatively small compared to the axial component of force which minimizes the required tangential assembly force necessary to overcome the tangential component of the shroud force and frictional forces.

A rhombic configured shroud, however, having a substantially larger tangential axis, i.e., on the order of about 40° – 60° , reduces the wedging action between the shroud contact surfaces as the blades are driven tangentially causing the required tangential assembly force to be substantially greater than for the steep angle design of the prior patent. This places limitation because of this shroud interference condition at the shroud contacting surfaces. The adjacent fork faces cannot be brought into full flush contact with one another until a rotation or twisting of the shroud occurs. By rotating the shroud about a blade radial axis, a change in the shroud cover tangential pitch occurs, which permits the blade assembly to accommodate the shroud interference condition. Because of the angle of the shroud edges, a twisting of the shroud reduces the tangential width of the shroud as the shroud rotates about the generally radial axis until all of the interference is taken up. By twisting the shroud, the airfoil acts as a torsional spring, which serves to maintain the contact load between adjacent shroud contact surfaces at all normal operating conditions of the blade to pre-twist the airfoil during assembly, a substantial tangential assembly force is required to generate the required twisting moment, i.e., torque on the shroud which occurs through the bearing forces on the shroud contact surfaces. The tangential assembly force must also overcome the frictional forces associated with sliding on contact surface relative to the adjacent contact surface.

Referring to Figs. 2 and 3, each fixture includes a portion which projects in a tangential direction from the lug to which the fixture is attached. The projection includes, on each axial downstream face, a leading chamfer as illustrated in Fig. 3. The size of step is adjusted based on the interference level at the shroud contact surfaces. Additionally, as seen in Fig. 3, the axial admission face of the lugs also include a chamfer complementary to the chamfer of adjacent blade, the chamfer being located on an adjacent lug to the lug having a registering taper (Fig. 4).

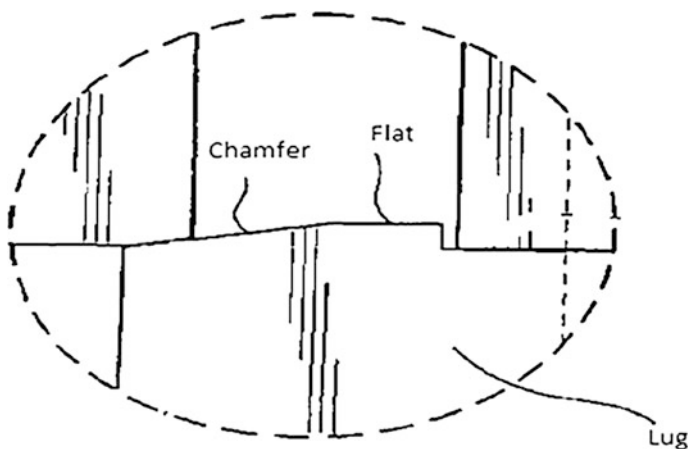
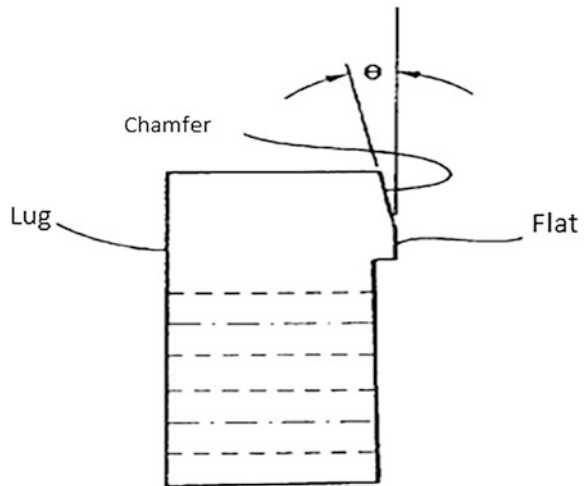


Fig. 3 Detail of lug engagement with adjacent blade

Fig. 4 Enlarged view of a fixture for securement to the lug on the shroud



3.3 Fixture Assembly

To assemble the blades on the rim of the rotor wheel, the fixtures are secured to the lug, e.g. using the bolts. Each successive blade to be assembled is side around the wheel rim to a location where the chamfer contacts the mating chamfer on the lug of the preceding blade. Once contact is made, a tangential assembly force is applied to the blade being installed to drive the blade toward the preceding blade. The fixture thus initially slides along the wedge angle created by the mating chamfers and causing a substantial twisting movement and corresponding rotation to occur at the shroud as illustrated in Fig. 5 as well as a twisting action of the airfoil. It will be appreciated that both of the mating blades will twist with the application of a tangential assembly force. When the axial step between the faces of the two blades equals the step size in the fixture, the flat surface of the fixture contacts the flat axially forward face of the shroud lug. The magnitude of rotation at the shroud is governed by the fixture step size and is set to slightly exceed the level of rotation that would naturally be created by the interference condition at the shroud contact surfaces. Thus, as the shroud twists and because of the angle of the shroud edges, the tangential width of the cover as the shroud is rotated is taken up to the extent that the faces of the fork surface of the blades contact one another. This enables the adjacent blades to slide together to enable the fork faces to contact one another with only the involved frictional forces resisting motion of the blades. Because of the small angle between the fixture and lug, i.e., 10° chamfer and the contact between flat and the adjacent lug, the frictional forces at such contact are larger than the forces tending to drive the blades apart. The blades will therefore remain in the partially assembled position after being driven together even when the assembly force is removed. This in turn enables additional blades to be assembled and likewise driven together without interference from the previously assembled blades.

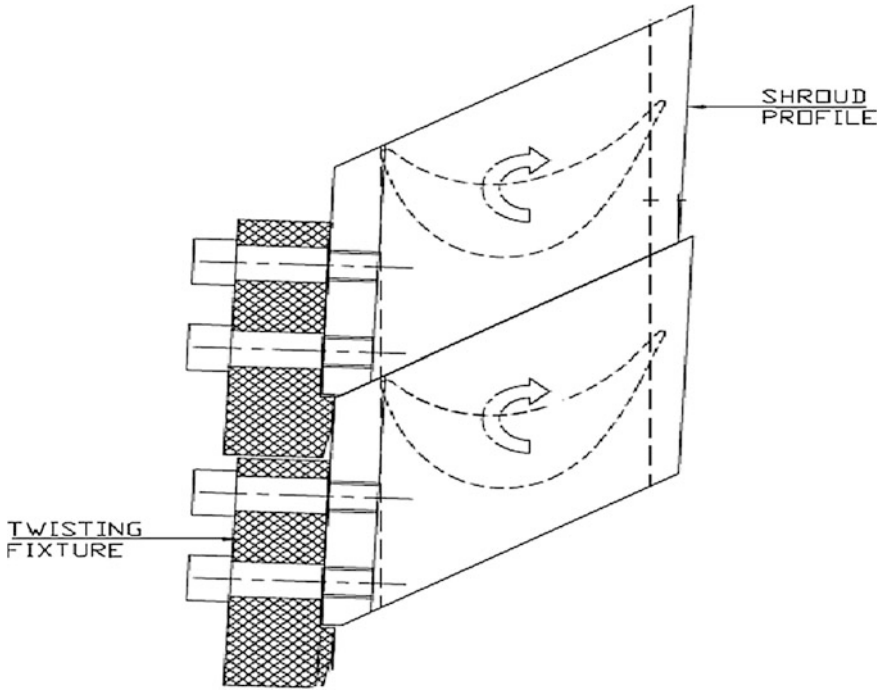


Fig. 5 Illustrating a direction of rotation or twist of the shroud and airfoils in the course of the assembly of the blades on the rotor wheel

3.4 Closing Blade Assembly

When all of the blades except for a closure blade have been applied about the wheel, the closure blade is inserted into a radial opening in the wheel fork. The assembly fixtures on the shrouds of the closure and adjacent blades aid in assembly of the closure blade since a pre-twist of the closure blade shroud can be applied with the fixtures. Thus, the closure blade is inserted and driven radially into the notch opening. After assembly of the closure blade, the assembly fixtures are removed from the shrouds. As the fixtures are removed, a rotation of the shrouds occurs in the opposite direction from the initial pre twist (i.e., compare Figs. 5 and 6). This opposite or negative rotation of the shrouds enables the contact surfaces of the shrouds to come into full flush contact with one another. It will be appreciated that the fork anti rotation key is in place during assembly of the blades to constrain fork rotation. Thus, the level of pre-twist in the blade airfoil created by the shroud rotation biases the shroud for rotation in the opposite direction into final assembly. Outer portions of the lugs may then be removed by machining.

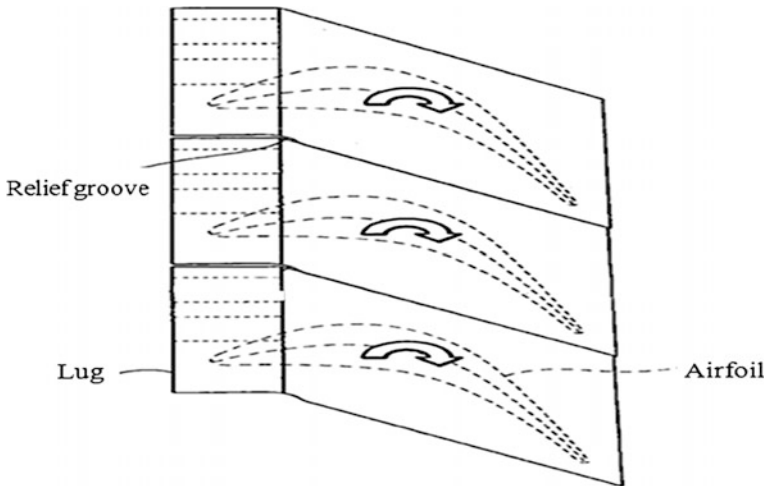


Fig. 6 View similar to Fig. 5 with the fixture removed illustrating a counter-rotation of the shroud and airfoil

Referring to Fig. 5, there is provided a relief groove on the shroud pressure side surface. The relief groove provides a low stress transition between the shroud contact and clearance surfaces.

4 Assembly Procedure

A method of assembling a plurality of blades on a rotor wheel wherein each blade includes an airfoil terminating at opposite ends in a shroud and a fork, respectively, comprising the step of pre-twisting the shroud and airfoil of each blade in a rotational direction about a generally radial axis in response to applying a tangential assembly force to interference fit shroud contacting surfaces thereby imparting a rotational bias to the airfoil enabling subsequent rotation of the airfoil into final assembly with the shroud edges of adjacent blades in contact with one another and fork faces of adjacent blades in contact with one another. A method including restraining rotational movement of the fork at the interface of the fork and rotor ring when said tangential assembly force is applied. A method including the step of wedging a fixture carried by the shroud each blade against a lug carried by the shroud of the adjacent blade to pre-twist the blade shroud and airfoils.

A method including sliding each blade being installed along the rotor rim to engage opposed contact faces of the forks as the shrouds and airfoils are being pre-twisted in excess of the level of rotation created by the interference fit between adjacent shroud contact surfaces.

A method according to any preceding claim including providing a lug on the shroud of each blade, releasable securing a fixture on each lug carried by the shroud of each blade, the fixture and lug of respective adjacent blades having generally complementary tapered surfaces at acute angles relative to the tangential direction, wedging the fixture carried by the shroud of each blade being installed against the tapered surface of the lug carried by the shroud of the adjacent blade previously installed on the rotor rim to pre-twist the shroud and airfoil of the blade. A method for each blade removing the fixture from the lug to enable rotation of the shrouds and airfoil, in the opposite rotational direction into final assembly.

5 Natural Frequency Test of Pre Twisted Blades

The natural frequency test results conducted to stage-7 turbine blades mounted on the rotor. Condition was that Blade was mounted on the turbine rotor and sensor mounted along the center axis of the blade 1/4th the distance from the blade tip. Weight of the accelerometer plus mounting stud used was 5 g.

5.1 Measurement System

The following instruments and measurement system were used for the study.

1. DI 440 FFT analyzer, Diagnostic Instruments make
2. Accelerometer: B&K make (Weighing 5 g) with 93 mv/g sensitivity
3. Polymate software for analysis and report generation.

5.2 Measurements

Following are the measurement parameters used while taking the data

- Frequency Spectrum 10–2000 Hz frequency bandwidth, 1600 lines of resolution was selected and the data collection was made.

5.3 Procedure

The vibration signatures were Fourier analyzed in the FFT analyzer to get the frequency spectra and was transferred to polymate software for detailed analysis of the signatures.

5.4 Comparison of Natural Frequency of Old Rotor Assembly and New Rotor Assembly

Natural frequency of pre twisted blades measured by using FFT analyser. Below is the following frequency measurement reading of Old and New rotor assembly (Figs. 7 and 8).

S. No.	Old rotor stage-07 blade frequency		New rotor stage-07 blade frequency	
	F1	F2	F3	F4
1	703	763	674	741
2	703	761	674	741
3	702	761	674	741
4	702	763	675	741
5	701	765	675	741
6	703	766	674	741
7	704	762	674	741
8	702	761	686	747
9	704	761.76	686	747
10	703	775	686	747
11	703	771	686	747
12	704	779	686	747
13	704	776	686	747
14	705	774	686	747
15	702	769	686	747
16	702	768	686	747
17	703	769	686	747
18	703	768	686	747
19	704	776	686	747
20	704	775	686	747
21	704	770	686	747
22	702	770	686	747
23	703	771	685	747
24	705	771	685	747
25	704	770	686	747

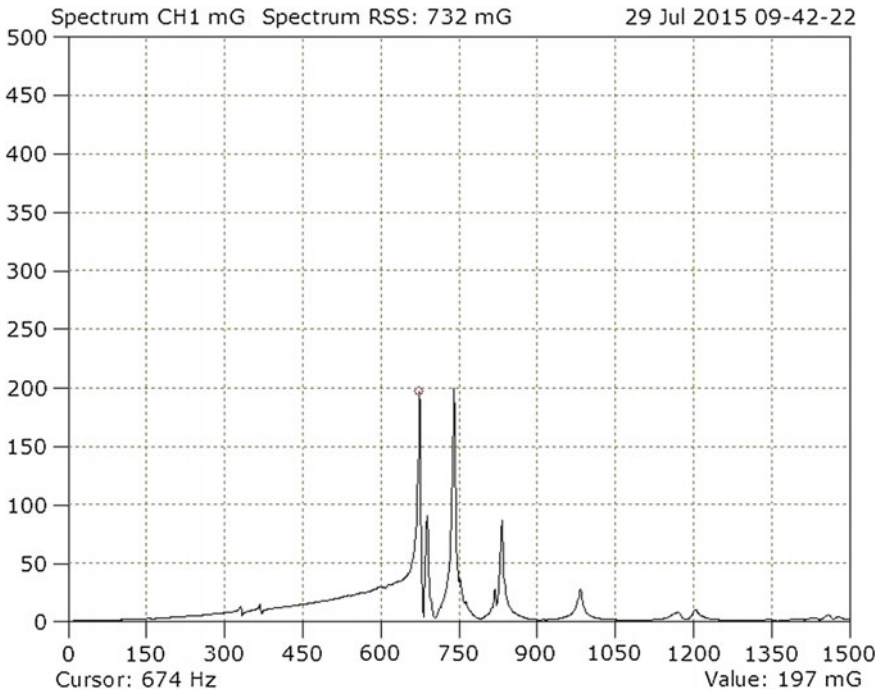


Fig. 7 Showing NFT spectrum recorded on blade-1 of 7th stage, first predominant natural frequency 674 Hz

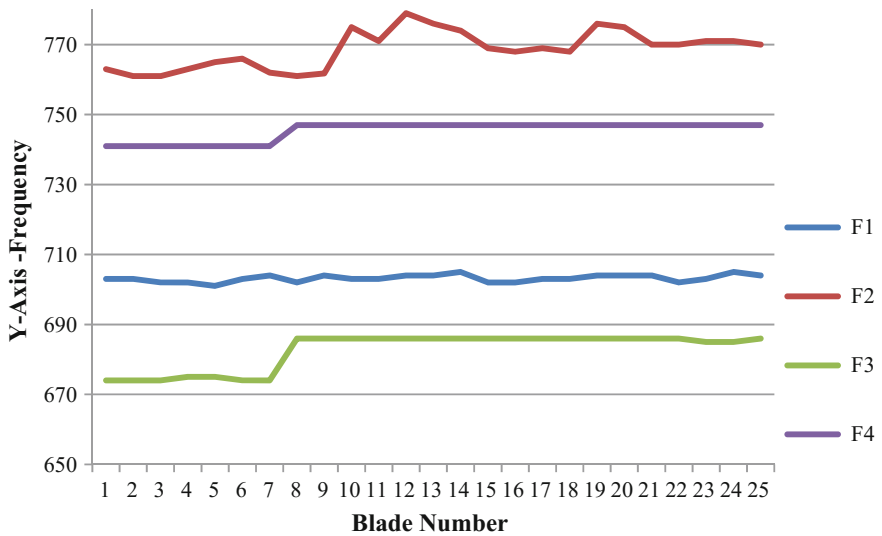


Fig. 8 Comparison of natural frequency of old rotor assembly and new rotor assembly

6 Conclusions

This system for blade assembly is successfully used for rhombic shroud and fork root blades. Blades are pre twisted to get shroud edges to be in mechanical contact with one another due to this gap between adjacent shroud edges is eliminated. It observed that the frequency values of the 7th stage blades are in the range of about 674–688 Hz. These values are in acceptable range. Steam leakages are eliminated. Thermal efficiency of turbine is improved. High level of mechanical reliability is increased.

References

1. Ramannagari DP, Masserey PA, Fleming RB, Calcagni C et al (2013) Shroud for pre twisted airfoils. Alstom Technology Ltd., United State Patent Application No. 2013/0323053A1, 5 Dec 2013
2. Tulsidasa D, Shantharaja M (2015) Effect of taper and twisted blade in steam turbine. Int J Sci Technol 04
3. Deallenbach RE et al Methods and systems for assembling shrouded turbine blade and tangential entry fork. European Patent No. EP 1 731 713 A2
4. Guengant P, Drancy, France, Assignor to Aktiengesell Schaft Brown, Boveri & Cie., Baden, Turbine blading. United State Patent Office, July 1967

Thermal Performance of Parabolic Dish Water Heater with Helical Coiled Receiver

Atul A. Sagade, Satish J. Aher and Narayani Sagade

Keywords Solar water heating systems · Instant water heating · Solar receivers · Industrial heating · Selective receiver coatings

Nomenclature

Pr	Prandalt's number
Re	Reynold's number
Gr	Grashoff's number
u_l	Overall heat loss coefficient ($W/(m^2 \text{ } ^\circ C)$)
Q_{loss}	Useful heat gain by water (W/m)
v	Wind velocity (m/s)
η_c	Collector efficiency (%)
(Q_{useful})	Useful heat gain (W/m)
(T_r)	Average receiver temperature ($^\circ C$)
(I_b)	Solar radiation (W/m^2)
(ΔT)	Temperature gradient ($^\circ C$)
T_{fi}	Inlet water temperature ($^\circ C$)
T_{fo}	Outlet water temperature ($^\circ C$)
T_{air}	Ambient temperature ($^\circ C$)

A.A. Sagade (✉)

Solar Thermal Research Lab, New Satara College of Engineering and Management, Korti, Pandharpur 413304, Maharashtra, India
e-mail: atulsagade@gmail.com

S.J. Aher

Department of Electrical Engineering, Amrutvahini College of Engineering, Sangamner 422605, Maharashtra, India
e-mail: satish1910@gmail.com

N. Sagade

REIRF, Pandharpur 413304, Maharashtra, India

1 Introduction

In India, different concentrating collectors are now in application to deliver a medium to high-temperature heat for industrial heating and (60–70%) of all the energy consumed in an industry is in the form of thermal energy. Thus, there is a great potential for utilizing solar energy for industrial process heat and domestic heating applications, especially in tropical countries like India where solar radiation is abundant. The demand for domestic heating is constant throughout the year and hence the capacity utilization of solar systems for these purposes can be very high. In several industries, 100% processes, the heat required is below 180 °C which can easily and economically be supplied by solar devices. Thus, this low temperature process heat requirement in industries makes the solar heating systems quite attractive. This paper aimed to explain the performance of novel truncated cone receiver for parabolic dish collector. Different researchers working on CSP for industrial heating and receiver geometry for parabolic dish systems and their brief literature is discussed in upcoming section. Sendhil Kumar and Reddy [1] explained a numerical investigation to study the natural convective heat loss from three types of receivers for a fuzzy focal solar dish concentrator, namely cavity receiver, semi-cavity receiver and modified cavity receiver. Authors reported the comparative study to predict the natural convection heat loss from the cavity, semi-cavity and modified cavity receivers. Larsen et al. [2] studied the heat loss of a linear absorber with a trapezoidal cavity and a set of pipes used for a linear Fresnel reflecting solar concentrator at laboratory scale. Authors observed that around 91% of the heat transferred to outdoors occurs at the bottom transparent window, for a pipe temperature of 200 °C. Wang and Siddiqui [3] designed a three-dimensional model of parabolic dish-receiver system with argon gas as a working fluid to simulate the thermal performance of a dish-type concentrated solar energy system. Authors explained an impact of the aperture size, inlet/outlet configuration of the solar receiver and the rim angle of the parabolic dish on the performance of proposed system. They concluded that the aperture size and different inlet/outlet configuration have a considerable impact on the receiver wall and gas temperatures, but the rim angle of the parabolic dish has negligible influence on the thermal performance of the system. Hahm et al. [4] described the performance of a cone concentrator combined with a solar cavity receiver and they compared its performance with a single cavity receiver. Authors explored that, the cone concentrator suffers from a high amount of rejected rays if the exit aperture is too small and larger exit aperture increases the thermal losses of the cavity. Fang et al. [5] reported a combined calculation method for evaluating the thermal performance of the solar cavity receiver. Using this approach, the thermal performance of a solar cavity receiver and a saturated steam receiver was simulated under different wind environments. Authors explained that change in the wind angle or velocity affects the air velocity inside the receiver. Harris and Lenz [6] discussed the Power profiles produced in cavities of varying geometry with concentrators of changing rim angle. They found that variation in concentrator rim angle and cavity geometry affects the

cavity power profile without a large effect on system efficiency. Authors concluded that the described methodology can be used to optimize concentrator/cavity design variables. Humphrey and Jacobs [7] investigated free-forced laminar flow convective heat transfer from a square cavity in a channel with variable inclination. They studied the influence on heat transfer of cavity orientation, channel inclination, flow direction and entrance profile for flow conditions. Authors concluded that the stable stratification of the flow in downward-facing cavity geometry was responsible for reducing the rate of heat transfer relative to an upward-facing geometry under equivalent flow conditions. Reddy and Sendhil Kumar [8] reported the numerical study of combined laminar natural convection and surface radiation heat transfer in a modified cavity receiver of solar parabolic dish collector using simulation model for combined natural convection and surface radiation. Authors investigated the influence of operating temperature, an emissivity of the surface, orientation and the geometry on the total heat loss from the receiver. Sagade [9, 10] described the effect of convective heat loss and effect of variation of mass flow rate on the thermal performance of parabolic dish solar water heater. He concluded that the system performance affected adversely because of convective heat loss. Also, the decreases in mass flow rate lead to increase in heat loss and decrease in collector efficiency. Plenty of similar literature is available on cavity receivers but avoided to discuss here because of space limitations.

From the literature discussed in above section, it is clear that the researchers evaluated thermal performance of cavity receiver geometries such as trapezoidal, square, conical, semi cavity and modified cavity and different design parameters such as rim angle, concentration ratio, receiver inclination, cavity orientation. The aim of present study is to report the thermal performance of a helical coiled truncated cone shape receiver with a small helix angle to enhance the efficiency of water heating and possible application in industrial heating, low-pressure steam generation, and water heating applications in the domestic sector. A helical coiled truncated cone shape receiver is coated with black nickel chrome as a selective receiver coating and covered with glass cover and mounted/coupled with a parabolic dish. A regression analysis technique is used to evaluate a simple relationship between the thermal performance parameters and the performance measurement.

2 Test Set Up and System Parameters

The prototype performance was evaluated under standard test condition of $I_b \geq 700 \text{ W/m}^2$ and $20 \text{ }^\circ\text{C} \leq T_{\text{air}} \leq 40 \text{ }^\circ\text{C}$ with water flow rate of 0.0056 kg/s . Figure 1 shows the experimental set up for the performance evaluation and Table 1 indicates the dimensions of the parabolic dish-helical coil receiver system.

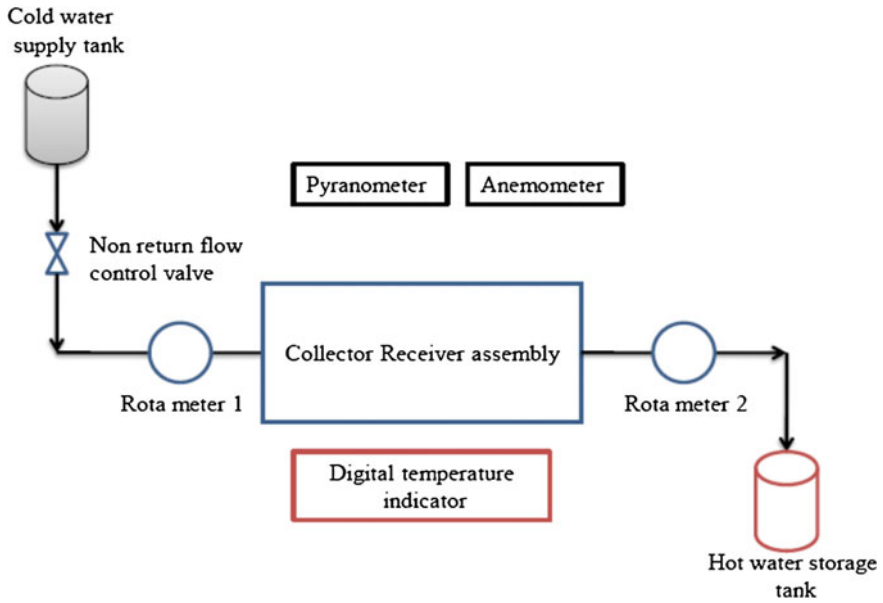


Fig. 1 Schematic of test setup

Table 1 Dimensions of the parabolic dish-helical coiled receiver system

Parameter	Value
Absorptivity (α)-Transmissivity (τ) product for receiver coating	0.93
Absorptivity (α)-Transmissivity (τ) product for copper	0.7
Aperture area of parabolic dish collector (A_c)	1.54 m ²
Depth of dish (D)	0.38 m
Diameter of parabolic dish (d)	1.4 m
Diameter of receiver at bottom (D_{rb})	0.135 m
Diameter of receiver at top (D_{rt})	0.095 m
Effective length of receiver coil (e_l)	3.96 m
Emissivity (ξ_c) of receiver coating	0.14
Emissivity (ξ_{cu}) of copper	0.725
Focal length of dish (f)	0.32 m
Mean diameter of receiver (D_{mean})	0.115 m ²
Reflectivity of parabolic dish mirrors (r)	0.86
Surface area of parabolic dish collector (A_s)	1.92 m ²
Surface area of receiver (A_{rec})	0.2357 m ²
Thermal conductivity (K) of copper	384 W/(m k)
Thickness (T) of mirrors of parabolic dish	2 mm

3 Calculations

The experiment was repeated for four times to check the reproducibility of the results. The equations used for the calculation of various thermal performance parameters were described below. For simplifying the calculations, it is assumed that,

- Heat transfer is steady state process.
- Solar radiation on the collector receiver system is constant at the instant.
- Axial heat transfer is neglected.
- Specific heat of water remains constant on temperature.

3.1 Useful Heat Gain by the Water

Useful heat gain by water is given by Eq. (1) [13]

$$Q_{useful} = E_{opt} - Q_{tl}(W) \quad (1)$$

where,

E_{opt} Optical radiation trapped receiver (W)

Q_{tl} Rate of heat loss from receiver (W)

3.2 Calculation of Heat Losses from the Receiver

Thermal losses from solar open cavity receivers include convective and radiative losses to air.

For focal plane i.e. cavity receiver overall heat loss is given by Eq. (2) [13]

$$Q_{loss} = A_{rec} \times u_l \times (T_r - T_{air})(W) \quad (2)$$

where,

T_{air} Temp of air surrounding a receiver ($^{\circ}C$)

T_r Average receiver temp ($^{\circ}C$)

u_l Overall heat loss coefficient

Overall heat loss coefficient (u_l) is given by Eq. (3) [13]

$$u_l = \left[\frac{1}{[h_{ct} + h_r]} \right]^{-1} (W/(m^2 \text{ } ^{\circ}C)) \quad (3)$$

where,

Radiative heat transfer coefficient (h_r) is given by Eq. (4) [13]

$$h_r = \frac{\xi_c \times \sigma (T_r^4 - T_{air}^4)}{T_r - T_{air}} \text{ (W/(m}^2 \text{ } ^\circ\text{C))} \quad (4)$$

Total convective heat loss coefficient (h_{ct}) can be given by Eq. (5) [13]

$$h_{ct} = h_{cn} + h_{cf} \text{ (W/(m}^2 \text{ } ^\circ\text{C))} \quad (5)$$

To estimate natural convective heat loss, following correlation developed by Eq. (6) [11]

$$\text{Nu} = 0.21G^{1/3} (1 + \cos(\theta_{rec}))^{3.2} (T_{mean}/T_{air})^{-1.5} \quad (6)$$

where,

G_r Grashof's number for natural convection

T_{mean} Mean temperature of water in receiver coils at natural convection ($^\circ\text{C}$)

θ_{rec} Receiver inclination angle = 90°

Forced convection loss coefficient (h_{cf}) is developed by Ma [12] and can be calculated by Eq. (7)

$$h_{cf} = f(\theta_{rec}) v^{1.401} \text{ (W/(m}^2 \text{ } ^\circ\text{C))} \quad (7)$$

The Instantaneous efficiency of the collector can be calculated by Eq. (8) [13]

$$\eta_c = \left(\frac{Q_{useful}}{I_b} \right) \times 100\% \quad (8)$$

4 Uncertainty Analysis

The errors occurred in the measuring instruments are calculated in this section. Thermocouples, pyranometer, cup type wind sensor, data logger and rotameter are used for measuring temperature, solar intensity and wind velocity, recording of continuous data and mass flow rate respectively. The minimum error occurred in any instrument is equal to the ratio between its least count and the minimum value of the output measured. The accuracies of various measuring instruments used in the experiments are given in Table 2.

Table 2 Uncertainty analysis

Instrument	Accuracy	Uncertainty (%)
Pyranometer	$\pm 2 \text{ W/m}^2$	1.2
Thermocouples	$\pm 1 \text{ }^\circ\text{C}$	1.3
Wind sensor	$\pm 1 \text{ m/s}$	2
Data logger	$\pm 1 \text{ units}$	0.5
Rotameter	$\pm 0.5 \text{ LPH}$	2.15

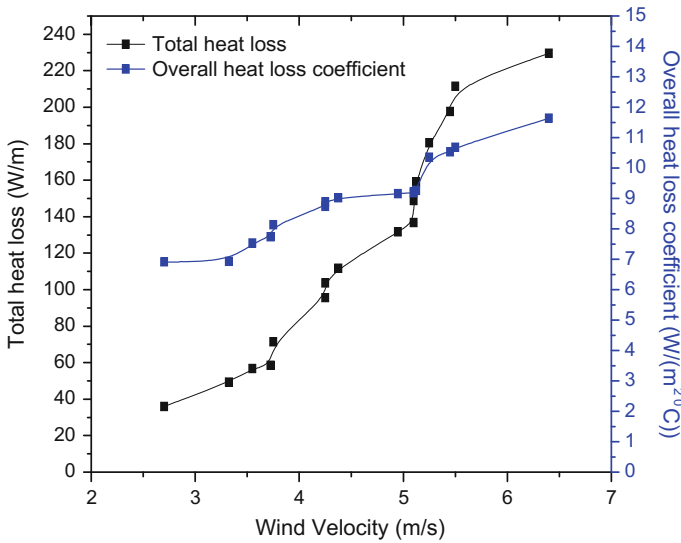


Fig. 2 Effect of wind velocity on overall heat loss coefficient and collector efficiency

5 Results and Discussion

5.1 Effect of Wind Velocity on Overall Heat Loss Coefficient and Collector Efficiency

Figure 2 indicates Variation of overall heat loss coefficient (u_l) and total heat losses (Q_{loss}) from a receiver with wind velocity (v). Regression Eq. (9) interprets that, when wind velocity increases by 1.04 m/s and heat loss increases by $0.0113 \text{ W m}^{-2} \text{ }^\circ\text{C}^{-1}$, heat loss coefficient will proportionally increase by $1 \text{ W}/(\text{m}^2 \text{ }^\circ\text{C})$

$$u_l = 2.74 + 1.04(v) + 0.0113(Q_{loss}) \tag{9}$$

With glass covered coated receiver, it is observed that heat losses are increased, when air gets heated due to rise in receiver temperature, air conductivity increases and heat losses also increase. But the main cause for heat loss is the temperature

gradient between receiver and ambient and wind velocity at the instant. Therefore there is an increase in convective and radiative heat losses from a receiver. An average receiver temperature was considered to provide accurate receiver loss predictions. The higher value of the linear regression coefficient of determination (R2) is 0.92 which shows the best fit of regression relation between the parameters.

5.2 Effect of Heat Loss on Collector Efficiency and Heat Gain

Figure 3 explores the effect of heat loss on collector efficiency (η_c) and heat gain (Q_u). Useful heat gained by water is a function of solar radiation, receiver temperature total heat loss and wind velocity at the instant. The system which yields more water temperature and will show better system performance. Equation (10) shows the relationship between collector efficiency with total heat losses and heat gain by water. Equation (10) indicates that when total heat loss, increases by 0.09 W/m, collector efficiency decrease by 1%. It also interprets that, when heat gain of water increase by 0.018 W/m proportionally collector efficiency increase by 1%. The value of the linear regression coefficient (R2) is 0.945 which shows a good linear relationship between the parameters. This model interprets that, the efficiency of collector decreases as the heat loss increases, which is confirmed by the negative slope coefficient.

$$\eta_c = 64.97 - 0.09(Q_{loss}) + 0.018(Q_{useful}) \tag{10}$$

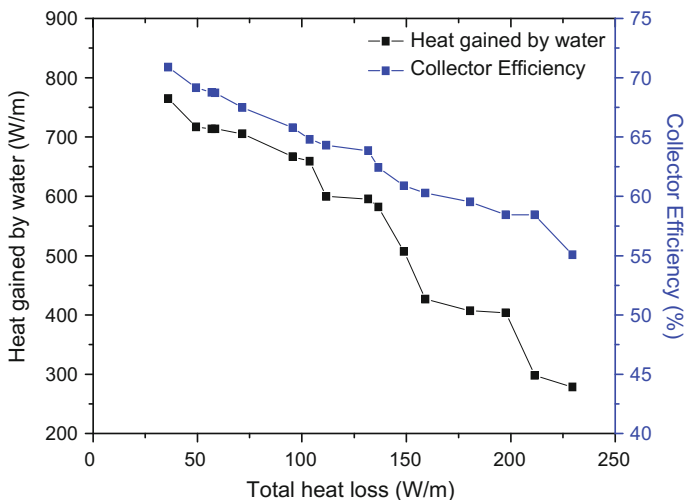


Fig. 3 Effect of heat loss on collector efficiency and heat gain

5.3 Effect of Receiver Temperature on Temperature Gradient and Collector Efficiency

From Fig. 4 it is observed that average receiver temperature (T_r) is majorly affected by solar radiation (I_b) and wind velocity at the instant. Receiver temperature increases sharply as solar radiation increases. Equation (11) shows the relation of receiver temperature and temp gradient (ΔT) with collector efficiency. Equation (11) interprets that, receiver temperature has negative impact on collector efficiency. When receiver temperature increases by 0.233 °C, proportionally collector efficiency decreases by 1%. When temperature gradient increases by 0.47 °C, collector efficiency decreases by 1%.

$$\eta_c = 74.01 - 0.233(T_r) + 0.47(\Delta T) \tag{11}$$

The linear regression coefficient (R2) for this linear model is 0.85 which shows the good linear relationship between the collector efficiency, receiver temperature and temperature gradient. This model interprets that, the efficiency of collector decreases as the receiver temperature increases, which is shown by the negative slope coefficient and collector efficiency increases as temperature gradient increases which is indicated by positive slope coefficient.

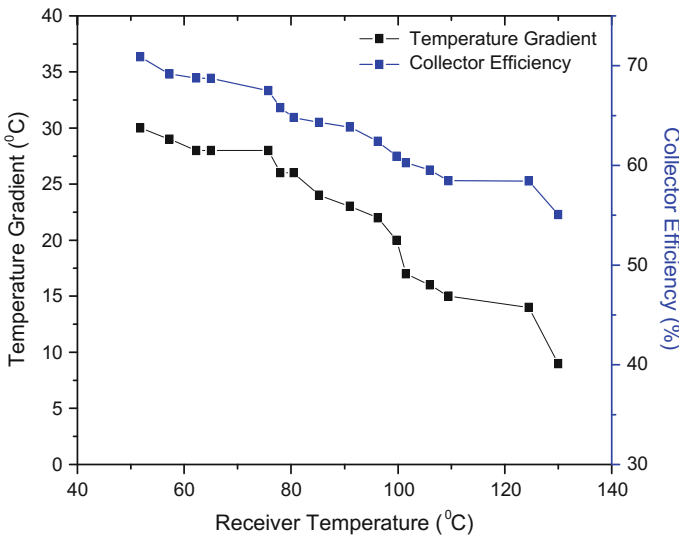


Fig. 4 Effect of receiver temperature on temperature gradient and collector efficiency

5.4 Effect of Beam Solar Radiation and Wind Velocity on Collector Efficiency

Figure 5 shows the variation of beam solar radiation and collector efficiency with wind velocity. Collector efficiency is a function of two environmental parameters solar radiation and wind velocity and out of which beam solar radiation has a negative effect on collector efficiency beyond the certain limit.

$$\eta_c = 74.53 - 0.35(v) - 0.009(I_b) \tag{12}$$

This is shown by Eq. (12). Equation (12) predicts that collector efficiency will decrease by 1% when wind velocity increases by 0.35 m/s and very little increase in solar radiation 0.009 W/m. When wind velocity and solar radiation shows no increase then collector efficiency will be equal to the intercept of Eq. (12).

5.5 Effect of Overall Heat Loss Coefficient and Receiver Temperature on Collector Efficiency

Equation (13) predicts that overall heat loss coefficient and receiver temperature has negative effect on collector efficiency.

$$\eta_c = 84.16 - 1.15(u_l) - 0.107(T_r) \tag{13}$$

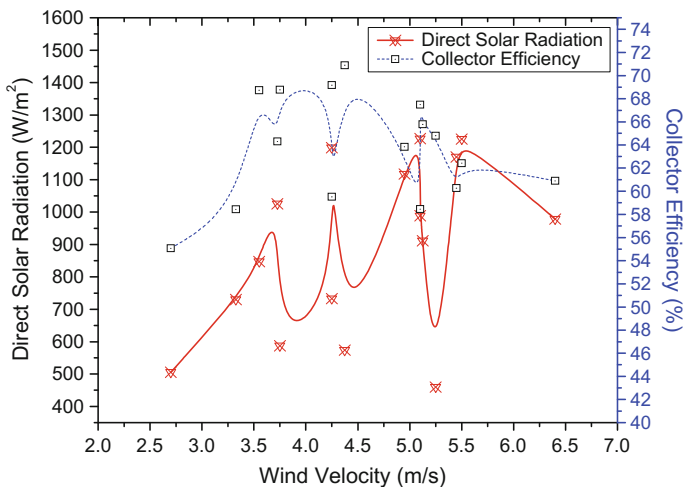


Fig. 5 Variation of beam solar radiation and collector efficiency with wind velocity

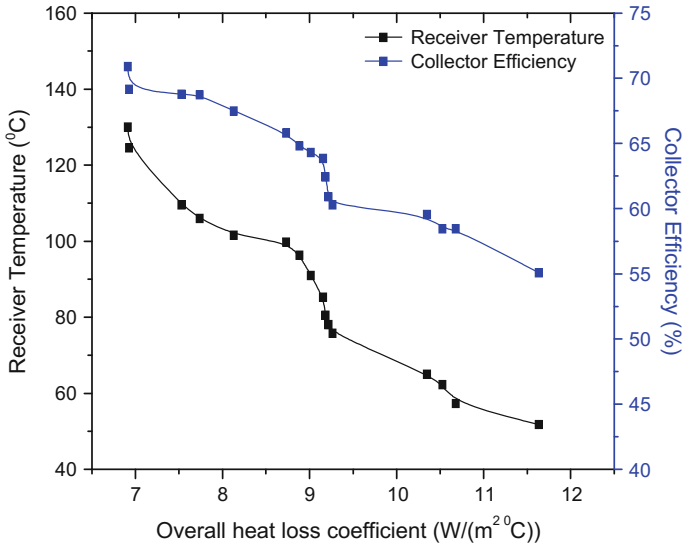


Fig. 6 Effect of overall heat loss coefficient and receiver temperature on collector efficiency

When overall heat loss coefficient and receiver temperature increases by 1.15 W/(m² °C) and 0.107 °C respectively, proportionally collector efficiency will decrease by 1% because collector efficiency is a function of parameters such as solar radiation, surface reflectance, receiver absorptance, atmospheric conditions, and wind velocity. The regression coefficient (R²) for this model is 0.81 which interpret the satisfactory relationship between the overall heat loss coefficient and receiver temperature on collector efficiency. This model predicts that the efficiency of collector decreases because of both parameters which are shown by the negative slope coefficients of overall heat loss coefficient and receiver temperature. Figure 6 indicates effect of overall heat loss coefficient and receiver temperature on collector efficiency.

6 Conclusions

From the field experiments, it is seen that, when receiver is coated black and covered with glass cover, system performance get enhanced. From the experimentation, it is clear that, the efficiency of the system achieved with considerable flow rate of 0.0056 kg/s flowing through the helical coiled receiver which was glass covered and coated with black nickel chrome is 63%. Total heat loss from the receiver adversely affects the overall efficiency of the system. Actual field experiments confirm the same. There is average rise of 40% in outlet water temperature with average outlet water temperature of 52 °C. Average increment in receiver

temperature was 35% from initial receiver temperature and average receiver temperature was noted as 88 °C. It also seen that, the theoretical regression modeling equations are satisfied by the actual experimental results; hence can be considered for design purpose and evaluation of thermal performance of the similar systems with different permutations and combinations. The experimental results are presented in the current work and the validity of the model is examined by comparison of the theoretical results with experimental results; and it demonstrates a good agreement between two results. It is to be noted here that, the results described in this paper are valid for water and similar fluids only. It is concluded that, the described parabolic dish-helical coiled receiver system can prove a good alternative for flat plate and evacuated tube water heaters and could be implemented effectively for low temperature small scale industrial process heat applications. It is further recommended to perform the comparative study of different receiver designs with the helical coiled receiver which can be used with the parabolic solar dish water heaters to select the best receiver.

References

1. Sendhil Kumar N, Reddy KS (2008) Comparison of receivers for solar dish collector system. *Energy Convers Manag* 49(4):812–819
2. Larsen SF, Altamirano M, Hernández A (2012) Heat loss of a trapezoidal cavity absorber for a linear Fresnel reflecting solar concentrator. *Renew Energy* 39(1):198–206
3. Wang M, Siddiqui K (2010) The impact of geometrical parameters on the thermal performance of a solar receiver of dish-type concentrated solar energy system. *Renew Energy* 35(11):2501–2513
4. Hahm T, Schmidt-Traub H, Leßmann B (1999) A cone concentrator for high-temperature solar cavity-receivers. *Sol Energy* 65:33–41
5. Fang JB, Wei JJ, Dong XW, Wang YS (2011) Thermal performance simulation of a solar cavity receiver under windy conditions. *Solar Energy* 85(1):126–138
6. Harris JA, Lenz TG (1985). Thermal performance of solar concentrator/cavity receiver systems. *Sol Energy* 34(1):35–142
7. Humphrey JAC, Jacobs W (1981) Free-forced laminar flow convective heat transfer from a square cavity in a channel with variable inclination. *Int J Heat Mass Transf* 24(10):1589–1597
8. Reddy KS, Sendhil Kumar N (2008) Combined laminar natural convection and surface radiation heat transfer in a modified cavity receiver of solar parabolic dish. *Int J Therm Sci* 47(12):1647–1657
9. Sagade AA (2013) Comparative experimental analysis of the effect of convective heat losses on the performance of parabolic dish water heater. *Int J Sustain Eng* 6(3):258–266
10. Sagade AA (2015) Experimental investigation of effect of variation of mass flow rate on performance of parabolic dish water heater with non-coated receiver. *Int J Sustain Eng* 34(10):645–656
11. Prakash M, Kedare SB, Nayak JK (2009) Investigations on heat losses from a solar cavity receiver. *Sol Energy* 83:157–170
12. Fraser PR (2008) Stirling dish system performance prediction model. A Master of Science (Mechanical Engineering) thesis. University of Wisconsin-Madison, USA
13. Duffie J, Beckman W (2006) *Solar engineering of thermal processes*. Wiley, New York

Application of MOORA Method for Friction Stir Welding Tool Material Selection

V.S. Gadakh, V.B. Shinde, N.S. Khemnar and A. Kumar

Keywords FSW · Tool material selection · Decision making · MOORA method

Nomenclature

Material M1	AISI H13 tool steel or SKD61
Material M2	AISI Type D2 tool steel
Material M3	HCS
Material M4	HSS (ASTM M35)
Material M5	AISI 1040 steel
Material M6	AISI 4140 steel
Material M7	M42 high speed tool steel
Material M8	O-1 tool steel
Material M9	MP159
Material M10	DIEVAR
Material M11	Orvar supreme
CTE	Linear coefficient of thermal expansion ($\mu\text{m}/\text{m } ^\circ\text{C}$)
M	Machinability
TC	Thermal conductivity (W/m K)
H	Hardness (HRc)
D	Density (kg/m^3)
SHC	Specific heat capacity (J/(kg K))
TD	Thermal diffusivity (m^2/s)
C	Cost (Rupees/kg)
YS	Yield strength (MPa)

V.S. Gadakh (✉) · V.B. Shinde · N.S. Khemnar
Amrutvahini College of Engineering, Sangamner 422608, Maharashtra, India
e-mail: vijay.gadakh@avcoe.org

A. Kumar
National Institute of Technology (NIT), Warangal 506004, Telangana, India

T	Toughness
HH	Hot hardness
RS	Resistance to softening
WR	Wear resistance

1 Introduction

Generally, for material selection, four general criteria are necessary as properties, manufacturing characteristics, environmental profile, and business considerations. The first task in materials selection is to decide which material properties are relevant to the application [1]. While selecting materials for engineering purpose, a distinct consideration of the functional requirements for each part is required, and various important measures need to be considered [2].

FSW process is the current research area of many researchers. FSW is a widely used as green welding process for soft materials such as aluminum alloys because it avoids many of the common problems of fusion welding. However, the FSW tool is subjected to severe stress and usually increase in temperature reduces the strength of material.

Different material characteristics can be considered important to friction stir, but ranking the material characteristics (from most to least important) will depend on the workpiece material, expected life of the tool, and the user's experiences and preferences [3]. Mishra and Ma [4] addressed that tool wear and shape optimization are associated with the tool materials and further research is needed for selection of tool material.

Figure 1 states the general tool material selection criteria. From Fig. 1 one cannot really judge the tool material as there are number of criteria's are involved for selecting the tool material. Although, different researchers have chosen the tool material based on literature, experience this does not guarantee the optimal tool material selection. Even though the selected tool material performs well in one of the characteristics, but it may or may not satisfy the other features. Padmanaban and Balasubramanian [5] considered five different tool materials for FSW of AZ31B magnesium alloys such as mild steel (MS), stainless steel (SS), armor steel (AS), high carbon steel (HCS) and high-speed steel (HSS). They have not given any methodology to select a tool material. They reported that using HCS or HSS as a tool material defect free welds are obtained. Besides, higher nugget hardness, joint efficiency, yield strength (YS) and ultimate tensile strength (UTS) were obtained using HCS.

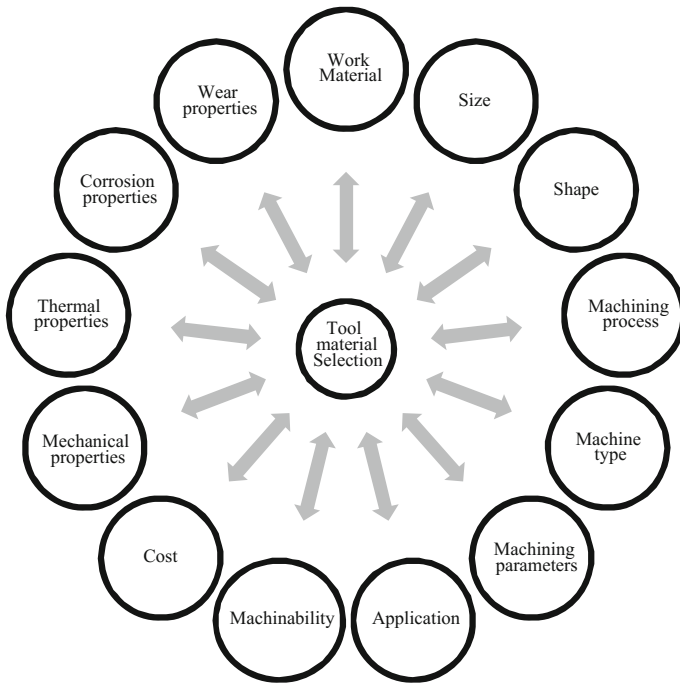


Fig. 1 Tool material selection criteria

So, in this paper, an attempt is made to apply the MOORA methodology for optimal tool material selection in FSW process. There are so a number of methods available such as multi-objective evolutionary methods, heuristic methods, classical methods, etc. for the collection of any phenomenon. Out of which MOORA method is considered, an advantage of this approach is very useful to the decision makers, who are not sound in mathematics.

The MOORA methodology is already used by many researchers for various applications for any selection problem involving any number of selection criteria [6, 7]. However, at this stage, no information available in the open literature about the tool material selection methodology for FSW process and careful attention is required in this context. In this paper, the MOORA method is employed as a tool to select the tool material for given application and prove its applicability for dealing with this type of complex decision-making situation. This method starts with a decision matrix showing the performance of different alternatives on various attributes (objectives).

- Step 1** Determine the objective, and identify the appropriate evaluation attributes/characteristics.
- Step 2** Represent all the information available for the attributes in the form of a decision matrix. The data described in Eq. (1) is known as matrix $X_{m \times n}$.

Where x_{ij} is the performance measure of i th alternative on a j th attribute, m is the number of options. Whereas n is the number of attributes. Then a ratio system is developed in which each performance of an alternative on an attribute is compared to a denominator which is a representative for all the options concerning to that attribute.

$$X = \begin{bmatrix} x_{11} & x_{11} & \cdot & x_{1n} \\ x_{21} & x_{22} & \cdot & x_{2n} \\ \cdot & \cdot & \cdot & \cdot \\ x_{m1} & x_{m2} & \cdot & x_{mn} \end{bmatrix} \quad (1)$$

Step 3 Brauers et al. [6, 7] concluded that for this denominator, the best choice is the square root of the sum of squares of each alternative per attribute. This ratio can be expressed as below:

$$x_{ij}^* = x_{ij} / \sqrt{\sum_{i=1}^m x_{ij}^2} \quad (j = 1, 2, \dots, n) \quad (2)$$

where x_{ij} is a dimensionless number which belongs to the interval $[0, 1]$ represents the normalized performance of i th alternative on j th attribute.

Step 4 Next, these normalized performances are added in case of maximization (for beneficial attributes) and subtracted in case of minimization (for non-beneficial attributes). Then the optimization problem is as:

$$y_i = \sum_{j=1}^g x_{ij}^* - \sum_{j=g+1}^n x_{ij}^* \quad (3)$$

where g is the number of characteristics to be maximized, $(n-g)$ is the number of attributes to be minimized, and y_i is the normalized assessment value of i th alternative on all the attributes. In some cases, it is often observed that some attributes are more important than the others. To give more importance to an attribute, it can be multiplied with its corresponding weight (significance coefficient) [6, 7]. When these attribute weights are taken into consideration, Eq. (3) becomes as follows:

$$y_i = \sum_{j=1}^g w_j \cdot x_{ij}^* - \sum_{j=g+1}^n w_j \cdot x_{ij}^* \quad (j = 1, 2, \dots, n) \quad (4)$$

where w_j is the weight of j th attribute, which can be determined applying analytic hierarchy process (AHP) or entropy method.

Step 5 The ranking obtained by arranging the alternatives in descending manner where the best alternative has the highest y_i value, while the alternative with the lowest y_i value is the worst choice.

2 FSW Tool Material Selection

This paper focuses on the selection of tool material in FSW process for aluminum alloy and its metal matrix composites (MMC). The tool materials considered here are based on the extensive literature survey. The information regarding the data of the attributes/characteristics was collected from various books, tool makers' manual/handbooks, the web [8] and CD-ROM [9]. As far as FSW process is the concern, the process is started from almost two and half decade ago. The technology is not yet fully full-grown, and it is expected that significant improvements in tool design, tool materials, process control, etc., will continue [10].

2.1 FSW Tool Material Selection Criteria

This problem considers eleven alternatives and thirteen attributes, and the data are given in Table 1. In this study, the objective is to evaluate the eleven options, and thirteen attributes are as CTE; Linear coefficient of thermal expansion, M; Machinability, TC; Thermal Conductivity, H; Hardness, D; Density, SHC; specific heat capacity, TD; Thermal Diffusivity, C; Cost, YS, T; toughness, HH; hot hardness, RS; resistance to softening, and WR; wear resistance. HH values shown in Table 1 was collected from ASM Handbook in 0–10 scale rating, i.e. 1 (low) to 9 (high). Similarly, RS and WR was qualitative terms (handbook values) converted into quantitative by the same scale rating. TD is the TC divided by D and SHC at constant pressure. SHC, often called specific heat, is calculated from Eq. (5). The general formula for TC is as:

$$TC = TD \times D \times SHC \quad (5)$$

For this particular problem, M, H, D, YS, T, HH, RS, and WR are considered as beneficial attribute (where higher values are desirable), whereas, CTE, TC, SHC, TD and C are regarded as non-beneficial attributes (where lower values are preferable) [2, 11, 12]. The weights (relative importance) of the thirteen attributes are determined using analytic hierarchy process (AHP) method and are given in Table 2. Eleven point scales was used to determine relative importance of thirteen attributes shown in Table 3.

Table 1 Quantitative data for FSW tool material selection

Mat. No.	CTE		M	TC		H	D	SHC		TD		C	YS		T	HH		RS		WR	
	Min	Max		Min	Max			Min	Max	Min	Max		Min	Max		Min	Max	Max	Max	Max	Max
	x_1	x_2	x_3	x_4	x_5	x_6	x_7	x_8	x_9	x_{10}	x_{11}	x_{12}	x_{13}								
M1	13.1	70	28.7	48	7760	460	6.88E-06	270	1365	8 (VH)	6	7 (H)	6 (M)								
M2	12.2	40	23	59.5	7700	460	7.23E-06	240	2200	3 (L)	6	7 (H)	8 (H)-(VH)								
M3	14.2	125	51.9	70	8260	669	1.72E-05	75	3200	5 (M)	5	3 (L)	6 (M)								
M4	11.5	30	28	67	8140	586	5.87E-06	1050	415	3 (L)	8	9 (HST)	7 (VH)								
M5	14.8	60	33.9	20	7845	1583	4.18E-06	90	448	3 (L)	3	9 (HST)	3 L								
M6	14.6	65	33	27	7850	561	9.67E-06	77	690	5 (M)	4	5 (M)	6 (M)								
M7	11.5	45	28	65.8	7980	600	5.85E-06	1200	475	3 (L)	9	9 (HST)	8 (VH)								
M8	11.4	70	34	62	7700	460	9.60E-06	400	634	5 (M)	3	3 (L)	4 (M)								
M9	14.3	40	35	50	8332	175	2.40E-05	650	400	7 (H)	4	3 (L)	6 (H)								
M10	5	35	98	90	15,700	480	1.30E-05	650	344	8 (VH)	6	3 (L)	8 (VH)								
M11	13.1	60	30	16	7780	460	8.38E-06	350	1520	8 (VH)	7	5 (M)	5 (M)								
$\sum_{j=1}^{11} x_{ij}^2$	1749.85	44,200	20,737.51	35,391.89	8,77E+08	5,078,992	1.48E-09	3,820,154	21,008,571	352	377	427	435								
$\sqrt{\sum_{j=1}^{11} x_{ij}^2}$	41.8312	210.238	144.0052	188.1273	29,606.96	2253.662	3.85E-05	1954.521	4583.511	18.7616	19.4164	20.6639	20.85665								

Table 2 Weights for different criteria

Criteria	CTE	M	TC	H	D	SHC	TD	C	YS	T	HH	RS	WR
Weight	0.10	0.07	0.11	0.08	0.10	0.09	0.08	0.10	0.08	0.07	0.05	0.04	0.02

Table 3 Value of material selection factor [2]

Qualitative measure of material selection factor	Assigned value
Exceptionally low	0.045
Extremely low	0.135
Very low	0.255
Low	0.335
Below average	0.410
Average	0.500
Above average	0.590
High	0.665
Very high	0.745
Extremely high	0.865
Exceptionally high	0.955

2.2 Application of MOORA Method for FSW Tool Material Selection

Table 3 shows the normalized performance scores of the alternatives on the considered attributes, the normalized assessment values (y_i) of all the options on the recognized attributes are computed. When the problem of selecting the most suitable tool material in FSW process for aluminum alloy series work material is solved using the MOORA method, AISI H13 is observed to be the best choice. The detailed calculations are shown in Table 4, from where it is also revealed that AISI type D2 tool steel is the second best option and Orvar Supreme is the last choice.

A closer look at the values of in Table 4 shows that there is the marginal change in the values of AISI H13 tool steel, AISI type D2 tool steel and HCS. In Table 1 values of some of the alternatives value shown as maximum value for following characteristics such as D, CTE, TC, YS and M. Just looking at the values of HCS in Table 1 one may conclude that HCS is better than AISI H13 tool steel and AISI type D2 tool steel, but, values shown in Table 1 for HCS are maximum values, and as such there is no particular class of HCS mentioned by past researchers.

3 Conclusions

FSW process is active and vibrant research area. Although, various researchers have selected the tool material based on literature, experience this does not guarantee the optimal tool material. Hence, there is an urgent need for an efficient method to solve the friction stir welding tool material selection problem. The paper focuses on a selection of tool material for FSW process of aluminum alloy and its MMCs using MOORA method. The method is decision-making tool to solve the given problem when the difficulty arises there are different criteria. Some researchers already explain the usefulness of the method. This approach can be applied for the selection of tool material of FSW for other alloys such as steel, titanium, magnesium, copper or dissimilar materials where tool wear has been identified as a serious problem then this method is very useful. The method with illustrated example will be guided for researchers who may not have the thorough knowledge of tool material selection in FSW.

Acknowledgements Support from the board of college and university development (BCUD), Pune, Grant #13ENG000074 is acknowledged. The authors would also like to thank the authorities of NIT, Warangal, India and also the authors expresses his gratitude to Prof. M.K. Negi, Amrutvahini College of Engineering, Sangamner, for their help.

References

1. Ipek M, Selvi IH, Findik F, Torkul O, Cedimoğlu, IH (2013) An expert system based material selection approach to manufacturing. *Mater Des* 47:331–340
2. Dieter GE, Schmidt LC (2007) *Engineering design*, 4th edn. McGraw-Hill, NY
3. Rao RV (2007) *Decision making in the manufacturing environment: using graph theory and fuzzy multiple attribute decision making methods*. Springer, London
4. Mishra RS, Mahoney MW (2007) Friction stir welding and processing. *ASM Int* 7–35
5. Mishra RS, Ma ZY (2005) Friction stir welding and processing. *Mater Sci Eng R* 50:1–78
6. Padmanaban G, Balasubramanian V (2009) Selection of FSW tool pin profile, shoulder diameter and material for joining AZ31B magnesium alloy—an experimental approach. *Mater Des* 30:2647–2656
7. Brauers WKM, Zavadskas EK, Peldschus F, Turskis Z (2008) Multiobjective decision-making for road design. *Transport* 23:183–193
8. Brauers WKM, Zavadskas EK, Peldschus F, Turskis Z (2008) Multi-objective optimization of road design alternatives with an application of the MOORA method. In: *Proceedings of 25th international symposium on automation and robotics in construction*. Vilnius Gediminas Technical University, Lithuania
9. MatWeb—Online materials information resource. Automation Creations, Inc., Blackburg, Virginia. <http://www.matweb.com>
10. Callister WD Jr, Rethwisch DG (2009) *Materials science and engineering: an introduction*, 8th edn. Wiley, NY

11. Lohwasser D, Chen Z (2010) Friction stir welding from basics to applications. Woodhead Publishing, New Delhi
12. Rai R, De A, Bhadeshia HKDH, DebRoy T (2011) Review: friction stir welding tools. *Sci Technol Weld Joining* 16(4):325–342
13. Zhang YN, Cao X, Larose S, Wanjara P (2012) Review of tools for friction stir welding and processing. *Can Metall Q* 51(3):250–261

Development of Prototype of Light Passenger Quarter Car for Improved Vehicle Ride Characteristics

Vijay R. Patil and Pradeep V. Jadhav

Keywords 2 DOF quarter-car model · Hydraulic assisted quarter car active suspension system · Hydraulic actuator · Vehicle ride characteristics

1 Introduction

Suspension system is one of the vital part of the vehicle. Therefore, it is quite necessary to design improved suspension system in order to improve the vehicles ride characteristics. An automobile is a nonlinear system in practical terms because it consists of many nonlinear components like suspensions, tires and other components having nonlinear properties. Vehicles moving on the randomly profiled road are exposed to vibrations which are damaging both for the passengers in terms of ride comfort and for the durability of the vehicle itself. Therefore the most important task of a vehicle suspension is to ensure holding and ride comfort road for a variety of road conditions, it is important to analyses the vibrations of the vehicle. The design of road vehicle is influenced by number of factors but in the design of suspension system the more focus is given on two parameters; in that one is to minimize the vertical forces transmitted to the sprung mass and to increase the tire-to-road contact for handling and safety.

The conventional passive suspension system consists of the spring and damper with fixed values of stiffness and damping coefficient and here the limited scope for its performance improvement. Hence there is compromise among the ride comfort and vehicle handling, as shown in Fig. 1.

V.R. Patil (✉)

Department of Automobile Engineering, Annasaheb Dange College of Engineering and Technology, Ashta, India
e-mail: vijaypatil872@gmail.com

P.V. Jadhav

Department of Mechanical Engineering, Bharati Vidyapeeth Deemed University College of Engineering, Pune, India
e-mail: pvjadhav@bvucoep.edu.in

Fig. 1 Conflict in ride and handling

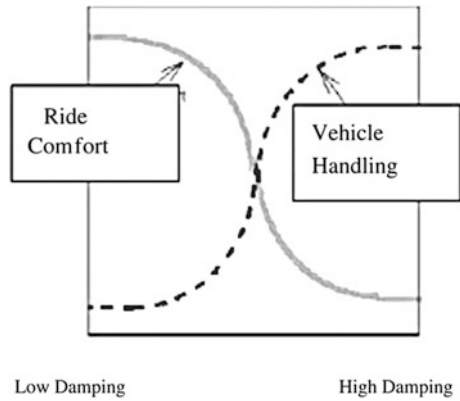
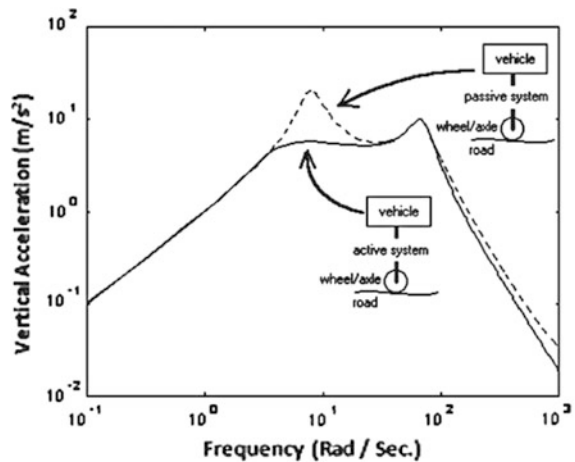


Fig. 2 Strategy for betterment of ride comfort



In semi-active suspension system, the variable dampers of different types are used along with a suspension spring. In the active suspension system, actuator is placed between the sprung and unsprung masses and with a correct control strategy there is possibility of improvement is shown in Fig. 2. The vehicle suspension system have been researched exhaustively by many researchers from all over the continents since long and now have reached to a very high level of sophistication. Crolla [1] has discussed that the extent to which theory has been put into practice in vehicle ride and handling performances. This paper provides the basic for road dynamic, handling dynamic, active control and vehicle dynamics. Dahlberg [2] has presented the suspension system of two degree freedom (2-DOF) vehicle travelling on randomly corrugated road is optimised with respect to both road holding and ride comfort. In this paper a linear 2-DOF system is used as a model for road vehicle for optimization. A conclusion is that an active suspension system could be controlled by the speed. Hrovat [3] demonstrates the connection between optimal

one and two degree of freedom vehicle structure consisting active suspensions. It is shown that the resulting, special one DOF system represents the limits of the best possible performance. Basari et al. [4] have presented the investigation on performance of nonlinear active suspension system with backstepping strategy. Dynamic model of suspension system has the rotational motion of control arm. Backstepping control is recursive control procedure which breaks a design problem for full system. Allenyne et al. [5] demonstrates analysis of a particular force tracking controls problem for rectilinear hydraulic actuators, and uses a revealing model reduction in classical analysis to explain physical phenomenon. Kaddassi et al. [6] have studied the control of an electro hydraulic active suspension with back stepping methodology. The active suspension system is extremely non liner due to the hydraulic components with the servo-valve and hence the powerful control strategy is needed. Kim et al. [7] has developed a model for an automotive suspension system which includes the dynamics of asymmetric hydraulic actuators. this model describes the force exerted by a single rode cylinder is considered as an internal state and the sum of oil flow rates through the orifice of servo valve as control input. Kaddassi and Kenne [8] have studied the real time position control of an electro hydraulic system using indirect adaptive back stepping, in which the hydraulic parameters variations occurs, it is therefore useful to utilize an adaptive control strategy in for update the controller with parameter variations.

From this review of research papers, it is seen that there is a ample scope to analyse the quarter car suspension system experimentally as well as theoretically, for improved vehicle characteristics by using some alternative methodologies with simulation technique using MATLAB SIMULINK software. Hence the conventional passive system has been modified to hydraulic assisted quarter car active suspension system (HA-QCSS) by placing a hydraulic actuator in between sprung and unsprung masses with required instrumentation. The results show considerable improvement in vehicle ride characteristics over the conventional passive system.

2 Development of Prototype of Quarter Car

The development of prototype of quarter car consists of designing of the various components of the prototype for experimental analysis. The components of the prototype has been designed and developed by referring standard SAE data of small passenger car with a mass ratio of 5. The physical prototype of 2 DOF quarter car has been developed for both passive quarter car active suspension system (P-QCSS) and hydraulic assisted quarter car active suspension system (HA-QCSS). The developed quarter car model consists of structure base, unsprung mass plate; two sprung mass Plates attached together.

2.1 2 DOF P-QCSS Model

The physical prototype of 2 DOF P-QCSS is developed, as shown in Fig. 3. The physical prototype is consist of structure base, unsprung mass plate, Two sprung mass Plates attached together as shown in Fig. 3. In the experimental test rig DC motor is used to drive the cam and follower system which is used for providing harmonic base excitation at desired amplitude and frequency to the base of unsprung mass plate. The DC motor and cam follower system is placed on a rigid cast iron base fixed on a firm concrete foundation.

The design calculation and selection of material has been carried out and the safe values for each of components selected with required factor of safety by referring the design data book. Design parameter for each component for passive suspension is given in Table 1. The shock Absorber with suspension spring and damper, Four springs below unsprung mass representing tyre stiffness, Four vertical circular bars for support and free vertical motion of plates, one upper plate for supporting bars used for development of physical setup. For experimental analysis instrumentation carried out for obtaining the real time-based data for sprung mass displacement and base excitation using FFT interface system.

Fig. 3 Physical prototype of 2 DOF P-QCSS

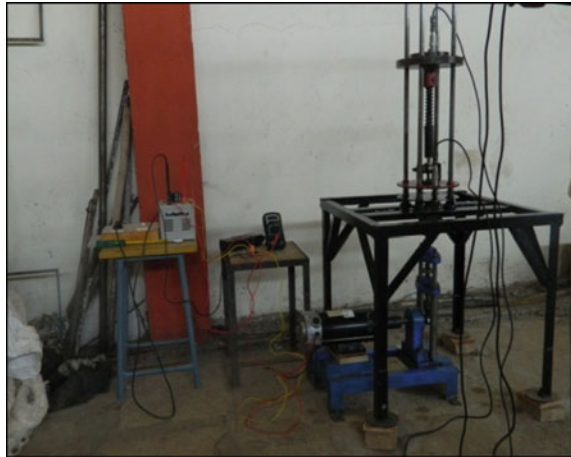


Table 1 Design parameter values for 2 DOF passive suspension system test rig

Parameter	Values
Sprung mass	8 kg
Unsprung mass	1.5 kg
Suspension spring stiffness	7950 N/m
Suspension damping coefficient	275 Ns/m
Tire spring stiffness	85,000 N/m

2.2 2 DOF HA-QCSS Model

Hydraulic assisted quarter car active suspension system adds hydraulic actuator to the passive components of passive suspension system to convert it to a 2 DOF hydraulic assisted quarter car active suspension system as shown in Fig. 4.

Block diagram of control system used to develop hydraulic assisted active suspension system is shown in Fig. 4. In order to develop hydraulic assisted active suspension system, the following hydraulic components has been used.

1. Pressurized hydraulic fluid source.
2. Servo valve to control the pressure of hydraulic fluid to hydraulic actuator.
3. Hydraulic actuator to convert the hydraulic pressure into force to be transmitted between the sprung and the unsprung mass.

In the hydraulic assisted quarter car active suspension system for actuation of the hydraulic actuator the advanced electromechanical servo valve (MOOG G761) has been used. The system has been controlled by PIC 16F870 Microcontrollers which is designed to meet the requirement. Figure 5 shows schematic of the hydraulic actuator and installed electromechanical servo valve top view as used in experimental test rig.

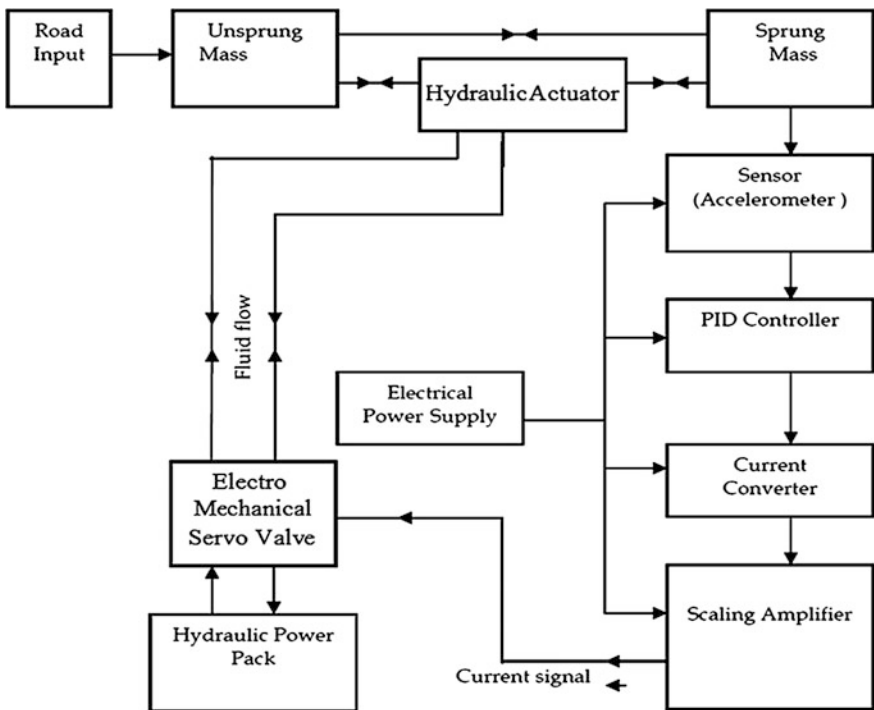


Fig. 4 Block diagram of control system used to develop active suspension system

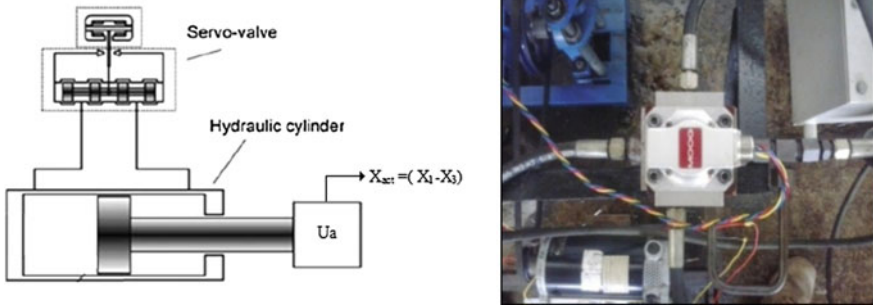


Fig. 5 Hydraulic actuator with servo valve and top view of installed electromechanical servo valve

This developed 2 DOF quarter car test set up for passive and hydraulic active suspension system is further used for the experimental analysis.

3 Simulation Analysis

The simulation analysis of 2 DOF quarter car passive suspension systems and 2 DOF hydraulic assisted quarter car active suspension system has been carried out. The response of the system is simulated by using MATLAB SIMULINK 2010 software. The acceleration amplitude has been taken as critical performance parameter because it is the most sensitive parameter than displacement amplitude or velocity amplitude. Figure 6 shows 2 DOF hydraulic assisted quarter car active suspension system.

3.1 Development of Program in SIMULINK for 2 DOF P-QCSS Model

A 2 DOF quarter-car model of passive suspension system is shown in Fig. 7. The sprung mass M_s represents mass of body. The unsprung mass M_{us} represent the equivalent mass due to the axle and tire. The vertical stiffness of the tire is represented by K_t , K_s for suspension spring stiffness and C_s damper coefficient. The variables X_s , X_{us} and r represent the vertical displacements from static equilibrium of the sprung mass, unsprung mass and the road respectively.

From Fig. 7 motion equations are as the following:

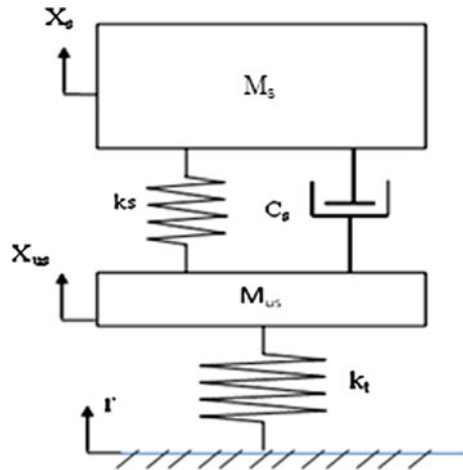
$$M_s \ddot{x}_s + K_s(x_s - x_{us}) + C_s(\dot{x}_s - \dot{x}_{us}) = 0$$

$$M_{us} \ddot{x}_{us} + K_s(x_{us} - x_s) + C_s(\dot{x}_{us} - \dot{x}_s) + K_t(x_{us} - r) = 0$$

Fig. 6 2 DOF hydraulic assisted quarter car active suspension system



Fig. 7 Schematic of 2 DOF quarter car passive suspension system model



The value of C_t for tires, compared to C_s , is very small, and hence, it is neglected to simplify the model. Using the state variables

$$\begin{aligned}
 x_1 &= x_s - x_{us} \\
 x_2 &= \dot{x}_s \\
 x_3 &= x_{us} - r \\
 x_4 &= \dot{x}_{us}
 \end{aligned}$$

where,

- $x_s - x_{us}$ suspension travel,
- \dot{x}_s sprung mass velocity,
- $x_{us} - r$ unsprung mass deflection,
- \dot{x}_{us} unsprung mass velocity.

The above state variable has been used state space equation, the space equation have been for formulation of program in MATLAB SIMULINK software.

3.2 Development of Program in SIMULINK 2 DOF HA-QCSS Model

Figure 8 shows a 2 DOF quarter-car modified to hydraulic assisted quarter car active suspension system by placing actuator as shown in Fig. 8. The model consists of all components in passive system with hydraulic actuator with an active control force u_a .

From Fig. 8 motion equations are as the following:

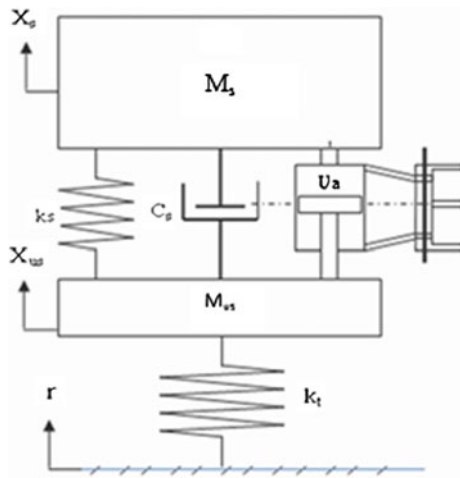
$$M_s \ddot{x}_s + K_s(x_s - x_{us}) + C_s(\dot{x}_s - \dot{x}_{us}) - u_a = 0$$

$$M_{us} \ddot{x}_{us} + K_s(x_{us} - x_s) + C_s(\dot{x}_{us} - \dot{x}_s) + K_t(x_{us} - r) + u_a = 0$$

where, u_a is the control force from hydraulic actuator.

Using the state variables $x_1 = x_s - x_{us}$, $x_2 = \dot{x}_s$, $x_3 = x_{us} - r$, $x_4 = \dot{x}_{us}$.

Fig. 8 Schematic of 2 DOF hydraulic assisted quarter car active suspension system



The above state variable has been used state space equation, the space equation have been for formulation of program in MATLAB SIMULINK software.

$$\begin{aligned}\dot{x} &= A(t)x(t) + B(t)u(t) \\ y(t) &= C(t)x(t) + D(t)u(t)\end{aligned}$$

4 Experimental Analysis

The performance analysis, the experimentation on the 2 DOF Quarter Car Test Rig, is carried out by employing state-of-the-art 4 Channel ADASH FFT Analyzer along with DDS 2011 Data Acquisition and Interpretation platform. The experimental analysis has been carried out with following sequence. Quarter car model was connected with the instrumentation as shown in Fig. 3. After completing the connection the power supply has been switched ON and by using voltage regulator DC motor set as per the requirement. The accelerometers are attached simultaneously on unsprung mass and sprung mass of the suspension test rig system. The cable of unsprung mass accelerometer was connected to the channel no. 1 of the FFT analyser for vertical acceleration of unsprung mass of the suspension system test rig. After connecting the accelerometers to channel no. 1 and 2 of the FFT, the exciter system has switched ON. After recording was completed, the FFT analyzer was connected to the computer for post processing the data and analyzing the results have been recorded.

4.1 Experimental Results of 2 DOF P-QCSS and HA-QCSS

Necessary instrumentation has been developed and, using FFT interfacing system vertical acceleration responses $\ddot{x}_s(t)$ and $\ddot{x}_{us}(t)$ have been recorded for sprung and unsprung masses when excitation frequency was set between 1 and 10 Hz.

It is seen from the results given in Table 2 that the maximum sprung mass acceleration of $7.76 \times 10^{-6} \text{ m/s}^2$ (Fig. 9b) for hydraulic assisted active suspension system has been obtained at frequency of 3 Hz where as for the passive system at the same frequency the sprung acceleration was obtained as $4.35 \times 10^{-5} \text{ m/s}^2$ (Fig. 9a). The maximum reduction of 82% in sprung mass acceleration was obtained for the same frequency of 3 Hz. The response obtained from the system at this frequency gives considerable reduction in the vertical vibration level, so it is observed that there is considerable improvement in the ride comfort characteristics of 2 DOF quarter car hydraulic assisted active suspension systems. The maximum reduction in sprung mass acceleration is obtained at 4 Hz frequency which is almost 92% (Fig. 10a, b). Whereas at 6 Hz, the sprung mass acceleration of

Table 2 Experimental results

Frequency in Hz	Sprung mass acceleration (m/s ²)		% Reduction
	P-QCSS	HA-QCSS	
3	4.35×10^{-5}	7.76×10^{-6}	82
4	8.42×10^{-6}	6.32×10^{-7}	92
5	3.40×10^{-5}	8.43×10^{-6}	75
6	9.9×10^{-6}	6.2×10^{-6}	47
7	4.4×10^{-5}	9.35×10^{-6}	78
8	1.36×10^{-5}	9.4×10^{-6}	30

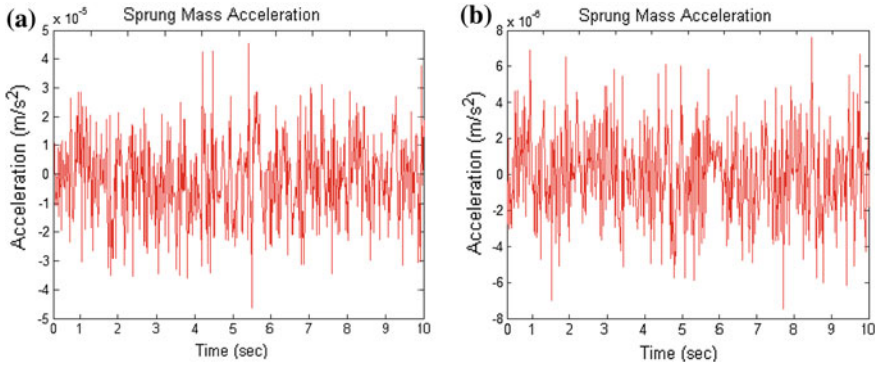


Fig. 9 Maximum sprung mass acceleration

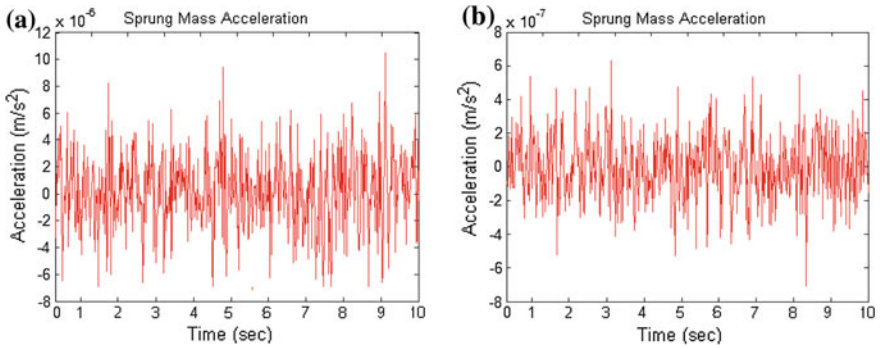


Fig. 10 Maximum reduction in sprung mass acceleration

$9.90 \times 10^{-6} \text{ m/s}^2$ has been obtained for active system and the sprung mass acceleration of $6.2 \times 10^{-6} \text{ m/s}^2$ is obtained for the passive system. So it is observed that at 6 Hz frequency the reduction is only 47%.

4.2 Simulation Results of 2 DOF P-QCSS and HA-QCSS

It is seen from the results given in Table 3 that the maximum sprung mass acceleration of $7.97 \times 10^{-6} \text{ m/s}^2$ (Fig. 11b) for hydraulic assisted active suspension system has been obtained at frequency of 3 Hz where as for the passive system at the same frequency the sprung acceleration was obtained as $4.0 \times 10^{-5} \text{ m/s}^2$ (Fig. 11a). The maximum reduction in sprung mass acceleration is obtained at 3 Hz frequency i.e. 80% (Fig. 12a, b). The response obtained from the system at this frequency gives considerable reduction in the vertical vibration level, so it is observed that there is considerable improvement in the ride comfort characteristics of 2 DOF Quarter Car Hydraulic Active Suspension System.

Table 3 The simulation results using MATLAB SIMULINK

Frequency in Hz	Sprung mass acceleration (m/s^2)		% Reduction
	P-QCSS	HA-QCSS	
3	4.0×10^{-5}	7.97×10^{-6}	80
4	1.19×10^{-5}	6.3×10^{-6}	47
5	3.3×10^{-5}	8.15×10^{-6}	75
6	1.32×10^{-5}	8.29×10^{-6}	37
7	4.3×10^{-5}	9.1×10^{-6}	78
8	1.45×10^{-5}	9.15×10^{-6}	38

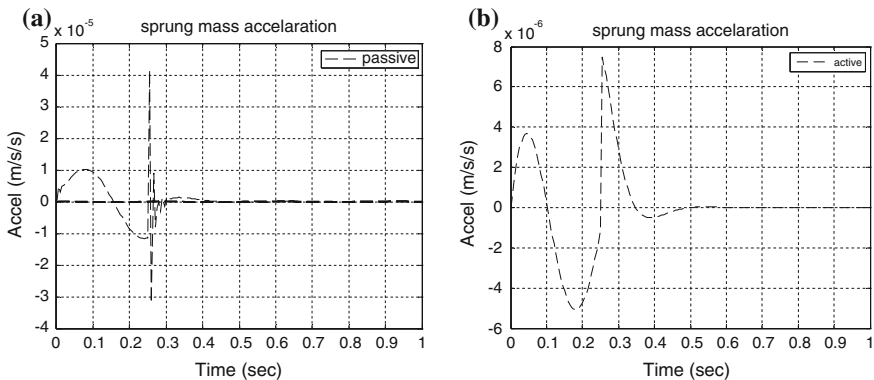


Fig. 11 Sprung acceleration was obtained as $4.0 \times 10^{-5} \text{ m/s}^2$

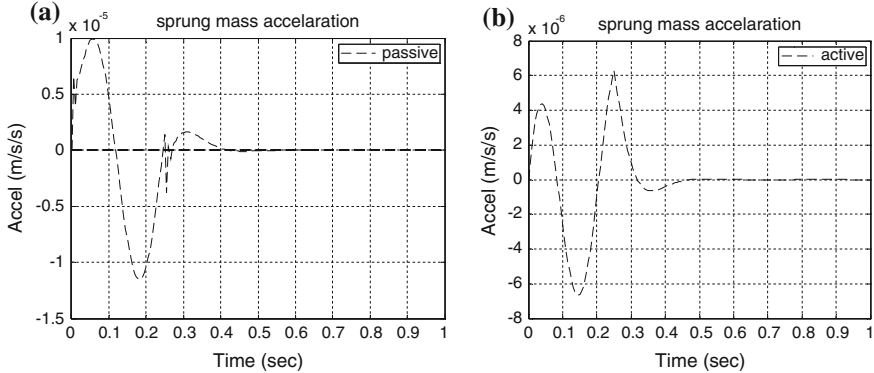


Fig. 12 Sprung mass acceleration is obtained at 3 Hz

5 Conclusion

In the light of the above-mentioned objective a quarter car 2 DOF passive quarter car suspension systems and 2 DOF hydraulic assisted active quarter car suspension system to obtain the improved vehicle characteristic, simulation and experimental analysis has been carried out and bounce response of sprung mass of quarter car suspension system model, in terms of vertical acceleration has been recorded. With developed experimental test set up for the 2 DOF quarter car passive suspension system and 2 DOF quarter active suspension system models, experimental and simulation analysis has been carried out. The vertical bounce characteristic in terms of acceleration of sprung mass and unsprung mass has been obtained for a excited frequency range of 3–8 Hz. It is observed that the 2 DOF quarter car hydraulic active suspension systems has shown significant improvement in ride parameters over that of the 2 DOF quarter car passive suspension systems. The values of active suspension parameters reduced substantially, over a range of excitation frequencies near the region of resonance. Thus by implementation of hydraulic assisted quarter car active suspension (HA-QCSS), the ride comfort of the occupants is improved to a reasonable degree.

References

1. Crolla DA (1996) Vehicle dynamics—theory into practice. In: The proceedings of the institution of mechanical engineers, research in automobile stability and control and in tyre performance, vol 210. IMech
2. Dahlberg T (1978) Ride comfort and road holding of A 2-DOF vehicle travelling on a randomly profiled road. *J Sound Vib* 58(2):179–187
3. Hrovat D (1990) Optimal active suspension for quarter car vehicle models. *Automats* 26(5):860
4. Basari AA et al (2007) Control of a quarter car nonlinear active suspension system. In: 2007 Asia-Pacific conference on applied electronics proceedings, 4–6 2007, Melaka

5. Allenyne A et al (1998) On the limitations of force tracking for hydraulic active suspension. In: Proceedings of the American control conference Philadelphia, Pennsylvania, June 1998
6. Kaddassi C et al (2005) Drive by wire control of an electro-hydraulic active suspension a backstepping approach. In: Proceedings of the 2005 IEEE control applications Toronto, Canada, 28–31 Aug 2005
7. Kim W et al (2001) Modelling and control for an asymmetric hydraulic active suspension system. JSME Int J Ser C No. 2
8. Kaddissi C, Kenne J-P (2011) Indirect adaptive control of an electro-hydraulic servo system based on nonlinear backstepping. IEEE/ASME Trans Mechatron 16(6)

Sheet Metal Piercing Punch Material Selection Using Complex Proportional Assessment Method

D.P. Hase and V.S. Gadakh

Keywords Material selection · Properties · Decision making · COPRAS method

1 Introduction

Press working is a chipless manufacturing process by which various components are made from sheet metal. During the sheet metal cutting operation the workpiece is stressed beyond its ultimate strength. The stresses caused in metal by the applied forces will be shearing stresses. Piercing is a metal cutting process that uses a punch press force a tool through the workpiece to create a hole diameter via shearing action takes when a punch and die are used [1, 2].

Punch is used in punching, blanking operations selecting the proper punch material for a particular punching operation. A correct punch material for particular piercing operation can give advantages including improved productivity increased material quality decreased cost, fine surface finish, minimized scrap material and consumption energy. Press tool failure investigations found five main failures such as wear, chipping, plastic deformation, cracking and galling. To avoid above failures of press components during the sheet metal operations tool steel material should have harder than sheet material. The tool material should have high hardness, good resistance to wear and plastic deformation, high microstructural toughness for resistance to cracking, high ductility for good resistance to chipping and low coefficient of friction between the tool surface and the sheet metal [2, 3].

To fulfill the requirement of the metal stamping industries, researchers have introduced and developed numerous multi criteria approaches and system for selection of appropriate materials. Wang and Chang [4] proposed a fuzzy multi-criteria decision-making (MCDM) approach to help selecting the best suited tool steel material for a specific manufacturing application, such as die design, jig and fixture design. Jee and Kang [5] applied techniques for order preference by

D.P. Hase (✉) · V.S. Gadakh
Amrutvahini College of Engineering, Sangamner 422608, Maharashtra, India
e-mail: dhanraj7hase@gmail.com

similarity to ideal solution (TOPSIS) method to solve a flywheel material selection problem taking into considerations several technical requirements simultaneously and also used entropy approach to evaluate the weights of material selection attributes. Chan and Tong [6] presented an integrated methodology of constructing an order pair of materials and end-of-life product strategy for material selection using grey relational analysis approach. Chatterjee et al. [7] suggested resolving material selections problems using two almost new MCDM methods, i.e. complex proportional assessment (COPRAS) method and evaluation of mixed data (EVAMIX) methods. These two methods were used to rank the alternative materials, for which several requirements were considered simultaneously approaches. Maity et al. [8] considered an exhaustive list of 19 cutting tools materials and evaluated their performances based on ten selection criteria. Grey COPRAS method was then applied to solve the cutting tool material selection problems considering grey data in the decision matrix.

It is found that literature lacks information on material selection of press tool components using MCDM method. Hence, in this paper a systematic evaluation model was proposed to help the press tool die designers for the optimum press tool material selection among the available alternatives in market. Entropy method was used to determine criteria weights and then alternative materials were ranked using COPRAS method in order to find out the best material for the press tool components by considering different material selection criteria's.

2 Multi-criteria Decision-Making Method

2.1 Complex Proportional Assessment Method

This preference ranking method of complex proportional assessment method, mainly developed by [9] assumes direct and proportional dependences of the priority and utility degree of the available alternatives under the presence of mutually conflicting criteria. It takes into account the performance of the alternatives with respect to different criteria and the corresponding criteria weights. The decision approach allows evaluating the direct and proportional dependence of the significance and utility degree of alternatives in a system of attributes, weights, and values of the attributes. The method determines a solution with the ratio to the ideal solution and the ratio with the best and worst solution. The degree of utility is determined by comparing the analysed alternatives with the best one. The values of the utility degree are from 0 to 100% between the worst and the best alternatives. The method is used here for evaluating and selecting the best punch material alternative for the given application uses a stepwise ranking and evaluating procedure of the alternatives in terms of their priority and utility degree. This method has already been successfully applied to solve various problems in the field of vendor selection and assessment [9, 10], material selection property management,

economics, etc. The procedural steps of the COPRAS method are presented as below [7].

The steps for COPRAS method are presented as below:

Step 1: Develop the decision matrix, X.

$$X = [x_{ij}]_{m \times n} \begin{bmatrix} x_{11} & x_{12} & \dots & x_{1n} \\ x_{21} & x_{22} & \dots & x_{2n} \\ \dots & \dots & \dots & \dots \\ x_{m1} & x_{m2} & \dots & x_{mn} \end{bmatrix} \tag{1}$$

where x_{ij} is the performance value of i th alternative on j th criterion, m is the number of alternatives compared and n is the number of criteria ($i = 1, 2 \dots m; j = 1, 2 \dots n$).

Step 2: Normalize the decision matrix using the following equation. The purpose of the normalization is to obtain dimensionless values of different criteria so that all of them can be compared.

$$R = [r_{ij}]_{m \times n} = \frac{x_{ij}}{\sum_{i=1}^m x_{ij}} \quad j = 1, 2, \dots, n; \quad i = 1, 2, \dots, m \tag{2}$$

Step 3: Determine the weighted normalized decision matrix, D.

$$D = [y_{ij}]_{m \times n} = r_{ij} \times w_j \quad j = 1, 2, \dots, n; \quad i = 1, 2, \dots, m \tag{3}$$

where r_{ij} is the normalized performance value of the i th alternative on j th criterion and w_j is the weight of j th criteria. The sum of dimensionless weighted normalized value of each criterion is always equal to weight for that criterion.

$$\sum_{i=1}^m y_{ij} = w_j \tag{4}$$

In other words it can be said that the weight, w_j of the investigated criterion is proportionally distributed among all the alternative according to their weighted normalized value, y_{ij} .

Step 4: The sums of weighted normalized values are calculated for both the beneficial attributes and non-beneficial attributes. The lower is value of non-beneficial attribute, such as cost, the better is the attainment of goal. On other hand, the larger is value of beneficial attribute, such as performance, the attainment of the goal is good.

These sums are calculated using the following equations.

$$S_{+i} = \sum_{j=1}^n y_{+ij} \tag{5}$$

$$S_{-i} = \sum_{j=1}^n y_{-ij} \tag{6}$$

where y_{+ij} and y_{-ij} are the weighted normalized value for the beneficial and non-beneficial attributes respectively.

The larger value of S_{+i} , alternative is the better and smaller value of S_{-i} alternative is the better. The S_{+i} and S_{-i} values express the degree of goals attained by each alternative. In any case, the sums of pluses S_{+i} and minuses S_{-i} of the alternatives are always respectively equal to the sums of weights for the beneficial and non-beneficial attributes as expressed by following equations.

$$S_{+} = \sum_{i=1}^m S_{+i} = \sum_{i=1}^m \sum_{j=1}^n y_{+ij} \tag{7}$$

$$S_{-} = \sum_{i=1}^m S_{-i} = \sum_{i=1}^m \sum_{j=1}^n y_{-ij} \tag{8}$$

In this way, Eqs. (7) and (8) can be used to verify the calculation.

Step 5: Determine the relative significances or priorities of the alternatives. The priorities of the candidate alternatives are calculated on the basis of Q_i . The greater the value of Q_i , the higher is the priority of the alternative. The relative significance value of an alternative shows the degree of satisfaction attained by that alternative. The alternative with the highest relative significance value Q_{max} is the best choice among the candidate alternatives.

Relative significance value (priority), Q_i of the i th alternative can be obtained below:

$$Q_i = S_{+i} + \frac{S_{-min} \sum_{i=1}^m S_{-i}}{S_{-i} \sum_{i=1}^m (S_{-min}/S_{-i})} \quad (i = 1, 2, \dots, m) \tag{9}$$

where S_{-min} is the minimum value of S_{-i}

Step 7: Calculate the quantitative utility U_i for i th alternative. The degree of an alternative's utility is directly associated with its relative significance value Q_i . The degree of an alternative's utility, leading to a complete ranking of the candidate alternatives, is determine by comparing the priorities of all the alternatives with the most efficient one and can be denoted as below:

$$U_i = \left[\frac{Q_i}{Q_{max}} \right] \times 100\% \tag{10}$$

where Q_{max} is the maximum relative significance value. With increase or decrease in the value of the relative significance for an alternative, it is observed that its degree of utility also increases or decreases. These utility values of the candidate

alternatives range from 0 to 100%. Thus, this approach allows for evaluating the direct and proportional dependence of significance and utility degree of the considered alternatives in a decision-making problem involving multiple criteria, their weights and performance value of the alternatives with respect to all the criteria.

3 Illustrative Example

In order to demonstrate and validate the COPRAS method for solving material selection problem, the following real time example is illustrated.

This example deals with the selection of the most appropriate material for punch of piercing die for press tool. Figure 1 shows that piercing die punch failure. During piercing operation of automobile sheet metal there is punch failure occurs. From the root cause analysis of punch failure, it was found that the material AISI D2 is defective one. Then it was decided that eliminate punch failure in piercing operation with cost effective solution. For the appropriate material selection of punch for press tool, have high hardness, adequate toughness, good resistance to softening, higher wear resistance and good machinability. Eight criteria's were selected from namely, cost in INR/Kg (C1), hardness in HRC (C2), non-deforming properties (C3), safety in hardness (C4), toughness (C5), resistance to softening effect of heat (C6), wear resistance (C7), and machinability (C8) [4] while selecting the most suitable material for designing a punch. Among these eight criteria's, hardness, non-deforming properties, safety in hardness, toughness, resistance to softening, effect of heat, wear resistance, and machinability are beneficial attributes where higher values are

Fig. 1 Punch failure. *Source* Hillman Gear Pvt. Ltd., Nashik



Table 1 Data of example [12–14]

AISI steel no.	C1	C2	C3	C4	C5	C6	C7	C8
D2	290	61	B	B	F	F	G	L
D3	195	61	G	B	L	F	B	L
A2	350	62	B	B	G	F	G	G
M2	800	64	G	G	G	B	B	F
M4	800	65	G	G	G	B	B	F

B best, *G* good, *M* medium, *F* fair and *L* low

Table 2 Decision matrix

Material	C1	C2	C3	C4	C5	C6	C7	C8
D2	290	61	5	5	2	2	4	1
D3	195	61	4	5	1	2	5	1
A2	350	62	5	5	4	2	4	4
M2	800	64	4	4	4	5	5	2
M4	800	65	4	4	4	5	5	2

Table 3 Weighted normalized decision matrix

Material	C1	C2	C3	C4	C5	C6	C7	C8
D2	0.0001	0.0051	0.0057	0.0054	0.0001	0.0002	0.0822	0.0441
D3	0.0007	0.0051	0.0045	0.0054	0.0001	0.0002	0.1027	0.0440
A2	0.0012	0.0052	0.0057	0.0054	0.0002	0.0002	0.0822	0.1764
M2	0.0027	0.0055	0.0045	0.0043	0.0002	0.0005	0.1027	0.0882
M4	0.0027	0.0055	0.0045	0.0043	0.0002	0.0005	0.1027	0.0882

desirable; on the other hand, cost is non-beneficial attribute where smaller values is preferable. Five different materials AISI D2, AISI D3, AISI A2, AISI M2 and AISI M4 were considered as candidate alternative. These materials are chosen by tool steel availability in market. Thus, the decision matrix of this MCDM problem consists of five alternative materials and eight criteria’s as shown in Table 1. The linguistic terms in Table 1 are converted into 0–5 scale as shown in Table 2 [11].

3.1 COPRAS Method

In this method, the decision matrix shown in Table 2 is first normalized using Eq. (2) and the corresponding weighted normalized decision matrix is constructed, as given in Table 3. The entropy method [7] is employed to determine different criteria weights as $W_{C1} = 0.0081$, $W_{C2} = 0.0263$, $W_{C3} = 0.0249$, $W_{C4} = 0.0250$, $W_{C5} = 0.0007$, $W_{C6} = 0.0016$, $W_{C7} = 0.4724$ and $W_{C8} = 0.4411$. The sum of all these weights are 1.

Now, the sums of the weighted normalized values are computed for both the beneficial attributes (S_{+i}) and non-beneficial attributes (S_{-i}) using Eqs. (5) and (6)

Table 4 Sum of weighted normalized values

Material	S_{+i}	S_{-i}
D2	0.1428	0.0009
D3	0.1621	0.0006
A2	0.2753	0.0012
M2	0.2058	0.0026
M4	0.2059	0.0026

Table 5 Q_i and U_i values

Material	Q_i	U_i	Rank
D2	0.1448	52.29	5
D3	0.1651	59.62	4
A2	0.2769	100	1
M2	0.2065	74.57	3
M4	0.2066	57.61	2

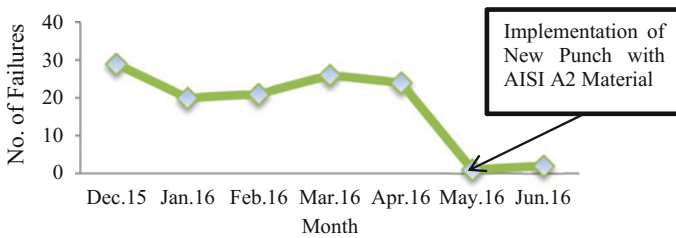


Fig. 2 Trend chart for punch failure after modification in die

respectively, as shown in Table 4. Table 5 shows the quantitative utility (U_i) value for each alternative material. Then, according to the descending values of (U_i), the alternative materials are ranked to fulfill the design requirements of the product.

COPRAS method gives the ranking of materials as 5-4-1-3-2. The best choice of material for the given application is material AISI A2. Material AISI M4 is the second choice and the last choice is material AISI D2. The advantage of COPRAS method is that it shows in what percent one alternative is better than another one [9]. It is a task of the degree of utility. The degree of utility (U_i) of the alternative indicates best to worst material selection process. The more goals are achieved and the more important they are, the higher is the degree of utility. In this Example, the preference of the difference between the utility degree of third alternative AISI A2 is 100% and the first alternative shows that the third alternative AISI D2 is 52.29% more useful than the first alternative by 44.71%. For the selection of any phenomenon, a unique performance criterion having higher value is desirable. In such a case, the decision-maker can directly select the alternative which gives higher performance without applying any statistical tool or method and rank them in descending order of their preference.

To understand the effectiveness of result it was required to monitor the results carefully, for this results were monitored for failure in field and results were plotted

and failure per month trend was monitored. Figure 2 shows trend chart for punch failure after modification in die Failure per month trend chart shows improvement and failure rate was drastically reduced which proves solution implemented is giving good results in actual application.

4 Conclusion

In this paper, COPRAS method is proposed for selection of punch material. The most appropriate punch material is selected among various alternatives, since data of different material given in the design handbook. In this work, five alternative materials and eight criteria were used for piercing punch material selection. AISI A2 tool steel use as suitable punch material and AISI D2 tool steel found worst chosen material. The application of the COPRAS method is suggested for decision-making in the punch material selection which helps in selecting the most suitable alternative from among a set of candidate alternatives for a given problem. The COPRAS method can consider all the attributes along with their relative importance, and hence it can provide a better accurate evaluation of the alternatives. The advantage of this method is that it shows in what percent one alternative is better than another one.

References

1. Sharma PC (2009) A textbook of production engineering: press tool design. S. Chand, New Delhi
2. Semiatin SL (1993) ASM forming and forging. ASM International Handbook Committee
3. Kumar S (2011) An intelligent system for selection of materials for press tools components. *J Eng Res Stud* 2:119–130
4. Wang MJJ, Chang TC (1995) Tool steel materials selection under fuzzy environment. *Fuzzy Sets Syst* 72:263–270
5. Jee DH, Kang KJ (2000) A method for optimal material selection aided with decision making theory. *Mater Des* 21:199–206
6. Chan JWK, Tong TKL (2007) Multi-criteria material selections and end-of-life product strategy: grey relational analysis approach. *Mater Des* 28:1539–1546
7. Chatterjee P, Athawale VM, Chakraborty S (2011) Materials selection using complex proportional assessment and evaluation of mixed data methods. *Mater Des* 32:851–860
8. Maity SR, Chatterjee P, Chakraborty S (2012) Cutting tool material selection using grey complex proportional assessment method. *Mater Des* 36:372–378
9. Zavadskas EK, Kaklauskas A, Turskis Z, Tamosaitiene J (2008) Selection of the effective dwelling housewalls by applying attributes values determined at intervals. *J Civil Eng Manag* 14:85–93
10. Gadakh VS (2013) Applications of complex proportional assessment method for vendor selection. *Int J Logistics: Res Appl* 17:23–34

11. Farag MM (2002) Quantitative methods of material selection: comparing alternative solutions. Handbook of material selection
12. Davis JR (1998) ASM metals handbook: tool steels. ASM International Handbook Committee
13. Smith DA (1990) Ferrous die materials: die materials and treatments. Die Design Handbook
14. Bayer AM Vasco T Walton LR (1990) ASM properties and selection: irons, steels, and high-performance alloys. ASM International Handbook Committee

Investigation of Thermal Performance of FRP Parabolic Trough Collector Using Different Receivers

Satish Aher, Atul Sagade and Narayani Sagade

Keywords Solar parabolic collector · Solar thermal heat for an industrial process · Solar collector materials · Selective coatings

1 Introduction

Solar and renewable heating is growing at a large rate all over the world. Especially, the hotter climatic counties planned to utilize full potential solar heating. From the Indian perspective, solar thermal systems can play a vital role in different low temperature (800–1500 °C) applications. The upcoming section discusses, a brief literature reported by researchers all over the world which explores the performance of such low temperature solar thermal systems that can be effectively implemented for domestic and industrial applications. García et al. [1] represents the overview of parabolic-trough collectors that were built and marketed during the past century, as well as the prototypes currently under development. This work also presents a survey of systems which could incorporate this concentrating solar system to supply thermal energy up to 400 °C, especially steam power cycles for electricity generation, including examples of each application. Tsai and Lin [2] proposed as a solar thermal concentrator system that is comprising a cylindrical heat pipe receiver and a variable-focus-parabolic-trough (VFPT) reflector. The authors analyzed the concentrator system using a ray tracing approach and optimized the geometry of the

S. Aher (✉)

Amrutvahini College of Engineering, Sangamner, Maharashtra, India
e-mail: satish1910@gmail.com

A. Sagade

New Satara College of Engineering and Management (Polytechnic), Korti-Pandharpur
413304, Maharashtra, India

N. Sagade

REIRF, Pandharpur 413304, Maharashtra, India

concentrator system for uniform irradiance distribution on the heat-pipe surface. They showed that the optimized VFPT concentrator yields a significant improvement in the irradiance uniformity and the heating efficiency compared to conventional cylindrical-trough and parabolic trough concentrators. Huang et al. [3] proposed a new analytical model for optical performance and a modified integration algorithm are proposed and applied to simulate the performance of a parabolic trough solar collector with vacuum tube receiver. The authors discussed the effects of different optical and design optical error, tracking error, position error from an installation of a receiver, optical properties of a reflector, transmittance and absorptivity of the vacuum tube receiver on the efficiencies of the trough system. Eck and Zerza [4] studied the direct steam generation (DSG) in parabolic trough collectors for solar thermal electricity generation as a part of pre-commercial DSG solar thermal power plant with the aim of minimizing the risk for potential investors. They investigated the DSG with steam cycles using superheated steam and concluded on the advantages, disadvantages, and design considerations of a steam cycle operated with saturated steam. Kalogirou [5] detailed thermal model of a parabolic trough collector and the thermal analysis of the collector–receiver system was done by considering all the modes of heat transfer. He developed a mathematical model and it validated with known performance of existing collectors and performed an analysis of the collector–receiver system described in his work. Tao et al. [6] explored an operation principle and design method of a new trough solar concentrator. They analyzed and optimized the new concentrator for design parameters. They commented on the applicability of their newly designed reflector for better thermal performance and indicated that the new concentrator can realize reflection, focusing for the sunlight using multiple curved surface compound method. Kalogirou et al. [7] compared the advantages and disadvantages of concentrating collectors against conventional flat-plate collectors. They designed a parabolic-trough solar collector system to optimize collector–aperture and rim angle and the receiver diameter selection. They showed that the variation in the collector characteristic curve can contribute to minimizing heat losses from the receiver. Sagade et al. [8–10] reported the thermal performance of the compound parabolic trough collector with the top glass cover for industrial heating. They explained the effect of receiver temperature and application of different absorber selective coatings on the thermal performance of parabolic trough using regression models. They concluded that the glass covered trough system can able to reduce heat losses from the absorber and may increase the life of the collector–receiver assembly. Sagade [11, 12] used parabolic dish collector for instant water heating application and investigated the effect of variation in natural and force convective heat losses and mass flow rates on the thermal performance of the proposed system. He reported instantaneous efficiencies of 63% and 48% for a parabolic dish- receiver system with coated and non-coated receivers. Although there is a massive similar literature is available on the proposed topic, but cannot be accommodated here because of space limitation. It is important to note that, the proposed system is designed with the aim of standalone low temperature industrial and domestic heating.

2 Theory of Basic Thermal Performance

The thermal performance of the proposed system can be evaluated using conventional equations and described in the upcoming section. The useful energy delivered from the concentrator can be calculated using Eqs. (1) and (2) [13, 14].

$$Q_u = mc_p(T_{out} - T_{in}) \quad (1)$$

$$Q_u = mc_p \left[\frac{CS}{U_l} + T_{air} - T_{in} \right] \left[1 - \exp \left\{ - \frac{F' \pi D_o U_l L}{mc_p} \right\} \right] \quad (2)$$

where,

- Q_u Useful energy delivered from the concentrator (W)
- m Mass flow rate (kg/s)
- T_{out} Outlet fluid temperature ($^{\circ}\text{C}$)
- T_{in} Inlet fluid temperature ($^{\circ}\text{C}$)
- C_p Specific heat of water (kJ/kg $^{\circ}\text{C}$)
- C Concentration ratio
- S Incident solar flux absorbed in the absorber plate (W/m^2)
- U_l Overall heat loss coefficient ($\text{W}/\text{m}^2 \text{ } ^{\circ}\text{C}$)
- T_{air} Ambient temperature ($^{\circ}\text{C}$)
- F' Collector efficiency factor
- D_o Outer diameter of tube (m)
- L Length of concentrator (m)

The useful energy gain per unit of the collector length can be expressed in terms of the local receiver temperature T_r using Eqs. (3) and (4) [13, 14].

$$Q_{u'} = \frac{Q_u}{L} \quad (3)$$

$$Q_{u'} = \frac{Q_u}{L} = F' \left[S - \frac{U_l}{C} (T_r - T_a) \right] (W - D_o) \quad (4)$$

where,

- $Q_{u'}$ Useful energy gain per unit of the collector length (W)
- T_r Mean receiver surface temperature ($^{\circ}\text{C}$)
- W Width of Parabolic reflector (m)

F' is the collector efficiency factor defined by Eq. (5) [13, 14]

$$F' = 1/U_l \left[\frac{1}{U_l} + \frac{D_{outer}}{D_{in} \times h_f} \right] \quad (5)$$

$$Q_u = F_R(W - D_o)L\left[S - \frac{U_l}{C}(T_{in} - T_{air})\right] \quad (6)$$

where,

D_{in} Inner diameter of tube, (m)

h_f Heat transfer coefficient on inside surface of tube, (W/(m² °C))

F_R Collector heat removal factor

The heat removal factor can be given by Eq. (7) [13].

$$F_R = \frac{mc_p}{\pi D_{outer} \times L \times U_l} \left[1 - \exp\left\{-\frac{F' \pi D_{outer} \times U_l \times L}{mc_p}\right\}\right] \quad (7)$$

And collector efficiency can be obtained by dividing Q_u by $I_b WL$. The instantaneous collection efficiency can also be calculated by Eq. (8) [13, 14].

$$\eta_{in} = \frac{Q_u}{I_b r_b WL} \quad (8)$$

where,

η_{in} instantaneous collection efficiency

I_b Incident beam radiation (W/m²)

2.1 Overall Loss Coefficient and Heat Correlations

Overall loss coefficients based on convection and re-radiation losses per unit length were computed by Eqs. (9) and (10) [13]

$$\frac{Q_l}{L} = h_{pc}(T_{receiver} - T_c)\pi D_{outer} + \sigma\pi D_{outer}(T_r^4 - T_c^4) / \left\{ \frac{D_{outer}}{\frac{1}{\varepsilon_p} + D_{ci}\left(\frac{1}{\varepsilon_c} - 1\right)} \right\} \quad (9)$$

$$\frac{q_l}{L} = h_w(T_c - T_a)\pi D_{co} + \sigma\pi D_{co}\varepsilon_c(T_c^4 - T_a^4) \quad (10)$$

where,

T_c Temperature of cover (°C)

h_w Wind heat transfer coefficient, W/m² K

ε_p Emissivity of absorber surface for long wavelength radiation

ε_c Emissivity of cover for long wavelength radiation

2.2 Heat Transfer Coefficient Between the Absorber Tube and the Cover

The heat transfer coefficient h_{pc} for the enclosed annular space between a horizontal absorber tube and a concentric cover is calculated using Eqs. (11), (12) and (13) [13]

$$\frac{K_{eff}}{k} = 0.317(Ra^*)^{0.25} \quad (11)$$

$$(Ra^*)^{0.25} = \frac{\ln\left(\frac{D_{ci}}{D_{outer}}\right)}{b^{0.75}\left(\frac{1}{D_o^{0.6}} + \frac{1}{D_c^{0.6}}\right)} Ra^{0.25} \quad (12)$$

where Ra^* = Rayleigh's Number

Thus,

$$h_{pc} = \frac{2K_{eff}}{D_{outer} \times \ln\left(\frac{D_{ci}}{D_{outer}}\right)} \quad (13)$$

2.3 Heat Transfer Coefficient on the Inside Surface of the Absorber Tube

The convective heat transfer coefficient h_f on the inside surface of the absorber tube can be calculated. For Reynolds Number greater than 2000, the flow is turbulent and heat transfer coefficient may be calculated from Eq. 14 [13]

$$Nu = 0.023Re^{0.8}P_r^{0.4} \quad (14)$$

3 System Description

Test Setup shown in Fig. 1 consist of solar collector of a storage tank of 100 L capacity, non- return valves fitted in the pipeline to define the flow direction and control valve is used to regulate the flow rate through the circuit. The necessary instruments were attached to the apparatus and then connected to the data acquisition system. Following measuring instrument were used for the data recording.

- (i) Solar radiation—Pyranometer (Kipp and Zonen CM6b).
- (ii) Wind Velocity—Digital Anemometer (Lutron AM-4201).
- (iii) Mass flow rate—Flowmeter.
- (iv) Temperature measurements—set of J type thermocouple with digital displays.

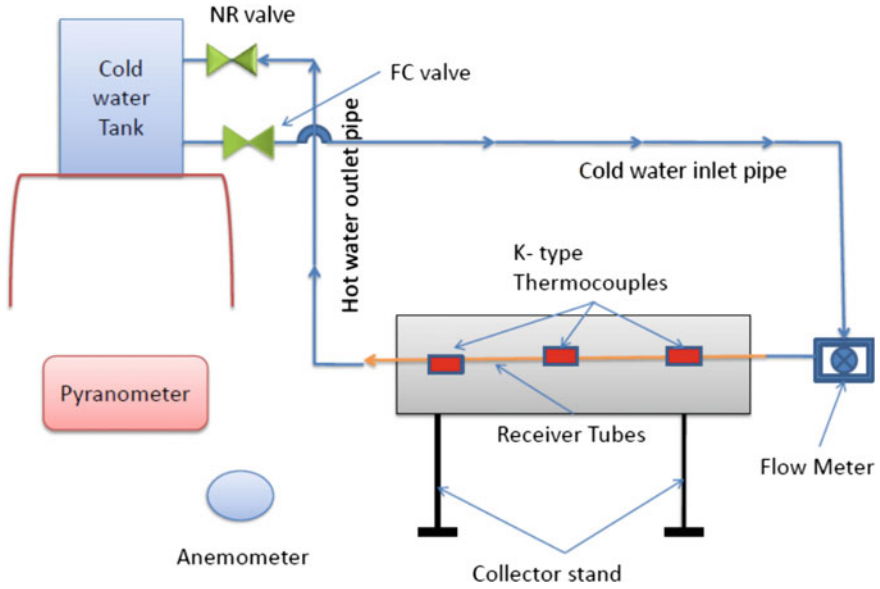


Fig. 1 Schematic diagram of test setup

Table 1 indicates the values of system parameters used in the experiments.

Table 1 Parameters used in the experimentation

System parameters	Values
Aperture of the concentrator (W)	1.10 m
Specular reflectivity of concentrator (ρ)	0.86
Outer diameter of glass tube	0.056 m
Outer diameter of absorber tube (D_o)	0.025 m
Length of parabolic trough	1.21 m
Intercept factor	0.95
Inner diameter of glass tube	0.050
Inner diameter of absorber tube (D_i)	0.020 m
Glass cover transitivity for solar radiation (τ)	0.85
Emissivity of glass (ϵ_c)	0.82
Emissivity of absorber tube surface (ϵ_p)	0.08
Concentration ratio (C)	13.69
Collector aperture area (A_c)	1.33 m ²
Absorber tube emissivity/emissivity (α)	0.15

4 Experimental Procedure

The field experiments for the current work is conducted at Shivaji University, Kolhapur at the latitude of 16.67°N and longitude of 74.25°E . At the start of every experiment, a system is flushed out to eliminate the air and other impurities in the absorber if any. The flow of water in the absorber is started and it is filled with water and the flow rate is adjusted to the required value. The whole system is exposed to the sun for over 20 min. To achieve quasi-steady state conditions before starting the experiments and checking is done for the proper working of all measuring instruments. The cold water storage tank is located above the level of the collector, to ensure that the cold water from the storage tank enters the absorber of the parabolic trough collector by gravity only and get heated up as shown in the Fig. 1. Heated water flows by thermosiphon into the top of the water tank and hot water is replaced by cold water from the bottom of the tank. The measurements of ambient temperature, fluid temperatures, receiver surface temperature, storage tank temperatures, solar radiation and wind speed were recorded at every 30 min. The experiments were performed 7 h after days from 9.00 am to 5.00 pm and each experiment is repeated for four times to check the reproducibility of the results.

During the experiment, the orientation of a cylindrical parabolic collector was kept such that its focal axis pointed in the east-west (E-W) direction and the focal axis is horizontal. Manual tracking was provided to the parabolic trough collector on experimental days. The trough was rotated about a horizontal E-W axis and adjusted manually so that the solar beam makes the minimum angle of incidence with the aperture plane at all times.

5 Results and Discussions

Figure 2 shows the variation of the inlet and outlet temperatures of water obtained with the two receivers. The trend explains that as solar radiation on receiver enhances, outlet water temperature increases. It is seen that, glass covered receivers both aluminum receiver and mild steel performs better as compared to uncovered receiver and it is possible to achieve higher outlet water temperature with a glass covered receivers. As the glass cover over the receiver acts as an insulator and outlet water temperature as well as temperature gradient between inlet and outlet water rises rapidly. It is observed that outlet water temperature and temperature gradient (i.e. The difference between the inlet and outlet water temperatures at the instant) increased by 68 and 29%, respectively, using the glass covered aluminum and mild steel receivers respectively. It is also observed that, when uncovered

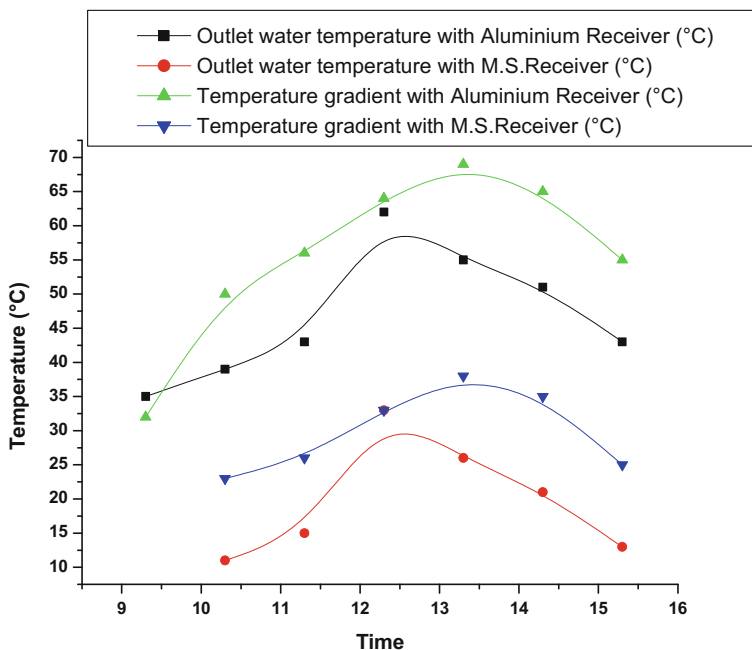


Fig. 2 Variation of outlet water temperatures and water temperature gradient throughout the day

receiver is exposed to the atmosphere, there are heavier convective heat losses from receiver due to the natural wind as compared to a glass covered receiver. But it is to be noted here that, the results of the system with uncovered receivers are not presented here as it is not the aim of the study discussed in this paper.

Figure 3 shows the effect of variation of the receiver temperature and heat loss coefficient of the collector efficiency. It is seen that as receiver surface temperature increases, heat loss coefficient and heat loss from the receiver increase affecting the collector efficiency adversely. Collector efficiency of 49.3 and 53.1% are obtained with the glass covered mild steel and aluminum receivers respectively. It is seen that, higher the wind speed, the higher the convective heat losses from the receiver and lower instantaneous collector efficiency. It is also seen that convective heat losses from receiver enhance with the increased temperature gradient between receiver and surrounding and instantaneous wind velocity. It is also observed that the average decrease in heat loss coefficient is 70% when receivers are covered with glass and at the same time the instantaneous efficiency of the collector is increased by 13% with glass covered receivers.

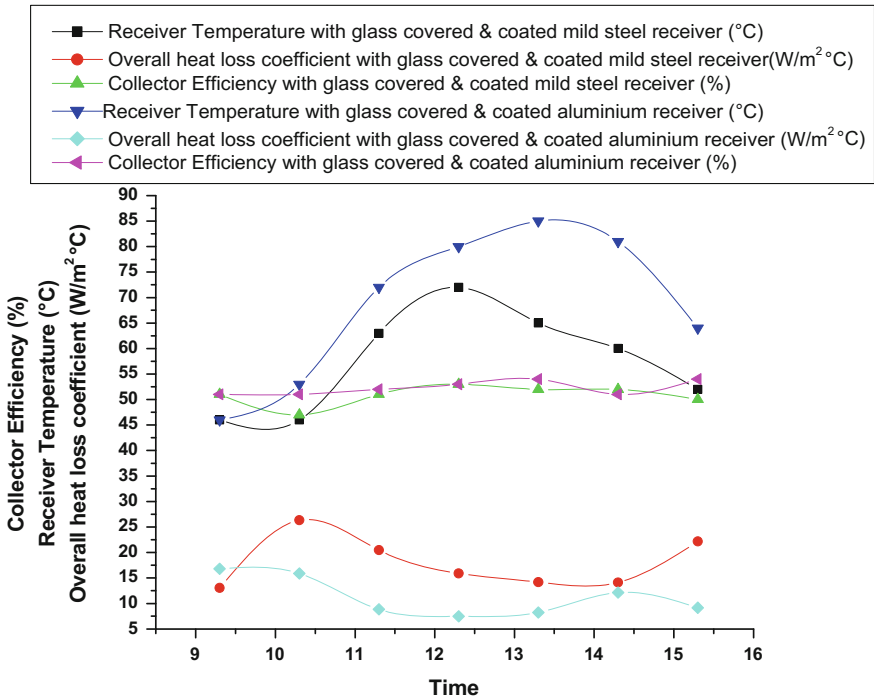


Fig. 3 Variation of collector efficiency, overall heat loss coefficient and receiver surface temperature throughout the day

Figure 4 shows useful heat gained by the water flowing through the receiver throughout the day. It is to be noted here that, the receiver temperature is the average of three values over the length of the receiver and not at the time. Useful heat gained by the water is affected by various parameters such as wind speed, receiver temperature, and solar radiation. The variation plotted shows that, as the receiver surface temperature increases, the thermal conductivity of air in the near vicinity of the receiver also enhances and therefore, the heat losses through the receiver also get advanced. But this is not only the reason of heat loss from the receiver. It is also observed that, as the beam solar radiation incident on the collector increases, the receiver captures more heat. It is seen that, when solar radiation and wind velocity reduces by 4 and 7%, respectively, average receiver temperature and useful heat gained by the glass covered aluminium receiver increases by 22 and 23% respectively as compared to a glass covered mild steel receiver.

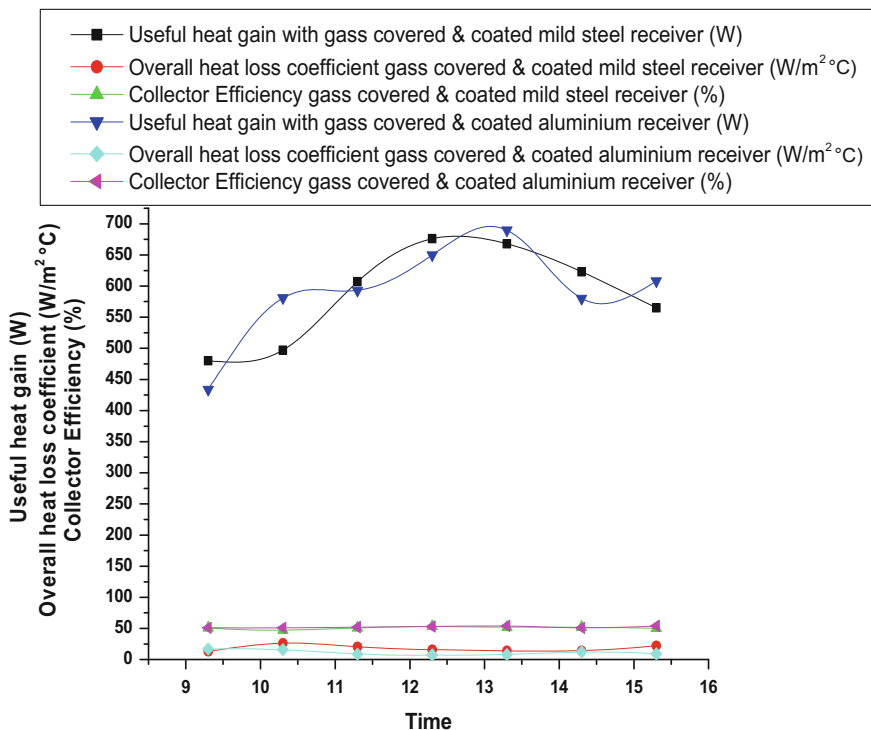


Fig. 4 Variation of useful heat gain by the receiver, overall heat loss coefficient and collector efficiency throughout day

6 Conclusions

Through the field experiments, it is seen that the proposed parabolic trough–receiver system shows better performance when a black epoxy coated aluminum and mild steel receivers are covered with glass cover. Average efficiencies of 53.1 and 49.3% are achieved with the proposed system using glass covered aluminum and mild steel receivers respectively. It is seen that, throughout the day, in comparison with glass covered mild steel receiver, average receiver temperature and useful heat gained by glass covered aluminum receiver increases by 22 and 23% respectively. It is concluded that, from the hotter climate perspective, proposed low-cost FRP parabolic trough system can able to play a vital role in low-temperature industrial heating and domestic heating applications. Particularly, the proposed system can be implemented to fulfill the needs of hot water and low-temperature steam in

restaurants and hotels, laundries. It is recommended to test the proposed system using the different receiver and selective coating materials for possible applicability in a high-temperature steam generation and similar systems.

Acknowledgements Authors want to acknowledge the lab and instrument support provided by Dept. of Energy Technology, Shivaji University, Kolhapur, to accomplish the current work.

References

1. Fernández-García A, Zarza E, Valenzuela L, Pérez M (2010) Parabolic-trough solar collectors and their applications. *Renew Sustain Energy Rev* 14:1695–1721
2. Tsai CY, Lin PD (2012) Optimized variable-focus-parabolic-trough reflector for solar thermal concentrator system. *Sol Energy* 86(5):1164–1172
3. Huang W, Peng H, Chen Z (2012) Performance simulation of a parabolic trough solar collector. *Sol Energy* 86(2):746–755
4. Eck M, Zarza E (2006) Saturated steam process with direct steam generating parabolic troughs. *Sol Energy* 80:1424–1433
5. Kalogirou SA (2012) A detailed thermal model of a parabolic trough collector receiver. *Energy* 48:298–306
6. Tao T, Hongfei Z, Kaiyan H, Mayere A (2011) A new trough solar concentrator and its performance analysis. *Sol Energy* 85:198–207
7. Kalogirou SA, Lloyd S, Ward J, Eleftheriou P (1994) Design and performance characteristics of a parabolic-trough solar collector system. *Appl Energy* 47:341–354
8. Sagade AA, Shinde NN, Patil PS (2014) Effect of receiver temperature on performance evaluation of silver coated selective surface compound parabolic reflector with top glass cover. *Energy Procedia* 48:212–222
9. Shinde NN, Sagade AA (2016) Experimental investigation into different selectively coated receivers and silver-coated selective surface compound parabolic reflector using regression modelling for industrial heating. *Int J Sustain Eng* 9(3):189–196
10. Sagade AA, Shinde NN, Patil S (2014) Experimental investigations on mild steel compound parabolic reflector with aluminum foil as selective surface and top cover. *Energy Procedia* 57:3058–3070
11. Sagade AA (2013) Comparative experimental analysis of the effect of convective heat losses on the performance of parabolic dish water heater. *Int J Sustain Eng* 6(3):258–266
12. Sagade AA (2015) Experimental investigation of effect of variation of mass flow rate on performance of parabolic dish water heater with non-coated receiver. *Int J Sustain Eng* 34(10):645–656
13. Duffie J, Beckman W (2006) *Solar engineering of thermal processes*. Wiley, New York
14. Yogi Goswami D, Kreith F, Kreider JF (2003) *Principals of solar engineering*. Taylor and Francis, Philadelphia, USA

Investigation of Load Carrying Capacity for Steering System with Polymer Helical Rack and Pinion Gear

Yogesh Ashok Ingale, A.P. Kadam, Digvijay G. Bhosale
and A.P. Bhosale

Keywords Nylon 6/6 · DELRIN · Helical rack and pinion gear · AGMA tooth bending stress · FEA · ESA

1 Introduction

Recently, a lot of efforts are being made for modification and optimization of the various parts, systems of a vehicle. To be more precise, more emphasis has been given on using alternative materials to achieve a combined benefit of reduction in weight and good performance. A conventional automobile steering gearbox (consisting of a rack and pinion gear unit) which is considered as more sophisticated are continuously being studied and investigated for the increase in transmissibility power level. This can be achieved by either selecting different material or the gear tooth geometry. Today the use of plastic gears or composite gears has been increased significantly in applications such as steering system. This is due to the availability of excellent polymer materials having extensive materials strength which can be varied in the broad range in comparison with steel. As the properties of polymers have got benefits compared to metallic gears like the low requirement of maintenance with functioning without any external lubrication, low weight, good noise-vibration damping properties, low cost and easy of manufacturing. This paper presents the design of rack and pinion gear with Nylon 6/6 and DELRIN materials

Y.A. Ingale (✉) · A.P. Kadam
Bharati Vidyapeeth's College of Engineering, Kolhapur, India
e-mail: ingaleyogesh20@gmail.com

A.P. Kadam
e-mail: apkadam75@rediffmail.com

D.G. Bhosale · A.P. Bhosale
Sanjeevan Engineering & Technology Institute, Kolhapur, India
e-mail: digvijay_bhosale@yahoo.co.in

A.P. Bhosale
e-mail: bhosaleamrut13@gmail.com

as per the AGMA standards. The comparative study of physical properties of both the gears has been done by using approaches such as FEA and experimental analysis. The compatibility of the materials has been checked for this particular application of steering system [1].

2 Design of Steering Rack and Pinion Gear Box

2.1 Loading Condition for Steering Gear Box

In this case steering load acting on pinion calculated by considering the weight of vehicle acting as a force on it. It is the normal force (W) acting on pinion gear when the car is stopped. The moment when the force is applied to turn the wheels it has the tangential component and resolving component (W^t & W^r). Further calculated the tangential component and resolving component acting on the pinion. For load analysis of plastic gear, the theory proposed by Civera [2] of Escuela technical industry was implemented.

$$\text{Normal force (W)} = 156.514 \text{ N}$$

$$\text{Tangential component (W}^t) = 147.075 \text{ N and,}$$

$$\text{Radial component (W}^r) = 53.53 \text{ N}$$

2.2 Selection of Suitable Gear Module

In this case of a hatchback car, the module for metal gear pair is usually between 2–3 mm. For plastic gear, following two methods are used to get the value of gear module. Module estimation as per the first method [3, 4]. The dimensional specifications of gear pair under investigation has been given in Table 1.

$$F_t = K_1 \times K_2 \times b \times P$$

$$\text{Module(m)} = 1.76 \text{ mm for Nylon 6/6} \quad (1)$$

$$\text{Module(m)} = 1.3448 \approx 1.4 \text{ mm for DELRIN} \quad (2)$$

And, module estimation as per second method [5],

$$(S_b) = m_n \times b \times Y \times \sigma_b$$

$$(S_b) = F.S. \times P_{\text{effective}}$$

$$P_{\text{effective}} = C_s \times P_t / C_v$$

Table 1 Dimensions of Nylon 6/6 and DELRIN material gear pair

Sr. No.	Properties	Nylon 6/6		DELRIN	
		Pinion	Gear	Pinion	Gear
01	Module (m) (mm)	2.75		2.25	
02	Pressure angle (\emptyset)	20°		20°	
03	Helix angle (φ)	30°		30°	
04	Face width (mm)	41.25		33.75	
05	No. of teeth (N)	07	21	05	21
06	Addendum (b) (mm)	2.75	2.75	2.25	2.25
07	Dedendum (d) (mm)	3.4375	3.4375	2.8125	2.8125
08	Circular pitch (mm)	19.25	8.6438	11.25	10.57
09	Base circle diameter (mm)	18.089	269.637	10.57	157.5

$$\text{Module (m)} = 1.669 \text{ mm for Nylon 6/6} \tag{3}$$

$$\text{Module (m)} = 1.37 \text{ mm for DELRIN} \tag{4}$$

2.3 Design of Helical Rack and Pinion Gear Pair by AGMA Approach

A. Design of Nylon 6/6 material gear pair by AGMA approach

Maximum Tooth bending stress equation (AGMA 2001-D04) [6]

$$\sigma_b = w^t \times K_o \times K_v \times K_s \times \frac{K_m \times K_B}{J} \times \frac{Pc}{F}$$

where,

$$\sigma = 147.075 \times 1.50 \times 1.3381 \times 1.112348 \times \frac{1.2971 \times 1.1234}{2.3} \times \frac{8.6394}{41.25}$$

$$\sigma = 43.58 \text{ Mpa}$$

This is AGMA Bending stress value for material Nylon 6/6 with module 2.75 mm and gear bending endurance strength is [6],

$$\sigma_{all} = \frac{S_t Y_N}{S_F K_T K_R}$$

$$\sigma_{all} = (103/2 \times) [1/(1 \times 1)] = 51.5 \text{ Mpa}$$

Now Safety Factors are,

$$S_F = \frac{S_t Y_N / K_T K_R}{\sigma}$$

Allowable bending stress, $S_t = 103 \text{ Mpa}$

$$S_F = \frac{(103 \times 1/1 \times 1)}{43.58} = 2.3635$$

The factor of safety is 2.36, which is in the limits of recommended factor of safety for gears between 1.5–2.5.

B. Design of DELRIN material gear pair by AGMA approach

Maximum Tooth bending stress equation (AGMA 2001-D04)

$$\begin{aligned} \sigma &= W^t \times K_O \times K_V \times K_S \times \frac{K_m \times K_B}{J} \times \frac{Pc}{F} \\ \sigma &= 147.075 \times 1.50 \times 1.0 \times 1.0884 \times \frac{1.3456 \times 1.6428}{0.298402} \times \frac{7.0686}{22.5} \\ \sigma &= 29.50 \text{ Mpa} \end{aligned}$$

This is AGMA Bending stress value for material DELRIN with module 2.25 mm and gear bending endurance strength is,

$$\begin{aligned} \sigma_{\text{all}} &= \frac{S_t Y_N}{S_F K_T K_R} \\ \sigma_{\text{all}} &= (110/2) \times [1/(1 \times 1)] = 55 \text{ Mpa} \end{aligned}$$

Safety Factors (S_F)

$$S_F = \frac{S_t Y_N / K_T K_R}{\sigma}$$

Allowable bending stress, $S_t = 110 \text{ Mpa}$

$$S_F = \frac{(110 \times 1/1 \times 1)}{29.50} = 3.72$$

The factor of safety is 3.72, which is more than recommended factor of safety for gears between 1.5–2.5.

3 Finite Element Analysis of Steering Gear Box

FEA results using ANSYS 12.1; the mesh independency is achieved by considering $\pm 5\%$ change in displacements.

3.1 Finite Element Analysis of Nylon 6/6 Gear Pair

From FEA results for pinion, (Figs. 1, 2 and 3)

σ = Tooth root bending strength for pinion = 44.453 N/mm²

σ_p = Permissible tooth root bending stress for pinion = 103 N/mm². We have,

$\sigma_p \geq \sigma$ and $\sigma_p = 103/SF$

$103/SF = 44.453$

SF = 2.318, safety factor.

3.2 Finite Element Analysis of Delrin Gear Pair

From FEA results for pinion, (Figs. 4, 5 and 6)

σ = Tooth root bending strength for pinion = 26.854 N/mm²

σ_p = Permissible tooth root bending stress for pinion = 110 N/mm². We have,

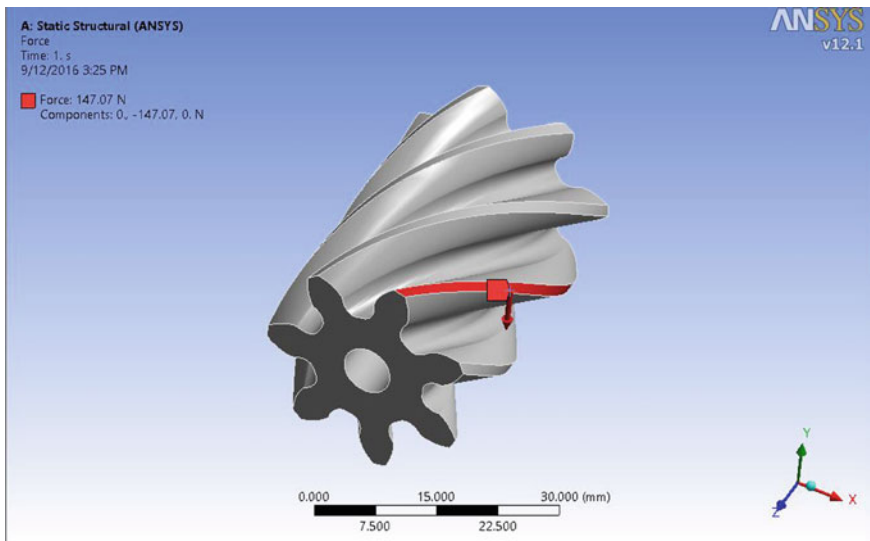


Fig. 1 Boundary conditions of Nylon 6/6 Pinion

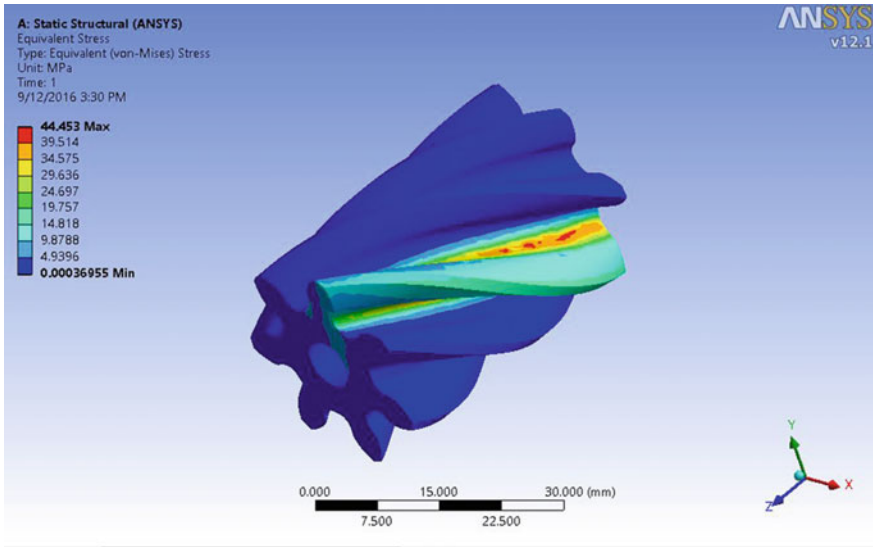


Fig. 2 Tooth Von-Mises stress for Nylon 6/6 Pinion

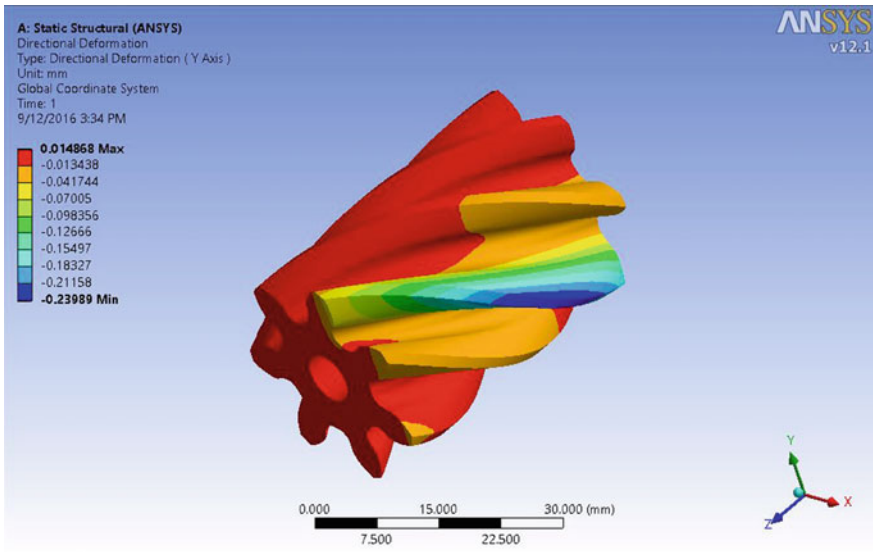


Fig. 3 Tooth deformation for Nylon 6/6 Pinion

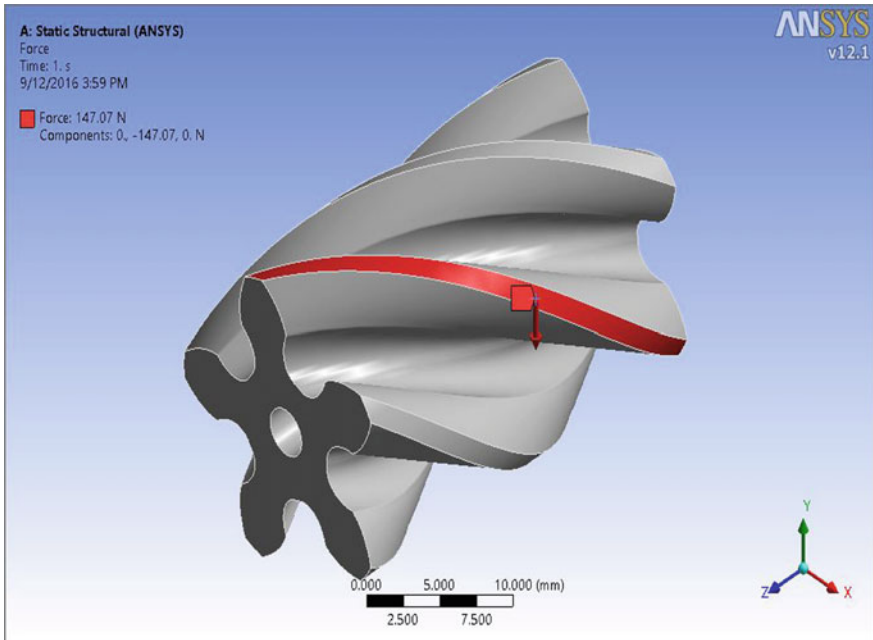


Fig. 4 Boundary conditions of DELRIN Pinion

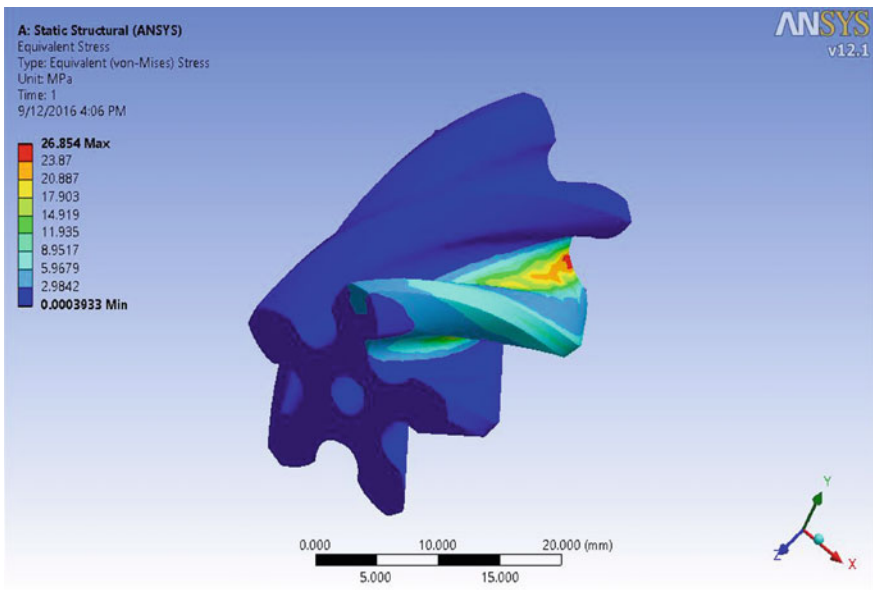


Fig. 5 Tooth Von-Mises stress for DELRIN Pinion

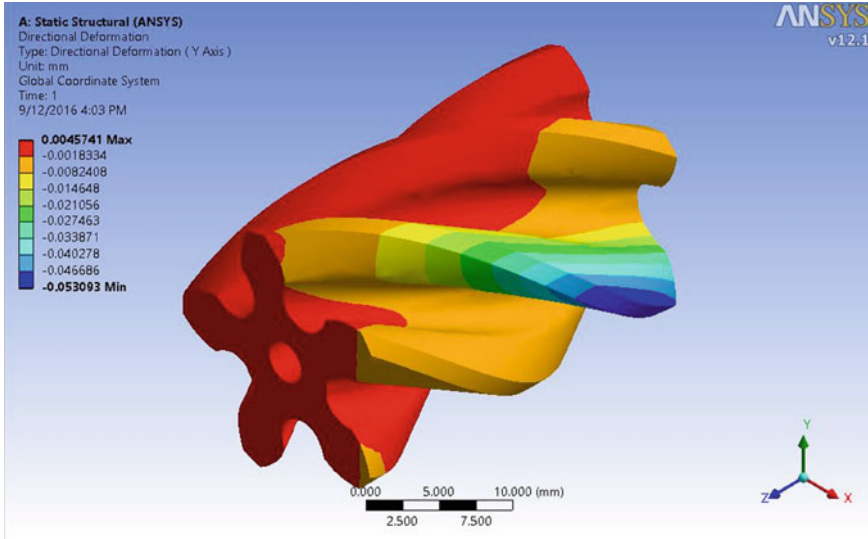


Fig. 6 Tooth deformation for DELRIN Pinion

$\sigma_p \geq \sigma$ and $\sigma_p = 110/SF$
 $110/SF = 26.854$
 $SF = 4.1$, safety factor.

4 Experimental Stress Analysis of Steering Gear Box

4.1 Experimental Strain Analysis Test Observations and Results

The stress can be found by general equation;

$$\sigma = E \times \mu\epsilon$$

where,

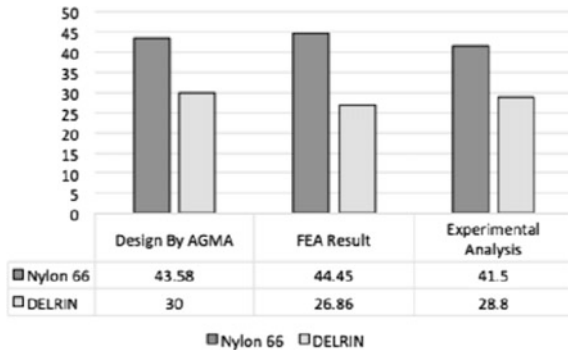
σ = maximum stress, E = Young’s Modulus and, $\mu\epsilon$ = micro strain
 Maximum Stress = Young’s Modulus of Elasticity \times Micro strain
 Maximum Stress $[\sigma] = E \times [\mu\epsilon \times 10^{-6}]$

The following are experimental strain analysis test results of Nylon 6/6 and DELRIN material gear pair [7], as per the loading condition mention in Rules of TED, New Delhi [8] (Table 2).

Table 2 Experimental analysis results

Sr. No.	% Load	Load on pinion (N)	Load on pinion (kg)	Strain gauge reading for Nylon 6/6 in micro strain ($\mu \epsilon \times 10^{-6}$)	Stress value for Nylon (Mpa)	Strain gauge reading for DELRIN in micro strain ($\mu \epsilon \times 10^{-6}$)	Stress value for DELRIN (Mpa)
01	5	7.4	1.00	708.19	2.075	232.25	1.44
02	10	14.70	1.50	1416.39	4.15	464.51	2.88
03	20	29.42	3.00	2832.76	8.30	929.03	5.76
04	25	36.77	4.00	3540.95	10.37	1161.29	7.20
05	30	44.12	4.50	4249.14	12.45	1393.54	8.64
06	50	73.54	7.50	7081.90	20.75	2322.58	14.4
07	80	117.66	12.0	11,331.05	33.20	3716.13	23.04
08	100	147.075	15.0	14,163.80	41.50	4645.17	28.8

Fig. 7 Stress results



5 Result and Discussion

5.1 Design, FEA and ESA Comparative Results of Gear Pair

Following are the results after design calculations, Finite Element analysis and Experimental analysis of gear pair for the same loading condition, (Figs. 7, 8 and 9).

As per AGMA standards gear design procedure, design of the gear pair has been carried out and it has been found that the design stresses are 43.58 and 30.00 Mpa for Nylon 6/6, DELRIN material respectively (Table 3).

The comparative results show that the Nylon 6/6 gear pair deformed more than the DELRIN gear pair for the same load.

Fig. 8 Strain results

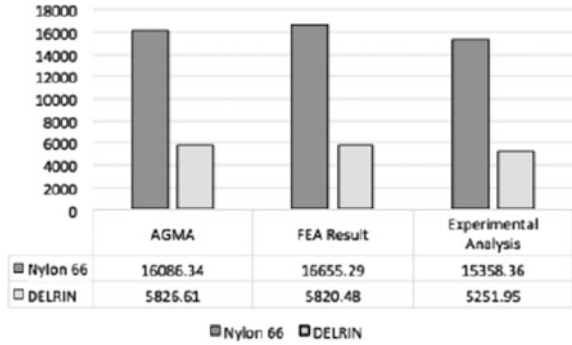


Fig. 9 Weight and cost result

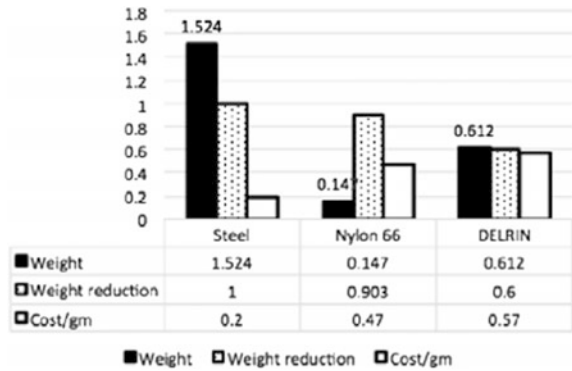


Table 3 Comparison between of Nylon 6/6 & DELRIN gear

Analysis methods	Parameter	Nylon 6/6	DELRIN
Design by AGMA approach	Tooth bending normal stress (max)	43.58	30.00
	Total deformation in micro strain	16,086.34	5826.61
Finite element analysis result	Von-Mises stress (max)	44.45	26.86
	Total deformation in micro strain	16,655.290	5820.48
Experimental analysis result	Von-Mises stress (max)	41.50	28.80
	Total deformation in micro strain	15,358.36	5251.95
Deviation in stress values (%)		3.32	4.31

Table 4 Weight and cost analysis

Parameter	Steel	Nylon 6/6	DELRIN
Pinion	0.124	0.032	0.05
Rack	1.4	0.115	0.562
Total weight	1.524	0.147	0.612
Weight reduction (%)	–	90.35	60.00
Cost per kg (Rs)	200	470	570
Total material cost (Rs)	305	70	306

5.2 Weight and Cost Analysis of Gear Pair

See Table 4.

5.3 LifeSpan of Gear

Pogacnik and Tavcar [9] suggest mathematical correlation between LifeSpan, load, and speed (tangential speed) of gear as,

$$(\text{LifeSpan})^{1/3} = 740 - 92.0 \times (\text{Load})^{1/2} - 67.7 \times \text{Speed}$$

LifeSpan = Number of load cycles gears can withstand without any failure

Load = Load level on gears as root stress (Mpa)

Speed = Tangential speed of gears (m/s)

Gear pair life for steering gear box application considering peak load is acting over the pinion as,

LifeSpan for Nylon 6/6 = 9.98×10^5 Number of cycles

LifeSpan for DELRIN = 7.86×10^6 Number of cycles

Thus, the lifespan of DELRIN gear pair is almost eight times more than that of Nylon 6/6 gear pair for the same loading conditions and working environment [2, 7, 9, 10].

5.4 Societal Application of Gear Pair

The study in this paper can be linked to the societal application from the cost point of view and employability. Nowadays every car manufacturer is working under stringent conditions to reduce the cost and provide the best to the customer. This paper includes the replacement of conventional steel gear pair set with a plastic or composite pair. The weight will be reduced and also in the case of mass production

the cost will be compatible with the conventional steel gears. On successful application, this would provide scope for new and aspiring vendors who has an interest in the field of plastic and composites and who would blend their interest with commercial aspects. The vendors when on the commercial application can provide employment to new engineers and other associated people with this field.

6 Conclusion

In this study, the weight and cost analysis suggests the benefit of weight reduction in polymer gears as compared to steels gears. It has been observed that about 90% weight reduction is achieved in Nylon 6/6 and 60% is seen in DELRIN as compared with metal gears. The cost reduction is also observed distinguished point in both polymer gears. The design of the gears has been carried by using AGMA approach and the tooth bending stress and deformation has been studied. The FEA and experimental results show that the Nylon 6/6 gears have more tooth bending stress and total deformation as compared to DELRIN gears. The value of factor of safety for the both the materials is also observed more than recommended for bending load. The fact that, the pitch line velocity in rack and pinion steering gear box is very low and so load transferred to gear pair is on the lower side. The work suggests that one can use non-metallic gears mentioned above for steering gearbox application provided as the study regarding the lifespan of the gear pair has also been carried out. It has been numerically found that the lifespan of DELRIN gear pair is almost eight times more than that of Nylon 6/6 gear pair for the same loading conditions and working environment.

References

1. Beermann S (2007) Estimation of lifetime for plastic gears
2. Civera DN (2011) Description and design of the steering system for a formula student car. Mechanical Engineering Department, Escuela University
3. Maitra GM, Prasad LV (2004) Handbook of mechanical design 2nd edn. Tata McGraw Hill Publishing Company Ltd
4. Dudley DW Dudley's gear handbook 2nd edn. McGraw-Hill Publishing Company Ltd
5. Bhandari VB (2012) Design of machine elements 3rd edn. Tata McGraw Hill Publishing Company Ltd
6. Shigley JE, Mischke CR Mechanical engineering design 6th edn. Tata McGraw Hill Publishing Company Ltd.
7. Patil SS, Karuppanan S, Atanasovska I (2016) Experimental measurement of strain and stress state at the contacting helical gear pairs. Science direct. Measurement
8. Transport engineering division council (2016) TED Norms, New Delhi
9. Pogacnik A, Tavcar J (2015) An accelerated multilevel test and design procedure for polymer gears. Science Direct. Mater Des
10. van Melick IHGH (2007) Influence on load sharing stresses and wears, studied by FEA

Dry Sliding Wear Performance Optimization of MoS₂ Filled PTFE Composites Using Taguchi Approach

Prasad M. Patare and G.S. Lathkar

Keywords PTFE · MoS₂ · Wear rate · COF · Taguchi · XRD · SEM

1 Introduction

Polymer matrix composites are used widely in the many engineering application nowadays. Polymer matrix composites are used many mechanical engineering components such as cams, brakes, bearings, and gears as they possess the self-lubrication properties, less friction, and better wear resistance. Due to their advantages, the polymer composites are widely used as sliding components in mechanical engineering systems, where only metal matrix composites were used previously.

Polytetrafluoroethylene (PTFE) is one of the key polymers used in the engineering application due to its low coefficient of friction. The properties of PTFE composites can be varied easily by addition of the other alloying elements in the base material of PTFE to increase the wear resistance of the material and to add other material properties in it.

But it shows a very high wear rate which can be reduced by addition of filler materials. Several researchers have observed the significant changes in the wear properties of PTFE reinforced with different fillers. Bijwe and Sen [1] have studied that with an inclusion of PEEK in PTFE wear rate decreases significantly. Li et al. [2] added Copper coated graphite to PTFE to improve the wear performance. Zhang et al. [3] demonstrated that in vacuum applications at room temperature and above, MoS₂, particularly when combined with various metal fillers, provides low coefficients of friction as well as low wear rates.

P.M. Patare (✉)
SRES COE, Kopargaon, India
e-mail: prasadpatare@gmail.com

G.S. Lathkar
MGM College of Engineering, Nanded, India

Hence, MoS_2 is considered as the filler material which when added to PTFE gives good sliding and wear characteristics, good thermal conductivity, low coefficient of friction and high-pressure resistance [3].

Design of experiment is a technique is used to conduct the experimentation using the minimum amount of time, work. This technique will provide the opportunity to conduct the experimentation work scientifically correct and with the proper methodology. The design of experimentation technique will require the appropriate process parameters and the factors selection to obtain the correct information from the experimentation.

The Taguchi method of the experimentation will give the set of the experimentation correctly with the appropriate combination of the all the parameters and the factors of the study. The results obtained from the experimentation are being analyzed using the appropriate techniques of the S/N curve and their interpretation.

2 Wear Testing

The experimentation work was conducted using the pin on disc test setup as per ASTM G99-05 Standard. This test setup is illustrated in Fig. 1.

The polymer composite material was prepared in the laboratory. The Mark [4, 5] have explained the various polymer material properties and their methods for mixture preparations. Initially, the base material named as polytetrafluorethylene was heated up to the melting temperature of $330\text{ }^\circ\text{C}$, then the alloying elements like the Molybdenum disulphide were poured into an open polymeric mold. The mixture is allowed to cool to the room temperature. While cooling the proper mixture care of



Fig. 1 Schematic diagram of pin-on-disc apparatus

continuous stirring is to taken so that the particles of the alloying elements should not get settled down at the base of the polymeric composition. Afterward, the composite materials are prepared in the appropriate dimensions for the experimentation purpose.

Wear test composites are made in the form of pins diameter 12 and 30 mm length and come in contact with (EN32 grade) carbon steel disc. EN32 is a low tensile steel suitable for lightly stressed components. The Table 1 shows the constituents of disk material EN32.

Before testing, the samples were polished with fine grade sand paper (1200 grit SiC) to ensure proper contact with the counter face.

3 Experimental Design

Experimentation work is carried out by using the technique like Taguchi Design. This method is helpful to analyze the control factors and levels. For the experimentation many control fable factors are listed as sliding distance, load, speed, lubrication condition, temperature, environmental conditions can be considered. For the present experimental work major factors considered as the load with three levels of 1, 2, and 3 kg, sliding distance as 2, 3 and 4 km, velocity as 1.09, 2.19 and 3.29 m/s. additionally filler content as 5% MoS₂, 10% MoS₂ and 15% MoS₂. For the experimentation work Taguchi design uses the orthogonal array with L27 (3¹³) [6]. All the control parameters and levels are shown in Table 2.

The L27 (3¹³) orthogonal array consists of the three levels and thirteen columns, out of these columns, column one, two, five and nine are used for the design of experimentation. The plan of the experiment is as follows: the first column of the Taguchi orthogonal array is assigned to the normal load, the second column to the sliding distance, the fifth column to the sliding velocity, the ninth column to filler content and remaining columns are assigned to their interactions and experimental errors as shown in Table 2.

After conducting the experimentation work, an analysis is done using the statistical analysis software like Minitab. From the statistical formulae, the signal to

Table 1 Constituents of EN32

Constituent	Percentage	Constituent	Percentage
Carbon	0.10–018	Phosphorous	0.05% max
Manganese	0.60–1.00	Sulphur	0.05% max
Silicon	0.05–0.35		

Table 2 Control factors and levels used in the experiment

Levels	Load (kg)	SD (m)	Velocity (m/s)	Filler content (%)
1	1	2000	1.09	5
2	2	4000	2.19	10
3	3	6000	3.29	15

noise ratio is evaluated for the further analysis. There are three different types of the signal to noise ratio are there namely: lower the better, nominal the best and higher is better. The selection of the signal to noise ratio is dependent on the requirement of the parameter which is to be evaluated. For the evaluation of the wear parameter, we have selected lower the better signal to noise ratio. Depending on the signal noise ration the ranking of the dominant parameters is decided. To determine the optimum process parameters confirmation tests were conducted.

4 Results and Discussion

4.1 Statistical Analysis of Wear Rate

The analysis was made using the software Design Expert 8.7.0.1 and MINITAB14 specifically used for the design of experiment applications. Test conditions with output results using orthogonal array are shown in Table 3.

The equations for calculation of S/N ratio are:

1. Lower is better:

$$S/N_{LB} = -10 \log \left(\frac{1}{r} \sum_{i=1}^r y_i^2 \right)$$

where, r = number of tests in trial

2. Nominal is best:

$$S/N_{NB1} = -10 \log(V_e) \quad (\text{variance only})$$

$$S/N_{NB2} = 10 \log(V_m - V_e/r * V_e) \quad (\text{mean and variance})$$

3. Higher is better:

$$S/N_{HB} = -10 \log \left(\frac{1}{r} \sum_{i=1}^r 1/y_i^2 \right)$$

From Table 3, it is observed that the maximum value of S/N ratio is observed at 1st reading which gives the minimum specific wear rate. Thus, minimum wear rate is obtained at the minimum value of normal load (A_1), sliding distance (B_1), velocity (C_1) and filler content (D_1).

Figure 2a, b show graphically the effect of the control factors on specific wear rate. Process parameter settings with the highest ratio always give the optimum quality with minimum variance. The graphs show the change of the ratio when the setting of the control factor has been modified from one level to the other. The best wear rate was at the lower values in the response graphs.

Table 3 Test conditions with output results using L₂₇ orthogonal array

Std.	Load (kg)	SD (km)	Velocity (m/s)	Material (%)	Wear (micron)	S/N ratio (dB)	COF	SN ratio (dB)
1	1	2	1.09	5	24.011	-27.6082	0.42	7.53501
2	1	4	3.29	5	43.87	-32.8433	0.32	9.89700
3	1	6	2.2	5	41.87	-32.4380	0.44	7.13090
4	2	2	3.29	5	35.82	-31.0823	0.34	9.37042
5	2	4	2.2	5	39.79	-31.9954	0.35	9.11863
6	2	6	1.09	5	31.39	-29.9358	0.42	7.53501
7	3	2	2.2	5	37.52	-31.4852	0.28	11.0568
8	3	4	1.09	5	38.38	-31.6820	0.27	11.3727
9	3	6	3.29	5	47.45	-33.5247	0.38	8.40432
10	1	2	2.2	10	26.33	-28.4090	0.32	9.89700
11	1	4	1.09	10	25.78	-28.2256	0.49	6.19607
12	1	6	3.29	10	42.52	-32.5718	0.27	11.3727
13	2	2	1.09	10	34.65	-30.7940	0.28	11.0568
14	2	4	3.29	10	45.93	-33.2419	0.24	12.3957
15	2	6	2.2	10	43.13	-32.6955	0.35	9.11863
16	3	2	3.29	10	41.23	-32.304	0.22	13.1515
17	3	4	2.2	10	39.35	-31.8988	0.25	12.0411
18	3	6	1.09	10	53.38	-34.5475	0.33	9.62972
19	1	2	3.29	15	32.85	-30.3307	0.21	13.5556
20	1	4	2.2	15	40.26	-32.0974	0.19	14.4249
21	1	6	1.09	15	39.87	-32.0129	0.23	12.7654
22	2	2	2.2	15	33.47	-30.4931	0.24	12.3957
23	2	4	1.09	15	45.92	-33.2400	0.21	13.5556
24	2	6	3.29	15	50.06	-33.9898	0.22	13.1515
25	3	2	1.09	15	40.27	-32.0996	0.17	15.3910
26	3	4	3.29	15	35.29	-30.9530	0.35	9.11863
27	3	6	2.2	15	56.114	-34.9814	0.25	12.0411

From the observation table, it is observed that values of the wear are measured in microns and values seem to be varying on the loading conditions. The wear for the loading conditions with load 1 kg, sliding distance 2 km, velocity as 1.09 m/s, and material composition as 5% of MoS₂, a volume of wear is 24.011 μm. The corresponding signal to noise ratio for lower is better is calculated as follows:

For wear = 24.011

$$\left(\frac{S}{N}\right)_s = -10 \cdot \log_{10} \left[\frac{\sum y^2}{n} \right]$$

where, y = Response factor, S² = Noise factors, n = Number of experiments.

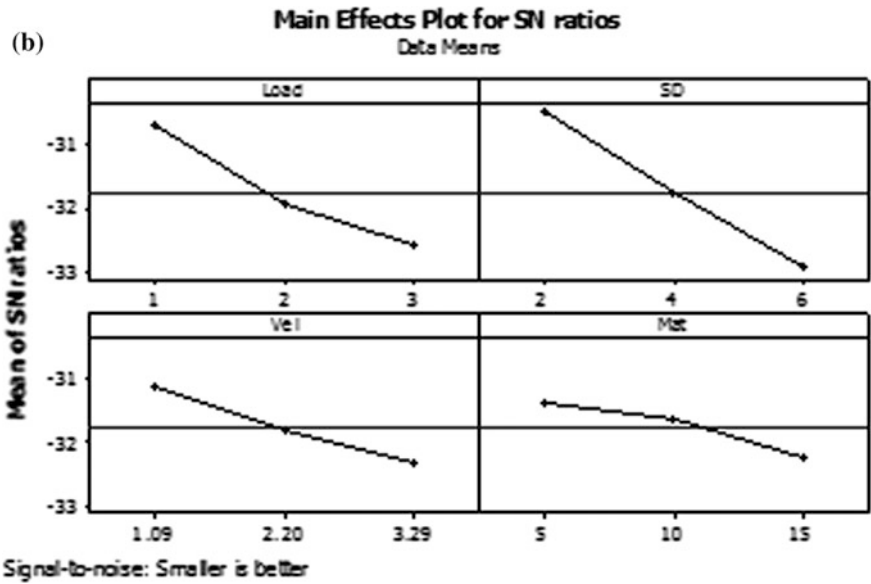
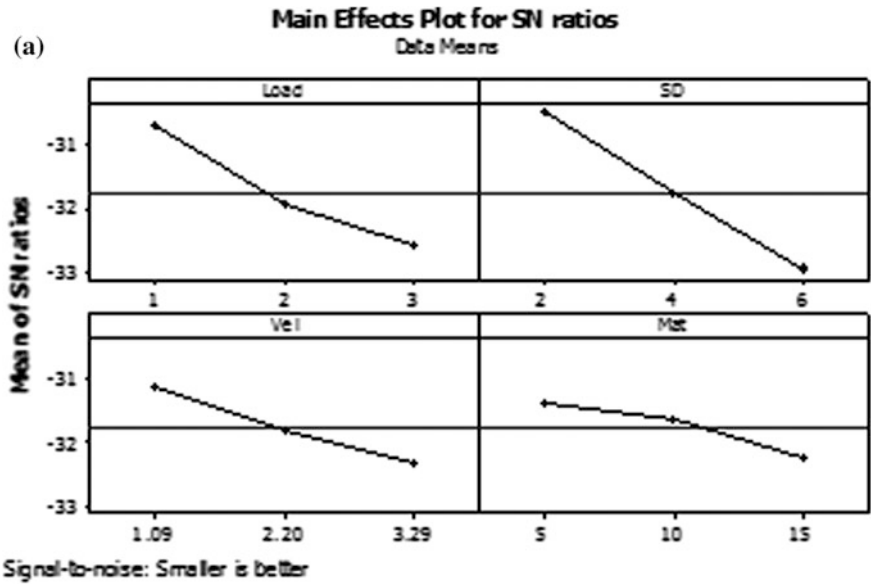


Fig. 2 Main effect plot for a SN ratios, b means

$$\left(\frac{S}{N}\right)_1 = -10 \cdot \log_{10} \left[\frac{\sum 24.011^2}{1} \right] = -27.608$$

For COF = 0.42

$$\left(\frac{S}{N}\right)_1 = -10 \cdot \log_{10} \left[\frac{\sum 0.42^2}{1} \right] = 7.535$$

After performing the analysis using the statistical tools on the experimental data, it has been observed that there is one observation for each input factor for which the response factors have optimum value. The S/N Ratio of each response factor also has the maximum and minimum value according to reading. So for finding the optimum parameter setting for each response parameter, the additive model of Taguchi Method is used. The S/N Ratio of each response parameter is calculated based on the formula containing the negative logarithmic value. This type of function is called as the monotonic decreasing function.

In an effort to identify the role of ceramic particles in the wear behavior of polymer composites, Durand et al. proposed several wear mechanisms such as surface cracking, particle detachment, thin and thick transfer layer at the interface, and so forth in case of polymer composites that provide the effective wear protection to the matrix material [7]. The Fig. 3 shows the interaction plot for wear.

From Table 4, one can observe that Sliding distance (B) has greater static influence of 34.78%, normal load (A) has greater static influence of 17.97%, sliding

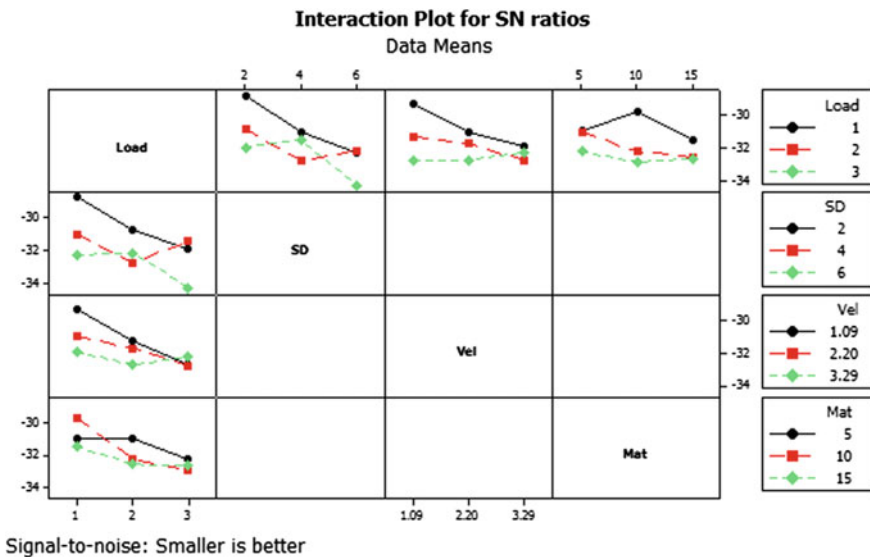


Fig. 3 Interaction graph between A, B, C and D for wear rate

velocity (C) has an influence of 6.00% and filler content (D) has an influence of 4.05% on specific wear rate. Normal load and velocity (AC) have an influence of 7.44%. However, the interaction between normal load and sliding distance (AB) and lastly normal load and filler content (AD) show less significance of contribution on specific wear rate.

In the material composition, one can observe that from Table 3 that PTFE + 5% of MoS₂ gives the most realistic result with less amount of wear while sliding against the steel disk using the pin on disk apparatus.

Table 5 shows the ranks of the influence of different factors on wear analyzed in Minitab. From the table, we can observe that Sliding distance has the greater impact on wear rate while filler content has the least effect.

4.2 Confirmation Experiment

The confirmation experiment was carried out to validate the experimentation work which is conducted is proper or not. The acceptance test also proves our accuracy the model which is developed.

From analysis in Minitab software, we obtained the graphs as indicated in Fig. 2a, b. By this analysis, we selected two sets of parameters as A₁B₁C₁D₁ and A₃B₃C₃D₃ for confirmation tests.

Table 4 ANOVA table for specific wear rate

Source	DOF	Seq SS	Adj SS	Adj MS	F test	P value	P (%)
Load (A)	2	16.39	16.39	8.195	12.64	0.007	17.9772
SD (B)	2	27.132	27.132	13.566	20.93	0.002	34.7876
Velocity (C)	2	6.43	6.43	3.215	4.96	0.054	6.0028
Material (D)	2	3.427	3.427	1.7136	2.64	0.15	4.0518
A × B	4	12.856	12.856	3.214	4.96	0.41	0.0519
A × C	4	8.156	8.156	2.039	3.15	0.102	7.4448
A × D	4	6.229	6.229	1.5573	2.4	0.162	0.1364
Error	6	3.89	3.89	0.6483			
Total	26	84.511					

Table 5 Wear response table for signal to noise ratio

Level	Load	SD	Velocity	Material
1	-30.726	-30.511	-31.127	-31.39
2	-31.94	-31.797	-31.832	-31.63
3	-32.608	-32.966	-32.315	-32.24
Delta	1.882	2.455	1.188	0.845
Rank	2	1	3	4

Table 6 Conformation tests

Load	SD	Velocity	Material	Wear	COF
1	2	1.09	5	24.011	0.42
2	6	3.29	15	47.3826	0.2907

Table 7 Conformation test for specific wear rate

Level	Optimal process parameter A ₁ B ₁ C ₁ D ₁		Improvement in the result (dB)
	Predicted	Experimental	
Specific wear rate (micron)	24.0110	24.3257	-27.60820495
Coefficient of friction	0.4200	0.4172	7.535014192

The results of experimental confirmation using optimal wear parameters and comparison of the predicted wear rate with the actual wear rate using the optimal wear parameters are shown in Tables 6 and 7.

5 SEM and EDX Results

The testing for the scanning electron microscope was conducted at Physics Department of Savitribai Phule Pune University, Pune using the SEM with the various resolution of the microscope and the micrograph obtained shows the availability of the Molybdenum Disulphide in the base combination of the polytetrafluoroethylene, as shown in the Fig 4.

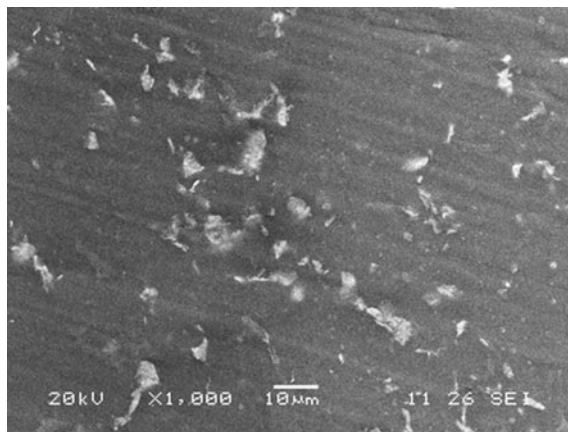


Fig. 4 SEM structure of MoS₂ with 5% addition

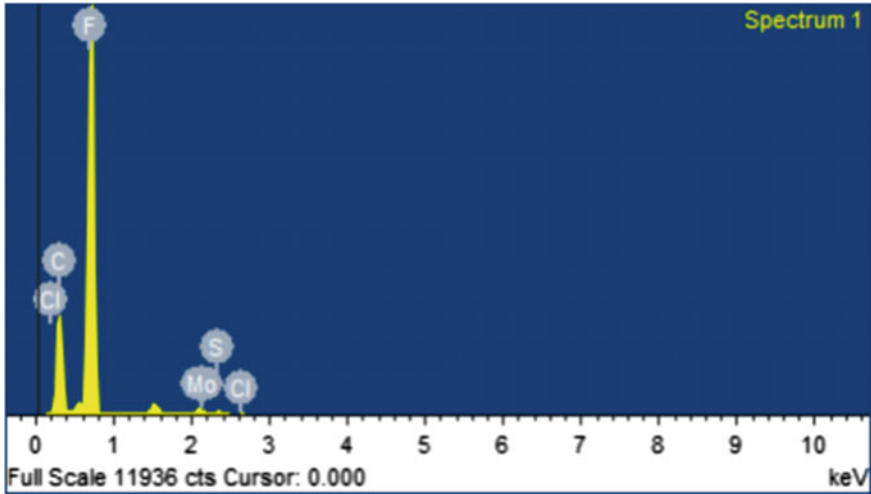


Fig. 5 EDX structure for 5% MoS₂

Table 8 Weight and atomic percentage in polymer composites of 5% MoS₂

Element	Weight %	Atomic %
C K	40.86	52.25
F K	58.98	47.69
S K	0.08	0.04
Cl K	0.04	0.02
Mo L	0.04	0.01
Totals	100.00	100.00

The energy dispersive X-ray spectroscopy was conducted at Indian Institute of Technology Mumbai for the evaluation of the various content in the mixture of the polymer composited as shown in following Fig. 5.

The corresponding element content are shown in Table 8.

6 Conclusions

The experimentation work conducted on the three different combinations of MoS₂ with the filler content of 5%, 10% and 15% with the base material of PTFE draws the following conclusion:

- (1) To minimize the wear rate of the polymer composite, the methodology of Taguchi technique is implemented with normal load, sliding distance, velocity and the filler content as the control factors for the experimentation using L27 (3⁴) orthogonal array having the three levels and four factors.

- (2) ANOVA results indicated that sliding distance is the factor which is having highest physical as well as a statistical influence of 34.78% followed by normal load (A) 17.97%, sliding velocity (C) 6.00% and filler content (D) 4.05% on specific wear rate. However, interactions of these factors have less significant effect on wear rate except AC combination which has an influence of 7.44%.
- (3) ANOVA results indicated that filler content has the greatest influence of 40.98% on coefficient of friction followed by sliding distance 5.21%, load 4.71% and sliding velocity 2.26%.
- (4) The results of the scanning electron micrograph (SEM) and the XRD results shows that filler content added to the base materials which is further used for the experimentation work is appropriate and same things are mentioned as per Table 8 in the results and discussions.

References

1. Bijwe J, Sen S (2005) Influence of PTFE content in PEEK-PTFE blends on mechanical properties and tribo-performance in various wear modes. *Wear* 258:1536–1542
2. Li F, Feng-yuan Y et al (2000) The tribological behaviors of copper-coated graphite filled PTFE composites. *Wear* 237:33–38
3. Zhang X, Vitchev RG et al (2004) Transfer of molybdenum sulphide coating material onto corundum balls in fretting wear tests. *Thin Solid Films* 446:78–84
4. Mark JE (1999) *Polymer data handbook*. Oxford University Press Inc., Oxford, pp 842–847
5. Mark JE (2007) *Physical properties of polymer handbook*, 2nd edn. Springer, New York, pp 319–340
6. Sudheer M et al (2012) Optimization of dry sliding wear performance of ceramic whisker filled epoxy composites using Taguchi's approach. *Adv Tribol* 431901:9 p
7. Durand JM et al (1995) Role of reinforcing ceramic particles in the wear behavior of polymer based model composites. *Wear* 181:833–839

Tribological Behavior of Al6061 Alloy Reinforced with Fly Ash Particles

D.A. Nayana, Mailareppa Marachakkanavar and Nagaraj Kantli

Keywords Al6061 MMC's · Fly ash · Stir casting · Pin and disk

1 Introduction

The present day of investigation, Aluminium is used as the matrix material due to its higher strength and ductility of the aluminium alloys. Aluminium alloy exhibits excellent mechanical properties like machinability and good bearing and wear properties [1]. Metal Matrix Composites is used to disperse or spread the reinforcing material into a matrix of metal, and which implies the name as ductile metal. Reinforcement improves the strength of the material, better thermal properties, specific weight and strength of the material, stiffness property and all mechanical properties holds good. By using these materials may aim at higher temperature service than the base metal parts [2]. The main aim is involved in designing the metal composite materials as matrix in order to incorporate the desirable qualities of metals and ceramics. This paper is to evaluate Tribological and Mechanical properties of composites with different volume fraction from their results. MMCs give better results for Hardness and Tensile properties [3] (Tables 1 and 2).

D.A. Nayana · N. Kantli
Department of Mechanical Engineering, Basaveshwar Engineering College,
Bagalkot 587102, Karnataka, India

M. Marachakkanavar (✉)
Department of Mechanical Engineering, Sinhgad Institute of Technology and Science,
Narhe, Pune 411041, Maharashtra, India
e-mail: mylari.sm@gmail.com

Table 1 Chemical composition of Al6061 alloy

Sl. no.	Material	Percentage
1	Iron	0.0–0.7
2	Silicon	0.4–0.8
3	Magnesium	0.8–1.2
4	Zinc	0.0–0.25
5	Manganese	0.0–0.15
6	Copper	0.15–0.40
7	Titanium	0.0–0.15
8	Chromium	0.04–0.35
9	Other elements	0.05–0.15

Table 2 Chemical composition of fly ash

Component lignite (%)	Bituminous	Sub bituminous	Lignite
SiO ₂	20–60	40–60	15–45
Al ₂ O ₃	5–35	20–30	20–25
Fe ₂ O ₃	10–40	4–10	4–15
CaO	1–12	5–30	15–40
LOI	0–15	0–3	0–5

2 Methodology

The Fly ash is a byproduct of thermal power plant and it is used as reinforcement material with aluminium alloy (Al6061). It is processed by stir casting method to prepare the specimen. Fly ash of 0, 2, 4, 6 and 8% were taken in the form of fine powder to prepare the specimen.

Preparation of wear specimen

The material should be turned to the diameter of 8 mm and a length of 30 mm in lathe machine and the end faces of specimen should be smooth. One end of the specimen should be polished smoothly by using emery paper of different grades. The shape of the pin is in cylindrical form which is equal to diameter of 8 mm and length of 30 mm. The disc has diameter of 180 and 12 mm of thickness.

3 Results and Discussions

3.1 Wear Test

Figure 1 shows the experimental results of wear test. Wear rate is plotted on y axis and composition of fly ash is plotted on x axis which is shown in the above graph. In first case wear of the specimen has increased at 0% of fly ash and then decreased

at 2% of fly ash then again wear rate of the specimen increased gradually at 4, 6 and 8% of fly ash is added for the speed of 1 m/s. In second case wear of the specimen has increased at 0% of fly ash then decreased at 2% again increased at 4% then again decreases at 6% and then increased at 8% for a speed of 2 m/s. In third case wear of the specimen has increased gradually as the % of fly ash has increased for a speed of 3 m/s.

Figure 2 shows that the, at 0 and 2% of fly ash wear of the specimen increases and decreases at 4% again then increased at 6 and 8% for a speed of 1 m/s at constant load of 2 kg as shown in above graph. For a speed of 2 m/s wear rate increases as the fly ash increases. At speed of 3 m/s wear of the specimen increases at 0, 2, 4, 6% and gradually decreases at 8%.

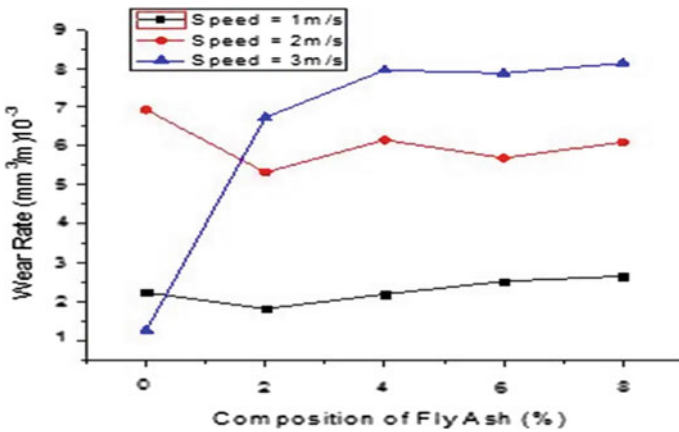


Fig. 1 Variation of wear rate versus fly ash at constant load 1 kg

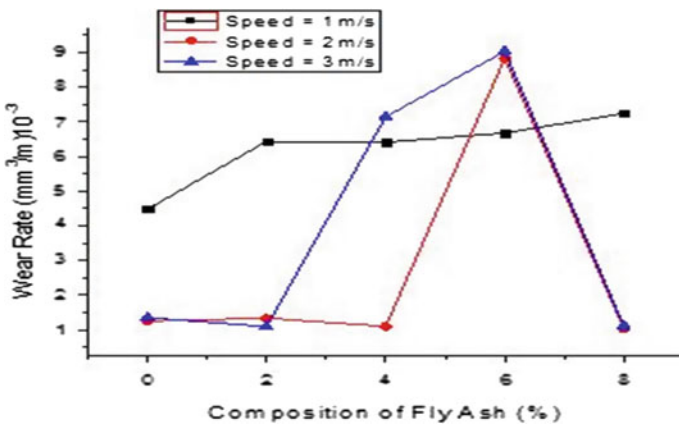


Fig. 2 Variation of wear rate versus fly ash at constant load 2 kg

Figure 3 shows that the wear of the specimen increases at 0% and gradually decreases at 2–8% for velocity of 1 m/s at a constant load of 3 kg. At 0% wear rate of the sample increases and gradually decreases at 2, 4, 6 and 8% for a speed of 2 m/s at a load of 3 kg.

Figure 4 shows that, wear of the specimen increased at 0% and gradually decreases in the weight fraction of fly ash of 2–8% for a speed of 1 m/s at constant load of 4 kg. In second case the wear increases at 0% and remains decreased at varying % of fly ash. Wear rate increase as the weight percentage of fly ash particles increases at 0% and decreases as the weight % of fly ash is increases and again decreases at 4–8% with a speed of 3 m/s at constant load of 4 kg.

Figure 5 shows the results of wear test. The wear rate is more in ductile material is more compared to brittle material. By addition of fly ash in ductile material

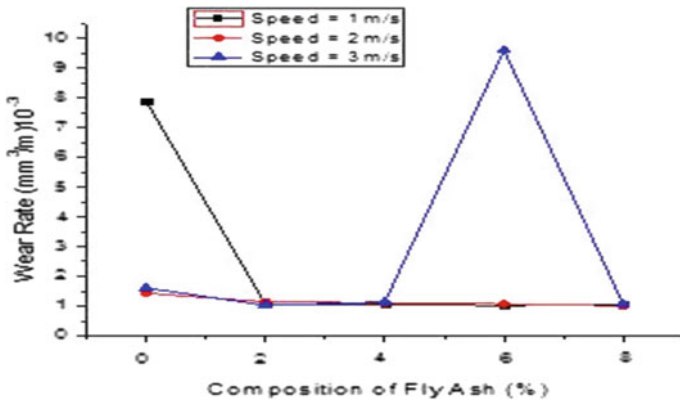


Fig. 3 Variation of wear rate verses fly ash at constant load 3 kg

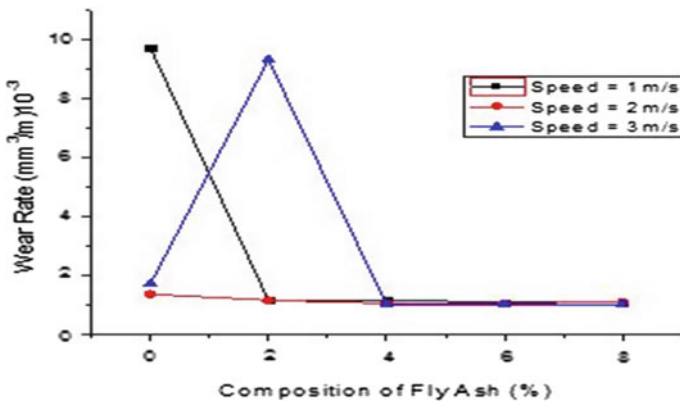


Fig. 4 Variation of wear rate verses fly ash at constant load 4 kg

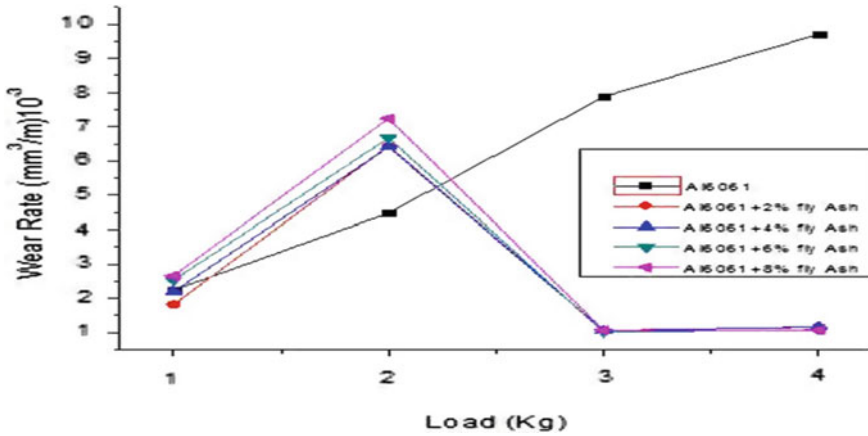


Fig. 5 Wear rate versus speed = 1 m/s

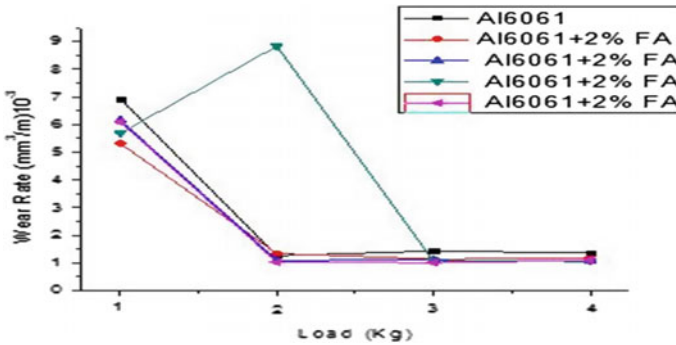


Fig. 6 Wear rate versus speed = 2 m/s

increases the ductility of material for some extent. As the fly ash increases wear rate of the specimen also increases with increase in load at 2%. Further addition of fly ash in Al6061 composite wear rate is reduced at constant speed of 1 m/s.

Figure 6 shows that as the load increases at a speed of 2 m/s Wear rate of the specimen also increases at 2 kg load and wear rate gradually decreases as the load increases for a constant speed of 2 m/s.

From Fig. 7 it shows that, as the load increases wear of Al increases but in the same way decreases with the addition of fly ash it is because of load is increased and it is due to friction at the contact surface and rotating disc increases.

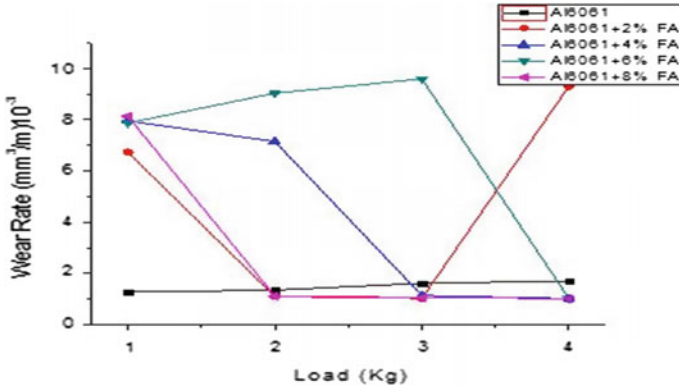
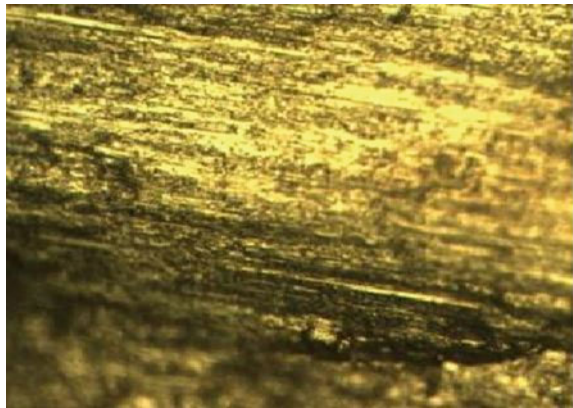


Fig. 7 Wear rate versus speed = 3 m/s

Fig. 8 Al6061 + 0% fly ash



3.2 Microstructure

Figures 8, 9, 10, 11, 12 and 13 clearly show the micrograph of wear test. The removal of material by impact, cracks which are generated along by particle pull at the outer surface can be observed clearly. Worn surfaces can also be viewed by this study. It also reveals the presence of a large number of narrow cut over the whole surface.

Fig. 9 Al6061 + 2% fly ash

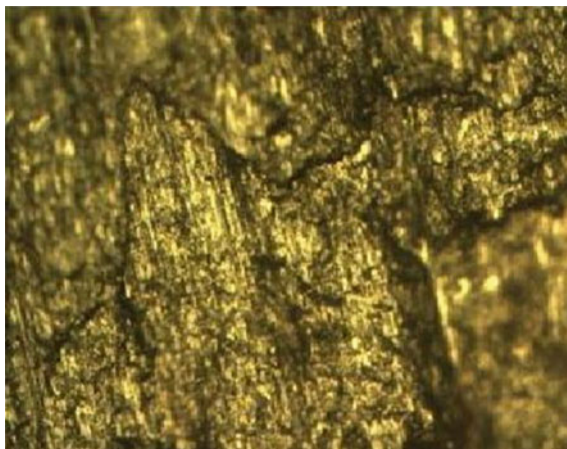


Fig. 10 Al6061 + 4% fly ash

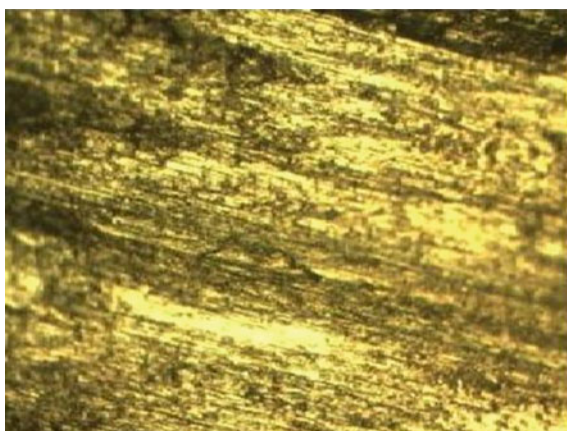


Fig. 11 Al6061 + 6% fly ash

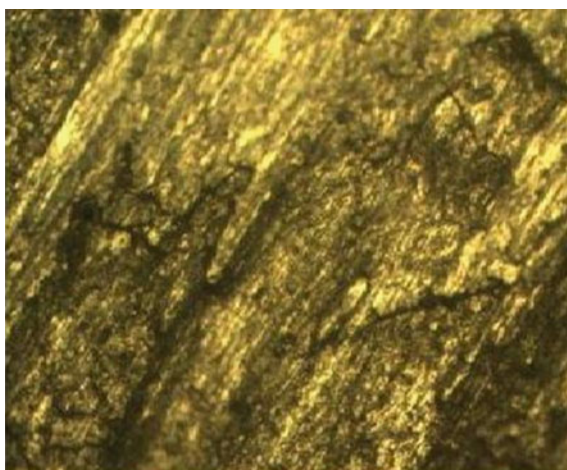


Fig. 12 Al6061 + 8% fly ash

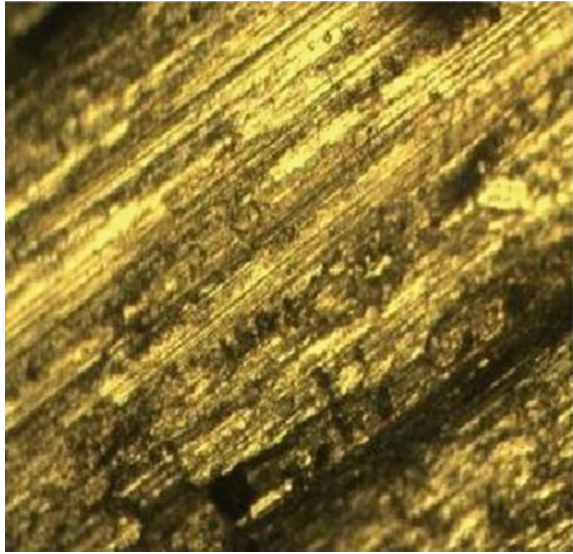
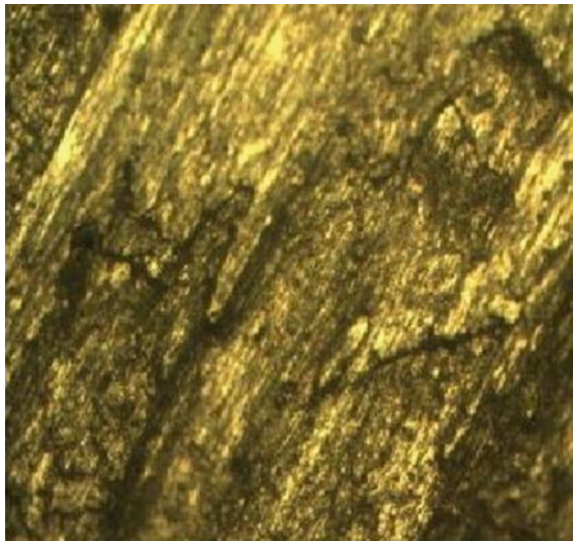


Fig. 13 Al6061 + 8% fly ash



4 Conclusion

Aluminium metal matrix had been fabricated successfully with the uniform dispersion of fly ash particles. Distribution of fly ash particles improves the wear behavior of composites. Wear rate decreases as the speed and load increases. By

addition of fly ash in ductile material increases the ductility of material for some extent. As the fly ash increases wear rate of the specimen also increases with increase in load.

References

1. Prasad N, Sutar H, Mishra SC, Shao SK, Acharya SK (2013) Dry sliding wear behaviour of aluminium matrix composite using red mud an industrial waste. *Int Res J Pure Appl Chem* 3 (1):59–74
2. Kumar V, Gupta RD, Batra NK (2014) Comparison of mechanical properties and effect of sliding velocity on wear properties of Al6061, Mg 4%, fly ash and Al6061, Mg 4%, graphite 4%, fly ash hybrid metal matrix composite. *Science Direct* 1365–1375
3. Anilkumar HC, Hebbar HS (2013) Effect of particle size of fly ash on mechanical and tribological properties of aluminium alloy (Al6061) composites and their correlations. *Int J Mech Syst Eng* vol 3

A Study on Partial Automation of Lac Bangle Manufacturing in Pandharpur

Rohini R. Bhosale and Nitin D. Misal

Keywords Lac bangle · Modern · Traditional · Automation · Livelihood

1 Introduction

Industrial growth of a country depends on the Economic development. The expansion of industrial sector helps to increase the use of natural resources, production of goods and services, creation of employment opportunities and improvement in the general standard of living of Indian population [1, 2]. Maharashtra is one of the major role playing states in Indian Economy.

In Maharashtra, there are many devotional places and Pandharpur is the most visited place by pilgrims. There are four main *Yatras (Vari)* in Pandharpur, and in a year more than 20 lakh pilgrims visits Pandharpur. There are five main businesses in Pandharpur viz. Essence Stick making, Lac bangles making, puffed rice manufacturing, Kumkum manufacturing, and pedha making. The all five businesses use the traditional method for manufacturing. So there is a great scope for automation in any process/partial automation/complete automation in the manufacturing of these businesses.

Bangles had been an important ornament of women since so many years in many parts of the world and particularly in the sub-continent. The pilgrim women visiting to Pandharpur depart wearing bangles as a part of a holy ritual. Generally maximum pilgrim women prefer to wear Lac bangles. Lac bangles with appealing colors and cultural patterns have become more fashionable for today's jet-set women [3].

The present study focuses on the change in livelihood of bangle manufacturers by automation and modernization of these industries. This paper discusses the

R.R. Bhosale (✉)

Department of MBA, SVERI's College of Engineering, Pandharpur, India
e-mail: rrbhosale@coe.sveri.ac.in

N.D. Misal

Department of Mechanical Engineering, SVERI's College of Engineering,
Pandharpur, India

significance of Lac bangles business in Pandharpur, SWOT analysis for Lac bangles manufacturing. Then the present (traditional) method of manufacturing bangles is presented. The scope for automation in Lac bangles manufacturing is discussed. The suggestions for improvement in Lac bangles manufacturing which will change the scenario are presented.

2 Literature Survey

2.1 History of Lac Bangles

The art of making bangles dates back almost 200 years but bangles remain an evergreen fashion accessory. Bangles or *bangdis* are decorative ornaments women of the Indian subcontinent have been wearing for ages. In the desert state of Rajasthan in India, the *churigars* (bangle makers) are scripting a story of communal amity with entire Muslim communities engaged in producing bangles, traditionally worn by Hindu married women as a symbol of marriage. In Maharashtra, green is considered an auspicious colour by married women. It is amazing when you think of the big role played by these delightful ‘circles of light’ in a woman’s life and the fascinating diversity of co-existing cultures in India [4, 5].

Lac is a coloured resin that is obtained from Hosts trees. It is collected from these hosts tree insects that accumulate this resin and then is thoroughly make pure before use [6, 7]. Owing to the plethora of artifacts’, varying tremendously in designs and patterns, lac craft has always been in huge demand. Reference to lac can be found in Vedas. The *Atharvaveda* provides a detailed account of lac, its production, and different uses. *Ayurveda* emphasize the importance of lac in medical therapies. India is one of the largest producers and its principal exporter of lac. It is used over a large area like food processing, textile, leather, cosmetics, varnish, and printing industries. Being bio-degradable and eco-friendly its usage is becoming highly popular [8–11].

2.2 Traditional Procedure of Bangle Making

Lac Bangles consist of *Chapdi* (black lac), orange *chapdi* (light golden lac), *beroza*, *giya pathar* powder, coal, sequins, semi-precious stones, and colors in powder form *pevdi* (yellow), *safeda* (lithophone), *mirgam* (copper), green, *chamki* (gold). The tools used are *Angethi* (coal burner with flat steel plates/*silla* on top), *kadai* (shallow vessel), wooden rod, stonepiece, *hattha* for pressing and shaping lac, iron bangles for sizing, tin foil, round wooden rod/*khali* for shaping bangles, cutter, tool for picking sequins, *haddi* or bone [8, 9].

During this process the, Lac pieces are first melted in a shallow vessel or *kadai*. When it is in a semi-molten state, *beroza*, *giyapathar* powder, and color are added to it. The mixture is stirred continuously. The colored lac is now stuck on the end of a wooden stick. The lac (without pigment) stuck around a wooden rod is heated slowly over the coal burner or *angethi*. It is simultaneously pressed with a stone or a wooden tool called *hattha* at regular intervals. When it is sufficiently warm and soft, it is wrapped with the desired color by rubbing the colored lac stick on it evenly. For this purpose the colored lac stick also has to be warm enough and is therefore heated over the burner. After the color has been applied to the lac base it is shaped into a thin coil with the help of *hattha* and cut off from the plain lac rod [10].

Heating the uncolored lac then uncolored lac pressed with *hattha*; Rubbing the colored lac. The coil is heated over the burner so that the ends can be joined together to form a bangle. After being joined it is slipped through a round wooden beam (with a tapering end for different sizes) and adjusted for size. The bangle is



Fig. 1 a Melting of Lac pieces (*in Kadai*), b Rolling of Lac as rods, c Heating the uncolored lac, d Rubbing colored Lac, e Coil formation using *hattha*, f Heating the coil, g Shaping the coil, h Putting the metal bangles, i Fixing the colored stones into coil into bangles

ready to be embellished with sequins, semi-precious stones, etc. The sequins are placed on a tin foil and heated over a burner. They are warmed so that they can melt the lac surface on which they are placed and stick there after solidification. They are picked up one at a time and stuck on the Bangle. The process requires great precision. It takes much longer when working with smaller sized sequins. The bangle manufacturing process is represented in Fig. 1.

2.3 Drawbacks of the Traditional Process

However many disadvantages are there for uniform mixing of raw material by manually for making LAC bangles, in this process involves many drawbacks are as listed below.

- (1) For mixing these raw materials, skilled worker is required
- (2) He has to take lots of efforts for uniform mixing of raw material.
- (3) Due to fumes health problem occurs to the operator.
- (4) Excess heat can change the property of raw material.
- (5) Less safety for the operator as surrounding is hazardous.

2.4 Lac Bangles Manufacturing Survey in Pandharpur

The lac bangle industry is growing a lot in India and it supplies extensively to the whole India as well as to the whole world. The Study was carried out in the state of Maharashtra where Solapur District Pandharpur Town was chosen as study location based on the existence of the lac industries.

There are around 30 bangle manufacturers in Pandharpur, who have been manufacturing them by the same traditional methods from five generations. It is the

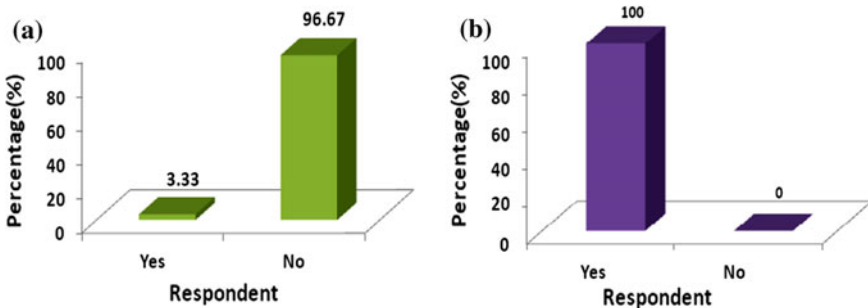


Fig. 2 a Automation in Lac bangle manufacturing process, b Scope for automation in same process

main source of income that supports their livelihood. Their standard of living is as yet not up to the mark. If they foresee it as their future source of livelihood and aim to survive and at the same time upgrade their standard of living, they need to change the method of manufacturing. In Pandharpur, only traditional bangles are manufactured. Keeping a check on the latest trends from across the country and the globe, the lac bangle-makers need to adapt to the modern trends. Figure 2a, b shows the present status of automation in lac bangle manufacturing and scope for automation, respectively.

2.5 *Swot Analysis*

Based on the survey data, a SWOT analysis for the Lac bangles manufacturing process has been presented as below:

Strength

- Abundant women labor hence can compete on price
- Low capital investment and high ratio of value addition
- Aesthetic and functional qualities
- Handmade and hence has few competitors
- Variety of products which are unique
- Increasing scope on product development and design upgradation

Weaknesses

- Competition from machine made goods
- Better terms of trade by competing countries
- Fluctuations of prices due to market conditions
- Irregular demand due to change in taste and Preferences
- Better packaging

Opportunities

- Rising appreciation for lac bangles by consumers in the developed countries
- Widespread novelty seeking
- Growth in search made by retail chains in major importing countries for suitable products and dependable suppliers.
- Opportune for agencies to promote marketing

Threats

- Better quality products manufactured by competitors.
- Good terms of trade by competing countries
- Consistent quality and increasing focus on R&D by competing countries
- Better packaging.

3 Automation in the Lac Bangle Manufacturing Process

3.1 Automation Is a Key for Survival of Lac Bangle Manufacturers

Many small scale units have turned sick due to lack of managerial competence on the part of entrepreneurs. An entrepreneur who is required to undergo training and counseling for developing his managerial skills will add to the problems of entrepreneurs. The small scale entrepreneurs have to encounter numerous problems relating to overdependence on institutional agencies for funds and consultancy services, lack of credit-worthiness, education, training, lower profitability and host of marketing and other problems. The Government of India has initiated various schemes aimed at improving the overall functioning of these units.

Lac bangle manufacturing unit has tremendous potential for automation. It starts from its first operation of stirring action of raw material to packing of bangle [12]. Now all these operations are manual operations where time, energy and money is wasting and production is also not possible. This is key failure of this business. This can be improved and livelihood of these artisans can be made only by automation introduction in this business aiming Pandharpur to be recognized for Lac bangle traditional as well as modern jewelry business on world map.

3.2 Lac Bangle Manufacturing Through Partial Automation

Stirring is the process to mix the fluid and powder to dissolve the powder thoroughly in given mixture and form a uniform product. The stirrer of conventional machine rotates in one direction only which creates a particular flow pattern in the fluids hence the particles tend to stick to the walls of container owing to the centrifugal force rather than mixing thoroughly in mixture, ultimately results into poor quality mixture of fluid there by poor quality output of fluid.

To overcome the above drawbacks and increase the production quality by introducing automatic mixing device with separate heating arrangement was developed. The trial for planetary stirrer and working of the planetary stirrer with heating arrangement is shown in Fig. 3a, b.

3.3 Scope for Automation in Lac Bangle Manufacturing

The possible automation in the process of mixing is developed as presented above. Further the automation can be possible in the following areas/ways

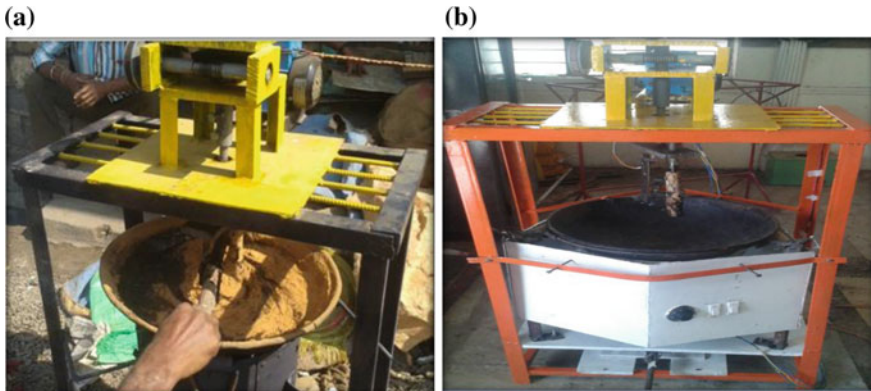


Fig. 3 a Trials for planetary stirrer, b Working device of planetary stirrer with heating arrangement

1. Use of Extrusion process for making of coil of lac
2. Use of mould for shaping of bangles
3. Automation in the golden paper attachment
4. Use of engraving machine for making design on the bangles
5. Use of automation for packing and dispatch activities
6. Overall automation in process like use of conveyors for transfer from one place to another.

4 Suggestions Based on the Study

- State of art research required for lac bangle in traditional manufacturing unit.
- The equipments used in manufacturing of the bangles are crude and heavily depend on the skill of the workers. Thus, the owner is dependent on skilled man power. These equipments can be converted into mass production equipment which does not depend on skill of the artisan/workers. By converting the traditional manufacturing industry into mass production industry with the same labour higher output can be achieved, which will enhance their earning, as these industries are currently running on pieces manufactured on per day basis.
- There is scope for manufacturing bangles with varied designs. This will sustain the sales of these bangles throughout the year and not limit it to seasonal sales like festivals. Also, customers will be getting more varied variety of bangle, which will help satisfy existing customers and attract potential customers. This in turn will help yield higher profit. So there is scope of increasing the income of present laborers as well as owners.
- This is potential business which is not depends upon recession in market.

- Well qualified proprietors need to take initiatives to develop lac bangle manufacturing business.
- There is strong need of marketing agencies for getting new market and taking out new design from market. With the result they are not in a position to upgrade their products keeping in mind market requirements. They are producing less of inferior quality and that too at higher costs. Therefore, in competition with better equipped large scale units they are placed in a relatively disadvantageous position.
- There is need of permanent chudi bazaar in this area like Hyderabad.
- No online business is done in Pandharpur area.
- Government must provide the subsidiary to this type of business.
- Lac Manufacturing Units have to encounter numerous problems relating to overdependence on institutional agencies for funds and consultancy services, lack of credit-worthiness, education, training, lower profitability and host of marketing and other problems. The Government of India has required initiating various schemes aimed at improving the overall functioning of these units.

References

1. Paramasivan C, Subramanian T (2012) Financial management. New Age International (P) Limited Publishers, New Delhi, pp 1–10
2. Mishra SK, Puri VK (2007) Economic environment of business, 4th edn. Himalaya Publishing House, Mumbai
3. Bhatnagar M (2009) Challenges and opportunities for rural lac bangle industry: a study of Jhunjhunu District (Rajasthan), IRJMSH, vol 5(1) online ISSN 2277–9809, pp 278–297
4. Norris D, Glover PM, Aldis RW (1934) Lac and the Indian Lac Research Institute, Namkum, 53 pp
5. Glover PM (1937) Lac cultivation in India. ILRI, Namkum Ranchi, 119 pp
6. Report of the Study on Lac Sub Sector For Chhattisgarh State Institute of Rural Development, Department of Panchayat & Rural Development, Govt. of Chhattisgarh
7. Reeves R (1967) Folk arts of India, Handicrafts and Handlooms Exportation Corp. of India
8. Desai V (2007) A study of rural economic. Himalaya Publishing House, Bombay
9. Chattopadhyay S (2011) Introduction to lac and lac culture
10. Department of Forest Biology & Tree Improvement Department of Forest Biology & Tree Improvement
11. Coxb SM, Finnb MD (2004) Reynolds number effects in a simple planetary mixer. Chem Eng Sci 59:3371–3379
12. Delaplacea G, Thakura RK, Bouviera L, Andreb C, Torrezb C (2007) Dimensional analysis for planetary mixer: mixing time and Reynolds. Chem Eng Sci 62: 1442–1447 (www.ierjournal.org International Engineering Research Journal (IERJ), Special Issue Page 127–130, ISSN 2395-1621 © 2015, IERJ All Rights Reserved Page 130 numbers)

Parametric Optimization for Photochemical Machining of Copper Using Grey Relational Method

Sandeep Sitaram Wangikar, Promod Kumar Patowari
and Rahul Dev Misra

Keywords Photochemical machining · Copper · Material removal rate · Edge deviation · Grey relational analysis

1 Introduction

For manufacturing of geometrically complex and dimensionally accurate machine parts from advanced materials, unconventional machining (UCM) processes are widely employed. In addition, the different unconventional machining processes have been utilized in micron-measure parts creation like microfluidic channels, silicon incorporated circuits, copper printed circuit sheets and enhancing things [1]. Photochemical machining (PCM) is the least studied processes amongst the UCM processes [2]. Photochemical machining (PCM) is one of the nonconventional machining process, which creates burr and stress-free level complex metal parts [1]. The PCM includes imaging of photoresist and chemical etching. A representative collection of relevant study in PCM is discussed below.

A systematic approach for PCM process, the PCM roadmap, and its examples was given by Allen [1]. For surface finishing of AISI 304 stainless steel utilizing hydrochloric acid, electrolytic photoetching process was used [3]. The chemical machining using ferric chloride and cupric chloride was performed and its effect on depth of etch and surface roughness was analyzed [4]. The better etching rate was observed for ferric chloride and good surface finish obtained using cupric chloride. The parametric effect study for chemical machining of copper and aluminium was performed by Cakir and also carried out the regeneration of cupric chloride etchant

S.S. Wangikar (✉) · P.K. Patowari · R.D. Misra
Department of Mechanical Engineering, National Institute of Technology,
Silchar, India
e-mail: Sandeep.wangikar@gmail.com

S.S. Wangikar
Department of Mechanical Engineering, SVERI's College of Engineering,
Pandharpur, India

[5, 6]. The PCM of SS 316 was conducted to study the effect of magnetic field on the etch rate and also PCM of a cardiovascular stent was performed [7, 8]. The parametric study of photochemical machining of different materials Monel 400, SS316L, ASME 316 steel, Brass and german silver and their optimization using different techniques was carried out [9–13]. The copper microchannel was manufactured using PCM, and its surface study was performed [14].

From the literature studied, it can be observed that very less study has been reported on parametric optimization for photochemical machining of copper. Also, there is scope for photo tool related research in PCM. In this study, photo tool analysis has been carried out for selecting the photo tool for PCM. The photochemical machining of copper using ferric chloride as etchant has been performed. The effects of etchant concentration, etching temperature with time on material removal rate and edge deviation have been studied.

2 Materials and Methods

2.1 Material

The material selected for the study is copper due to its applications in heat sinks, heat recovery units, molds for microfluidic applications, etc. The size of the specimen used was 20 mm × 20 mm × 1 mm (thick).

2.2 Experimental Procedure

The photochemical machining involves mainly seven stages as follows [1, 9–14]:

1. **Cleaning of Specimen:** The metal surface must be free of contaminants so that there will be good adhesion between metal and photoresist. Cleaning of the surface is carried out by a solvent like trichloroethylene or acetone to remove traces of grease or oil. After cleaning, washing the metal plates under running water is carried out.
2. **Photo tool generation:** The photo tool is nothing but a negative film of the image to be produced. Photo tools are normally generated by direct printing of the image from CAD drawings.
3. **Coating of photoresist:** Photoresists application is carried out by using an immersion process with the help of a photoresist dip coater followed by drying of the specimen.
4. **UV exposure:** The coated specimen is usually exposed to the ultraviolet source in contact with photo tool. Photoresist is sensitive to U.V. radiation and therefore a U.V tube based, U.V exposure unit can be used for exposure.

5. **Development:** After UV exposure, the specimen is kept in a solvent based developer. This will remove unexposed areas of the photoresist (Wet film negative method). The total development time is about 60–90 s.
6. **Rinsing:** The specimen should be washed in running water with neutral pH.
7. **Etching:** Process in which etchant chemically dissolves metal, their relative importance depends on the process parameters, such as temperature and dilution of the etchant solution.
8. **Cleaning:** The cleaning of the specimen is carried out by washing in running water and by using acetone.

2.3 Selection of Parameters

The PCM process performance is affected by many parameters. Based on the literature studied and some pilot experiments, the input parameters (control parameters) has been selected. To study their effect on the performance measures, the control parameters have been varied in a range during experimentation. The input parameters along with their range for experimentation are mentioned in Table 1. Along with the input parameters, there are some parameters which also have an effect on the performance of the photochemical machining. To study the effect of input parameters on the PCM process, these parameters are kept constant during the experimentation like specimen size, etchant (ferric chloride), photoresist, etc.

The performance of any photochemical machining process is stated by the undercut, material removal rate, etch factor, edge deviation. The output parameters considered for the experimentation are as follows.

1. **Edge Deviation (ED):** The non-conformity of the edge of a machined component is referred as Edge deviation. It is an important parameter for micro-fluidic applications.
2. **Material Removal Rate (MRR):** The higher value of MRR represents better etching performance. The material removal rate can be calculated from the depth of cut and the area etched.

Table 1 Control parameters with their levels

Control parameters	Concentration (g/l)	Temperature (°C)	Etching time (min)
Level 1	400	40	7
Level 2	500	50	14
Level 3	600	60	21

2.4 Taguchi Design of Experiments

The design of experiments includes proper selection of variables (input factors) and their interactions. The fractional factorial method developed by Taguchi is applied to optimize with process input variables. For three parameters with three levels (as given in Table 1) with a full factorial method, 27 experiments are required to be carried out. For the combination of parameters, only 9 experiments are needed to be performed as per Taguchi L-9 array. The photochemical machining on copper was carried out using Taguchi L-9 design matrix.

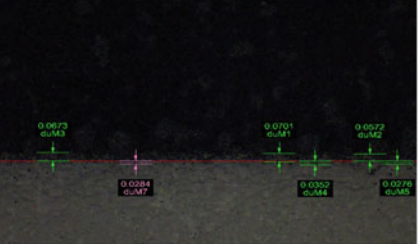

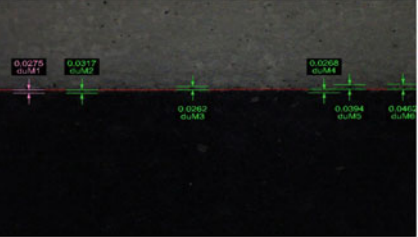


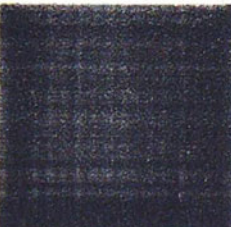

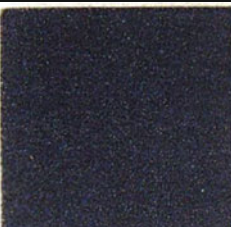
2.5 Photo Tool Analysis

- **Photo tool Generation:** The photo tool is nothing but a negative film of the image to be produced (machined). The accuracy of the photochemically machined specimen principally depends upon the accuracy of Photo tool. The photo tools are generated by direct printing of the image from CAD drawing. Thus the accuracy of the Photo tool is decided by the dpi (dots per inch) specification of the printer. The cartridge replacement and toner refilling also play a significant role in print quality. The Photo tool for the experimentation is generated with four different printers.
- **Photo tool Analysis:** The four photo tools have been analyzed for edge deviation and overall quality. The edge deviation (ED) measurement is has been carried out by using RAPID-I Vision5 microscope, and the sample images of Photo tool ED is presented in Table 2. The edge deviation should be minimum for a photo tool. Figure 1 shows the average edge deviation of the four photo tools. Amongst the four photo tools, Photo tool 4 has lowest edge deviation and a significant overall quality. Hence photo tool 4 is selected for the experimentation in photochemical machining.

2.6 Experimentation

The experimental set-up for PCM is as shown in Fig. 2. Using L9 array experimentation has been carried out with two replications. Thus total 27 experiments have been performed. Photochemical machining of the copper has been carried out using Ferric Chloride (FeCl_3) as etchant. For each experiment, the etchant used was 500 ml and the temperature was maintained within ± 1 °C. The single-sided chemical etching process was followed. The effect of input parameters on the material removal rate MRR (mm^3/min) and edge deviation (μm) has been studied.

Table 2 Edge deviation and overall image quality of different photo tools

Photo tool	Edge deviation measurement image	Image for Overall quality
1		
2		
3		
4		

The material removal rate has been calculated by calculating the volume of material removed and then dividing it by the etching time. The edge deviation of the specimen after photochemical machining has been measured using RAPID I Vision 5 microscope and Leica Optical Microscope. Figure 3 shows the edge deviation measurement of a sample specimen.

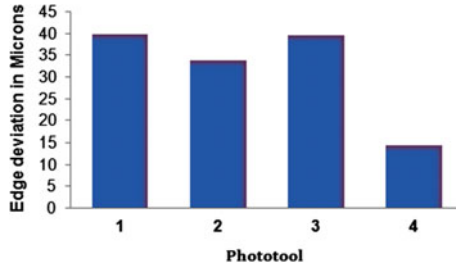


Fig. 1 Average edge deviation of photo tools

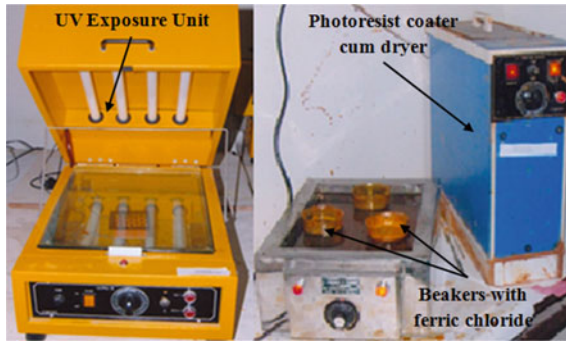


Fig. 2 Photochemical machining set-up

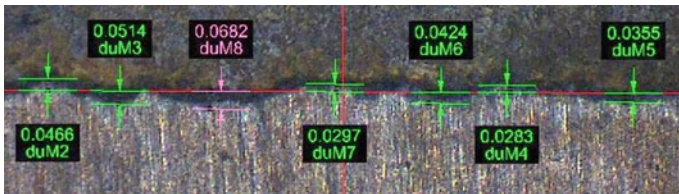


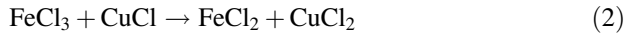
Fig. 3 Edge deviation measurement for a sample specimen

3 Results and Discussion

It is required to know the chemical reaction of the copper material with ferric chloride etchant. Every etchant reacts differently during a chemical machining process. The chemical reaction of $FeCl_3$ with copper is as follows:



The cuprous chloride (CuCl) and ferrous chloride (FeCl₂) are formed due to oxidation of copper by ferric ions. Further, CuCl is oxidized in the etchant solution to produce CuCl₂ as follows:



The CuCl₂ also reacts with copper and CuCl is formed as shown below:



3.1 Effect of Process Parameters on Edge Deviation (ED)

The Main Effect plots for ED are shown in Fig. 4a. Main effect plot gives the effect of control parameters on the response parameters. With an increase in concentration and temperature, the edge deviation increases. The edge deviation is observed decreasing with increasing etching time. The edge deviation always should be lesser. The lesser ED observed at concentration 400 g/L, temperature 40 °C, and the etching time of 21 min. From the probability plot as shown in Fig. 5a, it can be observed that the results of all nine experiments are within the upper and lower deviation limit.

3.2 Effect of Process Parameters on Material Removal Rate (MRR)

The Main Effect plots for MRR are shown in Fig. 4b. When the etching rate increases, the material removal rate increases. The MRR increases with increase in concentration and temperature and also with etching time. The maximum MRR observed at concentration 600 g/L, temperature 60 °C, and the etching time of

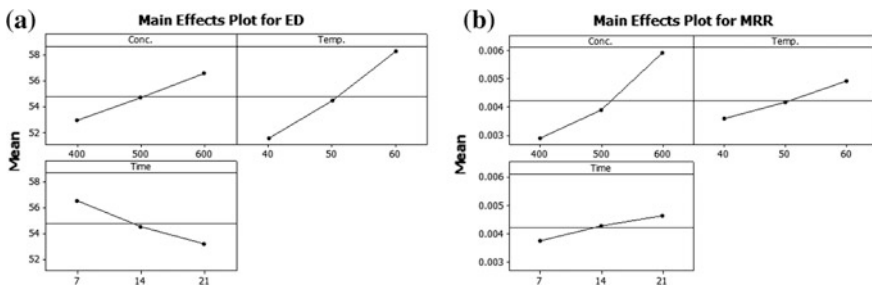


Fig. 4 a Main effects plot for ED, b Main effects plot for MRR

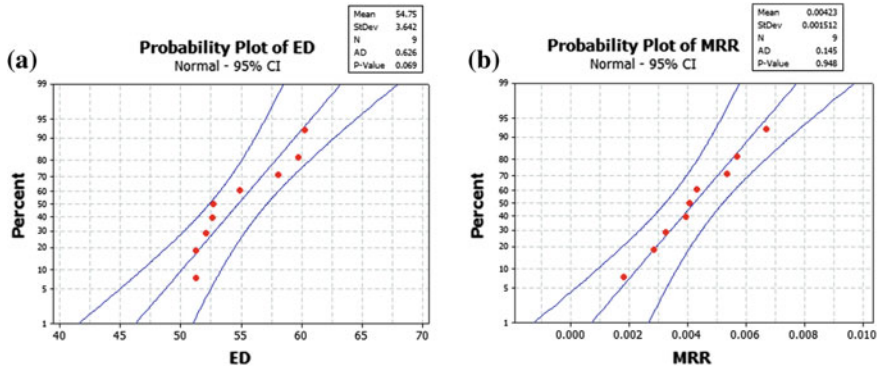


Fig. 5 a Probability plot for ED, b Probability plot for MRR

21 min. From the probability plot as shown in Fig. 5b, it can be noted that the results for MRR for all nine experiments are within the upper and lower deviation limit.

3.3 Optimization Using Grey Relational Analysis

If there are multiple response parameters, for the same conditions of independent variables, the best condition for a single parameter like ED and MRR can be obtained. But the MRR is always desired higher while ED should be always preferred lesser. For satisfying this condition, Grey relational analysis technique has been used for multi-objective optimization. Grey relational analysis determines the single parametric combination that optimizes the performance of an overall process. Grey relational analysis ranks the experiments based on the increasing order of their grey relational grade (GRG). The ten steps in Taguchi based grey relational analysis as given below.

- Step 1: Identify the response variables and corresponding S/N ratio
- Step 2: Identification of controllable parameters, interactions, and their levels
- Step 3: Identify orthogonal array and assign parameter levels to each column
- Step 4: Conduct the experiment and collect the data for response variables
- Step 5: Data preprocessing by normalizing of the response variables
- Step 6: Calculate grey relational coefficients for each sequence
- Step 7: Determine the grey relational grade by averaging the grey coefficients
- Step 8: Determine the optimum sequence, from the higher grey relational grade
- Step 9: Determination of optimum parameters
- Step 10: Predication of GRG for optimal parameters

The process of linear normalization of the original sequence is a problem of larger-the-better quality characteristic is used to normalize the original sequence using the following equation.

$$x_i^*(k) = \frac{x_i^{(o)}(k) - \min x_i^{(o)}(k)}{\max x_i^{(o)}(k) - \min x_i^{(o)}(k)} \tag{4}$$

For smaller-the-better quality characteristic of the original reference sequence, the following expression is used for normalization.

$$x_i^*(k) = \frac{\max x_i^{(o)}(k) - x_i^{(o)}(k)}{\max x_i^{(o)}(k) - \min x_i^{(o)}(k)} \tag{5}$$

The deviation sequence, $\Delta 0_i(k)$ is the absolute difference between the reference sequence $x_0^*(k)$ and the comparability sequence $x_i^*(k)$ after normalization. The value of $x_0^*(k)$ was considered as 1. It is determined using Eq. 6 as given below.

$$\Delta 0_i^*(k) = |x_0^*(k) - x_i^*(k)| \tag{6}$$

Grey relational coefficients (GRC) for all the sequences express the relationship between the ideal (best) and actual normalized response variables. If the two sequences agree at all points, then their grey relational coefficient is 1. The grey relational coefficient $\gamma(x_0(k), x_i(k))$ can be expressed by Eq. 7.

$$\gamma(x_0(k), x_i(k)) = \frac{\Delta \min + \zeta \Delta \max}{\Delta 0_i(k) + \zeta \Delta \max} \tag{7}$$

where $\Delta \min$ is the smallest value of $\Delta 0_i(k) = \min_i \min_k |x_0^*(k) - x_i^*(k)|$ and $\Delta \max$ is the largest value of $\Delta 0_i(k) = \max_i \max_k |x_0^*(k) - x_i^*(k)|$, $x_0^*(k)$ is the ideal normalized S/N ratio, $x_i^*(k)$ is the normalized comparability sequence and ζ is the distinguishing coefficient. The value of (ζ) is taken as 0.5 for all response variables and is substituted in Eq. 7. The GRC for all the experimental runs are calculated.

The overall evaluation of the multiple performance characteristics is based on the grey relational grade. The grey relational grade is an average sum of the grey relational coefficient, which is defined as follows:

$$\gamma(x_0, x_i) = \frac{1}{m} \sum_{i=1}^m \gamma(x_0(k), x_i(k)) \tag{8}$$

where $\gamma(x_0, x_i)$ the grey relational grade for the j th experiment and m is the number of performance characteristics.

The grey relational grade $\gamma(x_0, x_i)$ represents the level of correlation between the reference sequence and the comparability sequence. If the two sequences agree at

Table 3 GRG values for response parameters

Exp No.	Conc. (g/L)	Temp. (°C)	Time (min)	GRC MRR	GRC ED	GRG MRR	GRG in %	Rank
1	400	40	7	0.33	1.00	0.667	66.67	4
2	400	50	14	0.39	0.76	0.571	57.14	6
3	400	60	21	0.47	0.55	0.512	51.15	8
4	500	40	14	0.41	1.00	0.706	70.61	2
5	500	50	21	0.50	0.76	0.634	63.38	5
6	500	60	7	0.48	0.33	0.408	40.77	9
7	600	40	21	0.71	0.84	0.774	77.43	1
8	600	50	7	0.64	0.40	0.521	52.11	7
9	600	60	14	1.00	0.35	0.674	67.37	3

all points, then their grey relational coefficient is 1 everywhere, and therefore, their grey relational grade is equal to 1. The grey relational grade was determined by Eq. 8. A higher grey relational grade indicates that the corresponding condition is optimum.

From Table 3, the optimum condition is given at experiment number 7 (Concentration 600 g/L, temperature 40 °C, etching time 21 min).

3.4 Use of the Study for Societal Application

The photochemical machining can be applicable for manufacturing of jewelry items, ornaments from the material like german silver (a copper nickel alloy with silvery appearance). The heat sink and heat recovery units can be manufactured on copper using the above mentioned data of PCM. The moulds for fabrication of a microchannel using soft lithography technique can be manufactured very effectively using PCM.

4 Conclusions

Using Taguchi L9 design matrix, PCM of copper has carried out using. Based on the study, the main conclusion are summarized below

- The photo tool has significant effect on the etched specimen and thus photo tool selection has been carried out based on the edge deviation and overall quality.
- The edge deviation increases with increase in concentration, temperature and decreases with increase in etching time. The material removal rate increases with increase in concentration, temperature, and time.

- The maximum MRR observed at concentration 600 g/L, temperature 60 °C, and etching time of 21 min while lesser ED observed at concentration 400 g/L, temperature 40 °C, and etching time of 21 min.
- Grey relational analysis has been performed for deciding the optimum parametric condition.
- The concentration of 600 g/L, a temperature of 40 °C, and 21 min etching time are responsible optimum conditions as per GRG.

References

1. Allen DM (2004) Photochemical machining: from ‘manufacturing’s best kept secret’ to a \$6 billion per annum, rapid manufacture process. *CIRP Ann—Manuf Technol* 53(2):559–572. doi:[10.1016/S0007-8506\(07\)60029-8](https://doi.org/10.1016/S0007-8506(07)60029-8)
2. Gamage JR, DeSilva AKM (2015) Assessment of research needs for sustainability of unconventional machining processes. *Procedia CIRP* 26:385–390
3. Allen DM, Almond HJA (2004) Characterisation of aqueous ferric chloride etchants used in industrial photochemical machining. *J Mater Process Technol* 149:238–245
4. Cakir O, Temel H, Kiyak M (2005) Chemical etching of Cu-ETP copper. *J Mater Process Technol* 162–163:275–279
5. Cakir O (2006) Copper etching with cupric chloride and regeneration of waste etchant. *J Mater Process Technol* 175:63–68
6. Cakir O (2008) Chemical etching of aluminum. *J Mater Process Technol* 199:337–340
7. Saraf AR, Sadaiah M (2016) Magnetic field assisted photochemical machining (MFAPCM) of SS316L. *Materials and Manufacturing Process* 32(3):332–337. doi:[10.1080/10426914.2016.1198014](https://doi.org/10.1080/10426914.2016.1198014)
8. Saraf AR (2016) Sadaiah M, Photochemical machining of a cardiovascular stent. *Mater Manuf Processes* (Accepted Article). doi:[10.1080/10426914.2016.1198025](https://doi.org/10.1080/10426914.2016.1198025)
9. Sadaiah M, Patil DH (2015) Some investigations on surface texturing on Monel 400 using photochemical machining. In: *Proceedings of the 460 ASME 2015 international manufacturing science and engineering conference MSEC2015*, Charlotte, North Carolina, USA, 8–12 June 2015. doi:[10.1115/MSEC2015-9294](https://doi.org/10.1115/MSEC2015-9294)
10. Bhasme AB, Kadam MS (2016) Parameter optimization by using grey relational analysis of photochemical machining. *Int Res J Eng Technol* 3:992–997
11. Bhasme AB, Kadam MS (2016) Experimental investigation of PCM using response surface methodology on SS316L steel. *Int J Mech Eng Technol* 7:25–32
12. Mumbare P, Gujar AJ (2016) Multi objective optimization of photochemical machining for ASME 316 steel using grey relational analysis. *Int J Innovative Res Sci Eng Technol* 5:12418–12425
13. Wangikar SS, Patowari PK, Misra RD (2016) Effect of process parameters on surface characteristics of photochemically machined copper microchannel. *International conference on surface modification technologies SMT30*, Milan, Italy, June 29–July 1, 2016
14. Wangikar SS, Patowari PK, Misra RD (2016) Effect of process parameters and optimization for photochemical machining of brass and German silver. *Mater Manuf Processes* (Accepted Article). doi:[10.1080/10426914.2016.1244848](https://doi.org/10.1080/10426914.2016.1244848)

Part VI
Infrastructure Developments for Societal
Applications

Buried Pipelines Deformation Behavior in Different Soils Using Geof foam

A.S. Mane, Shubham Shete and Ankush Bhuse

Keywords Buried pipes · Geof foam · Image analysis · Small scale modelling

1 Introduction

Buried pipelines transports materials indispensable to the functioning and support of human life and repairable of property and hence are often referred to as lifelines. In industries, public supplies, and for transportation of oil, gas, water and many other fluids and goods buried pipelines are used. Buried pipeline generally spread over a large geographical region and encounter a wide variety of loading and soil condition. The deformation of pipelines caused by the different loading like earth pressure, traffic load and construction loading also. There are a many research have been done to calculate the nature forces acting on the pipelines buried under the soil [1–4]. Different types of soil loading affected on buried pipelines. The behavior of the cohesive soil, Frictional soil, and C-Phi soil greatly changes in soil stratum along the run and change in consistency of such soils. It is very necessary to protect the buried pipelines against different actions of loading. The results damage or crack of such pipes, disruption in the transportation on intended fluids caused by the different types of the loading which also unreasonable differential deformation in pipe. Several authors have suggested the use of geof foam to protect these pipes from surrounding soil [5]. These author's research is limited to the concept-based application than that of real modeling of the buried pipelines. To protect the buried pipelines could be using geof foam inclusion and several factors such as width of

A.S. Mane (✉)

Department of Civil Engineering, CSMSS, CSCOE, Aurangabad 431005, Maharashtra, India
e-mail: abhinavmane@gmail.com

S. Shete · A. Bhuse

Department of Civil Engineering, DIEMS, Aurangabad 431005, Maharashtra, India
e-mail: shubhamshete1231@gmail.com

A. Bhuse

e-mail: ankushbhuse94@gmail.com

geofoam, thickness, density of geofoam and soil type. The small-scale experimental evaluation of the buried pipelines with and without geofoam demonstrates in the present study.

2 Motivation Behind Present Study

Figure 1 shows the schematic cross section of the buried pipes with and without geofoam inclusion. Generally, the loosely placed fine grained soil, frictional sand and the mixture of these two soils experiences strip loading, a punching shear, general shear and local shear failure should occur simultaneously, which may transfer the majority of the surface load towards the pipe. When the geofoam placed below the strip loading at a certain depth of equal to the width (B) of the footing, geofoam compresses and the settlement due to strip loading gets distributed in the surrounding soil. With a geofoam case, the ultimately would result in lesser load transfer on the pipe from the footing. The wide spreading distribution in load transfer should heighten with the compressibility of the geofoam as well as the available volume for compression under the foundation. Due to the width of buffer below footing wider the spread of load and greater possibilities for clay, sand, and mixture of soil arching, increase in bearing area and shear strength development of soil.

3 Model Materials

3.1 Soil

Black cotton soils are found in many part of India. The black cotton used in this study is collected from Mukundwadi, Aurangabad (Maharashtra). Black cotton soils have been identified on igneous, sedimentary and metamorphic rocks. The optimum moisture content of black cotton is found 18% at maximum dry density is found 1.56 g/cm³. In the present study, soil is placed at 10% wet of optimum

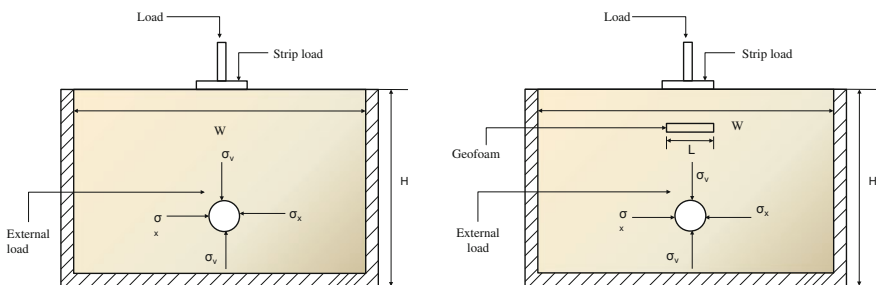


Fig. 1 Schematic cross section of buried pipe with and without geofoam

conditions. The sand used for this study is Bombay beach sand, composed of rounded and sub rounded particles. Sand is classified as Silty Sand (SM) in the unified soil classification system (USCS). The model sand is found to have internal frictional resistance of 32° for 55% relative density. The mixture of black cotton and sand is found to have optimum moisture content 1.715 gm/cm^3 at maximum dry density is 12%. In the present study, soil is placed at 10% wet of optimum conditions. The three types of model soils properties summarizes in Table 1. Figure 2 shvos the photographic veiw of model soils.

Table 1 Properties of the model materials used in present study

Properties	Values
<i>Sand</i>	
Specific gravity (G)	2.61
Soil classification (USCS)	SM
Coefficient of curvature (Cc)	1.17
Coefficient of uniformity (Cu)	1.99
Maximum void ratio (e_{\max})	0.943
Minimum void ratio (e_{\min})	0.691
Unit weight of soil at 55% relative density kg/m^3	1446.7
Angle of internal friction at 55% relative density ($^\circ$)	32°
<i>Black cotton</i>	
Soil classification	CH
Liquid limit (%)	68
Plastic limit (%)	26.40
Optimum moisture content (%)	18
Maximum dry density (g/cc)	1.56
Grain size distribution:	
Sand (%)	5.1
Silt + Clay (%)	94.9
<i>Mixture of BC and Sand</i>	
Optimum moisture content (%)	1.715
Maximum dry density (%)	12
<i>HDPE pipe</i>	
Diameter, $D_p(\text{m})$	0.05
Compressive load at 10% strain, (kN)	26
<i>Geofoam</i>	
Geofoam type	Expanded polystyrene
Geofoam legend	EPS8
Density (kg/m^3)	8
Compressive resistance at 1% strain (kPa)	10
Compressive resistance at 5% strain (kPa)	30
Compressive resistance at 10% strain (kPa)	35
Compressive elastic modulus (kN/m^2)	850

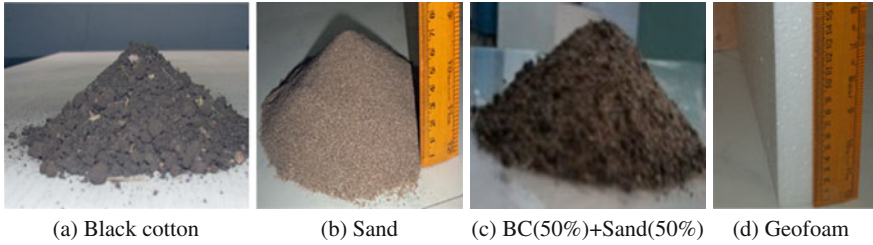


Fig. 2 Photographic view of model materials used in the present study

3.2 Geofoam

Expanded polystyrene (EPS) geofoam is used in the present study as a compressible inclusion behind reinforced zone. The compressive resistance in uniaxial unconfined compression tests is found to be 17 kPa for geofoam EPS8. At the same time, the elastic modulus is observed to be 850 kPa for geofoam EPS8. Properties of the model geofoam are summarized in Table 1.

3.3 HDPE Pipe

The model pipe stands for the flexible buried pipeline used for water, gas and oil transportation. In the present study, a commercially purchasable 2-inch diameter flexible HDPE pipe is used. On the model HDPE pipe to the extent, the deformation in the pipe for a particular load only one axis compression test is performed. Photographic view of the only one axis compression test on model HDPE pipe is used in the present study shown in Fig. 3. With the applied load the variation in

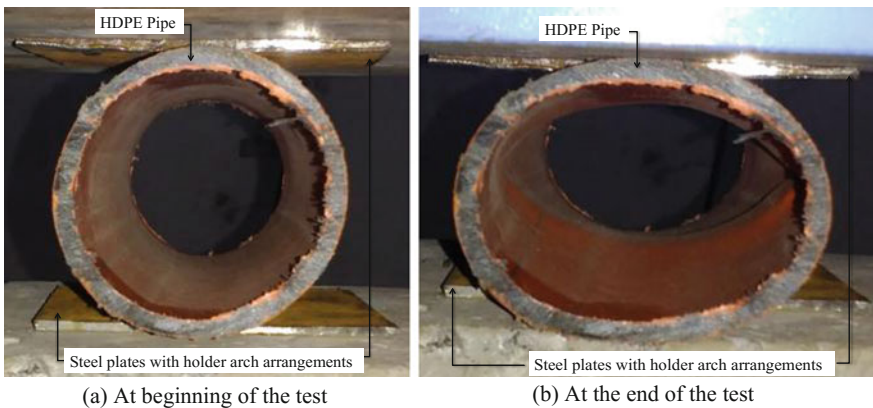
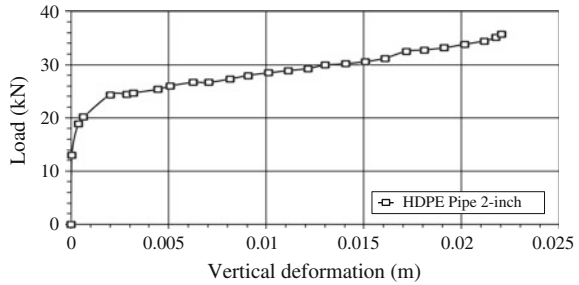


Fig. 3 Photographic view of uniaxial compression test on model HDPE pipe

Fig. 4 Uniaxial load deformation variation of model HDPE pipe



vertical deformation of the pipe is shown in Fig. 4. From the correlation in Fig. 4 deformations in the pipe were assessed with the help of image analysis technique and then the load required for indistinguishable deformation is marked.

4 Model Test Package and Test Procedure

For small-scale test model the strong MS box consists of a 10 mm thick steel panel from four sides i.e. bottom, back, and side panels. The front glass panel is made up of 12 mm thick for observation of buried pipeline model during test. The Fig. 5 shows front view of the buried pipeline model constructed with and without geofoam inclusion. In observation the moment occurring in the soil is capturing by using a digital camera at determinate time interval through the transparent glass panel. The MS box is proof tested for its capacity before starting of the test for different soil backfill and different loading intensities. Inside the glass panel number of thin polythene sheet strip were placed after the application of grease layer in such way that those moves along with the soil and on friction occur with boundary during the test. A benchmark is provided to measure movement of moveable markers during the test by using four permanent marker glued outside of the glass panel. Moveable plastic markers 'L' shaped were placed into the soil at specific interval to supervising the movement of soil during the test. A digital camera is fixed on a stand made up of PVC pipe. The lithium battery operated LED lighting panel is used to maintain constant intensity of clarification throughout the test. In the present study soil is placed likewise, cohesive soil at OMC 1.56 gm/cm^3 , sand at uniform relative density of 55% and mixture of clay and sand at 1.715 gm/cm^3 consistency. Geofoam of 8 kg/m^3 density with width of 100 mm is used which were placed exactly at depth equal to width of the footing (B_f) for the entire model test. In this study a constant height of surcharge above the pipe is 0.25 m maintained for the entire test.

The UTM (Universal Testing Machine) having maximum compressive and tensile capacity of 1000 kN were used to tested for all the experimental buried pipeline model in three type of soil at DIEMS Aurangabad. The geofoam of density 8 kg/m^3 and width 100 mm is placed above the buried pipeline at a constant height.

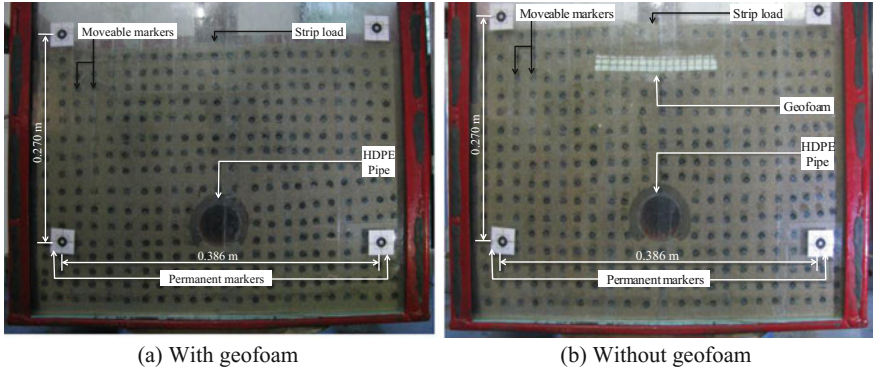


Fig. 5 Front view of the model test package

At the center of the test model and buried pipeline, the footing of size $0.023H$ wide is placed. A vertical load is gradually applied at the constant strain rate of 1.0 N/s . A digital camera (Canon make, 9 megapixels, enhanced shutter speed) were used to take images at a constant time interval. Images taken were stored in a connected computer located away from the test setup.

5 Test Program

The details of the model tests performed in the present study shown in Table 2. Entire 6 model tests were performed with and without geofoam inclusion below strip footing. Model BP01, BP03, and BP05 is tested without the inclusion of geofoam in the non-plastic fine sand soil, black cotton and mixture of these two soil respectively were treated as the base model for evaluation of the efficiency of the geofoam having 8 kg/m^3 density in a reduction of pressure on buried pipeline.

Table 2 Details of the model tests performed in the present study

Test legend	Type of soil	Geofoam width (mm)	Geofoam density (kg/m^3)
BP01	Sand	*NA	*NA
BP02		100	8
BP03	Black cotton	*NA	*NA
BP04		100	8
BP05	Mixture of sand and BC	*NA	*NA
BP06		100	8

6 Analysis and Interpretation

At the time of model, test images obtain at the constant interval with the help of a digital camera. Image analysis is performed on the images which are obtained from the tests performed with the help of Image J open source software [6]. By using the advanced template matching plugins and PIV (Particle Image Velocimetry) analysis in Image J, the displacements occurred above and around the pipe and geofoam is measured. The displacement vector diagrams for buried pipeline experimental models with and without geofoam is shown in Fig. 6. Vectors in the images are

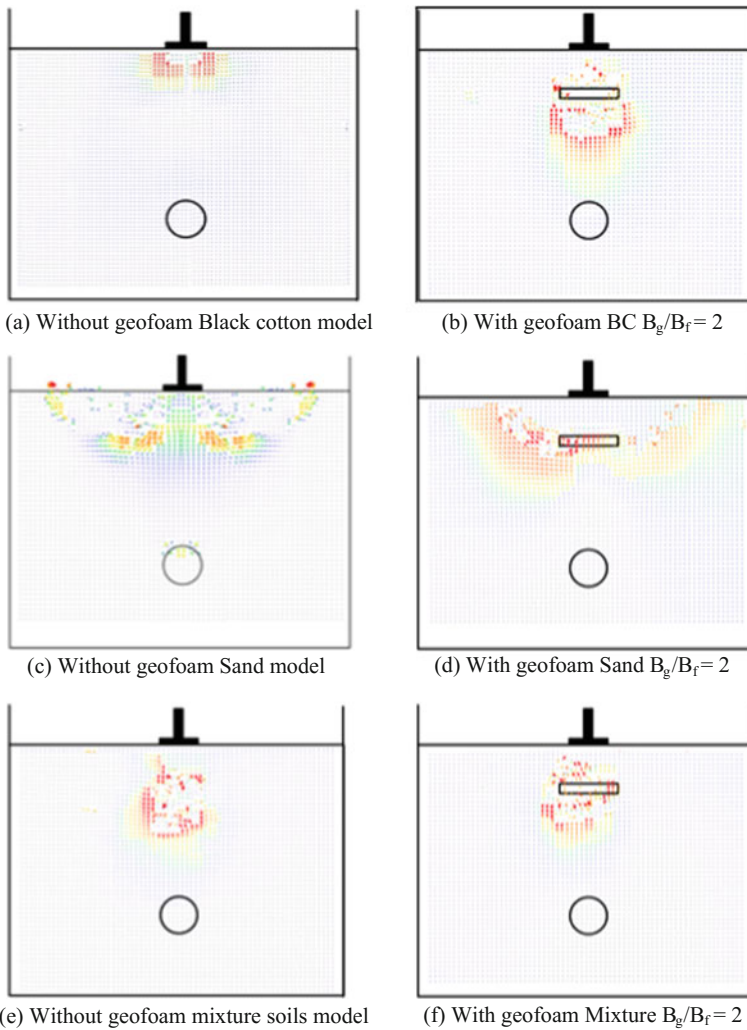


Fig. 6 Displacement vector for test models with and without geofoam

scaled up two times than original for better visualization of the results. After placing of geofoam compression zone at both side of buried pipeline is reduced and due to which deformation in buried pipeline also reduced. Geofoam is placed on the footing at height B_f (i.e. equal to the width of footing). Geofoam inclusion provides compressible bed below the footing which compresses according to the load transferred at corner minimum and at the center maximum forming a reverse arch. Due to this load transfer divert from axial direction to the outward diagonal direction and thus transfers less load on buried pipeline.

7 Results and Discussion

Deformations in the vertical direction were calculated from image analysis for all the model tests performed in the present study. It is observed that the deformations in the pipe are inversely proportional to the width of the geofoam and directly proportional to the density of the geofoam. Figure 6a shows the variation of vertical deformation occurred in the pipe with respect to the width of the geofoam for varying density of the geofoam. A similar representation about the load transferred on the pipe could be made as shown in Fig. 6b. The load transferred to the pipe is estimated based on the deformations measured through image analysis and the corresponding load from the load-deformation diagram of HDPE pipe as shown in Fig. 6. The vertical axis is normalized to the pipe diameter in Fig. 6a. A maximum reduction in load transferred of up to 33.33% is observed in the case of low-density geofoam (EPS8) having maximum width of 150 mm. Table 3 summarizes the results obtained from the series of the model tests performed in this study.

8 Conclusions

Based on the observations made in the present study, Conclusions made are as below,

1. Geofoam as a compressible inclusion placed below strip footing provides significant reduction in transferred load on buried pipes.
2. The load on buried pipes reduces the density of the geofoam inclusion decreases. So, the load transferred could be made minimum by decreasing the density of the geofoam inclusion.
3. With increase in width of the geofoam load reduction increase. This mainly due to the arching in soil above pipe as well as the wide distribution of the deformations in the soil mass mobilizes with the increase in width of the geofoam. A maximum decrease of 33.3% in load is obtained when a low-density (i.e. 8 kg/m^3) geofoam with a maximum width of $3B_f$ is used.

References

1. Bilgin O, Stewart HE (2012) Studying buried pipeline behavior using physical and numerical modeling. In: 'GeoCongress 2012: state of the art and practice in geotechnical engineering. 1, Oakland, California, United States, pp 2128–2137
2. Corey R, Han J, Khatri DK, Parsons RL (2014) Laboratory study on geosynthetic protection of buried steel reinforced HDPE pipes from static loading. *J Geotech Geoenviron Eng* 1(1):1–10
3. Johnson J, Hutson AC, Gibson RL, Verreault L (2010) Protecting existing PCCP subject to external transient loads. In: *Pipelines 2010: climbing new peaks to infrastructure reliability—renew, rehab, and reinvest. 1* ASCE, Keystone, Colorado, United States, pp 203–210
4. Stephen S (2011) Contribution of lateral earth pressure resistance to restrain horizontal thrust in buried pipelines. In: *Pipelines—a sound conduit for sharing solutions. 1*, ASCE, Carlsbad, CA, pp 358–371
5. Watkins RK (2004) Pipe and soil mechanics for buried corrugated HDPE pipe. In: *Pipelines 2004: pipeline engineering and construction. 1*, ASCE, San Diego, California, United States, pp 1–10
6. Schneider CA, Rasband WS, Eliceiri KW (2012) NIH image to imageJ: 25 years of image analysis. *Nat Methods* 9(7):67–671

A Time Dependent Scour Around Circular Piers Under Unsteady Flow

Anandrao R. Deshmukh and Rajkumar V. Raikar

Keywords Clear water scour · Froude's numbers · Sediment · Unsteady flow · Pier

Notations

B Channel width
D Depth of scour at time
 u_{*c} Critical shear velocity of sediment
 d_{50} Mean size of sediment
y Depth of flow
b Pier diameter of circular pier
U Average velocity of flow
Fr Froudes number
 U_c Average velocity of flow at critical condition
T Time at scour depth
 σ_g Geometric standard deviation
Q Discharge of flow
 u_* Shear velocity of sediment
 t_p Time corresponding peak discharge

1 Introduction

Hydraulic failure i.e. scours around bridge pier and abutments are amongst the prime reasons for bridge failures [1]. Scouring of stream bed elevation takes place in the close or around the structure like bridges piers, abutments, levees, and spur

A.R. Deshmukh (✉) · R.V. Raikar
Civil Engineering Department, KLE Society's Dr. M.S. Sheshgiri College
of Engineering and Technology, Belgaum 590008, India
e-mail: anand21desh@gmail.com

R.V. Raikar
e-mail: rvraikar@gmail.com

dikes, etc. When approaching channel does not supply sediment in scouring region, it is called as a clear-water scour. Garde and Kothyari [2] stated that when the ratio of u^*/u^*_c is less than one in the approaching channel, no sediment supply to the scour hole and clear water scour occurs. The condition of clear water scour is as $0.5 < U/UC < 1$; here U is the mean stream velocity, and UC is the mean critical velocity at which sediment starts moving. Scour was noticed to be maximum for U/UC equal to one and nearly independent of shear stress for U/UC values greater than one.

The horse shoe vortex and down flow at Pier upstream are main factors affects scouring due to which there is three dimensional flow separation around the structure. It is initiated when induced bed shear stress is strong enough to overcome the particle shear resistance in motion. The eroded sediment particles are washed out prominently on downstream by the influence of horse shoe vortex. In the downstream, the wake vortex system continues scouring which is shown in Fig. 1 [3].

When flow in streams is unsteady, scouring process around structure becomes very complicated. Scour depth estimation around piers and abutments is overestimated depth under steady flow using various models. Flood discharge of same intensity never remains for the same period, but it occurs for very few days instead of whole period. Hence there is the need to determine to scour depth under unsteady flow which may be less than the steady flow. Most bridge failures have mainly been caused by floods. The effects of flow unsteadiness of flow on bridge piers and abutments have not received adequate attention [4]. Numerous studies based on

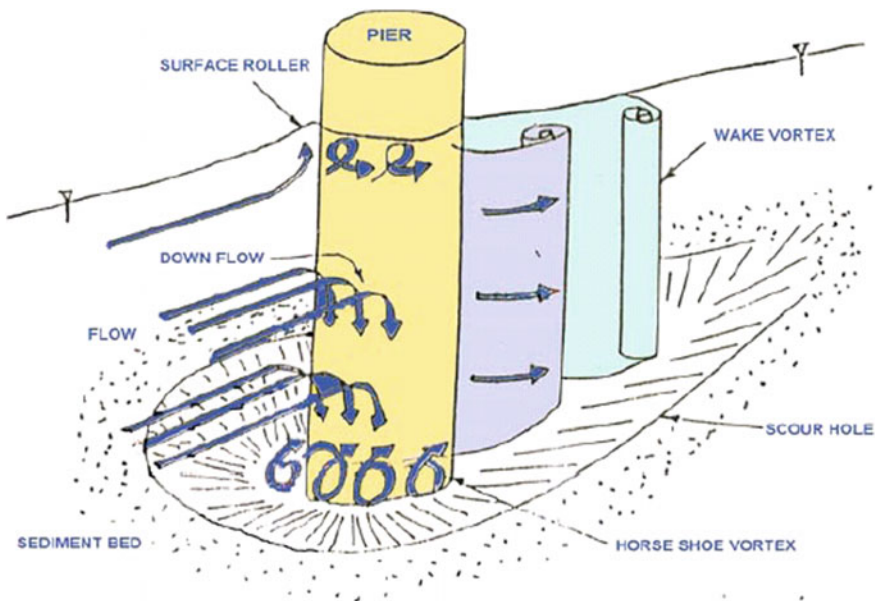


Fig. 1 Flow structure around circular bridge pier [3]

experimental and field data have investigated the temporal variation of scour depth at a pier and abutment under steady flow and clear-water scour [4–9]; However, only a few investigators have focused on the temporal evolution under un-steady flow [4, 7]. Parametric study of a flood wave is very limited. No unique model is developed for time-dependent scour but all model are suitable for their experimental and field conditions. As a result, effort on such topic is essential to evaluate the performance of different scours models under unsteady flows.

Most of the equations for estimation of maximum scour depth have been derived empirically from experimental studies in the laboratory. These equations are based on a limited range of data and apply to the conditions similar to those for which they are developed. Kothari et al. [7] developed a model for computing pier local scour depth under unsteady flow in a clear-water-scour condition. The assumption in his study was that a primary horse shoe vortex in front of the pier is the main responsible of scouring. Oliveto and Hager [4] investigated laboratory based empirical model in clear water local scour under unsteady condition in non-uniform sand and proposed a computational method of determination of local scour depth for stepped typed flood and concluded that scour depth is smaller in single peak flood discharge than scour depth for same peak discharge for a steady condition.

Many investigators have given conclusion from their work that as pier diameter increases maximum depth of scouring increases. The depth of scour is affected by bridge pier and abutment characteristics, such as shape size, alignment, and length, etc. [1, 6]. Ettema et al. [10] have shown that as Froude number of pier decreases scour depth around pier also decreases by keeping all other variables i.e. discharge, depth of flow and longitudinal slope of channel constant, etc because the frequency of horse shoe vortices and wake vortices on downstream side for pier of larger diameter decreases.

In this paper, experimental observations are presented for two different pier diameters and two different uniform sediments. Three stepped flood hydrographs with same base period were developed for experimentation.

The main objective study is to do a parametric study of local scour under unsteady flow condition for circular piers for uniform sediment. Final scour depth is compared for three different flood hydrograph. Comparisons of scour depth for flood hydrograph under study was made. It shows that for delayed flood wave it is maximum with d_{50} of 0.52 mm.

2 Experimental Set up and Procedure

Laboratory experiments were performed in tilting flume of rectangular cross section in Hydraulics laboratory in department of Civil Engineering at Rajarshi Shahu College of Engineering, Pune, having 0.30 m wide, 8 m long and 0.30 m deep with maximum discharge up to 0.015 cumecs. For discharge measurement orifice meter with pressure gage shaving a least count of 0.05 kg/cm^2 is used. It is fitted on delivery pipe of centrifugal pump. Recirculation system is adopted. Longitudinal

slope of flume is maintained 1 in 5000 with the help of mechanical jack towards tail end side of flume. The flow rate is adjusted by controlling valve. The valve and tail gate is slowly operated without disturbance to the bed surface until the desired discharge is obtained. Required water depth is obtained by tail gate. The water surface is measured using point gauges fixed on a carrier which moves along the length of channel section in to and fro on rail arrangement. It is sensitive to the variation of 0.1 mm.

3 Modification in Existing Flume

Existing bed level is elevated by 10 cm with Plexiglas sheets on upstream, and mobile bed zone of 185 cm long 30 cm wide, and 10 cm deep is prepared at distance of 2.25 m downstream of the flume and is false bed prepared is filled with sediment of desired size. To enter water in channel without turbulence, false bed was tapered and honey comb structure is kept vertically at entrance. Computation were done to ascertain a clear water condition for each step of hydrograph with help of empirical equations developed by V. Rijn to maintain clear water scour condition for given sediment size.

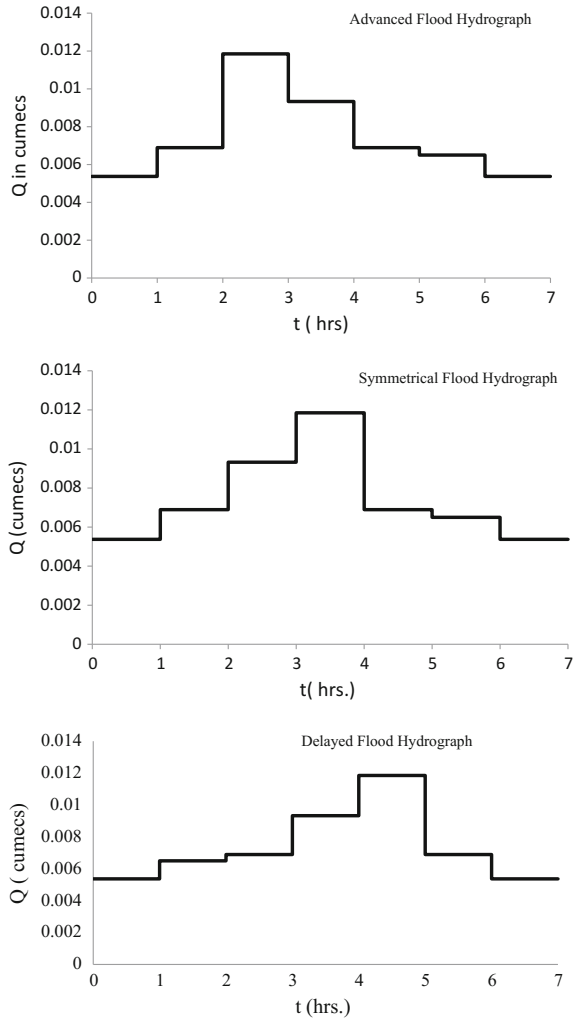
For experimentation, condition of flow intensity is kept less 1 (clear water scour condition). Flow shallowness (ratio of depth of flow to pier diameter) is more than 2.6 for all depth flow under all flood hydrographs and to avoid coarseness effect ratio of pier diameter to median sediment size of sediment is greater than 25. Also to avoid effect of contraction, diameter of pier should not more than 15% of channel width [8] and minimum dimension of pier and abutment normal to flow direction is kept 10% of channel width to avoid the influence of boundary layer thickness [9].

Before starting experimentation for unsteady flow, experimentation was done to decide optimum size of model to determine only local scour excluding contraction effect which is not part of present study. For median size of 0.52 mm with two different pier diameter, run of each flood hydrograph were taken. Total runs were 6 for same sediment. Similarly another 6 runs were taken for median size of 0.712 mm (Fig. 2)

Two piers made of a Plexiglas having diameter of 31.5 and 40 mm of circular cross section and river bed sediment of median size 0.52, and 0.712 mm was used. Before starting each run, experiments were conducted to maintain clear water scour for given sediment size without pier. Three different stepped flood hydrograph of same base period of 7 h were developed. Each step has duration of 1 h. But it was observed that local scour depth increases till peak discharge and remains constant when discharge recedes [5]. Hence runs were taken till end of peak discharge.

By using Shields diagram [11], u_{*c} is determined for both sediment size. u^* is also determined for each step of flood hydrograph to ascertain a clear water scour condition.

Fig. 2 Details of flood hydrographs experimented



4 Result and Discussion

The instantaneous scour depth is observed at the time interval of 5 min. The scale was pasted over a pier model having least count of 0.5 mm. It was observed through the transparent portion of the test section of the flume. The height of flume above the floor is approximately 1 m for each sediment size, observations were taken with both pier sizes. The scour pattern observed at 40 mm circular pier is shown in Fig. 3. For each flood hydrograph, experimentation of scour depth determination is done till peak flood because after peak flood, maximum scour

Fig. 3 Scour pattern observed around 40 mm pier



Table 1 Summary of experimentation for circular piers

Type of flood	u^*/u_{*c}	Q (m ³ /s)	y (m)	b (m)	d_{50} (m)	σ_g	t_p (s)
AHF	0.7	0.00537	0.09	0.0315,	0.00052,	1.28	10800
	0.762	0.00689	0.12	0.04	0.000712	1.31	
	0.85	0.01185	0.18				
SHF	0.70	0.00537	0.09				14400
	0.72	0.00689	0.1				
	0.808	0.00932	0.15				
	0.85	0.01185	0.18				
DHF	0.70	0.00537	0.09				18000
	0.72	0.0065	0.1				
	0.762	0.00689	0.12				
	0.808	0.00932	0.15				
	0.85	0.01185	0.18				

AHF Advanced flood hydrograph, DHF Delayed flood hydrograph, SHF Symmetrical flood hydrograph. Number of runs for each hydrograph-4

depth observed remains constant in clear water scour. Maximum scours depth is observed is on upstream side pier which is shown in Fig. 3.

The relation between local scour depth at circular bridge pier d_s and dependent parameters can be written

$$d_s = f(U, y, d_{50}, \sigma_g, b, t, t_p) \tag{1}$$

where t_p = peak flood time.

Assuming same specific gravity and non presence of viscous effects, an expression for scour depth for a local scour at a circular pier having diameter ‘b’ can be written as follows

$$d_s/b = f(y/b, d_{50}/b, t/t_p) \tag{2}$$

Summary of experimentation details for all flood hydrographs is given in Table 1 in which depth of scour observed at the end of each step of a flood are mentioned.

Summary of test condition is given in Table 1.

Figure 4 shows the comparison of scour depth evolution for circular piers. Figure 4a, b shows scour pattern for same pier diameter of 0.0315 m with different sediment. From Fig. 4a it reveals that final scour depth under delayed flood hydrograph depth of scour is maximum. It is because delayed flood wave occurs for longer period than other flood hydrograph.

In general, at sediment size of 0.52 mm final scour depth for all types hydrograph is more than 0.712 mm sediment for same pier diameter and the same type of hydrograph. Delayed hydrograph ends last as compared to others which result in maximum scour depth. At the end of peak flow, maximum scour is observed which continues till the end period of hydrograph because of a clear water scour condition.

Non-dimensional scour depth pattern observed for AFH, SFH and DFH is shown in Figs. 5, 6 and 7. For each step of flood wave initially scour rate is more and in later it diminishes. In general, scour variation trend is almost parallel to each other according to their sediment size and pier diameter. Dimensional less scour depth is more for smaller sediment size and larger pier diameter.

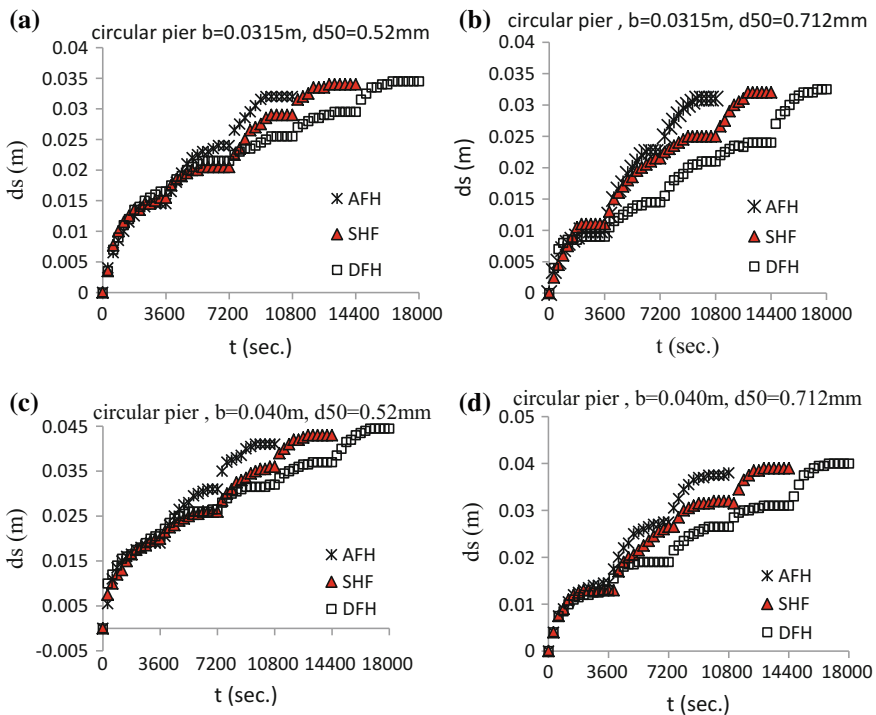


Fig. 4 Comparison of scour evolution at a circular pier under different flood hydrograph. **a** For $b = 0.0315$ m and $d_{50} = 0.52$ mm. **b** For $b = 0.0315$ m and $d_{50} = 0.712$ mm. **c** For $b = 0.040$ m with $d_{50} = 0.52$ mm. **d** For $b = 0.040$ m with $d_{50} = 0.712$ mm

Fig. 5 Dimensional less scours depth for AFH

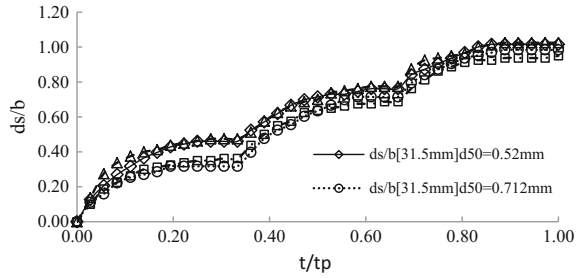


Fig. 6 Dimensional less scour depth for SFH

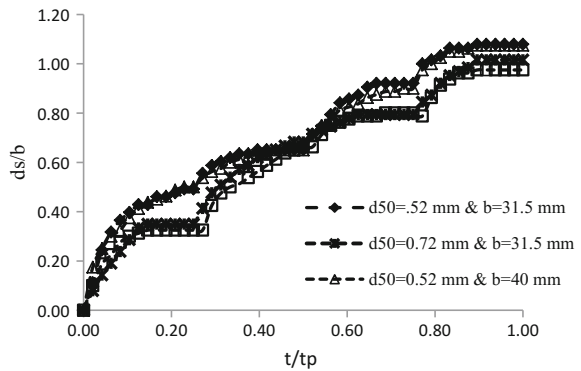
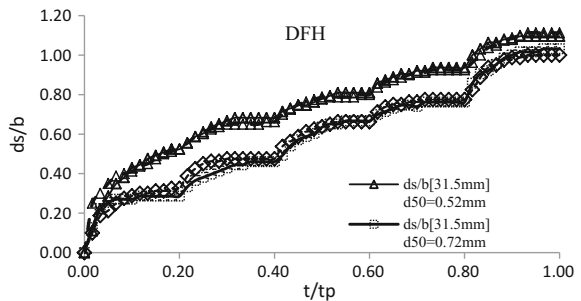


Fig. 7 Dimensional less scour depth for DFH



Besides this, it was observed that when the discharge of following the step in flood hydrograph suddenly increases to higher values, the rate of scouring rises significantly.

The comparison of non dimensional scour depth variation for different sediment size ($d_{50} = 0.52$ and 0.71 mm) at 0.040 m pier diameter is shown in Fig. 8a. Scour variation of sediment size 0.52 mm is overlying the scour variation of sediment size of 0.71 mm . Figure 8c shows similar variation pattern for 0.0315 m pier diameter.

Figure 8a, c compares non dimensional scour depth for same pier diameter with different sediment size which shows that scour depth is dependent on sediment size

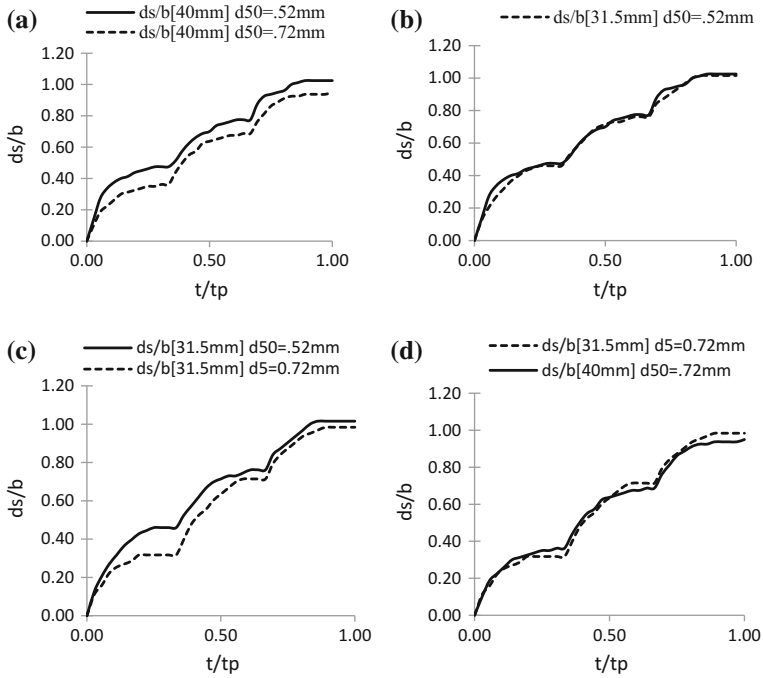


Fig. 8 Comparison of non dimensional scour depth for AFH **a** for 40 mm pier diameter, **b** for 0.52 mm sediment size, **c** for 31.5 mm pier diameter and **d** for 0.71 mm sediment size, **c** for 31.5 mm pier diameter and **d** for 0.71 mm sediment size

for both pier diameter. While Fig. 8b, d shows that almost scour pattern are overlapping for both pier diameters. It indicates that non dimensional scour depth w.r.t. is not dependent on pier diameter.

Similarly, comparison of scour depth under symmetrical flood and delayed flood is shown in Figs. 9 and 10 respectively. The Same trend of scour variation is observed. Under delayed flood wave scour variation for same pier diameter with different sediment are widely separated as compared to AFH and DFH which is shown in Fig. 10a, c for 40 mm pier diameter and 31.5 mm pier diameter respectively. Maximum scour depth is observed for DFH for 40 mm pier diameter with 0.52 mm median sediment size.

It is observed that rate of scouring at an initial period in each step of flood hydrograph is more and decreases in the later period. For same sediment size but for the different pier, diameter scours variation pattern are almost overlapping to each

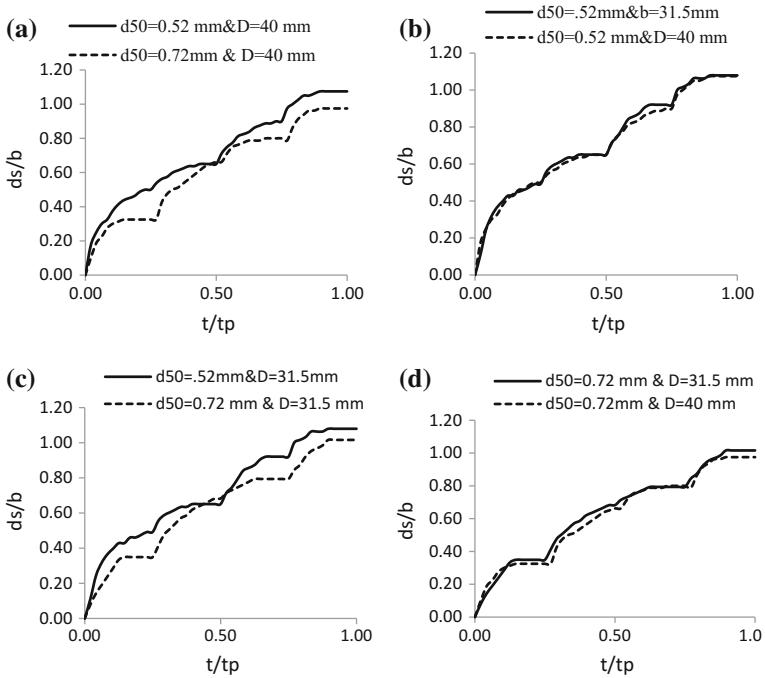


Fig. 9 Comparison for SFH **a** for 40 mm pier diameter, **b** for 0.52 mm sediment size, **c** for 31.5 mm pier diameter and **d** for 0.71 mm sediment size

other. And it differs for same pier diameter with different sediment size which is shown in Figs. 9 and 10b, d. Hence non dimensional scour depth depends on sediment size.

Non dimensional final scour depth (dsf/b) for different flood hydrograph for the different combination of pier diameter and sediment size is tabulated in Table 2. Peak discharge is same for all flood waves but peak time is different. For same pier diameter and same sediment size maximum scour depth observed is for DFH which indicates scour depth is dependent on peak time duration

In above table, dimensional less scour depth corresponding a peak discharge under delayed flood hydrograph is on higher side compared to other hydrograph. Also for pier of 0.040 m diameter in 0.52 mm sediment scour depth is maximum.

Figure 11 show that non dimensional final scour depth trend line versus non dimensional pier diameter under three flood waves. For symmetrical flood, there is more reliable with coefficient correlation above to 0.9 whereas for delayed and advanced flood hydrograph coefficient of correlation is not satisfactory. For $b/d_{50} = 76.92$ non dimensional final scour depth values are close to trend line.

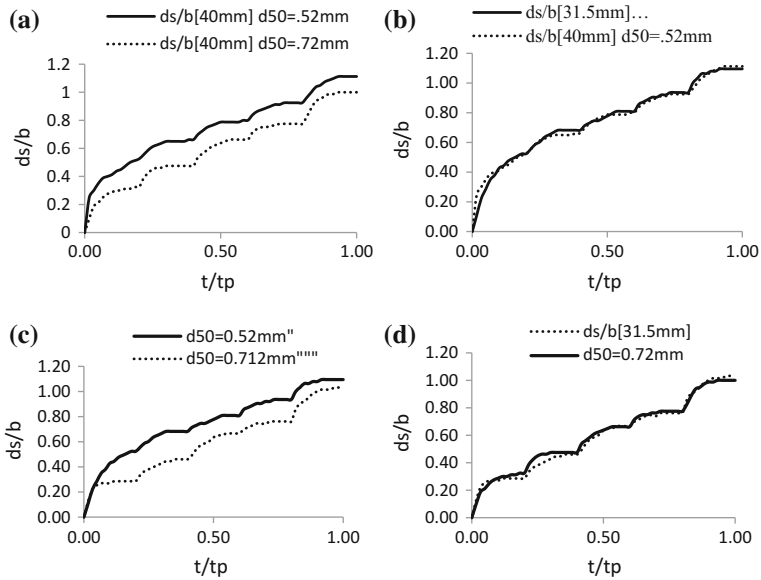
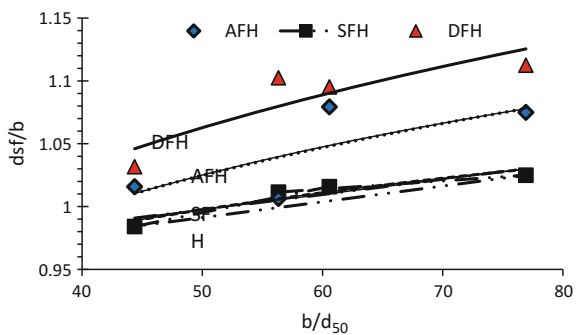


Fig. 10 Comparison of non dimensional scour depth for DFH **a** for 40 mm pier diameter, **b** for 0.52 mm sediment size, **c** for 31.5 mm pier diameter and **d** for 0.71 mm sediment size

Table 2 Non dimensional final scour depth for different floods

b (m)	d ₅₀ (mm)	b/d ₅₀	d _{s,f} /b		
			AFH	SFH	DFH
0.0315	0.52	60.58	10.08	1.02	1.10
0.0315	0.71	44.37	10.02	0.98	1.03
0.040	0.52	76.92	10.08	1.03	1.11
0.040	0.71	56.34	00.98	0.95	1

Fig. 11 Comparison of final scour depth determination for different flood hydrograph



5 Conclusion

The time-dependent variation of scour depth at circular piers in uniform sediments under unsteady flows with clear-water scour conditions are studied as a parametric approach. Unsteady flow of same base period with varying peak flow time experimented. Final scour depth observed for delayed flood hydrograph is maximum for a sediment of $d_{50} = 0.52$ and 40 mm pier diameter. And final scour depth trend for a symmetrical flood is more reliable than others. Dimensionless scour depth is dependent on mean sediment size and peak time. Parametric study of a local scour around a bridge pier under unsteady flow is carried out for small values of b/d_{50} and on uniform sand which is the limitation of present study.

References

1. Dargahi B (1982) Local scour at bridge piers-a review of theory and practice. Bulletin no TRITA-UBI-114, Stockholm (Sweden)
2. Garde RJ, Kothiyari UC (1995) State of art report on scour around bridge piers. IIBE, Mumbai
3. Garde RJ, Ranga Raju KG (2000) Mechanics of sediment transportation and alluvial streams problems. The New Age Publisher, New Delhi
4. Olivette G, Hager WH (2005) Further results to time dependent local scour at bridge elements. J Hydraul ASCE 131(2):97–105
5. Chang WY, Lai JS, Yen CL (2004) Evolution of scour depth at circular bridge piers. J Hydraul Eng ASCE 130(9):905–913
6. Dey S (1999) Local scour at pier (Part-I)-A review of development of research. Int J Sedim Res 12(2):23–44
7. Kothiyari UC, Garde RJ, Ranga Raju KG (1992) Temporal variation of scour around circular bridge piers. J Hydraul Eng ASCE 118(8):1091–1106
8. Melville BW, Chiew YM (1999) Time scale for local scour at bridge piers. J Hydraul Eng ASCE 125(1):59–65
9. Melville BW, Sutherland AJ (1988) Design method for local scour at bridge piers. J Hydraul Eng 114(10):22830
10. Ettema R, Kirkil G, Muste M (2006) Similitude of large-scale turbulence in experiments on local scour at cylinders. J Hydraul ASCE 132(1):33–40
11. C van Rijn (1984) Sediment transport, part I. Bed load transport. J Hydraul Engg ASCE 110(10):1431–1456
12. Kothiyari UC (2006) An assessment on Indian practice for estimation of scour around bridge piers. J Adv Eng, 89–100
13. Mia MF, Nago H (2003) Design model of time-dependent local scour at circular bridge pier. J Hydraul Eng ASCE 129(6):420–427

Implementation of Methodology for Wastewater Treatment from Textile Industry

D.A. Kumbhar

Keywords Physico-chemical · Equalization · Flotation · Sedimentation · Sludge

1 Introduction

Water is the major natural resource available for the living things on the earth. So it should be utilized carefully. Nowadays, there is a large amount of water required in the textile industry and that toxic water is not treated and let into the drainage. But according to the rule of government, every industry must do the pre-treatment and then let the water into drainage i.e. the industry should reduce the pollutants present in the effluent. The textile dyeing industry consumes bulk quantities of water and produces bulk volumes of wastewater from different steps in the dyeing and finishing processes. Dyeing mainly aims at dissolving the dye in water, which will be transferred to the fabric to produce colored fabric under certain conditions. In dyeing, color is applied in the form of solutions. The natural and synthetic textiles both are subjected to a variety of finishing processes. All of the finishing processes contribute to water pollution. Wastewater from dyeing units is often rich in color, containing residues of reactive dyes and chemicals, such as complex components, the high value of COD, along with BOD concentration as well as much more hard-degradation materials. The toxic effects of these dyestuffs and other organic compounds, as well as acidic and alkaline contaminants, from industrial establishments on the general public, are widely observed. Therefore, understanding and developing effective printing-dye industrial wastewater treatment technology is environmentally important. These effluents can be treated and will be reused for the dying process again in the industry, which leads to increase in environmental conditions [1–4].

D.A. Kumbhar (✉)

Department of Electronics and Telecommunication Engineering,
SVRI's COE Pandharpur, Solapur, Maharashtra, India
e-mail: dakumbhar@coe.sveri.ac.in

2 Intended Beneficiaries

The implementation of this project is very beneficial to the textile industries. Since the maximum amount of the water is wasted during the dyeing process. By this project, the textile industries will be able to reuse the water again for the dyeing process. Therefore, the similar setup can be established for the industries of type are stated below:

- Textile industry.
- Cotton spinning industry.
- Color printing industries.
- Locality near the industries.

The implementation of this project can control the water pollution, and also it will save the Environment.

After the water has been treated by the chemical process, the RO filter can be used to purify the water.

3 Methods

The waste water from the textile industry contains color, dyes, and oily chemicals. So there are various methods available to treat the waste water.

The treatment methods are as follows in Fig. 1.

From the mentioned methods, this project is carried under the physico-chemical treatment method as it is a less time-consuming process, cost effective and also easily applicable. This treatment process is explained below [2].

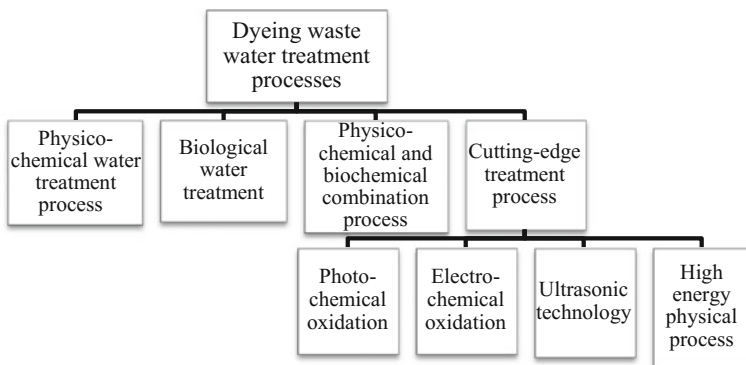


Fig. 1 Methods of waste water treatment

4 Physicochemical Waste Water Treatment

Wastewater treatment is a mixture of different unit processes, some physical, others chemical or biological in their action. The output (or effluent) of one process becomes the input (influent) of the next process. The first stage will usually be made up of physical processes. Physicochemical wastewater treatment has been widely used in the sewage water treatment plant having high removal of chroma and suspended substances, while it has a low removal of COD. The common physicochemical methods are shown as followed [2].

Step 1: Equalization and homogenization

In effluent, the quality of water is highly polluted, and quantity fluctuations, complex components, textile dyeing wastewater is required pretreatment to ensure the treatment effect and stable operation. In general, the regulating tank is set to treat the wastewater, and some chemicals are added to decrease harmful content (Fig. 2).

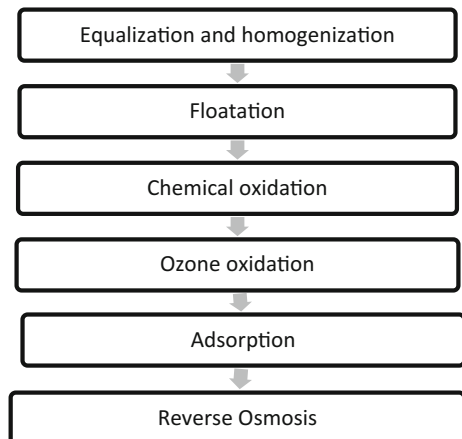
Step 2: Floatation

To separate the oil particles from the water, floatation is preferred, which forms the substrate in three-phase substances as, water, gas, and solid. Floatation produces a large number of micro-bubbles. Here the dissolved air under pressure is added to cause the Formation of tiny bubbles which will attach to particles. Due to its low density, the mixtures float to the surface so that the oil particles are separated from the water [2].

Step 3: Chemical oxidation

Chemical operations are those in which strictly chemical reactions occur, such as precipitation. Chemical treatment relies upon the chemical interactions of the contaminants we wish to remove from water. The chemical treatment method is applied both as in an integral part of the treatment process with physical methods.

Fig. 2 Flowchart of the physico-chemical process



Chemical operations can oxidize the pigment in the printing and dyeing wastewater as well as bleach the effluent. Currently, Fenton oxidation and ozone oxidation are often used in the wastewater treatment [2].

Step 4: Ozone oxidation

It is a very effective and fast decolorizing treatment, which can easily break the double bonds present in most of the dyes. Ozonation can also inhibit or destroy the foaming properties of residual surfactants, and it can oxidize a significant portion of COD. The advantage of this is, the treatment does increase neither the volume of wastewater nor the sludge mass [2].

Step 5: Adsorption

Adsorption is the heart of physicochemical wastewater treatment method, which can mix the wastewater and the porous material powder or granules, through this method, pollutants in the wastewater are adsorbed and removed from the surface of the porous material or filter. Commonly used adsorbents are activated carbon, silicon polymers and kaolin. Different adsorbents have selective adsorption of dyes. But, so far, activated carbon is still the best adsorbent of dye wastewater. The chroma can be removed 92.17%, and COD can be reduced 91.15% in series adsorption reactors, which meet the wastewater standard in the textile industry and can be reused as the washing water [2].

Step 6: Reverse osmosis

Reverse osmosis membranes have a retention rate of 90% or more for most types of ionic compounds and produce a high quality of permeate. Decolorization and elimination of chemical auxiliaries in dyehouse wastewater can be carried out in a single step by reverse osmosis. Reverse osmosis permits the removal of all mineral salts, hydrolyzed reactive dyes, and chemical auxiliaries [2].

5 Hardware Project

As shown in the Fig. 3 the wastewater from the textile industry is collected in the collection tank. Later it is dropped in the equalization tank. In equalization tank, there is a stirrer which always stirs the effluent such that there should be no effluent settled on the bottom surface. The solution of the lime, ferrous sulphate and the polyelectrolyte is added to the effluent to increase the pH value of the effluent. In the sedimentation tank, the sludge is collected in the funnel type container, and the supernatant flows over the sludge which helps in separation of sludge and the water. The water further can be provided to the water filter for filtration purpose. And the remaining sludge is collected in the sludge beds. The sludge is pressed in the hydraulic machines, and the water is separated, and the dry sludge is obtained (Fig. 4) [1, 5].

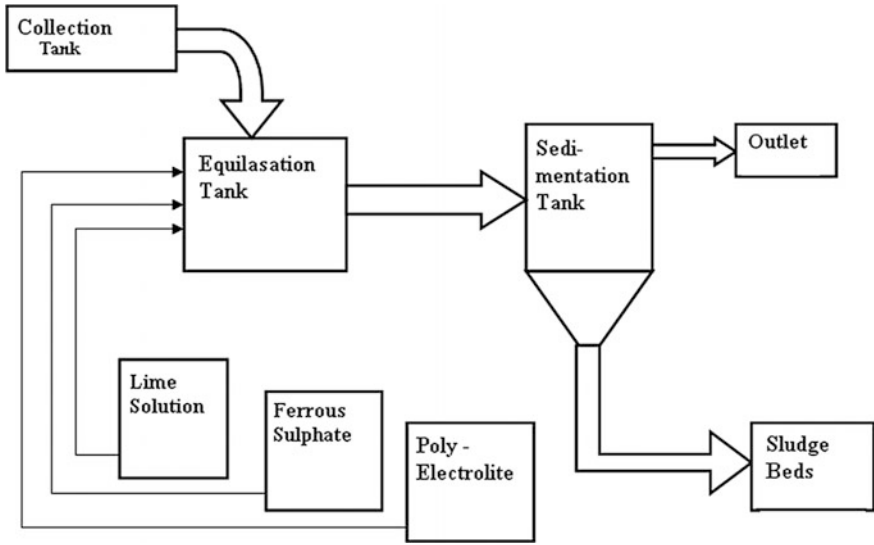


Fig. 3 Hardware structure of the treatment plant



Fig. 4 Hardware setup of the project

6 Chemical Components

- **Sodium Hydroxide (NaOH)**

Sodium Hydroxide is one of a series of water-soluble salts which can be produced when ammonia reacts with phosphoric acid. It is used as a fertilizer and as a water treatment chemical [3].

Specifications—Grade is Technical, overall Purity is 98–99%, PH is of 4–5.

– Applications

It is used as a fertilizer.

It can be used as a fire retardant.

It is also used as a yeast nutrient in winemaking.

• **Ferrous sulphate**

Iron sulphate or Ferrous Sulphate is the chemical compound with the formula FeSO_4 . It is used medically to treat iron deficiency, and also for industrial applications. Known since ancient times as copperas and as green vitriol, the blue-green heptahydrate is the most common form of this material [3].

– Application

It is used for Dewatering of organic sludge from sewage, human waste.

Ferrous Sulphate is used in feed, preserves, waste water treatment and water purity, disinfection, rubber, leather washing powder, livestock feed, pencils.

• **Polyelectrolyte**

Polyelectrolyte is a Water/Effluent Treatment Product used on a large scale in Industrial and Civil Water Treatments for flocculation of Impurities [3].

– Application

Industrial and Civil Water Treatment for flocculation, Related to modifying flow and stability properties of aqueous solutions and gels. They can be used to either stabilize or to initiate flocculation (precipitation). They can also be used to impart a surface charge to neutral particles, enabling them to be dispersed in aqueous solution.

They can be used as thickness, emulsifiers, conditioners, flocculants, and even drag reducers. They are used in water treatments and for oil recovery.

Many soaps, shampoos, and cosmetics incorporate poly electrolytes.

• **Hydrochloric Acid (HCL)**

Hydrogen chloride is a commodity inorganic chemical with a wide variety of uses, mainly by industry but also by professionals and consumers. It is used mainly within the industry as a pH regulator in water and waste-water treatment. The substance is used professionally as a cleaning agent to remove lime scale and for water treatment. The most common public use is a component of cleaning products to remove lime scale [3].

7 Results

In this project, there are certain chemical tests to be performed. So accordingly we have tested the textile effluent, and we got guidance and the results related to this is as mentioned below in the Table 1.

Table 1 Result of chemical tests

Testing parameters	Textile effluent	Test after treatment	Standards values
pH test	9.40	7.4	6–9
Suspended solids	1.350	1.290	200 mg/L
Dissolved solids	3880	4540	2100 mg/L
COD	639	150	400 mg/L
BOD	40	75	100 mg/L
Turbidity	20.40	0.5	0
Colour	1800	20	150 co-pt unit

8 Conclusion

1. This project plays an important role in the fields of textile industry. The treatment technique used is the physico-chemical treatment method. We have selected this method as it is less time consuming and cost effective process with the best result as follows,
 - (a) pH value has been improved up to 7.4 after the process
 - (b) Decolorization of waste water has done up to 20
 - (c) The BOD and COD values are kept within the standard limit
2. Treated water at this stage may be used for rinsing and washing purposes. As the improvement of the environmental protection laws and the raise of the awareness of environmental protection, the pollution of printing and dyeing enterprises has caught a lot of attention and the treatment of dyeing wastewater has become a focus.
3. We can reduce and eliminate the generation and emissions of wastes as well as the production of excessive use of resources and the risks to humans and the environment. Prevention and treatment of dyeing wastewater pollution are complementary. This will not only reduce water consumption but also effectively reduce the pollution of the printing and dyeing wastewater and achieve sustainable development of society.

References

1. Wang Z, Xue M, Huang K, Liu Z (2007) Textile dyeing wastewater treatment. Huazhong University of Science and Technology China
2. Gupta PK (2001) Methods in environmental analysis water, soil and air. AGROBIOS (India)
3. Gupta A (2007) Analytical chemistry, 2nd edn. Pragati Prakashan
4. Nordin N, Amir SFM, Othma MR (2013) Textile industries wastewater treatment by electrochemical oxidation technique. 20 Aug 2013
5. van Haandel A, van der Lubbe J (2011) Solutions in wastewater treatment. Aug 2011

Improving Torsional Seismic Response of Plan Asymmetric Structures Using Energy Dissipating Devices

Ravindra S. Desai and Shrirang N. Tande

Keywords Plan asymmetric buildings · Seismic analysis · Visco-elastic devices · Interstorey drift

1 Introduction

1.1 Background to the Study

Earthquakes are one of nature's greatest hazards to life on this planet and have destroyed countless cities and villages on virtually every continent. They are one of man's most feared natural phenomena producing almost instantaneous destruction of buildings and other structures. Unfortunately, many of earthquakes give very little or no warning before occurring and this is one of the reasons why earthquake engineering is complex.

On average about 200 large magnitude earthquakes occur in each decade (www.iris.edu). About 10–20% of these earthquakes occur in mid ocean, and hence cause no problems for human settlements. Others occur in the areas away from towns and cities and so similarly cause few problems. The problem occurs when an earthquake hits highly populated areas. Unfortunately, as the population of the earth increases the chances of this happening also increases. At the start of the century, less than one in three large earthquakes killed someone, it has now risen to two in three and this upward trend shows no signs of abating.

Some of the major problems relating to earthquake design are created by the original design concept chosen. The damages which have occurred during earthquake events clearly demonstrate that the shape of a building is crucial to how they respond to these events. The ideal aspects of a building form are simplicity, regularity and symmetry in both elevation and plan. These properties all contribute to a more predictable and even distribution of forces in a structure while any

R.S. Desai (✉) · S.N. Tande
Walchand College of Engineering Sangli, Sangli, India
e-mail: prof_rsdesai@yahoo.com

irregularities are likely to lead to an increased dynamic response, at least in certain locations of the structure. Torsion from ground motion could be of great concern due to eccentricity in the building layout. For instance if the center of mass (gravity) is not in the same position as the center of resistance a torsional moment about a vertical axis will be created which will have to be designed for.

1.2 Structural Irregularity in Buildings

The component of the building, which resists the seismic forces, is known as lateral force resisting system (L.F.R.S). The L.F.R.S of the building may be of different types. The most common forms of these systems in a structure are special moment resisting frames, shear walls and frame-shear wall dual systems. The damage in a structure generally initiates at location of the structural weak planes present in the building systems. These weaknesses trigger further structural deterioration which leads to the structural collapse. These weaknesses often occur due to presence of the structural irregularities in stiffness, strength and mass in a building system in vertical or horizontal directions or both.

1.3 Basic Principles of Seismic Response Control

Control systems add damping to the structure and/or alter the structure's dynamic properties. Adding damping increases the structural energy-dissipating capacity, and altering structural stiffness can avoid resonance to external excitation, thus reducing structural seismic response.

In order to achieve satisfactory earthquake response of a structure, three methods can be identified as being practical and efficient. These are; isolation, energy absorption at plastic hinges and use of mechanical devices to provide structural control. The first type, the method of structural isolation is very efficient, but expensive and difficult to carry out. The principle behind isolation is to change the natural period of the structure, substantially decouple a structure from the ground motion input and therefore reduce the resulting inertia force the structure must resist. This is done by the insertion of energy absorbing material between the substructures and superstructures, which will reduce the amount of seismic forces transmitted. In traditional structures, subjected to random and/or unpredictable loads, plastic hinges are provided. These plastic hinges, which suffer inelastic deformation are generally concentrated at the beam-column joints and are thus associated with damage to the primary structural elements.

In passive control systems, on the other hand, installations of mechanical energy dissipating devices, absorb the energy from the earthquake reducing the effects on the critical components of the structure, leaving the building undamaged. After the earthquake these absorbers, which do not themselves support the structure, are

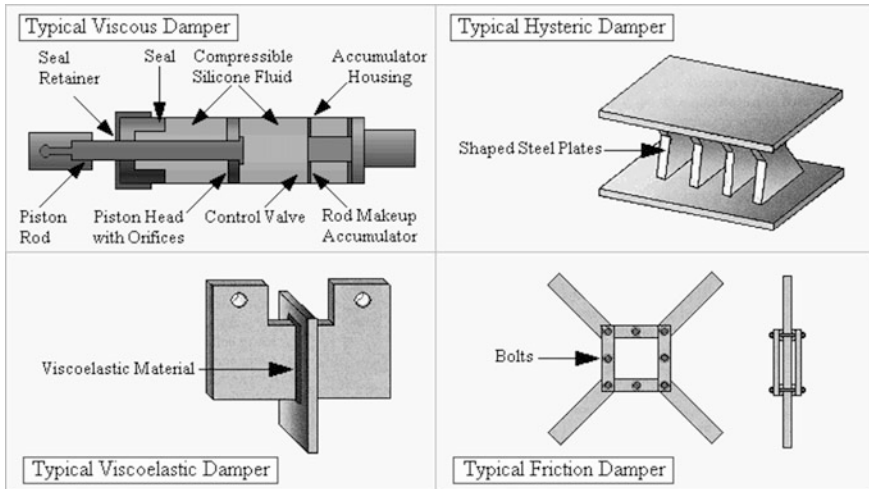


Fig. 1 Example of typical passive energy dissipating devices

easily replaceable, if required. Advantages of passive control system can be summarized in short as: they are usually relatively inexpensive, consumes no external energy, is inherently stable, and works even during a major earthquake. Figure 1 shows a few such devices.

Objectives of present study are:

1. To compensate torsional effect of plan asymmetric structure, find out difference in structural response of buildings with and without visco-elastic (VE) damper, to know the performance effectiveness of these energy dissipating devices.
2. To find out optimal locations of visco-elastic devices (VED) for cost effectiveness.

To achieve the stated objectives time history analysis are employed to investigate the effect of these damping systems under seismic loading of three different earthquake excitations. For the purposes of this study, the program selected for the numerical analysis is SAP2000 v15. This is a general purpose program that has been designed to solve a wide range of linear and non-linear problems involving static, dynamic response of systems.

1.4 Seismic Response Reduction by Visco-elastic Devices

In an experimental study by [1, 2], reduction in relative displacement and absolute accelerations was used as measure of effectiveness for the seismic behaviour of structures with added visco-elastic dampers. Significant improvement of structural

performance under seismic conditions was realized with the addition of visco-elastic dampers. It was shown, that damper effectiveness was strongly dependent upon environmental temperature. The importance of damper positioning within the structure was also stressed.

Top storey drift, absolute acceleration and base shear responses were analyzed by Tezcan and Uluca [3] by performing a nonlinear time history analysis on 7, 10, 20 storey symmetric buildings. It is shown that that visco-elastic dampers are quite effective when incorporated into the super-structure which behave like a break pedal and reduce the earthquake response significantly in proportion to the amount of damping supplied in these devices.

A parametric study performed by Kim and Bang [4] identifies the design variables that influence the torsional responses on a single storey plan asymmetric structure with one axis of symmetry. A simple and straightforward methodology to find out the optimum eccentricity of added VED to compensate for the torsional effect of a plan-wise asymmetric structure was developed using modal coefficients. It is found that the VED turn out to be more effective than viscous dampers in controlling torsional response of a plan-wise asymmetric building structure.

C, L and T shape buildings subjected to four different types of earthquake ground motions are compared [5] for their uncontrolled response with that controlled using VED. It is observed that controlled building shows moderate range of reduction for all response quantities as compared to uncontrolled building.

2 Seismic Analysis Considerations

2.1 *Torsion in Plan Asymmetric Buildings*

Seismic damage surveys and analyses conducted on modes of failure of building structures during past severe earthquakes concluded that most vulnerable building structures are those, which are asymmetric in nature. Asymmetric building structures are almost unavoidable in modern construction due to various types of functional and architectural requirements. Modern codes deal with torsion by placing restrictions on the design of buildings with irregular layouts and also through the introduction of an accidental eccentricity that must be considered in design. The lateral-torsional coupling due to eccentricity between Centre of Mass (CM) and Centre of Rigidity (CR) in asymmetric building structures generates torsional vibration even under purely translational ground shaking. During seismic shaking of the structural systems, inertia force acts through the CM while the resistive force acts through the CR as shown in Fig. 2.

2.2 Mathematical Modeling of Visco-elastic Device Response

2.2.1 Maxwell Spring-Dashpot Model

The Maxwell model can be represented by a purely viscous damper and a purely elastic spring connected in series, as shown in Fig. 3. In a series connection such as the Maxwell model, the stress on each element is the same and equal to the imposed stress, while the total strain is the sum of the strain in each element.

2.2.2 Kelvin–Voigt Model

The Kelvin–Voigt model, also known as the Voigt model, consists of a Newtonian damper and a Hookean elastic spring connected in parallel, as shown in the Fig. 4.

In a parallel connection such as the Kelvin model, the strain on each element is the same, while the total stress is the sum of the stress in each element.

This model represents a solid undergoing reversible, visco-elastic strain. Upon application of a constant stress, the material deforms at a decreasing rate, asymptotically approaching the steady-state strain.

Fig. 2 Torsion prone building

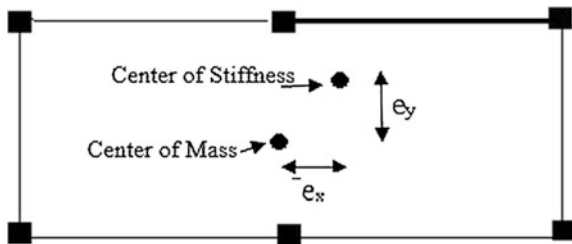
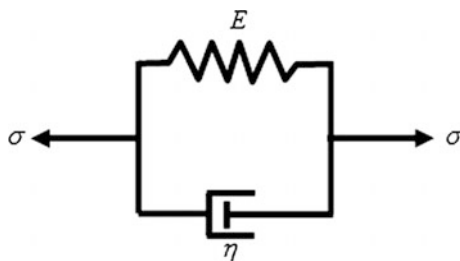


Fig. 3 Maxwell model



Fig. 4 Kelvin model



3 Methodology of Present Study

In this study two types of plan asymmetric building are used, L shape and T shape. Both, uncontrolled and controlled seismic response time history analyses are performed using SAP2000 V15. The controlled response is obtained for selected fundamental modal damping. Maximum response quantities of top floor displacement, top storey relative drift and base shear are compared for uncontrolled and controlled structures. In the second stage the location of VED is optimized using sequential search procedure (SSP) to find best response with minimum number of devices.

3.1 Strong Motions

Three time histories used are Elcentro, Chamoli, Uttarkashi; the later two from India.

3.2 Visco-elastic Device Design

By using fundamental frequency of uncontrolled structure design of visco-elastic devices is carried out in two steps. Firstly estimating additional amount of damping and corresponding stiffness for target modal damping. In the second step storage and loss moduli of dampers is calculated. The selection of VE damper stiffness (k_d) and loss factor (η) is trial and error procedure. These values can also be determined on the basis of the principle that the added stiffness that is due to VE damper should be proportional to the storey stiffnesses of the primary structure. In present study, total device stiffness and damping for each storey is obtained by transforming suitably, the modal strain energy for each storey [2]. The influence of temperature, frequency and strain amplitude on the shear storage and loss moduli of the visco-elastic material must be taken into account. The energy dissipation capacity of damper is affected by environmental temperature which is considered as 36 °C in this study.

3.3 Plan Asymmetric Buildings

Two 10 storey plan asymmetric buildings are considered for seismic analysis. Both buildings are designed using ETABS[®] software for zone-V in a medium soil strata.

The DL, LL are 5 KN/m^2 each along with wall loads lumped at floors. Figures 5 and 6 shows the PLAN of both buildings. The fundamental periods obtained are given in Table 1.

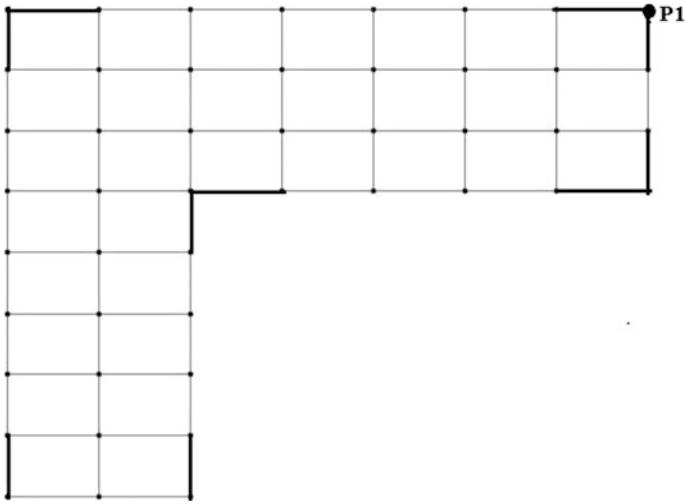


Fig. 5 VED positions in PLAN for L shape building (7 bays of 6 m in X and 8 bays of 4 m in Y)

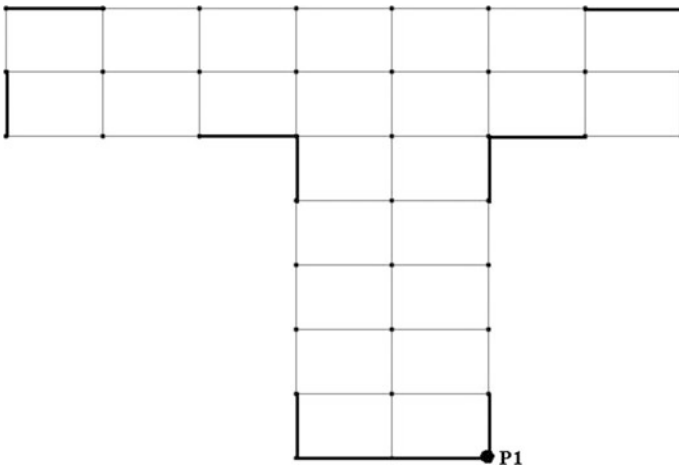


Fig. 6 VED positions in PLAN for T shape building (7 bays of 6 m in X and 7 bays of 4 m in Y)

Table 1 Structural fundamental frequency and period

Building	Frequency (Hz)	Time period (s)
L shape	0.703	1.43
T shape	0.68	1.46

3.4 Performance Requirement

The structure remains elastic, and the inter storey drift ratio shall not exceed 0.004 times the storey height.

3.5 Device Optimum Placement Strategy

In PLAN the position of devices is effective when they are placed at locations expected to experience maximum interstorey drift and/or velocity. These locations are generally identified as farthest locations from center of rigidity. In view of these considerations the PLAN Positions for the VED are fixed as shown in Fig. 5 for L shape and Fig. 6 for T shape building.

For deciding the number of dampers in any storey or height wise distribution of devices, successive drift reduction criteria is used. The response is calculated in terms of maximum interstorey drift, which is obtained during the earthquake ground motion. A parameter β_i^k is defined in order to evaluate the reduction of interstorey drift due to the application damper.

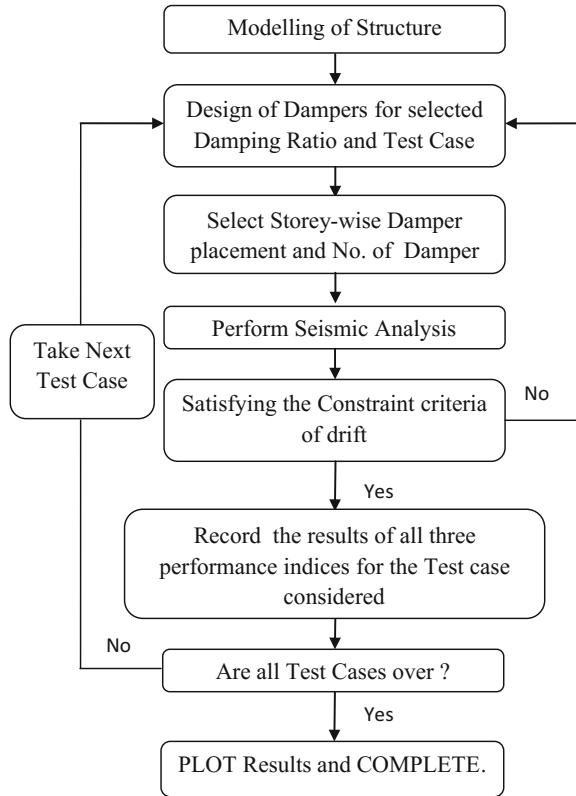
$$\beta_i^k = \frac{\Delta_i^k}{\Delta_i^0} \quad \beta_m^k = \frac{1}{n} \sum_{i=1}^n \beta_i^k$$

where Δ_i^k is the maximum drift on storey i in case when damper is used at k th storey, Δ_i^0 is the the maximum drift on storey i in case when damper in not used. It can be noted that β_i^k represent the benefit in drift reduction at story i when damper is used at k th storey, and β_m^k is the mean value β_i^k for all stories; β_m^k measures the overall benefit introduced by the dampers on the building when damper in used. A lower value of β_m^k means higher drift reduction [6].

3.6 Performance Evaluation and Optimized Selection

All the responses of building are measured at location P1 shown in Figs. 5 and 6 which is farthest point from the centre of rigidity of building.

Fig. 7 Flowchart of optimum selection method of devices



Performance evaluation is based on three criteria namely, lowest value of β_m^k , more reduction in top storey displacement and torsional moment at base of building. Based on results obtained from the bare frame a height-wise sequential search is carried out for the damper placement to fulfill the above criteria for six different configuration cases. The case which results into optimized achievement of reduction in structural quantities cited above, is selected as best of the choice. The flowchart shown in Fig. 7 elaborates the methodology. The methodology adopted here is effectively suitable for design offices.

4 Results and Discussion

Each of the two buildings are analyzed for six different storey groups (Test cases) such that VED are placed in those stories only which are member of a chosen group. Initially 10% added damping is considered in the structure and performance evaluation analysis is performed for each of test case as shown in Fig. 9. Results are

obtained for each of the three performance criteria for each test case and compared to find out the best test case which serves to be the optimized device configuration.

4.1 Results for L Shape Building

Following storey groups (Test Cases) are considered for optimal device placements.

- Case 1: damper is placed at first storey
- Case 2: damper at 1, 5, 6, 7 storey
- Case 3: at 1, 2, 5, 6, 7, 8 storey
- Case 4: at 1, 2, 5, 6, 7, 9, 10 storey
- Case 5: at 1, 5, 6, 7, 8 storey
- Case 6: at all storey.

It can be seen from Fig. 8 that substantial reduction upto 40% is achieved by VED placement. It can be noted from Fig. 9b that the Case no-3 results into optimum placement of dampers. Similar results are obtained for T shapes building resulting into case no-3 to be optimum.

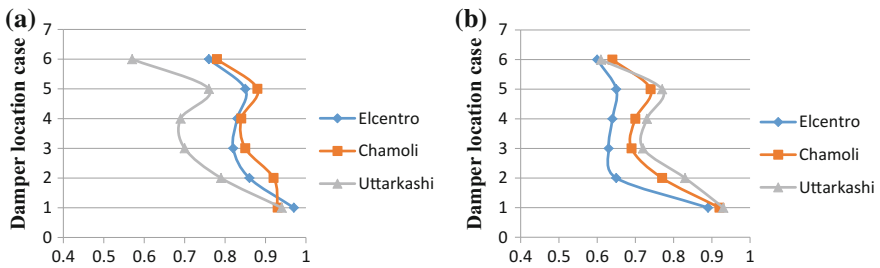


Fig. 8 Drift reduction ratio β for all 6 cases in **a** X direction. **b** Y direction

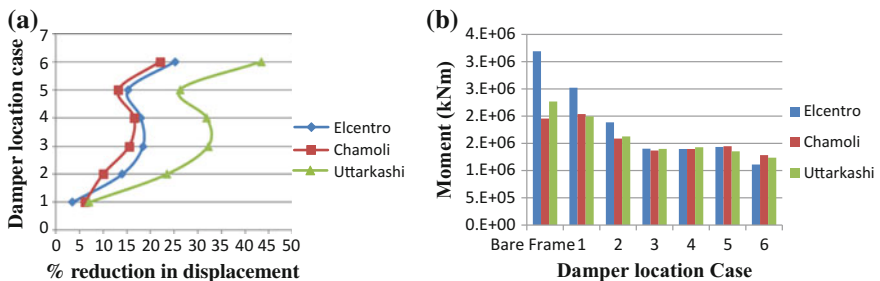


Fig. 9 **a** Reduction in X displacements. **b** Base torsional moment for each case

5 Conclusions

Conclusions of the study are listed below:

1. It is effective to introduce supplemental damping in plan asymmetric structure to substantially reduce the torsional response.
2. It is concluded that the plan positions selected for each type of building are quite satisfactory and balanced to take care of simultaneous components of earthquake loading.
3. Selection of damper position by sequential procedure is simplest and robust, as it leads to optimized configuration in minimum steps.
4. For L and T shape of building case 3 i.e. for L shape damper at 1, 2, 5, 6, 7, 8 storey and at 1, 2, 3, 6, 7, 8 storey for T shape gives better reduction in all the response values such as displacement, interstorey drift, torsional moment in columns and building.

References

1. Lin RC, Liang Z, Soong TT, Zhang RH (1991) An experimental study of seismic structural response with added viscoelastic dampers. *Eng Struct* 13(1):75–84
2. Chang KC, Soong TT, Oh ST, Lai ML (1991) Seismic response of a 2/5 scale steel structure with added viscoelastic dampers. Technical report NCEER-91-0012. State University of New York, Buffalo, NY
3. Tezcan Semih S, Uluca Ozan (2003) Reduction of earthquake response of plane frame buildings by viscoelastic dampers. *Eng Struct* 25:1755–1761
4. Kim Jinkoo, Bang Sunghyuk (2002) Optimum distribution of added viscoelastic dampers for mitigation of torsional responses of plan-wise asymmetric structures. *Eng Struct* 24:1257–1269
5. Patel V, Parmar A, Patel M, Mehta U (2014) Seismic response control of asymmetric building using viscoelastic damper. *IJCIET* 5(12):282–291
6. Tovar C, López OA (2004) Effect of the position and number of dampers on the seismic response of frame structures. 13th World Conference on Earthquake Engineering Vancouver, B.C., Canada, 1-6 Aug, Paper No. 1044

Optimization of Cables in Cable Stayed Bridge

Anuja J. Sohani and Smita Patil

Keywords Cable force tuning · Unknown load factor · Midas civil software · Cable stayed bridge

1 Introduction

Cable-stayed bridges are structural systems which are effectively composed of cables, the main girder and towers. This bridge form has a fine-looking appearance and fits in with most surrounding environments. The structural systems can be varied by changing the tower shapes and the cable arrangements. Up to a span length of 1000 m, the cable stayed system is considered as an economical solution. For cable-stayed bridges the cable forces are an important factor in the design process. Cables are one of the main parts of a cable-stayed bridge. They transfers the dead load and traffic load of the girders to the pylons. Determining the optimum distribution of tensioning forces of stay cables is an important step in the design process of cable-stayed bridge, which plays a major role in the construction of cable-stayed bridges. With pretensioning each cable, more stability and less simulation time will be achieved. Consequently, finding the tensile stresses in cables is critical in cost effective design of cable-stayed bridges. The structural complexity of cable-stayed bridges makes their design process a serious engineering concern. Negrão [1] were among the first to study the optimization of cable force in cable-stayed bridges. In recent years, different iterative methods have been proposed to improve the performance of cable-stayed bridges through optimization of

A.J. Sohani (✉) · S. Patil
Department of Civil Engineering, Datta Meghe College of Engineering,
Navi Mumbai 400708, India
e-mail: anuja.sohani@yahoo.co.in

S. Patil
e-mail: sbpatil_2009@rediffmail.com

cable forces. Haftka and Adelman [2] suggested a shape-finding procedure (zero displacement method) based on the dead load of the girders and pylons in which cable sag nonlinearity was included. A two-loop iteration method for shape finding was performed using the equilibrium iteration and shape iteration loops. In their study, a convex scalar function was used to minimize the cost of a box-girder deck cable-stayed bridge. The proposed function combines dimensions of the cross-sections of the bridge and post-tensioning cable forces. This method is very sensitive to the constraints, which should be imposed very cautiously to obtain a practical output.

The information below provides a critical review of the various approaches available for modeling and analysis of cable stayed bridge. Leonhardt and Zellner [3] in his paper proposed a non-iterative optimal analysis to find the post-tensioning cable forces in cable-stayed bridges. A transformed objective function is obtained using the post-tensioning forces. Then, by zeroing the partial derivatives of the transformed objective function, the post-tensioning cable forces are determined. Choi and Choi [4] in his paper has proposed an iterative approach to find the solution of the post-tensioning cable forces. This method is repeated until the cable forces are determined and the precision of the displacements of the deck and pylon converges to an allowable threshold.

Kasuga [5] from his paper he has shown Optimum design of a cable-stayed bridge structure is very complicated because of large number of design variables. Use of genetic algorithms (GAs) in optimizing such structure consumes significant computational time. Due to nonlinearity, structural analysis itself takes considerable computational time and the genetic algorithm has to perform a large number of iterations in order to obtain global minima reduces the computation time of optimization.

2 Optimization Methods of Cable Stayed Bridge

Most optimization methods available in literature for solving general nonlinear optimization problems could be classified into two groups known as direct and global optimization methods. Direct optimization methods are local search techniques as they begin with a starting guess solution and search for a local minimum, while the global optimization methods are global optimizers. In general, cable-stayed bridges are highly statically indeterminate structures, making the solution of the minimum weight of steel in stay cables not singular. Moreover, the search space of the current objective function is expected to contain several hills and valleys (local minima) due to the intersection of the design constraints with the objective function. Accordingly, a global search method is needed to find the global optimum solution and to avoid the possibility of being trapped in a local optimum. Since the control points of the B-spline curve are continuous in nature, the optimization method is more suited to continuous variables.

3 The Analysis Programme

Midas/Civil is an analysis programme for modeling and analyzing structural systems. It offers special features for analyzing civil structures, such as box girder or composite bridges. The programme provides the feature of unknown load factor method wherein the constraints for the bridge can be defined according to the structures requirement. The constraints are of reaction, moments, and displacement. In this paper the results are obtained by defining displacement constraints for nodes at cable locations. For modeling structural systems, the programme offers various element types. The main elements used for the analysis of cable stayed bridges are General Beam elements and Truss elements or Tension-Truss Cable elements. Initial pre-stressing forces can be calculated through optimizing the equilibrium state. The calculation of the ideal cable prestressing forces by the optimization is restricted to the linear analysis as the different loadings are superposed. The initial cable pre-stressing forces are obtained by the Unknown Load Factor function and the initial equilibrium state analysis of a completed cable stayed bridge.

4 Description of Bridge

The Bankot Bridge is taken as case study for the analysis purpose. The Bridge is situated between village Kolmandla in Raigad district and village Veshvi in Ratnagiri district across the Bankot creek. The Bridge under consideration is a 3-span composite cable-stayed bridge with an overall length of 250 m (62.5 + 125 + 62.5 m). The deck is 15.6 m wide. It comprises two longitudinal steel girders, 2 m deep, transverse steel girder at 3 m spacing and a reinforced concrete slab between 250 mm in depth. The deck of each cable-stayed cantilever section is supported by a total of 10 cables, with 10 cables arranged in each semi-fan configuration on each side of the pylon, in two planes, either side of the bridge deck. Each reinforced concrete pylon comprises two towers and two crossbeams, the lower one supporting the deck. The cable are spaced at every 9 m c/c. During construction, longitudinal motion of the deck was restrained at the pylon bearing to resist temporary out-of-balance.

4.1 *Location of Project Site, Geometry and Cross Section of Bankot Bridge*

The location of bridge site is given in Fig. 3. The geometry of bridge is given in Fig. 1 and the typical cross section of bridge is given in Fig. 2.

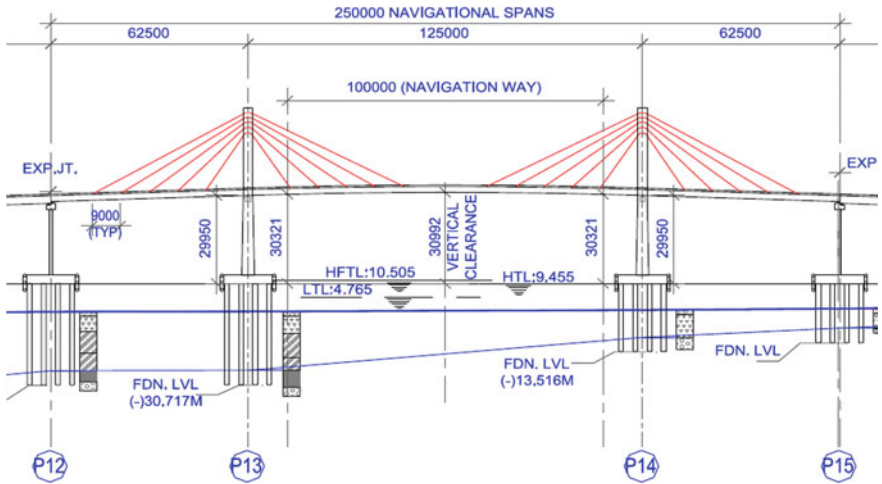


Fig. 1 Geometry of Bankot bridge

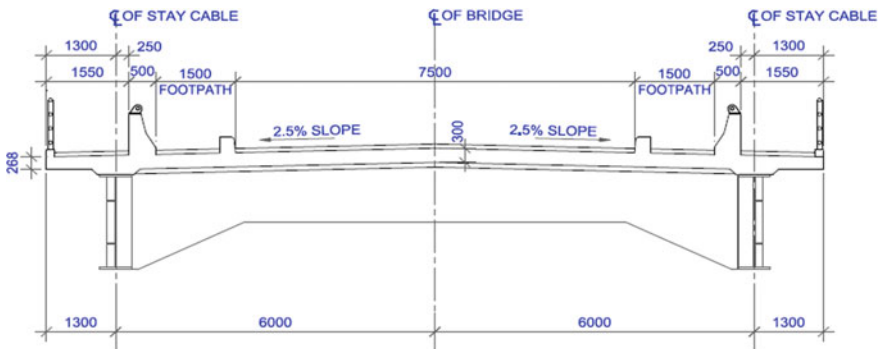


Fig. 2 Typical cross section of bridge

- Total length: 250 m.
- Clear carriageway width: 7.5 m.
- Side Footpath: 1.5 m.
- Overall width of deck: 14.6 m.
- Depth of superstructure: 2.3 m for full length of bridge including deck slab of 300 mm.
- Bearings: POT/POT-PFEE type bearings.
- Substructure: Cast in place Rectangular pylons with the cross beams at deck level and pylon level.
- Foundation: Combined pile foundation for pylons.



Fig. 3 Location of project site

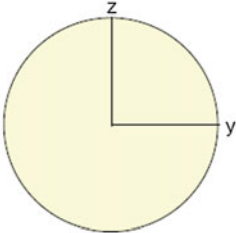
Table 1 Cross sectional properties of main girder

Before Composite					After Composite				
$A (m^2)$	$A_{sy} (m^2)$	$A_{sz} (m^2)$	$z (+) (m)$	$z (-) (m)$	$A (m^2)$	$A_{sy} (m^2)$	$A_{sz} (m^2)$	$z (+) (m)$	$z (-) (m)$
0.248	0.000	0.000	1.207	0.843	0.948	0.617	0.085	0.136	1.914
$I_{xx} (m^4)$	$I_{yy} (m^4)$	$I_{zz} (m^4)$	$y (+) (m)$	$y (-) (m)$	$I_{xx} (m^4)$	$I_{yy} (m^4)$	$I_{zz} (m^4)$	$y (+) (m)$	$y (-) (m)$
0.001	0.181	8.933	6.300	6.300	0.038	0.572	21.824	6.300	6.300
-	-	-	-	-	E_s/E_c	G_s/G_c	D_s/D_c	P_s	P_c
-	-	-	-	-	0.000	0.000	0.000	0.000	0.000

4.2 Properties Considered for Elements in Model

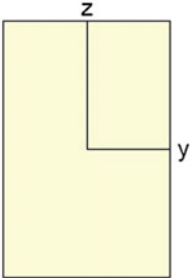
The properties considered for main girder, pylon, tie beam, pile cap and cables are presented in tabular format below along with the boundary elements considered (Tables 1, 2, 3, 4 and 5).

Table 2 Cross sectional properties of cable



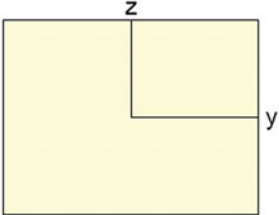
$A (m^2)$	$A_{sy} (m^4)$	$A_{sz} (m^4)$	$z (+) (m)$	$z (-) (m)$
0.002	0.002	0.002	0.025	0.025
$I_{xx} (m^4)$	$I_{yy} (m^4)$	$I_{zz} (m^4)$	$y (+) (m)$	$y (-) (m)$
0.000	0.000	0.000	0.025	0.025

Table 3 Cross sectional properties of pylon



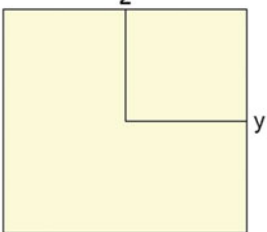
$A (m^2)$	$A_{sy} (m^4)$	$A_{sz} (m^4)$	$z (+) (m)$	$z (-) (m)$
6.000	5.000	5.000	1.500	1.500
$I_{xx} (m^4)$	$I_{yy} (m^4)$	$I_{zz} (m^4)$	$y (+) (m)$	$y (-) (m)$
4.695	4.500	2.000	1.000	1.000

Table 4 Cross sectional properties of tie beam



$A \text{ (m}^2\text{)}$	$A_{sy} \text{ (m}^2\text{)}$	$A_{sz} \text{ (m}^2\text{)}$	$z \text{ (+) (m)}$	$z \text{ (-) (m)}$
3.000	2.500	2.500	0.750	0.750
$I_{xx} \text{ (m}^4\text{)}$	$I_{yy} \text{ (m}^4\text{)}$	$I_{zz} \text{ (m}^4\text{)}$	$y \text{ (+) (m)}$	$y \text{ (-) (m)}$
1.215	0.563	1.000	1.000	1.000

Table 5 Cross sectional properties of pile cap



$A \text{ (m}^2\text{)}$	$A_{sy} \text{ (m}^2\text{)}$	$A_{sz} \text{ (m}^2\text{)}$	$z \text{ (+) (m)}$	$z \text{ (-) (m)}$
263.500	219.583	219.583	7.750	7.750
$I_{xx} \text{ (m}^4\text{)}$	$I_{yy} \text{ (m}^4\text{)}$	$I_{zz} \text{ (m}^4\text{)}$	$y \text{ (+) (m)}$	$y \text{ (-) (m)}$
9678.810	5275.490	6345.958	8.500	8.500

4.3 Midas Model and Methodology of Analysis

- The modeling of the Bridge has been done in MIDAS/CIVIL software as an analysis tool.
- The girder and the pylon has been modeled using the beam elements and the cable has been modeled using the truss elements.
- A steel-trusses ‘deck girder’ with diaphragms, is modeled with conventional three dimensional (3-D) beam elements, forms a ‘spine’ for the deck. To achieve this, all the bending, torsional and inertial properties of the steel trusses-deck composite girder are equivalent to that of the beam.
- User defined properties has been given to cables, girder and pylon.
- Form groups in MIDAS for the activation and deactivation of structural groups.
- Assign pretension forces in each cable.
- Section properties are calculated using tool “Section property calculator” available in analysis software.
- Cables connected to main girder with rigid link.
- Bearings are modelled using elastic links (locking and unlocking of bearings) as construction proceeds is also considered in model.
- Pylon, tower and cross beams are modeled as beam elements while foundation restraints are modeled as 3-D beam elements.
- Concrete of grade M40 is taken for deck and concrete of grade M50 is taken for pylon (Fig. 4).

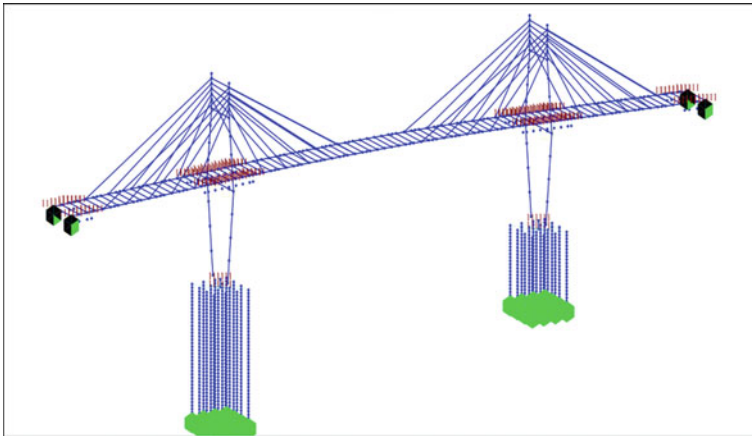


Fig. 4 Midas model of Bankot bridge modeling

5 Optimisation Technique Implemented in MIDAS

The model is analysed for self weight and pretension load of 1 kN is applied for each cables. In order to find the optimum cable forces under dead load condition, the cable stayed bridge is analyzed for a combination of dead load and pretension tension forces of 1 kN in each cable. After post processing the unknown load factor has to be defined in Midas. This is done as follows:

- The structure group of main girders and cross girders is created.
- The nodes at the cable locations are selected for defining the constraints.
- The constraints of displacement of lower and upper bound values of 1 cm are defined for each node.
- The unknown load factor can now be retrieved.
- The cable of pretension forces along with pretension forces is then generated in Midas.
- The excel file of pretension forces can be exported directly and it is given in Table 6.

6 Results

In the above table it can be seen that for the initial cable stress the forces can be calculated directly for the dead load condition. The deformed shape of the cable stayed bridge at the dead load condition and after the optimization of the girder displacement is given in Figs. 6 and 7. The graph shown in Fig. 8 gives the graph of displacement verses the pretension forces in cables (Fig. 5).

Table 6 Table of constraints and optimum cable forces for deck

Factor	Constraint	Node 302	Node 308	Node 311	Node 314	Node 324	Node 327	Node 330	Node 442	Node 514	Node 518
	Upper bound	0.01	0.01	0.01	0.01	0.01	0.01	0.01	0.01	0.01	0.01
	Lower bound	-0.01	-0.01	-0.01	-0.01	-0.01	-0.01	-0.01	-0.01	-0.01	-0.01
	Value	-0.005849	0.0024	0.008301	0.01	-0.0047	-0.00188	0.003406	-0.01	-0.00013	-0.000133
Self weight	1	0.0053	0.0012	-0.0050	-0.00713	0.00648	0.008139	0.00225	-0.1842	0.000308	0.000306
Pretension 1	1503.838	-9.9E-06	-1.1E-05	-7.8E-06	3.2E-07	-1E-05	-1.4E-05	-1.3E-05	3.4E-05	5.26E-08	5.25E-08
Pretension 2	928.01	-4.0E-06	4.E-07	7.5E-06	4.7E-06	-4E-06	-4.5E-06	4.45E-07	2.1E-05	-1.4E-07	-1.4E-07
Pretension 3	467.6496	1.3E-06	1.E-05	9.15E-06	5.8E-06	1.4E-06	4.7E-06	1.21E-05	1.1E-05	-1.9E-07	-1.8E-07
Pretension 4	169.290	6.1E-06	9.E-06	7.11E-06	4.2E-06	6.1E-06	1.26E-05	9.61E-06	3.8E-06	-1.4E-07	-1.4E-07
Pretension 5	47.537	1.2E-05	5.E-06	3.84E-06	2.1E-06	1.3E-05	7.97E-06	5.84E-06	1.1E-06	-7.1E-08	-7.1E-08
Pretension 6	1132.667	3.28E-06	6.E-06	6.13E-06	4.3E-06	3.3E-06	5.47E-06	6.53E-06	2.5E-05	-1.3E-07	-1.3E-07
Pretension 7	1357.41	1.45E-06	3.E-06	3.17E-06	2.2E-06	1.5E-06	2.7E-06	3.38E-06	3E-05	-6.9E-08	-6.8E-08
Pretension 8	980.995	1.04E-07	1.E-06	1.18E-06	8.5E-07	1E-07	7.64E-07	1.14E-06	2.2E-05	-2.6E-08	-2.6E-08
Pretension 9	528.658	-7.4E-07	3.E-08	2.02E-07	2E-07	-7E-07	-2.8E-07	2.70E-08	1.2E-05	-5.3E-09	-5.3E-09
Pretension 10	184.9291	-1.2E-06	-2.E-07	5.88E-09	8.8E-08	-1E-06	-6.7E-07	-2.7E-07	4.1E-06	-1.7E-09	-1.6E-09

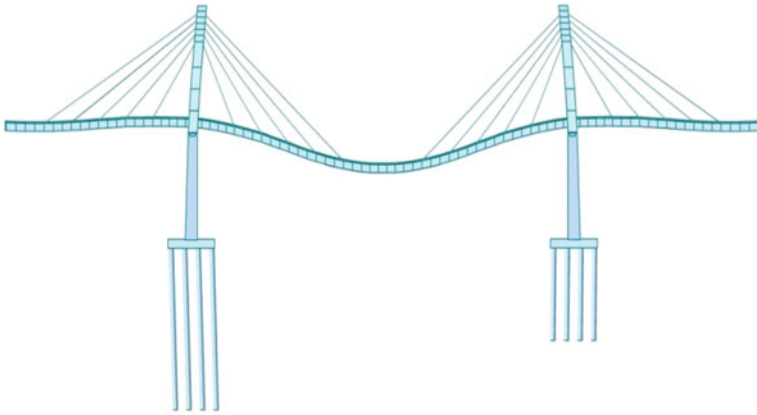


Fig. 5 Deformed shape in self weight condition

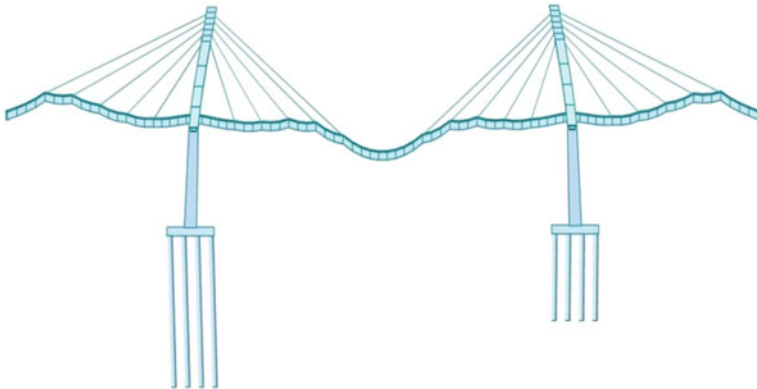


Fig. 6 Deformed shape after optimization of girder

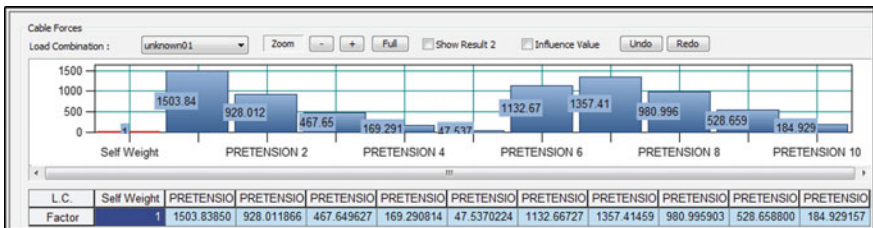


Fig. 7 Cable force tuning in Midas

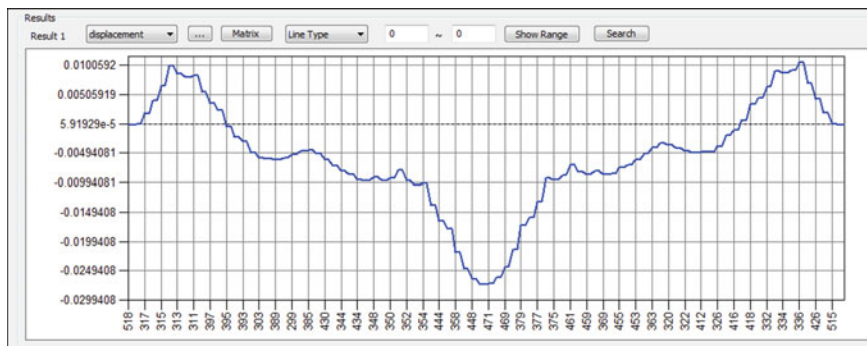


Fig. 8 Graph of displacement at girder location from the cable forces

7 Conclusion

The preceding paper presents the optimization methodology and cable force tuning, the method used is defining the constraints for displacement of 1 cm at nodes at girder location where cables are connected. Also including the understanding of the modeling, analysis technique. The determination of pretensioning cable forces is critical in the cable-stayed bridges design procedure. The results show that the unknown load factor method is a prominent method for optimizing the cable forces considering its easy extensibility, fast process, and applicability to real construction engineering problems. However, the cable forces optimized. A single constraint iterative algorithm is presented in this study to determine the cable pretensions of a cable-stayed bridge. As the optimizing cable forces, the time-dependent effects such as creep, shrinkage, or relaxations of pretensioning forces as well as geometrical nonlinearities can be considered. Furthermore, the proposed process can be used in the construction process of cable-stayed bridges. The benefits of the above optimization is that the stresses in the cables can be achieved directly without any tedious calculations.

References

1. Negrão JHO, Simões LMC (1997) Optimization of cable-stayed bridges with three-dimensional modelling. *Comput Struct* 741–758
2. Haftka RT, Adelman HM (1989) Recent developments in structural sensitivity analysis. *Struct Optim* 1:137–151
3. Leonhardt F, Zellner W (1991) Past, present and future of cable-stayed bridges. In: Ito M et al (eds) *Cable-stayed bridges, recent developments and their future*. Elsevier Science Publishers, New York
4. Choi CK, Choi IH (1993) An expert system for selecting types of bridges. *Comput Struct* 48:183–192
5. Kasuga A, Arai H, Breen JE, Furukawa K (1995) Optimum cable-force adjustment in concrete cable-stayed bridges. *J Struct Eng ASCE* 121(4):685–694

Vibration Isolation of Single-Degree-Freedom System Using Permanent Magnets

Supriya Choudhari and G.R. Patil

Keywords Permanent magnet · Vibration isolation · Spring-mass system · Single-degree-of-freedom · Shake table

1 Introduction

Isolation from ground during the seismic excitation has been one of the challenging subjects for researchers. The general principle is that structures will be decoupled from the horizontal components of the earthquake ground motion by interposing a layer with low horizontal stiffness between the structure and the foundation. It is the collection of structural elements which should substantially decouple a super-structure from its sub-structure resting on a shaking ground. Thus, protecting a building or non-building structures integrity. Base isolation is one of the most powerful tools of earthquake engineering pertaining to the passive structural vibration control technologies. Continuous vibrating machines are mainly the vibration inducing systems which cause change in the natural frequency of the structure. Most of the machines are mounted on foundations specially designed for the machine frequency. But there is some amount of transmission of vibration to the adjacent structure. The aim of the system is modification of dynamic interaction between structure and earthquake ground motion, in order to minimize the structure damage and to control the structural response. Passive vibration control system keeps the building to remain essentially elastic during large earthquakes and has fundamental frequency lower than both its fixed base frequency and dominant frequencies of ground motion. Introducing horizontal flexibility at base of structure helps in proper dissipation of energy at base level itself. The control is based on two different approaches, either the modification of dynamic characteristics or modification of energy absorption capacity of the structure.

S. Choudhari (✉) · G.R. Patil
JSPM's Rajarshi Shahu College of Engineering, Pune, India
e-mail: supriya.c41@gmail.com

Objectives of the paper are:

1. Obtain relation between the airgap and load weight applied to the SDOF system [3].
2. Relation between magnetic field and airgap and between pull force and airgap.
3. Obtain relation between the displacement amplitude and forcing frequency of spring and that of N35 grade permanent magnets.
4. Obtain the appropriate magnet type of PM-PM system [2] for isolation purpose.

2 Methodology

2.1 Problem Statement

Vertical isolation system. Combination of magnets using ring type-1, ring type-2 and plate magnets is arranged as top and bottom layers as follows:

Case-1: Ring-magnet-type-1 at top and bottom layer.

Case-2: Ring-magnet-type-2 at top and bottom layer.

Case-3: Plate-magnet-type at top and bottom layer. Airgap forms the medium to isolate the structure from ground. Such a representative prototype model is prepared and tested with varying load [1]. The displacement of beam from previous position is noted after loading the element at mid-span.

Horizontal isolation system. Using horizontal shake table, the prototype model is mounted on shake table with the repulsion acting horizontally and forcing frequency is applied to the setup. Displacement are evaluated for the respective forcing frequencies using spring and magnetic combinations. The shake table readings are observed and noted. In horizontal system, permanent magnet combinations of sizes mentioned for ring magnet type 1 and 2 and plate magnet adopted are as follows (Table 1):

Case 1: RMT-1—single magnet at one end.

Case 2: RMT-1—single magnet at both ends.

Case 3: RMT-1—double magnet at one end.

Case 4: RMT-1—double magnet at both ends.

Case 5: RMT-2—single magnet at one end.

Case 6: RMT-2—single magnet at both ends.

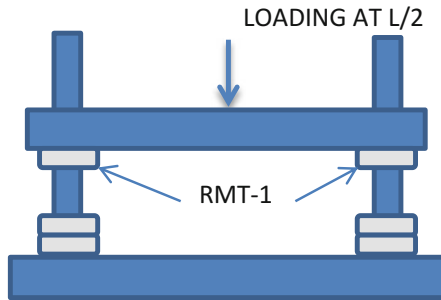
Case 7: PMT—single magnet at one end.

Case 8: PMT—single magnet at both ends.

Case 9: Spring (k)—5 different types of spring (k1, k2, k3, k4, k5).

Table 1 Specifications of model

Beam dimensions (scale = 1:10)	Dimension of neodymium magnets
Length, $l_{\text{eff}} = 160 \text{ mm}$	RMT-1: $20 \times 12 \times 5 \text{ mm}$
Total length of beam = 190 mm	RMT-2: $20 \times 10 \times 10 \text{ mm}$
Depth, $d = 30 \text{ mm}$	PMT: $20 \times 15 \times 6 \text{ mm}$
Width, $b = 26 \text{ mm}$	Grade of all magnets used: N35



Equation of motion for the forced damped vibration in single degree of freedom system is given as

$$m\ddot{y} + c\dot{y} + ky = F \sin \omega t$$

where,

- $m\ddot{y}$ inertial force,
- $c\dot{y}$ damping force,
- ky spring displacement and
- $F \sin \omega t$ external harmonic loading.

2.2 Procedure

Present work is carried out to study the effect of NdFeB permanent magnet as vibration isolation system in single-degree-of-freedom structure in which maglev phenomena is the governing mechanism isolating the structure from base. In vertical system, static analysis is performed by applying load on the vertical system [1, 4]. This gives minimum airgap achieved by the prototype to isolate vibration. In horizontal system, the forcing frequency is applied to spring and magnetic arrangement to obtain the displacement amplitude. The displacement amplitudes obtained are plotted graphically. Further, magnetic field and pull force is calculated

and compared with the types of magnet used. Stiffness of spring and the magnetic field is compared in order to get strong isolating system. The diagram above represents the model and validation of results in paper [1] is performed.

3 Results and Discussions

3.1 Results

Vertical system : The graphs showing variation of airgap with static loading for three types of magnet i.e. RMT-1, RMT-2 and PMT are plotted as below. From graphs in Figs. 1 and 2, decrease in airgap is observed up to a certain limit in all 3 types of magnet. The airgap varies as non-linear and the second degree curve shows combined behavior of the airgap. This validates the results of research paper [1]. The equation of second degree curve is represented in the respective graph.

Horizontal system: In horizontal system, the variation of displacement amplitude with forcing frequency i.e. harmonic loading is shown graphically below for spring and magnetic arrangement.

It is observed that the displacement increases with the applied forcing frequency in case of spring, RMT-1, RMT-2 and PMT from graphs in Figs. 3, 4, 5 and 6. As airgap decreases the repulsion value increases and is zero for airgap beyond 1.5 inches from Fig. 7. Figure 8 shows the comparison of magnetic field, magnetic stiffness and pull force. Magnetic field stiffness of PMT is higher than RMT-1 & RMT-2. Thus the variation of the stiffness of PMT is given by Fig. 9.

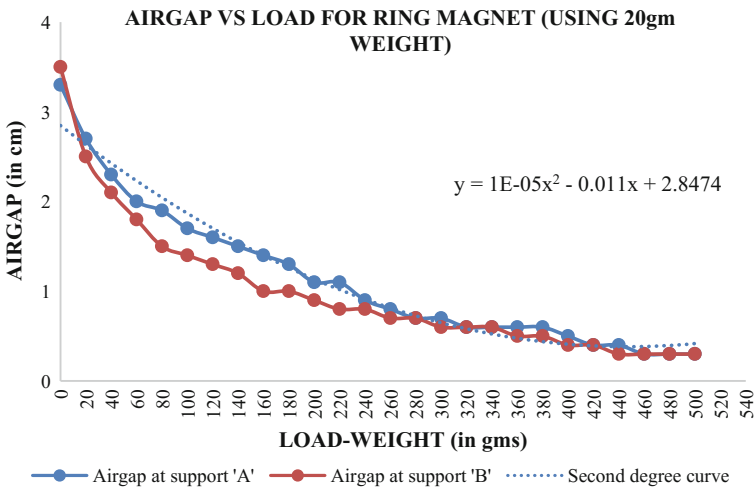


Fig. 1 Graph of airgap versus load weight for ring magnet type-1 using 20 gm weight

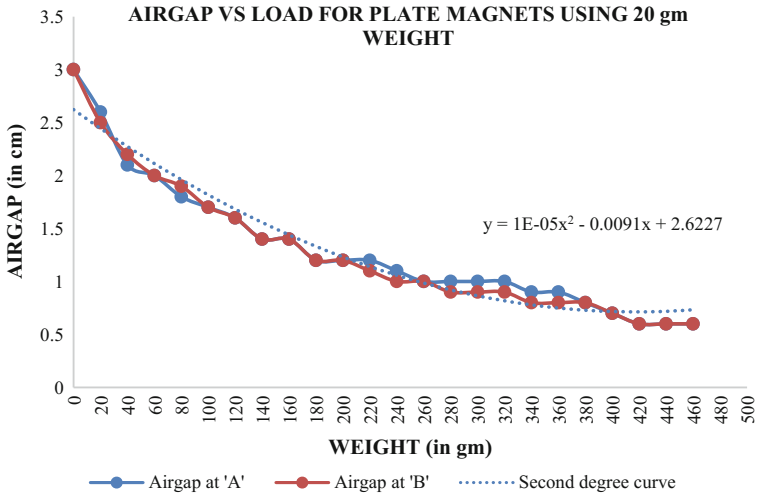


Fig. 2 Graph for airgap versus load weight for plate magnet using 20 gm weight

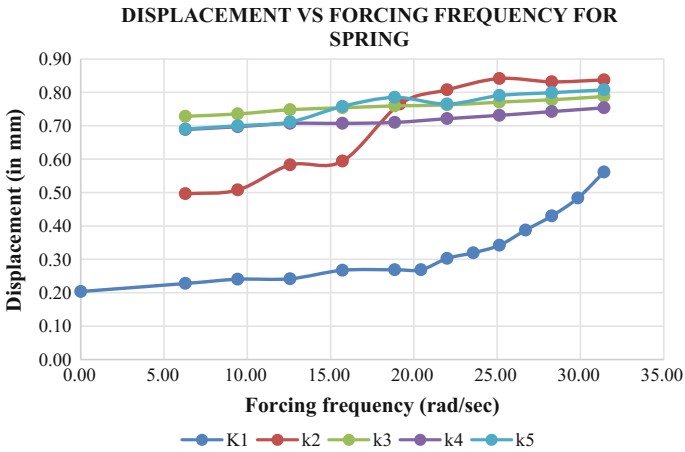


Fig. 3 Displacement versus forcing frequency graph for different springs

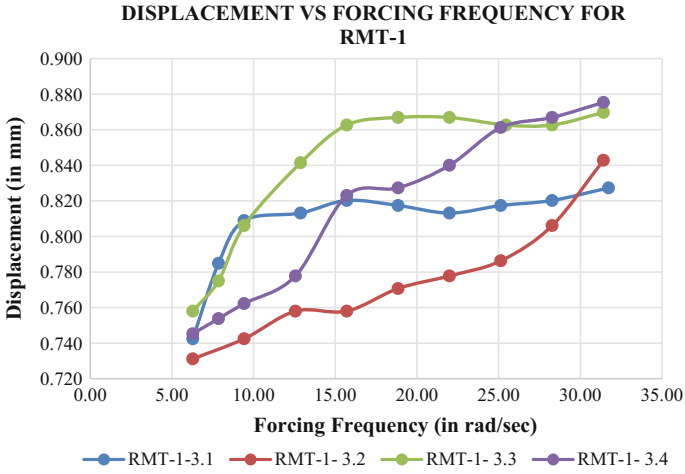


Fig. 4 Displacement versus forcing frequency graph for RMT-1

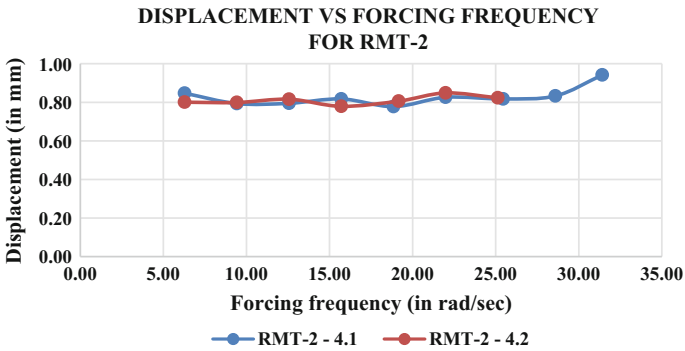


Fig. 5 Displacement versus forcing frequency graph for RMT-2

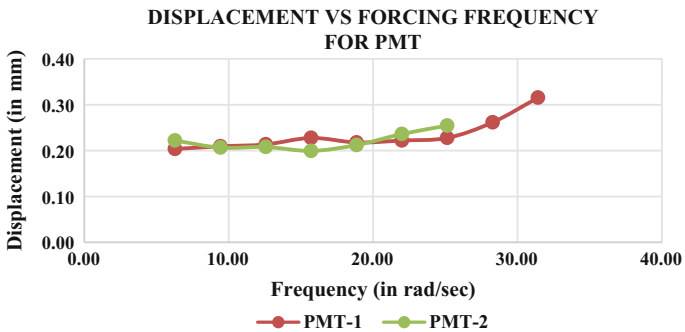


Fig. 6 Displacement versus forcing frequency graph for PMT

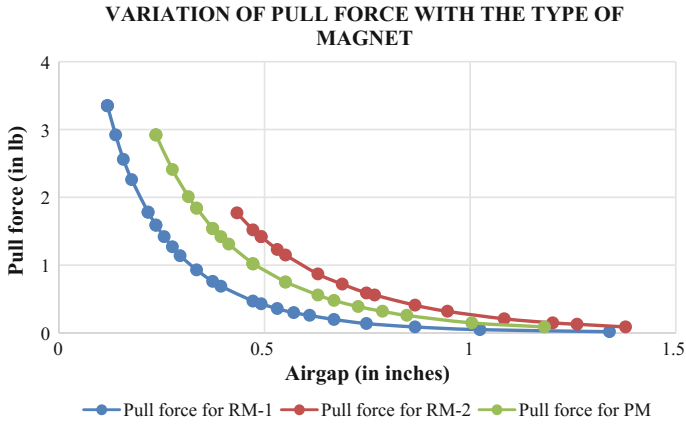


Fig. 7 Graph for variation of repel/pull force for three types of magnet

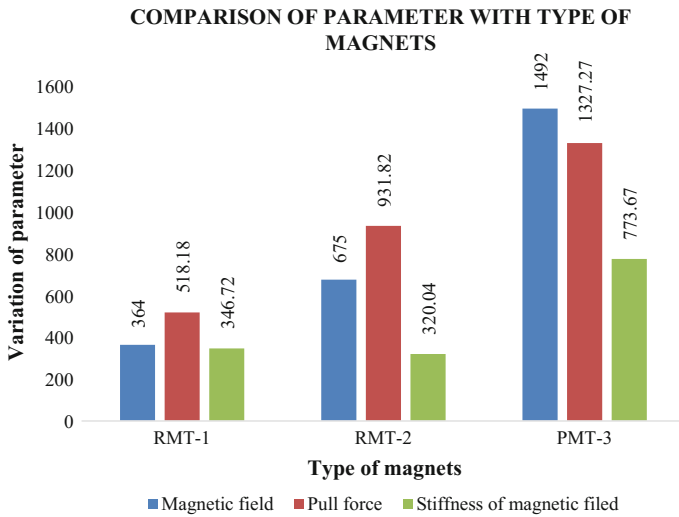


Fig. 8 Comparison of parameters of permanent magnets

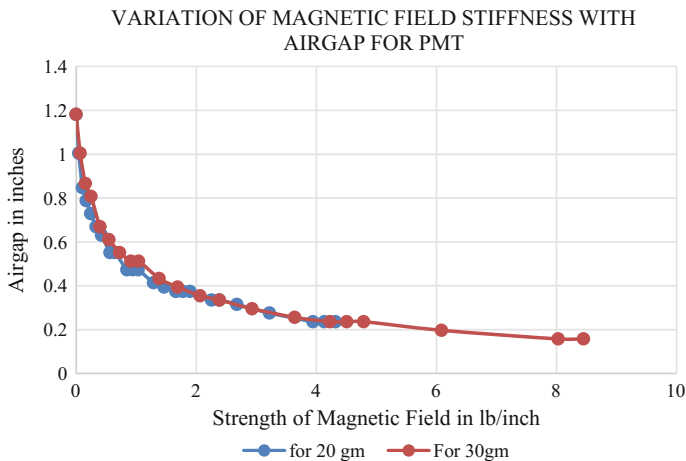


Fig. 9 Airgap versus strength of magnetic field variation for PMT

4 Conclusion

1. The variation of airgap with respect to load weight distribution is parabolic and non-linear in nature.
2. The magnetic field for RMT-1 is reversed when the airgap decreases below 7 mm, magnetic field for RMT-2 increases till airgap value 7 mm and magnetic field for PMT increases gradually with airgap and no reversing is seen. This shows that the magnetic field changes with the magnet distance apart 'd'.
3. Lesser the distance between the magnets, more is the pull/repel force acting. Due to such repulsion, tilting of horizontal beam while loading is seen.
4. The comparison shows that the plate magnets have high magnetic field, repulsion capacity and higher magnetic stiffness than the ring magnets. After plate magnets, the ring magnet type-2 has higher capacity and then the ring magnet type-1 with lower capacity.
5. Plate magnets can form stronger vibration isolation system due to its high repulsion and magnetic stiffness capacity.

5 Future Scope

The model is to be tested for vertical vibration deflection using vertical shake table.

References

1. Tsuda M, Kawasaki T, Yagai T, Hamajima T (2008) Dependence of horizontal vibration characteristics on load weight distribution in magnetic levitation type seismic isolation device. *IEEE Trans Appl Supercond* 18(2):832–835
2. Tsuda M, Kawasaki T, Yagai T, Hamajima T (2008) Improvement of levitation force characteristics in magnetic levitation type seismic isolation device composed of HTS bulk and permanent magnet. *J Phys: Conf Ser* 97. Available at: iopscience.iop.org
3. Tsuda M, Kojima T, Yagai T, Hamajima T (2007) Vibration characteristics in magnetic levitation type seismic isolation device composed of multiple HTS bulks and permanent magnets. *IEEE Trans Appl Supercond*. Available at: <http://www.researchgate.net/publication>
4. Fullerton LW et al (2012) Multi-level magnetic system for isolation of vibration (United States Patent, Patent no. US 8,279,031 B2, Date of Patent: Oct. 2, 2012)

Study on Behavior of Externally Bonded RC Beams Using Aramid Fiber Sheets

M.M. Deshmukh and M.M. Pawar

Keywords Numerical analysis · Flexural behavior · Strength · Load displacement response

1 Introduction

A structure is designed for a specific period and depending on the nature of the structure, its design life varies. For a domestic building, this design life could be as low as thirty to fifty years, whereas for a public building, it could be more than fifty years. Deterioration in concrete structures is a major challenge faced by the infrastructure and bridge industries worldwide. The deterioration can be mainly due to environmental effects, which includes gradual loss of strength with ageing, corrosion of steel, variation in temperature, repeated high intensity loading, freeze-thaw cycles, contact with chemicals and saline water and exposure to ultra-violet radiations. As complete replacement or reconstruction of the structure will be cost effective, strengthening or retrofitting is an effective way to strengthen the same [3, 5, 7].

The most popular techniques for strengthening of RC beams have involved the use of external epoxy-bonded steel plates [10, 11]. It has been found experimentally that flexural strength of a structural member can increase by using this technique. Although steel bonding technique is simple, cost-effective and efficient, it suffers from a serious problem of deterioration of bond at the steel and concrete interphase due to corrosion of steel. Other common strengthening technique involves construction of steel jackets which is quite effective from strength, stiffness and ductility considerations. However, it increases overall cross-sectional dimensions, leading to increase in self-weight of structures and is labour intensive. To eliminate these problems, steel plate was replaced by corrosion resistant and light-weight FRP Composite plates. FRPs help to increase strength and ductility without excessive

M.M. Deshmukh (✉) · M.M. Pawar
SVERI's College of Engineering, Pandharpur, India
e-mail: mdeshmukh00@gmail.com

increase in stiffness. Further, such material could be designed to meet specific requirements by adjusting placement of fibres. So concrete members can now be easily and effectively strengthened using externally bonded FRP composites.

Advanced fibre reinforced polymer (FRP) composite is very effectively being used worldwide for strengthening structures. It offers high strength with low self weight, corrosion resistance, high fatigue resistance, easy and rapid installation and minimal change in structural geometry. It provides a cost effective and technically more superior alternative to the traditional techniques in many specific situations. Conventional strengthening methods such as external post tensioning, member enlargement along with internal transverse steel, and bonded steel plates are very expensive. In addition to that these methods are time consuming; require extensive equipment and significant labour. FRP repair systems provide an economical and technically better alternative to traditional repair systems and materials [4, 6].

2 Experimental Investigation

2.1 Details of the Beam Specimen

The test program consisted of casting and testing of 8 beams, of which one was control beams, all having size of 150 mm \times 150 mm \times 700 mm length, reinforced with 2–12 Φ at bottom, 2–12 Φ at top using 8 mm diameter stirrups @125 mm c/c. The beams were cast using M 20 grade concrete and Fe 500 grade steel. The casting of beams was made as per IS code specification using M 20 grade concrete with 20 mm maximum size of coarse aggregate, locally available sand and 53 grade OPC cement [12]. These beams were cured for 28 days in pure water and were tested under two-point loading on a universal testing machine of capacity 1000 KN [13].

2.2 Preparation of Test Specimen

The description of test specimens is summarized in Table 1. The surfaces of the beams were cleaned using polish paper or grind to ensure a good bond between the FRP strip and concrete surface. Each of these beams was externally bonded with AFRP strips and epoxy to the beam as per the procedure given by the manufacturer [1–3, 8, 9].

Table 1 Strengthens patterns

Beam ID	L-section	C/S section	3D models
CB			
SBA 1			
SBA 2	FRP Sheet wrapping 		
SBA 3	FRP Sheet wrapping 		
SBA 4	FRP Sheet wrapping 		
SBA 5	FRP Sheet wrapping 		
SBA 6	FRP Sheet wrapping 		
SBA 7	FRP Sheet wrapping 		

2.3 Test Setup

All the specimens were tested on the universal testing machine (UTM) in the “Strength of Material” laboratory of SVERI’s College of Engineering Pandharpur. The testing procedure for the entire specimen will be same. After the curing period of 28 days, all the beam and its surface will clean for clear visibility of cracks. The most commonly used load arrangement for testing of beams consists of two-point loading [10–13, 15]. This has the advantage of a substantial region of nearly uniform moment coupled with very small shears, enabling the bending capacity of the central portion to be assessed. If the flexural capacity of the member is to be assessed, the load will normally be concentrated at a suitable shorter distance from a support.

Two-point loading can be conveniently provided by the arrangement. The load is transmitted through a load cell to beam. This beam bears on rollers seated on steel plates bedded on the test member with mortar, high-strength plaster or some similar material. The test member is supported on roller bearings acting on similar spreader plates.

The specimen was place over the two steel rollers bearing leaving 50 mm from the ends of the beam. Two point loading test shall be proposed. Loading is done by hydraulic jack of capacity 1000 KN. Cracks formed on the faces of the beams were marked and identified. All beam specimens were loaded and simply supported as shown in Fig. 1.

Load-deflection, stress and strains have been recorded for each specimen. Concrete having mean cube compressive strength of 22.50 MPa was used. For all the test beams, the parameters of interest were ultimate load, mid-span deflection, composite action, and failure modes.



Fig. 1 Experimental set up

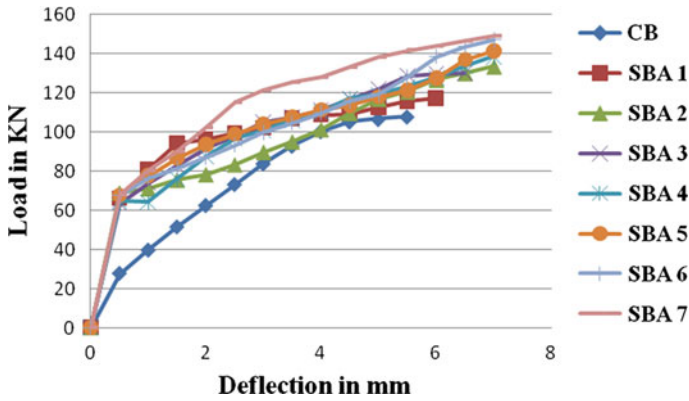


Fig. 2 Load versus deflection curve for CB and SBA 1, 2, 3, 4, 5, 6, 7

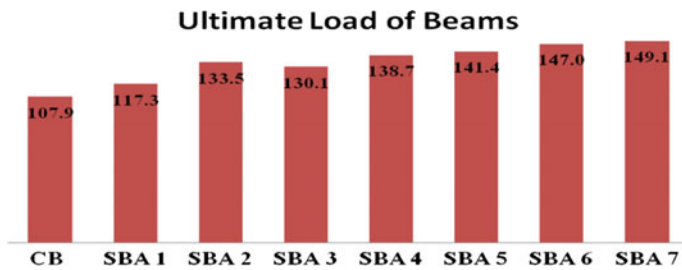


Fig. 3 Ultimate loads of beams CB and SBA 1, 2, 3, 4, 5, 6, 7 (in KN)

2.4 Test Result

During the experimental testing of beams it is observed that all the beams which strengthened, there is considerable increase in load values for initial cracks. For control beam initial cracks appeared at 25.5 KN and for all strengthen beam it was about 60–68 KN (Fig. 2).

2.5 Ultimate Load Carrying Capacity

The load carrying capacity of the control beams and the strengthen beams were found out is shown in Fig. 3. The control beams were loaded up to their ultimate loads. It was noted that of all the beams, the strengthen beams SBA 5, SBA 6 and SBA 7 had the higher load carrying capacity compared to the controlled beam. An important character to be noticed about the usage of AFRP sheets is the high ductile behavior of the beams. The shear failure

being sudden can lead to huge damage to the structure. But the ductile behavior obtained by the use of AFRP can give us enough warning before the ultimate failure. The use of FRP can delay the initial cracks and further development of the cracks in the beam.

3 Finite Element Modeling

Simulation has been carried out in ANSYS 14 which is a finite element package. In modeling 3D geometry of beams is drawn in CATIA 6 package. Concrete is a nonlinear behavior material during loading, its analysis in ANSYS version 14.0 (workbench) to conduct analysis (Fig. 4).

Similarly different configurations of beams which are modeled in CATIA 5.

CAD model is imported in ANSYS and it is meshed. Before mesh material properties are input to the software. Non-linear material properties are taken into consideration. These properties are obtained from experimentation. Following graph shows non linear behavior of CB 1 (Fig. 5).

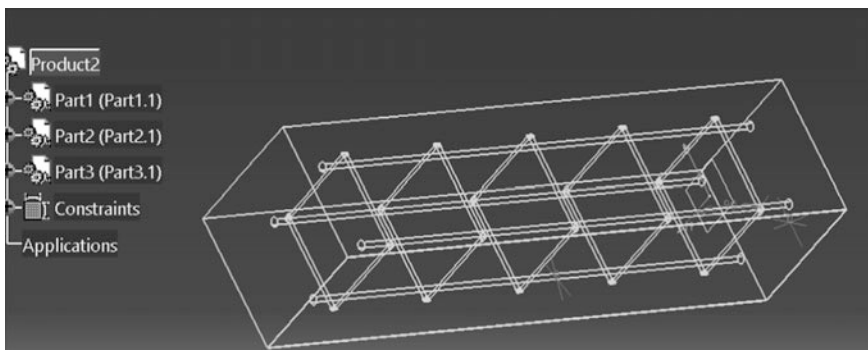


Fig. 4 CAD modeling of beam

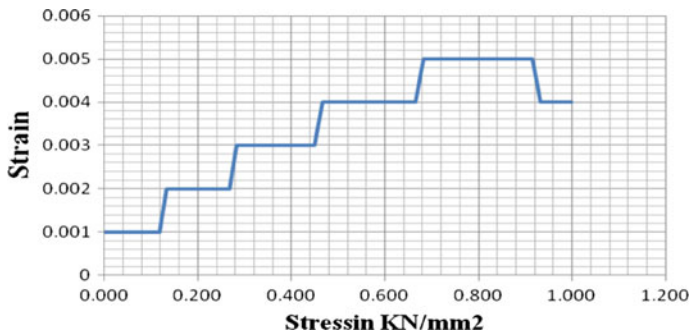


Fig. 5 Stress versus strain for CB

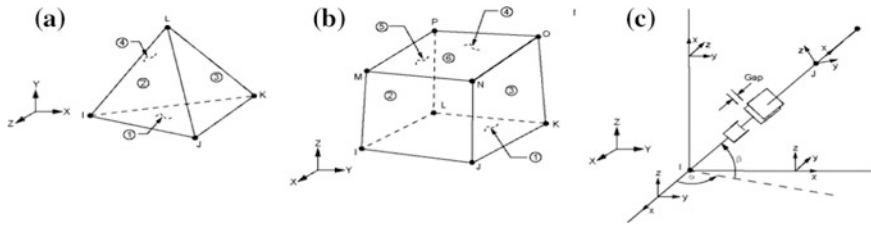


Fig. 6 Tetrahedron element (a), Brick 4 noded 20 element (b), Conta 178 element (c)

Table 2 Comparison of results for carbon FRP

Beams ID	Ultimate strength (KN)		% deviation
	By Expt.	By FEA	
CB	107.30	103.30	3.87
SBA 1	117.30	114.65	2.31
SBA 2	133.50	132.25	0.95
SBA 3	130.10	128.95	0.89
SBA 4	138.70	135.65	2.25
SBA 5	141.40	138.95	1.76
SBA 6	147.00	145.25	1.20
SBA 7	149.10	147.95	0.78

While meshing 10 node Tetrahedron and Brick 4 Noded 20 element are selected. Tetrahedron has been used for meshing steel bars and Brick 4 Noded 20 element was used for meshing remaining structure. Conta 178 element is used to model pair of steel bars with concrete and concrete with FRP (Fig. 6).

In Conta 178 pairing, perfect bonded contact is provided in between FRP and concrete. 8542 number of element and 1881 number of nodes is generated after meshing. Non-linear static analysis has been carried out.

In boundary condition, all degree of freedom of both ends of beams are making zero. i.e. Beam is simply supported at both ends. Two point loads are gradually applied at distant $L/3$ from supports. Loads are applied in negative Y direction. It is also observed that there is excessive distortion of elements when beam is broken.

In post processing, ultimate strength of beams are obtained as shown in Table 2. Deflection of simply supported beam is as shown in Fig. 7.

3.1 Ultimate Load Carrying Capacity

Finite element analysis has also carried out to find the ultimate load carrying capacity and compared with the experimental results. It was found that analytical analysis predicts lower value than the experimental findings. From the results, it is observed that there is maximum **3.87%** deviation in ultimate strength obtained by

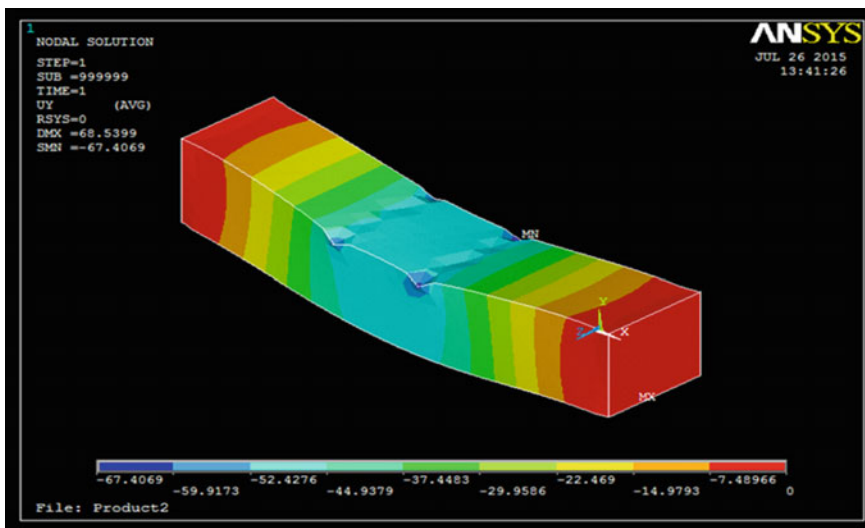


Fig. 7 Deflection of beam

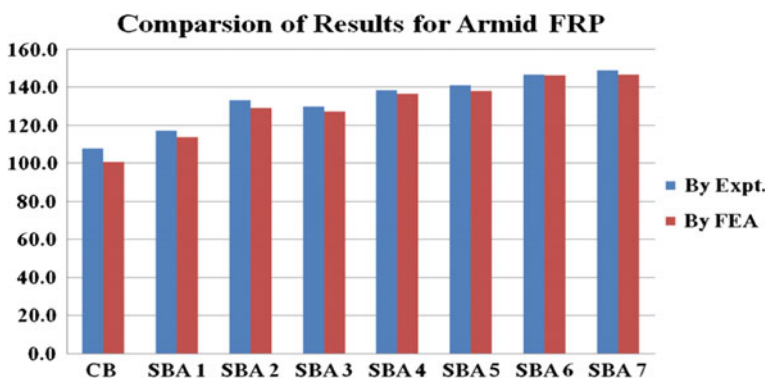


Fig. 8 Comparison of results for aramid FRP (Expt. and FEA)

experimentation and FEA; whereas minimum deviation is **0.89%**. The deviation, may occur because as during software analysis it considers all the ideal conditions for analysis. As a matter of fact practically or during experimentation work it is highly impossible to create ideal conditions to perform the ideal lab work for preparation of concrete and during casting. The deviation may be considering the difference between ideal assumption and actual work (Fig. 8).

4 Conclusions

Based on the results obtained from experiments, and ANSYS analyses, the following conclusions are drawn:

- (1) **AFRP** fabric properly bonded to the tension face of RC beams can enhance the ultimate strength up to **38.96%**.
- (2) Flexural strengthening of the beam increases the ultimate load carrying capacity, but the cracks developed were not visible up to a higher load. Due to invisibility of the initial cracks, it gives less warning compared to the control beam.
- (3) At any given load level, the deflections are reduced significantly thereby increasing the stiffness for the strengthened beams. At ultimate load level of the control specimens, the strengthened beams exhibit a decrease of deflection.
- (4) It is observed that load at initial cracks was increased for all strengthening the beam.
- (5) Finite element analysis has been carried out for result validation. It is observed that there is maximum **3.87%** deviation in ultimate strength obtained by experimentation and FEA.

References

Journal Papers

1. Belarbi A, Bora A (2013) FRP systems in shear strengthening of reinforced concrete structures. In: 11th International conference on modern building materials, structures and techniques, MBMST, pp 2–8
2. Djamaluddin R (2013) Flexural behaviour of external reinforced concrete beams. In: The 2nd international conference on rehabilitation and maintenance in civil engineering, pp 252–260
3. Ekenel M (2006) Flexural fatigue behavior of reinforced concrete beams strengthened with FRP fabric and precured laminate systems. *J Compos Constr ASCE* 433–442
4. Godat A (2010) Size effects for reinforced concrete beams strengthened in shear with CFRP strips. *J Compos Constr ASCE* 260–271
5. Grace NF (1999) Strengthening reinforced concrete beams using Fiber Reinforced Polymer (FRP) laminates. *ACI Struct J* 96(5):865–875
6. Sakuraba H, Matsumoto T, Hayashikawa T (2011) A study on the flexural behaviour of CFRP box beams with different laminate structures. In: 12th East Asia-Pacific conference on structural engineering and construction, pp 1845–1854
7. Satbhैया RK (2013) Rehabilitation and strengthening of R.C.C. STRUCTURES by using FRP composites. *Int J Emerg Technol Adv Eng* 3(10):261–273

Books

8. Shah MG, Kale CM (2010) RCC theory and design. Macmillan India, Reprint 2010
9. Shetty MS (2011) Concrete technology—theory and practice. S. Chand, Reprint 2011

ACI/IS Codes

10. ACI 440.2R-02: Guide for the Design and Construction of Externally Bonded FRP Systems for Strengthening Concrete Structures—American Concrete Institute—Effective from 11 July 2002
11. ACI 440.2R-08 Guide for the design and construction of externally bonded FRP systems for strengthening concrete structures—American Concrete Institute—Effective from July 2008
12. IS: 10262-1982, Recommended Guidelines For Concrete Mix Design—Bureau Of Indian Standards, New Delhi
13. IS: 516:1959, Methods Of Test For Strength of Concrete—Bureau Of Indian Standards, New Delhi
14. IS: 456-2000, Plain and Reinforced Concrete—Code of Practice—Bureau of Indian Standards, New Delhi
15. IS: 2185 (PART 4)-2008, Guidelines For Method of Testing—Bureau of Indian Standards, New Delhi

Part VII
ICT Based Societal Technologies

Forecasting Monsoon Rainfall Over India Based on Global Climate Parameters

Vaishalee S. Khotlande and Satishkumar S. Kashid

Keywords Long range forecast (LRF) · Genetic programming (GP) · Indian summer monsoon rainfall (ISMR)

1 Introduction

Indian Summer Monsoon Rainfall (ISMR) is always found to vary yearly, leading to profound impacts on agriculture based Indian economy. Spatiotemporal distribution of rainfall and amount of monsoon rainfall influences many policy decisions at National and state level. Prediction of Monsoon rainfall has been remained a great challenge for hydro-meteorologists due to intrinsic complexities in modeling the climatic systems.

The Indian Meteorological Department (IMD) has been issuing LRF of the southwest monsoon rainfall since 1886. It was, however the extensive and pioneering work of Walker [1, 2] that led to the development of the first objective models based on statistical correlations between monsoon rainfall and antecedent global atmosphere, land and ocean parameters. There are many reviews on the LRF of Indian southwest monsoon rainfall (ISMR) [3–8].

For the LRF of the ISMR, Genetic Programming approach has been taken up in this study, which uses the historical relationship between the ISMR and six global atmosphere-ocean parameters for monsoon rainfall forecast.

Pai [9] and Rajeevan et al. [10] have developed monsoon prediction models on the six predictors. On the similar lines, this study uses the various predictor combinations with similar set of inputs and Artificial Intelligence tool genetic programming. Thus in this study, the following six predictors are used for predication of Indian Summer Monsoon Rainfall.

V.S. Khotlande · S.S. Kashid (✉)
Department of Civil Engineering, Walchand Institute of Technology,
Solapur 413006, India
e-mail: sskashid@yahoo.com; sskashid@gmail.com

V.S. Khotlande
e-mail: vaishalikhotlande@gmail.com

- (a) North Atlantic Sea Surface Temperature anomaly
- (b) Equatorial South-East Indian Ocean Sea Surface Temperature anomaly
- (c) East Asia surface pressure anomaly
- (d) Nino3.4 Sea Surface Temperature anomaly
- (e) North Atlantic surface pressure anomaly
- (f) North Central Pacific zonal wind anomaly at 850 hPa (Fig. 1).

(a) **North Atlantic SST anomaly**

A relationship between the Atlantic Multidecadal Oscillation (AMO) and multi-decadal variability of the Indian summer monsoon rainfall has been recognized and studied [11, 12]. The fundamental link between the North Atlantic and the Indian summer monsoon is through the North Atlantic Oscillation. Strong negative (positive) NAO/NAM events lead to negative Tropospheric Temperature (TT) anomalies over Eurasia. These anomalies decrease (increase) meridional gradient of TT, resulting in below (above) normal monsoon rainfall. A positive AMO produces stronger monsoon by producing positive TT anomaly over Eurasia. It is also associated with enhanced La Nina type Pacific SST anomalies that stimulate stronger monsoon.

(b) **Equatorial SE Indian Ocean SST anomaly**

The Indian Ocean Dipole (IOD) phenomenon also affects the vigor of monsoons over the Indian subcontinent. A positive phase sees greater-than-average sea-surface temperatures and greater rainfall in the western Indian Ocean region, with a corresponding cooling of waters in the eastern Indian Ocean which tends to

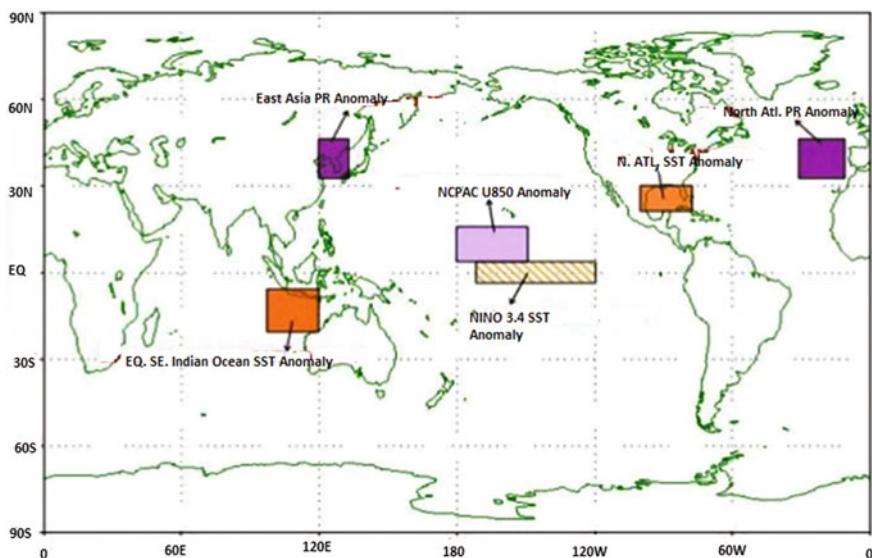


Fig. 1 Geographical locations of six predictors. *Source* India Meteorological Department

cause droughts in adjacent lands of Indonesia and Australia. The negative phase of the IOD brings about the opposite conditions, with warmer water and greater precipitation in the eastern Indian Ocean, and cooler and drier conditions in the west. The IOD is commonly quantified by an index that is the difference between sea surface temperature (SST) anomalies in the western (50°E – 70°E and 10°N – 10°N) and eastern (90°E – 110°E and 10°S – 0°S) equatorial Indian Ocean. The index is called the Dipole Mode Index (DMI).

(c) East Asia surface pressure anomaly

The Indian monsoon is found to be linked with the surface temperature contrast between the Indian Ocean and the rapidly warming Asian continent in late spring and summer. Variations of the Indian monsoon may be associated with variation of the surface temperature and other surface conditions, notably soil moisture. An increased (decreased) soil moisture can increase (decrease) evaporation which can cool (warm) the surface temperature and thereby decrease (increase) the temperature contrast that drives the mean monsoon.

(d) Nino3.4 SST anomaly [El Niño-Southern Oscillation (ENSO)]

El Niño-Southern Oscillation is a global coupled ocean-atmosphere phenomenon. The Pacific Ocean signatures, El Niño and La Niña are important temperature fluctuations in surface waters of the tropical Eastern Pacific Ocean. A higher El Niño southern oscillation (ENSO) is associated with droughts and La Niña is associated with excess rainfall [13, 14]. Sea surface temperature (SST) anomaly from the Niño 3.4 region is used as the ‘ENSO index’ in this study.

(e) North Atlantic surface pressure anomaly

The Atlantic Multidecadal Oscillation (AMO) is the low frequency variability in the Atlantic ocean is suggested to be induced by Atlantic thermohaline circulation (THC) variations and associated ocean heat transport fluctuations. The in-phase relationship between Indian rainfall and the AMO is consistent showing that Indian monsoon is significantly reduced when the Atlantic THC is substantially weakened. The current warm phase of the AMO persists in the coming decade; it will strengthen the summer rainfall over India. AMO is very important for understanding of the future climate change also.

(f) North Central Pacific zonal wind anomaly at 850 hPa

Climate is influenced by the temperatures of the surface waters, water currents as well as winds. The El Niño Southern Oscillation (ENSO) is a key component of global climate. For improving prediction the identification of ENSO’s dominant precursors, such as wind anomalies in the western Pacific Ocean (WPO) need to be considered. The variability of winds in the WPO is also a key factor in the transition from El Niño to La Niña via the responses of both equatorial oceanic Kelvin waves and an anomalous anticyclone in the Philippine Sea.

2 Data

The data used in this study were obtained from various sources, listed as following

- (a) North Atlantic SST anomaly (Longi. 20N–30N, Lati. 100W–80W) for the period Dec++Jan was obtained from (NCEP/NCAR reanalysis data)
- (b) Equatorial SE Indian Ocean SST anomaly (20S–10S, 100E–120E) for the period Feb++March was obtained from <http://www.ncdc.noaa.gov/oa/climate/research/sst/sst.html/>
- (c) East Asia surface pressure anomaly (35N–45N, 120E–130E) for the period Feb++March was obtained from (NCEP/NCAR reanalysis data)
- (d) Nino3.4 SST anomaly (5N–5S, 170W–120W) for the period MAM-DJF was obtained from (<http://www.cdc.noaa.gov/data/indices>).
- (e) North Atlantic surface pressure anomaly (35N–45N, 30W–10W) of May month only
- (f) North Central Pacific zonal wind anomaly at 850 hPa (5N–15N, 180E–150W) of May month only obtained from (NCEP/NCAR reanalysis data)

Monthly rainfall data over entire India as well as over homogeneous monsoon regions of India rainfall data used for this study were obtained from India Meteorological Department for a period 1901–2014. The data from 1950 through 2014 were only used, as the predictor data were available 1950 onwards. Monthly rainfall data from 1950 through 2000 were used for the training purpose. The data from 2000 to 2014 were used for the testing the GP models.

3 Methodology

Genetic Programming has been used by many researchers in Hydrology and Water Resources Engineering [15, 16, 17].

GP has the unique feature that it does not assume any functional form of the solution. GP can optimize both the structure of the model and its parameters. Genetic Programming evolves a computer program, relating the output and input variables. The specialty of GP approach lies with its ability to select input variables that contribute beneficially to the model and to disregard those that do not. Hence Genetic Programming is used for modeling rainfall prediction in this study.

GP evolves a function that relates the input information to the output information, which is of the form:

$$Y^m = f(X^n)(1) \quad (1)$$

where X^n is an n-dimensional input vector and Y^m is an m-dimensional output vector.

In the proposed study, the input vector consists of Historical Average Rainfall, North Atlantic SST anomaly, Equatorial SE Indian Ocean SST anomaly, East Asia surface pressure anomaly, Nino3.4 SST anomaly, North Atlantic surface pressure anomaly, and North Central Pacific zonal wind anomaly at 850 hpa. The output vector consists of monsoon rainfall for the particular month over the region under consideration.

In this work GP is implemented through software Discipulus [18] software that is based on an extension of the originally envisaged GP called Linear Genetic Programming (LGP).

3.1 Seasonal ISMR Prediction

Thus the seasonal rainfall is modeled as a function of

- (i) HR = Historical average monsoon rainfall (HR_{JJAS}),
- (ii) J1 = North Atlantic SST anomaly for the period Dec++Jan
- (iii) J2 = Equatorial SE Indian Ocean SST anomaly for the period Feb++March
- (iv) J3 = East Asia surface pressure anomaly Feb++March
- (v) J4 = Nino3.4 SST anomaly for the period MAM-DJF
- (vi) J5 = North Atlantic surface pressure anomaly of May month only
- (vii) J6 = North Central Pacific zonal wind anomaly at 850 hPa of May month only

The SST predictors were derived as the simple arithmetic average of the monthly ERSST.v2.

Anomalies over the respective geographical region (i.e. Dec++Jan and Feb++March).

The pairs of equations for the foresaid combinations for different models are listed as below

$$R_t = f\{(HR_t)(Predictor1, \dots, Predictor6)\}$$

1. $R_{seasonal} = f\{HR_{JJAS}, (J1, J2, J3, J5, J6)\}$ MODEL (1)
2. $R_{JJAS} = f\{(HR_{JJAS}), (J2, J3, J5, J6)\}$ MODEL (2)
3. $R_{JJAS} = f\{HR_{JJAS}, (J1 + J2 + J3 + J4 + J5 + J6)\}$ MODEL (3)
4. $R_{JJAS} = f\{HR_{JJAS}, (J3 + J4 + J5)\}$ MODEL (4)

The Pearson product and Correlation Coefficients for Training, and Testing for All India and four homogeneous monsoon regions with 6 predictors with different combinations are tabulated in Table 1. Root Mean Square Error for measurement of rainfall in mm during Training and Testing are enlisted in Table 2.

Table 1 Correlation coefficients between observed and predicted rainfall during training and testing periods

Region	CC	MODEL-1 (I1 + J2 + J3 + J5 + J6)	MODEL-2 (J2 + J3 + J5 + J6)	MODEL-3 (J1 + J2 + J3 + J4 + J5 + J6)	MODEL-4 (J3 + J4 + J5)
All India	Training	0.983	0.974	0.997	0.989
	Testing	0.653	0.643	0.252	0.747
Central NE India	Training	0.989	0.976	0.998	0.992
	Testing	0.565	0.435	0.401	0.678
NE India	Training	0.992	0.936	0.996	0.985
	Testing	0.592	0.703	0.267	0.224
NW India	Training	0.988	0.971	0.995	0.981
	Testing	0.411	0.718	0.649	0.573
Peninsular	Training	0.988	0.969	0.995	0.973
	Testing	0.027	0.242	0.331	0.441

Table 2 Root mean square error for measurement of rainfall in mm during training and testing

Regions	RMSE	MODEL-1 (I1 + J2 + J3 + J5 + J6)	MODEL-2 (J2 + J3 + J5 + J6)	MODEL-3 (J1 + J2 + J3 + J4 + J5 + J6)	MODEL-4 (J3 + J4 + J5)
All India	Training	26.3	32.6	8.0	22.0
	Testing	79.1	78.0	113.2	75.9
Central NE India	Training	30.8	51.7	11.2	25.8
	Testing	136.0	198.0	196.1	123.4
NE India	Training	23.3	67.8	11.6	14.6
	Testing	155.2	252.1	177.6	203.9
NW India	Training	25.6	43.6	17.4	36.0
	Testing	110.3	193.3	112.4	101.9
Peninsular	Training	25.2	39.5	16.2	36.6
	Testing	122.1	251.7	152.6	105.4

4 Discussion

The quantitative forecasts of rainfall for the southwest monsoon season (June–Sept) rainfall over the country as a whole and over the four broad geographical region are issued using six parameters.

Four different models with different combinations from six predictors are tried in this study. Model-1 includes 5 parameters, Model-2 uses 4 parameters, Model-3 uses 6 parameters and in Model-4 uses 3 parameters. The correlation coefficient and root mean square values for training and testing for all regions shown in above Tables 1 and 2 respectively. From these result it can be understood that Model no.4 with [East Asia surface pressure anomaly (J3), Nino3.4 SST anomaly (J4), North Atlantic surface pressure anomaly (J5)] combination gives the highest correlation coefficient for All India (0.747), Central India (0.678) and Peninsular India (0.441).

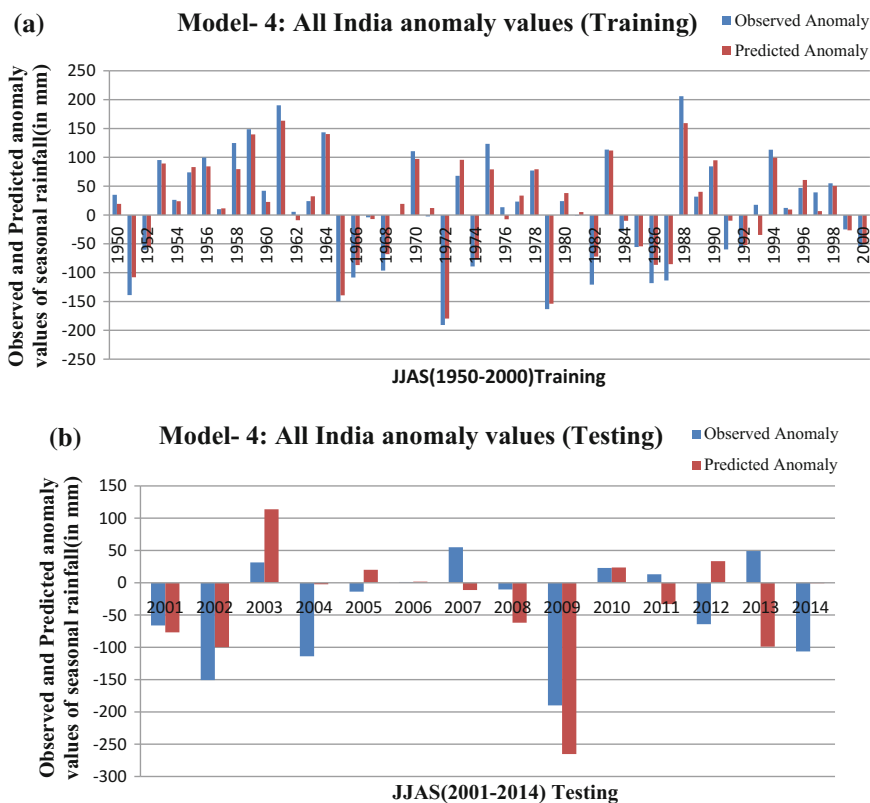


Fig. 2 a Graphical presentation of observed and predicted anomaly rainfall values of training period for all India. b Graphical presentation of observed and predicted anomaly rainfall values of testing period for all India

For North East India (0.703) and North West India (0.718) highest correlation coefficient is obtained by model 2 with combination (J2 + J3 + J5 + J6) i.e. Equatorial SE Indian Ocean SST anomaly, East Asia surface pressure anomaly, North Atlantic surface pressure anomaly and North Central Pacific zonal wind anomaly.

Figure 2a represents anomaly values of Observed and Predicted for All India with combination of predictors as [East Asia surface pressure anomaly (J3), Nino3.4 SST (J4), North Atlantic surface pressure anomaly (J5)] during training and Fig. 2b during testing respectively.

It can be observed from Fig. 2 that monsoon rainfall anomalies are nicely captured by GP models in most of the years.

5 Conclusions

This work uses the association between the global atmosphere, land and ocean parameters for prediction of Indian Summer Monsoon Rainfall over Homogeneous Monsoon Regions of India which is quite important for Indian hydro climatology. Genetic algorithm based approach (GP), is used for the complex relationship between inputs and outputs. Various combinations of predictors viz. North Atlantic SST anomaly, Equatorial SE Indian Ocean SST anomaly, East Asia surface pressure anomaly, Nino3.4 SST anomaly, North Atlantic surface pressure anomaly, North Central Pacific zonal wind anomaly at 850 hPa were explored for the seasonal ISMR prediction.

The highest correlation between observed rainfall and predicted rainfall was observed for [East Asia surface pressure anomaly (J3), Nino3.4 SST anomaly (J4), North Atlantic surface pressure anomaly (J5)] combination for All India Rainfall. AI tool Genetic Programming developed most optimum model for prediction of Indian Summer Monsoon Rainfall with correlation coefficient between observed and predicted rainfall as good as 0.747. However, considerably less correlation was observed for peninsular India, which covers Tamilnadu, Pondicherry, Coastal Andhra Pradesh, Rayalseema and South Interior Karnataka regions of India. The genetic programming tool was found to capture complex relationships between inputs and outputs satisfactorily.

References

1. Walker GT (1923) Correlation in seasonal variations of weather, VIII, a preliminary study of world weather. Mem India Meteorol Dept 24:75–131
2. Walker GT (1924) Correlation in seasonal variations of weather-IV, a further study of world weather. Mem India Meteorol Dept 24:275–332
3. Gadgil S, Rajeevan M, Nanjundiah R (2005) Monsoon prediction—why yet another failure? Curr Sci 88:1389–1400

4. Jagannathan P (1960) Seasonal forecasting in India: a review. FMU: 1-80, India Meteorological Department, Pune, India
5. Krishna Kumar K, Soman MK, Rupa Kumar K (1995) Seasonal forecasting of Indian summer monsoon rainfall. *Weather* 50:449–467
6. Normand C (1953) Monsoon seasonal forecasting. *QJR Meteorol Soc* 79:463–473
7. Rajeevan M (2001) Prediction of Indian summer monsoon: status, problems and prospects. *Curr Sci* 11:1451–1457
8. Thapliyal V, Kulshreshtha S (1992) Recent models for long range forecasting of southwest monsoon rainfall over India. *J Arid Environ* 43:239–248
9. Pai DS, Rajeevan M (2006) Long range prediction models for the Indian summer monsoon rainfall with different lead time periods based on the global SST anomalies. *Meteorol Atmos Phys* 92:33–43
10. Rajeevan M, Pai DS, Anil Kumar R (2006) New statistical models for long range forecasting of southwest monsoon rainfall over India. NCC research report No 1/2005, India Meteorological Department, Pune, India
11. Rajeevan M (2002) Winter surface pressure anomalies over Eurasia and Indian summer monsoon. *Geophys Res Lett* 29:94.1–94.4
12. Srivastava AK, Rajeevan M, Kulkarni R (2002) Teleconnection of OLR and SST anomalies over Atlantic Ocean with Indian summer monsoon. *Geophys Res Lett* 29(8):1284. doi:[10.1029/2001GL013837](https://doi.org/10.1029/2001GL013837)
13. Rasmusson EM, Carpenter TH (1983) The relationship between eastern equatorial Pacific sea surface temperatures and rainfall over India and Sri Lanka. *Mon Weather Rev* 111:517–528
14. Sikka DR (1980) Some aspects of the large-scale fluctuations of summer monsoon rainfall over India in relation to fluctuations in the planetary and regional scale circulation parameters. *Proc Indian Acad Sci Earth Planet Sci* 89:179–195
15. Kashid SS, Maity R (2012) Prediction of monthly rainfall on homogeneous monsoon regions of India based on large scale circulation patterns using genetic programming. *J Hydrol* 454–455:26–41
16. Babovic V, Keijzer M (2000) Genetic programming as a model induction engine. *J Hydroinform* 2 (1):35–60
17. Aytek A, Kisi O (2008) A genetic programming approach to suspended sediment modeling. *J Hydrol* 351:288–298
18. Francone FD (1998) *Discipulus owner's manual*. Machine Learning Technologies Inc, Littleton, Colorado

Augmented Reality in Higher Education Supported with Web 2.0: A Case Study in Chemistry Course

Trupti Satpute and Prakash Bansode

Keywords Augmented reality · Web 2.0 · E-learning · Spectroscopy

1 Introduction

For many learners across the world, chemistry is introduced for the first time in junior college level. Abstract concepts such as molecules, atoms, and electromagnetic fields inside and outside the molecules are formidable to undergraduate students; these students are often required to envision across micro- and macro-worlds, which can be extremely challenging. “The nuclear magnetic resonance for identification of substances” is a critical concept in chemistry learning, as it is the foundation of further learning about chemicals and organic chemistry. However, some students’ imaginative abilities are limited, and it is difficult for them to imagine how electron beam pass through particles and record resonance peaks. This problem necessitates improvement in the learning methods and tools used in chemistry teaching.

Augmented Reality (AR) is an extension of Virtual Reality (VR). By contrast to traditional VR, AR provides a seamless interface for users that combines both the real world and the virtual world. Users can interact with virtual objects that are interposed on real scenes around them and obtain the most natural and genuine human–computer interaction experience. With the rapid development of Augmented Reality, the integration of AR into disciplinary teaching has emerged to a significant extent. Regarding the “Type of AR” three types can be considered according to the classification of Wojciechowski and Cellary as in [1] marker-based AR, marker-less AR and location-based AR. Marker-based AR is based on the use of markers.

T. Satpute (✉)
SKN Sinhgad College of Engineering, Pandharpur, India
e-mail: satpute.trupti@gmail.com

P. Bansode
Sangola College, Sangola, India
e-mail: bansode.prakash4@gmail.com

Markers are labels that contain a colour or black and white pattern that is recognized or registered by the AR application through the camera. Marker-less AR is based on the recognition of the object's shapes. And location-based AR superimposes information according to the geographical location of the user.

According to [2] most of the studies used "Marker-based AR" (59.3%) which means that most of the applications developed for educational settings use markers. A possible explanation for this result is that currently the tracking process of markers is better and more stable compared to the marker-less tracking techniques. The use of static markers decrease the tracking work needed and reduce the number of objects to be detected [3]. Therefore for educational settings the use of markers could be recommended so that students can have a better experience with the technology. Most of the studies targeting AR benefits havent presented empirical results.

This research aims to develop a learning tool based on AR and web 2.0 for undergraduate chemistry courses, to examine its effect on students' cognitive performance, compare its effects on high-achieving and low-achieving students and investigate students' attitudes toward the software. The software is designed by using Moodle at core and Learning tool interoperability protocol for integrating AR tool with Moodle.

2 Literature Review

After a review of the related computer-assisted tools in chemistry education, we consider AR the most suitable and appropriate solution for the present problems. The main objective for our research was to develop a supplemental tool to perform AR based activity to enhance learning experience with LMS as well as add web 2.0 based functionality to marker based AR learning tool.

In the University of Panama, a research project was carried out where virtual world was used for teaching basic electronics course where AR is used to control actions in virtual world [4]. Another example is [5] where Black Board is used as LMS and social networking based on web 2.0 for educational purpose. AR is used for providing e-tutor in virtual environment and arranging an event in virtual gallery. They are more close to virtual reality which can be termed as augmented virtually than real world. So For having more interactive environment, the prototypes should be designed so as to augment the digital information in real world.

AR 2.0 as a user experience and networked medium has many parallel characteristics to Web 2.0 Hoang et al. [6] have developed a system which uses wearable device enabled with AR interface to share social network information which can capture location information using GPS co-ordinates. Such kinds of efforts are extended for combining location based augmented information to web 2.0 supports. By introducing ARML 2.0 which is an XML grammar that lets developers describe an augmented scene, the objects in the scene, and some essential aspects of their behaviour.

3 Research Methodology

3.1 Prototype Architecture

The prototype is a web application empowered with web 2.0 technologies. The AR modules “ChemAR” and “NMRChat” used in system are Rich Internet Applications which is a type of web 2.0 application. The system has been developed by using ARToolkit library and SilverLight runtime at client side. For providing web 2.0 based collaboration functionality, it is essential to have JavaScript enabled client so that chatting or collaborative editing of text is supported in real time. “NMRQuiz” is MVC based web application for conducting the quiz used for students’ evaluation (Fig. 1).

The system uses LMS (Moodle) for providing learning environment’s features and facilities. The web applications “ChemAR”, “NMRQuiz” and “NMRChat” are integrated with Moodle using Learning Tool Interoperability (LTI). Hence it can be used with Moodle inherently. This system can be used for classroom teaching or as revision tool. We have used it as supplemental tool for learning.

Figures 2 and 3 show the working of ChemAR and NMRChat respectively. ChemAR is AR module showing 3D structure of methane molecule formation. NMRChat has collaborative editing and chatting functionality. It can be used while performing AR activity. Students can share their experiences using chat function. It is showing apart of video where NMR spectrometer’s working is explained.

3.2 Experimental Setup

This study involved 24 students including 13 boys and 11 girls. The experiment of the software’s impact was conducted in a senior college in Sangola, India.

Research rationale and experiment preparation: This study mainly focuses on the supplemental learning effect of AR-based learning tools in a chemistry course. The testing class was taught the content of “NMR spectroscopy”. We interviewed

Fig. 1 Prototype architecture

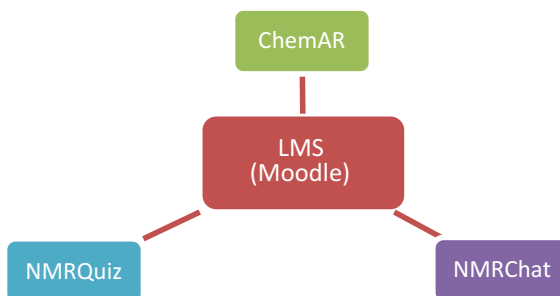
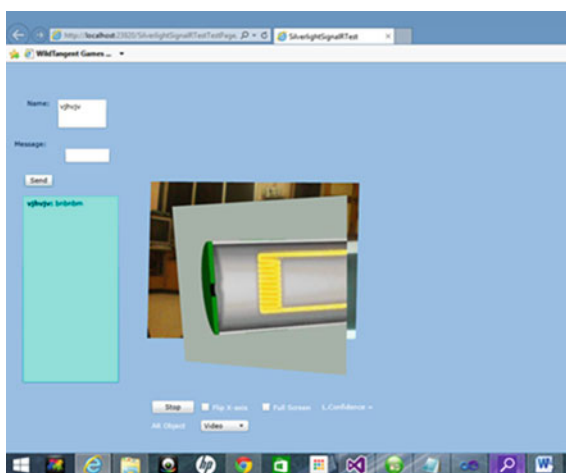


Fig. 2 ChemAR



Fig. 3 NMRChat



the chemistry teacher before the design and development of this AR tool, when he pointed out that students were not very motivated as the content is dull and abstract.

Therefore, he expressed a wish to review the content using an AR tool in order to stimulate learning interests and promote learning outcome of “NMR spectroscopy” content. For such reasons, the experiment did not include a control group. Pre-test scores will represent students’ learning outcomes when using textbooks, and post-test scores will represent students’ learning outcomes after using an AR inquiry-based learning tool. The questionnaire primarily surveys students’ learning attitudes toward this AR learning tool. Before the experiment, researchers installed the AR software on each computer in the computer laboratory. The experiment contains five sections, as shown in Table 1.

Table 1 Experiment setup

Experiment content	Operation methods
Pre-test	Each student is required to complete a test in Moodle independently
Grouping and inquiry-based learning using activity form	The class is randomly divided into groups of three. Each group is required to use the AR tool to learn as indicated on the activity form and cooperatively complete the form without the teacher's guidance (a set of AR tools contains AR-based software, markers and the activity form)
Post-test	Each student is required to independently complete the same test used for the pre-test inside Moodle
Questionnaire survey	Each student is required to independently complete a paper and pencil questionnaire

3.2.1 Measurement Instruments

Pre–post test: The quiz was devised by a chemistry teacher and further examined by a group of chemistry education experts. The pre test includes 20 questions out of which 10 were multiple choice questions and 10 were short answer type questions, associated to the learning content “NMR spectroscopy” and has a full mark of 20 points

Instruction and activity form: In this study, we designed an inquiry-based group learning scenario in which students were required to conduct explorations in groups of three without teacher instruction. They must use the AR tool and conclude the principles by themselves. The activity form is designed to assist them in the learning process, providing operation steps showing them what to do and asking introductory questions encouraging them to think and draw conclusions. The activity form was devised by us according to our application design. We want to clarify that the design of this activity form is not going to limit students' operations with the markers. As it is the first time students get knowledge of AR technology, and we put them in a self-exploration scenario without teachers' guidance, the activity form aims to show them how to use markers to interact with the computer and observe properly.

Post-questionnaire: The questionnaire adopts Likert scale with five options: a scale of 1, or “Strongly Disagree”, to 5, or “Strongly Agree”. The questionnaire consists of two constructs: cognitive validity and accessibility, and satisfaction with the software. Cognitive validity and accessibility construct includes ten items which are revisions from [7] and satisfaction with software construct has ten items which follow System Usability Scale.

4 Data Analysis and Findings

4.1 Overall Cognitive Performance

The experiment produced 24×2 test records (24 for the pre-test and 24 for the post-test), all of which are considered effective. The full mark of the test is 20 points. We conducted a paired t-test for the pre-test and post-test score variables. The tested variable is post-test score minus pre-test score, which stands for the difference yielded after using the AR tool for each student. Table 2 shows that the p-value (two-tailed) of the mean is close to zero ($t = 5.0251$, $p\text{-value} = 0.0001$). As a result, we conclude that with other unobserved variables controlled, the AR inquiry-based learning tool has a statistically significant improvement on the score of the adopted cognitive quiz test, and students' averages scores increased by 3.310 points.

Attitudes toward the AR tool through questionnaire analysis in the questionnaire analysis, we calculated the score of each construct by averaging all of the corresponding items within each construct. The descriptive statistics obtained are shown in Tables 3 and 4. Table 3 shows the items in "cognitive validity and accessibility". Here items 3 and 7 are negative statements and thus their mean score is less than other constructs. In Table 4, SUS based items are given with their mean score. SUS has alternative positive and negative statements. Hence the mean values are differing accordingly. The overall SUS score for our system to be 73.25% which is considered good.

From these findings we found that the AR inquiry-based learning tool has significant supplemental learning effects. The empirical study tested the software's supplemental effect. The pre-test scores represent students' learning outcomes when using textbooks and the post test score represent students' learning outcomes after using AR tool. The AR tool aims to aid students in exploring and generalizing concepts and to help students develop problem-solving skills, inquiry-based exploration skills instead of merely cognitive memorization.

Table 2 *t* test applied for pre and post test results

	Paired differences					<i>t</i>	Df	Sig (2-tailed)
	Mean	Std. deviation	Std. error mean	95% confidence interval of the difference				
				Lower	Upper			
Post-test score – pre-test score	3.375	2.43	0.680	2.05	4.79	5.0251	45	0.0001

Table 3 Descriptive statistics for the “cognitive validity and accessibility” constructs

No.	Statement	Mean	SD
1	I enjoyed the educational process performed with support of this e-learning application	4.416667	0.49307
2	“It was easier to learn difficult subjects, thanks to this e-learning application	4.25	0.661438
3	It was difficult to use the e-learning application	2.25	1.010363
4	With this e-learning application, I felt more self-confident about learning course subjects	4.208333	0.575845
5	By using this e-learning application, it was more effective to learn chemistry	4.45833	0.705878
6	I prefer using this e-learning application rather than other e-learning approaches	4.25	0.721688
7	I don't want to take part again in such an educational process	2.125	0.721688
8	Materials (animations, videos...etc.) viewed on the tool—application were attractive	4.333	1.64094
9	My academic achievement level has been improved, thanks to this e-learning application	4.16667	0.98601
10	This e-learning application has enabled me to learn faster	3.8333	0.687184

Table 4 Descriptive statistics for the “usability” constructs using SUS

No.	Statement	Mean	SD
1	I think that I would like to use this system frequently	4	0.91287
2	I found the system unnecessarily complex	2.625	1.2520816
3	I thought the system was easy to use	4.2083	0.49826
4	I think that I would need the support of a technical person to be able to use this system	3.0833	1.4117562
5	I found the various functions in this system were well integrated	4.04167	0.6757198
6	I thought there was too much inconsistency in this system	2.75	1.050793
7	I would imagine that most people would learn to use this system very quickly	4.08333	0.6400954
8	I found the system very cumbersome to use	2.29167	1.3987842
9	I felt very confident using the system	4.1667	0.942809
10	I needed to learn a lot of things before I could get going with this system	2.9167	1.255543

Figures 4 and 5 are the photographs taken while conducting the experiment. In Fig. 4, students are attempting the pre-test and in Fig. 5 some students are filling up the post questionnaire.

Fig. 4 Students solving post test



Fig. 5 Students who are filling up questionnaire



5 Conclusion

Empirical studies are meant to prove the benefits of technology to the society. The tests in such experiments are based on human behavioural characteristics. Results of our experiment show that the AR tool is beneficial in improving undergraduate students' cognitive test performance on corresponding content, and has relatively larger influence on low-achieving students. Additionally, students generally hold a positive attitude toward the AR tool and enjoyed the exploration experience. Based on the findings, we wish to further employ this AR tool as a remedial learning tool

and extend the method to other chapters and contents in chemistry course. Use of LMS has made the execution of experiment in easier and faster way. Use of AR based tools also claims to have more retention of knowledge. To prove that a post test after a long period can be conducted. The tool can be further modified so as to recognize the chemical structures instead of markers so as to increase relevance of learning material and augmented content.

Acknowledgements Authors are thankful to Dr. K.J. Ingole, Principal, Sangola College Sangola and Mr. Tathe, HOD, Department of Computer Science for their valuable support and co-operation.

References

1. Wojciechowski R, Cellary W (2013) Evaluation of learners' attitude toward learning in ARIES augmented reality environments. *Comput Edu* 68:570–585. doi:[10.1016/j.compedu.2013.02.014](https://doi.org/10.1016/j.compedu.2013.02.014)
2. Bacca J, Baldiris S, Fabregat R, Graf S, Kinshuk (2014). Augmented reality trends in education: a systematic review of research and applications. *Edu Technol Soc* 17(4):133–149
3. El Sayed NAM, Zayed HH, Sharawy MI (2011) “ARSC: augmented reality student card” an augmented reality solution for the education field. *Comput Edu* 56(4):1045–1061. doi:[10.1016/j.compedu.2010.10.019](https://doi.org/10.1016/j.compedu.2010.10.019)
4. Vernaza A, Ivan Armuelles V, Ruiz I (2012) Towards to an open and interoperable virtual learning environment using Metaverse at University of Panama. ISBN: 978-1-4673-2486-1/12/\$31.00, pp 320–325
5. Jin L, Wen Z (2009) An augmented social interactive learning approach through Web 2.0. In: *Proceedings of the international computer software and applications conference on 33rd annual IEEE*, pp 607–611
6. Hoang TN, Porter SR, Close B, Thomas BH (2009) Web 2.0 meets wearable augmented reality. In: *International symposium on wearable computers*, pp 151–152
7. Malinka I, Georgi I (2011) Enhancement of learning and teaching in computer graphics through marker augmented reality technology. *Int J New Comput Archit Appl (IJNCAA)* 1 (1):176–184

Implementation of QoS Based Policer in Routers for Next Generation Network (NGN)

Santosh D. Bhopale, S.V. Sankpal, D. Jayadevappa and Sharan Kumar

Keywords Weighted random early detection (WRED) · Multi-protocol label switching (MPLS) · Next generation network (NGN) · Class-based weighted fair queuing (CBWFQ) · Quality of service (QoS)

1 Introduction

Next Generation Networks are packet-based with capabilities to support multiple broadband networks and provide end-to-end Quality of Service (QoS) guarantees across multiple access networks. However, each technology implements its proprietary QoS solutions to satisfy its own network requirements. They define QoS classes based on their standard specifications which makes right mapping of QoS classes over heterogeneous networks a difficult task. Consequently, QoS parameters could seriously be affected at destination as a result of cumulative incorrect QoS mapping conversions. Providing QoS to the 5G network is contingent upon evolution of heterogeneous networks. A challenging task is how to transfer the QoS parameters over different networks to the end user in a unified environment. One possible solution is establishing a common interface among different types of network that can translate the QoS requirements from one type of network to the other. Vertical QoS mapping is associated with different layers within the same network. Each layer should understand and satisfy the QoS requirements for above and lower layers. Whereas, horizontal QoS mapping is considered between different network types, transferring QoS requirements from one technology to the other [1].

S.D. Bhopale (✉) · S. Kumar

Tatyasaheb Kore Institute of Engineering and Technology, Warananagar,
Maharashtra, India

e-mail: santoshbhopale@gmail.com

S.V. Sankpal

D.Y. Patil College of Engineering and Technology, Kolhapur, Maharashtra, India

D. Jayadevappa

JSS Academy Engineering and Technology, Bengaluru, Karnataka, India

Future NGN networks will also be characterized by high bandwidth content with speeds in excess of 10 Gb/s, various mobility levels, and energy and cost-efficient solutions with the augmentation of the wireless world's intelligence, but they should also meet the satisfaction of users, the so called quality of experience. Traditionally, in 3G-4G systems the QoS is considered in order to estimate the performance of the mobile network for a service with a guaranteed service level [2]. To support these highly bandwidth-intensive and time-sensitive multimedia services for the emerging 5G wireless networks, for the last several years the telecommunications academia and industry have made a great deal of effort/processes in investigating various advanced wireless techniques such as device-to-device (D2D) communications [3], wireless full-duplex (FD) communications, advanced cognitive radio (CR) communications, and so on, as well as quality of service (QoS) provisioning techniques. Because of the highly varying wireless channels, the deterministic delay-bounded QoS requirements for high-volume multimedia wireless traffic are usually hard to guarantee [3]. On the contrary, Relative DiffServ is simpler and more flexible to be used in dynamic network environments. The more promising algorithms to realize Relative DiffServ, also for efficient resource exploitation, are based on the Proportional Differentiation Model (PDM), in which the performance distance between classes is proportional to given differentiation parameters that can be configured as needed [4].

2 Related Work

2.1 Literature Survey

In the regard of present research work some literature survey has been done by many researchers. Al-Shaikhli et al. [1] expressed that in 5G, heterogeneous broadband networks will emerge to a common set of objectives to offer the end users higher capacity, robustness, security, QoS, and more in a unified and converged manner. They are proposing a common QoS framework, in order to provide end-to-end QoS support to application services over the heterogeneous networks. The framework consists of a two-level scheduling scheme: a Class-Based Weighted Fair Queuing (CBWFQ) discipline and a Rate-Controlled Priority Queuing (RCPQ) discipline. Gomez-Sacristan et al. [2] expressed that learning model developments that place greater weight on laboratory activities require investment in specific equipment that is often very expensive, difficult to manage, and soon obsolete. A virtual laboratory education platform, QoS Lab, for training in and research into quality-of-service (QoS) mechanisms used for Metro Ethernet access in next-generation networks (NGNs). Pierucci [5] proposed concept Quality of experience (QoE) is the subjective acceptability of the quality of a telecommunication service perceived by the user. An efficient QoE estimation method tailored for 5G systems is also proposed based on the neural network (NN) approach. Due

to their ability to fully learn the causal relationship between network parameters of quality of services (QoS) and the resulting QoE, NN can be suitable to gain QoE self-optimization for 5G. Panza et al. [4] expressed that Next-Generation Networks (NGNs), comprising for example, B4G and 5G cellular systems, will support Quality of Service (QoS) over a heterogeneous wired and wireless IP-based infrastructure. They describe an IP cross-layer scheduler which is able to support a Proportional Differentiation Model (PDM) for delay guarantees also over wireless. The key idea is to leverage feedbacks from the lower layers about the actual delays experienced by packets in order to tune at run-time the priority of the IP service classes in a closed-loop control. Their objective is to implement a PDM on the whole at the network interface, as relevant for the end users. Zhang et al. [3] are described that the 5G mobile wireless networks are expected to provide different delay-bounded QoS guarantees for a wide spectrum of services, applications, and users with extremely diverse requirements. Since the time-sensitive services in 5G multimedia wireless networks may vary dramatically in both a large range from milliseconds to a few seconds and diversity from uniform or constant delay-bound to different or variable delay-bound guarantees among different wireless links, the delay-bound QoS requirements for different types of services promote the newly emerging heterogeneous statistical delay-bounded QoS provisioning over 5G mobile wireless networks, to overcome these new challenges, they proposed a novel heterogeneous statistical QoS provisioning architecture for 5G mobile wireless networks. Gupta [6] expressed that Transition to Next Generation Networks is likely to raise questions about how inter-operator interconnections should take place in a heterogeneous environment. The NGN architecture introduces several degrees of complexity, requiring decisions on issues like the layers and planes at which the interconnection among different service provider. Domains should take place and how adequate quality of service can be ensured, over the interconnection, or various services. Sun [7] described that with the development of network technology, people's demand on real-time and multimedia feature of the network services has become more and more sophisticated, that requiring Quality of Service of Next Generation Networks with high features. In his work he systematically analyzes the characteristics and limitations of IntServ and DiffServ. Gardasevic et al. [8] proposed that the framework for cross-layer Quality of Service (QoS) adaptation in Next Generation Networks (NGN) based on Service-Oriented Architecture (SOA) principles of system design. The aim of this framework is to establish efficient communication mechanisms among the layers that will be able to adapt dynamically to the diversity of user/application requirements, networking technologies, and provider capabilities.

2.2 *QoS Mapping*

A general view of heterogeneous environment could potentially consist of satellite, radio, sensor, and cable networks as illustrated in Fig. 1. The interfaces between

different network types are shown in solid blue circles connecting each pair of networks in Fig. 1. QoS mapping over heterogeneous networks can be classified into vertical and horizontal QoS mapping as shown in Fig. 2.

Vertical QoS mapping is associated with different layers within the same network. Each layer should understand and satisfy the QoS requirements for above and lower layers.

Whereas, horizontal QoS mapping is considered between different network types, transferring QoS requirements from one technology to the other, Horizontal

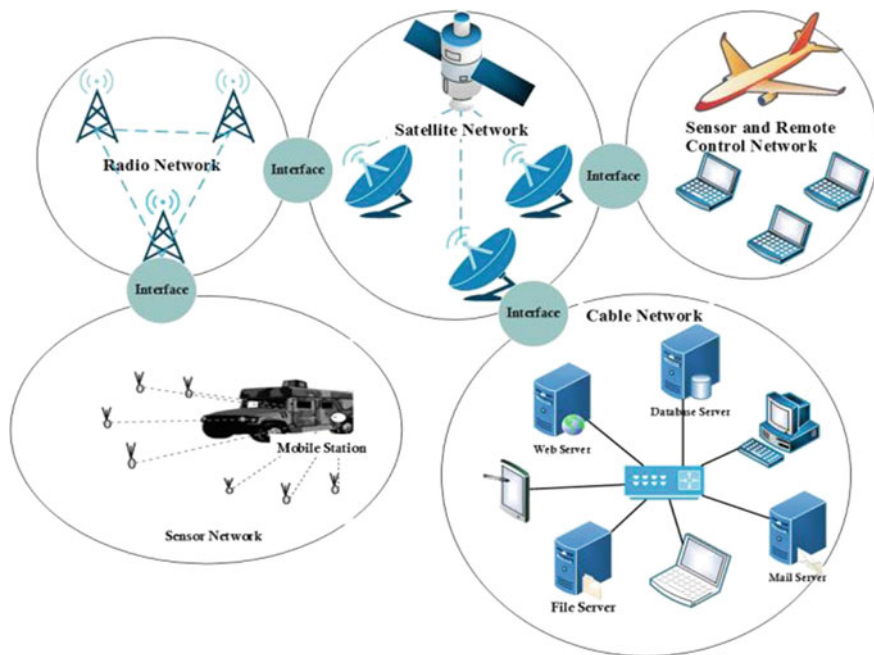


Fig. 1 Heterogeneous network environment in 5G

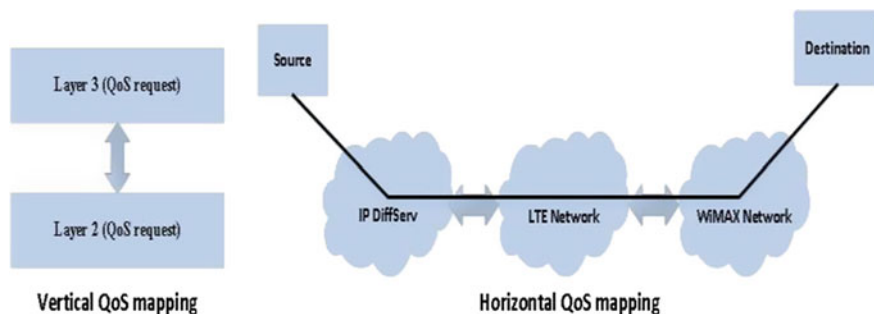


Fig. 2 Vertical and horizontal QoS mapping

QoS mapping over heterogeneous networks can be further classified into two categories: mapping according to QoS parameters or QoS classes.

(A) Mapping according to QoS parameters

The first category translates the QoS parameters such as delay and packet loss over heterogeneous networks. QoS Class Mapping framework based on Application Service Map (QCM-ASM) methods to achieve end-to-end QoS over heterogeneous networks. QCM-ASM determines the location information of each application on the two-dimensional graph based on packet loss and latency. QCM-ASM framework has fairness problem and it is difficult to implement since the mapping method is not clearly described in the paper. A QoS mapping scheme for multimedia services based on flow aggregation (QMS-FAG). In QMS-FAG, each QoS requirement is represented by a real number, and the overall QoS requirements are represented by a vector. Therefore, each service flow has a unique FAG identifier. This scheme is sitting at the edge of different QoS technologies and it considered users' QoE. Network between UMTS, DiffServ, and WiMAX2 [9] was simulated in this reference. Simulation results showed performance improvement in term of delay and packet loss, however, MOS value for three of four scenarios were set to 2.5, which provides poor QoE.

(B) Mapping according to QoS classes

QCM-IP method is performed in two stages: parameter-to class mapping which chooses the suitable QoS class that satisfies the QoS requirements of packets, and a class-to-class mapping table which is based on IP QoS class. QCM-IP has a limitation to provide QoS requirements for each application as it is based on direct mapping. The authors in [1] proposed a QoS support mechanism over hybrid optical and wireless network. A QoS mapping table between an Ethernet passive optical network (EPON), WiMAX and WLAN based on EPON classes was presented. This paper also showed proposed message exchange sequences for the hybrid system. The paper does not clearly describe the mapping method, the simulation, or analytical work for their proposed method. A dynamic mapping algorithm for a multiple participant session was proposed in [10]. RT traffic categorized into eight unified classes based on delay, bit rate, and packet loss. The first four classes belong to audio traffic while the other four classes belong to video. Simulation results showed that there was 72.88% satisfaction for the session participant QoS need. However, this algorithm did not consider the QoS parameters such as priority and QoE satisfaction level. Mapping table of integrated QoS classes is shown in Table 1. It consists of seven distinct QoS classes classified based on a set of performance parameters including end-to-end one way delay, jitter, and packet loss rate as recommended by Cisco in [11] and ITUT-T [12]. The first four classes from RT applications are sensitive to delay and can tolerate some degree of packet loss, while the last three classes, from NRT applications cannot tolerate any packet loss at all (e.g. zero loss information). Distinguishing NRT classes is based on latency.

Table 1 QoS metric and BW of integrated classes

Integrated QoS classes	Applications example	One way latency	One way jitter	Packet loss rate	Max. BW allowable percentage (%)
1	Interactive voice	≤ 150 ms	≤ 25 ms	≤ 3%	18
2	Interactive video	≤ 150 ms	≤ 30 ms	≤ 1%	25
3	Streaming video	≤ 4–5 s	N/A	≤ 1%	14
4	Control	≤ 100 ms	N/A	Zero	1
5	Interactive data	≤ 2–4 s	N/A	Zero	13
6	Bulk data	≤ 15–16 s	N/A	Zero	4
7	Best effort	Can be several min	N/A	Zero	25

3 Modeling Traffic on QoS Based Router for NGN

Following two basic approaches for QoS deployment in your NGN

Command line Interface (CLI) The CLI is the standard IOS interface that configures routers. CLI QoS features such as Priority Queuing (PQ) which is configured through the CLI.

Modular QoS CLI (MQC) Three step MQC process allows you to (1) place packets into different classes, (2) assign policy for those classes and (3) apply the policy to an interface. QoS mechanisms can not only provide for the allocation of a minimum amount of bandwidth for specific traffic but also limit the amount of bandwidth made available to that traffic.

Policing However, policing also can remark traffic that exceeds the specified rate and attempt to send the traffic anyway. Because policing drop behavior causes TCP retransmits, it is recommended for use on higher-speed interfaces. Also, note that policing can be applied inbound or outbound on an interface [13].

Shaping Shaping limits excess traffic, not by dropping it but by buffering it. This buffering of excess traffic can lead to delay. Because of this delay, shaping is recommended for slower-speed interfaces. Unlike policing, shaping cannot remark traffic. As a final contrast, shaping can be applied only in the outbound direction on an interface. It is impossible for an interface to send at a rate that is slower than the line rate.

4 Simulation Results and Analysis

In this simulation study, QoS metrics end-to-end delay, jitter and packet loss are collected and analyzed. End-to-end delay is the latency between the source and destination which directly affects user satisfaction. According to ITU-T, end-to-end one-way delay for both VoIP and video conference is recommended to be less than 150 ms. Jitter is the variations in the total end-to-end delay. Increased jitter causes asynchronous (i.e. out-of-order) packet arrivals. For an ideal system, jitter should be zero, which means there should be no delay variation in the time for the received packets. Packet delay variation for voice and video conference are recommended to be less than 25 and 30 ms respectively (Figs. 3, 4 and 5). Table 2 shows the confirmed and non confirmed packets and Table 3 shows outcome of WRED.

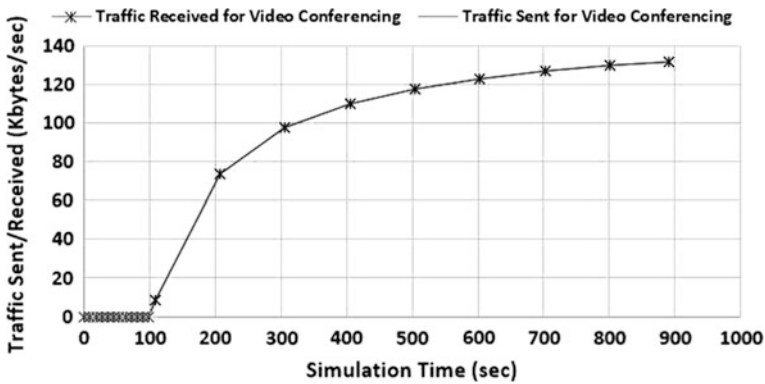


Fig. 3 Traffic sent and received for video conference

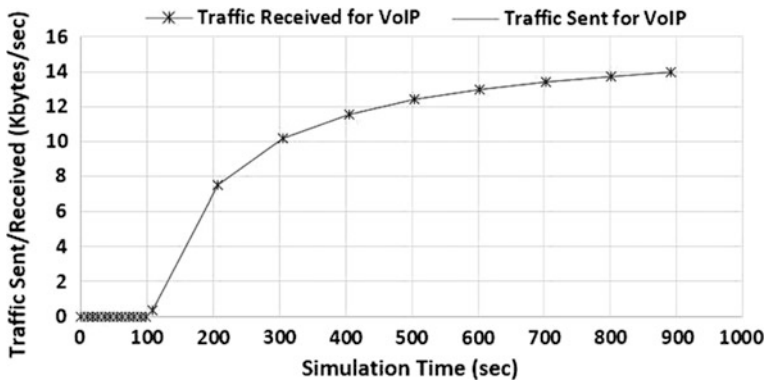


Fig. 4 Traffic sent and received for VoIP

Fig. 5 Outcome results of WRED

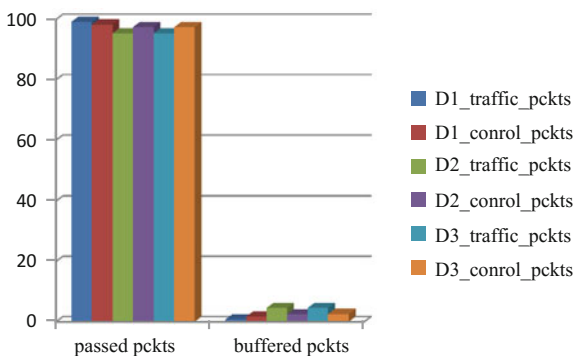


Table 2 Outcomes from proposed policer

Class	Confirmed bits	Non-confirmed bits
D1	1921	1961
D2	957	984
D3	957	984

Table 3 Outcomes of WRED

Classes	Passed packets	Randomly buffered packets	Tail buffered packets
D1_queue	1906	15	0
D2_queue	913	44	0
D3_queue	914	43	0
D1_control	58	01	1902
D2_control	118	03	863
D3_control	153	04	827

5 Conclusion

It seems that throughput of proposed NGN router model becomes 99.21–94.40% for D1 to D3 class with 256,000 Gb/s bit rate for 50% bandwidth and 12,800 Gb bit rate for 25% bandwidth. Proposed model outperforms in 60 ns as compare to existing routers.

References

1. Al-Shaikhli A, Esmailpour A, Nasser N (2016) Quality of service interworking over heterogeneous networks in 5G. In: IEEE ICC 2016—mobile and wireless networking symposium

2. Gomez-Sacristan A, Sempere-Paya VM, Rodriguez-Hernandez MA (2016) Virtual laboratory for QoS study in next-generation networks with metro ethernet access. *IEEE Trans Educ* 59 (3):187–193
3. Zhang X, Cheng W, Zhang H (2014) Heterogeneous statistical QoS provisioning over 5G mobile wireless networks. *IEEE Netw* 28:46–53
4. Panza G, Grilli S, Piri E, Vehkaperä J (2014) QoS provisioning by cross-layer feedback control. *IEEE J* 978-1-4799-8030-7/14
5. Pierucci L (2015) The quality of experience perspective toward 5G technology. *IEEE Wirel Commun* 22:10–16
6. Gupta L (2013) QoS in interconnection of next generation networks. In: 2013 5th international conference on computational intelligence and communication networks. *IEEE Comput Soci*, pp 91–96
7. Sun X (2012) Research on QoS of next generation network based on MPLS. In: *IEEE international conference on information science and technology*. Wuhan, Hubei, China, 23–25 March 2012, pp 294–296
8. Gardasevic G, Stjepanovic D, Damljanovic A, Cvijanovic D (2011) A SOA-based framework for cross-layer QoS adaptation in next generation networks. *IEEE J* 978-1-4673-2865-4/12
9. Vallejo A, Zaballo A, Selga JM, Dalmau J (2012) Next-generation QoS control architectures for distribution smart grid communication networks. *IEEE Commun Mag* 128–134
10. Chen C-L (2012) A proposal of next generation network: QoSMapping for MPLS-DiffServ and label forwarding. In: *IEEE, 5th international conference on biomedical engineering and informatics (BMEI 2012)*, pp 1416–1419
11. Ranaweera C, Lim C, Wong E, Nirmalathas A (2014) QoS performance of next generation optical-wireless converged network and PON cycle length. *IEEE J* 176–179
12. Kandhalu A, Rajkumar R (2012) QoS-based resource allocation for next-generation spacecraft networks. In: *IEEE 33rd real-time systems symposium*, 163–172
13. Tomkos I, Kazovsky L, Kitayama K-I (2012) Next-generation optical access networks: dynamic bandwidth allocation, resource use optimization, and QoS improvements. *IEEE Netw* 04–06

Wireless Sensor Networks for Societal Applications

Jayashri Joshi and Neeta Kulkarni

Keywords WSN · Data link layer · An end to end layer · Networking layer · Physical layer · Ad hoc network · Power aware protocols

1 Introduction

Multifunctional sensor nodes are less expensive, consumes low power and are small in size because of latest developments in wireless communications and MEMS technology. The sensor nodes (SN) are used to communicate for small distances. The components of SN are sensing, information processing and communication. Advantages of WSN over old sensors are as follows [1]:

- *Sensors* can be located at great distance from the real incident to detect an object. To do this, enormous sensors are required. The network of such huge sensors uses complicated techniques to determine the objects from surroundings [2].
- Many sensors may be mounted. Arrangements for sensors and communications links are done skilfully. All the sensors in the network send time of the detected incident to intermediate nodes. The data at the intermediate nodes are merged.

A WSN has many SN. These nodes are closely located near the incident. The installation of these sensors need not be arranged skilfully. In unreachable regions, the random instalment of sensor nodes can be allowed. Another advantage of WSN is the collective work of SN. SN consists of an integrated processor. Rather than transmitting fresh information to the nodes which make the mixture, SN uses their processing capability to locally pass easy calculations and send only the important and partly processed information [2]. WSN are used in several applications because

J. Joshi (✉)

Vishwakarma Institute of Information Technology, Pune, India
e-mail: jayashri.joshi@viit.ac.in

N. Kulkarni

SVERI College of Engineering, Pandharpur, India

of the features mentioned above. Understanding of these applications requires wireless ad hoc networking methods. There are several protocols and techniques are recommended for usual wireless ad hoc networks, but they do not match with the features and application needs of WSN. The comparison of sensor networks with ad hoc networks [3] is given as follows:

- The number of SN in WSN may be thousand times larger than ad hoc network nodes.
- SN can be heavily installed.
- SN are susceptible to failures.
- The sensor network topology varies regularly.
- SN mostly employ broadcast communication model wherein ad hoc networks employ point-to-point communication.
- SN have a restriction in cyber capabilities, power, and memory.
- SN do not contain a universal identification (ID) due to high overhead and several sensors.

As several SN are heavily installed, adjacent nodes are near to one another. Therefore, in a sensor network, multi-hop communication is expected to spend less energy than typical single hop communication. Moreover, the power transmission level should be made the minimum, which is greatly preferred in hidden operations. Few signal propagation effects practiced in long-distance wireless communication can be easily defeated in Multi-hop communication. The paper is structured as Sect. 2 explains few sensor network applications. Section 3 discusses the factors that help the sensor network design. Section 4 discusses the in-depth investigation of ongoing applications in this area and paper is concluded in Sect. 5.

2 Applications of Sensor Networks

WSN contains several various kinds of sensors like infrared, magnetic, seismic, thermal, acoustic and radar [2]. These sensors monitor a broad range of environment conditions which contains [2, 4]:

- Temperature and Humidity,
- Noise levels,
- Pressure,
- Vehicular movement,
- Soil makeup,
- Lightning condition,
- The availability or unavailability of specific types of things stress levels of mechanical objects.

2.1 Environmental Applications

It contains monitoring the activity of small animals, birds, and insects. The environmental conditions may influence irrigation, yields, chemical detection, precision agriculture, soil and atmospheric conditions, identification of forest fire, flood identification and bio-complexity plotting of the environment [5–20].

Forest fire Identification: As SN can be intentional, arbitrarily and heavily installed within a jungle, they should inform the end user about the location of fire before it goes out of control. Cores of SN may be installed using radio frequencies or optical systems. All the SN can also be fitted with useful power saving techniques [20], e.g., solar cells, as the sensors may be left idle for a long period (many months or even years). SN works together with one another in order to do distributed sensing and beat blockages like trees and rocks. The blockages obstruct the line of sight of wired sensors.

Biocomplexity plotting of the environment [21]: It needs an advanced technique for incorporating data beyond temporal and structural scales [22, 23]. The benefits of technology in isolated sensing and automatic information gathering have entitled higher structural, spectral, and temporal resolution at a linearly decreasing price per unit area [24, 25]. Also, SN can connect to the Internet. The Internet permits isolated users for limiting, watching and monitoring the biocomplexity of nature. Though satellite and airborne sensors give the best observation in huge bio-diversity, like the structural complexity of powerful plant species [2], these sensors are sufficient for monitoring small size bio-diversity [26]. Hence, ground level installation of wireless SN is required to monitor the biocomplexity [26, 27]. Three monitoring networks which contain 25–100 SN are used for constantly observing multimedia and weather sensor acquisition systems [9].

Flood Identification [19]: Example of flood identification is the ALERT system [28] installed in the United States. ALERT system contains different sensors like water level sensor, rainfall and environmental. Sensors provide information to the centralized database system in a planned manner [29].

Precision Agriculture: The advantages of this field are the capability to control the level of pesticides in drinking water, the level of soil erosion and air pollution in real time [2].

2.2 Military Applications

WSN is an important component of military command, computing, surveillance, communications, intelligence, and targeting (C4ISR) systems [2, 9]. Fast distribution, fault tolerance and self-organization features of WSN enables them a hopeful sensing method for military C4ISR. WSN are dependent on intense installation of excessive and less expensive SN. Therefore damage of few nodes by unfriendly behavior does not affect a military operation. This concept of WSN is

best for war fields. Few military applications are war field surveillance, observing friendly forces, inspection of opposing forces and land, equipment, and bullets, targeting, war damage evaluation, and nuclear, biological and chemical (NBC) attack identification and investigation [2].

Observing friendly forces, instruments, and ammunition: By using sensor networks, one can observe the conditions of armed forces, the condition and the availability of the instruments and bullets in a war field. Every vehicle, equipment, and important bullets are connected with sensors. These tiny sensors inform the status. The information is present in sink nodes and given to the head of the group.

War field surveillance: Important grounds, lands, and routes are closely monitored for the events of the opposing forces by using sensor networks. Sensor networks for new plans are installed immediately for battlefield surveillance as new plans are ready.

Investigation of opposing forces and land: WSN is installed in important lands. It provides some expensive, thorough and timely information about the opposing forces and land just before the opposing forces can stop them.

Targeting: WSN is combined with management systems of smart bullets.

War damage evaluation: Just before or after the war, WSN is installed in war region for collecting the data of war damage evaluation.

Detection and Inspection of Nuclear, biological and chemical attack: In chemical and biological war, it is necessary to be near ground zero for a prompt and correct finding of the operatives. WSN are used as chemicals in the responsive areas. The biological warning system may supply approachable forces with crucial reaction time. This crucial time is grieving casualties extremely. The sensor networks can also be used for complete inspection after an NBC attack is sensed. For example, a nuclear inspection is made without exposing a watch squad to nuclear radiation.

2.3 Home Applications

Home automation: Intelligent SN and actuators may be hidden in instruments like vacuum cleaners, microwave ovens, refrigerators, and VCRs [30]. These SN in the home appliances may communicate with one another and with an external network through the Internet. They permit users to achieve home appliances locally and isolated very easily.

Intelligent environment: The development of intelligent environment contain human-centred and technology-centred views [2]. In human-centred, an intelligent environment should change as per the user's requirements based on the input/output abilities. In technology-centred, new hardware technologies, networking solutions and middleware services are designed [2]. An explanation of how SN is utilized to build an intelligent environment is given in [31–33]. SN may be merged into furniture and devices. SN interacts with one another and also with space server. The space server also interacts with other space servers to know regarding the services

they provided like print, scan, and fax. These space servers and SN are put together with available embedded instruments to develop self-organizing, self-regulated system. The adaptive systems are dependent on models of control theory as explained in [32]. The computing and sensing in the smart environment should be dependable, determined and clear.

2.4 Health Applications

Few health applications of WSN are supplying communications; inbuilt patient monitoring, diagnostics, drug management, observing the activity and internal processes of insects or of small animals, telemonitoring of human physiological information and tracking and observing physicians and patients in the hospital [7, 14, 17, 34, 35].

Tele-monitoring of human physiological information: The physiological information gathered by the WSN is stored for very long time [36, 37]. It may be useful in medical research [37]. The implemented networks may also watch and sense behavior of old people, e.g., falling [21, 38]. These small SN provide enough freedom of movement and permit physicians to know pre-defined symptoms [39, 40]. A “Health Smart Home” is used in the Medical Department in France for checking the possibility of this system [35].

Tracking and observing physicians and patients in hospitals: Small and tiny SN is connected to every patient. Every SN performs its certain job. For, e.g., one SN is sensing the heart bit rate whereas another sensor is sensing the blood pressure (BP). Doctors too have an SN; that supports another doctor to trace them inside the hospital.

Drug administration in hospitals: When SN is connected to medicines, the possibility of receiving and suggesting incorrect medicines to patients is reduced. This is because, patients contains SN, which know their allergies and needed medicines [41].

2.5 Other Commercial Applications

Few commercial applications are as follows: controlling quality of product, watching material fatigue, managing inventory, constructing useful keyboards, building intelligent office premises, controlling environment in office premises, robot controlling and supervision in automatic manufacturing, local controlling of actuators, factory instrumentation, factory process control and automation, surveillance of disaster area, smart structures transportation, vehicle tracking and identification, instrument panel of semiconductor processing chambers, rotating machinery, wind tunnels, and temperature chambers [1, 4, 5, 7, 10, 14, 17, 42–46].

Controlling Environment in office premises: The air conditioning and maximum temperature of buildings are managed midway. Hence, the temperature in space changes by some degrees; one end of the room may be hotter than another end as only one control is available in the room and the flow of air from the main system is not equally shared. A distributed WSN may be used to manage the flow of air and temperature on all sides of the room. Such distributed technology may minimize power consumption by two quadrillions British Thermal Units (BTUs) in the United States, which saves around \$550 lakhs per annum and reduces 350 crores metric tons of carbon emissions [35].

Identifying and observing car thefts: SN are installed for finding fears within a particular area and inform about these fears to isolated users by using the Internet for examination [44].

Managing inventory control: Every element in a factory can contain SN. The users can detect the accurate position of the element and record the total number of elements in the similar group. When the users wish to put new inventories, the suitable SN should be connected to the inventories. The user can track and discover the inventories anytime.

Vehicle Tracking and Identification: There are a couple of ways as explained in [46] for tracing and finding the vehicle: In the first method, the line of bearing of the vehicle is decided inside the clusters and is then sent to the base station. In the second method, the basic information collected by the SN are passed on to the base station for finding the vehicle position.

3 Motivating Parameters of WSN Design

The motivating factors behind sensor network design are fault tolerance, scalability, sensor network topology, the production cost of SN, hardware constraints, transmission media, operating conditions and power consumption [2]. Many researchers have focused on these factors, but, none of these modules contains complete combined view of each and every factor which operate the development of WSN and SN. These factors are essential as they act as advice for developing a protocol for WSN. Moreover, these motivating factors are also useful for comparing various techniques.

3.1 Fault Tolerance

Few SN can fail to operate or be blocked. This may be because of less power, physical damage or environmental intrusion. The failure of SN should not affect WSN. It is known as fault tolerance issue. The talent to preserve WSN workings continuous without any interrupt because of SN failures is known as fault tolerance [47–49]. The fault tolerance or reliability of SN is denoted as ' $R_k(t)$ '. It is modelled

in [47] by using the Poisson distribution. The probability of successful operation of SN within the time interval $(0, t)$ is given as:

$$R_k(t) = e^{-\lambda_k t} \quad (1)$$

In (1), ' λ_k ' is failure rate of SN ' k ' and ' t ' is the time interval [2]. The arrangement of SN and techniques are intended to focus the amount of fault tolerance. The amount of fault tolerance is needed by the WSN. E.g., when SN are installed in a particular enclosed region or home to keep record of amount of temperature and humidity, the need of level of fault tolerance is less because such type of WSN is not freely destroyed or disturbed by atmospheric clamour. When SN are installed in battle stations for awareness and monitoring, then the need for level of fault tolerance becomes more high as the detected information is essential and sensors can be damaged because of unfriendly deeds. It means that the depth of fault tolerance is based on the type of application of WSN.

3.2 Flexibility

Several sensors are installed to study a phenomenon, based on the WSN application, the number of installation of sensors may access in millions. The advanced techniques must cooperate with such millions of nodes. These techniques also consider the large bulk type of WSNs. The thickness can change from some sensors to many sensors for a region, which may be small than 5 m in radius [10]. The thickness of such region can be measured as [7]

$$\mu(R) = \frac{N\pi R^2}{A} \quad (2)$$

In (2), N is the number of distributed sensors in region A . The R is the frequency transmission range among sensors. Mainly, $\mu(R)$ provides the count of sensors involved in the transmission radius of every node in area A . Moreover, the count of sensors in unit area show the density of node. The density of node based on the demand in which the sensors are used. In WSN application of machine diagnosis, the SN density is near about 300 SN in a $5 \times 5 \text{ m}^2$ area. In WSN application of vehicle tracking, the density of node is near about 10 SN per area [48]. Generally, the maximum density of node may be 20 SN/m³ [46]. For example, a house having approximately more than two dozens of home appliances carrying with sensor nodes [30], the sensor nodes will be increased when used into small fittings and other units. In habitat monitoring, the count of sensors will change from 25 to 100 per area [9]. The thickness of node will be maximum when a human carries thousands of SN. These SN are used in human wearing units such as clothing, eye glasses, shoes, watch, purse and jewellery [2]. These SN are also used while viewing a cricket, basketball and football match inside stadium.

3.3 Hardware Cost of SN

As sensor networks are made up of a huge SN, the value of each SN is necessary to defend the total value of WSN. If the value of WSN is costly than installing the conventional sensors, then WSN is very costly. To make WSN cost-effective, the price of every sensor node should be as minimum as possible. Though the Bluetooth technology is very famous for a low price, it is 10 times costlier than the designed cost for a node though the SN contains more hardware like sensing unit and processing unit. Additionally, SN is used with a mobilizer, Global Positioning System (GPS) or power generator based on the demands of WSN. As a result, the price of an SN becomes an interesting thing in current days.

3.4 Hardware Bounds

Figure 1 shows four basic units of the sensor node. The basic units are sensing unit, processing unit, a transceiver unit, and a power unit. SN also contain application based extra units like a position determining system, power generator, and mobilizer.

Sensing unit has sensors and ADCs. The ADC will change the analog signals generated by the sensors depending on the monitored data into digital signals. The digital signals are then applied to the processing unit. The processing unit carries a small storage unit and processor. The storage unit accomplishes the methods that make the SN work together with the neighboring nodes to pass out the allocated sensing jobs. The transceiver unit links the node to the network. A power unit is an essential unit of SN. It is composed of energy saving cell like solar cells. The routing protocols and sensors need the report of position with maximum efficiency. Hence position finding system is essential for sensor node. A mobilizer is required to shift sensor nodes when the allocated task becomes necessary to pass on. All sub-components may be installed in a small module [1]. The installation area is

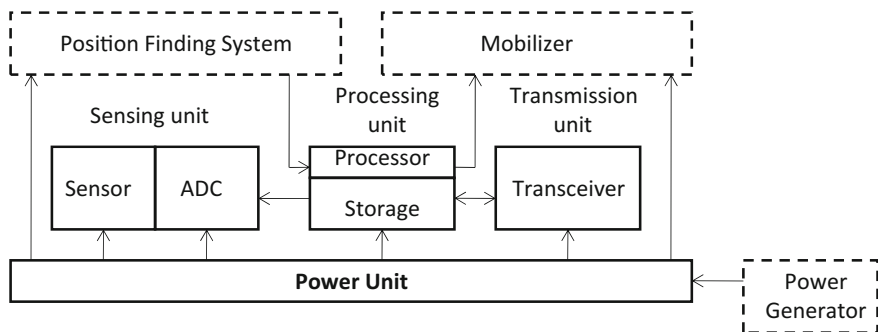


Fig. 1 Hardware parts of SN

smaller than a cubic cm [45]. The tough bounds for sensor nodes are as follows [14]. The sensor node must:

- use very less power,
- work in large volumetric bulks,
- exhibit less hardware cost and be expendable,
- be independent and work untended,
- be flexible to nature.

As the SN are not accessible frequently, the life of WSN is based on the continuance of the energy savings of the nodes. Power is a limited asset because of restriction of the mass of sensor node. The smart dust mote stores energy of 1 J [44]. In Wireless Integrated Network Sensors (WINS), the maximum supply currents should be less than 30 μA for enhancing life span [50]. In WINS, SN is charged from lithium (Li) batteries. The diameter and thickness of these cells are 2.5 and 1 cm respectively [50]. The life span of WSN can be enhanced by obtaining energy from nature [35]. Solar cells are used for energy saving [35]. The component of transmitter and receiver of SN can be passive or active as dust motes [44]. They may also be a radio frequency (RF) device. The communications between transmitter and receiver need modulation, filter, demodulation and multiplexing. Hence RF communication becomes more tough, complex and costly. The path loss of the sending signal between two nodes can be as maximum as the fourth order exponent of the distance between two nodes as the antennas are near to the earth [44]. Wireless communication is chosen in many current WSN projects because the data packets carried in WSN are less in size [35]. The frequency re-use in WSN is maximum because of minimum communication distances. These features make easy to use low duty cycle transmitter and receiver for WSN. The design of energy saving technique and low duty cycle transmitter and receiver is still tough, and present industrial wireless technologies like those used in Bluetooth is not sufficient for WSN as turning ON, and OFF of transmitter and receiver of SN needs more power [46].

Several sensing jobs need the report of the position of nodes. As sensors are randomly installed and left alone, such sensors need to be united by using position finding system. Position finding systems are essential for routing protocols. It is frequently considered that every sensor node has GPS unit. GPS has minimum 5 m accuracy [51, 52]. In [53] it is induced that fitting every SN with a GPS is not feasible for WSN. Another method in which fewer nodes utilize GPS and help other nodes to locate their areas drastically is urged in [53].

3.5 WSN Technology

Complete numbers of unreachable and unwatched SN are sensitive to usual failures. Because of this, a continuation of WSN become a difficult task. Several nodes are installed everywhere in the sensor region. SN are installed in tens of feet from one another [1]. The maximum node densities is 20 nodes/m³ [46]. Installing large SN

closely needs careful control of continuation of WSN topology. It checks problems corresponding to topology maintenance and modification in three phases:

1. *Pre-deployment and deployment phase*

SN are thrown in a region or kept one at a time in sensor area. SN are used by

- sloping from a plane,
- transmitting in a weapon shell, rocket or missile,
- dropping a throw from a shipboard, etc.,
- mounting in a factory, and
- mounting one sensor at a time by a human or a robot.

Though all the sensors and their abandoned instalment frequently prevent them from skillful instalment of plan, the ways for basic implementation must

- minimize the value of installation,
- remove the need for any reorganization and preplan,
- rise the flexibility of arrangement and
- advanced fault tolerance and self-organization.

2. *Post-deployment phase*: After instalment, topology changes because of modification in SN [13, 54]

- location,
- Sociability because of obstructing, noise and moving objects,
- Existing energy,
- damaging,
- task information.

SN are installed at a fixed position. The failure of the device is a usual or constant event because of energy reduction or havoc. It is also easy to include WSN with huge migrant nodes. Also, SN and WSN go through varying task dynamics and there may purposeful block. Thus, WSN topologies are sensitive to usual modifications after implementation.

3. *Re-deployment of additional node phase*: More SN is re-installed anytime to change the damaging nodes because of changes in task oscillations. The network should be re-structured if new nodes are added. Lamination with usual topology modifies an ad hoc network which contains variables of nodes, and strict power consumption bounds need certain routing protocols.

3.6 Nature

SN is closely installed near or within the phenomenon to be seen. Thus, SN frequently is unobserved in isolated locations. They may be operating in:

- Busy communications,
- Inside huge machines,
- At the base of a sea,
- Within a tornado,
- On the base of a sea at the time of tornado,
- A biologically or chemically dirty area,
- A war field past the enemy lines,
- In a building or warehouse,
- In a river flowing with current.

The above example informs us under which conditions SN are proposed to operate. Sensors operate under high pressure at the base of a sea, in severe nature like wreckage or a war field, in maximum heat and cold like the nozzle of an aircraft engine, and in tremendously noisy conditions like intentional jamming [2].

3.7 Transmission Channel for WSN

In a multi-hop WSN, interacting nodes are connected by a wireless channel. These channels are produced by radio, infrared or optical media. For allowing universal working of these networks, the selected transmission medium should be present all over the world. One way for radio channels is the use of industrial, medical (ISM) and scientific bands that provide license-free interaction at many locations.

Table 1 shows the table for Frequency Assignment made feasible for ISM applications. Few of the above frequency bands are already utilized for interacting with a cordless phone and wireless LANs. In WSNs, low expensive, small-sized, very low power transceiver is essential. As mentioned in [55] specific hardware limitations and agreement between the antenna efficiency and energy eating restrict the selection of a carrier frequency for transmitters and receivers to very

Table 1 Frequency assignment feasible for ISM applications

Frequency band (MHz)	Center frequency (MHz)
6.765–6.795	6.780
13.553–13.567	13.560
26.957–27.283	27.120
40.66–40.70	40.68
433.05–434.79	433.92
902–928	915
2400–2500	2450
5725–5875	5800
24,000–24,250	24,125
61,000–615,000	61,250
122,000–123,000	122,500
244,000–246,000	245,000

high-frequency range. The use of the 0.433 GHz band in European countries and 14,000 kHz band in North America is suggested. The transceiver development problems in ISM bands are focused in [56, 57]. The important benefits of using ISM bands are free radio, large bandwidth assignment, and availability around the globe. Much of the present hardware for SN relies on the design of RF circuit. Micro AMPS wireless SN explained in [48] utilizes Bluetooth suitable with 2.4 GHz transceiver containing an inbuilt frequency synthesizer. The sensor device explained in [58] utilizes one channel RF transceiver working at 916 MHz. The WINS architecture [46] utilizes radio channels for interaction among nodes. Infrared is another simple mode of inter-node interaction in WSN. Transceivers based on Infrared are not expensive and simple to construct. Most of the present day laptops, PDAs, and cell phones provide an infrared data connection interface. The basic disadvantage is that it needs line of sight between transmitter and receiver. Because of this disadvantage infrared may not be used for a transmission channel in WSN set up. An exciting improvement is that of the intelligent dust mote [14]. This is an independent sensing, computing and communication mode which utilizes optical medium for transmission. Two transmission methods are explained in [17]. The first method is the passive transmission by using a corner-cube retroreflector (CCR) and second is the active communication by using a laser diode and steerable mirrors. A structure of three mirrors (CCR) is useful for interacting with a digital high or low device.

3.8 Power Intake for WSN

The wireless SN is a very small electronic device. It may only be fitted with a restricted power supply. It should be less than 0.5 Ah, and 1.2 V. In few applications, replacement of power supplies may be inaccessible. Hence lifetime of SN indicates a strong reliance on battery life. In a multihop ad hoc WSN, every node acts as information originator and information router [2]. The improper functioning of some nodes may create notable topological modifications and may need re-routing of data packets and re-organization of the network. Thus, power management and power preservation are of utmost importance. Because of all the above reasons, researchers are presently paying attention on the development of power saving techniques and sensor network protocols. In mobile and ad hoc networks, power preservation is an essential development, but it is not a basic aspect as a user can modify the power resources. The importance is more on Quality of Service instead of power efficiency. In WSN, power efficiency is an essential parameter which motivates the network lifetime. Protocols based on the particular application may be developed by properly dealing with other parameters like delay and throughput with power efficiency. The major job of SN in a WSN is to sense events, execute fast information processing and deliver the information.

4 Architecture of SN

Figure 2 shows the distribution of SN in sensor region. Every distributed SN carry the abilities to gather information and pass information to the sink node and the users. As seen in Fig. 2, information are delivered back to the user using a multi-hop infrastructure less architecture via sink node. Sink node interacts with the task manager node by using Internet/Satellite.

The protocol stack used by SN and the sink node is as shown in Fig. 3. This protocol stack unites power and routing alertness, gathers information with networking protocols, interacts power effectively via wireless medium and sponsors collective work for SN. The protocol stack is composed of:

- Application layer
- Transport layer
- Network layer
- Data link layer
- Physical layer
- Power management plane
- Mobility management plane
- Task management plane.

Application layer: Based on the sensing events, various kinds of application software are designed and utilized in the application layer.

Transport layer: It supports the flow of information if WSN needs it.

Network layer: It supports the routing of data provided by the transport layer. As nature is noisy and SN are movable, the MAC protocol should be power saver and should reduce crash with the broadcast of the adjacent node.

Physical layer: It requires easy and sensitive modulation, sending and receiving schemes.

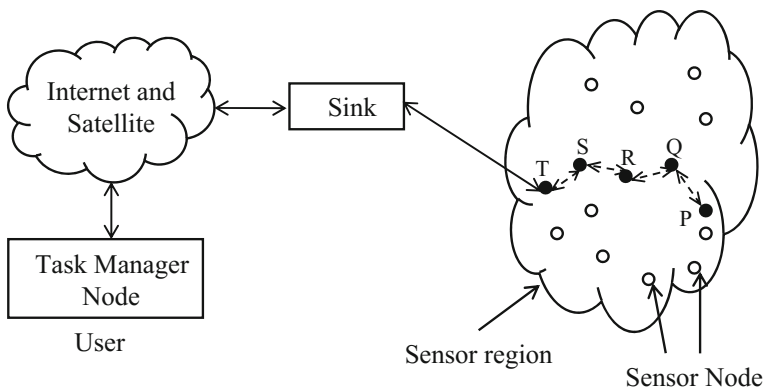
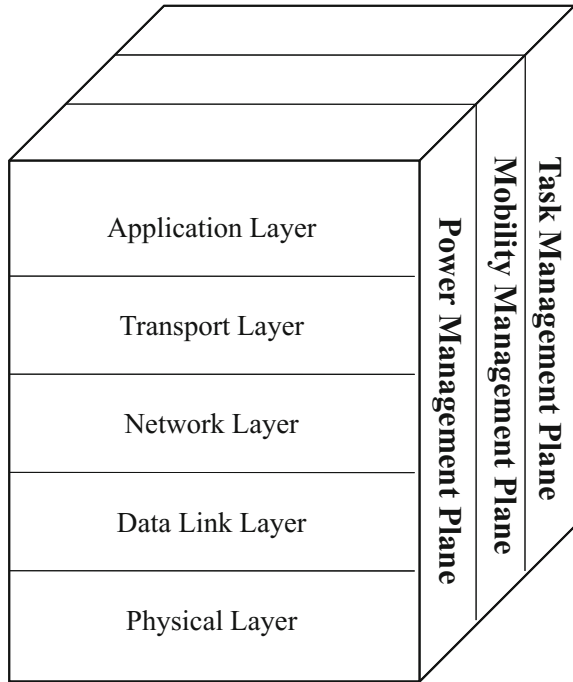


Fig. 2 Distribution of SN in sensor region

Fig. 3 Protocol stack of WSN



Additionally, the Power Management Plane controls the power within SN; the Mobility Management Plane controls the motion within the SN, and Task Management Planes control the task distribution within the SN. These planes support SN to start the sensing job and minimize the total power dissipation. The power management plane handles usage of power by SN. For, e.g., the SN can switch off its receiver after the message is obtained from the adjacent node. This is done to neglect obtaining multiplied messages. If the power level of SN is below the threshold, then SN announces to its neighbors about its low power and is unable to participate in routing data.

Rest of the power can be booked to sense an event. The mobility management plane finds and records the effort of SN, so a route back to the user is continuously kept and the SN can maintain the record of its adjacent SN. By keeping a record of their neighboring SN, the SN can manage the usage of task and power. The task management plane supports and plans the sensing events offered to a certified area. It is not important that every SN in that area should do the sensing job at a time. Therefore, few SN does the job more than other SN based on their power. The management plans are essentials to cooperate SN in a power saving, travel information in a migrant WSN and divide power resources between SN. From Fig. 3 it is seen that the presented work in [14, 44, 46] has been mapped to the protocol stack. In WINS [44], a scattered network and Internet access are supplied to SN, control and processor units. WINS networks are benefited of this small space between SN

to offer multi-hop communication and reduce energy utilization because the SN used are in huge number. In WINS information is ordered back to the user and uses the same method as seen in Fig. 2. In WINS, the SN finds the ecological information and this information is ordered step by step via WINS nodes till it arrives at WINS gateway. Hence, the WINS nodes are SN like P, Q, R, S, and T. The WINS gateway uses Internet services to interact with the user. According to [44], a low-power protocol group which talks about the limitations of WSN should be improved. Motes [14] can be connected to devices or can stay in the air due to their tiny size and weight. Such SN needs MEMS technique for optical fiber transmission and sensing. The SN have solar cells to gather energy during the sunny hours. SN need line of sight (LoS) for interacting visually with Base Station (BS), transmitter, receiver or other sensors. By comparing the intelligent dust architecture with the architecture of SN shown in Fig. 2, the intelligent dust mote interacts directly with the BS transceiver as a sink. Though peer to peer interaction is easy, collision issues may be present in medium access layer because of “concealed nodes”. The application layer, MAC layer, and physical layer include bright dust motes in the protocol layers stack shown in Fig. 3. Another way to development techniques and protocols for WSN is run by the needs of the physical layer [46]. The techniques and protocols must be well advanced depending on the selection of physical layer units like the type of processors and receivers. This bottommost way of the micro AMPS WSN also talks about the significance of the different types of layers shown in Fig. 3 to be strongly combined with the SN. Micro AMPS WSN also interacts with the user as seen in Fig. 2. Various techniques like TDMA, FDMA, etc. are being discussed in [46]. This bottommost way informs that the sensor network protocols must have knowledge of hardware and can utilize certain features of microprocessors, transmitter, and receivers for reducing power utilization of the SN. This may take towards a routine solution for various kinds of SN development. Various kinds of SN installed also guide to various kinds of WSN. This can also guide to various kinds of cooperative protocols and techniques.

5 Conclusion

The adaptability, fault acceptance, large sensing reliability, less cost and fast improving features of sensor networks from several advanced and thrilling application areas for isolated sensing. In coming days, this application region will build WSN as an essential part of human lives. Nevertheless, understanding of WSN requires meeting the limitations put by factors like fault tolerance, scalability, cost, hardware, modification in network topology, nature and power utilization. As above limitations are largely tough and certain for WSN, ad hoc networking protocols are essential. Most of the current research is involved in improving the protocols required for various layers of WSN protocol stack.

References

1. Intanagonwiwt C, Govindan R (2000) Directed diffusion: a scalable and robust communication paradigm for sensor networks. In: Proceedings of the annual international conference on mobile computing and networking '00, vol 11(1), Boston, pp 56–67
2. Ian FA, Su W, Cayirci E (2001) A survey on sensor networks. *IEEE Commun Mag* 38: 393–422
3. Perkins C (2000) Ad hoc networks. Addison-Wesley, Boston
4. Estrin D, Govindan R, Heidemann J, Kumar S (1999) Next century challenges: scalable coordination in sensor networks. In: Annual international conference on mobile computing and networking '99, United States, pp 263–270
5. Agre J, Clare L (2001) An integrated architecture for cooperative sensing networks. In: *IEEE Computer Magazine*, pp 106–108
6. Bhardwaj M, Garnett T, Chandrakasan A (2001) Upper bounds on the lifetime of sensor networks. In: International conference on communication '01, pp 1–37
7. Bulusu N (2001) Scalable coordination for WSN: self-configuring localization systems. ISCTA, United Kingdom
8. Cerpa A (2004) Adaptive self-configuring sensor network topologies. *IEEE Trans Mobile Comput* 2:272–285
9. Cerpa A (2000) Habitat monitoring: application driver for wireless communication technology. In: Annual conference on special interest group on data communication '00, vol 31, pp 20–41
10. Cho SH, Chandrakasan A (2000) Energy-efficient protocols for low duty cycle wireless microsensor. In: Annual Hawaii international conference on system sciences, vol 2, pp 272–286
11. Halweil B (2001) Study finds modern farming is costly. *World Watch* 13(1):9–10
12. Heinzelman WR (1999) Adaptive protocol information dissemination in wireless sensor networks. In: Proceeding of annual international conference on mobile computing and networking '99, UK, pp 174–185
13. Jaikaeo C (2001) Diagnosis of sensor networks. *ICC'01* 5:1627–1632
14. Kahn JM (1999) Next century challenges: mobile networking for smart dust. In: Annual international conference on mobile computing and networking '99, United States, pp 271–278
15. Fire spreads to 40000 acres. vol 150, New York, pp 1–7, 2001
16. Slijepcevic S, Potkonjak M (2001) Power efficient organization of wireless sensor networks. *IEEE ICC* 2001, vol 2, pp 472–476
17. Warneke B (2001) Smart dust: communicating with a cubic-millimeter. *IEEE Transl* 34 (1):44–51
18. <http://www.fao.org>
19. Bonnet P (2000) Querying the physical world. *IEEE Transl* 7:10–15
20. Chandrakasan A (1999) Design considerations for distributed microsensor system. In: *IEEE international conference on custom integrated circuits*, IEEE '99, California, pp 279–286
21. Celler B (1994) An instrumentation systems for the remote monitoring changes in functional health status of elderly at home. In: International conference on IEEE-engineering in medicine and biology society, vol 2. New York, pp 908, 909
22. Estrin D, Girod L, Pottie G, Srivastava M (2001) Instrumenting the world with wireless sensor networks. International conference on acoustic, speech and signal processing 2001, Utah, pp 608–615
23. Girod L, Estrin D (2001) Robust range image estimation using acoustic and multimodal sensing. In: Proceedings of the IEEE/RSJ, international conference on robots and systems '01, Hawaii, pp 980–986
24. Colwell R, Testimony of Dr. Rita Colwell. Director, National Research Foundation
25. <http://www.consecolo.org/vol1/iss1/art4>
26. <http://www.jamesreserve.edu/news>

27. Gell-Mann M (1995) What is complexity?
28. <http://www.alertsystems.org>
29. Imielinski T, Goel S (2000) DataSpace: querying and monitoring deeply networked collections in physical space. *IEEE Transl Personal Commun* 7(5):4–7
30. Petriu EM, Georganas ND, Petriu DC, Makrakis D (2000) Sensor based information based appliances. *IEEE Mag Instrum Meas* 3(4):31–35
31. Abowd GD, Sterbenz JPG (2000) Final report on the inter-agency workshop on research issues for smart environments. *IEEE Trans Pers Commun* 7(5):36–40
32. Herring C, Kaplan S (2000) Component-based software systems for smart environments. *IEEE Trans Pers Commun* 7(5):60–61
33. Essa I (2000) Ubiquitous sensing for the smart and aware environment. *IEEE Trans Pers Commun* 7(5):47–49
34. Noury N, Herve T, Rialle V, Virone G (2000) Monitoring behavior in home using a smart fall sensor. *IEEE conference on microtechnologies in medicine and biology*, pp 607–610
35. Rabaey JM, Ammer MJ, da Silva JL, Patel D, Roundy S (2000) PicoRadio supports ad hoc ultra-low power wireless networking. *IEEE Comput Mag* 33(7):42–48
36. Johnson P, Andrews DC (1996) Remote continuous physiological monitoring in the home. *J Telemed Telecare* 2:107–113
37. Ogawa M, Tamura T, Yoda M, Togawa T (1997) Fully automated biosignal acquisition system for home health monitoring. In: *International conference on IEEE-EMBS*, vol 6, Hong Kong, pp 2403–2405
38. Trappenburg JCA et al (1995) Home telecare for the elderly patients by use of passive infrared sensor in ‘small room’. *J Telemedicine Telecare* 14(14):183–184
39. Nam YH (1998) Development of remote diagnosis system integrating digital telemetry for medicine. In: *Proceeding of IEEE-engineering in medicine and biology society*, Hong Kong, vol 3, pp 1170–1173
40. Bauer P (2000) The mobile patient: wireless distributed sensor networks for patient monitoring and care. *Proceedings of IEEE EMBS 2000, international conference on information technology applications in biomedicine*, pp 17–21
41. Sibbald B (2001) Use computerized systems to cut adverse drug events: report. *Can Med Assoc J* 164(13):1878
42. Estrin D (2000) Embedding the Internet communication. In: *Proceedings of ACM43*, pp 38–41
43. Priyantha N (2000) The cricket location-support system. In: *Proceedings of ACM MobiCom '00*, pp 32–43
44. Pottie GJ, Kaiser WJ (2000) Wireless integrated network sensors. In: *Proceedings of ACM43*, pp 551–558
45. Rabaey J (2000) Pico-Radio: ad-hoc wireless networking sensor/monitor nodes. In: *Proceedings of VLSI WVLSI '00, Florida*, pp 9–12
46. Shih E (2001) Physical layer driven protocol and algorithm design for energy efficient wireless sensor networks. In: *Proceedings of ACM MobiCom '01, Italy*, pp 272–286
47. Hoblos G, Staroswiecki M, Aitouche A (2000) Optical design of fault tolerant sensor networks. In: *Proceeding of ICCA '00, Anchorage, AK*, pp 467–472
48. Nadig D, Iyengar SS, Jayasimha DN (1993) A new architecture for distributed sensor integration. In: *Proceedings of IEEE Southeastcon '93, NC*, pp 8
49. Shen C, Srisathapornphat C, Jaikao C (2001) Sensor information networking architecture and applications. *IEEE Trans Pers Commun* 8(4):52–59
50. Vardhan S (2000) Wireless integrated network sensors (WINS): distributed in situ sensing for mission and flight systems. In: *Proceedings of IEEE aerospace conference '00, vol 7*, pp 459–463
51. Perrig A (2001) SPINS: Security protocols for sensor networks. In: *Proceedings of ACM MobiCom '01, Italy, vol 7*, pp 189–199
52. Li L, Halpern JY (2001) Minimum energy mobile wireless Minimum energy mobile wireless. In: *IEEE international conference on communication '01, vol 1, Finland*, pp 278–283

53. Savvides A (2001) Dynamic fine-grained localization in ad-hoc networks of sensors. In: Proceedings of ACM MobiCom '01, Italy, pp 166–179
54. Meguerdichian S (2001) Exposure in wireless ad-hoc sensor networks. In: Proceedings of ACM MobiCom '01, Italy, pp 139–150
55. Porrect A, Melly T, Enz CC, Vittoz EA (2000) A low-power low-voltage transceiver architecture suitable for wireless distributed sensors network. In: Proceedings of IEEE ISCAS '00, vol 1, Geneva, pp 56–59
56. Favre P (1998) A2V, 600 μ A, 1-GHz BiCMOS super regenerative receiver for ISM applications. IEEE J Solid State Circuits 33(12):2186–2196
57. Porrect AS, Melly T, Enz CC, Vittoz EA (1999) A 1.2 V, 430 MHz, 4 dBm, power amplifier and 250 μ W Frontend, using standard digital CMOS process. In: IEEE international symposium on low power electronics and design, pp 233–237
58. Woo A, Culler DE (2001) A transmission control scheme for media access in sensor networks. In: Proceedings of ACM MobiCom '01, Italy, pp 221–235

Topology-Hiding Multipath Routing Protocol: A Modified Approach for Wireless Network

Akshay Suhas Phalke and Manohar S. Chaudhari

Keywords MANET · Topology hiding · THMR · M-THMR

1 Introduction

Mobile ad hoc networks are a unique wireless environment with far reaching application possibilities. It is dynamic, ad hoc, infrastructure less and self configurable having autonomous nodes. These very characteristics offer huge security challenges [1, 2]. It is vulnerable to topology exposure as the message hops from network to network in an untrusted environment. Ad hoc routing protocols such as AODV, DSR and wireless MAC protocols cater to security issues [3–6] but exposing the topology thereby making it more vulnerable. Literature from [7–11] discuss security protocols such as BAODV, IAODV, NDMR, AODVM, AODV-BR respectively. Scarce MANET resources make it more difficult to be secure proof from malicious attacks.

In this paper, we present Modified Topology-Hiding Multipath Routing protocol (M-THMR) to address the security challenges in MANET specifically focusing on topology exposure. M-THMR employs the following mechanisms: Hide topology-M-THMR does not carry the link information to in route messages, using this mechanism it is able to hide the topology. Find node-disjoint routes—After construction of any route to the destination it advertises the set of node in that path, so that next path will not contain the previously chosen nodes. Exclude unreliable routes-M-THMR able to detect the malicious as well as faulty node over the routing path to avoid unreliable paths. To evaluate the proposal we compared with THMR with respect to delay, packet delivery ratio and packet loss ratio.

A.S. Phalke (✉) · M.S. Chaudhari
Sinhgad Institute of Technology, Lonavala, India
e-mail: akshayphalke3@gmail.com

M.S. Chaudhari
e-mail: Mschaudhari20@gmail.com

The paper is divided into Sect. 1 as introduction, Sect. 2 gives literature review of related routing protocols. In Sect. 3, we describe the Modified Topology-Hiding Multipath Routing protocol (M-THMR); Sect. 4 describes the experiment and results evaluation and Conclusions in Sect. 5.

2 Related Works

AODV [12] a reactive routing protocol constructs route on demand. Sequence numbers ensure prevention from routing loop. RREQ, RREP and RRER are the messages in the protocol. It uses table driven routing mechanism for routing data packets to destination nodes.

Secure-AODV (SAODV) [13] secures from malicious intermediate node for spoofing its identity illegally. It modifies the hop count on route request messages by fabricating route error messages. SAODV extends AODV. It uses RREQ, RREP and RERR routing messages. Digital sign is used to secure the integrity and authenticity.

In Geographic routing protocols [14, 15]: each node learns its location through some localization techniques or location services. The malicious nodes can utilize the location information to deduce network topology. Hence the geographic routing protocols also expose network topology.

Marina and Das [12] proposed AOMDV, an on-demand multipath distance vector protocol which computes multiple loop-free link disjoint paths during route discovery.

In Wang et al. [16] discussed the concept of trust for the selection of trustworthy candidate for routing packet to the destination. An idea of trust is used for detection of faulty nodes in the network. The paper discussed the security of the packet being forwarded to the destination using trustworthiness concept.

Chai et al. [17]: discuss the various load metrics and summarizes the principles behind several existing load balanced ad hoc routing protocols. Also qualitative comparison of the various load metrics and load balanced routing protocols is presented. Abusaleh et al. [18] made an indepth survey of all secure protocols. References [3, 4, 13, 14, 19–31] explored secure protocol proposals such as AODV, DSR, HADOF.

Zhang et al. [32] focused on topology-exposure and proposed a Topology-Hiding Multipath Routing protocol (THMR): THMR disallows packets to carry routing information thereby malicious nodes cannot identify topology information protecting from attacks based on that. THMR establishes multiple node-disjoint routes in a route discovery attempt and exclude unreliable routes before transmitting packets. They proved that THMR is loop-free and topology-hiding. THMR has three phases: Route Request Phase, Route Reply Phase and Route Probe Phase. In these phases, no routing information is carried in route messages. In Route Request Phase, the source node broadcasts a route request message. Every intermediate node creates a reverse route to the source node for

every received copy, but only rebroadcasts the first copy. After Route Request Phase, every node can establish multiple reverse routes back to the source node. This is to facilitate the discovery of multiple node-disjoint routes for the source in Route Reply Phase. In Route Reply Phase, a node excluding mechanism is designed to find as many node-disjoint routes as possible. Route Probe Phase is to detect the malicious nodes and ensure the availability of the candidate routes before transmitting packets. THMR system considered the topology exposure problem and discussed its mitigation technique, but does not give solution over fault nodes detection. This protocol does not give details of mitigation for fault node avoidance. THMR hides topology, find node disjoint routes, defends against attacks and avoids unreliable routes. The data structures used are routing table (RT) and sequence number table (SNT). The notations used are: S, D, seq, hopCt, RREQ, RREP, exNodeSet, ID, T_D, mHop for source, destination, sequence number, route distance, route request, route reply, set of nodes not containing intermediate route, destination ID, timer initiated at destination, temporary hop count of the best route. Our proposal improvises on this and simulation validates our hypothesis.

3 Modified Topology-Hiding Multipath Routing Protocol (M-THMR)

In MANET nodes exchange information to neighbours and form network for data packet routing to their desired destination. This can be targeted by any malicious adversary who intentionally wants to disrupt the functionality of the network. Attackers can inject malicious information to repeat previous routing messages, or modify the valid routing information and eventually bring the network down. Sometime due to internal attacks, it causes severe damages as these nodes are not up to their initial commitments. Such nodes also can send erroneous information to modify the local view of the network. Usually, it is very difficult to identify the internal attacker, since they already have some sort of credentials that everybody believes. Trust value of a node is calculated by using following equation,

$$T_j(k, n) = R_{kj}(n) / F_{kj}(n)$$

$T_j(k, n)$ = Trust value of node j assigned/calculated by node k during n th topology cycle. Where $R_{kj}(n)$ and $F_{kj}(n)$ are the number of packet that have been received by k and forwarded from j at time t respectively, and $0 \leq T(k, t) \leq 1$.

Trust value of a node is updated after every topology change using following mathematical equation.

$$T_j(k, n) = \alpha \cdot T_j(k, n - 1) + (1 - \alpha) \cdot T_j(k, n)$$

where, $T_j(k, n)$ is node j 's trust value measured during n th topology updating cycle. $0 < \alpha < 1$ is a weighting factor used to trade off between current measurement and

previous estimation. Fault detection is an important task in wireless networks. We propose a method to detect the faulty nodes and faulty nodes over a path. When node joins the network it is assigned with a security parameter value called a trust. The trust value is updated after every topology change. If node has a trust value lower than the threshold trust value then that node is treated as faulty or malicious node and corresponding link as faulty link.

M-THMR overcomes this attack exposure by hiding route information through the intermediate routes. In M-THMR: When an intermediate node n_i receives a RREP copy, it takes several actions. The first action is to prune its routing table based on the received information. n_i removes all the routes whose destination is the source node in the RREP and whose Next Hop is in $exNodeSet$ of the RREP. The action is to remove all the routes which use some nodes on an already established route and ensure all the established routes are node-disjoint. Only in two cases, node n_i takes additional actions. The first case is $nextNode$ is n_i itself, which means the RREP sender has selected n_i as the next hop to the source node or the previous node to the destination on the route. The second case is $nextNode$ is NULL, which means this RREQ comes from destination D and n_i is a direct neighbor of D . Only in these two cases, n_i is on an established route to the destination through the RREP sender or to the destination directly from the source. In the above two cases, n_i needs to further do some processing task as follows. Firstly, n_i creates a route to destination D through the RREP sender. Secondly, n_i finds the closest neighbor n_j to source S by checking its routing table, which will be placed on route as the previous node and be filled in $nextNode$ field in the RREP to be rebroadcasted. Then, n_i removes all the other routes except the one that is closest to source S . In addition, n_i updates and rebroadcasts the RREP message. n_i sets $nextNode$ to be the closest neighbor n_j , inserts it into $exNodeSet$, increases $hopCt$ by 1, and then rebroadcasts the RREP message.

From the description above, we can see that

- $ExNodeSet$ greatly reduces the probability that a node is placed on more than one route.
- Every node independently makes routing decisions by checking the reverse routes.
- Only the nodes that are placed on established routes needs to rebroadcast the RREP message.
- Only two routes in routing table remains finally, which means that the established routes are bidirectional.

At the source node, the RREP message keeps getting rebroadcasted until it arrives at source S . Once source S receives the first copy, it initiates a timer TS to collect the following copies. Source S only accepts the copies that arrive before TS times out, and processes them as the intermediate nodes but does not rebroadcast them. When TS times out, source S stops accepting RREP message and multiple node-disjoint routes to destination D are established. The detailed routing protocol is shown in Algorithm.

Hence, M-THMR protocol is capable of determining secure route by comparing the security parameters while performing route hiding.

Algorithm 1: *Trust Value Calculation for Secure Route Discovery Mechanism*

```

Input: Ti (trust value of nodes)
Output: FaultNode [ ], TrustNode [ ].
N [ ] =GetNeighbour[ ];//find all neighboring nodes
For all node i in N [ ]
CalculateTrust[ ]// obtain trust
UpdateTrust () //
If(Ti<TThreshold)
FaultNode U
node(i) else
TrustNode U
node(i) End for

```

Algorithm 2: *M-THMR Protocol at node i*

Method 1: *Route request Phase*

```

Upon receiving RREQ < S,D, seq, hopCt > from nj
: if ni == D then
set a timer TD
/* enter Route Reply Phase upon timeout*/return
end if
Insert <S,nj, hopCt + 1> into RT /*reverse route*/ if <S,seq> doesn't exist in SNT then
Insert <S,seq> into
SNT if ni! = D then
Rrebroadcast RREQ < S,D, seq, hopCt + 1
> end if

```

Method 2: *Route reply Phase*

```

Upon receiving RREP < S,D, seq,
hopCt, exNodeSet, nextNode > from nj:
for each route R in RT do
if R.D == S and R.nextHop ∈ exNodeSet then Remove route R
end if
end for
if nextNode == NULL or nextNode == ni
then Insert < D, nj, hopCt + 1 > into RT
/* two temporary parameters */
Set mHop = 65535 and R1 =
NULL for each route R in RT do
if R.D == S and R.hopCount < mHop
then Set mHop = R.hopCount and R1 = R
end if
end for
for each route R in RT do
/* remove all reverse routes to source */ if R.D == S then
Remove route
R end if
end for
if R1! = NULL then

```

(continued)

(continued)

Algorithm 2: *M-THMR Protocol at node i*

```

Insert R1 into RT
nextNode = R1.nextHop
exNodeSet = {R1.nextHop}  $\cup$  exNodeSet Broadcast RREP < S,D, seq, hopCt + 1,
exNodeSet, nextNode>
end if
end if

```

Method 3: *Route probe Phase*

```

Upon Timeout at the Destination:
Set exNodeSetHop = NULL for
each route R in RT do
exNodeSet = {R.nextHop}  $\cup$  exNodeSet end for
Broadcast RREP <S,D, 0, exNodeSet,NULL>

```

4 Experimental Evaluations

To evaluate our proposal we focused on route, delay, delivery and loss. We experimentally simulated M-THMR protocol using NS2 Simulator to evaluate the performance. It provides scalable and parameter driven environment for wireless protocol simulation. We compared the performance of M-THMR with THM for evaluation.

4.1 Simulation Setup

To simulate the protocol we setup the parameter described in Table 1. The simulation runs on Random Way-point mobility model with a speeds variation up to 100 m/s and capacity of 2 Mb/s. We perform the simulation in two sets. First set does not having any malicious node while second set contains 40% of malicious nodes.

Table 1 Simulation parameters

Configurations	Parameters values
Simulation area	1000 m \times 1000 m
No. of nodes	20, 40, 80
Source-destination pairs	15
Packet size	512 bytes
CBR rates	4 bytes
Mobility	RWP
Max. speed (ms)	4–24 ms
Pause time	0 s
Simulation time	600 ms

During route discovery process all nodes behave normally. During data routing, we configure the simulator to choose 40% node as malicious randomly. It was observed that those nodes behave abnormally and tries to modify data packets and tries drops all data packets routed through them.

4.2 Performance Analysis

End-to-End delay: Figure 1 shows the throughput performances of the protocol in the form of end-to-end delay in adversarial scenario. M-THMR achieves 12% improvisation of packet delay in compare to the base protocol.

This is to check the performance of the protocol in the form delay in the adversarial scenarios, the simulation is checked by considering 20, 40 & 80 nodes as shown in Fig. 1. The delay of node 20 is less because the node 20 is near to the source node, and the delay of time taken to deliver a data is less than that of node 40 and node 80. Figure 1, specifies that the speed of the node increases with simulation time, and averagely proposed protocol (M-THMR) minimizes the delay as compare to the existing protocol (THMR).

Packet delivery ratio: Packet delivery ratio comparison with base protocol. As the malicious packets increases packet delivery increase with a convergence of 98% as per base protocol. PDR is checked by the total packet transmitted from the source to that of packet received by the destination. Figure 2, depict the value of PDR of 20 nodes and as the ratio of traffic increases so we have to check the PDR ratio by selecting 40 and 80 nodes shown in Fig. 2.

Figure 2 shows the comparison of the existing and proposed. Result shows that the packet delivery ratio is better for proposed protocol (M-THMR) as compared to existing protocol (THMR).

Overhead: It is the processing time taken by the system to deliver the packet from source to the destination.

Overhead is checked by the total processing time taken by the source to deliver packet to the destination. Figure 3 depict the value of overhead of node 20, 40 and 80 as shown. The overhead of node 20 is less because the node 20 is near to the

Fig. 1 Comparison of delay versus number of nodes

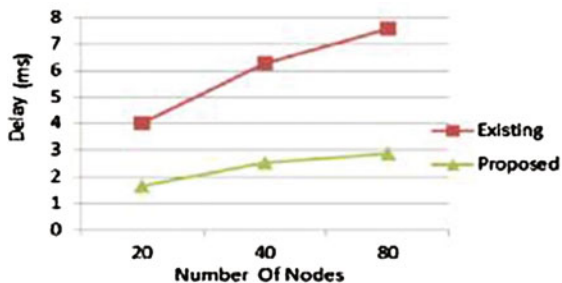


Fig. 2 Comparison of packet delivery ratio versus number of nodes

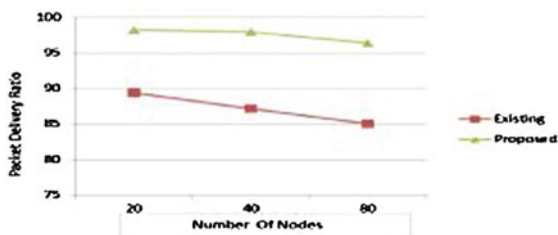


Fig. 3 Comparison of overhead versus number of nodes

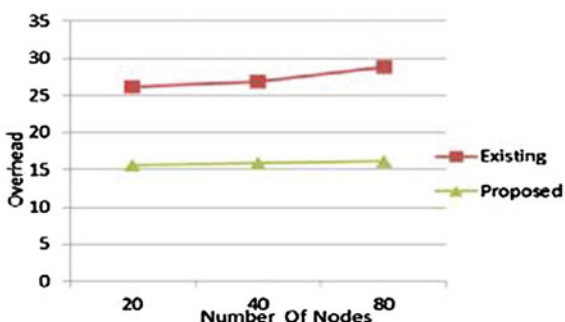
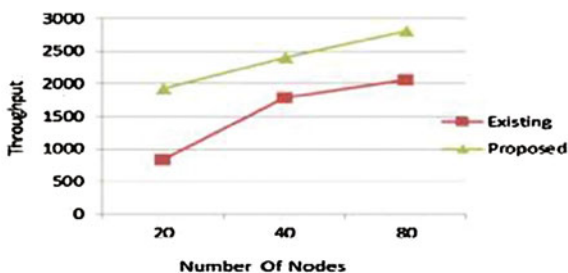


Fig. 4 Comparison of throughput versus number of nodes



source node, and therefore the time taken to deliver a data is less than that of node 40 and node 80. Figure 3 shows the comparison of the existing and proposed. Result shows that the Overhead is better for proposed protocol (M-THMR) as compared to existing protocol (THMR).

Throughput: The Throughput specifies the amount of data transmitted from the source to the destination. The throughput of M-THMR is high with a small size of the network.

Figure 4 shows the comparison of the existing (THMR) and proposed (M-THMR) protocol. Results shows that packet lost is low in proposed than that of existing.

5 Conclusion

After analyzing the common attacks and their dependence on the acquisition of network topology, this paper points out the necessity of hiding topology in designing the routing protocols for MANET. The paper also formally defines topology-hiding and proposes a Modified Topology-Hiding Multipath Routing protocol (THMR). Performance evaluation shows that Modified-THMR (M-THMR) has better capability of finding routes. M-THMR doesn't degrade the performance when there is no attack. While in the adversarial scenario, the simulation results show that M-THMR can resist attacks at a low overhead and short routing convergent time. As for the future work, we plan to design the data transmission strategy with fault detection mechanism based on M-THMR.

References

1. Lacuesta R, Lloret J, Garcia M, Penalver L (2013) A secure protocol for spontaneous wireless ad hoc networks creation. *IEEE Trans Paral Distrib Syst* 24(4)
2. Sahadevaiah K, Prasad Reddy PVGD (2011) Impact of security attacks on a new security protocol for mobile ad hoc networks. *Netw Protoc Alg* 3(4):122–140
3. Liu K, Deng J, Varshney PK, Balakrishnan K (2007) An acknowledgment-based approach for the detection of routing misbehavior in MANETs. *IEEE Trans Mob Comput* 6(5):488–502
4. Perkins CE, Royer EM, Das SR (2003) Ad hoc on-demand distance vector (AODV) routing. IETF INTERNET DRAFT, MANET working group. Feb 2003
5. Yang H, Luo H, Ye F, Lu S, Zhang L (2004) Security in mobile ad hoc networks: challenges and solutions. *IEEE Wirel Commun* 11(1):38–47
6. Kong J, Zerfos P, Luo H, Lu S, Zhang L (2001) Providing robust and ubiquitous security support for wireless mobile networks. In: *ICNP*, pp 251–260
7. Huang TC, Huang SY et al (2010) AODV-based backup routing scheme in mobile ad hoc networks. In: *International conference on communications and mobile computing (CMC)*, pp 254–258
8. Yang YB, Chen HB (2009) An improved AODV routing protocol for MANETs. In: *International conference on wireless communications, networking and mobile computing (WiCom)*, pp 1–4
9. Li X, Cuthbert L (2004) Stable node-disjoint multipath routing with low overhead in mobile ad hoc networks. In: *IEEE annual international symposium on modeling, analysis, and simulation of computer and telecommunications systems (MASCOT)*, pp 184–191
10. Ye Z, Krishnamurthy SV et al (2004) A routing framework for providing robustness to node failures in mobile ad hoc networks. *Ad Hoc Netw* 2(1):87–107
11. Lee SJ, Gerla M (2000) AODV-BR: backup routing in ad hoc networks. In: *IEEE wireless communications and networking conference (WCNC)*, pp 1311–1316
12. Marina MK, Das SR (2001) On-demand multipath distance vector routing in ad hoc, p 23. doi:[10.1109/ICNP.2001.992756](https://doi.org/10.1109/ICNP.2001.992756)
13. Sanzgiri K, Dahill B, Levine BN, Shields C, Royer EM (2002) A secure routing protocol for ad hoc networks (pdf). Technical report: UM-CS-2002-032
14. Papadimitratos P, Haas Z (2002) Secure routing for mobile ad hoc networks. In: *SCS communication networks and distributed systems modeling and simulation conference (CNDS 2002)*, San Antonio, TX

15. Burmester M, Medeiros B (2009) On the security of route discovery in MANETs. *IEEE Trans Mob Comput* 8(9):1180–1188
16. Wang B, Huang C, Yang W, Wang T (2010) Trust opportunistic routing protocol in multi-hop wireless networks. In: 2010 IEEE international conference on wireless communications, networking and information security (WCNIS), Beijing, China, pp 563–567. doi:[10.1109/WCINS.2010.5541842](https://doi.org/10.1109/WCINS.2010.5541842)
17. Chai K, Le A-N, Cho Y-Z (2009) Load balanced routing protocols for ad hoc mobile wireless networks. *Art IEEE Commun Mag* (Sept 2009)
18. Abusalah L, Khokhar A, Guizani M (2008) A survey of secure mobile ad hoc routing protocols. *IEEE Commun Surv Tutor* 10(4):78–93 (Fourth quarter 2008)
19. Pirzada A, McDonald C (2005) Secure routing with the AODV protocol. In: Proceedings of the Asia-Pacific conference on communications, pp 57–61
20. Johnson DB, Maltz DA, Hu YC (2004) The dynamic source routing protocol for mobile ad hoc networks (DSR). IETF INTERNET DRAFT, MANET working group, July 2004
21. Yu W, Sun Y, Liu KJR (2005) HADOF: defense against routing disruption in mobile ad hoc networks. In: Proceedings of conference on IEEE INFOCOM
22. Yu W, Sun Y, Liu KJR (2005) Stimulating cooperation and defending against attacks in self-organized mobile ad hoc networks. Proceedings of second annual IEEE CS conference on sensor and ad hoc communication and networks (SECON '05)
23. Yang H, Luo H, Ye F, Lu S, Zhang L (2004) Security in mobile ad hoc networks: challenges and solutions. *IEEE Wireless Commun* 11(1):38–47
24. Luo H, Zerfos P, Kong J, Lu S, Zhang L (2002) Self-securing ad hoc wireless networks. In: Proceedings of seventh IEEE symposium on computers and communication (ISCC '02)
25. Abedi O, Fathy M (2008) Enhancing AODV routing protocol using mobility parameters in VANET, IEEE/ACS international conference on computer systems and applications, AICCSA 2008
26. Asokan N, Ginzboorg P (2000) Key agreement in ad-hoc networks. *Comput Commun Rev* 23:1627–1637
27. Kong J, Zerfos P, Luo H, Lu S, Zhang L (2001) Providing robust and ubiquitous security support for wireless mobile networks. In: ICNP, pp 251–260
28. Xiao Y, Rayi VK, Sun B, Du X, Hu F, Galloway M (2007) A survey of key management schemes in wireless sensor networks. *Comput Commun* 30(11/12):2314–2341
29. Zhu S, Xu S, Setia S, Jajodia S (2006) LHAP: a lightweight hop by-hop authentication protocol for ad-hoc networks. *Ad Hoc Netw J* 4(5):567–585
30. Yan J, Ma J, Li F, Moon SJ (2010) Key pre-distribution scheme with node revocation for wireless sensor networks. *Ad Hoc Sens Wirel Netw* 10(2/3):235–251
31. Mukesh M, Rishi KR (2010) Security aspects in mobile ad hoc network (MANETs): technical review. *Int J Comput Appl* 12(2):37–43
32. Zhang Y, Wang G, Hu Q, Li Z, Tian J (2012) Design and performance study of a topology-hiding multipath routing protocol for mobile ad hoc networks. In: INFOCOM, 2012 proceedings IEEE, Orlando, FL, pp 10–18. doi:[10.1109/INFCOM.2012.6195468](https://doi.org/10.1109/INFCOM.2012.6195468)

A Cloud Computing Based WSNs for Agriculture Management

Gorakhnath U. Waghmode and Avinash D. Harale

Keywords Agricultural management · Wireless sensing element actor networks · Cloud storage · Mobile or computer etc.

1 Introduction

Agriculture plays a vital role in India's Economy. Major portion of Indian economy depends on agricultural products. In developing countries like India, Lower productivity in agriculture is commonly observed as most important issues due to drastically changes in climate. Most of the problems related to agriculture are connected to atmosphere watching and management of inexperienced house.

According to Economic Survey of India (2015–16), agriculture contributes about 17.4% to GDP and more than 60% rural population's income depends on agricultural resources [1]. A cloud computing applications plays an important role in different domains such as: agriculture, medical, transportation systems, manufacturing and financial service [2]. A cloud related application allows the farmers to receive or upload the information related to the cultivation and information related to the soil moisture, temperature, humidity. This paper introduces cloud computing as brand new technique to be utilized in addition to WSNs to enhance their application and benefits to the area of agriculture.

Change in climate and lack of precaution in agricultural field have resulted in poor yield as compared to population growth. To increase the productivity there is a need of continuous monitoring environmental parameters like temperature, humidity, soil moisture, light and that parameters should be shared between all the farmers [3, 4].

In proposed system farmers can upload their data on cloud database through the wireless sensors network as shown in Fig. 1. Data include various parameters such

G.U. Waghmode (✉) · A.D. Harale
Department of Electronics Engineering, SKN SCOE, Pandharpur, Solapur, India
e-mail: gorakhwaghmode1990@gmail.com

A.D. Harale
e-mail: haraleavinash@yahoo.co.in

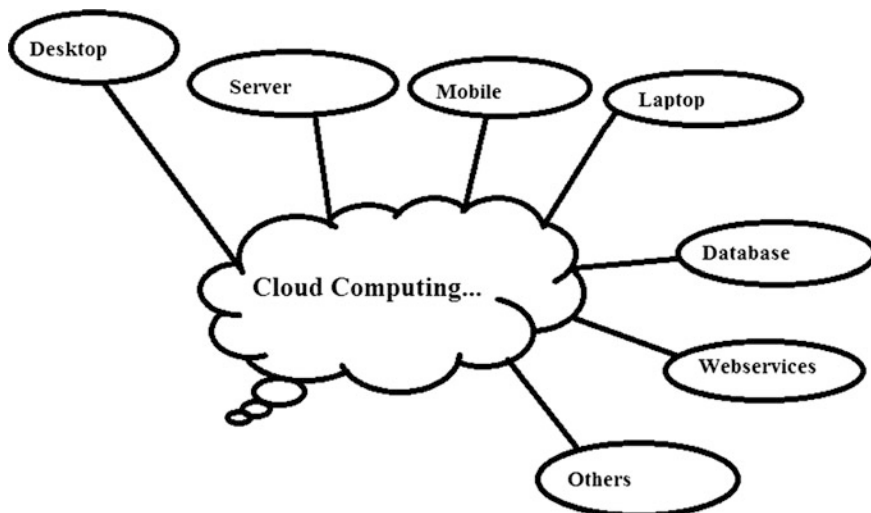


Fig. 1 Cloud services

as temperature, humidity, soil moisture, light etc. which are helpful in agricultural productivity. The data will be shared among all other farmers. Farmers on farmland can get easily information about work plans and they can also enter field data into the cloud system. The uploaded information is stored in big database also referred as cloud. The stored information is shared to head office as well as farmers in real time by using PC or smart phone. The importance of development in agriculture field has been promoted by the numerous developments within the field of wireless sensing element networks (WSAN) [5].

2 Proposed System

See Fig. 2.

2.1 WSN (*Wireless Sensor Networks*)

Various sensors such as temperature, light, moisture, rainfall are used to sense different parameters. These sensors are used in various fields such as agriculture, industry, forest, coal mining, railway etc. [6]. Here temperature sensor is used to sense existing temperature in agricultural field. To sense the strength of light the LDR is used. The amount of moisture present in the soil can be measured by using moisture sensor. Rainfall sensors are used to sense the amount of rainfall. In this way different sensors are used to sense the environmental parameters which will increase the productivity in agriculture [7] (Fig. 3).

Fig. 2 Proposed block diagram

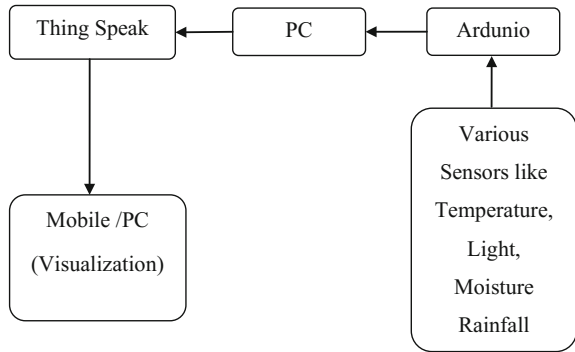
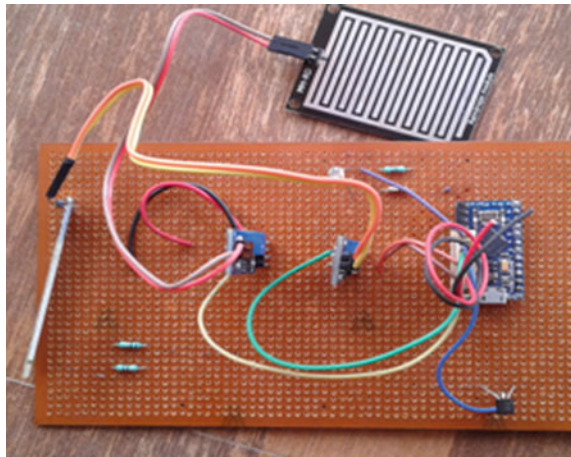


Fig. 3 Different sensors

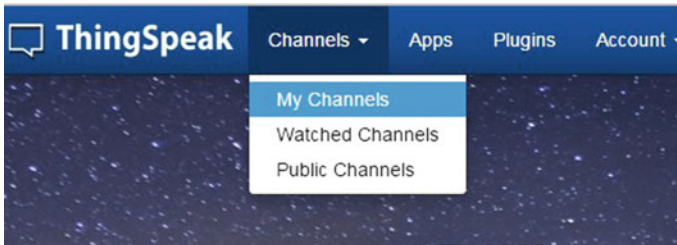
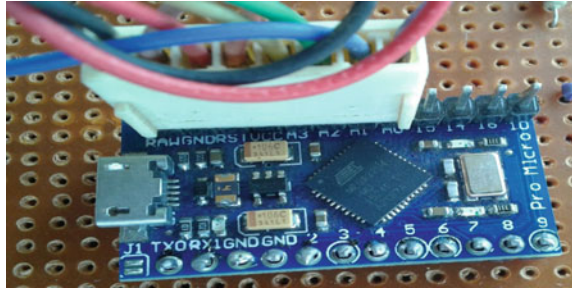


2.2 *Arduino*

Arduino is used to create microcontroller-based kits for building digital devices and interactive objects that can sense and control physical devices. Here arduino is used as controller. All the sensing parameters are given to analog channels of arduino. Arduino convert that analog sense parameter into equivalent digital value (Fig. 4).

2.3 *Personal Computer*

The data is received by serial communication from arduino. The PC will act as database for sensor data and in that data is also processed in respective values. The data base is prepared by using Dot Net.

Fig. 4 Arduino board**Fig. 5** Open source cloud service

2.4 *Thingspeak*

Internet of Things is a new paradigm of connecting devices like microcontrollers and smart objects to cloud. Using IoT services, we can now connect sensors to internet directly. Thingspeak is an open source cloud service used for general purpose applications. The proposed research work aims at addressing the issues and challenges with the aforementioned objective of integrating sensor network over cloud using Internet of Things services. So Internet of Things or IoT basically is connecting Embedded System to internet. In Thingspeak we have to upload the data in their own database through channel. The uploaded data will be converted into respective values which are able to show the data in terms of graph (Fig. 5).

2.5 *Mobile/PC (Visualization)*

Smart phone or computer is used to receive the data from things speak or any open source cloud service. Received data is represented as graph of respective values versus time or date. User can give the suggestion like in particular area which crop will be beneficial etc. In future this system can be connecting with government's agricultural organizations to communicate directly with farmers.

3 System Flow Chart

See Fig. 6.

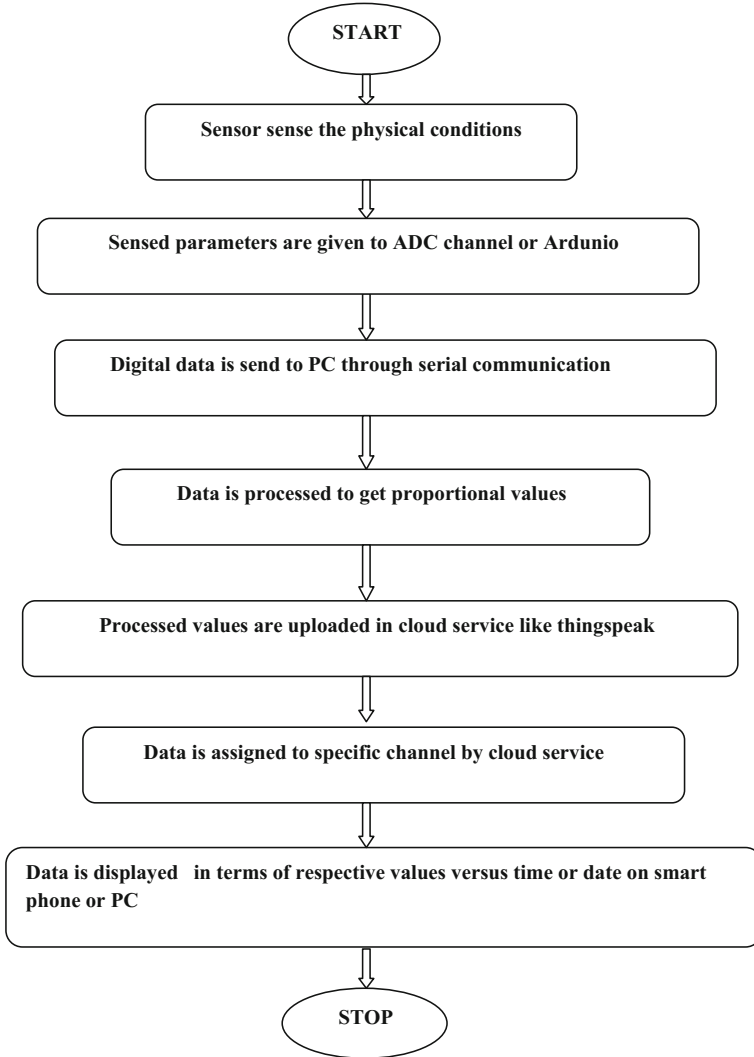


Fig. 6 System flowchart

4 Results and Discussions

Proposed system i.e. a cloud computing based WSNs for Agriculture Management is designed for a proper combination of wireless sensor networks with cloud computing services for the agricultural field. Arduino controller converts environmental sensed parameters into proportional digital values. Digital values are uploaded in the cloud by using cloud service i.e. thing speak. By accessing the channel of cloud service, system can display to user, the real time information in terms of graph.

As shown in Figs. 7 and 8 computer is used to display the graph of real time environmental conditions while in second part information is displayed on smart phone.

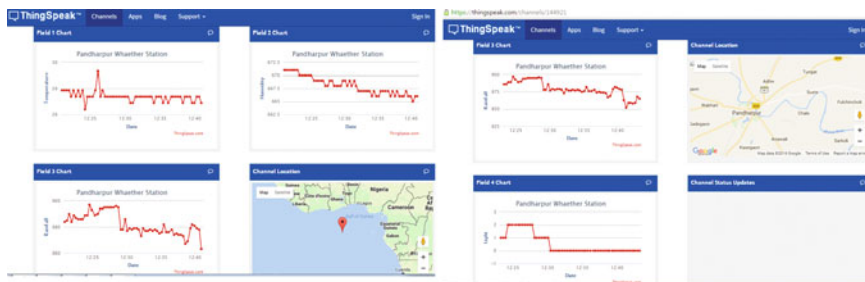


Fig. 7 System output on computer

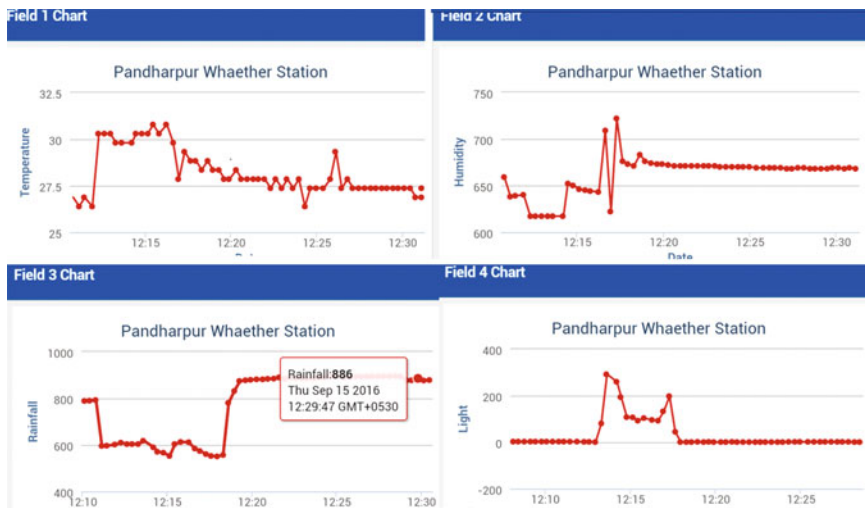


Fig. 8 System output on smart phone

5 Conclusion

Proposed system is designed for cloud based system which is used in agricultural field. Traditionally systems were designed for the prediction purpose, but cloud based system can be used for storage of large database required to data analysis of farming activity. By using open source cloud computing facility farmers are able to see agricultural information on smart phone as well as computer. All the displaying parameters are graph of respective values versus time or date. In future user can share this system with government's agricultural organization to communicate directly with farmers which will be one of the best methods to increase the productivity in agricultural field.

Acknowledgements I would like to express thanks towards my guide prof. Avinash D. Harale. I am thankful to my colleague Miss. Surekha R. Patil for her uncountable support. I am also thankful to all those who guided me during this work.

References

1. Yesugade KD, Bathiya S (2014) Agro-sense: a cloud-enabled mobile app and efficient farming system using WSNs. *IJSRD Int J Scientific Res Dev* 2(08):2321–0613 (ISSN online)
2. Thakur A, Kumar M, Yadav RK (2014) Cloud computing: demand and supply in banking, healthcare and agriculture. *IOSR J Comput Eng (IOSR-JCE)* 16(3, Ver. II):96–101
3. Tian M, Xia Q, Yuan H (2013) Discussion on the application of cloud computing in agricultural information management. *Res J Appl Sci Eng Technol* 5(8):2538–2544
4. Kalghatgi S, Sambrekar KP (2015) Review: using cloud computing technology in agricultural development. *IJISSET Int J Innov Sci Eng Technol* 2(3)
5. Chung W-Y, Yu P-S, Huang C-J (2013) Cloud computing system based on wireless sensor network, vol 2. *IEEE*
6. Hodge VJ, O'Keefe S, Weeks M, Moulds A (2015) Wireless sensor networks for condition monitoring in the railway industry. *IEEE Trans Intell Transp Syst* 16
7. Murakami Y, Utomo SKT (2013) iFarm: development of cloud-based system of cultivation management for precision agriculture. In: 2013 IEEE 2nd global conference on consumer electronics (GCCE)

Analysis on an MHT Based Integrity Authentication Framework for Cloud Data Security

R.S. Sajjan, Vijay Ghorpade and B.D. Arkas

Keywords Public auditing · Private key · Multi replica

1 Introduction

Cloud computing has taken best popularity in the current trends. The system ability performs the cloud to maintain on demand services for the cloud user. It may be computed with different resource techniques that help for making the secure connection and secure data storage on the cloud. The data has to be stored on the cloud in the form of speciality that measures data access and data management. In the formulation of cloud data security the cloud system measure efficiency and effectiveness [1].

Due to the public network, the attacker can easily break the network. Hence the system fails in database security and efficiency. The system can create the number of replica, which are updated one by one, that takes more time to manage and access the data [2]. To enhance and achieve the proposed system goal cloud user has to be covering the efficiency problem of data on the cloud. Hence especially the proposed system enables the special type of authentication and need to process the data through the structure made by the cloud source.

R.S. Sajjan · B.D. Arkas (✉)

VVP Institute of Engineering and Technology, Solapur (Soregaon), India
e-mail: arkasbapuraje@gmail.com

V. Ghorpade

D. Y. Patil College of Engineering and Technology, Kolhapur, Kolhapur, India

2 Related Work

Cloud has become popular with scalability and integrity. For the data security and privacy protection nature of cloud uses specific techniques. The current updates are through cloud applications with symmetric business trends. Efficient storage of cloud data has become helpful for secure access and updating of data. Hence the public auditing is the scheme that overcomes with efficiency and complexity problem. Intensively the integrity verification and digital signature is research issue in the current field. Existing scheme manage generation of integrity proofs and to sign the proofs which give the signature of verification [3–5]. The proposed first scheme support with verification of all data updates on cloud and authenticated data structure modified under public auditing and integrity verification.

3 Problem Statement Analysis

The cloud server are much more scalable when the system fails then stored replica on multiple locations are playing the important role of data recovery service. The current tradition uses data authentication structure to enable public auditing scheme, hence the digestion of system which becomes powerful at the time of verification of each block in every replica. The proposed system addressing audit problem of data blocks becomes separated with factors that are addressed with the combination of all dynamic public auditing scheme. In the proposed system of the author, multi-replica can be elaborated effectively by the factor of efficiency.

The verification process requires verifier who is able to analyze and to have better knowledge of integrity checking. So information leakage and public auditing are preserved. Hence the multi-replica scheme is not secure in the verification process of TPA.

4 System Design

In the proposed system we are implementing secure and scalable cloud storage system. Firstly in this system user has to register with Cloud Service Provider (CSP), which generate the private key for the user. Using the MHT algorithm, the files are splits into batches and those parts will be encrypted using the AES algorithm. Data auditing encapsulated with TPA to audit data from files that stored on the cloud server. The MHT algorithm happens for the different purpose; actually, hash function is used for calculation of each leaf node of the data block. The system collision avoided by this hash function traversal algorithm also system security and efficiency are enhanced. The proposed system proves authentication and integrity with improving the public data auditing and replication of secure cloud storage (Fig. 1).

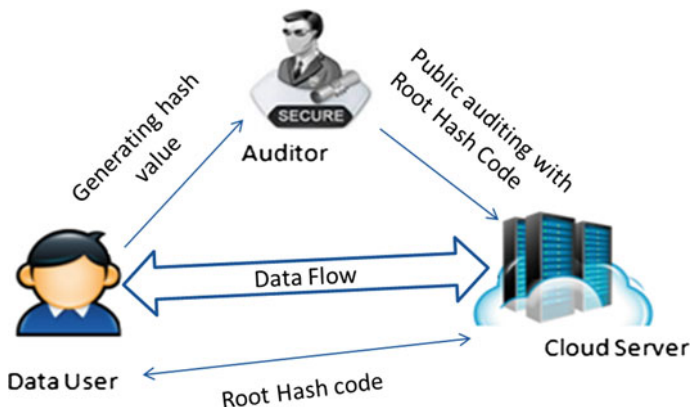


Fig. 1 An system architecture of MHT based authentication integrity system

4.1 Data Owner

In this module, we are going to create a User application by which the data owner is allowed to access the application provided by the cloud. First, the data owner registers his details with the Cloud Service Provider. Once registered the private key generated will be sent to the Data Owner mail id given at the time of registration. The registered Data owner is allowed to upload the files into the Cloud Sever. The file can be encrypted using Advanced Encryption Scheme and then upload into the Cloud Server.

4.2 Cloud Service Provider

Cloud Service Provider (CSP) contains a large amount of data in their Data Storage. The CSP can maintain all the User information to authenticate when they want to login into their account. Also, the Cloud Server would redirect the User requested job to any of the Queue to process the User requested the job. Request of all Users can be processed by the Virtual machines in the Queue.

4.3 Merkle Hash Tree

Merkle Hash Tree is the tree in which every non-leaf node is labelled with the hash of labels of its children node. MHT is based on the binary tree which is useful because they allow efficient and secure verification of the contents of data structures. Those encrypted form of data would be split into batches, and those batch

files are stored in the cloud. The root node top hash key stored in the local database of the data owner.

4.4 Trusted Third Party

Trusted Party Auditor audit the data that are uploaded by data owner based on the file's top hash key stored in their database. TPA can retrieve the particular batch file hash key and compares with the hash key value in the database. If the validation results in top hash value match, then data integrity is ensured.

5 Implementation

5.1 System Requirements

<i>Hardware Requirements</i>	Memory: 4 GB RAM. Processor: Intel(R) Core(TM) i5-4210U CPU@ 2.40 GHz.
<i>Software Requirements</i>	Operating system: Windows 8v and above, System type: 64 bit operating system.
Language	apex, JQuery, Angular JS, etc.
Public Cloud Data Service	Salseforce Framework.

5.2 Setup

The setup algorithm takes no input. It outputs the root hash code for the input. The setup phase is used to generate security keys like private key and public key by enhancing KeyGen () function.

5.3 Encryption Phase

Encrypt (spk, M, I). The encryption algorithm fetches as input the public parameters spk, a message M, and an access structure I over the universe of attributes. Algorithm will encrypt M and produce a cipher text CT such that only a user that possesses attribute set that satisfies the access structure will do decryption the message.

5.4 Key Generation Phase

The client generates a secret value $\alpha \in Z_p$ and a generator g of G , then compute $v = g^\alpha$. A secret signing key pair $\{\text{spk}, \text{ssk}\}$ is chosen with respect to a designated provably secure signature scheme whose signing algorithm is denoted as $\text{Sig}()$. This algorithm outputs $\{\text{ssk}, \alpha\}$ as the secret key sk and $\{\text{spk}, v, g\}$ as the public key pk . For simplicity, in our settings, we use the same key pair for signatures, i.e., $\text{ssk} = \alpha$, $\text{spk} = \{v, g\}$.

5.5 Decryption Phase

Decrypt ($\text{spk}, \text{CT}, \text{ssk}$). The decryption algorithm takes as input the public parameters spk , a cipher text CT , which contains an access policy I , and a private key ssk , which is a private key for a set S of attributes. If the set S of attributes satisfies the access structure I then the algorithm will decrypt the cipher text and return a message M .

5.6 Data Update and Verification

The public auditing of dynamic data is supported by the verification scheme by proving without any cheating with the dishonest server. For the data dynamics the Insertion I , Modification M , Deletion D are the minimum requirements. In Multi-replica block m_i block needs to be updated, with all corresponding blocks b_{ij} . Server perform the update request $\text{UpdateReq} \{\text{Type}, i, \{b'_{ij}\}\}$.

With the replica block client firstly nodes N_h for verification. Next process to deletion, the client wants to update the replica i.e. $h'(b_{ij})$. And finally, replica structure may have to identify h' and has to compute R_{new} also compare R_{new} with R' .

5.7 Public Auditing with All Replica

Suppose to authenticate the verification of $H(b_{ij})$ by verifying if $h(b_{ij}) = H(1||l(b_{ij})||H(b_{ij}))$ sign with particular block (Fig. 2).

$$e(\sigma_j, g) = e(\Pi_i H(b_{ij})^{v_i} u^{w_j}, v), j \in [1, c]$$

With the help of this equation the verification output produced by ACCEPT and REJECT statement. The cloud computing has several technologies and architectures should be merged to utilize the features, in particular, multi-tenancy and virtualization; but they bring their security issues with concerns security of cloud Fig. 3 computing.

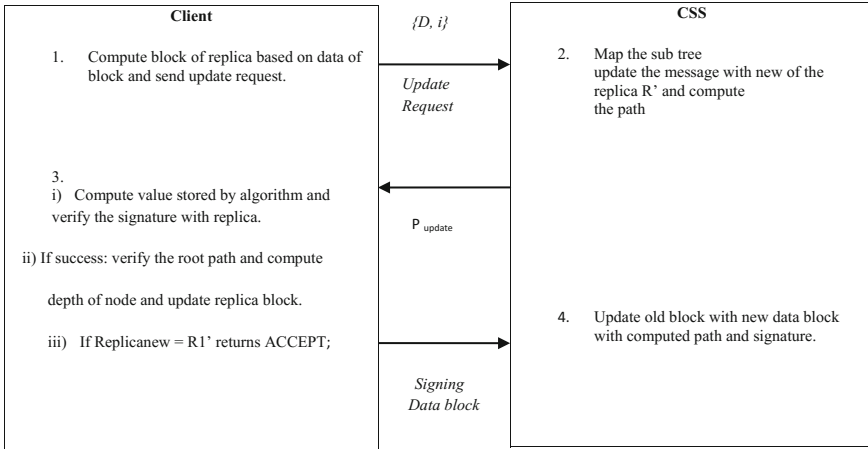


Fig. 2 Data update and data verification

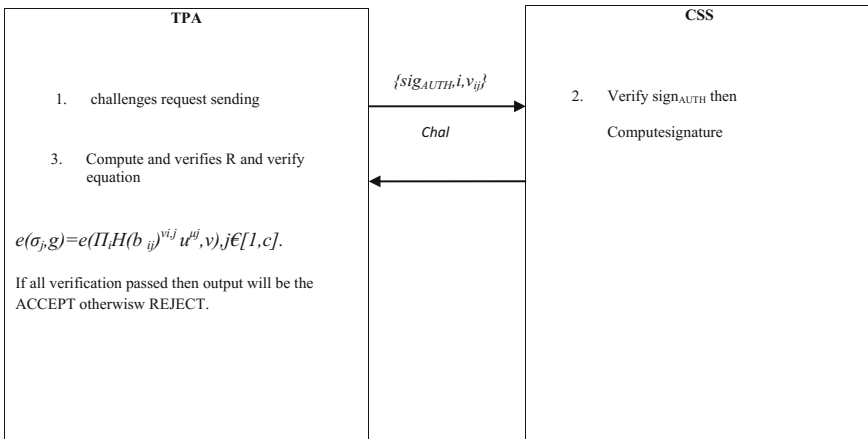


Fig. 3 Public auditing with all replicas

6 Performance Analysis

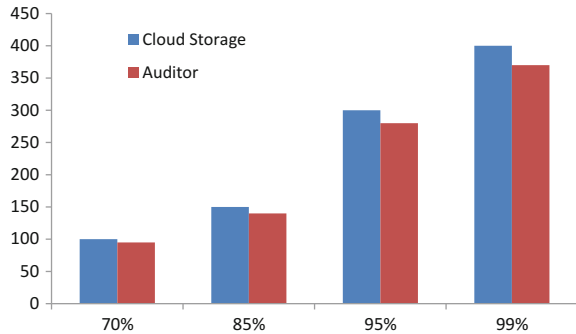
In the system provided experimental results has to achieve the improved efficiency of MuR-DPA when deployed on cloud data storage. We compare our new scheme with MuR-DPA MR-PDP, DPDP, SIR-DPA schemes and our proposed system is once who providing the system public auditing and all replica updating with the single iteration [3] (Table 1).

This session provides building of sales force cloud testing with measure better performance. As for cloud storage behavior and the time cost for auditing the file

Table 1 Comparisons of external authentication and integrity verification scheme

	MR-PDPPDP		SIR-DPA	FU-DPA	Proposed system
	[3]	[4]	[2]	[5]	
Public auditability	NO	NO	YES	NO	YES
One iteration for updating replica	NO	NO	NO	NO	YES

Fig. 4 File audit and secure storage



with maximum confidence. The TPA can allow the user to verify both data updates and position lack of secrete knowledge. It is the important issue that challenges sent by the client will not follow the wrong way (Fig. 4).

7 Conclusion

Both the data integrity and public auditing aims to achieve system goal. In this paper, the purpose of the proposed system has taken charge of ability to enhance replica update and integrity verification. With the comparison of the existing system; performance increased by public data auditing and the one at replica updation. Merkle Hash Tree structure allowing data blocks in a sufficient manner as authentic block processing; Instead of another data block. The One Iteration for Updating All Replicas scheme isolating updation of recent data block on cloud server.

References

1. Stalling W (2011) A handbook on cryptography and network security, principles and practices, 5th ed. Pearson Education
2. Wang Q, Wang C, Ren K, Lou W, Li J (2011) Enabling public audit ability and data dynamics for storage security in cloud computing. *IEEE Trans Paral Distrib Syst* 22(5):847–859

3. Curtmola R, Khan O, Burns RC, Ateniese G (2008) MR-PDP: multiple-replica provable data possession. In: Proceedings of 28th IEEE international conference on distributed computing system, Beijing, China, 2008, pp 411–420
4. Erway C, Papamanthou AC, Tamassia R (2009) Dynamic provable data possession. In: Proceedings of 16th ACM conference on comput. commun. security, Chicago, USA, 2009, pp 213–222
5. Liu C, Chen J, Yang LT, Zhang X, Yang C, Ranjan R, Ramamohanarao K (2014) Authorized public auditing of dynamic big data storage on cloud with efficient verifiable fine-grained updates. *IEEE Trans Paral Distrib Syst*

Historical Drought Analysis of Maharashtra State by Using SPI Index

Ajay Chavadekar and S.S. Kashid

Keywords Standardized precipitation index (SPI) · Meteorological drought

1 Introduction

Drought is a deficit of water. Droughts are perceived as some of the most expensive and the least understood natural disasters. Based on deficits observed in various hydrologic quantities, droughts are interpreted differently. Scarce rainfall in monsoon leads to drought situations. Shortage of food and fodder leads to a massive, devastating effect on human and animal and it may also have impacts on social, environmental and economic factors. Drought effect on the environment is the result of damages to wild animals' habitats, animals, and plants, degradation of soil and water quality. It also increases soil erosion, which causes loss of biological productivity. It gives great impact on agriculture and allied industries. The government can plan for mitigation of droughts, if it receives a reliable forecast of drought, before the onset of monsoon.

Drought modeling is done using the Standardized Precipitation Index (SPI). SPI is simple to calculate, powerful and flexible index. In the year 2012, WMO recommends that SPI may be used as official drought index. In the computation of SPI index, only rainfall data is required as data input. Using SPI indices, we can identify dry periods and wet periods effectively. Poor distribution, deficiency and prolonged absence of precipitation resulting in a drought like situations [1]. Precipitation is the main controlling factor in drought events in the central plane region of Maharashtra. Vegetation growth is dependent upon some additional environmental factors, such as high temperature, high winds, low soil moisture content, or low relative humidity. In particular, hydrologic soil properties play an important role in affecting vegetation growth [2]. The total amount of water available for plant growth in a field is a function of the depth and water-holding capacity of the soil. Water holding

A. Chavadekar (✉) · S.S. Kashid
Walchand Institute of Technology, Solapur 413005, India
e-mail: ajaychavadekar@gmail.com

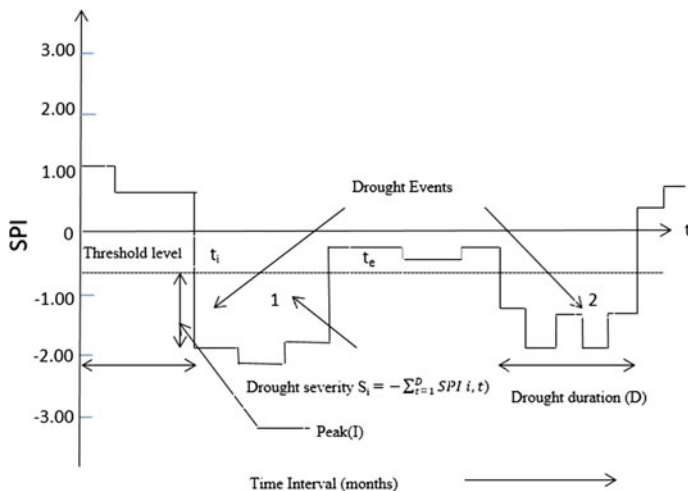


Fig. 1 Depiction of drought characteristics (Severity S ; Duration D ; and peak I) based on standardized precipitation index (SPI)

capacity is considered as one of the most influential hydrologic soil variables in calculating the amount of water storage in a soil profile [2]. Figure 1 depicts the drought characteristics based on Standardized Precipitation Index (SPI).

2 Objectives of Work

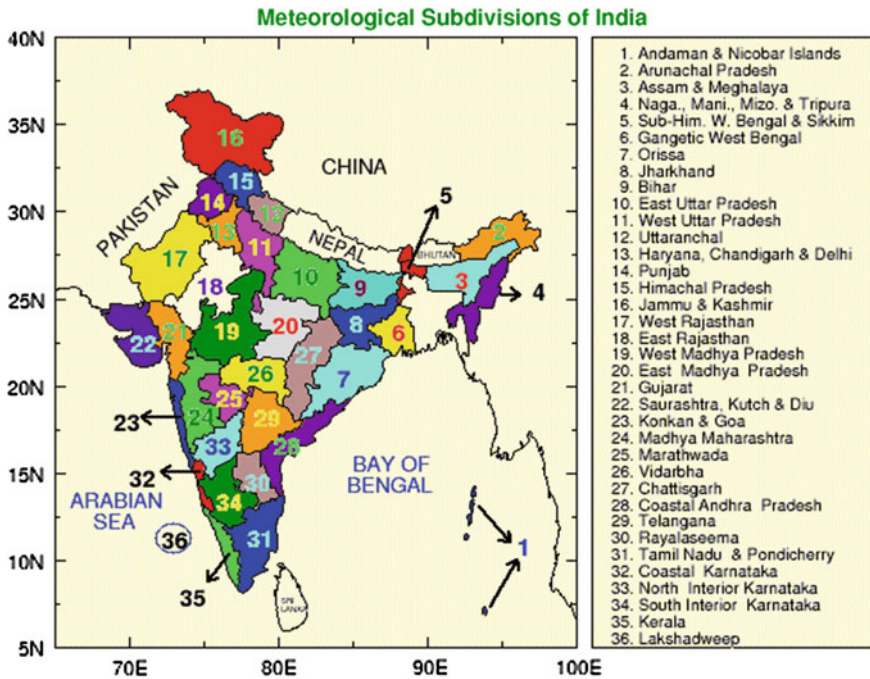
This work intends to analyze historic droughts and computes drought intensity, duration, and frequency for four meteorological subdivisions of Maharashtra. It also focuses on drought occurrence patterns and recurrence of drought events.

3 Data

Monthly rainfall data over various sub divisions of India (<http://www.tropmet.res>) [3, 4] are used for this study. Data were collected by India Meteorological Department for a period 1871–2010. Table 1 illustrates the areal extent of meteorological subdivisions of Maharashtra and available rain gauge stations. Sub-divisional monsoon regions of India are shown in Fig. 2.

Table 1 Details Maharashtra meteorological subdivisions

Subdivision No.	Subdivision name	Area in (km ²)	No. of rain gauge	Average area per rain gauges km × km
23	Konkan and Goa	34,905	5	83 × 83
24	Madhya Maharashtra	115,309	9	113 × 113
25	Marathwada	64,525	5	114 × 114
26	Vidarbha	97,537	8	110 × 110



© 2005, Indian Institute of Tropical Meteorology

Fig. 2 Sub-divisional monsoon regions of India. *Source* Indian Institute of Tropical Meteorology

4 Methodology

Rainfall is the only input required for computing the SPI index. This SPI can characterize drought at multiple timescales such as 3, 6, 9 or 12 months to capture different drought states ranging from short-term, medium-term and long-term drought conditions. In this study, SPI at a 12-month timescale (SPI-12) is chosen for drought modeling, which can be useful for assessing seasonal drought conditions. The details of computation of the SPI can be found in McKee [5-7].

Steps in involved in computation of SPI are as following

1. The transformation of the precipitation value into standardized precipitation index (SPI) has the purpose of:
 - a. Transforming the mean of the precipitation value adjusted to 0;
 - b. Standard deviation of the precipitation is adjusted to 1.0; and
 - c. Skewness of the existing data has to be readjusted to zero.

When these goals have been achieved the standardized precipitation index can be interpreted as mean 0 and standard deviation of 1.0.

2. Computation of Mean of the precipitation
3. Computation of the standard deviation for the precipitation
4. Computation of the skewness of the given precipitation
5. The precipitation is converted to lognormal values and the statistics, shape and scale parameters of gamma distribution are computed. The resulting parameters are then used to find the cumulative probability of an observed precipitation event.
6. The cumulative probability is then transformed to the standard normal random variable Z with mean zero and variance of one, which is the value of the SPI and classification is done as per Table 2.

SPI gives early warnings for multiple time scales, which helps to analyse drought and it is calculate better compare to PDSI. However, based on given rainfall data, input interpretations and conclusions may differ significantly. SPI considers low values of precipitation, soil moisture storage, groundwater, reservoir, stream flow and snow melt. Advantages of SPI are, it has simple calculations, which requires only precipitation values.

The Gamma distribution used for the SPI is given by

$$g(x) g(x) = \frac{1}{\beta^\alpha \gamma(\alpha)} x^{\alpha-1} + e^{-x/\beta} \tag{1}$$

β is scale factor, α is shape factor, $\gamma(\alpha)$ is ordinary gamma function of α . Probabilities are given by distribution function as

$$g(x) = \int_0^x g(t) dt \tag{2}$$

Table 2 Classification of droughts according to SPI index

SPI index	Drought intensity designation
2.0+	Extremely wet
1.5–1.99	Very wet
1.0–1.49	Moderately wet
–0.99 to 0.99	Near normal
–1.0 to –1.49	Moderately dry
–1.5 to –1.99	Severely dry
–2 to less	Extremely dry

Mixed distribution function used by SPI as the precipitation distribution may contain zeroes as given by where q is the probability of a zero, and is estimated by m/n , in which m is the number of zeros in a precipitation time series n

$$H(x) = q + (1 - q)G(x) \tag{3}$$

SPI calculated using a rational approximation approach

$$SPI = \left(t - \frac{C_0 + C_1t + C_2t^2}{1 + d_1t + d_2t^2 + d_3t^3} \right) \tag{4}$$

For $0 < H(x) \leq 0.5$

$$SPI = \left(t - \frac{C_0 + C_1t + C_2t^2}{1 + d_1t + d_2t^2 + d_3t^3} \right) \tag{5}$$

For $0.5 < H(x) \leq 1.0$

$$c_0 = 2.515517 \quad c_1 = 0.802853 \quad c_2 = 0.010328$$

$$d_1 = 1.432788 \quad d_2 = 0.189269 \quad d_3 = 0.001308$$

The length of the precipitation record plays an important role in calculating the SPI. Different lengths of record and similar gamma distributions over different time periods would give consistent results in the SPI. In contrast, the SPI values might be inconsistent when the distributions are different. Hence, it is recommended that the SPI user should be aware of the numerical differences in the SPI values, if different lengths of records are used [8].

5 Results and Discussions

SPI-12 indices were calculated for all four meteorological subdivisions of Maharashtra State. The indices are listed in Table 3. According to drought analysis, it is observed that ‘Marathwada’ sub-division is the most drought prone sub-division of Maharashtra State. From 1871 to 2012, total six extremes, six severe and 14 moderate droughts events were observed. Similarly, the second drought prone area of Maharashtra is ‘Madhya Maharashtra,’ where four extremes, nine severe and 14 Moderate drought events were observed. Vidarbha and Konkan and Goa subdivisions receive good rainfall as compared to other two meteorological subdivisions. But these sub-divisions are also affected by droughts several times. In last 141 years, since 1871, Vidarbha experienced three extremes, eight severe and 16 moderate droughts. Coastal region Konkan and Goa faced four

Table 3 Classification of droughts according to SPI-12 index

Madhya Maharashtra				Marathwada			
Sr. No.	Year	Duration	Type of drought	Sr. No.	Year	Duration	Types of drought
1	1871–72	8	Severe	1	1871–72	9	Extreme
2	1876–77	7	Extreme	2	1875	4	Severe
3	1881	6	Moderate	3	1876–77	7	Moderate
4	1884	2	Severe	4	1896	6	Moderate
5	1899	9	Extreme	5	1899	8	Extreme
6	1902	4	Moderate	6	1902	5	Moderate
7	1904	9	Severe	7	1904	4	Moderate
8	1905	6	Moderate	8	1905	9	Moderate
9	1911	10	Severe	9	1907	6	Moderate
10	1914	6	Moderate	10	1912	6	Severe
11	1918–19	8	Extreme	11	1914	3	Severe
12	1920–21	11	Severe	12	1918–19	7	Severe
13	1925	9	Moderate	13	1920–21	12	Extreme
14	1930	5	Moderate	14	1925	4	Moderate
15	1936–37	9	Severe	15	1929	6	Moderate
16	1939	6	Moderate	16	1936	5	Moderate
17	1941–42	7	Moderate	17	1939	7	Moderate
18	1952–53	6	Severe	18	1941	6	Severe
19	1972–73	13	Extreme	19	1971	4	Moderate
20	1977	5	Moderate	20	1972–73	9	Extreme
21	1982	5	Moderate	21	1984	6	Severe
22	1985	8	Severe	22	1986	5	Moderate
23	1986–87	6	Moderate	23	1991–92	5	Extreme
24	1992	5	Severe	24	2003	3	Extreme
25	2003–04	8	Moderate	25	2008	3	Moderate
26	2009	4	Moderate	26	2012	10	Moderate
27	2012	10	Moderate	27			

extreme and five severe and 15 moderate drought events. By historical analysis of droughts, it is observed that major drought events were observed in 1877, 1899, 1911, 1918, 1920, 1951, 1965, and 1972. Graphical representation of different drought events observed in Maharashtra shown in Fig. 3 (Table 4).

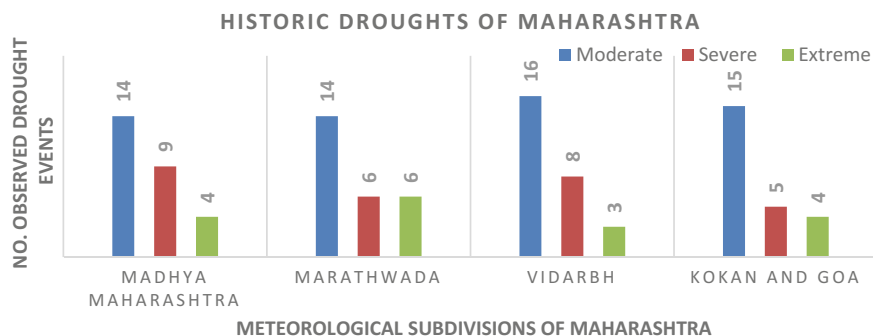


Fig. 3 Historic observed drought events of Maharashtra

Table 4 Classification of droughts according to SPI-12 index

Konkan and Goa				Vidarbha			
Sr. No.	Year	Duration	Type of drought	Sr. No.	Year	Duration	Types of drought
1	1873-74	7	Severe	1	1871	6	Moderate
2	1876-77	7	Extreme	2	1873	4	Moderate
3	1881	6	Extreme	3	1876	6	Severe
4	1884	5	Severe	4	1880	4	Moderate
5	1891	9	Severe	5	1892	3	Severe
6	1899	11	Extreme	6	1899	10	Extreme
7	1901-02	5	Moderate	7	1902	8	Severe
8	1911	9	Severe	8	1904	6	Moderate
9	1913-14	10	Moderate	9	1918-19	5	Moderate
10	1915	6	Moderate	10	1920-21	10	Extreme
11	1918-19	8	Severe	11	1929	6	Moderate
12	1920	6	Moderate	12	1939	5	Moderate
13	1925	3	Moderate	13	1950-51	7	Severe
14	1926	4	Moderate	14	1952	7	Severe
15	1935	5	Moderate	15	1965-66	8	Moderate
16	1941	6	Extreme	16	1967-68	5	Moderate
17	1952-53	7	Moderate	17	1969	4	Moderate
18	1965	6	Moderate	18	1972-73	8	Extreme
19	1972-73	10	Moderate	19	1974	6	Severe
20	1983	5	Moderate	20	1982	4	Moderate
21	1986-87	9	Moderate	21	1984-85	8	Moderate
22	2002	4	Moderate	22	1987	6	Moderate
23	2008	4	Moderate	23	1991-92	8	Severe
				24	1996	6	Severe
				25	2000-01	4	Moderate
				26	2004-05	5	Moderate
				27	2009-10	10	Moderate

6 Conclusions

Madhya Maharashtra and Marathwada are highest drought prone sub-divisions of Maharashtra State. The years when most of subdivisions reported drought conditions are 1877, 1899, 1905, 1911, 1918, 1920, 1951, 1972, 1986, 1987, 2002, 2008 and 2012. In the period 1965–1984 and 1899–1920 the Maharashtra experienced the highest frequencies of large-scale droughts. SPI index is found to be the most suitable index for analysis of meteorological droughts,

References

1. Ogallo LA (1994) Drought and desertification: an overview. *Bull World Health Organ* 43:18–22
2. Wolter K, Timlin MS (1993) Monitoring ENSO in COADS with a seasonally adjusted principal component index. In: *Proceedings of the 17th climate diagnostics workshop*, Norman, OK, NOAA/NMC/CAC, NSSL, Oklahoma Climate Survey, CIMMS and the School of Meteor, University of Oklahoma, pp 52–57
3. Parthasarathy B, Munot AA, Kothawale DR (1995) Monthly and seasonal rainfall series for all-India homogeneous regions and meteorological subdivisions: 1871–1994. IITM Research, Report No. RR-065
4. Parthasarathy B, et al (1987) Droughts/floods in the summer monsoon season over different meteorological subdivisions of India for the period 1871–1984. *J Climatol* 7(1):57–70
5. McKee TB, Doesken NJ, Kleist J (1993) The relationship of drought frequency and duration of time scales. In: *Eighth conference on applied climatology*, American Meteorological Society, Anaheim, CA, pp 179–186, 17–23 Jan 1993
6. Ganguli P, Janga Reddy M (2013) Spatio-temporal analysis and derivation of copula-based intensity–area–frequency curves for droughts in western Rajasthan (India)
7. Janga Reddy M, Ganguli P (2012) Application of copulas for derivation of drought severity-duration-frequency curves. *Hydrol Process* 26(11):1672–1685
8. Mishra AK, Singh VP (2010) A review of drought concept. *J Hydrol* 391:202–221

Statistical Downscaling of GCM Output for Generating Future Rainfall Scenarios Using SDSM for Upper Godavari Basin, Maharashtra

S.S. Motegaonkar and S.S. Kashid

Keywords Statistical downscaling · Climate change · Global climate model · CanESM2

1 Introduction

During the 20th century, the global surface temperature has increased by more than half a degree Celsius and the 1990s was, on average, the hottest decade for the last 1000 years [1]. The fourth assessment report (AR4) of the Intergovernmental Panel on Climate Change [2] has listed the various climate scenarios and its drivers. The rising demand for water and the possible decline in future water resources due to climate change, will pose a significant challenge to water resources planners [3]. Therefore, a proper assessment of probable future precipitation and its variability over time should be included in climate change studies [4]. Global Circulation Models (GCMs) are considered as effective tools available today, which uses transient climate simulations to generate climatic conditions for hundreds of years into the past and the future. They play a crucial role in generating future projections of climate change using different emission scenarios [5]. However, GCMs are available at a coarse grid resolution of 1° – 2° . Consequently, products of GCMs cannot be used directly for climate impact assessment on a local scale. This has led researches to undertake to development of suitable downscaling methodologies to transfer the GCM information to local scale information. A study of the impacts of

S.S. Motegaonkar · S.S. Kashid (✉)
Walchand Institute of Technology, Solapur 413005, India
e-mail: sskashid@yahoo.com

S.S. Motegaonkar
e-mail: motegaonkarshilpa@gmail.com

climate change on the environment and the surroundings includes an account of the hydrological regime for the present and the future years. In order to accurately assess the water balance, generation of future hydrological scenario is essential.

2 Downscaling

Downscaling, or translation across scales, is a set of techniques that relate local and regional scale climate variables to the larger scale atmospheric forcing [6]. The downscaling process plays a crucial role in driving impact assessment models such as drought analysis, water resources management, water demand availability, ecological impacts and risk and vulnerability assessments. Statistical downscaling technique involves transformation using statistical regressions. In order to study the impacts of global warming on a small scale, it is necessary to develop and apply the scenarios to specific issues being faced by the region [7]. It has been emphasized that one of the most important challenges while framing policies is the lack of impact assessment at appropriate scales. Hence it is important to “downscale” in order to address the mismatch in the resolution of the GCM and the local catchment.

2.1 Statistical Downscaling Model (SDSM)

SDSM is a software tool that has been designed for climate change impact assessment studies using a robust downscaling model. The model is also capable of generating scenarios for variables that can not be directly obtained from GCMs. SDSM is a combination of stochastic weather generator and regression-based method. This is because the large scale synoptic variables and the moisture variables are used to condition the small scale variables (like rainfall frequency, intensity and occurrences). SDSM can be used as a windows-based free open source tool for the development of a single site downscaling of data under current and future forcings.

3 Study Area

One of the largest river basins of India, Godavari Basin, has been selected as study area for the present study. Godavari basin extends over states of Maharashtra, Andhra Pradesh, Chhattisgarh and Odessa in addition to smaller parts in

Madhya Pradesh, Karnataka and Union Territory of Puducherry having a total area of 3,12,812 km² with a maximum length and width of about 995 and 583 km. Table 1 gives details of study area (Fig. 1; Table 2).

Table 1 Salient features of the Godavari basin

Basin extent	
Longitude	73° 24'–83° 4'E
Latitude	16° 19'–22° 34'N
Total length of Godavari River (km)	1465
Catchment area (km ²)	312,812
Mean annual rainfall (mm)	1093.21



Fig. 1 Godavari river basin. *Source* Central Water Commission, GOI Ministry of Water Resources, 2014

Table 2 Characteristics of climate stations covered in the basin area

Climate station (Upper Godavari basin)	Catchment area (km ²)	Latitude	Longitude
Nasik	650	20°12'	73°32'
Nanded	52,038	19°08'	77°19'
Kopergaon	6840	19°33'	74°14'
Purna	15,000	19°10'	77°02'

3.1 Data Used

In the present study, data from the following sources is used

1. **Large-scale atmospheric variables** (predictors): These were extracted for the grid point closer to each climate station from the Canadian Institute for Climate Studies (CICS) website (<http://www.cics.uvic.ca/scenarios>).
2. **Observed Data**: The observations used in this study are daily gridded precipitation data, obtained from India Meteorological Department (IMD), Pune. It is available at high spatial resolution $0.25^\circ \times 0.25^\circ$ (latitude \times longitude) for a period 1971–2010 (40 years).

4 Methodology

Simulations can be performed through combinations of regressions and weather generators, sequences of daily climatic data for present and future periods by extracting statistical parameters from observed data series.

The first step in SDSM is screening of predictor variables. Calibration of the model is done by using the data for the period 1970–2000 and simulation is performed using precipitation data series. The percentage of variance is calculated which is tabulated below.

Climate scenario is generated from the model by simulation of daily precipitation data series for the whole 1961–1990 period with both ‘Observed’ (NCEP) and ‘Modeled’ (CanESM2) predictors. Monthly means and variances are compared using t-tests and. Raw CanESM2 precipitation data are used for comparison of monthly residuals with downscaled data. Future climate change projection is divided into three periods, namely 2030s (2011–2040), 2060s (2041–2070) and 2090s (2071–2100).

5 Results and Discussions

Results in terms of ‘explained variance’ during the calibration at each meteorological station is presented in Table 3 in terms of statistical parameters by giving the percentage of explained variance for the selected predictors. For precipitation, the best and the worst performance of the model is seen to be 45.6 and 20.5%.

Table 3 Calibration result at selected meteorological stations

Climate station	Explained variance (%)
Nasik	45.6
Nanded	31.2
Kopargaon	23.1
Purna	20.5

Table 4 Statistical performance of simulated result compared to observed data at four stations

Sr. No.	Station	Statistical parameter	Precipitation			
			Calibration period (1961–1990)		Validation period (1996–2005)	
			Observed	Simulated	Observed	Simulated
1	Nasik	Std. dev (mm)	123.62	130.28	128.22	118.41
		R ²	–	0.73	–	0.83
2	Nanded	Std. dev (mm)	143.19	136.34	120.62	131.91
		R ²	–	0.81	–	0.87
3	Kopargaon	Std. dev (mm)	119.71	126.14	134.74	140.11
		R ²	–	0.65	–	0.70
4	Purna	Std. dev (mm)	104.43	117.22	130.16	124.75
		R ²	–	0.79	–	0.74

The results variation in mean precipitation residual is due to unrealistic representation of CanESM2 predictors. It is clearly shown that SDSM performed better using Raw predictors than CanESM2 predictors (Table 4).

5.1 Climate Change Scenarios (CCCma Under RCP2.6, RCP4.5, RCP8.5) by Downscaling Future Rainfall

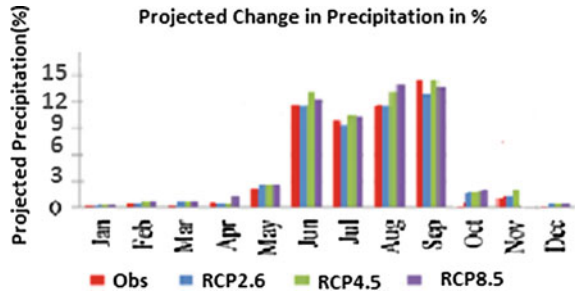
The projected annual precipitation in four meteorological stations for three future periods, compared to the baseline period of 1976–2005 is presented in Table 5. The future rainfall at Godavari basin have been downscaled for the RCP2.6, RCP4.5 and RCP8.5 scenarios.

It is noted that for Nasik region, the annual rainfall is likely to be increased by 2–11% in three of the scenarios respectively. At Nanded station, the annual rainfall is likely to be increased by 2–13% during three scenarios but during RCP4.5 and RCP8.5 in 2060s it may decrease by 4 and 2% respectively. At Kopargaon station also, it may be improved by 1 and 15% but for RCP4.5 over 2060s it is likely to decrease by 9%. However at Purna station, it may be decreased by 2 and 11% except RCP4.5 in 2060s and RCP8.5 2030s. Thus it shows increasing trend for these two RCPs as shown in Table 5 (Fig. 2).

Table 5 Projected Change in annual precipitation for future period compared to baseline period under three RCPs

Sr. No.	Station	Annual precipitation in baseline period	RCP2.6			RCP4.5			RCP8.5		
			2030s	2060s	2090s	2030s	2060s	2090s	2030s	2060s	2090s
			Percentage change compared to baseline period (%)								
1	Nasik	1029.6	3	7	11	2	6	9	3	-7	10
2	Nanded	954	2	4	4	8	-4	13	8	-2	6
3	Koparg-aon	832	1	3	9	15	2	3	-9	10	4
4	Purna	608	-5	-7	-6	-11	8	-2	15	-5	-2

Fig. 2 Projected change in precipitation on the basin



6 Conclusion

The future climate projection for the Upper Godavari basin has been carried out using the outputs of CanESM2 developed by Canadian Centre for Climate Modeling and Analysis (CCCma). In regression based statistical downscaling techniques, the choice of predictors becomes one of the most challenging issues, as different sets of predictors will likely give different results. In SDSM, the choice is made using quantitative tests (explained variance and partial correlation). Study can be carried out by selecting more predictors which are strongly influencing on rainfall as a hydrological parameter. The study shows likely increase in the rainfall at three raingauge stations viz. Nasik, Nanded, and Kopargaon station and decrease in the rainfall at Purna station in Godavari basin, in future, due to climate change.

References

1. Srivastava AK, Rajeevan M, Kshirsagar SR (2008) Development of a high resolution daily gridded temperature data set (1969–2005) for the Indian Region
2. Giorgi F, Hewitson B et al (2001) Regional climate information—evaluation and projections. In: Climate change 2001: the scientific basis. IPCC TAR. Cambridge University Press, Cambridge
3. Huang C, Barnett AG, Wang X, Vaneckova P, FitzGerald G, Tong S (2011) Projecting future heat-related mortality under climate change scenarios: a systematic review. *Environ Health Perspect* 119:1681–1690
4. Goswami BB, Mukhopadhyay P, Mahanta R, Goswami BN (2010) Multiscale interaction with topography and extreme rainfall events in the northeast Indian region. *J Geophys Res* 115:D12
5. Fowler HJ, Blenkinsop S, Tebaldi C (2007) Linking climate change modelling to impacts studies: recent advances in downscaling techniques for hydrological modelling. *Int J Climatol* 27:1547–1578
6. Labat D, Godd eris Y, Probst JL, Guyot JL (2004) Evidence for global runoff increase related to climate warming. *Adv Water Resour* 27:631–642
7. Wentz FJ, Ricciardulli L, Hilburn K, Mears C (2007) How much more rain will global warming bring? *Science* 317:233–235

Design of MIMO Antenna for WLAN and Wi-Max Application

Vivek D. Kamble and Mandar R. Jadhav

Keywords MIMO antenna · Return loss · Band width · WLAN · Wi-Max

1 Introduction

The use of wireless devices is the latest trend in communication technology, and there is a constant demand for compactness or miniaturization of wireless electronic devices, as well as an increase in speed and data rate for these devices. The potential of UWB technology is enormously owing to its tremendous advantages such as the capability of providing high-speed data rates at short transmission distances with low power dissipation. The rapid growth in wireless communication systems has made UWB an outstanding technology to replace the conventional wireless technologies in today's use of Blue tooth and wireless LANs, etc. [1].

Development of wireless technology has raised the capacity and reliability requirements of wireless communication. It has become increasingly difficult to fulfill the requirements with traditional SISO systems due to the limitation in channel capacity. MIMO is a new wireless technology conveyed in the mid-90s. One of the main benefits of MIMO is that the additional paths can be used to increase the capacity of the link without increasing transmit power. MIMO can transmit multiple de-correlated signals with same power level, simultaneously through the spatially parallel channel. For any MIMO application wide band antenna is desirable, hence we can use stacked antenna to achieve wideband in conjunction with MIMO systems [2].

Recently, there is a demand to increase the data rate of existing wireless communication systems. The application of diversity techniques, most commonly assuming two antennas in a mobile terminal, can enhance the data rate and

V.D. Kamble (✉) · M.R. Jadhav
Trinity College of Engineering and Research, Pune, India
e-mail: vivekkamble2010@gmail.com

M.R. Jadhav
e-mail: jadhavmandar58@gmail.com

reliability without sacrificing additional spectrum or transmitted power in rich scattering environments. MIMO technology has attracted attention in modern wireless communication systems MIMO systems transmit the same power using multiple antennas at the transmitter and receiver thereby increasing the channel capacity without the need for additional bandwidth or power. MIMO UWB systems can further increase the channel capacity as compared to conventional MIMO systems for narrow band applications. To combat the multipath fading problem in an indoor UWB wireless communication system, a UWB diversity antenna system is a promising candidate. However, for an efficient MIMO antenna system, mutual coupling between the individual antennas should be as low as possible [3].

2 Single Antenna Design

2.1 Designing of UWB MSA Antenna

The antenna is designed on a substrate printed on both sides, on one side is the patch, and another side is a ground plane. The patch is fed by a microstrip feed line, appropriate matching of the feed line is required to produce desired characteristics of the antenna. The geometry of the given antenna is illustrated in Fig. 1. It is fabricated on a $23 \times 19.4 \text{ mm}^2$ FR-4 substrate with a dielectric constant of 4.4 and a substrate thickness of 1.6 mm. Design parameters are shown in Table 1. The proposed antenna has been simulated by High-Frequency Structure Simulator.

Fig. 1 Antenna geometry with dimensions in mm

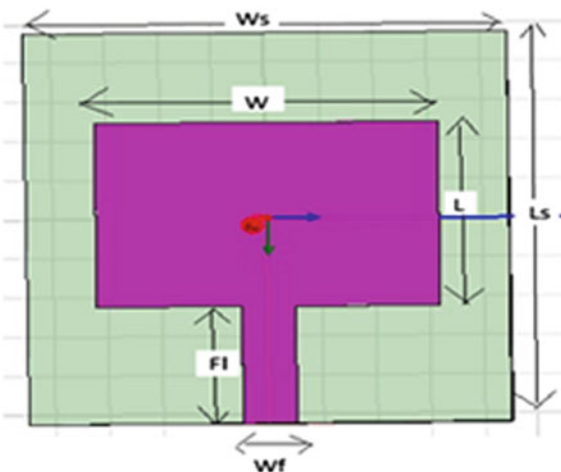


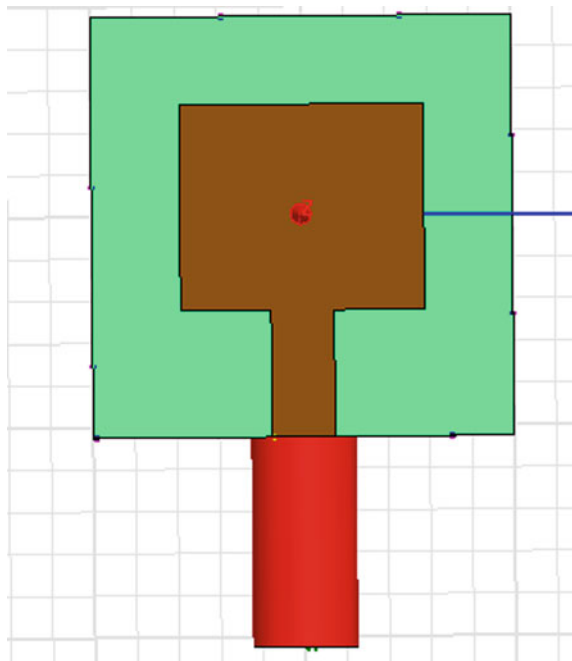
Table 1 Single antenna dimensions

Sr. No.	Parameters	Calculated dimensions (mm)
1.	L	9.8
2.	W	13.4
3.	Ls	19.6
4.	Ws	23.0
5.	Fl	5.5
6.	Wf	2.7
7.	D	22.0

2.2 Antenna Simulation Analysis

The simulation results of the antenna are shown in Fig. 2, from the simulated graph it is observed at BW 8.7 GHz, S11 < -10 dB. The VSWR plot for the antenna is also shown in Fig. 3 which is about 1.05 GHz frequency showing good matching conditions (Figs. 4, 5, 6, 7, 8 and 9).

Fig. 2 Antenna designs in HFSS



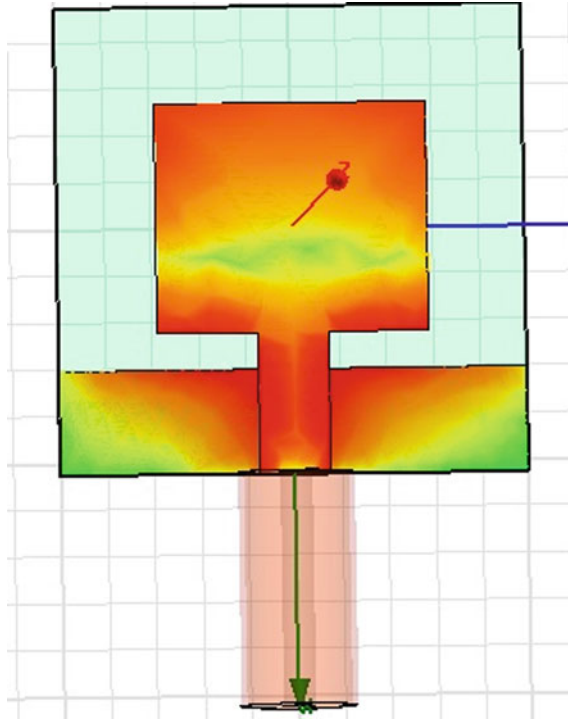


Fig. 3 Current distribution

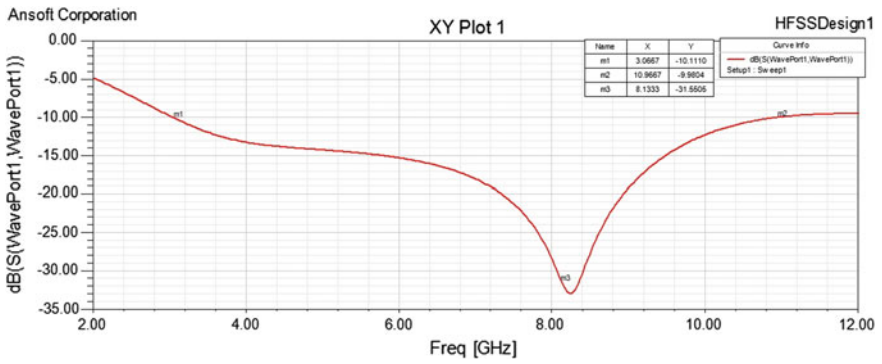


Fig. 4 Return loss for the antenna

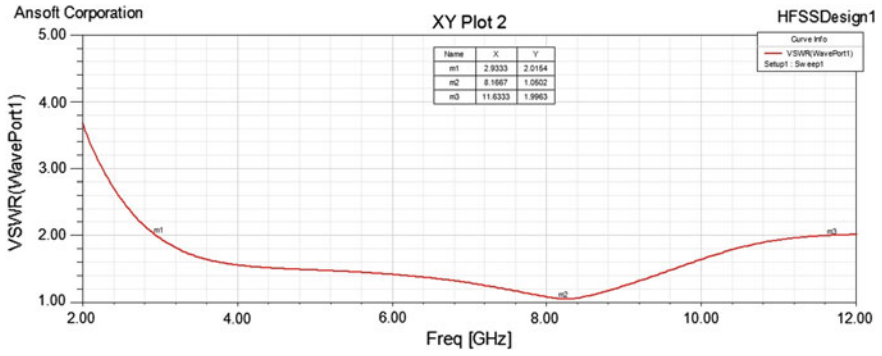


Fig. 5 VSWR plot for the antenna

Fig. 6 Radiation pattern for the antenna

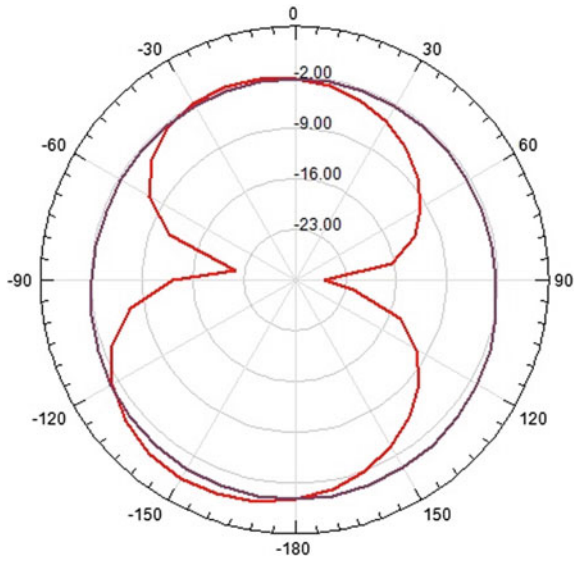


Fig. 7 3D polar plot for the antenna

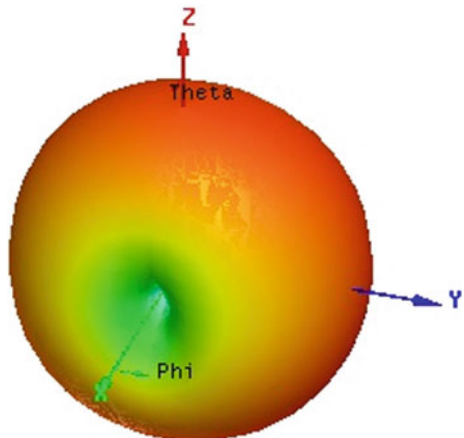


Fig. 8 MIMO antenna designs in HFSS

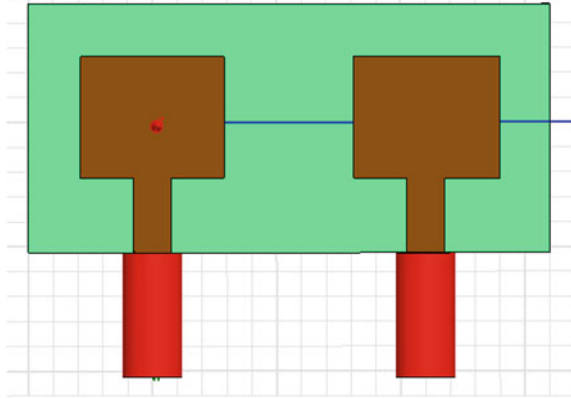
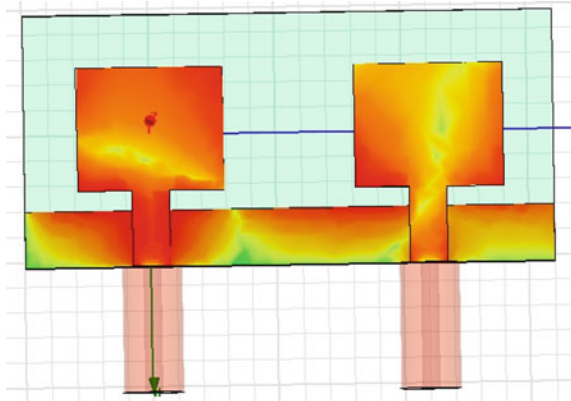


Fig. 9 MIMO antenna current distribution



3 MIMO Antenna Design and Analysis

The main criteria for MIMO system design are mutual coupling, which mainly arises due to the smaller spacing between the two antennas when multiple antennas are involved at closer spacing the design issues are more complicated. The mutual coupling mainly depends on the distance between the elements of an antenna array, by increasing the distance between the elements of the antennas, the mutual coupling can be reduced.

(A) VSWR

The plots in Figs. 10 and 11 show the corresponding VSWR at the two ports for the two antennas. We can observe that VSWR for the 6.8 GHz center frequency which is less than 2 indicating improved matching conditions.

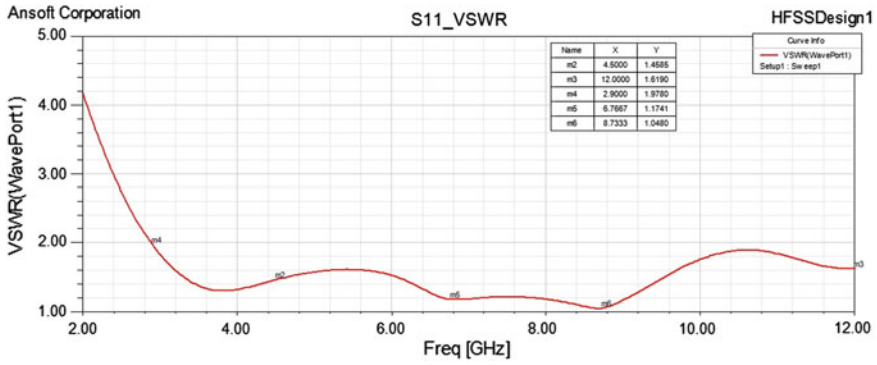


Fig. 10 Port 1 VSWR for the MIMO antenna

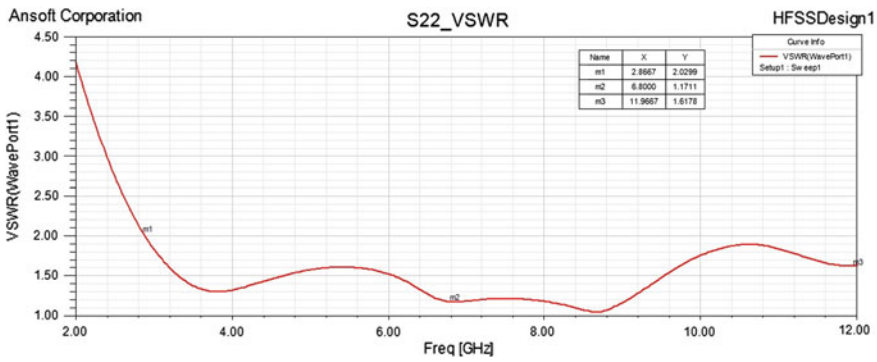


Fig. 11 Port 2 VSWR for the MIMO antenna

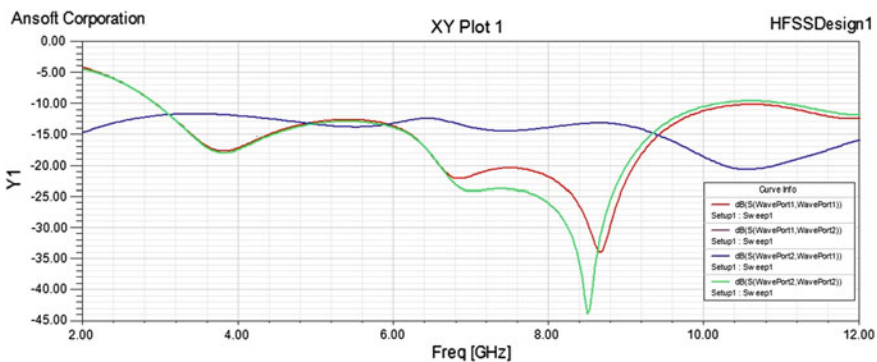


Fig. 12 S11_S22_S21_S12 parameters for MIMO antenna

(B) Return Loss

The plots in Fig. 12 show the S11, S22, S12 and S21 plots respectively after simulation. We can observe that $S_{11} < -10$ dB for the 6.8 GHz frequency and also $S_{22} < -10$ dB for this frequency. Thus, both antennas are meeting the specified requirement of return loss (Figs. 13 and 14).

Fig. 13 Radiation pattern for MIMO antenna

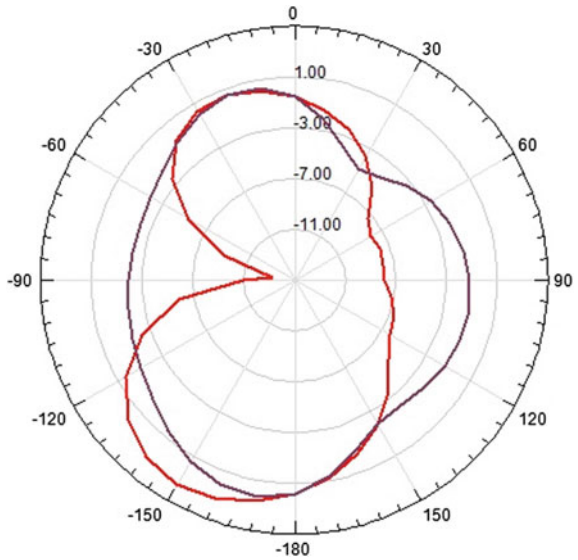


Fig. 14 3D polar plot for MIMO antenna

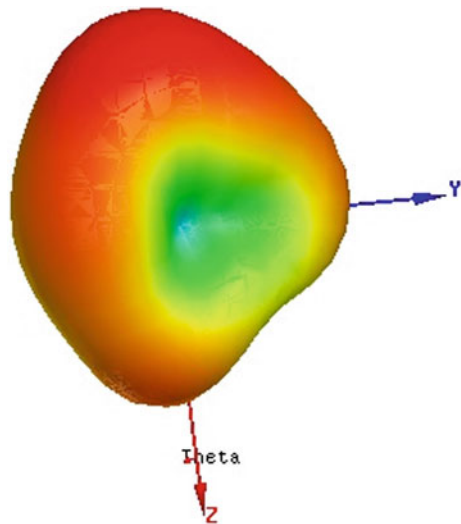


Table 2 Single antenna and MIMO antenna results comparison

Sr. No.	Type of antenna	Freq. range (GHz)	Return loss (dB)	VSWR	BW (GHz)	BW (GHz)	BW (%)	Gain (dB)
1.	Without MIMO	2.93–11.63	–31.55	1.05	8.7	8.7	127	2.55
2.	With MIMO	2.90–12.00	–34.05	1.04	9.1	9.1	133	4.12

4 Comparison of Single Antenna and MIMO Antenna

Table 2 shows the comparison between the single antenna and MIMO antenna. As compared to a single antenna, BW and gain of MIMO antenna are greater also MIMO antenna is operated in the higher frequency range.

5 Conclusion

The system is operating on 2.90–12.00 GHz frequency band using practical antennas designed on High-Frequency Structure Simulator. We have compared various parameters of a single antenna and MIMO antenna and found that the antennas in the MIMO system are operating independently of each other which is a requirement for MIMO system design. MIMO systems offer an increased capacity, but this requires a complex design.

References

1. Sorin V, Artemenko A, Sevastyanov A, Maslennikov R (2011) Compact bandwidth-optimized two element MIMO antenna system for 2.5–2.7 GHz band. In: Proceedings of 5th European conference on antenna and propagation
2. Nigam H, Kumar M (2014) Design and analysis of 2X2 MIMO system for 2.4 GHz ISM band applications. IJAR CET 3(5)
3. Agarwal A, Kaur A (2015) A review paper on stacked microstrip antenna for MIMO application. In: RIEECE-2015

Secure Ration Dispensing System Using HAN and Geofencing Through Li-Fi

Aashish A. Gadgil, Apoorva S. Bendigeri, Diksha D. Halagi,
Gautam Prakash and Shivani A. Nadgouda

Keywords Li-Fi · Geofencing · HAN · Embedded system

1 Introduction

Public distribution system (PDS) is an Indian food security system, established by the Government of India under Ministry of Consumer Affairs, Food, and Public Distribution and managed jointly with state governments in India. India's Public Distribution System (PDS) is the largest retail system in the world. Public distribution system [1] provides a ration card issued under the authority of State Government for the purchase of essential consumer materials like rice, wheat, kerosene and oil at subsidized rate. State Government issues distinctive ration cards like yellow ration card, saffron ration card, and white ration card depending on family annual income. The consumer material is supplied to ration card holders in the first week of every month by ration shopkeeper. Public Distribution System is one of the widely controversial issues that involve malpractice. The manual intervention in weighing of the materials leads to inaccurate measurements and/or it may happen, the ration shop owner illegally uses consumer materials without prior knowledge of ration card holders. The proposed system aids to control malpractices which are present in ration shop by replacing manual work with automatic system based on three emerging technologies—HAN, Li-Fi and Geofencing. Every consumer, i.e., family head is provided with HAN transmitter card which acts as ration card [1]. The HAN card has unique identification number. The consumer needs to scan the card on HAN reader which is interfaced with microcontroller. Once consumer is validated by password, the system asks the consumer to select appropriate material and quantity of material through keypad. Based on material chosen by consumer, appropriate circuitry will be activated and consumer gets material.

A.A. Gadgil (✉) · A.S. Bendigeri · D.D. Halagi · G. Prakash · S.A. Nadgouda
KLS's Gogte Institute of Technology, Belagavi, Karnataka, India
e-mail: aashishgadgil@gmail.com

Human Area Networking (HAN) technology [1], which is under development, uses the surface of the human body as a safe, high speed network transmission path. A transmission path is formed at the moment a part of the human body comes in contact with a HAN transceiver. Communication is possible using any body surfaces, such as the hands, fingers, arms, feet, face, legs or torso. HAN works through shoes and clothing as well. When the physical contact gets separated, the communication is ended. This technology is dealt in detail in Sect. 2.

Light Fidelity (Li-Fi) is transmission of data through a LED light bulb that varies in intensity faster than the human eye can follow. When a constant current is applied to an LED light bulb a constant stream of photons are emitted from the bulb which is observed as visible light. If the current is varied slowly the output intensity of the light dims up and down. Because LED bulbs are semi-conductor devices, the current, and hence the optical output, can be modulated at extremely high speeds which can be detected by a photo-detector device and converted back to electrical current. The intensity modulation is imperceptible to the human eye, and thus communication is just as seamless as RF [2]. Using this technique, high speed information can be transmitted from an LED light bulb.

Geofencing is the use of the Global Positioning System (GPS) satellite network and/or local radio-frequency identifiers (such as Wi-Fi nodes or Bluetooth beacons or Li-Fi) to create virtual boundaries around a location called geofence [4]. The geofence is then paired with a hardware/software application that responds to the boundary in some fashion as dictated by the parameters of the program.

2 Design and Implementation

In this section a brief introduction to the technologies used in the implementation of the system is presented followed by the design and implementation of the system.

2.1 *Human Area Networking (HAN)*

Human Area Network, abbreviated as HAN, is based on RedTacton technology [3]. Human Area Networking (HAN) technology uses the surface of the human body as a safe, high speed network transmission path. It uses the minute electric field emitted on the surface of the human body as medium for transmitting the data. It can achieve duplex communication over the human body at a maximum speed of 10 Mbps [1, 3]. HAN transmits the data between the human-centered electronics devices and computers and other network devices via total human natural physical activities. The block diagram of RedTacton [3] transceiver is shown in Fig. 1. The signal from the interface is sent to the data sense circuit and the transmitter circuit. The data sense circuit senses the signal and if the data is present it sends control signal to the transmitter which activates the transmitter circuit. The transmitter

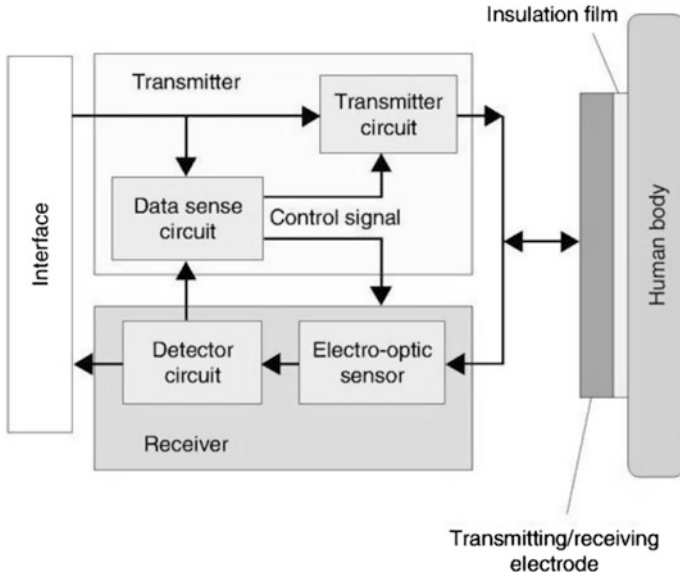


Fig. 1 Block diagram of RedTacton transceiver

circuit varies the electric field on the surface of our body. This change in the electric field is detected by the electro-optic sensor. The output of the electro-optic sensor is given to the detector circuit, which in turn is given to the interface of the receiving Red Tacton device. The receiving Red Tacton [3] transceiver recognizes the change in the electric field. Electro-optic sensor measures the weak electric field induced, which is finally converted back to original form by laser to read the signal.

2.2 Geofencing Through Li-Fi

A Geofence is a virtual perimeter for a real world geographic area. It could be dynamically generated as in a radius around a store or point location, or a geofence can be a predefined set of boundaries. Geofencing [4] is the creation of virtual boundaries by the use of the Global Positioning System (GPS) satellite network and/or local radio-frequency identifiers such as Wi-Fi nodes or Bluetooth beacons or Li-Fi. The geofence is then paired with a hardware/software application that responds to the boundary in some fashion as dictated by the parameters of the program. The use of a geo-fence is called geo-fencing [4], and one example of usage involves a location-aware device of a location-based service (LBS) user entering or exiting a geo-fence. This activity could trigger an alert to the device's user as well as messaging the geo-fence operator. This info, which could contain the location of the device, could be sent to a mobile telephone or an email account.

Light Fidelity (Li-Fi) is a bidirectional, high-speed and fully networked wireless communication technology similar to Wi-Fi. The term was coined by Harald Haas and is a form of visible light communication and a subset of optical wireless communications (OWC) and could be a complement to RF communication (Wi-Fi or cellular networks), or even a replacement in contexts of data broadcasting [2]. It is so far measured to be about 100 times faster than some Wi-Fi implementations, reaching speeds of 2.24 Gbps [1, 2]. It is wireless and uses visible-light communication or infrared and near-ultraviolet instead of radio-frequency spectrum, part of optical wireless communications technology, which carries much more information, and has been proposed as a solution to the RF-bandwidth limitations.

Geofencing Through Li-Fi

As discussed, Geofence is a virtual perimeter for a real world geographic area. This geofence, a predefined set of boundaries, can be created using Wi-Fi nodes or Bluetooth beacons or Li-Fi. This section deals with creation of geofence using Li-Fi. Light illuminated from power LED, used in Li-Fi, will create a geofence around it which can be assumed as virtual boundary. This virtual boundary can be used in many applications such as vehicle security, fleet management etc.

2.3 Implementation

This section deals with the methodology of implementation of secure ration dispensing system in the proposed system.

HAN (Human Area Networking) technology uses the surface of the human body as a safe, high speed network transmission path. It is completely distinct from wireless and infrared technologies as it uses the minute electric field emitted on the surface of the human body. A transmission path is formed at the moment a part of the human body comes in contact with a HAN transceiver. Communication is possible using any body surfaces. HAN works through shoes and clothing as well. When the physical contact gets separated, the communication is ended.

Li-Fi is transmission of data through a LED light bulb that varies in intensity faster than the human eye can follow. When a constant current is applied to an LED light bulb a constant stream of photons are emitted from the bulb which is observed as visible light. If the current is varied slowly the output intensity of the light dims up and down. Because LED bulbs are semi-conductor devices, the current, and hence the optical output, can be modulated at extremely high speeds which can be detected by a photo-detector device and converted back to electrical current. The intensity modulation is imperceptible to the human eye, and thus communication is just as seamless as RF. Using this technique, high speed information can be transmitted from an LED light bulb.

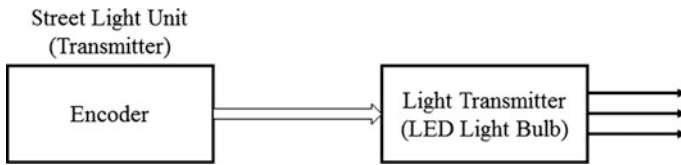


Fig. 2 Li-Fi transmitter (street light unit)

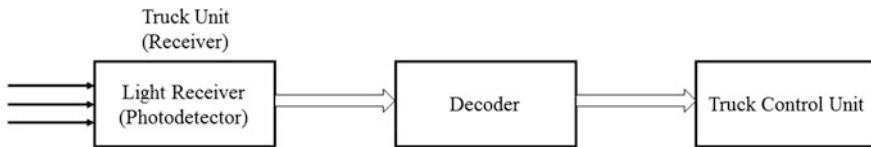


Fig. 3 Li-Fi receiver (truck unit)

Geofencing is the use of the Global Positioning System (GPS) satellite network and/or local radio-frequency identifiers (such as Wi-Fi nodes or Bluetooth beacons or Li-Fi) to create virtual boundaries around a location. The geofence is then paired with a hardware/software application that responds to the boundary in some fashion as dictated by the parameters of the program.

Geofencing through Li-Fi: The block diagram of Li-Fi transmitter is shown in Fig. 2. The encoder will generate one tone and one frequency. That frequency is amplified by amplifier circuits and fed into the LED light bulb. The LED light bulb used in our case is power LED Street light. The illumination from street light i.e. power LED will create a geofence.

The Li-Fi receiver will be mounted on truck. The block diagram of Li-Fi receiver is shown in Fig. 3. It consists of a light dependent resistor (photodiode) and a decoder circuitry. Whenever the truck with Li-Fi receiver module comes under the vicinity of the illumination from the power LED (street light) i.e. geofence, the photodiode will receive the light signal and generate an electrical signal proportional to it. This electrical signal is processed by a demodulator circuit (DTMF Decoder), and the output of decoder is then fed to a truck control unit and turns on the Truck Control Unit (TCU).

Truck Control Unit: The block diagram of Truck Control Unit [1, 4] is as shown in Fig. 4. Major components of truck control unit are HAN receiver, microcontroller unit and dispensing unit.

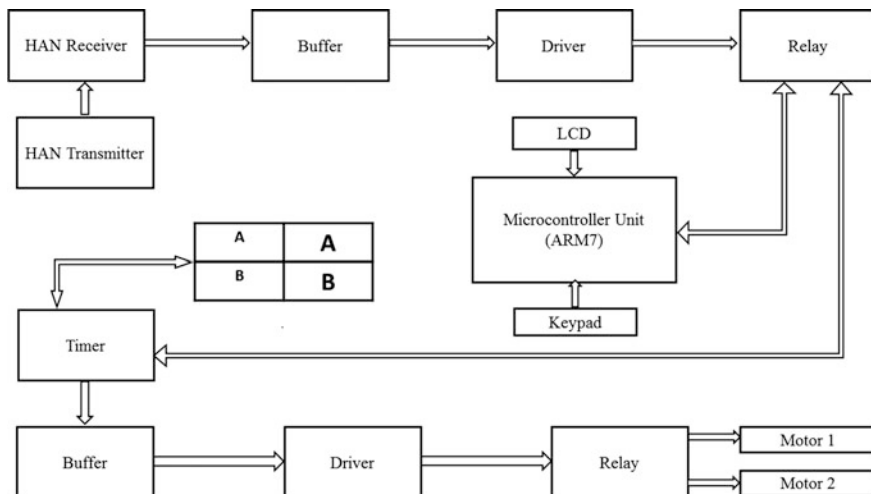


Fig. 4 Truck control unit

3 Working

The section deals with the flow of the system.

- i. The truck consisting of Li-Fi receiver should come under the vicinity of the street light of the city that has Li-Fi transmitter mounted on it. The Li-Fi transmitter has encoder which generates one tone one frequency for every city. That frequency is amplified by the amplifier circuits and fed into the power LED.
- ii. The Li-Fi receiver has light dependent resistor, which will receive the light signal and correspondingly generate an electrical signal proportional to it. This electrical signal is processed by a demodulator circuit (DTMF Decoder), and the output of decoder is then fed to Truck Control Unit (TCU). If the electrical signal is valid it will activate the TCU and door of truck will open. Otherwise truck door can't be opened if code will not match with the light transmitter and receiver.
- iii. Every authorized person is provided with the HAN transmitter similar to Ration Card and confidential pin for authentication. HAN transmitter consists of DTMF encoder which generates both valid and invalid signals, uses body of human being for transmission of signals.
- iv. The HAN receiver mounted on the TCU senses changes in the weak electric field on the surface of the body caused by the transmitter.
- v. The HAN receiver, which detects the change in electric field on the body, has DTMF decoder. It identifies the transmitted signal. If the signal is valid one, authorized person clears one level of authentication. If the signal is invalid the

system will not activate the microcontroller unit hence he/she will not get the ration.

- vi. Once microcontroller unit is activated, a message to ENTER PASSWORD is displayed on the LCD display. The authorized person has to enter the confidential pin using 4×4 keypad which is interfaced with the microcontroller. This level of security is to ensure the authorization of the person. This is because anybody can may steal the HAN transmitter. By entering valid Secret Password, which is regularly or randomly changed and is known to concerned persons only, one can clear the second level of security.
- vii. If both the levels are cleared then only the dispenser unit is activated.
- viii. Upon clearing both the levels of security the person is asked to select the commodity as per their requirement.
- ix. The selected commodity will be dispensed as per the selection made by the person.
- x. The dispenser unit is made to dispense the selected quantity based on the selection made by the person. It is well calibrated and depends on the rotation of motor, which is controlled by the timer.

4 Benefits

- i. The system is fully automatic and easy to use thus eliminating the man power involved in ration distribution.
- ii. Only authorized person will get the ration and the right amount.
- iii. Corruption and mediator malpractice is reduced.
- iv. No need of tracking the vehicle since vehicle gets activated only in the vicinity area.
- v. The system is based in advanced chip technology, thus enabling to track and protect the database of the user.
- vi. With its centralized server connectivity, the system can be made real time and thus helping resource management effectively.

5 Limitations

- i. During day time street light needs to be ON.
- ii. If street light is damaged immediate action needs to be taken.

6 Results

The secure ration dispensing using Li-Fi and HAN has been implemented successfully and it is tested on hardware components in the model which has been explained previously. Results obtained from the model made the overall system fully automatic. Also when we compare the RedTacton technology with the other technologies it's a fully secured and faster way to transmit the data, as our body itself acts has a transmitting media therefore there is no problem of hackers and thieves. The main intention to automate the overall system of ration dispensary is achieved.

7 Conclusion

The concept of Li-Fi can be great life changing experience if implemented. Every bulb, every LED light used at home, offices, education centre medical centre would be used as a data transmitting device. By the implementation of this technology we can make this world a better place to live which is cleaner and greener. This technology will not only empower us with higher bandwidth, availability and capacity but also more of the security and efficiency. The proposed system ensures there is no need for the electrode to be in direct contact with the skin; communication environment can be shaped simply and at low-cost, can spread data at a rate greater than that of peer technologies (max. of 10 Mbps) and Security is more. The system is fully automatic and easy to use, eliminating the man power; hence we can control the corruption. With the centralized server connectivity this system can be made real time and thus helping resource management effectively. RedTacton transceivers are programmable and we can choose what to part with whom and what plans you communicate with. This new technology gives solution and this research work will make a great change in public distribution system and is beneficial for the government.

8 Future Scope

The automated and secure system as implemented in our proposed project can have a great future in coming days. The secure way of transmitting data through Li-Fi technology and HAN technology can be implemented by different organizations.

- i. Defense can use Li-Fi technology to transmit secure data.
- ii. HAN can be used by the different institutions where ID card are required for attendance. The generic way of attendance in educational institutions can be modified by using HAN, where students or employees will only have to touch

the HAN receiver and hence it will save the time and resources required to maintain the record.

- iii. HAN can be used by banks as well. Instead of using credit cards and debit cards they can provide HAN transmitter.
- iv. Li-Fi is the newest technology that can offer wildest speed internet access. So, it can substitute Wi-Fi at educational societies and at companies so that all the people can make use of Li-Fi with the same speed envisioned in a specific area.
- v. Operation theatres (OTs) do not allow Wi-Fi due to radiation worries. Practice of Wi-Fi at hospitals interferes with the mobile and PC which blocks the signals for monitoring equipment's. So, it may be detrimental to the patient's health. To overcome this Li-Fi can be used to retrieving internet and to control medical equipment. This can even be beneficial for robotic surgeries and other computerized processes.

References

1. Mahesh C, Shrinivas Mayya D (2015) Automatic ration dispensary system using HAN. IJSRD 3(06)
2. Sapsagare VS (2014) Next of Wi-Fi an future technology in wireless networking Li-Fi using led over internet of things. IJERMT 3(03)
3. Gopi G, Ravi Kumar R (2013) Red Tacton—a human area networking technology. IJETT 4 (04)
4. Anthony C et al (2010) Geofencing components and existing models. IMECS 02(03)

Enhanced Digital Image Watermarking in Combination with Encryption

Ashwini B. Babar, J.A. Kendule and S.M. Shinde

Keywords Digital image · Copyright protection · Digital image watermarking · MATLAB

1 Introduction

In the proposed system, DCT and SVD Transforms are used for preprocessing of the images and for encryption Diffie-Hellman key exchange algorithm is used. Image Watermarking techniques are mainly categorized into two—(a) spatial domain and (b) frequency domain techniques [1, 2]. The frequency domain methods are found to be more robust when compared to spatial domain techniques. Discrete Wavelet Transform (DWT), Discrete Cosine Transform (DCT), Discrete Fourier Transform (DFT), etc. are various transform domain techniques. Among that, DCT is beneficial because in DCT need low processing power but it has blocks artifacts means loss of some information but has the most important feature of Energy Concentration. Block based watermarking is another suitable watermarking method which divides the image into different blocks, and the watermark is embedded in these blocks. Embedding capacity is increased with the number of blocks in the cover image. This method is more robust and efficient compared to

A.B. Babar · J.A. Kendule (✉) · S.M. Shinde
E&TC Department, SVERI's College of Engineering, Pandharpur, India
e-mail: jyotikendule@rediffmail.com

A.B. Babar
e-mail: babarashwini27@gmail.com; ashwinibabar027@gmail.com

S.M. Shinde
e-mail: smshinde@coe.sveri.ac.in

non-block based watermarking techniques. Different methods are introduced to attack the watermarked images at transmission time. So, it is a challenging task to find out the best watermarking method. The challenge of the attacker is to obtain the embedding bits of the cover image. If the owner randomly chooses the embedding bits, it will be difficult for the attacker to find out the pieces. So new methods can be used to find out the positions of the cover image to which the watermark bits are to be embedded. The proposed method uses the keys generated from Diffie-Hellman Key exchange algorithm to find the positions of the cover image to which the watermark bits are to be embedded. This is the blind watermarking technique as the host image is required for the extracting watermark.

The Watermarking Algorithm used in wide applications including owner identification, transaction tracking and copy control [3, 4].

1.1 Proposed Method

Watermarking Algorithm consists of two stages, Watermark Embedding and Watermark Extraction. Watermark Embedding is achieved by taking Watermark image and host image as input and then watermark image is embedded in the host image. The extraction can be done in two ways i.e. depending upon whether the host image is taken or not at the time of extraction. If the host image is taken at the time of extraction, then it is called as non-blind and otherwise it is called as the blind image watermarking. In the proposed design can be used to avoid the disadvantages of previous methods. That is in watermark embedding process, instead of embedding sequentially, we use the cryptographic algorithm for embedding the bits randomly. The singular value decomposition is used to increase the quality of the image.

The objectives which will be fulfilled by the proposed system are:

1. To achieve improvement in fidelity by increasing Normalized correlation i.e. getting the value approximately equal to 1 and this is done by using the DCT-SVD pair of transformation.
2. To improve PSNR value as compared to the values in the previous papers.
3. To achieve the Multi-layered security by achieving randomness for embedding positions by comparing the PSNR, Normalized correlation values with another system in the presence of attacks.

Hence more security with better image quality can be achieved by this method.

1.2 Proposed Methodology

By taking DCT Transform and SVD Transform consequently of both the images and then convert those images into blocks. Up to this is all about the preprocessing of the images. In most of the watermarking algorithms, the bits of the watermark are embedded directly into the Host picture. This will make the task of the attacker easier to find out the positions where the watermark is present. So the positions are to be selected randomly to provide security. In the proposed method the help of cryptographic algorithm is used to find out the positions. The positions in the cover image to which the watermark bits are to be embedded are found out by using Diffie-Hellman Key Exchange algorithm. Then after scaling the Watermark image by the strength factor, it is embedded in the Host image to get the Watermarked image. The original image and the watermarked image are input for watermark extraction hence the technique is the nonblind image watermarking method. With the help of the Host image and the keys, the watermark image is extracted from the watermarked image. The cover image and the watermarked image are converted into DCT domain then SVD domain and then divided into 32×32 blocks. The same procedure of embedding is also done in extraction using the keys to finding out the positions where the watermark is present. Watermark image is extracted by subtracting the Host image from Watermarked image and then dividing by the strength factor (Fig. 1).

In image processing applications, due to the resistance of singular values of SVD, it has become an attractive domain for watermarking applications [3].

General Review of Singular Value Decomposition (SVD): Singular value decomposition is a linear algebra technique used to solve many mathematical problems. In image processing applications the theoretical background of SVD technique to be noticed is:

- (a) The SVs (Singular Values) of an image has very good stability, which means that when a small value is added to an image, this does not affect the quality with great variation.
- (b) SVD is able to productivity represent the intrinsic algebraic properties of an image, where singular values correspond to the brightness of the image, and singular vectors reflect geometry characteristics of the image.
- (c) An image matrix has many small singular values compared with the first singular value. Even ignoring these minute singular values in the reconstruction of the image does not affect the quality of the reconstructed image [5-7].

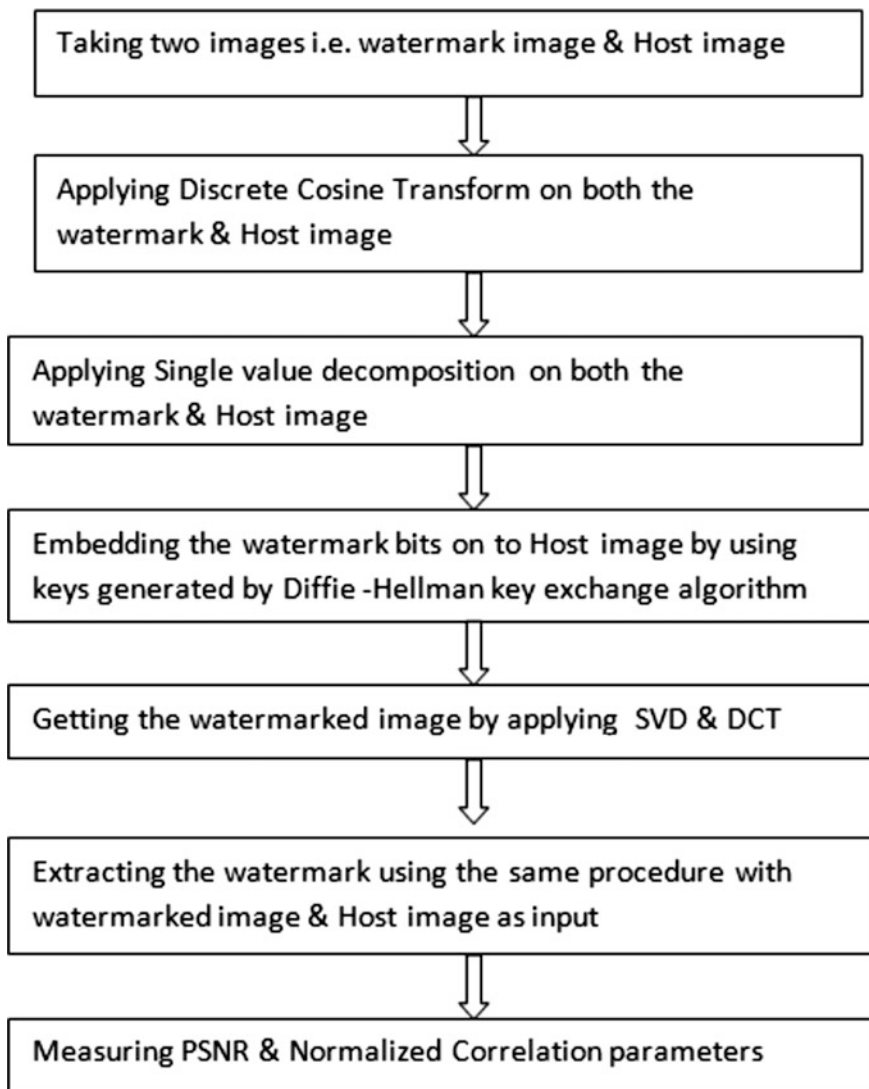


Fig. 1 Flow chart of proposed methodology

2 Experiments and Results

The proposed algorithm has experimented for two times with different types of two watermark image, and the cover image is taken the same image both times. Here at the time of embedding Cover image and watermark image is taken then the cover image is divided into blocks the positions for embedding are find out by using D-H algorithm and DCT and SVD are applied simultaneously on the watermark image

then after we are getting the embedded image. This image is saved because for the further processing we require this image in the second half of the experiment i.e. Extraction process.

Then at last by comparing the watermarked image and extracted watermark image we are calculating the two parameters i.e. PSNR and NC. The formulae used for the calculation of the parameters are as follows:

$$PSNR = 10 \log_{10} \frac{M^2}{\frac{1}{m \times n} \sum_{i=0}^{m-1} \sum_{j=0}^{n-1} [I(i,j) - K(i,j)]^2}$$

PSNR is calculated to analyze concealing the effect of the watermark whereas, Normalized correlation is calculated to get the degree of similarity between the two compared imaged.

$$NC = \frac{\sum_{i=1}^{M_1} \sum_{j=1}^{M_2} W(i,j)W'(i,j)}{\sqrt{\sum_{i=1}^{M_1} \sum_{j=1}^{M_2} [W(i,j)]^2} \sqrt{\sum_{i=1}^{M_1} \sum_{j=1}^{M_2} [W'(i,j)]^2}}$$

Here we are using Singular value decomposition hence the results we are getting are better than as mentioned in the previous papers on watermarking. i.e. we are getting the better image quality as well as better fidelity [3, 8] (Figs. 2, 3, 4, 5, 6, 7, 8 and 9).

- PSNR: 76.6375
- Normalized Correlation: 0.94385
- PSNR: 75.1328
- Normalized Correlation: 0.97685.

Fig. 2 Cover image



Fig. 3 Watermark image 1



Fig. 4 Watermarked image



Fig. 5 Extracted watermark



Fig. 6 Cover image



Fig. 7 Watermark image 2

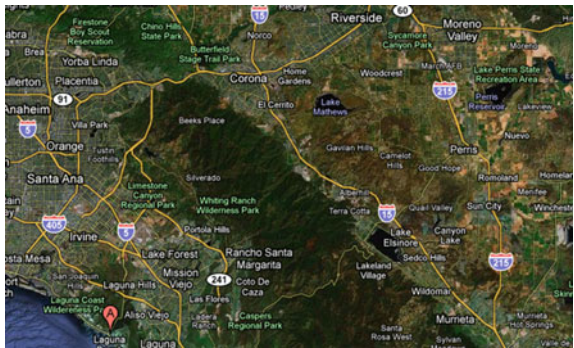
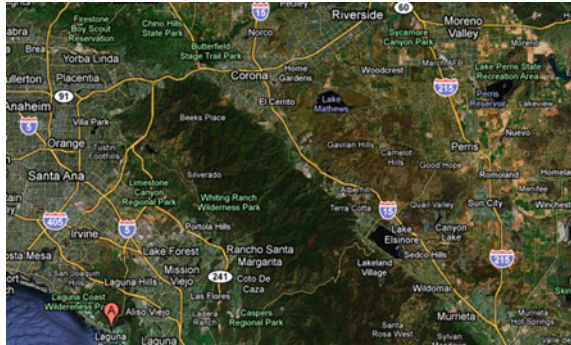


Fig. 8 Watermarked image



Fig. 9 Extracted watermark

3 Conclusion

By using this method for watermarking, we will achieve better Security by using cryptographic encryption algorithm which provides randomness for embedding positions. The proposed method will provide the watermarking algorithm with multi-layered security and improvement in peak signal to noise ratio and also the improvement in fidelity by increasing normalized correlation.

References

1. Chandrakar N, Bagga J (2015) Performance analysis of DWT based digital image watermarking using RGB color space. *Int J Sci Res Eng Technol* 4(1):1
2. Sharma P (2013) Digital image watermarking using 3 level discrete wavelet transform. In: *Conference on advances in communication and control systems*
3. Aparna JR, Ayyappan S (2014) Image watermarking using Diffie-Hellman key exchange algorithm. In: *International conference on information and communication technologies*
4. Saxena R, Tiwari N, Ramaiya MK (2015) Blind digital watermarking using AES technique for color images. *Int J Emerg Technol Comput Appl Sci* 15–129:1–3
5. Tikariha M, Dev AK (2015) An efficient JND based digital image watermarking using hybrid DWT-DCT-SVD approach. *Int J Sci Prog Res* 10(01)
6. Vaishnavi D, Subashini TS (2014) Robust and invisible image watermarking in RGB color space using SVD. In: *International conference on information and communication technologies*
7. Sarkardeh F, Khalili M (2015) Effective SVD-YCBCR color image watermarking. *Int J Comput Netw Commun Secur* 3(3):2–3
8. Kaur S, Gill R (2015) A robust technique of digital watermarking using hybrid method of DWT & SVD on RGB color space. *Int J Sci Res* 4(5):2–3

SNR Versus BER Performance and Effect of Changes in Hysteresis on Different Modes of IEEE 802.11a

Swapnita R. Dhabre

Keywords IEEE 802.11a · AMS · SNR · BER · OFDM

1 Introduction

The IEEE 802.11a has eight different data transmission modes. Each mode corresponds to a particular data rate, Modulation scheme and code rate [1]. It is as follows.

The standard uses OFDM technique instead of FDM to achieve the higher spectral efficiency. A large number of closely spaced orthogonal subcarrier used to carry the data [2]. The Modulator uses convolution codes. In Sect. 2 we will see about Adaptive modulation technique.

This standard operates over 5 GHz frequency band using OFDM modulation. There are eight different transmission modes available for this standard with various data rates from 6 to 54 Mbps, three different code rates and four types of modulations (BPSK, QPSK, 16-QAM, 64-QAM). The mode selection in IEEE 802.11a has been made by using Receiver Based Auto Rate (RBAR) mechanism. This selection depends on sender and receiver current states.

Table 1 shows the mode of transmissions in IEEE 802.11a standard [1]. If the channel condition is suitable station can increase its sending rate by selecting a new mode. RBAR mechanism tries to select the best mode with the help of SNR computed at the receiver side. In Sect. 2 the effectiveness of OFDM as the modulation technique for wireless application is studied. In Sect. 3, the different aspects of hysteresis factor have been described. In Sect. 4, the propagation characteristics of Multipath Channel have been discussed. In Sect. 5 the results are presented. Finally, the conclusion and future work have been presented in Sect. 6.

S.R. Dhabre (✉)

Vishwakarma Institute of Information Technology, Pune, India
e-mail: srdtgf12@gmail.com

Table 1 PHY modes of IEEE 802.11a

Modulation	Mode	Code rate	Data rate (Mbps)
BPSK	1	1/2	6
BPSK	2	3/4	9
QPSK	3	1/2	12
QPSK	4	3/4	18
16-QAM	5	1/2	24
16-QAM	6	3/4	36
64-QAM	7	2/3	48
64-QAM	8	3/4	54

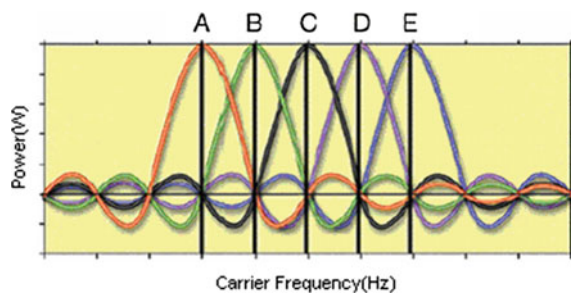
2 OFDM Principles

In OFDM technique many no of closely-spaced orthogonal subcarriers are used to carry the data. The subcarrier frequencies are selected such that the subcarriers are orthogonal to each other. This property avoids the cross-talk between subchannels and also eliminates the need for inter-carrier guard bands [2] (Fig. 1).

Elimination of inter-carrier guard bands greatly simplifies the design of both transmitter and receiver. It allows efficient modulator and demodulator implementation using the FFT algorithm. To generate OFDM successfully, the relationship between all the carriers must be carefully controlled to maintain the orthogonality of the carriers. In IEEE 802.11a there are total 52 sub-carriers out of which 48 sub-carriers are used to send the data, and four sub-carriers have been used as pilot signals [3]. The Pilot signals have been inserted for the measurement of the channel condition, i.e. the equalizer gain for each subcarrier. Pilot signals are also used for synchronization [4].

The orthogonal carriers can be easily generated by setting frequency bin, then performing the IFFT. Since each bin of an IFFT corresponds to the amplitude and phase of a set of orthogonal.

Fig. 1 Orthogonal OFDM subcarriers



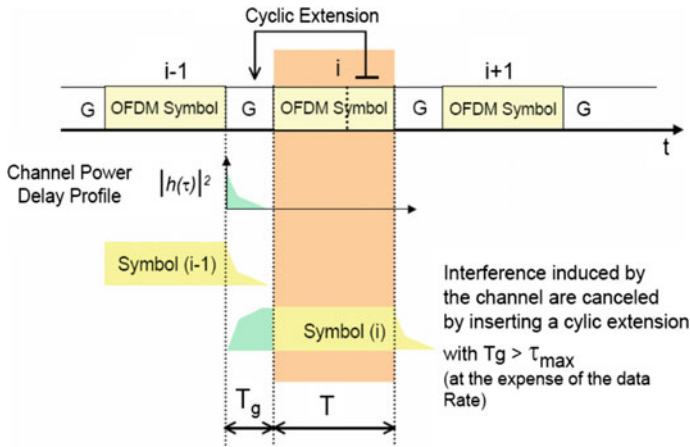


Fig. 2 Adding cyclic prefix

A Guard period or cyclic prefix is inserted between two sequential OFDM symbols. It helps reduce Intersymbol Interference. The cyclic prefix preserves orthogonality between sub-carriers. If two OFDM symbols interfere with each other, it is just because the other one has overlapped the cyclic prefix and part of the data field of one of them. This can happen when the transmission delay of the symbols is bigger than the cyclic prefix duration. Thus to eliminate the ISI the last 16 subcarriers are copied into the beginning of the OFDM symbol. The four main criteria are its tolerance to multipath delay spread, peak power clipping, channel noise and time synchronization errors (Fig. 2).

3 Effect of Changes in Hysteresis on Different Modes

The following Simulink block is used to change the different mode.

If we want to select the mode two, then we should write the value of SNR of the channel in between 10 and 11. To select mode four, the SNR of the channel should be between 14 and 18. To select mode six, it should be between 22 and 26. To select mode eight, it should above 28. If we want to remain in particular mode, then the hysteresis factor comes into the picture. And hysteresis plays the major role.

Suppose we want to select the mode 2 and want to remain in mode two then low SNR the threshold should be as follows.

The value SNR wrote should be less than three by the values 14 and greater than three by value six as the hysteresis factor is 3. Let it as 10 in the following block.

If we make the SNR of the channel as seven then even though it is between 6 and 14 the mode one is selected randomly as the difference between 6 and 7 is one which is less than hysteresis 3. Thus based upon hysteresis the mode changes. The Multipath Channel contains Multipath Rayleigh Fading Channel which is followed by AWGN channel. Because the channel is often modeled by random attenuation (known as fading) of the transmitted signals followed by the Additive noise [5] in wireless communication.

4 Different Fading Modes

The different fading modes are discussed in this section. Fading is the distortion that a carrier—modulated telecommunication signal experiences over certain propagation media. In the wireless system, fading is caused due to multipath propagation. Fading can cause poor performance in a communication system because it can result in a loss of signal power without reducing the power of the noise. If the fading is more, then there is the severe drop in the channel signal-to-noise ratio, which may cause the temporary failure of the communication.

4.1 Dispersive Fading Mode

The channel in this mode has a dispersed gain (scattered). Since the gain is scattered the strength of the transmitted is weakened heavily over the distance. In this manner, the spectral characteristics of the transmitted signal are dispersed (scattered) and cannot be preserved. There is the severe drop in the SNR of the multipath channel.

4.2 Flat Fading

Because of the constant gain over the channel, the strength of the transmitted signal is weakened slowly over the distance. Spectral characteristics of the transmitted signal are preserved correctly at the receiver side as compared to the dispersive fading mode. There is no severe drop in the SNR of the multipath channel.

4.3 No Fading Mode

In this mode, there are no fluctuations in the gain of the channel hence the strength and spectral characteristics of the signal are well preserved in as compared to above modes [6].

5 Simulation Environment

The required PHY mode specified with the modulation scheme, code rate, and the data rate has been achieved by the particular SNR and Low SNR Threshold Setting. Each mode has different BER in different fading modes. Figures 3, 4, 5 and 6 show

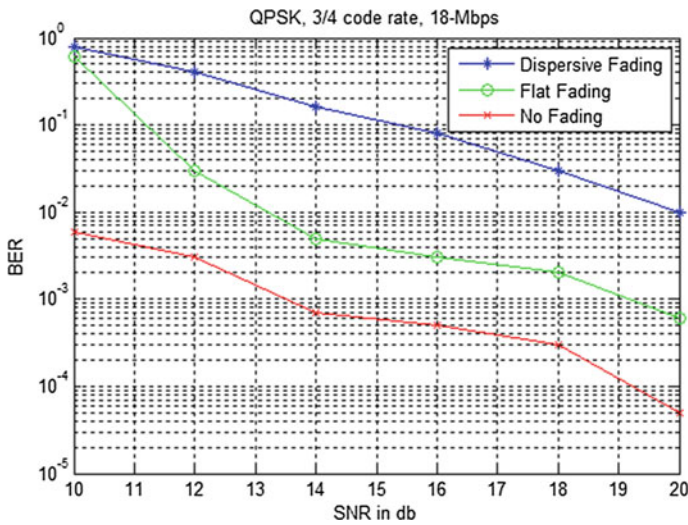


Fig. 3 QPSK modulation scheme

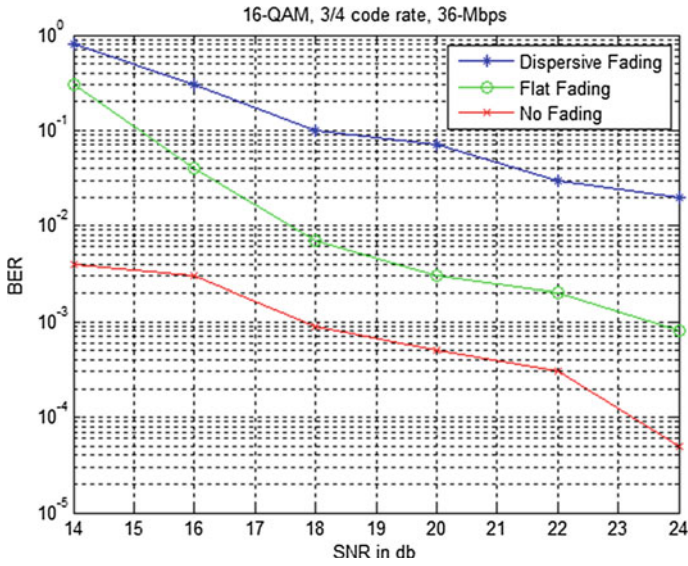


Fig. 4 16-QAM modulation scheme

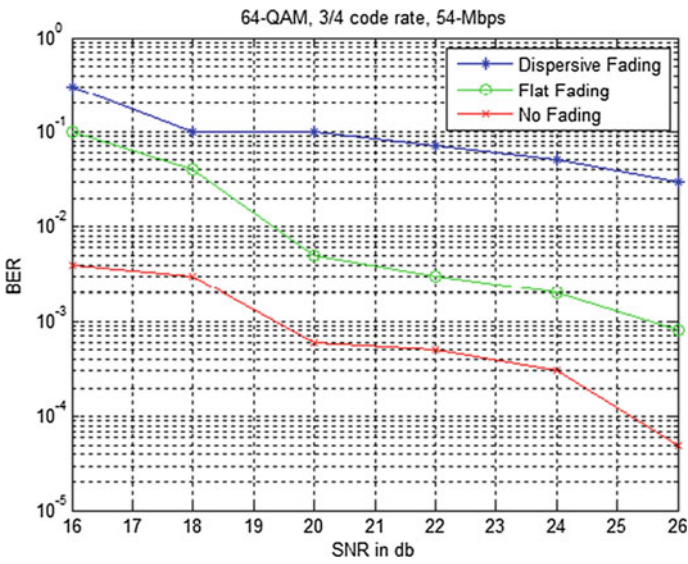


Fig. 5 64-QAM modulation scheme

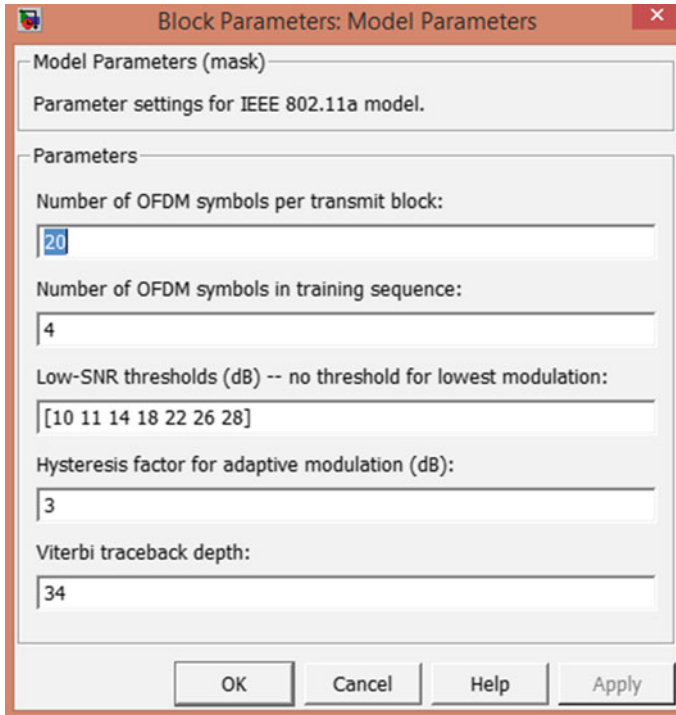


Fig. 6 Block parameters: model parameters

the calculated BER versus SNR for different simulation setting mode. The simulation setting blocks which are used for simulation setting are as shown below in Figs. 7, 8 and 9.

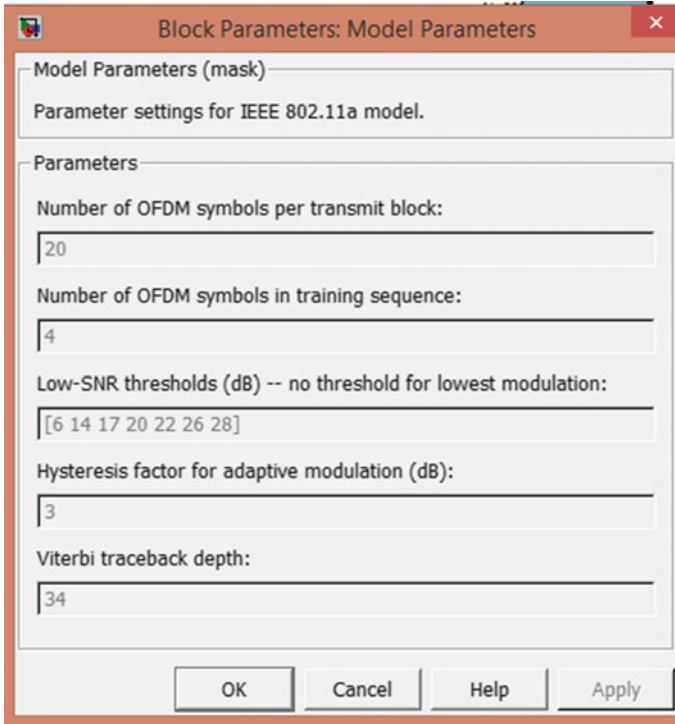


Fig. 7 Calculated BER versus SNR

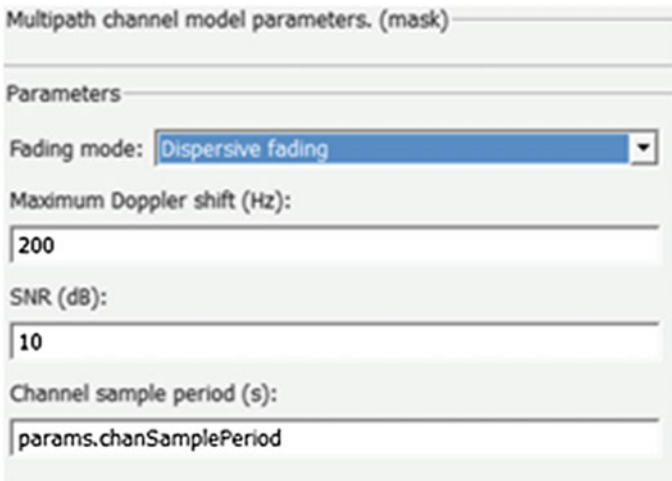


Fig. 8 Multipath channel model parameters (mask)

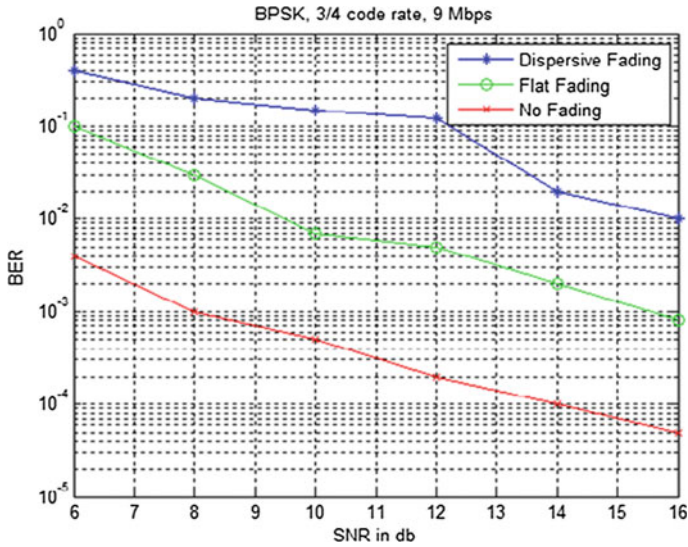


Fig. 9 BPSK modulation scheme

6 Conclusions

We can see that for BPSK, QPSK, 16-QAM, 64-QAM modulation scheme the BER decreases with the increase in SNR. Notice that for a given SNR, the increase in data rate results in the increase of BER.

From Figs. 6 and 7, it is clear that for the SNR of 8 dB, the BER is 0.2 bits in dispersive fading mode, it is 0.03 bits in flat fading mode and 0.001 in no fading mode (PHY mode). Thus it can be observed that in each distinct PHY mode for the same value of SNR the BER is high in dispersive fading mode, it is reducing in flat fading mode and highly reduced in no fading mode.

Acknowledgements I would like to thank Electronics and Telecommunication Engineering Department, Vishwakarma Institute of Information Technology, Pune, India for great support. I am thankful to Prof. Radhika Punrandare for her guidance and all valuable discussions and suggestions.

References

1. Doo KY, Song J, Cho DH (2004) Enhanced transmission mode selection in IEEE 802.11a WLAN system. 0-7803-8521-7/04/\$20.00 (c) 2004 IEEE
2. Cimini LJ Jr (1985) Analysis and simulation of a digital mobile channel using orthogonal frequency division multiplexing. IEEE Trans Commun 33(7):665–675
3. VOCAL Technologies, Ltd. Homepage. White Paper <H:\Modulation\80211b5.html>

4. Lawrey E (2001) The suitability of OFDM as a modulation technique for wireless telecommunication. White paper
5. Institute of Electrical and Electronics Engineers, Inc. (1997) IEEE standard for wireless LAN access control (MAC) and physical layer (PHY) specifications. IEEE, 445 p (IEEE PHY layer)
6. Rappaport TS (2002) Wireless communication principles and practice, 2nd edn. Publisher PHI